Dieter Bäuerle

Laser Processing and Chemistry

Fourth Edition

Springer

Laser Processing and Chemistry

Fourth Edition

Dieter Bäuerle

Laser Processing and Chemistry

Fourth Edition

With 332 Figures

Springer

Prof. Dr. Dr.h.c. Dieter Bäuerle
Johannes-Kepler-Universität Linz
Inst. Angewandte Physik
Altenbergerstr. 69
4040 Linz
Austria
dieter.baeuerle@jku.at

ISBN 978-3-642-17612-8 e-ISBN 978-3-642-17613-5
DOI 10.1007/978-3-642-17613-5
Springer Heidelberg Dordrecht London New York

Library of Congress Control Number: 2011923073

© Springer-Verlag Berlin Heidelberg 1986, 1996, 2000, 2011
This work is subject to copyright. All rights are reserved, whether the whole or part of the material is concerned, specifically the rights of translation, reprinting, reuse of illustrations, recitation, broadcasting, reproduction on microfilm or in any other way, and storage in data banks. Duplication of this publication or parts thereof is permitted only under the provisions of the German Copyright Law of September 9, 1965, in its current version, and permission for use must always be obtained from Springer. Violations are liable to prosecution under the German Copyright Law.
The use of general descriptive names, registered names, trademarks, etc. in this publication does not imply, even in the absence of a specific statement, that such names are exempt from the relevant protective laws and regulations and therefore free for general use.

Cover design: eStudio Calamar S.L., Heidelberg

Printed on acid-free paper

Springer is part of Springer Science+Business Media (www.springer.com)

To my family and my friends around the world

Preface

Materials processing with lasers is an expanding field which is captivating the attention of scientists, engineers, and manufacturers alike. The aspect of most interest to scientists is the basic interaction mechanisms between the intense light of a laser and materials exposed to a chemically reactive or non-reactive surrounding medium. Engineers and manufacturers see in the laser a tool which will not only make manufacturing cheaper, faster, cleaner, and more accurate but also open up entirely new technologies and manufacturing methods that are simply not available using standard techniques. The most established applications are laser machining (cutting, drilling, shaping), and laser welding, surface hardening, annealing, recrystallization, and glazing. Laser *chemical* processing which includes micropatterning and extended-area processing by laser-induced etching, material deposition, chemical transformation, etc. has actual and potential applications in micromechanics, metallurgy, integrated optics, electronic device and semiconductor manufacture, optoelectronics, sensor technology and chemical engineering. Increasingly, lasers are also being used in biotechnology, medicine, and in art conservation and restoration.

This book concentrates on various aspects of laser–matter interactions, in particular with regard to laser material processing. Special attention is given to laser-induced chemical reactions and non-equilibrium processes at gas–, liquid–, and solid–solid interfaces. The intention is to give scientists, engineers, and manufacturers an overview of the extent to which new developments in laser processing are understood at present, of the various new possibilities, and of the limitations of laser techniques. Students may prefer to read the book selectively, not troubling themselves unduly with detailed calculations or descriptions of single processes.

The book is divided into seven parts, each of which consists in turn of several chapters. The main symbols, conversion factors, abbreviations and acronyms used throughout the text are listed in Appendix A. For convenience, some mathematical functions and relations of particular interest are listed in Appendix B. Tables I, II, III, IV and V are intended to encourage the reader to use the formulas presented for rapid estimation of various quantities. An extensive subject index can be found at the end of the book.

The publication of this fourth edition was motivated by both the excellent reviews and responses from colleagues and students and, importantly, the fact that the third edition was almost sold out within only 3 years. In the present edition I

have included some of the most fascinating new developments in the field. Among those are fundamental investigations and applications using ultrashort laser pulses, the synthesis of metastable materials, and the increasing importance of lasers in nanotechnology, including nanopatterning and the synthesis of both nanoparticles and nanocomposite films. More attention is also given to fields of practical interest such as 3D-microfabrication and rapid prototyping, different types of surface functionalizations covering applications in microtechnology, chemical analysis, combustion engines, etc. Two additional chapters have been added. These summarize new developments and applications of lasers in medicine, biotechnology, and art conservation and restoration.

Finally, I wish to thank my students and all my staff for valuable discussions. Many of our "own" results incorporated in this book have been achieved together with colleagues and friends during world-wide cooperations within various different national and international projects. In particular I would like to thank M. Aspelmeyer, M. Dinescu, C. Grigoropoulos, P. Leiderer, T. Lippert, A. Pikulin, and many others for valuable discussions and N. Bityurin, J.D. Pedarnig, and B. Rethfeld for critical reading and comments on parts of the present manuscript. Valuable discussions and contributions to several chapters of the previous edition, in particular by B. Luk'yanchuk, N. Arnold, and N. Bityurin are gratefully acknowledged. Our close cooperation over many years, mainly on theoretical aspects of laser-material interactions, is reflected in numerous publications cited throughout the text. Last but not least, I wish to express my deep gratitude to my outstanding secretary, Irmengard Haslinger, for her tireless assistance in preparing this new edition.

Linz, March 2011 Dieter Bäuerle

Contents

Part I Overview and Fundamentals

1 Introduction 3
1.1 Conventional Laser Processing 4
1.2 Laser Chemical Processing 7
1.2.1 Thermal Activation 7
1.2.2 Non-thermal Activation 9
1.2.3 Local and Large-Area Processing 10
1.2.4 Comparison of Techniques 10
1.2.5 Planar and Non-planar Processing 12

2 Thermal, Photophysical, and Photochemical Processes 13
2.1 Excitation Mechanisms, Relaxation Times 13
2.1.1 Thermal Processes 15
2.1.2 Photochemical Processes 16
2.1.3 Photophysical Processes 17
2.1.4 A Simple Model 17
2.1.5 Chemical Relaxation 18
2.2 The Heat Equation 19
2.2.1 The Source Term 19
2.2.2 Dimensionality of Heat Flow 21
2.2.3 Kirchhoff and Crank Transforms 21
2.2.4 Phase Changes 22
2.2.5 Limits of Validity 23
2.3 Selective Excitations of Molecules 25
2.3.1 Electronic Excitations 26
2.3.2 Infrared Vibrational Excitations 29
2.4 Surface Excitations 35
2.4.1 External Photoeffect 35
2.4.2 Internal Photoeffect 35
2.4.3 Electromagnetic Field Enhancement, Catalytic Effects 37
2.4.4 Adsorbed Molecules 37

3 Reaction Kinetics and Transport of Species 39
3.1 Photothermal Reactions 41
3.2 Photochemical Reactions 43
3.3 The Concentration of Species 45
3.3.1 Basic Equations 45
3.3.2 Dependence of Coefficients on Temperature and Concentration 49
3.4 Heterogeneous Reactions 51
3.4.1 Stationary Equations 52
3.4.2 Transport Limitations 53
3.4.3 Dynamic Solutions 57
3.4.4 Heterogeneous Versus Homogeneous Activation 59
3.5 Combined Heterogeneous and Homogeneous Reactions 59
3.5.1 The Boundary-Value Problem 60
3.5.2 Approximate Solutions 61
3.6 Homogeneous Photochemical Activation 62

4 Nucleation and Cluster Formation 63
4.1 Homogeneous Processes 63
4.1.1 Classical Kinetics 64
4.1.2 Droplets Within a Laser Beam 66
4.1.3 Transport of Clusters, Thermophoresis, Chemophoresis 70
4.1.4 Fragmentation of Particles 70
4.2 Nanoparticle Formation by Pulsed-Laser Ablation 71
4.2.1 Gaseous Ambient 71
4.2.2 Liquid Ambient 76
4.3 Heterogeneous Processes 76
4.3.1 Nucleation in LCVD 77
4.3.2 Condensation of Clusters from Vapor/Plasma Plumes 79
4.3.3 Nanotube Formation by Laser-CVD 82
4.3.4 Shaping of Nanoparticles 83
4.3.5 Cluster Formation Within Solid Surfaces 83

5 Lasers, Experimental Aspects, Spatial Confinement 85
5.1 Lasers 85
5.1.1 CW Lasers, Gaussian Beams 85
5.1.2 Pulsed and High-Power CW Lasers 87
5.1.3 Semiconductor Lasers 89
5.2 Experimental Aspects 90
5.2.1 Micro-/Nanoprocessing 90
5.2.2 The Reaction Chamber; Typical Setup 95
5.2.3 Large-Area Processing 96
5.2.4 Substrates 98
5.3 Confinement of the Excitation 98
5.3.1 The Thermal Field 99
5.3.2 Non-thermal Substrate Excitations 99

5.3.3 Gas-, Liquid- and Adsorbed-Phase Excitations 99
5.3.4 Plasma Formation 100
5.3.5 Material Damages 100
5.3.6 Non-linearities 100
5.3.7 Optical Near-Field and Field-Enhancement Effects ... 104

Part II Temperature Distributions and Surface Melting

6 General Solutions of the Heat Equation 111
6.1 The Boundary-Value Problem 111
6.1.1 The Attenuation Function, $f(z)$ 112
6.1.2 Boundary and Initial Conditions 113
6.2 Analytical Solutions 116
6.3 Pulse Shapes 118
6.3.1 Single Rectangular Pulse 118
6.3.2 Triangular Pulse 120
6.3.3 Smooth Pulse 120
6.3.4 Multiple-Pulse Irradiation 121
6.4 Beam Shapes 122
6.4.1 Circular Beam 122
6.4.2 Rectangular Beam 123
6.4.3 Uniform Illumination 123
6.5 Characteristics of Temperature Distributions 123
6.5.1 Center-Temperature Rise 124
6.5.2 Width of Distribution 124
6.6 Numerical Techniques 126

7 Semi-infinite Substrates 127
7.1 The Center-Temperature Rise 127
7.1.1 Gaussian Beam 127
7.1.2 Circular Laser Beam 128
7.1.3 Rectangular Beam 128
7.2 Stationary Solutions for Temperature-Independent Parameters .. 129
7.2.1 Surface Absorption 130
7.2.2 Finite Absorption 131
7.3 Stationary Solutions for Temperature-Dependent Parameters ... 134
7.4 Scanned CW-Laser Beam 137
7.5 Pulsed-Laser Irradiation 139
7.5.1 Gaussian Intensity Profile 139
7.5.2 Uniform Irradiation 141
7.6 Dynamic Solutions for Temperature-Dependent Parameters 142

8 Infinite Slabs 147
8.1 Strong Absorption 147
8.1.1 Thermally Thin Film 147
8.1.2 Scanned CW Laser 148

8.2 The Influence of Interferences 151
8.3 Coupling of Optical and Thermal Properties 153

9 Non-uniform Media 155
9.1 Continuous Changes in Optical Properties 155
9.2 Absorption of Light in Multilayer Structures 157
9.2.1 Thin Films 157
9.2.2 Two-Layer Structures 159
9.2.3 Three-Layer Systems 160
9.3 Temperature Distributions for Large-Area Irradiation 160
9.3.1 Stationary Solutions for Thin Films 160
9.3.2 Dynamic Solutions 162
9.4 Temperature Distributions for Focused Irradiation 163
9.4.1 Strong Film Absorption 164
9.4.2 Finite Film Absorption 165
9.5 The Ambient Medium 167
9.5.1 Influence on Substrate Temperature 168
9.5.2 Indirect Heating 170
9.5.3 Free Convection 170
9.5.4 Temperature Jump 173

10 Surface Melting 177
10.1 Temperature Distributions, Interface Velocities 178
10.1.1 Boundary Conditions 181
10.1.2 Temperature Dependence of Parameters 186
10.2 Solidification 186
10.3 Process Optimization 189
10.4 Convection 190
10.5 Surface Deformations 192
10.5.1 Surface Patterning 193
10.6 Welding 194
10.6.1 Ultrashort-Pulse Laser Welding 196
10.7 Liquid-Phase Expulsion 196

Part III Material Removal

11 Vaporization, Plasma Formation 201
11.1 Energy Balance 203
11.2 One-Dimensional Model 204
11.2.1 Stationary Evaporation 207
11.2.2 Non-stationary Evaporation 212
11.2.3 Optimal Conditions 214
11.3 Knudsen Layer, the Recoil Pressure 215
11.4 Influence of a Liquid Layer 217
11.5 Limitations of Model Calculations 220
11.6 Plasma Formation 221

11.6.1 Ionization 222
11.6.2 Optical Properties of Plasmas 223
11.6.3 Optical Breakdown 225
11.7 Laser-Supported Absorption Waves (LSAW) 227
11.7.1 Laser-Supported Combustion Waves (LSCW): $I_p \leq I \leq I_d$ 227
11.7.2 Laser-Supported Detonation Waves (LSDW): $I \geq I_d$ 229
11.7.3 Superdetonation 230
11.8 Abrasive Laser Machining 231
11.8.1 Cutting, Drilling, Shaping 231
11.8.2 Non-metals 233
11.8.3 Scribing, Marking, Engraving 234
11.8.4 Comparison of Techniques 234

12 Nanosecond-Laser Ablation 237
12.1 Surface Patterning 238
12.2 Ablation Mechanisms 242
12.2.1 Models 244
12.3 Photothermal Surface Ablation 247
12.3.1 Influence of Screening 249
12.3.2 Post-pulse Ablation 250
12.4 Interactions Below Threshold 251
12.5 The Threshold Fluence, ϕ_{th} 253
12.5.1 Thin Films 256
12.6 Ablation Rates 256
12.6.1 Dependence on Photon Energy and Fluence 256
12.6.2 Dependence on Pulse Duration 259
12.6.3 Influence of Spot Size, Screening 260
12.6.4 Dependence on Pulse Number 261
12.6.5 Influence of an Ambient Atmosphere 263
12.7 Photothermal Volume Decomposition 265
12.8 Photochemical Ablation 266
12.8.1 Dissociation of Polymer Bonds 267
12.8.2 Defect-Related Processes, Incubation 268
12.9 Photophysical Ablation 270
12.9.1 Long Pulses 271
12.9.2 Short Pulses 272
12.9.3 Thermal Versus Photochemical and Photophysical Ablation 272
12.10 Thermo- and Photomechanical Ablation 273
12.10.1 Basic Equations 274
12.11 Material Damage, Debris 276
12.11.1 Strong Absorption 276
12.11.2 Finite Absorption 277
12.11.3 Debris 278

13 Ultrashort-Pulse Laser Ablation 279
13.1 Material Patterning and Damage 279
13.1.1 Wide-Bandgap Materials, Glasses, Polymers 281
13.1.2 Nanostructures 283
13.2 Overview on Interaction Mechanisms 283
13.3 Low Fluence Photoexcitations 285
13.3.1 Thermal Volume Decomposition 286
13.3.2 Thermal Versus Photophysical Ablation 287
13.3.3 Ablation Dynamics 288
13.4 Molecular Dynamics (MD) Simulations 288
13.5 The Two-Temperature Model 292
13.5.1 Electron Transport, Damage Thresholds 296
13.5.2 Melting, Surface Deformation and Ablation 298
13.5.3 Processing of Metals and Semiconductors 301
13.6 Multiphoton- and Avalanche Ionization 302
13.6.1 Dielectrics 303
13.6.2 Coulomb Explosion 306
13.6.3 Processing of Dielectrics 308
13.7 Comparison of Nanosecond and Ultrashort-Pulsed Laser Ablation 311

14 Etching of Metals and Insulators 315
14.1 Photochemistry of Precursor Molecules 317
14.1.1 Halides 317
14.1.2 Halogen Compounds 319
14.2 Concentration of Reactive Species 320
14.2.1 Ballistic Approximation 321
14.2.2 Diffusion 323
14.2.3 Influence of the Reaction Chamber 324
14.2.4 Gas-Phase Recombination 326
14.2.5 Gas-Phase Heating 327
14.3 Dry-Etching of Metals 327
14.3.1 Spontaneous Etching Systems 328
14.3.2 Diffusive Etching Systems 329
14.3.3 Passivating Reaction Systems 329
14.4 Dry-Etching of Inorganic Insulators 332
14.4.1 SiO_2 Glasses 332
14.4.2 Oxides 333
14.5 Wet-Etching 334
14.5.1 Front-Side Etching 335
14.5.2 Backside Etching 335

15 Etching of Semiconductors 339
15.1 Dark Etching 339
15.2 Laser-Induced Etching of Si in Cl_2 342

15.2.1 Surface Patterning 342
15.2.2 Photochemical and Thermal Etching 343
15.2.3 Chlorine Radicals 345
15.2.4 Electron–Hole Pairs 346
15.2.5 Crystal Orientation and Doping 348
15.2.6 Nanopatterning 349
15.3 Si in Halogen Compounds 350
15.3.1 Si in XeF_2 350
15.3.2 Si in SF_6 351
15.4 Microscopic Mechanisms 352
15.4.1 Photochemical Etching 353
15.4.2 Combined Photochemical and Thermal Etching 354
15.4.3 Thermal Etching 354
15.5 Dry-Etching of Compound Semiconductors 354
15.5.1 III–V Compounds 354
15.5.2 Laser Etching of Atomic Layers 357
15.5.3 Dopants, Impurities, and Defects 357
15.6 Wet-Etching 357
15.6.1 Silicon 358
15.6.2 Compound Semiconductors 359
15.6.3 Interpretation of Results 360
15.6.4 Spatial Resolution, Waveguiding 364

Part IV Material Deposition

16 Laser-CVD of Microstructures 369
16.1 Precursor Molecules 369
16.2 Pyrolytic LCVD of Spots 370
16.2.1 Deposition from Halides 370
16.2.2 Deposition from Carbonyls 375
16.3 Modelling of Pyrolytic LCVD 375
16.3.1 Gas-Phase Processes 376
16.3.2 The Coupling Between $T(\boldsymbol{x})$ and $h(\boldsymbol{x})$ 379
16.4 Temperature Distributions on Circular Deposits 382
16.5 Simulation of Pyrolytic Growth 385
16.6 Photolytic LCVD 389
16.6.1 Metals 389
16.6.2 Other Materials 392
16.6.3 Process Limitations 392

17 Growth of Fibers 393
17.1 In Situ Temperature Measurements 394
17.2 Microstructure and Physical Properties 395
17.3 Kinetic Studies 397

17.3.1 Silicon . . . 398
17.3.2 Carbon . . . 398
17.4 Gas-Phase Transport . . . 399
17.4.1 The Coupling of Fluxes . . . 399
17.4.2 Thermal Diffusion (Soret Effect) . . . 402
17.5 Simulation of Growth . . . 405

18 Direct Writing . . . 407
18.1 Characteristics of Pyrolytic Direct Writing . . . 407
18.1.1 Dependence on Laser Parameters and Substrate Material . . . 408
18.1.2 Electrical Properties . . . 410
18.2 Temperature Distributions in Direct Writing . . . 411
18.2.1 Center-Temperature Rise . . . 411
18.2.2 1D Approach, $\kappa^* \gg 1$ . . . 413
18.2.3 Numerical Solutions . . . 414
18.3 Simulation of Direct Writing . . . 415
18.3.1 1D Model . . . 415
18.3.2 Comparison with Experimental Data . . . 417
18.3.3 2D Model . . . 421
18.4 Photophysical LCVD . . . 422
18.5 Applications of LCVD in Microfabrication . . . 424
18.5.1 Planar Substrates . . . 424
18.5.2 Non-planar Substrates, 3D Objects . . . 426

19 Thin-Film Formation by Laser-CVD . . . 429
19.1 Direct Heating . . . 430
19.1.1 Stationary Solutions . . . 430
19.1.2 Non-stationary Solutions . . . 434
19.2 Pyrolytic Processing Rates . . . 434
19.2.1 Diffusion . . . 435
19.2.2 Recombination . . . 437
19.3 Photolytic Processing Rates . . . 438
19.4 Metals . . . 439
19.4.1 Deposition from Metal Halides . . . 439
19.4.2 Deposition from Alkyls and Carbonyls . . . 442
19.5 Semiconductors . . . 443
19.5.1 Photodecomposition of Silanes . . . 444
19.5.2 Crystalline Ge and Si . . . 446
19.5.3 Amorphous Hydrogenated Silicon (a-Si:H) . . . 446
19.5.4 Compound Semiconductors . . . 450
19.5.5 Carbon . . . 451
19.6 Insulators . . . 451
19.6.1 Oxides . . . 452
19.6.2 Nitrides . . . 452
19.7 Heterostructures . . . 453
19.8 Comparison of LCVD and Standard Techniques . . . 454

20 Adsorbed Layers, Laser–MBE 457
20.1 Fundamental Aspects 458
20.1.1 Influence of Laser Light 462
20.2 Deposition from Adsorbed Layers 463
20.2.1 Vacuum 463
20.2.2 Gaseous Ambient 466
20.3 Combined Laser and Molecular/Atomic Beams 470
20.3.1 Laser-MBE 471
20.3.2 Laser-ALE 472
20.3.3 Laser-OMBD 473
20.3.4 Laser-Focused Atomic Deposition 474

21 Liquid-Phase Deposition, Electroplating 477
21.1 Liquid-Phase Processing Without an External EMF 477
21.1.1 Thermal Decomposition 477
21.1.2 Electroless Plating 480
21.1.3 Metal–Liquid Interfaces 481
21.1.4 Semiconductor–Liquid Interfaces 483
21.1.5 Further Experimental Examples 484
21.2 Electrochemical Plating 484
21.2.1 Jet-Plating 486

22 Thin-Film Formation by Pulsed-Laser Deposition and Laser-Induced Evaporation 489
22.1 Experimental Requirements 490
22.1.1 Congruent and Incongruent Ablation 493
22.1.2 Targets 494
22.1.3 Uniform Ablation 495
22.1.4 Cross-Beam PLD 497
22.2 Volume and Surface Processes, Film Growth 497
22.2.1 Plasma and Gas-Phase Reactions 498
22.2.2 Substrate Temperature, Laser-Pulse-Repetition Rate 499
22.2.3 Energy of Species 500
22.2.4 Particulates 501
22.2.5 Chemical Composition and Thickness of Films 504
22.3 Overview of Materials and Film Properties 505
22.4 High-Temperature Superconductors 506
22.4.1 Non-reactive Deposition 507
22.4.2 Reactive Deposition 507
22.4.3 Heterostructures 508
22.4.4 Metastable Compounds, Mixed Systems 510
22.4.5 Films with Step-Like Morphology 512
22.4.6 Buffer Layers, Applications 513
22.5 Metals, Semiconductors, and Insulators 515
22.5.1 Metals 515
22.5.2 Semiconductors 515

22.5.3 Carbon Films 517
22.5.4 Insulators 519
22.5.5 Heterostructures 521
22.6 Nanostructured Materials 521
22.6.1 Nanoparticle films 522
22.6.2 Nanocomposites 522
22.7 Organic Materials 524
22.7.1 MAPLE 527
22.8 Laser-Induced Forward Transfer 528
22.8.1 Transfer films 530

Part V Material Transformations, Synthesis and Structure Formation

23 Material Transformations, Laser Cleaning 535
23.1 Transformation Hardening 535
23.2 Laser Annealing, Recrystallization 537
23.2.1 Ion-Implanted Semiconductors 537
23.2.2 Thin Films 540
23.3 Glazing 541
23.4 Shock Hardening 542
23.5 Surface Polishing 542
23.6 Transformations Within Bulk Materials 544
23.6.1 Non-erasable Marking 545
23.6.2 Gratings 545
23.6.3 Waveguides 546
23.6.4 3D-Optical Storage 547
23.7 Laser Cleaning 549
23.7.1 Adhesion Forces 550
23.7.2 Dry Cleaning 552
23.7.3 Steam Cleaning 557
23.7.4 Wet Cleaning 558
23.7.5 Matrix Cleaning 559

24 Doping 561
24.1 Solid-Phase Diffusion 562
24.2 Liquid-Phase Transport 565
24.3 Sheet Doping 565
24.3.1 Silicon 566
24.3.2 Compound Semiconductors 569
24.4 Local Doping 570
24.5 Laser Implantation 571

25 Cladding, Alloying, and Synthesis 573
25.1 Laser-Assisted Cladding and Sintering 573
25.1.1 3D Rapid Prototyping 575
25.2 Alloying 575

25.2.1 Laser–Surface Alloying 575
25.2.2 Formation of Metastable Materials 576
25.2.3 Silicides 576
25.3 Synthesis 577
25.3.1 Thin Films 577
25.3.2 Fibers 578

26 Oxidation, Nitridation, and Reduction 581
26.1 Basic Mechanisms 582
26.1.1 Very Thin Films 583
26.1.2 Thin Films 583
26.1.3 Thick Films 585
26.1.4 Influence of Laser Light 585
26.2 Metals 587
26.2.1 Photothermal Oxidation 587
26.2.2 Photochemical Contributions 589
26.2.3 Oxidation by Pulsed-Laser Plasma Chemistry 590
26.2.4 Nitridation 591
26.3 Elemental Semiconductors 592
26.3.1 Photothermal Oxidation of Si 592
26.3.2 Photochemically Enhanced Oxidation of Si 594
26.3.3 Nitridation of Silicon 596
26.4 Compound Semiconductors 596
26.4.1 Summary 597
26.5 Oxide Transformation, Reoxidation 597
26.5.1 Silicon Oxide 597
26.6 Reduction and Metallization of Oxides 598
26.6.1 Qualitative Description 599
26.6.2 Oxidic Perovskites and Related Materials 600
26.6.3 Superconductors 602

27 Transformation and Functionalization of Organic Materials 605
27.1 Surface Modification of Polymers 605
27.1.1 Laser-Enhanced Adhesion 605
27.1.2 Swelling, Amorphization, Crystallization 607
27.1.3 Photochemical Exchange of Species 608
27.1.4 Chemical Degradation 609
27.2 Chemical Transformations Within Thin Films and Bulk Materials 611
27.2.1 Laser Lithography 613
27.2.2 Maskless Techniques 616
27.2.3 Decomposition of Precursor Films 617
27.2.4 3-D Photopolymerization 619
27.3 Laser-LIGA, LAN 620

28 Instabilities and Structure Formation 623
28.1 Coherent and Non-coherent Structures 623
28.1.1 Equations 624
28.1.2 Stability 625
28.1.3 Coherent Structures 626
28.1.4 Non-coherent Structures 626
28.2 Ripple Formation 626
28.2.1 Interference Pattern 627
28.2.2 Distribution of Energy 632
28.2.3 Feedback 634
28.2.4 Comparison of Experimental and Theoretical Results . 635
28.2.5 Ripples Generated by Ultrashort-Laser Pulses 638
28.2.6 Embedded Periodic Structures 643
28.3 Spatio-Temporal Oscillations 644
28.3.1 Zero Isoclines 645
28.3.2 Instabilities in Laser-Induced Oxidation 646
28.3.3 Explosive Crystallization 647
28.3.4 Exothermal Reactions 648
28.3.5 Instabilities in Direct Writing 649
28.3.6 Discontinuous Deposition and Bistabilities 652
28.4 Instabilities and Structure Formation in Laser Ablation 655
28.4.1 Fundamental Aspects 655
28.4.2 Conical and Columnar Structures 659
28.5 Hydrodynamic Instabilities 664
28.5.1 Kelvin–Helmholtz Instabilities 664
28.5.2 Rayleigh–Taylor Instabilities 666
28.5.3 Surface Corrugations, Droplets 668
28.6 Stress-Related Instabilities 671
28.7 Technological Aspects 676

Part VI Diagnostic Techniques, Plasmas

29 Diagnostic Techniques 681
29.1 Characterization of Laser-Beam Profiles 681
29.2 Homogenization of Laser Beams 681
29.2.1 Diffractive Methods 682
29.2.2 Reflective Methods 682
29.2.3 Refractive Methods 683
29.3 Deposition, Etch, and Ablation Rates 683
29.3.1 Optical Techniques 683
29.3.2 Other Techiques 686
29.4 Temperature Measurements 689
29.4.1 Photoelectric Pyrometry 689
29.4.2 Other Optical Techniques 693
29.4.3 Other Techniques 693

29.5 Analysis of Surfaces and Thin Films 694
29.5.1 Surface Topologies, Microstructures 694
29.5.2 Transport Measurements 695

30 Analysis of Species and Plasmas 697
30.1 Precursor and Product Species 697
30.1.1 Optical Spectroscopy 697
30.1.2 Mass Spectrometry 699
30.1.3 MALDI, LAESI 701
30.2 Species in Vapor and Plasma Plumes 702
30.2.1 Species at Subthreshold Fluences 702
30.2.2 Atomic and Molecular Neutrals 703
30.2.3 Electrons and Ions 704
30.2.4 Plasma Radiation, X-Rays 705
30.2.5 Clusters and Fragments 705
30.3 Plume Expansion in Vacuum 706
30.3.1 Spherical Plume 706
30.3.2 Elliptical Plume 707
30.3.3 Mass- and Ion-Flux Measurements 708
30.4 Plume Expansion in Gases, Shock Waves 708
30.4.1 Point Blast Model 710
30.4.2 Combined Propagation of Plume and SW 711
30.4.3 Formation of Nanoparticles 713
30.4.4 Comparison with Experimental Investigations 715
30.5 Optical Breakdown in Liquids, Cavitation 719
30.5.1 Absorbing Targets 720
30.5.2 Transparent Media 721

Part VII Lasers in Medicine, Biotechnology and Arts

31 Lasers in Medicine and Biotechnology 727
31.1 Medical Applications 728
31.1.1 Ophthalmology 728
31.1.2 Dermatology and Surgery 728
31.1.3 Photodynamical Therapy 729
31.1.4 Prosthesis 729
31.2 Biotechnology 729
31.2.1 Laser Microdissection 729
31.2.2 Micro-/Nanosurgery and Manipulation 730
31.2.3 Biopolymers 730
31.3 Interaction Mechanisms 731
31.3.1 Chemical Effects 733

32 Restoration and Conservation of Artworks 735
32.1 Cultural Heritages 735
32.1.1 Metal Artworks 736
32.1.2 Oil-paintings, Frescos 736

32.2 Analysis and Origin of Artworks 737
32.3 Architecture, Modern Artwork 737

Appendix A Definitions and Symbols 739
A.1 Symbols and Conversion Factors 739
A.2 Abbreviations, Acronyms 745

Appendix B Mathematical Functions and Relations 749

Appendix C Tables 757

References 783

Index 843

Part I
Overview and Fundamentals

Chapter 1
Introduction

The current interest in the use of lasers, be it for scientific investigations or for industrial applications, is directly linked to the unique properties of laser light. The high spatial coherence achieved with lasers permits extreme focusing and directional irradiation at high energy densities. The monochromaticity of laser light, together with its tunability, opens up the possibility of highly selective narrow-band excitation. Controlled pulsed excitation offers high temporal resolution and often makes it possible to overcome competing dissipative mechanisms within the particular system under investigation. The combination of all of these properties offers a wide and versatile range of quite different applications.

Materials processing with lasers takes advantage of virtually all of the characteristics of laser light. The high energy density and directionality achieved with lasers permits strongly localized heat- or photo-treatment of materials with a spatial resolution of better than 10 nm. Pulsed lasers or scanned cw lasers allow time-controlled processing between about 10^{-15} s and continuous operation. The monochromaticity of laser light allows for control of the depth of heat treatment or selective, non-thermal excitation – either within the surface of the material and/or within the molecules of the surrounding medium – simply by changing the laser wavelength. Because laser light is an essentially massless tool, there is no need for mechanical holders with all the attendant problems these pose in the case of either brittle or soft materials (workpieces). Furthermore, laser beams can be moved at speeds which can never be obtained by using mechanical tools or conventional heat sources. Contrary to mechanical tools, laser light is not subject to wear and tear. This avoids any contamination of the material being processed and, if the beam is properly controlled, also guarantees constant processing characteristics. With medical and biological applications it is also important that laser beams are absolutely sterile tools. Laser technology is completely compatible with present-day electronic control techniques. Naturally, a particular processing application will require only one or a few of these properties.

Laser processing can be classified into two groups: conventional laser processing and laser chemical processing. *Conventional* laser processing can be performed, at least in principle, in an inert atmosphere and can take place without any changes in the overall chemical composition of the material being processed. This is the most important difference to laser *chemical* processing, which is characterized by

D. Bäuerle, *Laser Processing and Chemistry,* 4th ed.,
DOI 10.1007/978-3-642-17613-5_1, © Springer-Verlag Berlin Heidelberg 2011

an overall change in the chemical composition of the material or the activation of a real chemical reaction. In many situations, a unique classification into chemical and non-chemical laser processing is difficult or impossible.

1.1 Conventional Laser Processing

The interaction mechanisms between laser light and matter depend on the parameters of the laser beam and the physical and chemical properties of the material. Laser parameters are the wavelength, intensity, spatial and temporal coherence, polarization, angle of incidence, and dwell time (illumination time at a particular site). For pulsed-laser irradiation it is often more appropriate to introduce instead of the intensity the energy density (fluence). The material is characterized by its chemical composition and microstructure (the arrangement of atoms or molecules within a solid), which determine the type of elementary excitations and the interactions between them.

Conventional laser processing is mainly performed with *infrared* (IR) laser light. This can excite free electrons within a metal, or vibrations within an insulator. In semiconductors both types of excitations are possible in the IR. In general, the excitation energy is dissipated into heat within a time which is short compared to any other time involved in the process. As a consequence, with low to medium intensities, the laser beam can just be considered as a heat source which induces a temperature rise on the surface and within the bulk of the material. This is schematically shown in Fig. 1.1.1a. The temperature distribution is determined by the optical

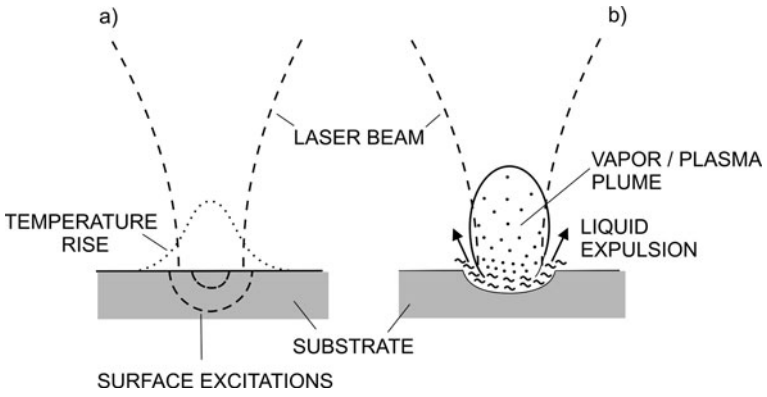

Fig. 1.1.1 a, b The picture illustrates two regimes of laser–material interactions employed in conventional laser processing. (**a**) Heat treatment of surface with laser-light intensity below the vaporization threshold, $I < I_v$. The absorbed laser light causes a temperature rise with or without surface melting. This intensity regime is mainly employed with laser-induced surface modifications. If surface melting takes place, abrasive processing by liquid-phase expulsion using a gas jet is possible. (**b**) The intensity regime $I > I_v$ is characterized by liquid-phase expulsion, vaporization, and plasma formation. This regime is employed in most cases of abrasive laser processing

and thermal properties of the material and, near phase transitions, by transformation energies for crystallization, melting, boiling, etc.

When the laser-light intensity, I, reaches a certain intensity, I_v, which causes significant material vaporization, a vapor plume above the substrate surface is formed (Fig. 1.1.1b). With further increasing intensity, the number of species within the plume increases and interactions between the laser light and the vapor become important. These result in an ionization of species. Above a certain intensity, I_p, the vapor is more appropriately denoted as a plasma. The plasma strongly absorbs the laser light, which now couples to the substrate mainly via the plasma plume. This is the dominating interaction mechanism in most types of abrasive metal processing by means of CO_2 lasers. Because of the strong non-linearity in this interaction, small changes in laser parameters may cause strong changes in processing results. For this reason, proper control of the various parameters is a prior condition for reproducible processing.

Figure 1.1.2 gives an overview of the various applications and parameter regimes employed in laser processing. The intensities and interaction times shown in the figure refer to different types of lasers.

The best-established application is abrasive laser machining, such as drilling, scribing, cutting, trimming, and shaping. Here, the material is removed from the workpiece as liquid, vapor, or plasma (Fig. 1.1.1b). The liquid is expelled by the recoil pressure of the vapor or by an additional gas jet. With conduction-limited laser welding and with bonding, the material is only melted. Typical light intensities employed in these applications range from about 10^5 to $10^{10}\,\mathrm{W/cm^2}$, with irradiation times $10^{-7}\,\mathrm{s} < \tau_\ell < 10^{-1}\,\mathrm{s}$. Most commonly used are high-power CO_2 lasers ($\lambda \approx 10.6\,\mu\mathrm{m}$) and Nd:YAG lasers ($\lambda \approx 1.064\,\mu\mathrm{m}$; see Table I). Here, in general, the laser beam is focused onto the workpiece to a spot size of, typically, between some ten micrometers and several millimeters.

Besides these well-established applications, laser-induced morphological, structural and compositional transformations of material surfaces and thin films are attracting increasing interest. These applications are performed, in general, with laser-light intensities $I < I_v$ (Fig. 1.1.1a). Among the most common processing applications of this type are laser annealing, transformation hardening, glazing, recrystallization, many types of alloying, and shock hardening. These applications are based on the short heating and cooling cycles achieved with lasers. Here, the laser-induced surface temperature is either kept just below the melting temperature or slightly above it. Shock hardening is performed with high intensity short pulses that cause a strong mechanical compression.

Processing applications that involve an overall change in the chemical composition of the surface – without the necessity of a chemical reaction – are cladding and those cases of alloying where new material is added to the surface. These processes, in general, require surface melting.

The somewhat lower laser-light intensities employed in many of these applications, typically $10^3 - 10^8\,\mathrm{W/cm^2}$, make it possible to process larger areas by using unfocused or defocused laser beams. The lateral dimension of the area that can be processed in a single scan is therefore much wider, typically up to several

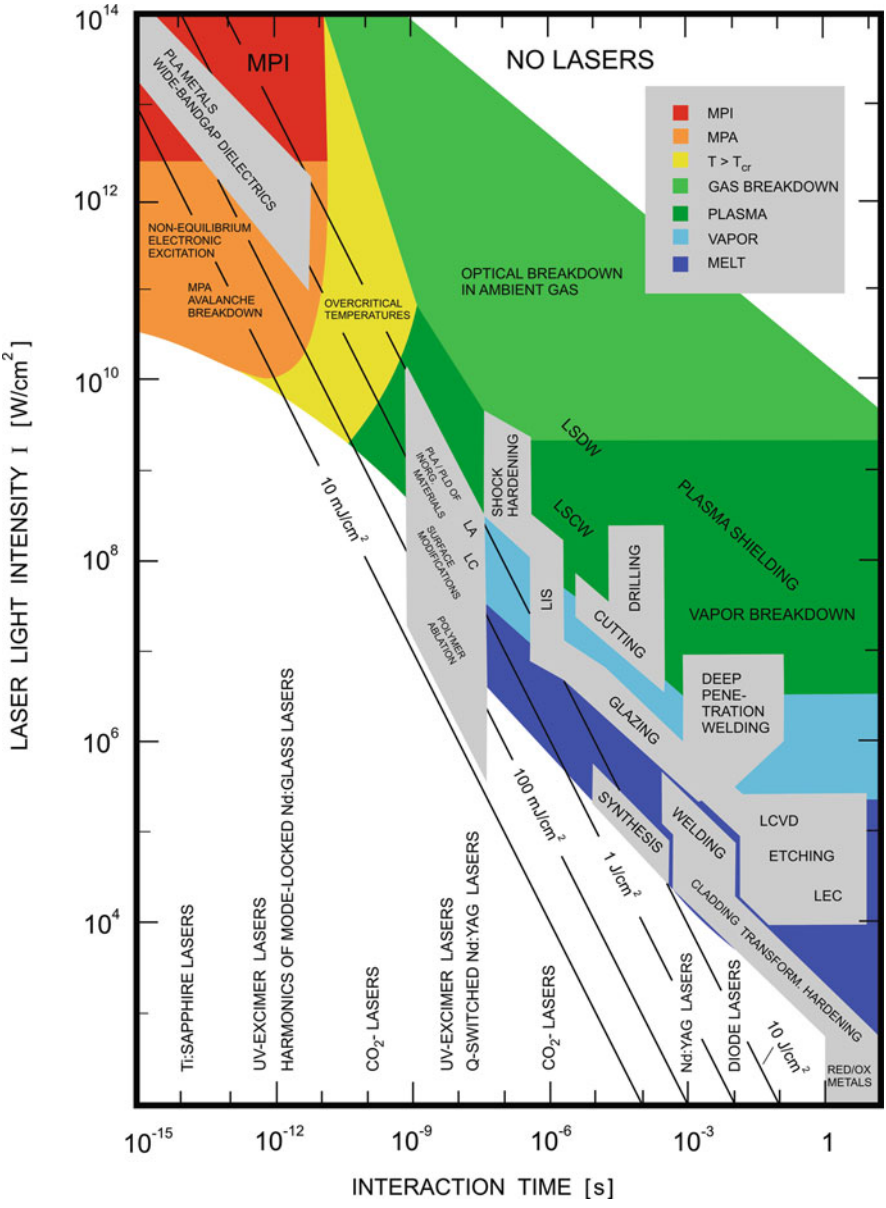

Fig. 1.1.2 Applications of lasers in materials processing. PLA/PLD: pulsed-laser ablation/deposition. Surface modifications include laser-induced oxidation/nitridation of metals, surface doping, etc. LA: laser annealing. LC: laser cleaning. LIS: laser-induced isotope separation/IR-laser photochemistry. MPA/MPI: multiphoton absorption/ionization. LSDW/LSCW: laser-supported detonation/combustion waves. LCVD: laser-induced CVD. LEC: laser-induced electrochemical plating/etching. RED/OX: long pulse or cw CO_2-laser-induced reduction/oxidation. Laser-light intensities exceeding 10^{16} W/cm^2 generate X-rays that gain increasing importance in nanotechnology [adapted from *Bäuerle* 1996]

centimeters. The processed depth is between some ten Ångstroms and several centimeters, depending on the material being processed and the type of laser employed. With some of these large-area processing applications, and in particular with the annealing of semiconductor surfaces, high-intensity lamps instead of lasers are used on real production lines.

1.2 Laser Chemical Processing

The object of laser-induced chemical processing (LCP) of materials is the patterning, coating and physicochemical modification of solid surfaces by activation of real chemical reactions. An overview of the various possibilities is presented in Fig. 1.2.1. The figure includes reactions that result in material deposition, ablation/pulsed-laser deposition (PLD), etching, synthesis, surface modification (doping, alloying, oxidation, reduction, nitridation, exchange of surface atoms/molecules), metallization, decomposition, and polymerization. Laser-induced activation or enhancement of a reaction can take place heterogeneously or homogeneously or via a combination of both. A *heterogeneous* reaction is induced in an adsorbate–adsorbent system, at a gas–solid or liquid–solid interface, or within the solid surface itself (Fig. 1.2.1a, b, d, e). A *homogeneous* reaction is activated within the ambient medium (Fig. 1.2.1c) or within the bulk of the material. Symbolically, the first step in a laser-induced reaction can be described, in many cases, by

$$\mathrm{AB} + \mathrm{M} + \mathrm{Photons} \rightarrow \mathrm{A}(\downarrow) + \mathrm{B}(\uparrow) + \mathrm{M}\,, \tag{1.2.1}$$

including the case $\mathrm{B} \equiv \mathrm{A}$. 'A' shall be the relevant species for surface processing. If $\mathrm{B} \neq \mathrm{A}$, the interaction of species B (atoms or molecules) with the substrate surface shall be weak or negligible. 'M' can be a gas, a liquid solvent, or a solid.

Both heterogeneous and homogeneous laser-induced reactions may be activated *thermally* (photothermally, pyrolytically), or *photochemically* (photolytically), or by a combination of both (photophysically).

1.2.1 Thermal Activation

We shall denote a reaction as thermally activated if the thermalization of the (laser) excitation energy is fast compared to any other process. In this case, the laser can be considered simply as a heat source. This is schematically shown in Fig. 1.2.2. In case (a) the laser light is absorbed exclusively by the substrate. If we ignore any heat flow into the ambient medium, molecules AB are decomposed only within the laser-heated area. While species A stick on or subsequently further react with the substrate, species B desorb. Heating of the ambient medium via the substrate may result in homogeneous activation of the reaction.

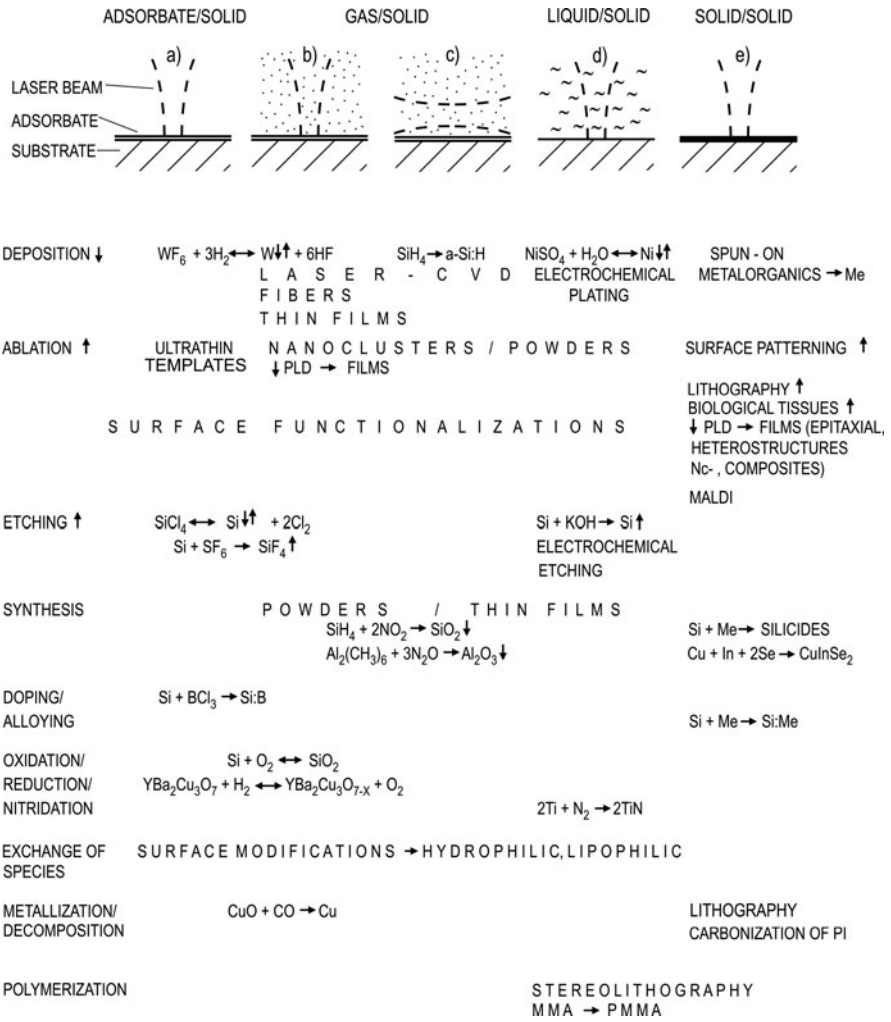

Fig. 1.2.1 a–e Laser chemical processing at or near solid surfaces. The laser beam is always shown at perpendicular incidence to the substrate (workpiece) except in case (**c**) where it propagates parallel to the surface within a gaseous- or liquid-ambient medium. For simplicity, not all reaction products are included in the formulas. ↓ refer to deposition or condensation of products, and ↑ to desorption of species, surface ablation, or etching. ↔ denotes reactions that can be reversed by shifting the chemical equilibrium to the other side. PLD = pulsed-laser deposition. In PLD, the material ablated from the substrate (target) is condensed on another substrate (*not* shown in the figure). Additional abbreviations are: nc = nanocrystalline, Me = metal. PTFE = polytetrafluoroethylene (Teflon); PI = polyimide; MMA = methyl-methacrylate; PMMA = polymethyl-methacrylate

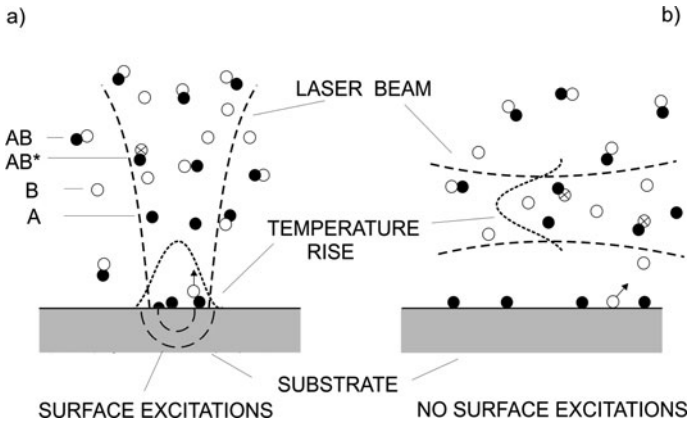

Fig. 1.2.2 Illustration of laser-induced chemical processing (LCP) at perpendicular (case (**a**)) and parallel laser-beam incidence (case (**b**)). Thermal (photothermal, pyrolytic) LCP at perpendicular incidence is, in general, performed with precursors AB that do not absorb the laser radiation. Non-thermal (photochemical, photolytic) LCP is based on selective excitation/dissociation of precursor molecules and/or the substrate. In a purely photochemical process, the laser-induced temperature rise can be ignored

In Fig. 1.2.2b the laser beam propagates parallel to the surface and can only be absorbed by molecules AB. The excitation energy shall be rapidly transformed into heat and the molecules are thermally decomposed. On their way to the substrate, some of the fragments A and B recombine. Those species A (or products AC formed in a subsequent reaction $A + CD \rightarrow AC + D$) that reach the substrate can either just stick on the surface or react with it. The situation is similar in cases where gas-phase molecules are not directly decomposed but thermally excited into higher vibrational states, AB^*. Some of the molecules AB^* reach the substrate, while others thermalize via collisions with molecules AB that are in the vibrational ground state or in a lower excited state. Molecules AB^* may also decompose due to collisions with each other or with the substrate. The sticking probabilities of AB^* and AB on the substrate surface may differ significantly.

1.2.2 Non-thermal Activation

In photochemical laser processing, the first reaction step is faster than the thermalization of the excitation energy. Non-thermal excitations are included in Fig. 1.2.2. With both perpendicular and parallel irradiation, precursor molecules AB are dissociated as a consequence of *selective* electronic or vibrational excitation within the volume of the laser beam. Species A will diffuse and, if they do not recombine on their way, may hit the surface. The situation is similar if AB is not decomposed but only selectively excited. With perpendicular incidence the laser light may also excite the solid surface, thermally or non-thermally. Non-thermal surface excitations are photoelectrons generated on metal surfaces, electron–hole pairs in semiconductors,

selective excitations of surface polaritons, etc. Surface excitations may significantly influence reactions between species A or AB* and the substrate, and they often permit one to localize the reaction in space. For purely photochemical processes the temperature rise within the ambient medium and on the substrate surface can be ignored.

In many cases, different excitation mechanisms contribute *simultaneously* to the reaction, but often one of them dominates. Frequently, a reaction is initiated photochemically and proceeds thermally, and vice versa.

Finally, changes in the optical, thermal, mechanical, and chemical properties of the processed surface or the ambient medium may cause various *feedbacks* and different kinds of *instabilities*.

1.2.3 Local and Large-Area Processing

As in conventional laser processing, laser chemical processing can be performed locally or on a more extended scale.

Local laser-induced *chemical* processing allows for single-step direct substrate patterning with lateral dimensions down into the nanometer range. This can be performed by scanning a focused laser beam across the substrate surface (direct writing), by projecting the laser light via a mechanical mask, by interference of laser beams, by means of microlens arrays, or by SXM-type techniques (SXM stands for scanning probe microscopy).

Large-area chemical processing can be performed with the laser beam propagating either perpendicular (normal incidence) or parallel to the surface. The latter irradiation geometry permits thin-film fabrication with or without uniform substrate heating.

1.2.4 Comparison of Techniques

Local and large-area material deposition, surface modification, compound formation, material transformation, and etching are needed in many areas of technology, such as mechanics, metallurgy, electronic and semiconductor device fabrication, integrated optics, optoelectronics, sensor and chemical technology, etc. In virtually all of these fields light-assisted processing, and in particular laser processing, offers new and unique processing possibilities that are impossible with currently available technologies. On the other hand, there are many applications where laser processing has to compete with standard and well-established techniques. Among those are: conventional chemical vapor deposition (CVD); plasma-CVD (PCVD) or plasma etching (PE); electron-beam (EB) processing; ion-beam processing, e.g., reactive ion-beam etching (RIE), etc.

With the exception of electron- and ion-beams, these conventional techniques are all large-area processing techniques. Thus, surface patterning can be achieved only in combination with mechanical masking or lithographic methods. Here, typically, 10–20 different dry- and wet-processing steps are required to produce a particular

pattern or single feature. The repeated physical and chemical treatment influences the *whole* substrate or device in each cycle. The fabrication of a microstructure, for example by CVD, requires the substrate to be uniformly heated up to several hundred degrees. In conventional liquid-phase etching, the exposure of the whole substrate to an aggressive etching solution may result in serious damage. Problems associated with photoresist masks are sometimes also difficult to overcome. In other words, the conventional techniques may become problematic or even inadequate whenever sensitive materials or prefabricated devices are to be processed.

With lasers, thermal and chemical treatment can be strongly localized, thereby leaving the material otherwise unaffected. Consequently, the laser technique allows one to thermally transform thin films on heat-sensitive substrates, or to process materials such as compound semiconductors, high-temperature superconductors (HTS), piezoelectric ceramics, polymers, etc. For instance, in laser-induced CVD (LCVD) heating takes place only locally or not at all. Furthermore, laser processing avoids material damage from ion or electron bombardment, or from overall vacuum-ultraviolet (VUV) radiation, which is inherent in plasma processing. Laser processing is *not* limited to planar substrates but also allows three-dimensional fabrication. The nonlinearity of laser-induced chemical reactions makes it possible to increase the process resolution over that achieved in standard photolithography. Unlike ion- or electron-beams, laser radiation can propagate through a great variety of media, or it can be made strongly absorbable, e.g., by changing its wavelength. These and other properties of laser processing are important in micromechanics and semiconductor device technology, and a prior condition for the fabrication of new multicomponent microdevices. Laser processing for surface profiling by doping, etching, etc., often yields superior results with respect to those achieved with conventional techniques. The strong non-equilibrium conditions that can be achieved with lasers permit one to synthesize (metastable) materials that cannot be fabricated by any other technique. Finally, the unique possibilities to control interaction processes between laser light and matter, including soft materials, biological tissues etc. have opened up completely new applications in biotechnology, medicine, and even in art conservation and restoration.

It is evident that in all cases where standard techniques can be applied equally well or where the quality of a particular processing step can be tolerated, economical arguments will be decisive. Here, the most serious limitations of laser processing are, at present, the total process rates and throughputs. This severe problem refers not only to laser-direct writing, but also to many cases of large-area laser processing. The local processing rates for deposition, etching, etc., can be extremely high, $100\,\mu m/s$ and more. Nevertheless, the processed surface area per unit time is quite small. Many of the conventional large-area techniques permit fabrication of a large number of devices simultaneously. Thus, despite being multiple-step processes, the total throughput is very high. Therefore, in the foreseeable future, laser direct writing of complete complex structures may be interesting for the design of prototypes and the fabrication of masters but not for direct mass production.

To resolve the throughput problem one needs more powerful laser systems than those currently available, and further developments in optical projection, interference, and fiber techniques. For these reasons, laser micro- and nanoprocessing

should be considered for the time being as a *complementary* technique that can be used when standard techniques become inadequate. In such cases fabrication of tools, devices, wafers, etc., on a piece-by piece basis becomes quite conceivable. Even today laser micro-/nanoprocessing substitutes conventional techniques in cases where small-area complementations and modifications (for example for customization) or repair of prefabricated devices or tools are necessary. In such cases multiple-step conventional techniques become very inefficient or cannot be applied at all. Here, laser micro-processing can significantly improve the total production yield. Furthermore, localized deposition may be advantageous when recovery of precious materials such as rare metals from liquid or solid admixtures, for example from photoresists, is expensive or altogether uneconomic. Clearly, economic arguments are less relevant in biological (biophotonics, microdissection, micro-/nanosurgery, etc.) and medical applications (opthalmology, surgery, etc.), and in many cases of art conservation.

1.2.5 Planar and Non-planar Processing

Laser processing is frequently classified into two-dimensional planar processing and three-dimensional non-planar processing:

- If the substrate is planar *and* if the lateral dimensions of the processed feature are larger than or comparable to the axial dimensions, we define processing to be planar (two-dimensional). This includes large-area etching, deposition, alloying, and compound formation, but also most cases of laser direct writing on planar substrates.
- If the substrate is non-planar, or if the lateral dimensions of the laser processed feature are small compared to its axial dimensions, we define processing to be non-planar (three-dimensional). This includes many cases of material cutting and drilling, the etching of deep grooves and via holes, the growth of fibers, etc. Clearly, this classification is sometimes somewhat arbitrary.

Chapter 2
Thermal, Photophysical, and Photochemical Processes

A proper definition of *thermal* (photothermal) and *non-thermal* (photochemical) laser processing would require a detailed knowledge of the fundamental interactions between laser light and matter, and of the various relaxation times involved. This information is available only for a few special systems. For this reason, the definitions usually employed are not very strict. We shall consider a laser-induced process as thermally activated if the thermalization of the excitation energy is fast compared to both the excitation rate and the initial processing step. The term photochemical is used if the laser-induced process proceeds *mainly* non-thermally. If both thermal and non-thermal mechanisms are significant, we denote the process as *photophysical*. Particularly in connection with photo-decomposition processes, we frequently use, instead of photothermal and photochemical, the terms pyrolytic and photolytic, respectively.

If laser processing is thermally activated, the state of the system is described by the temperature and the total enthalpy. The latter is relevant only if phase changes or chemical reactions take place. For a quantitative analysis and optimization of a particular process, the laser-induced temperature distribution must be known. In laser-microchemical processing, direct temperature measurements have been performed with a reliable degree of accuracy in only a very few cases. Frequently, laser-induced temperatures can only be calculated. In fact, many features in thermal processing can be qualitatively, and in some cases even quantitatively, analyzed on this basis.

Photochemical laser processing is determined by the *selectivity* of the excitation. In a gas or liquid, the selectivity is characterized by the number density of (selectively) excited, ionized, or dissociated species. In a solid, the degree of selectivity is determined by the number density of non-equilibrium photoelectrons, electron–hole pairs, photodissociated bonds, etc.

2.1 Excitation Mechanisms, Relaxation Times

The *primary* interactions between light and matter are always non-thermal. In laser processing, the relevant excitations can be classified into those of the solid substrate to be processed, those of the ambient medium, and those of the adsorbate–adsorbent system.

D. Bäuerle, *Laser Processing and Chemistry,* 4th ed.,
DOI 10.1007/978-3-642-17613-5_2, © Springer-Verlag Berlin Heidelberg 2011

In solids, light can interact with elementary excitations that are optically active. Among those are different types of electronic excitations (inter- and intraband excitations, excitons, plasmons, etc.) and excitations of phonons, polaritons, magnons, etc. Additionally, there may be localized or non-localized electronic or vibrational states that are related to defects, impurities, or the solid surface itself. Some of these transitions are schematically shown in Fig. 2.1.1. The energy E_g describes the distance between the highest valence band and the lowest conduction band. In recent years, excitations of material surfaces/interfaces have gained increasing interest. Of particular importance in nanooptics are surface-plasmon polaritons (SPPs) excited at nanostructured metal/dielectric *interfaces* (Sect. 27.2.2). SPPs are surface electromagnetic waves that are coupled to (coherent) oscillations of conduction band electrons at the interface with a dielectric medium.

In liquids and gases, light can induce electronic, vibrational, and rotational transitions within single molecules.

If molecules or atoms become adsorbed on a solid surface, their electronic and vibrational properties change. As a consequence, one observes changes in absorption cross sections and selection rules for optical absorption, additional vibrational transitions, etc. Light can increase or decrease the density of adsorbed species,

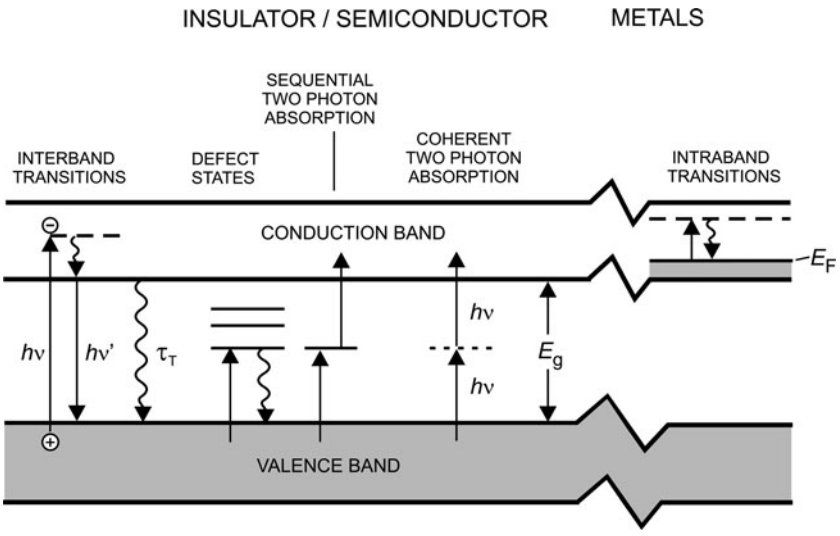

Fig. 2.1.1 Schematic of different types of electronic excitations in a solid. Only the highest valence band (VB) and the lowest conduction band (CB) are shown. *Straight lines* indicate absorption or emission of photons with different energies, $h\nu$. *Oscillating lines* indicate non-radiative processes. Interband transitions VB→CB take place if $h\nu \geq E_g$. In this process, electron–hole pairs are generated. Band-gap excitations are located in the near infrared (NIR) and visible (VIS) for semiconductors and in the ultraviolet (UV) for insulators. Defect, impurity and surface states often permit sub-bandgap excitations with $h\nu < E_g$. At high laser-light intensities, sequential multiphoton excitations via defect states or coherent multiphoton excitations become important. Intraband electronic transitions are typical for laser excitations in metals, and in semiconductors at elevated temperatures. E_F is the Fermi-energy

e.g., via excitations of the solid, the (free) gas- or liquid-phase molecules, or the adsorbate–adsorbent complex.

In all systems, different elementary excitations are coupled via anharmonic or higher order dipolar (multipolar) interactions.

High laser-light intensities allow high excitation densities to be generated, thermally or non-thermally. The density of excited molecules, atoms, ions, radicals, electrons, etc., can exceed 10^{22} species/cm^3. The coupling of elementary excitations among each other and with the intense laser radiation can cause a number of *new* phenomena. Prominent examples are changes in absorption cross sections, thermal runaway in metals and semiconductors, thermal self-focusing in transparent media (including the ambient medium), high densities of free carriers generated by interband excitation or impact ionization in semiconductors and insulators. With even higher laser-light intensities, *non-linear* optical phenomena such as self-focusing, multiphoton processes, etc., become important. With very high intensities, the formation of plasmas, shock waves, detonation waves, etc., is observed.

The time for the thermalization of the excitation energy depends on the type of material and the laser parameters.

In *metals*, light is almost exclusively absorbed by conduction band electrons within a skin layer of, typically, 10 nm (intraband transitions, Fig. 2.1.1). The time between electron–electron collisions, τ_e, is of the order of 10^{-14} to 10^{-12} s (10 fs to 1 ps). Electron-phonon relaxation times, τ_{e-ph}, are much longer, due to the big difference between electron and ion masses. Depending on the strength of electron-phonon coupling, one finds $10^{-12}\,\text{s} \leq \tau_{e-ph} \leq 10^{-10}\,\text{s}$. Similar relaxation times are found for quasi-free (conduction band) electrons in semiconductors like Si.

In *non-metals*, interband electronic excitations can last much longer, ranging from, typically, 10^{-12} to 10^{-6} s. Excitations of *localized* electronic states associated with defects, impurities or surfaces may have much longer lifetimes. Optically active phonons and localized vibrations in non-metals can be directly excited by IR light.

In single, isolated molecules, electronic excitations decay within 10^{-14} to 10^{-6} s. The lifetime of *low* excited vibrational levels is, typically, 10^{-3} s. With the (high) molecular densities employed in laser-chemical processing, energy randomization between molecules with vibrational mismatches $\leq k_B T$ occurs via collisions within, typically, 10^{-10} to 10^{-4} s.

It should be emphasized that with the *high* light intensities achieved with lasers, excitation and energy relaxation mechanisms can be significantly altered with respect to those relevant at low to medium intensities. For example, in polyatomic molecules highly excited vibrational states may have lifetimes of 10^{-13} to 10^{-11} s only.

2.1.1 Thermal Processes

The thermalization of the excitation energy shall be described by the relaxation time τ_T. For a thermal process $\tau_T \ll \tau_R$, where τ_R characterizes the initial processing step or the inverse excitation rate, depending on which is smaller. For some systems,

however, this condition must be modified. τ_R can be the time required for desorption of species from the surface, or, for structural rearrangements of atoms or molecules within the surface, the time which characterizes the *initial* step in a chemical reaction, etc.

Let us consider a simple example: Assume a reaction that is mediated by collisions of gas-phase molecules with a Si surface. The reaction probabilities for thermal and non-thermal processes shall be equal. The Si shall be irradiated by a picosecond laser pulse with $h\nu > E_g(\mathrm{Si})$ and an intensity that generates a carrier density, $N_c \approx 10^{22}/\mathrm{cm}^3$ near the surface. This carrier density decreases via Auger recombination to 1% within about 10^{-10} s (Sect. 2.4). Due to electron–phonon coupling, the recombination energy is dissipated into heat within, typically, 10^{-12} to 10^{-11} s. With a gas pressure of 100 mbar and a temperature of 300 K, the impingement rate onto the surface is some 10^{22} molecules/cm^2 s. The number of surface atoms is about 10^{14} atoms/cm^2. The time for the initial reaction step between a gas-phase molecule and a surface atom is then $\tau_R \geq 10^{-8}$ s, which is very long compared to $\tau_T \leq 10^{-10}$ s. Thus, the effect of laser radiation is purely thermal. In other words, if $\tau_T \ll \tau_R$ the detailed excitation mechanisms become irrelevant and the laser can be considered simply as a heat source.

In spite of their thermal character, laser-driven thermophysical and thermochemical processes may be quite different from those initiated by a conventional heat source. There are various reasons for this: The laser-induced temperature rise can be localized in space and time. Temperatures of more than 10^4 K can be induced in a *small* volume which is defined by the laser focus and the material parameters. With short high-intensity laser pulses, heating rates up to more than 10^{15} K/s can be achieved. With such heating rates, the chemical relaxation time may be slow in comparison, and the chemical reaction takes place far from equilibrium. Another possibility is the selective excitation of a particular species, e.g., in a gas mixture. Furthermore, laser heating may change the optical properties of the medium and thereby introduce non-linearities in the interaction process. As a consequence of these various mechanisms, novel chemical reaction pathways and reaction products, novel material microstructures and phases, novel surface morphologies, and novel evaporation characteristics may occur.

2.1.2 Photochemical Processes

The term photochemical (photolytic) laser processing is used if the overall thermalization of the excitation energy is slow, i.e., if $\tau_T \geq \tau_R$. This condition frequently holds for chemical reactions of excited molecules among themselves or with the substrate surface, for photoelectron transfer and subsequent chemisorption of species on solid surfaces, for photochemical desorption of species from surfaces, etc. If we consider the example discussed above, but assume that the molecules are already adsorbed on the Si surface, photocarriers can *directly* interact with the adsorbate and thereby initiate a reaction. In this case τ_R is the time for charge

transfer (Sect. 15.1). With purely photochemical processes, the temperature of the system remains (almost) unchanged under laser-light irradiation.

Due to the high excitation densities, laser photochemistry can be quite different from standard photochemistry using lamps.

2.1.3 Photophysical Processes

Thermal and photochemical processes can be considered as limiting cases of photophysical processes. We denote a process as photophysical if both thermal and non-thermal mechanisms *directly* contribute to the overall processing rate. The degree of thermal and non-thermal contributions depends on the relative yield of the respective reaction channels.

2.1.4 A Simple Model

The classification into thermal, photophysical, and photochemical processes is often quite complex. Consider the situation shown in Fig. 2.1.2. A and A^* shall characterize the system in the ground state and in the excited state, respectively. If we ignore spontaneous emission, non-radiative transitions $A^* \rightarrow A$ are described by the thermal relaxation time, τ_T. The characteristic times for the reaction of A and A^* with C are $\tau_A(T)$ and $\tau_{A^*}(T)$. It is often convenient to use, instead of relaxation times, τ_i, rate constants, $k_i \equiv k_i(T) = \tau_i^{-1}$. Let us consider *low* excitation rates where $\tau_T \leq h\nu/\sigma I$ (σ is the excitation cross section).

If $\tau_T \ll \tau_{A^*}$ and $\tau_A \ll \tau_{A^*}$ the excitation energy is immediately dissipated into heat and the reaction is thermally activated. The reaction rate is determined by k_A.

If $\tau_T > \tau_{A^*}$ and $\tau_{A^*} \ll \tau_A$ the process is mainly photochemically activated. The reaction takes place via excited species A^*.

If $\tau_T \ll \tau_A, \tau_{A^*}$ but $\tau_{A^*} \ll \tau_A$, or if all these times are comparable, both the 'thermal channel' and the 'photochemical channel' are important. We denote this process as photophysical. Let us study this situation in further detail and consider the kinetic equations

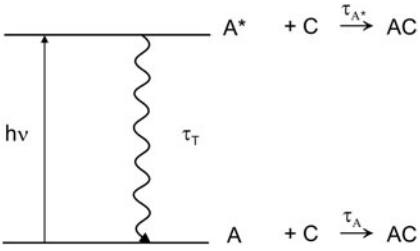

Fig. 2.1.2 A simple model for the competition between a thermal and a photochemical reaction. Stimulated emission is not indicated

$$\frac{\mathrm{d}N_\mathrm{A}}{\mathrm{d}t} = \frac{\sigma I}{h\nu}\,(N_{\mathrm{A}^*} - N_\mathrm{A}) + \frac{N_{\mathrm{A}^*}}{\tau_\mathrm{T}}\ ,$$
$$\frac{\mathrm{d}N_{\mathrm{A}^*}}{\mathrm{d}t} = \frac{\sigma I}{h\nu}\,(N_\mathrm{A} - N_{\mathrm{A}^*}) - \frac{N_{\mathrm{A}^*}}{\tau_\mathrm{T}}\ . \tag{2.1.1}$$

Here, the reaction of A and A^* with C has been assumed to be so slow that the related changes in N_A and N_{A^*} can be ignored. The total density of species is then $N = N_\mathrm{A} + N_{\mathrm{A}^*}$ and quasi-stationary conditions are achieved after time $t \approx \tau_\mathrm{T}$. With $\mathrm{d}N_\mathrm{A}/\mathrm{d}t = \mathrm{d}N_{\mathrm{A}^*}/\mathrm{d}t = 0$, we obtain from (2.1.1) the quasi-stationary densities $\tilde{N}_\mathrm{A}$ and $\tilde{N}_{\mathrm{A}^*}$. The sum of reaction rates via the thermal channel, $W_\mathrm{T} \approx k_\mathrm{A}\tilde{N}_\mathrm{A}$, and the photochemical channel, $W_\mathrm{PC} \approx k_{\mathrm{A}^*}\tilde{N}_{\mathrm{A}^*}$, is then

$$W = W_\mathrm{T} + W_\mathrm{PC} = k_\mathrm{A}\tilde{N}_\mathrm{A}\left[1 + \frac{k_{\mathrm{A}^*}}{k_\mathrm{A}}\left(1 + \frac{h\nu}{\sigma I \tau_\mathrm{T}}\right)^{-1}\right]\ . \tag{2.1.2}$$

The relative importance of the photochemical and thermal channels is determined by the second term in the parentheses. When the laser beam is switched off, the contribution of the photochemical channel decays within the characteristic time τ_T. Afterwards, the process is determined by k_A only.

This example shows, in a transparent way, how the competition between thermal and photochemical processes is determined by different time constants.

2.1.5 Chemical Relaxation

Let us consider a thermochemical process which is characterized by a chemical relaxation time, τ_ch, given by

$$\frac{1}{\tau_\mathrm{ch}} \equiv k_\mathrm{ch} = -\frac{1}{\Delta N_i}\frac{\mathrm{d}N_i}{\mathrm{d}t}\ , \tag{2.1.3}$$

where N_i is the number density of species i, and ΔN_i its deviation from the equilibrium value. If the heating rate

$$\frac{1}{\tau_\mathrm{t}} \equiv k_\mathrm{t} = \frac{1}{T}\frac{\mathrm{d}T}{\mathrm{d}t} \tag{2.1.4}$$

is small compared to k_ch, the system is in chemical equilibrium. If, on the other hand, $k_\mathrm{t} \gg k_\mathrm{ch}$, the system is far from equilibrium. This is the regime of non-equilibrium thermochemistry where novel reaction pathways and reaction products may be observed. The situation is analogous to the case of fast cooling (quenching) of systems. In this case, a non-equilibrium chemical state can be frozen.

Non-equilibrium chemistry is important in laser-induced surface modification, alloying, synthesis, etc. Quenching of non-equilibrium states is also important with structural transformations where no chemical reactions take place (Chap. 23).

2.2 The Heat Equation

Temperature distributions induced by the absorption of laser radiation within gases, liquids, and solids have been calculated on the basis of the heat equation. In the most general case, the temperature $T \equiv T(\boldsymbol{x}, t) = T(x_\alpha, t)$ is a function of both the spatial coordinates, x_α, and the time, t. With fixed laser parameters the temperature distribution depends on the optical absorption within the irradiated zone, on the transport of heat out of this zone and, if relevant, on transformation enthalpies for crystallization, melting and vaporization, chemical reaction enthalpies (exothermal or endothermal), etc. In the absence of heat transport by convection and thermal radiation, the heat equation can be written, in a coordinate system that is fixed with the laser beam, as

$$\varrho(T)c_\mathrm{p}(T)\frac{\partial T(\boldsymbol{x}, t)}{\partial t} - \nabla[\kappa(T)\nabla T(\boldsymbol{x}, t)] + \varrho(T)c_\mathrm{p}(T)\boldsymbol{v}_\mathrm{s}\nabla T(\boldsymbol{x}, t) = Q(\boldsymbol{x}, t) \,, \tag{2.2.1}$$

where $\varrho(T)$ is the mass density and $c_\mathrm{p}(T)$ the specific heat at constant pressure. $\boldsymbol{v}_\mathrm{s}$ is the velocity of the substrate (medium) relative to the heat source, Q (W/cm^3) (here, the substrate moves with a velocity $\boldsymbol{v}_\mathrm{s}$ whose direction is opposite to that shown in Fig. 6.1.1). If the substrate (workpiece) is uniform and isotropic, its thermal properties are characterized by a single thermal conductivity, κ, and a single heat diffusivity, D, which are related by

$$D = \frac{\kappa}{\varrho c_\mathrm{p}} \,. \tag{2.2.2}$$

If all temperature dependences in material parameters are ignored, the heat equation becomes linear. Values of ϱ, c_p, κ, and D are listed for various materials in Table II.

2.2.1 The Source Term

Subsequently, we assume that the light energy absorbed within the medium is totally transformed into heat. The source term can then be written as

$$Q(\boldsymbol{x}, t) = -\nabla \langle \boldsymbol{S} \rangle + U(\boldsymbol{x}, t) \,. \tag{2.2.3}$$

The function $U(\boldsymbol{x}, t)$ shall describe the additional energy per unit volume and time that is required or provided if phase changes or chemical reactions take place. $\langle \boldsymbol{S} \rangle = c\langle \boldsymbol{E} \times \boldsymbol{H} \rangle / 4\pi = I\hat{\boldsymbol{k}}_\ell$ is the time average of the Poynting vector. $\hat{\boldsymbol{k}}_\ell$ is a unit vector in the direction of the propagating light. This general expression for $\langle \boldsymbol{S} \rangle$ should be used if interference phenomena, optical inhomogeneities in the material, etc., must be considered. The propagation of light is characterized by the dielectric and magnetic permittivities of the medium, $\varepsilon = \varepsilon' + \mathrm{i}\varepsilon''$ and $\mu = \mu' + \mathrm{i}\mu''$. Henceforth,

we set $\mu' = 1$ and $\mu'' = 0$. The complex index of refraction can then be written as $\tilde{n} = \varepsilon^{1/2} = n + \mathrm{i}\kappa_\mathrm{a} \equiv n(1 + \mathrm{i}\kappa_0)$. Frequently, only the real part, n, is termed the refractive index. $\kappa_\mathrm{a} = n\kappa_0$ is the absorption index, and κ_0 the attenuation index. In the case of weak absorption and $\varepsilon'' \ll \varepsilon'$ we have $n \approx \varepsilon'^{1/2}$ and $\kappa_\mathrm{a} \approx \varepsilon''/2\varepsilon'^{1/2}$. In the low-density approximation which holds, for example, for dilute gases, $n - 1 \approx [\varepsilon' - 1]/2$ and $\kappa_\mathrm{a} \approx \varepsilon''/2$.

For monochromatic light and an isotropic medium, the first term in (2.2.3) can be written as

$$-\nabla \langle \boldsymbol{S} \rangle = \frac{\omega}{8\pi} \varepsilon'' |E_0|^2 \ ,$$

where $E(\boldsymbol{x}, t) = [E_0(\boldsymbol{x}) \exp(-\mathrm{i}\omega t) + \text{c.c.}]/2$ is the electric field. In the approximation of a (single) plane-wave and low absorption we obtain

$$\langle \boldsymbol{S} \rangle = \frac{c}{8\pi} n |E_0|^2 \hat{\boldsymbol{k}}_\ell = I \hat{\boldsymbol{k}}_\ell \ .$$

If we assume that the laser beam propagates in the z-direction, these two expressions yield the Bouguer–Lambert–Beer law,[1]

$$\frac{\mathrm{d}I(z)}{\mathrm{d}z} = -\alpha I(z) \ , \tag{2.2.4}$$

where

$$\alpha = \frac{4\pi\kappa_\mathrm{a}}{\lambda} = \frac{2\omega\kappa_\mathrm{a}}{c} = \frac{4\pi n\kappa_0}{\lambda} \tag{2.2.5}$$

is the (linear) absorption coefficient. λ is the wavelength in a vacuum. Values of α are listed for different materials in Table III. Instead of α, we often introduce the optical penetration depth, $l_\alpha = \alpha^{-1}$. The absorbed energy per unit volume and time is αI.

If the attenuation of the laser radiation is not solely caused by absorption but also by scattering, described by α_s, we have to replace α in (2.2.4) by the extinction coefficient, $\beta = \alpha + \alpha_\mathrm{s}$.

In a strict sense, Beer's law can be applied only if ε is uniform in space. Nevertheless, (2.2.4) is often also employed in photothermal processing, where the refractive index is *not* constant. Then, α is simply replaced by $\alpha = \alpha(T)$. Furthermore, for a tightly focused laser beam, the plane-wave approximation holds only within the Rayleigh length, z_R (Chap. 5).

---

[1] Throughout the literature, (2.2.4) is often termed the Lambert–Beer law or simply Beer's law; it was first derived experimentally in its integral form by *P. Bouguer* (1729), and theoretically by *I. G. Lambert* (1760). A mesoscopic interpretation of α was first given by *A. Beer* (1852).

2.2.2 Dimensionality of Heat Flow

An important quantity in thermal processing is the heat diffusion length,

$$l_{\mathrm{T}} \approx \zeta (D\tau_\ell)^{1/2} \; . \tag{2.2.6}$$

In *most* cases of transient heating that are characterized by a laser-beam dwell time, τ_ℓ, we choose $\zeta = 2$. This definition describes the $1/\mathrm{e}$ (spatial) decay in the temperature distribution

$$T(\boldsymbol{x}, t) \approx \frac{Q}{\varrho c_{\mathrm{p}} (4\pi\, Dt)^{m/2}} \exp\left(-\frac{|\boldsymbol{x}|^2}{4Dt}\right) \; , \tag{2.2.7}$$

which is a (fundamental) solution of the linear heat equation for a *point source* in infinite space,

$$\frac{\partial T}{\partial t} = D\nabla^2 T + \frac{Q}{\varrho c_{\mathrm{p}}} \delta(\boldsymbol{x}, t) \; .$$

The number m characterizes the (spatial) dimensionality of the problem, i.e., $m = 1, 2, 3$. Q is the total energy release and ϱ the density in $(\mathrm{g/cm^m})$.

It must be emphasized, however, that in all other cases the characteristic length, l'_{T}, which defines $T(l'_{\mathrm{T}}, t)/T(0, t) = 1/\mathrm{e}$, depends on the particular boundary-value problem under consideration and may differ significantly from (2.2.6).

The *dimensionality* of the heat flow is characterized by the relative size of l_{T} and other characteristic quantities such as the radius of the laser beam, w, the optical penetration depth, l_α, the thickness of the substrate, h_{s}, etc. If, for example, $l_{\mathrm{T}} \gg w, l_\alpha$, one has to consider the propagation of heat in three dimensions. On the other hand, for moderate absorption with $l_\alpha \leq l_{\mathrm{T}}$ and $l_{\mathrm{T}} \ll w$, lateral heat flow can be ignored and the temperature distribution in z-direction is obtained from the one-dimensional heat equation.

2.2.3 Kirchhoff and Crank Transforms

If the irradiated medium is isotropic, the temperature dependence of the thermal conductivity, $\kappa(T)$, can be eliminated from the heat equation by performing the Kirchhoff transform,

$$\theta(T) = \int_{T(\infty)}^{T} \frac{\kappa(T')}{\kappa(T(\infty))} \mathrm{d}T' \; , \tag{2.2.8}$$

where θ is a linearized temperature, and $T(\infty)$ the temperature at infinity, i.e., far away from the processed region. If κ is independent of temperature, the linearized

temperature is equal to the temperature rise, i.e., $\theta = \Delta T$. In terms of θ, the heat equation (2.2.1) has the form

$$\frac{1}{D(T(\theta))}\frac{\partial\theta}{\partial t} - \nabla^2\theta + \frac{\boldsymbol{v}_\mathrm{s}}{D(T(\theta))}\nabla\theta = \frac{Q}{\kappa(T(\infty))} \,. \tag{2.2.9}$$

An analytical solution of (2.2.9) is possible only in special cases. For an arbitrary geometry and temperature-dependent parameters D, α, and the reflectivity, R, only numerical solutions can be found.

With similar types of equations where D depends on time only, i.e. $D = D(t)$, and where $\boldsymbol{v}_\mathrm{s} = 0$ (see, e.g., Sect. 24.1), the Crank transform,

$$\tau = \int_0^t D(t')\,\mathrm{d}t' \,, \tag{2.2.10}$$

yields the linear equation

$$\frac{\partial\theta}{\partial\tau} - \nabla^2\theta = \frac{Q}{\kappa(T(\infty))} \,, \tag{2.2.11}$$

which can be solved analytically in many cases.

2.2.4 Phase Changes

If the laser power exceeds the threshold power for surface melting and evaporation, the temperature distribution can be calculated from the heat equation only when the latent heats of melting, ΔH_m, and evaporation, ΔH_v, are taken into account (because the experiments are, in general, performed at constant pressure, we use the enthalpy). Henceforth, the enthalpy is used with different dimensions, as convenient. The conversion of the enthalpy per *atom* is $\Delta H^\mathrm{a} \equiv \Delta H(\mathrm{J/atom}) = \Delta H(\mathrm{J/mol})/L = \Delta H(\mathrm{J/cm^3}) \times M/(\varrho L) = \Delta H(\mathrm{J/g}) \times M/L$ where L is the Avogadro number and M the atomic weight per mol. Values of ΔH_m and ΔH_v are listed in Table IV. The table shows that the latent heat of evaporation is, typically, 2−4 eV/atom (50–100 kcal/mol), while the latent heat of melting is, typically, 0.1−0.5 eV/atom (2–10 kcal/mol).

If phase changes take place, $U(\boldsymbol{x}, t)$ in (2.2.3) is non-zero and given by

$$U(\boldsymbol{x}, t)\,\mathrm{d}V \approx \boldsymbol{v}_{ls}\Delta H_\mathrm{m}\,\mathrm{d}F_{ls} + \boldsymbol{v}_{\mathrm{v}l}\Delta H_\mathrm{v}\,\mathrm{d}F_{\mathrm{v}l} \,, \tag{2.2.12}$$

where $\boldsymbol{v}_{ls}(\boldsymbol{x}, t)$, $\boldsymbol{v}_{\mathrm{v}l}(\boldsymbol{x}, t)$ and $\mathrm{d}F_{ls}$, $\mathrm{d}F_{\mathrm{v}l}$ are the respective velocities and surface elements of the liquid–solid and vapor–liquid interface within the volume element $\mathrm{d}V$. It is often convenient to introduce the *total* enthalpy, which can be approximated by

$$\Delta H(T) \approx \int_{T(\infty)}^{T} \varrho(T')c_\mathrm{p}(T')\,\mathrm{d}T' + \mathscr{H}(T - T_\mathrm{m})\Delta H_\mathrm{m} + \mathscr{H}(T - T_\mathrm{b})\Delta H_\mathrm{v}\ . \tag{2.2.13}$$

Here, the kinetic energy of the vapor is ignored. The first term describes the enthalpy density (J/cm^3; with solids and liquids this is equal to the energy density) required to heat the material from the temperature $T(\infty)$ to T. Note that in the case of vaporization this term includes the enthalpy change within the solid, liquid, and gas phases. The latter can be approximated, for an ideal gas, by $\Delta H_\mathrm{G} = \gamma R_\mathrm{G}\varrho_\mathrm{v}\Delta T/M(\gamma - 1)$, where $\gamma = c_\mathrm{p}/c_\mathrm{v}$ is the adiabatic index.

The second term describes the additional energy density necessary for melting. $\mathscr{H}$ is the Heaviside function, which is zero if $T < T_\mathrm{m}$ and unity if $T > T_\mathrm{m}$. The third term describes the latent heat of evaporation at the boiling temperature, T_b. Note, however, that vaporization may take place at temperatures $T_\mathrm{v} \lesssim T_\mathrm{b}$ (Chap. 11).

If we consider the liquid–solid system only and ignore density changes and also convective fluxes, the heat equation can be written together with (2.2.13) in the form

$$\frac{\partial \Delta H(\boldsymbol{x}, t)}{\partial t} - \nabla[\kappa(T)\nabla T(\boldsymbol{x}, t)] + \boldsymbol{v}_\mathrm{s}\nabla\Delta H(\boldsymbol{x}, t) = -\hat{\boldsymbol{k}}_\ell \nabla I(\boldsymbol{x}, t)\ , \tag{2.2.14}$$

where $\boldsymbol{v}_\mathrm{s}$ is the substrate velocity with respect to the laser beam. Equation (2.2.14) is most conveniently used with problems where latent heat effects play an important role (for a more general discussion see *Landau* and *Lifshitz*: Fluid Mechanics 1974). The situation is analogous with exothermal or endothermal chemical reactions when the energy of formation, ΔH, cannot be ignored with respect to the absorbed laser-light energy. In general, (2.2.14) can be solved only numerically [*Fell* et al. 2008].

2.2.5 *Limits of Validity*

The heat equation describes temperature distributions in many cases of thermal laser processing quite well. Nevertheless, one should be aware of the restrictions and uncertainties of calculated temperature distributions:

- The heat equation gives a macroscopic description of the medium averaged over a volume where thermal fluctuations are small. To estimate the length scale where such a description is appropriate, we consider a cube of side length l with N atoms (molecules) per unit volume. Then, the relative temperature fluctuation is $\delta T/T \approx (Nl^3)^{-1/2}$ and thus $l \approx (\delta T/T)^{-2/3}N^{-1/3}$. For $\delta T/T = 10^{-3}$ this yields $l \approx 0.02\,\mu\mathrm{m}$ for solids ($N \approx 10^{23}$ atoms/cm^3) and $l \approx 1\,\mu\mathrm{m}$ for gases with $N = 10^{18}$ atoms/cm^3. Thus, with submicrometer structures and with gases at low pressures, the application of the heat equation becomes inappropriate (Sect. 9.5.4).
- The values of α, R, κ, D, etc., are usually derived from static or quasi-static measurements where only small temperature gradients are involved. In laser

processing, however, the temperature gradients may be very strong and the interaction times very short. The temperature gradients are, typically, of the order $\nabla T \approx \Delta T/l$. Here, l is a characteristic length, for example, the radius of the laser focus, w, the heat diffusion length, l_T, the optical penetration depth, l_α, etc., depending on the particular problem. In any case, ∇T may be 10^5-10^{10} K/cm. As a consequence, the parameter values relevant in photothermal processing may significantly differ from those in conventional heat conduction problems.

- The optical properties of a specific medium depend on the laser parameters, which, in turn, affect the thermophysical properties via their temperature dependences. These dependences are often known in small temperature intervals only.
- The optical and thermal properties of a solid also depend on its surface morphology and crystallinity (amorphous, ceramic, poly- or single-crystalline), on surface contaminations (adsorbates, oxide layers, etc.), on defects (both physical defects such as dislocations, cracks, etc., and chemical defects such as isolated impurities, aggregate centers, etc.).
- The optical and thermal properties of liquids and gases depend on admixtures; with gases they also depend on pressure.
- Changes in parameter values originating from laser-induced changes in material properties introduce additional complications. Let us consider laser-CVD (Fig. 1.2.2a). Before nucleation takes place, α, R, D, κ, and the total emissivity, ε_t, are determined by the physical properties of the substrate material. When deposition commences, these quantities will rapidly change with the density and size of nuclei, and therefore with time. When a compact film is formed, e.g., a metal film, and when the penetration depth of the laser light is small compared to the film thickness, α, R, and ε_t will refer only to this deposited film. Similarly, D and κ will be quite different for such a combined structure compared to a uniform plane substrate. The situation is very similar in laser-induced surface modification and compound formation. Further complications arise if changes in surface geometry become significant. This is sometimes the case in materials deposition, etching, and ablation.
- The coupling between different degrees of freedom (e.g., the temperature, the density of species, N_i, etc.) causes feedbacks in the laser–matter interactions. Thus, from a theoretical point of view, a proper description of laser processing would require, in many cases, consideration of coupled non-linear equations.
- Whenever Knudsen effects are important, the kinetic Boltzmann equation instead of the heat equation should be solved. In reality, it is often possible to solve the problem for the Knudsen layer separately and derive modified boundary conditions for the heat equation.
- With ultrashort pulses where $\tau_\ell \leq D/v_0^2$ (v_0 is the sound velocity), the finite velocity of the heat front must be taken into account. Thus, the term $v_0^{-2}\partial^2 T/\partial t^2$ should be added to $D^{-1}\partial T/\partial t$ in the heat equation. This will result in a significant increase in temperature because the energy cannot be removed sufficiently fast enough from the heated volume (see, e.g., [*Vedavarz* et al. 1994]).

- With ultrashort pulses, the electrons and phonons are *not* in thermal equilibrium and 'hot' electron diffusion becomes important. In such cases one has to employ the 'two-temperature' model (Sect. 13.5).

In spite of these difficulties and restrictions, we will demonstrate in later chapters that essential features observed in laser processing can be understood from model calculations. In inhomogeneous media the propagation of light and heat must be calculated in a different way (Chap. 9).

In any case, the knowledge of laser-induced temperature distributions is a prerequisite for the modelling of processing rates, the clarification of the chemical kinetics, and the enlightenment of the basic microscopic interaction mechanisms. It is evident that it is desirable to measure as many of the relevant quantities as possible in situ, i.e., during laser processing.

2.3 Selective Excitations of Molecules

Laser photochemistry near or at molecule–solid interfaces can be based on selective electronic excitations of both the molecules and the solid surface, on selective vibrational excitations of the molecules, or on a combination of them. The excitation energy can also be transferred indirectly via an intermediate species as in photosensitization.

Electronic transitions of molecules are located mainly in the UV and VIS. Vibrational transitions are located in the IR. Both electronic transitions and vibrational transitions can be excited by single-photon (linear) processes or by multiphoton (MP) non-linear processes.

Laser-photochemical (non-thermal) processing is frequently based on *electronically* excited molecules and photofragments of them. There are, however, very few examples where selective single- or multiphoton *vibrational* excitations are of importance.

Different fundamental mechanisms involved in selective optical excitations of molecules and, to some extent, of solids have been studied for model systems. However, apart from a very few exceptions, only little is known about the photochemistry of systems relevant to LCP. Here, the physical conditions are very complex compared to the conditions in model systems.

The degree of selectivity achieved in a particular photoexcitation process is determined by the ratio of the excitation rate, W_{exc}, and the relaxation rate, W_{relax}. The selectivity is more pronounced the better the condition

$$W_{\mathrm{exc}} > W_{\mathrm{relax}} \tag{2.3.1}$$

is fulfilled. We shall term an excitation as selective if the system is *not* in local equilibrium. This shall include cases where the laser light induces a local temperature rise but without complete thermalization, e.g., between vibrational and translational degrees of freedom. In a mixture, selectivity can also denote the excitation of a

particular kind of species. The term non-selective or thermal excitation is used if the absorbed light energy is, at least locally, thermalized between the different degrees of freedom *and* the different kinds of species.

Subsequently, we shall summarize some basic aspects of selective electronic excitations and IR vibrational excitations.

2.3.1 Electronic Excitations

Electronic excitations of molecules can be based on single-photon or multi-photon processes. They are, in general, accompanied by simultaneous changes in the vibrational and rotational energy of the molecule.

Single-Photon Excitations

Let us consider some characteristic cases of single-photon (linear) excitations. Figure 2.3.1 shows potential energy curves for the electronic ground state and excited states of different molecules. According to the Franck–Condon principle, transitions occur vertically between maxima in the densities $|\psi_1|^2$ and $|\psi_2|^2$, where ψ_i are vibrational wave functions for the lower and upper electronic states. If the excited electronic state is unstable (Fig. 2.3.1a), excitation results in direct dissociation within times of, typically, 10^{-14} to 10^{-13} s. Clearly, relaxation and energy transfer between gas-phase molecules is unlikely within such short times. If the excited electronic state is stable, dissociation only occurs for photon energies $h\nu \geq E'_{\mathrm{D}}$ (Fig. 2.3.1b). However, in many cases dissociation of isolated molecules is even observed for $h\nu \leq E'_{\mathrm{D}}$ (Fig. 2.3.1c, d). This phenomenon is termed spontaneous predissociation. It is related to transitions from the initially excited electronic state to an unstable state (Fig. 2.3.1c) or to a stable electronic state whose dissociation energy is below the originally excited state (Fig. 2.3.1d). The final state can also be the electronic ground state itself; then, the molecule dissociates if $h\nu \geq E_{\mathrm{D}}$. Such intramolecular radiationless transitions result from the mixing of states near crossings of potential curves. They are therefore more common in polyatomic molecules than in diatomic molecules. The typical times for predissociation are between 10^{-12} and 10^{-6} s. Radiationless transitions are also termed internal conversion and intersystem crossing [*Avouris* et al. 1977; *Bixon* and *Jortner* 1968] or as Landau–Zener transitions [*Levine* and *Bernstein* 1987].

The main limitation of single-photon excitation/dissociation processes relevant to laser-chemical processing is the lack of flexibility of available lasers to match the maxima of dissociative transitions in the medium to far UV.

Densities of Excited and Dissociated Species

In photochemical laser processing, reaction rates are directly related to the average number of excited or dissociated molecules. Let us consider the problem for the simple photochemical process

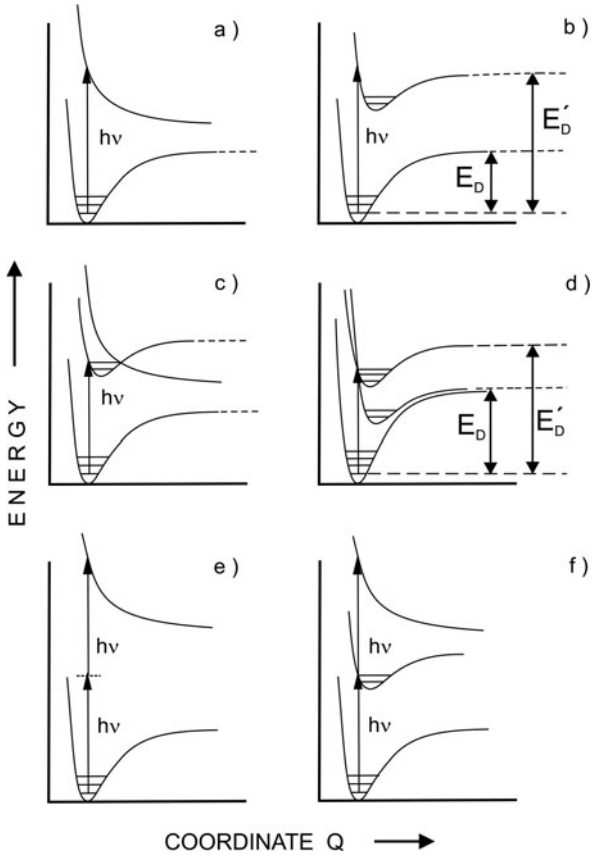

Fig. 2.3.1 a–f Potential energy curves for the electronic ground state and excited states of molecules, showing different cases of optical excitation and dissociation. E_D and E_D' are dissociation energies. Vibrational energy levels are only indicated. Rotational levels are not shown at all. Cases (**a**) to (**d**) show single-photon excitations. (**e**) Coherent two-photon excitation. (**f**) Sequential two-photon excitation. The energies of photons in cases (**e**) and (**f**) are not necessarily equal

$$\mathrm{AB}_\mu + h\nu \underset{\tau_{\mathrm{em}}}{\overset{\sigma}{\longleftrightarrow}} \mathrm{AB}_\mu^* \underset{\tau_{\mathrm{rec}}}{\overset{\tau_{\mathrm{d}}}{\longleftrightarrow}} A + \mu B\,. \qquad (2.3.2)$$

The excitation of molecules AB_μ is characterized by the effective cross section, σ, at the particular laser wavelength. σ depends on the type of reactant, the gas pressure, etc. The effect of pressure broadening, line shifts, etc., also depends on the bandwidth of the laser light. The situation is similar for species AB_μ dissolved in a liquid. The effective cross section can significantly differ from the excitation (absorption) cross section for a single *isolated* molecule, σ_a. The latter is measured under collisionless conditions, and it has large values only if the photon energy

matches the distance between respective energy levels of the molecule and if the transition is allowed by symmetry (selection rules), i.e., if it is optically active. For $h\nu \geq E'_{\mathrm{D}}$ and negligible fluorescence, the absorption cross section is equal to the dissociation cross section, σ_{d}.

The relaxation time for deactivation of AB^*_μ is denoted by τ_{em}. τ_{d} describes the time for dissociation of AB^*_μ in a first-order decomposition process (Chap. 3). τ_{rec} and τ'_{rec} characterize the recombination of A and B to AB_μ and AB^*_μ, respectively. The relaxation times depend on gas pressure.

Electronic absorption and dissociation cross sections of molecules that are of particular relevance in laser processing are summarized in Table V for different laser wavelengths. Most of the values of σ found in the literature refer to effective cross sections.

For an estimation of photochemical processing rates, the concentrations of species A and AB^*_μ, x_{A} and x_{AB^*}, must be known. Stationary values of these are given in [*Bäuerle* 1996].

Multiphoton Excitations

Multiphoton (MP) processes open up additional excitation/dissociation channels and thereby permit one to use the laser light at a particular wavelength more efficiently or to use a much wider variety of precursor molecules.

The number of molecules excited in a MP process depends non-linearly on photon flux. Figures 2.3.1e, f show two different kinds of MP excitations. If the photon energy is smaller than the energy difference between the first optically active excited state and the ground state, excitation is possible only via *coherent* two-photon absorption (case e). The absorption cross section for coherent n-photon excitations is henceforth denoted by ${}^{(n)}\sigma$. The situation is different in case f. Here, the molecule is transferred to the first excited state by absorption of a single photon. The absorption of an additional photon results in dissociation. This process is denoted as *sequential* two-photon absorption. In the simplest case, the cross section of a sequential n-photon excitation is proportional to $\prod_i^n {}^{(1)}\sigma_i$, where ${}^{(1)}\sigma_i$ is the single-photon absorption cross section; $\prod$ denotes the product. The energies of the single photons involved in a MP process are not necessarily equal.

Efficient MP processing can only be performed with high-power pulsed lasers. Because such laser pulses may cause substrate damage, most applications of MP processing are performed with an irradiation geometry where the laser beam propagates parallel to the substrate surface (Fig. 1.2.2b). The relevant processing step can be based on MP ionization (MPI), MP dissociation (MPD), or MP excitation of the precursor molecules.

Photosensitization

Photosensitization denotes a process where photons are absorbed by intermediate species which transfer their excitation energy to acceptor molecules via

collisions [*Calvert* and *Pitts* 1966]. For example, direct photolysis of CH_4 is only possible below 144 nm,

$$CH_4 + h\nu(\lambda < 144\,\text{nm}) \rightarrow CH_2 + H_2\,, \tag{2.3.3}$$

while the Hg-photosensitized reaction can take place at a longer wavelength,

$$Hg(^1S_0) + h\nu(\lambda = 253.7\,\text{nm}) \rightarrow Hg(^3P_1) \tag{2.3.4}$$

$$Hg(^3P_1) + CH_4 \rightarrow Hg(^1S_0) + CH_3 + H\,. \tag{2.3.5}$$

As can be seen from this example, the photoproducts are not necessarily the same in both cases.

Photosensitized reactions are very common in photochemical studies, but cannot be employed in laser microchemistry due to the delocation of the reaction in this process. However, the technique has been applied for large-area, low-temperature growth of epitaxial layers of HgTe [*Irvine* et al. 1984], the deposition of hydrogenated amorphous silicon (a-Si : H) [*Kamimura* and *Hirose* 1986], and etching reactions [*Loper* and *Tabat* 1984].

2.3.2 Infrared Vibrational Excitations

In this subsection we shall discuss some fundamentals on vibrational excitations of free molecules in the electronic ground state. Special emphasis is put on aspects that are relevant to LCP.

Excitation of Isolated Diatomic Molecules

Vibrational excitation of single *isolated* molecules can be realized within the collisionless environment of a molecular beam. Figure 2.3.2 shows an anharmonic potential which shall represent the electronic ground state. Because of anharmonicity, the vibrational levels are not equally spaced. Rotational levels are ignored in the figure although they are essential in excitation processes. For simplicity, we always use the term vibrational transition, even when the rotational state of the molecule is changed simultaneously.

The simplest absorption process is a one-photon (linear) excitation of the vibrational state, $v = 1$, as shown by arrow a. The excitation energy $h\nu = E_{v=1} - E_{v=0}$ is, typically, between $100\,\text{cm}^{-1}$ and some $1000\,\text{cm}^{-1}$ (about 0.01 eV to some 0.1 eV). Arrows b and c indicate excitations of the third and fourth vibrational level by *coherent* two- and three-photon processes, respectively. Such MP processes become quite unlikely for excitations $v > 4$, because of the rapid decrease in σ with such highly non-linear processes. Vibrational levels $v = 2, 3, \ldots$ can also be excited, although with low probability, in a one-photon overtone absorption process using a photon energy $h\nu' = E_v - E_{v=0}$. This is indicated for $v = 2$ by arrow d. MP absorption by *sequential* excitation (case e) becomes quite unlikely for high vibrational levels as

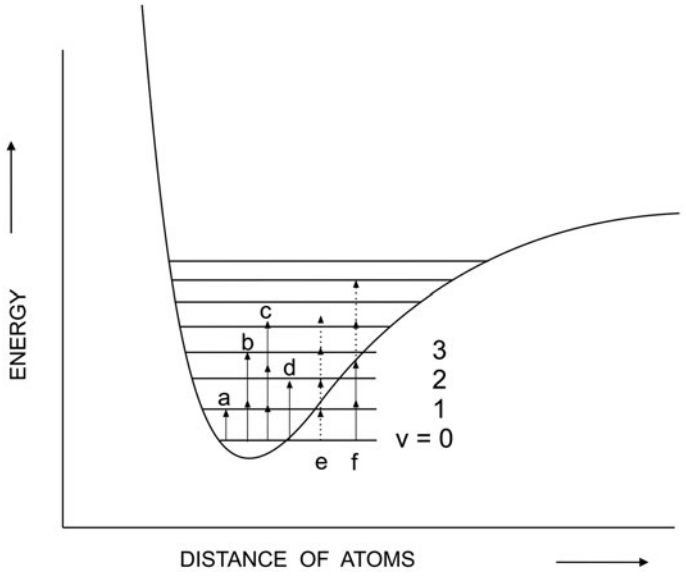

Fig. 2.3.2 Various types of IR vibrational excitations of a single isolated diatomic molecule. For simplicity, rotational levels have been ignored, **a**: one-photon excitation; **b, c**: coherent two- and three-photon excitation; **d**: one-photon overtone excitation; **e**: sequential four-photon excitation; **f**: two-photon coherent excitation (*solid arrows*) followed by sequential excitation (*dotted arrows*). The energies of photons employed in multiphoton excitation processes are not necessarily equal

well, simply because of the (increasing) mismatch between the photon energy and the vibrational energy levels. A combined excitation process is shown in case f. Here, two-photon coherent absorption (solid arrows) is followed by two-photon sequential absorption (dotted arrows). In this way, higher vibrational levels can be excited.

Excitation of Isolated Polyatomic Molecules

In contrast to diatomic molecules, polyatomic molecules can absorb a great number of monochromatic photons even under collisionless conditions. This can be seen from Fig. 2.3.3. The 'superposition' of different vibrational-level systems, corresponding to different normal modes of the molecule, results in different regions of vibrational-level densities. At low energies the vibrational levels are discrete. With increasing energy, their density increases rapidly. The region above a certain energy, E_s, is denoted as *quasi-continuum*. E_s corresponds to, typically, three to ten vibrational quanta for simple polyatomic molecules and to only one vibrational quantum for molecules consisting of many atoms, or such with heavy atoms.

Selective excitation of the particular mode that is in resonance with the IR laser frequency takes place as discussed with diatomic molecules. If this resonant mode is excited up to the quasi-continuum, even a weak intermode anharmonicity is

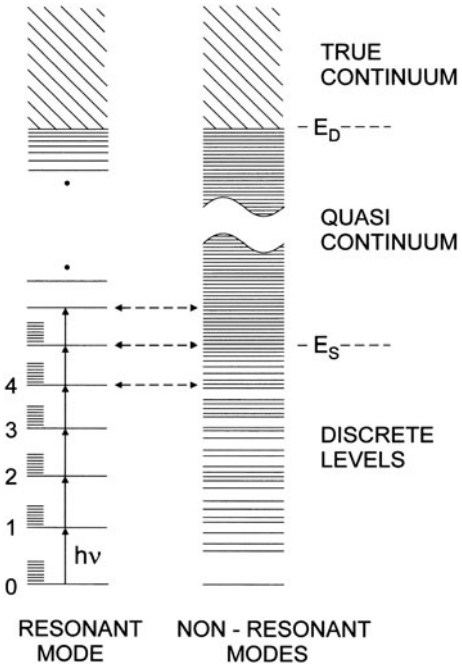

Fig. 2.3.3 Multiphoton vibrational excitation and dissociation of a polyatomic molecule by intense IR radiation. *Left*: vibrational-rotational levels for the mode that is selectively excited by the IR radiation. *Right*: three regimes of vibrational level densities: discrete levels of non-resonant modes, vibrational quasi-continuum, and true continuum

sufficient to cause stochastization of the vibrational energy. In other words, when the vibrational energy stored in the selectively driven mode approaches E_s, it will spread over all the different modes. This mechanism diminishes the number of vibrational quanta in the resonant mode and thereby permits further laser-light absorption. This process takes place again and again. Thus, the vibrational degrees of freedom are subjected to strong heating. The true continuum is reached at the dissociation energy, E_D. Dissociation of the vibrationally excited molecule will take place, in general, via the *lowest* dissociation channel. With the high excitation rates that can be achieved with intense IR lasers, many-photon *superexcitation* of polyatomic molecules far above the dissociation energy has been observed.

The rate of vibrational excitation of a single polyatomic molecule is often written as

$$W_{ex} = \sigma \frac{I}{h\nu}\,, \tag{2.3.6}$$

where σ is the *average* absorption cross section, which depends on laser fluence and pulse length. For polyatomic molecules, σ has values of, typically, 10^{-20} to $10^{-18}\,\mathrm{cm}^2$. The average number of IR photons absorbed per pulse by a *single*

molecule is $\langle n \rangle = \sigma\phi/h\nu$. With polyatomic molecules, 10–100 IR photons can be absorbed with fluences $\phi \approx 1-10\,\mathrm{J/cm^2}$.

Collisionless IR-MP excitation and dissociation of many molecules which are used as precursors in laser-chemical processing, such as SF_6, BCl_3, $CO(CF_3)_2$, CF_3I, and CDF_3, is consistent with the model in Fig. 2.3.3. Highly vibrationally excited molecules and radicals produced by IR-MP excitation/dissociation interact with solid surfaces quite differently than molecules in the vibrational ground state. Examples will be given in various chapters.

The Role of Collisions

Collisions will not only change the lifetime of a particular excitation, but also permit high-level vibrational excitation and dissociation of even diatomic molecules via near-resonant energy transfer. For *pure* gaseous CO, this process can be described by

$$\begin{aligned} \mathrm{CO}(v=0) + h\nu &\leftrightarrow \mathrm{CO}(v=1) \\ \mathrm{CO}(v=1) + \mathrm{CO}(v=1) &\leftrightarrow \mathrm{CO}(v=2) + \mathrm{CO}(v=0) \\ \mathrm{CO}(v=2) + \mathrm{CO}(v=1) &\leftrightarrow \mathrm{CO}(v=3) + \mathrm{CO}(v=0) \end{aligned} \qquad (2.3.7)$$

etc. The transition $v = 0 \rightarrow 1$ which is in resonance with the photon energy $h\nu$ is excited in a one-photon process (Fig. 2.3.2). Subsequently, the energy is transferred to other excited molecules. Thereby, high vibrational states, up to the dissociation limit, can be reached. The same process can take place with lower efficiency (unless there is a coincidence in vibrational energies), between *different* molecules, A and B, including isotopes.

Selectivity

The selectivity of a particular photo-excitation process is determined by (2.3.1). The redistribution of vibrational energy is determined by different relaxation times:

- The time required for spontaneous radiative (dipolar) transitions between low-lying, well-separated vibrational levels which determines the natural linewidth. This is, typically, of the order of 10^{-3} s.
- The time required for *intra*molecular transfer of vibrational energy between different vibrational modes being excited, $\tau_{\text{v-v}}^{\text{A}}$. This time decreases with increasing vibrational anharmonicity and increasing density of vibrational levels. Within the quasi-continuum it is, typically, of the order of 10^{-13} to 10^{-11} s.
- The time required for *inter*molecular transfer of vibrational energy via collisions between molecules either of the *same* kind, $\tau_{\text{v-v}}^{\text{A-A}}$, or of *different* kinds, $\tau_{\text{v-v}}^{\text{A-B}}$. For low-level excitations, energy exchange between molecules of different kinds is less efficient because of the mismatch of vibrational energy levels. For highly excited states the type of colliding molecules becomes almost unimportant.

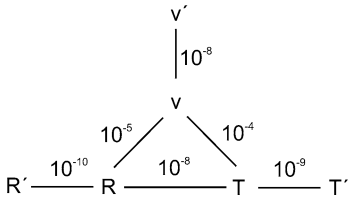

Fig. 2.3.4 Different relaxation channels for energy transfer during binary collisions of molecules, $v' - v$ stands for vibrational-vibrational, $v - T$ for vibrational-translational, and $R - T$ for rotational-translational processes. The numbers represent typical relaxation times for pure gases at 300 K in units of sbar [*Eyring* et al. 1980]

- The time required for molecular vibrational energy to be transferred to translational degrees of freedom, $\tau_{v\text{-}T}$. This is the time required to reach thermal equilibrium within the molecular mixture.

Clearly, $\tau_{v\text{-}v}^{A\text{-}A}$, $\tau_{v\text{-}v}^{A\text{-}B}$, and $\tau_{v\text{-}T}$ vary with experimental conditions such as the molecular density, temperature, and the type of admixtures or solvents. Figure 2.3.4 shows, schematically, various energy-transfer processes and the corresponding relaxation times that are typical for *binary collisions* of gas-phase molecules at 300 K and 1000 mbar. With these conditions, the time between successive collisions is $\tau_c \approx 10^{-10}$ s ($\tau_c^{-1} \approx N\langle\sigma_c v\rangle$; σ_c is the cross section for collisions and v the velocity of molecules).

Classification of IR-MP Photochemistry

IR-MP photochemistry based on pulsed-laser excitation of high vibrational states can be classified into four different cases:

Mode- or *bond-selective* photochemistry requires an excitation rate that is large compared to the rate of intramolecular vibrational energy transfer. This would need both a mode which is fairly isolated from other vibrational modes and high-intensity picosecond or femtosecond resonant excitation. Mode isolation is well fulfilled for diatomic molecules, because they have only one vibrational degree of freedom. In fact, vibrationally enhanced photochemical reactions based on low-level excitations of diatomic molecules have been reported. Collisionless MP, high-level excitation/dissociation by monochromatic infrared radiation is, however, unlikely/impossible (Fig. 2.3.2). For polyatomic molecules the situation is somewhat complementary. They permit high-level vibrational excitation but no bond selectivity (Fig. 2.3.3). Laser processing based on bond-selective vibrational excitation/dissociation of precursor molecules has not been demonstrated.

The (three) remaining cases of selective vibrational excitations have been employed in laser processing:

Molecule-selective excitation requires

$$W_{ex} \gg \frac{1}{\tau_{v\text{-}v}^{A\text{-}B}} . \tag{2.3.8}$$

The vibrational energy within molecules A which interact with the IR light is in equilibrium. Other molecules within the mixture, B, that are *not* directly excited are in lower vibrational states. Thus, molecules in resonance with the laser frequency acquire a higher vibrational temperature than all other molecules. High-level, molecule-selective vibrational excitation can take place as discussed with regard to Fig. 2.3.3, and via collisions analogous to (2.3.7). The time for energy transfer from A to B or from A to surface atoms, $\tau_{\text{v-v}}^{\text{A-B}}$, must be long compared to the time of resonant energy transfer, A to A.

Molecule-selective excitation and dissociation is of practical interest, e.g., in laser *isotope separation* [*Letokhov* 1983]. With isotopes whose mismatch between vibrational levels is of the order of $k_{\text{B}}T$, collisional excitations of the type (2.3.7) must be avoided.

Non-equilibrium excitation is achieved if

$$W_{\text{ex}} \gg \frac{1}{\tau_{\text{v-T}}} \,. \tag{2.3.9}$$

In this case, there may be vibrational equilibrium among all molecules in the mixture, but no equilibrium between vibrational and translational degrees of freedom. Condition (2.3.9) can only be fulfilled if the gas mixture does not contain any component with fast v − T relaxation. For example, with pure SF_6 one finds that with gas pressures $p(SF_6) \approx 0.1$ mbar and low cw CO_2-laser-light intensities, about 50% of the molecules can be in a non-equilibrium state. Because of the difference in the vibrational and translational temperatures, non-selective vibrational photochemistry is possible when the time constant for the *fastest* reaction channel is shorter than $\tau_{\text{v-T}}$. The most important application is IR laser-induced radical synthesis [*Letokhov* 1988].

Photothermal excitation is characterized by

$$W_{\text{ex}} \ll \frac{1}{\tau_{\text{v-T}}} \,. \tag{2.3.10}$$

All molecules within the reaction volume defined by the laser beam are in thermal equilibrium. The vibrational energy is immediately thermalized.

Since σ in (2.3.6) and $\tau_{\text{v–T}}$ depend on temperature, (2.3.9) transforms to

$$W_{\text{ex}}\tau_{\text{v–T}} = \sigma(T)\frac{I}{h\nu}\tau_{\text{v–T}}(T) \gg 1 \,. \tag{2.3.11}$$

The decrease in relaxation time with temperature can be described by the Landau–Teller relation, $\tau_{\text{v–T}}(T) = \tau_{\text{v–T}}(0)\exp(\mu/T^{1/3})$, where $\mu > 0$. The cross section $\sigma(T)$ can increase or decrease with temperature. Because $T = T(I)$, (2.3.11) is a non-monotonic function of intensity with regions that correspond to either thermal or non-thermal gas-phase excitations.

2.4 Surface Excitations

In this section we give an overview on non-thermal or not purely thermal excitations of solid surfaces and adsorbate–adsorbent systems.

2.4.1 External Photoeffect

The external photoeffect denotes the ejection of electrons from a solid surface that is irradiated with photons. With metals, photoelectron emission is observed if $h\nu \geq h\nu_G$, where ν_G denotes a threshold frequency which is located within the VIS and UV [λ_G(Cs, Cu, Pt) $\approx$ 639, 277, 231 nm]. Photoelectron emission has also been observed with semiconductors and insulators. With photon energies $h\nu < E_g$, such electrons may originate from single-photon excitations of occupied electron traps within the band gap or from MP excitations across E_g (Fig. 2.1.1). The latter mechanism seems to be quite common with ps- and fs-laser pulses. In any case, if the solid is immersed in a reactive ambient, molecules that capture an electron can become unstable. Spontaneous decay or partial fragmentation of the molecule may be the consequence [*Schröder* et al. 1987]. Further fragmentation can take place via collisions with other molecules or with the substrate surface (Fig. 2.4.1).

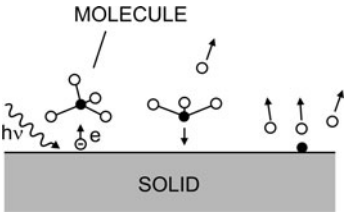

Fig. 2.4.1 Decomposition of a molecule by photoelectron capture

2.4.2 Internal Photoeffect

The internal photoeffect is the generation of electron–hole pairs in semiconductors or insulators by single-photon or multiphoton excitation (Fig. 2.1.1; we will not bother with direct and indirect processes as this is outlined in standard textbooks). Electrons and holes change the optical properties of the material and thereby its interaction with laser light (Sect. 7.6). Moreover, photocarriers play a fundamental role in many types of molecule–surface interactions relevant in LCVD, surface modification, and etching (Fig. 15.1.1). The analysis of such processes requires detailed information on the carrier distribution.

Carrier Densities

For an intrinsic semiconductor, the carrier density can be described, in a simple approximation, by

$$\frac{\partial N_c(\boldsymbol{x},t)}{\partial t} = \alpha(\nu)\frac{I(\boldsymbol{x},t)}{h\nu} - k^{\mathrm{rec}}[N_c(\boldsymbol{x},t) - \overline{N}_c(T)] + \nabla[D_c(\boldsymbol{x},t)\nabla N_c(\boldsymbol{x},t)]\,. \tag{2.4.1}$$

The first term describes the generation of photocarriers by inter-band absorption. The second term represents the loss of carriers by recombination, where $k^{\mathrm{rec}} = \tau_{\mathrm{rec}}^{-1}$ is the rate constant for electron–hole pair recombination and $\overline{N}_c(T)$ the carrier density in (thermal) equilibrium. The last term describes the diffusion of carriers.

The recombination time, τ_{rec}, depends on the material and the concentration of photocarriers. It is determined by direct or indirect band-to-band recombination, by multicarrier (Auger) recombination, and by defects and impurities. Thus, values of τ_{rec} near the surface differ somewhat from those within the bulk. τ_{rec} is, typically, between a few picoseconds and several seconds.

The diffusion coefficient can be written as

$$D_c = \frac{\sigma_e D_e + \sigma_h D_h}{\sigma_e + \sigma_h}\,. \tag{2.4.2}$$

D_e and D_h are the actual diffusion coefficients of electrons and holes and σ_e and σ_h the corresponding conductivities.

Equation (2.4.1) ignores laser-induced heating and collective (plasma) phenomena which are observed at very high carrier densities [*Yoffa* 1980].

Let us consider electron–hole pair generation in some more detail for silicon. Because E_g (Si; 300 K) $\approx$ 1.1 eV, bandgap excitations become possible with $\lambda < 1\,\mu$m. With increasing temperature, E_g decreases, and thereby the minimum photon energy for excitation. With carrier densities $N_c > 10^{18}\,/\mathrm{cm}^3$, Auger recombination becomes dominant. Then, the carrier lifetime decreases with increasing concentration as

$$\tau_{\mathrm{rec}} = \frac{1}{k^{\mathrm{rec}}} \propto \frac{1}{N_c^2}\,. \tag{2.4.3}$$

For room temperature, the second term in (2.4.1) can be substituted by ζN_c^3 with $\zeta \approx 4 \times 10^{-31}\,\mathrm{cm}^6/\mathrm{s}$. For example, an initial carrier density of $N_c = 10^{22}\,/\mathrm{cm}^3$ decreases via Auger recombination within about 10^{-10} s to 1%.

Avalanche Ionization

With high laser-light intensities, the rate of electron excitation may overtake the rate of energy loss via generation of phonons. Then, electrons become highly excited and, eventually, attain sufficient energy to generate secondary electron–hole pairs by impact ionization of lattice atoms/molecules (the contribution of holes can often be ignored because of their low mobility, in particular in insulators and large bandgap semiconductors). Because of the positive feedback involved in this process, very high electron densities can be generated. This effect is often termed avalanche ionization. With such conditions, even originally highly transparent materials can become strongly absorbing and, as a consequence, *optical breakdown* and plasma formation is often observed.

With very high laser-light intensities, electrons may even be generated when $h\nu < E_g$. This is mediated via highly non-linear processes such as defect enhanced or coherent MP absorption (Fig. 2.1.1), light-induced defect formation, thermal ionization, and MP ionization (MPI). Further details on multiphoton- and avalanche-ionization are presented in Sect. 13.6.

2.4.3 Electromagnetic Field Enhancement, Catalytic Effects

Various types of electromagnetic field enhancements observed on solid surfaces can significantly alter both surface morphologies and reaction rates in laser-material processing [*Plech* et al. 2009; *Brodoceanu* et al. 2007; *Aussenegg* et al. 1983]. Such field enhancements may be related to surface roughnesses, nucleation centers, clusters, the excitation of surface polaritons or plasmons, interference phenomena, particulates etc. Further details are outlined in Sect. 5.3.7.

The physical and chemical properties of surfaces change during laser ablation, etching, deposition, doping, and surface modification. Changes in surface properties may cause autocatalytic effects, as observed during laser-induced metal deposition, catalyze electroless plating, as observed after polymer ablation, etc.

Some of these different effects are discussed in detail in other chapters.

2.4.4 Adsorbed Molecules

Adsorption of molecules on solid surfaces changes their electronic and vibrational properties and thereby the absorption cross section for the interaction with light. Additionally, the number of vibrational degrees of freedom can increase. With a diatomic molecule such as CO, adsorption changes the number of vibrational degrees of freedom from one to six (Fig. 2.4.2). *Selective* electronic or vibrational excitation of adsorbate–adsorbent systems may result in selective desorption or photolysis of adsorbed species, in changes in the catalytic properties of the surface, etc. [*Aussenegg* et al. 1983].

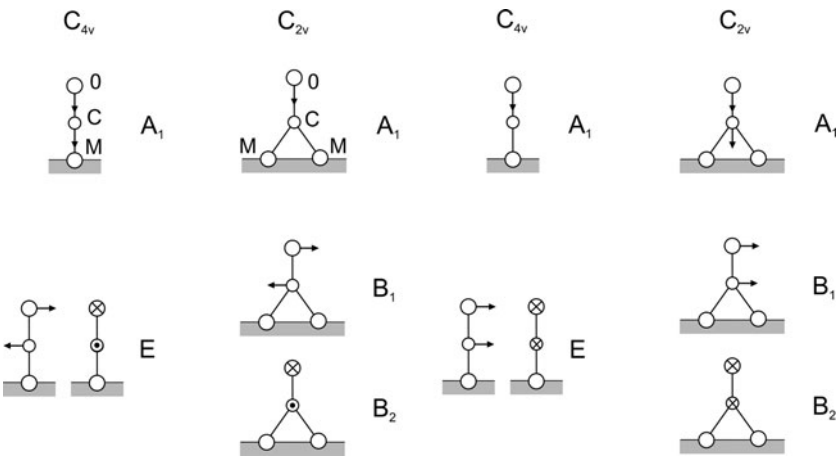

Fig. 2.4.2 Normal modes of CO molecules adsorbed on a metal surface in top site (C_{4v} symmetry) and bridging site (C_{2v} symmetry) positions; ⊗ and ⊙ indicate elongations perpendicular to the plane of the drawing. Vibrations with A and B symmetry are non-degenerate, vibrations with E symmetry are two-fold degenerate

It should be emphasized that the consideration of *single* effects oversimplifies the situation. A real understanding of chemical reactions at interfaces requires simultaneous treatment of the different interactions in the gas phase, adsorbed phase, and solid phase and, in addition, the often subtle couplings between them.

Chapter 3
Reaction Kinetics and Transport of Species

An estimation of processing times in LCP requires the knowledge of reaction rates. In this chapter we shall outline some fundamentals of the kinetics and mass transport of laser-induced chemical reactions, with special emphasis on heterogeneous reactions at gas–solid interfaces (Fig. 1.2.1).

Heterogeneous activation of a chemical reaction by direct laser-light irradiation of the substrate can take place within adsorbed layers or at gas–solid, liquid–solid, or solid–solid interfaces (Fig. 1.2.1a, b, d, e). The reaction zone, i.e., the area on the substrate surface where the reaction takes place, is not necessarily the same size as the laser spot but it can be smaller or larger (Sect. 5.3). If laser light at parallel incidence is used to excite or dissociate species that do *not* react within the ambient medium (except recombination) but only on the substrate surface, we still term the reaction heterogeneous.

With *homogeneous* activation, the first step of excitation *and* subsequent reaction takes place within a certain volume of the gas, the liquid, or the solid. In LCP, such reactions are activated mainly by using parallel incidence of the laser beam (Fig. 1.2.1c).

Let us consider a chemical reaction of the type

$$\zeta_{AB}AB + \zeta_{CD}CD + \ldots \rightleftarrows \zeta_{AD}AD + \zeta_{BC}BC + \ldots , \qquad (3.0.1)$$

where AB, CD, etc., are reactants which may include the substrate as, for example, in laser-induced chemical etching of Si in Cl_2. AD, BC, etc., are reaction products which may desorb from the substrate surface or may stick on it. The ζ_i are stoichiometric coefficients which characterize the particular reaction path and may differ for heterogeneous and homogeneous reactions. In general, reactions of type (3.0.1) will consist of a number of consecutive steps:

- Transport of reactants into the reaction volume.
- Transport of product atoms or molecules generated, for example, in the gas phase, to the surface with possible recombination or secondary reactions on the way.
- Adsorption of one or more reactants on the surface.
- Pyrolytic or photolytic activation of molecules at or near the substrate surface.
- Pyrolytic or photolytic activation of the substrate surface.

D. Bäuerle, *Laser Processing and Chemistry,* 4th ed.,
DOI 10.1007/978-3-642-17613-5_3, © Springer-Verlag Berlin Heidelberg 2011

- Transport of electrons, atoms, molecules, etc., within the solid surface.
- Condensation or further reactions of excited molecules on the surface.
- The chemical reaction itself.
- Desorption of reaction products from the surface.
- Transport of reaction products out of the reaction volume.

Clearly, in different types of LCP, one or more of these steps either will not occur at all or will differ significantly.

The *net* reaction rate in (3.0.1) is given by

$$W = W_{\rightarrow} - W_{\leftarrow} \,, \tag{3.0.2}$$

where $W_{\rightarrow}$ and $W_{\leftarrow}$ denote the reaction rates in forward and backward directions. The (dynamic) equilibrium is characterized by $W_{\rightarrow} = W_{\leftarrow}$. Away from equilibrium, the concentration of reactants and reaction products changes with time. If the concentration is uniform and if mass transport limitations are ignored, the temporal change in reaction rate for a closed system is described by

$$\begin{aligned} W &= -\frac{1}{\zeta_{\mathrm{AB}}}\frac{\mathrm{d}N_{\mathrm{AB}}}{\mathrm{d}t} = -\frac{1}{\zeta_{\mathrm{CD}}}\frac{\mathrm{d}N_{\mathrm{CD}}}{\mathrm{d}t} = \cdots \\ &= \frac{1}{\zeta_{\mathrm{AD}}}\frac{\mathrm{d}N_{\mathrm{AD}}}{\mathrm{d}t} = \frac{1}{\zeta_{\mathrm{BC}}}\frac{\mathrm{d}N_{\mathrm{BC}}}{\mathrm{d}t} = \cdots \,. \end{aligned} \tag{3.0.3}$$

The total number density of species is given by

$$N = \sum_i N_i \,. \tag{3.0.4}$$

In homogeneous gas-, liquid-, or solid-phase reactions, N_i is the number of atoms (molecules) per unit volume. Here, N_i includes both reactants and reaction products. In adsorbed-phase processing, N_i is the number of species per unit area. Instead of N_i we often introduce molar ratios, $x_i = N_i/N$, with $\sum x_i = 1$.

In many cases of LCP, the concentration of reaction products is kept small so that $x_{\mathrm{AD}}, x_{\mathrm{BC}} \ll 1$. Thus, $W_{\rightarrow} \gg W_{\leftarrow}$ and the net reaction rate can be approximated by $W \approx W_{\rightarrow}$.

Irrespective of the type of reaction or the detailed activation mechanism, the reaction rate is either limited by the chemical kinetics or by mass transport.

Within the *kinetically* controlled regime, the reaction rate depends on the detailed activation mechanisms, the density of reactants, the physical and chemical properties of the substrate, and the laser parameters.

Within the *mass transport* limited regime, the reaction rate depends on the maximum flux of species into the reaction zone, but not on the detailed activation mechanisms. Here, strong gradients in the concentration of reactants occur near the reaction zone.

3.1 Photothermal Reactions

For thermally activated reactions of type (3.0.1) and $W_{\rightarrow} \gg W_{\leftarrow}$, the (net) reaction rate can be described by

$$W(\boldsymbol{x},t) = k(T) N_{\mathrm{AB}}^{\gamma_{\mathrm{AB}}} N_{\mathrm{CD}}^{\gamma_{\mathrm{CD}}} \cdots = W_0(\boldsymbol{x},t) \exp\left(-\frac{\Delta E}{k_{\mathrm{B}} T(\boldsymbol{x},t)}\right) , \tag{3.1.1}$$

where the (phenomenological) rate constant is given by the Arrhenius law

$$k(T) = k_0 \exp\left(-\frac{\Delta E}{k_{\mathrm{B}} T(\boldsymbol{x},t)}\right) , \tag{3.1.2}$$

where ΔE is the *apparent* chemical activation energy. In gas-phase reactions, typical values of ΔE are between 0.5 and 5 eV (about 10–100 kcal/mol). k_0 is a pre-exponential factor whose dimension depends on the total reaction order. It also depends on temperature, the spatial orientation of colliding species (steric factor), the distribution of rotational and vibrational energy of molecules, etc. [*Hirschfelder* et al. 1964; *Hänggi* et al. 1990]. k_{B} is the Boltzmann constant (if ΔE is given in kcal/mol, k_{B} is replaced by the gas constant, R_{G}). The temperature distribution can be written as $T(\boldsymbol{x},t) = T(\infty) + \Delta T(\boldsymbol{x},t)$, where $\Delta T(\boldsymbol{x},t)$ is the laser-induced temperature rise and $N_i \equiv N_i(\boldsymbol{x},t)$. γ_i are partial reaction orders. The total reaction order is

$$\gamma = \gamma_{\mathrm{AB}} + \gamma_{\mathrm{CD}} + \cdots = \sum_i \gamma_i \ . \tag{3.1.3}$$

Here, the summation includes the reactants only. γ is, typically, within the range $0 \le \gamma \le 3$ and includes fractional numbers. In thermodynamic equilibrium, or close to it, γ_i coincide, for elementary reactions, with the stoichiometric coefficients, ζ_i, as introduced in (3.0.1).

Sometimes, it is more convenient to use instead of (3.1.2) the Frank–Kamenetsky expansion:

$$k(T) \approx k_0 \exp\left(-\frac{\mathscr{E}}{T_{\mathrm{c}}}\right) \exp\left(-\frac{\mathscr{E}}{T_{\mathrm{c}}} \frac{T_{\mathrm{c}} - T}{T_{\mathrm{c}}}\right) , \tag{3.1.4}$$

where T_{c} is the maximum temperature and $\mathscr{E} \equiv \Delta E / k_{\mathrm{B}}$.

The reaction enthalpy (reaction heat at constant pressure) is given by $\Delta H = \Delta H_{\rightarrow} - \Delta H_{\leftarrow}$, where $\Delta H_{\rightarrow} \equiv \Delta E$ (Fig. 3.1.1). We term a reaction exothermal if $\Delta H < 0$ and endothermal if $\Delta H > 0$. The reaction coordinate represents the energetically most favorable path in the (multidimensional) phase space in which the molecules participating in the reaction are described.

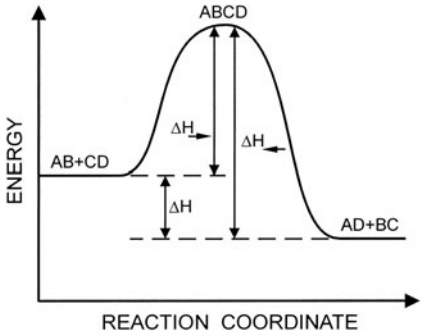

Fig. 3.1.1 Illustration of the reaction enthalpy $\Delta H = \Delta H_{\rightarrow} - \Delta H_{\leftarrow}$. The activation energy for the reaction AB + CD → AD + BC is $\Delta E \equiv \Delta H_{\rightarrow}$. The reaction is exothermal if $\Delta H < 0$ and endothermal if $\Delta H > 0$

If the reaction proceeds within a closed system, the *net* reaction rate decreases continuously with time and, finally, becomes zero when $W_{\rightarrow} = W_{\leftarrow}$. From the law of mass action we can calculate the equilibrium constant for a homogeneous reaction as follows:

$$K_{\mathrm{ce}} \equiv K_{\mathrm{ce}}(T) = \frac{k_{\rightarrow}}{k_{\leftarrow}} = \frac{N_{\mathrm{AD}}^{\gamma_{\mathrm{AD}}} N_{\mathrm{BC}}^{\gamma_{\mathrm{BC}}} \cdots}{N_{\mathrm{AB}}^{\gamma_{\mathrm{AB}}} N_{\mathrm{CD}}^{\gamma_{\mathrm{CD}}} \cdots} \,. \tag{3.1.5}$$

The index ce denotes chemical equilibrium.

Equation (3.1.5) can also be applied to heterogeneous systems in which one of the reactants or reaction products is solid while the other constituents are gaseous or liquid. Consider, for example, etching of Si in a Cl_2 atmosphere:

$$\mathrm{Si} + 2\mathrm{Cl}_2 \rightleftarrows \mathrm{SiCl}_4 \,. \tag{3.1.6}$$

The law of mass action can be written in the form

$$K'_{\mathrm{ce}} = \frac{k \rightarrow}{k \leftarrow} = \frac{N_{\mathrm{SiCl_4}}}{N_{\mathrm{Cl_2}}^2 N_{\mathrm{Si}}} \,, \tag{3.1.7}$$

where N_{Si} is the *gas-phase* concentration of Si atoms which is determined by the saturation pressure p_{Si} above the (solid) silicon surface. Because p_{Si} depends only on temperature, it is commonly included into K_{ce}, i.e.,

$$K_{\mathrm{ce}} = \frac{N_{\mathrm{SiCl_4}}}{N_{\mathrm{Cl_2}}^2} \,, \tag{3.1.8}$$

where $K_{\mathrm{ce}} = K'_{\mathrm{ce}} N_{\mathrm{Si}}$. In other words, in reactions of type (3.1.6) the solid phase is, in general, not explicitly considered in the law of mass action. The situation is

similar in homogeneously induced reactions if one of the reaction products condenses. Consider (3.1.6) from right to left. Assume that gaseous $SiCl_4$ is decomposed within a laser beam at parallel incidence to the substrate (Fig. 1.2.1c). If the partial pressure of Si atoms exceeds the saturation pressure, Si condenses and forms clusters and a solid film.

The Arrhenius law implies several assumptions. In particular, it is valid when the translational, vibrational and rotational temperatures are equal, i.e., if $T_{\mathrm{trans}} = T_{\mathrm{vib}} = T_{\mathrm{rot}}$, and if the system is close to equilibrium. In many cases, however, the Arrhenius law can even be applied to systems that are far from equilibrium.

A further comment seems to be appropriate. Equation (3.0.1) describes a *net* reaction which may include many intermediate steps and parallel reaction pathways. Each of these is characterized by a (different) rate constant, k_j. The *overall* reaction rate observed experimentally is dominated by the slowest step within the fastest reaction channel, and this channel can change with experimental parameters. This is the reason why k_0 and ΔE in (3.1.2) can be considered as constants only within certain ranges of temperatures, molecular densities, etc. It also explains why ΔE in (3.1.2) is denoted as an *apparent* activation energy. For the same reasons, γ_i do not coincide, in general, with ζ_i of the corresponding net reaction.

As a final point we note that the reaction rate, W, is proportional to but not identical with the processing rate. This becomes evident from the (heterogeneous) reaction

$$\mathrm{C_2H_2} \rightarrow 2\mathrm{C}(\downarrow) + \mathrm{H_2}\ , \tag{3.1.9}$$

where the *deposition* rate is given by

$$W_{\mathrm{D}}(\mathrm{cm/s}) = \frac{Zm}{\varrho} W(\mathrm{species/cm^2\ s})\ . \tag{3.1.10}$$

Here Z is the number of atoms (molecules) deposited per formula unit, and m and ϱ their mass and mass density, respectively.

3.2 Photochemical Reactions

For photochemically activated reactions the rate can be described by

$$W(\boldsymbol{x}, t) = W_0' \prod_i \left[{}^{(n)}\sigma_i \left(\frac{I(\boldsymbol{x}, t)}{h\nu} \right)^n \right]^{\gamma_i} = k'(I) N_{\mathrm{AB}}^{\gamma_{\mathrm{AB}}} N_{\mathrm{CD}}^{\gamma_{\mathrm{CD}}} \cdots\ , \tag{3.2.1}$$

where

$$W_0' = k_0' N_{\mathrm{AB}}^{\gamma_{\mathrm{AB}}} N_{\mathrm{CD}}^{\gamma_{\mathrm{CD}}} \cdots\ , \tag{3.2.2}$$

and

$$k'(I) = k'_0 \prod_i \left[{}^{(n)}\sigma_i \left(\frac{I(\boldsymbol{x}, t)}{h\nu} \right)^n \right]^{\gamma_i} . \tag{3.2.3}$$

$\prod$ denotes the product over all species i to be excited; k'_0, and thereby W'_0, depends on the relaxation times relevant for selective excitation of species (Chap. 2). To illustrate (3.2.1), we consider a number of different cases:

- Single-photon excitation of a single type of reactant, AB, that reacts in a first-order reaction which is characterized by $i = \mathrm{AB}$, $n = 1$, $\gamma_{\mathrm{AB}} = 1$, and $\gamma_{\mathrm{CD}} = 0$. Thus, the rate constant is

$$k'(I) = k'_0 \sigma_{\mathrm{AB}} \frac{I}{h\nu} . \tag{3.2.4a}$$

  $\sigma_{\mathrm{AB}} \equiv {}^{(1)}\sigma_{\mathrm{AB}}$ is the single-photon excitation cross section.
- Coherent n-photon excitation of species AB that react in a first-order reaction where $i = \mathrm{AB}$, $n \neq 1$, $\gamma_{\mathrm{AB}} = 1$, and $\gamma_{\mathrm{CD}} = 0$. Thus,

$$k'(I) = k'_0 {}^{(n)}\sigma_{\mathrm{AB}} \left(\frac{I}{h\nu} \right)^n . \tag{3.2.4b}$$

- Single-photon excitation with two excited species, AB and CD, that react with partial reaction orders γ_{AB} and γ_{CD}. Thus, $i = \mathrm{AB}, \mathrm{CD}$ and $n_{\mathrm{AB}} = n_{\mathrm{CD}} = 1$ so that

$$k'(I) = k'_0 \left(\frac{\sigma_{\mathrm{AB}} I}{h\nu} \right)^{\gamma_{\mathrm{AB}}} \left(\frac{\sigma_{\mathrm{CD}} I}{h\nu} \right)^{\gamma_{\mathrm{CD}}} . \tag{3.2.4c}$$

- Sequential n-photon excitation of a single reactant, AB, that react with partial reaction order γ_{AB}

$$k'(I) = k'_0 \left({}^{(1)}\sigma_{\mathrm{AB}} \frac{I}{h\nu} \right)^{n\gamma_{\mathrm{AB}}} . \tag{3.2.4d}$$

Here, the cross sections for sequential excitation steps have been assumed to be equal, and any deactivation of species during these steps has been ignored.

In the case of a mixture of AB and CD where, however, only molecules AB are excited in a coherent n-photon process, the reaction rate is described by

$$W = k'_0 \left[{}^{(n_{\mathrm{AB}})}\sigma_{\mathrm{AB}} \left(\frac{I}{h\nu} \right)^{n_{\mathrm{AB}}} \right]^{\gamma_{\mathrm{AB}}} N_{\mathrm{AB}}^{\gamma_{\mathrm{AB}}} N_{\mathrm{CD}}^{\gamma_{\mathrm{CD}}} . \tag{3.2.5}$$

3.3 The Concentration of Species

The reaction rates in LCP depend on the density of relevant species within the reaction zone. This density can be calculated from the following basic equations:

- The equations of continuity for the individual species (diffusion equations).
- The equation of overall continuity.
- The heat transport equation.
- The Navier–Stokes equation. If the viscosity is ignored, this is also called the Euler equation.

Besides the transport equations, we have the equation of state, which relates between the pressure, the temperature, and the concentration of species.

The formulas presented subsequently apply to both heterogeneous and homogeneous laser-induced reactions. However, the meaning of the various quantities, the reaction rates, and the reaction pathways may be quite different in both cases. With heterogeneous reactions, W describes the number of species that react per unit time per unit area, while with homogenous reactions W is the number of species that react per unit time per unit volume. Furthermore, with a heterogeneous reaction the relevant temperature distribution, $T(\boldsymbol{x}, t)$, is that induced on the solid surface, while with a homogeneous reaction it is that induced within the volume.

3.3.1 Basic Equations

Let us consider a non-equimolecular first-order reaction of the type

$$\mathrm{AB}_\mu + \mathrm{M} \underset{k_2,k_4}{\overset{k_1,k_3}{\rightleftharpoons}} \mathrm{A} + \mu\mathrm{B} + \mathrm{M}\,. \tag{3.3.1}$$

The decomposition of molecules AB_μ shall take place heterogeneously at the solid surface, i.e., at the interface between the solid and the ambient medium and/or homogeneously within the volume just above the substrate surface. Surface and volume forward reactions shall be characterized by rate constants k_1 and k_3, respectively. M shall be a carrier gas, a liquid solvent, or a solid. In gas-phase reactions a carrier gas (diluent) is often added simply because it is more convenient to work at normal total pressure instead of reduced pressure. The carrier gas, M, can be inert or it can participate in the reaction as, e.g., $\mathrm{H_2}$ during deposition of Si from $\mathrm{SiH_4} + \mathrm{H_2}$. In any case, in the presence of a carrier gas, $N_{\mathrm{AB}} \ll N_{\mathrm{M}}$. A and B are products of the forward reaction. A shall be the relevant species for surface processing. If A is generated in the volume, it must first diffuse to reach the substrate surface to be processed. Species A can simply stick on the surface and form a deposit or else react further. In the backward reaction, species A react with B to form the original constituent. The backward reaction between condensed species A and molecules B

is characterized by k_2, while the recombination between A and B within the volume is described by k_4. Henceforth we make the following assumptions:

- The mean free path of molecules, λ_m, should be much smaller than the width of the reaction zone, $\mathscr{w}$, i.e., $\lambda_m \ll \mathscr{w}$. Otherwise, the transport of heat and species must be calculated from the Boltzmann equation.
- The reaction shall be so slow that pressure gradients can be ignored (isobaric conditions).
- External forces are ignored.
- The contribution of the Dufour effect (transport of energy originating from a concentration gradient) to the thermal flux is omitted.
- Any generation of heat due to the finite viscosity of the medium is ignored.
- The substrate shall not be melted.

The basic equations are listed in the following for the example of the reaction (3.3.1).

Diffusion Equations

The equations of continuity for the *individual* species can be written in the form

$$\frac{\partial N_i}{\partial t} + \nabla \boldsymbol{J}_i = Q_{\mathrm{v},i} \ , \tag{3.3.2}$$

where i stands for all species within the volume of the ambient medium, i.e., $i = 1, 2, \ldots, j$. For the example of (3.3.1) we have $i \equiv \mathrm{AB}_\mu$, A, B, and M. $\boldsymbol{J}_i = \boldsymbol{J}_i(\boldsymbol{x}, t)$ is the flux, and $Q_{\mathrm{v},i}$ the source term, which is the *net* rate of species i generated within the volume:

$$Q_{\mathrm{v,AB}} = -W_\mathrm{v} = -k_3(T) N_\mathrm{AB} + k_4(T) N_\mathrm{A} N_\mathrm{B}^\mu \ . \tag{3.3.3}$$

The flux of species i with respect to stationary coordinates is

$$\boldsymbol{J}_i = N_i \boldsymbol{v}_i \ , \tag{3.3.4}$$

where $\boldsymbol{v}_i \equiv \boldsymbol{v}_i(\boldsymbol{x}, t)$ is the mean velocity of species i, i.e., the sum of the velocities of molecules i within a small volume element divided by the number of molecules. With the approximations made, each flux, $\boldsymbol{J}_i$, can be written as a sum of the diffusion flux and the hydrodynamic flux, for example,

$$\boldsymbol{J}_\mathrm{AB} = -N D_\mathrm{AB} \left(\nabla \frac{N_\mathrm{AB}}{N} + k_\mathrm{T}^\mathrm{AB} \nabla \ln T \right) + N_\mathrm{AB} \boldsymbol{v} \ , \tag{3.3.5}$$

where $N = \sum_i N_i$. The first term in (3.3.5) describes ordinary diffusion, where $D_\mathrm{AB} = D_\mathrm{AB}(T(\boldsymbol{x}, t))$ is the molecular diffusion coefficient. The second term describes thermal diffusion of species AB_μ, where $k_\mathrm{T}^\mathrm{AB} \equiv k_\mathrm{T}^\mathrm{AB}(x_i(\boldsymbol{x}, t))$ is the

thermal diffusion ratio and $x_i = N_i/N$. Diffusion is superimposed on the hydrodynamic flow (third term); $\boldsymbol{v}$ is the average velocity of *all* species and it is given by

$$\boldsymbol{v} = \frac{1}{N}\sum_i N_i \boldsymbol{v}_i = \frac{1}{N}\sum_i \boldsymbol{J}_i = \frac{1}{N}\boldsymbol{J} \ , \tag{3.3.6}$$

where $\boldsymbol{J}(\boldsymbol{x}, t)$ is the total flux. $\boldsymbol{v}$ can be determined from the equation of (overall) continuity.

Equation (3.3.5) is exact only for binary diffusion. For a gas mixture, in principle, the multicomponent Stefan–Maxwell equations for diffusion should be employed [*Bird* et al. 1960]. However, it is a common approximation to use (3.3.5) even in such cases, but consider D_{AB} as an effective molecular diffusion coefficient. If a diluent is present, binary diffusion is certainly a good approximation as long as $N_{\mathrm{AB}} \ll N_{\mathrm{M}}$. The flux of the other species can be written in analogy to (3.3.5).

The Equation of Continuity

The sum of equations (3.3.2) yields the equation of (overall) continuity

$$\frac{\partial N}{\partial t} + \nabla(N\boldsymbol{v}) = \sum_i Q_{\mathrm{v},i} \ . \tag{3.3.7}$$

Heat Transport Equation

For the present problem, the heat equation is most conveniently written in the form

$$\frac{\partial}{\partial t}\left(\sum_i N_i E_i^{\mathrm{a}}\right) + \nabla \boldsymbol{S}_{\mathrm{T}} = Q \ , \tag{3.3.8}$$

where $\boldsymbol{S}_{\mathrm{T}}$ is the total energy flux, which is given by

$$\boldsymbol{S}_{\mathrm{T}} = \sum_i \boldsymbol{J}_i H_i^{\mathrm{a}} - \kappa \nabla T \ . \tag{3.3.9}$$

The (internal) energy per molecule is

$$E_i^{\mathrm{a}}(T) = E_{i0}^{\mathrm{a}} + \int_{T(\infty)}^{T} c_{\mathrm{v},i}(T')\,\mathrm{d}T' \ .$$

The corresponding enthalpy is

$$H_i^{\mathrm{a}}(T) = H_{i0}^{\mathrm{a}} + \int_{T(\infty)}^{T} c_{\mathrm{p},i}(T')\,\mathrm{d}T' \ .$$

Here $c_{\mathrm{v},i}$ and $c_{\mathrm{p},i}$ are the heat capacities per molecule at constant volume and constant pressure, respectively. Equation (3.3.8) means that the change in energy per unit volume is determined by the flux of enthalpy and the heat flux. The source term Q (W/cm^3) includes the absorbed laser power density only. Any heats of reaction are included in the first term. $\partial N_i/\partial t$ can be eliminated by means of (3.3.2). With an isobaric system E_i^{a} can be replaced by H_i^{a}. For gas mixtures with $N_{\mathrm{M}} \gg N_{\mathrm{AB}}, N_{\mathrm{A}}, N_{\mathrm{B}}$, the energy is determined by the carrier gas only. The same approximation holds for liquids where the precursor molecules are diluted within a solvent. Additionally, for liquids $c_{\mathrm{p}} \approx c_{\mathrm{v}}$.

If we assume the molecular heat capacities to be equal for all species and ignore their temperature dependences, we obtain

$$c_{\mathrm{v}} \frac{\partial}{\partial t}(NT) + \nabla(c_{\mathrm{p}} NT\boldsymbol{v} - \kappa \nabla T) = Q \ . \tag{3.3.10}$$

Equation of State

Because the diffusion equations for the individual species and the equation of continuity are not independent of each other, we need one additional equation, which is the equation of state:

$$N(\boldsymbol{x}, t) = \frac{N(\infty)}{T^{*q}(\boldsymbol{x}, t)} \ . \tag{3.3.11}$$

$N(\infty)$ is the total number density far away from the reaction zone. $T^*(\boldsymbol{x}, t) = T(\boldsymbol{x}, t)/T(\infty)$ is the normalized temperature. For an ideal gas, the exponent is $q = 1$, while for a liquid the approximation $q \approx 0$ can be employed.

The boundary-value problem for N_i, N, $\boldsymbol{v}$, and T is then described by the $j + 3$ equations (3.3.2), (3.3.7), (3.3.8), and (3.3.11). One of the variables, N_i, and therefore one of the Eqs. (3.3.2) can be excluded because $N = \sum N_i$.

Boundary Conditions

The temperature at the interface is assumed to be continuous:

$$T(\boldsymbol{x}_{\mathrm{s}}, t) = T_{\mathrm{s}} \ . \tag{3.3.12}$$

Thus, any temperature jump at the surface $\boldsymbol{x}_{\mathrm{s}}$ is ignored. T_{s} must be calculated by taking into account possible changes in the shape of the reaction zone. At sufficiently large distances from the reaction zone,

$$T(\boldsymbol{x} \to \infty, t) = T(\infty) \ . \tag{3.3.13}$$

At the surface $\boldsymbol{x}_{\mathrm{s}}$ the net flux (normal component; the surface normal shall be directed from the solid surface into the ambient medium) of species AB_μ shall be

equal to the net reaction rate, $W_s \equiv W(\boldsymbol{x}_s, t)$:

$$-J_{AB}(\boldsymbol{x}_s, t) = W_s \ , \tag{3.3.14}$$

where $W_s = k_1(T_s)N_{AB} - k_2(T_s)N_B^{\mu}$ is the net amount of molecules AB decomposed at the surface per unit area and time. Correspondingly, we have

$$J_B(\boldsymbol{x}_s, t) = \mu W_s \ . \tag{3.3.15}$$

From (3.3.6), (3.3.14), and (3.3.15) we obtain for the normal component of the average velocity at the surface

$$v(\boldsymbol{x}_s, t) = \frac{bW_s}{N} \ , \tag{3.3.16}$$

where $b = \mu - 1$ describes the net increase in particle number density per formula unit. Far away from the reaction zone we assume

$$\begin{aligned} &N_{AB}(\boldsymbol{x} \to \infty, t) = N_{AB}(\infty) \quad \text{and} \\ &N_A(\boldsymbol{x} \to \infty, t) = N_B(\boldsymbol{x} \to \infty, t) = 0 \ , \end{aligned} \tag{3.3.17}$$

and at the surface

$$N_A(\boldsymbol{x}_s, t) = 0 \ . \tag{3.3.18}$$

The latter condition implies that all species A impinging onto the surface $\boldsymbol{x}_s$ stick on it.

In the following sections, we will investigate different solutions of this boundary-value problem. In many laser processing situations, one can assume steady-state conditions.

The assumptions made clearly oversimplify the real situation of laser-activated chemical reactions at or near interfaces. In particular, the omission of ordinary (free) convection is certainly a crude approximation if we are dealing with high-density ambient media, i.e., with high gas pressures or with liquids. It should also be emphasized that the equations discussed in this section are coupled. Thus, the single contributions to the reaction rate are not independent of each other. The *coupling* of fluxes results in the appearance of *new* phenomena (Sect. 17.4.1).

3.3.2 Dependence of Coefficients on Temperature and Concentration

For *gases*, the temperature and pressure dependence of the *molecular* diffusion coefficient, for example of species AB_μ, can often be described by

$$D_{\mathrm{AB}} \equiv D_{\mathrm{AB}}(T_{\mathrm{g}}, p) \approx D_{\mathrm{AB}}(T(\infty), p_{\mathrm{s}}) \frac{T_{\mathrm{g}}^{*n}}{p^*} \ , \tag{3.3.19}$$

where $T_{\mathrm{g}}^* = T_{\mathrm{g}}(\boldsymbol{x}, t)/T(\infty)$. $D_{\mathrm{AB}}(T(\infty), p_{\mathrm{s}})$ is the diffusion coefficient at a standard pressure, p_{s}, far away from the reaction zone. Within the elementary kinetic theory of gases the exponent is $n = 1.5$. Experimental values are within the range $1.5 \leq n \leq 2$ [*Hirschfelder* et al. 1964]. At low to medium gas pressures, $D_{\mathrm{AB}} \propto 1/p^*$, where $p^* = p/p_{\mathrm{s}}$. The total pressure is $p = \sum p_i$ if $N_{\mathrm{M}} = 0$, and $p \approx p_{\mathrm{M}}$ if $N_{\mathrm{M}} \neq 0$ ($N_{\mathrm{M}} \gg N_i$).

The dependence of D_{AB} on the relative concentrations of gaseous constituents can, to a good approximation, be ignored [*Ferziger* and *Kaper* 1972].

In the phenomenological theory of *liquids*, the temperature dependence of the molecular diffusion coefficient is described by

$$D_i(T_l) = D_0 T_l^* \exp\left(-\frac{\mathscr{E}^*}{T_l^*}\right) \approx D_0 T_l^{*n} \ . \tag{3.3.20}$$

The latter approximation can be employed for small temperature intervals where n is within the range $1 \leq n \leq 10$. Typical values of diffusion coefficients in liquids are $D_i(300\,\mathrm{K}) \approx 10^{-5}\,\mathrm{cm}^2/\mathrm{s}$. Hereafter, we often use the abbreviation $D_i(\infty) \equiv D_i(T(\infty))$.

Thermal Conductivity

The thermal (heat) conductivity of a *gas* mixture depends on temperature and concentration

$$\kappa \equiv \kappa(T_{\mathrm{g}}, x_i) = \sum \kappa_i(T_{\mathrm{g}}) x_i \approx \kappa_{\mathrm{M}} \ , \tag{3.3.21}$$

where κ_i are the thermal conductivities and $x_i \equiv x_i(\boldsymbol{x}, t)$ the molar ratios of (pure) gases i. The latter approximation refers to $N_{\mathrm{M}} \neq 0$. The temperature dependence can be described by

$$\kappa_i(T_{\mathrm{g}}) = \kappa_i(T(\infty)) T_{\mathrm{g}}^{*m_i} \ . \tag{3.3.22}$$

The exponents m_i are, in the general case, different for different gases. In the elementary kinetic theory of gases, all m_i are equal, with $m_i \equiv m = 1/2$. Experimental values are within the range $0.5 \leq m \leq 1.5$. If not otherwise indicated, the exact concentration dependence of κ is ignored and an average value is used instead.

The thermal conductivity of *liquid solutions* can also be described, in good approximation, by (3.3.21) and (3.3.22) [*Hirschfelder* et al. 1964].

Thermal Diffusion Ratio

The thermal diffusion ratio, k_T, for species AB_μ and $N_M = 0$ can be described by

$$k_T^{AB} = \alpha_T x_{AB}(1 - x_{AB}) \,, \tag{3.3.23a}$$

and for $N_M \neq 0$ by

$$k_T^{AB} = \alpha_T x_{AB} x_M \approx \alpha_T x_{AB} \,. \tag{3.3.23b}$$

α_T is the thermal diffusion coefficient, whose sign depends on the relative size of masses and the interaction between different types of molecules. For rigid spheres and $N_M = 0$

$$\alpha_T = \alpha_0 \frac{m_{AB} - m_B}{m_{AB} + m_B} \,, \tag{3.3.24a}$$

while with $N_M \neq 0$ we have, correspondingly,

$$\alpha_T = \alpha_0' \frac{m_{AB} - m_M}{m_{AB} + m_M} \,. \tag{3.3.24b}$$

Henceforth, we assume $\alpha_T = \text{const.}$; in reality, α_T depends weakly on concentration and temperature and, with very high temperatures ($\geq 10^3$ K), it may even change sign. If $m_{AB} \ll m_M$, we can use the approximation $\alpha_T \approx 1/2$.

3.4 Heterogeneous Reactions

This section deals mainly with the modelling of reaction rates in laser-induced gas- and liquid-phase processing. In particular, we shall investigate static and dynamic solutions of the boundary-value problem formulated in the preceding section. The model employed is schematically shown in Fig. 3.4.1. The reaction zone is described by a hemisphere of radius $r_D = d/2$ which is placed on a semi-infinite substrate. The reaction shall take place exclusively on the surface of the hemisphere, whose temperature shall be uniform and given by

$$T_s = T(\infty) + \Delta T_s \,, \tag{3.4.1}$$

where $\Delta T_s \equiv \Delta T_s(r_D)$. We assume $T_s = T(r_D)$, where $T(r_D)$ is the temperature of the gas or liquid at the surface r_D. This approximation holds as long as r_D is much larger than the mean free path of molecules, λ_m. The heat and particle (mass) flux calculated within this model shall have *spherical* symmetry with respect to the center of the hemisphere. Thus, we ignore ordinary convection.

In order to permit a direct comparison between the various results, we often introduce normalized quantities, which are indicated by asterisks.

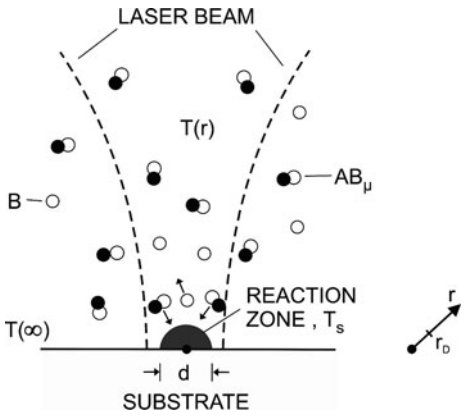

Fig. 3.4.1 Spherical reaction zone with radius $r_D = d/2$. The surface temperature, T_s, shall be uniform. The origin of the radius vector, r, is in the center of the hemisphere. Laser radiation is exclusively absorbed on the surface $r = r_D$. The model applies to laser-induced gas- and liquid-phase processing with ambient temperature $T(r)$. Carrier gas or solvent molecules possibly present are not indicated [*Bäuerle* 1986]

If we assume the temperature of the ambient medium to be *uniform*, i.e., $T = T(\infty)$, the situation applies to those cases of thermal processing where gas-phase heating via the laser-heated surface can be ignored. It applies also, however, to photochemical processing from an adsorbed phase that is in dynamic equilibrium with the gas phase. Here, the *whole* system, including the surface $r = r_D$, can be isothermal.

Let us consider again a first-order non-equimolecular heterogeneous reaction,

$$\mathrm{AB}_\mu + \mathrm{M} \rightarrow \mathrm{A}(\downarrow) + \mu\mathrm{B}(\uparrow) + \mathrm{M}\,. \tag{3.4.2}$$

In contrast to (3.3.1), decomposition of precursor (reactant) molecules takes place exclusively at the interface $r = r_D$ and no backward reaction is considered. Any heat of reaction is ignored.

3.4.1 Stationary Equations

It is convenient to solve the equations given in Sect. 3.3.1 using dimensionless variables: $r^* = r/r_D$, $v^* = v/k_0$, $T^* = T/T(\infty)$, $\mathscr{E}^* = \Delta E/k_B T(\infty)$, $J_i^* = J_i r_D/N(\infty)D_i(\infty)$, $S_T^* = S_T/c_p k_0 N(\infty)T(\infty)$, and $\kappa^* = \kappa/c_p k_0 N(\infty) r_D$. We assume $N_M = 0$, and c_p to be constant and equal for all components. From the equation of continuity and the equation of state we obtain

$$v^*(r^*) = \left(\frac{T^*}{T_s^*}\right)^q \frac{v^*(1)}{r^{*2}}\,, \tag{3.4.3}$$

where $v^*(1) \equiv v^*(r^* = 1)$. With (3.3.5), (3.3.11) and (3.4.3), the flux can be written as

$$J^*_{\mathrm{AB}}(r^*) = \frac{J^*_{\mathrm{AB}}(1)}{r^{*2}} = -\frac{D_{\mathrm{AB}}}{D_{\mathrm{AB}}(\infty)T^{*q}}\left(\frac{\partial x_{\mathrm{AB}}}{\partial r^*} + k_{\mathrm{T}}^{\mathrm{AB}}\frac{\partial}{\partial r^*}\ln T^*\right) + k_0^*\frac{v^*(1)}{T_{\mathrm{s}}^{*q}}\frac{x_{\mathrm{AB}}}{r^{*2}} \; . \tag{3.4.4}$$

$k_0^* = k_0 r_{\mathrm{D}}/D_{\mathrm{AB}}(\infty)$ is the pre-exponential factor in the rate constant $k \equiv k_{\rightarrow}$ in (3.4.2). The energy flux (3.3.9) can be written as

$$S^*_{\mathrm{T}}(r^*) = \frac{S^*_{\mathrm{T}}(1)}{r^{*2}} = \frac{T^*}{T_{\mathrm{s}}^{*q}}\frac{v^*(1)}{r^{*2}} - \kappa^*(T^*)\frac{\partial T^*}{\partial r^*} \; . \tag{3.4.5}$$

In analogy to (3.3.14) and (3.3.16) we obtain

$$-J^*_{\mathrm{AB}}(1) = k_0^*\frac{x_{\mathrm{AB}}(1)}{T_{\mathrm{s}}^{*q}}\exp\left(-\frac{\mathscr{E}^*}{T_{\mathrm{s}}^*}\right) \; , \tag{3.4.6}$$

and

$$v^*(1) = b x_{\mathrm{AB}}(1)\exp\left(-\frac{\mathscr{E}^*}{T_{\mathrm{s}}^*}\right) \; . \tag{3.4.7}$$

The *coupled* (ordinary) differential equations (3.4.4) and (3.4.5) can be solved together with the conditions

$$T^*(1) = T_{\mathrm{s}}^*; \quad T^*(\infty) = 1; \quad x_{\mathrm{AB}}(r^* \rightarrow \infty) = x_{\mathrm{AB}}(\infty) \; . \tag{3.4.8}$$

From these equations we obtain $x_{\mathrm{AB}}(r^*)$, $T(r^*)$, and $S_{\mathrm{T}}(1)$. $x_{\mathrm{AB}}(1)$ can then be determined self-consistently.

The application of this boundary-value problem to heterogeneous pyrolytic *gas-phase* reactions and the phenomena that arise from the coupling of fluxes are discussed in Sect. 17.4.1.

3.4.2 Transport Limitations

An adequate description of laser-induced reactions requires one to solve the transport equations simultaneously. In many cases, however, it is quite illuminating to investigate the effect of *single* contributions to the reaction rate. Let us consider the problem discussed in the preceding subsection, but ignore any temperature gradients within the ambient medium. Thus, we obtain from (3.3.6) for the total flux $\boldsymbol{J} = \boldsymbol{J}_{\mathrm{AB}} + \boldsymbol{J}_{\mathrm{B}} = -b\boldsymbol{J}_{\mathrm{AB}} = N\boldsymbol{v}$. Using this and (3.3.5) this yields

$$\boldsymbol{J}_{\mathrm{AB}}(r) = -\frac{N D_{\mathrm{AB}} \nabla x_{\mathrm{AB}}}{1 + b x_{\mathrm{AB}}(r)} \,. \tag{3.4.9}$$

The dimensionless factor $[1 + b x_{\mathrm{AB}}(r)]$ accounts for the drift velocity . This means that diffusion is superimposed on an overall flow caused by the change in particle number density (chemical convection).

Together with (3.4.4) and boundary conditions analogous to those in (3.4.6) and (3.4.8) we obtain

$$\frac{b x_{\mathrm{AB}}(r^*) + 1}{b x_{\mathrm{AB}}(\infty) + 1} = \exp\left(-\frac{b k^*}{r^*} x_{\mathrm{AB}}(1)\right) \,, \tag{3.4.10}$$

with $k^* = k r_{\mathrm{D}} / D_{\mathrm{AB}}(\infty) = k_0^* \exp(-\mathscr{E}^*/T_{\mathrm{s}}^*)$. If the reaction order $\gamma_{\mathrm{AB}} \neq 1$, the product $k^* x_{\mathrm{AB}}(1)$ in the exponent has to be replaced by $k'^* N^{\gamma-1} x_{\mathrm{AB}}^{\gamma}(1)$. Equation (3.4.10) permits one to calculate the molar ratio at the surface and thereby the reaction rate:

$$W = k N x_{\mathrm{AB}}(1) \,. \tag{3.4.11}$$

With isothermal conditions, N is independent of r, i.e., $N(r) = N(\infty)$. The solution is unique with all parameter values. The average velocity of the gas in the radial direction is

$$v(r^*) = \frac{b k x_{\mathrm{AB}}(1)}{r^{*2}} \equiv \frac{v(1)}{r^{*2}} \,. \tag{3.4.12}$$

Equimolecular Reactions: $b = 0$

With equimolecular reactions, the total number of species remains constant, i.e., with each molecule AB decomposed, a single atom/molecule B is generated. The solution (3.4.10) yields

$$x_{\mathrm{AB}}(r^*) = x_{\mathrm{AB}}(\infty)\left(1 - \frac{k^*}{r^*(1 + k^*)}\right) \,. \tag{3.4.13}$$

The reaction rate is then

$$W = \frac{k N_{\mathrm{AB}}(\infty)}{1 + k^*} \,. \tag{3.4.14}$$

This relation is often termed the Smoluchowski equation. If diffusion is fast compared to the reaction, i.e., if $D_{\mathrm{AB}}/k \gg r_{\mathrm{D}}$ and thus $k^* \ll 1$, the reaction is *kinetically* controlled. In this approximation, the concentration of species AB is almost uniform and given by

$$x_{\mathrm{AB}}(r^*) \approx x_{\mathrm{AB}}(\infty)\left(1-\frac{k^*}{r^*}\right) \approx x_{\mathrm{AB}}(\infty)\ . \tag{3.4.15}$$

The reaction rate within the kinetically controlled regime becomes

$$W^{\mathrm{kin}} = kN_{\mathrm{AB}}(\infty)\ . \tag{3.4.16}$$

In this regime the reaction rate is proportional to the rate constant and does not depend on any geometrical factor. If, on the other hand, $D_{\mathrm{AB}}/k \ll r_{\mathrm{D}}$ and thus $k^* \gg 1$, the reaction rate is limited by the *transport* of species:

$$W^{\mathrm{tr}} \approx \frac{D_{\mathrm{AB}}N_{\mathrm{AB}}(\infty)}{r_{\mathrm{D}}}\ . \tag{3.4.17}$$

Within the approximations made, this is the *highest* rate that can be achieved in a specific chemical reaction. Within the transport-limited regime, the detailed activation mechanisms are unimportant. The transition from the kinetically controlled regime to the mass-transport-limited regime takes place when $k^* \approx 1$. An Arrhenius plot of the normalized reaction rate, $W^* = W/k_0N_{\mathrm{AB}}(\infty)$, for $b = 0$ is shown in Fig. 3.4.2a by the dash-dotted curve. The kinetically controlled regime and the transport-limited regime can clearly be visualized.

From (3.4.16) it becomes evident that within the kinetically controlled regime of a first-order reaction the particle flux, and thus the reaction rate, increases linearly with partial pressure, $p_{\mathrm{AB}}(\infty)$. This is shown in Fig. 3.4.2b. Solid and dashed curves

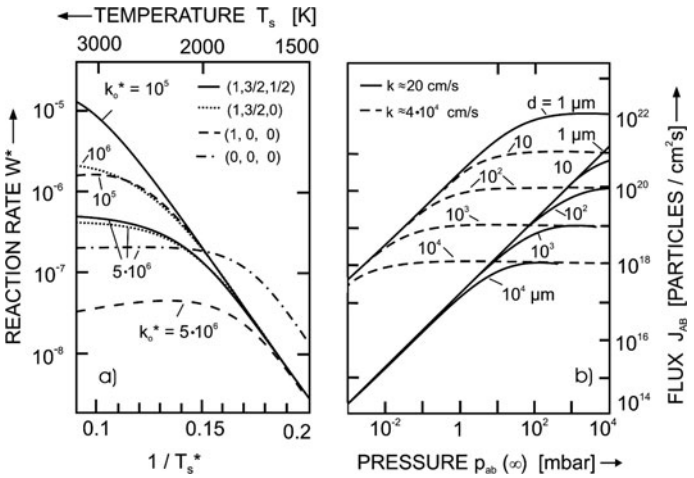

Fig. 3.4.2 (**a**) Arrhenius plot of normalized reaction rate, W^*, for various values of k_0^* and parameter sets (q, n, m). $\mathscr{E}^* = 90$ and $T(\infty) = 300\,\mathrm{K}$, adapted from [*Bäuerle* et al. 1990]. (**b**) Dependence of reaction flux on pressure, $p_{\mathrm{AB}}(\infty)$, in a reaction of type (3.4.2) with $N_{\mathrm{M}} = 0, b = 0$, $p_{\mathrm{AB}}(\infty) \times D_{\mathrm{AB}} \approx 80\,\mathrm{mbar\,cm^2/s}$, and $r_{\mathrm{D}} = d/2$ (Fig. 3.4.1). *Solid curves*: $k = 20\,\mathrm{cm/s}$ $(\eta = 10^3)$. *Dashed curves*: $k \approx 4 \times 10^4\,\mathrm{cm/s}$ $(\eta \to 1)$ [adapted from *Bäuerle* 1996]

refer to rate constants $k \approx 20\,\mathrm{cm/s}$ ($\eta = 10^{-3}$) and $k \approx 4 \times 10^4\,\mathrm{cm/s}$ ($\eta \to 1$), respectively. Sometimes, we use, instead of k, reaction probabilities, η. If $\eta \ll 1$ we can use the approximation $k \approx \eta\langle v_{AB}\rangle/4$. This relation can also be applied for arbitrary η, including $\eta \to 1$ as long as $r_D \leq \lambda_m$.

If $N_{AB}(\infty) \gg N_B(\infty)$, the total pressure is $p \approx p_{AB}(\infty)$. With the approximation $D_{AB} \propto 1/p \approx 1/p_{AB}(\infty)$, the particle flux within the transport-limited regime becomes independent of pressure.

The Influence of *b*

Chemical convection affects only the transport-limited regime. This is quite understandable. Within the kinetically controlled regime $k^* \ll 1$ and the consumption/generation of species is so small that the total number density remains almost unchanged; consequently, the influence of a hydrodynamic flow can be ignored.

The molar ratio at the surface of the reaction zone, $x_{AB}(r_D)$, calculated from (3.4.10) as a function of b is shown in Fig. 3.4.3. The solid curve represents $x_{AB}(\infty) = 1$; the dashed curves show the influence of finite concentrations $x_B(\infty)$. The reaction rates with $b > 0$ are significantly smaller than those with $b = 0$. The physical reason is that species B generated within the reaction zone hinder the transport of species AB_μ into this zone.

In thermal processing, the coupling of fluxes may significantly diminish the effect of b and, with certain parameters, may even cause an inverse behavior (Sect. 17.4.1). In the limit of full absorption of species AB_μ at the surface r_D, which is described by $b = -1$, and with $x_B(\infty) = 0$, the transport of AB_μ is purely convective and the concentration $x_{AB}(r_D)$ equals unity.

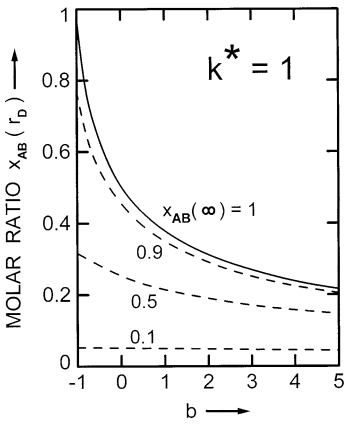

Fig. 3.4.3 Molar ratio $x_{AB}(r_D)$ as a function of b for $k^* = 1$ and various values of $x_{AB}(\infty)$. The influence of finite concentrations $x_B(\infty)$ is shown (*dashed curves*). With the restriction $x_{AB} \ll x_M$, the results can be adapted to the case $x_M \neq 0$ [*Kirichenko* et al. 1990]

The velocity of the convective flow can be calculated from (3.4.12). With $r^* = 1$, $x_{AB}(\infty) = 1.0$, $k^* = 1$, $D_{AB} = 0.1\,\mathrm{cm^2/s}$ and $r_D = 1\,\mu\mathrm{m}$, we obtain $v(r_D) \approx 4\,\mathrm{m/s}$ and $v(r_D) \approx 10\,\mathrm{m/s}$ for $b = +1$ and $b = -1$, respectively (the velocity vectors are oriented in opposite directions).

The Influence of Scanning and Convection

Scanning of the laser beam or ordinary (free) convection provides an additional supply of reactant molecules to the reaction zone. This can be taken into account, in a crude approximation, by substituting k^* in (3.4.14) by

$$k^* = \frac{k}{v + D_{AB}/r_D}\,, \tag{3.4.18}$$

where v is the scanning velocity of the laser beam, $v \equiv v_s$, or the velocity of the convective flow, $v \equiv v_c$ (Sect. 9.5.3). The influence of convection on mass transport can be ignored as long as $v_c r_D / D_{AB} \ll 1$.

The Influence of Gas-Phase Heating

Let us consider the influence of gas-phase heating on the reaction rate for $b = 0$ and *arbitrary* exponents q, n, m which describe the temperature dependences in the number density of species (3.3.11), the diffusion coefficient (3.3.19), and the thermal conductivity (3.3.22). Different cases are included in Fig. 3.4.2a. The temperature dependences of N and D influence the reaction rate considerably, while the temperature dependence of κ has only little influence.

3.4.3 Dynamic Solutions

For spherical symmetry (Fig. 3.4.1) with $T(r > r_D) = T(\infty)$, $\mu = 1$, and $W_v = 0$ we obtain from the diffusion equation (3.3.2), the boundary conditions (3.3.14), (3.3.15), (3.3.16), (3.3.17) and (3.3.18), and the initial conditions $N_{AB}(t = 0) = N_{AB}(\infty)$ the time-dependent density of species AB:

$$\begin{aligned} N_{AB}(r^*, t^*) = N_{AB}(\infty) \Bigg\{ 1 - \frac{k^*}{r^*[1+k^*]} \Bigg[\operatorname{erfc}\left(\frac{r^*-1}{2t^{*1/2}}\right) \\ - \exp[(1+k^*)(r^*-1) + (1+k^*)^2 t^*] \\ \times \operatorname{erfc}\left(\frac{r^*-1}{2t^{*1/2}} + (1+k^*)t^{*1/2}\right) \Bigg] \Bigg\}\,, \end{aligned} \tag{3.4.19}$$

where $t^* = D_{AB} t / r_D^2$. In the limit $t \to \infty$, this yields the steady-state profile (3.4.13). The (normalized) particle flux at the surface r_D is given by

$$J^*_{AB}(r_D, t) = \frac{J_{AB}(r_D, t)}{J_{AB}(r_D, 0)} = -\frac{J_{AB}(r_D, t)}{kN_{AB}(\infty)} = \frac{1 + k^*\Psi}{1 + k^*} , \qquad (3.4.20)$$

with

$$\Psi = \exp[(1 + k^*)^2 t^*] \operatorname{erfc}[(1 + k^*)t^{*1/2}] .$$

Figure 3.4.4 shows the temporal dependence of J^*_{AB} for various values of $d = 2r_D$. Full curves have been calculated for $k \approx 20\,\mathrm{cm/s}$ and dashed curves for $k \approx 4 \times 10^4\,\mathrm{cm/s}$. Within the kinetically controlled regime ($k^* \ll 1$), J^*_{AB} remains almost constant, while in the diffusion-limited regime ($k^* \gg 1$) it strongly decreases with increasing time.

The characteristic time to reach the *stationary* flux is given by

$$\tau(\delta) \approx \frac{r_D^2 k^{*2}}{D_{AB}\pi[1 + k^*]^2} \frac{1}{\delta^2} , \qquad (3.4.21)$$

where $\delta \equiv [J_{AB}(t) - J_{AB}(\infty)]/J_{AB}(\infty)$. The time $\tau(\delta)$ increases with increasing diameter of the reaction zone. With $\delta = 0.1$ and $k^* \ll 1$, we obtain $\tau(0.1) \approx 2d^4k^2/D^3_{AB}$, while with $k^* \gg 1$ this time becomes $\tau(0.1) \approx 8d^2/D_{AB}$. If both k and d are small, the reaction flux is almost unity and independent of time.

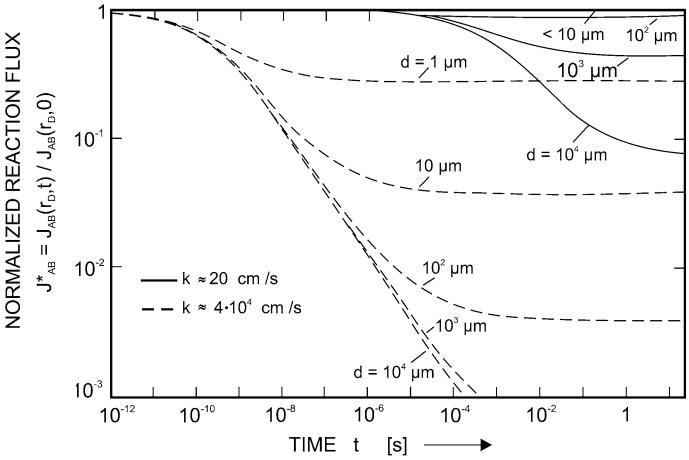

Fig. 3.4.4 Temporal dependence of the normalized flux (3.4.20) for various diameters of the reaction zone, $d = 2r_D$. The parameters employed were $p_{AB}(\infty)D_{AB} = 80\,\mathrm{mbar\,cm^2/s}$, with $p \approx p_{AB}(\infty) = 100\,\mathrm{mbar}$ [*Bäuerle* 1996]

3.4.4 Heterogeneous Versus Homogeneous Activation

Up to now we have assumed 'purely' heterogeneous activation of the chemical reaction. There are, however, many situations where a clear separation of heterogeneous and homogeneous contributions to thermally activated reactions becomes difficult.

Let us again consider the model in Fig. 3.4.1. Even if the ambient medium does *not* absorb the laser light, it will be indirectly heated via the laser-induced temperature rise on the surface $r = r_D$. As a consequence, a *homogeneous* reaction within a hemispherical shell above this surface can be activated. The thickness of this shell, estimated from (3.1.4) and (9.5.6), is

$$\Delta r = r - r_D < \frac{k_B T_s}{\Delta E} r_D \,. \tag{3.4.22}$$

For $T_s = 2000\,\mathrm{K}$, $\Delta E = 0.4\,\mathrm{eV}$ ($10\,\mathrm{kcal/mol}$) and $r_D = 1\,\mu\mathrm{m}$, we obtain $\Delta r \leq 0.4\,\mu\mathrm{m}$. Within this model, a distinction between homogeneous and heterogeneous reactions loses sense when $\Delta r \ll r_D$.

In reality, the situation is more complicated. First, a proper estimation of the width of the heated zone must include consideration of convection, the temperature jump at the interface, if relevant, and the influence of temperature dependences in parameters. Second, the densities of species relevant to surface processing can differ significantly with heterogeneous and homogeneous activation. For example, in adsorbates the densities of species, N_i, as well as their cross sections for dissociation, σ_i, may differ significantly from the corresponding gas-phase values. There are also many other light–molecule–surface interactions which influence heterogeneous but not homogeneous reactions. The situation is similar with photochemically activated reactions.

3.5 Combined Heterogeneous and Homogeneous Reactions

A model particularly useful for the description of many types of laser-induced surface modifications and the deposition and etching of flat patterns is depicted in Fig. 3.5.1. Here, we assume *cylindrical* symmetry. The laser light which shall exclusively be absorbed by the substrate causes a surface temperature rise, and thereby indirect heating of the adjacent medium. We consider a thermally activated reaction similar to (3.3.1):

$$\zeta_{AB}\mathrm{AB} + \zeta_C\mathrm{C} + \mathrm{M} \underset{k_2}{\overset{k_1,k_3}{\rightleftarrows}} \zeta_A\mathrm{A}(\downarrow) + \zeta_{BC}\mathrm{BC} + \mathrm{M} \,. \tag{3.5.1}$$

In contrast to the spherical model, we assume a Gaussian intensity distribution of the laser beam and *inhomogeneous* substrate heating. The maximum temperature, T_c,

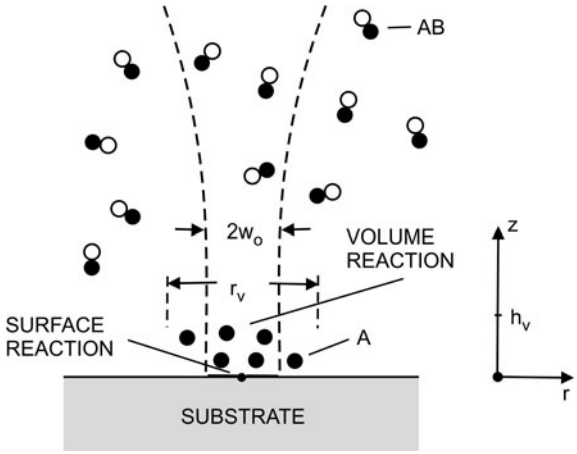

Fig. 3.5.1 Cylindrical model for the description of pyrolytic LCP. The origin of the coordinate system is on the substrate surface in the center of the laser beam. The laser light is exclusively absorbed on the surface $z = 0$. The temperature distribution on the surface is $T_s(r)$; in the gas phase it is $T(r, z)$ [*Kirichenko* and *Bäuerle* 1992]

occurs in the center of the beam at $r = z = 0$. Due to inhomogeneous heating, the rate constants and transport properties of species will vary from point to point. For simplicity, we assume that the temperature distribution remains unchanged during laser processing. This is a good approximation as long as we consider only flat structures and ignore changes in the physical properties within the irradiated area. With stationary conditions, the temperature distribution on the substrate surface is given by

$$T_s(r) \equiv T(r, z = 0) = T(\infty) + \Delta T_s(r) \; . \tag{3.5.2}$$

3.5.1 The Boundary-Value Problem

Approximate solutions of the boundary-value problem for a reaction of type (3.5.1) and gas-phase precursors have been derived by *Kirichenko* and *Bäuerle* (1992). Chemical convection and thermal diffusion have been ignored. With stationary conditions, the equations in Sect. 3.3.1 yield for species AB:

$$\begin{aligned} -\nabla(N D_{AB} \nabla x_{AB}) &= Q_{v,AB} = -W_v \; , \\ x_{AB}(r, z \to \infty) &= x_{AB}(\infty) \; , \\ -J_{AB} &= N D_{AB} \left.\frac{\partial x_{AB}}{\partial z}\right|_{z=0} = W_s \; . \end{aligned} \tag{3.5.3}$$

W_v and W_s are the net reaction rates in the volume and on the surface, respectively. These rates are given by

$$W_\mathrm{v} = k_3(T) N_\mathrm{AB}^{\gamma_\mathrm{AB}^\mathrm{v}} N_\mathrm{c}^{\gamma_\mathrm{c}^\mathrm{v}} \ ,$$

and

$$W_\mathrm{s} = k_1(T_\mathrm{s}) N_\mathrm{AB}^{\gamma_\mathrm{AB}} N_\mathrm{c}^{\gamma_\mathrm{c}} - k_2(T_\mathrm{s}) N_\mathrm{BC}^{\gamma_\mathrm{BC}} \ .$$

γ_i^v and γ_i are partial reaction orders for volume and surface reactions, respectively (Sect. 3.1). Analogous equations hold for species BC and A.

The temperature dependence of D_i is described by (3.3.19); with an exponent $n = 1$, we obtain, with

$$N D_i = N(\infty) D_i(T(\infty)) \tag{3.5.4}$$

and $N \equiv N(T) = N(\infty)/T^*$, the conservation law

$$\begin{aligned} &N(T)[D_\mathrm{AB}(T) x_\mathrm{AB}(r,z) + D_\mathrm{BC}(T) x_\mathrm{BC}(r,z)] \\ &= N(\infty) D_\mathrm{AB}(T(\infty)) x_\mathrm{AB}(\infty) \ , \end{aligned} \tag{3.5.5}$$

where we have assumed $x_\mathrm{BC}(r, z \to \infty) = 0$.

3.5.2 Approximate Solutions

An analytical solution of the boundary-value problem (3.5.3), (3.5.4), and (3.5.5) is not possible. Solutions can be obtained by employing an iteration approach where the concentrations x_AB and x_BC are calculated self-consistently.

The rate constants k_j contain exponential factors for which, typically, $T \ll \mathscr{E}_j$. This permits further simplifications. Near the origin $r = z = 0$ we can use the expansion

$$T(r,z) \approx T_\mathrm{c} - \Delta T_\mathrm{c} \left(\frac{r^{*2}}{2} + \frac{2z}{\sqrt{\pi} w_0} \right) \ . \tag{3.5.6}$$

For the *surface* reactions, the rate constants (3.1.4) can then be written as

$$k_j(T_\mathrm{s}) = k_j(T_\mathrm{c}) \exp\left(-\frac{r^2}{r_j^2} \right) \ , \tag{3.5.7a}$$

with $j = 1, 2$. For the *volume* reaction, $j = 3$, we obtain

$$k_3(T) \approx k_3(T_\mathrm{c}) \exp\left(-\frac{r^2}{r_3^2} - \frac{z}{h_\mathrm{v}} \right) \ , \tag{3.5.7b}$$

where

$$h_{\mathrm{v}} = \frac{\sqrt{\pi}}{2}\frac{w_0 T_{\mathrm{c}}^2}{\mathscr{E}_3 \Delta T_{\mathrm{c}}} \quad \text{and} \quad r_j = w_0 \left(\frac{2T_{\mathrm{c}}^2}{\mathscr{E}_j \Delta T_{\mathrm{c}}}\right)^{1/2} . \tag{3.5.8}$$

h_{v} describes the extension of the volume reaction in the z-direction. Explicit expressions for the molar ratios x_i and further details on the calculations can be found in [*Kirichenko* and *Bäuerle* 1992]. An illustration of the results is given in Sect. 16.2.

Reaction rates achieved by homogeneous gas-phase heating using *parallel* laser-beam incidence are discussed in Chap. 19.

3.6 Homogeneous Photochemical Activation

The analysis of photochemical processing requires the modelling of the spatial and temporal distribution of photogenerated species and of reaction rates. Consider, for example, a photolytic reaction of the type

$$\mathrm{A}_{\mu_\mathrm{A}}\mathrm{B}_{\mu_\mathrm{B}} + \mathrm{M} + h\nu \rightarrow \mu_\mathrm{A}\mathrm{A}(\downarrow) + \mu_\mathrm{B}\mathrm{B} + M \; . \tag{3.6.1}$$

Such reactions are employed in LCVD of metals from alkyls or carbonyls (B $\neq$ A), and in many cases of dry etching (B $\neq$ A or B $\equiv$ A). Equation (3.6.1) can also be applied to situations where dissociation of $[\mathrm{A}_{\mu_\mathrm{A}}\mathrm{B}_{\mu_\mathrm{B}}]^*$ takes place via subsequent molecular collisions or other interactions.

Molecules AB are excited/dissociated within the total *volume* of the incident laser beam (Fig. 1.2.2). The photoproducts diffuse into the surrounding medium and recombine, or they react at the substrate surface and, to some extent, at the walls of the reaction chamber. In the case of localized irradiation (Fig. 1.2.2a), species A will also condense *outside* the reaction zone and thereby decrease the spatial confinement. Non-thermal excitations of the substrate surface (Sect. 2.4) may also play an important or even decisive role in the molecule–surface interactions.

Because of the interrelation between the different quantities determining single effects, the concentration of photoproducts and the reaction rates depend on the size of the reaction zone, the reaction probabilities at the different material surfaces, the size of the reaction chamber, etc. This will be outlined in Sect. 14.1.

Chapter 4
Nucleation and Cluster Formation

The formation of nuclei and clusters from single atomic or molecular species plays an important or even decisive role in laser-induced gas-phase synthesis of powders, laser-CVD, pulsed-laser deposition (PLD) etc. Of similar importance are (heterogeneous) nucleation processes in laser-annealing, recrystallization, thin-film formation, etc. Depending on the particular application, nucleation and cluster formation can be desirable or undesirable. An example is PLD, where clusters formed within the vapor plume may condense on the substrate and thereby deteriorate epitaxial film growth. However, by employing a moderate background pressure, the same technique can be used to fabricate thin nanocrystalline films with unique physical properties.

Laser radiation can influence both homogeneous and heterogeneous nucleation and cluster formation in various ways:

- Laser-induced decomposition of precursor molecules generates atomic or molecular radicals, ions, etc., which may serve as nucleation centers.
- Selective laser-light absorption results in heating or ionization of nuclei/clusters and thereby favors either their further growth or their decomposition, depending on the particular system under consideration.
- The degree of non-equilibrium that can be achieved in laser-induced processes is significantly higher than in any classical system. For example, within the initial phase of the vapor plume generated in pulsed-laser ablation, the degree of oversaturation exceeds that of classical systems by many orders of magnitude.
- The strong gradients in temperature, concentration of species, etc., influence both the kinetics of nucleation and cluster formation and the transport of particles. For example, in (heterogeneous) pyrolytic LCVD the temperature gradients near the deposit are, typically, 10^7 K/cm. With such temperature gradients, thermophoretic and chemophoretic forces, thermal diffusion, etc., become important.

4.1 Homogeneous Processes

In this section we consider homogeneous nucleation and cluster formation within a metastable phase, mainly an oversaturated vapor.

D. Bäuerle, *Laser Processing and Chemistry,* 4th ed.,
DOI 10.1007/978-3-642-17613-5_4, © Springer-Verlag Berlin Heidelberg 2011

4.1.1 Classical Kinetics

Nuclei are homogeneously formed within an oversaturated vapor due to fluctuations. The growth of nuclei is favored by the free energy of condensation and suppressed by the interface energy. For spherical nuclei (droplets) and isothermal conditions, the critical radius can be described by

$$r_c = \frac{2\sigma V_n}{\mu(p) - \mu_n(p)} = \frac{2\sigma V_n}{k_B T \ln S} \approx \frac{2\sigma V_n}{|\Delta H^a|\,\theta}\,, \tag{4.1.1}$$

where σ is the surface tension coefficient, and V_n the volume available per atom/molecule within the nucleus. The chemical potentials for the metastable vapor and the nucleus, μ and μ_n, depend on partial pressure, $p \equiv p_i$. $S = p/p_s(T) = N(\infty)/N_s$ characterizes the degree of oversaturation, and $p_s(T) \equiv p_s(T, r \to \infty)$ the saturated vapor pressure over a plane surface. The latter approximation can be used for small values of supercooling, θ. $\Delta H^a < 0$ is the heat of condensation per molecule. Figure 4.1.1 shows the Gibbs free energy, ΔG, as a function of particle radius. The dashed curve corresponds to the situation observed without laser light. If a nucleus with radius $r > r_c$ is formed, it continues to grow. If, however, $r < r_c$ the nucleus decomposes.

The probability for the formation of a nucleus with radius r_c is given by [*Landau* and *Lifshitz*: Statistical Physics 1980]

$$\mathcal{W} \propto \exp\left(-\frac{16\pi\sigma^3 V_n^2 p^2}{3k_B^3 T^3 \Delta p^2}\right) \equiv \exp\left(-\frac{T_1}{T}\cdot\frac{1}{\theta^2}\right) \tag{4.1.2}$$

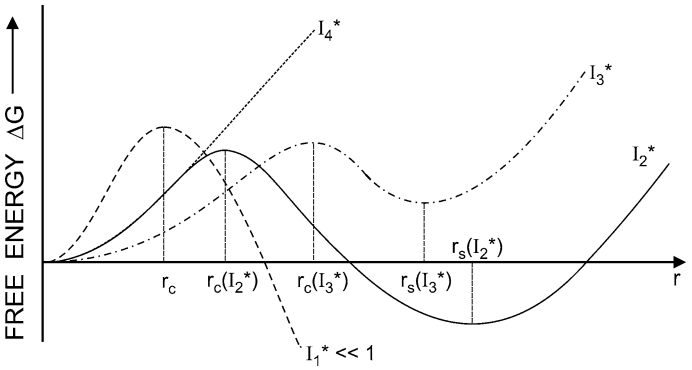

Fig. 4.1.1 Free energy of droplets as a function of their radius. The situation without laser light or with very low intensities, $I_1^* \ll 1$ (Sect. 4.1.2) is shown by the *dashed curve*. For medium laser-light intensities (*solid curve*) there exists a critical radius, $r_c(I_2^*) > r_c$ and a stable size of the particle, $r_s(I_2^*)$. For very high intensities (*dotted curve*) formation of a stable nucleus becomes impossible. An intermediate situation is shown by the *dash-dotted curve*

with $\Delta p = p - p_s \ll p$. This equation can be rewritten by using the Clausius–Clapeyron relation

$$\Delta p = \frac{\Delta H^a}{T_0 V_g} \Delta T \tag{4.1.3}$$

with $\Delta T = T - T_0$. T_0 characterizes the phase equilibrium with $p = p_s(T_0)$. V_g is the volume available per molecule/atom within the gas phase, and $\theta = -\Delta T/T_0$. Equation (4.1.2) shows that nucleation is determined by the (material) parameter T_1 and the supercooling, θ. With $\theta \to 0$, the critical radius of clusters can be described by $r_c \propto 1/\theta$ [see (4.1.1)].

The temporal behavior of the droplet radius is schematically shown in Fig. 4.1.2. The ambient atmosphere of droplets shall consist of the vapor and a buffer gas.

- The formation of critical nuclei takes place within a latent time $t_n \propto \omega^{-1}$.
- In the kinetically controlled region, the nuclei are small compared to their mean free path within the gas, i.e., their radius is within the range $r_c < r \ll \lambda_m$. Their growth in volume is proportional to the number of collisions, which, in turn, is proportional to the cross section, so that $\mathrm{d}/\mathrm{d}t\,(r^3) \propto r^2$. Thus, the radius of nuclei increases linearly with time, $r \propto t$.
- In the diffusion-limited region, r is comparable to λ_m, and much larger than r_c. The nuclei are in quasi-equilibrium with the surrounding vapor. The diffusion equation yields $\mathrm{d}/\mathrm{d}t\,(r^3) \propto J \propto r^2 D_i[N(\infty) - N_s(r)]/r$, where J is the total flux onto the surface of the droplet. $N_s(r)$ is the density of saturated vapor over the curved surface of the droplet with radius r. It is related to the saturated vapor over a plane surface, N_s, via $N_s(r) = N_s(1 + 2\sigma V_n/k_B T r)$ (Laplace formula). Together with (4.1.1) this yields for low oversaturation $N_s(r) = N_s +$

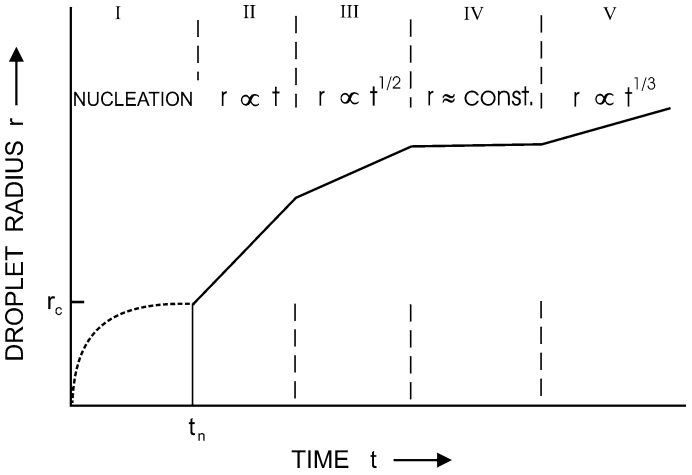

Fig. 4.1.2 Evolution of droplet formation. I: nucleation; II: kinetically controlled growth; III: diffusion limited growth; IV: transition region; V: Ostwald ripening region

$[N(\infty) - N_s]r_c/r$. Thus, $\mathrm{d}/\mathrm{d}t\,(r^3) \propto r^2[N(\infty) - N_s](r - r_c)/r^2 \propto (r - r_c) \propto r$, and thereby $r \propto t^{1/2}$.

- Within the transition region, IV, the radius of droplets remains almost constant. This can be due to the competition in growth between different droplets of similar size [*Pflügl* and *Titulaer* 1993], or due to changes in local vapor pressure related to fluctuations in the density of nuclei, which yields $r \propto t^{1/15}$ [*Tokuyama* and *Enomoto* 1992].
- In the Ostwald ripening (coalescence) region, V, growth can be described by $r \propto t^{1/3}$ [*Gunton* et al. 1983].

Due to the growth of nuclei, the degree of oversaturation, S, decreases and r_c increases. As a consequence, all nuclei are approximately of critical size, i.e., $r \approx r_c$. We can apply the diffusion equation as in region III, but replace $N(\infty)$ with N_s so that $N(\infty) - N_s(r) \approx N_s - N_s(r) \propto N_s/r$, where the Laplace formula was again employed. Thus, $\mathrm{d}/\mathrm{d}t\,(r^3) \propto r^2[N(\infty) - N_s(r)]/r \propto N_s \propto$ const., and thereby $r \propto t^{1/3}$.

This *mean-field* type description of the growth process ignores *direct* interactions between droplets. It can be applied to those cases of laser processing that can be described by *quasi-stationary* equations. In this regime, the size of big clusters increases, while that of small clusters decreases. This description cannot be applied to vapor/plasma plumes generated by pulsed-laser ablation – because of both the fast expansion of the plume and the presence of charged particles.

A detailed introduction to nucleation and cluster formation in standard systems can be found, e.g., in [*Abraham* 1978; *Maissel* and *Glang* 1970].

4.1.2 Droplets Within a Laser Beam

Let us consider an oversaturated vapor with droplets formed by vapor condensation in the presence of laser light. Here, we employ the term droplet for *spherical* clusters and nanoparticles (NPs) with crystalline or amorphous microstructure, including liquids. The laser radiation shall be absorbed by the droplets but not by the vapor. Thus, the temperature of droplets, T_n, increases with respect to the temperature of the ambient vapor, T, and their growth behavior will be changed.

For large droplets (typically, $r > 10\,\mathrm{nm}$), which can be described by macroscopic variables, the absorptivity can be calculated on the basis of the Mie theory [*Born* and *Wolf* 1980]. The energy balance for such droplets can be written as

$$\frac{\mathrm{d}E}{\mathrm{d}t} = \pi r^2 A I - 4\pi r^2 I_{\mathrm{loss}} + 4\pi r^2 \varrho \Delta H_v(r) \frac{\mathrm{d}r}{\mathrm{d}t}\,, \tag{4.1.4}$$

where E is the sum of the volume and surface energy of droplets, i.e., $E = \varrho c_p(4\pi r^3/3)T_n + 4\pi r^2\sigma$. A is the effective absorptivity of the droplet and I_{loss} the heat exchange with the ambient vapor. The last term describes the heat of condensation.

For droplets whose radius is small compared to both the laser wavelength, λ, and the penetration depth, l_α, the effective absorptivity can be approximated by

$$A = \frac{\sigma_a}{\pi r^2} = \frac{32}{3}\pi^2 \frac{r}{\lambda} \mathrm{Im}\{\alpha_e\} = 8\pi \frac{r}{\lambda} \mathrm{Im}\left\{\frac{\varepsilon - 1}{\varepsilon + 2}\right\} = \frac{r}{\lambda} f(\varepsilon) \,. \tag{4.1.5}$$

Here, terms of higher orders in r/λ have been ignored. σ_a is the absorption cross section. The electric polarizability of the particle, α_e, has been approximated by $\alpha_e = 3(\varepsilon - 1)/4\pi(\varepsilon + 2)$. With $\varepsilon = \tilde{n}^2 = [n + i\kappa_a]^2$, the function $f(\varepsilon)$ becomes

$$f(\varepsilon) = \frac{48\pi n \kappa_a}{(n^2 - \kappa_a^2 + 2)^2 + 4n^2\kappa_a^2} \,. \tag{4.1.6}$$

In the simplest case, we can approximate the loss term by

$$I_{\mathrm{loss}} = \eta'(T_n - T) \,. \tag{4.1.7}$$

If $r \gg \lambda_m$, the heat exchange coefficient can be approximated by $\eta' \approx \kappa_g / r$, where κ_g is the thermal conductivity of the vapor. If $r \ll \lambda_m$, we can use $\eta' = \zeta m c_v J$, where $\zeta \leq 1$ is the accomodation coefficient which characterizes the degree of inelasticity of collisions. c_v is the specific heat, and J the flux of molecules onto the droplet surface. In the elementary kinetic theory, J is described by

$$J = \frac{1}{4} N \langle v \rangle = \frac{1}{4} N \left(\frac{8 k_B T}{\pi m}\right)^{1/2} \,, \tag{4.1.8}$$

where $\langle v \rangle$ is the mean velocity of gas molecules of mass m. Thus we can write

$$\eta' = \zeta(l + 1) \frac{p_t}{T} \left(\frac{k_B T}{8\pi m}\right)^{1/2} \,, \tag{4.1.9}$$

where $l = 6Z - 6$. Z is the number of atoms per molecule. For a linear molecule $l = 6Z - 5$, and for a monatomic gas $l = 3$. p_t is the total gas pressure.

For *stationary* conditions, (4.1.4) yields

$$T_n = T + \frac{I f(\varepsilon)}{4\eta' \lambda} r \,. \tag{4.1.10}$$

Due to the difference in temperatures, $T_n \neq T$, the critical radius of droplets in the presence of laser light, $r_c(I)$, will differ from (4.1.1). In addition, droplets with finite (stable) radii, $r_s(I)$, will appear. The equilibrium values, $r_e(I) = r_c(I), r_s(I)$ can be calculated from the condition that the flux of condensing molecules, $J = J(T)$, must be equal to the flux of evaporating molecules, $J_v = J_v(T_n)$. This is analogous to the condition that the saturated vapor pressure near the surface of the droplet,

$p_s(T_n, r_c(I))$, is equal to the (oversaturated) partial pressure of the vapor, p, within the ambient gas, i.e.,

$$p_s(T_n, r_c(I)) = p \ . \tag{4.1.11}$$

The pressure p_s near a surface of radius r and temperature T is given by

$$p_s(T_n, r) = p_0 \exp\left(-\frac{\Delta E_v^a(r)}{k_B T_n}\right) \ , \tag{4.1.12}$$

where

$$\Delta E_v^a(r) = \Delta E_v^a - \frac{2\sigma V_n}{r} \ . \tag{4.1.13}$$

p_0 is a constant. $\Delta E_v^a \approx \Delta H_v^a$ is the enthalpy of vaporization per atom (molecule) from a plane surface. With $S = p/p_s(T)$ we obtain from (4.1.11), (4.1.12), and (4.1.13)

$$\frac{2\sigma V_n}{k_B T_n r_e(I)} = \ln S + \frac{\Delta H_v^a}{k_B T_n} - \frac{\Delta H_v^a}{k_B T} \ . \tag{4.1.14}$$

In the absence of laser radiation $T = T_n$ and we obtain (4.1.1). Equations (4.1.14) and (4.1.1) yield

$$r_e^* = \left[1 + \left(1 - \frac{\mathscr{H}_v^*}{\ln S}\right)\Delta T_n^*\right]^{-1} \ . \tag{4.1.15}$$

Here, we have introduced dimensionless quantities $r_e^* = r_e(I)/r_c$, $\mathscr{H}_v^* = \Delta H_v^a/k_B T$, and $\Delta T_n^* = T_n/T - 1$. Note that $\mathscr{H}_v^*/\ln S > 1$. Equation (4.1.10) can then be rewritten as

$$\Delta T_n^* = \left(\frac{I f(\varepsilon) r_c}{4\eta' \lambda T}\right) r_e^* = I^* r_e^* \ . \tag{4.1.16}$$

The two functions $r^*(\Delta T_n^*)$ are schematically drawn in Fig. 4.1.3. The dashed lines represent (4.1.16). The behavior of (4.1.15) is shown by the combined solid and dash-dotted curve. The number of solutions depends on the parameter values. Two solutions exist for laser-beam intensities

$$I^* < \frac{1}{4}\left(\frac{\mathscr{H}_v^*}{\ln S} - 1\right)^{-1} \ . \tag{4.1.17}$$

The branch of *critical* solutions corresponds to the solid curve and the branch of stable solutions to the dash-dotted curve. For very *low* laser-light intensities, I_1^*, the situation is essentially the same as in the absence of laser light. The (lower)

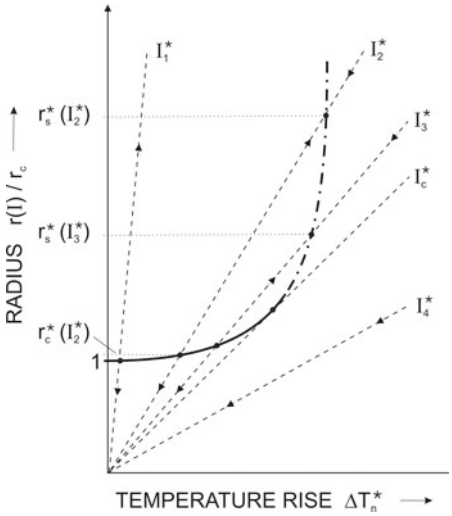

Fig. 4.1.3 Critical and stable radii of droplets normalized to the radius $r_c \equiv r_c(I = 0)$ in the presence of laser light as a function of the temperature rise $\Delta T_n^* = (T_n/T) - 1$. The (normalized) laser-beam intensities are $I_1^* < I_2^* < I_3^* < I_c^* < I_4^*$. The branch of critical solutions (*solid curve*) and the branch of stable solutions (*dash-dotted curve*) are shown [*Luk'yanchuk* and *Bäuerle* 1994]

intersection point yields a critical radius, $r_c(I_1^*) \approx r_c$, as given by (4.1.1). The second intersection point between curves is beyond the range of applicability of the model. For *medium* laser-light intensities, I_2^*, there are two intersection points. The lower corresponds to the critical radius, $r_c(I_2^*)$. If $r < r_c(I_2^*)$, the nucleus decomposes. If $r > r_c(I_2^*)$, the droplet grows until it reaches a stable size, $r_s(I_2^*)$. This behavior is included in Fig. 4.1.1 (solid curve). If the laser-light intensity is increased to I_3^* the critical radius increases. The radius of stable droplets decreases and the minimum becomes more shallow (see dash-dotted curve in Fig. 4.1.1). For intensities I_c^* the critical points collapse and *no* stable solution exists. For $I_4^* > I_c^*$, no solution exists (dotted curve in Fig. 4.1.1). The formation of droplets is suppressed by laser-induced evaporation. Thus, if we choose an appropriate laser-light intensity, for example, I_2^*, droplets of almost equal size, $r_s(I_2^*)$, can be grown.

In the present model we have employed macroscopic quantities to describe droplets of spherical shape. In cases of strong oversaturation, which are, in fact, relevant in laser processing, critical nuclei may consist of a small number of atoms/molecules only. For such small aggregates a macroscopic description is inadequate.

In spite of its simplicity, the model shows that droplet formation in the presence of laser radiation differs significantly from the standard behavior. The possibility of growing droplets with a relatively small size-distribution is used for the synthesis of fine-grain powders. In most of these investigations CO_2-laser radiation has been employed. Depending on the particular experimental conditions, the grain sizes are, typically, between 10 nm and some μm. Among the materials that have been

synthesized are ultrafine powders of Al_2O_3 [*Borsella* et al. 1993a], MgO [*Vorobyev* et al. 1991], SiC [*Scholz* et al. 1993], and Si, Si_3N_4, ternary Si–C–N, etc. [*Borsella* et al. 1993b and references therein].

4.1.3 Transport of Clusters, Thermophoresis, Chemophoresis

With laser-light intensities that produce high concentrations of product species by homogeneous decomposition of precursor molecules within gases or liquids, clusters may significantly contribute to the processing rate. With the condensation of clusters, the deposition rate strongly increases and the morphology of the deposit changes, in general, to large-grain, low-density material.

Laser light not only changes the kinetics of the nucleation process, but also influences the transport of nuclei and clusters. Besides their Brownian motion, the particles will be accelerated by convective forces related to laser-induced temperature gradients. Due to these temperature gradients, additional driving forces based on thermophoresis and chemophoresis may also become important. Thermophoretic forces are directed from the hotter to the colder regions, because the momentum transfer from molecules that hit the cluster on the hotter side exceeds that from molecules on the colder side. The situation is similar to thermal diffusion of heavy molecules. If a chemical reaction takes place, differences in momentum transfer from precursor and product molecules on the hotter and the colder sides of the cluster give rise to chemophoretic forces. While both thermophoretic and chemophoretic forces are directed from the hotter to the colder regions, they can contribute to the transport of clusters towards the substrate surface. The reason is simple: with the formation of clusters, the temperature distribution within the medium may be strongly changed. Both the energy of condensation and direct absorption of laser light by the clusters can produce a maximum in the temperature distribution above the surface.

4.1.4 Fragmentation of Particles

Laser fragmentation of micro-/nano particles has been studied within gas streams and liquids.

Laser fragmentation of polystyrene (PS), soot, NaCl, and Au particles in flowing N_2 and air has been investigated by means of 193 nm ArF-laser radiation [*Choi* et al. 2007]. Depending on the material and laser parameters, fragmentation and/or decomposition of the particles is observed. Atomic/molecular species generated in this process, subsequently undergo homogeneous nucleation and/or they condense on the (smaller) fragments. Laser fragmentation permits the fabrication of powders with particle sizes that can be controlled within the range of a few nanometers and several micrometers.

Laser fragmentation of micron-sized powders in liquids, mainly in water, has been applied for the synthesis of semiconducting nanopowders [*Kosalathip* et al. 2008] and the preparation of organic fluorescent colloidal solutions [*Yasukuni* et al. 2008].

4.2 Nanoparticle Formation by Pulsed-Laser Ablation

A rapidly growing field is the synthesis of nanomaterials by laser vaporization (Chap. 11) and pulsed-laser ablation (Chaps. 12 and 13) of solid or liquid targets in inert or reactive gases or liquids. Here, the condensation of atoms/molecules to clusters – with or without any chemical reactions – occurs *during* the fast expansion of the vapor/plasma plume generated in front of a target material. The time of nucleation and the size and composition of clusters depend on the type of material, the laser parameters and, importantly, on the ambient medium. In fact, the formation of nanoparticles (NPs) with well-defined physical and chemical properties, small size distribution, etc. can be controlled via the ambient medium.

With optimized laser parameters and ambient atmosphere, PLA permits to fabricate various nanomaterials with *controlled* size distribution and different physical/chemical properties. Among those are particles with amorphous, poly- or single-crystalline microstructure, "coated" particles, core/shell spheres, etc. Another class of nanomaterials are nanowires, nanotubes, and nanohorns (Sect. 4.3). In particular with the latter materials, classification into homogeneous and heterogeneous processes is somewhat arbitrary. The fabrication of nanoparticle (NP) and nanocomposite *films* by pulsed-laser deposition (PLD) is discussed in Sect. 22.6. Because of their unique physical and chemical properties, nanoparticles have many real and potential applications in various different areas of technology, biotechnology and medicine. Among those are applications in nanophotonics, optoelectronics, plasmonics, material synthesis, high-quality printing of high-performance flexible electronics (Sect. 25.1), etc. Nanoparticles can also be employed for coatings and catalysts, sensors for gas- and bioanalysis, bio-imaging, tumor treatment, drug delivery, etc. In contrast to many conventional pathways using toxic chemicals for the synthesis and purification of nanoparticles, PLA is a relatively simple and clean technique that yields essentially no waste material.

Within liquids, e.g. water, formation of (toxic) nanoparticles by ablation of solid targets can be well controlled with respect to possible contaminations of the environment. Furthermore, by simultaneous or subsequent fragmentation using, e.g., an additional laser beam at parallel incidence to the target surface and/or by addition of capping ligands, NPs with small mean size and narrow size distribution can be fabricated. A drawback to these advantages of NP control, are the lower ablation rates in liquids with respect to gaseous environments. With metal targets, fs-lasers are the preferred sources for NP formation (Chap. 13).

4.2.1 Gaseous Ambient

Cluster formation during plume expansion has been studied mainly in vacuum and for background atmospheres of noble gases, and of N_2 and O_2 at pressures up to several 100 mbar. Experimentally, the dynamics of cluster formation was studied in situ by time-resolved optical spectroscopy, including emission and absorption spectroscopy, laser-induced photoluminescence (PL), Rayleigh scattering (RS), X-ray absorption spectroscopy, etc. (Chaps. 29 and 30). Among the target materials

employed are metals such as Ag, Au, Cu, Co, Ni, Ti, and various metal alloys [*Jegenyes* et al. 2008; *Liu* et al. 2007; *Barcikowski* et al. 2007; *Seto* et al. 2006; *Pászti* et al. 1997], semiconductors, in particular Si/SiO_x [*Patrone* et al. 2000; *Makino* et al. 1999; *Geohegan* et al. 1998; *Marine* et al. 1998] and ZnTe [*Lowndes* et al. 1998]. Carbon targets have been employed to study the formation of carbon clusters [*Puretzky* et al. 2008; *Madsen* et al. 2007], nanohorns and, in the case of Co- or Ni-doped targets, the growth of nanotubes (Sect. 4.3). Mainly ceramic targets were used for the synthesis of oxide clusters [*Ullmann* et al. 2002] including high temperature superconductors such as $YBa_2Cu_3O_7$ (YBCO) [*Geogehan* et al. 1999], $Ca_xFe_yO_z$ [*Sasaki* et al. 1998], and glasses [*Hiromatsu* et al. 2008]. Particulates accompanying laser ablation of PTFE targets have been studied by *Heitz* and *Dickinson* (1999).

The synthesis of compounds and core/shell nanoparticles formed in inert or reactive atmospheres has been studied for a number of materials. Among those are core/shell particles of CdSe/ZnS [*Gallardo* et al. 2009] and of Ni/NiO. The latter have been synthesized by ablation of Ni targets in O_2 atmosphere. Depending on the laser parameters and the O_2 pressure, formation of NiO cubes or Ni/NiO core/shell spheres is observed [*Liu* et al. 2007]. At high gas pressures, clusters condense on the target surface and form a nanocrystalline overlayer. This technique is denoted as pulsed-laser plasma chemistry (PLPC) (Sect. 26.2.3).

Detailed studies on the dynamics of cluster-formation during plasma plume expansion have been performed mainly for silicon and carbon.

Silicon

The formation of SiO_x ($0 < x < 2$) clusters was studied during ns excimer-laser ablation of Si in He and Ar atmospheres. Expansion of the Si plume into He results in an only gradual deceleration of the plume due to the large difference in atomic masses ($m_{Si} = 28$). The resulting flow pattern and cluster distribution lead to a turbulent ring of clusters. The situation is quite different with Ar ($m_{Ar} = 40$). Here, efficient deceleration *and* reflection of Si atoms and the formation of a uniform, stationary cloud of nanoparticles were observed. With 1.3 mbar Ar- and 248 nm KrF-laser radiation ($\phi = 5 - 8\,J/cm^2$, $\tau_\ell \approx 28$ ns) the expansion of the Si plume slows down from initially 2×10^6 cm/s to 10^4 cm/s within $t \approx 20\,\mu s$ [*Geohegan* et al. 1998]. Expansion velocities have been studied also by time-of-flight (TOF) techniques, time-resolved photography etc. (Chap. 30).

The onset times for nanocluster formation derived from PL and RS experiments were 3 ms in 1.3 mbar Ar and 0.15 – 0.2 ms in 13 mbar He. Clearly, the times derived from the PL signals yield no information on the initial stage of formation, when the clusters are still in liquid form. In any case, with both He and Ar, three broad PL bands at 1.8, 2.5, and 3.2 eV were observed and ascribed to 1 – 10 nm vapor-phase SiO_x clusters. The PL bands agree well with those found for oxidized nanocrystalline Si films and porous silicon.

The distribution of cluster sizes and its dependence on laser fluence, the type and pressure of the ambient gas atmosphere, and the distance from the target surface were studied by condensing the clusters onto a substrate, either directly or embedded

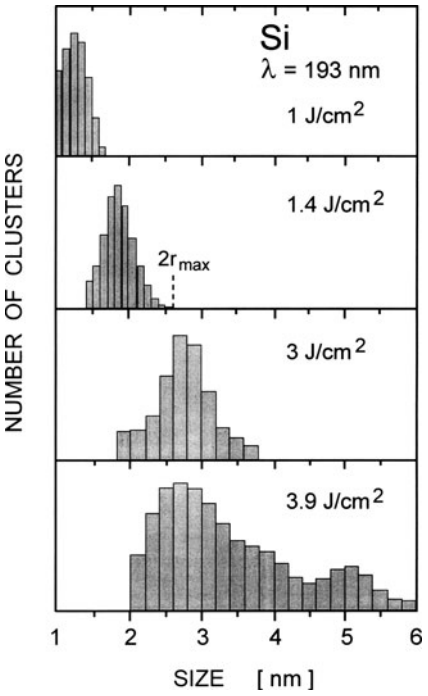

Fig. 4.2.1 Distribution of cluster size (diameters) obtained by ArF-laser ($\tau_\ell = 15$ ns) ablation of Si in 5 mbar He. The second maximum observed with $\phi = 3.9\,\mathrm{J/cm^2}$ is probably due to coalescence of clusters on the substrate [*Marine* et al. 1998]

into a matrix (Sect. 22.6). The experimental arrangement employed in such investigations is the same as in PLD (Fig. 22.1.1). Figure 4.2.1 shows the size distribution of clusters obtained by ArF-laser ablation of Si into He at different laser fluences. At a given pressure, the mean size of nanocrystals increases with increasing fluence and decreases with increasing distance from the target (Fig. 4.2.2). Investigations on the PL of these clusters revealed a clear size-dependence [*Patrone* et al. 2000]. By increasing the mean cluster size from about 1.3 nm ($\phi \approx 1\,\mathrm{J/cm^2}$) to the largest sizes, about 5 nm, the PL spectrum shifts from the near UV to the near IR. This shift in PL is consistent with quantum confinement effects. The shift in band gap energy scales inversely with cluster size. A fit to the experimental data yields

$$\Delta E_\mathrm{g}(d) \equiv E_\mathrm{g}(d) - E_\mathrm{g}(\infty) = A/d^n \tag{4.2.1}$$

where $A = 3.283\,\mathrm{eV\,nm^n}$, $n = 1.34$, and $E_\mathrm{g}(\infty) \equiv E_\mathrm{g}$ (bulk). In fact, this fit is consistent with calculations on the electronic structure of Si nanocrystals. Within this picture, the main effect of cluster oxidation is the diminished size of the crystalline Si core.

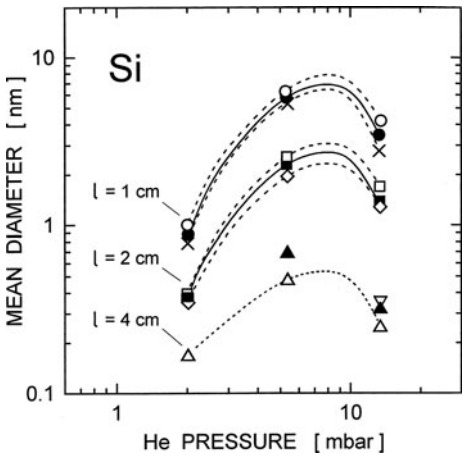

Fig. 4.2.2 Average diameter of Si/SiO_x nanoparticles formed in He after ArF-laser ablation ($\phi = 1.04\,J/cm^2$, $N_\ell = 500$). The particles were condensed on a Si substrate and their sizes were analyzed by atomic force microscopy (AFM). l is the distance between the target and the substrate (Fig. 22.1.1). Measurements taken at different parts of the sample are also shown (*open symbols, dashed curves*) [*Lowndes* et al. 1998]

The effect of background pressure on average particle sizes is still under discussion. *Yoshida* et al. (1996) find an increase in cluster size with increasing pressure. On the other hand, *Lowndes* et al. find a pronounced maximum at a He pressure of about 8 mbar (Fig. 4.2.2). According to numerical calculations based on the hydrodynamic equations and the Zeldovich-Raizer theory of condensation, the differences in the observations are related to the different laser pulse energies employed in the experiments. With the "low" laser-pulse energies employed by *Yoshida* et al. the theory predicts a maximum in size distribution at a much higher background pressure [*Ohkubo* et al. 2003]. Experimental verification would be desirable.

At constant pressure, the average cluster size increases with increasing mass of gas-phase atoms/molecules. It should be noted, however, that the distribution of cluster sizes derived from such investigations may differ from that in the vapor phase. Formation of bigger clusters by coalescence ($A_m + A_n \rightarrow A_{m+n}$; m, n are the number of atoms A within a cluster), surface tension effects, etc., may result in changes in cluster sizes, shapes, etc.

Carbon

The synthesis of single-wall carbon nanotubes (SWNT) and nanohorns (SWNH) was studied by Nd:YAG and CO_2-laser vaporization of pure and Ni-/Co-doped graphite targets in Ar atmosphere (Sect. 4.3). By means of time-resolved spectroscopy and spectroscopic imaging of the ablation plume, the dynamics of cluster-formation from atomic and molecular species has been studied. After ablation of doped targets, the formation of carbon clusters occurs, typically, within several

100 µs to 1 ms, while metal catalyst clusters are formed within times 1 ms $< t <$ 2 ms. The growth of nanotubes within the plume of mixed nanoparticles requires times of several seconds [*Puretzky* et al. 2008; see also Sect. 4.3].

Theoretical Considerations

The appearance of clusters during laser-induced evaporation or ablation of solid or liquid targets has been studied theoretically for various different regimes of laser-matter interactions and by means of quite different models and physical approaches. For the reasons already mentioned in the introduction to this section, we subsequently make only a few remarks to direct the reader to the original literature and to those sections within this book where cluster and particle formation mechanisms are discussed.

First of all, the occurrence of particles or fragments in PLA may have quite different origins. Particles may be *directly* ejected from the target due to hydrodynamic sputtering, phase explosion or thermo-/photomechanical mechanisms. Hydrodynamic sputtering refers to droplets that are ejected from the target either due to transient melting and motion of the liquid caused by strong temperature gradients and relaxation of the laser-induced pressure, or due to different types of hydrodynamic instabilities. It also includes droplet formation during the development of cones/columnar structures, etc. Phase explosion (binodal decomposition) refers to a state where short high-intensity laser pulses cause strong overheating of the material and thereby a transition to a mixed state consisting of vapor and liquid droplets. Photo- and thermomechanical effects cause exfoliation or spallation of large solid or liquid particles and even big fragments due to the relaxation of laser-induced stresses. All of these mechanisms are discussed throughout this book, and in particular in Chaps. 10, 11, 12, 13, 22, 28, and 30. Furthermore, as mainly discussed within this section, clusters may be formed by condensation of atoms/molecules during expansion of a vapor/plasma plume. In vacuum, the high cooling rates and the strongly non-uniform density of ablated species during plume expansion do *not* permit to fabricate NPs with a small size distribution (Sect. 30.4). In the presence of a background gas, plume expansion becomes confined. This favors collision-induced condensation – with our without chemical reactions. The confinement depends on the laser parameters, the pressure *and* the type of the background atmosphere. In particular, with increasing laser-light intensity, the average size of particles increases. This is quite plausible, because the total mass ablated during the pulse increases, and thereby the density of the vapor and the number of collisions between atoms/molecules. This is confirmed by numerical calculations [*Ohkubo* et al. 2003]. Thus, for well-defined NP formation, the background atmosphere is essential because it mediates vapor/gas mixing. In other words, the number of collisions of vapor-phase species and thereby their size and chemical composition, can be controlled via the background atmosphere. Gas-phase mixing and chemical reactions can be enhanced by a number of quite different mechanisms. These are related to shock waves (Sect. 30.4), Rayleigh-Taylor instabilities (Sect. 28.5), etc. For the latter mechanism, the characteristic time for mixing is

related to the increment γ by $t_{\mathrm{mix}} \propto 1/\gamma \propto 1/p^{1/3}$, where p is the pressure of the background atmosphere. For He and pressures of a few mbar, typical values are $t_{\mathrm{mix}} \approx 5 - 10\,\mu\mathrm{s}$.

4.2.2 Liquid Ambient

Laser ablation within liquids permits synthesis of nanoparticles (NPs) under controlled and environmental friendly conditions. The physical properties of the NPs depend on size *and* the type of liquid employed [*Umezu* et al. 2007]. Among the materials investigated are different metals such as Au, Ag, Gd, Fe, Ti, etc. [*Abdolvand* et al. 2008; *Besner* et al. 2008; *Takada* et al. 2008; *Tarasenko* et al. 2008; *Barcikowski* et al. 2007; *Masai* et al. 2007; *Sylvestre* et al. 2004]. Among the semiconductors studied in detail were Si [*Takada* et al. 2008; *Umezu* et al. 2007] and II-VI compounds [*Semaltianos* et al. 2009; *Said* et al. 2007]. Ablation and cluster formation has been studied also for oxides, polymers [*Elaboudi* et al. 2008], and biomaterials like hydroxyapatite (*Mhin* et al. 2009; Sect. 22.5).

In most of these experiments, particle-size distributions have been investigated as a function of laser fluence for multiple-pulse irradiation. Thus, fragmentation of clusters and/or ablation products within the suspension during subsequent pulses will be very important. Furthermore, with the pulse repetition rates employed, the local laser-induced temperature rise results in convective flows (microstirring) within the liquid. Convection will influence the local concentration of product species and thereby the efficiency of subsequent fragmentation processes. For these reasons, an analysis of particle size distributions on the basis of fundamental interaction processes is very difficult. The addition of capping ligands during PLA enables the synthesis of NPs with diameters $d < 10\,\mathrm{nm}$ and a small size distribution. This has been demonstrated for Au targets ablated in aqueous solutions of oligosaccharides or biopolymers [*Besner* et al. 2008].

Both, PLA and laser fracture (Sect. 4.1.4) in liquids are versatile techniques for the fabrication of colloidal solutions and nanoparticle powders of various types.

4.3 Heterogeneous Processes

This section deals with nucleation and cluster formation at or near interfaces. Such processes are extremely important in standard and laser-induced thin-film formation techniques. Equally important are nucleation processes during solidification and recrystallization. Nucleation and cluster formation within the gas phase *and* on the substrate surface are important in many cases of nanoparticle and nanocomposite film formation and during synthesis of nanowires, nanohorns, and nanotubes.

The theory of heterogeneous nucleation in connection with thin-film growth is outlined, e.g., in [*Maissel* and *Glang* 1970; *van Stralen* and *Cole* 1979]. The probability for the formation of a nucleus of critical radius, r_{c}, is given in analogy to (4.1.2) by

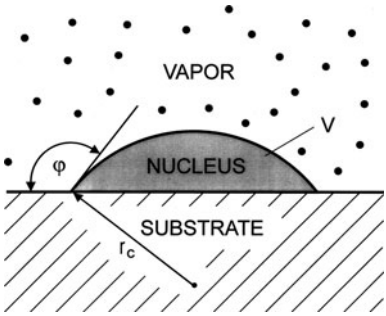

Fig. 4.3.1 Schematic picture of a nucleus of radius r_c and volume V on a substrate surface

$$\omega \propto \exp\left(-\frac{T_1'}{T}\frac{1}{\theta^2}\right) , \tag{4.3.1}$$

where $T_1' = T_1 \cdot f$, with

$$f = \frac{1}{4}\left(2 + 3\cos\varphi - \cos^3\varphi\right) = \frac{V}{\frac{4}{3}\pi r_c^3} \tag{4.3.2}$$

V is the volume of the nucleus and φ the wetting angle, which depends on the type of material of the nucleus and the substrate (Fig. 4.3.1). For $\varphi = \pi$, the (liquid) nucleus completely wets the surface ($f = 0$). It should be mentioned that the wetting angle is frequently defined also by $\varphi' = \pi - \varphi$.

4.3.1 Nucleation in LCVD

In the presence of laser light, nucleation is strongly modified with respect to standard thin-film growth and additional mechanisms must be considered. Laser light can change the sticking probability of species and their migration on and desorption from the substrate surface, and it can photodecompose molecules within the gaseous atmosphere or within adsorbed layers, etc. In any case, for nucleation to take place, a certain concentration of species, and thereby a threshold intensity for deposition is required. Subsequently, we consider two cases: absorbing substrates and transparent substrates that do not or only very slightly absorb the laser light.

Absorbing Substrates

With (strongly) absorbing substrates, precursor molecules are thermally dissociated at or near the laser-heated area on the substrate surface. The free atoms form clusters on the surface, which provide nucleation centers for further film growth. With most processing conditions employed in LCVD, the time of nucleation, t_n, is short compared to the laser-beam illumination time, τ_ℓ. The main differences to nucleation in

standard CVD are related to temporal changes in the laser-induced temperature distribution, e.g., due to changes in the reflectivity and thermal conductivity provided by the nuclei. In laser micropatterning, nucleation processes will also be influenced by the confinement of the temperature distribution and the strong (lateral) temperature gradients.

Transparent Substrates

For transparent substrates, nucleation may depend on the quality of the substrate surface. Surface defects such as pinholes and scratches, but also dust particles, etc., absorb the laser light and thereby may allow nucleation to be initiated at such 'hot spots'.

Nucleation may also be initiated by atoms that result from selective excitation/dissociation of *adsorbed* molecules (Fig. 4.3.2). Because of the high density of adsorbed molecules, the free atoms may form clusters which, even when of subcritical size, may strongly absorb the laser radiation. Such heated clusters can provide nucleation sites and film growth can proceed mainly thermally. Both the degree of photodecomposition of adsorbed species and the light intensity absorbed by the nuclei depend sensitively on the laser wavelength (adsorption may significantly change the effective absorption/dissociation cross section with respect to free gas-phase molecules; Chap. 20). This is an important difference to nucleation on strongly absorbing substrates, where the temperature rise is determined by the optical and thermal properties of the substrate. With transparent substrates, latent times for nucleation of several seconds or even minutes have been observed. Examples are Ar^+- or Kr^+-laser-induced metal deposition from alkyls or carbonyls on quartz or (standard) glass substrates.

In photolytic CVD based on (non-thermal) dissociation of gas- or adsorbed-phase molecules, multiatom clusters originally formed on the substrate surface by thermal or non-thermal processes may serve as nucleation centers for film growth. For

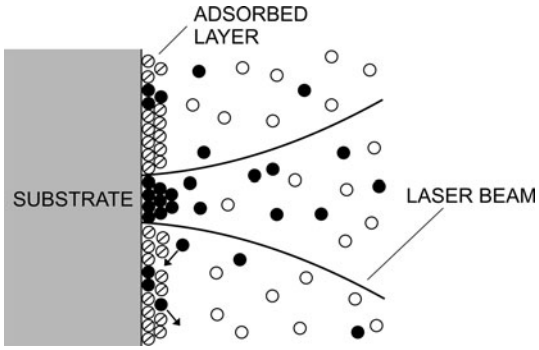

Fig. 4.3.2 Influence of adsorbed-layer photolysis on nucleation and condensation of gas-phase photofragments. Free gas-phase precursors (*open circles*) and photofragments (*solid circles*) are indicated

example, metal structures have been grown on transparent substrates by UV-laser photolysis of gas-phase molecules. While the metal atoms are produced within the *total* volume of the laser beam, they condense *preferentially* on the nuclei generated within the irradiated area (Fig. 4.3.2). For Cd, for example, the critical number of atoms necessary for the formation of a stable nucleus in the gas phase is about 10 at 300 K. For nuclei adsorbed on solid surfaces, this number depends on the physical properties of the material. Atoms that neither form stable nuclei nor attach themselves to nucleation centers formed within and around the area of the laser focus will diffuse across the surface and then evaporate, with high probability. The surface diffusion length is, approximately, $l \approx (2D_i t_v)^{1/2}$, where D_i is the coefficient for surface diffusion of atoms and t_v the average residence time before reevaporation. If an atom impinges on the substrate within an area defined by the radius $r \leq r_n + l$, where r_n is the radius of a stable nucleus, it will, on average, be captured by this nucleus. Atoms impinging on the substrate at distances outside of this zone will reevaporate prior to capture. In other words, the sticking probability for free gas- or liquid-phase atoms, or small clusters of atoms, impinging on or near the nuclei formed within the irradiated substrate area is much bigger than anywhere else on the substrate surface. For Cd atoms, the sticking coefficient is about unity on a Cd film, but $< 10^{-3}$ on SiO_2 glass. Thus, nucleation thresholds suppress, to some extent, isotropic deposition and thereby enhance the contrast in photolytic surface patterning. Nevertheless, depending on the particular precursor molecules, the formation of stable nuclei *outside* of the irradiated area may take place. Furthermore, incorporation of impurities due to incomplete photofragmentation is frequently observed.

4.3.2 Condensation of Clusters from Vapor/Plasma Plumes

If the nanoparticles produced during PLA (Sect. 4.2) are condensed onto a substrate, a nanoparticle or cluster-assembled film is formed. Such films have unique physical properties. This is discussed in Sect. 22.6.

The condensation of clusters generated during PLA in a reactive or an inert atmosphere may also play an important role in various types of surface modifications. Among those are oxidation and nitridation by pulsed-laser plasma chemistry (Sect. 26.2.3), surface transformations of polymer films (Sect. 27.1), etc. Other interesting phenomena include the growth of dendritic structures or self-assembled nanowires, nanohorns, or nanotubes from condensed material.

The growth of dendrites has been observed for PET (polyethylene-terephthalate) after single-pulse UV excimer-laser irradiation (Fig. 4.3.3). The dendrites are of fractal shape, they are randomly distributed over the irradiated area, and they start to grow at different nucleation centers at different times after laser irradiation. Irradiation at shorter wavelengths results in larger dendrites with more filigree arms and a larger number of bifurcations. The size and number density of dendrites also depend on the type and pressure of the ambient atmosphere. With increasing mass of gas-phase atoms/molecules, the size of dendrites decreases while their number

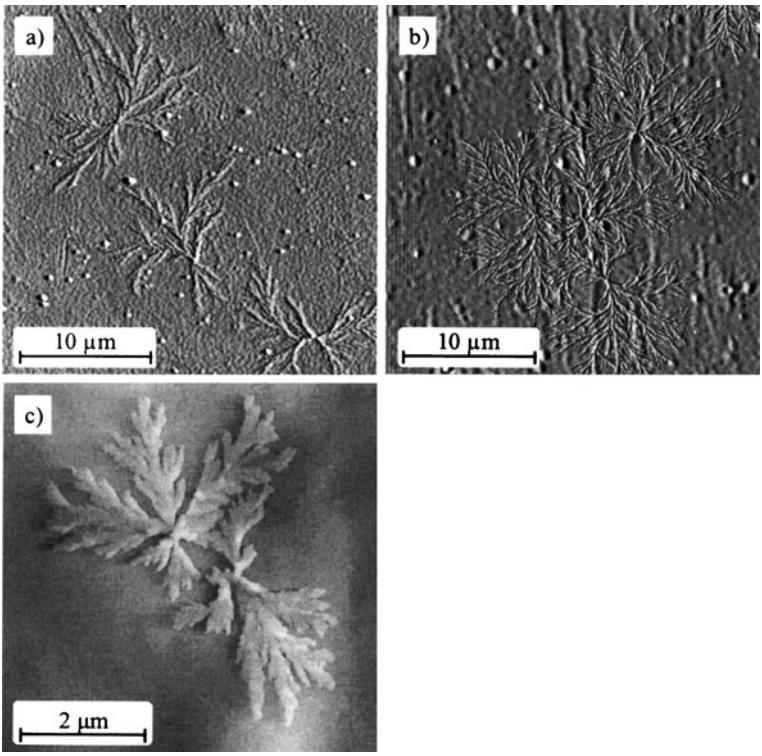

Fig. 4.3.3 (**a**)–(**c**) AFM picture of dendrites observed after single-pulse excimer-laser irradiation of PET and annealing at $T_{gr} = 55°C$ for 120 min. (**a**) $\lambda = 193$ nm, $\phi \approx 45\,mJ/cm^2$; (**b**) $\lambda = 248$ nm, $\phi \approx 90\,mJ/cm^2$; (**c**) $\lambda = 308$ nm, $\phi \approx 255\,mJ/cm^2$ [*Arenholz* et al. 1998]

density increases (Fig. 4.3.4). At a certain pressure, the polymer surface is completely covered with dendrites. Such a morphology may be quite favorable for applications where a nano-roughness of the polymer surface improves the adhesion of evaporated films, avoids the collapse of magnetic heads, etc. (Sect. 27.1).

Because dendritic growth is observed *only* within the laser-irradiated spot *and* is influenced by the type and pressure of the ambient atmosphere, the growth of dendrites must be related to both the laser-induced modification of the polymer surface *and* the condensation of back-scattered material after ablation. This can be tentatively understood on the basis of the partial recrystallization of the amorphized polymer surface and segregational growth from redeposited material. Both the thickness of the amorphized layer and the size of ablated fragments depend on the laser wavelength.

Nanowires, Nanohorns and Nanotubes

Sponge-like webs and columns of nanowires have been grown by PLA using different types of targets and Ar or N_2 atmospheres at pressures of up to 700 mbar.

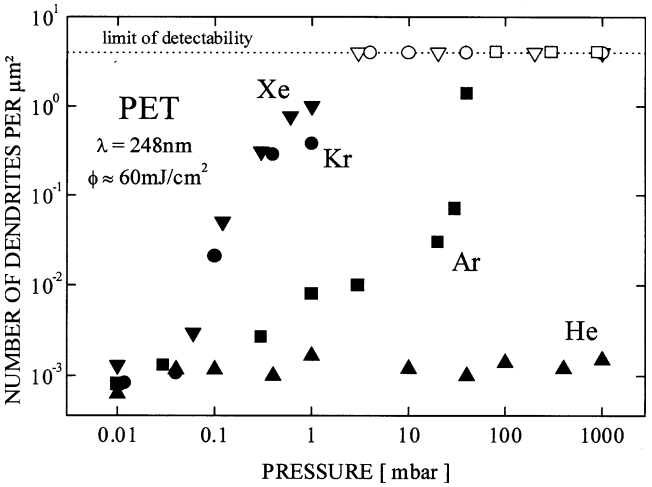

Fig. 4.3.4 Number density of dendrites observed after single-pulse KrF-laser irradiation of PET in various ambient atmospheres: (▲) He, (■) Ar, (●) Kr, (▼) Xe. The AFM measurements were performed after annealing the sample for $t_{gr} = 60$ min at $T_{gr} \approx 55°C$. Dendrite densities exceeding the limit of detectability are also shown (*open symbols*) [*Klose* et al. 1999]

Some of the experiments were performed in quartz tubes placed within an oven at temperatures up to 1200°C. For the fabrication of Si nanowires and C nanotubes, the targets were doped with about 0.5–1 % of Fe, Co or Ni. Figure 4.3.5 shows a TEM image of Si nanowires. They consist of a crystalline Si core and a ∼ 5 nm amorphous outer sheath. Their diameter is, typically, within the range of a few to several tens of nm, and their lengths up to a few hundred µm. The growth rates

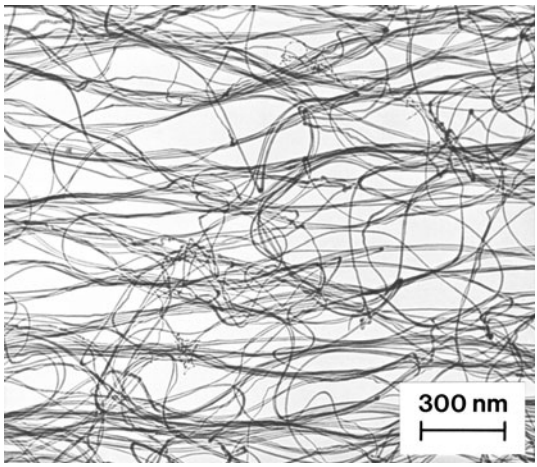

Fig. 4.3.5 TEM image of Si nanowires fabricated by KrF-laser ablation in 665 mbar Ar. The target was pressed Si powder doped with 0.5% Fe [*Y.F. Zhang* et al. 1998]

were 10–80μm/h. Here, the growth process seems to be catalyzed by the metal dopants. However, with mixed Si/SiO_2 targets, SiO_2 may play an important or even dominating role in nanowire formation [*Wang* et al. 1998]. Doping of Si nanowires (Si core 37 ± 5 nm, SiO_x shell ≈ 20 nm) through ion implantation and subsequent annealing with $3 - 5$ ns Nd:YAG-laser pulses was studied by *Misra* et al. (2008).

Nanowires seem to grow from seed nanoclusters formed within the vapor/plasma plume within micro- to milliseconds (Sect. 4.2). The growth of nanowires that takes place on the substrate, proceeds on a much longer time scale.

Quartz tube furnaces were also used for the growth of single-wall carbon nanotubes (SWNT) and nanohorns (SWNH). Nanosecond laser ablation of Co or Ni-doped carbon targets at temperatures around 1100°C favors growth of SWNT. High growth yields ($\approx$ 6 g/h) were achieved by cumulative ablation with spatially overlapping 0.5 ms Nd:YAG-laser pulses [*Puretzky* et al. 2008; *Gorbunov* and *Jost* 2007]. Efficient growth requires good confinement of carbon and metal clusters over relatively long times. This requirement is better fulfilled with 'short' laser pulses.

Growth of vertically aligned carbon nanotube arrays (VANTAs) by *standard* CVD from mixtures of C_2H_2 and N_2 has also been demonstrated on KrF-laser modified multilayer catalyst films consisting of Al, Mo, Fe, or $Fe(NO_3)_3$ on Si(100) substrates. VANTAs grow only at sites that have been laser-irradiated prior to CVD. This behavior has been ascribed to the strong catalytic effect of nanoparticles formed within the laser-irradiated film area [*Rouleau* et al. 2008; *Zimmer* et al. 2007].

Efficient growth of carbon nanohorns ($\approx$ 10 g/h) is achieved by ablation of *pure* graphite targets and 20 ms Nd:YAG-laser pulses [*Puretzky* et al. 2008]. In contrast to CO_2-laser synthesis, no or negligible amounts of graphitic impurities were found.

Vertically well-aligned ZnO nanowires were grown on metal-patterned sapphire substrates by KrF-laser ablation of *undoped* ZnO targets [*Guo* et al. 2008; *Rahm* et al. 2007].

4.3.3 Nanotube Formation by Laser-CVD

Carbon nanotubes were also grown by laser-CVD (LCVD) using both cw- and pulsed-laser irradiation. In all cases, the substrate materials employed were coated with either catalyst thin films or with nanoparticles, e.g. Fe/Co, Co/Mo, etc. The precursor gases employed include mixtures of CH_4/C_2H_4, C_2H_5OH in Ar and H_2. With cw-laser irradiation, sponge-like 'films' consisting of mixtures of multi- and single-walled carbon nanotubes (MWNT/SWNT) have been grown in well-localized regions on substrate surfaces [*Chiashi* et al. 2007; *Kasuya* et al. 2007]. *Pulsed*-laser irradiation, however, permits to grow pure SWNT. This effect is ascribed to the strong temperature gradients in pyrolytic LCVD that are further enhanced by the rapid heating/cooling cycles with pulsed irradiation. Thus, gas-phase pyrolysis is suppressed even more efficiently [*Liu* et al. 2008]. In these latter investigations, pulsed Nd:YAG-laser radiation ($\lambda = 1064$ nm, $\tau_\ell \approx 0.5$–50 ms, 1–500 pps) together

with mixtures of CH_4/C_2H_4 in Ar and H_2 have been employed. The SWNT had lengths between 1 μm and 10 μm. Depending on laser parameters, growth rates of 10–100 μm/s have been achieved. Laser-assisted growth of carbon nanotubes is another example which demonstrates the versatility of LCVD and the differences in growth kinetics in comparison to standard CVD (Chaps. 16, 17 and 18).

4.3.4 Shaping of Nanoparticles

Metal nanoparticles (NPs) with well-defined dimensions and very small size distributions can be fabricated by selective laser ablation/evaporation. This has been demonstrated for nanoparticles on dielectric substrates [*Hubenthal* 2009]. For example, deposition of a submonolayer metal film on a dielectric substrate results in the formation of nanoclusters due to surface diffusion and nucleation of atoms (Volmar-Weber growth). Shaping of NPs is based on selective excitation of surface plasmons. Because the resonance frequencies of surface plasmons (SPR) depend on the size d of NPs, the absorption cross section, and thereby the heating of NPs depends on d. By using two or several different laser frequencies, it is possible to totally evaporate the smallest clusters of the distribution and to shrink the largest ones. By this means, only clusters with a well-defined size and a small size distribution remain on the substrate. For example, Ag clusters have been fabricated with a size of 5 ± 1 nm. Clearly, for non-spherical particles the frequencies of SPRs depend on the orientation of particles with respect to the electric field of the laser light. By applying successively different laser wavelengths, the shaping of ellipsoidal Au nanoparticles to sizes with mean axial ratios between 0.19 and 0.98 has been demonstrated [*Hubenthal* et al. 2005]. Shape tailoring of triangular Au deposits formed by nanosphere lithography has been discussed by *Morarescu* et al. (2009). An important quantity for many applications of metal-nanoparticles is the damping of localized surface plasmon polaritons. For colloidal elliptically shaped Au-nanoparticles with an equivalent radius $< r > \approx 17$ nm a dephasing time $T_2 \approx 3.7$ fs has been found [*Hubenthal* 2007].

4.3.5 Cluster Formation Within Solid Surfaces

Laser light can decompose a material within a certain penetration depth and thereby generate clusters of product species. Examples are nanoparticles of Ca formed in CaF_2 under 157 nm F_2-laser radiation [*Cramer* et al. 2006], Si precipitates in SiO_2 surfaces [*Kurosawa* et al. 1993], Ag and Au nanoparticles in doped glasses [*Shin* et al. 2008], etc. Clearly, precipitation of Ag clusters is well known from some types of sun glasses.

Hg-lamp irradiation of strained $Si_{0.8}Ge_{0.2}$ layers in O_2 results in selective formation of SiO_2 under which a Ge-rich layer of SiGe accumulates. Further irradiation and oxidation results in the formation of Ge NPs within the SiO_2 layer. The samples show photoluminescence within the range 550–800 nm [*Craciun* et al. 1995a].

Chapter 5
Lasers, Experimental Aspects, Spatial Confinement

5.1 Lasers

The lasers most commonly used in materials processing are listed in Table I. In the following sections, we will discuss only some characteristic properties of various lasers and their particular areas of application in materials processing.

5.1.1 CW Lasers, Gaussian Beams

Microfabrication by laser direct writing is mainly performed with continuous wave (cw) Ar^+ or Kr^+ lasers, including frequency-doubled lines. The good spatial coherence of such lasers permits tight focusing; together with their good stability in beam profile (mode), output power, frequency, and beam pointing, these lasers allow accurate microfabrication with constant and well-defined morphology. The main disadvantages of ion lasers for applications are their low efficiencies and high costs.

The TEM_{00} mode, which has been used in most of the experiments, is of Gaussian shape (Fig. 5.1.1). The laser-beam intensity within the focal plane has the form

$$I(r) = I_0 \exp\left(-\frac{r^2}{w_0^2}\right) , \tag{5.1.1}$$

where w_0 is the radius of the laser focus defined by $I(w_0) = I_0/\mathrm{e}$. (Frequently, one uses the definition $I(w_\mathrm{e}) = I_0/\mathrm{e}^2$ instead so that $w_\mathrm{e} = \sqrt{2}w_0$.) The *total laser power* is

$$P = 2\pi \int_0^\infty r I(r)\,\mathrm{d}r = \pi w_0^2 I_0 . \tag{5.1.2}$$

Throughout this book, the laser power always refers to the *effective* power incident onto the substrate surface, i.e., it is corrected for losses at the entrance window of the reaction chamber, etc.

D. Bäuerle, *Laser Processing and Chemistry,* 4th ed.,
DOI 10.1007/978-3-642-17613-5_5, © Springer-Verlag Berlin Heidelberg 2011

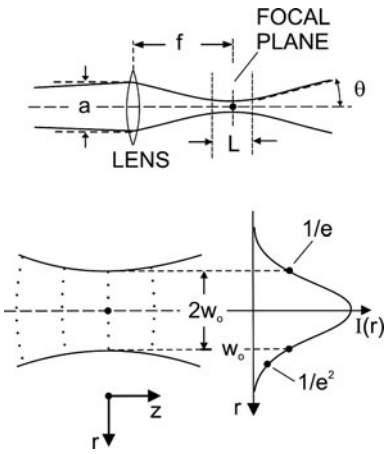

Fig. 5.1.1 Intensity distribution and shape of a Gaussian laser beam near the focal plane. $2w_0$ is the beam waist, $L = 2z_R$ the length (depth) of the focus, and Θ the beam divergence angle. The shape of the wave front is indicated (*dotted curves*)

In order to obtain a tight focus, the laser beam is first expanded and then focused by a lens (Fig. 5.1.1). For small divergence of the incident beam and $a \gg \lambda$, the beam waist occurs approximately at the focal distance (length), f, from the lens. The radius of the *laser focus* within the focal plane is approximately given by

$$w_0 \approx \zeta \frac{f\lambda}{\pi a} \,. \tag{5.1.3}$$

ζ depends on the definition of a, which is the diameter of the beam in the middle of the focusing lens. If we define this diameter by the $1/\mathrm{e}$ and $1/\mathrm{e}^2$ intensity levels, $a(1/\mathrm{e})$ and $a(1/\mathrm{e}^2)$, the respective values are $\zeta = 1$ and $\zeta = \sqrt{2}$. The intensity profile within the focal plane is Gaussian only if the diameter of the lens significantly exceeds the diameter of the laser beam.

If we confine the diameter of the laser beam by a real aperture of diameter d, the intensity profile within the focal plane becomes non-Gaussian. With $d = a(1/\mathrm{e})$ and $d = a(1/\mathrm{e}^2)$, the transmitted power is 63 and 86%, respectively. With $d = \pi a(1/\mathrm{e})/\sqrt{2}$, about 99% of the total power is transmitted. Within the focal plane, the variation in intensity due to diffraction is then $\pm 17\%$. With $d \approx 3.3a(1/\mathrm{e})$ this variation is diminished to below $\pm 1\%$ [*Siegman* 1986].

It is evident that the diffraction-limited diameter of the laser focus, $2w_0$, decreases with decreasing wavelength. Clearly, w_0 is one of the essential parameters determining the lateral resolution of patterns. If not otherwise noted, we henceforth use w_0 and a defined by the $1/\mathrm{e}$ intensity level.

The *radius of the laser beam* at distance z from the focal plane is

$$w(z) = w_0 \left[1 + \left(\frac{z}{z_\mathrm{R}} \right)^2 \right]^{1/2} , \tag{5.1.4}$$

where z_R is the Rayleigh length, i.e., the distance over which the diameter of the focused beam changes by a factor of $\sqrt{2}$. The region $|z| \leq z_\mathrm{R}$ is often denoted as the *Rayleigh range*. The length (depth) of the laser focus is defined by

$$L = 2z_\mathrm{R} = \frac{4\pi w_0^2}{\lambda} = \frac{4f^2\lambda}{\pi a^2} . \tag{5.1.5}$$

Sometimes, L is also denoted as the confocal parameter. With decreasing w_0, accurate positioning of the substrate into the focal plane becomes more and more difficult. For $z \gg z_\mathrm{R}$, the beam radius increases linearly with z and the *divergence angle* (Fig. 5.1.1) is

$$\Theta = \frac{w_0}{z_\mathrm{R}} = \frac{a}{2f} . \tag{5.1.6}$$

5.1.2 Pulsed and High-Power CW Lasers

Pulsed lasers are the preferred sources in all types of laser processing where high heating rates and well-defined localization of the energy input within the substrate/workpiece is desirable. The optimum laser fluence for processing and the heat diffusion length are both controlled via the laser-pulse length, τ_ℓ. The strong nonlinearities in laser-material interactions which are particularly pronounced with ultrashort-laser pulses, are a prerequisite for laser micro- and nanofabrication. The intensity profile of many types of pulsed lasers is non-Gaussian. The beam width is then defined by the full width at half maximum (FWHM), which is henceforth denoted by $2w$. Spatial and temporal pulse shaping for laser manufacturing is described, e.g., in [*Landolt-Börnstein* 2004].

At laser-light intensities $>10^8\,\mathrm{W/cm^2}$, the optical properties of the material to be processed (workpiece) become less important. In this regime, all materials become absorbing at any wavelength due to surface breakdown and plasma formation (Chap. 11).

Among the problems that arise with the presently commercial pulsed lasers are: difficulties in the precise control of the output power, at least on a shot-to-shot basis, and changes in the beam profile and pointing. These problems may result in surface damage due to uncontrolled melting or ablation, and in a poor uniformity and morphology of generated patterns in microprocessing. Additionally, with UV lasers, in particular with excimer lasers and frequency-tripled or frequency-quadrupled Nd:YAG lasers, only moderate pulse energies are available.

Excimer Lasers

For laser micropatterning and some types of surface modifications and thin-film deposition, excimer lasers and F_2-lasers are almost ideal sources. This is related to their high photon energies (short wavelengths), their short pulse lengths (typically 10–40 ns), and their relatively poor coherence (an excimer laser's output is highly multimode and contains as many as 10^5 transverse modes). The high photon energy of excimer lasers allows for direct photodissociation of many molecules and strong optical absorption with many solids. The short pulse length is a prerequisite for spatially well-defined and chemically stoichiometric ablation with low damage of the surrounding material, in particular for heat-sensitive and multicomponent substrates. The poor spatial coherence of excimer-laser light diminishes interference effects. Interferences cause severe problems in imaging applications with lasers of high spatial coherence. High photon energies, rapid heating and cooling rates, and good energy localization within a thin surface layer are prior conditions in laser lithography, in sheet doping of semiconductor surfaces, and in *congruent* laser ablation for surface patterning and thin film formation by PLD. Modern excimer lasers can be operated with pulse repetition rates of several kHz and average powers up to several 100 Watts. At low repetition rates pulse energies $E_\ell \gtrsim 1$ J are achieved. Among the disadvantages of excimer lasers are their low efficiency (the laser output power is only about 1–3% of the electrical input power), their moderate pulse-to-pulse stability, and the high operating costs. F_2-laser processing requires the beam path to be purged with dry N_2 because water and O_2 absorb 157 nm radiation. For fundamental and technological aspects on excimer- and F_2-lasers see [*Basting* and *Marowsky* 2005].

With some types of large-area applications, e.g., surface modifications of organic polymers, excimer lasers may be substituted by excimer lamps [*Gumpenberger* et al. 2005, 2003; *Vollkommer* and *Hitzschke* 1997].

CO_2 Lasers

CO_2 lasers with high average power in cw or pulsed operation are the most commonly used sources in laser machining (cutting, drilling, shaping, etc.), laser welding, and many types of large-area surface modifications (hardening, glazing, etc.). CO_2 lasers combine a high efficiency with great reliability and low-cost operation. They are presently the most important laser sources for technical applications. Fundamental aspects of CO_2 lasers [*Siegman* 1986] and the specific requirements on such lasers in conventional laser processing [*Steen* 2003; *Duley* 1976] are widely discussed in the literature.

Nd:YAG and Nd:Glass Lasers

High-power pulsed and cw Nd:YAG lasers are employed in various types of laser machining (scribing, trimming, cutting, etc.) and surface modifications. Nd:YAG lasers and, in particular, diode-pumped lasers are very reliable. Besides CO_2 lasers,

they are the most important sources in conventional laser processing [*Steen* 2003]. While Nd:YAG lasers allow high cw powers and high average powers at high pulse repetition rates, Nd:glass lasers are particularly suitable for applications that require short, high-intensity pulses. Frequency-multipled lines of both Nd:YAG and Nd:glass lasers are used in different areas of laser microprocessing.

Ultrashort-Pulse Lasers

The most established ultrashort-pulse laser is the Ti:Sapphire (Ti-S) laser. By using special pulse stretching and compression techniques, pulse durations between some hundred ps and about 1 fs can be achieved. The wavelength most commonly employed is around 800 nm. Higher harmonics of Ti-S lasers are frequently used as well.

Diode-pumped ps Nd:YVO_4 and fs Yb:YAG systems may become a promising alternative to Ti-sapphire lasers [*Kleinbauer* et al. 2004].

Fiber Lasers

Rare-earth-doped fiber lasers gain increasing importance because of their compactness, flexibility, high efficiency, and low pump thresholds. They are pumped by diode laser arrays and can be operated in cw- and pulsed-modes. Cw-fiber lasers with an output power of several kW and diffraction limited beam quality have been demonstrated. With Yb-doped fiber CPA (chirped-pulse amplification) systems average powers of more than 100 W at 1030 nm wavelength, repetition rates of 75 MHz, and pulse lengths of less than 30 fs have been achieved. The fundamentals and applications of ultrashort-pulse fiber lasers are reviewed by *Tünnermann* et al. (2004).

5.1.3 Semiconductor Lasers

Diode lasers are becoming increasingly important for pumping solid-state lasers such as Nd:YAG, Ti:Sapphire, or fiber lasers. In laser materials processing diode lasers are employed for soldering, transformation hardening, and some cases of cladding, welding, and cutting [*Bachmann* et al. 2007].

The photon energy of semiconductor lasers is directly related to the bandgap energy and the doping of the material (Fig. 2.1.1). The wavelengths of the lasers that are most important for applications in materials processing are within the range between about 0.4 µm (GaN) and 8–12.5 µm ($Pb_{1-x}Sn_xSe$). At present, the most commonly used semiconductor laser is the $Al_{1-x}Ga_xAs$ laser with output wavelengths ranging from about 780 to 880 nm (Table I). The exact wavelength of a particular diode laser depends on the operating temperature and the current. Semiconductor lasers may operate continuously, quasi-continuously ($\tau_\ell \approx 100\,\mu s$) or with pulse durations in the ns or ps regime. A single p-n junction of a conventional *horizontal cavity* (edge emitting) diode laser emits, typically, a few milliwatts.

The spatial beam profile is often elliptical due to diffraction of the radiation perpendicular to the narrow junction, which is around 1 μm thick. The astigmatism can often be corrected by employing anamorphic lenses (these have different magnifications in the two directions perpendicular to k_ℓ). Because of the large beam divergence, diode lasers cannot be focused very well.

High-power linear diode-laser *arrays* emit up to 10^3 W in cw operation and stacks of 2D arrays up to 10^4 W in quasi-cw operation. The most attractive features of diode lasers are their high efficiency (up to more than 50%), their small size, light weight, low operating voltage, tunability and, very importantly, their low prime and operating costs. Among the main disadvantages of diode lasers are their bad spatial beam profile, the low power density, and the short working distances that can be employed.

As well as the conventional horizontal cavity diode lasers, *vertical cavity surface emitting lasers* (VCSEL) have become increasingly important [*Li* and *Iga* 2003]. Such lasers can be fabricated as two-dimensional arrays and they have a much better beam characteristic than edge-emitting diode lasers.

Semiconductor lasers based on quantum dots exhibit some properties that are superior to those based on quantum wells. Among those are the low threshold current, high temperature stability, and the relatively high power, at present about 1.5 W. Both edge emitting and surface emitting quantum dot lasers have been demonstrated.

5.2 Experimental Aspects

The main components to be considered in laser processing are the laser, the imaging optics, the substrate and, in many cases of LCP, the reaction chamber. Subsequently, we shall discuss different kinds of irradiation geometries and experimental setups employed in different kinds of localized and large-area laser processing.

5.2.1 Micro-/Nanoprocessing

Laser micro-/nanoprocessing allows for *single-step* direct substrate patterning with lateral dimensions down to several 10 nm. It can be performed by direct writing, by projection of the laser light via a mechanical mask, by employing a direct-contact mask, by interference of laser beams, by means of microlens arrays, or by SXM-type techniques (Fig. 5.2.1).

Direct Writing

In direct writing, the laser beam, in general a cw laser, is expanded and then focused at normal incidence onto the substrate surface (Fig. 5.2.1a). In most cases of micro- and submicropatterning, the substrate is translated with respect to the fixed laser beam.

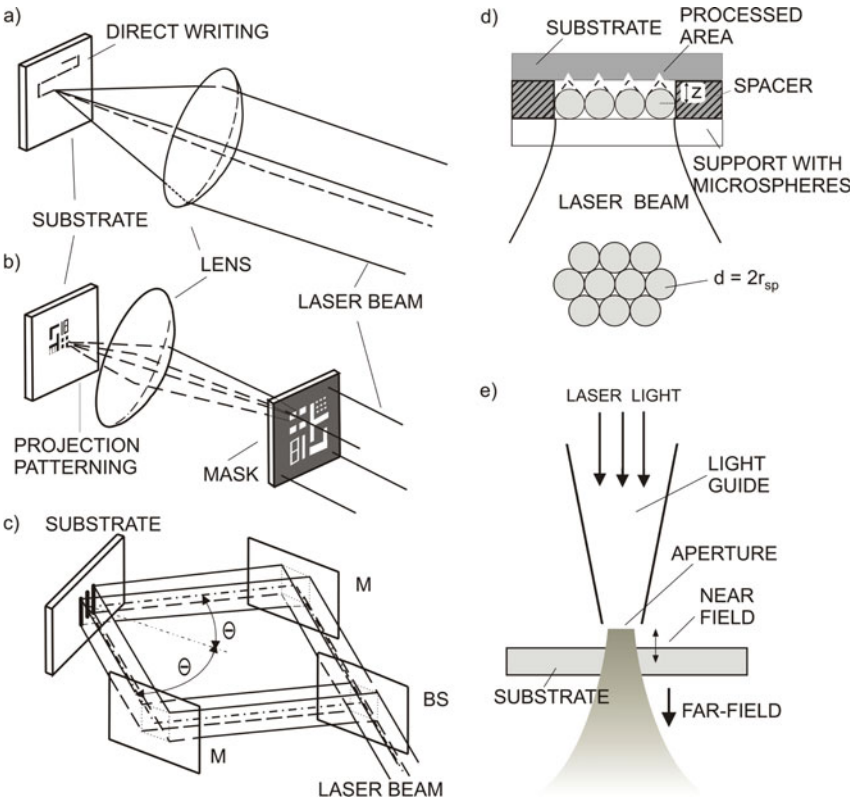

Fig. 5.2.1 a–e Optical configurations employed in laser micro-/nanoprocessing. (**a**) Direct writing. (**b**) Projection patterning (the optical path is indicated for one feature only). (**c**) Patterning by interference of laser beams (M: mirror, BS: beam splitter, Θ: angle of incidence). (**d**) Patterning by means of microlens arrays. The diameter of microspheres is $d = 2\,r_{\mathrm{sp}}$. (**e**) SNOM-type setup. Aperture sizes are, typically, $a \lesssim 100$ nm and the separation between probe and sample is, typically, 5–50 nm

The diffraction-limited diameter of a Gaussian laser beam focus is given by (5.1.3). Thus, for $f/a \approx 1$, the minimum laser spot size becomes $2w_{0\,\mathrm{min}} \approx \lambda$. With Ar^+ and Kr^+ lasers this is, typically, around 0.5 µm. In practical applications, however, values $f/a > 1$ are frequently employed. There are several reasons for this: In order to minimize diffraction effects, the diameter of the laser beam at the focusing lens, $a(1/\mathrm{e})$, should be considerably smaller than the diameter of the lens, d, and thus $f/a > f/d \geq 1$. To minimize image aberrations, special lenses or elaborate lens combinations must be used, and this increases f/d even further. Moreover, all types of laser processing require a certain working distance between the lens and the substrate to be processed, e.g., to suppress contaminations of the lens by species desorbing/evaporating from the substrate, or due to a window of a reaction chamber, etc. Furthermore, some applications require a certain depth of focus, L, e.g., for processing of non-planar substrates. This also limits the size of the

focus that can be employed, since $L \propto f^2/a^2$. In summary, in practical applications one has to compromise between the size of the focus, the working distance, the focal depth, and the price of the imaging optics.

For 3D laser machining (cutting, welding, etc.) beam-guiding is often performed by means of flexible arms or optical fibers. Fiber optics combines high flexibility for 3D motion with simple beam guiding over long distances.

Projection Patterning

Laser-light projection (Fig. 5.2.1b) allows one to generate whole patterns with a single or a few laser shots.

As well as the simple imaging shown in the figure, telecentric optical schemes, Schwarzschild telescopes, and complex optical systems, either all-refractive systems or catadioptric (refractive/reflective) systems, are employed. Distortion free flat field imaging is of particular importance in microlithography (Sect. 27.2).

The smallest resolvable feature size achieved in projection patterning is often defined by the smallest distance between two points that can be resolved according to the Rayleigh criterion

$$d = \xi_1 \frac{\lambda}{NA} \,. \tag{5.2.1}$$

$NA = n \sin \Theta$ is the numerical aperture of the imaging system (2Θ is the total angle of the focused beam near the image; see Fig. 5.1.1). ξ_1 is a factor which depends on the spatial and temporal coherence of the light, the shape of features which are projected, and the criterion which defines 'separation' of features. With the 'classical' definition, the value ξ_1 is, typically, within the range $0.5 \leq \xi_1 \leq 0.8$. For dense equidistant lines, e.g., one finds $\xi_1 = 0.5$ and for dots $\xi_1 = 0.61$ [*Born* and *Wolf* 1980]. There are, however, different definitions for the separation of features, e.g., $d_{\min} \approx d/2$ in (5.2.1) so that $\xi_1' = 0.5\xi_1$ [*Rothschild* 1998]. For the imaging of equal lines and spaces by means of incoherent light one obtains $\xi_1' = 0.25$. Another important processing parameter is the depth of focus. In photolithography, one frequently uses the notation DOF, instead of L, with

$$\mathrm{DOF} \equiv L = \xi_2 \frac{\lambda}{NA^2} \,, \tag{5.2.2}$$

where ξ_2 may depend on ξ_1. Projection patterning requires, in general, a DOF $\geq$ 1 µm, depending on the particular processing application (surface/thin-film transformation, etching, deposition, etc.). In microlithography a DOF of 0.5 µm may become tolerable. Equations (5.2.1) and (5.2.2) reveal that a reduction in feature size is achieved more easily by decreasing λ, than by increasing NA, because the DOF decreases with the second power of NA.

Surface patterning using a contact mask can be performed with laser light that is either focused to a line or unfocused with perpendicular or/and parallel incidence (Fig. 5.2.4). Here, the resolution is determined by the mask.

Interference

Laser-beam interference (Fig. 5.2.1c) allows one to generate patterns with periods

$$\Lambda = \frac{\lambda}{2n \sin \Theta} \tag{5.2.3}$$

over several square centimeters. The technique has been successfully demonstrated for material deposition, surface modifications, chemical etching, and (well-defined) surface roughening. It permits one to fabricate diffraction gratings, holograms, etc.

By means of phase-controlled multiple-beam interferences, complex periodic patterns can be generated [*Ihlemann* et al. 2007; *Klein-Wiele* and *Simon* 2003].

Light Modulators

For rapid maskless processing, liquid crystal devices (LCDs) and digital micromirror devices (DMDs) have been employed as electrically controllable spatial light modulators. With LCDs line patterns with widths of around 10 μm have been fabricated [*Hayashi* et al. 2008]. By combining a DMD and near-field optics, feature sizes down to 100 nm have been achieved [*Pan* et al. 2010].

Microlens Arrays

Regular two-dimensional (2D) lattices of micro-/nanospheres formed by self-assembly processes, e.g. from colloidal suspensions, can be employed to produce on a substrate surface millions to some billions of micrometer-/nanometer-sized features with a single or a few laser shots [*Bäuerle* et al. 2002]. Transparent microspheres with radii $r_{sp} > \lambda$ behave like microlenses that focus the radiation onto the substrate. A schematic experimental arrangement is shown in Fig. 5.2.1d. Due to (spherical) aberration, the maximum intensity is shifted from the geometrical focus

$$f = \frac{r_{sp}}{2} \frac{n}{n-1} \tag{5.2.4a}$$

to the diffraction focus

$$f_d \approx f \left(1 - \sqrt{\frac{3\lambda}{8 r_{sp}} \frac{n(3-n)-1}{n(n-1)}} \right) . \tag{5.2.4b}$$

where n ist the refractive index of the microspheres. Figure 5.2.2a shows a white light image generated by a 2D-lattice of a-SiO_2 microspheres at a distance $z = f$.

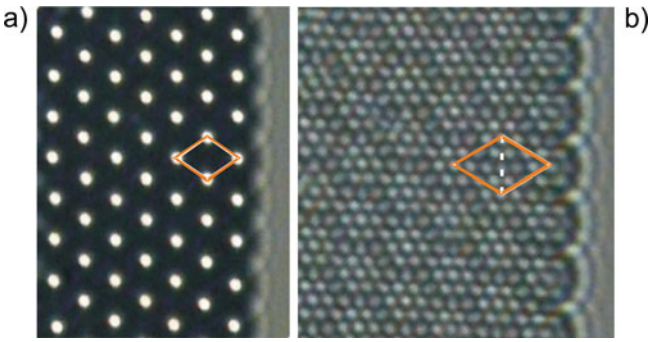

Fig. 5.2.2 a, b White-light microscope pictures of primary and secondary intensity maxima generated by a 2D-lattice of a-SiO_2 microspheres of diameter $d = 3 \pm 0.15\,\mu\text{m}$. (**a**) $z \approx f$; in this case the distance between the intensity maxima is equal to the diameter of spheres (see *rhombus*). (**b**) $z = f + \varepsilon$. The distance between interference maxima is about 800 nm. At the right side of the figures the boundary of the array of spheres can be seen [*Bäuerle* et al. 2002]

In this case, the microscope picture reveals the hexagonally close-packed structure of the lattice formed by the microspheres. The distance between intensity maxima is equal to the diameter of microspheres. If the distance z in Fig. 5.2.1d is increased by an amount ε, so that the total distance between the center of the microspheres and the substrate surface is given by $z = f + \varepsilon$, we can generate different interference patterns in the Fresnel region, which show periodically ordered well-defined maxima of similar intensities. The distances between these maxima are much smaller than the diameter of the spheres. This can be seen in the white-light microscope picture shown in Fig. 5.2.2b. The changes in the spatial frequency of the hexagonal pattern can be qualitatively understood along the following lines. Spheres create waves, which first converge, and then diverge behind the foci. These waves interfere in the region where they significantly overlap. Due to their localization, mainly adjacent beams will interact. This can be approximated by a superposition of single Gaussian beams. The interference pattern obtained in this way is in good agreement with the pattern shown in Fig. 5.2.2b. The intensity enhancement behind mirospheres and optical near-field effects are discussed in Sect. 5.3.7. "Direct writing" by means of microlens arrays can be performed by angular scanning of the incident laser beam [*Guo* et al. 2007]. Subwavelength direct writing by means of *single* optically trapped microspheres has been demonstrated by *McLeod* and *Arnold* (2008).

Combined Laser-SXM Techniques

Scanning-probe microscopy (SXM) such as scanning near-field optical microscopy (SNOM), or scanning tunneling microscopy (STM) and atomic force microscopy (AFM) in combination with laser light, permits surface processing with very high spatial resolution.

SNOM-type setups have been employed for nanolithography, local reduction of oxides, material etching, ablation, and nanodiagnostics [*Hwang* et al. 2009a; *Wysocki* et al. 2004; *Nolte* et al. 1999a; *Pedarnig* et al. 1998]. In this technique, the laser light is coupled into the tip of a solid or hollow fiber as shown in Fig. 5.2.1e.

By positioning the substrate within the near field of the fiber tip, one can produce structures that are *not* limited by optical diffraction (Sect. 5.3.7).

Laser-illuminated STM and AFM tips have been used for local surface modification, deposition, and material removal with a spatial resolution down to about 10 nm. Here, field-enhancement effects underneath the tip play an important or even a dominant role in the patterning process [*Hwang* et al. 2009a; *Hwang* et al. 2002]. The first experiments by *Jersch* et al. (1997) were based on thermal expansion of the tip, causing a "printing" effect on the surface.

5.2.2 The Reaction Chamber; Typical Setup

In LCP, the reaction chamber is often operated with a constant flow of the gaseous or liquid reactant with or without a carrier. In microchemical processing, the reaction chamber can be sealed off, in many cases, because of the small amount of species consumed in most of the reactions. The type of material used for the fabrication of the reaction chamber is often of great importance. Spontaneous reactions of precursor molecules, intermediate species, reaction products, and carrier gases or solvents with the chamber material can result in significant changes in the number densities of species, and reaction pathways and, more importantly, in additional reaction products that contaminate the substrate surface, the deposited film, the microstructure, etc. Thus, proper materials selection for the reactor, including its windows, o-rings, etc., is a prerequisite for well-defined processing.

A typical setup employed in direct writing is schematically shown in Fig. 5.2.3. Laser-beam illumination times are electronically controlled via a mechanical shutter

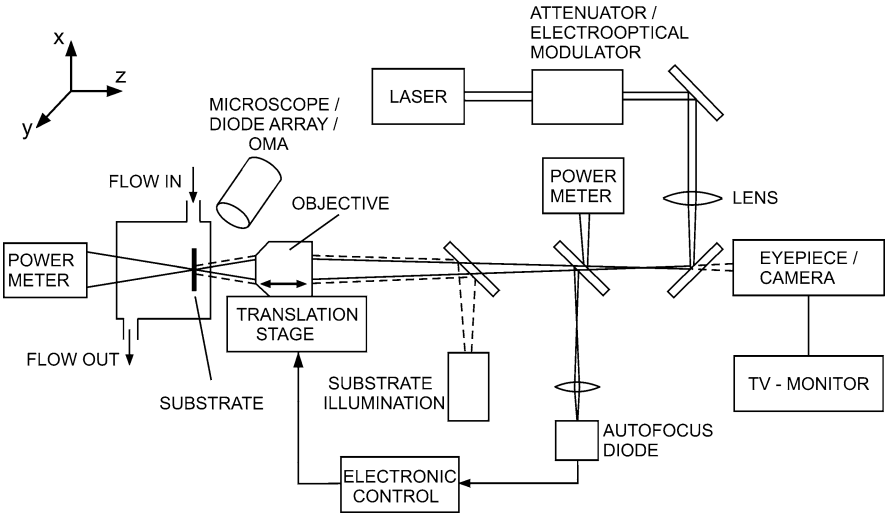

Fig. 5.2.3 Typical experimental setup employed in microchemical processing. The substrate is mounted on an xyz stage. The position of the objective is optically and electronically controlled (autofocus). The eyepiece, or a CCD camera together with a monitor, is used for direct observation of patterns

or via an electro-optical modulator. In micropatterning, the laser beam is first expanded and then focused onto the substrate, for example by employing an objective. An eyepiece, or a CCD camera in combination with a monitor, is used for direct observation of patterns. The position of the objective is optically and electronically controlled (autofocus). Additionally, a polarizer and a $\lambda/4$ plate are introduced, in general, in order to avoid optical feedback from the substrate or the processed area. Optical coupling can generate relaxation oscillations, mode instabilities, or chaotic temporal behavior, which result in spatial and temporal intensity fluctuations. The lasers most commonly used in direct writing are cw lasers, mainly Ar^+ and Kr^+ lasers. Typical (effective) power densities employed, are between 10^3 and some 10^7 W/cm^2. The main features of setups used in micropatterning by laser-light projection and interference are similar.

5.2.3 Large-Area Processing

Extended thin-film formation by LCVD and different kinds of large-area surface transformations, modifications, etching, and ablation are performed with the optical arrangements shown in Fig. 5.2.4.

For *perpendicular* (normal) laser-beam incidence, the substrate is scanned with respect to the laser beam, which is either unfocused or defocused, or focused to a line by means of a cylindrical lens. The latter arrangement is shown in Fig. 5.2.4a. The experimental setup and laser–molecule–substrate interactions are very similar to those described for microprocessing. Direct substrate irradiation can clean the surface, assist nucleation processes, enhance surface diffusion of species, promote surface catalyzed reactions, etc. With large-area gas- or liquid-phase processing, transport limitations become important at lower (thickness) deposition rates than in microchemical processing. This is a consequence of the dimensionality of transport. Transport will be determined by two-dimensional diffusion if a tight line focus is used, and by one-dimensional diffusion if the laser beam is unfocused or defocused. Besides irradiating the substrate through the ambient medium, the entrance window can itself be used as a substrate (Fig. 9.5.1b). This irradiation geometry can be employed with strongly absorbing media, or with gases of moderate absorption at high pressures.

Films deposited at perpendicular laser-beam incidence are often of better morphology and higher purity than those deposited at parallel incidence. This is mainly a consequence of laser-induced surface heating.

Parallel laser-beam incidence opens up the ability to investigate the influence of species excited within the gas phase only. With both pyrolytic and photolytic processes, excitation of species will take place within the total volume of the laser beam. The absence of direct substrate or film irradiation, permits high-power cw or pulsed lasers to be employed. In order to increase the laser-light intensity above the surface, the mirror on the right side in Fig. 5.2.4b can be positioned perpendicular to the laser beam.

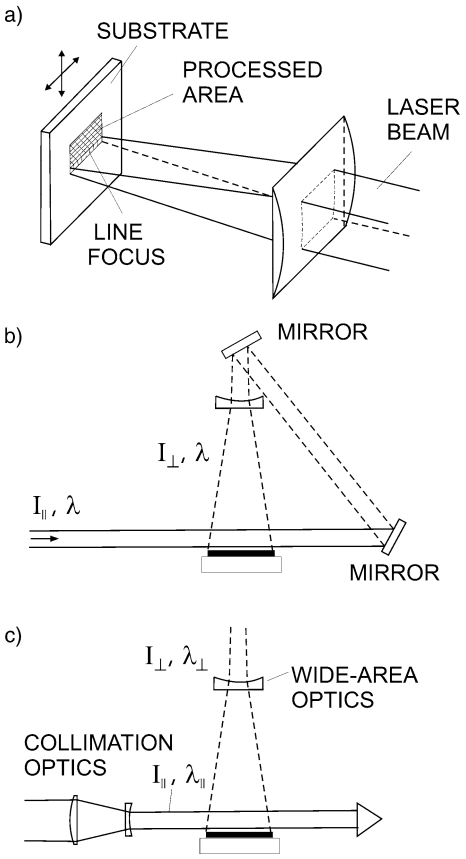

Fig. 5.2.4 a–c Large-area surface processing by employing: (**a**) a line focus; (**b**) parallel laser-beam incidence, eventually combined with perpendicular incidence of the transmitted light; and (**c**) combined parallel and perpendicular incidence of different laser beams

For the production of high-quality films, the substrate is often preheated to a certain temperature, T_s. This allows for proper control of the surface temperature and film thickness. The substrate temperatures typically employed are much lower than those used in standard CVD. LCVD permits one to control film thicknesses within, typically, 0.01 Å/pulse. This allows accurate growth of multilayer structures.

Combined parallel and perpendicular irradiation can be achieved by either directing the emerging beam onto the surface as shown in Fig. 5.2.4b or by using two lasers, for example, at different wavelengths (Fig. 5.2.4c). In the latter case, one can separately optimize homogeneous and heterogeneous pyrolytic or photolytic reactions by proper selection of the intensities and wavelengths of beams at parallel ($I_\parallel, \lambda_\parallel$) and perpendicular ($I_\perp, \lambda_\perp$) incidence. For perpendicular irradiation the laser can often be substituted by a lamp.

5.2.4 Substrates

Proper pretreatment, material selection, and temperature control of the substrate is of great importance in many types of laser processing.

The surface quality (cleanliness, roughness, morphology, surface oxides, etc.) and, if relevant, the crystallographic orientation of a particular substrate influence the laser-induced surface temperature, the sticking of impinging species, solid-phase in/out diffusion of species, the adherence of deposited films, etc.

Cleaning of the substrate surface is performed by employing the standard techniques that are widely described in the literature for gas-phase epitaxy, CVD, plasma deposition, etc. Efficient surface cleaning can sometimes be performed by irradiating the substrate (mainly in a vacuum or an inert atmosphere) prior to surface processing with a single or a few laser pulses. Here, excimer lasers have proved to be of particular suitability.

During LCVD or PLD, the substrate can be kept at either ambient or elevated temperature. This permits deposition onto heat-sensitive materials such as organic polymers, compound semiconductors, piezoelectric ceramics, etc. The as-deposited films are amorphous, polycrystalline, or monocrystalline, depending on the specific film and substrate material, surface temperature, and ambient atmosphere. For the growth of high-quality films, the substrate must fulfil a number of conditions:

- The mismatch in thermal expansion between substrate and film should be as small as possible. Otherwise, strains and even microcracks build up during cooling or post-deposition annealing.
- High chemical and thermal stability of the substrate material are required in order to avoid interface reactions. Interdiffusion of substrate/film elements causes contaminations and changes in film stoichiometry.
- The lattice constants of the substrate surface should closely match the lattice constants of the deposited material. This is a prior condition for oriented large-grain polycrystalline or epitaxial film growth.

For the integration of thin films in device technology, the substrate material that yields the best-quality films is not always the most suitable one (see, e.g., Sect. 22.4.2). With practical substrates, the mismatch in lattice parameters and thermal expansion, as well as material interdiffusion, can often be diminished by means of a buffer (intermediate) layer.

5.3 Confinement of the Excitation

The resolution achieved in laser micropatterning is determined by the width of the laser focus, by the spatial confinement of the laser-induced excitation, by material damages, and by different types of non-linearities. The quantity which determines the confinement of the excitation depends on the particular system under consideration. In some types of conventional laser processing and most cases of pyrolytic

microchemical processing, the important parameters are the width and depth of the thermal field induced on the substrate (workpiece) to be processed. In photochemical laser processing, the confinement of the interaction process is determined by (non-thermal) excitations of the ambient gas or liquid, of adsorbed layers, *and* of the substrate. With high laser powers, the spatial extension of the plasma plume becomes the relevant quantity. New mechanisms become important in ultrashort-pulse laser processing.

With special processing techniques using microlenses, thin wires, or SXM-techniques, optical near field effects become important.

5.3.1 The Thermal Field

The width and depth of the thermal field induced within the irradiated substrate is discussed in various chapters of this book, and in particular in Sect. 6.5. It is essentially determined by the width of the laser focus, the heat diffusion length, and the optical penetration depth, depending on the particular system.

5.3.2 Non-thermal Substrate Excitations

The spatial resolution achieved in a particular processing application can depend on non-thermal excitations of the substrate (Sect. 2.4). For example, the diffusion of photogenerated carriers in crystalline semiconductors may decrease the resolution in laser-induced dry-etching (Chap. 15). With ultrashort laser pulses, energy transport by ballistic propagation and diffusion of hot electrons in metals may significantly exceed the (lattice) heat transport (Chap. 13).

5.3.3 Gas-, Liquid- and Adsorbed-Phase Excitations

Apart from substrate excitations, adsorbed-phase and homogeneous gas- or liquid-phase excitations may decrease the spatial confinement in LCP. Species that are photoexcited/dissociated within the gaseous or liquid ambient medium will randomly diffuse towards the solid surface. Consequently, deposition on or etching of areas beyond the laser spot will occur. The loss in resolution can be minimized by a careful selection of the processing parameters.

In *pyrolytic* gas- or liquid-phase processing, thermal or photochemical excitations within the volume of the laser beam can be avoided, to a large extent, by the correct choice of the intensity and wavelength of the laser radiation.

In *photochemical* gas- or liquid-phase processing, a confinement of the reaction to the illuminated area is possible only if the dissociative continuum of adsorbed molecules is considerably shifted (in general, towards longer wavelengths). In such cases, proper selection of the laser-light frequency allows mainly adsorbed-phase

photolysis instead of gas- or liquid-phase photolysis (Chap. 20). If the interaction between adsorbed species and the substrate is strong enough, adsorbed-layer photolysis can also be performed by removing the ambient medium prior to laser-light irradiation. In all other cases, photoexcitation/dissociation will take place within the *total* volume of the laser beam. Here, tight focusing not only limits the area of excitation on the substrate, but also confines the relevant volume of excitation within the ambient medium. Species that are generated at a distance larger than their mean free path for collision-induced deactivation, recombination, or reactions with parent or other molecules will not reach the substrate. In other words, the flux of such species onto the substrate is limited to a small region around the laser spot. This depends on the collision rate and the incident light flux. In gas-phase processing, the reaction volume can sometimes be further diminished by correct selection of the type of buffer gas and the respective partial pressures of gaseous constituents.

The spatial confinement is also decreased by surface diffusion of adsorbed precursors, or of photofragments impinging on the substrate.

For the broad range of experimental conditions used in LCP, the relevant diffusion lengths may be smaller than, comparable to, or larger than the diffraction-limited diameter of the laser beam.

5.3.4 Plasma Formation

With the formation of a plasma, the confinement of the laser–solid interaction decreases, in both conventional and chemical laser processing. With dense plasmas, laser–solid interactions are mediated only via the plasma. The processing width is then determined by the size of the plasma plume. With ultrashort laser pulses, plasma shielding is strongly diminished or even irrelevant.

5.3.5 Material Damages

Laser-induced material damages and disturbances around the laser-processed zone may substantially decrease the spatial resolution in laser micropatterning. Strong temperature gradients may cause material cracking, the depletion of a certain component, material segregation, etc. Changes in the optical index of refraction, convection, turbulence, bubbling, etc., play an important role, in particular in liquid-phase processing and in all cases where the surface is melted. The desorption of species or fragments from the surface, the formation of clusters, the coating of entrance windows, etc., may attenuate and scatter the incident light.

5.3.6 Non-linearities

It has been demonstrated in different processing applications that, under certain conditions, it is possible to produce patterns with lateral dimensions that are

significantly *smaller* than the diffraction-limited diameter of the laser focus. This observation is related to thermal and/or optical non-linearities in the laser-matter interactions.

Thermal Activation

To illustrate the influence of non-linearities in thermally activated laser processing, we have plotted in Fig. 5.3.1 the intensity profile of a Gaussian laser beam (solid curve), the temperature distribution induced on a semi-infinite substrate (dotted curve) and (normalized) processing rates $W^*(r) \propto \exp[-\Delta E/k_B T(r)]$ (dashed curves). Activation energies of $\Delta E = 22\,\text{kcal/mol}$ (curve a) and $\Delta E = 46.6\,\text{kcal/mol}$ (curve b) are characteristic, for example, for laser-induced deposition of Ni from $Ni(CO)_4$ and of Si from SiH_4. The non-linear dependence of the processing rate on temperature causes the lateral variation in W to be substantially narrower than in temperature, $T(r)$, *and* the laser-beam intensity, $I(r)$. The spatial confinement of the reaction increases with increasing ΔE.

Let us now study, in more detail, the influence of ΔE and the center temperature, T_c, on the spatial confinement. The increase in spatial confinement shall be described by the ratio w_0/r_e, where r_e is given by the $1/e$ point in processing rate, $W(r)$. For a circular laser beam, the temperature distribution can be written as

$$T(r) = T_0 + \Delta T(r) = T_0 + \Delta T_c f(r)\ . \tag{5.3.1}$$

If we assume a Gaussian beam, surface absorption, and temperature-independent parameters, $f(r)$ is given by (7.2.4). The definition of r_e yields for an *arbitrary* function $f(r)$

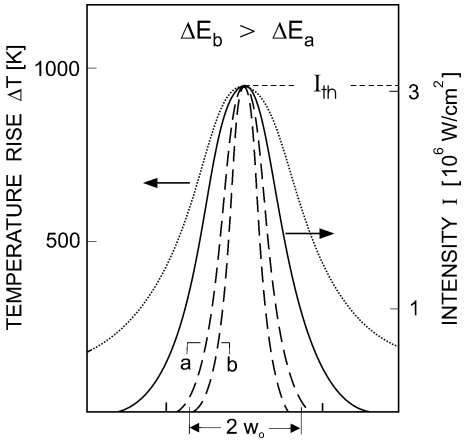

Fig. 5.3.1 Spatial confinement in pyrolytic laser processing. *Solid curve*: intensity profile of the laser beam ($2w_0$ is the $1/e$ diameter). *Dotted curve*: calculated temperature rise ($\kappa = 0.50\,\text{W/cm K}$, $P_{abs} = 0.3\,\text{W}$, $\alpha \to \infty$, $w_0 \approx 1.8\,\mu\text{m}$). *Dashed curves*: normalized processing rates for $\Delta E = 22\,\text{kcal/mol}$ (*curve a*) and $\Delta E = 46.6\,\text{kcal/mol}$ (*curve b*) [*Bäuerle* 1986]

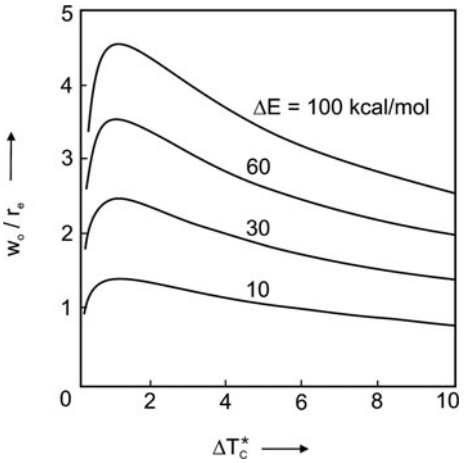

Fig. 5.3.2 Ratio w_0/r_e [$W(r_e) = W(0)/e$] versus (normalized) laser-induced center temperature rise $\Delta T_c^* = \Delta T_c/T(\infty)$ for various activation energies, ΔE [*Bäuerle* 1986]

$$r_e = f^{-1}\left[\frac{1 - T_0(1 + T_0/\Delta T_c)/\mathscr{E}}{1 + T_0(1 + \Delta T_c/T_0)/\mathscr{E}}\right] \equiv f^{-1}(\gamma) \ , \tag{5.3.2}$$

where $f^{-1}(\gamma)$ is the inverse function of $f(r)$ and $\mathscr{E} \equiv \Delta E/k_B$. In Fig. 5.3.2 we have plotted the ratio w_0/r_e versus $\Delta T_c^* = \Delta T_c/T_0$ for $T_0 = T(\infty) = 300\,\mathrm{K}$. For a certain value of ΔE, there exists a maximal value of w_0/r_e at a certain optimal center temperature, $T_{c\,opt}$. Because the function $f^{-1}(\gamma)$ is monotonic, $T_{c\,opt}$ can easily be calculated from

$$\frac{\partial r_e}{\partial \Delta T_c} = \frac{\partial f^{-1}}{\partial \gamma}\frac{\partial \gamma}{\partial \Delta T_c} = 0 \ ,$$

which yields

$$\Delta T_{c\,opt} = T_0\left(\frac{\mathscr{E} + T_0}{\mathscr{E} - T_0}\right) \approx T_0 \ .$$

Thus, with systems where $\mathscr{E} \gg T_0$ we find $T_{c\,opt} \approx 2T_0$. Clearly, efficient processing requires the practical center temperature to be well above the threshold temperature for the particular processing application, i.e., $T_{c\,prac} > T_{c\,opt}$. Thus, the confinement will be decreased with respect to the optimal value.

If $\Delta T_c \approx T_c \gg T_0$, the processing rate can be approximated by

$$W = k_0 \exp\left(-\frac{\mathscr{E}}{T(r)}\right) \approx k_0 \exp\left(-\frac{\mathscr{E}}{T_c}\right) \exp\left(-\frac{\mathscr{E}}{T_c}\frac{r^2}{w_T^2}\right) . \qquad (5.3.3)$$

Here, we have used the expansion $T(r) \approx T_c(1 - r^2/w_T^2)$. Equation (5.3.3) then yields

$$r_e = w_T \left(\frac{T_c}{\mathscr{E}}\right)^{1/2} .$$

For the case of surface absorption we obtain $w_T \approx 1.5 w_0$ (Sect. 6.5).

Other non-linearities, for example, in the absorptivity, $A = A(T), A(h)$, etc., may also influence the confinement of the reaction.

Photophysical and Photochemical Processing

Non-thermal excitations depend on the particular interaction process. For example, in laser photolysis based on *multiphoton* dissociation of adsorbed molecules, or surface bonds, the reaction rate is given by $W \propto I^n$, where n is the number of coherently absorbed photons. The situation is analogous to that shown in Fig. 5.3.1. With increasing n, the width of the intensity distribution I^n decreases. Such optical nonlinearities increase the confinement in photochemical laser processing (Sect. 3.2). Among the examples is the two-photon polymerization employed for 3D lithography (Sect. 27.3), and the processing of dielectrics with ultrashort laser pulses and photon energies $h\nu << E_g$. Here, multiphoton- and impact ionization generate a plasma layer *within* the material. This causes strong absorption and optical breakdown. The strong nonlinearity of this process causes a confinement of the interaction volume (Sect. 13.6). In other words, with optimized laser parameters, the width of the processed zone is small compared to the width of the *linear* intensity distribution.

Nucleation

Whenever nucleation processes are involved in a particular processing step, such as in material deposition, compound formation, recrystallization, etc., they may be of importance for the spatial confinement, simply because of their strong non-linearity (Chap. 4).

Instabilities, Periodic Structures

While the non-linear interactions mentioned above will, in general, improve the confinement of the laser process, the occurrence of instabilities and periodic structures will, within certain parameter regions, deteriorate it. This will be discussed in detail in Chap. 28.

5.3.7 Optical Near-Field and Field-Enhancement Effects

New phenomena are observed, if so-called near field effects become important. Within the near field of a fiber tip, i.e. at distances, typically between zero (contact mode) and some ten nanometers, the "light spot" resulting from the evanescent wave is not limited by optical diffraction, but by the diameter of the tip (Fig. 5.2.1e).

The high resolution obtained with a fiber tip can be made plausible from the uncertainty principle. For an *undamped* wave propagating in x-direction we obtain with $\Delta p_x = 2\hbar k$ and $\Delta x\ \Delta p_x \gtrsim \mathrm{h}$ for $\Delta \mathrm{x} \gtrsim \lambda/2$. This corresponds to the Abbe limit. A wave propagating in k-direction within a fiber tip whose radius becomes small compared to the wavelength is strongly damped. For an evanescent wave in z-direction we obtain with $k_\mathrm{z} = \mathrm{i}\gamma$ and $k^2 = {k_\mathrm{x}}^2 + {k_\mathrm{z}}^2$ for strong damping, i.e. with big values of γ, a "resolution" $\Delta \mathrm{x} << \lambda$. Thus, within the near field of the fiber tip, i.e. within the region of the evanescent wave leaving the tip, the optical resolution is *not* limited by the wavelength. By this means, nanopatterning of surfaces by direct writing has been demonstrated.

Optical near-field effects are also observed in the vicinity of small structures, particles, or curved interfaces.

Let us first consider transparent particles, whose size is much bigger than the wavelength. In this "classical limit", the local electromagnetic field strongly depends on the particle shape. For example, spherical particles with radii $r_\mathrm{sp} >> \lambda$ focus the incident radiation as shown in Fig. 5.3.3. The *average* intensity on the plane $z = r_\mathrm{sp}$ "behind" the sphere can be approximated by

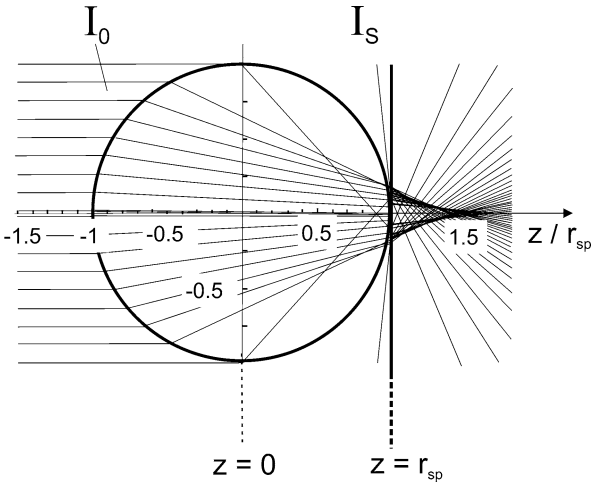

Fig. 5.3.3 Focussing properties of a (transparent) microsphere with radius $r_\mathrm{sp} >> \lambda$. I_s is the intensity within a radius $\rho < \rho_\mathrm{c}$ on the substrate which is placed directly behind the sphere within the plane $z = r_\mathrm{sp}$

$$I_S \approx \begin{cases} \dfrac{27\,n^4}{(4-n^2)^3}\, I_0 & \text{with} \quad \rho < \rho_c \\ 0 & \text{with} \quad \rho > \rho_c \end{cases} \tag{5.3.4}$$

where n is the index of refraction of the microsphere and I_0 the (uniform) incident intensity. With a-SiO_2 microspheres ($n = 1.42$) we obtain $I_S/I_0 \approx 14$. Note that this intensity enhancement is *independent* of r_{sp}. If the sphere, e.g. PS, is placed on a substrate such as Si, the radiation reflected from the substrate yields an additional contribution to the electromagnetic field. It further increases the overall intensity I_s [*Luk'yanchuk* et al. 2004]. However, with other material combinations, the situation may be opposite [*Bityurin* 2011]. ρ is the distance from the axis of symmetry on the substrate surface and ρ_c the caustic radius which is given by

$$\rho_c = \frac{(4-n^2)^{3/2}}{3\sqrt{3}\,n^2}\, r_{sp} \tag{5.3.5}$$

With a-SiO_2 we obtain ρ_c (a-SiO_2) $\approx 0.27\, r_{sp}$. While the *overall* intensity enhancement by microspheres is qualitatively well described by the approximation (5.3.4), the real situation is much more complex.

For isolated particles in free space, the scattered electromagnetic field can be described by the Mie theory. Figure 5.3.4 shows the intensity $EE^* \equiv |E|^2$ within the xy-plane at $z = r_{sp}$. Depending on the Mie parameter, $k\,r_{sp}$, the intensity distribution shows single-, double- or multiple-peak structures. In laser processing, such near-field structures become relevant with strongly nonlinear processes and short laser pulses. In fact, experiments using microspheres in contact with the substrate surface together with ultrashort laser pulses, give clear evidence for such different distributions. Among the examples are single-hole and double-hole structures observed after irradiation of PS particulates on Si substrates with 100 fs Ti:Sapphire-laser pulses [*Münzer* et al. 2002] and of SiO_2 particulates on Ni

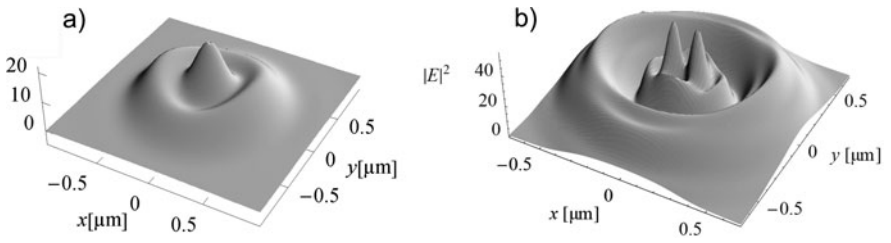

Fig. 5.3.4 Intensity $|E|^2$ underneath a focusing microsphere at $z = r_{sp}$. The origin of the coordinate system is located in the center of the sphere (see Fig. 5.3.3). The incident electric field is a plane wave, propagating in z- and polarized in x-direction with unity strength. The refractive index of the sphere is $n = 1.42$. (**a**) Mie parameter $k\,r_{sp} = 2\,\pi\,r_{sp}/\lambda \approx 15.7$ ($r_{sp} = 2\,\mu$m; $\lambda = 800$ nm) (**b**) $k\,r_{sp} \approx 78.5$ ($r_{sp} = 3.1\,\mu$m; $\lambda = 248$ nm). Here, a pronounced double-peak structure in the direction of initial polarization occurs [after *Kofler* 2004]

foils with 500 fs KrF-laser pulses [*Bäuerle* et al. 2003]. Observations related to single- and multiple-peak structures have been made with metal-coated microspheres [*Langer* et al. 2006]. With nanosecond pulses, such "fine" structures are smeared out due to spatial dissipation of the excitation energy. If the microsphere is not in contact with the substrate, near-field effects are washed out. For distances beyond the decay length of evanescent waves, the field is determined by propagating modes only. This has been demonstrated by *Guo* et al. (2007). The intensity distribution as a function of the distance behind a sphere is shown in Fig. 5.3.5. Both the geometrical focus and the diffraction "focus" are indicated. The "line-type" diffraction focus has a number of consequences for surface patterning applications (Sect. 12.1). Further details on the imaging properties and near-field effects of microspheres and microsphere arrays are outlined by *Huang* et al. (2009), *Kofler* and *Arnold* (2006), *Kofler* (2004), and others.

The situation changes significantly with particles having sizes comparable or smaller than the wavelength. In this case, the influence of the particle shape becomes less pronounced. The local electromagnetic field is not any more concentrated below the particle, but develops into a dipolar shape similar to that of a Hertz oscillator. This effect can be demonstrated, e.g. in ablation experiments using subthreshold fluences [*Leiderer* et al. 2004]. With laser fluences that result in "uniform" substrate ablation, i.e. with $\phi > \phi_{th}$ (uniform), such structures are washed out.

Experimental and theoretical investigations of different types of field enhancement effects below and around dielectric and metallic nanoparticles, metallic triangular structures, etc. have been performed by *Geldhauser* et al. 2011, *Plech*

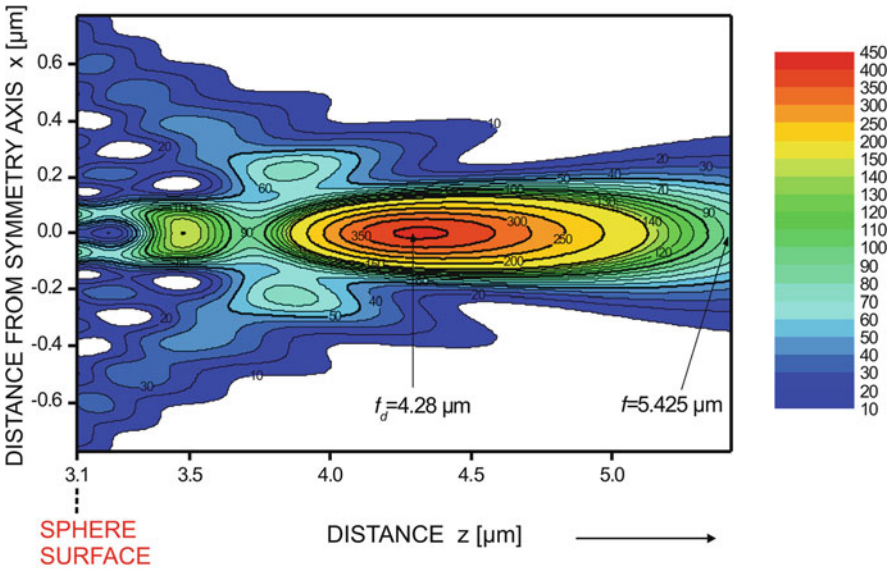

Fig. 5.3.5 Intensity distribution as a function of the distance "behind" a (transparent) sphere of radius $r_{sp} = 3.1\,\mu m$ ($\lambda = 248\,nm$, $E \parallel x$, $n = 1.4$) [adapted from *Kofler* 2004]

et al. 2009, *Boneberg* et al. 2007; *Luk'yanchuk* et al. 2007a; *Tribelsky* and *Luk'yanchuk* 2006, and many others. With metallic structures, field enhancement effects related to individual and/or coupled plasmonic excitations become important. Optical near-field effects and the importance of resonant plasmon excitations in combined laser-STM techniques have been discussed by *Wang* et al. 2007.

Field enhancement effects at the tip of conical/columnar structures are employed in matrix-free laser desorption ionization (Sect. 28.7).

Part II
Temperature Distributions and Surface Melting

One of the basic quantities in laser processing is the temperature rise induced by the absorbed laser radiation on a material surface or within its bulk. A knowledge of the temperature distribution is a prerequisite for both fundamental investigations and technical applications. In fact, before starting laser processing at all, the temperature distribution, or at least the maximum temperature, should first be estimated. Only on this basis can one select the type of laser and the parameters adequate for the particular processing application.

Laser-induced temperature distributions can be estimated by solving the heat equation for the particular irradiation geometry and the substrate under consideration. This is the main content of Part II of the book. The limits of such calculations have already been discussed in Chap. 2.

Chapter 6
General Solutions of the Heat Equation

6.1 The Boundary-Value Problem

The substrate shall be an infinite slab of uniform thickness, h_s, that is irradiated by a cw- or pulsed-laser beam which is either focused or extended over a wider area (Fig. 6.1.1). For *localized* irradiation, the absorbed laser light generates a local temperature rise, $\Delta T(\boldsymbol{x}, t)$, which can be calculated by solving the *three-dimensional* heat equation (2.2.1). For *large-area* (uniform) irradiation, the temperature is uniform within planes $z = \text{const.}$, and the temperature rise, $\Delta T(z, t)$, can be calculated by solving the *one-dimensional* heat equation.

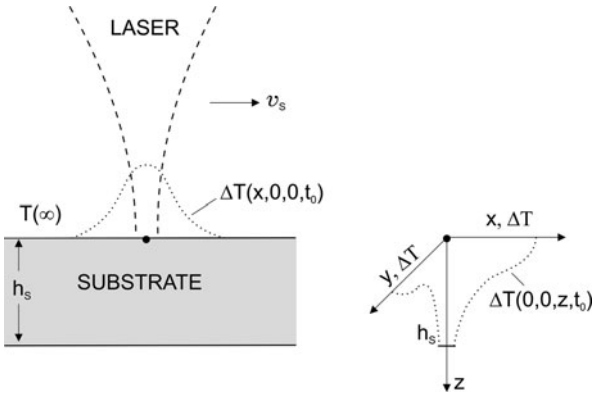

Fig. 6.1.1 Infinite slab of uniform thickness, h_s, irradiated by a laser beam at perpendicular incidence. In the absence of scanning, the origin of the coordinate system is on the surface in the center of the laser beam. If $v_s \neq 0$, the origin of the coordinate system is either fixed with the substrate or with the laser beam, depending on the particular problem under consideration. The laser-induced temperature rise on the surface $z = 0$ and along the z-direction is indicated (*dotted curves*). The temperature far away from the irradiated area is $T(\infty)$. With increasing focal width, $2w$, the temperature distribution becomes wider. In the limit $w \to \infty$ (large-area irradiation) the temperature rise becomes uniform within planes $z = \text{const}$

D. Bäuerle, *Laser Processing and Chemistry,* 4th ed.,
DOI 10.1007/978-3-642-17613-5_6, © Springer-Verlag Berlin Heidelberg 2011

The Source Term

In most cases of thermal laser processing, the Rayleigh length is long compared to the optical penetration depth. Then, in a coordinate system that is fixed with the laser beam, the source term in the heat equation can be written in the form

$$Q(x_\alpha, t) = I(x, y, t)(1 - R) f(z) = I_\mathrm{a} g(x, y) f(z) q(t) \,, \tag{6.1.1}$$

where $I_\mathrm{a} = I_0(1 - R)$ is the (maximum) laser-light intensity that is not reflected from the surface $z = 0$. $g(x, y)$ describes the (arbitrary) intensity distribution (beam shape) within the xy-plane. $f(z)$ describes the attenuation of the laser light in z-direction, and $q(t)$ its temporal dependence (pulse shape). Thus, we have $\max[g(x, y)] = \max[q(t)] = 1$. Frequently, we introduce cylindrical coordinates, so that $I = I(r, \varphi, t)$, where φ describes the angle between the radius vector $\boldsymbol{r}$ and the x-axis.

$R \equiv R(T, \lambda)$ denotes the temperature- and wavelength-dependent normal-incidence reflectivity within the processed area. In the general case, the reflectivity depends on the angle of incidence, the polarization of the laser beam, and the thickness of the slab. The latter dependence can be ignored if the optical penetration depth $l_\alpha \ll h_\mathrm{s}$. If, on the other hand, $l_\alpha > h_\mathrm{s}$, interference phenomena due to multiple reflections of the laser light may become important. The reflectivity, and also the absorptivity, will then depend on h_s. In this chapter we ignore multiple reflections within the slab.

Values of R and α are listed in Table III for different materials and various wavelengths. For metals, reflectivity values in the near UV and VIS spectral range are, typically, between 0.4 and 0.95. In the IR, typical values are between 0.9 and 0.99. It should be noted, however, that these values can be applied only if the wavelength, λ, is small compared to the radius of the laser spot, w. Additionally, in the dependence $R = R(T, \lambda)$ we can employ the surface temperature $T = T(x, y, 0, t)$ only if the variation of $T \equiv T(\boldsymbol{x}, t)$ in z-direction is slow over the distance l_α, i.e., if $l_\alpha(\mathrm{d}T/\mathrm{d}z) \ll T$. Finally, with very high laser-light intensities, optical non-linearities become important.

6.1.1 The Attenuation Function, $f(z)$

The function $f(z)$ in (6.1.1) describes the attenuation of the laser beam in z-direction. For a *uniform* material, it can be written as

$$f(z) = \alpha(T(z)) \exp\left[- \int_0^z \alpha(T(z'))\, \mathrm{d}z' \right] \,, \tag{6.1.2}$$

where $\alpha(T)$ is the temperature-dependent linear absorption coefficient at the laser wavelength under consideration. Because of this temperature dependence, the optical properties of the material become inhomogeneous under laser-light irradiation.

This case is discussed in Chap. 9. In the present chapter we mainly consider either finite absorption with α being a constant, or surface absorption.

If α is *finite* but independent of temperature, we obtain

$$f(z) = \alpha \exp(-\alpha z) \ . \tag{6.1.3a}$$

For *surface absorption*, $l_\alpha = \alpha^{-1}$ is small compared either to the heat diffusion length, $l_\mathrm{T} \approx 2(D\tau_\ell)^{1/2}$, or to another characteristic length, $\mathscr{L}$, depending on which is smaller. $\mathscr{L}$ can be the radius of the laser beam, w, the thickness of the slab, h_s, a length which characterizes the heat exchange, κ/η, the surface curvature or roughness, etc. The criterion for surface absorption can be written as $l_\alpha \ll \min(l_\mathrm{T}, \mathscr{L})$. Henceforth, surface absorption is often denoted, symbolically, by $\alpha \to \infty$ (for metals, one often introduces instead of l_α the skin depth $l_\mathrm{s} = c/(2\pi\sigma\omega)^{1/2}$, where σ is the frequency-dependent ac conductivity). In many practical cases with laser beam dwell times $\tau_\ell > 10^{-9}$ s, the assumption of surface absorption is satisfied with coefficients $\alpha > 10^5\,\mathrm{cm}^{-1}$. In this approximation, the light intensity that penetrates into the material can be ignored. Thus, the source term, Q, vanishes, except at the irradiated surface, where it is given by the absorbed laser power, so that

$$f(z) = \delta(z) \ , \tag{6.1.3b}$$

where $\delta(z)$ (cm^{-1}) is the delta function. This approximation holds for metals within the near UV to near IR spectral region, where the absorption coefficients are, typically, between 10^5 and $10^7\,\mathrm{cm}^{-1}$. It also holds for many semiconductors at elevated temperatures and laser wavelengths $\lambda \ll hc/E_\mathrm{g}$ (E_g denotes the bandgap energy). For crystalline Si, the approximation $\alpha \to \infty$ is reasonably well fulfilled for laser wavelengths $\lambda < 0.5\,\mu\mathrm{m}$.

6.1.2 Boundary and Initial Conditions

The solution of the heat equation (2.2.1) requires the consideration of boundary conditions. We shall assume that the slab is immersed in a gaseous or liquid medium M and that the temperature is continuous at the interfaces, i.e.,

$$T_\mathrm{s}(x_\alpha, t) = T_\mathrm{M}(x_\alpha, t) \quad \text{at} \quad z = 0, h_\mathrm{s} \ . \tag{6.1.4}$$

Another boundary condition is obtained from the balance of energy fluxes at the surface $z = 0$:

$$-\kappa_\mathrm{s} \left.\frac{\partial T_\mathrm{s}(x_\alpha, t)}{\partial z}\right|_{z=0} - J_\mathrm{ch}(x, y, 0, t) = -\kappa_\mathrm{M} \left.\frac{\partial T_\mathrm{M}(x_\alpha, t)}{\partial z}\right|_{z=0} \ . \tag{6.1.5}$$

The same boundary condition applies at the surface $z = h_\mathrm{s}$, except there is a change in sign of J_ch. The heat conductivities κ_s and κ_M refer to the substrate and the

ambient medium, respectively. J_{ch} is the heat flux originating from phase changes and/or chemical reactions at the surface $z = 0$. Clearly, the heat flux at $z = 0$ is continuous only if $J_{ch} = 0$. In the case of surface absorption, the source term, Q, is included in (6.1.5). The boundary conditions (6.1.4) and (6.1.5) are good approximations as long as any temperature jump at the interfaces can be ignored. This approximation holds if the mean free path of molecules, λ_m, is small compared to the size of the heated zone. For the case of localized irradiation (Fig. 6.1.1) this is fulfilled if $\lambda_m \ll w$, where w is the radius of the laser focus. For a liquid ambient medium, this condition always holds. For laser microchemical processing in gases at medium to low pressures it may not be fulfilled and $\lambda_m \geq w$. In this case, *no* complete thermal equilibrium between the laser-heated area and the adjacent gas is reached (Sect. 9.5.4).

In many practical cases one can use, instead of (6.1.5), the *effective* boundary condition

$$-\kappa_s \left.\frac{\partial T_s(x_\alpha, t)}{\partial z}\right|_{z=0} \approx J_{ch}(x, y, 0, t) - J_{loss}(x, y, 0, t) \,, \tag{6.1.6}$$

where

$$\begin{aligned} J_{loss} &= J_c + J_r \\ &\approx \eta[T_s(x, y, 0, t) - T_M(\infty)] + \sigma_r \varepsilon_t [T_s^4(x, y, 0, t) - T_M^4(\infty)] \,. \end{aligned} \tag{6.1.7}$$

J_c is the energy flux into the ambient medium. Here, η is the surface conductance (coefficient of surface heat transfer). It depends on κ_s and κ_M, on the geometry of the substrate, the flow velocity of the ambient – if relevant, on the surface morphology, and the thickness of surface coverages – for example, native oxide layers, adsorbates, water films, etc. In the absence of convection one can often use the approximation $\eta \approx \kappa_M / l$, where l is some characteristic length.

In the presence of *free* convection, η is temperature-dependent and can be described by

$$\eta(T_s) = \eta_0' \left(\frac{T_s - T_M(\infty)}{T_M(\infty)} \right)^{1/4} \,. \tag{6.1.8}$$

For substrates with areas of several square centimeters that are immersed in air at standard conditions, typical values of η_0' are around $10^{-4}\,\mathrm{W/cm^2\,K}$. For small areas, η_0' may exceed this value by a factor of 10 or more. For a liquid, η_0' is, typically, within the range $0.1–0.3\,\mathrm{W/cm^2\,K}$.

With *forced* convection one can often employ the approximation

$$\eta_f = \eta(T) + \eta_1(T) \left(\frac{v_c}{v_1} \right)^{1/2} \,, \tag{6.1.9}$$

as long as $v_c \ll v_0$, where v_0 is the sound velocity and v_c the velocity of the ambient with respect to the substrate. For air at standard conditions $v_1 \approx 1\,\mathrm{m/s}$ and $\eta_1 \approx 0.2\eta$. All coefficients η_i depend on the geometry of the substrate and its orientation with respect to the gas flux.

The consideration of the heat conductance in the boundary conditions is quite useful, because it permits the influence of an ambient medium on the substrate temperature to be estimated by solving the (single) heat equation for the substrate only. A more physical description of the problem is given in Sect. 9.5.

J_r describes the energy flux by thermal radiation. The Stefan–Boltzmann constant is $\sigma_r \approx 5.7 \times 10^{-12}\,\mathrm{W/cm^2K^4}$. $\varepsilon_t \equiv \varepsilon_t(T_s)$ is the total emissivity. For polished metals, $\varepsilon_t \approx 0.02$–$0.05$. For thermally oxidized metals, $\varepsilon_t \approx 0.6$–$0.7$. For standard glass and fused quartz, $\varepsilon_t \approx 0.93$. For (carbon) soot, $\varepsilon_t \approx 0.98$.

The comparison of fluxes J_c and J_r shows that with substrate materials immersed in gases at standard conditions and with $\varepsilon_t \approx 0.4$, $J_c > J_r$ for temperatures $T_s < 1000\,\mathrm{K}$ and $J_c < J_r$ if $T_s > 1000\,\mathrm{K}$. At $T_s = 1000\,\mathrm{K}$, we have $J_c \approx J_r \approx 1$–$3\,\mathrm{W/cm^2}$. In most processing cases, this energy loss can be ignored in comparison to the energy dissipated within the substrate.

If there are no phase transformations and/or chemical reactions, or if the related energies are small, we can also ignore J_{ch}.

Summary

The boundary-value problem described by the heat equation, the source term (6.1.1), and the above boundary and initial conditions, is herein summarized. For convenience, we introduce the linearized temperature, θ, see (2.2.8). The heat equation can then be written as

$$\frac{\kappa}{D}\frac{\partial\theta}{\partial t} - \kappa\nabla^2\theta = Q\ , \tag{6.1.10a}$$

where $D \equiv D(T(\theta))$ and $\kappa \equiv \kappa(T(\infty))$ refer to the substrate (we drop indices if the meaning of quantities is evident). Henceforth, we mainly assume D to be independent of temperature. In a coordinate system that is fixed with the slab (for more general representations of Q see Sect. 2.2) the source term (6.1.1) can be written as

$$Q = I_a(x, y, t)\, f(z) = I_a g(x - v_s t, y)\, f(z) q(t)\ . \tag{6.1.10b}$$

If $v_s \neq 0$, the laser beam is scanned with constant velocity in x-direction. If losses by thermal radiation are ignored, the boundary conditions have the form

$$-\kappa \left.\frac{\partial\theta}{\partial z}\right|_{z=0} = -\eta_0[T(\theta(z=0)) - T(\infty)] \tag{6.1.10c}$$

$$-\kappa \left.\frac{\partial\theta}{\partial z}\right|_{z=h_s} = \eta_h[T(\theta(z=h_s)) - T(\infty)] \tag{6.1.10d}$$

$$\theta(r \to \infty) = 0\,. \tag{6.1.10e}$$

Here, we have introduced different surface conductances η_0 and η_h for planes $z = 0$ and $z = h_s$, respectively. The initial condition is

$$\theta(t \le 0) = 0\,. \tag{6.1.10f}$$

For surface absorption, the source term, Q, is more conveniently considered in the boundary condition. The right side of (6.1.10c) is then replaced by $I_a(z = 0) - \eta_0[T(\theta(z = 0)) - T(\infty)]$.

6.2 Analytical Solutions

The most frequently employed analytical techniques to solve the boundary-value problem described in the preceding section are the method of integral transformations and the Green's function technique [*Carslaw* and *Jaeger* 1988]. If analytical solutions are found, they can frequently be presented in integral form only. These integrals can be calculated either numerically or by employing additional assumptions. There are also other analytical techniques which are less well known but very useful, in particular with non-linear problems. Among those are methods that are based on the theory of functions with complex variables (method of conformal mapping) and methods which are related to the symmetry properties of the heat equation. The latter techniques are based on the theory of Lie groups. In addition, there are a number of approximation methods such as variational techniques, the method of averaging, the Galerkin method, etc.

In the following, we first present quite general solutions of the boundary-value problem (6.1.10) and then consider special cases. For convenience, we introduce dimensionless variables. The normalized coordinates are

$$x^* = \frac{x}{l}\,; \quad y^* = \frac{y}{l}\,; \quad z^* = \frac{z}{l}\,, \tag{6.2.1a}$$

where l is some characteristic length. In many problems, the radius or width of the laser beam is an appropriate normalization factor, i.e., $l \equiv w_0$, w, w_x or w_y (which refers to a Gaussian beam, a circular beam with constant intensity, or a rectangular beam). For thin infinite slabs of thickness h_s we sometimes choose $l \equiv h_s$. The normalized time and scanning velocity are defined as

$$t^* = \frac{D}{l^2}t \quad \text{and} \quad v_s^* = \frac{v_s l}{D}\,. \tag{6.2.1b}$$

We also introduce the dimensionless absorption coefficient and thickness

$$\alpha^* = \alpha l \quad \text{and} \quad h_\mathrm{s}^* = \frac{h_\mathrm{s}}{l} \,. \tag{6.2.1c}$$

The dimensionless coefficients of heat transfer are

$$\eta_0^* = \frac{\eta_0 l}{\kappa} \quad \text{and} \quad \eta_\mathrm{h}^* = \frac{\eta_\mathrm{h} l}{\kappa} \,. \tag{6.2.1d}$$

We also introduce the dimensionless quantities $\kappa_0^* = \kappa_0/\kappa$ and $\kappa_\mathrm{h}^* = \kappa_\mathrm{h}/\kappa$, which are equal to unity, except if one of the surfaces is kept at a constant temperature, e.g., if $\theta(z = h_\mathrm{s}) = 0$, we have $\kappa_\mathrm{h}^* = 0$.

The most general solution of the boundary-value problem (6.1.10) obtained with the Green's function technique can be written as [*Luk'yanchuk* and *Bäuerle* 1994]

$$\theta(\boldsymbol{x}^*, t^*) = \frac{l^2}{\kappa} \int_0^{t^*} \int_0^{h_\mathrm{s}^*} \int_{-\infty}^{+\infty} \int_{-\infty}^{+\infty} \mathbb{G}(\boldsymbol{x}^*, t^*, \boldsymbol{x}_1^*, t_1^*)\, Q(\boldsymbol{x}_1^*, t_1^*)\, \mathrm{d}\boldsymbol{x}_1^*\, \mathrm{d}t_1^* \,,$$

where $Q = Q(\boldsymbol{x}_1^*, t_1^*)$ is an arbitrary source term. Here, we have assumed linear boundary conditions. The Green's function $\mathbb{G}$ can be obtained by the method of integral transformations. For a coordinate system that is fixed with the laser beam, $\mathbb{G}$ is given by

$$\mathbb{G} = \frac{1}{4\pi(t^* - t_1^*)} \exp\left(-\frac{(x^* - x_1^*)^2 + (y^* - y_1^*)^2}{4(t^* - t_1^*)}\right) \mathbb{F}(z^*, z_1^*, t^*, t_1^*)$$

and

$$\mathbb{F}(z^*, z_1^*, t^*, t_1^*) = \sum_{n=-\infty}^{\infty} B_n Z_n(z^*) Z_n(z_1^*) \exp[-\nu_n^2 (t^* - t_1^*)] \,,$$

in which

$$Z_n(z^*) = \cos \nu_n z^* + \frac{\eta_0^*}{\kappa_0^* \nu_n} \sin \nu_n z^* \,,$$

$$B_n = \frac{\zeta \kappa_0^{*2} \nu_n^2}{(\kappa_0^{*2} \nu_n^2 + \eta_0^{*2})(\zeta h_\mathrm{s}^* + \kappa_\mathrm{h}^* \eta_\mathrm{h}^*) + \zeta \kappa_0^* \eta_0^*} \,,$$

where $\zeta = \kappa_\mathrm{h}^{*2} \nu_n^2 + \eta_\mathrm{h}^{*2}$. Here, ν_n are roots of the equation

$$\tan(h_\mathrm{s}^* \nu_n) = \frac{\nu_n (\kappa_0^* \eta_0^* + \kappa_\mathrm{h}^* \eta_\mathrm{h}^*)}{\kappa_0^* \kappa_\mathrm{h}^* \nu_n^2 - \eta_0^* \eta_\mathrm{h}^*} \,.$$

Subsequently, we shall consider this solution in further detail by employing the source term (6.1.10b) with $f(z)$ given by (6.1.3a). Thus, we assume a finite but temperature-independent absorption coefficient and ignore interference phenomena within the slab. With this simplification we can perform the integration over z_1^*. We shall also assume equal surface conductances at both sides of the slab, i.e., $\kappa_0^* = \kappa_h^* = 1$ and $\eta_0^* = \eta_h^* = \eta^*$. The laser beam shall be switched on at $t = 0$ in the position $x = y = 0$ and it shall be scanned with constant velocity, v_s, in the x-direction. For a coordinate system that is fixed with the slab, the solution can be written as

$$\theta(x^*, t^*) = \frac{l}{\kappa} I_a \int_0^{t^*} q(t^* - t_1^*) \mathscr{G}(x^*, y^*, t^*, t_1^*) \mathscr{F}(z^*, t_1^*) \, \mathrm{d}t_1^* \, . \tag{6.2.2}$$

The function $\mathscr{G}$ is given by

$$\begin{aligned} &\mathscr{G}(x^*, y^*, t^*, t_1^*) \\ &= \frac{1}{4\pi t_1^*} \int_{-\infty}^{+\infty} \mathrm{d}x_1^* \int_{-\infty}^{+\infty} \mathrm{d}y_1^* g(x_1^*, y_1^*) \\ &\quad \times \exp\left(- \frac{[(x_1^* - x^*) - v_s^*(t_1^* - t^*)]^2 + (y_1^* - y^*)^2}{4t_1^*} \right) \, . \end{aligned} \tag{6.2.3}$$

The solution (6.2.2) can be applied to many practical cases. It contains three *independent* functions. $\mathscr{G}$ and $\mathscr{F}$ describe the temperature field within the xy-plane and in the z-direction, respectively. $\mathscr{F}$ depends on the absorption coefficient, the heat exchange coefficient, and the thickness of the substrate (Appendix B).

6.3 Pulse Shapes

We now consider various *temporal* dependences of laser-beam intensities that are most commonly used in laser processing. With a static cw-laser beam, the intensity is *constant* with respect to time, i.e.,

$$I(t) \equiv I_0 q(t) = I_0 \mathscr{H}(t) \, , \tag{6.3.1}$$

where $\mathscr{H}$ is the Heaviside function and $I_0 = \text{const}$. This is a good approximation also for long laser pulses where stationary solutions ($t^* \to \infty$) of (6.2.2) can be employed.

6.3.1 Single Rectangular Pulse

For a single rectangular pulse of duration τ_ℓ (solid curve in Fig. 6.3.1) the intensity can be described by

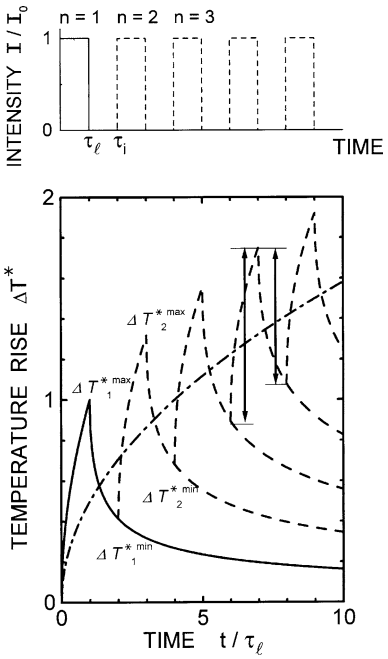

Fig. 6.3.1 Temporal variation of the (normalized) surface temperature rise ΔT^* for a single rectangular pulse (*solid curve*) and for multiple-pulse irradiation (*dashed curve*; (6.3.7)). *Arrows* indicate heating and cooling cycles. The *average* temperature rise is also shown (*dash-dotted curve*)

$$I(t) = I_0 \mathscr{H}(\tau_\ell - t)\mathscr{H}(t) \; . \tag{6.3.2}$$

The laser fluence (energy density) is

$$\phi = I_0 \tau_\ell \; . \tag{6.3.3}$$

The temperature rise calculated from (6.2.2) is then

$$\Delta T \equiv \theta(x^*, y^*, z^*, t^*) = \frac{I_a l}{\kappa} \int_{t_0^*}^{t^*} \mathscr{G}(x^*, y^*, t^*, t_1^*) \mathscr{F}(z^*, t_1^*) \, \mathrm{d}t_1^* \; , \tag{6.3.4}$$

where $t_0^* = 0$ with $t < \tau_\ell$ and $t_0^* = t^* - \tau_\ell^*$ with $t > \tau_\ell$. The temporal dependence of the normalized temperature rise, $\Delta T^* = \Delta T / \Delta T_{\max}$, is schematically shown in the lower part of Fig. 6.3.1 by the solid curve. For normalization we have employed the maximum temperature rise $\Delta T_{\max}(\alpha \to \infty) = I_0 2(D\tau_\ell)^{1/2}/(\pi^{1/2}\kappa)$.

6.3.2 Triangular Pulse

For a triangular pulse (Fig. 6.3.2a) the intensity can be written as $I(t) = I_0 q(t)$, with

$$q(t) = \begin{cases} \dfrac{t}{\tau_0}\,\mathscr{H}\left(\dfrac{t}{\tau_0}\right) & \text{for } t < \tau_0 \\ \dfrac{\tau_1 - t}{\tau_1 - \tau_0} & \text{for } \tau_0 \le t \le \tau_1 \\ 0 & \text{for } t > \tau_1 \end{cases} , \tag{6.3.5}$$

where I_0 is the maximum intensity that is reached at τ_0. The duration of the pulse defined by the full width at half maximum is $\tau_{\mathrm{FWHM}} \equiv \tau_\ell = \tau_1/2$.

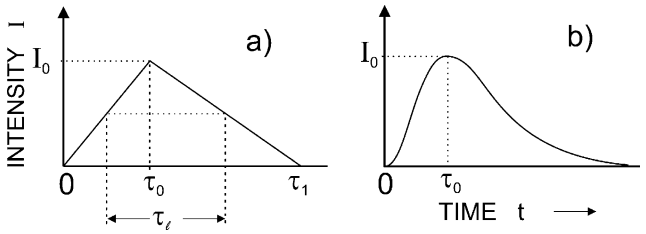

Fig. 6.3.2 Temporal variation of the intensity for (**a**) a triangular and (**b**) a smooth pulse

6.3.3 Smooth Pulse

The intensity of the pulse shown in Fig. 6.3.2b can be approximated by

$$I(t) = I_0 \left(\frac{t}{\tau_0}\right)^{\beta} \exp\left[\beta\left(1 - \frac{t}{\tau_0}\right)\right] , \tag{6.3.6}$$

where β describes the temporal shape of the pulse. The laser fluence is

$$\phi = I_0 \tau_0 \exp(\beta) \frac{\Gamma(\beta + 1)}{\beta^{\beta+1}} ,$$

where we have introduced the Γ function (Appendix B).

Figure 6.3.3 compares the normalized surface temperature rise $\Delta T^* = \Delta T/\Delta T_{\max}$ for three different pulse shapes of *equal* fluence and τ_{FWHM}. Both the temperature and the time were normalized to the *rectangular* pulse. The figure demonstrates that the maximum surface temperature depends significantly on pulse shape. This effect is most pronounced at the surface $z = 0$ and for $\alpha \to \infty$. For the triangular pulse, the maximum temperature rise and the corresponding time

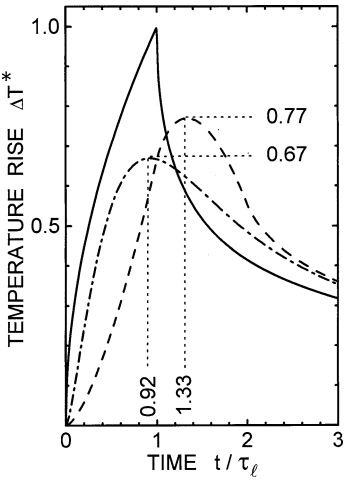

Fig. 6.3.3 Temporal variation of surface temperature rise $\Delta T^* = \Delta T/\Delta T_{\max}$ calculated for large-area irradiation with three different pulse shapes and surface absorption ($\alpha \to \infty$). All *curves* were calculated for the *same* fluence $\phi^* = \int_0^\infty I(t)\,\mathrm{d}t/(I_0\tau_\ell) = 1$ and time $t^* = t/\tau_\ell$, where I_0 is the intensity and τ_ℓ the duration of the *rectangular* pulse. *Solid curve*: single rectangular pulse of width τ_ℓ. *Dashed curve*: triangular pulse of the *same* pulse duration $\tau_{\mathrm{FWHM}} = \tau_\ell$ with $\tau_1 = 2\tau_\ell$ and $\tau_0 = \tau_\ell$ (symmetric pulse). *Dash-dotted curve*: smooth pulse with $\beta = 1$ and $\tau_{\mathrm{FWHM}} = \tau_\ell$. $\Delta T^*_{\max} = 0.67$ is reached at $t = 0.92\tau_\ell$

depend on the ratio τ_0/τ_ℓ and they are given by $\Delta T^*_{\max} = 4/[3(4 - \tau_0/\tau_\ell)^{1/2}]$ and $t'_{\max} = 4/(4 - \tau_0/\tau_\ell)$.

6.3.4 Multiple-Pulse Irradiation

The temperature rise for *multiple*-pulse irradiation can also be calculated from (6.2.2). With laser pulses that are rectangular in time (Fig. 6.3.1) the intensity can be described by

$$I(t) = I_0 \sum_{n=1}^{m} [\mathscr{H}(t - \tau_{\mathrm{i}}^n) - \mathscr{H}(t - \tau_{\mathrm{f}}^n)] \,, \tag{6.3.7}$$

where $\tau_{\mathrm{i}}^n = (n-1)\tau_{\mathrm{i}}$ and $\tau_{\mathrm{f}}^n = \tau_{\mathrm{i}}^n + \tau_\ell$. The temporal dependence of ΔT^* is shown in the lower part of Fig. 6.3.1 by the dashed curve. The temperature oscillates between a maximum value at the end of the pulse, $\Delta T_n^{*\max}$, and a minimum value before the next pulse, $\Delta T_n^{*\min}$.

The *average* temperature rise $\langle \Delta T(z,t) \rangle$ can be calculated from the solutions of the heat equation by using the average intensity $\langle I(t) \rangle = \phi \nu_{\mathrm{r}}$, where ν_{r} is the laser-pulse repetition rate. The dash-dotted curve in Fig. 6.3.1 shows

$\langle \Delta T^*(0, t') \rangle$ for rectangular pulses. The average heat penetration depth is given by $l_T = 2(DN_\ell/\nu_r)^{1/2}$.

With some types of pulsed lasers or modulated cw lasers, the temporal behavior of the intensity can be described by

$$I(t) = I_0 \left[1 - \cos\left(\frac{\pi t}{\tau_\ell} \right) \right] . \tag{6.3.8}$$

6.4 Beam Shapes

Among the most important beam shapes employed in laser processing is the *Gaussian beam* whose (spatial) intensity distribution is given by (5.1.1)

$$I(r^*) = I_0 \exp(-r^{*2}) . \tag{6.4.1}$$

The characteristic length for normalization of variables is $l = w_0$. Thus, $r^* = r/w_0$, with $r^2 = x^2 + y^2$. For a moving laser beam the distribution (6.4.1) remains unchanged in a system fixed with the beam. The $\mathscr{G}$-function that enters (6.2.2) is obtained by integration of (6.2.3) with

$$g(x^*, y^*) = \exp(-x^{*2} - y^{*2}) .$$

This yields

$$\mathscr{G}(x^*, y^*, t^*, t_1^*) = \frac{1}{1 + 4t_1^*} \exp\left(-\frac{[x^* - v_s^*(t^* - t_1^*)]^2 + y^{*2}}{1 + 4t_1^*} \right) . \tag{6.4.2}$$

6.4.1 Circular Beam

For a circular beam with constant intensity over its cross section $F = \pi w^2$, the intensity can be written as

$$I(r^*) = I_0 \mathscr{H}(1 - r^*) , \tag{6.4.3}$$

where $r^* = r/l = r/w$. Integration of (6.2.3) yields

$$\begin{aligned} \mathscr{G}(x^*, y^*, t^*, t_1^*) = {} & \frac{1}{2t_1^*} \exp\left(-\frac{[x^* - v_s^*(t^* - t_1^*)]^2 + y^{*2}}{4t_1^*} \right) \\ & \times \int_0^1 r^* \mathbf{I}_0(\xi r^*) \exp\left(-\frac{r^{*2}}{4t_1^*} \right) \mathrm{d}r^* , \end{aligned} \tag{6.4.4}$$

where $\mathbf{I}_0$ is the modified Bessel function and

$$\xi = \frac{1}{2t_1^*}\left\{\left[x^* - v_s^*(t^* - t_1^*)\right]^2 + y^{*2}\right\}^{1/2} .$$

6.4.2 Rectangular Beam

For a rectangular beam with constant intensity over its cross section $F = 2w_x 2w_y$, we can write

$$I(x, y) = I_0 \mathscr{H}(w_x^2 - x^2)\mathscr{H}(w_y^2 - y^2) . \tag{6.4.5}$$

Integration of (6.2.3) yields

$$\mathscr{G}(x^*, y^*, t^*, t_1^*) = \frac{1}{4}\sum_{\pm} \operatorname{erf}\left(\frac{w_x^* \pm x^* \mp v_s^*(t^* - t_1^*)}{2\sqrt{t_1^*}}\right) \times \sum_{\pm} \operatorname{erf}\left(\frac{w_y^* \pm y^*}{2\sqrt{t_1^*}}\right) , \tag{6.4.6}$$

where $w_x^* = w_x/l$ and $w_y^* = w_y/l$. It is convenient to use either $l = w_x$ or $l = w_y$. The $\sum_{\pm}$ implies the sum of terms taken once with the upper and once with the lower sign, i.e., $\sum_{\pm} \exp(a \pm b \mp c) = \exp(a + b - c) + \exp(a - b + c)$.

6.4.3 Uniform Illumination

For large-area uniform illumination of the substrate surface, the intensity is constant within the plane $z = 0$, i.e.,

$$I(x, y) = I_0 = \text{const.}$$

and we obtain $\mathscr{G} = 1$.

6.5 Characteristics of Temperature Distributions

In many applications it is essential to estimate the characteristic features of the laser-induced temperature distribution. These are the maximum temperature, and the width of the temperature distribution within the xy-plane and in the z-direction.

6.5.1 Center-Temperature Rise

With the beam shapes given in Sect. 6.4 and the assumptions made throughout this chapter, the maximum temperature rise on the substrate surface occurs in the *center* of the laser beam at $\boldsymbol{x}^* = 0$. This center-temperature rise, $\Delta T_\mathrm{c}(0,0,0) = \theta_\mathrm{c}$, is estimated in Chaps. 7 and 8 for different cases.

6.5.2 Width of Distribution

For *transient* laser-beam irradiation and $\eta = 0$, the width of the thermal field in axial direction, w_T^a, and in lateral direction within the xy-plane, w_T^l, is of the order

$$w_\mathrm{T}^a(t) \approx l_\alpha + l_\mathrm{T} \quad \text{and} \quad w_\mathrm{T}^l(t) \approx w \tag{6.5.1a}$$

for $l_\alpha \ll w$ and times $t \ll w^2/D$. If $l_\alpha \gg w$, we obtain

$$w_\mathrm{T}^a(t) \approx l_\alpha \quad \text{and} \quad w_\mathrm{T}^l(t) \approx w + l_\mathrm{T}\,, \tag{6.5.1b}$$

with $t \ll l_\alpha^2/D$. As before we use, in general, $l_\mathrm{T} \approx 2(D\tau_\ell)^{1/2}$. Note, however, that in many cases of (thermal) laser processing the temperature distribution is non-exponential and described by a power-like dependence on coordinates. Thus, there is *no* universal characteristic length, l (see also Sect. 2.2.2). The *stationary* temperature distribution is characterized by

$$w_\mathrm{T}^a(t \to \infty) \approx \max(\xi^a w, l_\alpha) \quad \text{and} \quad w_\mathrm{T}^l(t \to \infty) \approx \xi^l w\,, \tag{6.5.1c}$$

where ξ^a and ξ^l are constants. The temporal dependence of w_T^a and w_T^l is shown by the isotherms in Fig. 6.5.1. Here, a semi-infinite substrate, a Gaussian laser beam, and $l_\alpha = 0$ have been assumed. The isotherms are defined by $\theta(r^*, z^*, t^*)/\theta_\mathrm{max}(0,0,t^*) = 1/\mathrm{e}$, with $r^* = r/w_0$, $z^* = z/w_0$, and $t^* = Dt/w_0^2$. The stationary values are $w_\mathrm{T}^a(t \to \infty) \approx 1.25 w_0$ and $w_\mathrm{T}^l \approx 1.73 w_0$. The temporal development of the temperature distribution for surface absorption and finite absorption is also shown in Fig. 7.2.3.

For focused *cw-laser* irradiation, the width w_T^l of the stationary temperature field is often described by the relation

$$\theta(x = w_\mathrm{T}^l) = \zeta \theta_\mathrm{c}\,, \tag{6.5.2}$$

where ζ has a value of 0.5, $1/\mathrm{e}$ or $1/\mathrm{e}^2$. With a Gaussian beam and a semi-infinite substrate as well as $\alpha^* \to \infty$ and $\eta^* = 0$, the respective values yield $w_\mathrm{T}^l \approx 1.38 w_0$, $1.50 w_0$, and $1.79 w_0$.

Another definition of w_T^l is given by the so-called *parabolic approximation* (Fig. 6.5.2). Here, the real temperature distribution, $\theta(x)$, is approximated by $\theta_\mathrm{c}(1 - x^2/w_\mathrm{T}^{l2})$, with

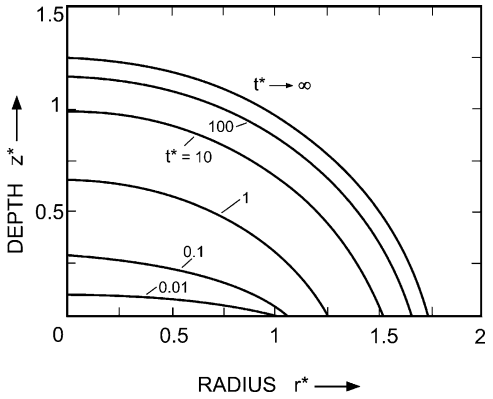

Fig. 6.5.1 Temporal dependence of isotherms calculated for a semi-infinite substrate, $\alpha \to \infty$, and a Gaussian laser beam

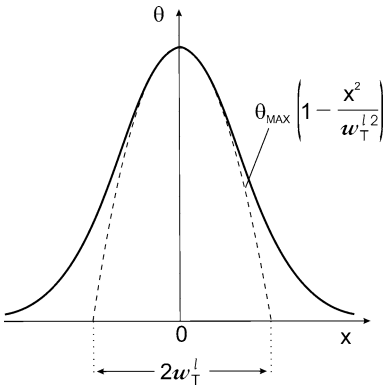

Fig. 6.5.2 Width of temperature distribution, $2w_{\mathrm{T}}^{l}$, defined by the parabolic approximation

$$w_{\mathrm{T}}^{l} = \left(-\frac{1}{2\theta} \frac{\mathrm{d}^2\theta}{\mathrm{d}x^2} \right)_{x=0}^{-1/2} . \tag{6.5.3}$$

With a Gaussian beam and a semi-infinite substrate, this yields $w_{\mathrm{T}}^{l}(t \to \infty) = \sqrt{2}w_0$. Thus, the different definitions yield similar results. This is also true for other definitions used throughout the literature. The reason is that all these definitions are related to the size of the laser beam.

With $\eta \neq 0$, the temperature distribution becomes more localized, i.e., the widths w_{T}^{a} and w_{T}^{l} are diminished.

6.6 Numerical Techniques

Numerical techniques for solving differential equations such as the heat equation, permit one to easily include arbitrary variations in material parameters in the calculations. Furthermore, such calculations can be performed for almost any geometry of the substrate (workpiece). The main disadvantage is that such solutions do not provide general relationships and they are always limited to finite regions. In order to satisfy boundary conditions at infinity, calculations should be performed over a wide range of variables. Here, one has to compromise between the accuracy in calculations and the total computer time required. Additionally, inappropriate discretizations of the problem can cause artefacts like oscillations, instabilities, and even chaos in non-linear equations.

Depending on the geometry of the physical problem, it is advantageous to employ either *finite difference* or *finite element* techniques. These techniques have been widely described in the literature [*Marsal* 1976; *Akin* 1998; *Press* et al. 1992], and they will not be discussed any further in this book.

Throughout this book we often compare analytical solutions, where they are possible, with numerical solutions based on finite difference or finite element techniques.

Chapter 7
Semi-infinite Substrates

In this chapter we discuss various specific solutions of the heat equation for semi-infinite substrates. The irradiation geometry and the definition of the coordinate system shall be the same as in Fig. 6.1.1 but with $h_s \to \infty$. Any phase changes and chemical reaction energies are ignored.

7.1 The Center-Temperature Rise

For many applications, the knowledge of the *maximum* laser-induced temperature rise is of great importance. With the beam shapes discussed in Sect. 6.4, the maximum surface temperature always occurs in the center of the laser beam at $\boldsymbol{x}^* = 0$. Subsequently, we present analytic expressions for semi-infinite substrates, stationary conditions, and temperature-independent material parameters. Thus, the linearized temperature is equal to the laser-induced temperature rise, see (2.2.8), so that $\theta_c(\alpha^*, \eta^*) \equiv \Delta T(\boldsymbol{x}^* = 0, \alpha^*, \eta^*)$. With low to moderate values of η^* or with $\alpha^* \to \infty$, the center-temperature rise at the substrate surface is equal to the maximum temperature rise.

7.1.1 Gaussian Beam

From the equations presented in Sects. 6.2 and 6.4, we obtain for a Gaussian beam, finite absorption, and finite heat losses [*Luk'yanchuk* and *Bäuerle* 1994]

$$\theta_c^G(\alpha^*, \eta^*) = \frac{I_a w_0}{\kappa} \left\{ \int_0^\infty \frac{dt^*}{1+4t^*} \alpha^* \exp(\alpha^{*2} t^*) \operatorname{erfc}(\alpha^* t^{*1/2}) \right.$$
$$- \frac{\sqrt{\pi}}{2} \frac{\alpha^* \eta^*}{\eta^* - \alpha^*} \int_0^\infty \frac{dt^*}{(1+4t^*)^{1/2}} \left[\eta^* \exp(\eta^{*2} t^*) \right.$$
$$\left. \left. \times \operatorname{erfc}(\eta^* t^{*1/2}) - \alpha^* \exp(\alpha^{*2} t^*) \operatorname{erfc}(\alpha^* t^{*1/2}) \right] \right\} . \quad (7.1.1)$$

DOI 10.1007/978-3-642-17613-5_7, © Springer-Verlag Berlin Heidelberg 2011

In the absence of heat losses, i.e., with $\eta^* = 0$, we obtain

$$\theta_c^G(\alpha^*, \eta^* = 0) = \frac{\alpha^* I_a w_0}{\kappa} \int_0^\infty \frac{dt^*}{2t^* + \alpha^*} \exp(-t^{*2}) \; . \tag{7.1.2}$$

For surface absorption, $\alpha^* \to \infty$, (7.1.1) yields

$$\theta_c^G(\eta^*) = \frac{\sqrt{\pi}}{2} \frac{I_a w_0}{\kappa} \left\{ 1 - \eta^* \int_0^\infty \frac{dt^*}{(1+4t^*)^{1/2}} \times \left[\frac{1}{(\pi t^*)^{1/2}} - \eta^* \exp(\eta^{*2} t^*) \operatorname{erfc}(\eta^* t^{*1/2}) \right] \right\} \; . \tag{7.1.3}$$

For surface absorption and no heat losses we obtain

$$\theta_c \equiv \theta_c^G(\alpha^* \to \infty, \eta^* = 0) = \frac{\sqrt{\pi}}{2} \frac{I_a w_0}{\kappa} = \frac{P(1-R)}{2\sqrt{\pi}\kappa w_0} \approx 0.89 \frac{I_a w_0}{\kappa} \; . \tag{7.1.4}$$

Subsequently, θ_c is often used for normalization.

7.1.2 Circular Laser Beam

For a circular beam we obtain with $\alpha^* \to \infty$ and $\eta^* = 0$

$$\theta_c^C(\alpha^* \to \infty, \eta^* = 0) = \frac{I_a w}{\kappa} \; . \tag{7.1.5}$$

7.1.3 Rectangular Beam

For a rectangular beam of area $F = 2w_x 2w_y$ and with $\alpha^* \to \infty$ and $\eta^* = 0$ the center-temperature rise is

$$\begin{aligned} &\theta_c^R(\alpha^* \to \infty, \eta^* = 0) \\ &= \frac{I_a (w_x w_y)^{1/2}}{\pi\kappa} \left[\left(\frac{w_x}{w_y} \right)^{1/2} \ln \left(\frac{(w_x^2 + w_y^2)^{1/2} + w_y}{(w_x^2 + w_y^2)^{1/2} - w_y} \right) \right. \\ &\quad \left. + \left(\frac{w_y}{w_x} \right)^{1/2} \ln \left(\frac{(w_x^2 + w_y^2)^{1/2} + w_x}{(w_x^2 + w_y^2)^{1/2} - w_x} \right) \right] \end{aligned} \tag{7.1.6}$$

For a square beam with $w_x = w_y = w_s$ this yields

$$\theta_c^S(\alpha^* \to \infty, \eta^* = 0) = \frac{2 I_a w_s}{\pi\kappa} \ln \left(\frac{\sqrt{2}+1}{\sqrt{2}-1} \right) \approx 1.12 \frac{I_a w_s}{\kappa} \; . \tag{7.1.7}$$

7.2 Stationary Solutions for Temperature-Independent Parameters

In this section the values of the absorption coefficient, $\alpha = \alpha(T_0)$, the thermal conductivity, $\kappa = \kappa(T_0)$, and the reflectivity, $R = R(T_0)$, are taken at a fixed temperature, T_0. For this (linear) problem stationary solutions of the heat equation can be obtained from (6.2.2) with $v_s^* = 0$, $h_s \to \infty$ and an upper integration variable $t^* \to \infty$. This yields

$$\theta(\boldsymbol{x}) = \frac{I_a l}{\kappa} \int_0^\infty \mathscr{G}(x^*, y^*, t_1^*) \mathscr{F}(z^*, t_1^*)\, \mathrm{d}t_1^* \,, \tag{7.2.1}$$

where

$$\mathscr{G}(x^*, y^*, t_1^*) = \frac{1}{4\pi t_1^*} \int_{-\infty}^{\infty} \mathrm{d}x_1^* \int_{-\infty}^{\infty} \mathrm{d}y_1^* g(x_1^*, y_1^*) \times \exp\left(-\frac{(x_1^* - x^*)^2 + (y_1^* - y^*)^2}{4t_1^*}\right) , \tag{7.2.2a}$$

or, in cylindrical coordinates,

$$\mathscr{G}(r^*, \varphi, t_1^*) = \frac{1}{4\pi t_1^*} \int_0^\infty \mathrm{d}r_1^* r_1^* \int_0^{2\pi} \mathrm{d}\varphi_1 g(r_1^*, \varphi_1) \times \exp\left(-\frac{r^{*2} + r_1^{*2} - 2r^* r_1^* \cos(\varphi - \varphi_1)}{4t_1^*}\right) , \tag{7.2.2b}$$

with $x^* = r^* \cos\varphi$ and $y^* = r^* \sin\varphi$. The $\mathscr{F}$-function for semi-infinite substrates is listed for different cases in Appendix B. The characteristic length, l, for the normalization of variables is the laser beam radius w_0 or w, or, in the case of a rectangular beam, w_x or w_y. Solutions for uniform large-area illumination are obtained with $l \to \infty$.

With a *Gaussian beam*, we obtain from (7.2.1) in the absence of heat losses to the surrounding medium

$$\theta(r^*, z^*) = \frac{\alpha^*}{\sqrt{\pi}} \theta_c \int_0^\infty \frac{\mathrm{d}\xi}{\alpha^{*2} - \xi^2} \mathbf{J}_0(\xi r^*) \times \left[\alpha^* \exp(-\xi z^*) - \xi \exp(-\alpha^* z^*)\right] \exp\left(-\frac{\xi^2}{4}\right) . \tag{7.2.3}$$

$\theta_c = \pi^{1/2} I_a w_0 / 2\kappa$ is the center-temperature rise given by (7.1.4). $\mathbf{J}_0$ is the Bessel function of order zero, and ξ an integration variable. We shall now discuss (7.2.3) for surface absorption and for finite absorption.

7.2.1 Surface Absorption

With $\alpha^* \to \infty$, the temperature rise within the plane $z = 0$ becomes

$$\Delta T(r^*, 0) = \theta_c \mathbf{I}_0 \left(\frac{r^{*2}}{2}\right) \exp\left(-\frac{r^{*2}}{2}\right) , \tag{7.2.4}$$

where $\mathbf{I}_0$ denotes the modified Bessel function of order zero, with $\mathbf{I}_0(0) = 1$. The result (7.2.4) is included in Fig. 7.2.1 by the dashed curve. In order to permit a comparison with temperature distributions that apply to other cases (see below), we have chosen parameter values that correspond to crystalline Si.

The temperature distribution around the center of the irradiated area can be approximated by the interpolation formula

$$\Delta T(r^*, 0) \approx \frac{\theta_c}{(1 + r^{*2})^{1/2}} \tag{7.2.5}$$

(dotted curve in Fig. 7.2.1). For $1 < r^* \leq 3$ the temperature rise is $\Delta T(r^*) \approx \theta_c / r^*$. The temperature rise along the z-axis is

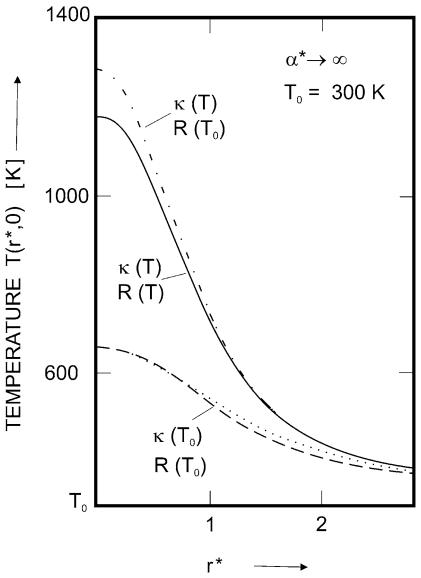

Fig. 7.2.1 Stationary temperature distribution induced by a Gaussian laser beam at normal incidence ($P = 0.5\,\mathrm{W}$, $w_0 \approx 1.8\,\mu\mathrm{m}$, $T_0 = T(\infty) = 300\,\mathrm{K}$). The radius is measured from the center of the laser beam. All cases calculated apply to surface absorption, i.e., $\alpha^* \to \infty$. The other parameters employed were: *Dashed curve*: $\kappa = \kappa(\mathrm{Si}, T_0) \approx 1.50\,\mathrm{W/cmK}$, $R(\mathrm{Si}, T_0) = 0.324$. *Dotted curve*: interpolation formula (7.2.5) with otherwise the same parameters as for the dashed curve. *Dash-dotted curve*: $\kappa = \kappa(\mathrm{Si}, T)$, see (7.3.4). *Solid curve*: numerical solution for $\kappa = \kappa(\mathrm{Si}, T)$, $R = R(\mathrm{Si}, T)$, see (7.3.5) [*Piglmayer* and *Bäuerle* 1994]

$$\Delta T(0, z^*) = \theta_c \operatorname{erfc}(z^*) \exp(z^{*2}) \ . \tag{7.2.6}$$

With large values of either r or z, (7.2.3) approaches

$$\Delta T(r^* \gg 1 \text{ and/or } z^* \gg 1) = \frac{1}{\sqrt{\pi}} \frac{\theta_c}{(r^{*2} + z^{*2})^{1/2}} \ , \tag{7.2.7}$$

which holds for typical values $r^*, z^* \geq 10$; it holds also for finite absorption if $r^*, z^* \gg \alpha^{*-1}$.

The assumption of surface absorption and temperature-independent parameters is a fairly good approximation with many metals. Here, the thermal conductivity is dominated by conduction electrons and can be described, in a first approximation, by the Wiedemann–Franz law, $\kappa = \pi^2 k_B^2 T \sigma / 3 e^2$, where σ is the electrical conductivity, which with temperatures greater than the Debye temperature, θ_D, can be described by $\sigma \propto T^{-1}$ [*Ashcroft* and *Mermin* 1976]. Inspection of Table II reveals, however, that with some metals the thermal conductivity can significantly decrease, in particular for high temperatures. This is mainly a consequence of the increase in electron–phonon interactions.

7.2.2 Finite Absorption

We shall characterize the influence of finite absorption by the normalized temperature rise

$$\Delta T^*(0, 0; \alpha^*) = \frac{\Delta T(0, 0; \alpha^*)}{\Delta T(0, 0; \alpha^* \to \infty)} \equiv \frac{\theta_c(\alpha^*)}{\theta_c} \ , \tag{7.2.8}$$

where θ_c is given by (7.1.4). Figure 7.2.2 shows $\theta_c(\alpha^*)/\theta_c$ versus α^* (solid curve). The figure demonstrates that the approximation $\Delta T(0, 0) \approx \theta_c$ holds very well as long as $\alpha^* > 10^2$. With decreasing values of α^*, however, the center temperature strongly decreases. With $\alpha^* > 10$, ΔT^* can be approximated by

$$\Delta T^*(0, 0; \alpha^* > 10) \approx 1 - \frac{2}{\sqrt{\pi}} \frac{1}{\alpha^*} \tag{7.2.9a}$$

(dotted curve in Fig. 7.2.2). With $\alpha^* < 0.1$ we have

$$\Delta T^*(0, 0; \alpha^* \ll 1) \approx \frac{\alpha^*}{\sqrt{\pi}} \left(\ln \frac{2}{\alpha^*} - \frac{C}{2} \right) \tag{7.2.9b}$$

(dash-dotted curve). $C = 0.577$ is Euler's constant. The intermediate region $0.1 \leq \alpha^* \leq 10$ can be approximated by the linear dependence

$$\Delta T^*(0, 0; 0.1 \leq \alpha^* \leq 10) \approx 0.53 + 0.165 \ln \alpha^* \tag{7.2.9c}$$

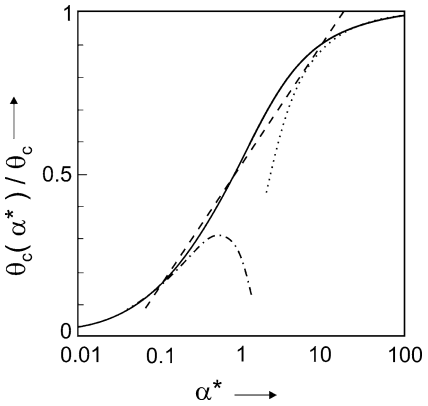

Fig. 7.2.2 Normalized center-temperature rise induced on a semi-infinite substrate of finite absorption as a function of $\alpha^* = \alpha w_0$ (*solid curve*). The approximations given in (7.2.9) are also shown (*dotted, dash-dotted*, and *dashed curves*)

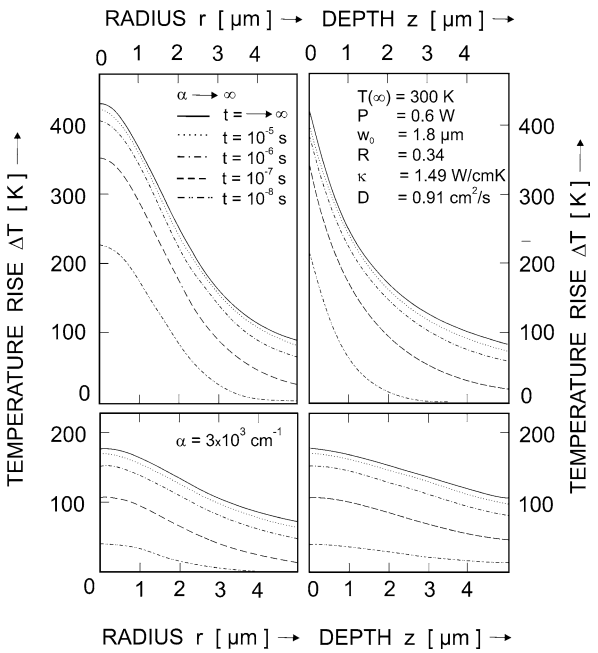

Fig. 7.2.3 Temperature distribution in radial (*left-hand side*) and axial (*right-hand side*) directions for various durations of laser light irradiation. *Upper part*: Strong absorption with $\alpha \to \infty$. *Lower part*: Finite absorption with $\alpha = 3 \times 10^3\,\mathrm{cm}^{-1}$. All other parameters employed were equal for both cases, with values as indicated in the figure [$\kappa = \kappa(\mathrm{Si}, 300\,\mathrm{K})$; $R = R(\mathrm{Si}, 300\,\mathrm{K})$; $D = D(\mathrm{Si}, 300\,\mathrm{K})$]

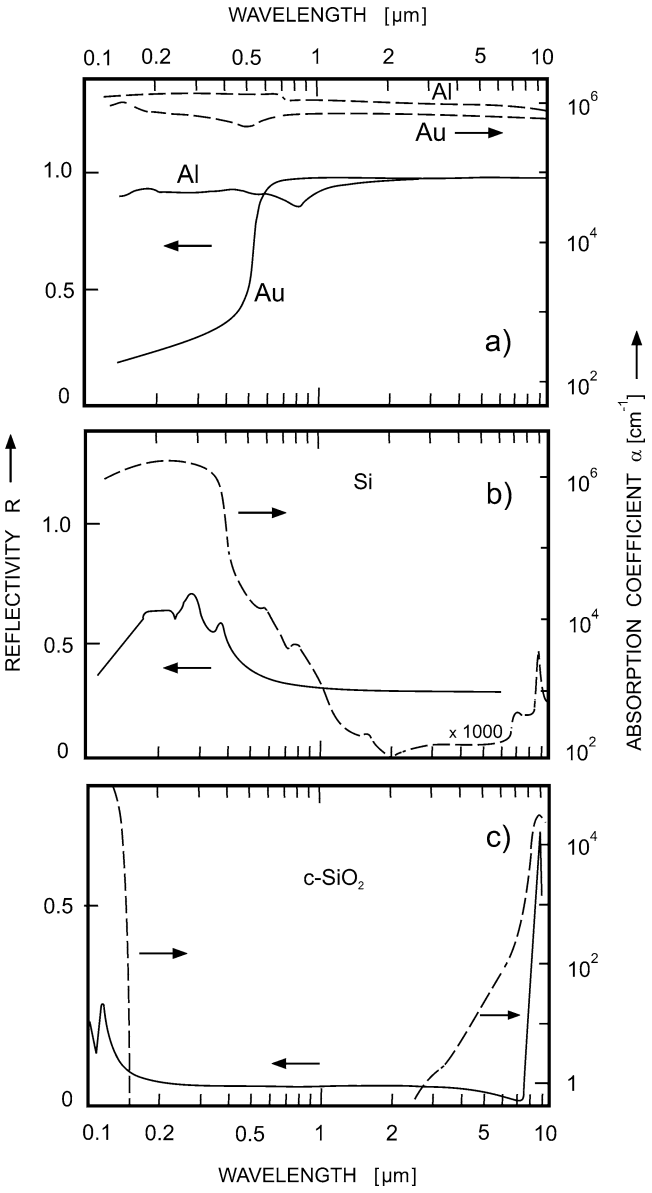

Fig. 7.2.4 a–c Reflectivity R (*solid curves*) and absorption coefficient α (*dashed curves*) as a function of wavelength for two typical metals, a semiconductor and an insulator. (**a**) Evaporated films of Al and Au. (**b**) Crystalline silicon (Si). (**c**) Crystalline quartz (c-SiO_2) [adapted from *von Allmen* and *Blatter* 1995]

(dashed curve). The steady-state temperature distribution, in both r- and z-directions, calculated from (7.2.3) with $\alpha = 3 \times 10^3\,\mathrm{cm}^{-1}$ is included in the lower part of Fig. 7.2.3 by the solid curves. The comparison with curves for $\alpha^* \to \infty$ (upper part of figure) shows that with a penetration depth $l_\alpha \approx 3\,\mu\mathrm{m}$ ($l_\alpha^* = l_\alpha / w_0 \approx 1.67$), the steady-state center-temperature rise on the surface, $\Delta T(0, 0; \alpha^*)$, decreases by more than a factor of two. On the other hand, in both r- and z-directions, the temperature distributions are only little affected with distances $r, z > l_\alpha$.

With $z \ll w_0$ and $l_\alpha \ll w_0$, the temperature rise can be described by

$$\Delta T(r^*, z^*) = \theta_\mathrm{c} \left[\mathbf{I}_0 \left(\frac{r^{*2}}{2} \right) \exp\left(-\frac{r^{*2}}{2} \right) - \frac{2}{\sqrt{\pi}\alpha^*} \left[\alpha^* z^* + \exp(-\alpha^* z^*) \right] \exp\left(-r^{*2} \right) \right] , \quad (7.2.10)$$

where $\mathbf{I}_0$ is the modified Bessel function of zero order.

The consideration of a finite penetration depth is important in all cases where the absorption coefficient of the material at the laser wavelength employed, $\alpha(\lambda)$, is smaller than, typically, $10^4\,\mathrm{cm}^{-1}$. This is the case with insulators and semiconductors for photon energies within the range $h\nu_\mathrm{ph} < h\nu < E_\mathrm{g}$, where $h\nu_\mathrm{ph}$ is the phonon (vibrational) energy of the highest IR-active dispersion oscillator (Reststrahl oscillator). Figure 7.2.4 shows the absorption coefficient and the reflectivity as a function of wavelength for two metals, a semiconductor and an insulator.

It is important to note, however, that at higher temperatures and high laser-light intensities, the absorption coefficient may change considerably due to free-carrier generation via highly non-linear mechanisms such as thermal ionization, multiphoton ionization, and impact ionization. These mechanisms become particularly important with pulsed-laser irradiation.

7.3 Stationary Solutions for Temperature-Dependent Parameters

In this section we investigate changes in temperature distribution caused by the temperature-dependent parameters $\kappa = \kappa(T)$ and $R = R(T)$.

From a mathematical point of view, consideration of a temperature dependence in the *thermal conductivity* yields no new aspects. We can use all of the solutions given in the previous section and calculate the temperature from the Kirchhoff transform (2.2.8). Subsequently, we assume surface absorption and ignore heat losses to the ambient medium, i.e., $\eta^* = 0$.

Case 1: $\alpha \to \infty$, $\kappa(T)$, $R(T_0)$

For crystalline insulators and semiconductors, the thermal conductivity is dominated by phonon–phonon interactions and decreases with increasing temperature. With temperatures much higher than the Debye temperature, the thermal conductivity can be described by

$$\kappa(T) \approx \frac{\kappa(T(\infty))}{T^{*m}} , \tag{7.3.1}$$

where $T^* = T/T(\infty)$. The exponent has values within the range $1 \leq m \leq 2$. By employing the Kirchhoff transform we obtain with (7.3.1) and arbitrary $m \neq 1$

$$T(\theta) = T(\infty)\left(1 + (1-m)\frac{\theta}{T(\infty)}\right)^{1/(1-m)} , \tag{7.3.2a}$$

and with $m = 1$

$$T(\theta) = T(\infty)\exp\left(\frac{\theta}{T(\infty)}\right) . \tag{7.3.2b}$$

For Si, the temperature dependence of κ can be described, in good approximation, by $\kappa(T(\infty)) = 1.54\ (\mathrm{W/cm\,K})$ and $m = 1.22$. The experimental data within the range $300\,\mathrm{K} < T < 1400\,\mathrm{K}$ can be fitted even more properly by [*Ho* et al. 1974]

$$\kappa(T) \approx \frac{k}{T - T_\mathrm{k}} , \tag{7.3.3}$$

where $k = 299\,\mathrm{W/cm}$ and $T_\mathrm{k} = 99\,\mathrm{K}$. With (7.3.3) we obtain

$$T(\theta) = T_\mathrm{k} + [T(\infty) - T_\mathrm{k}]\exp\left(\frac{\theta}{T(\infty) - T_\mathrm{k}}\right) . \tag{7.3.4}$$

The dash-dotted curve in Fig. 7.2.1 is calculated for this case. Clearly, this curve can be obtained directly from $\Delta T(r, 0) = \theta(r, 0)$ as given by (7.2.4), the Kirchhoff transform (2.2.8), and the temperature dependence of $\kappa(T)$. From the comparison of curves it becomes evident that consideration of a temperature-dependent κ with $\mathrm{d}\kappa/\mathrm{d}T < 0$ strongly increases the temperature near the center of the laser beam. The region $r \gg w_0$ is only slightly affected. In other words, with $\mathrm{d}\kappa/\mathrm{d}T < 0$, the width of the temperature distribution decreases significantly. This *sharpening* of the temperature field plays an important role in many cases of thermal laser processing.

Case 2: $\alpha \to \infty$, $\kappa(T)$, $R(T)$

The reflectivity of most insulators and semiconductors shows a complex dependence on temperature. For the example of Si and photon energies $h\nu < 3\,\mathrm{eV}$, we can use for temperatures $T \leq 1000\,\mathrm{K}$ the approximation [*Jellison* and *Modine* 1983]

$$R(\lambda, T) \approx R(\lambda, T_0) + 5 \times 10^{-5} T \quad (T < 1000\,\mathrm{K}) \,, \tag{7.3.5a}$$

where $T_0 = 300\,\mathrm{K}$. With higher temperatures and 694 nm ruby-laser radiation the experimental data can be fitted by [*Toulemonde* et al. 1985]

$$R(694\,\mathrm{nm}, T) \approx 0.584 - 4.8 \times 10^{-4} T + 2.6 \times 10^{-7} T^2 \quad (1000\,\mathrm{K} < T < T_\mathrm{m}) \,. \tag{7.3.5b}$$

The result of numerical calculations that employ (7.3.5) with $R(\lambda = 694\,\mathrm{nm}, T_0) = 0.324$ is included in Fig. 7.2.1 as the solid curve. The increase in reflectivity diminishes the laser-induced temperature at the center of the irradiated zone by more than 10%. The figure clearly demonstrates that the temperature dependences in the material parameters κ and R strongly influence the laser-induced temperature distribution. At the melting temperature of c-Si the reflectivity at 514.5 nm is $R(T \lesssim T_\mathrm{m}) \approx 0.44$; for c-Ge it is $R(T \lesssim T_\mathrm{m}) \approx 0.47$ [*Chaoui* et al. 2001].

The increase in the reflectivity of *semiconductors* observed in the low to medium temperature range originates from thermally activated electrons.

The reflectivity of *metals*, in general, decreases with increasing temperature. This is mainly a consequence of the increase in electron–phonon interactions. With many metals, this behavior can be described, in good approximation, by the linear relationship

$$R(T) = R_0 - R_1 (T - T_0) \,, \tag{7.3.6}$$

where $R_0 \equiv R(T_0)$. R_1 is a constant. For Ag, Al, Au, and Cu, typical values of R_1 within the near IR are around $2 \times 10^{-5}\,\mathrm{K}^{-1}$. With laser-beam intensities $I \gg 10^2\,\mathrm{W/cm^2}$ one has $I R_1 \gg \eta$ for typical values of η (Sect. 6.1). For this reason, consideration of a temperature-dependent reflectivity is more important than the consideration of heat losses to a gaseous ambient medium.

One should be aware, however, that at high temperatures with almost all materials, changes are observed in the reflectivity due to surface contaminations (oxidation, nitridation, etc.) and near melting due to surface deformations (corrugations, ripples, etc.). These effects are often of greater importance than those related to inherent reflectivity changes.

7.4 Scanned CW-Laser Beam

We now consider temperature distributions induced by scanned cw-laser irradiation of a substrate of finite absorption and temperature-independent material parameters, $\eta = 0$ and $l \equiv w_0$. Scanning shall be performed in x-direction with constant velocity, v_s (Fig. 6.1.1). The laser beam shall be of Gaussian shape, switched on at $t = -\infty$ and pass the position $x = y = 0$ at $t = 0$. In a reference frame that is fixed with the substrate, the temperature rise at the origin, $\Delta T(0, t^*; v_s^*) \equiv \Delta T(0, 0, 0, t^*; v_s^*)$, becomes

$$\Delta T(0, t^*; v_s^*) = \frac{2}{\sqrt{\pi}} \alpha^* \theta_c \int_0^\infty \frac{dt_1^*}{1 + 4t_1^*} \exp\left(-\frac{v_s^{*2}(t^* - t_1^*)^2}{1 + 4t_1^*}\right) \times \operatorname{erfc}(\alpha^* t_1^{*1/2}) \exp(\alpha^{*2} t_1^*) \,, \tag{7.4.1}$$

where θ_c is given by (7.1.4). With $\alpha^* \to \infty$ this solution becomes

$$\Delta T(0, t^*; v_s^*) = \frac{2}{\pi} \theta_c \int_0^\infty \frac{dt_1^*}{t_1^{*1/2}(1 + 4t_1^*)} \exp\left(-\frac{v_s^{*2}(t^* - t_1^*)^2}{1 + 4t_1^*}\right) . \tag{7.4.2}$$

In order to obtain further insight, we show in Fig. 7.4.1a the time evolution of the normalized temperature rise $\Delta T^*(0, t^*; v_s^*) \equiv \Delta T(0, t^*; v_s^*)/\Delta T(0, 0; 0)$ as a function of $v_s^* t^*$ for $\alpha^* = 1$ and for different scanning velocities. Note that $v_s^* t^* = v_s t / w_0 = 2t/\tau_\ell$, where $\tau_\ell = 2w_0/v_s$ is the dwell time of the laser beam. The figure shows that the maximum temperature rise occurs at times $t > 0$, i.e., *after* the laser beam has passed the position $x_\alpha = 0$. This demonstrates that for high scanning velocities heat diffusion lags behind the beam center. For velocities $v_s^* \gg 1$ the heat diffusion length becomes smaller than the laser focus. If $l_T = 2(D\tau_\ell)^{1/2} \ll w_0$, the energy absorbed during the dwell time cannot diffuse out of the focus region.

Figure 7.4.1b shows for $t^* = 0$ the normalized temperature rise at the origin, $\Delta T^*(0, 0; v_s^*) \equiv \Delta T(0, 0; v_s^*)/\Delta T(0, 0; v_s^* = 0)$, and the maximum temperature rise as a function of v_s^*. The solid curves have been calculated for the case of surface absorption, while the dashed curves refer to finite absorption with $\alpha^* = 1$. As v_s^* increases, ΔT^* decreases, since the total energy delivered to any point on the surface decreases with decreasing laser-beam dwell time. Let us consider the result for $\alpha^* \to \infty$, $w_0 \approx 1.8\,\mu\text{m}$, and $D = D(\text{Si}, T_0 = 1680\,\text{K}) = 0.084\,\text{cm}^2/\text{s}$. The figure reveals that with these parameters and with scanning velocities $v_s < 10^2\,\text{cm/s}$ the decrease in center temperature is less than 5%. This approximation also holds, for example, in direct writing of patterns by LCVD, if the thermal conductivities of the deposit and the substrate are about equal. With scanning velocities $v_s > 10^2\,\text{cm/s}$, which are common in laser annealing and laser synthesis, the surface temperature decreases significantly with increasing v_s.

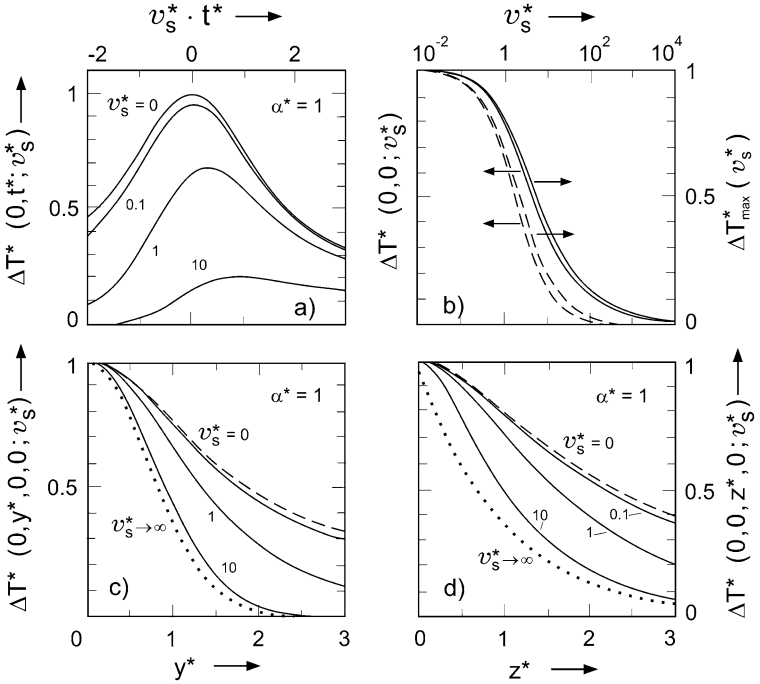

Fig. 7.4.1 a–d Normalized surface temperature rise induced by a Gaussian laser beam on a semi-infinite substrate (reference frame fixed with substrate) as a function of (**a**) the dimensionless product $v_s^* t^* = v_s t/w_0$, where $v_s^* \equiv v_s w_0/D$ and (**b**) the normalized scanning velocity. Surface absorption (*solid curves*) and finite absorption, $\alpha^* = \alpha w_0$ (*dashed curves*), are shown. For comparison, we have also included the maximum temperature rise. (**c**) Profiles perpendicular to scanning direction for various scanning velocities, v_s^*, $\alpha^* = 1$, and $t^* = 0$. (**d**) Same as (**c**) but in the z-direction

The (normalized) surface temperature rise perpendicular to the scanning direction, $\Delta T^*(0, y^*, 0, 0; v_s^*) = \Delta T(0, y^*, 0, 0; v_s^*)/\Delta T(0, 0, 0, 0; v_s^*)$, is illustrated in Fig. 7.4.1c. If $v_s^* \gg 1$, the profile can be described by

$$\Delta T^*(0, y^*, 0, 0; v_s^*) \approx \exp(-y^{*2}) \; . \tag{7.4.3}$$

In this approximation, the temperature profile has the same shape as the (Gaussian) profile of the laser beam. No significant amount of heat can diffuse out of the laser-irradiated area. With $v_s^* \ll 1$ the temperature profile approaches the steady-state limit, $v_s^* = 0$. The limits $v_s^* \to \infty$ and $v_s^* \to 0$ are included in the figure by dotted and dashed curves, respectively.

Figure 7.4.1d shows the corresponding results for the z-direction. With $v_s^* \gg 1$ the profile approaches the form

$$\Delta T^*(0, 0, z^*, 0; v_s^*) \approx \exp(-\alpha^* z^*) \; . \tag{7.4.4}$$

This is equal to the shape of the beam attenuation in the z-direction. With decreasing v_s, the profile is broadened by heat transport.

Of further concern is the temperature dependence of the material parameters. In the dynamic case one has to consider, in addition, the temperature dependence of the thermal diffusivity, D. For semiconductors, D decreases, in general, with increasing temperature. For the example of Si, we can use the approximation

$$D(T) = \frac{C}{T - T_d} , \tag{7.4.5}$$

with $C = 128\,\mathrm{cm}^2\,\mathrm{K/s}$ and $T_d = 159\,\mathrm{K}$. Consideration of a temperature-dependent diffusivity requires one to solve the heat equation numerically. However, a rough estimation of the influence of $D(T)$ can be obtained from Fig. 7.4.1b if for v_s^* the value for the diffusivity is taken once at $T_0 = 300\,\mathrm{K}$ and once at a temperature near the melting point, $T_0 \approx T_m$. The temperature dependence of D, which is mainly related to $\kappa = \kappa(T)$ in (7.3.3), causes a strongly non-linear increase in the laser-induced temperature rise (Fig. 7.6.1).

7.5 Pulsed-Laser Irradiation

In this section we discuss pulsed-laser irradiation of a semi-infinite substrate with finite absorption, temperature-independent material parameters, and $\eta = 0$. The laser-beam intensity shall be Gaussian or uniform. Solutions for other beam shapes are obtained from (6.2.2) and the intensity distributions given in Sect. 6.4.

7.5.1 Gaussian Intensity Profile

For a Gaussian laser beam we obtain from (6.3.4) with (6.4.2) and (B.10) for a *single* rectangular pulse the temperature rise at the origin $r = 0$, $z = 0$

$$\Delta T(0, 0, t^*) = \frac{2\alpha^*}{\sqrt{\pi}}\theta_c \int_{t_0^*}^{t^*} \frac{\mathrm{d}t_1^*}{1 + 4t_1^*} \operatorname{erfc}(\alpha^* t_1^{*1/2}) \exp(\alpha^{*2} t_1^*) . \tag{7.5.1}$$

For the heating cycle ($0 \le t \le \tau_\ell$) we set $t_0^* = 0$, while for the cooling cycle ($t > \tau_\ell$) we set $t_0^* = t^* - \tau_\ell^*$.

Surface Absorption

Let us first consider the limiting case $\alpha^* \to \infty$. Then, (7.5.1) yields for the *heating cycle*

$$\Delta T(0, 0, t^*) = \frac{2}{\pi}\theta_c \arctan(2t^{*1/2}) , \tag{7.5.2}$$

with $\theta_c = \sqrt{\pi} I_a w_0 / 2\kappa$ from (7.1.4). Thus, for $t^* = Dt/w_0^2 \ll 1$, we find

$$\Delta T(0, 0, t) = \frac{I_a l_T}{\sqrt{\pi}\kappa} \propto t^{1/2} , \tag{7.5.3}$$

where $l_T = 2(Dt)^{1/2}$. Clearly, the maximum temperature is reached at $t = \tau_\ell$. The average temperature rise can be estimated from the energy balance. The energy absorbed, $I_a t$, heats a layer of thickness l_T. Thus, $c_p \varrho \Delta T = I_a t / l_T$.

If the heat equation is linear, the *cooling cycle* can be described by subtracting the solution for the heating cycle starting at $t = \tau_\ell$ from the heating cycle starting at $t = 0$; i.e., for $t > \tau_\ell$

$$\begin{aligned} \Delta T(0, 0, t^*) &= \frac{2}{\pi}\theta_c\{\arctan(2t^{*1/2}) - \arctan[2(t^* - \tau_\ell^*)^{1/2}]\} \\ &= \frac{2}{\pi}\theta_c \arctan\left(\frac{2t^{*1/2} - 2(t^* - \tau_\ell^*)^{1/2}}{1 + 4t^{*1/2}(t^* - \tau_\ell^*)^{1/2}}\right) . \end{aligned} \tag{7.5.4}$$

For times $t \gg \tau_\ell$, (7.5.4) approaches

$$\Delta T(0, 0, t^* \gg \tau_\ell^*) = \frac{\theta_c \tau_\ell^*}{2\pi t^{*3/2}} = \frac{I_a w_0^2 \tau_\ell}{4\sqrt{\pi}\kappa t (Dt)^{1/2}} . \tag{7.5.5}$$

The solid curves in Fig. 7.5.1 show the normalized center-temperature rise, $\Delta T_c^* = \Delta T(0, 0, t^*; \alpha^*)/\Delta T(0, 0, \infty; \alpha^*)$, as a function of normalized time for the heating and the cooling cycle, and for laser-pulse lengths between $\tau_{\ell 1}^* = 10^{-5}$ and $\tau_{\ell 4}^* = 10$. With increasing pulse length, ΔT_c^* first increases rapidly and then levels off, when $\tau_\ell \le w_0^2/D$. For pulse lengths $\tau_\ell^* > 1$, the temperature rise can well be approximated by the *steady-state* solution $\Delta T_c^* = 1$.

The temporal behavior of temperature distributions calculated from (6.2.2) for the radial (xy-plane) and axial (z-axis) directions is included in the upper part of Fig. 7.2.3.

Finite Absorption

The radial and axial temperature rise calculated from (7.5.1) with $\alpha = 3 \times 10^3\ \mathrm{cm}^{-1}$ is included in the lower part of Fig. 7.2.3. Finite penetration of the laser light affects the temperature distributions around the center more strongly than at distances farther away.

In the limit $l_T \ll l_\alpha$, (7.5.1) yields

$$\Delta T(0, 0, t) \approx \frac{\alpha I_a t}{\varrho c_p} . \tag{7.5.6}$$

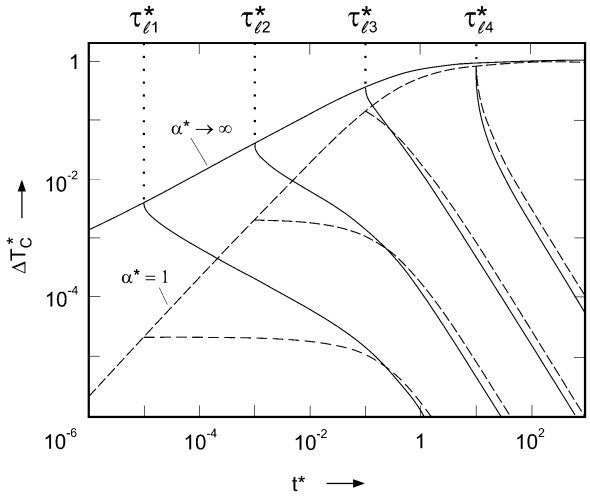

Fig. 7.5.1 Normalized center-temperature rise as a function of $t^* = Dt/w_0^2$ for laser pulse lengths (dwell times) between $\tau^*_{\ell 1} = 10^{-5}$ and $\tau^*_{\ell 4} = 10$

The solution (7.5.6) is termed the energy-density solution or calorimetric solution because it directly follows from the heat balance. The energy density absorbed, $I_\mathrm{a}t$, heats a layer of thickness l_α. Thus, $\varrho c_\mathrm{p} \Delta T l_\alpha = I_\mathrm{a} t$.

For the beginning of the cooling cycle, the energy balance yields, in analogy,

$$\frac{\mathrm{d}T}{\mathrm{d}t} \approx -\frac{\alpha^3 I_\mathrm{a} D \tau_\ell}{\varrho c_\mathrm{p}} \ . \tag{7.5.7}$$

Thus, the cooling rate strongly increases with α.

7.5.2 *Uniform Irradiation*

For uniform (large-area) irradiation by a *single* rectangular laser pulse, the temperature rise in the z-direction can be described for the *heating cycle* by

$$\Delta T(z,t) = \frac{I_\mathrm{a}}{\kappa} \left\{ l_\mathrm{T} \,\mathrm{ierfc}\left(\frac{z}{l_\mathrm{T}}\right) - \frac{1}{\alpha}\exp(-\alpha z) + \frac{1}{2\alpha}\exp\left(\frac{\alpha l_\mathrm{T}}{2}\right)^2 \right.$$
$$\left. \times \sum_{\pm} \left[\exp(\pm\alpha z)\,\mathrm{erfc}\left(\frac{\alpha l_\mathrm{T}}{2} \pm \frac{z}{l_\mathrm{T}}\right)\right]\right\} \ , \tag{7.5.8}$$

where $l_\mathrm{T} = 2(Dt)^{1/2}$. With $\alpha \to \infty$, only the first term in the parentheses remains; with $z = 0$, the solution coincides with (7.5.3). With finite α and $z = 0$, we obtain

$$\Delta T(0,t) = \frac{I_\mathrm{a}}{\kappa}\left\{\frac{l_\mathrm{T}}{\sqrt{\pi}} - \frac{1}{\alpha}\left[1 - \exp\left(\frac{\alpha l_\mathrm{T}}{2}\right)^2 \operatorname{erfc}\left(\frac{\alpha l_\mathrm{T}}{2}\right)\right]\right\} . \tag{7.5.8a}$$

In analogy to (7.5.6) we can approximate (7.5.8a) by the energy balance

$$I_\mathrm{a} t \approx \varrho c_\mathrm{p} \Delta T(0,t)\left[l_\alpha + l'_\mathrm{T}\right] , \tag{7.5.8b}$$

which takes into account heat diffusion out of l_α. This approximation is asymptotically correct for $t \to \infty$ if we choose $l'_\mathrm{T} = \sqrt{\pi}(Dt)^{1/2}/2$.

Similar to (7.5.4), the *cooling cycle* after single-pulse irradiation ($t > \tau_\ell$) can be described by

$$\Delta T(z,t) = \frac{2I_\mathrm{a}D^{1/2}}{\kappa}\left[t^{1/2}\operatorname{ierfc}\left(\frac{z}{2(Dt)^{1/2}}\right) - (t-\tau_\ell)^{1/2} \times \operatorname{ierfc}\left(\frac{z}{2D^{1/2}(t-\tau_\ell)^{1/2}}\right)\right] . \tag{7.5.9}$$

Note that $\operatorname{ierfc}(z=0) = 1/\sqrt{\pi}$.

7.6 Dynamic Solutions for Temperature-Dependent Parameters

We now discuss the influence of temperature-dependent parameters on temperature distributions induced by uniform (large-area) pulsed-laser irradiation.

Case 1: $0 \le t \le \tau_\ell$, $\alpha \to \infty$, $\kappa(T_0)$, $D(T_0)$, $R(T)$

With many metals, the reflectivity decreases with increasing temperature, and it can be described by the ansatz (7.3.6).

For large-area pulsed-laser irradiation with uniform intensity, the boundary-value problem (6.1.10) can directly be solved by taking into account $I_\mathrm{a} = I_0[1 - R(T(\infty)) + R_1\Delta T] \equiv I_0[A_0 + R_1\Delta T]$, where $A_0 \equiv A_0(T(\infty))$ is the absorptivity at $T(\infty)$. For the heating cycle $0 \le t \le \tau_\ell$ we obtain

$$\Delta T(z,t) = \frac{A_0 I_0}{R_1 I_0 - \eta}\left[\operatorname{erf}\left(\frac{z}{l_\mathrm{T}}\right) - 1 + \operatorname{erfc}\left(\frac{z}{l_\mathrm{T}} - \Lambda\right)\exp\left(\Lambda^2 - \frac{2\Lambda}{l_\mathrm{T}}z\right)\right] , \tag{7.6.1}$$

where $T(\infty) = 300\,\mathrm{K}$ and

$$\Lambda = \frac{l_\mathrm{T}}{2\kappa}(R_1 I_0 - \eta) .$$

The decrease in reflectivity causes the temperature to increase more rapidly. It can easily be proved that with $R_1, \eta \to 0$ (7.6.1) becomes identical to (7.5.8) with $\alpha^* \to \infty$.

Case 2: $0 \le t \le \tau_\ell$, α, $\kappa(T_0)$, $D(T_0)$, $R(T)$, $\eta = 0$

This case is the same as case 1, except that α is finite, and $\eta = 0$. The temperature rise at the surface is

$$\Delta T(0,t) = \frac{A_0}{R_1}\left\{\exp(\Lambda^2)[1+\operatorname{erf}\Lambda]-1\right\} + \frac{I_0 A_0}{\alpha\kappa}\left\{\exp\left(\frac{\alpha l_\mathrm{T}}{2}\right)^2 \operatorname{erfc}\left(\frac{\alpha l_\mathrm{T}}{2}\right)-1\right\} . \tag{7.6.2}$$

With $\alpha \to \infty$ the second term vanishes and (7.6.2) becomes identical to (7.6.1) with $\eta = 0$ and $z = 0$. With constant reflectivity (absorptivity), i.e., $R_1 = 0$, the first term becomes

$$\frac{I_0 A_0 l_\mathrm{T}}{\sqrt{\pi}\kappa} \propto t^{1/2} \tag{7.6.2a}$$

and the result is identical to (7.5.8a). After a very long time, i.e., with $I_0^2 R_1^2 t / \kappa c_\mathrm{p} \varrho \gg 1$ we obtain

$$\Delta T(0,t) \approx \frac{2A_0}{R_1}\exp\left(\frac{I_0^2 R_1^2}{\kappa c_\mathrm{p}\varrho} t\right) . \tag{7.6.2b}$$

Such exponential growth is typical, e.g., in conventional laser processing of metals.

Case 3: $0 \le t \le \tau_\ell$, $\alpha = \alpha(T)$, $\kappa = \kappa(T)$, $D = D(T)$, $R = R(T)$

If the material parameters are temperature dependent, the laser-induced temperature rise can only be calculated numerically. The influence of temperature-dependent parameters on the temperature distribution is most pronounced for non-metals, and in particular for semiconductors at temperatures below melting.

In semiconductors, the total absorption coefficient can be described by

$$\alpha = \alpha_\mathrm{f} + \alpha_\mathrm{c} = \alpha_\mathrm{f} + \sigma_\mathrm{a} N_\mathrm{c} . \tag{7.6.3}$$

α_f is the lattice or the interband absorption coefficient, depending on the laser wavelength under consideration (see Fig. 7.2.4). α_f depends only slightly on temperature, except for photon energies that are close to either the energy of a Reststrahl

oscillator, $h\nu_{\mathrm{ph}}$, or the bandgap energy, $E_{\mathrm{g}} \times \alpha_{\mathrm{c}}$ describes the absorption by free carriers, which depends on the concentration of electron–hole pairs, N_{c}, and on their absorption cross section, σ_{a}. In semiconductors, both electrons and holes are mobile and both contribute to the electrical conductivity. σ_{a} can be written in the form

$$\sigma_{\mathrm{a}} = \frac{e^2}{\varepsilon_0 n c \omega^2} \left(\frac{1}{m_{\mathrm{e}}^* \tau_{\mathrm{e}}} + \frac{1}{m_{\mathrm{h}}^* \tau_{\mathrm{h}}} \right) , \tag{7.6.4}$$

where e is the electron charge, ε_0 the vacuum dielectric constant, n the refractive index (real part), c the velocity of light, and $\omega = 2\pi\nu$. The quantities m_{e}^* and m_{h}^* are the effective masses and τ_{e} and τ_{h} the collision times for electrons and holes, respectively. Equation (7.6.4) reveals that the absorption cross section of the carriers increases with decreasing photon energy.

For Si, the absorption cross section of Nd:YAG-laser radiation is $\sigma_{\mathrm{a}}(300\,\mathrm{K}, 1.06\,\mu\mathrm{m}) \approx 5 \times 10^{-18}\,\mathrm{cm}^2$ [*Svantesson* and *Nilsson* 1978] and for CO_2-laser radiation $\sigma_{\mathrm{a}}(300\,\mathrm{K}, 10.6\,\mu\mathrm{m}) \approx 10^{-16}\,\mathrm{cm}^2$ [*Bhattacharyya* and *Streetman* 1980].

The temperature dependence of the absorption coefficient (7.6.3) originates *mainly* from the temperature dependence in electron–hole pair concentration, $N_{\mathrm{c}}(T) = N_{\mathrm{e}}(T) = N_{\mathrm{h}}(T)$. In thermal equilibrium, the carrier concentration in intrinsic (undoped) crystalline semiconductors is given by [*Ziman* 1972]

$$\overline{N}_{\mathrm{c}}(T) = 2 \left(\frac{k_{\mathrm{B}} T}{2\pi\hbar^2} \right)^{3/2} (m_{\mathrm{e}}^* m_{\mathrm{h}}^*)^{3/4} \exp\left(-\frac{E_{\mathrm{g}}(T)}{2 k_{\mathrm{B}} T} \right) , \tag{7.6.5}$$

where, in general, E_{g} decreases with increasing temperature. From (7.6.3) and (7.6.5) it becomes evident that the absorption coefficient strongly increases with temperature, even faster than exponentially. This can cause *thermal runaway*: As the material heats up due to its absorption by initially present free carriers, lattice defects, impurities, etc., N_{c} increases. The increase in N_{c} produces an increase in absorption and thereby an increase in heating rate, etc.

Let us consider this in further detail for the example of crystalline Si. Here, the experimental data on the temperature dependence of the absorption coefficient can well be fitted, within the range $300\,\mathrm{K} \leq T \leq 1000\,\mathrm{K}$ and for photon energies below 3 eV ($\lambda > 410\,\mathrm{nm}$) by *Jellison* and *Modine* (1983)

$$\alpha(T) \approx \alpha_0 \exp\left(\frac{T}{T_{\mathrm{R}}} \right) . \tag{7.6.6}$$

The parameters α_0 and T_{R} are listed in Table 7.6.1. For wavelengths $\lambda < 410\,\mathrm{nm}$, the fit (7.6.6) becomes less satisfactory. The range where the approximation $\alpha \to \infty$ becomes adequate can be derived directly from (7.6.6) and the parameters listed in the table.

Let us first consider thermal runaway for photon energies $h\nu < E_{\mathrm{g}}$. This is the case with CO_2-laser radiation, which is only weakly absorbed in pure Si [$E_{\mathrm{g}}(300\,\mathrm{K}) \approx 1.1\,\mathrm{eV}$; $\lambda = 10.6\,\mu\mathrm{m} \mathrel{\widehat{=}} 0.12\,\mathrm{eV}$]. The absorption coefficient

Table 7.6.1 Temperature dependence of the absorption coefficient $\alpha(T) = \alpha_0 \exp(T/T_R)$ for c-Si

λ (nm)	α_0 (10^3 cm^{-1})	T_R (K)
10 μm	2×10^{-5}	110
694	1.34	427
633	2.08	447
532	5.02	430
515	6.28	433
488	9.07	438
485	9.31	434
458	14.5	429
405	55.1	420
308	1400($T \leq 1100$ K)	4545
	1800($T > 1100$ K)	

in pure (undoped) Si is $\alpha(300\,\text{K}; 10.6\,\mu\text{m}) \leq 0.3\,\text{cm}^{-1}$ [in heavily doped Si, $\alpha(300\,\text{K}; 10.6\,\mu\text{m}) \leq 10^3\,\text{cm}^{-1}$]. Absorption is mainly related to the photoexcitation of free (thermally activated) carriers within the conduction band. These carriers transfer their energy rapidly to the lattice via electron–phonon scattering within, typically, 10^{-12} to 10^{-13} s. As a result, the lattice is locally heated and the absorption coefficient increases exponentially, see (7.6.6). Simultaneously, $l_\alpha = \alpha^{-1}$ shrinks and thus causes absorption to take place in a smaller volume. The heating rate is further enhanced by the decrease in $\kappa(T)$ and $D(T)$, see (7.3.3) and (7.4.5). This dynamic feedback increases the overall heating rate extremely rapidly.

If the photon energy exceeds the bandgap energy, i.e., if $h\nu > E_g$, the laser radiation *directly* generates electron–hole pairs. With Si, the condition is fulfilled for visible light. The carrier concentration generated is shown in Fig. 15.2.5. Because

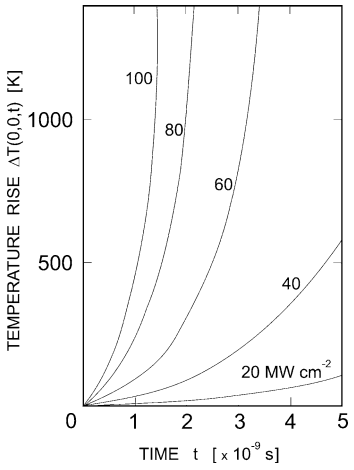

Fig. 7.6.1 Center-temperature rise, $\Delta T(0, 0, t)$, for Si versus time ($t < \tau_\ell$) for pulsed ruby-laser ($\lambda = 694$ nm) irradiation at various pulse intensities [*Kwong* and *Kim* 1983]

the quantum yield for interband absorption is near unity, very high carrier densities can be produced. For $N_c > 10^{18}$ /cm^3, carrier recombination is dominated by Auger processes (Sect. 2.4.2). The time of energy transfer to the lattice is then of the order of some picoseconds.

A theoretical treatment of transient heating requires the solution of the heat equation by taking into account the temperature dependences of material parameters. Figure 7.6.1 shows the results of one-dimensional calculations for Si and pulsed ruby-laser radiation. The dramatic rise in heating rate with increasing laser-pulse intensity becomes evident.

In *insulators* and, with certain conditions, also in semiconductors, the laser light may itself change the effective absorption coefficient via other non-linear mechanisms. For example, with very intense short pulses, substrate heating related to laser-induced impact ionization can become very important or even dominant.

Chapter 8
Infinite Slabs

In this chapter we consider the absorption of light and laser-induced temperature distributions in isotropic slabs (substrates) of finite uniform thickness, h_s, and infinite extension in the xy-plane (Fig. 6.1.1).

8.1 Strong Absorption

The laser-induced temperature distribution within a slab is similar to that within a semi-infinite substrate, as long as $l_\alpha, l_T \ll h_s$. In such cases, the solutions presented in Chap. 7 can directly be applied.

Subsequently, we will consider solutions of (6.2.2) for several limiting cases and different types of laser-beam irradiation. The material parameters are assumed to be independent of temperature. The laser beam intensity shall be *Gaussian*. The temperature rise in a coordinate system that is fixed with the (scanned) laser beam can be written as [*Luk'yanchuk* and *Bäuerle* 1994]

$$\Delta T(r^*, \varphi, z^*, t^*) = \frac{I_a w_0}{\kappa} \int_0^{t^*} \frac{\mathrm{d}t_1^*}{1+4t_1^*} q(t^* - t_1^*) \times \exp\left(-\frac{r^{*2} + v_s^* t_1^* (v_s^* t_1^* + 2r^* \cos\varphi)}{1+4t_1^*}\right) \mathscr{F}(z^*, t_1^*) \ , \quad (8.1.1)$$

where $q(t)$ describes the (arbitrary) pulse shape of the Gaussian laser beam (Sect. 6.3). The characteristic length introduced for normalization is $l \equiv w_0$. The $\mathscr{F}$-function is given in Appendix B for different cases characterized by the heat exchange coefficient, η, and the absorption coefficient, α.

8.1.1 Thermally Thin Film

The laser beam and the substrate shall be both fixed ($v_s^* = 0$) and illumination, pulsed or cw, shall start at $t^* = 0$. For a thermally thin film ($\eta^* h_s^* = \eta h_s/\kappa \ll 1$) the heat conductivity is so large, or the film so thin, that the temperature variation

D. Bäuerle, *Laser Processing and Chemistry,* 4th ed.,
DOI 10.1007/978-3-642-17613-5_8, © Springer-Verlag Berlin Heidelberg 2011

within the film is small compared to the average temperature. The $\mathscr{F}$-function (B.7) can then be approximated by

$$\mathscr{F}(t_1^*) \approx \frac{1}{h_s^*} \exp\left(-\frac{2\eta^* t_1^*}{h_s^*}\right) .$$

The temperature rise becomes

$$\Delta T(r^*, t^*) = \frac{I_a w_0^2}{\kappa h_s} \int_0^{t^*} \frac{\mathrm{d}t_1^*}{1+4t_1^*} q(t^* - t_1^*) \exp\left(-\frac{r^{*2}}{1+4t_1^*}\right) \times \exp\left(-\frac{2\eta^* t_1^*}{h_s^*}\right) . \tag{8.1.2}$$

For $q(t) = \text{const.}$, the center-temperature rise is

$$\Delta T_c(t^*) = \frac{I_a w_0^2}{4\kappa h_s}\left[\mathrm{Ei}\left(-\zeta(1+4t^*)\right) - \mathrm{Ei}(-\zeta)\right]\exp(\zeta) , \tag{8.1.3}$$

where $\zeta = \eta^*/2h_s^*$. The function Ei is given in Appendix B. With $\zeta t^* \ll 1$, we obtain

$$\Delta T_c(t^*) \approx \frac{I_a w_0^2}{4\kappa h_s} \ln(1+4t^*) . \tag{8.1.4}$$

Stationary solutions exist only in the case of finite heat losses, $\eta^* \neq 0$. With $t^* \to \infty$, we obtain from (8.1.3)

$$\Delta T_c = -\frac{I_a w_0^2}{4\kappa h_s} \exp(\zeta)\,\mathrm{Ei}(-\zeta) . \tag{8.1.5}$$

With the approximation $\zeta \ll 1$ this yields

$$\Delta T_c \approx \frac{I_a w_0^2}{4\kappa h_s}\left[\ln\left(\frac{2h_s^*}{\eta^*}\right) - \mathrm{C}\right] . \tag{8.1.6}$$

With $\zeta \gg 1$ where $\mathrm{Ei}(-\zeta) \approx (1-\zeta)\exp(-\zeta)/\zeta^2$, we obtain $\Delta T_c \approx I_a/2\eta$.

8.1.2 Scanned CW Laser

With scanned cw-laser irradiation and surface absorption, the temperature rise for quasi-stationary conditions ($t^* \to \infty$) and $\eta^* = 0$ can be obtained from (8.1.1) and (B.8). In a coordinate system that is fixed with the laser beam, we obtain

$$\Delta T(r^*, z^*, \varphi) = \frac{I_a w_0^2}{\kappa h_s} \int_0^\infty \frac{dt_1^*}{1 + 4t_1^*} \boldsymbol{\theta}_3^J \left[\frac{\pi z^*}{2h_s^*} \middle| \exp\left(-\frac{\pi^2 t_1^*}{h_s^{*2}} \right) \right] \times \exp\left(-\frac{r^{*2} + v_s^* t_1^* (v_s^* t_1^* + 2r^* \cos\varphi)}{1 + 4t^{*\prime}} \right) , \quad (8.1.7)$$

where $\boldsymbol{\theta}_3^J$ is the Jacobian theta function (Appendix B).

Figure 8.1.1 shows isotherms calculated from (8.1.7) with $h_s^* \equiv h_s/w_0 = 1$, $v_s^* = 2$ at a depth $z = 0.4h_s$. The figure shows that the maximum temperature rise along the x-axis, $\Delta T_{max} \equiv \theta_{max} = \theta(x_0^*, z^*, \pi)$, remains behind the center of the laser beam at $x^* = y^* = 0$.

Figure 8.1.2 shows the maximum temperature rise, $\theta_{max}^* = \theta_{max}/\theta_c$, as a function of scanning velocity at the depth $z = h_s$, i.e., on the rear (non-irradiated) side of the substrate. If we set $\theta_{max}(z = h_s) \approx T_m^{eff} - T(\infty)$, with $T_m^{eff} = T_m + \Delta H_m/c_p$, we can estimate the scanning velocity for which the slab is melted through the whole thickness (ΔH_m is the enthalpy of melting, Chap. 10). This permits a rough estimation of cutting and welding velocities in laser machining.

The following approximations can be employed: For scanning velocities $v_s^* \ll 1$, one obtains on the surface $z = 0$

$$x_0^*(z^* = 0) \approx -\frac{v_s^*}{4} \ln\left(\frac{16}{\xi v_s^{*2}} \right) , \quad (8.1.8)$$

where $\xi = \exp(C + 1)$ and $C = 0.577$. The maximum temperature is

$$\Delta T_{max}(z^* = 0) \equiv \theta_{max}(z^* = 0) \approx \frac{\theta_c}{2\sqrt{\pi} h_s^*} \ln\left(\frac{16}{\xi v_s^{*2}} \right) . \quad (8.1.9)$$

For high scanning velocities $v_s^* \gg 1$, one obtains for $z^* = 0$

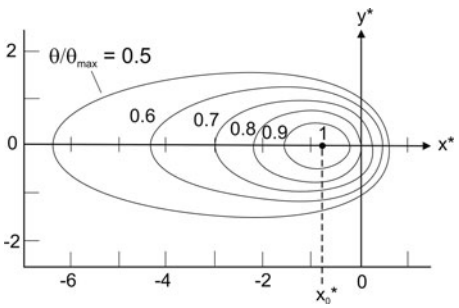

Fig. 8.1.1 Isotherms calculated at a depth $z = 0.4h_s$ of a slab of thickness $h_s^* = 1$. The coordinate system x^*, y^* is fixed with the center of the Gaussian laser beam at $x^* = y^* = 0$. The scanning velocity is $v_s^* = 2$. The maximum temperature occurs at a distance $-x_0^*$ from the beam center [*Bunkin* et al. 1978]

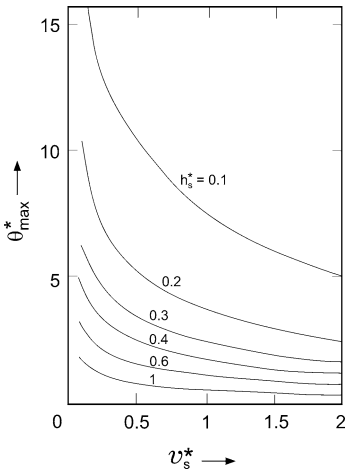

Fig. 8.1.2 Normalized maximum temperature rise at the rear side of a slab ($z = h_s$) as a function of normalized scanning velocity

$$x_0^*(z^* = 0) \approx 0.54$$
$$\Delta T_{max}(z^* = 0) \approx 1.37 \frac{\theta_c}{v_s^{*1/2}} \,. \tag{8.1.10}$$

Correspondingly, one obtains for the depth z*

$$x_0^*(z^*) \approx x_0^*(0) + \frac{1}{2} v_s^* z^{*2} \tag{8.1.11}$$

and

$$\Delta T_{max}(z^*) \approx \frac{\theta_c}{0.74 v_s^{*1/2} + v_s^* z^*} \,. \tag{8.1.12}$$

The dependence (8.1.11) can also be derived from simple arguments. The time required for heat diffusion over a distance z is $t \approx z^2/4D$. Thus, $x_0(z) - x_0(0) \approx v_s t \approx w_0 v_s^* z^{*2}/4$. Equation (8.1.12) may be rewritten as

$$z^* \approx \frac{\theta_c}{v_s^* \Delta T_{max}(z^*)} - \frac{0.74}{v_s^{*1/2}} \,. \tag{8.1.13}$$

This equation can conveniently be used to estimate the processing depth for high v_s^*.

The minimum energy deposit per unit length (J/cm), necessary to induce a temperature rise ΔT_{max} at the depth z is

$$E \approx \frac{\pi w_0^2 I_a(0)}{v_s} \,, \tag{8.1.14}$$

where $v_s \equiv v_s(z, \theta_{max}(z))$ must be determined from (8.1.13).

8.2 The Influence of Interferences

For weak to moderate absorption ($l_\alpha \geq h_\mathrm{s}$), multiple reflections within the slab cannot be ignored and the absorptivity becomes dependent on the thickness of the slab, i.e., $A = A(h_\mathrm{s})$.

Let us consider the situation for *uniform* irradiation of a slab with permittivity ε_s in an ambient medium with $\varepsilon_\mathrm{M} \approx 1$. Due to energy conservation, the absorptivity, A, is related to the reflectivity, $R = |r|^2$, and the transmittivity, $D = |d|^2$, by

$$A + R + D = 1 \,. \tag{8.2.1}$$

The amplitude reflection and transmission coefficients are given by

$$r = \frac{r_\mathrm{Ms}[1 - \exp(-\mathrm{i}2\psi)]}{r_\mathrm{Ms}^2 - \exp(-\mathrm{i}2\psi)} \quad \text{and} \quad d = \frac{(r_\mathrm{Ms}^2 - 1)\exp(-\mathrm{i}\psi)}{r_\mathrm{Ms}^2 - \exp(-\mathrm{i}2\psi)} \,,$$

where

$$r_\mathrm{Ms} = \frac{1 - \sqrt{\varepsilon_\mathrm{s}}}{1 + \sqrt{\varepsilon_\mathrm{s}}} \qquad \text{and} \qquad \psi = \frac{2\pi h_\mathrm{s}}{\lambda}\sqrt{\varepsilon_\mathrm{s}} = k_\ell h_\mathrm{s}\sqrt{\varepsilon_\mathrm{s}} \,,$$

in which $\sqrt{\varepsilon_\mathrm{s}} = n + \mathrm{i}\kappa_\mathrm{a}$. Indices M and s refer to the ambient medium and the substrate (slab), respectively. Let us consider two limiting cases.

Case 1: Semi-infinite Substrate, $h_\mathrm{s} \to \infty$

For a semi-infinite substrate there is, of course, no interference and we obtain the well-known Fresnel formulas

$$R = \frac{(1-n)^2 + \kappa_\mathrm{a}^2}{(1+n)^2 + \kappa_\mathrm{a}^2} \,, \quad A = \frac{4n}{(1+n)^2 + \kappa_\mathrm{a}^2} \quad \text{and} \quad D = 0 \,. \tag{8.2.2}$$

Case 2: Finite Thickness, Weak Absorption, $l_\alpha \gg h_\mathrm{s}$ and $\kappa_\mathrm{a} \ll 1$

If we consider only terms linear in κ_a and αh_s, we obtain

$$\begin{aligned} R &= \frac{(1-n^2)^2 \sin^2(\beta h_\mathrm{s}/2)}{\xi}(1 - A) \\ A &= 2\kappa_\mathrm{a}\frac{(1+n)\beta h_\mathrm{s} - (1-n)\sin(\beta h_\mathrm{s})}{\xi} \\ D &= \frac{4n^2}{\xi}(1 - A) \,, \end{aligned} \tag{8.2.3}$$

with

$$\xi = 4n^2 + (1-n^2)^2 \sin^2\left(\frac{\beta h_\mathrm{s}}{2}\right)$$

and $\beta = 4\pi n/\lambda$. The heat source term for a slab of finite thickness is given by

$$Q(z) = I_0(1-|r_\mathrm{Ms}|^2) f(z)\ , \tag{8.2.4}$$

with $f(z) = \alpha f'(z)$, where

$$f'(z) = \left| \frac{r_\mathrm{Ms}\exp(-\mathrm{i}\psi z/h_\mathrm{s}) - \exp(-\mathrm{i}2\psi)\exp(\mathrm{i}\psi z/h_\mathrm{s})}{r_\mathrm{Ms}^2 - \exp(-\mathrm{i}2\psi)} \right|^2 . \tag{8.2.5}$$

If $\kappa_\mathrm{a} \ll n$, this equation can be approximated by

$$f'(z) = \frac{\exp[\alpha(h_\mathrm{s}-z)] - 2\zeta\cos[\beta(h_\mathrm{s}-z)] + \zeta^2\exp[-\alpha(h_\mathrm{s}-z)]}{\exp(\alpha h_\mathrm{s}) - 2\zeta^2\cos(\beta h_\mathrm{s}) + \zeta^4\exp(-\alpha h_\mathrm{s})}\ , \tag{8.2.6}$$

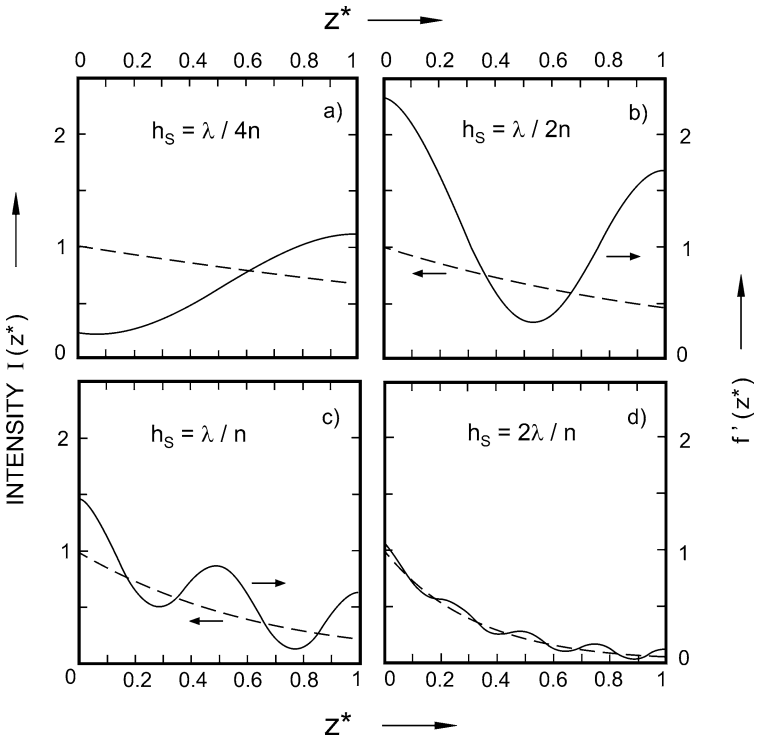

Fig. 8.2.1 a–d $f'(z^*)$ calculated from (8.2.5) for different thicknesses of an infinite slab, h_s (*solid curves*). The parameters employed correspond to 10.6 μm CO_2-laser radiation and doped Ge ($n = 4$, $\kappa_\mathrm{a} = 0.5$). The *dashed curves* have been calculated from Beer's law

where $\zeta = (1-n)/(1+n)$. The solid curves in Fig. 8.2.1 show $f'(z^*)$ as calculated from (8.2.5) with $z^* = z/h_s$. The dashed curves represent Beer's law, $f'(z) = \exp(-\alpha z)$. For thin films, considerable differences between the curves are observed. With $h_s = \lambda/4n$, the intensity at $z = 0$ becomes very small due to interference between the incident and the reflected beams. With larger thicknesses, $f'(z^*)$ shows oscillations. With $h_s > 2\lambda/n$, Beer's law becomes a good approximation.

8.3 Coupling of Optical and Thermal Properties

Some important features arising from the coupling between the optical and thermal properties of a material can be derived most simply from the heat balance. For a thermally thin slab and uniform irradiation this yields

$$h_s \varrho c_p \frac{dT}{dt} = I_0 A - I_{loss} , \tag{8.3.1}$$

where $A \equiv A(T)$. The thermal losses can be described by

$$I_{loss}(T) = \eta[T - T(\infty)] . \tag{8.3.2}$$

$T(\infty)$ is the initial temperature. The absorptivity of the slab is given by (8.2.1). For *weak* absorption, A can be approximated by (8.2.3). This temperature dependence, $A = A(T)$, is related to the index of refraction, $n = n(T)$, the absorption index, $\kappa_a = \kappa_a(T)$, and the thermal expansion of the slab, $h_s(T)$. If the temperature rise is small, we can use the expansion

$$n(T) = n(T(\infty)) + [T - T(\infty)]\frac{dn}{dT} \tag{8.3.3}$$

and

$$h_s(T) = h_s(T(\infty))\{1 + \beta_T[T - T(\infty)]\} ,$$

where β_T is the linear thermal expansion coefficient. The temperature dependence of κ_a can be described in analogy to n; outside of resonances, it can be ignored.

For weak absorption, the laser-induced temperature can then be estimated from (8.3.1) to (8.3.3), together with (8.2.3). Due to the temperature dependence of its optical thickness, transient heating of the slab shows an oscillating behavior. Another phenomenon is the occurrence of bistabilities or even multistabilities. This is schematically shown in Fig. 8.3.1. The stationary temperature rise $\Delta T \equiv \Delta T(t \to \infty)$ as a function of incident laser-beam intensity shows unstable branches, which are indicated by dashed lines.

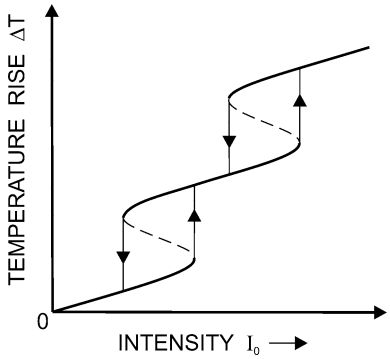

Fig. 8.3.1 Stationary temperature rise of an infinite slab as a function of laser-beam intensity for a temperature-dependent absorptivity, $A(T)$

Chapter 9
Non-uniform Media

Continuous or discontinuous changes in thermophysical and optical properties of materials significantly change laser-induced temperature distributions with respect to those estimated for plane uniform (homogeneous) substrates. *Continuous* changes in physical properties may be related to temperature dependences of material parameters or to slow changes in the material structure or composition. *Discontinuous* changes in physical properties occur in some types of composite materials, in multilayer structures, and in combined structures. Such structures may only be generated during laser processing, as in laser-induced surface oxidation or deposition of thin films or microstructures.

9.1 Continuous Changes in Optical Properties

Laser-induced heating changes the optical properties of materials via their temperature dependence. The change in absorbed laser-light intensity, in turn, changes the temperature distribution. This feedback, if strong enough, may cause *new phenomena* in laser–matter interactions. Among the examples already discussed are thermal runaway (Sect. 7.6) and oscillations or multistabilities (Sect. 8.3). In more general cases, the reflectivity and absorptivity become complex functionals of $\tilde{n}(\boldsymbol{x})$. The distribution of dissipated energy must then be calculated from the Maxwell equations (see, e.g., [*Born* and *Wolf* 1980]). The problem can be simplified considerably if we assume:

- Laser-beam irradiation at normal incidence.
- A temperature-dependent dielectric permittivity $\varepsilon = \varepsilon(T)$ only, and $\mu' = 1$, $\mu'' = 0$ (Sect. 2.2.1).
- A variation of ε only in the z-direction, $\varepsilon = \varepsilon(z)$, which is a good approximation for large-area illumination.
- Weak absorption, with $\kappa_\mathrm{a} \ll n$, where $\kappa_\mathrm{a} = \kappa_\mathrm{a}(z)$.
- The validity of geometrical optics. This means that the change in refractive index over the wavelength within the medium, $\lambda_\mathrm{M} = \lambda/n$, shall be small so that $(\lambda/n)(\mathrm{d}n/\mathrm{d}z) \ll n$.
- The beam shape to remain unchanged.

D. Bäuerle, *Laser Processing and Chemistry,* 4th ed.,
DOI 10.1007/978-3-642-17613-5_9, © Springer-Verlag Berlin Heidelberg 2011

With these assumptions, the source term in the heat equation can be written as

$$Q(z) = [1 - R(T(z = 0))]I_0 f(z) \,, \tag{9.1.1}$$

where $f(z)$ is given by (6.1.2). If any of these assumptions becomes relaxed, the propagation of the laser light becomes more complicated.

Consider, for example, an optical inhomogeneity $n = n(z)$, with $\mathrm{d}n/\mathrm{d}z < 0$. This may originate from a temperature distribution, $T(z)$, a chemical inhomogeneity, $N_i(z)$, etc. Then, for oblique laser-beam incidence, the light may propagate as schematically shown in Fig. 9.1.1a. This is the situation in optical *waveguides* produced by laser-induced surface doping.

If n changes in the direction perpendicular to the wavevector of the laser beam, non-linear refraction will result in self-focusing or defocusing phenomena (Fig. 9.1.1b). *Self-focusing* occurs if the refractive index of the medium changes with intensity so that $n(r) = n_0 + n_1 I(r)$, with $n_1 > 0$, and if the power exceeds the critical power

$$P_{\mathrm{cr}} = \zeta \frac{\lambda^2}{n_0 n_1} \,. \tag{9.1.2}$$

For a Gaussian beam and consideration of aberration effects, $\zeta = (1.22)^2\pi/32$. For $P > P_{\mathrm{cr}}$ and an initially non-diverging beam, self-focusing occurs at a distance

$$z_{\mathrm{f}} = \frac{z_{\mathrm{R}}}{\sqrt{2}\left[(P/P_{\mathrm{cr}})^{1/2} - 1\right]} \,, \tag{9.1.3}$$

where z_{R} is the Rayleigh length in (5.1.5). The (non-inertial) non-linearity of n depends directly on the amplitude of the electric field. In this case, the propagation of light can be described by the solution of the non-linear Maxwell equations.

There are, however, other (inertial) non-linearities where changes in optical properties are only indirectly related to the action of the laser light. An example is the laser-induced heating of a medium which causes an inhomogeneity $\varepsilon = \varepsilon(T(r, z))$. Then, a description of light propagation requires one to solve the Maxwell equations together with the heat equation. In media where the optical properties do not only

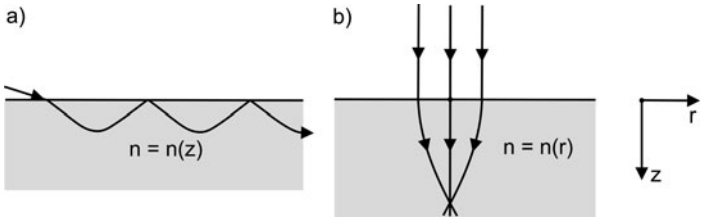

Fig. 9.1.1 (**a**) Optical waveguiding due to a refractive index $n = n(z)$, with $\mathrm{d}n/\mathrm{d}z < 0$. (**b**) Self-focusing related to (lateral) changes $n = n(r)$

change with temperature but also with chemical composition, i.e., $\varepsilon = \varepsilon(T, N_i)$, multiple non-linearities arise.

In ultrashort-pulse laser processing, self-focusing and filamentation result in the formation of voids within material volumes (Sect. 13.6). Theoretical studies on filamentation are summarized in [*Gaižauskas* 2006].

9.2 Absorption of Light in Multilayer Structures

Discontinuous changes in material properties occur in multilayer structures. In the following, we concentrate on the optical properties of multilayer structures, with special emphasis on systems that are relevant to laser processing. The situation considered is shown in Fig. 9.2.1. Different layers are characterized by their thickness, $h_1, h_2, \ldots, h_s$, and their permittivity, $\varepsilon_1, \varepsilon_2, \ldots, \varepsilon_s$ (the same indices are added to other related quantities). The ambient medium shall be air ($\varepsilon_M \approx 1$). The results obtained for uniform irradiation can also be employed with a collimated beam whose diameter is sufficiently large.

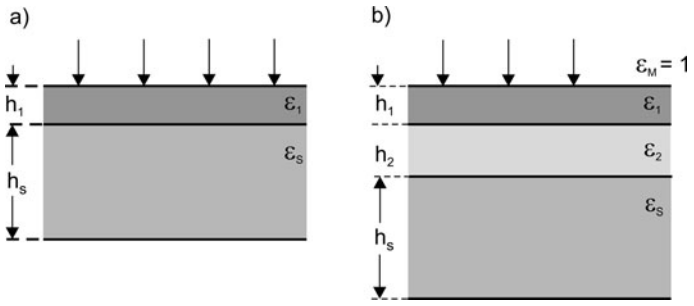

Fig. 9.2.1 Uniform irradiation of substrates covered with (**a**) a single layer and (**b**) with two layers

9.2.1 Thin Films

First, we consider a thin extended film placed on a substrate with $h_1 \ll h_s$ (Fig. 9.2.1a). If $h_s \gg l_{\alpha s}$, the substrate can be considered semi-infinite with respect to its optical behavior. Because $D = 0$, we have

$$A + R = 1 \,. \tag{9.2.1}$$

The amplitude reflection coefficient is

$$r_{M1s} = \frac{r_{1s} + r_{M1} \exp(-i2\psi_1)}{r_{M1} r_{1s} + \exp(-i2\psi_1)} \,, \tag{9.2.2}$$

with

$$r_{ij} = \frac{\sqrt{\varepsilon_i} - \sqrt{\varepsilon_j}}{\sqrt{\varepsilon_i} + \sqrt{\varepsilon_j}} \quad \text{and} \quad \psi_i = \frac{2\pi h_i}{\lambda}\sqrt{\varepsilon_i} = k_\ell h_i \sqrt{\varepsilon_i} \ ,$$

where $\sqrt{\varepsilon_i} = n_i + \mathrm{i}\kappa_{\mathrm{a}_i}$. The indices i and j refer to the different media, in the present case to those characterized by ε_M, ε_1, and ε_s.

Weak Absorption

For weakly absorbing films, the absorptivity changes with film thickness, h_1, due to interferences. This situation applies to metal oxides on metal substrates irradiated with IR or VIS light, for which $\kappa_{\mathrm{a}1} \ll n_1$. Additionally, for metals $A_\mathrm{s} = 1 - |r_{\mathrm{Ms}}|^2 \ll 1$. If we only consider terms linear in $\kappa_{\mathrm{a}1}$ and A_s, we obtain

$$A(h_1) \approx \frac{n_1^2 A_\mathrm{s} + 2\kappa_{\mathrm{a}1}[\beta h_1 - \sin(\beta h_1)]}{n_1^2 + (1 - n_1^2)\sin^2(\beta h_1/2)} \ , \tag{9.2.3}$$

with

$$\beta = \frac{4\pi n_1}{\lambda} = 2k_\ell n_1 \ . \tag{9.2.4}$$

The oscillations in the absorptivity (9.2.3) are due to interferences of the laser light within the thin layer. Their period is $\Delta h = 2\pi/\beta = \lambda/2n_1$. The number of oscillations is

$$Z = \frac{h_1}{\Delta h} \approx \frac{n_1}{2\pi\kappa_{\mathrm{a}1}} \ . \tag{9.2.5}$$

The latter approximation estimates the number of *pronounced* oscillations which occur up to $h_1 \approx l_{\alpha 1} = \alpha_1^{-1}$. For an oxide layer of Cu_2O and 10.6 µm CO_2-laser radiation, the number of pronounced oscillations is $Z = 14$ (Fig. 9.2.2). If we consider, in contrast, an SiO_2 layer on Si and UV-laser radiation, we find $Z \approx 10^6$. The number of oscillations observed experimentally depends also on the surface roughness, the spectral width of the laser light, etc. Via (9.2.5) the type of layer material can be analyzed.

For very thin films we can approximate (9.2.3) by

$$A(h_1) \approx A_\mathrm{s}(1 + \xi h_1^2) \ , \tag{9.2.6}$$

where $\xi = k_\ell^2(n_1^2 - 1)$ and $\xi h_1^2 \ll 1$. If we set $\kappa_{\mathrm{a}1} = \kappa_{\mathrm{as}} = 0$, we obtain from (9.2.2) the reflectivity

$$R(h_1) = |r_{\mathrm{M1s}}|^2 = \frac{n_1^2(1 - n_\mathrm{s})^2\cos^2\varphi + (n_\mathrm{s} - n_1^2)^2\sin^2\varphi}{n_1^2(1 + n_\mathrm{s})^2\cos^2\varphi + (n_\mathrm{s} + n_1^2)^2\sin^2\varphi} \ , \tag{9.2.7}$$

where $\varphi = k_\ell n_1 h_1$.

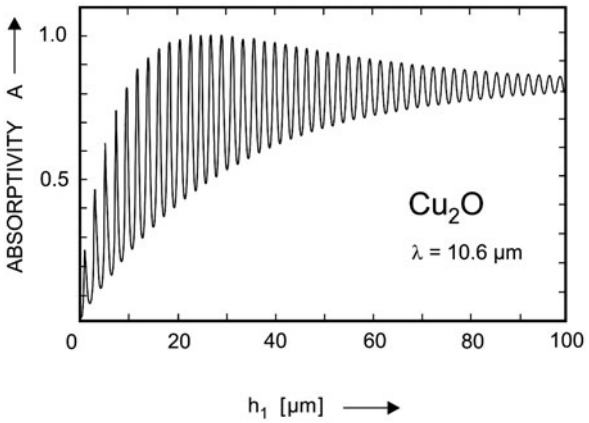

Fig. 9.2.2 Absorptivity calculated as a function of layer thickness. The parameters $A_s = 0.02$, $n_1 = 2.45$, and $\kappa_{a1} = 0.027$ correspond to a Cu_2O layer on a Cu substrate and CO_2-laser radiation

Strong Absorption

If $\kappa_{a1} > n_1$, the absorptivity changes smoothly from A_s to $A(h_1) \approx A_1 = 1 - |r_{M1}|^2$ within a film thickness of a few absorption lengths. The averaged absorptivity (with respect to the oscillations) is

$$\langle A(h_1)\rangle = \frac{1}{\Delta h_1}\int_0^{\Delta h_1} A(h_1 + x)\,\mathrm{d}x \approx A_1 + (A_s - A_1)\exp(-2\alpha_1 h_1)\ .$$

9.2.2 Two-Layer Structures

A two-layer structure (Fig. 9.2.1b) describes, for example, the situation in many cases of laser-induced oxidation of copper (Chap. 26). Here, h_1 corresponds to CuO, and h_2 to Cu_2O. The absorptivity is

$$A = 1 - |r_{M12s}|^2\ , \tag{9.2.8}$$

where the amplitude reflection coefficient is

$$r_{M12s} = \frac{r_{12s} + r_{M1}\exp(-\mathrm{i}2\psi_1)}{r_{M1}r_{12s} + \exp(-\mathrm{i}2\psi_1)}\ . \tag{9.2.9}$$

r_{M1} is defined as in (9.2.2). r_{12s} can be calculated from r_{M1s} by changing indices $M \rightarrow 1$ and $1 \rightarrow 2$. This procedure can be extended to an arbitrary number of layers.

For two-layer systems, the absorptivity may show double interference behavior. For example, high-frequency oscillations may be modulated by low-frequency oscillations. This has in fact been observed during cw Nd:YAG-laser oxidation of Cu.

The reflectivity of two free standing layers – without the semi-infinite substrate – is obtained from (9.2.9) by changing S → M.

9.2.3 Three-Layer Systems

For a three-layer system, the amplitude reflection coefficient is given by

$$r_{\mathrm{M123s}} = \frac{r_{123\mathrm{s}} + r_{\mathrm{M1}} \exp(-\mathrm{i}2\psi_1)}{r_{\mathrm{M1}} r_{123\mathrm{s}} + \exp(-\mathrm{i}2\psi_1)} \,, \tag{9.2.10}$$

where $r_{123\mathrm{s}}$ can be calculated from (9.2.9) by changing indices M → 1, 1 → 2, 2 → 3.

This model can be applied, in a first approximation, to laser-induced oxidation of Fe. Here, h_1 corresponds to Fe_2O_3, h_2 to Fe_3O_4, and h_3 to FeO. While for Cu and Fe the boundaries between different oxide layers are relatively sharp, they are washed out for other oxides, e.g., those of Ti and V.

9.3 Temperature Distributions for Large-Area Irradiation

Consider uniform laser-light irradiation which directly or indirectly heats a thin film placed on a substrate (Fig. 9.2.1a).

In the simplest case, the film changes only the absorptivity from A_s to A, but has no influence on the overall *thermal* properties. A can be constant or it can change with time, for example, due to changes in film thickness. In the latter case, the (single) heat equation for the substrate must be solved together with the equation for $A = A(h)$. This approximation can be applied to laser-induced growth of films whose thermal properties are similar to those of the substrate.

If the film influences both the optical and thermal properties of the system, the heat equation must be solved for both the thin film and the substrate.

9.3.1 Stationary Solutions for Thin Films

The influence of the film on the surface temperature can be estimated from the boundary condition at the interface to the ambient medium,

$$\eta \Delta T = \kappa_1 \left.\frac{\partial T}{\partial z}\right|_{z=0} \approx \kappa_1 \frac{\delta T_1}{h_1} \,, \tag{9.3.1}$$

which yields

$$\frac{\delta T_1}{\Delta T} \approx \frac{\eta h_1}{\kappa_1} \,, \tag{9.3.2}$$

where δT_1 is the change in temperature within the film, and ΔT its *average* temperature rise. For gases $\eta h_1/\kappa_1 \ll 1$ and thus $\delta T_1 \approx 0$. The average temperature rise is then

$$\Delta T \approx \frac{I_0 A}{2\eta} \,, \tag{9.3.3}$$

where $A = A_1 + A_\mathrm{s}$ is the *total* absorptivity of the system. For surface absorption $A \equiv A_1$. For *finite* absorption, the distribution of the absorbed intensity must be considered in the source term for the film and the substrate so that

$$Q_1 = I_0 f_1(z) \qquad \text{and} \qquad Q_\mathrm{s} = I_0 f_\mathrm{s}(z) \,. \tag{9.3.4}$$

For simplification we assume the substrate to be optically semi-infinite, i.e., $l_{\alpha\mathrm{s}} \ll h_\mathrm{s}$. This applies to metal oxidation and, for laser wavelengths $\lambda < 500\,\mathrm{nm}$, also to the oxidation of Si. In this approximation, the functions $f_1(z)$ and $f_\mathrm{s}(z)$ can be written as

$$f_1(z) = \alpha_1(1 - R_1) \left| \frac{r_{1\mathrm{s}} \exp(-\mathrm{i}\varphi) + \exp(-\mathrm{i}2\psi) \exp(\mathrm{i}\varphi)}{r_{\mathrm{M}1} r_{1\mathrm{s}} + \exp(-\mathrm{i}2\psi)} \right|^2 \,, \tag{9.3.5}$$

and

$$f_\mathrm{s}(z) = \alpha_\mathrm{s} n_\mathrm{s} \left| \frac{(1 + r_{\mathrm{M}1})(1 + r_{1\mathrm{s}})}{r_{\mathrm{M}1} r_{1\mathrm{s}} + \exp(-\mathrm{i}2\psi)} \right|^2 \exp(\alpha_1 h_1) \exp[-\alpha_\mathrm{s}(z - h_1)] \,,$$

with

$$1 - R_1 = \frac{4n_1}{(1 + n_1)^2 + \kappa_{\mathrm{a}1}^2} \quad \text{and} \quad \varphi \equiv \varphi(z) = k_\ell z \sqrt{\varepsilon_\mathrm{s}} \,,$$

where $r_{\mathrm{M}1}$, $r_{1\mathrm{s}}$, $r_{\mathrm{M}\mathrm{s}}$ and ψ are given by (9.2.2). With the present assumptions, laser-beam interference takes place within the film, while the attenuation within the substrate is described by Beer's law. The total energy absorbed within the film and the substrate is proportional to

$$A_1 = \int_0^{h_1} f_1(z)\,\mathrm{d}z \qquad \text{and} \qquad A_\mathrm{s} = \int_{h_1}^{\infty} f_\mathrm{s}(z)\,\mathrm{d}z \,. \tag{9.3.6}$$

Due to energy conservation

$$A = A_1 + A_\mathrm{s} = 1 - |r|^2 \,,$$

where the amplitude reflection coefficient, $r \equiv r_{\mathrm{M}1\mathrm{s}}$, is given by (9.2.2).

Figure 9.3.1 shows the absorptivities, reflectivities and transmissivities for a substrate of thickness h_s as a function of film thickness, h_1. The parameters employed correspond to an SiO_2 layer on a 300 µm Si wafer. The results shown in Fig. 9.3.1a

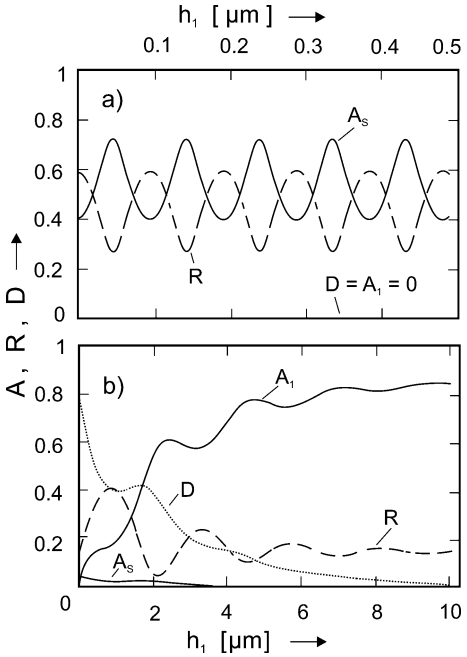

Fig. 9.3.1 a, b Absorptivities, A, reflectivities, R, and transmissivities, D, calculated for uniform laser-light irradiation as a function of film thickness, h_1. The parameters employed correspond, approximately, to an SiO_2 layer on a Si wafer ($h_s = 300\,\mu m$). (**a**) 308 nm XeCl-laser radiation ($R_1 = 0.05$, $\alpha_1 = 0$, $R_s = 0.59$, $\alpha_s = 1.47 \times 10^6\,cm^{-1}$). (**b**) CO_2-laser radiation ($R_1 = 0.15$, $\alpha_1 = 4 \times 10^3\,cm^{-1}$, $R_s = 0.31$, $\alpha_s = 0.86\,cm^{-1}$)

were calculated from (9.3.6) and (9.2.2) for (uniform) XeCl-laser radiation. SiO_2 is transparent to 308 nm radiation, while Si absorbs strongly at this wavelength. Due to interferences within the SiO_2 layer, the reflectivity, R, oscillates and thereby so does the (surface) absorptivity of the silicon, A_s. The situation is different for CO_2-laser radiation (Fig. 9.3.1b). SiO_2 strongly absorbs at $10.6\,\mu m$, while Si is almost transparent at this wavelength. For this reason, the finite thickness of the silicon wafer must be taken into account. Here, A_1 strongly increases with h_1, while the transmissivity, D, decreases. A_s can be described, in good approximation, by Beer's law. The oscillations of R, and thereby of A_1 and D, are due to interferences within the SiO_2 layer.

According to (9.3.3) the temperature rise behaves in the same way as the total absorptivity, $A = A_1 + A_s$.

9.3.2 Dynamic Solutions

For *large-area* uniform irradiation and $h_s \to \infty$, the temperature distribution within the film for $\alpha \to \infty$ and $\eta = 0$ is

$$\Delta T_1(z,t) = \frac{I_0(1-R_1)l_T}{\kappa_1} \sum_{n=-\infty}^{+\infty} \Lambda^{|n|} \,\mathrm{ierfc}\left(\frac{|z-2nh_1|}{l_T}\right) , \qquad (9.3.7)$$

where $l_T = 2(D_1 t)^{1/2}$ and

$$\Lambda = \frac{\kappa^* - D^{*1/2}}{\kappa^* + D^{*1/2}} , \qquad \text{and} \qquad D^* = D_1/D_s . \qquad (9.3.8)$$

The effect of temperature-dependent thermal conductivities can be taken into account if the functional form of the temperature dependences $\kappa_1(T)$ and $\kappa_s(T)$ is the same, so that $\kappa^* = \kappa_1(T)/\kappa_s(T)$ is independent of temperature. In this case, a Kirchhoff transform in analogy to (2.2.8) can be performed.

9.4 Temperature Distributions for Focused Irradiation

In this section, we shall investigate temperature distributions induced within a thin film and a substrate by a *focused* laser beam (Fig. 9.4.1). We assume $h_s \to \infty$ and cylindrical symmetry. Before presenting (approximate) solutions of the boundary-value problem, we shall estimate, in a crude way, the influence of the film on the surface temperature rise. Heat transport to the ambient medium is ignored, i.e., we set $\eta = 0$.

The temperature gradient induced by a focused laser beam absorbed at the surface is of the order $\nabla T \approx \Delta T/w$. The power transported from the illuminated area $F \approx \pi w^2$ into the substrate is $P_s \approx F\kappa_s \nabla T$. In the absence of the film and with stationary conditions, this must be equal to the laser power absorbed on the surface, $P_a \approx I_0 A \pi w^2$. This yields $\Delta T(z=0, h_1=0) \approx I_0 A w/\kappa_s$. In the presence of the

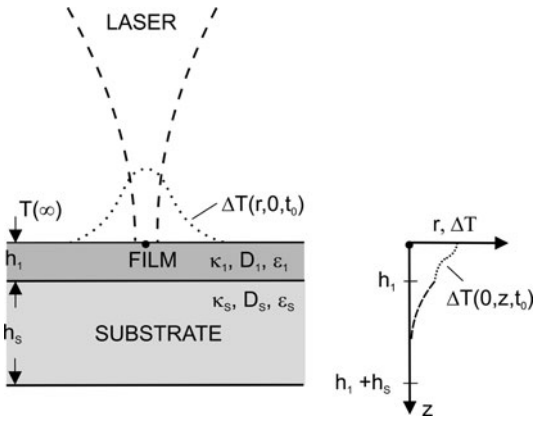

Fig. 9.4.1 Irradiation geometry and laser-induced temperature rise on a substrate covered with a thin film of thickness h_1. The origin of the coordinate system is on the film surface in the center of the laser beam

film, we have to consider the change in lateral heat flux. If $\kappa_1 \gg \kappa_s$, the additional power transported in lateral direction is $P_1 \approx 2\pi w h_1 \times \kappa_1 \nabla T$. With $P_a = P_s + P_1$, the relative change in surface temperature rise caused by the film becomes

$$\Delta T^* \equiv \frac{\Delta T(z=0,h_1)}{\Delta T(z=0,h_1=0)} \approx \left(1 + \frac{2h_1}{w}\frac{\kappa_1}{\kappa_s}\right)^{-1} . \tag{9.4.1}$$

Thus, the increase in lateral heat flux decreases the surface temperature. The case $\kappa_1 \gg \kappa_s$ can be applied to thin films of metals or semiconductors on thermally insulating substrates. With $\kappa_1/\kappa_s \approx 50$, a laser focus $w = 10\,\mu\text{m}$, and a film thickness of $h_1 = 100\,\text{Å}$, the surface temperature will decrease by about 10%.

These simple arguments cannot be applied to thermally insulating films where $\kappa_1 \ll \kappa_s$. A more accurate estimation which also includes this case is given by (9.4.5).

9.4.1 Strong Film Absorption

For $\alpha_1 \to \infty$, temperature-independent material parameters, and $h_s \to \infty$, a Gaussian laser beam induces the following steady-state temperature rise within the film [*Burgener* and *Reedy* 1982]:

$$\Delta T_1(r^*,z^*) = \frac{P(1-R_1)}{2\pi w_0 \kappa_1}\int_0^\infty \mathrm{d}\xi \mathbf{J}_0(\xi r^*)\exp\left(-\frac{\xi^2}{4}\right) \times\left[\exp(-\xi z^*) + \frac{(\kappa^*-1)\cosh(\xi z^*)\exp(-\xi h_1^*)}{\kappa^*\sinh(\xi h_1^*)+\cosh(\xi h_1^*)}\right], \tag{9.4.2}$$

where ξ is an integration variable, $\mathbf{J}_0$ the Bessel function of order zero, $r^* = r/w_0$, $z^* = z/w_0$, $h_1^* = h_1/w_0$, and $\kappa^* = \kappa_1/\kappa_s$. Figure 9.4.2 shows the center-temperature rise $\Delta T_c^* = \Delta T(r = z = 0, h_1)/\Delta T(r = z = 0, h_1 = 0) \equiv \Delta T_c(h_1)/\Delta T_c(h_1 = 0)$ calculated from (9.4.2) for parameters h_1^* and κ^*. For $h_1^* > 1$, the temperature rise becomes independent of layer thickness.

The temperature rise within the *substrate* is

$$\Delta T_s(r^*,z^*) = \frac{P(1-R_1)}{2\pi w_0 \kappa_1}\int_0^\infty \mathrm{d}\xi \mathbf{J}_0(\xi r^*)\exp\left(-\frac{\xi^2}{4}\right) \times\left[\exp(-\xi z^*) + \frac{(\kappa^*-1)\cosh(\xi h_1^*)\exp(-\xi z^*)}{\kappa^*\sinh(\xi h_1^*)+\cosh(\xi h_1^*)}\right]. \tag{9.4.3}$$

For large values of z and r this can be approximated by

$$\Delta T_s(r^* \gg 1, z^* \gg 1) = \frac{P(1-R_1)}{2\pi w_0 \kappa_s (r^{*2}+z^{*2})^{1/2}} . \tag{9.4.4}$$

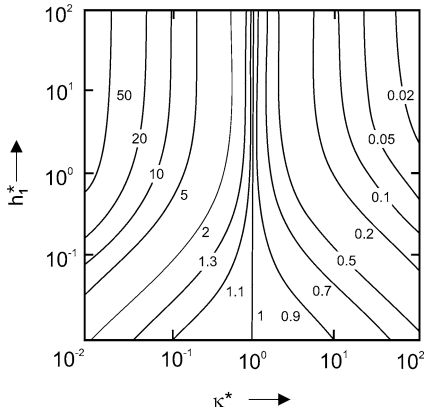

Fig. 9.4.2 Normalized center-temperature rise $\Delta T_c^* = \Delta T_c(h_1)/\Delta T_c(h_1 = 0)$ (*numbers on curves*), as a function of film thickness h_1^* and heat conductivity κ^*

This result is obvious. For large distances from the source, the temperature distribution must be equal to (7.2.7).

Another approximation seems to be interesting. If we assume $h_1^* \ll \min(\kappa^*, 1, \kappa^{*-1})$, we can expand (9.4.2) and obtain

$$\Delta T_c^* \equiv \frac{\Delta T_c(h_1)}{\Delta T_c(h_1 = 0)} = 1 + \frac{2}{\sqrt{\pi}} \frac{h_1}{w_0} \frac{(\kappa_s - \kappa_1)(\kappa_s + \kappa_1)}{\kappa_1 \kappa_s} . \tag{9.4.5}$$

For $\kappa_1 \gg \kappa_s$, this yields

$$\Delta T_c^* = 1 - \frac{2}{\sqrt{\pi}} \frac{h_1}{w_0} \frac{\kappa_1}{\kappa_s} .$$

Except for the factor $1/\sqrt{\pi}$, this result agrees with (9.4.1).

For $\kappa_1 \ll \kappa_s$, we obtain

$$\Delta T_c^* = 1 + \frac{2}{\sqrt{\pi}} \frac{h_1}{w_0} \frac{\kappa_s}{\kappa_1} . \tag{9.4.6}$$

Thus, the film increases the surface temperature. This case applies to surface oxidation of metals or semiconductors.

9.4.2 Finite Film Absorption

We now assume finite film absorption and all material parameters to be independent of temperature. Furthermore, if $h_1 \geq l_{\alpha 1}$, the real intensity distributions within the

film can be approximated by an exponential (Fig. 8.2.1d). Thus, we can define an *effective* absorption coefficient,

$$\alpha_1 = \frac{1}{h_1} \ln\left(\frac{P(z=0)}{P(z=h_1)}\right) . \tag{9.4.7}$$

The reflection coefficient, R, depends on film thickness and oscillates with a period of, approximately, $\lambda/2n_1$.

Multilayer Structures

The steady-state temperature distribution induced by cw-laser irradiation of multilayer structures has been calculated by *Calder* and *Sue* (1982).

For a semi-infinite substrate covered by a *single* film, the temperature rise induced within the film by a cylindrical beam of radius w can be described by

$$\begin{aligned}\Delta T_1(r^*, z^*) = \frac{P(1-R)\alpha_1^{*2}}{2\pi w \kappa_1 F(0)} \int_0^\infty \mathrm{d}\xi \frac{F(\xi)\mathbf{J}_0(\xi r^*)}{\alpha_1^{*2} - \xi^2} \\ \times\Bigg(\Big\{\kappa^* \cosh[\xi(h_1^* - z^*)] + \sinh[\xi(h_1^* - z^*)] \\ +\Big[\frac{\xi}{\alpha_1^*} - \kappa^* + \Big(1 - \frac{\xi}{\alpha_s^*}\Big)\Lambda \exp(-\alpha_s^* h_1^*)\Big] \\ \times \exp(-\alpha_1^* h_1^*)\cosh(\xi z^*)\Big\} \\ \times[\cosh(\xi h_1^*) + \kappa^* \sinh(\xi h_1^*)]^{-1} - \frac{\xi}{\alpha_1^*}\exp(-\alpha_1^* z^*)\Bigg) ,\end{aligned} \tag{9.4.8}$$

where $\Lambda \equiv \Lambda(\xi)$ is given by

$$\Lambda = \kappa^* \frac{\alpha_s^{*2}(\alpha_1^{*2} - \xi^2)}{\alpha_1^{*2}(\alpha_s^{*2} - \xi^2)}$$

and

$$F(\xi) = \int_0^\infty g(r^*)\mathbf{J}_0(\xi r^*) r^* \,\mathrm{d}r^* , \tag{9.4.9}$$

with $r^* = r/w$, $z^* = z/w$, and $\alpha_i^* = \alpha_i w$. The function $g(r^*)$ describes the radial intensity distribution of the (circular) laser beam.

With a Gaussian beam, $F(\xi)$ simplifies to

$$F(\xi) = \frac{1}{2} \exp\left(-\frac{\xi^2}{4}\right) . \tag{9.4.10}$$

Figure 9.4.3 shows the (normalized) center-temperature rise, $\Delta T_1(0,0)/P$, calculated from (9.4.8) and (9.4.10) as a function of the thickness of a p-Si film on a glass substrate. The overall change in surface temperature, and the interference pattern superimposed, originates from changes in the reflection coefficient (Sect. 9.2.1). If the film thickness exceeds the optical penetration depth, i.e., if $h_1 > l_{\alpha 1}$, the laser power absorbed remains almost constant, while the heat transport within the film ($\kappa_1 \gg \kappa_s$) further increases with h_1.

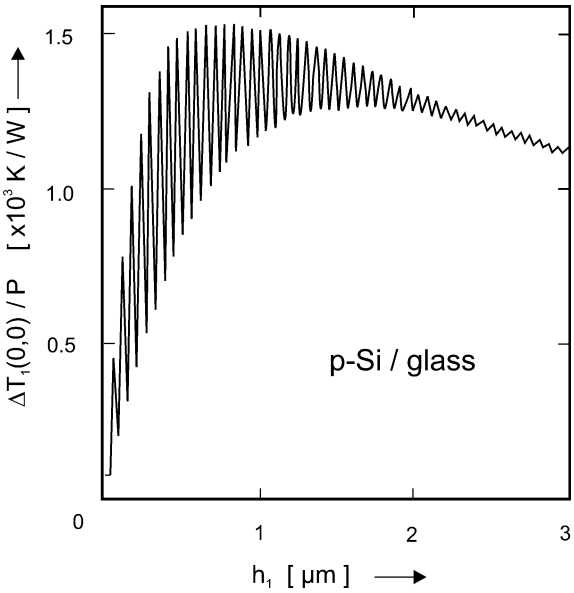

Fig. 9.4.3 Normalized temperature rise induced on the surface of a thin film on a semi-infinite substrate, calculated as a function of film thickness, h_1 [$P(\lambda = 501\,\text{nm})$ is the incident laser power, $2w_0 = 40\,\mu\text{m}$]. The material parameters employed correspond to a polycrystalline silicon (p-Si) film and a glass substrate: $\kappa_s(T_0 = 300\,\text{K}) = 0.02\,\text{W/cm K}$, $\alpha_s(T_0) = 0$, $n_s(T_0, \lambda = 501\,\text{nm}) \approx 1.35$, $\kappa_1(T_0 = 300\,\text{K}) = 0.3\,\text{W/cm K}$, $\alpha_1(T_0, \lambda = 501\,\text{nm}) \approx 1.5 \times 10^4\,\text{cm}^{-1}$, $n_1(T_0, \lambda = 501\,\text{nm}) \approx 4.2$ [adapted from *Calder* and *Sue* 1982]

9.5 The Ambient Medium

The analysis of laser processing rates requires, in many cases, knowledge of the temperature distribution within the ambient medium, and the influence of this medium on the substrate temperature.

The ambient medium can be heated either *directly* if it absorbs the incident laser radiation (Sect. 19.1), or *indirectly* via the heated substrate area. Heat transport within a gas or a liquid takes place via heat conduction, convection, and thermal radiation. Convection may originate from density gradients related to temperature gradients (free convection), from changes in particle number density in non-equimolecular reactions (chemical convection), or from an external flow (forced convection).

9.5.1 Influence on Substrate Temperature

An ambient medium changes the substrate temperature. Let us consider Fig. 9.5.1.

Case a: The laser radiation shall be exclusively absorbed by the substrate. In the absence of a chemical reaction, the ambient medium will lower the surface temperature, $T_s(z = 0)$. If an exothermal surface reaction related to the ambient medium takes place, T_s can increase or decrease, depending on the relative amount of the reaction enthalpy and the loss of energy by heat transport into the medium.

Case b: The laser radiation shall exclusively be absorbed by the medium at the backside of the sample. Then, the maximum temperature rise occurs within this medium at a distance $z_0 \propto \alpha^{-1}$. This irradiation scheme permits *localized* processing by means of strongly absorbing ambient media. Initial investigations have been performed for CO_2-laser-induced etching of Si and Ge in an atmosphere of CF_3I+SF_6. Here, SF_6 was used as a sensitizer that strongly absorbs CO_2-laser radiation [*Karlov* et al. 1985]. By using this irradiation geometry, real material patterning with reasonable "etch" rates has been demonstrated by laser-induced backside wet etching (LIBWE, Sect. 14.5). Femtosecond-laser pulses open up *new* possibilities of laser-induced backside processing. Due to nonlinear processes, *all* linearly transparent materials become strongly absorbing (Sect. 13.6). Thus, by focusing the laser light to the rear side of the substrate and/or into the ambient medium, different types

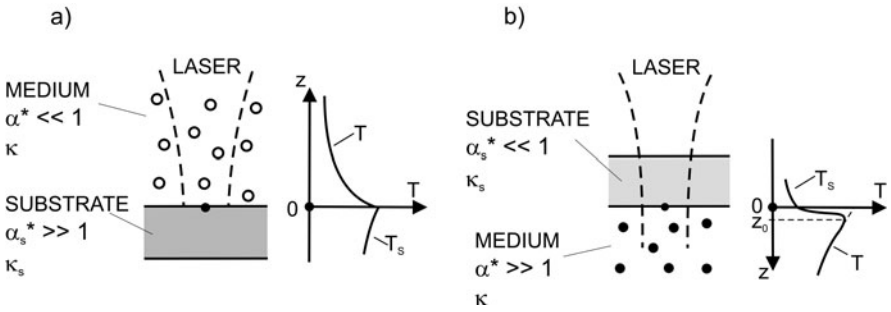

Fig. 9.5.1 a, b Influence of an ambient medium on the substrate temperature, T_s. The quantity $\alpha^* = \alpha w_0$ is the normalized absorption coefficient, and κ the thermal conductivity. (**a**) Non-absorbing ambient medium, strongly absorbing substrate. (**b**) Non-absorbing substrate, strongly absorbing ambient medium [*Bäuerle* 1996]

of thermally- and/or non-thermally- (photochemically) induced processes can take place. This permits almost all types of laser processing discussed throughout this book.

In the following, we shall discuss the situation shown in Fig. 9.5.1a only. To estimate the change in laser-induced surface temperature caused by the ambient medium, a number of simplifying assumptions are made: The laser beam shall be fixed, of Gaussian shape, and exclusively absorbed on the substrate surface, i.e., $\alpha = 0$ and $\alpha_s \to \infty$. In the absence of convection, the boundary-value problem can be formulated as described in Sect. 6.1. The heat equation can be written in the form

$$\frac{1}{D}\frac{\partial T}{\partial t} - \nabla^2 T = 0 \; . \tag{9.5.1}$$

The region $z \leq 0$ refers to the substrate with temperature T_s and thermal diffusivity $D \equiv D_s$, while $z > 0$ refers to the ambient medium with temperature T and diffusivity D. The boundary conditions are as follows:

- The balance of energy fluxes at the interface $z = 0$,

$$\kappa \left.\frac{\partial T}{\partial z}\right|_{z=0} = \kappa_s \left.\frac{\partial T_s}{\partial z}\right|_{z=0} - I_a(r) \; . \tag{9.5.2}$$

  For a Gaussian laser beam $I_a(r) = I(0)(1 - R)\exp(-r^2/w_0^2)$.
- The continuity of temperatures at $z = 0$,

$$T(r, 0, t) = T_s(r, 0, t) \; . \tag{9.5.3}$$

- The temperature rise at infinity shall vanish,

$$T(r \to \infty, z \to \infty, t) = T_s(r \to \infty, z \to -\infty, t) = T(\infty) \; . \tag{9.5.4}$$

With steady-state conditions we obtain the same solution as in (7.2.4), except that the center-temperature rise on the substrate surface, $\theta_c = \Delta T_c \equiv \Delta T_s(0, 0)$, is now

$$\theta_c = \Delta T_c = \frac{P(1 - R)}{2\sqrt{\pi}\, w_0 \kappa_s} \left(1 + \frac{\kappa}{\kappa_s}\right)^{-1} \; . \tag{9.5.5}$$

The physical reason for the additional term κ/κ_s can easily be understood. With stationary conditions, the heat flux from the surface is simply shared between the ambient medium and the substrate as $J : J_s = \kappa I_a/(\kappa + \kappa_s) : \kappa_s I_a/(\kappa + \kappa_s) = \kappa : \kappa_s$. Note that (9.5.5) is the same as (7.1.4) if $\kappa/\kappa_s \ll 1$. This is certainly a good approximation with gases at low to medium pressures. Thus, in the absence of convection, the temperature rise induced on a semi-infinite substrate changes only little in the presence of a gaseous atmosphere.

If convection becomes important, (9.5.5) cannot strictly be applied. This is the case with gases of medium to high pressures and with liquids and 'long' laser pulses (Sect. 9.5.3). In general, the substrate temperature will be decreased by convection.

Some further comments seem to be appropriate: In Sect. 6.1 we introduced the surface conductance, η. This permits one to describe, phenomenologically, the influence of an ambient medium on the substrate temperature by solving the (single) heat equation for the substrate. If we consider energy transport by heat conduction only, a simple consideration of the energy flux yields $\eta \approx \kappa/w_0$. This can be proved by comparing (9.5.5) and (7.1.3). The second term in the parenthesis of (7.1.3) is of the order of $\eta^* = \eta w_0/\kappa_s$. Thus, if $\kappa/\kappa_s \ll 1$, (9.5.5) and (7.1.3) yield the same result if $\eta = \kappa/w_0$. It should be noted, however, that (7.1.3) also permits one to estimate the influence of convection, if the appropriate form of η is known (Sect. 6.1).

9.5.2 Indirect Heating

For *cylindrical* symmetry the stationary temperature field induced within a *non-absorbing* ambient medium due to heat transport from the laser heated solid surface, $T(r, z)$, can be approximated by (3.5.6), where ΔT_c is now given by (9.5.5).

For *spherical* symmetry (Fig. 3.4.1) the temperature distribution is, in the simplest approximation,

$$T(r) = T(\infty) + \Delta T_s \frac{r_D}{r} \,. \tag{9.5.6}$$

If the temperature dependence of κ is taken into account [see (3.3.22)], we obtain instead

$$T^*(r^*) = \left[1 + (T_s^{*m+1} - 1)\frac{1}{r^*}\right]^{1/(m+1)} \,, \tag{9.5.7}$$

with $T_s^* = T_s/T(\infty)$ and $r^* = r/r_D$. Equation (9.5.7) can directly be derived from the heat equation by employing a Kirchhoff transform. $T^*(r^*)$ is shown in Fig. 9.5.2 for different values of m. Clearly, the temperature distribution depends on the surface temperature, T_s, and it becomes flatter with increasing exponent m. With the approximations made, (9.5.7) describes temperature distributions in gases *and* liquids.

9.5.3 Free Convection

Consideration of convection is certainly essential if we are dealing with gases at medium to high pressures or with liquids. Free convection is described by the set of (coupled) equations mentioned in the beginning of Sect. 3.3. It is evident that the overall problem can be solved only numerically and for each particular system

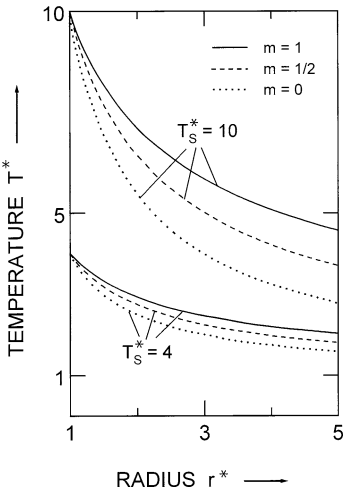

Fig. 9.5.2 Temperature distribution within a gaseous or liquid ambient medium, $T^*(r^*)$, for various temperature dependences of the thermal conductivity, $\kappa(T)$. Calculations have been performed for two surface temperatures, $T_s^* = T^*(1)$

(geometry, medium, etc.) only. For this reason, approximate solutions and even crude estimations are often quite useful. For example, the influence of free and forced convection on the substrate temperature can be estimated for many solutions given in Chaps. 7, 8 and 9 if we approximate η by (6.1.8) and (6.1.9), respectively.

The temperature within the ambient medium can be described by the (simplified) heat equation

$$\varrho c_p \frac{\partial T}{\partial t} - \nabla[\kappa(T)\nabla T] + \varrho c_p v_c \nabla T = 0 \,, \tag{9.5.8}$$

where the third term describes heat transport by convection.

The velocity of the convective flow, v_c, can be described by [*Landau* and *Lifshitz*: Fluid Mechanics 1974]

$$v_c \approx \frac{\nu_k}{l} \boldsymbol{f}\left(\frac{\boldsymbol{x}}{l}, \mathscr{P}_r, \mathscr{G}_r\right) \,, \tag{9.5.9}$$

where ν_k (cm^2/s) is the kinematic viscosity and l a characteristic length which has the dimension of the hot zone. Depending on the particular problem under consideration, l is given by the size of the laser focus, the size of the laser-processed structure, etc. For spherical symmetry $l \approx r_D T_c / T(\infty)$ (Fig. 3.4.1). The Prandtl number $\mathscr{P}_r = \nu_k / D$ describes the properties of the medium where $D = \kappa / \varrho c_p$.

Free convection is often characterized by the (dimensionless) Grashof number

$$\mathscr{G}_r = g\beta_T l^3 \frac{\Delta T}{\nu_k^2} \,, \tag{9.5.10}$$

where g is the acceleration due to gravity, β_T the coefficient of thermal expansion of the gas or liquid, and ΔT the temperature difference. For ideal gases with constant pressure

$$\beta_\mathrm{T} = -\frac{1}{\varrho}\left.\frac{\partial \varrho}{\partial T}\right|_p = \frac{1}{T} \propto \varrho \ , \tag{9.5.11}$$

where ϱ is the (mass) density of the gas. If $\mathscr{G}_r \to 0$, the function $\boldsymbol{f}$ in (9.5.9) tends to zero.

Instead of the Grashof number one often introduces the Rayleigh number

$$\mathscr{R}_a = g\beta_\mathrm{T} l^3 \frac{\Delta T}{D\nu_\mathrm{k}} = \mathscr{G}_r \times \mathscr{P}_r \ . \tag{9.5.12}$$

Note the strong dependence of $\mathscr{G}_r$ and $\mathscr{R}_a$ on the characteristic length, l. The viscosity of gases is about equal to the thermal diffusivity, $\nu_\mathrm{k} \approx D$, and inversely proportional to the total pressure, $\nu_\mathrm{k} \propto 1/p$, so that $\mathscr{R}_a \approx \mathscr{G}_r$.

At $T \approx 300\,\mathrm{K}$, typical values of the kinematic viscosity are $\nu_\mathrm{k} \approx 0.15\,\mathrm{cm}^2/\mathrm{s}$ for air, and $\nu_\mathrm{k} \approx 0.01\,\mathrm{cm}^2/\mathrm{s}$ for water. The Prandtl number is about 0.73 for air, 6.75 for water, 7250 for glycerol, and 0.044 for Hg.

The heat flux into the medium is often described by

$$J_\mathrm{c} = \kappa \frac{\Delta T}{l} \mathscr{N}(\mathscr{G}_r, \mathscr{P}_r) = \eta \Delta T \ , \tag{9.5.13}$$

where $\mathscr{N}$ is the Nusselt number. For $\mathscr{N} = 1$, heat transport takes place by conduction only. The function $\boldsymbol{f}$ in (9.5.9) and $\mathscr{N}$ depend on the geometry of the problem. η is the surface conductance introduced in Sect. 6.1 and $\Delta T = T_\mathrm{s} - T(\infty)$. By comparing single terms in (9.5.8) the influence of heat transfer caused by convection and conduction can be estimated from $v_\mathrm{c}^* = \varrho c_\mathrm{p} v_\mathrm{c} T l^{-1} / l^{-1} \kappa T l^{-1} = v_\mathrm{c} l / D$, where we have used $\nabla T \approx T/l$.

With *stationary* conditions and $-\nabla T \parallel \boldsymbol{g}$, heat transport by convection can be ignored as long as the Rayleigh (Grashof) number stays below a critical value, $\mathscr{R}_a < \mathscr{R}_a^\mathrm{cr} \approx 10^3$.

If, however, ∇T has a component $\perp \boldsymbol{g}$, the liquid is unstable and convection starts with all $\mathscr{R}_a > 0$. For the stationary case, v_c can be estimated from the balance between buoyancy and (Stokes) friction forces within the liquid

$$\Delta\varrho l^3 g \approx \varrho l^2 \nu_\mathrm{k} \frac{v_\mathrm{c}}{l} \ .$$

With (9.5.11) and (9.5.12), this yields

$$v_\mathrm{c}^* = \frac{v_\mathrm{c} l}{D} = \frac{g\beta_\mathrm{T} l^3 \Delta T}{D\nu_\mathrm{k}} = \mathscr{R}_a \ . \tag{9.5.14}$$

These estimations show that the influence of convection becomes significant with Rayleigh numbers $\mathscr{R}_a > 1$.

For *transient* laser heating, free convection becomes effective only with longer illumination times. The time constant involved can be estimated as follows: If we ignore viscosity, the acceleration in the initial phase of heating is

$$\frac{\mathrm{d}v_\mathrm{c}}{\mathrm{d}t} \approx \frac{\Delta\varrho}{\varrho} g = \beta_\mathrm{T} g \Delta T \ .$$

For a pulse length τ_ℓ this yields

$$v_\mathrm{c} \approx \beta_\mathrm{T} g \Delta T \tau_\ell \ . \tag{9.5.15}$$

The influence of free convection on the temperature distribution can be ignored if $v_\mathrm{c}^* \ll 1$. This is fulfilled for low laser pulse repetition rates and pulse lengths $\tau_\ell \ll D/\beta_\mathrm{T} g l \Delta T = l^2/\nu_\mathrm{k}\mathscr{R}_a$. Note that in liquids the influence of convection on mass transport (Sect. 3.4.2) may become effective earlier because $D_\mathrm{AB} \ll D$.

A convective flow can be laminar or turbulent. Turbulence is observed with Grashof numbers, typically, $\mathscr{G}_r > 5 \times 10^4$. The influence of convection on the temperature distribution is sometimes estimated by substituting κ and D by other phenomenological parameters, κ' and D', that contain – besides κ and D – convective terms κ_c and D_c respectively [*Levich* 1962].

The effect of convection in LCP can often be diminished by changes in the irradiation geometry or in the geometry of the reaction chamber. Estimations of temperature and velocity profiles near heated spots and lines and near heated cylinders [*Kuehn* and *Goldstein* 1980] have been performed. Temperature profiles near heated wires immersed in various gaseous atmospheres have been measured with high spatial resolution by employing Raman spectroscopy [*Leyendecker* et al. 1983a]. From these results we conclude that in laser microchemical gas-phase processing at low to medium pressures the effect of free convection is small or negligible.

9.5.4 Temperature Jump

If the mean free path of molecules, λ_m, becomes comparable to or larger than the size of the heated zone, r_D, a discontinuity (jump) in temperature at the interface between the laser-processed zone and the ambient medium occurs. Let us consider this in further detail for spherical symmetry (Fig. 3.4.1). If $\lambda_\mathrm{m} \ll r_\mathrm{D}$, we can ignore any temperature jump. If, however, $\lambda_\mathrm{m} \geq r_\mathrm{D}$, the temperature at the laser-heated surface, $T_\mathrm{s}(r_\mathrm{D})$, is *not* equal to the temperature of the gas at this surface, $T_\mathrm{g}(r_\mathrm{D})$, but given by [*Smoluchowski* 1911]

$$T_\mathrm{s}(r_\mathrm{D}) = T_\mathrm{g}(r_\mathrm{D}) - g_\mathrm{T} \left.\frac{\partial T_\mathrm{g}}{\partial r}\right|_{r_\mathrm{D}} \ , \tag{9.5.16}$$

where g_T is the temperature-discontinuity coefficient, which is inversely proportional to the gas pressure and thus directly proportional to the mean free path,

$$g_T = \beta\lambda_m \propto \frac{1}{p} . \tag{9.5.17}$$

Here, β is a factor of the order of unity which depends on the accomodation coefficient [*Landau* and *Lifshitz*: Physical Kinetics 1974]. For rigid spheres, the mean free path can be described by

$$\lambda_m \approx \frac{1}{\sqrt{2}\sigma N} \propto \frac{1}{p} , \tag{9.5.18}$$

where σ is the scattering cross section and N the number of gas molecules per volume, i.e., $N = p/k_B T$. For a two-component system consisting of molecules AB and M, the simplest approximation is $\sigma \approx \pi(r_{AB} + r_M)^2 \approx 4\pi r_{eff}^2$. Figure 9.5.3 shows λ_m as a function of temperature for various gas pressures and $r_{eff} = 2.5$ Å. At low to medium pressures, λ_m becomes comparable to or larger than the typical dimensions of structures produced in laser microprocessing. In such cases, the temperature jump at the gas–solid interface cannot be ignored. For temperature-independent thermal conductivity, the temperature distribution within the gas phase is then given by

$$T_g(r) = \frac{T_s(r_D) - T(\infty)}{1 + g_T/r_D} \frac{r_D}{r} + T(\infty) . \tag{9.5.19}$$

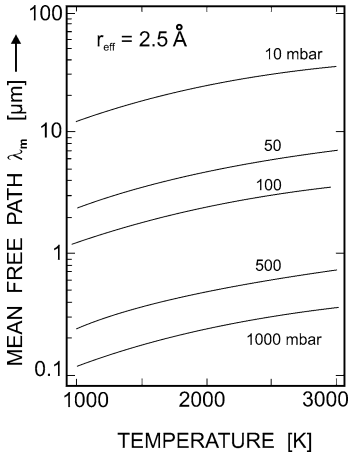

Fig. 9.5.3 Mean free path of gas molecules as a function of gas-phase temperature for various pressures. The model of rigid spheres with an effective radius $r_{eff} = 2.5$ Å has been used

Depending on the ratio g_T/r_D, the temperature jump can significantly modify the gas-phase temperature. This has been proved experimentally for micron-sized W spheres in H_2 atmospheres of different pressures by using Raman scattering spectroscopy [*Kullmer* 1996]. Its effect on the temperature distribution within the *substrate* can be ignored, in general. The heat flux from the solid surface to the gas is given by

$$J = \kappa_g \frac{T_s(r_D) - T(\infty)}{r_D + g_T} \,. \tag{9.5.20}$$

Thus, at a constant surface temperature, T_s, and radius, r_D, the heat flux decreases with decreasing gas pressure.

Chapter 10
Surface Melting

Surface melting, also termed as *heterogeneous* melting, is involved in many types of *conventional* and *chemical* laser processing. Among the examples are surface homogenization, planarization, microstructure refinement, glass formation, sealing of porous materials, alloying, some types of surface hardening, laser sintering, surface cladding, many types of engraving and marking, laser bending, laser welding, abrasive laser machining, some types of laser-chemical etching and deposition, and most types of laser doping and synthesis.

With all kinds of laser-induced surface modifications that involve the diffusion of species or the mixing of material components, the processing rates are increased by several orders of magnitude when the surface melts. Sometimes, there are problems in achieving surface melting in a well-defined way. This originates mainly from temperature-dependent changes in the surface morphology and physical properties, and from various kinds of feedbacks. For many systems, the region of laser parameters that can be employed for controlled melting without significant surface damage is small. Surface warping and cracks resulting from mechanical stresses are frequently observed.

Clearly, material melting is a prerequisite in laser welding. The amount of energy required in abrasive laser machining such as drilling, cutting, and shaping is considerably smaller if the process is based on mainly liquid-phase expulsion instead of mainly vaporization. It should be noted that with ultrashort laser pulses *homogeneous* melting, i.e. homogeneous nucleation of liquid inclusions within superheated (metastable) bulk materials plays an essential or even dominating role [*Ivanov* and *Zhigilei* 2007]. However, there are still many open questions. With intensities, typically in excess of $10^{12}\,\mathrm{W/cm^2}$ and pulse lengths $\tau_\ell \lesssim 100$ fs, non-thermal (cold) melting, in particular in tetrahedrally bonded semiconductors, has been observed. These phenomena are discussed in Chap. 13.

In the following, we shall present simple models for *heterogeneous* melting and process optimization. Here, we consider mainly laser-beam intensities that do *not* cause significant vaporization.

D. Bäuerle, *Laser Processing and Chemistry,* 4th ed.,
DOI 10.1007/978-3-642-17613-5_10, © Springer-Verlag Berlin Heidelberg 2011

10.1 Temperature Distributions, Interface Velocities

Let us consider a semi-infinite substrate that is *uniformly* irradiated by a *single* rectangular laser pulse of duration τ_ℓ (Fig. 10.1.1). Material evaporation shall be ignored.

The temporal behavior of the surface temperature, $T_s \equiv T(z = 0)$, is schematically shown in Fig. 10.1.2. T_s reaches the (equilibrium) melting point, T_m, within a time $\tau_m(0)$. Subsequently, T_s increases much slower or not at all, as the absorbed laser-light energy is spent not only on heating, but also on melting, which requires enthalpy ΔH_m. After a time $\tau_m(h_l)$ the surface is molten to a depth h_l. T_s increases further when the melt front matches the heat front. The maximum in T_s is reached at τ_ℓ. For times $t > \tau_\ell$, the system cools and resolidifies within a time τ_s. In many types of laser material processing, the heating and cooling cycles are so short that, except with metals, overheating of the solid phase and undercooling of the liquid phase is significant (dotted curves). Clearly, the exact temporal behavior of T_s depends on the material under consideration, on the intensity, duration and shape of the laser pulse, on convective flows and, if relevant, on the type of the ambient medium. For example, with laser-induced melting of metals within an oxidizing atmosphere, the maximum in T_s is shifted to times $t > \tau_\ell$ due to the release in exothermal energy. In

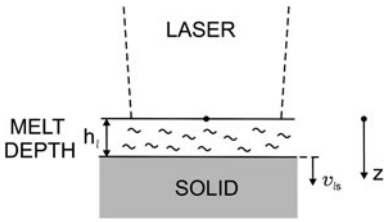

Fig. 10.1.1 Large-area laser-induced surface melting. The melt depth is denoted by h_l and the velocity of the liquid–solid interface by v_{ls}

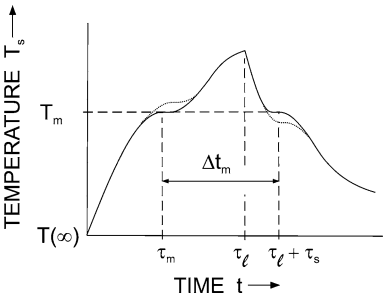

Fig. 10.1.2 Temporal dependence of the surface temperature induced by a single rectangular laser pulse of duration τ_ℓ. τ_m is the time required to reach the melting temperature, T_m. τ_s is the time of resolidification

many applications the time during which the surface is molten, Δt_m, is of particular interest. This time depends on τ_m and thereby on the melt depth required in the process.

The solution of the general problem, i.e., the calculation of the total spatial and temporal behavior of the temperature distribution within the liquid and the solid material can be obtained only numerically. Here, one can solve the heat equation in the form (2.2.9) for the solid and liquid phase and include the heat of melting into the boundary condition for the moving interface. Alternatively, one can solve the (single) heat equation (2.2.14) for the whole temperature region and include the heat of melting in $c_\mathrm{p}(T)$. For $T = T_\mathrm{m}$, one can set $c_\mathrm{p} = \Delta H_\mathrm{m}\delta(T - T_\mathrm{m})$. In numerical calculations the δ function is often approximated by a Gaussian profile.

Analytical solutions of the melting problem are possible only in a very few cases, as, for example, with uniform surface heating and special boundary conditions [*Carslaw* and *Jaeger* 1988; *Crank* 1988]. For this reason, crude estimations of the time, τ_m, the threshold intensity for surface melting, I_th, and the melt depth, h_l, are often quite useful. In a simple way, these quantities can be estimated from the solutions presented in Chaps. 7 and 8. For example, if for the laser-induced temperature rise we set

$$\Delta T(\boldsymbol{x}) = T_\mathrm{m} - T(\infty) \;, \tag{10.1.1}$$

we obtain for $\boldsymbol{x} = 0$ the intensity I_th. The time $\tau_\mathrm{m}(h_l)$ can be estimated in a similar way.

The Time $\tau_\mathrm{m}(h_l)$

For large-area irradiation and finite absorption with $l_\alpha \gg l_\mathrm{T}$ we find from (7.5.6)

$$\tau_\mathrm{m} \equiv \tau_\mathrm{m}(0) \approx \frac{\theta_\mathrm{m}\kappa_\mathrm{s} l_\alpha}{D I_\mathrm{a}} \;, \tag{10.1.2a}$$

with $\theta_\mathrm{m} = T_\mathrm{m} - T(\infty)$. The time $\tau_\mathrm{m}(h_l)$ required to melt a layer of thickness $h_l = l_\alpha$ can be obtained by substituting T_m with $T_\mathrm{m}^\mathrm{eff} = T_\mathrm{m} + \Delta H_\mathrm{m}/c_\mathrm{p}$.

For the case of surface absorption, i.e., with $l_\alpha \ll l_\mathrm{T}$, we obtain from (7.5.3)

$$\tau_\mathrm{m} \equiv \tau_\mathrm{m}(0) \approx \frac{1}{D}\left(\frac{\theta_\mathrm{m}\kappa_\mathrm{s}}{I_\mathrm{a}}\right)^2 \;. \tag{10.1.2b}$$

For $h_l = l_\mathrm{T} = 2(D\tau_\mathrm{m})^{1/2}$, the time $\tau_\mathrm{m}(h_l)$ can again be estimated by substituting θ_m with $\theta_\mathrm{m}^\mathrm{eff}$.

Maximum Melt Depth

For fluences around the melting threshold, i.e., with $\phi \gg \phi_{\mathrm{th}} = I_{\mathrm{th}}\tau_\ell \equiv \phi_{\mathrm{m}}$, the maximum melt depth near T_{m} can be estimated in analogy. Here, the liquid–solid interface is considered as an isotherm which can be calculated from (10.1.1) by substituting T_{m} with $T_{\mathrm{m}}^{\mathrm{eff}}$.

Let us assume large-area irradiation (Fig. 10.1.1) and surface absorption. The solution (7.5.8) yields for fluences near the melting threshold $\phi \approx \phi_{\mathrm{m}}$ the approximate relation

$$h_l^{\max} \approx \frac{l_{\mathrm{T}}}{\sqrt{\pi}} \frac{\phi - \phi_{\mathrm{m}}}{\phi_{\mathrm{m}}} , \tag{10.1.3a}$$

where ϕ_{m} is the fluence necessary for surface melting,

$$\phi_{\mathrm{m}} = \frac{\sqrt{\pi}}{2} \kappa_{\mathrm{s}} \theta_{\mathrm{m}} \left(\frac{\tau_\ell}{D}\right)^{1/2} .$$

For somewhat higher fluences, $\phi > \phi_{\mathrm{m}}$, we can approximate (7.5.8) by

$$\Delta T(h_l^{\max}, \tau_\ell) = \Delta T_{\max} \exp\left(-\frac{h_l^{\max 2}}{l_{\mathrm{T}}^2}\right) = T_{\mathrm{m}}^{\mathrm{eff}} - T(\infty) ,$$

where $\Delta T_{\max} = I_{\mathrm{a}} l_{\mathrm{T}} / \sqrt{\pi}\kappa_{\mathrm{s}}$ and $l_{\mathrm{T}} = 2(D\tau_\ell)^{1/2}$. With $\Delta T \propto \phi$, this yields for $\phi \geq \phi_{\mathrm{m}}$

$$h_l^{\max} \approx l_{\mathrm{T}} \left[\ln\left(\frac{\phi}{\phi_{\mathrm{m}}}\right)\right]^{1/2} \approx l_{\mathrm{T}} \left(\frac{\phi - \phi_{\mathrm{m}}}{\phi_{\mathrm{m}}}\right)^{1/2} . \tag{10.1.3b}$$

For $\phi < \phi_{\mathrm{m}}$ we obtain $h_l^{\max} = 0$. The latter approximation in (10.1.3b) is obtained for $\phi - \phi_{\mathrm{m}} \ll \phi_{\mathrm{m}}$.

It should be emphasized that such a description of the non-linear melting problem by linear solutions is a crude approximation only.

For fluences well above the melting threshold, i.e., with $\phi > \phi_{\mathrm{m}}$, the simplest estimation of the maximum melt depth is based on the *energy balance*

$$h_l^{\max} \approx \frac{P(1-R) - P_{\mathrm{L}}}{F\varrho\Delta H}\tau_\ell \leq \frac{I_{\mathrm{a}}}{\varrho\Delta H}\tau_\ell \leq \frac{\phi_{\mathrm{a}}}{\varrho\Delta H} . \tag{10.1.3c}$$

R is the reflectivity and F the area of the molten surface. ΔH is the total enthalpy, i.e., $\Delta H = \Delta H_{\mathrm{m}} + c_{\mathrm{p}}[T_{\mathrm{m}} - T(\infty)]$. P_{L} describes the energy loss by heat conduction and thermal radiation. The latter relation refers to very short high-intensity laser pulses, where P_{L} can often be ignored.

Both regimes, $h_l^{\max} \propto (\phi - \phi_{\mathrm{m}})^n$ with $n \leq 1$ and $h_l^{\max} \propto \phi$, have been verified in various experiments and with different materials. Figure 10.1.3 shows experimental

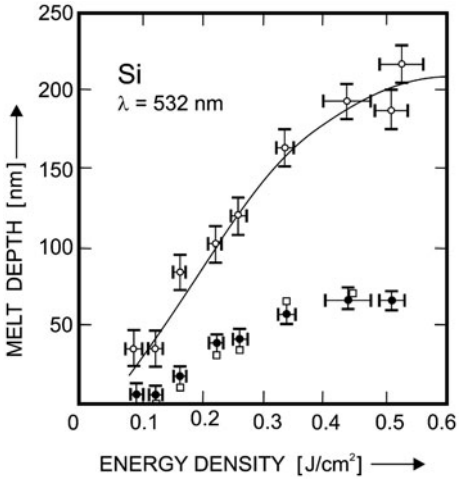

Fig. 10.1.3 Maximum melt depth in (100)Si as a function of Nd:YAG-laser fluence ($\lambda = 532\,\text{nm}$, $\tau_\ell = 7.5\,\text{ns}$). The data (*open circles*) were derived from concentration profiles of Cu^+ ions implanted into the surface. A calculated curve is also shown (*solid curve*). The position of the buried Cu peak derived from RBS (*solid circles*) and reflectivity measurements (*open squares*) is given. This peak indicates the position where solidification fronts starting from the liquid–solid interface and from the surface collide (see also Sect. 10.2) [*Bruines* et al. 1986]

data for Si. The linear regime (open circles) is clearly visible. The accuracy of data for fluences $\phi \approx \phi_\text{m}$ is not good enough to derive any functional dependence.

10.1.1 Boundary Conditions

In the following, we discuss different types of boundary conditions employed to solve the heat equation.

The Stefan Problem

Within the frame of the Stefan problem, it is assumed that the temperature at the liquid–solid interface, $z = h_l(t)$, is continuous and equal to the melting temperature,

$$T(z = h_l(t)) \equiv T_l(h_l) = T_\text{s}(h_l) = T_\text{m} \; . \tag{10.1.4}$$

The velocity of the liquid–solid interface, $v_{l\text{s}} = \dot{h}_l$, is described by

$$v_{l\text{s}}(t)\varrho\Delta H_\text{m} - \kappa_\text{s} \left.\frac{\partial T}{\partial z}\right|_{h_l} = J_{l\text{s}} \; . \tag{10.1.5}$$

Here, $\Delta H_\text{m}(\text{J/g})$ is the latent heat of melting. κ_s and κ_l are the thermal conductivities of the material in the solid and liquid phases, respectively. $J_{l\text{s}}$ is the energy flux from

the liquid to the interface $z = h_l$. If convection within the liquid is ignored, J_{ls} is given by

$$J_{ls} = -\kappa_l \left.\frac{\partial T}{\partial z}\right|_{h_l} .$$

Exact solutions of the Stefan problem can be found only in special cases; among those are the Neumann solutions.

In the presence of strong convective flows (Sect. 10.4) the temperature within the liquid is almost uniform, $T_l \approx T_m$ (note, however, that convection is only driven by temperature gradients). If we assume that the total energy absorbed at the liquid surface is (instantaneously) transported by convection to the interface, we can set $J_{ls} = I_a$. We then obtain

$$v_{ls}\varrho\Delta H_m - \kappa_s \left.\frac{\partial T}{\partial z}\right|_{h_l} = v_{ls}\varrho\{\Delta H_m + c_p[T_m - T(\infty)]\} = I_a ,$$

which yields

$$v_{ls} = \frac{I_a}{\varrho\Delta H} .$$

This solution is equal to (10.1.3c). The temperature distribution for this case is schematically shown in Fig. 10.1.4 by the solid curve.

If the laser light is absorbed at the liquid surface, and if we ignore convection, there is no analytical solution of the Stefan problem. In this case we have in addition to (10.1.4) and (10.1.5) the boundary condition

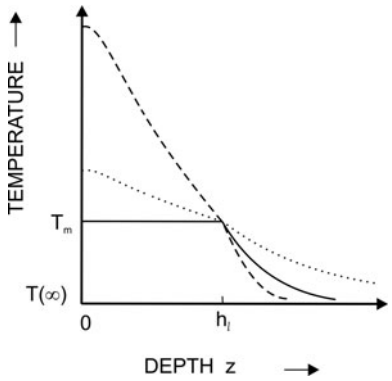

Fig. 10.1.4 Schematic picture of temperature distributions in laser surface melting. T_m is the melting temperature, z the distance from the surface, and h_l the melt depth. The temperature distribution in the presence of strong convection (*solid curve*), long laser pulses with $l_T \ll h_l$ (*dotted curve*), and short high-intensity laser pulses which cause strong overheating (*dashed curve*) are shown

$$-\kappa_l \left.\frac{\partial T}{\partial z}\right|_{z=0} = I_\mathrm{a} \ .$$

Qualitatively, the temperature distribution will be similar to that shown by the dashed and dotted curves in Fig. 10.1.4.

The Stefan model is often employed to describe melting and solidification in cases where the interface velocities are very small compared to the sound velocity, so that overheating (undercooling) at the liquid–solid interface can be ignored. From a physical point of view, this model is invalid, because it assumes that the phase transition takes place instantaneously.

In reality, the temperature at the liquid–solid interface, T_i, should exceed the equilibrium melting temperature, i.e., $T_\mathrm{i} > T_\mathrm{m}$ (overheating), while in the case of solidification we should have $T_\mathrm{i} < T_\mathrm{m}$ (undercooling).

Kinetic Model (Frenkel–Wilson Law)

For the case of melting (solidification) with 'moderate' overheating (undercooling) the velocity of the liquid–solid interface can be described by the difference in rate constants for melting, k_{sl}, and solidification, k_{ls}, i.e.,

$$v_{ls} = k_{sl} - k_{ls} \ . \tag{10.1.6}$$

Melting of a solid is a thermally activated process which can be described by

$$k_{sl} = k_{sl}^0 \exp\left(-\frac{\Delta E_{sl}^\mathrm{a}}{k_\mathrm{B} T_\mathrm{i}}\right) \ , \tag{10.1.7}$$

where k_{sl}^0 is a preexponential factor and ΔE_{sl}^a the activation energy per atom for melting. The situation is schematically shown in Fig. 10.1.5 for quasi-equilibrium conditions. In analogy, solidification can be described by

$$k_{ls} = k_{ls}^0 \exp\left(-\frac{\Delta E_{ls}^\mathrm{a}}{k_\mathrm{B} T_\mathrm{i}}\right) \ . \tag{10.1.8}$$

Clearly, the melting enthalpy per atom is given by $\Delta H_\mathrm{m}^\mathrm{a} = \Delta E_{sl}^\mathrm{a} - \Delta E_{ls}^\mathrm{a}$. Because $v_{ls} = 0$ at $T_\mathrm{i} = T_\mathrm{m}$, i.e., $k_{sl} = k_{ls}$, the velocity of the melt front can be described by

$$v_{ls} = v_0 \left[1 - \exp\left(-\frac{\Delta H_\mathrm{m}^\mathrm{a}}{k_\mathrm{B} T_\mathrm{m}} \frac{\Delta T_\mathrm{i}}{T_\mathrm{i}}\right)\right] \exp\left(-\frac{\Delta E_{sl}^\mathrm{a}}{k_\mathrm{B} T_\mathrm{i}}\right) \ . \tag{10.1.9}$$

Here, we have introduced the velocity $v_0 \equiv k_{sl}^0$ and $\Delta T_\mathrm{i} = T_\mathrm{i} - T_\mathrm{m}$. Equation (10.1.9) is often termed the Frenkel–Wilson law. It applies to heterogeneous melting which starts at the material surface. During solidification $T_\mathrm{i} < T_\mathrm{m}$, the velocity of the solid–liquid interface, v_{sl}, can be described by the same equation with $v_{sl} = -v_{ls}$ and the direction of the z-axis in Fig. 10.1.1 reversed. This law can be applied

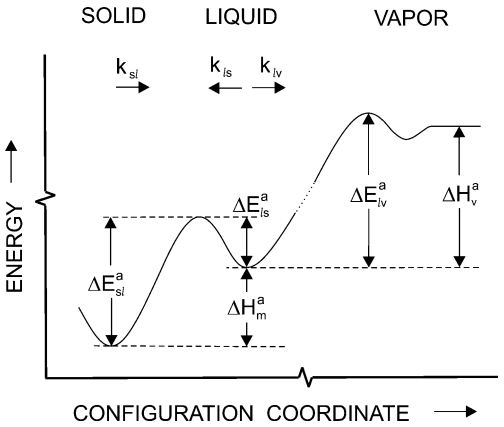

Fig. 10.1.5 Schematic picture to describe melting (solidification) and vaporization. $\Delta E^{\mathrm{a}}_{sl}$ and $\Delta E^{\mathrm{a}}_{ls}$ are the activation energies for melting and solidification; k_{sl} and k_{ls} are rate constants. The corresponding quantities for vaporization are included. $\Delta H^{\mathrm{a}}_{\mathrm{m}}$ and $\Delta H^{\mathrm{a}}_{\mathrm{v}}$ are the enthalpies (per atom/molecule) for melting and vaporization, respectively. The picture refers to a certain (fixed) temperature. Note that the values of ΔH_{m} and ΔH_{v} in Table IV refer to T_{m} and T_{b}, respectively

successfully to laser melting of semiconductors with interface velocities of 10^3–10^4 cm/s.

If the degree of overheating is small, we can expand (10.1.9) near $T_{\mathrm{i}} \approx T_{\mathrm{m}}$. This yields

$$v_{ls} \approx \tilde{v}_0 \frac{\Delta H^{\mathrm{a}}_{\mathrm{m}}}{k_{\mathrm{B}} T^2_{\mathrm{m}}} \Delta T_{\mathrm{i}} \approx \tilde{v}_0 \frac{c_{\mathrm{p}} \Delta T_{\mathrm{i}}}{3 \Delta H_{\mathrm{m}}\,(\mathrm{J/g})} \,. \tag{10.1.10}$$

This approximation can be employed with metals, where, typically, $\tilde{v}_0 \equiv k_{sl}(T_{\mathrm{m}}) \approx 10^4$ cm/s. The latter approximation is obtained with $\Delta H^{\mathrm{a}}_{\mathrm{m}}\,(\mathrm{J/atom}) = \Delta H_{\mathrm{m}}\,(\mathrm{J/g}) M/L \approx k_{\mathrm{B}} T_{\mathrm{m}}$ and $c_{\mathrm{p}} \approx 3 L k_{\mathrm{B}}/M$ (Dulong–Petit law), where M is the atomic weight per mol and L the Avogadro number. In analogy, (10.1.10) can also be applied to solidification.

Surface Melting of Si

We now discuss numerical calculations for the example of a Si wafer. Here, the heat equation (2.2.14) has been solved together with (10.1.9) and

$$\begin{aligned} &T_l(h_l) = T_{\mathrm{s}}(h_l) = T_{\mathrm{i}} \,, \\ &\left.\frac{\partial T}{\partial z}\right|_{z=0} = 0 \,, \quad T(h_{\mathrm{s}}, t) = T_0 \,, \quad T(z, 0) = T_0 \,. \end{aligned} \tag{10.1.11}$$

Figure 10.1.6 shows temperature distributions calculated for different times during and after 532 nm Nd:YAG-laser irradiation. The arrows indicate the position

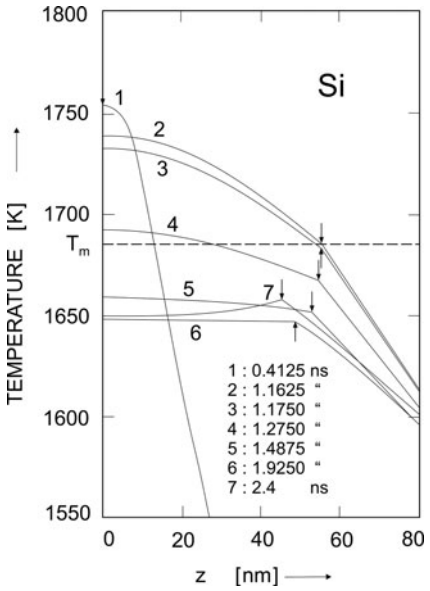

Fig. 10.1.6 Temporal development of temperature distribution during laser-induced surface melting and solidification of Si ($\lambda = 532\,\text{nm}$ Nd:YAG, $\phi = 0.3\,\text{J/cm}^2$, $\tau_\ell = 0.5\,\text{ns}$, $T_\text{m} = 1685\,\text{K}$, $\Delta H_\text{m} = 0.495\,\text{eV}$, $\Delta E_{sl} = 1.22\,\text{eV}$, $v_0 = 6\times10^5\,\text{m/s}$, and $T_0 = 150\,\text{K}$). Only a *single* liquid–solid interface (*arrows*) was taken into account [*Stock* et al. 1985]

of the liquid–solid interface. During the laser pulse, the solid surface is overheated (curve 1) and the heat front moves in the z-direction. The maximum melt depth is reached with $T_\text{i} = T_\text{m}$ where $v_{sl} = 0$. Subsequently, the liquid is undercooled due to the strong temperature gradient (curves 4–6). Due to solidification, the interface moves back towards the surface. The maximum in the temperature distribution that appears at the liquid–solid interface (curve 7) is related to the heat of crystallization. Note that this heat release takes place at $T_\text{i} \neq T_\text{m}$, where T_i depends on time. During solidification, the lowest temperature within the melt occurs at the surface. Thus, nucleation in the undercooled melt at the surface becomes quite likely. By this means, a second solidification front that starts from the surface may develop. This has been ignored in Fig. 10.1.6.

Strong Overheating, Localized Irradiation

If the degree of overheating (undercooling) is very high, i.e., if $c_\text{p}\Delta T_\text{i} \geq \Delta H_\text{m}$, the Frenkel–Wilson law cannot be applied, mainly because of homogeneous melting (solidification) within the bulk of the solid (liquid).

For high-intensity laser pulses and focused laser-beam irradiation, liquid-phase expulsion and vaporization become important. Here, the deformation of the surface (deep-penetration melting, formation of droplets, etc.) must be taken into account. New phenomena are observed with high-intensity ultrashort laser pulses (Chap. 13).

10.1.2 Temperature Dependence of Parameters

At the melting temperature, some of the material parameters that enter the calculations show discontinuities. Figure 10.1.7 shows the behavior of $\kappa(T)$ and $c_p(T)$ for the example of Si and Cu.

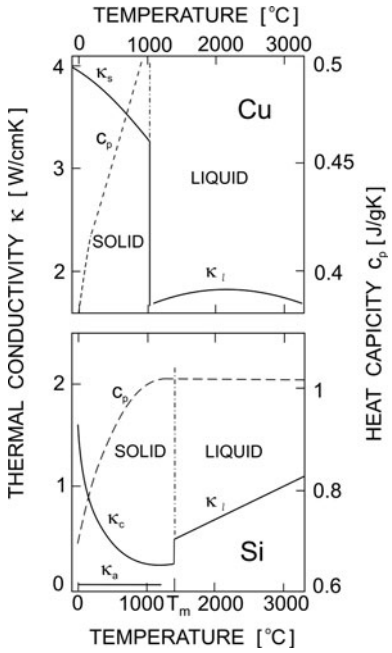

Fig. 10.1.7 Temperature dependence of the thermal conductivity, κ, and the specific heat, c_p. For Cu, κ_s and κ_l refer to the (crystalline) solid and the liquid phase. Adapted from [*Duley* 1976]. For Si, κ_c and κ_a denote thermal conductivities of crystalline and amorphous material. Adapted from [*Wood* and *Geist* 1986]

Experimental data on $\kappa(T)$, $D(T)$, and $c_p(T)$ are listed for a large number of materials in Table II.

The reflectivity of liquid metals is, in general, smaller than for solid metals, $R_l < R_s$. With many metals, one finds for the absorptivity $A_l(T_m) \approx 2A_s(T_m)$. For semiconductors, such as Ge and Si, the situation is opposite, i.e., $R_l > R_s$. The abrupt change in R at T_m, monitored by a probe beam, permits the direct measurement of Δt_m.

10.2 Solidification

For many applications it is a good approximation to consider materials processing only during the time Δt_m, when the surface is molten (Fig. 10.1.2). The estimation of this time is therefore very important. Precise calculations can be performed only

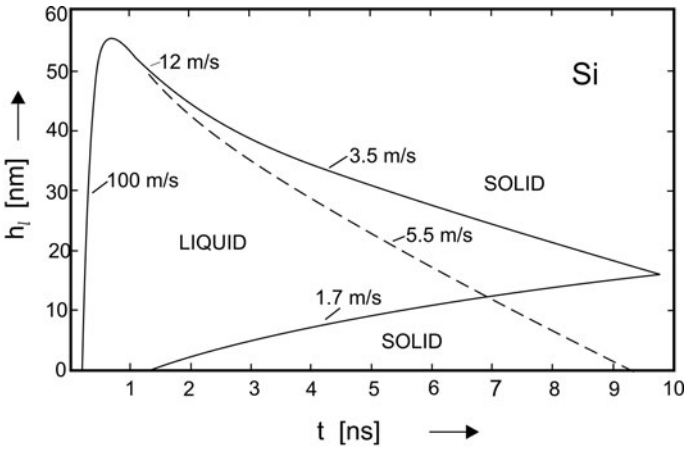

Fig. 10.2.1 Position of liquid–solid interfaces in Si versus time. Interface velocities (derivatives of curves) in different regions are indicated. For comparison, the path of one interface alone (*dashed curve*, no nucleation at the surface) is drawn. The parameters employed are the same as in Fig. 10.1.6 [*Stock* et al. 1985]

numerically by solving the correct boundary-value problem. Figure 10.2.1 shows the results of such calculations for the example of Si. Here, the same boundary conditions and parameters as in Fig. 10.1.6 have been employed. The maximum melt depth is reached after about 0.8 ns. Without surface nucleation, solidification occurs exclusively at the liquid–solid interface (dashed curve). The interface velocity (derivative in Fig. 10.2.1) is first very high and then slows down. If surface nucleation is taken into account (solid curves), a solidification front starts from the surface and both interfaces collide after about 10 ns at a depth of about 15 nm. While these details refer, of course, to the special system under consideration, the overall behavior shown in the figure is very typical for material solidification.

For Si, experimentally determined *solidification velocities* are of the order of 10 m/s; for metals, they are of the order of 10 to 10^3 m/s.

In the following, we will present a simple estimation of Δt_m. Consider a laser pulse that induces large-area surface melting. With the definitions given in Fig. 10.1.2, we find

$$\Delta t_\mathrm{m} \approx \tau_\ell - \tau_\mathrm{m} + \tau_\mathrm{s} \; . \tag{10.2.1}$$

The time τ_m has already been estimated in Sect. 10.1. For *high-intensity* laser pulses that are long in comparison to τ_m, the approximation $\Delta t_\mathrm{m} \approx \tau_\ell + \tau_\mathrm{s}$ can often be employed. Then, we have to estimate only τ_s.

For *slow* solidification (in Fig. 10.2.1 for $t > 2$ ns) we can employ the Stefan model. Let us introduce a new time scale, $t' = t - \tau$, where τ is defined by the maximum melt depth, $h_l(\tau) = h_l^\mathrm{max}$. For $t' > 0$, the thickness of the molten layer can then be described by

$$h_l(t') = h_l^{\max} - h(t') \; . \tag{10.2.2}$$

Solidification shall start at a time τ, when the liquid is at a (uniform) temperature, T_m. We assume that at this time the temperature distribution within the solid is characterized by the heat-diffusion length $l_\mathrm{T} \approx 2(D\tau)^{1/2}$, where $\tau \approx \tau_\ell$ and $T(z \to \infty) = T(\infty)$. The situation is described by the solid curve in Fig. 10.1.4. Solidification ($t' \geq 0$) can then be described by a special Neumann solution of the Stefan problem, where solidification starts at $t = 0$ at a depth $z' = h_l^{\max} + \zeta l_\mathrm{T}$, with $T_l(z \leq z') = T_\mathrm{m}$ and $T_\mathrm{s}(z \geq z') = T(\infty)$. For this case the solution is [*Carslaw* and *Jaeger* 1988]

$$h(t') = \zeta l_\mathrm{T} \left[\left(1 + \frac{4Dt'}{l_\mathrm{T}^2} \right)^{1/2} - 1 \right] , \tag{10.2.3}$$

where ζ is given by the solution of

$$\zeta \cdot [1 + \mathrm{erf}(\zeta)] \exp(\zeta^2) \equiv f(\zeta) = \frac{c_\mathrm{p} \theta_\mathrm{m}}{\pi^{1/2} \Delta H_\mathrm{m}} \; , \tag{10.2.4}$$

with $\theta_\mathrm{m} = T_\mathrm{m} - T(\infty)$. Physically reasonable values are within $0.25 < \zeta < 1$. From (10.2.3) the time of resolidification becomes

$$\tau_\mathrm{s} = \frac{h_l^{\max 2}}{4\zeta^2 D} \left(1 + \frac{2\zeta l_\mathrm{T}}{h_l^{\max}} \right) \; . \tag{10.2.5}$$

Because of the solidification front which starts from the surface, this time may be modified (Fig. 10.2.1). For fluences $\phi - \phi_\mathrm{m} \ll \phi_\mathrm{m}$ where $h_l^{\max}$ is very small, we obtain

$$\tau_\mathrm{s} \approx \frac{l_\mathrm{T} h_l^{\max}}{2\zeta D} \approx \frac{l_\mathrm{T}^2}{2\zeta D} \left(\frac{\phi - \phi_\mathrm{m}}{\phi_\mathrm{m}} \right)^{1/2} \; . \tag{10.2.6a}$$

The latter relation follows from (10.1.3b). Clearly, if we use (10.1.3a) instead, we obtain $\tau_\mathrm{s} \propto \phi - \phi_\mathrm{m}$. For high fluences $\phi > \phi_\mathrm{m}$ the melt depth $h_l^{\max}$ is large and the second term in the parentheses in (10.2.5) can be ignored, i.e.,

$$\tau_\mathrm{s} \approx \frac{h_l^{\max 2}}{4\zeta^2 D} \approx \frac{(1-R)^2}{4D} \left(\frac{\phi - \phi_\mathrm{m}}{\varrho \Delta H \zeta} \right)^2 \approx \frac{1}{4\zeta^2} \frac{\phi^2}{\phi_\mathrm{m}^2} \tau_\ell \; , \tag{10.2.6b}$$

where we have substituted $h_l^{\max}$ from (10.1.3c) with $\phi_\mathrm{a} = (1-R)(\phi - \phi_\mathrm{m})$. The latter approximation holds for $\phi_\mathrm{m} \ll \phi$.

The functional dependence of τ_s expected from (10.2.6) has in fact been observed experimentally. Figure 10.2.2 shows results for Q-switched Nd:Glass laser radiation and various semiconductor substrates. The inset shows the situation near the melting

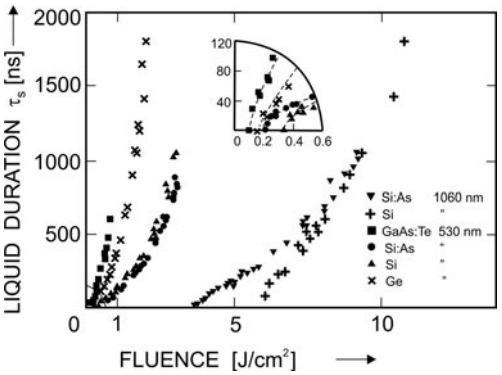

Fig. 10.2.2 Duration of the liquid phase at the surface of Si, Ge, and GaAs as a function of Nd:Glass laser fluence ($\tau_\ell \approx 40$ ns; $\lambda = 1{,}060$ and 530 nm) [*Auston* et al. 1979]

threshold, where, in fact, τ_s can be approximated by $\tau_s \propto (\phi - \phi_m)^n$ with $0.5 \leq n \leq 1$. For large fluences the measured data can be approximated well by the parabolic law. If we consider the data for Si and 530 nm radiation with $\phi = 3\,\mathrm{J/cm^2}$, we obtain from (10.2.6b) with $\zeta = 0.3$ a value of $\tau_s \approx 1{,}450$ ns. This value is in reasonable agreement with the experimental data.

The behavior of the solidification front velocity in the initial phase, i.e., immediately after the maximum melt depth has been reached, can qualitatively be understood from Fig. 10.1.4. For short laser pulses (dashed curve), the temperature gradient at $z = h_l$ is very large and the velocity v_{ls} will be very high. For long laser pulses (dotted curve) the temperature gradient is much smaller, and therefore so is v_{ls}. By differentiation of $h(t')$ in (10.2.3) we obtain for times $t' \approx 0$ the (maximum) velocity

$$v_{ls}(t' \approx 0) \approx \frac{2\zeta D}{l_T} \approx \zeta \left(\frac{D}{\tau_\ell}\right)^{1/2} . \tag{10.2.7}$$

Note, however, that for very short laser pulses temperature gradients within the liquid cannot be ignored.

10.3 Process Optimization

For many technical applications the optimization of the surface melting process with respect to the energy required is of interest. For a certain melt depth, the smallest energy consumption can be found by minimizing the integral

$$\int_0^{\tau_\ell} P(t')\,\mathrm{d}t' \;\rightarrow\; \text{minimum} . \tag{10.3.1}$$

This is achieved, to a good approximation, if the maximum melt depth required, is of the order of the heat-diffusion length. Thus, the condition to fulfill (10.3.1) is

$$h_l^{\max} \approx l_{\mathrm{T}} \approx 2(D\tau_\ell)^{1/2} \,. \tag{10.3.2}$$

Here, $h_l^{\max}$ is characterized by the effective melting temperature $T_{\mathrm{m}}^{\mathrm{eff}} = T_{\mathrm{m}} + \Delta H_{\mathrm{m}}/c_{\mathrm{p}}$. Convection may strongly modify this condition.

The situation can most easily be understood from Fig. 10.1.4: From an energetical point of view, the solid curve shows an almost optimal situation. The material is just molten up to the depth $h_l^{\max}$ and the heat front penetrates only slightly into the solid. Obviously, this idealized situation can never be achieved with realistic material parameters. For very long laser pulses with $l_{\mathrm{T}} \gg h_l^{\max}$, there is a considerable waste of energy because the solid material is heated to a very large depth (dotted curve). For very short high-intensity laser pulses additional energy is consumed due to strong overheating at the surface (dashed curve). Thus, (10.3.2) is quite plausible. From a practical point of view, overheating of the surface or deep penetration heating may be advantageous or disadvantageous. A crude estimation of the optimized laser-beam intensities is obtained from (10.1.3c) and (10.3.2)

$$I_{\mathrm{opt}} \approx \frac{2\varrho\Delta H}{1-R}\left(\frac{D}{\tau_\ell}\right)^{1/2} \,, \tag{10.3.3}$$

where $\Delta H \approx \Delta H_{\mathrm{m}} + c_{\mathrm{p}} T_{\mathrm{m}}$.

For *finite* absorption and heat losses at the surface, the temperature distribution (in the z-direction) is non-monotonic. Then, an estimation of the optimized laser-beam intensity becomes more complex.

10.4 Convection

Surface melting under the action of laser light may result in the excitation of convective fluxes within the liquid layer. Such convective fluxes play an important or even decisive role in material transport involved in many types of laser processing, such as in surface doping, surface alloying, etc.

With *uniform* laser-light irradiation and intensities that do not cause significant evaporation, convection may originate from changes in material density related to temperature gradients in the z-direction and from surface tension effects. In laser processing, the latter usually dominate, because the depth of the molten layer is smaller than the capillary length, i.e., $h_l < l_{\mathrm{c}} \approx (\sigma/g\varrho)^{1/2}$, where σ is the surface tension (for a volume element l_{c}^3, the gravitational force and surface tension forces balance if $g\varrho l_{\mathrm{c}}^3 \approx \sigma l_{\mathrm{c}}$). With strongly absorbing materials the highest temperature is reached at the surface and, as a consequence, Rayleigh–Benard and Marangoni (Pearson) instabilities will not develop. However, in such cases an instability due to parametric interactions between gravity-capillary waves and thermocapillary waves may become important [*Anisimov* and *Khokhlov* 1995]. Free

convection is characterized by the Rayleigh number, $\mathscr{R}_a$ [(9.5.12); here, l must be replaced by h_l], or, if surface-tension effects dominate, by the Marangoni number, $\mathscr{M} = |\mathrm{d}\sigma/\mathrm{d}T| \cdot h_l \Delta T/\varrho D \nu_\mathrm{k}$.

With *focused* laser light, convective fluxes driven by changes in the surface tension of the material become even more pronounced (Marangoni convection). If the changes in surface tension originate from gradients in the laser-induced temperature distribution along the surface, this phenomenon is also denoted as the thermocapillary effect. The direction of the convective fluxes depends on the sign of $\mathrm{d}\sigma/\mathrm{d}T$. Marangoni convections frequently result in surface deformations, as schematically shown in Fig. 10.4.1.

The r-component of the velocity of the convective flow, v_c, related to the thermocapillary effect can be estimated from (Fig. 10.4.1)

$$\eta \left.\frac{\partial v_\mathrm{c}}{\partial z}\right|_{z=h_l(r)} = \frac{\partial \sigma}{\partial r} = \frac{\mathrm{d}\sigma}{\mathrm{d}T}\frac{\partial T}{\partial r} \,, \tag{10.4.1}$$

and $v_\mathrm{c}(z=0) = 0$, which yields

$$v_\mathrm{c} \approx \frac{h_l \Delta T}{\eta w_\mathrm{T}} \frac{\mathrm{d}\sigma}{\mathrm{d}T} \,, \tag{10.4.2}$$

where ΔT is the temperature rise, w_T the width of the temperature distribution, and $\eta = \varrho \nu_\mathrm{k}$ the dynamic viscosity. Typical values of v_c are between 1 cm/s and some 10 cm/s. For high laser-light intensities, v_c exceeds some critical value and the 'laminar' convective flow loses its stability (Sect. 28.5).

The time for one convective cycle due to the thermocapillary effect can be estimated from $\tau_\mathrm{c} \approx w_\mathrm{T}/v_\mathrm{c}$ and $h_l = 2(D\tau_\mathrm{c})^{1/2}$. With (10.4.2), this yields

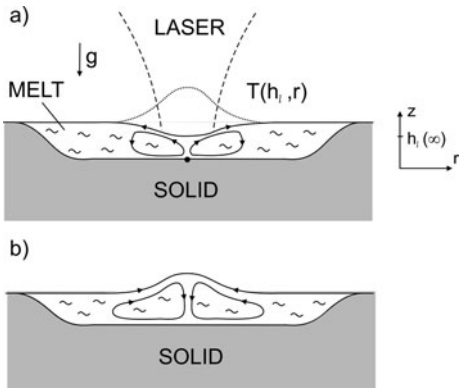

Fig. 10.4.1 a, b Convection due to localized melting. $h_l(\infty)$ is the melt depth away from the laser-irradiated zone and $\boldsymbol{g}$ the vector of gravity. The width of the molten layer is approximately given by the thermal width, w_T. (**a**) Surface tension decreases with increasing temperature, i.e., $\mathrm{d}\sigma/\mathrm{d}T < 0$. (**b**) $\mathrm{d}\sigma/\mathrm{d}T > 0$

$$\tau_c \approx \left(\frac{\eta w_T^2}{2D^{1/2}\Delta T} \frac{dT}{d\sigma} \right)^{2/3} . \tag{10.4.3}$$

Typical values of ΔT are 10^2–10^3 K. In a crude approximation we can set $d\sigma/dT \approx \sigma/T_{cr}$. For liquid metals, σ is of the order of 10^{-4} J/cm^2 and $\eta \approx 10^{-2}$ g/cm s. If we consider a situation similar to that shown in Fig. 10.4.1a with $w_T \approx 0.5$ cm, we find that typical values of τ_c are between 10^{-3} and 10^{-5} s. It is evident that convective mixing is relevant only if $\tau_c < t_d = N_\ell \tau_\ell$, where t_d is the laser beam dwell time and N_ℓ the number of laser pulses.

Another mechanism that excites convective flows is related to the recoil pressure due to laser-induced vaporization ($p_{rec} = p_{rec}(I)$; Sect. 11.3). Empirically, the time for one convective cycle can be estimated from (10.4.3) if we substitute $\Delta T \approx T_v$ and w_T by $w_s = w_s(I)$, which is a characteristic width of the surface perturbation that depends on the laser-light intensity. Typical values of τ_c are of the order of 10^{-6} s. The corresponding convection velocities are, typically, 10^2–10^3 cm/s. This mechanism is relevant to surface processing with μs CO_2 lasers.

Besides the instabilities already mentioned, other instabilities of the Rayleigh–Taylor or Kelvin–Helmholtz type (Sect. 28.5) can result in mixing times $\tau_c \leq 10^{-7}$ to 10^{-8} s. The typical velocities related to these instabilities are $v_c > 10^3$ cm/s.

10.5 Surface Deformations

In many cases, surface melting and convection result in surface deformations and in structural and chemical inhomogeneities of the resolidified material. The shape of the surface around the center of the laser beam is determined by the thermal expansion of the material and the surface tension of the liquid. If we assume the thickness of the molten layer to be small compared to the width of the laser focus, i.e., $h_l \ll 2w_0$, and ignore any temperature gradients in the z-direction, we can estimate the shape of the surface from the solution of the corresponding hydrodynamical problem [*Landau* and *Lifshitz*: Fluid Mechanics 1974]. In this approximation one obtains

$$h_l^2(r) \approx h_l^2(\infty) \left(\frac{\varrho(\infty)}{\varrho(r)} \right)^{3/4} + \frac{3}{g\varrho(r)} [\sigma(r) - \sigma(\infty)] , \tag{10.5.1}$$

where $h_l(\infty)$ is the thickness of the molten layer and $\varrho(\infty)$ the mass density for distances $r > w_0$. If we ignore thermal expansion, i.e., assume $\varrho(r) \approx \varrho(\infty)$, the thickness of the liquid layer within the beam center can be approximated by

$$h_l(0) \approx h_l(\infty) + \frac{3}{2\varrho(\infty) g h_l(\infty)} [T(0) - T(\infty)] \frac{d\sigma}{dT} , \tag{10.5.2}$$

where $T(0)$ is the center temperature (Fig. 10.4.1). For a rough estimation we can set $h_l(\infty) \approx l_T$, as before. The surface tension coefficient $\sigma(r) \equiv \sigma(T(r))$ decreases, in most cases, with increasing temperature as [*Hirschfelder* et al. 1964]

$$\sigma = \sigma_0 \left(1 - \frac{T}{T_{cr}}\right)^{\nu} , \tag{10.5.3}$$

where σ_0 is a constant, T_{cr} the critical temperature, and $\nu \approx 1$. With $d\sigma/dT < 0$, (10.5.2) directly yields $h_l(0) < h_l(\infty)$. This is schematically shown in Fig. 10.4.1a.

It should be noted, however, that as laser-light intensities generate significant material evaporation the recoil of particles leaving the surface can produce a deformation similar to that depicted in the figure.

The situation may be even more complex. For example, in some cases of surface alloying, a surface deformation as shown in Fig. 10.4.1b is observed. This type of deformation can be obtained only if the direction of the flow changes sign due to the concentration dependence of σ. Consider the alloying of A and S. The concentration of A in S depends on temperature, i.e., $N_A = N_A(T)$. Thus, for certain types of species we may have

$$\frac{d\sigma}{dT} = \frac{\partial\sigma}{\partial T} + \frac{\partial\sigma}{\partial N_A}\frac{\partial N_A}{\partial T} > 0 . \tag{10.5.4}$$

The previous remarks apply also to cases where the laser beam is scanned with velocities $v_s^* = v_s w_0/D \ll 1$ perpendicular to the plane of the paper in Fig. 10.4.1. Scanning of the laser beam changes the surface morphology mainly via the change in temperature distribution $\Delta T(v_s^*) = T(v_s^*) - T(v_s^* = 0)$ (Sect. 7.4). Changes in the hydrodynamics are of higher order in v_s^* and shall be ignored.

10.5.1 Surface Patterning

Laser-induced *local* heating and/or melting has been employed for micro-/nanopatterning of surfaces. Examples based on surface tension effects are microholes on PET [*Denk* et al. 2002], microbumps on BK7-glass [*Zahariev* et al. 2009], etc. It should be noted that the formation of microbumps observed on some types of polymers are of quite different origin. They are based on a *real* increase in local volume, mainly due to scission of polymer chains (Sect. 12.4).

A quite different mechanism is involved in the formation of cones/bumps on Si substrates. Figure 10.5.1a shows an array of such bumps generated by means of a regular lattice of a-SiO_2 microspheres placed on a quartz support (Fig. 5.2.1). In this case, cone formation is based on the anomalous behavior of the density of liquid and solid Si with $\rho_l(\text{Si}) > \rho_S(\text{c-Si})$ (Table II). Thus, local melting results in a local *decrease* in volume. Resolidification starts at the edge of the molten zone and proceeds towards the center. Due to the volume increase during solidification, the liquid Si is squeezed radially towards the center and forms a protrusion. As a

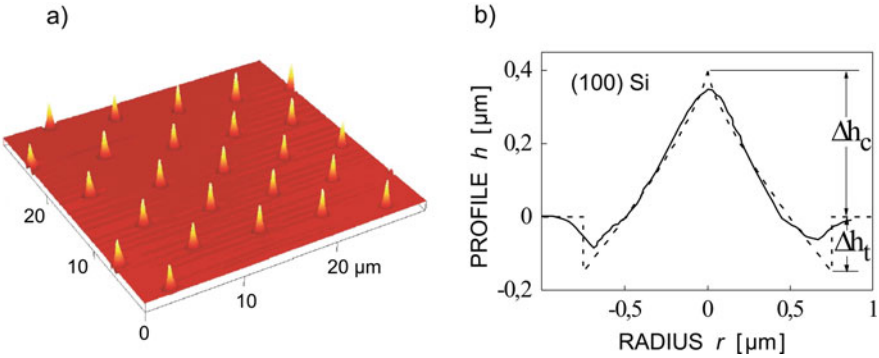

Fig. 10.5.1 (**a**) Silicon cones fabricated on a (100) Si surface by single KrF-laser pulses ($\phi = 250\,\mathrm{mJ/cm^2}$, $\tau_\ell = 28\,\mathrm{ns}$) using a regular lattice of SiO_2-microspheres ($d = 6\,\mu\mathrm{m}$) for focussing. The height of cones with respect to the original surface is $350 \pm 30\,\mathrm{nm}$. (**b**) The full curve shows an AFM profile of a silicon cone. The dashed curve was calculated from Eq. (10.5.5) using $h_l = 1.73\,\mu\mathrm{m}$ and $w_\mathrm{m} = 0.75\,\mu\mathrm{m}$ as fit parameters [*Wysocki* et al. 2003]

result, a solid cone surrounded by a ring-shaped trench is formed. In fact, the shape of features, $h = h(r)$, can be almost quantitatively explained by mass conservation only. This yields

$$h = h_l \left(1 - \frac{1}{\beta}\right)\left(\frac{r}{w_m}\right)^\beta + \frac{1}{\beta} h_l \tag{10.5.5}$$

with $\beta = 3\,\rho_\mathrm{S}/\rho_l - 2$. Figure 10.5.1b shows the good agreement between measured and calculated cone profiles. When taking into account heat diffusion and surface tension effects, the singularities at $r = 0$ and $r = w_\mathrm{m}$ are washed out.

The melt depth h_l can be estimated *independently* from the heat balance (10.1.3c). If we compare the energy focused by a microsphere of radius r_sp into the molten zone, w_m, we obtain $h_l \approx A\phi\, r_{sp}^2/w_m^2\, \rho_l(c_p \Delta T_m + \Delta H_m)$. With material parameters averaged between 300 K and ΔT_m (Table II), we obtain $h_l = 1.88\,\mu\mathrm{m}$. This value is in good agreement with the value derived from the fit in Fig. 10.5.1b.

10.6 Welding

Lasers are used as a high-speed and high-quality welding tool. They permit autogeneous welding (without filler) at atmospheric pressure with low porosity welding seams, little material distortions, fracturing, and contaminations. The good localization of the temperature profile (small extention of heat-affected zone [HAZ]) allows accurate and narrow welding even near temperature-sensitive material components. The lasers most commonly employed are cw CO_2 and Nd:YAG lasers. As with standard material welding, protection (shrouding) of the laser-processed zone, and

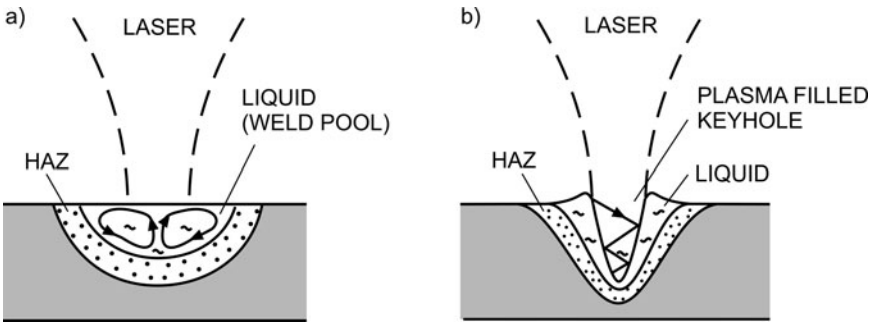

Fig. 10.6.1 a, b Models for the two intensity ranges of laser welding. HAZ stands for heat-affected zone. (**a**) Conduction-limited welding. (**b**) Deep-penetration (keyhole) welding

of the laser optics, by an adequate inert gas is of importance. Laser welding can be classified according to two intensity ranges:

- With low to moderate laser-light intensities, the material is locally melted without significant vaporization. Heat transport is mediated via heat conduction and convection within the melt pool. This is schematically shown in Fig. 10.6.1a. This type of laser welding is denoted as *conduction-limited welding*. It is applied for low-penetration (depth) welding.
- With laser-light intensities that cause sufficient material vaporization, a deep vapor cavity (keyhole) within the melt pool is formed (Fig. 10.6.1b). This is denoted as *deep-penetration (keyhole) welding*. The incident laser light can penetrate deep into the keyhole and is strongly absorbed due to multiple reflections and plasma-enhanced coupling (Chap. 11). Because the keyhole acts like a 'light trap', this processing range is not very sensitive to the wavelength of the laser light. With a tight focus located below the material surface, very high aspect ratios, typically up to $\Gamma = h/d \approx 5$–20, can be achieved (h and d are the weld depth and width, respectively). The strong feedback among the amount of the absorbed laser light, the plasma, and the depth of the hole within the starting phase may cause problems in process control. With optimized conditions, the material is welded through the whole thickness without any material dropout.

With a scanned laser beam, an egg-shaped melt region is formed (see, e.g., Fig. 8.1.1). The molten material ahead of the laser beam flows around the keyhole and solidifies behind it. The maximum welding speed can be estimated, in the simplest form, from the energy balance, which yields

$$v_{\mathrm{s}}^{\max} \leq \frac{AP - P_{\mathrm{L}}}{dh\Delta H} \,, \tag{10.6.1}$$

where ΔH (J/cm^3) $\approx \Delta H_{\mathrm{m}} + \varrho c_{\mathrm{p}} T_{\mathrm{m}}$. P_{L} corrects for heat losses by conduction and radiation. The penetration depth, h, increases with laser power and decreases with increasing scanning velocity. This is shown in Fig. 10.6.2 for stainless steel and CO_2-laser radiation.

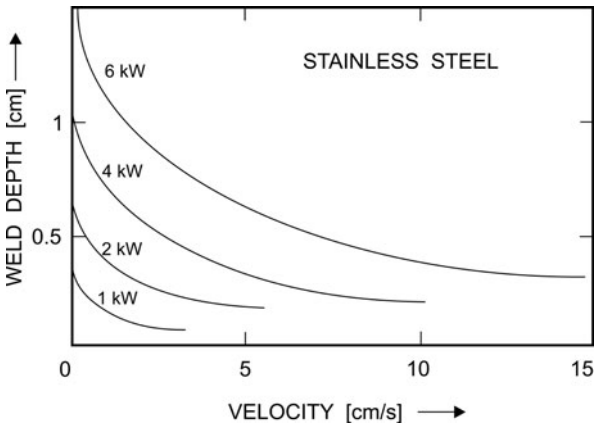

Fig. 10.6.2 Weld depth achieved in deep-penetration (keyhole) welding of stainless steel (AISI 304) with a fast axial flow CO_2 laser as a function of scanning velocity. Adapted from [*Industrial Laser Annual Handbook* 1990]

Mainly because of economic reasons, a wide field of additional applications opens up with high-power diode lasers. Already today, such lasers permit one to join hard and soft plastics and metal sheets. Deep-penetration welding of steel plates with thicknesses up to several millimeters has been reported as well [*Bachmann* et al. 2007].

10.6.1 Ultrashort-Pulse Laser Welding

Real welding using high-repetition rate ultrafast laser pulses ($\lambda = 1045\,\text{nm}$, $\tau_\ell = 350\,\text{fs}$, $\nu_\text{r} = 700\,\text{kHz}$) has been demonstrated for combinations of glasses, glasses and silicon, etc. [*Horn* et al. 2008]. The underlying mechanisms are discussed in Sect. 13.6. They are mainly based on the short laser-material interaction times and the strong absorption of (linearly) transparent materials due to multiphoton- and avalanche-processes.

It should be noted that ultrashort-pulse laser welding is quite different to the *bonding* of organic-inorganic or organic-organic materials and the *joining* of materials by means of an adhesive interlayer. These processes are based on (thermal) material softening and/or on *non-thermal* laser-induced surface modifications. This latter process is often denoted as 'photochemical welding'. The mechanisms are discussed in Sect. 27.1.

10.7 Liquid-Phase Expulsion

Abrasive laser processing based on laser-induced melting requires *much* less energy than laser-induced vaporization. This can directly be verified from a simple estimation of the total enthalpy, ΔH, required in both cases (see Table IV). Thus,

laser machining based mainly on laser-induced melting is to be preferred as long as the specifications of the particular application can be fulfilled. Efficient processing requires strong absorption of the laser radiation and, in the case of abrasive laser machining, fast removal of the liquefied material from the solid surface. The latter can be achieved in different ways:

- By the surface tension of the liquid. This causes the liquefied material to flow to the edge of the molten zone (Sect. 10.5). This mechanism is of particular relevance for the fabrication of holes or cuts in *thin* films or foils, and direct writing of shallow grooves. Certain types of laser marking and laser scribing are based on this mechanism.
- By employing an ambient atmosphere which reacts heavily with the melt to give a gaseous product.
- By using a high-pressure gas jet. This technique is denoted as liquid-phase expulsion. Here, the gas jet expels the liquefied material as schematically shown in Fig. 10.7.1. The molten material accumulates near the bottom of the slab (substrate) due to surface tension which retards the liquefied material from leaving the kerf. The exact width and shape of this zone depends on the scanning (cutting) velocity, v_s, and the gas jet. With optimized parameters, resolidified material formed on the lower surface can be avoided. Liquid-phase expulsion is frequently employed in abrasive laser machining, in particular in metal processing. The Mach numbers of the jet are, typically, around 0.2. In many cases, the proper selection of a gas which exothermally reacts with the liquid, for example, oxygen,

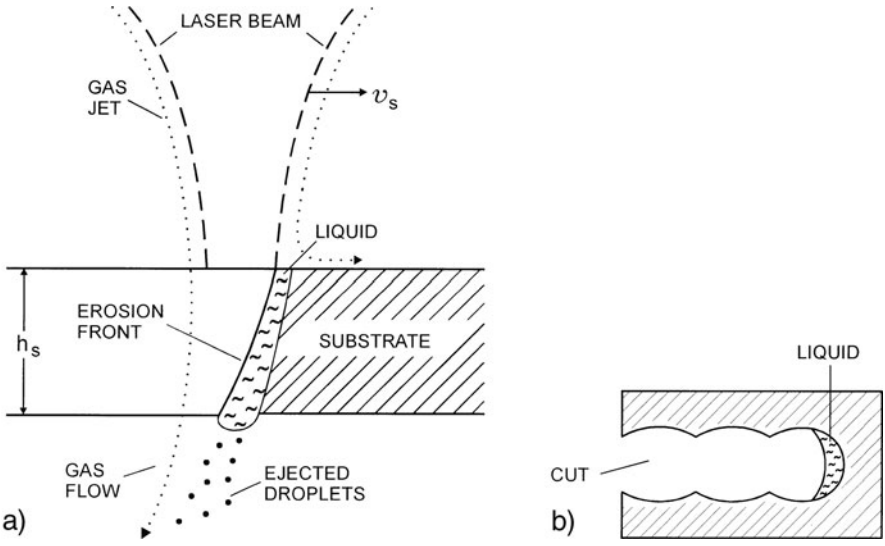

Fig. 10.7.1 a, b Laser cutting by liquid-phase expulsion. The gas jet expels the molten substrate mainly as droplets. (**a**) Cross section. The width of the molten zone depends on the laser and material parameters, the scanning (cutting) velocity, v_s, and the gas jet. (**b**) Plan view showing striations

permits one not only to compensate for gas-jet cooling but even to contribute to the overall energy input. In such cases, striations (oscillations of the kerf width) related to the exothermal heat release are frequently observed. The mechanism is similar to that in explosive crystallization (Sect. 28.3.3). With high laser powers, when material evaporation becomes significant, periodical screening of the incident laser light by the vapor/plasma or a too steep slope of the cutting edge can cause oscillations of the kerf as well.

There are, of course, advantages and disadvantages of melt-phase processing (see Sect. 11.8). In particular, with metals, efficient coupling of CO_2-laser radiation to the substrate is mediated only via the plasma. With the high laser-light intensities involved in vaporization cutting, the liquefied material is expelled by the recoil pressure of the vapor (Chap. 11).

For further details on laser welding and fusion cutting, the reader is referred to the extensive literature on this topic [*Hügel* and *Graf* 2009; *Bachmann* et al. 2007; *Landolt-Börnstein* 2004; *Steen* 2003; *Schuöcker* 1999; *Ready* 1997]. Sophisticated theoretical models have been developed by *Schulz* et al. (1999), *Yabe* (1998), and others.

Part III
Material Removal

Laser-induced material removal can be based on either ablation or etching. The basic mechanisms involved can be thermal, photophysical, or photochemical in nature.

The term laser-induced ablation, or simply laser ablation, is used if material removal can be performed, at least in principle, in a vacuum or in an inert ambient medium. Thus, ablation takes place only if the laser light is *directly* absorbed by the material to be ablated. Clearly, absorption may be based on linear- and/or nonlinear interaction processes.

Thermal ablation requires material melting and vaporization, or sublimation. At high laser powers and laser-beam dwell times in excess of picoseconds, interactions between the laser light and the laser-induced vapor/plasma plume become important. Laser-induced melting, vaporization, and plasma–solid interactions are the dominant mechanisms used in conventional abrasive laser machining, in particular of metallic workpieces (Fig. 1.1.2). Here, the lasers most commonly used are CO_2 lasers, Nd:YAG lasers, and diode lasers in either cw- or pulsed-mode operation. The laser-beam dwell times and pulse widths employed are, typically, between some 100 ns and some 100 ms. With such 'long' dwell times, laser-induced vaporization can often be treated as a *quasi-stationary* process (Chap. 11).

If materials are subjected to nanosecond UV-laser pulses obtained, e.g., from excimer lasers or frequency-multipled Q-switched solid-state lasers, ablation becomes strongly *non-stationary* and additional interaction mechanisms may become important. The pulse lengths in this regime are, typically, between 100 ps and 100 ns. This range of nanosecond pulsed-laser ablation is employed in many cases of micropatterning (Chap. 12) and in most cases of thin-film formation by pulsed-laser deposition (PLD). While most of the experimental results obtained in this regime can be interpreted on the basis of thermal and thermomechanical mechanisms, there are clear indications for non-thermal (photochemical) and photomechanical mechanisms, in particular with non-metals.

With materials that thermally conduct well, in particular with metals, high-quality and high-resolution surface patterning can only be achieved with ultrashort pulses with widths 1 fs $\lesssim \tau_\ell \lesssim$ 100 ps. In this regime of laser–material interactions, the linear optical properties of the material become less important. For this reason, ultrashort pulses allow the patterning of transparent materials for which no efficient laser sources for direct bandgap excitation exist. The dominant physical

mechanisms include thermal ablation at overcritical temperatures, the desorption of excited species, non-equilibrium electronic excitations, avalanche breakdown, and multiphoton ionization (Chap. 13).

Laser-induced chemical *etching* denotes thermal or non-thermal material removal in a *reactive* ambient medium (Chaps. 14 and 15).

Chapter 11
Vaporization, Plasma Formation

Subsequently, we consider mainly quasi-stationary interaction processes with laser-beam dwell times of 100 ns and longer. The laser-light intensity shall be so high that significant material vaporization takes place and a dense vapor plume is formed (Fig. 11.0.1). With increasing laser-light intensities, an increasing fraction of vapor-phase species becomes ionized. In this stage, one talks about a laser-induced plasma. The vapor-/plasma-plume consists of electrons, atoms/ions, molecules and clusters.

Species leaving the *surface* take along some kinetic and, eventually, internal energy. The binding energy required to remove an atom from a solid can be estimated from $\Delta H^{\mathrm{a}}\,(\mathrm{J/atom}) = \Delta H\,(\mathrm{J/g})/N_{\mathrm{s}} \approx \Delta H_{\mathrm{v}}\,(\mathrm{J/g})/N_{\mathrm{s}}$, where $\Delta H_{\mathrm{v}} \equiv \Delta H_{\mathrm{v}}(T_{\mathrm{b}})$ is the enthalpy of evaporation at the boiling temperature, T_{b}; $N_{\mathrm{s}} = L/M$

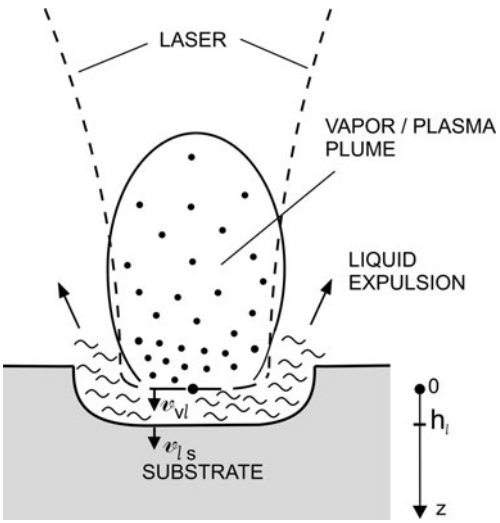

Fig. 11.0.1 Laser-induced surface melting, vaporization, and liquid-phase expulsion

D. Bäuerle, *Laser Processing and Chemistry,* 4th ed.,
DOI 10.1007/978-3-642-17613-5_11, © Springer-Verlag Berlin Heidelberg 2011

is the (atom) number density, L the Avogadro number, and M the atomic weight per mol (see also Sect. 2.2.4). For clusters formed by collective effects, or for droplets related to hydrodynamic instabilities, or for big material fragments ejected due to stress relaxation, the average energy per atom required for material removal may be significantly smaller.

Thermalization of species leaving the surface is mediated via collisions within a few mean free paths from the surface. This region is called the *Knudsen layer*. The strong temperature and pressure gradients in the axial direction of the vapor plume – compared to the corresponding gradients in the lateral direction – cause the plume to have a strongly forward directionality.

In the simplest model, the expansion of the vapor beyond the Knudsen layer is described by an adiabatically expanding gas [*Anisimov* et al. 1993]. Here, the temperature within the plume decreases with distance from the substrate surface. In a vacuum, the expansion velocity increases with time up to some limiting value. In the presence of an ambient gas, the expansion velocity reaches some maximum and decreases thereafter. This hydrodynamic description does not consider any non-equilibrium effects, which may become important with short high-intensity laser pulses. In this case, the species desorbed from the surface may have a *non*-Maxwellian velocity distribution which is 'between' that for quasi-equilibrium thermal evaporation and that for a 'monochromatic' molecular beam.

In any case, the species leaving the surface generate a recoil pressure on the substrate. In the presence of a molten surface layer and with focused laser-beam irradiation, the recoil pressure expels the liquid in part (Fig. 11.0.1). The ablated material may also generate a shock wave (Chap. 30). The vapor plume absorbs and scatters the incident laser radiation.

In Sects. 11.1, 11.2, 11.3 and 11.4, we consider laser-light intensities which exceed the intensity for material vaporization, $I_v \equiv I_v(\lambda)$, but do not significantly ionize the vapor. For CO_2-laser radiation and metal substrates this intensity is within the range 10^4–10^6 W/cm^2. In this range, interactions of the laser light with the vapor can often be ignored. If this approximation is too crude, the laser-light intensity reaching the substrate can be described by an effective intensity which takes into account losses due to absorption and scattering within the plume (Sect. 12.3). Local intensity changes due to distortions of the beam shape by the hot vapor plume can be taken into account in a similar way. With the intensities under consideration, the rate of material removal is determined by both evaporation *and* liquid-phase expulsion. In the presence of a reactive gas this rate can be enhanced by chemical reactions.

In the following, we will present simple models which permit one to estimate vaporization rates, mainly for flat structures whose depth is very small compared to their width, $h \ll d$. The problem becomes much more difficult for deep holes and grooves where $h \geq d$. Some typical cross sections which are observed in experiments are shown in Fig. 11.0.2. The quantity $\Gamma \equiv h/d$ is often termed the *aspect ratio*. With deep structures, calculations of the laser-induced temperature distribution must take into account the changes in geometry during the ablation/etching process.

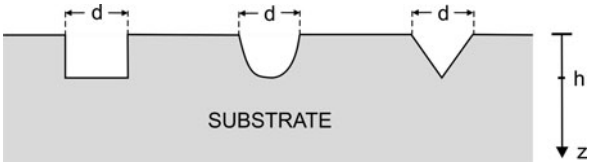

Fig. 11.0.2 Model structures for deep holes or grooves (oriented perpendicularly to the plane of the page). d is defined as the width at the substrate surface, while h is the maximum depth

11.1 Energy Balance

The simplest approximation to estimate processing rates, with both shallow and deep structures, is based on the energy balance.

Let us assume that material removal is governed by vaporization. The light energy absorbed can then be divided into bulk heating, melting, and vaporization of the material. For laser-light intensities in excess of the threshold intensity for ablation, $I = P/F > I_{\mathrm{th}}$, the depth, Δh, ablated during the dwell time of the laser beam, τ_ℓ, can be estimated from

$$\Delta h \approx \frac{AP - P_{\mathrm{L}}}{F\left[\varrho c_{\mathrm{p}}(T - T_0) + \Delta H_{\mathrm{m}} + \Delta H_{\mathrm{v}}\right]}\tau_\ell \approx \frac{A\phi - \phi_{\mathrm{L}}}{\Delta H_{\mathrm{v}}} \,. \qquad (11.1.1)$$

In this approximation, shielding of the incident laser light by the vapor plume, recondensation of ablated material within the processed area, and the ejection of clusters, fragments, etc., is ignored. This is certainly a good approximation for laser powers that are around the threshold power for vaporization. P_{L} corrects for losses due to thermal radiation and the energy which remains within the non-ablated material volume (due to heat conduction, convection, the finite absorption of the material, chemical reaction enthalpies, etc.). F is the ablated area and T the average temperature at which evaporation takes place. With very short pulses, T may significantly exceed the boiling temperature, T_{b}. The specific heat of the solid, the liquid, and the gas phase have been assumed to be equal, i.e., $c_{\mathrm{p}} \equiv c_{\mathrm{ps}} = c_{\mathrm{pl}} = c_{\mathrm{pv}}$ (Sect. 2.2.4). Any temperature dependences of the material parameters have been ignored. At a *fixed* laser fluence, optimum ablation conditions are reached if the absorbed laser-light energy is used as efficiently as possible. This is the case with low overheating of the ablated material and with small values of P_{L}. For surface absorption, $l_{\mathrm{T}} \gg l_\alpha$, and the fluences commonly used, this is fulfilled, in good approximation, if $\Delta h \approx l_{\mathrm{T}}$. This condition permits one to estimate the optimum pulse duration (Sect. 11.2.3). If the energy losses are small compared to the energy spent for evaporation, we can set $P_{\mathrm{L}} \approx 0$. Then, (11.1.1) suggests an increase in the ablated layer thickness which is proportional to the laser fluence, $\Delta h \approx \phi_{\mathrm{a}}/\Delta H_{\mathrm{v}}$. Even with materials with a high thermal conductivity such as metals, where ϕ_{L} cannot be neglected, Δh increases often linearly with ϕ. The reason is that ϕ_{L} remains almost constant as long as τ_ℓ is fixed. Strong non-linearities arise when laser–plasma–solid interactions become important.

11.2 One-Dimensional Model

Surface evaporation of a semi-infinite liquid or solid at temperature T, can be approximated by the *Hertz–Knudsen* equation

$$J_\mathrm{i} = s\,\frac{p_\mathrm{s}(T) - p_\mathrm{i}}{(2\pi m_\mathrm{i} k_\mathrm{B} T)^{1/2}}\ , \tag{11.2.1}$$

where J_i (species/cm^2 s) is the flux and m_i the mass of species i that leaves the surface. $s \le 1$ is a correction factor which depends on the particular mechanism of evaporation. It is often denoted as the evaporation or condensation (sticking) coefficient. p_i is the partial pressure of molecules at infinity. The saturated vapor pressure can be described by the Clausius–Clapeyron relation

$$p_\mathrm{s}(T) = p_0 \exp\left(-\frac{\mathscr{E}_\mathrm{v}}{T}\right) \equiv p_1 \exp\left(-\frac{\mathscr{E}_\mathrm{v}}{T} + \frac{\mathscr{E}_\mathrm{v}}{T_\mathrm{b}}\right)\ , \tag{11.2.2}$$

where p_1 is 1 atm, and $\mathscr{E}_\mathrm{v} \approx M\Delta H_\mathrm{v}/R_\mathrm{G} = \Delta H_\mathrm{v}^\mathrm{a}/k_\mathrm{B}$. With equilibrium conditions, i.e., when $p_\mathrm{i} = p_\mathrm{s}(T)$, there is *no* overall evaporation. The maximum evaporation rate is obtained with $p_\mathrm{i} = 0$. The maximum velocity of the evaporation front is

$$v = \frac{m_\mathrm{i}}{\varrho} J_\mathrm{i}^\mathrm{max} = \left(\frac{m_\mathrm{i}}{2\pi k_\mathrm{B} T}\right)^{1/2} \frac{p_\mathrm{s}(T)}{\varrho}\ . \tag{11.2.3}$$

Depending on whether evaporation takes place from a liquid surface or a solid surface (sublimation), v is identical to $v_{\mathrm{v}l}$ or v_vs. It should be noted that a more detailed treatment of surface evaporation requires the consideration of the Knudsen layer (Sect. 11.3).

Let us now consider *laser-induced* evaporation of a substrate. The laser beam shall propagate in the z-direction; the ablated surface shall be placed within the plane $z = 0$ (Fig. 11.2.1). The influence of the plasma plume shall be ignored. The radius of the laser beam, w, shall be large compared to l_α and l_T. With this condition, the problem can be treated in one dimension (1D). It also applies to shallow structures, where $h \ll d$. We consider a single laser pulse of duration τ_ℓ and a uniform laser-light intensity on the surface $z = 0$. The laser-induced surface temperature can be estimated from the 1D heat equation. In a reference frame that is attached to the interface $z = 0$ and which moves with the velocity $v(t)$, the heat equation has the form

$$\varrho c_\mathrm{p}\left(\frac{\partial T}{\partial t} - v\frac{\partial T}{\partial z}\right) = \frac{\partial}{\partial z}\left(\kappa_\mathrm{s}\frac{\partial T}{\partial z}\right) - \frac{\partial I}{\partial z}\ , \tag{11.2.4}$$

where ϱ is the mass density. c_p is the specific heat and κ_s the heat conductivity of the solid ($T < T_\mathrm{m}$) and liquid ($T > T_\mathrm{m}$) substrate material. Convection within the liquid is ignored. We employ the boundary condition

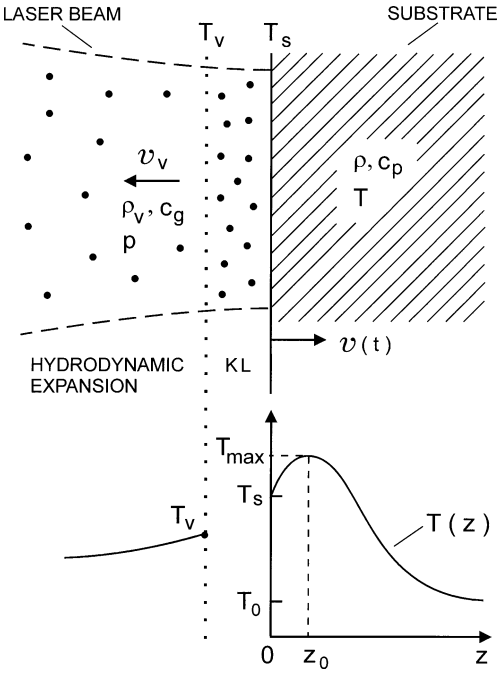

Fig. 11.2.1 Irradiation geometry and laser-induced temperature distribution within the solid (finite absorption) and within the ambient medium. The liquid layer, if present, is not drawn. Condensation effects are ignored. KL denotes the Knudsen layer

$$-\kappa_s \left.\frac{\partial T}{\partial z}\right|_{z=0} = S_s = -J_i \Delta H_v^a(T_s) \; . \tag{11.2.5}$$

S_s (J/cm^2 s) is the total energy flux at the surface. If we introduce the total enthalpy of the (condensed) substrate, ΔH_s, we can rewrite (11.2.4) in analogy to (2.2.14)

$$\frac{\partial \Delta H_s}{\partial t} = v \frac{\partial \Delta H_s}{\partial z} + \frac{\partial}{\partial z}\left(\kappa_s \frac{\partial T}{\partial z}\right) - \frac{\partial I}{\partial z} \; . \tag{11.2.6}$$

Note that this equation does *not* contain ΔH_v, as this enters the boundary condition (11.2.5) only. ΔH_m is included in ΔH_s.

The temporal behavior of the surface temperature, $T_s \equiv T(z = 0, t)$, and the velocity, v, are shown schematically in Fig. 11.2.2. At the beginning of the laser pulse, the temperature T_s increases and reaches within a time t_v an almost constant (stationary) value, T_{st}. After the laser pulse, i.e., with $t > \tau_\ell$, T_s decreases (cooling cycle). The situation is somewhat different with the ablation velocity, v. Here, the stationary regime is only reached after a time $t_{st} > t_v$. The evaporated layer thickness is

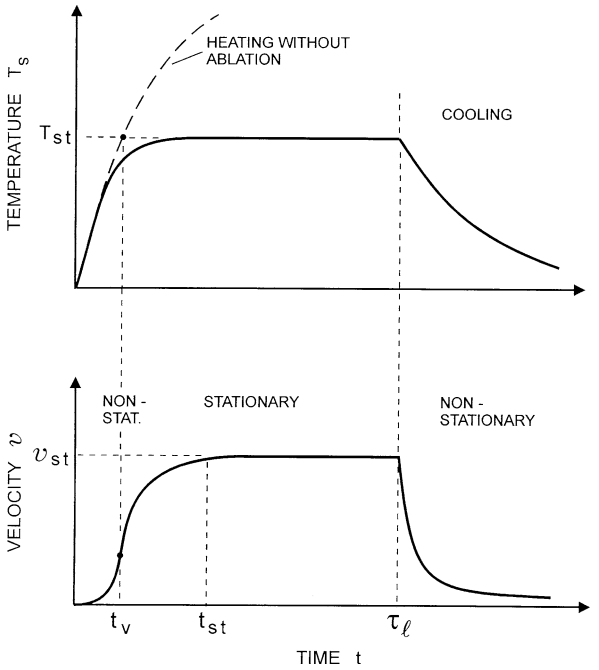

Fig. 11.2.2 Schematic of the temporal dependence of the temperature, T_s, and velocity, v, of the ablation front. The laser-induced temperature rise that would be expected *without* evaporation is shown (*dashed curve*). τ_ℓ is the laser-pulse length. T_s reaches the stationary value T_{st} after a time t_v, while v becomes constant only after a time $t_{st} > t_v$. The influence of a liquid layer has been ignored. With certain materials and laser parameters, the surface temperature in the initial phase may exceed T_{st}, i.e., $T_s(t_v < t < t_{st}) > T_{st}$

$$\Delta h = \int_0^\infty v(t)\,\mathrm{d}t \approx v_{st}(\tau_\ell - t_v)\ . \tag{11.2.7}$$

The latter approximation can be employed only if ablation can be ignored for times $t > \tau_\ell$.

Finally, it should be noted that within the literature different treatments of material evaporation can be found. Almost all of them start from the heat equation. The main differences in the physical mechanisms appear in the boundary conditions. For example, with *normal boiling*, formation of vapor bubbles within the (bulk) liquid is of great importance. This is *not* the case in many types of laser-induced material evaporation. Here, the time of formation depends on the thermophysical and optical properties of the material and on the laser parameters. For conventional (quasi-stationary) metal processing, *surface* evaporation dominates for (moderate) intensities of, typically, $I \lesssim 10^9\ \mathrm{W/cm^2}$ and pulse lengths of the order of 10 ns or longer. However, with fluences in excess of several $\mathrm{J/cm^2}$, the melt is overheated up to its thermodynamic stability and undergoes a rapid transition to a mixed gaseous/liquid state. This is often denoted as explosive volume evaporation or *phase explosion*

[*Bulgakova* and *Bulgakov* 2001]. The transition from surface evaporation to phase explosion is correlated with a dramatic increase in ablation rate. The corresponding fluence is often denoted as a 'second' threshold. Phase explosion is the dominant mechanism for material removal under the action of *high* intensity ultrashort-pulse laser-radiation (Chap. 13). Subsequently, we consider the regime where material removal via surface evaporation is the dominating process.

For strongly absorbing materials ($\alpha \to \infty$) and *slow* evaporation, one can assume that 'boiling' takes place within a thin surface layer and use instead of (11.2.5) the boundary condition

$$-\kappa_s \left.\frac{\partial T}{\partial z}\right|_{z=0} = I_a - v\Delta H_v \ .$$

Here, v is determined from the condition $T(z = 0) = T_b$. These conditions do not allow overheating at the surface or below the surface. Both effects are, however, important in many cases of laser-induced evaporation, in particular when short high-intensity laser pulses are used.

For these reasons, in the next sections we analyze stationary and non-stationary regimes of T_s and v on the basis of (11.2.3–6).

11.2.1 Stationary Evaporation

With stationary conditions, T_s is independent of time, i.e., $T_s = \text{const}(t) \equiv T_{st}$. Spatial integration of (11.2.6) yields, with (11.2.5),

$$-S_s + v\Delta H_s(T_s) = I_a \ . \tag{11.2.8}$$

This result reflects the energy conservation. The energy flux is related to the flux of species that evaporate from the surface at temperature T_s by (11.2.5). S_s is proportional to the difference of the enthalpies of the gas and the condensed phases. Here we use the approximation

$$\begin{aligned} -S_s \approx v\Delta H_v(T_s) &= v\left[H_g(T_s) - H_s(T_s)\right] \\ &\approx v\left[\Delta H_v^0 + \Delta H_g(T_s) - \Delta H_s(T_s)\right] \ , \end{aligned} \tag{11.2.9}$$

where $\Delta H_v^0 \equiv \Delta H_v(T_0) = H_g(T_0) - H_s(T_0)$ is the enthalpy of sublimation at T_0. It is related to the enthalpy of vaporization, which is usually given at T_b by $\Delta H_v^0 = \Delta H_v(T_b) - \varrho\langle c_g\rangle\Delta T_b + \varrho\langle c_p\rangle\Delta T_b + \Delta H_m$, with $\Delta T_b = T_b - T_0$ and $T_0 = 298\,\text{K}$. We approximate the enthalpy of the gas (vapor) per unit volume of evaporated material by

$$\Delta H_g(T_s) = \int_{T_0}^{T_s} \varrho c_g(T)\,\mathrm{d}T \approx \varrho\left\langle c_g\right\rangle \Delta T_s \ ,$$

where the specific heat of the vapor at constant pressure is denoted by $c_g \equiv c_{pv}$. The relative contributions of the terms are, e.g., for Fe at $T_s = T_b$ (in units of $10^4\,\mathrm{J/cm^3}$), the following: $\Delta H_v \equiv \Delta H_v(T_b) = 4.9$, $\varrho\langle c_g\rangle \Delta T_b = 1.0$ and $\varrho\langle c_p\rangle \Delta T_b = 1.7$. Correspondingly, we obtain at $T_s = 6000\,\mathrm{K}$ the following: $\Delta H_v(T_s) = 4.4$, $\varrho\langle c_g\rangle \Delta T_s = 2.3$, and $\varrho\langle c_p\rangle \Delta T_s = 3.5$. Additionally, we have $\Delta H_m = 0.2 \times 10^4\,\mathrm{J/cm^3}$ and $\Delta H_v^0 \approx 5.8 \times 10^4\,\mathrm{J/cm^3}$. The relative sizes of terms are, in fact, typical for metals. Thus, we can often employ the approximation $\Delta H_v^0 \approx 1.2\Delta H_v \approx \Delta H_v$. With inorganic insulators this factor can be 1.4–1.6.

With (11.2.9), the energy balance (11.2.8) can be written as

$$I_a = v\tilde{H}(T_s) \approx v\left(\Delta H_v^0 + \frac{5R_G\varrho\Delta T_s}{2M}\right), \tag{11.2.10}$$

where $\tilde{H}(T_s) \equiv \Delta H_v^0 + \Delta H_g(T_s) \approx (1.2{-}1.4)\Delta H_v^0 \approx 1.5\Delta H_v$ is the effective enthalpy for 1D stationary evaporation. The approximation in (11.2.10) refers to monoatomic gases. Note that this equation does *not* contain $\Delta H_s(T_s)$ and ΔH_m. This result can be understood in terms of (equilibrium) thermodynamics: we can argue that evaporation (sublimation) takes place at T_0 and that the gas is subsequently heated to T_s.

To calculate the temperature T_s, we need another equation in addition to (11.2.10), because v is unknown. In terms of the vaporization kinetics, the interface velocity can be described by (11.2.3). In a simplified form this can be written as

$$v(T_s) \approx v_0 \exp\left(-\frac{\mathscr{E}_v}{T_s}\right), \tag{11.2.11}$$

where v_0 is of the order of the sound velocity within the solid/liquid, i.e., 10^5–$10^7\,\mathrm{cm/s}$ [$v_0(\mathrm{Fe};\, T = 1{,}800\,\mathrm{K}) \approx 5.6 \times 10^6\,\mathrm{cm/s}$, $v_0(\text{c-}SiO_2) \approx 2.2 \times 10^5\,\mathrm{cm/s}$]. Equations (11.2.10) and (11.2.11) permit one to calculate the stationary temperature, T_{st}, and velocity, v_{st}. According to (11.2.10) the velocity v_{st} depends approximately linearly on intensity I_a. Thus, we find from the kinetic equation (11.2.11) that T_{st} changes approximately logarithmically with I_a. In *dimensionless* variables, these equations can be written as

$$I_a^* = (\Delta H^* + T_{st}^*)\exp\left(-\frac{1}{T_{st}^*}\right) \tag{11.2.10a}$$

and

$$v_{st}^* = \exp\left(-\frac{1}{T_{st}^*}\right), \tag{11.2.11a}$$

where

$$I_a^* = I_a/v_0\varrho c_g\mathscr{E}_v\,, \quad \Delta H^* = \Delta H_v^0/\varrho c_g\mathscr{E}_v - T_0/\mathscr{E}_v\,,$$
$$v_{st}^* = v_{st}/v_0\,, \quad \text{and} \quad T_{st}^* = T_{st}/\mathscr{E}_v\,.$$

This result does *not* depend on the absorption coefficient, α. It reflects the purely energetic nature of the stationary solution. For conventional metal processing with CO_2 or Nd:YAG lasers, $I_a^* \ll 1$. With short high-intensity pulses and materials with a low activation temperature, $\mathscr{E}_v$, the range $I_a^* \approx 1$ becomes relevant. Note that $I_a^* \approx 1$ corresponds to $I \approx 10^{10}$–$10^{12}\,\mathrm{W/cm^2}$. In this regime, laser–plasma interactions cannot be ignored.

Figure 11.2.3 shows the normalized velocity, v_{st}^*, and temperature, T_{st}^*, as a function of the laser-light intensity, I_a^*. $\Delta H^* = 0.4$ is typical for metals. $\Delta H^* = 0$ applies to materials that evaporate in large molecules, e.g., polymers.

For metals where $\Delta H_v^0 \gg \varrho c_g T_s$, a rough estimation yields, for moderate fluences,

$$v_{st} \approx \frac{I_a}{\Delta H_v^0} \quad \text{and} \quad T_{st} \approx \mathscr{E}_v \left[\ln\left(\frac{v_0 \Delta H_v^0}{I_a}\right)\right]^{-1}\,. \tag{11.2.12a}$$

With laser-light intensities $I_a \lesssim 10^6\,\mathrm{W/cm^2}$ and metals, the stationary temperature can be approximated by the boiling temperature, i.e., $T_{st} \approx T_b$. With intensities $I \approx 10^9\,\mathrm{W/cm^2}$, we estimate $T_{st} \approx 1.5\,T_b$. If $\Delta H_v^0 \ll \varrho c_g T_s$, instead of (11.2.12a) one can use

$$v_{st} \approx \frac{I_a}{\varrho c_g \mathscr{E}_v} \ln\left(\frac{v_0 \varrho c_g \mathscr{E}_v}{I_a}\right) \quad \text{and } T_{st} \approx \mathscr{E}_v \left[\ln\left(\frac{v_0 \varrho c_g \mathscr{E}_v}{I_a}\right)\right]^{-1}. \tag{11.2.12b}$$

This case may be relevant for the ablation of polymers. As polymers often ablate in large fragments, one can use the approximation $c_g \approx c_p$.

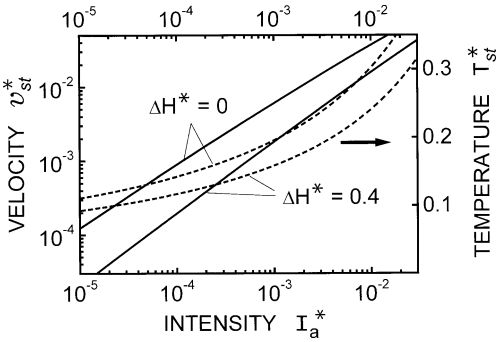

Fig. 11.2.3 Normalized stationary velocity of the ablation front (*solid curves*) and surface temperature (*dashed curves*) as a function of the normalized laser-light intensity for two different values of ΔH^* [*Arnold* and *Bäuerle* 1998]

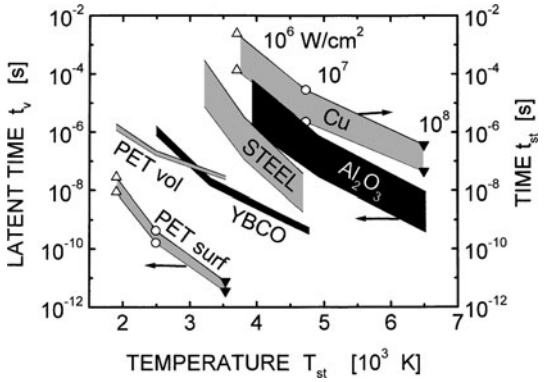

Fig. 11.2.4 The lower boundary of *shaded regions* gives the latent time, t_v, during which the stationary temperature, T_{st}, is reached (see also Fig. 11.2.2). The upper boundary is the time t_{st} after which the stationary ablation velocity, v_{st}, is reached. Calculations have been performed for different materials and absorbed laser-light intensities $I_a = IA(\mathrm{W/cm^2})$: $\triangle\ 10^6$, $\circ\ 10^7$, $\blacktriangledown\ 10^8$. For PET results for both surface absorption and volume absorption are shown

Temperatures T_{st} calculated for different materials and absorbed laser-light intensities $I_a = AI = 10^6$–10^8 W/cm^2 are shown in Fig. 11.2.4.

Two Exponent Solution

For constant material parameters, the stationary solution of (11.2.4) can be written as

$$\Delta T(z) = C\exp(-\alpha z) + (\Delta T_{st} - C)\exp\left(-\frac{z}{l_T}\right) \tag{11.2.13}$$

with

$$C = \frac{I_a}{\kappa_s(l_T^{-1} - \alpha)}$$

and $\Delta T_{st} = T_{st} - T_0$. Here, we have employed Beer's law. The *stationary* thermal penetration depth is

$$l_T = \frac{D}{v_{st}} \approx \frac{D\Delta H_v}{I_a}\ . \tag{11.2.14}$$

Thus, during stationary ablation, l_T remains *constant*. For *finite* absorption, the maximum in the temperature distribution (11.2.13) occurs *below* the surface (Fig. 11.2.1) at the position

$$z_0 = \frac{l_T}{1 - \alpha l_T}\ln\left(\frac{1 + \xi/\alpha l_T}{1 + \xi}\right)\ , \tag{11.2.15}$$

where $\xi = \Delta H_v^0/\varrho c_p \Delta T_{st} = \Delta H_v^0/\Delta H_s(T_{st})$. Here, we have assumed $\Delta H_g = \Delta H_s$ and therefore $S_s = -v\Delta H_v^0$. Subsurface superheating can then be described by

$$\frac{\Delta T(z_0) - \Delta T_{st}}{\Delta T_{st}} = (1+\xi)\exp(-\alpha z_0) - 1 \; . \tag{11.2.16}$$

For *surface absorption* ($\alpha \to \infty$) and moderate laser-light intensities, we have $\alpha l_T = \alpha D/v_{st} \approx \alpha D \Delta H_v^0/I_a \gg 1$, and thereby $z_0 \approx l_\alpha \ln(1+\xi) \approx 0$ and $C \approx -I_a/\kappa_s \alpha \approx 0$. Thus,

$$\Delta T(z) = \Delta T_{st} \exp\left(-\frac{z}{l_T}\right) \; . \tag{11.2.17}$$

Here, the maximum temperature rise occurs at the surface. This is a good approximation with metals.

Finite Size of Laser Beam (3D Case)

With long pulses and focused laser beams, three-dimensional (3D) heat conduction becomes important. Thus, we have to add a radial term to (11.2.4),

$$\kappa_s \frac{1}{r}\left[\frac{\partial}{\partial r}\left(r\frac{\partial T}{\partial r}\right)\right] \approx -\kappa_s \frac{\Delta T(z)}{w^2} \; . \tag{11.2.18}$$

Consideration of this term results in both an increase in l_T and additional losses due to radial heat conduction. For a top-hat laser beam and a hole with parabolic cross section $d \ll 2w$ (Fig. 11.0.2) and a constant apex radius, w', the energy balance (11.2.10) can be approximated by [*Sobol* 1995]

$$I_a = v[\Delta H_v^0 + \varrho c_g \Delta T_s f(\beta)] \; , \tag{11.2.19}$$

where

$$f(\beta) = -\frac{\exp(-\beta)}{\beta\,\mathrm{Ei}(-\beta)} \quad \text{and} \quad \beta = \frac{vw'}{2D} \; .$$

The exponential integral function Ei is defined in Appendix B. In order to find v and T_s one must solve (11.2.19) together with (11.2.11). With $\beta \gg 1$, we obtain $f(\beta) \to 1$ and (11.2.19) becomes identical to (11.2.10). For estimations one can substitute w' by the laser-beam radius, w.

11.2.2 Non-stationary Evaporation

As indicated in Fig. 11.2.2, the temperature T_s changes strongly during the heating cycle $0 \le t \le t_v$ and the cooling cycle $t > \tau_\ell$. The situation is similar for the velocity of the evaporation front, v, for time intervals $0 \le t \le t_{st}$ and $t > \tau_\ell$. Non-stationary effects also become important when the incident laser-light intensity is not constant, i.e., if $I = I(t)$. Moreover, even if $I = \text{const}(t)$, the intensity absorbed at the substrate surface may strongly change due to screening (Sect. 11.6), or due to changes in the absorptivity $A = A(t)$ related to changes in temperature, the surface morphology, the growth of an oxide layer, etc. With very short pulses, i.e., with $\tau_\ell < t_{st}$, the stationary regime will not be reached at all. In this case, we have to solve the time-dependent equations (11.2.6) and (11.2.11), together with the boundary condition (11.2.5), where S_s is given by (11.2.9). Thus, all quantities become time dependent, i.e., $v = v(t)$, $\Delta h = \Delta h(t)$, $l_T = l_T(t)$, etc. Integration of (11.2.6) yields the overall energy balance

$$\int_0^\infty I_a \, dt = \phi_a \approx \Delta h \tilde{H}(T_{st}) + (l_T + l_\alpha) \Delta H_s(T_{st}) \, , \tag{11.2.20}$$

where $\tilde{H}(T_{st})$ was defined for (11.2.10) or, if we correct for effects of the Knudsen layer, it is defined by (11.3.2). T_{st} corresponds to an average intensity $I_a = \phi_a/\tau_\ell$, where τ_ℓ is some average pulse width. The first term is the enthalpy necessary to evaporate the layer thickness, Δh. The second term approximates the enthalpy stored at $t = \tau_\ell$ within the non-ablated (condensed) material volume, $z > 0$ (Fig. 11.2.1). This energy, i.e., $P_L = (l_T + l_\alpha) \varrho c_p \Delta T_{st}$ is lost in single-pulse ablation. The heat penetration depth, $l_T = l_T(t)$, shows a complicated temporal dependence [*Arnold* et al. 1998]. If, however, $\tau_\ell < t_{st}$ and/or if Δh is very small, we can use the approximation $l_T \approx (D\tau_\ell)^{1/2}$. If $\tau_\ell > t_{st}$, we have $l_T \approx D/v_{st}$, where v_{st} can be approximated by (11.2.12). With surface absorption and high-intensity long pulses, the energy stored within the non-ablated material may *decrease* with time, i.e., $l_T(t > t_v) < l_T(t_v)$.

For uniform irradiation and a constant intensity, I_a, the temperature rise during the heating cycle can be calculated from (7.5.8a) or, in good approximation, from (7.5.8b). These equations can also be employed to calculate the latent time t_v (Fig. 11.2.2) from the condition

$$\Delta T(0, t_v) = \Delta T_{st} \, , \tag{11.2.21}$$

where ΔT_{st} is obtained from (11.2.10) and (11.2.11), or from the approximations (11.2.12). For *surface* absorption ($\alpha \to \infty$) we obtain from (7.5.8b)

$$t_v \approx \frac{\pi}{4} \left(\frac{\Delta H_s(T_{st})}{I_a} \right)^2 D \approx \left(\frac{c_p \varrho \mathscr{E}_v}{I_a \ln(v_0 \Delta H_v / I_a)} \right)^2 D \, , \tag{11.2.22a}$$

with $\Delta H_s(T_{st}) = \varrho c_p \Delta T_{st}$. The second approximation holds mainly for metals [see (11.2.12a)]. Typical values of t_v obtained with absorbed laser-light intensities $I_a = AI = 10^6$–$10^8\,\mathrm{W/cm^2}$ are plotted in Fig. 11.2.4 for various materials. For Al_2O_3 surface absorption can be assumed only for heavily doped material, or for laser wavelengths $\lambda < 150\,\mathrm{nm}$ or $\lambda \gtrsim 8\,\mu\mathrm{m}$.

For *finite* (volume) absorption we obtain

$$t_v \approx \frac{\Delta H_s(T_{st})}{\alpha I_a} \approx \frac{c_p \varrho \mathscr{E}_v}{\alpha I_a \ln(v_0 \Delta H_v / I_a)} \tag{11.2.22b}$$

In the latter approximation we have employed (11.2.12a). The corresponding values obtained for PET with $A = 1$ and $\alpha(308\,\mathrm{nm}) = 4 \times 10^3\,\mathrm{cm^{-1}}$ are included in Fig. 11.2.4 and denoted by PET vol.

Threshold Fluence and Minimum Intensity

The minimum absorbed laser-light intensity, I_a^{min}, or fluence, ϕ_a^{min}, necessary to initiate significant material evaporation within a (fixed) laser pulse length, τ_ℓ, can be calculated from (11.2.22). With $\alpha \to \infty$, we obtain

$$I_a^{min} = \frac{\sqrt{\pi}}{2} \Delta H_s(T_{st}) \left(\frac{D}{\tau_\ell}\right)^{1/2}$$

or

$$\phi_a^{min} = \frac{\sqrt{\pi}}{2} \Delta H_s(T_{st}) (D\tau_\ell)^{1/2} \tag{11.2.23a}$$

and with finite α

$$I_a^{min} = \frac{\Delta H_s(T_{st})}{\alpha \tau_\ell} \quad \text{or} \quad \phi_a^{min} = \frac{\Delta H_s(T_{st})}{\alpha} . \tag{11.2.23b}$$

Note that in this latter case ϕ_a^{min} is almost independent of τ_ℓ.

The Time Required to Reach Stationary Ablation, t_{st}

The temperature of the ablation front, $T_s \equiv T(0)$, reaches its stationary value within the time t_v. The temperature *profile* within the ablated material, $T(z > 0)$, and the velocity of the ablation front, v, will become stationary only with times $t \geq t_{st}$. For $l_\alpha \ll D/v_{st}$, this time is given by

$$t_{st} = \frac{D}{v_{st}^2} \approx D \left(\frac{\tilde{H}(T_{st})}{I_a}\right)^2 . \tag{11.2.24a}$$

A similar dependence can also be derived from the condition that with t_{st} the thermal penetration depths without and with ablation should become equal, i.e., $(Dt_{st})^{1/2} \approx D/v_{st}$. Typical values found with $A = 1$ and intensities between $I = 10^6$ and $10^8\,\mathrm{W/cm^2}$ are included in Fig. 11.2.4 for different materials. For $l_\alpha \gg D/v_{st}$, we obtain

$$t_{st} = \frac{1}{\alpha v_{st}} \approx \frac{\tilde{H}(T_{st})}{\alpha I_a} \,. \tag{11.2.24b}$$

In some cases one can use the approximation $\tilde{H} \approx \Delta H_v$. The comparison shows that the time t_{st} significantly exceeds t_v. From (11.2.22) and (11.2.24) we can estimate typical values of t_{st}/t_v. For *metals* ($\alpha \to \infty$, $\Delta H_v^0 \gg \varrho c_g T_s$) we obtain

$$\frac{t_{st}}{t_v} \approx \left(\frac{\tilde{H}(T_{st})}{\Delta H_s(T_{st})}\right)^2 \approx 10 \text{ to } 20 \,. \tag{11.2.25a}$$

With *insulators* (α finite, $l_\alpha > D/v_{st}$, $\Delta H_s(T_{st}) \approx \Delta H_v$) this ratio is given by

$$\frac{t_{st}}{t_v} \approx \frac{\tilde{H}(T_{st})}{\Delta H_s(T_{st})} \approx 1 \text{ to } 4 \,. \tag{11.2.25b}$$

With times $t > t_{st}$, the thermal energy stored within the volume $z > 0$ remains constant and the thermal penetration depth, l_T, reaches its stationary value (11.2.14).

Non-stationary material evaporation is of particular importance in thermal (photothermal) pulsed-laser ablation using nanosecond to picosecond laser pulses (Chaps. 12 and 13).

11.2.3 Optimal Conditions

For laser ablation based on material evaporation, an optimization of the evaporation process with respect to the energy required is of relevance. Thus, we search for the maximum thickness, Δh, which can be evaporated for a given fluence, ϕ.

Let us assume that material removal takes place only at T_{st} (Fig. 11.2.2) and ignore evaporation for times $t < t_v$ and $t > \tau_\ell$. This is a good approximation for nanosecond and longer pulses, in particular for *metals*, where $z_0 \approx 0$ (Fig. 11.2.1). With the differential $\mathrm{d}(\Delta h) = 0$ and $l_\alpha \ll l_T$, we obtain from (11.2.20) with $l_T = D/v_{st}$

$$\left(\Delta h + \frac{\Delta H_s(T_{st}) D\tau_\ell}{\phi_a}\right)^2 = D\tau_\ell \left(\frac{\mathscr{E}_v}{T_{st}} - \frac{\Delta H_v^0}{\tilde{H}(T_{st})}\right) \,, \tag{11.2.26}$$

where we have employed $\tilde{H}(T_{st}) v_{st} = \phi_a/\tau_\ell$ and (11.2.11) for $v(T_{st})$. With metals, we can use the approximations $\Delta H_s(T_{st}) D\tau_\ell/\phi_a \ll \Delta h$ and $\Delta H_v^0/\tilde{H}(T_{st}) \ll \mathscr{E}_v/T_{st} \approx 10$. Thus, with optimal conditions we obtain

$$\Delta h \approx \zeta (D\tau_\ell)^{1/2} \approx l_\mathrm{T}, \tag{11.2.27}$$

where ζ is between 2 and 4. This confirms the statement that optimal conditions are achieved when the ablated-layer thickness is of the order of the heat penetration depth (Sect. 11.1). Thus, if the pulse is too long, the intensity (at fixed fluence), and thereby the ablation rate, is very low. As a consequence, too much energy is spent to heat the non-ablated material. If τ_ℓ is too short, ablation proceeds at a very high surface temperature, T_s. Then, the contribution of the second term in (11.2.10) to $\tilde{H}_\mathrm{st}$, which enters (11.2.20), becomes very high and too much energy is lost to overheating of the evaporated material. To some extent, the situation is similar to that shown in Fig. 10.1.4. The present result is confirmed if we use the relation $\Delta h \approx v_\mathrm{st}(\tau_\ell - t_\mathrm{v})$ instead of (11.2.20), or if we solve the complete non-stationary problem (11.2.3), (11.2.4), (11.2.5) and (11.2.6). If one uses the approximation $\Delta h \approx \phi_\mathrm{a}/\Delta H_\mathrm{v}$ in (11.2.26), the optimum laser-beam dwell time is

$$\tau_\ell \approx \frac{1}{D}\frac{T_\mathrm{st}}{\mathscr{E}_\mathrm{v}}\left(\frac{\phi_\mathrm{a}}{\Delta H_\mathrm{v}}\right)^2 \approx \frac{0.1}{D}\left(\frac{\phi_\mathrm{a}}{\Delta H_\mathrm{v}}\right)^2 , \tag{11.2.28}$$

with ΔH_v (J/cm^3). If we choose $\phi_\mathrm{a} = 10^3$ J/cm^2, we obtain for τ_ℓ(stainlesssteel) $\approx 10^{-3}$ s and for τ_ℓ(Cu) $\approx 5 \times 10^{-5}$ s. Clearly, this treatment does not account for screening. With temperature-dependent screening (Sect. 11.6) the optimal pulse duration increases with respect to (11.2.28), mainly because of the lower temperature involved in the process.

11.3 Knudsen Layer, the Recoil Pressure

With high laser fluences, the boundary condition (11.2.9) becomes inaccurate. The correct condition should consider the macroscopic (hydrodynamic) motion of the vapor, the decrease in gas-phase temperature due to expansion and maxwellization, and the backward flux of species. Initially, the molecules leave the surface at temperature T_s with non-zero average velocity ($-z$-direction in Fig. 11.2.1). Due to collisions, the vapor will finally propagate with a hydrodynamic velocity v_v. This transformation from a non-equilibrium (half-maxwellian distribution) to the equilibrium distribution (shifted maxwellian) occurs within a thin layer of the order of a few mean free paths of species. This layer is denoted as the *Knudsen layer*. If we assume that v_v is equal to the velocity of sound within the vapor (Mach number $\mathscr{M}_a = 1$), which is the case for adiabatic expansion in a vacuum, we have

$$v_\mathrm{v} = \left(\gamma \frac{p}{\varrho_\mathrm{v}}\right)^{1/2} = \left(\gamma \frac{R_\mathrm{G} T_\mathrm{v}}{M}\right)^{1/2} , \tag{11.3.1}$$

where $\gamma = c_\mathrm{p}/c_\mathrm{v} \approx 5/3$. Due to the (partial) transformation of thermal energy into (macroscopic) kinetic energy of the forward-directed vapor plume, the temperature

of the vapor, T_v, will be lower than T_s. For velocities v_v given by (11.3.1), one finds for a monoatomic gas $T_v = 0.67\,T_s$. The energy conservation which also takes into account the backward flux of species can then be written as [*Anisimov* et al. 1971]

$$I_a = v\left(\Delta H_v^0 + 2.23\frac{R_G \varrho T_s}{M}\right) = v\tilde{H}\ , \tag{11.3.2}$$

which almost coincides with (11.2.10). The same analysis yields for the number density of species and the pressure of the vapor behind the Knudsen layer

$$N_v = 0.31 N_s(T_s) \quad \text{and} \quad p = N_v k_B T_v = 0.21\, p_s(T_s)\ , \tag{11.3.3}$$

where $N_s(T_s)$ is the equilibrium number density of species within the saturated vapor. Because of the exponential increase of N_s with temperature, $N_v = 0.31 N_s(T_s = 1.49 T_v)$ is much bigger than $N_s(T_v)$. Thus, the vapor is significantly oversaturated and condensation may start. Instead of (11.2.3) the velocity of the evaporation front becomes

$$v = 0.32\left(\frac{m_i}{k_B T_s}\right)^{1/2}\frac{p_s(T_s)}{\varrho}\ . \tag{11.3.4}$$

In the more general case with $\mathscr{M}_a \neq 1$, all of the quantities T_v, N_v, and p_v become dependent on $\mathscr{M}_a$. For example, one obtains

$$\frac{T_v}{T_s} = \left[(1+\xi^2)^{1/2} - \xi\right]^2\ ,$$

where $\xi = (\pi\gamma/8)^{1/2}\cdot\mathscr{M}_a\cdot(\gamma-1)/(\gamma+1)$. $\mathscr{M}_a$ must be determined experimentally or theoretically from the gas flow within the region of hydrodynamic expansion (Fig. 11.2.1). With very high fluences the expansion of the vapor/plasma plume must be described by the complete hydrodynamic equations [*Krokhin* 1972]. In this regime, plasma shielding, the influence of surface instabilities, etc., must also be taken into account.

Because of momentum conservation, species evaporated from the surface cause a *recoil pressure*,

$$p_{rec} \approx (1+\gamma)p = 0.56\, p_s(T_s) \approx p_s(T_s)\ , \tag{11.3.5a}$$

which acts on the non-ablated material. Thus, the recoil pressure is of the order of the saturated vapor pressure. The factor 0.56 can be understood from the momentum 'carried away' by the evaporating species. With (11.3.2) and (11.3.4) we can write p_{rec} as a function of I_a as follows:

$$p_{\mathrm{rec}} = 1.79\varrho v \left(\frac{k_{\mathrm{B}}T_{\mathrm{s}}}{m_{\mathrm{i}}}\right)^{1/2} = 1.4\varrho v v_{\mathrm{v}}(T_{\mathrm{s}})$$
$$= 1.79\left(\frac{k_{\mathrm{B}}T_{\mathrm{s}}}{m_{\mathrm{i}}}\right)^{1/2} \frac{\varrho I_{\mathrm{a}}}{\Delta H_{\mathrm{v}}^{0} + 2.23\varrho R_{\mathrm{G}}T_{\mathrm{s}}/M} \approx 10^{-5} I_{\mathrm{a}} \ , \quad (11.3.5b)$$

where p is in atm and I_{a} in W/cm^2. Thus, p_{rec} increases *almost* linearly with I_{a}, because of the logarithmic behavior of $T_{\mathrm{s}}(I_{\mathrm{a}})$ [see (11.2.12)]. The latter approximation refers to 'average' parameters for inorganic materials.

For comparison, the *radiation pressure* is $p_{\mathrm{rad}} \approx (1 + R)I/c \ll p_{\mathrm{rec}}$, where c is the velocity of light. This may become incorrect for ultrashort pulses and temperatures in excess of the critical temperature, i.e., with $T > T_{\mathrm{cr}}$, where (11.3.5b) does not hold.

11.4 Influence of a Liquid Layer

Up to now, we have considered mainly 1D material evaporation from a liquid, or sublimation from a solid surface. With *focused* laser-beam irradiation, however, the recoil pressure will squeeze the liquid out of the irradiated spot, mainly near its edges (Fig. 11.0.1). This is denoted as *liquid-phase expulsion*.

Let us first consider the *non-stationary* initial phase of heating and melting. During the time interval $t_{\mathrm{v}} - \tau_{\mathrm{m}}$ (Fig. 10.1.2), a molten layer of thickness h_0 is formed. If we assume a parabolic pressure profile over a circular laser spot with radius w and consider material evaporation to be negligible in comparison to liquid-phase expulsion, the decrease in liquid layer thickness can be described by [*Luk'yanchuk* et al. 1997]

$$h_l(t) = h_0 \cosh^{-2}(\Gamma t) \ , \quad (11.4.1)$$

with

$$\Gamma = \left(\frac{2p_{\mathrm{rec}}}{\varrho w^2}\right)^{1/2} \approx \frac{1}{w}\left(\frac{I_{\mathrm{a}} v_{\mathrm{v}}}{\Delta H_{\mathrm{v}}}\right)^{1/2} \ ,$$

where p_{rec} has been taken from (11.3.5b). Here, and in the following, we ignore all numerical coefficients. The value of h_0 can be estimated from the boundary condition

$$I_{\mathrm{a}} = \kappa_{\mathrm{s}} \frac{\partial T}{\partial z} \approx \frac{\kappa_{\mathrm{s}}(T_{\mathrm{b}} - T_{\mathrm{m}})}{h_0} \approx \frac{\kappa_{\mathrm{s}} T_{\mathrm{b}}}{h_0} \ ,$$

where we have set $T_{\mathrm{s}} = T_{\mathrm{b}}$. This yields

$$h_0 \approx \frac{\kappa_{\mathrm{s}} T_{\mathrm{b}}}{I_{\mathrm{a}}} \ . \quad (11.4.2)$$

The maximum velocity of the vapor–liquid interface is of the order of

$$v_{vl}^{\max} \approx h_0 \Gamma \approx \frac{\kappa_s T_b}{w} \left(\frac{v_v}{I_a \Delta H_v} \right)^{1/2} . \tag{11.4.3}$$

The maximum acceleration is

$$\dot{v}_{vl}^{\max} \approx h_0 \Gamma^2 \approx \frac{\kappa_s T_b v_v}{w^2 \Delta H_v} . \tag{11.4.4}$$

This acceleration may play an important role in the development of hydrodynamic instabilities (Sect. 28.5).

Depending on the laser and material parameters, *stationary* conditions may be reached after the initial phase of liquid expulsion. In this regime, the evaporation and melting fronts propagate with equal velocities, $v_{vl} = v_{ls} = v_{st}$. The thickness of the molten layer is, in analogy to (11.2.14), of the order of

$$h_l \approx \frac{D}{v_{st}} , \tag{11.4.5}$$

where $v_{st} \equiv v_{st}^{liq} + v_{st}^{vap}$. Here, v_{st}^{liq} denotes the contribution of (radial) liquid-phase expulsion to the (axial) front velocity. Using the Bernoulli equation and mass conservation for the liquid, we obtain with (11.4.5)

$$v_{st} \approx \left(\frac{p_{rec}}{\varrho} \right)^{1/2} \frac{h_l}{w} + v_{st}^{vap} = \left(\frac{p_{rec}}{\varrho} \right)^{1/2} \frac{D}{v_{st} w} + v_{st}^{vap} . \tag{11.4.6}$$

If liquid-phase expulsion dominates, i.e., if $v_{st}^{liq} \gg v_{st}^{vap}$, we obtain

$$v_{st}^{liq} \approx \left(\frac{D}{w} \right)^{1/2} \left(\frac{p_{rec}}{\varrho} \right)^{1/4} \approx \left(\frac{D}{w} \right)^{1/2} \left(\frac{I_a v_v}{\Delta H_v} \right)^{1/4} \tag{11.4.7}$$

and

$$h_l \approx \frac{D}{v_{st}^{liq}} \approx (wD)^{1/2} \left(\frac{\Delta H_v}{I_a v_v} \right)^{1/4} \tag{11.4.8}$$

Thus, the thickness of the molten layer *decreases* with increasing laser-light intensity, mainly due to the increase in recoil pressure. The overall rate of liquid-phase expulsion slowly *increases* with I_a. A rough estimation for titanium yields, for a power of $P = 2 \times 10^4$ W and a focus of $w = 0.5$ mm, a layer thickness $h_l \approx 20\,\mu$m.

When material removal due to evaporation becomes important, the relative contributions to the overall velocity of the evaporation front in (11.4.6) can be estimated

from

$$\frac{v_{\mathrm{st}}^{\mathrm{vap}}}{v_{\mathrm{st}}^{\mathrm{liq}}} \approx \frac{I_{\mathrm{a}}}{\Delta H_{\mathrm{v}}} \left(\frac{w}{D}\right)^{1/2} \left(\frac{\Delta H_{\mathrm{v}}}{I_{\mathrm{a}} v_{\mathrm{v}}}\right)^{1/4} \approx \left(\frac{w^2}{D^2} \frac{I_{\mathrm{a}}^3}{v_{\mathrm{v}} \Delta H_{\mathrm{v}}^3}\right)^{1/4} . \tag{11.4.9}$$

This ratio exceeds unity for

$$I_{\mathrm{a}} > \Delta H_{\mathrm{v}} \left(\frac{D^2}{w^2} v_{\mathrm{v}}\right)^{1/3} . \tag{11.4.10}$$

For Al this is about $10^7\,\mathrm{W/cm^2}$ for a focus of $w \approx 0.5\,\mathrm{mm}$. If $v_{\mathrm{st}}^{\mathrm{vap}} \gg v_{\mathrm{st}}^{\mathrm{liq}}$, we find with (11.4.5)

$$h_l \approx \frac{D}{v_{\mathrm{st}}} \approx \frac{D}{v_{\mathrm{st}}^{\mathrm{vap}}} \approx \frac{D \Delta H_{\mathrm{v}}}{I_{\mathrm{a}}} . \tag{11.4.11}$$

Thus, h_l decreases with I_{a} faster than in (11.4.8), mainly due to the increase of v_{st} due to vaporization. With (11.4.6) we obtain

$$v_{\mathrm{st}}^{\mathrm{liq}} \approx \left(\frac{p_{\mathrm{rec}}}{\varrho}\right)^{1/2} \frac{D \Delta H_{\mathrm{v}}}{I_{\mathrm{a}} w} \approx \left(\frac{\Delta H_{\mathrm{v}} v_{\mathrm{v}}}{I_{\mathrm{a}}}\right)^{1/2} \frac{D}{w} . \tag{11.4.12}$$

Thus, in this regime $v_{\mathrm{st}}^{\mathrm{liq}}$ *decreases* with I_{a}. Comparing (11.4.7) and (11.4.12) one finds that there exists an intensity of the order of (11.4.10) where $v_{\mathrm{st}}^{\mathrm{liq}}$ has a maximum. This behavior is related to the interdependence between the recoil pressure and the thickness of the liquid layer. Sophisticated numerical calculations which include both liquid-phase expulsion and vaporization have been performed by many authors [*Chan* and *Mazumder* 1987; *Zweig* 1991]. Figure 11.4.1 shows the results of such calculations. The typical thickness of the liquid layer, h_l, is some $10\,\mu\mathrm{m}$, depending on the physical properties of the material. This result is in reasonable agreement with (11.4.8) and (11.4.11). Figure 11.4.1b shows that the vaporization rate increases continuously with absorbed laser power, while liquid-phase expulsion, first increases, then reaches a maximum, and then decreases. At low laser powers, material removal is governed by liquid-phase expulsion while at high laser powers vaporization dominates. All of these features are in qualitative agreement with the equations presented in this section. It should be noted, however, that any direct coupling between the vapor plume and the laser light has been ignored in both descriptions. With the laser-light intensities considered in the figures, this is certainly a crude approximation.

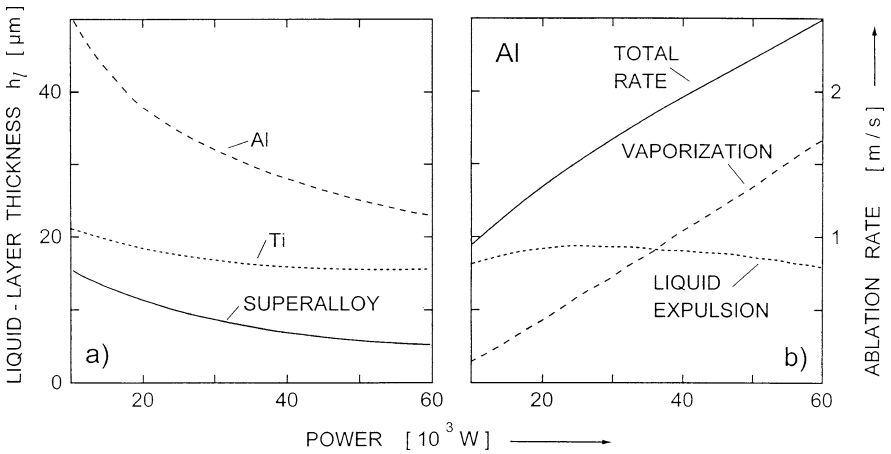

Fig. 11.4.1 (**a**) Calculated thickness of liquid layer, h_l, and (**b**) thermal ablation rate for Al as a function of CO_2-laser power ($w = 0.5$ mm). The total rate in (**b**) is the sum of liquid-phase expulsion and vaporization [*Chan* and *Mazumder* 1987]

11.5 Limitations of Model Calculations

Experimentally observed ablation rates often deviate considerably from theoretical predictions. In addition to the limitations in temperature calculations discussed already in previous chapters (see, e.g., Sect. 2.2.5), there are many additional reasons for the discrepancies in results:

- Surface melting changes the absorbed laser-light intensity, the dissipation of energy (including heat conduction, convection, liquid-phase expulsion, thermal radiation, etc.) and, in the presence of a reactive ambient medium, the surface chemistry and interaction with reactive species.
- Hydrodynamic instabilities may result in the ejection of (liquid) droplets (Sect. 12.6.5).
- Overheating and bubble formation can cause *explosive* melt ejection. This becomes effective, in particular, with a penetrating source, $l_\alpha > l_T$. In such cases, the laser light heats a large material volume. Because evaporation cools the surface, the maximum temperature, and thus overheating, can occur *below* this surface (Fig. 11.2.1).
- Part of the evaporated material recondenses within the area being processed. Besides its direct effect on ablation rates, recondensation diminishes surface cooling caused by vaporization and also changes the absorption behavior within the processed area.
- The incident laser light will be attenuated by absorption and scattering within the vapor/plasma plume. Thus, the overall ablation rates will be significantly lower than those expected from the preceding model calculations, especially for high laser-light intensities. In this regime, the width of the processed area becomes dependent on the (lateral) extension of the plasma plume.

- With deep holes/grooves (Fig. 11.0.2), the parameters determining the absorption of laser radiation, the dissipation of heat, the shielding of the incoming laser light, etc., will change with the geometry of the structure, and thereby with time. Obviously, the various effects are mutually coupled.
- With multicomponent or composite materials, material segregation and decomposition becomes important, except when very short laser pulses are employed (Chap. 13). If material segregation takes place, all parameters will change in a complicated way, single constituents will be enriched, etc.

These different contributions explain why calculated temperature distributions and processing rates, in particular for deep holes/grooves, do not permit proper modeling of laser-induced ablation, except in a few particular cases. Additional problems with quantitative analyses arise from the often significant uncertainties in material parameters and their temperature dependences.

11.6 Plasma Formation

Up to now we have ignored any interaction between the incident laser beam and the vapor/plasma plume. This is a good approximation only for low laser-light intensities and/or for ultrashort pulses with $\tau_\ell \ll t_\mathrm{p}$. Here, t_p is the time after which laser–vapor/plasma interactions become relevant.

If $\tau_\ell \gtrsim t_\mathrm{p}$, screening of the incident laser light by absorption and scattering within the vapor plume diminishes the intensity that reaches the substrate. With many systems, this effect is relevant even with laser-light intensities that do *not* cause significant ionization within the vapor plume. In this regime, I_a can often be calculated from the output intensity of the laser, by employing Beer's law and an effective extinction coefficient α_p. Local intensity changes due to refraction of the incident radiation by the hot vapor plume can be estimated as well. The time t_p can be approximated by the time t_v (Fig. 11.2.2) after which significant material evaporation starts. This time, which is given by (11.2.22) is shown in Fig. 11.2.4 for different materials and absorbed laser-light intensities, I_a.

With increasing laser-light intensity I, an increasing fraction of atoms/molecules becomes ionized. When the vapor becomes substantially ionized, it is more appropriately described as a plasma. With the onset of plasma formation, α_p becomes strongly non-linear with temperature. In this regime and with nanosecond pulse lengths, we can employ the approximation $t_\mathrm{p} \approx t_\mathrm{v} + t_\mathrm{v}^\mathrm{opt}$, where $t_\mathrm{v}^\mathrm{opt}$ is the time for optical breakdown. Here, both t_v and $t_\mathrm{v}^\mathrm{opt}$ are often of the order of a few nanoseconds. With subpicosecond pulses, laser-plasma interactions can be ignored. This follows from the observation that the expansion velocities are $v_\mathrm{v} \lesssim 10^6$ cm/s.

To classifiy the scenario of laser–plasma–substrate interactions, it is convenient to introduce different laser-output intensities that are characterized by their response onto the plasma and the solid surface.

We have already introduced the laser-light intensity which causes significant vaporization of the substrate surface, I_v. The onset of plasma formation shall be

characterized by the intensity $I_p \equiv I_p(\lambda)$. Clearly, no sharp boundaries between these ranges exist. With these definitions, the intensities considered in the previous sections are within $I_v < I \ll I_p$ where absorption of the laser radiation within the vapor/plasma plume can be ignored, in good approximation. With the formation of a plasma, the plume strongly absorbs the laser radiation and shields the substrate. When increasing the intensity above I_p, the plasma plume expands in volume and its forward direction becomes more pronounced (Fig. 11.0.1). If I is even further increased, the plasma decouples from the substrate and propagates towards the incident beam.

Such a plasma is often termed a laser-supported absorption wave (LSAW). The dynamic behavior of LSAW is determined by the laser-light energy absorbed within the plasma plume and the energy loss via heat conduction and via plasma and particle radiation. If the LSAW propagates towards the laser beam with *subsonic* velocity, it is also termed laser-supported combustion wave (LSCW). The propagation velocity of this wave increases with laser-light intensity and reaches the velocity of sound (with respect to the ambient medium) at the intensity I_d. LSAW that propagate with *supersonic* velocity are also denoted as laser-supported detonation waves (LSDW).

Propagating LSAW may result in an *oscillating* behavior of the laser–plasma–substrate coupling. The different ranges of interactions have been extensively described in the literature.

11.6.1 Ionization

Within a gas of temperature T_g, collisions between (thermal) electrons and gas-phase atoms/molecules result in a certain degree of ionisation, ξ. In dynamic *equilibrium*, where the rate of generation is equal to the rate of recombination, ξ is given by the *Saha* equation

$$\frac{\xi^2}{1-\xi} = \frac{K(T_g)}{N_g} = \frac{2g_i}{g_a N_g}\left(\frac{2\pi m_e k_B T_g}{h^2}\right)^{3/2} \exp\left(-\frac{E_i}{k_B T_g}\right) , \qquad (11.6.1)$$

with $\xi = N_e/N_g$ and $N_g = N_e + N_a$. Here, N_e and N_a are the number densities of electrons and atoms/molecules, respectively. In the present form (11.6.1) holds only for single ionization, i.e., with $N_e = N_i$, where N_i is the number of ions. g_i and g_a denote the degeneracy of states for ions and atoms/molecules, respectively. E_i is the ionization energy. For *low* temperatures $\xi \ll 1$ and thus

$$\xi \approx \left[\frac{K(T_g)}{N_g}\right]^{1/2} \approx 5.8 \times 10^{-4} \frac{T_g^{5/4}}{p^{1/2}} \exp\left(-\frac{E_i}{2k_B T_g}\right) , \qquad (11.6.2)$$

with $g_i = 1$ and $g_a = 2$. p (bar) $= N_g k_B T_g$ is the pressure of the gas under consideration, and $N_e N_i = N_e^2 \propto N_a \approx N_g \propto p$. With normal conditions and

low temperatures T_g, the number of 'seed' electrons is usually not determined by (11.6.2) but by impurities that become easily ionized as, e.g., by moisture.

In laser processing, the Saha equation is only of limited value. Here, the laser light may *directly* ionize species via sequential or coherent multiphoton excitation, or via collisions with electrons accelerated within the laser field (impact ionization). With focused and/or pulsed-laser beams, the diffusion of electrons out of the vapor/plasma plume, and the strong non-equilibrium conditions must be taken into consideration.

11.6.2 Optical Properties of Plasmas

The optical properties of a plasma are determined by the complex index of refraction, $\tilde{n} = n + i\kappa_a = \varepsilon^{1/2} = (\varepsilon' + i\varepsilon'')^{1/2}$ (see Sect. 2.2).

For *low* degrees of ionization, typically $\xi \lesssim 10^{-2}$, the absorption coefficient can be derived from the Drude theory if we apply a damping term that is mainly determined by collisions between electrons and neutral atoms/molecules. With increasing ionization, i.e., within the range $10^{-2} < \xi \lesssim 0.3$, we can apply the Kramers–Unsöld equation, in particular in UV-laser processing. For $\xi \approx 1$, absorption by inverse Bremsstrahlung becomes dominant. In the IR, this regime can be described semi-quantitatively by the Drude theory as well, except that damping is now dominated by collisions between electrons and ions.

Drude Model, $\xi \lesssim 10^{-2}$

According to the Drude theory, the dielectric constant is given by

$$\varepsilon = \varepsilon' + i\varepsilon'' = 1 - \frac{\omega_p^2}{\omega^2 + \omega_c^2} + i\frac{\omega_p^2}{\omega^2 + \omega_c^2}\frac{\omega_c}{\omega} , \tag{11.6.3}$$

where ω_c is the frequency of 'collisions' (interactions), mainly between electrons and neutral atoms/molecules. It can be approximated by $\omega_c \approx \sigma_{ev} v_e N_v$, where σ_{ev} is the cross section for electron–neutral collisions and v_e the velocity of electrons. ω_p is the plasma frequency, which is related to the density of electrons

$$\omega_p^2 = \frac{4\pi e^2 N_e}{m_e} = 3.18 \times 10^9 N_e . \tag{11.6.4}$$

While $\omega_c \ll \omega_p$ with most laser-induced plasmas, collisions between electrons and neutrals and/or ions (free–free electron transitions) *are required* for light absorption. With *low* density plasmas, i.e., with $\omega_c \ll \omega_p \ll \omega$, we can use the approximation $\alpha = 2\omega\kappa_a/c \approx \omega\varepsilon''/c$ for the absorption coefficient and thus obtain

$$\alpha_D \approx \frac{\omega_p^2 \omega_c}{c\omega^2} \propto \frac{N_e N_v}{\omega^2} \propto \lambda^2 \tag{11.6.5}$$

and $\mathrm{Re}\,\tilde{n} \equiv n \approx 1$. c is the velocity of light. In the latter approximation we have assumed the frequency of collisions to be proportional to the density of species within the vapor, N_v. Within this range, absorption within the vapor/plasma plume is proportional to λ^2. It should be noted, however, that with VIS and UV radiation the energy of photons is much higher than the energy gained by the electrons within the light field. In such cases, the process should be treated quantum mechanically.

Kramers–Unsöld Equation

For laser parameters that still cause a relatively low degree of ionisation with, typically, $10^{-2} \lesssim \xi < 0.3$, and a large number of highly *excited* atoms/molecules N_a^*, so that $N_\mathrm{a}^* \gg N_\mathrm{e}, N_\mathrm{i}$, photo-ionization of excited atoms/molecules (bound–free electron transitions) becomes important. For hydrogen-like atoms and $\hbar\omega \ll E_\mathrm{i}$ the absorption coefficient can be described by the Kramers–Unsöld equation

$$\alpha_\mathrm{KU} = \alpha_\mathrm{IB} \cdot \exp\left(\frac{\hbar\omega}{k_\mathrm{B}T_\mathrm{p}}\right) \approx 2.43 \times 10^2 \lambda^3 p \left[\exp\left(\frac{\hbar\omega}{k_\mathrm{B}T_\mathrm{p}}\right) - 1\right] \times \exp\left(-\frac{E_\mathrm{i}}{k_\mathrm{B}T_\mathrm{p}}\right), \tag{11.6.6}$$

where α_IB (cm^{-1}) is given by (11.6.7). The second approximation is obtained by employing the Saha equation for low degrees of ionization, (11.6.2). T_p is the temperature and p (bar) the pressure within the vapor/plasma plume; λ (μm) is the laser wavelength. Equation (11.6.6) is of particular importance for UV-laser processing with $\hbar\omega \gtrsim k_\mathrm{B}T_\mathrm{p}$ and low-to-medium laser-light intensities. In this regime, α_KU is dominated by the exponential factor (bound–free transitions). With IR radiation, $\hbar\omega \ll k_\mathrm{B}T_\mathrm{p}$ and $\alpha_\mathrm{KU} \approx \alpha_\mathrm{IB}$, i.e., absorption becomes dominated by inverse Bremsstrahlung.

Inverse Bremsstrahlung

With laser-light intensities that cause a high degree of ionization with $\xi \approx 1$ and laser-light frequencies $\omega > \omega_\mathrm{p}$ the dominating absorption mechanism is *inverse Bremsstrahlung* within the field of the ions. This process is based on free–free electron transitions. The absorption coefficient can then be described by

$$\alpha_\mathrm{IB} \approx C \cdot \lambda^3 \frac{Z^2 N_\mathrm{i} N_\mathrm{e}}{T_\mathrm{p}^{1/2}} \left[1 - \exp\left(-\frac{\hbar\omega}{k_\mathrm{B}T_\mathrm{p}}\right)\right], \tag{11.6.7}$$

where $C \approx 2\sqrt{2}e^6/[3(3\pi)^{1/2}\hbar c^4 m_\mathrm{e}^{3/2} k_\mathrm{B}^{1/2}] \approx 1.37 \times 10^{-35}$ and λ is in μm. Z is the average ion charge. Within the approximations made, equilibrium between electron and ion temperatures is assumed, i.e., $T_\mathrm{p} = T_\mathrm{e} = T_\mathrm{i}$. With thermal equilibrium with respect to ionization, $N_\mathrm{i}N_\mathrm{e}$ can be derived from the Saha equation (11.6.1). For $\xi \approx 1$, we have $N_\mathrm{i}N_\mathrm{e} \approx N_\mathrm{v}^2$. It is important to note that α_IB can be applied to

non-equilibrium situations as well. For IR radiation $\hbar\omega \ll k_B T_p$. In this case, one can expand the exponential function in a Taylor series and (11.6.7) becomes similar to the Drude formula, if ω_c is calculated for electron–ion collisions [*Raizer* 1991]. Equation (11.6.7) takes into account stimulated emission. Additionally, instead of 'collisions' one considers the interaction of the electrons with the laser field in the (non-screened) Coulomb field of the ions. This modifies the expression for ω_c. For UV radiation and $\xi \ll 1$, however, one has to employ the Kramers–Unsöld equation, which takes into account both free–free *and* bound–free electron transitions.

11.6.3 Optical Breakdown

When the intensity approaches a critical value, I_p^{opt}, the laser light becomes increasingly absorbed by inverse Bremsstrahlung and by photo-excitation and photo-ionization of atoms/molecules. These processes increase the number of energetic electrons which can ionize atoms/molecules (impact ionization). This positive feedback results in *avalanche ionization* of the vapor, i.e., in optical breakdown. In the initial phase of optical breakdown, the concentration of electrons increases *exponentially* with time. This phenomenon has been studied mainly with focused, but *freely* propagating laser beams (i.e., in the absence of any targets) within various different atmospheres [*Raizer* 1991].

With *low* gas pressures, the electrons have to gain enough energy within the strong field of the laser to ionize gas-phase species before they escape from the plasma volume. In this regime, the threshold intensity for optical breakdown can be described by

$$I_p^{opt} \approx \frac{m_e c E_i \omega^2}{12\pi e^2 \sigma_{eg}^2 w^2 N_g^2} \propto \frac{\omega^2}{w^2 p^2} \,. \tag{11.6.8}$$

Thus, I_p^{opt} decreases with *increasing* λ, as expected from (11.6.5). Here, and in the following equations, linear polarization of the laser light has been assumed. The typical time for the development of optical breakdown, t_p^{opt}, can be estimated from the rate equation for the electrons, which is similar to (2.4.1). If we ignore recombination, this can be written as

$$\frac{\partial N_e}{\partial t} = \zeta_a I N_e + D_e \Delta N_e \approx \zeta_a I N_e - \frac{D_e N_e}{w^2} \,, \tag{11.6.9}$$

where $\zeta_a = \sigma_a / h\nu$ is the avalanche coefficient and σ_a the corresponding cross section. The first term describes the impact ionization of species by multiple collisions with electrons. With the ansatz $N_e(t) = N_e(0) \exp(t/t_e)$, we obtain

$$t_e = \left[\frac{D_e}{w^2} \left(\frac{I}{I_p^{opt}} - 1 \right) \right]^{-1} \,, \tag{11.6.10}$$

with an initial electron density $N_e \approx 10^6\,\mathrm{cm}^{-3}$ (in air, at normal conditions, $N_e \approx 10^3\,\mathrm{cm}^{-3}$) and complete ionization at 1 atm, i.e., $N_e \approx 10^{19}\,\mathrm{cm}^{-3}$, we find

$$t_p^{opt} \approx t_e \ln 10^{13} \approx 30 t_e(I) \; . \tag{11.6.11}$$

With *high* pressures, the electron energy losses are mainly due to collisions with atoms, and not due to electron escape. In this regime one obtains

$$I_p^{opt} \approx \frac{m_e^2 c \omega_c^2 E_i}{2\pi m_g e^2} \propto p^2 \; , \tag{11.6.12}$$

where m_g is the mass of atoms/molecules within the gas, and $\omega_c = \sigma_{eg} v_e N_g$. The turnover from (11.6.8) to (11.6.12) occurs at a pressure where these intensities are about equal. With laser-light frequencies that permit *direct* single- and/or multiphoton ionization (MPI) of species, I_p^{opt} *decreases* with increasing ω (decreasing λ).

Experimentally, typical values of I_p^{opt} in *clean* air at atmospheric pressure are about $10^{11}\,\mathrm{W/cm^2}$ for ruby-laser radiation and about $2 \times 10^9\,\mathrm{W/cm^2}$ for CO_2-laser radiation for spot sizes $2w = 0.1$ mm [*Raizer* 1991]. These intensities are by about two to three orders of magnitude *higher* than the corresponding breakdown intensities, I_p, observed in front of solid or liquid targets. This is due to the following facts:

- Electron and ion emission from the target.
- The temperature increase near a target, as compared to in a gas.
- The lower average energy for ionization of the hot and dense vapor.
- Local enhancements of the surface electric field due to surface roughnesses.
- The increase in local electric field due to the reflection of the radiation from the target.

For laser ablation with nanosecond pulses, the mechanism underlying (11.6.12) is probably dominant. This is due to the high vapor pressure caused by the ablated species, which is, typically, in excess of 10^2 atm. With femtosecond pulses, optical breakdown due to multiphoton absorption within the *ambient gas* in front of the target enhances the thermal energy coupling to the substrate [*Bulgakova* et al. 2008] (Chaps. 13 and 30).

Experimental Examples

Laser-induced plasma formation plays an important role in metal processing, in particular with IR radiation. Because of the high reflectivity of metals in the IR, efficient coupling of the laser-light energy to the substrate is only mediated via the plasma.

Figure 11.6.1 shows this effect for the example of steel. Here, the reflectivity is plotted versus the intensity of CO_2-laser radiation. At low intensities, the reflectivity corresponds to that of steel. With increasing surface temperature, R decreases as

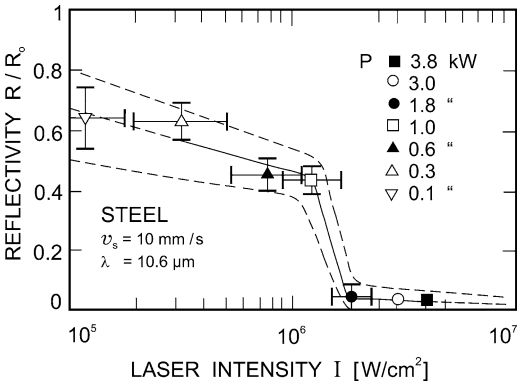

Fig. 11.6.1 Reflectivity as a function of CO_2-laser-beam intensity and different laser powers. The strong drop in reflectivity is due to plasma formation [*Herziger* and *Kreutz* 1986]

with most metals (Sect. 7.3). Near the intensity $I \approx I_p$ a sharp drop in reflectivity occurs. The CO_2-laser radiation now becomes strongly absorbed within the laser-induced plasma. The figure shows that I_p is some $10^6\,W/cm^2$. For Nd:YAG-laser radiation plasma formation in front of metal targets is observed at laser-light intensities of some $10^8\,W/cm^2$. These values are lower than those obtained in clean air, by roughly two to three orders of magnitude. Additionally, the threshold intensity for optical breakdown near material surfaces is often described more properly by $I_p \propto \omega$.

Because of the short times involved in the generation of the plasma and because of the avalanche-type increase in carrier concentration, the absorptivity rises almost instantaneously and, with certain experimental conditions, can reach a value near unity. This range of strong plasma absorption is employed in particular in metal processing (Sect. 11.8), and it has been investigated for a large number of different materials and a wide range of laser wavelengths [*Prokhorov* et al. 1990].

11.7 Laser-Supported Absorption Waves (LSAW)

If the laser-light intensity is increased well above I_p, the expansion of the plasma plume towards the direction of the incident laser beam becomes increasingly pronounced. With even higher laser-light intensities, an oscillating behavior of the laser–plasma–substrate coupling is observed. Subsequently, we discuss the dynamic behavior of LSAW for different regimes.

11.7.1 Laser-Supported Combustion Waves (LSCW): $I_p \leq I \leq I_d$

We first consider an intermediate regime where the laser-light intensity is high enough to cause optical breakdown within the gas/vapor in front of the substrate,

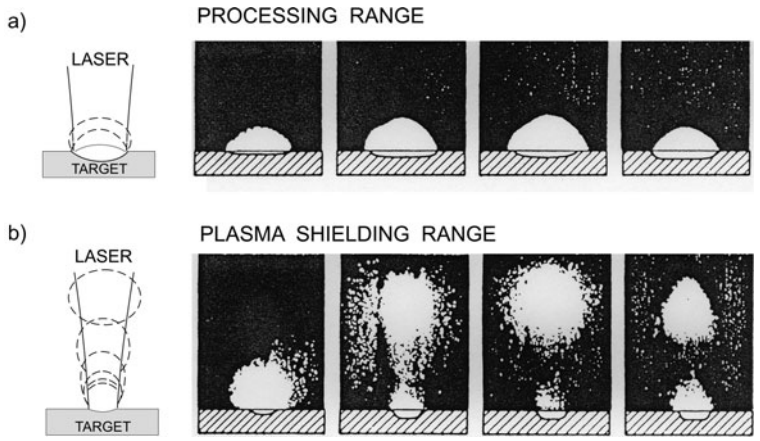

Fig. 11.7.1 a, **b** Development of a plasma in front of a steel target irradiated by 10.6 μm CO_2-laser light (TEM_{00}). The figure shows selected regimes (temporal distance 50 ns) of high-speed photography. (**a**) Intensity range employed in most types of laser machining. (**b**) Plasma-shielding range [*Herziger* and *Kreutz* 1984]

but too low for to generate a detonation wave. This is the regime of LSCW. Here, the laser radiation is absorbed within a large volume of the plasma plume.

With laser-light intensities just above I_p, the plasma is confined to a region near the surface. This is shown in Fig. 11.7.1a for CO_2-laser radiation and steel. This intensity regime is employed in most types of laser machining. Here, the temperature of the plasma is, typically, of the order of $T_p \approx 10^4$ K (≈ 1 eV). If the intensity is increased, the plasma plume expands towards the laser beam; nevertheless, it remains stationary. The spreading of the plasma increases the width of the temperature distribution on the substrate with respect to that which would be induced with the same laser focus in the absence of the plasma. Thus, the interaction of the laser radiation with the solid via the plasma reduces the spatial resolution.

If the intensity reaches some critical value, typically $10^7\,\mathrm{W/cm^2} < I_{cr} < 10^{10}\,\mathrm{W/cm^2}$, depending on the wavelength, the laser light is essentially absorbed within the plasma and does not reach the substrate. This is the range of *plasma shielding*. Here, the coupling of the plasma to the substrate can become so weak that energy transfer is interrupted and, as a consequence, laser-induced material vaporization ceases. Then, the plasma decouples from the substrate surface (Fig. 11.7.1b). Due to the propagation and expansion of the plasma plume, the laser-light intensity on the substrate surface increases again, until plasma ignition is restarted.

When the incident laser-light energy is strongly absorbed within the plasma, it only just increases the internal energy of the plume. This energy is dissipated into the ambient medium via heat conduction and thermal radiation and, in part, it is converted into the kinetic energy of the hydrodynamic motion of the plume. The simplified energy balance yields [*von Allmen* and *Blatter* 1995]

$$\kappa_{\text{eff}} \frac{T_\text{p}}{l} \approx A_\text{p} I - J_\text{L} l \approx (\alpha_\text{p} I - J_\text{L}) l \ , \tag{11.7.1}$$

where κ_{eff} is an effective transport coefficient which describes both heat conduction and thermal radiation, i.e., $\kappa_{\text{eff}} \approx \kappa_\text{g} + \kappa_\text{r}$. In this regime, the temperature of the plasma is, typically, $T_\text{p} \approx (0.5-2) \times 10^4$ K. J_L includes all energy losses. $l \approx l_\text{T} = D_\text{p}/v_\text{cw}$ is the heat diffusion length [see (11.2.14)]. D_p is the thermal diffusivity, and v_cw the propagation velocity of the LSCW towards the laser beam. For laser-light intensities well above the critical intensity, v_cw is determined by heat conduction from the hot plasma to the cold gas of the medium ahead of the plume. From (11.7.1) one obtains

$$v_\text{cw} \approx D_\text{p} \left(\frac{\alpha_\text{p} I - J_\text{L}}{\kappa_{\text{eff}} T_\text{p}} \right)^{1/2} \propto I^{1/2} \ . \tag{11.7.2}$$

Any shock wave generated in this intensity range travels far ahead of the front of ablated material (Sect. 30.3). LSCW are similar to combustion waves observed with (self-sustained) exothermal chemical reactions where $v_\text{cw} \propto \Delta H^{1/2}$ (ΔH is the reaction enthalpy).

For intensities $I \approx I_\text{cr}$, the absorbed laser-light energy just balances the energy losses, i.e., $\alpha I = J_\text{L} \approx \kappa_{\text{eff}} T_\text{p}/w^2$. The approximation assumes losses in radial direction only and ignores the kinetic energy of the hydrodynamic motion. I_cr can be shifted to higher intensities by increasing κ_{eff}. This can be achieved by appropriate changes of the ambient atmosphere, for example, the admixture of He. With $v_\text{cw} \approx 0$, the LSCW become stationary. Such stationary plasmas are frequently denoted as *plasmatrons*. They can be generated within focused laser beams even in the absence of any target. With cw CO_2 lasers, stationary temperatures within the plasmatron of, typically, 2×10^4 K can be achieved. This temperature is higher than that obtained, for example, with microwave (up to 6×10^3 K) or RF ($\approx 1 \times 10^4$ K) discharges.

11.7.2 Laser-Supported Detonation Waves (LSDW): $I \geq I_\text{d}$

At higher laser-light intensities, e.g., with CO_2 lasers and $I > 10^8\,\text{W/cm}^2$, the ablated material propagates with supersonic velocity towards the laser beam and drives a shock wave into both the ambient medium *and* the substrate material.

An ambient gas within the region ahead of the expanding vapor becomes strongly compressed, heated, and ionized. As a consequence a shock wave is formed. The velocity of the shock wave in the ambient is about equal to the velocity of the ionization front. The plasma frequency, ω_p, can exceed the laser-light frequency, ω. Then, we find from (11.6.3) that $\varepsilon' < 0$, i.e., the plasma becomes metal-like, i.e., it reflects strongly, and partly absorbs the laser radiation within a thin layer at the shock-wave/ionization front. Additional heating within this front is caused by the UV radiation of the plasma. The temperature can reach more than 10^5 K (≈ 10 eV)

and explosive propagation of the plasma with supersonic velocity is observed. This is denoted as a LSDW.

In the case of large-area irradiation, the velocity of this detonation wave can be approximated by [*Zeldovich* and *Raizer* 1966]

$$v_{\mathrm{dw}} \approx \left(2(\gamma^2-1)\frac{I}{\varrho_{\mathrm{g}}}\right)^{1/3} \propto I^{1/3}\,, \tag{11.7.3}$$

where $I \gg I_{\mathrm{p}}$. The adiabatic coefficient is $\gamma \approx 5/3$; ϱ_{g} is the density of the ambient medium. With $I = 10^9\,\mathrm{W/cm^2}$ and air at standard conditions ($\varrho_{\mathrm{g}} \approx 1.3\times10^{-3}\,\mathrm{g/cm^3}$) we obtain $v_{\mathrm{dw}} \approx 3\times10^6\,\mathrm{cm/s}$. The pressure just behind the detonation wave (11.7.3) can be approximated by

$$p_{\mathrm{dw}} \approx \frac{2\varrho_{\mathrm{g}} v_{\mathrm{dw}}^2}{\gamma+1} \propto I^{2/3}\,. \tag{11.7.4}$$

With the above parameters, we obtain $p_{\mathrm{dw}} \approx 10^4\,\mathrm{bar}$. Almost the same pressure acts upon the substrate surface.

The intensity regime under consideration is employed with special applications as, for example, in shock hardening (Chap. 23). Shock waves also play an important role in many cases of pulsed-laser ablation and material fragmentation.

11.7.3 Superdetonation

At very high laser-light intensities, typically, $\geq 10^9\,\mathrm{W/cm^2}$, new phenomena are observed. The ionization front propagates *ahead* of the shock wave. The reason is that species in front of the shock wave are first excited by the UV-plasma radiation and subsequently ionized by the laser light. This process is much faster than ionization via electron impact. The velocity of such fast ionization waves can be described by

$$v_{\mathrm{sd}} \propto I^n\,,$$

with $n > 1$ [*Fisher* and *Kharash* 1982]. The properties of ionization waves depend on the laser parameters and on the type and pressure of the ambient gas. v_{sd} can reach values of some $10^9\,\mathrm{cm/s}$. Due to the (non-thermal) excitation of species by the UV-plasma radiation, the temperature within the plume scales *inversely* with laser-light intensity, i.e., $T \propto I^{\beta}$, with $\beta < 0$.

The intensity regime considered in this subsection is applied for the generation of pulsed X-rays and fast ions.

11.8 Abrasive Laser Machining

Applications of laser-induced (quasi-stationary) vaporization include drilling, cutting, scribing, and shaping of materials, and also some types of trimming, engraving, marking, paint stripping, surface cleaning, etc. These applications have been described extensively in the literature [*Hügel* and *Graf* 2009; *Landolt-Börnstein* 2004; *Steen* 2003; *Schuöcker* 1999; *Ready* 1997; *Duley* 1983, 1976]. A field that becomes increasingly important is the laser machining of strongly *heterogeneous* materials. Among those are compound materials, stacks of different materials consisting, e.g., of sheets of metals and non-metals, etc.

The laser sources most commonly used in abrasive laser machining are CO_2 lasers, Nd:YAG lasers and, with some of the applications, diode lasers [*Bachmann* et al. 2007]. The laser-beam intensities employed depend on the laser wavelength. For CO_2-laser radiation they are, typically, between some 10^3 W/cm^2 and some 10^8 W/cm^2 (Fig. 1.1.2).

Laser *microprocessing* of metals and non-metals based on nanosecond, picosecond, and femtosecond pulsed-laser ablation is discussed in Chaps. 12 and 13.

11.8.1 Cutting, Drilling, Shaping

Laser machining frequently requires laser-induced melting only (Sect. 10.7). However, with many materials, and in particular with metals, efficient coupling of the laser-light energy to the substrate is mediated only via the generation of a plasma.

The energy flux onto the substrate surface is then determined by the laser-light intensity penetrating the plasma plume, and the net amount of energy transferred from the plasma. Important mechanisms of energy coupling between the plasma and the substrate are as follows:

- Heat conduction. This is governed by the density and mean free path of electrons within the plasma plume.
- Plasma radiation. This contains a wide spectrum of frequencies, including UV radiation, which is strongly absorbed by metals; it may even exceed the energy which would be directly absorbed from a CO_2 laser in the absence of the plasma. The situation can be different with an insulator when this has a strong dispersion oscillator whose frequency coincides with the CO_2-laser frequency (Fig. 7.2.4).
- Particle bombardment and condensation. Both contribute to the thermal energy available for substrate processing.

A proper estimation of the total energy absorbed by the substrate must consider all of the various contributions. From an experimental point of view, efficient plasma-enhanced coupling is observed as long as the plasma plume stays close to the surface (Fig. 11.7.1).

Metals strongly reflect IR- and VIS-laser radiation (Table III). Thus, efficient processing becomes possible only via strong plasma absorption. This is the reason

why laser machining of metals such as drilling, cutting, shaping, deep-penetration welding, etc., but also some laser-induced surface transformations, in particular surface alloying, are often performed in this regime.

For materials cutting, the maximum scanning velocity depends, for fixed laser parameters and a particular material, on the thickness of the workpiece, h_s. In the simplest approximation, the cutting speed can be estimated from the energy balance (11.1.1). If we assume, for example, a cw-laser beam of focus $2w$ and a scanning velocity v_s, the dwell time of the laser beam is $\tau_\ell \approx 2w/v_s$. With $\Delta h \equiv h_s$, (11.1.1) yields

$$v_s^{\max} \leq \frac{AP - P_L}{dh_s \Delta H} , \tag{11.8.1}$$

where $d \leq 2w$ is the *kerf width*, which is, typically, a few millimeters. ΔH is the total enthalpy. A similar approximation is obtained from the equations given in Sect. 8.1. More refined estimations for keyhole-like cutting and welding (Fig. 10.6.1b) based, e.g., on the Rosenthal solution, permit one to study the dependence of the kerf width on cutting velocity, $d = d(v_s)$, etc. [*Hügel* and *Graf* 2009; *Steen* 2003]. In many cases of abrasive laser machining, however, the laser beam is used in combination with a gas jet. The role of this jet can be twofold: it expels the liquefied material (Fig. 10.7.1), and it may also induce an exothermic reaction which can provide a significant amount of energy to the area being processed.

With a typical setup employed for laser cutting of metals in combination with an oxygen gas jet, the exothermal energy delivered by the oxidation reaction contributes about 60% (stainless steel) to 90% (Ti) to the total energy. Thus, with unchanged laser parameters, the cutting speed can be significantly increased. Figure 11.8.1 shows v_s for stainless steel as a function of plate thickness for several laser powers. The dependence shown in the figure is qualitatively described by (11.8.1). With many applications, however, reactive gases cannot be used because of their influence on material properties. In metal-sheet processing with kW CO_2 lasers, cutting speeds in excess of 10^2 cm/s and positioning speeds of up to 10^3 cm/s are achieved.

Figure 11.8.2 shows drilling velocities for Al, Cu, and steel as a function of Nd:YAG-laser-light intensity. The drilling velocity rises steeply just above the threshold for ablation and saturates at higher intensities. Here, the plasma determines the efficiency and quality of the process. Typical velocities achieved in cw-/single-pulse laser drilling of metals are between a few cm/s and some 10^3 cm/s.

Other types of drilling technique employ a sequence of pulses. By removing smaller material volumes per pulse, the quality of holes is improved. Multiple-pulse laser drilling is also denoted as percussion drilling. The best results concerning the roundness and aspect ratio of holes, in particular in microfabrication, is the trepanning technique. Here, the laser beam is rotated and translated with respect to the workpiece. By this means, the quality of holes becomes less dependent on beam profile.

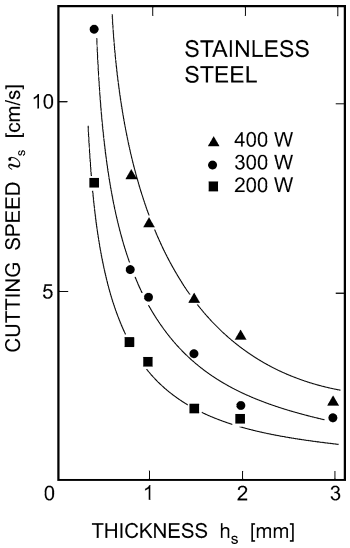

Fig. 11.8.1 Cutting speed versus thickness of stainless steel slabs for CO_2-laser radiation in combination with an oxygen gas jet (diameter of nozzle 1.2 mm; flow rate 20 normal liters per minute). Adapted from [*Sona* 1987]

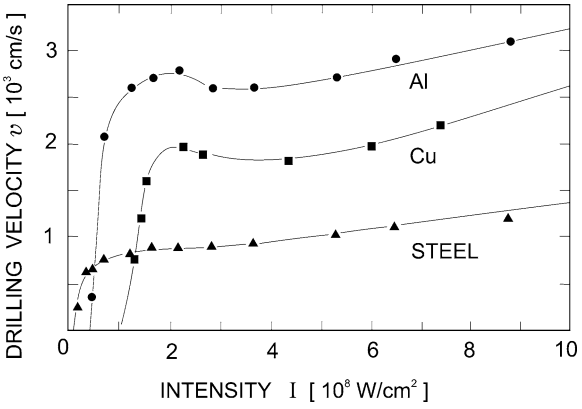

Fig. 11.8.2 Drilling velocity as a function of Nd:YAG-laser-light intensity ($\lambda = 1.06\,\mu m$) for different metals [*Herziger* and *Kreutz* 1984]

11.8.2 Non-metals

Laser machining has also been investigated for a large number of non-metals Among those are semiconductors, inorganic insulators, organic materials, etc. Many of these materials, e.g., some types of ceramics and organic polymers, but also textile, paper and wood, show *no* pronounced melt phase or even sublimate only. In such cases, abrasive processing with IR-laser radiation is based mainly on

material decomposition and evaporation of fragments. Here the laser-beam intensities employed are $10^5\,\mathrm{W/cm^2} < I < 10^9\,\mathrm{W/cm^2}$.

The cutting speeds achieved with 0.5 kW cw-CO_2-laser radiation and a kerf width of about $d \approx 0.2$ mm are, typically, between a few cm/s and some 10^3 cm/s (SiO_2, $h_s \approx 2$ mm, $v_s \approx 2$ cm/s; mylar, $h_s \approx 0.03$ mm, $v_s \approx 5 \times 10^2$ m/s ; textile, 0.5 g/m^2, $v_s \approx 10^2$ m/s; newsprint paper, $v_s \approx 10^3$ m/s). Depending on the material and the specific experimental conditions, the width of the damaged zone is some ten to several 10^3 µm wide. With many of these applications, diode lasers are increasingly used.

11.8.3 Scribing, Marking, Engraving

With brittle materials like silicon, ceramics, glasses, etc., scribing is an alternative to cutting. In this technique, shallow grooves or patterns of blind holes are fabricated within the surface of the material, mainly by laser-induced vaporization. The depth of grooves/holes is, typically, $h < h_s/4$. Subsequently, the workpiece can be mechanically broken into segments. Compared with direct (full penetration) cutting, laser scribing requires less energy (about a factor of 10–50 less), it is a fast and clean process with a small heat-affected (damaged) zone (HAZ), and it produces only little debris. The quality of edges is satisfactory for many applications, e.g., the fabrication of chips from silicon wafers.

Another technique is laser-induced controlled *fracture*. Here, the laser heats the small interaction volume within the substrate. Rapid heating/cooling causes stresses that may result in local crack formation. By this means, some types of brittle materials can be separated without significant material removal. The process is extremely fast, cheap, and clean. However, this process is presently hardly used because of problems with uncontrolled fracturing.

Laser *marking* and *engraving* are widely used for logos, product identification, or for functional informations, e.g. on cables, electronic or medical devices, etc. Laser marking can be based on material evaporation, ablation (Chaps. 12 and 13), etching (Chaps. 14 and 15), physical and/or chemical material transformations, including foam formation (Chaps. 23 and 27), etc. [*Faißt* 2008]. Marking can be performed by direct writing, by projection patterning, or by means of a contact mask (Sect. 5.2.1). Non-erasable laser marking *within* the volume (bulk) of transparent materials is described in Sect. 23.6.

11.8.4 Comparison of Techniques

The advantages of laser cutting, drilling, and shaping based mainly on material *evaporation* (vaporization cutting) include smooth material edges (no or little solidified melt structure), and a relatively small extension of the transformed (e.g., oxidized) surface and the HAZ. Among the disadvantages are the high laser-light

intensities required, problems in process control, and the relatively low processing velocities.

The advantage of abrasive laser machining based mainly on material *melting* (Sect. 10.7) is the much lower energy consumption. For *non-reactive* liquid-phase expulsion the power required is by about a factor of 2–10 lower than in vaporization cutting. Thus, for a certain laser-beam intensity, much higher processing velocities can be achieved. Disadvantageous are the lower quality in surface morphology and, in general, the wider extension of the HAZ.

Abrasive laser processing based on material melting and *liquid-phase* expulsion by a reactive gas (reactive fusion cutting) yields the highest processing velocities and permits cutting of thick metal slabs. Disadvantageous is the transformation of the material surface, e.g., by oxidation, the wide extension of the HAZ and, quite frequently, an even lower quality in surface morphology than in melt-phase processing using an inert gas atmosphere.

Chapter 12
Nanosecond-Laser Ablation

Material removal caused by short high-intensity laser pulses is often termed pulsed-laser ablation (PLA). Throughout the literature, the terms laser-assisted evaporation, laser sputtering and, wrongly, laser etching, are also used. Within the regime under consideration, material removal takes place far from equilibrium and may be based on thermal or non-thermal microscopic mechanisms. For this reason, we will prefer the term laser ablation, which is less suggestive with respect to the fundamental mechanisms involved in the process. PLA permits one to widely suppress the dissipation of the excitation energy beyond the volume that is ablated during the pulse. For nanosecond pulses, this is fulfilled if the thickness of the layer ablated per pulse, Δh, is of the order of the heat penetration depth, $l_\mathrm{T} \approx 2(D\tau_\ell)^{1/2}$, or the optical penetration depth, $l_\alpha = \alpha^{-1}$, depending on which is the larger, i.e.,

$$\Delta h \approx \max\{l_\mathrm{T}, l_\alpha\} \; . \tag{12.0.1}$$

This (simplified) condition is, in fact, the basic requirement for applications of the technique.

Laser ablation has been demonstrated to be a powerful tool in micropatterning of hard, brittle, and heat-sensitive materials, and in the fabrication of thin films with complex stoichiometry. The latter technique is termed pulsed-laser deposition (Chap. 22). It is evident that (12.0.1) is a crude estimation. Because of the fast heating and cooling rates achieved with pulsed lasers, material damage or material segregation in multicomponent systems can often be ignored even in cases where the ablated layer thickness is considerably smaller than the value obtained from (12.0.1). With many materials, (12.0.1) can be reasonably well fulfilled with UV-laser light and nanosecond pulses. With VIS- and IR-laser radiation, this condition is often more difficult to fulfill because of the lower absorption observed with many materials at longer wavelength. Additionally, with increasing wavelength, laser–plasma interactions become more pronounced; these result in plasma shielding, oscillations in the energy–substrate coupling, etc. (Chap. 11). With both longer wavelengths and enhanced laser–plasma interactions, the resolution achieved in micropatterning decreases.

With certain materials, nanosecond laser pulses are too long for high-quality and high-resolution surface patterning. Among those are metals, many semiconductors,

D. Bäuerle, *Laser Processing and Chemistry,* 4th ed.,
DOI 10.1007/978-3-642-17613-5_12, © Springer-Verlag Berlin Heidelberg 2011

thin films of high-temperature superconductors, etc. Because of the high thermal conductivity of these materials, (12.0.1) can be well fulfilled only with picosecond- or femtosecond-laser pulses. A similar problem arises with materials whose bandgap energy, E_g, exceeds the photon energy of the UV-laser sources presently available. In such cases $l_\alpha \gg \Delta h$, and (12.0.1) cannot be fulfilled. An exception is materials in which the laser radiation itself generates defects (incubation centers) that, in turn, absorb the laser light. Other wide-bandgap materials, e.g., glasses such as a-SiO_2, are quite stable even to ArF-laser radiation. However, well-defined patterning of such materials has been demonstrated with picosecond and femtosecond laser pulses. With ultrashort laser pulses the linear optical properties of materials become less relevant. Due to multiphoton absorption, (linearly) transparent materials can be precisely patterned with subwavelength resolution (Chap. 13).

Because PLA preserves the stoichiometry during the ablation process (this is known as congruent ablation), this technique, in combination with an optical spectrometer and a mass spectrometer, can be used for chemical analysis of multicomponent materials by LIBS and MALDI, respectively (Sect. 30.1).

The present chapter summarizes experimental results and theoretical models that apply mainly to nanosecond-laser ablation. Tabular presentations of previous investigations can be found in [*Bäuerle* 2000, 1996, 1986]. The regime of *ultrashort*-pulse laser ablation is discussed in Chap. 13.

12.1 Surface Patterning

The efficiency of material removal under the action of laser light is described by the *ablation rate*. This is defined by the *total* layer thickness ablated per laser pulse, $W_A \equiv \Delta h$ (μm/pulse), by the *average* ablation velocity per pulse, $v \equiv \Delta h/\tau_\ell$ (μm/s), or by the ablated volume per pulse, $W_A \equiv \Delta m/\varrho$ (μm^3/pulse), where Δm is the mass loss. W_A depends on the photon energy, fluence, pulse length, and width of the laser focus, the heat or optical penetration depth, the enthalpy of vaporization, internal stresses, the type and pressure of the ambient atmosphere, etc. If incubation and/or structure formation and/or changes in the chemical composition become important, or if deep holes or grooves are fabricated, W_A becomes dependent also on the number of laser pulses, N_ℓ.

Surface patterning by PLA can be performed by focusing the laser light onto the substrate by means of a single lens or a microlens array, by direct masking, by laser-light projection, interference, or by laser-SXM techniques (Sect. 5.2.1). In contrast to most conventional techniques, laser ablation permits one to pattern or to shape *non-planar* workpieces.

Significant material ablation is observed only if the laser fluence, ϕ, exceeds a certain threshold fluence, ϕ_{th}. The fluences employed in surface patterning are above the ablation threshold, $\phi > \phi_{th}$, and they are, typically, between 0.1 J/cm^2 and several J/cm^2, depending on the particular material and laser parameters. The corresponding ablation rates are between some 0.01 μm/pulse and several

μm/pulse. The physical properties required for estimating the thermal and optical penetration depth are listed in Tables II and III for various materials.

Among the *inorganic* materials where patterning by PLA is advantageous are oxidic perovskites, perovskite-related oxides including high-temperature superconductors (HTS), and glasses.

Figure 12.1.1 shows scanning electron microscope (SEM) pictures of patterns fabricated in ceramic $PbTi_{1-x}Zr_xO_3$ (PZT) by XeCl-laser radiation. The top surface next to the groove shows agitation due to radiation from the low fluence tail of the line focus and/or the laser-induced plasma. In the vicinity of groove walls, no changes in morphology or any material transformations have been detected. The pattern shown in Fig. 12.1.1b was produced by scanning a line focus over the directly masked sample surface. A contact mask permits one to avoid laser-induced surface damage.

Patterning by laser-light projection is demonstrated in Fig. 12.1.2. The bottom of the hole produced in $LiNbO_3$ is very smooth and almost no damage around the hole, apart from an approximately 1-μm-thick brittle layer at the rim, can be detected. Patterns of similar quality have also been produced in other materials. Figure 12.1.2b shows a HTS film which was patterned by KrF-laser-light projection. The deepening at the edge of the hole in (a) and the fringes near the bar in (b) originate from Fresnel diffraction. Clearly, arbitrary shapes of holes (rectangular, triangular, etc.) and patterns can be fabricated by employing a corresponding mask, eventually together with beam shaping in order to utilize the laser light most efficiently.

Figures 12.1.2c, d show a micro-lens-tipped optical fiber and a diffraction grating fabricated by F_2-laser radiation in combination with a mask. In the former case the beam was shaped by mask projection and at perpendicular incidence to the rotating fiber [*J. Li* et al. 2007].

Among the *organic polymers* studied in most detail are PET (polyethyleneterephthalate [Mylar]), PI (polyimide), PMMA (polymethyl-methacrylate), and PTFE (polytetra-fluorethylene [Teflon]). The chemical structures of these polymers

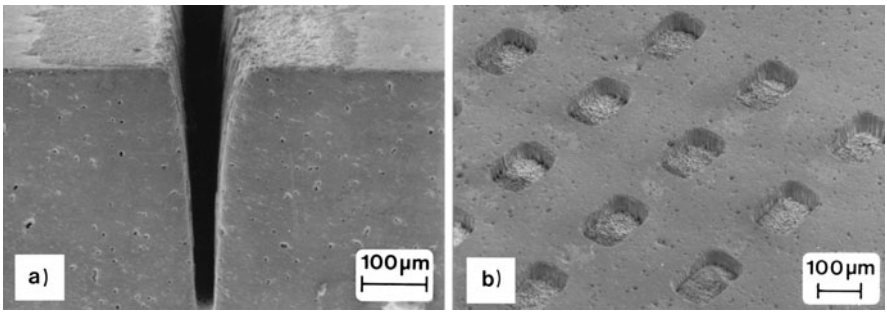

Fig. 12.1.1 a, b SEM pictures showing different patterns produced on ceramic PZT by means of 308 nm XeCl-laser radiation ($\tau_\ell \approx 15$ ns). The groove in (**a**) was obtained with a *stationary* line focus ($\phi = 10.8\,\mathrm{J/cm^2}$, $w = 50\,\mu\mathrm{m}$, $N_\ell = 4 \times 10^3$, pulse repetition rate, $\nu_\mathrm{r} = 5$ Hz). (**b**) Line focus scanned perpendicular to directly masked sample ($\phi = 15\,\mathrm{J/cm^2}$, $\nu_\mathrm{s} = 0.84\,\mu\mathrm{m/s}$) [*Eyett* et al. 1987]

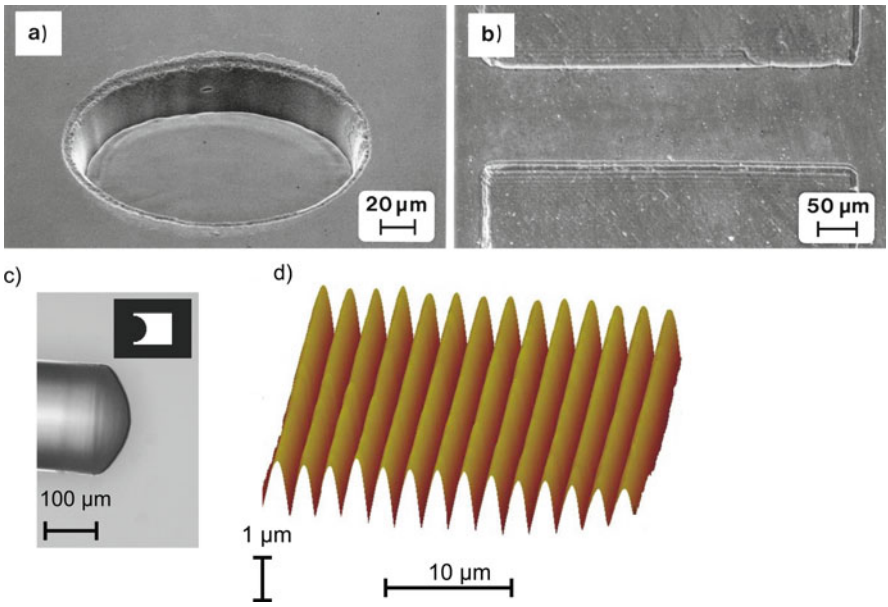

Fig. 12.1.2 a, b, c, d Projection patterning by excimer-laser ablation. (**a**) Single-crystalline $LiNbO_3$ ($\lambda = 308\,\text{nm}$, $\phi = 2.7\,\text{J/cm}^2$, $2w = 175\,\mu\text{m}$, $N_\ell = 500$; vacuum) [*Eyett* and *Bäuerle* 1987]. (**b**) $YBa_2Cu_3O_7$ film on (100) $SrTiO_3$ substrate ($\lambda = 248\,\text{nm}$, $\phi \approx 1.5\,\text{J/cm}^2$, $\tau_\ell \approx 17\,\text{ns}$; $h_1 \approx 0.1\,\mu\text{m}$) [*Heitz* et al. 1990]. (**c**) Micro-lens-tipped optical fiber shaped by 157 nm F_2-laser radiation. The surface roughness is 30 nm rms (**d**) AFM image of part of a diffraction grating fabricated on the end facet of a multimode silica optical fiber [*J. Li* et al. 2007]

are shown in Fig. 12.1.3. A comprehensive overview including various chemical aspects of different polymers and their ablation behavior is given by *Lippert* (2005).

Figures 12.1.4 and 12.1.5 show examples for the ablation of organic materials. The pattern of holes in PI was fabricated by using a microlens array together with single-pulse KrF-laser radiation (Fig. 12.1.5). The technique permits large-area parallel processing. Furthermore, in comparison to holes fabricated by means of a high-quality lens, much higher aspect ratios can be achieved. This phenomenon is related to the small intensity variation over the 'long focus' that is caused by spherical aberration (Fig. 5.3.5).

At present, the fields of real and potential applications of nanosecond PLA can be summarized as follows:

- Surface patterning of materials that cannot, or only very inefficiently, be patterned by means of standard techniques [*Ihlemann* et al. 2008; *Pedarnig* et al. 2005a; *Peruzzi* et al. 2004; *Eyett* and *Bäuerle* 1987; *Eyett* 1987].
- Fabrication of microholes and grooves with variable aspect ratios for ink-jet printers, sensors, microfluidic devices, etc.
- Components for micromechanical devices, motors, sensors, etc. (Fig. 12.1.4a).

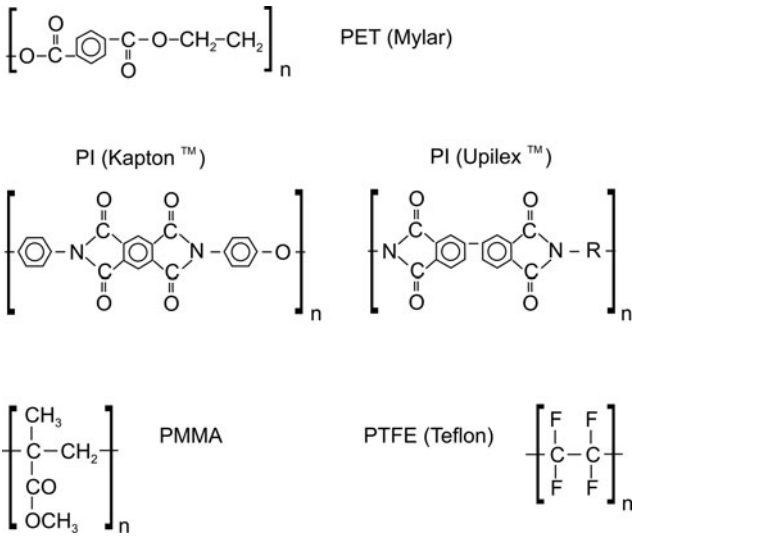

Fig. 12.1.3 Chemical structures of some synthetic polymers. PET (polyethylene-terephthalate; Mylar). PI (polyimide; Kapton is a Du Pont TM; Upilex is a Ube TM). PMMA (polymethyl-methacrylate; Plexiglas, Lucite). PTFE (polytetra-fluoroethylene; Teflon)

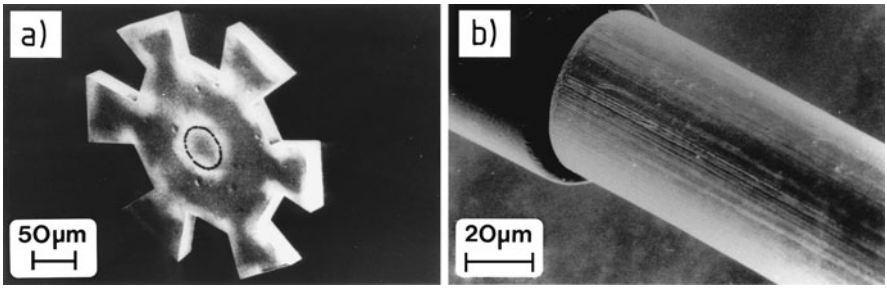

Fig. 12.1.4 (**a**) Microgear fabricated from a PI foil by 248 nm KrF-laser-light projection [*Endert* et al. 1995]. (**b**) A 50 µm Cu wire with the insulation stripped off by KrF-laser ablation [*Lambda-Physik*, Industrial Report, Nov. 1994]

- Fabrication of microoptical devices such as micromirrors [*Böhm* et al. 2006; *Gigan* et al. 2006], fiber optical devices [*Dou* et al. 2008; *J. Li* et al. 2007], etc.
- Formation of surface-relief gratings, graded transmission dielectric masks, metal foil and thin films masks [*Bekesi* et al. 2008; *Ihlemann* et al. 2003], etc.
- Fabrication of optoelectronic devices such as waveguides.
- Via formation (for vertical interconnections) for semiconductor device fabrication, e.g. thin-film packaging of multichip modules (MCM), fabrication of high-power transistors [*O. Krüger* et al. 2007], etc.
- Formation of holes with shallow wall angle in passivation layers on semiconductors wafers [*Wolbold* et al. 1997].

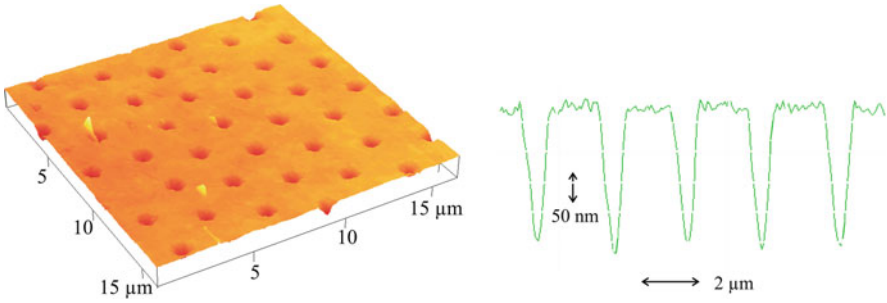

Fig. 12.1.5 Holes produced by local KrF-laser-induced ablation of PI (polyimide) using a 2D-lattice of a-SiO_2 microspheres ($d = 3 \pm 0.15\,\mu m$). The (uncorrected) depth profile was measured by means of an AFM [*Bäuerle* et al. 2002]

- Micromachining of thin films for applications in solar cells fabrication [*Bovatsek* et al. 2010; *Green* 2009; *Haas* et al. 2008; *Pfleging* et al. 2000; see also Sect. 11.8.3], nanotechnology [*Guo* et al. 2007] etc.
- Wirestripping (Fig. 12.1.4b).
- Marking.
- Surface cleaning from particulates and contamination layers (Sect. 23.7).
- Different types of trimming.
- Link cutting, in particular in redundancy technology.
- Certain types of lithography (Sect. 27.2).
- The fabrication of masters which are subsequently used for economic replication by standard techniques. Such masters are, e.g., masks or real 3D structures. Among those are moulding tools fabricated by direct laser patterning [*Pfleging* et al. 2003b] or by laser LIGA (Sect. 27.4).
- Laser plasma thrusters [*Fardel* et al. 2009].

An overview on the applications of laser ablation in medicine and biotechnology is given in Chap. 31.

12.2 Ablation Mechanisms

Nanosecond-laser ablation has been analyzed on the basis of thermal, mechanical, photophysical, photochemical, and defect models. Almost all of these models try to describe ablation by a single dominant mechanism. For this reason, each of these models permits one to analyze experimental results only for a particular material and within a narrow range of parameters. A more general description requires simultaneous consideration of the different interaction mechanisms and the coupling between them. Let us discuss this in further detail by means of the block diagram shown in Fig. 12.2.1.

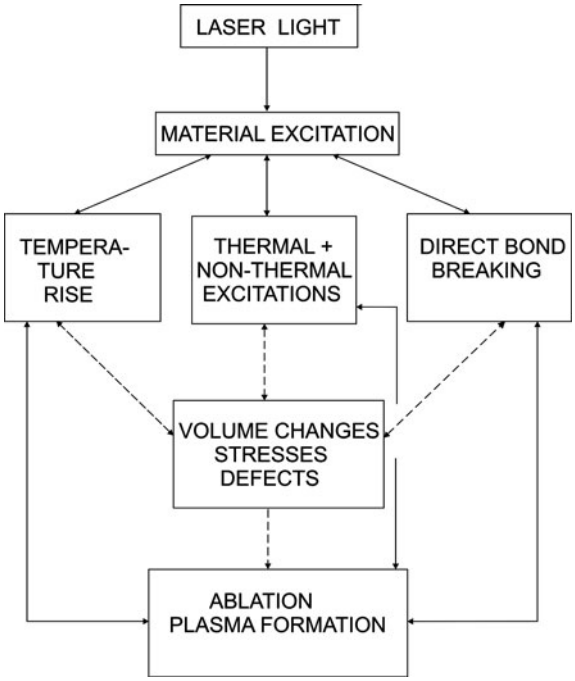

Fig. 12.2.1 Different interaction and feedback mechanisms involved in PLA. Ablation can be based on thermal activation only (*left path*), on direct bond breaking (photo-chemical ablation; *right path*), or on a combination of both (photophysical ablation; *intermediate path*)

The process starts with single-photon or multiphoton material excitation. If the excitation energy is instantaneously transformed into heat, the increase in temperature changes the optical properties of the material and thereby the absorbed laser power. This coupling between the thermal field and the optical properties is indicated in the figure by a double-headed arrow. The temperature rise can result in (thermal) material ablation (vaporization) with or without surface melting. There is, however, another channel (dashed arrows) which may also result in ablation. The temperature rise induces stresses which can be so high that explosive-type ablation or, with thin films on thick substrates, material pop-off is observed. Stresses also change the optical properties of the material and thereby influence the laser-induced temperature rise. Another feedback could be related to thermally induced defects. Irrespective of whether thermally induced stresses or defects are important or not, we henceforth refer to this overall process as *thermal ablation*.

If the photon energy is high enough, laser-light excitation can result in direct bond breaking. As a consequence, single atoms, molecules, clusters or fragments desorb from the surface. Besides this direct channel, there is again an indirect channel (dashed arrows). Light-induced defects, for example, photochemically dissociated bonds, can build up stresses which result in (mechanical) ablation. Both the direct and indirect paths can take place, in principle, without any

change in surface temperature. For this reason we term this process *photochemical ablation*.

Photophysical ablation shall describe a process in which both thermal and non-thermal mechanisms contribute to the overall ablation rate. An example would be a system in which the lifetime of electronically excited species or of broken bonds is so long that species desorb from the surface before the total excitation energy is dissipated into heat. The desorption process is enhanced by the temperature rise. Thermally or non-thermally generated defects, stresses, and volume changes may again influence the overall process. Thermal ablation and photochemical ablation can be considered as limiting cases of photophysical mechanisms.

The different mechanisms and feedback channels included in Fig. 12.2.1 are by no means complete: Additional complications arise from plasma formation, the ejection of electrons and ions which can build up surface electric fields, etc. Such electric fields, for example, may change activation energies for thermal desorption, for direct bond breaking, etc.

12.2.1 Models

In a simplified picture, the most important processes involved in PLA include the optical excitation and energy dissipation, and the decomposition and removal of the material itself.

Let us start with the consideration of the electronic energy scheme shown on the left side of the schematic in Fig. 12.2.2. In organic polymers S_0, S_1, S_2, ... denote singlet states, while T_1, T_2, ... denote triplet states. In inorganic insulators or semiconductors, S_0, S_1, S_2, ... indicate electronic energy bands. For example, S_0 would correspond to the highest valence band and S_1 to the lowest conduction band. For metals there is no energy gap and S_0 and S_1 can directly overlap. Apart from these 'intrinsic' states, there may be defect states, D_1, D_2, ..., related to excitons, F-centers, surface states, broken bonds, molecular fragments, etc. (Sect. 12.8.2). Between these various different energy states, radiative transitions (straight lines) and/or non-radiative transitions (oscillating lines) can take place (see also Fig. 2.1.1). For simplicity, only a single defect state and only a few of the possible excitation/relaxation channels are drawn.

Infrared laser light excites electrons within the conduction band (intraband transitions) of metals and semiconductors, vibrations in semiconductors and insulators, defect states, etc. Here, the thermalization of the excitation energy is, in general, so fast that the laser can simply be considered as a heat source (Chap. 2). The situation may change with high-intensity, ultrashort laser pulses (Chap. 13).

With non-metals and *ultraviolet* laser radiation, the situation can be quite different. Here, the laser light can induce single-photon or multiphoton interband transitions, $S_0 \rightarrow S_1, S_0 \rightarrow S_2, \ldots$, or excite defect states, $D_1, D_2, \ldots$, etc. The excitation of defect states – or their generation by UV-laser radiation – is of particular importance when the photon energy is smaller than the bandgap energy,

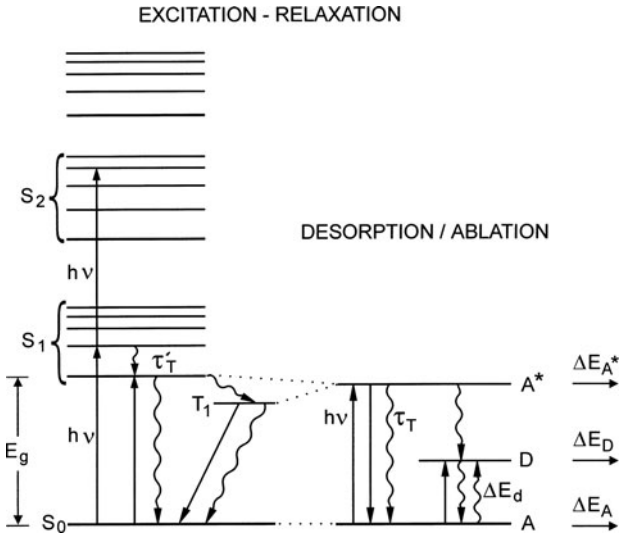

Fig. 12.2.2 Schematic showing different excitation and energy relaxation channels. Straight lines indicate the absorption or emission of photons, while oscillating lines indicate non-radiative transitions. The photophysical model describes the electronic states of the material (*left-hand side*) by two states A, A^* (*right-hand side*). ΔE_A and ΔE_{A^*} are the activation energies for (thermal) desorption of ground-state and excited-state species, respectively. In addition to these 'intrinsic' states there may be defect states, D, that are initially present or only generated during laser-light irradiation

i.e., with $h\nu < E_g$ (Sect. 12.8.2). Non-radiative transitions between different electronic energy bands or defect levels shall be characterized by (thermal) relaxation times, τ_T, and those within energy bands by $\tau_T' \ll \tau_T$ (clearly, these times significantly differ for different energy bands). If τ_T becomes comparable to, or even exceeds, the characteristic time, τ_R, for instance, the time for activated desorption of 'excited' species, electronically excited states will play an important role in the ablation process (Sect. 2.1).

In this and the following chapter we will discuss different macroscopic phenomenological models (photophysical, thermal, photochemical, mechanical, etc.), and microscopic models (molecular dynamics simulations, defect-related models, etc.). All of these models can be applied within certain regimes that are determined by the particular material and the laser parameters.

Let us start with a *photophysical* model and its limiting cases. Here, we describe the various excitation and energy-relaxation channels by a two- or three-level system. Thus, we concentrate on the absorption process, the relaxation of the system into states with *long* lifetimes, and the thermal desorption of species. Consider the three-level system shown on the right-hand side of Fig. 12.2.2. Species A refer to the electronic ground state and A^* to intrinsic electronically excited states, e.g., conduction-band states. As before, D shall describe defect states that can be electronically or thermally excited or which are generated only during laser-light

irradiation. In any case, electronic or vibrational excitation shall diminish the binding energy of 'species' and thereby enhance their desorption from the surface. Thus, the excitation and energy relaxation processes are described by electronic transitions, $A \rightarrow A^*$, radiative and non-radiative transitions, $A^* \rightarrow A$, and electronic and/or vibrational transitions, $A^*, A \rightarrow D$.

Within the present model we assume that material removal is dominated by thermal 'desorption' of species related to the electronic ground state, A, excited state, A^*, and defect states, D. These *desorption* rates are determined by activation energies ΔE_i ($i \equiv A, A^*$, and D), and by the local temperature rise, which is controlled by the excitation rate and the thermal relaxation time, τ_T. The total ablation velocity can be described by

$$v = f(N_A^*, N_{A^*}^*, N_D^*) \approx v_A N_A^*(0) + v_{A^*} N_{A^*}^*(0) + v_D N_D^*(0) \; . \qquad (12.2.1)$$

The approximation can be made as long as collective effects can be ignored. Here, $v_i = v_i^0 \exp[-\mathscr{E}_i/T(0)]$ are rate constants for thermally activated desorption. The coefficients v_i^0 are proportional to the corresponding attempt (vibrational) frequencies. As before, we use the abbreviations $\mathscr{E}_i \equiv \Delta E_i / k_B$. $T(0)$ is the surface temperature. N_i^* are the normalized number densities of states i. N_D may strongly depend on temperature, the number of laser pulses, stresses, etc. For the activation energies we assume ΔE_{A^*} and ΔE_D to be significantly smaller than ΔE_A. Hereafter, we will *mainly* consider ablation processes that are based on material decomposition within a thin *surface* layer, $z \ll \Delta h$. This certainly holds if the lifetime of defects generated within the *volume* of the material, i.e., for depths $z > \Delta h$, is so short that they do *not* contribute to the surface concentration, $N_D(0)$ (we assume that volume contributions to $N_{A^*}(0)$ can be ignored because of the 'short' lifetime of A^*). In the opposite case, however, $N_D(0)$ does depend on excitation/decomposition processes within the bulk material. In such cases, the term $v_D N_D^*(0)$ must be replaced by a function $g(N_D^*(0))$. Ablation starts when some critical defect concentration, N_D^{cr}, is reached. The function $g(N_D^*(0))$ increases sharply near N_D^{cr}. In contrast to the average ablation rate defined in Sect. 12.1, (12.2.1) describes the *instantaneous* ablation velocity.

Purely *thermal* and purely *photochemical* laser ablation can be described by limiting cases of this photophysical model, which is discussed in further detail in Sect. 13.3.

In a purely *thermal* process the second term in (12.2.1) can be ignored. With strong material absorption, optical excitation results in material heating within a depth l_T and ablation takes place via channel A and/or D. For materials with finite absorption, thermally excited/generated defects, D, may accumulate within a depth l_α and strongly contribute or even determine the overall ablation rate. With multicomponent materials and long laser pulses, material segregation *can* take place, at least at the surface. In such cases, the ablation velocity is given by the sum over the different material constituents j

$$v = \sum_j v_j(T) N_j^*(0, t) \; . \qquad (12.2.2)$$

Here, $N_j^*(x,t)$ must be calculated from the transport equations for the constituents j within the material.

A purely *photochemical* process requires long relaxation times τ_T and low activation energies $\mathscr{E}_{A^*} \approx 0$ and/or $\mathscr{E}_D \approx 0$. Then, we can ignore the first term in (12.2.1). In this case, ablation is dominated by the desorption of excited species, A^*, and/or by species related to (non-thermally) excited/generated defects, D. Such a *purely* photochemical process seems to be unlikely, at least for pulse lengths $\tau_\ell > 10-100$ ps.

The present description can be applied to materials that sublimate and to all cases where the time of laser–material interaction is so short that structural modifications of the material can be ignored. These cases include nanosecond-laser ablation of some non-metals, and many cases of picosecond-laser ablation.

If the material is modified or if it melts during the laser pulse, or if its microstructure changes with *subsequent* pulses, the electronic and vibrational structure, and thereby the various excitation/dissipation channels, may significantly change. This is certainly the situation with the majority of materials that are ablated with nanosecond and longer pulses. However, such cases can be described by (12.2.1) as well. The main difference is that the activation energies, pre-exponential factors, and number densities are changed. This is probably the reason why laser-ablation experiments performed with completely different systems can often be described by essentially the same formalism.

12.3 Photothermal Surface Ablation

If the thermal relaxation time, τ_T, is very short (Sect. 2.1), laser ablation can simply be treated as a thermal process. This regime applies to PLA by IR- and VIS-laser radiation, and to most cases of UV-laser ablation with nanosecond and longer pulses. Thermal 'evaporation' is, in most cases, the dominant mechanism in systems where surface melting is observed. The situation becomes more complicated, however, when stress-related effects (Sect. 12.9), liquid-phase expulsion (Sect. 11.4) or the ejection of liquid droplets (Sect. 12.6.5) contribute significantly to the overall ablation rate.

Let us first ignore such effects and consider the simplest case of surface evaporation based on the first term in (12.2.1), a single laser pulse of duration τ_ℓ, and a *uniform* intensity distribution. With this latter assumption, the problem can be treated in one dimension (Fig. 11.2.1). Here, we can employ all of the equations derived in Chap. 11.

The layer thickness ablated per laser pulse can be tentatively divided into different terms

$$\Delta h = \int_0^\infty v(t)\,\mathrm{d}t \approx \Delta h_1 + \Delta h_2 + \Delta h_3 + \Delta h_4\,, \tag{12.3.1}$$

where $\Delta h_1 \equiv \Delta h_1(t < t_v)$ is the ablated-layer thickness up to the time t_v (see Fig. 11.2.2). In many cases, Δh_1 can be ignored. Δh_2 is the layer thickness ablated within the interval $t_v \le t \le t_{st}$. In this regime, ablation and (bulk) heating are non-stationary, though the surface temperature is already close to T_{st} (Sect. 11.2). Δh_3 is the layer thickness ablated within the stationary regime, i.e., within the interval $t_{st} \le t \le \tau_\ell$. With nanosecond pulses, the stationary regime is often *not* reached. With picosecond and femtosecond pulses, stationary conditions are *never* reached. If the energy stored within the volume $z > 0$ (Fig. 11.2.1) is large, ablation may continue for a certain time *after* the laser pulse, $t > \tau_\ell$. The layer thickness ablated during this time shall be described by the term Δh_4.

The contribution of the single terms in (12.3.1) to the *overall* ablation rate depends on the particular material under investigation, the laser pulse length, τ_ℓ, and fluence, ϕ. With microsecond and longer pulses, we can approximate (12.3.1) by (11.2.7). With picosecond and femtosecond pulses we can often use $\Delta h \approx \Delta h_4$. The situation is particularly complicated with nanosecond pulses, where Δh_2, Δh_3, and Δh_4 may significantly contribute to Δh.

A classification of regimes similar to (12.3.1) can be employed if we consider a constant laser pulse length, τ_ℓ, and variable fluences, ϕ. In this case, both t_v and t_{st} decrease with increasing fluence/intensity (Sect. 11.2.2). With $\phi \lesssim \phi_{th}$, we can describe the ablated-layer thickness by an *Arrhenius-type* law

$$\Delta h \equiv \Delta h_1 \approx C_1 \exp\left(-\frac{C_2}{\phi}\right) . \tag{12.3.2}$$

With fluences $\phi > \phi_{th}$, the surface temperature, T_s, changes only logarithmically with ϕ and it is close to $T_{st}(\phi/\tau_\ell)$ (see Fig. 12.3.1). Here, the *overall* ablated-layer thickness contains contributions Δh_2, Δh_3, and Δh_4. From (11.2.20) we obtain the *linear* law

$$\Delta h \approx B(\phi - \phi_{th}) , \tag{12.3.3}$$

with $B = A/\tilde{H}(T_{st})$, where A is the absorptivity, $\tilde{H}(T_{st}) = \Delta H_v^0 + \Delta H_g(T_{st})$, and

$$\phi_{th} = \frac{\Delta H_s(T_{st})}{A}\left([D(T_{st})\tau_\ell]^{1/2} + l_\alpha\right) . \tag{12.3.4}$$

Here, we have employed $l_T \approx [D(T_{st})\tau_\ell]^{1/2}$. This is a good approximation for fluences $\phi \approx \phi_{th}$. The relation (12.3.4) is an implicit equation for ϕ_{th}, because $T_{st} = T_{st}(\phi_{th}/\tau_\ell)$. T_{st} can be estimated from (11.2.12), or it can be directly derived from Fig. 11.2.3. Approximations similar to (12.3.3) and (12.3.4) hold, in fact, even within wide ranges of temperature-dependent parameters, as long as $D\tau_\ell\alpha^2 > 0.1$. Equation (12.3.4) is more general than (11.2.23). It even holds for time-dependent intensities $I = I(t)$ if we substitute τ_ℓ by τ_{FWHM}. For surface absorption we find $\phi_{th} \propto \tau_\ell^{1/2}$ and with weak absorption $\phi_{th} \approx \text{const}(\tau_\ell)$. For 'long' pulses with $\tau_\ell > w^2/D$, heat transport changes from 2D to 3D and we obtain $\phi_{th} \propto \tau_\ell$.

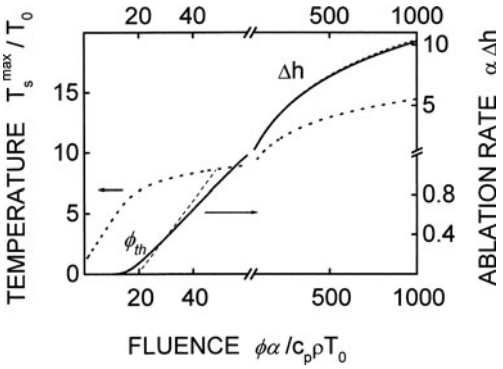

Fig. 12.3.1 Normalized ablated depth (*solid curve*) and maximum surface temperature (*dotted curve*) calculated for a smooth laser pulse (Sect. 6.3). For fluences $\phi \lesssim \phi_{\rm th}$ the behavior is described by the Arrhenius tail and for $\phi > \phi_{\rm th}$ by the linear approximation (12.3.3) (*dashed curve*). For higher laser-light intensities, screening results in the logarithmic dependence (12.3.6). The parameters employed were: $A = 1$, $\alpha^2 D\tau_\ell = 1$, $v_0/D\alpha = 10^3$, $\Delta H_{\rm v}^0/c_{\rm p}T_0 = 20$, $\mathscr{E}_{\rm A}/T_0 = 70$, $H_{\rm g} = H, \alpha_{\rm g} = 0.2\alpha$. These parameters are, e.g., characteristic for strongly absorbing dielectrics with $\alpha = 10^5\,{\rm cm}^{-1}$, $D = 10^{-2}\,{\rm cm}^2/{\rm s}$, $v_0 = 10^6\,{\rm cm/s}$, $\mathscr{E}_{\rm v} = 21000\,{\rm K} \equiv 1.81\,{\rm eV}$, $T_0 = 300\,{\rm K}$, $c_{\rm p} = 1\,{\rm J/g\,K}$, $\varrho = 1\,{\rm g/cm}^3$, $\Delta H_{\rm v}^0 = 6\,{\rm kJ/cm}^3$, and $\tau_\ell = 10\,{\rm ns}$. With these numbers, the unit of time is 10 ns and of temperature 300 K. The spatial unit is 0.1 μm, and the unit of fluence 3 mJ [*Arnold* et al. 1998]

Experimentally, the Arrhenius tail can be seen only in measurements that can detect small mass losses as, e.g., those using a quartz-crystal microbalance (Sect. 29.3). The 'ablated depth', Δh_1, derived from such measurements is, with most systems, an artificial quantity which is related to the depletion of volatile species from the surface or the laser-induced desorption (LID) of sub-monolayers, or a few monolayers only. With certain materials one often observes a roughening of the surface or even the formation of a hump (Sect. 12.4).

In the present model the ablation 'threshold' corresponds to the fluence $\phi_{\rm th}$, where ablation starts to influence the surface temperature (Fig. 11.2.2). The different ablation thresholds observed for metals and insulators are mainly due to the differences in optical and thermal properties. Experimentally, $\phi_{\rm th}$ is determined from the intersection of the linear fit of data $\Delta h(\phi)$ for fluences $\phi > \phi_{\rm th}$ (see, e.g., Figs. 12.4.1 and 12.6.3).

12.3.1 Influence of Screening

With moderate-to-high laser output intensities, $I_\ell(t)$, and pulse lengths longer than picoseconds, screening of the incident radiation by the vapor/plasma plume becomes important [*Schmidt* et al. 1998; *Eyett* and *Bäuerle* 1987]. The laser-light intensity that reaches the substrate can be estimated from

$$I \equiv I(0,t) = I_\ell(t)\exp(-\alpha_{\rm p}\Delta h)\ , \tag{12.3.5}$$

where $\Delta h \equiv \Delta h(t)$ is the ablated-layer thickness at the time t. α_p is the absorption coefficient of the vapor plume recalculated to the density of the condensed phase, i.e., $\alpha_p = \alpha\sigma_v/\sigma_s$. Here, σ_v and σ_s are the absorption cross sections of species in the vapor and the condensed phases, respectively. Equation (12.3.5) ignores any lateral expansion of the plume, which becomes important with $v_v\tau_\ell \geq w$. From the differential form of (11.2.20) and (12.3.5) one obtains the *logarithmic* law

$$\Delta h = \frac{1}{\alpha_p} \ln\left[1 + \alpha_p B(\phi - \phi_{th})\right] . \tag{12.3.6}$$

With $\alpha_p \Delta h \ll 1$, we obtain (12.3.3) with the same values of B and ϕ_{th}.

With laser fluences $\phi \gg \phi_{th}$, the layer thickness ablated per pulse may become almost *independent* of ϕ because of strong plasma shielding (Chap. 11). However, surface modifications (Chaps. 26 and 27) or structure formation, in particular the formation of cones (Sect. 28.4), can cause similar behavior.

The overall dependence $\Delta h = \Delta h(\phi)$ is shown in Fig. 12.3.1 for normalized quantities. With $\phi < \phi_{th}$, we can see the Arrhenius tail (12.3.2), then the linear regime (12.3.3), and with moderate-to-high fluences the logarithmic behavior (12.3.6). Such a dependence is often reflected well in measured ablation curves as, e.g., in Fig. 12.6.1.

In the following, we discuss the various different regimes described by (12.3.2), (12.3.3), and (12.3.6).

12.3.2 Post-pulse Ablation

After the end of the laser pulse, only the material whose temperature is high enough will ablate. The temperature corresponding to the $1/e$ decrease in ablation velocity can be estimated from (11.2.11)

$$T(\Delta h_4) \approx T_{st} - \frac{T_{st}^2}{\mathscr{E}_v} .$$

For surface absorption we obtain, together with (11.2.17) and $T_{st} \approx \Delta T_{st}$, for the layer thickness ablated *after* the pulse

$$\Delta h_4 \approx \frac{T_{st} D}{v_{st} \mathscr{E}_v} , \tag{12.3.7}$$

where v_{st} can be estimated from (11.2.12). The thickness of the layer ablated *during* the pulse is $\Delta h_3 \approx v_{st}\tau_\ell$ and, therefore, $\Delta h_4 \ll \Delta h_3$ if

$$\frac{T_{st}}{\mathscr{E}_v} \frac{D}{v_{st}^2 \tau_\ell} \ll 1 . \tag{12.3.8}$$

This condition is in fact fulfilled for the parameters commonly employed in ablation experiments with materials that absorb strongly.

The situation is different in the case of *finite* absorption. Here, the overheated layer of thickness z_0 may have accumulated enough energy to be ablated after the pulse (Fig. 11.2.1). This is the case if the dissipation of energy by heat conduction, characterized by the time $t_T \approx z_0^2/4D$, is slow compared to the ablation process, characterized by $t_A \approx z_0/v_{st}$. The condition $t_T > t_A$ yields $v_{st}z_0/4D > 1$. In this case, a layer of thickness $\Delta h_4 \approx z_0 \approx l_\alpha$ may be ablated *after* the pulse.

12.4 Interactions Below Threshold

Irradiation of a solid with laser fluences $\phi < \phi_{th}$ frequently results in changes in surface morphology and microstructure, in the generation of defects, and in the depletion of one or several components of the material (Sect. 12.8.2, Chaps. 26, 27, 28 and 30). For this reason, the meaning of experimental data obtained for low laser fluences is strongly related to the technique employed in the measurements. If, for example, the layer thickness ablated per pulse is derived from the depth of holes, h, generated during N_ℓ laser pulses, i.e., from $\Delta h = h/N_\ell$, one finds $\Delta h(\phi < \phi_{th}) \approx 0$. This can be seen in Fig. 12.4.1. The accuracy of such measurements depends on the experimental technique employed and on the extent the surface morphology changes due to roughening, the development of surface instabilities, etc. If, however, Δh is derived from mass loss measurements, one finds $\Delta h(\phi < \phi_{th}) \neq 0$. This is a very general behavior that has been found for many different materials. The reason is that even for very low fluences, laser-induced desorption (LID) of submonolayers, or a few monolayers, or the depletion of single species takes place.

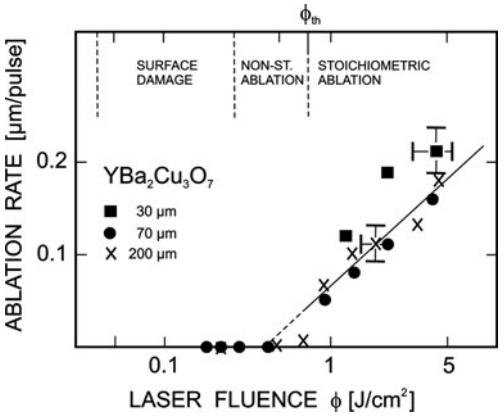

Fig. 12.4.1 Surface damage/ablation of $YBa_2Cu_3O_7$ films on (100) MgO substrates as a function of KrF-laser fluence. Different laser-beam spot sizes on the film surface, $2w$, are indicated by different symbols. Film thicknesses were between 0.5 and 1.5 µm [*Heitz* et al. 1990]

Let us discuss this in further detail for $YBa_2Cu_3O_7$ (YBCO) films irradiated by KrF-laser light (Fig. 12.4.1). Fluences of $\phi < 0.04\,\mathrm{J/cm^2}$ cause no detectable film damage. Within the range $0.04\,\mathrm{J/cm^2} \lesssim \phi \lesssim 0.27\,\mathrm{J/cm^2}$, surface damage together with the depletion of oxygen and small amounts of Cu is observed. With $\phi \geq 0.27\,\mathrm{J/cm^2}$, non-stoichiometric ablation starts. Microprobe analyses reveal a depletion of Cu and, to a smaller extent, of Ba. This is expected from the vapor pressures of the metal oxides and metallic species formed during (thermal) decomposition of YBCO. The depletion of single material components increases with fluence. With $\phi > \phi_{\mathrm{th}} \approx 0.75\,\mathrm{J/cm^2}$, ablation becomes stoichiometric. While the laser fluences corresponding to the different ranges of surface damage and ablation depend on the particular material and laser parameters, the overall behavior shown in the figure is characteristic of multicomponent materials subjected to nanosecond laser pulses.

The situation can be even more complex. Figure 12.4.2 shows the surface topology of (semi-crystalline) PI after *single-pulse* Ar^+-laser irradiation. With center fluences $\phi_0 \lesssim \phi_{\mathrm{th}}$, the irradiated area shows a hump. The increase in specific volume has been related to both the amorphization of crystalline domains (about 10% of the total volume; $\varrho_{\mathrm{C}}/\varrho_{\mathrm{A}} = 1.11 \pm 0.02$) and to polymer fragments that are trapped within the interaction volume. Molecular fragments, such as CO, HCN, etc., are totally or in part released from the sample (Sect. 30.2.5). Here, the threshold fluence for ablation, ϕ_{th}, was defined by the average of the lowest fluence at which a dip appears in the center of the hump (Fig. 12.4.2b) and the highest fluence for which this dip is absent (Fig. 12.4.2a). Clearly, mass loss measurements would reveal an Arrhenius tail from which one can derive an 'ablated'-layer thickness, Δh_1

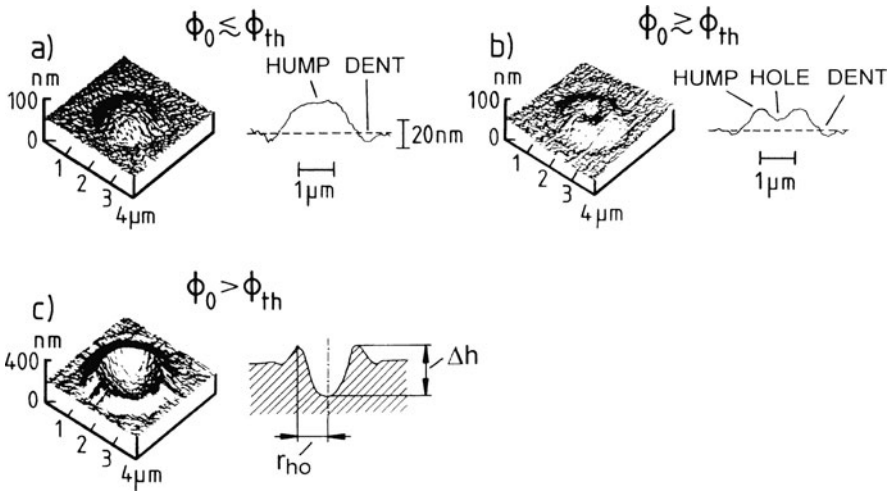

Fig. 12.4.2 a–c AFM pictures of single-pulse Ar^+-laser-induced surface-topology changes and ablation of PI ($\lambda = 302\,\mathrm{nm}$, $\phi(r) = \phi_0 \exp[-(r/w_0)^2]$, $w_0 \approx 2.1\,\mu\mathrm{m}$). (**a**) $\phi_0/\phi_{\mathrm{th}} \approx 0.96$, $\tau_\ell = 5\,\mu\mathrm{s}$. (**b**) $\phi_0/\phi_{\mathrm{th}} \approx 1.01$, $\tau_\ell = 2.1\,\mu\mathrm{s}$. (**c**) $\phi_0/\phi_{\mathrm{th}} \approx 1.25$, $\tau_\ell = 800\,\mathrm{ns}$; the cross section on the right is schematic [*Himmelbauer* et al. 1996b]

(Fig. 12.6.1), while, in reality, a hump appears. For fluences $\phi_0 > \phi_{th}$, real ablation, i.e., the formation of a hole, is observed.

12.5 The Threshold Fluence, ϕ_{th}

With a thermally activated process as described by the Arrhenius-type law (11.2.11), no real threshold exists. However, *significant* ablation is observed only above a certain fluence, which we henceforth denote as the threshold fluence, ϕ_{th}. ϕ_{th} depends on the particular material, its microstructure and concentration of physical and chemical defects, and on the laser parameters, in particular the laser wavelength and pulse duration (dwell time). Typical values for metals are within the range $1-10\,\mathrm{J/cm^2}$. With inorganic insulators and strong-to-medium absorption ϕ_{th} is, typically, between 0.5 and $2\,\mathrm{J/cm^2}$, and with organic materials between 0.01 and $1\,\mathrm{J/cm^2}$. With thin films, ϕ_{th} becomes dependent also on the film thickness and the substrate material.

For finite absorption, ϕ_{th} decreases with an increasing absorption coefficient, irrespective of whether this is related to a decrease in laser wavelength, the addition of dopants, or to the generation of defects. A decrease of ϕ_{th} with increasing α is expected for *both* thermal and non-thermal ablation mechanisms, because the excitation energy will be localized within a smaller volume.

The *effective* absorption coefficient can be described by

$$\alpha = \alpha_0 + \sigma_i N_i + \alpha_D(N_\ell) + \alpha^{NL} \,. \tag{12.5.1}$$

Here, α_0 denotes the linear temperature-dependent absorption coefficient of the pure material (Chap. 7; note that α in Beer's law is the extinction coefficient, which may differ significantly for solids in crystalline and ceramic form). The second term describes the effect of light-absorbing impurities/dopants, where N_i is the number of impurity/dopant atoms or molecules per unit volume. The third term takes into account changes in absorption caused by radiation-induced defects (incubation centers). α_D is a function of laser intensity, I, and it saturates after a certain number of laser pulses, N_ℓ. With transient defects, α_D depends on the laser-pulse repetition rate. The last term, $\alpha^{NL} \equiv \alpha(I)$, stands for multiphoton (non-linear optical) absorption processes. With very high laser-light intensities, when self-induced transparency, thermal runaway, avalanche ionization, etc., become important, the approximation (12.5.1) loses sense.

The effect of doping on ϕ_{th} is shown in Fig. 12.5.1 for PMMA. Here, the absorption coefficient for XeCl-laser radiation was tuned via the concentration of pyrene. By investigating additional host–dopant combinations, it has been found that the threshold fluence and the ablation rate are determined by the absorption strength of the dopant and not by its chemical nature or any charge-transfer interactions between the excited dopant and the monomer units of the host polymer. Thus, the role played by the dopant is simply to absorb the light rather than to channel the electronic excitation to the host polymer. Similar results have been obtained with PTFE

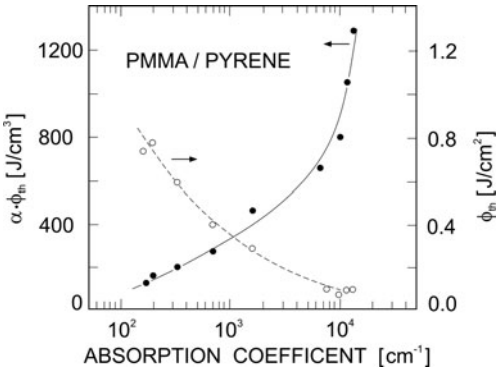

Fig. 12.5.1 Threshold fluence, ϕ_{th}, and $\alpha\phi_{th}$, for PMMA doped with pyrene. The absorption coefficient, α, refers to 308 nm XeCl-laser radiation [*Chuang* et al. 1988]

doped with PI [*Egitto* and *Davis* 1992]. However, with dopants that significantly change the thermal relaxation time, the interpretation of data may be different.

Defects generated by the laser radiation itself are frequently denoted as *incubation* centers. Among those are color centers in ionic crystals, vacancies, broken bonds, molecular fragments, etc. (Sect. 12.8). Radiation-induced defects are of particular importance for the ablation behavior of wide-bandgap materials and photon energies $h\nu < E_g$. Here, successive laser pulses increase the number of defects and thereby the absorptivity within the irradiated volume. The increase in energy absorption causes a decrease in ϕ_{th}. Thus, ϕ_{th} for multiple-pulse ablation is lower than for single-pulse ablation. In other words, if ϕ is just below ϕ_{th} for single-pulse ablation, ablation starts after a certain number of pulses. With further pulses, stationary conditions are obtained (Fig. 12.5.2). ϕ_{th} can also be reduced via defects generated by electron- or ion-beam irradiation.

Another characteristic feature is the decrease in ϕ_{th} with pulse duration, τ_ℓ (Fig. 12.5.3). With shorter pulses, the spatial dissipation of the excitation energy is reduced and ϕ_{th} is reached at lower fluences. This observation can be related to a decrease in heat penetration depth and/or an increase in absorption coefficient due to multiphoton excitation. For a thermal process and strong absorption, i.e., $l_\alpha \ll l_T$,

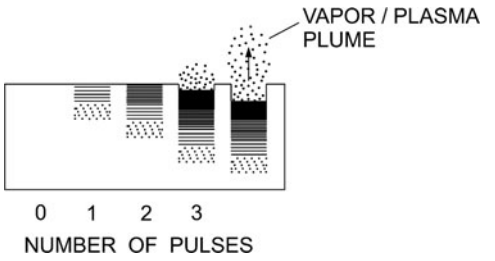

Fig. 12.5.2 Schematic showing the increase in absorption with successive laser pulses

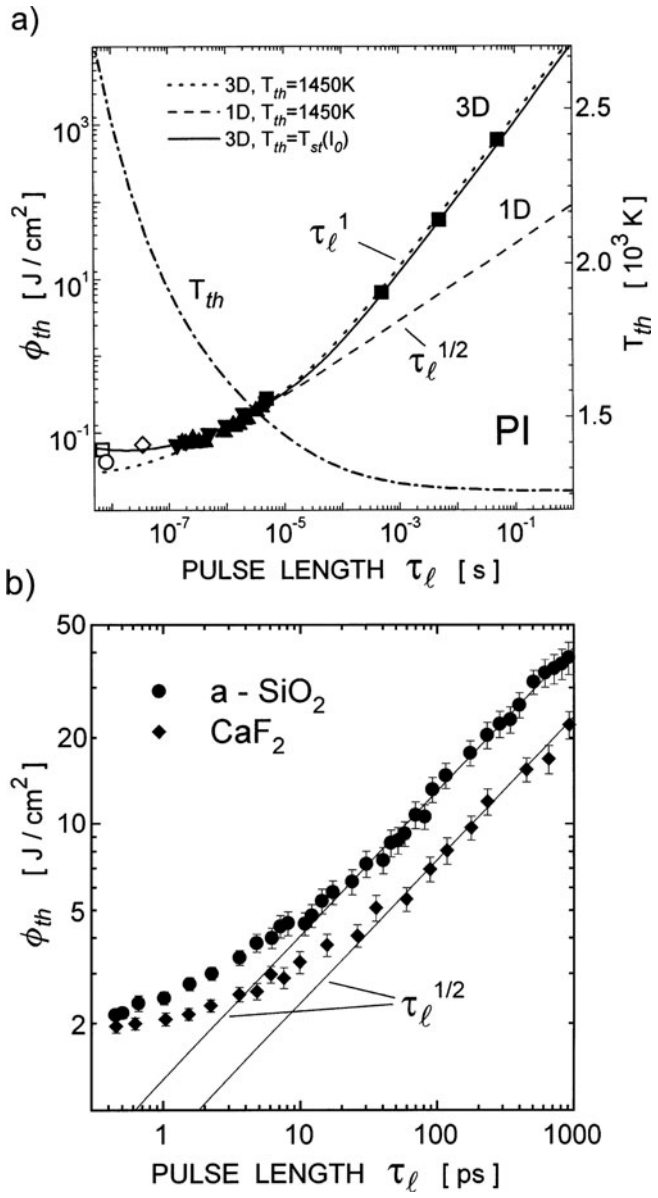

Fig. 12.5.3 a, **b** Dependence of threshold (damage) fluence, ϕ_{th}, on laser pulse duration, τ_ℓ. (**a**) Single-shot laser irradiation of PI. *Solid symbols* refer to 302 nm Ar^+-laser (Fig. 12.4.2) and *open symbols* to 308 nm XeCl-laser radiation. The scattering in XeCl-laser data could be related to differences in the laser pulse shapes employed (Sect. 6.3). *Dotted and dashed curves* were calculated from (7.5.1) with $T_{th} = 1,450$ K for 3D- and 1D-heat transport, respectively. *Solid curve*: 3D heat transport with $T_{th} = T_{st}(I_0)$; the *dash-dotted curve* shows the corresponding dependence of T_{th} on τ_ℓ. For $\tau_\ell > 10^{-4}$ s, *dotted and solid curves* can be described by $\phi_{th} \propto \tau_\ell^{\varepsilon}$, with $\varepsilon \approx 1$ [*Piglmayer* et al. 1998]. (**b**) Damage threshold for a-SiO_2 (•) and CaF_2 (♦) exposed to 1053 nm Ti:sapphire-laser radiation. *Solid lines* are $\tau_\ell^{1/2}$ fits to the 'long' pulse results [*Stuart* et al. 1995; see also Sect. 13.6]

we expect $\phi_{\text{th}} \propto l_{\text{T}} \propto \tau_\ell^\varepsilon$, with $\varepsilon = 1/2$ and $\varepsilon = 1$ for 1D and 3D heat transport, respectively (Sect. 12.3). Non-linear excitations become important in particular for wide-bandgap materials and/or optically strongly non-linear materials exposed to picosecond or femtosecond laser pulses (Sect. 13.6).

12.5.1 Thin Films

The absorptivity of light in thin films and multilayer structures depends strongly on the optical properties of films, the film thicknesses, and the laser parameters (Chap. 9). Additionally, the optical and thermal properties of the *substrate* may strongly influence the laser-induced temperature profile, and thereby ablation rates.

With *thin films* on thermally insulating transparent substrates, ϕ_{th} is significantly lower than on thermally well conducting substrates. If $\kappa_1 > \kappa_\text{s}$, the fluence ϕ_{th} increases with film thickness, h_1, until it reaches a constant value which is characteristic for the bulk material. Energy transport can be described by heat diffusion. Within the range $l_\alpha < h_1 < l_{\text{T}}$, ϕ_{th} is diminished by a factor $h_1/l_{\text{T}} \cdot \phi_{\text{th}}$ becomes independent of h_1 when $h_1 > l_{\text{T}}$.

In fact, the influence of absorption and heat diffusion could widely explain experimental data on ablation rates of thin polymer films on various different substrates [*Fardel* et al. 2008]. With very thin films, changes in the kinetics due to photochemical and thermally activated bond breaking and thermal degradation may become important. The situation may, however, be much more complex. Phase transformations, depletion of single species, exfoliation, etc. may contribute to the overall ablation behavior. Such effects have been observed, e.g., during ablation of thin films of a-C:H [*Daminelli* et al. 2006]. Thus, it seems questionable whether experiments of this type are suitable for clarifying ablation mechanisms. Even with well adherent single element thin films, both finite size and surface effects may strongly influence the experimental results. With ultrashort pulses, additional mechanisms become important (Chap. 13).

12.6 Ablation Rates

The ablation rate (velocity) was defined in Sect. 12.1. It should be noted, however, that the *average* ablation velocity derived from experimental data may differ significantly from the instantaneous velocity, $v = \Delta\dot{h}$.

In the following, we discuss the dependence of ablation rates on laser and material parameters.

12.6.1 Dependence on Photon Energy and Fluence

Figure 12.6.1 shows the ablation rate for PI as a function of fluence for different excimer-laser wavelengths. The ablated-layer thickness, Δh, has been derived

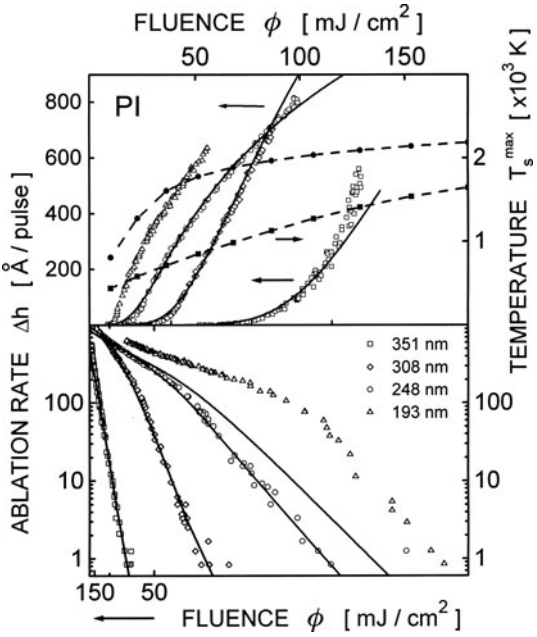

Fig. 12.6.1 Ablation rate of polyimide as a function of laser fluence for different excimer laser wavelength. Data points were derived from mass-loss measurements using a quartz crystal microbalance [*Küper* et al. 1993]. The *solid curves* were calculated by employing the method of moments [*Arnold* et al. 1998]. The parameters employed were: $\tau_\ell = 6.13\,\text{ns}$ ($\tau_{\text{FWHM}} = 15\,\text{ns}$), $v_0 = 3 \times 10^6\,\text{cm/s}$, $\mathscr{E}_\text{A} = 17500\,\text{K}$, $T_0 = 300\,\text{K}$, $c_\text{p} = 2.55 - 1.59\exp[(300 - T)/460]\text{J/g K}$, $c_\text{g} = 2.55\,\text{J/g K}$, $\kappa = 1.55 \times 10^{-3}(T/300)^{0.28}\text{W/cm K}$, $\varrho = 1.42\,\text{g/cm}^3$, $\Delta H_\text{v} = 0.5\,\text{kJ/g}$, $\alpha_\text{p} = 0.45\alpha$. *Triangles* ($\lambda = 193\,\text{nm}$): $A = 0.93$, $\alpha = 4.25 \times 10^5\,\text{cm}^{-1}$. *Circles* ($\lambda = 248\,\text{nm}$): $A = 0.88$, $\alpha = 3.1 \times 10^5\,\text{cm}^{-1}$. *Diamonds* ($\lambda = 308\,\text{nm}$): $A = 0.89$, $\alpha = 10^5\,\text{cm}^{-1}$. *Squares* ($\lambda = 351\,\text{nm}$): $A = 0.9$, $\alpha = 0.32 \times 10^5\,\text{cm}^{-1}$. The calculated maximum surface temperature rise, $\Delta T_\text{s}^\text{max}$, is shown (*dashed curves, solid symbols*)

from mass-loss measurements using a quartz crystal microbalance (Sect. 29.3). The increase in intrinsic absorption of PI with decreasing wavelength is responsible for the decrease in ϕ_th. With high fluences, the absorbed laser-light energy is more efficiently used if the optical penetration depth is longer. This explains, in part, why the ablation rates achieved with longer wavelength may exceed those observed with shorter ones. A more detailed discussion also requires the consideration of laser–vapor/plasma interactions. The solid curves in Fig. 12.6.1 have been calculated by employing the method of moments. The overall shape of measured ablation curves is quite similar to the theoretical curve presented in Fig. 12.3.1. For low fluences one finds the Arrhenius tail (12.3.2), then the linear regime (12.3.3) and for high fluences the logarithmic behavior (12.3.6). This becomes even more evident from separate plots for the three regimes shown in Fig. 12.6.2 for KrF-laser radiation. The figures show that the experimental data are well described by the respective equations.

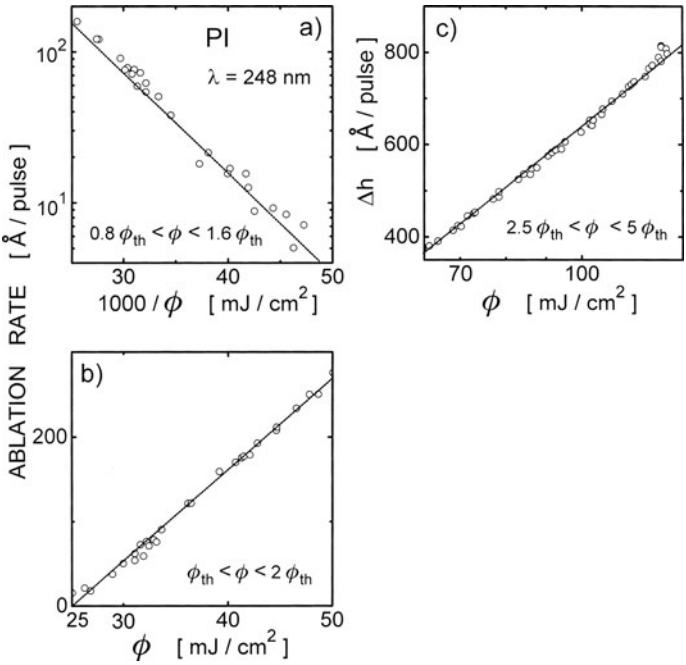

Fig. 12.6.2 a–c Ablation rate of PI. Data refer to the 248 nm KrF-laser radiation in Fig. 12.6.1. Calculated fits of the following are shown (*lines*): (**a**) Arrhenius law (12.3.2); (**b**) linear law (12.3.3), with $\phi_{\mathrm{th}} = 25\,\mathrm{mJ/cm^2}$; (**c**) logarithmic law (12.3.6) for *high* fluences

Heuristically, one can describe the *overall* behavior $\Delta h = \Delta h(\phi)$ by the *single* interpolation formula [*Luk'yanchuk* et al. 1994]

$$\Delta h = C_1 \exp\left(-\frac{C_2}{\phi \exp(-\alpha_0 \Delta h)}\right) , \tag{12.6.1}$$

where α_0 describes the attenuation of the laser light within the vapor plume. Because of (temporal) averaging, α_0 deviates from α_{p} in (12.3.6), i.e., $\alpha_0 \neq \alpha_{\mathrm{p}}$. For fluences $\phi \lesssim \phi_{\mathrm{th}}$, where $\alpha_0 \Delta h \to 0$, (12.6.1) becomes identical to (12.3.2). For fluences $\phi > \phi_{\mathrm{th}}$, this equation has a real physical meaning only for strong plasma-plume absorption. In any case, (12.6.1) fits experimental data for various different materials quite well. The 'ablated-layer thickness' shown in Fig. 12.6.1 for fluences $\phi < \phi_{\mathrm{th}}$ is an artificial quantity. In this regime, the measured mass loss is *not* related to real ablation, but to the desorption of volatile species (Sect. 12.4). A further point to note is the significant disagreement between the experimental data obtained for ArF-laser radiation and the calculated curve. Apparently, these data cannot be described within the frame of photothermal surface ablation only.

While the dependences of the ablation rates on fluence and laser wavelengths shown in Figs. 16.6.1 and 16.6.2 are characteristic for some types of polymers, there are significant differences between experimental results achieved by different

groups for similar polymers. For example, gravimetric and profilometric measurements of ablation rates on Durimid^{TM}, a polyimide similar to that used by *Küper* et al., did *not* exhibit Arrhenius tails for any of the laser wavelengths (193, 248, 308 nm) employed [*Dumont* et al. 2005]. The differences are, probably, related to the differences in data collection. *Küper* et al. measured single-pulse ablation rates but on the same samples for a whole sequence of fluences. Thus, it seems that each sample surface was irradiated by multiple pulses. As described in various sections, already a *single* pulse may cause physical and chemical modifications of a surface (Sect. 12.6.4). In particular with PI, surface carbonization and roughening lowers the ablation rate near the threshold ϕ_{th} (Sect. 27.1.4). *Dumont* et al. collected the data by using a fresh surface after each single pulse. For all of the polymers investigated by this group (two types of PI and triazene), the ablation data near the threshold fluence can be directly related to the UV absorption spectra. For higher fluences, indications for bleaching and shielding effects have been found. For some of the polymers and wavelengths investigated, significant mass losses prior to ablation have been measured. Thus, there are still a number of open questions including the influence of debris, desorption of adsorbed molecules, such as water, etc.

IR-Laser Ablation

The most detailed studies on laser ablation of polymers based on resonant and non-resonant *infrared* vibrational excitation have been carried out by *Haglund* et al. In these experiments *tunable* free-electron laser (FEL) radiation ($10 - 30$ mJ; $v_{\text{r}} = 30$ Hz) has been employed. The pulse structure consists of 4 µs macropulses which comprise 1 ps micropulses. The latter seem to be unimportant with respect to the interpretation of experimental data. The ablation dynamics, the type of ablated species and the expansion of the plasma plume depend strongly on the absorption strength of the particular vibrational mode excited by the FEL radiation. For example, for PEG (polyethylene glycol), the C-H stretching mode shows a strong absorption band near $\lambda = 3.45$ µm. With the FEL fluences employed, excitation of this mode results in strong overheating, material ablation, and shielding of the incident laser radiation by the gaseous species. On the other hand, selective excitation of the O-H stretching mode that shows only weak absorption at $\lambda = 2.94$ µm, results in material decomposition and normal boiling [*Johnson* et al. 2009a]. The ablation rates for 3.45 and 2.94 µm excitations can be described by Eqs. (12.3.6) and (12.3.3), respectively. IR-laser ablation has also been studied for PMMA [*Spyratou* et al. 2008] and PS (polystyrene) [*Johnson* et al. 2009b].

12.6.2 Dependence on Pulse Duration

The ablated depth as a function of Ar^+-laser pulse length is shown in Fig. 12.6.3 for PI and various (constant) intensities, I_0. With decreasing I_0 the (average) ablation velocity, $v \approx \Delta h/(\tau_\ell - t_{\text{v}})$ (slope of solid lines), decreases, while ϕ_{th} increases. For lines $I_0 = \text{const.}$, the temperature T_{s} is about the same and equal to the stationary

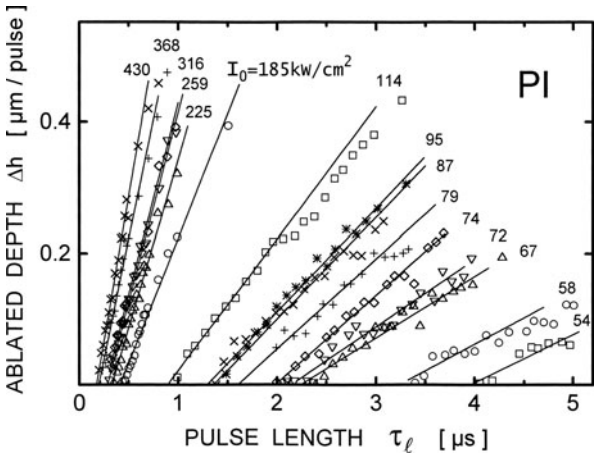

Fig. 12.6.3 Dependence of the ablated depth for PI (Kapton H) on the duration of 302 nm Ar^+-laser pulses of intensities I_0. Linear interpolations are shown (*solid lines*) [data derived from *Himmelbauer* 1996]

value, $T_{st}(I_0)$ (11.2.12b). Therefore, the data permit one to estimate the activation energy, ΔE_A, from $v \approx v_0 \exp(-\Delta E_A / k_B T_{st})$. The analysis yields $\Delta E_A \approx 1.5$ eV. This value is independent of pulse length within the regime under consideration.

The effect of τ_ℓ on the ablation rate has also been investigated for PMMA [*Schmidt* et al. 1998], for FEP [*Nakamura* et al. 1996] and, within the nanosecond to femtosecond regime, for CaF_2 and different types of inorganic glasses (Chap. 13).

12.6.3 Influence of Spot Size, Screening

The size of the laser spot on the substrate surface, $2w$, determines the width of the generated pattern and the expansion of the plasma plume. Both the transport of ablated species and the attenuation of the incident laser light are thereby related to w. With deep holes, both depend also on the depth, h. In the following, we consider the case $w \gg h$.

Figure 12.6.4 shows the ablation rates for $LiNbO_3$ as a function of laser fluence for different laser-beam spot sizes. For nanosecond pulses, the ablation rates are higher for smaller spot sizes. Above a 'saturation' value, about 80 µm, the ablation rate becomes independent of w. Similar observations have been made with various other materials and longer laser pulses [*Wolff-Rottke* et al. 1995; *Heitz* et al. 1990]. This effect originates from the attenuation of the incident laser radiation by the expanding plasma plume. For semi-infinite surfaces and *shallow* patterns, the attenuation decreases with decreasing spot size because 3D transport of ablation products becomes effective. This is consistent with time-dependent reflectivity measurements performed during such experiments. From a practical point of view, this effect has

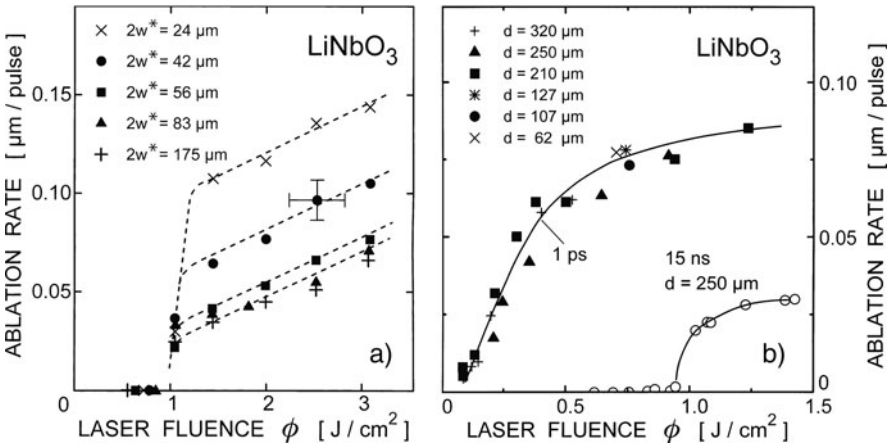

Fig. 12.6.4 a, **b** Ablation rate of $LiNbO_3$ versus XeCl-laser fluence for various spot diameters. The *dashed* and *solid curves* are to guide the eye. (**a**) $\tau_\ell = 11$ ns [*Eyett* and *Bäuerle* 1987]; (**b**) $\tau_\ell = 1$ ps and 15 ns [*Beuermann* et al. 1990]

to be considered when employing projection masks with different feature sizes. In this case the depths of single features will differ from each other.

As already mentioned, the initial velocity of species ejected from the ablated surface is of the order of 1–10 μm/ns. Thus, even if ablation would start instantaneously, almost no plasma plume can develop during a picosecond or femtosecond pulse, and plasma shielding should be strongly reduced or even avoided. This has in fact been demonstrated (Fig. 12.6.4b). With picosecond pulses, the ablation rate becomes independent of laser-beam spot size ($d \approx 2w$ is the diameter of the hole). The ablation rate obtained in the regime of high fluences is approximately equal to that obtained with the smallest spot size in Fig. 12.6.4a.

These experiments show that ultrashort pulses allow strong material excitation prior to the expansion of the plasma plume.

12.6.4 Dependence on Pulse Number

With strongly absorbing materials, the total ablated depth increases initially linearly with the number of laser pulses, N_ℓ. This is shown in Fig. 12.6.5b for the example of ceramic PZT. Here, the slope depends on laser fluence, and also on pulse duration. Similar results have been obtained with PZT doped with Sr (PSZT) and La (PLZT) [*Leech* et al. 2008].

With weak absorbers, where laser-generated defects may become important, material removal can be slow or zero for the first 'incubation' pulses and then increase linearly or non-linearly, depending on the material and the laser parameters.

With *deep* holes or grooves, the ablation rate may strongly decrease with increasing N_ℓ. This is shown in Fig. 12.6.5a. A similar behavior has been found for

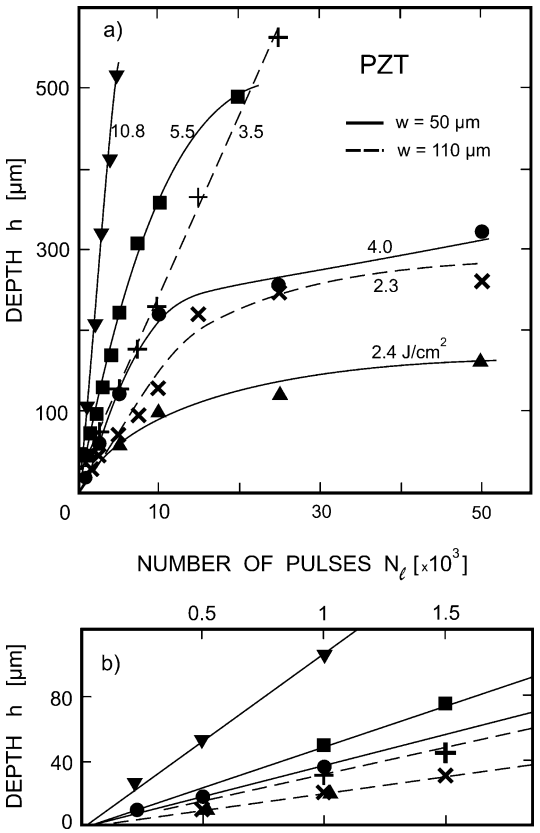

Fig. 12.6.5 (**a**) Depth of grooves as a function of the number of laser pulses, N_ℓ, for different fluences and widths of the line focus. *Solid* and *dashed curves* are guides for the eye. (**b**) Increase in depth for small N_ℓ. Focus $w = 50\,\mu$m: ▲ $\phi = 2.4\,\mathrm{J/cm^2}$; ● $\phi = 4.0\,\mathrm{J/cm^2}$; ■ $\phi = 5.5\,\mathrm{J/cm^2}$; ▼ $\phi = 10.8\,\mathrm{J/cm^2}$. Focus $w = 110\,\mu$m: × $\phi = 2.3\,\mathrm{J/cm^2}$; + $\phi = 3.5\,\mathrm{J/cm^2}$ [*Eyett* et al. 1987]

other systems as, e.g., for nanosecond excimer-laser ablation of various polymers [*Srinivasan* 1994] and for picosecond to femtosecond Ti:sapphire-laser ablation of different crystalline and amorphous materials (Chap. 13). The drop-off in rate observed with *high* N_ℓ, i.e., with the formation of deep holes or grooves, can be related to the following different effects:

- With increasing hole depth, the loss of energy by heat conduction increases and thereby decreases the laser-induced temperature rise. This effect becomes significant when $h \approx w$.
- With increasing depth, the transport of ablated species becomes less efficient and favors material recondensation within the hole/groove. The depth at which the gradual decrease in slope is observed increases with the width of the focus, $2w$. With wider holes/grooves, recondensation of species becomes less likely.

- With nanosecond pulses, the attenuation of the incident laser-light by the ejected material becomes of great relevance. This can be made plausible from a simple estimation. The velocity of species ejected out of the hole is 10^5–10^6 cm/s. During a laser pulse of 20 ns, these species will travel about 20–200 μm. Thus, for deep holes/grooves the attenuation of the incident light by scattering and secondary excitation of product species is important and becomes more efficient with increasing h. With higher fluences, secondary photolysis increases and results in smaller fragments with smaller attenuation cross sections. Laser–vapor/plasma interactions are strongly reduced or even absent with picosecond and femtosecond pulses. The vapor/plasma plume cannot develop on a sub-picosecond time scale.

A dependence similar to that shown in Fig. 12.6.5a has also been observed in certain cases of *large-area* irradiation. Here, the decrease in ablation rate is related to changes in the surface morphology and/or the chemical composition of the surface. Both effects are important, for example, when PI is irradiated with KrF-laser light at fluences $\phi < 0.26\,\mathrm{J/cm^2}$. Here, ablation even ceases after a certain number of pulses. This effect is related to roughening and carbonization of the surface (Sect. 27.1.4). Surface roughening results in a strong increase in surface area and thereby in a decrease in effective fluence. Carbonization changes the optical and thermal properties of the surface and thereby the coupling and action of the laser light. With intermediate fluences, cone formation, which is observed with many different materials, may suppress or even stop ablation (Sects. 22.1 and 28.4).

An increase in laser-pulse *repetition rate* increases the (average) laser-induced temperature rise (Sect. 6.3) and thereby the rate of thermally activated processes. This effect has been observed in connection with surface carbonization of PI [*Ball* et al. 1996] and the ablation of PI and a PMMA-based polymer [*Burns* and *Cain* 1996].

12.6.5 Influence of an Ambient Atmosphere

A *non-reactive* atmosphere may influence the transport of ablated material, the attenuation of the laser light, and the development of surface instabilities. All of these effects become more pronounced with increasing gas pressure.

Due to collisions with gas-phase molecules, the transport of ablated species away from the irradiated surface area is hindered with respect to free expansion into vacuum. This favors cluster formation (Sect. 4.1.4) and the recondensation of product species (debris) on the substrate surface. As a consequence, the (net) ablation rate is, in general, reduced and debris outside of the ablated region is observed. Additionally, the confinement of the vapor plume increases the attenuation of the incident laser light and thereby reduces the effective laser fluence. The situation may change, however, when surface corrugations related to instabilities and/or to surface-tension effects in thin films become effective.

Instabilities

Figure 12.6.6 shows the ablation rate for an Au film on quartz as a function of fluence for KrF-laser radiation. The rate significantly *increases* with Ar pressure. Such an increase in rate was also observed with increasing laser spot size. This effect can be tentatively related to the development of surface instabilities. Their formation may be enhanced if the vapor stays over the molten surface longer either due to a larger spot size or due to a higher ambient pressure. Instabilities result in surface corrugations which enhance the absorptivity of the material and reduce the vaporization enthalpy (Sect. 28.4). The effect is particularly pronounced with thin thermally high-conductance films on insulating substrates. When $\kappa_1 \gg \kappa_s$, the time during which the material is molten, Δt_m, is very long and instabilities can build up even with a single laser pulse. With the Au film and $\phi = 1\,\mathrm{J/cm^2}$, one finds that Δt_m equals several microseconds; with the same parameters and bulk Au one finds $\Delta t_m \approx 30\,\mathrm{ns}$. With thin films, surface corrugations lead to the formation of islands and thereby to a strong suppression of heat conduction. With thick films or bulk material and multiple-pulse irradiation, hydrodynamic instabilities can result in the formation and ejection of (liquid) droplets and thereby in an increase in the overall ablation rate [*Bennett* et al. 1995].

A *reactive* atmosphere can increase the rate of material removal. This is known as dry etching (Chaps. 14 and 15). Additionally, such an atmosphere can change the physical and chemical properties of the ablated surface, which is the basis of many types of laser-induced surface modifications (Chaps. 26 and 27). A reactive atmosphere can also change the chemical composition of ablated species. This is of particular importance in PLD (Chap. 22).

Within any type of medium, PLA can generate shock waves (Chap. 30).

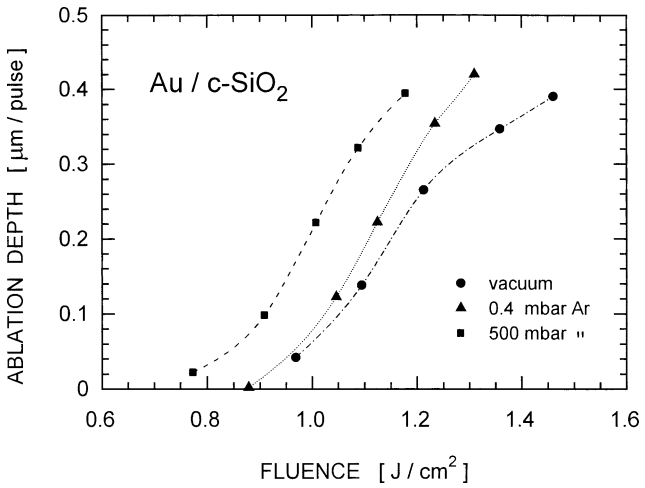

Fig. 12.6.6 Single shot (average) ablation rate of an Au film ($h_1 = 0.54\,\mu\mathrm{m}$) on a quartz crystal microbalance as a function of KrF-laser fluence ($\tau_\ell \approx 26\,\mathrm{ns}$). Different symbols refer to different Ar gas background pressures [*X. Zhang* et al. 1997]

12.7 Photothermal Volume Decomposition

If the lifetime of defects, broken bonds, etc., generated within the material volume is long enough, the surface concentration of defects, $N_D(z = 0)$, increases during single-pulse or multiple-pulse irradiation. $N_D(0)$ can be calculated from the heat equation and the kinetic equation. The heat equation has the same form as (11.2.6), except for the source term, which now contains the additional energy (per volume and time) that is required for bond breaking (Sect. 2.2)

$$Q(z,t) = -\frac{\partial I}{\partial z} - \Delta H_d (1 - N_D^*) k_d^0 \exp\left(-\frac{\mathscr{E}_d}{T(z,t)}\right) . \tag{12.7.1}$$

Here, we have assumed a first-order 'reaction' with activation temperature $\mathscr{E}_d$ and pre-exponential factor k_d^0. $N_D^* = N_D/N$, where N is the total number density of bonds. ΔH_d is the (total) enthalpy of (all) bonds. If we ignore any backward or subsequent reaction, i.e., if we assume the lifetime of the defects (broken bonds) to be infinite, the kinetic equation can be written in the form

$$\frac{\partial N_D^*}{\partial t} = v \frac{\partial N_D^*}{\partial z} + (1 - N_D^*) k_d^0 \exp\left(-\frac{\mathscr{E}_d}{T(z,t)}\right) . \tag{12.7.2}$$

The heat equation and (12.7.2) are coupled via the ablation velocity, v. The position of the interface between the gas and condensed phases is determined by the condition

$$N_D(z = 0) = N_D^{cr} . \tag{12.7.3}$$

Thus, v depends on the kinetics of defect formation and thereby on the temperature distribution within the *bulk* material. This is significantly different to pure surface evaporation, where v is determined by the *surface* temperature only [see (11.2.11)]. The most important results of this model are the following [*Bityurin* et al. 2003, 1998]:

- The maximum temperature always occurs at the surface.
- With fluences $\phi < \phi_{th}$, volatile species may result in a mass loss.
- Near the onset of ablation, the temporal behavior of the ablated-layer thickness is described by

$$\Delta h(t) = C(t - t_{cr})^{1/2} \tag{12.7.4}$$

  where C is a constant and t_{cr} the time during which the critical concentration N_D^{cr} is built up. This leads to a sharp onset of ablation

$$v = \frac{C}{2(t - t_{cr})^{1/2}} . \tag{12.7.5}$$

- For stationary ablation, the results are equivalent to those obtained for surface evaporation (Sect. 11.2.1). We can directly employ (11.2.10) and (11.2.11) if we substitute $v_0 \rightarrow v_0'(\alpha, N_D^{cr}, k_d^0, \Delta H_d)$, $\Delta H_v^0 \rightarrow \Delta H_d N_D^{cr}/N$, and $\mathscr{E}_v \rightarrow 2\mathscr{E}_d/3$ for low intensities or $\mathscr{E}_d$ for high intensities.
- For fluences $\phi \gtrsim \phi_{th}$ the ablated-layer thickness can be described by

$$\Delta h \approx \frac{1}{\alpha}\zeta\left[\frac{\phi - \phi_{th}}{\phi_{th}}\right]^{1/2} , \tag{12.7.6}$$

  with $\phi = I_0\tau_\ell$. ζ depends on pulse shape and on $D\alpha^2\tau_\ell$, and it is of the order of unity, i.e., $\zeta \sim 1$.
- When ablation ceases, some volatile species still exist below the surface and may leave the material afterwards.
- If the lifetime of defects is finite, i.e., if recombination or secondary reactions become important, stationary ablation can develop only above a certain threshold intensity, even with cw irradiation.

Both bulk and surface photothermal models fit the experimental data on the ablated-layer thickness, $\Delta h = \Delta h(\phi)$, for ns-laser pulses equally well. Thus, such measurements do *not* permit to differentiate between these models. The situation is different for ultrashort-pulse laser ablation. Here, time-resolved measurements should yield different results (Chap. 13). With fluences $\phi >> \phi_{th}$ the overall ablation behavior becomes dominated by shielding and is independent of the mechanism of material decomposition.

12.8 Photochemical Ablation

Purely non-thermal (photochemical) laser ablation has been discussed for organic polymers, inorganic insulators, and semiconductors.

Let us assume that photochemical ablation is based on direct (non-thermal) bond breaking. With an irradiation geometry as depicted in Fig. 11.2.1, the number of broken bonds for a single-step reaction is obtained from the rate equations (3.0.3) and (3.2.1)

$$N_D(z) = \eta\frac{\sigma N\phi(z)}{h\nu} ,$$

where $\phi(z) = \int_0^\infty I(z,t')dt'$ is the dose and η the quantum yield. N is the total number density of absorption centers (chromophores). Subsequently, we assume that ablation occurs if the number of broken bonds within the layer Δh exceeds some critical value, i.e., if $N_D(z \le \Delta h) \ge N_D^{cr}$. Then, we obtain from the Lambert-Beer law

$$\Delta h = \frac{1}{\alpha} \ln\left(\frac{\phi}{\phi_{\text{th}}}\right) , \tag{12.8.1}$$

with

$$\phi_{\text{th}} = \frac{h\nu}{A\eta\sigma}\frac{N_{\text{D}}^{\text{cr}}}{N} = \frac{h\nu}{A\eta\alpha}N_{\text{D}}^{\text{cr}} . \tag{12.8.2}$$

and $\Delta h = 0$ if $\phi < \phi_{\text{th}}$. The absorption coefficient α is often used as a *fit* parameter. It can significantly differ from measured (linear) absorption coefficients. Clearly, (12.8.1) does *not* hold if $\alpha = \alpha(I)$ and/or if incubation plays an important role. If screening of the incident laser light cannot be ignored, instead of (12.8.1) one can derive the relation

$$\Delta h = \frac{1}{\alpha_{\text{p}}} \ln\left(1 + \frac{\alpha_{\text{p}}}{\alpha}\frac{\phi - \phi_{\text{th}}}{\phi_{\text{th}}}\right) \equiv \frac{1}{\alpha_{\text{p}}} \ln\left[1 + \alpha_{\text{p}} B(\phi - \phi_{\text{th}})\right] . \tag{12.8.3}$$

If $\alpha_{\text{p}}\Delta h \ll 1$, i.e., with fluences $\phi \gtrsim \phi_{\text{th}}$ and/or if $\alpha_{\text{p}} \approx 0$, we can employ a Taylor expansion and obtain

$$\Delta h \approx \frac{1}{\alpha}\frac{\phi - \phi_{\text{th}}}{\phi_{\text{th}}} \equiv B(\phi - \phi_{\text{th}}) , \tag{12.8.4}$$

where the slope $B = A\eta/h\nu N_{\text{D}}^{\text{cr}}$ is independent of α and α_{p}. Equations (12.8.3) and (12.8.4) have the same form as (12.3.6) and (12.3.3) respectively, but with different meanings for B and ϕ_{th}. If $\alpha = \alpha_{\text{p}}$, one obtains (12.8.1) again. If $\alpha \neq \alpha_{\text{p}}$, $\Delta h(\phi)$ initially follows (12.8.1). At high fluences it approaches the same law but with α substituted by α_{p}, including (12.8.2). In reality, one has to take into account that plasma formation depends strongly on laser wavelength and that $\alpha_{\text{p}} \neq$ const. in many cases (Sect. 11.6). Furthermore, with increasing intensity, bleaching due to saturation effects may result in ablation rates in excess of those calculated from (12.8.1) [*Pettit* and *Sauerbrey* 1993]. The influence of multiple reaction pathways and the critical number density of broken bonds, N_D^{cr}, has been described by *Bityurin* et al. (2003).

12.8.1 Dissociation of Polymer Bonds

Polymers are composed of long molecular chains that consist of sequences of monomers, i.e. molecular groups of the same nature (Fig. 12.1.3). Within the same chain, the monomers are strongly bound. The bonds between neighbouring molecular groups that belong to *different* chains are comparatively weak. Efficient ablation requires the breaking of intrachain bonds. The length of fragments should be smaller than Z. Here, Z is the number of monomers per persistent length (Kune segment; correlation length with respect to the direction of the polymer chain). Z is

determined by geometrical factors and the stiffness of chains. Typically, $Z = 5 - 10$ monomer units. The chemical structure and design of polymers for high-quality laser ablation has been described by *Lippert* (2005).

Direct (non-thermal) bond breaking may be an important or even dominant mechanism in polymer ablation by means of deep UV-laser light with $\lambda \leq 200$ nm. Dissociation of polymer chains or side groups into smaller fragments leads to an expansion of the irradiated volume. This creates an internal pressure which reduces the activation energy for bond breaking and converts it to translational energy of ablation products (Sect. 12.9).

The influence of thermal, mechanical and different types of chemical reactions on ablation thresholds of PMMA subjected to UV-laser, and in particular to 157 nm F_2-laser radiation, has been studied by means of molecular-dynamics (MD) simulations in combination with Monte Carlo-based techniques [*Prasad* et al. 2008; see Sect. 13.3]. For PTFE, the principal ablation product observed with 248 nm KrF-laser radiation is the monomer $[CF_2]_n$ with $n = 2$ (Fig. 12.1.3). With 157 nm F_2-laser radiation, fragments with $n = 1 - 6$ have been detected [*John* et al. 2008]. These differences in ablation products observed with KrF and F_2 lasers can be attributed to photothermal and mainly photochemical ablation mechanisms, respectively. Direct bond breaking seems to play a significant role also in ArF-laser ablation of PI (Fig. 12.6.1) and PMMA.

12.8.2 Defect-Related Processes, Incubation

Physical and chemical defects, including those that are generated by the laser radiation itself (incubation centers), can significantly influence microscopic interaction mechanisms which finally result in laser-induced emission of species from solid surfaces. Defects permit sub-bandgap electronic excitations in non-metals, enhance multiphoton bandgap excitations, alter binding energies of neighboring atoms and their coupling to the crystal lattice, trap electronic excitation energies, electrons, holes, etc. Energy trapping can have two consequences: it suppresses fast thermal relaxation and permits local energy transfer to a single or a few atoms only.

The mechanisms described in the following are mainly discussed in connection with laser-induced desorption (LID) where sub-monolayer quantities of atoms, molecules, ions, clusters, etc., are ejected from the surface without any significant modification of the surface morphology [*Miller* and *Haglund* 1998]. Nevertheless, defect formation by these mechanisms may be responsible for material 'incubation', and for the 'tail' observed in mass-loss measurements for fluences $\phi \leq \phi_{th}$ (see, e.g., Fig. 12.6.1). With fluences $\phi \geq \phi_{th}$, where significant ablation takes place, such mechanisms may *initiate* the ablation process.

The effect of laser radiation with photon energies $h\nu < E_g$ has been studied in particular for wide-bandgap insulators such as alkali halides, alkaline earth fluorides, a-SiO_2, etc. Here, bandgap excitation based on *multiphoton* absorption is

strongly enhanced if there are 'intermediate' (defect) states (Fig. 2.1.1). In these materials, the generation of electron–hole pairs can result in the formation of self-trapped excitons (STE). An exciton in an alkali halide, for example, consists of a hole that is localized on a (negative) halogen ion – thereby forming a halogen atom – and an electron which is bound by the Coulomb potential of the surrounding (positive) alkali ions. Because of the strong electron–phonon coupling in these materials, such excitons can become self-trapped. The major contribution to the lattice relaxation energy (for one-center excitons) originates from the Jahn–Teller energy [*Itoh* et al. 1991]. STE states are located in the bandgap and may be excited by laser light. Non-radiative decay of STE can result in the formation of F center–H center pairs (an F center is an electron in an anion vacancy; a H center denotes a molecular X_2^- ion, where X stands for a halogen atom) [*Haglund* 1998; *Itoh* et al. 1991]. X_2^- ions generated in this way are very mobile and diffuse over large distances. At the surface, they can dissociate and thereby lead to (preferential) emission of halogen atoms (the mobility of X_2^- ions depends on the crystal orientation and the emission of halogen atoms will therefore be anisotropic). What remains are F centers and an alkali-rich surface layer (F centers are not very mobile and neutralize metal ions only to some extent). At higher temperatures the metal atoms/ions are thermally desorbed from the surface. The defects generated in the halogen sublattice can be considered as 'incubation' centers. In any case, they increase the trapping of holes and the optical absorption coefficient, etc.

Laser-induced photoelectron emission and desorption of neutrals and ions has been studied for various wide-bandgap oxides, nitrates, alkali halides, carbonates, and phosphates. Sub-bandgap laser irradiation of these materials at *low* fluences results in positive ion emission with very high energies. A model system that has been studied in great detail is MgO ($E_g \approx 7.8$ eV). Here, 248 nm (5 eV) KrF-laser irradiation results in the emission of Mg^+ and Mg^{++} ions with energies of up to 11 and 20 eV, respectively. The intensities of emitted ions are strongly enhanced by surface treatments that increase the defect density. These observations, and the low laser-light intensities employed in these experiments, are inconsistent with an interpretation based on multiphoton absorption processes. The emission mechanism is attributed instead to the Coulomb repulsion of Mg^+ or Mg^{++} ions that are located over oxygen vacancies from which one or two electrons have been removed by photoexcitation. The ion energies observed are consistent with the Madelung energies of such defects. Similar mechanisms have been discussed in connection with the emission of K^+ and K^- ions from KCl, Na^+ and Na_2^+ ions from $NaNO_3$, and of Ca^+ ions from $CaCO_3$ and $CaHPO_4 \cdot 2H_2O$. The emission of both photoelectrons and ions from these materials may be responsible for the initial phase of plume formation and laser ablation [*Dickinson* 2008, 1998]. A mesoscopic modelling of such processes has been performed by *Stoneham* et al. (1999).

Even with metals, translational energies of atoms desorbed from the surface may significantly exceed the photon energy. An example is the desorption of Au atoms from polycrystalline Au irradiated with nanosecond KrF-laser radiation [*Bennett* et al. 1996].

12.9 Photophysical Ablation

Thermal *and* non-thermal ablation mechanisms become important if, for example, the second term in (12.2.1) cannot be ignored. This can be the case for relatively low surface temperatures (fluences) and activation energies $\Delta E^* \ll \Delta E$.

In order to elucidate the main ideas, we only consider a two-level system (Fig. 12.2.2). We ignore temperature dependences in parameters, spontaneous emission, any influence of defects, thermo- and photomechanical contributions related to stresses, etc. [*Luk'yanchuk* et al. 1993a, b].

In a (moving) reference frame that is fixed with the surface to be ablated, the density of species A^* and A can be described by

$$\frac{\partial N_{A^*}}{\partial t} = v\frac{\partial N_{A^*}}{\partial z} + \frac{\sigma I}{h\nu}(N_A - N_{A^*}) - k_T N_{A^*} \,, \tag{12.9.1}$$

$$\frac{\partial N_A}{\partial t} = v\frac{\partial N_A}{\partial z} - \frac{\sigma I}{h\nu}(N_A - N_{A^*}) + k_T N_{A^*} \,, \tag{12.9.2}$$

where σ is the absorption cross section, and $k_T = \tau_T^{-1}$ the rate constant for thermalization of the excitation energy. Here, we ignore any diffusion processes, which are slow compared to all other processes under consideration.

The propagation of the laser light within the substrate is given by

$$\frac{\partial I}{\partial z} = -\sigma(N_A - N_{A^*})I \,. \tag{12.9.3}$$

The heating of the solid surface is described by the heat equation

$$\frac{\partial T}{\partial t} = v\frac{\partial T}{\partial z} + D\frac{\partial^2 T}{\partial z^2} + \frac{D}{\kappa}Q \,. \tag{12.9.4}$$

The heat source, Q, is determined by non-radiative transitions,

$$Q = k_T h\nu N_{A^*} \,. \tag{12.9.5}$$

The heat flux at the surface $z = 0$ is dominated by the heat loss due to ablation of species A and A^*,

$$\kappa \left.\frac{\partial T}{\partial z}\right|_{z=0} \approx v_A \Delta H_A N_A^*(0) + v_{A^*}\Delta H_{A^*} N_{A^*}^*(0) \,. \tag{12.9.6}$$

For the transition enthalpies we set $\Delta H_A = \varrho \Delta E_A/m$ and $\Delta H_{A^*} = \varrho \Delta E_{A^*}/m$, where m is the (average) mass of ablated fragments A and $A^* \times N_A^* = N_A/N$, with $N = N_A + N_{A^*}$. Besides (12.9.6) we employ the boundary conditions

$$N_{\mathrm{A}}(z \to \infty) = N\,, \quad N_{\mathrm{A}^*}(z \to \infty) = 0\,,$$
$$T(z \to \infty) = T(\infty)\,, \quad \text{and} \quad I(z = 0, t) = I_{\mathrm{a}}(t)\,. \tag{12.9.7}$$

Here, $I_{\mathrm{a}}(t) < I_\ell(t)(1 - R)$ due to the attenuation of the laser-output intensity, I_ℓ, within the vapor/plasma plume [see (12.3.5)]. The initial conditions are

$$N_{\mathrm{A}}(t = 0) = N\,, \quad N_{\mathrm{A}^*}(t = 0) = 0\,, \quad \text{and} \quad T(t = 0) = T(\infty)\,. \tag{12.9.8}$$

Equations (12.2.1) and (12.9.1), (12.9.2), (12.9.3), (12.9.4), (12.9.5), (12.9.6), (12.9.7) and (12.9.8) characterize the boundary-value problem. Similar models can also be applied to cases where transitions A $\to$ A* $\to$ D or direct non-thermal excitation/generation of defects is most important.

12.9.1 Long Pulses

Photophysical ablation may be important for the description of systems where the activation energy $\Delta E_{\mathrm{A}^*} \ll \Delta E_{\mathrm{A}}$. For long pulses we can consider quasi-stationary conditions with $\partial N_{\mathrm{i}}/\partial t \approx 0$. The first term on the right-hand side of (12.9.1) is usually small, and it yields

$$N_{\mathrm{A}^*}(0) \approx \frac{N I}{2 I_{\mathrm{sat}}(1 + I/I_{\mathrm{sat}})} \approx \frac{\sigma N I \tau_{\mathrm{T}}}{h\nu} = \frac{\alpha I \tau_{\mathrm{T}}}{h\nu} = \frac{\alpha \phi \tau_{\mathrm{T}}}{h\nu \tau_\ell}\,, \tag{12.9.9}$$

where $I_{\mathrm{sat}} = h\nu/2\sigma\tau_{\mathrm{T}}$ is the saturation intensity. If we assume that the second term in (12.2.1) and (12.9.6) dominates and if we substitute N_{A^*} by (12.9.9), we end up with the same stationary problem as in Sect. 11.2.1, except that $\mathscr{E}_{\mathrm{v}}$ is replaced by $\mathscr{E}_{\mathrm{A}^*}$, ΔH_{v}^0 by ΔH_{A^*}, and

$$v_0 \equiv v_0(I) = v_{0\mathrm{A}^*} \frac{N_{\mathrm{A}^*}(0)}{N} \approx v_{0\mathrm{A}^*} \frac{\sigma I \tau_{\mathrm{T}}}{h\nu}\,. \tag{12.9.10}$$

The second equality in (12.9.9) and (12.9.10) refers to the case $I \ll I_{\mathrm{sat}}$, which is fulfilled well with short relaxation times, τ_{T}. Due to the weak dependence of $v_{\mathrm{st}}(v_0)$ in (11.2.12), the overall behavior of (theoretical) ablation curves will be similar for photophysical and purely thermal models, i.e., we obtain almost the *same* laws as in Sect. 12.3. The main difference is that efficient ablation can take place at relatively low temperatures, mainly due to the low activation energy $\mathscr{E}_{\mathrm{A}^*}$.

Another interesting feature of the model is the behavior of the intensity distribution. From (12.9.3) and (12.9.9) it becomes evident that with increasing concentration N_{A^*} (increasing τ_{T}), the penetration depth of the laser light increases. This *bleaching* effect becomes important when $I/I_{\mathrm{sat}} \to 1$ [see also *Pettit* and *Sauerbrey* 1993].

The photophysical model permits one to fit the experimental data in Fig. 12.6.1 with an accuracy similar to that obtained with the thermal model. With a relaxation

time $\tau_T \geq 10^{-9}$ s, the surface temperature derived for fluences $\phi \approx \phi_{th}$ is about 2000°C. This temperature is in agreement with direct temperature measurements [*Brunco* et al. 1992] and with experimental data on the vibrational temperature of product species [*Srinivasan* and *Braren* 1989]. One should emphasize, however, that the relaxation times required for this fit are unrealistically long. In reality, typical relaxation times in polymers are of the order of some 10 ps. The value $\Delta E_A = 3$ eV employed in the calculations is realistic for PI (polyimide) where the dissociation energy of C–N bonds is about 3.15 eV. In many cases, for example, in aromatic compounds, bond-breaking energies may exceed this value considerably ($\Delta E_A \approx$ 4.8 eV for C–H and C–O bonds, and 4.5 eV for C–N bonds).

12.9.2 Short Pulses

Photophysical effects may become of particular importance if in (12.9.9) the intensity $I/I_{sat} \approx \alpha\phi\tau_T/Nh\nu\tau_\ell > 1$. This is often fulfilled for laser pulses that are shorter than the thermal relaxation time, i.e., $\tau_\ell < \tau_T$. For such short pulses, the photophysical model allows a number of predictions that differ significantly from the theoretical and experimental results obtained for purely thermal ablation: During the pulse, a bleached zone near the surface is formed. Significant thermal relaxation $A^* \rightarrow A$, and thus *material heating* and ablation take place mainly *after* the laser pulse. Ablation is maintained during the time τ_T, when the temperature remains high enough due to transitions $A^* \rightarrow A$ within the bleached zone. For further details see *Luk'yanchuk* et al. (1998).

12.9.3 Thermal Versus Photochemical and Photophysical Ablation

The most important differences and characteristics between thermal, photochemical and photophysical ablation models can be summarized as follows:

- With short pulses and in particular with ps- or fs-pulses, the *dynamical* behavior of the ablation process may be quite different for purely thermal and photophysical mechanisms, even when the overall ablated-layer thicknesses are comparable.
- The efficiency of photophysical ablation via channel A^* increases approximately linearly with increasing relaxation time, τ_T. Purely thermal ablation remains almost unaffected or may even decrease with increasing τ_T.
- Purely photochemical ablation can be described by $\Delta E_{A^*} \rightarrow 0$. For cw-laser irradiation this channel dominates if $I\sigma\tau_T/h\nu = \tau_T/\tau_0 > \exp(-\mathscr{E}_A/T)$ (see also Sect. 2.1). This holds also for pulsed irradiation if $\tau_\ell \gg \tau_T\tau_0/(\tau_T + \tau_0)$. For short laser pulses the condition is $\tau_\ell(\tau_T + \tau_0)/\tau_0\tau_T > \exp(-\mathscr{E}_A/T)$.
- Ablation experiments using *two* successive pulses with variable time delay, t_d, may show opposite behavior within certain parameter ranges [*Preuss* et al. 1993].

For example, the total ablated-layer thickness may increase with t_d for a photophysical mechanism and decrease for a purely thermal mechanism.

- If the analysis of measured ablation curves yields activation energies that are significantly smaller than bond-breaking energies, i.e., if $\Delta E_{exp} < \Delta E_A$, photophysical mechanisms may play an important role. Such low activation energies can, however, also be explained by (thermal) material degradation, in particular with polymers.
- The dependence of the overall ablated depth on laser fluence, $\Delta h = \Delta h(\phi)$, is not very sensitive to the particular model. In any case, high fluences cause high temperatures. Thus, photochemical effects will become less important.
- With all models, low surface temperatures, T_s, can be explained by small values of ΔE_A, or ΔE_{A^*}.
- The photophysical model can explain the absence of certain types of surface instabilities (Chap. 28).
- The activation energy ΔE_{A^*}, which strongly affects the results, is unknown for bulk material. For free molecules, the assumption $\Delta E_{A^*} < \Delta E_A$ certainly holds in most cases.
- In the present form, the photophysical model takes into account only the desorption of species from the *surface*. In reality, volume effects often play an important or even dominating role in laser ablation (Sects. 12.7 and 13.3). For example, when the maximum in the temperature distribution is located below the surface (Fig. 11.2.1), volatile product species formed within the material volume may cause explosive-type ablation.
- To exclude stimulated emission, at least one additional energy level should be taken into account. This would describe single-photon excitation and relaxation processes as shown on the left-hand side of Fig. 12.2.2. Because $\tau_T' \ll \tau_T$, the energy $h\nu - E_g$ is dissipated into heat. Ablation rates calculated on the basis of a four-level system for wavelengths $\lambda = 351\,\text{nm}$, 308 nm, and 248 nm almost coincide with the solid curves in Fig. 12.6.1. For further details on the photophysical model see *Bityurin* et al. (2003) and references therein.

12.10 Thermo- and Photomechanical Ablation

Mechanical ablation is caused by built-up stresses generated by the laser light (Fig. 12.2.1). Depending on whether these stresses originate from thermal effects (thermal expansion, vaporization, thermally generated defects, etc.) or non-thermal effects (expansion due to direct bond breaking, non-thermal defect formation, etc.), we use the terms thermomechanical or photomechanical ablation, respectively. Such mechanisms are important in the following:

- Liquid-phase expulsion under the action of the recoil pressure of species evaporated from the surface (Sect. 11.4).
- Inorganic insulators and semiconductors, where light-induced stresses may change the optical properties of the material.

- Polymer ablation, where both thermal and non-thermal fragmentation of polymer chains may lead to a volume increase. A well-known example is the depolymerization of PMMA.
- Cases where mechanical stresses change bond-breaking energies.
- Strongly inhomogeneous systems that consist of different materials with different physical (thermal, optical, etc.) properties, such as layered structures, certain types of ceramics, compound materials, etc.
- PLA of biological tissues.

12.10.1 Basic Equations

Let us first consider the influence of stresses on laser-induced defect formation. In 1D approximation, the generation of defects can be described by

$$\frac{\partial N_{\mathrm{D}}(z,t)}{\partial t} = \eta \frac{\sigma I(z,t)}{h\nu} N + k_0 N \exp\left(-\frac{\Delta E_{\mathrm{d}} - \zeta S_{zz}(z,t)}{k_{\mathrm{B}} T(z,t)}\right) , \quad (12.10.1)$$

where N_{D} is the number density of defects. N is the total number of sites, bonds, chromophores, etc. The first term describes direct (photochemical) defect formation with quantum yield η, which may depend on stress as well, i.e., $\eta = \eta(S_{zz})$. The second term describes the thermal generation of defects with an activation energy ΔE_{d} that is reduced by mechanical stresses, depending on the 'strength of coupling', ζ. A possible influence of *electronically* excited species can be described in analogy. The stress component, S_{zz}, can be calculated from the equation of thermoelasticity [*Landau* and *Lifshitz*: Theory of Elasticity 1976].

$$\frac{\partial^2 S_{zz}}{\partial t^2} = v_0^2 \frac{\partial^2 S_{zz}}{\partial z^2} - \frac{Y}{3(1-2\mu)} \frac{\partial^2}{\partial t^2} \left[\beta_{\mathrm{T}}(T - T_0) + \xi \frac{N_{\mathrm{D}}}{N}\right] , \quad (12.10.2)$$

where v_0 is the sound velocity, Y Young's modulus, and μ the Poisson ratio. The first term in parentheses describes the influence of normal thermal (volume) expansion with coefficient β_{T}. The second term describes the volume change caused by broken bonds $\Delta V/V = \xi N_{\mathrm{D}}/N$.

The decrease in activation energy by mechanical stresses can cause a significant decrease in threshold fluence. Clearly, the number of defects will strongly influence the ablation rate.

Equations (12.10.1) and (12.10.2) must be solved together with the heat equation and Beer's law. They can be applied to many systems where laser-induced defect formation, structural transformations, chemical transformations, etc., generate stresses that, in turn, affect the corresponding 'reaction' rate. Thermomechanical and photomechanical mechanisms may be responsible also for high ablation rates at relatively low temperatures.

It is evident that in most experiments *tangential* stresses cannot be ignored, in particular in laser micropatterning.

Let us start with the effect of stresses caused by normal (linear) *thermal expansion*. This occurs with any material and only depends on the laser-induced temperature rise and material parameters, i.e., $S \propto p \propto \Delta T \propto I$. This stress (pressure) can cause crack formation, exfoliation (removal of macroscopic fragments or flakes), instabilities (see, e.g., Fig. 28.6.1), etc. The rapid vertical expansion during large-area, pulsed-laser irradiation is the dominating mechanism of particle removal in laser dry cleaning (Sect. 23.7).

Let us now discuss the influence of (additional) stresses in polymer ablation. While UV-laser ablation of PI can be described well within the frame of the thermal or photophysical models, which both ignore stresses, the situation is different with PMMA. Here, ArF-laser ablation seems to be strongly influenced by built-up stresses related to the local volume increase due to photochemical and thermal *bond breaking*. In fact, the large discrepancy between the threshold fluence calculated from (12.8.2) and the experimental value derived from ablation-rate measurements may be explained along these lines (Sect. 12.8.1). If we take into account the decrease in activation energy due to mechanical stresses, we find, with $\eta(\mathrm{ArF}) = 10^{-2}$ and $\zeta = 1.7 \times 10^{-21}\,\mathrm{cm}^3$, a threshold fluence that is about two orders of magnitude smaller [*Kitai* et al. 1990]. The remaining discrepancy to the experimental value can be explained, in principle, if we take into account the influence of electronically excited defects.

It is evident, however, that the values of many of the parameters that enter these calculations are known only approximately or not at all. For these reasons, the modelling of systems where laser-induced stresses significantly influence ablation rates can reveal only qualitative results and trends. With many systems, the situation is even more complicated. For example, laser-induced defect formation or chemical transformations may result in *volatile species* which are trapped within the material and which may even accumulate in multiple-pulse experiments. The built-up pressure, however, is strongly determined by the diffusion of species and, possibly, their enhanced transport along permanent cracks, or transient cracks which open up during the thermal shock induced by the laser pulse. Such effects are not only important in many cases of laser ablation, but also in laser-induced surface oxidation, nitridation, and reduction (Chap. 26).

In particular with low-to-moderate laser-light absorption and high fluences, the pressure built up by volatile species within the material volume may become so high that big clusters or even fragments are ejected. In cases of thermally induced volume *chemical reactions*, this pressure is proportional to the reaction rate, which depends exponentially on temperature. With quasi-stationary conditions, T depends logarithmically on intensity I [see, e.g., (11.2.12)]. Then, we find again $p \propto I$. The same applies to subsurface material transformations, including melting and bubble formation, which can result in explosive material removal as well. With intensities that cause significant material evaporation, the *recoil pressure*, p_{rec}, becomes of greater importance (Sect. 11.3). With even higher intensities, the (primary) shock related to the generation of a *shock wave*, $p_{\mathrm{sw}} \propto (\phi/\tau_\ell)^{1/2}$, or, in dense media, in particular in liquids, the (secondary) shock related to bubble collapse, $p_{\mathrm{bubble}} \propto E$, may dominate (Sect. 30.3).

12.11 Material Damage, Debris

One of the most important questions for applications of PLA in surface micropatterning is the degree and extension of material damage beyond the volume ablated during the laser pulse. Among the different kinds of damage observed are defect formation, changes in morphology and chemical composition, material distortions, indications for melting, cracks, exfoliation, etc. The type and degree of damage caused by the ablation process depends on the laser parameters and the specific material, including its microstructure, pureness, internal stresses, etc. In many cases, material damage can be reduced by either increasing the absorption strength via the laser wavelength or material doping, and/or by decreasing the laser-pulse duration (dwell time). This is understandable because the spread of the damaged zone is related to the degree of localization of the absorbed laser-light energy and thereby to the heat diffusion length and the optical penetration depth.

Another important point for applications is the smoothness of the ablated surface. With many materials, the ablated surface is relatively rough for fluences just above ϕ_{th} and becomes smoother with higher fluences, or shorter wavelengths and pulse lengths. This observation may be related to the suppression of surface instabilities, convective flows, or material segregation (Chaps. 10 and 28). In some cases, e.g., in materials with strong internal stresses, the surface smoothness can be improved by thermal annealing of the material prior to ablation (Sect. 28.6).

12.11.1 Strong Absorption

For strong absorption, (12.0.1) yields $\Delta h \approx l_{\mathrm{T}}$. With nanosecond pulses, the condition $l_\alpha \ll l_{\mathrm{T}}$ is fulfilled if the laser wavelength matches a strong elementary excitation of the material to be ablated. With inorganic insulators and semiconductors, strong absorption occurs when the photon energy exceeds the bandgap energy. On this basis, we can understand, for many systems, the degree of material damage observed in surface patterning.

For oxidic perovskites, the bandgap energies are, typically, $E_{\mathrm{g}} \approx 3\,\mathrm{eV}$. Thus, the requirement $h\nu > E_{\mathrm{g}}$ can be achieved with laser wavelengths $\lambda \lesssim 410\,\mathrm{nm}$. Let us consider the experiments performed with PZT (Fig. 12.1.1): With $D \approx 4 \times 10^{-3}\,\mathrm{cm}^2/\mathrm{s}$ and $\tau_\ell(\mathrm{XeCl}) \approx 15\,\mathrm{ns}$, we obtain $l_{\mathrm{T}} \approx 0.1\,\mu\mathrm{m}$. This is comparable to the layer thickness ablated per pulse at the fluence employed. Thus, the absence of any detectable damage on the side walls and the bottom of grooves is consistent with this explanation. On the other hand, for typical dwell times employed with scanned cw Ar^+ or Kr^+ lasers, $\tau_\ell \approx 2\,\mathrm{s}$, we obtain $l_{\mathrm{T}} \approx 10^3\,\mu\mathrm{m}$. Thus, thermal damage becomes widely extended, in agreement with the experiments [*Eyett* et al. 1986].

The present argument can also be applied to organic polymers such as PET, PI, etc., whose absorption cross sections for 248 nm and 193 nm excimer-laser radiation are very high (Table III). These materials can be patterned without detectable damage by means of nanosecond KrF- or ArF-laser pulses. The same effect is

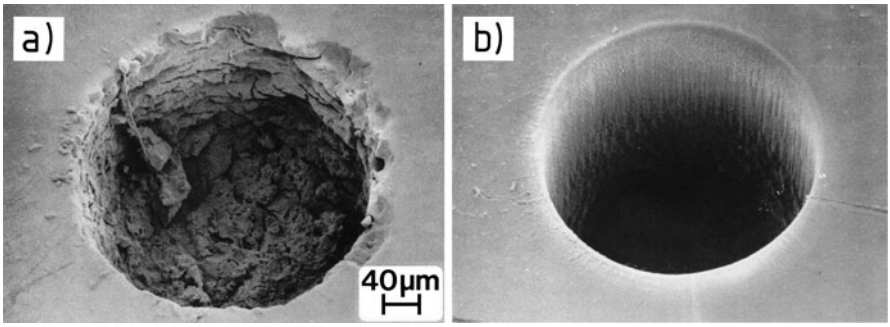

Fig. 12.11.1 a, **b** SEM pictures of holes fabricated in PS (polystyrene) by 308 nm XeCl-laser radiation ($\phi = 9\,\mathrm{J/cm^2}$, $\tau_\ell = 30\,\mathrm{ns}$, $N_\ell = 70$). (**a**) Pure PS. (**b**) PS doped with 2% diphenyl-triazene [*Ihlemann* et al. 1990]

achieved if a material with *low* intrinsic absorption is doped with an adequate dopant (Fig. 12.11.1).

For materials with large values of the thermal diffusivity, D, damage-free patterning can only be achieved with femtosecond pulses (Chap. 13). Here, nanosecond pulses are too long to suppress heat transport out of the ablated area/volume. As a result, a wide heat-affected zone (HAZ) is observed. The width of the HAZ depends not only on τ_ℓ, but also on laser fluence, pulse-repetition rate, material parameters and, for thin films, on film thickness. One should note, however, that with brittle materials and with biological tissues laser-induced damage may be determined by the shock-affected zone (SAZ), which may increase with shorter pulse lengths (Sect. 12.10.1).

12.11.2 Finite Absorption

Many materials with low absorption cannot be patterned in a well-defined way when employing standard nanosecond excimer-laser pulses. An exception is those materials in which, after a certain number of pulses, absorption is sufficiently increased due to defects (incubation centers) generated by the laser radiation itself (Sects. 12.5 and 12.8.2). Many inorganic insulators are, however, quite insensitive to UV-laser radiation. As a consequence, the number of pulses that would cause significant defect absorption is very high. For applications this is impractical. There are, however, a number of techniques to achieve good-quality surface patterning with such materials:

- One possibility is to generate surface or near-surface defects by using deep UV or even vacuum UV (VUV) radiation. Among the examples are a-SiO_2 [*Endert* et al. 1999], $GaPO_4$ [*Pedarnig* et al. 2005a], etc. that have been directly patterned by means of 157 nm F_2-laser radiation. Note that a-SiO_2 is quite stable under 193 nm ArF-laser light.

- Another possibility is the coating of the surface with an absorbing layer [*Ihlemann* 2008].
- Efficient ablation has also been demonstrated by using a combination of F_2-laser and KrF-laser pulses [*Obata* et al. 2001].
- The same effect can be achieved by electron- or ion-beam irradiation of the sample prior to laser ablation [*Dickinson* et al. 1991] or by laser-induced plasma-assisted ablation [*Hanada* et al. 2004].
- Another possibility is to employ ultrashort pulses. This is discussed in Chap. 13.

Damage thresholds in optical multimode fibers with core diameters of 180 – 600 µm were recently investigated for ns Nd:YAG-laser radiation. The threshold fluences for 1064 nm and 532 nm pulses were 140 – 570 J/cm^2 and 45 – 175 J/cm^2, respectively [*Mann* et al. 2009].

12.11.3 Debris

The condensation of ablation products (debris) on the processed surface must be avoided with many applications. Here, it is very efficient to ablate the material in a vacuum. This, however, is often impractical in production lines, and it is sometimes even impossible, as, for example, with medical applications. Debris can often be reduced or even avoided by proper selection of the ambient atmosphere, e.g., a flow of H_2 or He, or by reactive gases [*Küper* and *Brannon* 1992]. With certain conditions, debris can also be removed by subsequent laser treatment (Sect. 23.7).

After XeCl- and KrF-laser ablation of PET, PI, and PES (polyethersulfone) in air, a positive surface potential has been observed. This was ascribed to cationic fragments redeposited onto the ablated area; the process has been applied for selective electroless plating (Sect. 21.1.2).

Chapter 13
Ultrashort-Pulse Laser Ablation

Picosecond- and femtosecond-laser ablation has been proved to be a powerful technique for the patterning of both thermally high-conductance materials and wide-bandgap materials. Because both the influence of heat conduction within the material and screening of the incident laser light are strongly diminished with picosecond pulses, and can even be ignored with femtosecond pulses, material removal is very localized and requires less energy.

With ultrashort pulses, ablation mechanisms that are of minor relevance or not at all present in nanosecond-laser ablation become increasingly important. These include the desorption of excited species from material surfaces, nonlinear optical absorption within both the substrate material and the ambient medium, non-equilibrium effects related to electronic and/or vibrational excitations, multiphoton ionization (MPI) and avalanche breakdown, Coulomb explosion, and phenomena related to overcritical heating. Such strongly nonlinear interaction processes can further enhance or diminish the localization of the excitation energy. This, in turn, increases/diminishes the resolution in surface patterning and also opens up completely novel material-processing possibilities.

In the following, we give an overview on the various different aspects of ultrashort-pulse laser ablation and on the theoretical models employed for different materials and regimes of laser parameters. Liquid-assisted ultrashort-pulse laser processing is discussed in Sect. 14.5.

13.1 Material Patterning and Damage

For materials with *high thermal diffusivity*, damage-free patterning requires picosecond or even femtosecond pulses. This has been demonstrated for metals, many types of semiconductors, and for thin films of high-temperature superconductors (HTS) as, e.g., $YBa_2Cu_3O_7$ [*Proyer* et al. 1994]. Figure 13.1.1 shows the situation for a thick steel foil. With nanosecond pulses, heat transport out of the ablated volume results in a heat-affected zone (HAZ) which is related to melting. In the simplest approximation, and as long as the laser pulse length exceeds the electron-phonon relaxation time, i.e. $\tau_\ell >> \tau_{\text{e-ph}}$, the width of the HAZ can be estimated from

D. Bäuerle, *Laser Processing and Chemistry,* 4th ed.,
DOI 10.1007/978-3-642-17613-5_13, © Springer-Verlag Berlin Heidelberg 2011

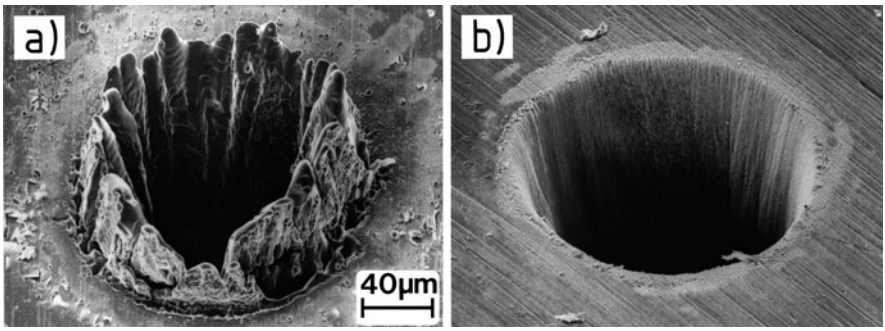

Fig. 13.1.1 a, **b** SEM pictures of holes fabricated in a 100 µm thick steel foil with 780 nm Ti:sapphire-laser radiation. (**a**) $\tau_\ell = 3.3$ ns, $\phi = 4.2\,\mathrm{J/cm^2}$. (**b**) $\tau_\ell = 200$ fs, $\phi = 0.5\,\mathrm{J/cm^2}$ [*Tönshoff* et al. 1999]. The quality of holes as shown in (**b**) can be further improved by rotating the polarization during drilling [*Nolte* et al. 1999b]

the heat penetration depth, $l_T \approx 2(D\tau_\ell)^{1/2}$. Thus, with ultrashort pulses, the HAZ can be significantly diminished, or even avoided completely (Fig. 13.1.1b). Clearly, the width of the HAZ depends not only on material parameters and on τ_ℓ but also on laser fluence, pulse-repetition rate and, with thin films, on film thickness and substrate material. If, on the other hand, $\tau_\ell << \tau_{\text{e-ph}}$, the width of the HAZ is no longer determined by τ_ℓ, but by the particular type of material and the corresponding relaxation times. Tentatively we can approximate the width of the damaged zone by $l_\mathrm{e} \approx 2(D_\mathrm{e}\tau_{\mathrm{e-ph}})^{1/2}$, where D_e is the electron diffusivity. However, with fs-pulses, and in particular with noble metals, energy transport by ballistic propagation of electrons must be considered as well. This can be done in a heuristic way, as described in Sect. 13.5. In fact, in the regime, $\tau_\ell << \tau_{\text{e-ph}}$ the effective penetration depth may exceed l_T by a factor of 10–100. For heat-sensitive compounds, the width of the zone where chemical modifications, e.g. the depletion of single species have been detected, can be explained along these lines [*Bonse* and *Krüger* 2010; Sect. 29.5].

Typical ablation rates achieved with metal targets and picosecond to femtosecond Ti:sapphire-laser pulses are 0.01 µm/pulse to 0.2 µm/pulse. The corresponding fluences are between $0.5\,\mathrm{J/cm^2}$ and $10\,\mathrm{J/cm^2}$. In multiple-pulse laser machining, the (highest) repetition rate that can be employed depends on the scanning velocity, v_s, and/or on beam distortions and shielding related to interactions with material ablated by previous pulses.

Applications of ultrashort-pulse lasers for processing materials with high thermal diffusivity can be summarized as follows:

- Patterning of material surfaces and foils that cannot be satisfactorily patterned by conventional techniques or by nanosecond-laser ablation [*Ostendorf* et al. 2006; *Weikert* and *Dausinger* 2004]. Here, a resolution down to several 10 nm has been achieved.
- Patterning of thin films [*Zoppel* et al. 2007; *Proyer* et al. 1994]. However, for certain systems and laser parameters, film and/or substrate melting and/or swelling may result in the formation of microbumps, protrusions, etc. Structure formation

observed with 30 fs 800 nm Ti:sapphire laser pulses is particularly pronounced for Au films on a-SiO_2 substrates [*Kuznetsov* et al. 2009; *Ivanov* et al. 2008]. For the same system, similar structures have been observed also with 8 ns 266 nm Nd:YAG laser pulses [*Moening* et al. 2009]. The thermally insulating substrate causes a long existence of the melt and thereby permits the development of hydrodynamic flows. The fact that such structures develop even under fs-laser irradiation may be related to the weak electron-phonon coupling in Au. Due to the ballistic propagation of electrons, the energy is rapidly distributed over the whole film depth. There are, however, alternative explanations related, e.g., to the laser-induced shock-wave or/and to optical breakdown within the ambient gas and thermal energy coupling to the substrate (Sect. 11.6.3). In any case, structures of this type can be applied for surface marking or 'on-the-fly' 2D photofabrication [*Koch* et al. 2006].

- Drilling of high-aspect-ratio microholes in metals for fuel-injector nozzles, hydraulic or pneumatic equipment, etc. In ultrashort-pulse laser drilling – as in 'standard' laser drilling (Sect. 11.8.1) – the trepanning technique yields the best results with respect to the roundness and aspect ratio of microholes. [*Ancona* et al. 2009, 2008; *Ostendorf* et al. 2006; *Breitling* et al. 2004a].
- Machining of memory metals, masks, etc.
- Fabrication of medical implants, e.g., metallic stents used as cardiovascular implants (Fig. 13.1.4).
- Synthesis of nanoclusters and powders (Sect. 4.1).

13.1.1 Wide-Bandgap Materials, Glasses, Polymers

Another field of applications of ultrashort pulses is the patterning and micromachining of materials for which the photon energy of practical lasers is not high enough either for efficient single-photon absorption or defect generation (Sect. 12.10.2). Among those are wide-bandgap (crystalline) materials with $E_g > h\nu$, but also glasses and polymers with low absorptivity. Examples for wide-bandgap materials are alkali and earth-alkali halides, and various oxides such as Al_2O_3, SiO_2, etc. Among the amorphous materials (glasses) most frequently investigated are a-SiO_2, glass filters, etc. Enhanced absorption of ultrashort-pulse laser radiation due to nonlinear effects permits precise patterning of such materials.

Figures 13.1.2 a and b show NaCl irradiated, respectively, with 16 ns and 300 fs KrF-laser pulses. Well-defined patterning without detectable thermal damage is only achieved with femtosecond pulses. This has been ascribed to coherent two-photon absorption, which reduces the optical penetration depth and thus permits sufficient energy to be absorbed per unit volume and time to initiate ablation without damage. Similar results have been obtained with different types of glasses [*Matsuoka* 2007; *Krüger* et al. 2003; *Lenzner* et al. 1999b], and polymers [*Krüger* and *Kautek* 2004; *Küper* and *Stuke* 1989]. However, the situation may be more complicated. Amorphous and crystalline SiO_2 are most precisely ablated with the shortest pulses employed, about 5 fs. On the other hand, brittle materials like

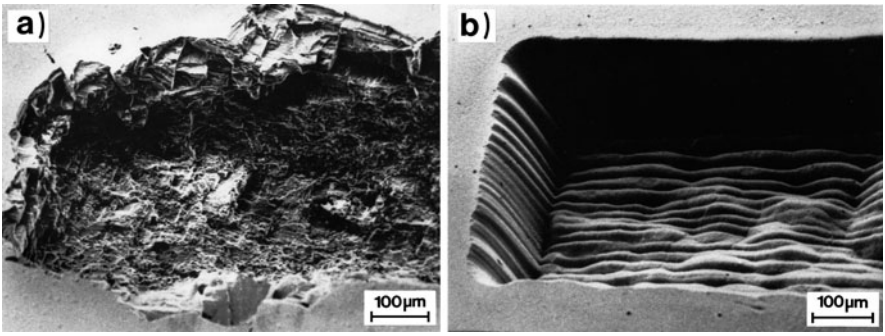

Fig. 13.1.2 a, **b** SEM pictures of NaCl ablated by 248 nm KrF-laser radiation. (a) With nanosecond pulses an undefined crater is observed. Cracks are reaching deep into the surrounding material ($\phi = 4.2\,\mathrm{J/cm^2}$, $\tau_\ell \approx 16\,\mathrm{ns}$, $N_\ell = 15$). (b) With femtosecond pulses well-defined patterning without crack formation is possible ($\phi = 500\,\mathrm{mJ/cm^2}$, $\tau_\ell \approx 300\,\mathrm{fs}$, $N_\ell = 500$) [*Küper* and *Stuke* 1989]

MgF_2, CaF_2 and MgO are most precisely machined with picosecond pulses. Here, nanosecond- and femtosecond-laser ablation results in strong fracturing and exfoliation within and far around the interaction volume. With nanosecond pulses, this observation is mainly related to thermal stresses. With femtosecond pulses, mechanical stresses related to isochoric heating, defect/void formation and mechanical fragmentation and spallation cause the material damage (Sect. 13.4). Here, the width of structures, including the damaged zone, can be significantly diminished by using temporally shaped laser pulses. This has been demonstrated for a number of materials such as a-SiO_2, Al_2O_3, and MgF_2, etc. [*Englert* et al. 2008; *Stoian* et al. 2003; see also Sect. 6.3].

Real and potential applications include:

- Drilling of deep holes [*Stoian* et al. 2003].
- Micromachining of materials for microoptical and optoelectronic devices such as micromirrors [*Brodoceanu* et al. 2010], special lenses, lens arrays [*Lin* et al. 2009], gratings [*K. Chen* et al. 1997], etc.
- Micromachining of crystalline materials such as diamond, for the fabrication of collimators, undulators, etc. [*Balling* et al. 2009].
- Chemical and physical modification and functionalization of surfaces (Chap. 23).
- Surface and buried marking (Sect. 23.6).
- Fabrication of 3D buried hollow structures for microchannel devices, gratings, lenses, etc. (Sect. 13.6).
- Microfabrication of metamaterials [*Chen* et al. 2010].
- Material modifications for the fabrication of gratings, waveguides, optical data storage, etc. (Sect. 23.6).
- Polymerization and shaping of organic and organic-inorganic materials (Sect. 27.3).
- Synthesis of nanoclusters and powders (Sect. 4.1).
- Ablation of soft and hard biological tissues (Chap. 31).
- Some cases of restoration of artworks (Chap. 32).

13.1.2 Nanostructures

The combination of ultrashort laser pulses with SXM-techniques (Sect. 5.2.1) permits to fabricate well-defined nanostructures. Here, the laser light is either coupled into a glass fiber (SNOM-technique) or it directly irradiates the tip of an atomic force (AFM) or scanning tunneling microscope (STM) [*Hwang* et al. 2006; *Klein-Wiele* and *Simon* 2003].

Periodic nanopatterns have been produced by either phase-controlled multiple-beam interference techniques [*Klein-Wiele* and *Simon* 2003] or by means of 2D-microlens arrays (Sect. 5.2.1). Figure 13.1.3 shows an example for the case of a (100) Si surface that has been patterned by using a self-assembled lattice of a-SiO_2 microspheres together with 300 fs 266 nm Ti-sapphire laser radiation.

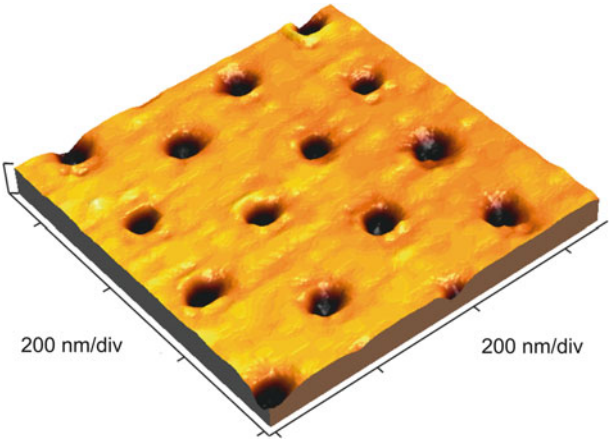

Fig. 13.1.3 Silicon nanoholes fabricated on a (100) Si surface by using a regular lattice of SiO_2-microspheres ($r_{sp} = 150$ nm) together with single-shot 265.7 nm Ti-sapphire laser radiation ($\phi = 15 \pm 3.5$ mJ/cm^2, $\tau_\ell \approx 300$ fs). The width of holes at FWHM is 57 ± 6.5 nm and their depth with respect to the original silicon surface is 6 ± 1 nm [*Brodoceanu* et al. 2007]

Real and potential applications include:

- Nanopatterning of material surfaces [*Zhou* et al. 2008; *Brodoceanu* et al. 2007; *Eversole* et al. 2007; *Hong* et al. 2007; *Miyaji* and *Miyazaki* 2007; *Hwang* et al. 2006; *Klein-Wiele* and *Simon* 2003].
- Direct write laser lithography, fabrication of photonic structures (Chap. 27).
- Fabrication of transparent templates [*Hartmann* et al. 2008].

13.2 Overview on Interaction Mechanisms

Many of the mechanisms and models discussed for nanosecond-laser ablation, hold also with pulses that are longer than several 10–100 ps. With shorter pulses, however, new phenomena are observed. The most important differences can be summarized as follows:

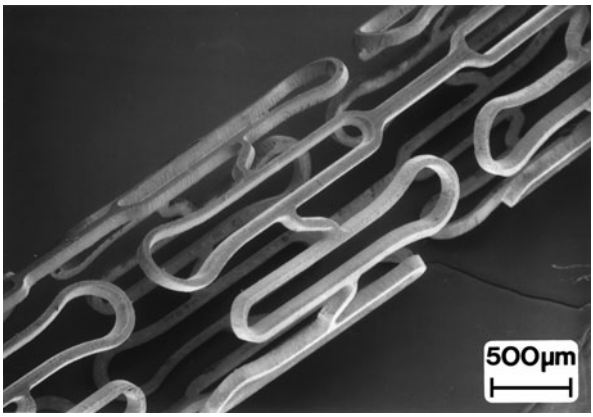

Fig. 13.1.4 Stent fabricated from a Ta tube by femtosecond-laser machining ($\lambda = 780\,\text{nm}$, $\phi = 21\,\text{J/cm}^2$, $\tau_\ell = 150\,\text{fs}$, $\nu_\text{r} = 1\,\text{kHz}$, $v_\text{s} \approx 300\,\mu\text{m/s}$) [*C. Momma* 1999, private communication]

- With all types of materials, ablation is strongly non-stationary and starts only *after* about 1 to several 10 ps. In other words, material excitation takes place mainly prior to the expansion of the plasma plume. Thus, plasma shielding is strongly diminished or even avoided (Sect. 12.6.3).
- At present, the most practical femtosecond laser is the Ti:sapphire laser, which emits radiation within the near IR. Thus, for *low* laser-light intensities, thermal *surface* ablation is expected only for metals, many semiconductors, and for materials with strongly nonlinear optical absorption. Most inorganic insulators and organic polymers are, however, transparent within this spectral region. With those materials, thermally induced defect formation and decomposition within the material *volume* take place. With higher harmonics of Ti:sapphire- or ultrashort-pulse excimer-laser radiation, *single* photon electronic excitations of these materials become important or even dominating.
- With increasing laser-light intensities, nonlinear optical processes, and nonequilibrium effects play an important or even decisive role. Multiphoton processes will increase the absorption coefficient α, and thereby decrease the threshold fluence $\phi_\text{th} \propto \alpha^{-1}$.
  This influence becomes more and more pronounced with decreasing pulse duration, τ_ℓ. If we assume, in the simplest approximation, that for an n-photon process $\alpha \propto I^{n-1} \propto (\phi/\tau_\ell)^{n-1}$, we find $\phi_\text{th} \propto \tau_\ell^{(n-1)/n}$. This coincides with the multiphoton ionization limit discussed in Sect. 13.6.
- With metals, fs-laser pulses generate a hot electron gas in a ‘cold’ lattice. This transient nonequilibrium is described by the two-temperature model (TTM).
- In semiconductors hot electron-hole pairs are generated by single-photon and/or multiphoton- and impact (avalanche) ionization.
- With dielectrics, multiphoton- and avalanche ioniziaton result in the formation of a plasma within a thin surface layer. At very high intensities, Coulomb explosion is observed.

- *Very high* intensity ultrashort laser pulses lead to very high heating rates with or without material melting. Heating is almost isochoric, i.e. much faster than thermal expansion of the lattice. Thus, the laser-pulse length is shorter than the time τ_s required for mechanical relaxation (expansion) of the interaction volume, i.e. $\tau_\ell < \tau_s \approx l/v_0$, where l is the characteristic depth of laser energy deposition and v_0 the sound velocity. For fs-pulses and metal targets, the relevant parameters are *not* the laser pulse duration and the optical penetration depth, but the electron-phonon relaxation time $\tau_{e\text{-}ph}$ and the depth of heating due to hot electrons. In this case, the condition for stress confinement is $\tau_{e\text{-}ph} < \tau_s$. In a more compact form this condition can be written as

$$\tau_s > \max\{\tau_\ell, \tau_{e\text{-}ph}\} \tag{13.2.1}$$

  where the parantheses denote the selection of the longer time constant [*Zhigilei* et al. 2009; *Schäfer* et al. 2002]. Stress 'confinement' yields very high thermoelastic pressures within the interaction volume. Stress relaxation results in void (bubble) formation and macroscopic thermomechanical ablation (spallation). With even higher intensities phase explosion is observed. This scenario is universal for almost all types of materials.

Depending on the type of material and the laser parameters, these quite different photoexcitation pathways are responsible for the onset of ablation. Subsequently, these mechanisms are discussed in further detail.

For the proof of laser-material interactions and ablation models, time-resolved measurements are of fundamental importance. Among the various different techniques employed are time-resolved beam deflection, pump-probe optical measurements, acoustic methods, etc. Such investigations yield information on the dynamics of electrons in metals and semiconductors, on the importance of multiphoton absorption/ionization, avalanche ionization and plasma formation within dielectric materials, on defect formation, the 'latent' time between the incident laser pulse and the ejection of species from the surface, the influence of plasma shielding, etc.

Time-resolved X-ray and electron diffraction permit to study the dynamics of *atoms* under fs-laser irradiation of materials (Chaps. 29 and 30).

13.3 Low Fluence Photoexcitations

In this section we consider mainly picosecond pulses, *low* laser-light intensities, and dielectric materials, including organic polymers. If the photon energies are too low for direct (non-thermal) bond breaking or band-gap excitations, laser-induced heating via the absorption of 'seed' electrons or physical or chemical defects, including incubation, take place. If the photon energies are high enough for *direct* photoexcitation, both thermal and/or non-thermal processes become possible. Subsequently, we will discuss such processes separately.

13.3.1 Thermal Volume Decomposition

For the materials under consideration we tentatively ignore heat conduction and the role of mechanical stresses. In other words, we consider pulses of 100 ps or somewhat longer, where we can assume thermal confinement without stress confinement. We also neglect ablation during the pulse and consider only thermal decomposition of the material within the heated volume. The calorimetric solution (7.5.6) yields for the temperature distribution after the pulse

$$\Delta T(z) \approx \frac{\alpha \phi_\mathrm{a}}{\varrho c_\mathrm{p}} \exp(-\alpha z) \; . \tag{13.3.1}$$

If we consider a first-order thermally activated 'reaction', the number of defects, e.g., broken bonds, is given by (12.7.2). If we assume $N_\mathrm{D}^\mathrm{cr} \approx N$, we obtain with $v = 0$, i.e., in the laboratory system,

$$t k_\mathrm{d}^0 \exp\left(-\frac{\mathscr{E}_\mathrm{d}}{T}\right) \approx 1 \; . \tag{13.3.2}$$

If we approximate t by the cooling time $t \approx 1/\alpha^2 \, D$, which follows from (7.5.7), we obtain the ablated depth

$$\Delta h \approx \frac{1}{\alpha} \ln\left(\frac{\phi}{\phi_\mathrm{th}}\right) \; , \tag{13.3.3}$$

with

$$\phi_\mathrm{th} \approx \frac{\varrho c_\mathrm{p} \mathscr{E}_\mathrm{d}}{\alpha A} \left[\ln\left(\frac{k_\mathrm{d}^0}{\alpha^2 D}\right)\right]^{-1} \; . \tag{13.3.4a}$$

With *multiple-pulse* irradiation and infinite lifetime of defects, we have $t \approx N_\ell/\alpha^2 D$ so that

$$\phi_\mathrm{th} \approx \frac{\varrho c_\mathrm{p} \mathscr{E}_\mathrm{d}}{\alpha A} \left[\ln\left(\frac{k_\mathrm{d}^0 N_\ell}{\alpha^2 D}\right)\right]^{-1} \; . \tag{13.3.4b}$$

In addition to the assumptions already made, this simple treatment also ignores the enthalpy of defect formation/bond breaking, any effects due to the moving boundary, non-linear optical absorption, possible non-equilibrium effects of subsystems, avalanche breakdown, etc. Nevertheless, it permits a tentative description of some of the features that have been observed experimentally: The ablated-layer thickness increases logarithmically with ϕ. This is consistent with picosecond ablation-rate measurements for dielectrics such as $LiNbO_3$ (see, e.g., Fig. 12.6.4). The decrease of ϕ_th observed with multiple-pulse irradiation of CaF_2 (Fig. 13.3.1),

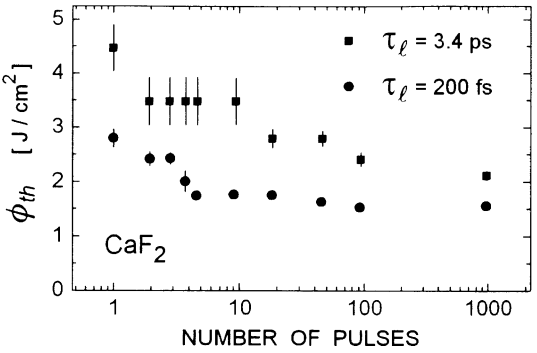

Fig. 13.3.1 Threshold fluence, ϕ_{th}, for Ti:sapphire-laser-irradiated ($\lambda = 790\,\text{nm}$) CaF_2 as a function of N_ℓ and two different pulse lengths, τ_ℓ [*Rosenfeld* et al. 1999]

Al_2O_3, amorphous and crystalline SiO_2, and LiF [*Rosenfeld* et al. 1999] can be tentatively described by (13.3.4b) as well. However, alternative explanations based on photoinduced defects, changes in absorptivity due to surface roughening [*Campbell* et al. 1999], etc. may be possible as well.

With fluences $\phi \gtrsim \phi_{\text{th}}$, initially slow material removal during the first few "incubation" pulses and strong ablation after a certain number of pulses have been observed. Such a crossover from gentle ablation to strong ablation is consistent with volume decomposition, the accumulation of defects, and subsequent optical breakdown within the material.

13.3.2 Thermal Versus Photophysical Ablation

The influence of thermal and photochemical pathways on the initiation of polymer ablation under ultrashort-pulse laser irradiation has been studied for PMMA, PI, PET, PTFE, etc.

For PMMA, the number of either thermally or photochemically broken bonds has been calculated on the basis of a combined Molecular Dynamics (MD) / Monte Carlo (MC) reaction scheme (Sect. 13.4). For purely *thermal* decomposition, the evolution of broken bonds has been found to be in good agreement with the analytical Eq. (12.7.2). According to the MD simulations and for 150 ps F_2–laser pulses, ablation should start with the desorption of small polymer fragments from the surface. This process should last up to about 170 ps. Subsequenlty, the ejection of large fragments should occur [*Prasad* et al. 2008]. Excitation and heating of the PMMA matrix and indirect heating via the excitation of embedded point thermal absorbers should *not* influence the yield of ejected particles [*Conforti* et al. 2008].

The influence of *photochemical* bond breaking on ablation yields has been studied by MD/MC simulations for the same system, PMMA and 157 nm F_2-laser radiation [*Prasad* et al. 2008]. Here, *direct* breaking of C-CO bonds (Norrish type I reaction) and of C-CH_2 bonds (Norrish type II reaction) has been considered.

Depending on the type of reaction pathway, various different (small) molecules are formed and *thermally* ejected from the surface. These combined photochemical and thermal processes should result in lower ablation thresholds and higher yields.

13.3.3 Ablation Dynamics

Bulk and surface photothermal models fit the experimental data on the ablated layer thickness, $\Delta h = \Delta h(\phi)$, for ns-laser ablation of polymers equally well (Chap. 12). Thus, such experiments do *not* permit to elucidate the underlying ablation mechanisms. For ultrashort-laser pulses, however, the ablation dynamics expected for these models should be quite different. For the surface model, the maximum ablation rate should coincide with the maximum surface temperature. For bulk heating, however, ablation should start much later [*Bityurin* et al. 2003]. Thus, from a comparison of single- and pair-pulse laser ablation experiments one should be able to distinguish between these models. Such experiments have been performed by using 0.5 ps KrF-laser pulse-pairs of variable delay. The materials studied were mainly PMMA and PTFE [*Preuss* et al. 1993]. According to these experiments, there was *no* indication for material removal within time intervals of 200 ps. Thus, the results are in favor of the bulk model. Nevertheless, systematic experimental and more sophisticated theoretical studies are needed. For example, with ultrashort pulses, the influence of mechanical stresses and the generation of a plasma on or near the material surface can significantly alter the ablation behavior (Sect. 13.6). The importance of plasma effects in pico- and femtosecond UV-laser ablation of PMMA and PI has been studied by *Beinhorn* et al. (2004). For PMMA the maximum in the reflected energy observed at about 5 ps, coincides with a minimum in the ablation rate at the same pulse duration.

13.4 Molecular Dynamics (MD) Simulations

Molecular dynamics simulations have been successfully employed for modelling the response of target materials subjected to picosecond- and, in particular, to femtosecond-laser pulses. Such simulations permit a time-resolved analysis of local laser-matter interactions. In many cases, MD methods are combined with other techniques/models. These have been employed for the description of laser-induced heating, melting, photomechanical spallation, ablation, phase explosion and even for matrix-assisted laser desorption ionization (MALDI).

In MD simulations the target atoms or molecules are described by interacting rigid or breathing spheres with three translational and, in the latter case, one internal degree of freedom. The excitation of atoms/molecules is modeled by depositing the absorbed energy into the motion of the system. In the simplest case, one attributes to each atom a velocity $\sqrt{2E_a/m}$ in random direction, where m is the mass and E_a the kinetic energy per atom. If photochemical (non-thermal) effects are important, the

laser energy is channelled in part or totally into chemical excitation/bond breaking pathways. In order to limit the times for (computer) simulations, the total number of atoms/molecules employed in such calculations is, typically, between several 10^3 and 10^8. Such a small number of atoms/molecules explains, why MD simulations are suitable in particular for ultrashort-pulse laser irradiation where the interaction volumes are 'small'. The absorption probability can be modulated by Lambert-Beer's law to describe the exponential attenuation of the laser-light intensity with propagation depth. Multiphoton absorption can be introduced in a similar way.

Interatomic interactions have been described in quite different ways. For example, for metals the delocalized metallic binding has been described by many-body potentials, while for non-metals with localized bonds, Lennard-Jones potentials have been employed [*Upadhyay* et al. 2008; *Agranat* et al. 2007]. Interestingly, even with such different interaction potentials, the *overall* response of materials to ultrashort laser pulses is almost 'universal'. For the description of photophysical (combined thermal and non-thermal) ablation of polymers, combined harmonic/Morse-type potentials have been used [*Prasad* et al. 2008].

Figures 13.4.1 show MD simulations of the material response to ultrashort-pulse laser radiation. Fig. 13.4.1a exhibits the temporal evolution of the process. In the initial phase of interaction, the absorbed energy amorphizes a surface layer and 'slow' evaporation (desorption) of material from the surface takes place. Subsequently,

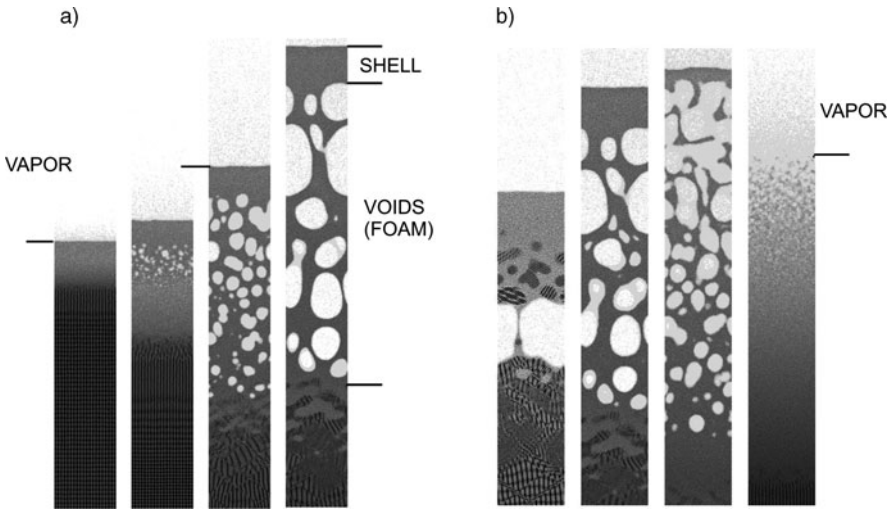

Fig. 13.4.1 Molecular dynamics simulation of the material response to ultrashort-pulse laser radiation. a) Temporal evolution of material removal. "Slow" evaporation, subsurface void/bubble formation, coalescence of voids (foam) and formation of a spallation layer (shell). b) Dependence on increasing laser-light intensity (surface temperature) from left to right. The thickness of the spallation layer decreases. The last picture on the right side shows the situation during phase explosion. Below the dash, a two-phase state consisting of vapor and liquid droplets is observed [after *Agranat* et al. 2007]

voids (bubbles) nucleate *below* the surface and coalesce. This results in a foam-type structure with a liquid layer (shell) on top. This layer is denoted as spallation layer. Its thickness increases during separation from the foam due to the surface tension of the liquid. Finally, this layer spalls off. With increasing laser-light intensity (surface temperature), the thickness of the spallation layer decreases (Fig. 13.4.1b). The fraction of liquid material below this layer increases. When the fluence increases further, the spallation layer disappears and an abrupt transition to the regime of phase explosion (binodal decomposition) occurs. The dash on the right side separates the vapor from the two-phase state consisting of vapor and liquid droplets.

Figure 13.4.2 shows the average material density for the case of the second plot in Fig. 13.4.1b. The coordinate z^* is normalized to the Lennard-Jones parameter σ. The origin $z^* = 0$ corresponds to the target surface at $t = 0$. The spallation layer has almost constant density (left side). Below this layer, strong density fluctuations due to voids are observed. Stretching of the material (negative pressure) is observed within the whole region. Its maximum is around the 'boundary' between the foam and the bubbleless material with almost the bulk density. This boundary corresponds to the surface of the non-ablated target material.

In connection with the analysis of 'vapor' plumes and various different applications, one should be aware that cluster/droplet formation under the action of ultrashort laser pulses can originate from: the condensation of vapor (phase above the upper dashes in Fig. 13.4.1), the breaking of the liquid shell, and from the 'bubbly liquid' in the two-phase region [*Zhigilei* et al. 2009; *Inogamov* et al. 2008; *Agranat* et al. 2007]. Due to their different origins, the clusters/droplets have a large size distribution which is disadvantageous for the fabrication of homogeneous powders and high-quality thin films by pulsed-laser deposition (PLD). These clusters cause also debris and redeposition of particulates which cause problems in laser micropatterning.

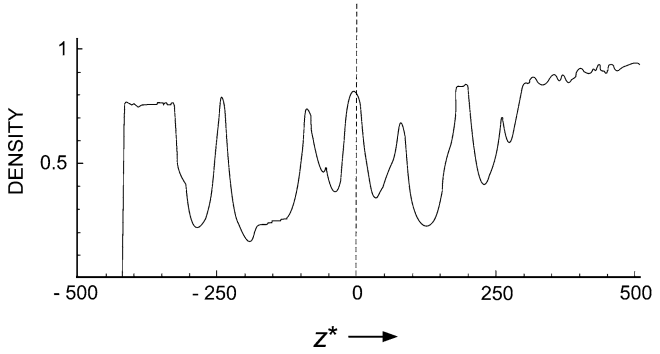

Fig. 13.4.2 Average density of the material as a function of normalized coordinate z^*. The parameters are the same as those employed in the second plot in Fig. 13.4.1b. The origin $z^* = 0$ corresponds to the position of the target surface at $t = 0$. Below the spallation layer (left side) strong density fluctuations due to voids are observed [after *Agranat* et al. 2007]

Summary

Let us summarize the results of MD simulations in connection with ultrashort-pulse laser ablation. With increasing laser-light intensities the scenario can be described as follows:

- Material heating
- Stress relaxation and surface expansion may result in 'normal' acoustic surface oscillations or photomechanical exfoliation.
- Amorphization/melting of the surface and resolidification on a time scale of several hundred ps to several ns. From the melt, 'slow' evaporation of mainly single atoms and a small number of dimers and trimers takes place.
- The threshold fluence, ϕ_{th}, for ablation decreases with decreasing pulse length, τ_ℓ; the ablation rate increases nonlinearly with ϕ.
- For laser pulses that are shorter than the time of thermal expansion (isochoric heating), stress confinement results in huge thermoelastic pressures.
- Stress relaxation may cause long lasting surface deformations related to temporary void (bubble) formation below the surface.
- Increasing number of voids and coalescence. Formation of a two-phase 'foamy' material structure and a condensed spallation layer on top.
- Macroscopic material ablation (spallation). The separated spallation layer strongly decreases the energy transfer to the remaining material.
- The spallation layer becomes increasingly thinner and disappears at the evaporation threshold.
- Strong non-equilibrium evaporation (ablation).
- Above a 'second threshold', strong overheating results in *phase explosion*, i.e. in a *collective* transition from the solid or liquid phase to a mixed gaseous/liquid phase (binodal decomposition). The ablation plume consists of a mixture of sublimated species and a substantial fraction of large molecular clusters of different sizes, and droplets [*Zhigilei* et al. 2009; *Agranat* et al. 2007].

Depending on the material and the laser parameters, one or several of these steps may be unimportant or will not occur at all.

Other applications

MD simulations in connection with ultrashort-pulse laser-material interactions have also been applied to study

- Structural changes in covalently bounded nanostructures and solids. Detailed calculations were performed on the damage and healing of defects in carbon nanotubes, and on nonequilibrium melting of bulk Ge [*Jeschke* et al. 2009].
- The role of defect formation in surface alloying, annealing, and hardening [Chaps. 23 and 25; *Lin* et al. 2008a].
- The mechanisms of nanobump formation on thin metal films [Chap. 28; *Ivanov* et al. 2008]

In spite of the success of MD calculations, the small interaction volumes (number of species and laser foci) considered, are, in many cases, far away from experimental conditions, even in picosecond- and femtosecond-laser processing. The size of the simulation volume, however, can significantly influence the response of the material. Such problems become even more severe with low laser-light absorption. Furthermore, the predicted thresholds for ablation and spallation, as well as stress amplitudes, etc. *do* depend on the interatomic potential employed in the calculations [*Zhakhovskii* et al. 2009]. For all of these reasons, but also because of the many unknown parameters 'classical' MD simulations do only permit a qualitative comparison with experimental data. However, MD simulations combined with other techniques or model descriptions of laser excitation and relaxation processes, may change this situation.

13.5 The Two-Temperature Model

In metals, light is almost exclusively absorbed by free–free electron transitions within the conduction band (Sect. 2.1). Within the electron system, the excitation energy is thermalized within, typically, 10 fs to 1 ps. Thermalization between the electron subsystem and the lattice is much slower, typically of the order of 1–100 ps, depending on the strength of electron–phonon coupling, $\Gamma_{\text{e-ph}}$. Thus, femtosecond-laser excitation generates a hot electron gas. The transient non-equilibrium between the hot electrons and the lattice can be described by temperatures T_e and T, which can be calculated from the corresponding heat equations [*Anisimov* et al. 1974]. This description is denoted as the two-temperature model (TTM). In the laboratory system, the (coupled) nonlinear equations for T_e and T can be written, in a more general form, as

$$C_\text{e}(T_\text{e})\frac{\partial T_\text{e}}{\partial t} = \nabla[\kappa_\text{e}(T_\text{e}, T)\nabla T_\text{e}] - \Gamma_{\text{e–ph}}(T_\text{e})[T_\text{e} - T] + Q(x_\alpha, t) \qquad (13.5.1a)$$

and

$$C(T)\frac{\partial T}{\partial t} = \nabla[\kappa(T)\nabla T] + \Gamma_{\text{e–ph}}(T_\text{e})[T_\text{e} - T]\,, \qquad (13.5.1b)$$

where C_e and C are the heat capacities (per unit volume) of the electron and lattice subsystems, respectively. In a 1D approximation the source term can be written as $Q(z, t) = \alpha A I(t) \exp(-\alpha z)$. With femtosecond pulses and, in good approximation, also with picosecond pulses heat conduction within the lattice subsystem [first term on the right-hand side of (13.5.1b)] can be ignored. Here, heat conduction occurs much more rapidly through the free electron gas than via phonons. For 'medium' levels of excitation $C_\text{e} << C$ and the electrons can be heated to very high transient temperatures. If T_e is much lower than the Fermi temperature, $T_\text{F} \equiv E_\text{F}/k_\text{B}$, the heat capacity of electrons can be approximated by $C_\text{e} = C_0 T_\text{e}$, where $C_0 =$

$\pi^2 N_e k_B/2T_F$ is a constant. C can be assumed to be constant for temperatures above the Debye temperature, θ_D [θ_D(Au) $\approx$ 165 K; θ_D(Cu) $\approx$ 343 K; θ_D(Ni) $\approx$ 450 K]. The (non-equilibrium) thermal conductivity of electrons can be approximated by $\kappa_e = \kappa(T)T_e/T \times \kappa(T)$ is the normal equilibrium heat conductivity of the metal. A more appropriate approximation is given by *Anisimov* and *Rethfeld* (1997). For *intense* fs-laser pulses, i.e. with strong electron-phonon nonequilibrium, the linear approximation $C_e \propto T_e$ becomes inadequate. In such cases, C_e can exhibit positive (Au, Ag, Cu, ...) or negative (Ni, Pt, ...) deviations from the linear dependence. Similarly, the strength of electron-phonon coupling $\Gamma_{\text{e-ph}}$ becomes dependent on T_e. $\Gamma_{\text{e-ph}}$ can either increase (Au, Ag, Al, Cu, ...) or decrease (Ni, Pt, ...) with increasing temperature T_e [*Lin* et al. 2008b].

Clearly, the general problem (13.5.1) can only be solved numerically. Let us now consider different regimes of laser-metal interactions.

Femtosecond Pulses

In this regime, the laser-pulse duration is short compared to the characteristic time for cooling of the hot electron gas due to energy exchange with the lattice, i.e., $\tau_\ell \ll \tau_e \equiv C_e/\Gamma_{\text{e-ph}}$. For $t \ll \tau_e$, i.e., $\Gamma_{\text{e-ph}} T_e \ll C_e T_e/t$, electron–phonon coupling can be ignored. If we also ignore heat conduction by electrons, which is a reasonable approximation with $D_e \tau_{\text{e-ph}} < \alpha^{-2}$, where $D_e = \kappa_e/C_e$ is the thermal diffusivity of electrons, (13.5.1a) simplifies to

$$\frac{1}{2} C_0 \frac{\partial T_e^2}{\partial t} = \alpha I_a \exp(-\alpha z) \ ,$$

which yields

$$T_e(t) = \left[T_0^2 + \frac{2\alpha \phi_a(t)}{C_0} \exp(-\alpha z) \right]^{1/2} \ , \tag{13.5.2}$$

where $\phi_a(t) = \int_0^t I_a(t')\,dt'$. T_0 is the initial temperature, which is henceforth ignored. At the end of the pulse, i.e., with $t = \tau_\ell$, we obtain

$$T_e(\tau_\ell) \approx \left(\frac{2\alpha \phi_a}{C_0} \right)^{1/2} \exp\left(-\frac{\alpha z}{2} \right) \ . \tag{13.5.3}$$

The evolution of the temperature for times $t \geq \tau_\ell$ is described by (13.5.1) with $Q = 0$. In this regime, T_e rapidly decreases due to electron energy transfer to the lattice. As heat conduction can be ignored, from (13.5.1) we obtain the lattice temperature

$$T \approx \frac{\alpha \phi_a}{C} \exp(-\alpha z) \ . \tag{13.5.4}$$

Here, we have employed the energy balance $CT = \int_0^{T_e} C_e(T_e')\,dT_e'$ and (13.5.3). Significant ablation occurs if $CT = \varrho c_p T \approx \Delta H_v$. This approximation can be employed as long as $T_e \ll E_F/k_B$. Together with (13.5.4), we then obtain the ablated depth

$$\Delta h = \frac{1}{\alpha} \ln \frac{\phi}{\phi_{th}} , \tag{13.5.5}$$

with

$$\phi_{th} = \frac{\Delta H_v}{\alpha A} . \tag{13.5.6}$$

Equation (13.5.5) has the *same* form as 13.2.3 and (12.8.1). However, the meaning of α and ϕ_{th} is quite different (see, e.g., Sect. 13.5.3).

Picosecond Pulses

In this regime we have $\tau_\ell \gg \tau_e$. Thus, (13.5.1a) becomes quasi-stationary, i.e., we can set $\partial T_e/\partial t \approx 0$. Heat conduction by electrons cannot be ignored in this regime. The hot electrons diffuse over a length $l_e \approx (D_e \tau_\ell)^{1/2} \approx (\kappa_e/\Gamma_{e\text{-}ph})^{1/2}$ before they transfer their energy to the lattice. In this case from (13.5.1b) one can derive

$$T(0,t) \approx \frac{\phi_a(t)}{C(l_e + l_\alpha)} \exp\left(-\frac{t}{\tau_{ph}}\right) , \tag{13.5.7}$$

where $\tau_{ph} = C/\Gamma_{e\text{-}ph}$ is the characteristic time for lattice heating. If the energy is absorbed at the surface, i.e. if $l_\alpha \ll l_e$, and $\tau_\ell \ll \tau_{ph}$, we obtain, with $\kappa_e \approx$ const. for the maximum lattice temperature at the end of the pulse,

$$T(0,\tau_\ell) \approx \frac{\phi_a}{C l_e} \approx \frac{\phi_a}{C}\left(\frac{\Gamma_{e\text{-}ph}}{\kappa_e}\right)^{1/2} . \tag{13.5.8}$$

With the characteristic times for electron-gas cooling, τ_e, and lattice heating, τ_{ph}, we can define the electron-phonon relaxation time

$$\frac{1}{\tau_{e-ph}} = \frac{1}{\tau_e} + \frac{1}{\tau_{ph}} \tag{13.5.9a}$$

or

$$\tau_{e-ph} = \frac{C_e\, C}{(C_e + C)\Gamma_{e-ph}} \tag{13.5.9b}$$

For 'medium' levels of excitation $C_e << C$ and $\tau_{e\text{-}ph} \approx C_e/\Gamma_{e\text{-}ph}$. For strong excitations with $C_e \approx C$ we have $\tau_{e\text{-}ph} \approx C_e/2\,\Gamma_{e\text{-}ph}$.

The two-temperature model describes the laser excitation of conduction band electrons and the subsequent energy transfer from the hot electrons to the lattice vibrations via the electron-phonon coupling. The model assumes the validity of the heat equation for ultrashort laser pulses. In other words, it assumes that the energy distribution of the electrons is thermalized and can be described by a temperature T_e. In many applications of Eqs. (13.5.1) the coefficients have been assumed as constants. This is, however, inadequate in most cases. The consideration of the influence of the electron temperature T_e on the electron-phonon coupling and electron heat capacity, is quite important [*Lin* et al. 2008b].

Figure 13.5.1 shows the temporal dependence of the electron and lattice temperatures calculated from the TTM for 100 nm thick films of Au and Ni. These metals are representative examples for weak and strong electron-phonon coupling [$\Gamma_{e-ph}(\text{Au}) \approx 2.3 \times 10^{10}\,\text{W/cm}^3\,\text{K}$; $\Gamma_{e-ph}(\text{Ni}) \approx 3.6 \times 10^{11}\,\text{W/cm}^3\,\text{K}$]. The differences in Γ_{e-ph} are directly revealed in the different behavior of temperatures T_e and T. In particular, the time required to reach thermal equilibrium in Au is almost ten times longer than for Ni. Another consequence is the temperature gradient that

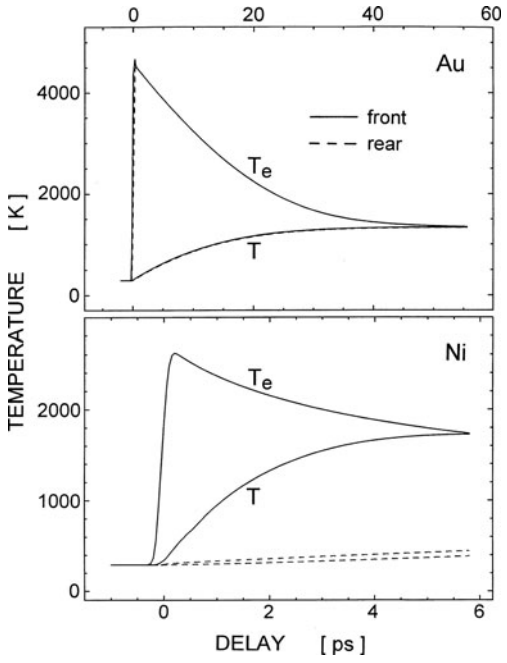

Fig. 13.5.1 Temporal dependence of the electron temperature, T_e, and lattice temperature, T, calculated from the TTM for 100 nm films of Au and Ni irradiated with 200 fs pulses ($\lambda = 400$ nm and $\phi \approx \phi_m$, where ϕ_m is the melting fluence). Solid curves show the temperature at the surface (front side) of films; *dashed curves* show the temperature at the rear side. With Ni, thermal equilibrium is reached about 10 times faster in comparison to Au. With Au, *solid* and *dashed curves* almost coincide [*Wellershoff* et al. 1999]

builds up between the front and the rear sides. In Au, Γ_{e-ph} is small and thus l_e large. Therefore, the absorbed energy can spread into deeper parts of the sample and thereby diminishes the energy density in the surface region. Films with a thickness comparable to l_e, are heated almost homogeneously. The opposite behavior is found for Ni. Strong electron-phonon coupling causes rapid cooling of the hot electrons and thereby prevents long-range energy transport by electron diffusion.

The TTM permits a qualitative and, in certain cases, an even semi-quantitative interpretation of ultrashort-pulse laser-metal interactions. For example, Fig. 13.5.1 explains the differences in damage (melting) thresholds for noble metals and transition metals, and thereby the importance of the electron-phonon coupling. Due to rapid energy transport by hot electrons (large l_e), the damage threshold observed (experimentally) with Au is higher than for Ni. This agreement also proves the thermal character of laser-metal interactions for fs-laser pulses. It should be noted, however, that with ns-pulses the damage threshold is higher for Ni in comparison to Au.

In spite of the success of the TTM, there are a number of experimental observations and physical processes that require an extension of this model. Some of these processes can be described via phenomenological extensions of the parameters in Eqs. (13.5.1). Among the examples is the inclusion of the energy transport by ballistic propagation of electrons [*Hohlfeld* et al. 2000], the consideration of surface/grain boundary scattering [*Hopkins* and *Norris* 2007], etc. Laser-induced phase transformations of the target material and changes in its microstructure have been described by combining molecular dynamics (MD) simulations with the TTM [*Lin* and *Zhigilei* 2006; *Ivanov* and *Zhigilei* 2003; *Schäfer* et al. 2002]. The results are consistent with time-resolved X-ray and electron diffraction experiments [*Hillyard* et al. 2007; *Siwick* et al. 2003].

For intense fs-laser pulses, the initial strongly non-thermal distribution of the electrons cannot be ignored. In a simple extension of the TTM, transient electronic excitations are described by corresponding source terms in Eqs. (13.5.1a) and (13.5.1b) [*Carpene* 2006]. A more rigorous treatment employs the Boltzmann equation for the partition function of the electrons. At low excitation levels, a nonequilibrium distribution of electrons results in a delayed cooling of the electron gas [*Rethfeld* et al. 2002a; *Groeneveld* et al. 1995]. For fluences near the damage threshold, the energy exchange between electrons and phonons can be described by the TTM, in spite of the nonequilibrium within the electron gas.

13.5.1 Electron Transport, Damage Thresholds

The nonequilibrium dynamics of electrons and the competition between ballistic and hot-electron transport and electron-phonon coupling has been investigated by pump/reflectivity probe experiments [*Bonn* et al. 2000; *Hohlfeld* et al. 2000]. Typical experimental arrangements are discussed in Sect. 29.3. Among the metals investigated in great detail are Au, Cu, Ni, etc. Transient reflectivity measurements clearly reveal three different regimes of the electron transport:

- For metals, whose electronic behavior can be described by the model of the so-called 'free-electron gas' (see, e.g., *Kittel* 2005), *ballistic* motion of excited electrons is observed during and immediately after a fs-laser pulse. The velocities of such hot electrons are close to the Fermi velocity of, typically, 10^8 cm/s. Thermalization within the electron gas occurs by collisions of these highly excited electrons with those near the Fermi energy. This has been proved by measuring reflectivity changes as a function of the pump-probe delay for different film thicknesses (Fig. 13.5.2). The depth for ballistic motion derived from the measurements is for Au $l_{\text{ballistic}} \approx 100$ nm. Thus, with films up to thicknesses $h \lesssim 100$ nm, ballistic transport cannot be ignored and becomes even dominant with the 20 nm film. In this case, the film is almost homogeneously heated. The change in reflectivity in the initial phase is almost linear. This can be easily understood from Eq. (13.5.1a). Due to ballistic transport, the temperature gradient within the film (first term on the right side) can be ignored. Thus, with $T << T_e$ integration directly yields $T_e(t) - T_{e,\max} \approx -\Gamma_{e-ph} \times t/C_0$. The coupling constant $\Gamma_{e\text{-}ph}$ can directly be derived from the slope of the linear regime. Qualitatively, a similar behavior has been observed for Cu, Ag, etc. On the other hand, for d-band metals, such as Ni, Cr, Mo, etc., *no* ballistic motion of electrons has been detected. This is in agreement with the much shorter mean free paths of electrons, which is within the range of 10–20 nm only. This length is comparable to the optical penetration depth for the laser radiation employed in the experiments.

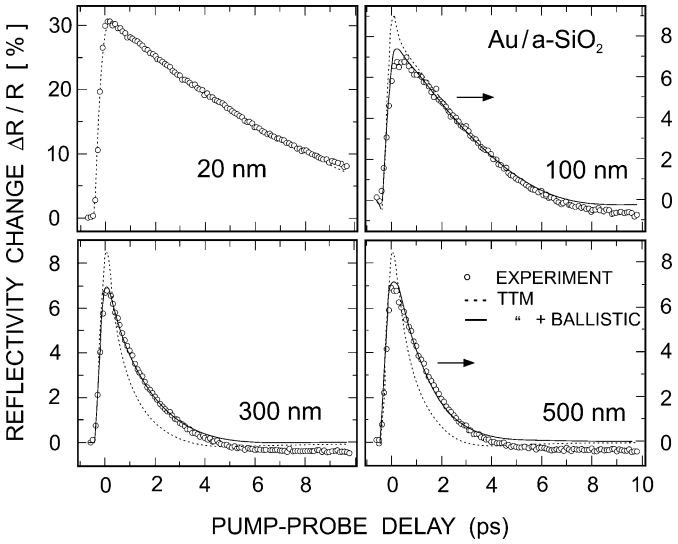

Fig. 13.5.2 Transient reflectivities for Au films of various thicknesses on fused silica (a-SiO_2) substrates. The change in reflectivity is defined as $\Delta R = R(T_e) - R$ with $R \equiv R(293\,\text{K})$. The experimental data were taken with 100 fs (p-polarized) probe pulses ($\lambda = 500$ nm) and 200 fs pump pulses ($\lambda = 400$ nm, $\phi = 1\,\text{mJ/cm}^2$). *Dashed curves* were calculated with the TTM. *Full curves* take into account ballistic energy transport with $l_{\text{ballistic}} = 105$ nm [adapted from *Hohlfeld* et al. 2000]

- Once the electron gas is thermalized, it can be described by an electron temperature, T_e. In this regime, we can apply the TTM, i.e. Eqs. (13.5.1). The dashed curves in Fig. 13.5.2 have been calculated in this way. Due to the temperature gradient, the electrons *diffuse* into deeper parts of the film / bulk. The diffusion length is determined by the electron-phonon coupling, $\Gamma_{\text{e-ph}}$ (see Eq. (13.5.7)). In this regime, a clear change in the time-dependence of the reflectivity measurements is observed. Inhomogeneous heating due to diffusive transport results in an exponential decay of $\Delta R/R$. It becomes evident, however, that in the initial phase of excitation, electron transport by diffusion overestimates the density of electrons near the surface and thereby overestimates the changes in reflectivity. This discrepancy between results is a clear indication that electron transport is enhanced by ballistic motion. Phenomenologically, this has been taken into account by employing an effective penetration depth $l_\alpha^{eff} = l_\alpha + l_{ballistic} = \alpha_{eff}^{-1}$ in the source term of Eq. (13.5.1a). The full curves in the figure have been calculated in this way with $l_{\text{ballistic}} = 105\,\text{nm}$. These curves are in good agreement with the experimental data. Electron emission from the surface has not been taken into account.
- For times $t > \tau_\ell$ thermal equilibrium between the lattice and the electrons is reached, i.e. $T \approx T_e$.

While this description of the electron transport upon fs-laser irradiation of metals is widely accepted, the exact values of parameters and damage thresholds derived from similar investigations using somewhat different laser parameters and film thicknesses may differ by a factor of 2 or more [*J. Krüger* et al. 2007]. In any case, the differences in electron dynamics explain, why fs-laser patterning of thin films is more efficient and more well-defined for transition metals in comparison to noble metals. Thus, high resolution patterning is more difficult to achieve with noble metals, where the absorbed energy is rapidly distributed by ballistic transport and electron diffusion.

Pump/reflectivity probe experiments were also performed for a large number of semiconductors [*Bonse* et al. 2009a; *Temnov* et al. 2006; *Bonse* et al. 2006; *Sokolowski-Tinten* et al. 1998]. Here, a strong increase in surface reflectivity caused by photoexcited electron-hole pairs is observed during several 100 fs. Depending on the laser fluence, melting takes place within about 1 ps. With liquid Si, which behaves like a metal, melting goes along with a strong increase in surface reflectivity. With higher fluences, surface deformations, the appearance of Newton rings, and material ablation is observed. This scenario that is typical for many metals and semiconductors is subsequently discussed in further detail.

13.5.2 Melting, Surface Deformation and Ablation

Strong excitation of metals and semiconductors by ultrashort laser pulses can result in strong overheating with transient temperatures that exceed the equilibrium melting temperature by a factor of two or more. This can be easily verified from

Eqs. (13.5.1). Such strong overheating may cause a transition from heterogeneous to *homogeneous* melting within the bulk material [*Ivanov* and *Zhigilei* 2007; *Rethfeld* et al. 2002b]. For femtosecond pulses, the time for lattice heating is of the order of some ps and short in comparison to typical expansion times of the lattice which are, typically, in excess of 100 ps. Thus, heating of the interaction volume is almost isochoric. The (compressive) thermoelastic pressure related to this process can reach values of 10^3 to several 10^4 bar (0.1 to several GPa). This pressure causes rapid surface expansion and the generation of a rarefaction wave which propagates from the surface into the bulk. Thus, unloading of this pressure causes high tensile stresses which favor the nucleation and growth of voids within the melt. As revealed from MD calculations, typical nucleation times for voids are several ps (Sect. 13.4). In fact, this scenario is supported by experimental findings using ultrafast microinterferomety. By this means, long lasting deformations on different material surfaces such as Au [*Agranat* et al. 2007] and GaAs [*Temnov* et al. 2006] have been observed at laser fluences slightly below the threshold for ablation. For Si, amplitudes of 10 nm have been detected over times of 150 ps. For GaAs values of 150 nm over 5 ns have been measured. These extremely long lasting deformation times cannot be explained by the acoustic time t_s, which normally controls the response of the system. A simple estimation yields $t_s \approx \Delta h/v_o$, where Δh is the thickness and v_o the sound velocity within the excited material layer. Assuming $\Delta h \approx 150$ nm and $v_o \approx 3 \times 10^5$ cm/s, we obtain $t_s \approx 50$ ps. This time is very short in comparison to the experimentally observed deformation times. Thus, the 'slow' dynamics of surface deformations may be tentatively explained by the nucleation, growth, and collapse of voids or gas bubbles *below* the irradiated surface [*Zhigilei* et al. 2009; *Inogamov* et al. 2008; *Upadhyay* et al. 2008; *Agranat* et al. 2007]. Temporary void formation may also explain the absence of 'normal' acoustic oscillations that are observed for lower laser-light intensities or longer pulses.

Within a certain range of laser fluences close to the ablation threshold, the surface deformations become so large that Newton fringes can be observed. They appear, typically, several 100 ps after the pulse and last up to several ns. First investigations of this type using time-resolved optical microscopy have been performed for various types of metal films on glass substrates and for (bulk) Si [*Sokolowski-Tinten* et al. 1998]. Meanwhile, similar observations have been reported for many other materials. The Newton fringes originate from interferences of the (visible) light that is reflected from the surface of the (partially transparent) 'bubble-like' shell and the transmitted light that is reflected from the surface of the non-ablated target material. The density of the shell is similar to that of the condensed phase (Fig. 13.4.2). For metals, the thickness of the shell corresponds, approximately, to the skin depth of, typically, 20 nm. According to MD simulations, the volume between the expanding shell and the "crater" on the target surface is filled with a two-phase mixture of gaseous and liquid material (Fig. 13.4.1). Beyond the shell there is a thin layer of supercooled vapor [*Inogamov* et al. 2008; *Agranat* et al. 2007].

While microinterferometry permits to detect surface displacements of a few nanometers, Newton rings can only be observed for shell displacements of the order of a few microns, i.e. at later times / higher fluences. Furthermore, for pump-probe

delay times of several 100 fs to a few ps, i.e. *before* the development of surface deformations, microinterferometry permits to measure local transient laser-induced changes of the optical properties of the material. Newton fringes are *not* observed for nanosecond and longer laser pulses. With such 'long' pulses the stress amplitudes are too small.

With sufficiently high laser-light intensities this scenario results in (macroscopic) thermomechanical material ablation (spallation). Thus, the liquid shell leaves the surface and it propagates with almost constant velocity (Sect. 13.4). For Ge and 130 fs-laser pulses of $1.35\,\mathrm{J/cm^2}$ [ablation threshold ϕ_{th} ($\lambda = 800\,\mathrm{nm}$, $\tau_\ell = 130\,\mathrm{fs}$) $\approx 1.32\,\mathrm{J/cm^2}$], the velocity and lifetime of the shell (spallation layer) was found to be $10^4\,\mathrm{cm/s}$ and 40 ns, respectively. The corresponding values for $2.08\,\mathrm{J/cm^2}$ were $5 \times 10^4\,\mathrm{cm/s}$ and 5 ns [*Bonse* et al. 2006]. For metals and semiconductors, the surface of the non-ablated material (the crater) is covered with a thin molten layer. This is in agreement with MD simulations.

When further increasing the laser-light intensity, explosive *volume* evaporation, which is also denoted as phase explosion or binodal decomposition, is observed (Fig. 13.4.1b). In this regime the ablation plume consists of big clusters (droplets) with a wide size distribution. This is quite different to the regime of surface evaporation where the vapor plume consists of small fragments, mainly atoms, ions, and small molecules, depending on the material and the laser parameters (Chaps. 11, 12 and 30).

As already mentioned, molecular dynamics (MD) simulations have revealed that this scenario is almost 'universal'. In other words, the response of quite different materials, metals and non-metals, upon ultrashort-pulse laser irradiation is very similar (Sect. 13.4). Nevertheless, there are also some important differences: Depending on the type of materials, the melting thresholds for metals and non-metals may differ significantly. Furthermore, the ablation of metals takes place always via liquefaction, while non-metals may ablate from the solid phase as well. 'Classical' MD simulations ignore the quite different excitation mechanisms for metals and non-metals. In metals, the laser-light energy is mainly absorbed via intraband transitions of free or quasifree conduction band electrons (Fig. 2.1.1). With intense fs-laser pulses, however, the electron temperature, T_{e}, can reach several $10^4\,\mathrm{K}$, comparable to the Femi temperature. In such cases, thermal excitation of lower band electrons, e.g. d-band electrons in Au, Cu, Ni, Pt etc. becomes important [*Lin* et al. 2008b]. This is supported by calorimetric measurements on the energy absorption upon fs-laser irradiation [*Chan* et al. 2009]. In crystalline semiconductors, band-gap excitations result in the generation of electron-hole pairs. With very high intensities non-thermal (cold) melting and avalanche ionization become relevant as well. In dielectrics with $E_{\mathrm{g}} > h\,\nu$ multiphoton band-gap excitation and impact-ionization are the dominating mechanisms. Thus, absorption occurs only locally where the intensity exceeds the threshold for MPI. Under high-intensity fs-laser pulses photoemission of electrons may result in a local depletion of negative charges and, as a consequence, in Coulomb explosion.

13.5.3 Processing of Metals and Semiconductors

The functional dependence of the ablation rate of metals is still under discussion. For 100 fs Ti:sapphire laser radiation the data for Ag, Cu and W can be fitted by the logarithmic law (13.5.5) for low fluences, while for higher fluences, typically above $3\,\mathrm{J/cm^2}$, a linear fit seems to be more appropriate [*Byskov-Nielsen* et al. 2010]. As already described in Chap. 12, the accuracy of measurements does often not allow a clear distinction between such different functional dependences.

Figure 13.5.3 shows the ablation rate of Cu as a function of laser fluence for different pulse lengths. The regime $\phi < 0.4\,\mathrm{J/cm^2}$ is observed only with subpicosecond pulses. Here, *no* traces of molten material are observed. With fluences $0.4\,\mathrm{J/cm^2} < \phi < 5\,\mathrm{J/cm^2}$, the ablation rate changes only very little with τ_ℓ. In this regime, a thin layer of molten material appears. This ablation behavior has been analyzed on the basis of the two-temperature model. The two regimes $\phi < 0.4\,\mathrm{J/cm^2}$ and $\phi > 0.4\,\mathrm{J/cm^2}$ observed with femtosecond pulses have *both* been ascribed to logarithmic laws with threshold fluences ϕ_{th}^{l} and energy deposition depths $l \equiv \alpha^{-1}$ with $l_\alpha > l_\mathrm{e}$ and $l \equiv l_\mathrm{e}$ with $l_\alpha < l_\mathrm{e}$ [*Nolte* et al. 1997]. For fluences $\phi > 5\,\mathrm{J/cm^2}$ and picosecond pulses, a decrease in slope is observed. This behavior has been ascribed to changes in the optical and thermal properties of the material during the pulse. An alternative explanation of the two fluence regimes is given by *Zhigilei* et al. (2009).

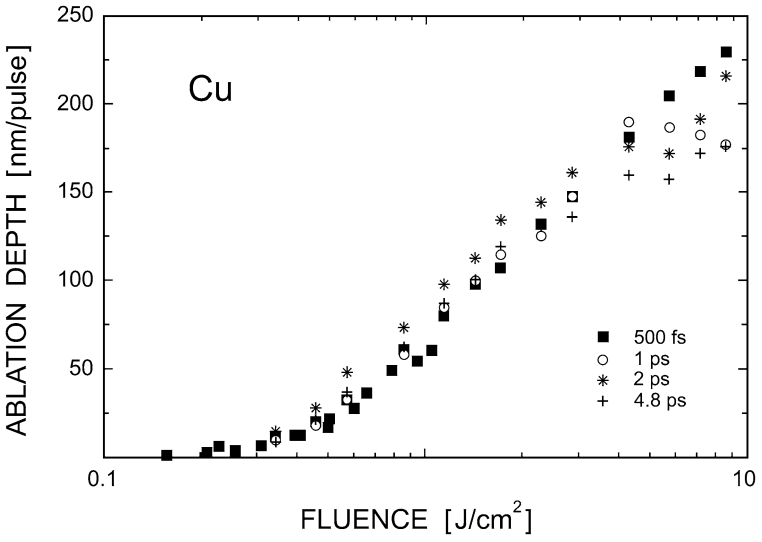

Fig. 13.5.3 Ablation depth per pulse for Cu and 500 fs to 4.8 ps Ti:sapphire-laser radiation ($\lambda = 780\,\mathrm{nm}$, $E_\ell = 1\,\mathrm{mJ}$, $\nu_\mathrm{r} = 1\,\mathrm{kHz}$) [*Nolte* et al. 1997]

Microdrilling of Cu, carbon steel, and stainless steel by means of 100 ps fiber-amplified microchip laser pulses was also described, with good accuracy, by a logarithmic law. Except of a thin molten layer, the quality of holes is similar to that obtained with sub-picosecond pulses. Ablation rates up to several 10 nm/pulse have been achieved. At high pulse repetition rates, particle shielding and heat accumulation (Sect. 6.3) become important [*Ancona* et al. 2009, 2008]. It should be noted, however, that with such 'long' pulses stress confinement is relaxed or even negligible at all. Thus, the laser-induced pressure wave may be not strong enough to cause spallation.

Nanopatterning of thin films of Au and of Au/Cr layers was demonstrated by using a SNOM-type setup in combination with 800 nm laser pulses ($\tau_\ell \approx 83$ fs). Feature sizes well below 20 nm have been achieved [*Chimmalgi* et al. 2005; *Hwang* et al. 2006]. Similar experiments have been performed for bulk Si.

In some cases, the situation may be more complicated. For example, single-pulse Ti:sapphire laser ablation of InP with fluences in excess of about $0.78\,\mathrm{J/cm^2}$ yields a crater with a central plateau of several ten nanometers in height ($\lambda = 800$ nm, $\tau_\ell = 10$ fs). This plateau is surrounded by a deeper annular ring [*Bonse* et al. 2009a]. Thus, the ablation rate, defined by the layer thickness ablated per pulse in the center of the crater, measured as a function of fluence, shows a step-like discontinuity. This phenomenon is explained by the formation of a high-density plasma and optical breakdown during the laser pulse. Due to combined single-and multiple-photon excitation and avalanche ionization the carrier density in the center of the Gaussian beam becomes so high, that the pulse energy is totally absorbed within a very shallow surface layer (Sect. 13.6).

13.6 Multiphoton- and Avalanche Ionization

In semiconductors and insulators laser-light intensities of 10^{11} to $10^{14}\,\mathrm{W/cm^2}$ generate very high electron densities via single-/multiphoton ionization and electron-electron impact ionization processes. The positive feedback in this latter process results in avalanche (cascade) ionization.

In tetrahedrally bonded semiconductors such as Si, the high density of photogenerated electron-hole pairs can result in a lattice instability, i.e. in a disordering of atoms within times $t \lesssim 100$ fs. During this time, the lattice remains almost 'cold'. This process is often denoted as cold- or non-thermal melting [*Choi* and *Grigoropoulos* 2004; *Rousse* et al. 2001; *Shank* et al. 1983]. Non-thermal melting has also been observed in a number of other materials, such as Ge, InP, InSb, etc. Recently, time-resolved X-ray scattering has been employed to study the *atomic* dynamics of InSb under fs-laser irradiation [*Hillyard* et al. 2007; *Lindenberg* et al. 2005]. With 'medium' laser fluences, large (coherent) atomic displacements have been observed. The transition to lattice disordering (cold-melting) with increasing carrier densities (laser fluences) has been clearly detected. Computations for the example of fs-laser excitation of InSb are in agreement with the

experimental results. These studies, based on a density functional theory, reveal that ultrafast melting is related to the softening of transverse acoustic phonons [*Zijlstra* et al. 2008].

In the following, we concentrate on *wide-bandgap* dielectrics with $h\nu < E_g$ and on glasses.

13.6.1 Dielectrics

With *high-quality* dielectric materials, the threshold fluence for ablation or surface damage for pulse lengths longer than a few tens of picoseconds is so high that even the 'low' amount of laser-light energy absorbed by surface states, by the 'small' number of bulk defects, and by quasi-free 'seed' electrons causes strong heating and breakdown at or near the materials surface. Heat transport is determined by diffusion which yields for the 1D case $\phi_{th} \propto \tau_\ell^\varepsilon$, with $\varepsilon \approx 0.5$ (Sect. 12.3). Experimentally, such a dependence has been observed for many wide-bandgap dielectrics and glasses (Fig. 12.5.3b). The situation changes with shorter pulses. In this range, ϕ_{th} continues to decrease with decreasing pulse length. Because of the short time scales involved, ϕ_{th} is *not* determined by heat conduction, but by rapid electron-hole production via *multiphoton* absorption, impact ionization and optical breakdown (Sect. 2.4.2). Within the time scales under consideration, typically shorter than 10 ps, the electrons cannot completely couple their energy to the lattice during the pulse. The evolution of the "free" electron density can be described by the rate equation

$$\frac{dN_e}{dt} = {}^{(n)}\Xi\, I^n + \zeta_a I N_e - k^{rec} N_e^q \tag{13.6.1}$$

The first term on the right hand side describes multiphoton ionization. Here, ${}^{(n)}\Xi$ is proportional to the n-photon absorption cross section, ${}^{(n)}\sigma$, with the smallest n satisfying $nh\nu \geq E_g$ (Sect. 3.2). The second term represents impact ionization where ζ_a is the avalanche coefficient (Sect. 11.6). The last term accounts for electron recombination/loss where $1 \leq q \leq 2$. The scenario can be described as follows: The intense laser pulse generates conduction band electrons by multiphoton absorption. The 'free' electrons *linearly* absorb the laser radiation by intraband transitions within the conduction band, like in a metal (Fig. 2.1.1). If the kinetic energy of these electrons is large enough, they transfer it, or part of it, to valence-band electrons which, as a consequence, can overcome the band-gap energy. This process rapidly increases the number of electrons, resulting in avalanche breakdown. In any case, Eq. (13.6.1) includes two limiting cases: multiphoton ionization (MPI) and electron avalanche ionization. Optical breakdown within the material occurs when the density of free electrons reaches a critical value, N_e^{cr}, which is, typically, of the order of 10^{21} per cm^3.

Figure 13.6.1 shows experimental data on the damage threshold for a-SiO_2 as a function of the laser pulse length and different laser wavelengths.

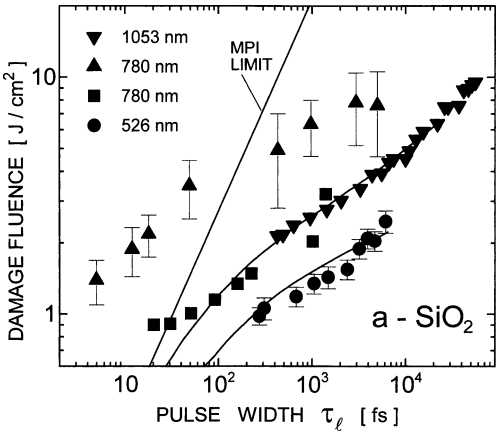

Fig. 13.6.1 Threshold fluence for surface damage of fused silica as a function of the duration of Ti:sapphire-laser pulses. Data refer to different laser wavelengths, number of laser pulses, and authors. ▼, ● $N_\ell = 600$ [*Stuart* et al. 1996]; ■ $N_\ell = 50$ [*Krüger* et al. 1997]; ▲ $N_\ell = 50$ [*Lenzner* et al. 1998]. The *solid curves* have been calculated from (13.6.1); the *straight line* represents the multiphoton ionization limit calculated with the same parameters [*Stuart* et al. 1996]

The damage thresholds calculated from (13.6.1) with $k^{\text{rec}} = 0$, for $\lambda = 1053\,\text{nm}$ and 526 nm laser radiation, are included in the figure as solid curves. The figure shows that with decreasing τ_ℓ the thresholds first decrease much slower, i.e., with exponents $\varepsilon < 0.5$, and then asymptotically approach the limit where MPI alone creates the critical electron density N_e^{cr}. While the data obtained by *Stuart* et al. and *Krüger* et al. are in reasonable agreement, investigations by *Lenzner* et al. yield a much higher MPI limit. This difference could be related to the hollow-fiber beam profile employed in the latter experiments. Such a beam profile should be free of 'hot' spots frequently observed with solid-state lasers. Such hot spots can significantly reduce the damage threshold (see also Sect. 6.3). Another important point is the different number of laser pulses employed in the experiments. With high-quality a-SiO_2 and the laser wavelengths under consideration, the degree of incubation, and thereby $\alpha_{\text{D}}(N_\ell)$, may change up to large numbers N_ℓ (Sects. 12.5 and 12.8; see also Fig. 13.3.1). For 5 fs pulses, damage thresholds $\phi_{\text{th}}(N_\ell = 1) \approx 4\,\phi_{\text{th}}$ $(N_\ell = 50)$ have been measured [*Lenzner* et al. 1999a].

Damage thresholds have also been determined for various fluorides and 400 fs-laser pulses. Here, it has been found that ϕ_{th} for BaF_2 ($1.6\,\text{J/cm}^2$), CaF_2 ($2.0\,\text{J/cm}^2$), MgF_2 ($2.1\,\text{J/cm}^2$), and LiF ($2.5\,\text{J/cm}^2$) scales with the bandgap energy. With the pulse durations employed, this is in reasonable agreement with what is expected for multiphoton-initiated avalanche ionization. Again, ϕ_{th} decreases with increasing number of pulses (Fig. 13.3.1).

Apart from the various differences in laser parameters and materials employed in these investigations, there are a number of objections referring to the interpretation of experimental data for ultrashort laser pulses:

- In the nonstationary regime, i.e. in the initial stage of ionization, Eq. (13.6.1) is a very crude approximation. In this regime, the 'free' electrons generated by MPI and avalanche ionization within the surface of the dielectric, act like a 'plasma' which determines the amount of reflected, transmitted, and absorbed light. This is the reason why even for transparent dielectrics, the absorbed laser-pulse intensity changes *during* the pulse and becomes dependent on the depth z within the material, i.e. $I_a \equiv I_a(t, z)$. Thus, Eq. (13.6.1) must be solved self-consistently. Such calculations have been performed by *Feit* et al. (2004). When further increasing the pulse energy, the absorbed and transmitted energy saturates while the reflected energy continues to increase. The thickness of the plasma layer depends on the material and the laser parameters. For $N_e \gtrsim N_e^{cr}$ it is, typically, between 10 and 100 nm [*Agranat* et al. 2009; *Bhardwaj* et al. 2006; *Feit* et al. 2004]. The temporal evolution of the surface reflectivity of a-SiO_2 upon 120 fs-laser irradiation with fluences below the ablation threshold has been investigated by *Siegel* et al. (2007). Interestingly, a time delay of $t \approx 1.5$ ps between the end of the pump pulse at 800 nm and the maximum in surface reflectivity, measured at 400 nm, has been observed.
- In the initial phase of excitation, the fraction of 'free' electrons whose energy is sufficiently high for impact ionization is certainly much smaller than the *total* number of electrons, N_e. This was pointed out by *Rethfeld* (2004). Qualitatively, the situation is quite evident. MPI generates electrons with an energy corresponding to the lower edge of the conduction band. Their kinetic energy is, roughly speaking, $E_{kin} \lesssim h\nu << E_g$. For impact ionization, these electrons must first gain enough energy by (linear) absorption of the incident radiation, which causes intraband transitions, as described above. On a femtosecond time scale, these processes cannot be considered as instantaneous. Thus, the transient number density of electrons with energy $E_{kin} \gtrsim E_g$ is smaller than the total number of electrons, i.e. $N_e^t(E_{kin} \gtrsim E_g) < N_e$. In other words, there is a certain time delay between the generation of electrons by MPI and that by avalanche ionization. Quantitative calculations that account for this scenario have been performed on the basis of a multiple-rate equation (MRE) [*Rethfeld* 2006, 2004]. This modified rate equation has the same form as the single-rate equation (13.6.1), except that the total electron density, N_e, in the second term on the right side is substituted by N_e^t. The deviations of results are particularly important as long as N_e^t/N_e changes in time. Trapping/recombination of electrons was ignored, i.e. the calculations were performed for $k^{rec} = 0$. Depending on the type of material, the laser light intensity and pulse duration, the transition from the initial stage, where MPI dominates, to the avalanche regime can last several 10 fs to several ps. For SiO_2 and a laser-light intensity of $I = 4.3 \times 10^{13}$ W/cm^2 (corresponding to an electric field of $E \approx 10^8$ V/cm) impact ionization was estimated to contribute to the free electron density only after about 100 fs. Avalanche ionization dominates after about 1.5 ps [*Rethfeld* 2006]. Thus, the contribution of avalanche ionization to the overall rate depends strongly on pulse duration. The influence of fast electron trapping on the transient free electron density and on dielectric breakdown have

been recently studied as well [*Rethfeld* et al. 2010]. Both, a modified MRE and a kinetic approach based on Boltzmann collision integrals have been employed. A MRE has been used also to describe the changes in optical properties of materials on the basis of a Drude model (*Christensen* and *Balling* 2009; see also Sect. 28.2.5). This model provides a reasonable fit to ablation rates measured for c-Al_2O_3 upon single-shot 100 fs Ti:sapphire laser irradiation [*Christensen* et al. 2010].

- The experimental results in Fig. 13.6.1 refer to *fused* SiO_2. Glasses, however, do *not* have a real band structure as crystalline materials and trapping/localization of electrons cannot be ignored [*Mott* and *Davis* 1979]. In a-SiO_2, e.g., defect states are related to (non-bridging) oxygen atoms bonded to single Si atoms. The lifetimes of electrons in the conduction band of crystalline dielectrics exceed those in the amorphous state significantly, depending on the type of material. Moreover, with fs laser irradiation the loss of electrons by photoemission may become important (Sect. 13.6.2).
- For laser-light intensities exceeding 10^{13} W/cm^2 and the wavelength under consideration, the multiphoton approximation starts to become inadequate. With such intensities, the electric field is of the order of the internal (atomic) electric field. For a semiconductor with band gap energy E_g the 'atomic' field is, approximately, given by E_g/ea where e is the electron charge and a the lattice constant. With such fields, tunnelling ionization becomes important [*Keldysh* 1965]. The "transition" is characterized by the Keldysh parameter $\gamma = \omega(2m_e E_i)^{1/2}/eE$ where E_i is the ionization potential. For 'moderate' laser-light intensities (electric field strengths), i.e. with $\gamma >> 1$, coherent absorption of multiple photons is an adequate description of the ionization process (MPI). For *very* high laser-light intensities, i.e. with $\gamma << 1$, tunnelling ionization becomes dominating.

13.6.2 Coulomb Explosion

Optical breakdown observed in dielectrics under high-intensity pulsed-laser irradiation changes the optical properties from transparent to 'metal-like', as discussed in the preceding section. The strong energy coupling to the 'plasma-layer' may yield intense photoemission of electrons, which results in a local accumulation of positive charges and surface electric fields of several 10^8 V/cm. As a consequence, the repulsive forces between ions may exceed the binding forces within the lattice, resulting in strong ion emission. This process is known as Coulomb explosion. Coulomb explosion is inhibited in metals due to the fast transport of electrons which counterbalances the laser-induced charge deficiency within the interaction volume.

The most detailed experimental studies on Coulomb explosion have been carried out for c-Al_2O_3, a-SiO_2, Si, and Au targets [*Stoian* et al. 2002a]. Figure 13.6.2 shows measurements for Al_2O_3. The yield of Al^+ ions was measured by

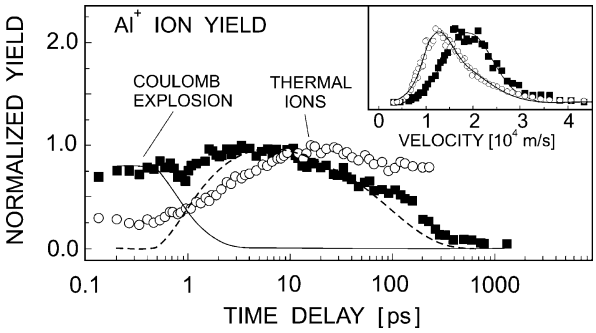

Fig. 13.6.2 Evidence for Coulomb explosion for Al_2O_3. Normalized yield of Al^+ as a function of the delay between two equal, subthreshold 100 fs pulses. *Squares*: 'fast' ions with a velocity of 2×10^6 cm/s showing a double-peak structure. *Full and dashed curves* are drawn to guide the eye. *Circles*: 'thermal' ions with a velocity of 1.2×10^6 cm/s. *Inset*: velocity distributions for Al^+ measured at two pump-probe delays: *circles*: 12 ps; *squares*: 0.6 ps [adapted from *Stoian* et al. 2002a; Copyright *American Physical Society*]

time-of-flight (TOF) mass spectroscopy. The time delay refers to two equal intensity subthreshold pulses with $\tau_\ell = 100$ fs. The circles refer to plasma ions that are characteristic for 'strong' thermal ablation. Their peak velocities are around 1.2×10^6 cm/s (see inset). For short delay times and 'gentle' ablation, fast ions with velocities of 2×10^6 cm/s are observed (squares). The fast ions show a double peak structure. The ions related to the first peak occur on a *sub-ps* time scale (the full curve is a guide for the eye). They are too fast for a thermal process. These ions are related to Coulomb explosion. The second peak in the fast ion signal (dashed curve) is due to the high energy tail of thermal ions. In contrast to the fast non-thermal ions ejected due to repulsive electrostatic forces, the thermal ions appear at a delay of about 20 ps. This time is determined by the electron-phonon coupling and the heating of the lattice. In fact, the calculated damage threshold for sapphire (c-Al_2O_3) is in good agreement with the experimental observations. The emission of Si^+ ions from a-SiO_2 behaves similarly to that of Al^+ ions shown in Fig. 13.6.2.

With Si and Au targets ion emission is only observed after surface melting, i.e. after 4–10 ps and 10–100 ps, respectively. Investigations on the photoemission of electrons from Si under ArF-laser irradiation ($\lambda = 193$ nm, $\tau_\ell \approx 15$ ns) did not show evidence for Coulomb explosion as well [*Marine* et al. 2008]. Nevertheless, whether Coulomb explosion can occur in semiconductors remains an open question. A unified approach for modelling the charge dynamics in dielectrics, semiconductors, and metals and the problem of Coulomb explosion is given by *Bulgakova* et al. (2007, 2005). At least with metals, it is quite clear that space charge effects significantly diminish the overall yield of electron emission [*Wendelen* et al. 2010]. Thus, surface electric field strengths obtained in earlier studies on dielectrics should be reconsidered.

13.6.3 Processing of Dielectrics

The interaction mechanisms between ultrashort laser pulses and materials discussed in the previous sections are of fundamental importance for the understanding of many processing applications discussed throughout this book. Subsequently, we present some further examples and peculiarities of ultrashort-pulse laser processing, in particular of dielectrics. Besides of the surface patterning of wide-band gap materials and glasses already discussed in Sect. 13.1, fs-laser processing is an attractive field for the fabrication of 3D embedded structures within transparent materials. By focusing fs-laser light of 'moderate' intensity into a *transparent* solid or liquid medium, multiple-photon absorption – with or without plasma formation – can cause material modifications such as local changes in refractive index, photopolymerization, etc. Embedded structures based on local refractive index changes are used as waveguides and diffractive optical elements, for 3D optical data storage, etc. (Sect. 23.6). Multiphoton photopolymerization *within* organic or organic-inorganic polymers is employed in stereolithography, the fabrication of photonic structures, etc. (Sect. 27.3). High-intensity fs-laser radiation focused into a transparent material causes local decomposition and void formation by multiphoton and avalanche ionization. In contrast to plasma formation at surfaces, which is confined to a thin layer of 10–100 nm, there is no such restriction if the laser beam is focused *into* the material volume. In this case, optical breakdown and plasma formation can 'grow' towards the incident laser beam. By this means, *hollow* structures within the bulk of a material can be generated. Beam focusing through an air-dielectric interface causes spherical aberration that elongates the excited material volume. Thus, for high resolution processing, in particular at large focusing depths, adaptive temporal pulse shaping is required [*Mermillod-Blondin* et al. 2008a].

Embedded Structures

Embedded 3D hollow microstructures are desirable for the fabrication of optical elements such as Fresnel zone plates and micrograting, for micromechanical and microfluidic devices, etc. The materials preferred for such applications are quartz glass (a-SiO_2) and Foturan. The latter is a commercially available photosensitive glass (Schott Corp., Germany) that consists of lithium aluminosilicate doped with (photoactive) Ce. Photoexcitation and phase separation processes in Foturan have been studied by *Livingston* et al. (2008). Foturan can be decomposed with moderate laser-light intensities.

Buried microfluidic devices are applied for chemical analysis, medical testing, drug-discovery, photonic biosensing, etc. Increasing importance find so-called 'all-in-one' lab-on-a-chip devices such as micro-total analysis systems (μ-TAS), where different functionalities are integrated into a single chip. A schematic picture of such a device is shown in Fig. 13.6.3a. The waveguides and hollow channels can all be fabricated by laser direct writing. Figure 13.6.3b shows real microchannels embedded 200 μm below the surface of a Foturan glass chip. These microchannels with a diameter of 45 μm connect several reservoirs at the surface. Patterning

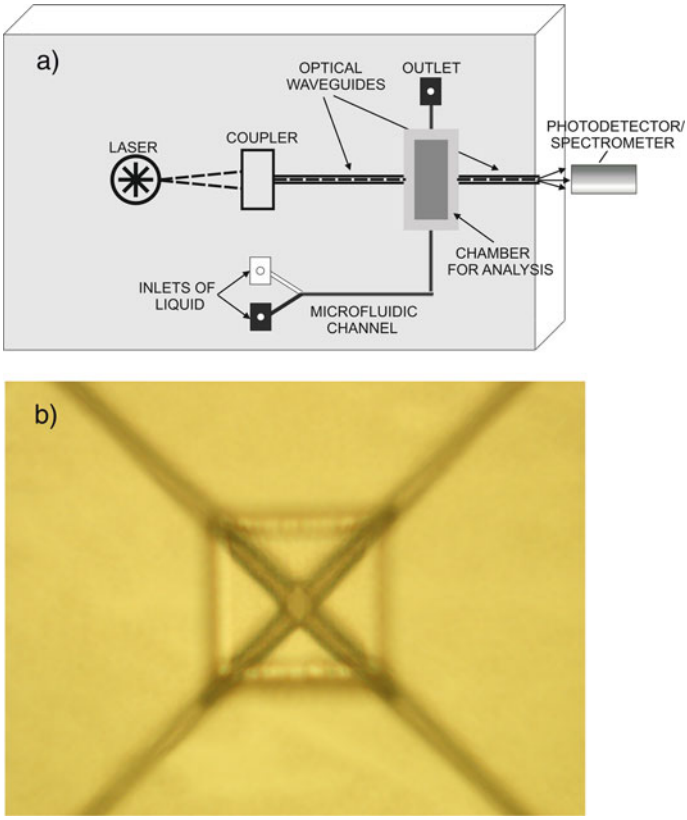

Fig. 13.6.3 (**a**) Example of an 'all-in-one' lab-on-a-chip device [adapted from *Sugioka* et al. 2007a]. (**b**) Microchannels of 45 μm width embedded 200 μm below the surface of a photostructurable glass (Foturan). The square is one of several microreservoirs at the surface. Patterning has been performed by fs-laser direct writing followed by post annealing and successive wet etching [adapted from *Sugioka* et al. 2007b]

was achieved by fs-laser direct writing followed by post annealing and successive wet etching. The functionality of such microfluidic structures generated in Foturan [*Hanada* et al. 2009a] and a-SiO_2 [*Hwang* et al. 2009b] has been demonstrated, e.g. in connection with dynamic cell analysis.

The formation of hollow structures in a-SiO_2 requires higher laser-light intensities than in Foturan. Within this intensity regime, self-focusing and filamentation of the laser beam is frequently observed. The *dynamics* of femtosecond void formation in a-SiO_2 was investigated by time-resolved phase-contrast microscopy [*Mermillod-Blondin* et al. 2009]. Here, 100 fs 800 nm pump pulses together with frequency-doubled probe pulses have been employed. The temporal resolution was better than 0.6 ps. The pulse energy was around the critical power for self-focusing. The scenario can be described as follows: For times $0.5\,\text{ps} \leq t \leq 2\,\text{ps}$ a negative refractive index change that can be attributed to a strong electron-hole plasma

is observed. For $t > 2$ ps electron-lattice relaxation becomes important and the appearance of a void surrounded by a shallow region of higher refractive index is observed. This indicates high pressure relaxation together with rarefaction within the excited volume. The refractive index within this volume decreases continuously over several 100 ps to 10 ns. This overall scenario is consistent with the mechanisms discussed throughout Sects. 13.4, 13.5 and 13.6. Spherical aberration which results from the mismatch of the refractive index at the interface does not only elongate the excited volume around the focal depth, but can even result in the formation of self-organized void arrays [*Song* et al. 2008].

Femtosecond void formation in a-SiO_2 and other dielectric materials has been employed for the fabrication of Fresnel zone plates [*Watanabe* and *Itoh* 2006] and different types of embedded optical components [*Terakawa* et al. 2010].

Figure 13.6.4 shows voids generated by picosecond laser pulses of different pulse lengths. At the upper surface, $\phi < \phi_{th}$. Thus, no damage occurs. The depth at which material decomposition starts, z_m, can be controlled via the laser power and/or the pulse length, i.e., $z_m = z_m(P, \tau_\ell)$. With increasing number of laser pulses, the cavities grow towards the (entrance) surface of the sample. The cavities show internal structures reminescent of micro-explosions, and they are surrounded by compacted material. Self-focusing at a depth z_f occurs if the laser-light intensity causes a sufficiently high positive non-linear contribution to the refractive index, n, and if the laser power exceeds the critical power, P_{cr}, (Sect. 9.1). With ps pulses, self-focusing is mainly determined by the electronic Kerr effect and not by electrostriction, heating, etc.

Figure 13.6.5 shows the inverse depth, z_m, versus the square root of the laser power. This plot reveals that $z_m \propto z_f$ and behaves in a way similar to (9.1.3). The ratio z_m/z_f depends on τ_ℓ. A linear fit to the experimental data shows that P_{cr} is

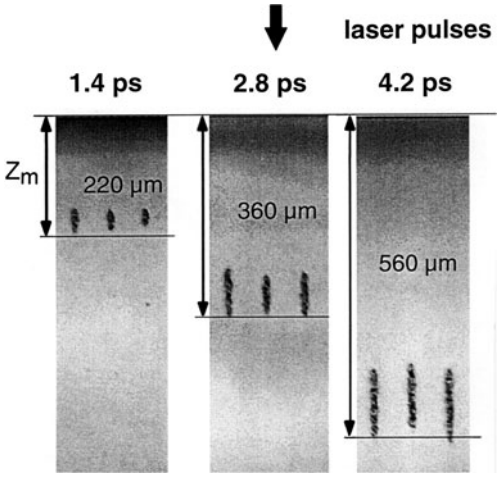

Fig. 13.6.4 Side view of modifications in bulk a-SiO_2 after 100 laser shots using three different pulse durations ($\lambda = 790$ nm, $E_\ell = 20\,\mu$J, spot size $= 920\,\mu m^2$) [*Ashkenasi* et al. 1998]

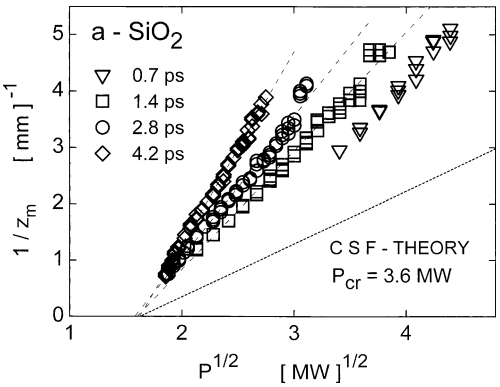

Fig. 13.6.5 Experimentally determined reciprocal modification depths in a-SiO_2 versus the square root of the laser power using side-view analysis, as depicted in Fig. 13.6.3. *Lines* are linear fits to experimental data. The expected catastrophic self-focusing depth assuming a critical self-focusing power threshold of 3.6 MW is shown (*dotted line*) [*Ashkenasi* et al. 1998]

approximately constant with pulse lengths $\tau_\ell \geq 1.4$ ps and somewhat higher with the shortest pulse. If the depth z_m is moved close to the exit (lower) surface of the sample, material removal occurs in the direction of laser-light propagation. By this means, holes can be fabricated on the *rear* side of the sample by using a relatively large focus at the entrance surface; additionally, this geometry avoids damage or contamination of the laser optics.

13.7 Comparison of Nanosecond and Ultrashort-Pulsed Laser Ablation

Thermal, photophysical, and photochemical ablation models often yield similar logarithmic dependences of the ablated-layer thickness on laser fluence, but with different meanings of ϕ_{th} and α. This is the main reason why ablation rate measurements using nanosecond pulses have been 'successfully' analyzed on the basis of all of these different models in parallel. This is not astonishing. The logarithmic law follows from the assumption that absorption takes place either within the material which is subsequently ablated or within the vapor/plasma plume. With nanosecond pulses, screening of the incident laser light by the vapor/plasma plume cannot be ignored, at least with fluences $\phi \gtrsim (2-3)\phi_{th}$. In the limiting case of very strong screening, the overall ablation behavior becomes determined by the interactions between the laser light and the product species, and *not* by *direct* laser-substrate interactions. Thus, ablation-rate measurements $\Delta h = \Delta h(\phi)$ for fluences $\phi >> \phi_{th}$ and pulse lengths exceeding 10–100 ps are not very conclusive with respect to the elucidation of microscopic mechanisms determining laser-material interactions. With even higher fluences, multiphoton absorption and optical breakdown occurs,

and α itself becomes dependent on fluence (Sect. 11.6). This may result in an even faster saturation in the dependence $\Delta h(\phi)$.

From these considerations it becomes clear that any information on microscopic material interactions with laser pulses longer than some 10–100 ps can only be revealed from the response of the system to fluences at or around ϕ_{th}, where interactions of the incident laser light with the vapor/plasma plume can be ignored.

If we linearize the logarithmic law for fluences $\phi \gtrsim \phi_{\text{th}}$, we obtain for the thermal and photochemical models the linear relations (12.3.3) and (12.8.4), respectively. These laws follow also from energetic considerations (11.2.20), or from the notion that the ablated depth is proportional to the number of photons, if absorption within the plume can be ignored. While these laws have again the same form, the parameters B and ϕ_{th} have different meanings. Most conclusive with respect to a separation between thermal and photochemical processes are investigations of the threshold fluence on laser-pulse length. For a thermal process which is controlled by 1D heat diffusion, we expect from (12.3.3) for the case of strong absorption $\phi_{\text{th}} \propto \tau_\ell^\varepsilon$, with $\varepsilon \approx 0.5$. Such a dependence has, in fact, been proved experimentally for many dielectrics, including organic polymers, where exponents within the range $0.3 < \varepsilon < 0.6$ have been found. For 'long' pulses and/or very small laser-spot diameters, 3D heat transport becomes important. In this limit, ϕ_{th} increases linearly with τ_ℓ, i.e., with an exponent $\varepsilon \approx 1$. This has been observed for PI and laser-pulse lengths $\tau_\ell \gtrsim 10\,\mu\text{s}$ (Fig. 12.5.3a). With photochemical processes, the decomposition rate should depend only on the dose $\int_o^t I(t')dt'$. This is certainly in contradiction to reliable experimental results on the ablation of most inorganic materials. Thus, in spite of the fact that the different models for nanosecond laser ablation result in the *same* laws, there is a clear preference for the thermal model (Sect. 12.3). This model permits one to describe almost all of the experimental data on the ablation of inorganic materials with nanosecond and longer pulses (Chap. 12). Exceptions are cases where stress-related effects (Sect. 12.9), liquid-phase expulsion (Sect. 11.4) or instabilities resulting in the ejection of liquid droplets (Sect. 12.6.5) contribute significantly to the overall ablation rate. Additionally, most of the experiments performed with organic polymers can be analyzed along similar lines, at least for wavelengths $\lambda > 200\,\text{nm}$. However, non-thermal effects may become important with deep UV-laser radiation (Sect. 12.8) and with ultrashort laser pulses (Sect. 13.3).

An equation that permits an analytical description of the ablation rate over a wide range of fluences is (12.3.6). This formula yields the linear law for fluences $\phi \gtrsim \phi_{\text{th}}$ and the logarithmic behavior for $\phi \gg \phi_{\text{th}}$. It does *not* describe Arrhenius tails and strong non-linearities related to plasma formation.

If experimental data obtained with nanosecond pulses cannot, or not satisfactorily, be explained on the basis of the thermal model, it does not necessarily mean that non-thermal processes are important. It can equally well indicate the limits of validity in the standard description of laser-induced thermal processes (Chap. 2), and the approximations made in the model calculations.

With femtosecond pulses, *no* vapor/plasma plume can develop during the pulse and ablation takes place only after the pulse.

With metals and small-bandgap semiconductors, the laser light generates a hot electron gas that can transport the absorbed energy much faster than normal (quasi-equilibrium) heat diffusion. This effect is most pronounced for s-band metals, e.g., Au, where the electron-phonon coupling is weak and where ballistic motion of electrons becomes important (Sect. 13.5). With very high laser-light intensities and pulse lengths up to some 10 fs, non-thermal (cold) melting, in particular in tetrahedrally bonded semiconductors, has been observed.

With wide-bandgap materials, the high intensities generated with picosecond and in particular with femtosecond pulses can produce very high concentrations of 'free' electrons via multiphoton absorption and impact ionization. Under certain conditions, the latter process results in avalanche ionization. This causes plasma formation and optical breakdown *within* the material. In this regime, the threshold (damage) fluence still decreases with pulse duration. For avalanche ionization one finds a slower decrease, i.e., an exponent $\varepsilon < 0.5$. If MPI with $n \gg 1$ dominates, an exponent $\varepsilon \approx 1$ is expected (Sect. 13.6). With nanosecond and low intensity ultrashort-pulse laser radiation the surface temperature remains *below* the critical temperature, i.e. $T_s < T_{cr}$. A 'sharp' boundary between the vapor and the liquid/solid phase exists. The vapor/plasma plume consists of atoms, ions, and small molecules. Its dynamics can be described by normal adiabatic expansion (*Anisimov* et al. 1993).

High intensity ultrashort-pulse laser radiation causes *homogeneous* heating within the bulk material, the formation of voids (foam) and a spallation layer.

With very high intensities, the initial surface temperature may exceed the critical temperature, i.e. $T_s > T_{cr}$. In this case, *no* sharp boundary between phases exists. Thus, both plume expansion *and* ablation must be described by the *hydrodynamic* equations and the equation of state.

Chapter 14
Etching of Metals and Insulators

Material removal by a gaseous, liquid, or solid etchant may be enhanced or only induced under the action of laser light. This is called laser-induced chemical etching. Symbolically, etching can often be described by the reversal of a corresponding deposition reaction, as already indicated in Fig. 1.2.1. Consider the deposition of Si according to $SiCl_4 \rightleftarrows Si(\downarrow) + 2Cl_2$. If the chemical equilibrium is shifted to the other side, the reaction describes the etching of Si in a Cl_2 atmosphere. Another example is laser-enhanced electrochemical processing. Here, the course of the reaction can be turned around by simply changing the polarity of the substrate with respect to the counterelectrode.

With many materials, standard (dark) etching starts spontaneously when they become immersed in a gaseous or liquid etchant. With some systems, the reaction continues and the material becomes dissolved. With other systems there is an initial reaction which passivates the surface and thereby suppresses further reactions. Clearly, there are materials which are just inert in a particular medium.

Laser light can influence molecule–surface interactions by excitation of gas- or liquid-phase molecules, excitation of the solid surface or of adsorbate–adsorbent complexes. The etching mechanisms can be thermal or photochemical in nature. Laser chemical etching may be classified into dry-etching, which employs gaseous precursors, and wet-etching, which is performed in liquids. Etching reactions using a solid etchant are quite rare.

In *dry-etching*, the precursor molecules most commonly used are halides, in particular Cl_2 and Br_2, and halogen compounds. The etching mechanisms are often based on the interaction between halogen radicals and charge carriers at or within the solid surface. These interaction mechanisms are, in many aspects, similar to those in surface oxidation (Chap. 26). The halogen radicals are formed spontaneously, for example by molecule–surface collisions, or only under the action of laser light. In a metal the free carriers are electrons, while in a semiconductor both electrons and holes are mobile. Dry-etching of metals and semiconductors is often classified into spontaneous etching, diffusive etching, and passivating reactions.

Wet-etching is mainly performed in aqueous solutions of acids like HCl, HNO_3, H_2SO_4, and H_3PO_4, or in lyes like NaOH and KOH, or in neutral salt solutions of NaCl, $NaNO_3$, K_2SO_4, etc. In addition, mixtures of different acids or of different

D. Bäuerle, *Laser Processing and Chemistry,* 4th ed.,
DOI 10.1007/978-3-642-17613-5_14, © Springer-Verlag Berlin Heidelberg 2011

lyes with or without other additives have been employed. Neutral salt solutions have the advantage of being less corrosive than acids or lyes. In laser-induced wet etching, the laser light enhances or induces the chemical reaction between the etchant and the substrate material. In many cases of liquid-phase processing, however, material removal is based on ablation only. In such cases, the liquid is used for efficient removal of ablation debris by either chemical reactions and/or for enhanced transport out of the interaction zone. In cases, where the absorbed laser light only softens or melts the substrate surface, cavitation bubbles may enhance surface erosion. In fact, in many cases of so-called laser-induced backside wet-etching (LIBWE), these mechanisms are important or even dominating (Sect. 14.5).

The most important dry-etching techniques currently used in micromechanics and microelectronics are plasma-assisted etching (PE) and reactive ion etching (RIE). Basically, PE and RIE involve reactive radicals and charged particles which interact with the solid surface, which is commonly kept at or near ambient temperature. Laser-induced etching can be considered as a *new* technique that not only permits direct maskless etching at high rates but also makes it possible to process a wide variety of materials that cannot be processed by standard techniques, or only very inefficiently. The general trend in semiconductor micro fabrication is definitely towards dry-etching, because wet-etching, in general, introduces high levels of contamination. Nevertheless, wet-etching is still of great importance, mainly due to the high rates that can be achieved. A further advantage is its great versatility, which is related to the large variety of reactants available without restrictions on volatility etc. Laser-induced wet-etching is therefore a useful tool in *micro*machining such as cutting, drilling, shaping, etc.

Most of the work on laser-induced etching has concentrated on metals and semiconductors. Localized etching by direct writing, projection patterning, and laser-beam interference has been demonstrated with both gas-phase and liquid-phase precursors. Large-area etching with the laser-beam parallel to the substrate has been investigated mainly with gaseous etchants. Under otherwise identical experimental conditions, the etch rate strongly depends on the microstructure and morphology of the material, crystal orientation, the type and concentration of admixtures, impurities, dopants, etc. Laser etching can be highly selective. This has been demonstrated for p-Si on SiO_2 and for W on Si substrates [*Loper* and *Tabat* 1984]. Here, the etch rates with respect to the substrate are, typically, 10^2-10^3 times higher.

Etch rates achieved in laser-induced dry-etching can compete with those in conventional techniques. For example, with a 200 W excimer laser and Cl_2 atmosphere it is possible to remove Si from a $10\,cm^2$ SiO_2 wafer, or a Si wafer, with a rate of 20 Å/s. This rate is similar to typical removal rates obtained with RF-plasma etching (PE). For W in a COF_2 atmosphere, ArF-laser radiation of comparable intensity would yield etch rates that are 3–4 times higher than those in PE. For many other metals, PE is even less efficient than for W. The high etch rates achieved with laser light, in particular at perpendicular incidence, are not only due to thermal or photochemical enhancement of the etching reaction itself, but also to thermal or non-thermal desorption of non-volatile reaction products, which are very often rate limiting in PE.

14.1 Photochemistry of Precursor Molecules

The precursor molecules mainly employed in laser chemical etching are halides and halogen compounds. Overviews on the photophysics and photochemistry of these molecules can be found in *Ben-Shaul* et al. (1981) and *Calvert* and *Pitts* (1966).

14.1.1 Halides

Many materials are inert against Cl_2, Br_2, and I_2 molecules, but are heavily attacked by the (atomic) radicals. Halides show strong continua in the VIS and UV, which result, at least in part, from optically active dissociative transitions $^1\Pi_u \leftarrow {}^1\Sigma_g$. The most detailed investigations on laser-induced photochemical etching have been performed with metals and semiconductors in a chlorine atmosphere. For these reasons we will further outline the photochemistry of halides for the example of chlorine. The photodecomposition of Cl_2 can be described by

$$Cl_2 + h\nu(\lambda \leq 500\,\text{nm}) \rightarrow 2Cl\ . \tag{14.1.1}$$

The maximum in the dissociative continuum occurs at about 330 nm. At wavelengths $\lambda > 480$ nm, the continuum is very weak and has vibrational structure superimposed on it, resulting from transitions into the bound $^3\Pi(O_u^+)$ state. If absorption occurs at wavelengths shorter than 498.9 nm, this bound state predissociates with near unity yield by crossing over to a repulsive state [*Heaven* and *Clyne* 1982; and references therein]. For Br_2 and I_2 the corresponding wavelengths for dissociation are below 628.4 nm and 803.7 nm, respectively. Photoexcitation together with energy transfer via *collisions* permits predissociation at somewhat longer wavelengths. Furthermore, at elevated temperatures, excitation from higher vibrational levels ($v'' > 0$) becomes possible. These are the reasons why, for example, Cl_2 can even be photodissociated with 514.5 nm radiation, though with low efficiency (Table V).

Halogen radicals are very aggressive and strongly chemisorb on many material surfaces or even diffuse into these surfaces and break chemical bonds. Photochemical etching of silicon can be described by

$$Si + xCl \rightarrow SiCl_x(\uparrow)\ , \tag{14.1.2}$$

with $x \leq 4$. The product molecules desorb from the surface. In this reaction the etch rate is proportional to the radical concentration at the surface (Chap. 15). A quantitative analysis of such reactions thus requires the knowledge of the gas-phase chemistry that follows the photogeneration of radicals. For chlorine this can be described by

$$\mathrm{Cl_2} + h\nu \longrightarrow 2\mathrm{Cl}$$

$$\mathrm{Cl} + \mathrm{Cl} + \mathrm{Cl_2} \xrightarrow{k_1} \mathrm{Cl_2} + \mathrm{Cl_2} \tag{14.1.3a}$$

$$\mathrm{Cl} + \mathrm{Cl} + \mathrm{Cl_2} \xrightarrow{k_2} \mathrm{Cl_2^*} + \mathrm{Cl_2} \tag{14.1.3b}$$

$$\mathrm{Cl_2^*} \xrightarrow{k_3} \mathrm{Cl_2} + h\nu' \tag{14.1.3c}$$

$$\mathrm{Cl_2^*} + \mathrm{Cl_2} \xrightarrow{k_4} \mathrm{Cl_2} + \mathrm{Cl_2} \tag{14.1.3d}$$

$$\mathrm{Cl_2^*} + \mathrm{Cl} \xrightarrow{k_5} \mathrm{Cl_2} + \mathrm{Cl}\ . \tag{14.1.3e}$$

The recombination of Cl atoms occurs via three-particle collisions (14.1.3a, b). The latter recombination channel has a probability of a few percent only. Reaction (14.1.3c) results in chemiluminescence (afterglow) between about 450 and 1400 nm. This chemiluminescence permits one to measure the chlorine-atom concentration in situ, e.g., during laser-induced chemical etching [*Kullmer* and *Bäuerle* 1988a]. The *total* chemiluminescence intensity observed during chlorine-atom recombination is proportional to the density of excited $\mathrm{Cl_2^*}$ molecules

$$I \propto N_{\mathrm{Cl_2^*}}\ . \tag{14.1.4}$$

With (14.1.3b–e) we obtain the rate equation

$$\frac{\mathrm{d}}{\mathrm{d}t} N_{\mathrm{Cl_2^*}} = k_2 N_{\mathrm{Cl}}^2 N_{\mathrm{Cl_2}} - k_3 N_{\mathrm{Cl_2^*}} - k_4 N_{\mathrm{Cl_2^*}} N_{\mathrm{Cl_2}} - k_5 N_{\mathrm{Cl_2^*}} N_{\mathrm{Cl}}\ . \tag{14.1.5}$$

For stationary conditions one obtains

$$N_{\mathrm{Cl_2^*}} = \frac{k_2 N_{\mathrm{Cl}}^2 N_{\mathrm{Cl_2}}}{k_3 + k_4 N_{\mathrm{Cl_2}} + k_5 N_{\mathrm{Cl}}}\ . \tag{14.1.6}$$

Thus, N_{Cl} can be determined from (14.1.4) and (14.1.6). Under certain circumstances, however, it is more appropriate to measure, instead of (14.1.4), the *spectrally resolved* intensity, $I(\lambda)$. In the short wavelength region around 550 nm, this intensity can be described by [*Clyne* and *Stedman* 1968]

$$I(\lambda \approx 550\,\mathrm{nm}) \propto N_{\mathrm{Cl_2^*}}(v' \approx 12) \propto N_{\mathrm{Cl}}^2 N_{\mathrm{Cl_2}}^{\gamma} \tag{14.1.7}$$

with $\gamma \approx 0.6$. Experimentally, the relative chlorine-atom concentration, N_{Cl}, can then be determined from the measured intensity $I(550\,\mathrm{nm})$ and the chlorine-gas pressure (Fig. 30.1.1b).

14.1.2 Halogen Compounds

Laser-chemical etching by UV and VIS radiation or by IR radiation is often performed by using halogen compounds such as HCl, XeF_2, NF_3, COF_2, CF_4, CF_2Cl_2, CF_3Cl, CF_2Br_2, CF_3Br, CF_3I, CCl_4, CF_3NO, SF_6, $CO(CF_3)_2$, etc.

Electronic Excitations

The halogen compounds listed, can be photodissociated by UV- or VIS-laser radiation. The products are radicals such as F, Cl, CF_2, CF_3, etc. These radicals are highly reactive and therefore predestined for etching.

The pyrolytic and photolytic decomposition kinetics of many halides and halogen compounds has been reviewed by *Armstrong* and *Holmes* (1972).

IR Vibrational Excitations

There are only a few examples for photochemical material processing with IR-laser radiation. The reason is that with the complex molecules and the high molecular densities employed in LCP, condition (2.3.9), and to an even greater extent (2.3.8), is difficult to fulfill.

Molecule-selective multiphoton vibrational excitation and dissociation (MPD) has been demonstrated for dry-etching with precursors such as SF_6, CF_3Br, CF_3I, and CDF_3. Here, SF_6 has been most extensively studied with respect to both its fundamental excitation mechanisms and its etching characteristics for pulsed CO_2-laser radiation. For *low* laser fluences (0.1–1 J/cm^2 or about 2–20 MW/cm^2), non-dissociative coherent excitation is observed,

$$SF_6 + n_c h\nu(CO_2) \rightarrow SF_6^* \,, \tag{14.1.8}$$

with $n_c \geq 3$. Asterisks now indicate vibrational excitation of the molecules. Because of the dense rotational structure in heavy polyatomic molecules such as SF_6, pumping into the quasi-continuum is possible *without* intermediate collisions (Sect. 2.3).

For fluences of 5–10 J/cm^2 a combination of coherent and sequential MPD of SF_6 is observed. This may be described, symbolically, by

$$SF_6 + nh\nu(CO_2) \rightarrow SF_5 + F \,, \tag{14.1.9}$$

with $n \gtrsim 30$. SF_5 is unstable and further decomposes into SF_4 and another F atom.

The intensity of multiphoton absorption spectra depends on the laser fluence. Additional characteristic features are: a distinct resonance behavior and a broadening and shifting of the resonance to lower frequencies with increasing laser fluence. For SF_6, these characteristics have been studied by *Bagratashvili* et al. (1976). They compare favorably with laser etching experiments performed in a SF_6 atmosphere. A further point to consider is the dependence of the dissociation yield on gas pressure and composition [*Letokhov* 1983; and references

therein]. For many monomolecular gases, the dissociation yield is independent of gas pressure, within a certain range. For SF_6 this range is $0.1\,\text{mbar} \leq p(SF_6) \leq 5\,\text{mbar}$. This behavior is related to the fact that the v–v exchange between molecules of the same type can take place without a reduction of the average vibrational energy. Collisions between *different* types of molecules can result in a decrease or an increase in dissociation yield. For SF_6 [*Fuss* and *Cotter* 1977], CF_3I [*Bagratashvili* et al. 1978], etc., an admixture of monoatomic buffer gases decreases the dissociation yield. For other molecules such as CDF_3, C_2H_4, $C_2H_2F_2$, however, the dissociation yield shows a pronounced maximum when the buffer-gas pressure is increased. In the case of CDF_3 with Ar, this maximum occurs at a pressure of $p(\text{Ar}) \approx 25\,\text{mbar}$ and exceeds the monomolecular yield by a factor of about 45. Vibrational energy transfer between vibrational modes is more efficient with complex polyatomic molecules than with simple species (Sect. 2.3).

14.2 Concentration of Reactive Species

The time-dependent concentration of gas-phase radicals, A, generated in a (purely) photochemical reaction of the type

$$\text{A}_{\mu_\text{A}}\text{B}_{\mu_\text{B}} + h\nu \rightarrow \mu_\text{A}\text{A} + \mu_\text{B}\text{B}$$

is given by the diffusion equation (3.3.2), which is approximated by

$$\frac{\partial N_\text{A}(\boldsymbol{x}, t)}{\partial t} \approx Q_{\nu,\text{A}}(\boldsymbol{x}, t) + D_\text{A}\nabla^2 N_\text{A}(\boldsymbol{x}, t) + f(N_\text{AB}, N_\text{A}, N_\text{B})\ . \quad (14.2.1)$$

The first term on the right-hand side describes the generation of species A within the gas (volume), and the second term the transport of these species by ordinary diffusion. The last term denotes the loss of radicals A by gas-phase recombination. The source term can be written as

$$Q_{\nu,\text{A}}(\boldsymbol{x}, t) = \mu\alpha_\text{AB}(\nu, N_\text{AB}(\boldsymbol{x}, t))\frac{I(\boldsymbol{x}, t)}{h\nu}\ , \quad (14.2.2)$$

where $\mu \equiv \mu_\text{A}$. The boundary conditions are determined by the reaction (net) fluxes of species onto the various surfaces within the reaction chamber, including the substrate.

Henceforth, we assume cw-laser irradiation at normal incidence to the substrate and cylindrical symmetry (Fig. 14.2.1). In the simplest case, the reaction fluxes at the surfaces (normal components) can then be described by

$$-J_\text{A} = D_\text{A}\hat{\boldsymbol{n}}_\text{r}\nabla N_\text{A} = k_\text{r}N_\text{A}\ , \quad (14.2.3)$$

where $\hat{\boldsymbol{n}}_\text{r}$ are unit vectors (directed into the reaction chamber) normal to the various surfaces (Fig. 14.2.1a); k_r are the corresponding reaction rate constants which are

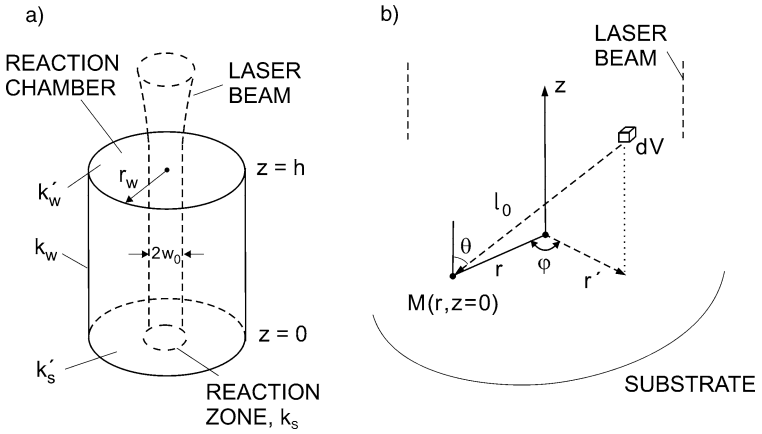

Fig. 14.2.1 (**a**) Reaction chamber and irradiation geometry employed in model calculations. The origin of coordinates is in the center of the basal plane. The radius of the reaction zone is $\sqrt{2}w_0$. (**b**) Magnification of laser-irradiated surface area. For notation see text

different for the different areas within the chamber: For the cylinder jacket defined by $r = r_w$ and $0 \leq z \leq h$, $k_r \equiv k_w$. The top surface (window) at $z = h$ with $r \leq r_w$ is characterized by $k_r \equiv k_w$. In the basal plane ($z = 0$) we define the reaction zone by $r \leq w_e = \sqrt{2}w_0$ and the corresponding rate constant by $k_r \equiv k_s$. Outside of this zone, the rate constant is $k_r \equiv k'_s$. Finally, we set up:

$$N_A(r, z, t) = 0 \qquad \text{with} \qquad t < 0\,. \tag{14.2.4}$$

The reaction rate in the center of the reaction zone is $W(0, 0, t) = -J_A(0, 0, t) = k_s N_A(0, 0, t)$. Equation (14.2.1), together with (14.2.3) and (14.2.4), can only be solved numerically.

Some general aspects can be demonstrated by employing (crude) simplifications that permit an analytical treatment of the problem. Different approximations are discussed in the next subsections. Specific solutions of (14.2.1) for parallel laser-beam incidence are presented in Sect. 19.4.

14.2.1 Ballistic Approximation

An analytical expression for the reaction rate can be obtained if we assume a ballistic motion of A without recombination ($\lambda_m \gg I_0 \approx w_0$; Fig. 14.2.1b).

For low gas-phase absorption, where $I(r, z) \approx I(r, h) = I(r)$, the generation rate of species A at a point $(r', z > 0)$ is given by

$$\frac{\partial N_A}{\partial t} \approx \mu \sigma_{AB} N_{AB} \frac{I(r')}{h\nu}\,. \tag{14.2.5}$$

The number of species A generated per second in $\mathrm{d}V = r'\,\mathrm{d}r'\,\mathrm{d}\varphi\,\mathrm{d}z$ is then $[\partial N_\mathrm{A}/\partial t]\,\mathrm{d}V$. These species shall propagate isotropically out of $\mathrm{d}V$. By integrating contributions from the entire gas volume above the substrate, the total flux at $M(r, z = 0)$ becomes

$$-J_\mathrm{A}(r,0) \approx \frac{\eta\mu\sigma_\mathrm{AB}N_\mathrm{AB}P}{\pi h\nu w_0^2}\int_0^{2\pi}\mathrm{d}\varphi\int_0^h \mathrm{d}z \times \int_0^{r_\mathrm{w}} \frac{r'z}{4\pi l_0^3}\exp\left(-\frac{r'^2}{w_0^2}\right)\mathrm{d}r' \,. \tag{14.2.6}$$

If *no* further reactions of A on the substrate take place, as, for example, in some cases of photolytic LCVD, η becomes equivalent to a sticking coefficient. In the case of etching, η is the reaction probability that contains the sticking probability of A on the surface, the probability for further decomposition or reaction of A on the surface, the desorption of reaction products, etc. If both $h, r_\mathrm{w} \gg w_0$ (Fig. 14.2.1a), (14.2.6) can be approximated by

$$-J_\mathrm{A}(r,0) \approx \frac{\eta\mu\sigma_\mathrm{AB}N_\mathrm{AB}}{4\sqrt{\pi}h\nu w_0} P\mathbf{I}_0\left(\frac{r^{*2}}{2}\right)\exp\left(-\frac{r^{*2}}{2}\right) \,, \tag{14.2.7}$$

where $\mathbf{I}_0$ is the modified Bessel function. In the center of the laser focus this becomes

$$-J_\mathrm{A}(0,0) \approx \frac{\eta\mu\sigma_\mathrm{AB}N_\mathrm{AB}P}{4\sqrt{\pi}h\nu w_0} \propto \frac{1}{w_0} \,. \tag{14.2.8}$$

Thus, with the approximations made, the flux in the case of *gas-phase* photolysis at constant laser power, P, is $J_\mathrm{A} \propto w_0^{-1}$. For *adsorbed-phase* photolysis we find $J_\mathrm{A} \propto I \propto w_0^{-2}$. The reason for this difference is that species created at distances larger than w_0 are distributed over such a large area that they do not significantly contribute to the rate at the center of the laser focus. While these considerations are very simple and transparent, we should be aware of the many approximations made:

- The assumption of a constant coefficient η does not apply in many cases.
- With the gas pressures commonly employed in LCP, the assumption $\lambda_\mathrm{m} \gg l_0$ does not hold.
- The assumption of a semi-infinite gas phase and the omission of product recombination is often inadequate. Their influence will be considered in the next two subsections.

14.2.2 Diffusion

In order to obtain further insight into the problem, we investigate the influence of diffusion on the number density of species A on the substrate surface. Here, we assume $k_s = k'_s$ and $h, r_w \gg w$ (Fig. 14.2.1a). In this limit, the interaction of species with the walls and the entrance window of the reaction chamber can still be ignored. With these approximations, an analytical solution of the stationary problem can be found. With $z > 0$ we have

$$D_A \nabla^2 N_A + Q_{\nu,A}(r) = 0 \,, \tag{14.2.9}$$

and with $z = 0$

$$D_A \frac{\partial N_A}{\partial z} = k_s N_A \,. \tag{14.2.10}$$

With a Gaussian laser beam and low gas-phase absorption, the source term can be written as

$$Q_{\nu,A} = Q_0 \exp\left(-\frac{r^2}{w_0^2}\right) \,, \tag{14.2.11}$$

where

$$Q_0 = \frac{\mu \sigma_{AB} N_{AB} I_0}{h\nu} \,.$$

By using integral transforms, we find

$$N_A(r = 0, z = 0) = \frac{Q_0 w_0^2}{2D_A} \int_0^\infty \frac{\exp(-\zeta^2)\,\mathrm{d}\zeta}{\zeta + k_s^*/2} \,, \tag{14.2.12}$$

where $k_s^* = k_s w_0 / D_A$. If $k_s^* \gg 1$, this yields

$$N_A(0, 0) \approx \frac{\mu \sigma_{AB} N_{AB} P}{2\sqrt{\pi} h\nu k_s w_0} \,. \tag{14.2.13a}$$

This result differs from (14.2.8) by a factor of 2 (in the ballistic approximation half of the species never reach the substrate). This approximation proves to be reasonable with $k_s^* \geq 5$ (see below). If $k_s^* \ll 1$, from (14.2.12) we obtain

$$N_A(0, 0) \approx \frac{\mu \sigma_{AB} N_{AB} P}{2\pi h\nu D_A} \ln\left(\frac{2}{k_s^*}\right) \,. \tag{14.2.13b}$$

14.2.3 Influence of the Reaction Chamber

The concentration of photoproducts impinging on the substrate surface depends on the size of the reaction chamber and on the material from which it is fabricated. This has been demonstrated by solving (14.2.1) together with (14.2.2), (14.2.3) and (14.2.4) for the reactor geometry depicted in Fig. 14.2.1a. The calculations reveal that for constant laser power the exponent n, according to the ansatz

$$W(0,0) \propto \frac{1}{w_0^n} , \tag{14.2.14}$$

strongly depends on the rate constants $k_r\{k_s, k'_s, k_w, k'_w\}$ and, under certain conditions, on the reactor size, which is characterized by the dimensionless quantity $\Gamma = h/w_e$, where $w_e = \sqrt{2}w_0$ and $h = r_w$.

Let us first consider the situation where species A react at the *total* sample surface (inside and outside of the laser-irradiated area) and at the walls and windows of the reaction chamber with equal rates $k^* \equiv k_s^* = k_s^{*\prime} = k_w^* = k_w^{*\prime}$. Examples would be photolytic etching of metal and glass substrates by halogen radicals within metal and glass reactors, respectively.

Figure 14.2.2 shows the concentration $N_A^*(0,0)$ and the exponent n (right-hand scale) as a function of k^*. Solid and dotted curves belonging to values $\Gamma = 10^4$ and $\Gamma = 10^3$, respectively, almost coincide.

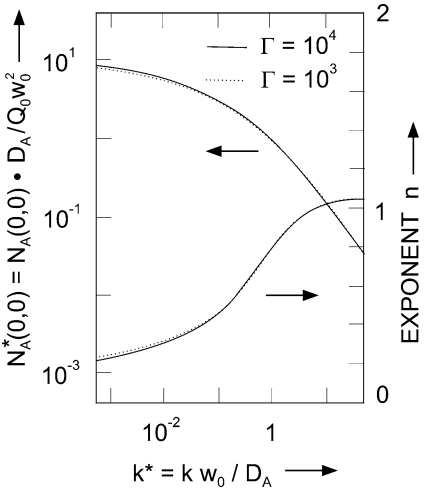

Fig. 14.2.2 Dependence of the stationary concentration of photogenerated species $N_A^*(0,0)$ (*left-hand scale*) and of the exponent n (*right-hand scale*) on the normalized rate constant $k^* \equiv k_s^* = k_s^{*\prime} = k_w^* = k_w^{*\prime}$ with $\Gamma = 10^4$ (*solid curves*) and $\Gamma = 10^3$ (*dotted curves*) [*Piglmayer* and *Bäuerle* 1989]

If k becomes very large, i.e., $k \to k_m \equiv k_{max}$ ($\eta \approx 1$; Sect. 3.4.2), species A react with unit probability on all surfaces. This limit is described by (14.2.13a). (Note that these calculations refer to a Gaussian beam, while the present model uses a constant intensity.) The numerical calculations yield $n \approx 1$ for $k^* \geq 5$ (the slightly larger value of n is a numerical artefact originating from the 'coarse' discretization).

If k decreases, i.e., $k < k_m$, the fraction $(1-\eta)$ of molecules impinging on the various surfaces is reflected into the volume of the reaction chamber, thereby increasing the concentration N_A. The dependence of $W(0,0)$ on w_0 can be described, approximately, by (14.2.14), where, however, the exponent n is not constant. With very small values of k^*, the density N_A^* becomes more uniform within the reaction chamber and is no longer affected by w_0. Therefore, n approaches zero for $k^* \to 0$.

We now assume that species A react with equal probability on the *total* substrate surface, while the walls of the reaction chamber are inert. This situation is described by $k^* \equiv k_s^* = k_s^{*\prime}$ and $k_w^* = k_w^{*\prime} \to 0$. It applies, for example, to photolytic dry-etching of metals in a chlorine atmosphere, where the reaction chamber is fabricated out of glass. The results are similar to those shown in Fig. 14.2.2, as long as $k^* \geq 10^{-4}$. With $\Gamma = 10^4$, the deviations are negligible. With $\Gamma = 10^3$ and $k^* = 10^{-4}$, however, the deviations amount to a decrease of about 12% in n and an increase of about 25% in $N_A^*(0,0)$. The latter originates from the increase in back reflection of species A from the reactor walls into the gas volume.

Figure 14.2.3 shows the temporal dependence of W^* for different values of k^* where $k^* \equiv k_s^{*\prime} = k_w^* = k_w^{*\prime}$ and $k_s^* \to k_m^*$. The times necessary to reach steady-state conditions depend strongly on k^*. With very small values of k^*, these times can become longer or comparable to typical laser-beam dwell times involved in LCP.

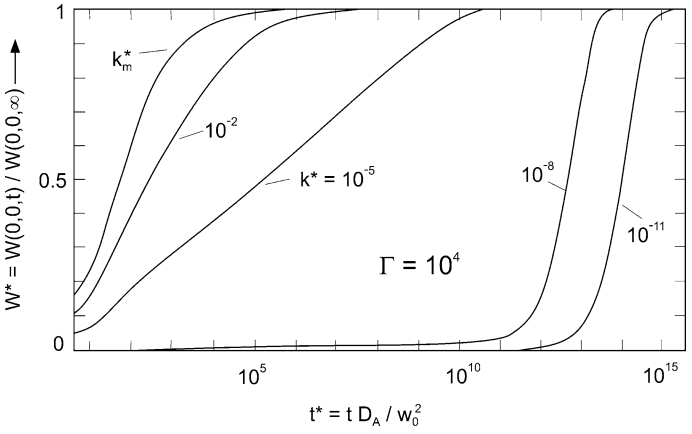

Fig. 14.2.3 Reaction rate W^* as a function of time t^* for various rate constants k^* and $\Gamma = 10^4$ [*Piglmayer* and *Bäuerle* 1989]

14.2.4 Gas-Phase Recombination

Let us consider the simplest case of gas-phase recombination, where

$$f(N_A, N_B) = -k_A^{rec} N_A \ . \tag{14.2.15}$$

This ansatz permits an analytical solution of (14.2.1). The number density within the center of the laser beam is

$$N_A(0,0) = \frac{Q_0 w_0^2}{2D_A} \int_0^\infty \frac{\zeta \exp\left(-\zeta^2\right) \mathrm{d}\zeta}{\zeta^2 + k_A^{rec*} + \frac{k_s^*}{2}\left(\zeta^2 + k_A^{rec*}\right)^{1/2}} \ , \tag{14.2.16}$$

where Q_0 and k_s^* are defined as in (14.2.12), and $k_A^{rec*} \equiv k_A^{rec} w_0^2 / 4D_A$. With $k_A^{rec*} = 0$, (14.2.16) and (14.2.12) become identical. If the reaction is very fast and recombination very slow, so that $k_s^* \gg 1$ and $k_A^{rec*} \ll 1$, we obtain

$$N_A(0,0) = \frac{\pi^{1/2} Q_0 w_0}{2k_s} \ . \tag{14.2.17a}$$

This equation coincides with (14.2.13a). If, on the other hand, $k_A^{rec*} \gg 1$, we obtain

$$N_A(0,0) = \frac{Q_0 w_0}{w_0 k_A^{rec} + 4k_s (k_A^{rec*})^{1/2}} \ . \tag{14.2.17b}$$

More general cases of gas-phase recombination introduce a non-linearity into (14.2.1). Then, calculations can only be performed numerically. As an example, we study the photolysis of chlorine. The recombination of chlorine radicals (atoms) generated within the *gas phase* takes place via three-particle collisions (14.1.3a, b), which can be described by

$$f(N_{Cl_2}, N_{Cl}) = -2k_{Cl\text{-}Cl} N_{Cl}^2(r,z,t) N_{Cl_2} \ , \tag{14.2.18}$$

where

$$k_{Cl\text{-}Cl} = k_1 + k_2 = 5.5 \times 10^{-32}\,\mathrm{cm}^6/\mathrm{s} \ . \tag{14.2.19}$$

The substrate surface shall be characterized by $k_s \to k_m \approx \langle v_{Cl} \rangle / 2 = 2.13 \times 10^4\,\mathrm{cm/s}$. We choose $k_s' = k_w = k_w' \equiv k = 0.1\,\mathrm{cm/s}$. This very small value should be considered as a *minimal* rate constant for reactions between chlorine radicals and material surfaces [*Clyne* and *Stedman* 1968].

Figure 14.2.4 shows the reaction rate, $W^*(0,0,t)$, as a function of time, t, for various chlorine pressures, $p(Cl_2)$. The time necessary to reach stationary conditions, t_∞, increases with decreasing chlorine pressure. The comparison of the 100 mbar curves shows that recombination reduces t_∞. With 1 mbar, t_∞ is of the

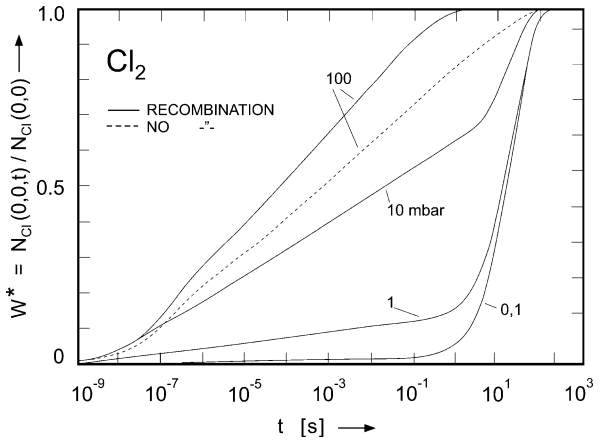

Fig. 14.2.4 Temporal dependence of the photolytic dissociation rate of chlorine. *Solid curves* have been calculated by incorporating the proper recombination kinetics (14.2.18) into (14.2.1). The *dashed curve* shows the behavior without recombination. The parameters were $\alpha_{Cl_2}(514.5\,\text{nm}, 1000\,\text{mbar})I = 33\,\text{W/cm}^3$, $w_0 = 5\,\mu\text{m}$, $p_{Cl_2} D_{Cl} = 79\,\text{cm}^2\,\text{s}^{-1}$ mbar, $k_s \to k_m = 2.13 \times 10^4$ cm/s, $k'_s = k_w = k'_w = 0.1$ cm/s, and $\Gamma = 10^4$ [*Piglmayer* and *Bäuerle* 1989]

order of 100 s. Such times can be longer than or comparable to typical laser-beam dwell times employed in laser-induced dry-etching.

14.2.5 Gas-Phase Heating

The influence of gas-phase heating on the reaction flux of species can be calculated from the equations presented in Sect. 3.5. For pure etching we employ the boundary condition $x_{BC}(r, z \to \infty) = x_{BC}(\infty)$ and set $k_2 \neq 0$ and $k_1 = k_3 = 0$ in (3.5.1). The spatial distribution of the reaction rate is essentially the same as shown in Fig. 16.3.1, except that the height of the deposit is now replaced by the depth of the etched hole. At low temperatures, the depth of the hole decreases monotonically with increasing distance r^*. At higher temperatures, the maximum etch depth can occur at a certain distance, $r > 0$.

14.3 Dry-Etching of Metals

Laser-enhanced dry-etching has been studied for many metals – both elements and compounds (see previous edition).

In the following, we will discuss spontaneous etching systems, diffusive etching systems, and passivating reaction systems separately.

14.3.1 Spontaneous Etching Systems

Spontaneous etching denotes a situation where the material dissolves within the ambient medium *without* any external influence. Among the examples are Al in a Cl_2 atmosphere or Mo, Ta, Ti, W in XeF_2, etc. Small mass losses due to etching can be measured conveniently by means of a quartz crystal microbalance (QCM; Sect. 29.3). In most of these experiments, the metal film is directly evaporated onto the quartz.

Figure 14.3.1 shows measurements for the Al–Cl_2 system. Curve a shows the situation *without* laser light. After exposure of the Al film to Cl_2, the frequency of the QCM first decreases due to chlorine chemisorption and then increases due to etching. Etching continues until the chlorine gas is pumped off.

Light can significantly enhance the etch rate. This is shown in the lower part of Fig. 14.3.1 for (pulsed) N_2-laser radiation (note change in scales). The enhancement in etch rate depends on the laser parameters and the chlorine-gas pressure (curves b and c). With $\phi = 0.12\,\mathrm{J/cm^2}$ and $p(Cl_2) = 0.13\,\mathrm{mbar}$ the etch rate was $W_E \approx 11\,\text{Å/pulse}$; with XeCl-laser radiation ($\phi = 0.3\,\mathrm{J/cm^2}$, $p(Cl_2) = 1.3\,\mathrm{mbar}$) it was $W_E \approx 30\,\text{Å/pulse}$.

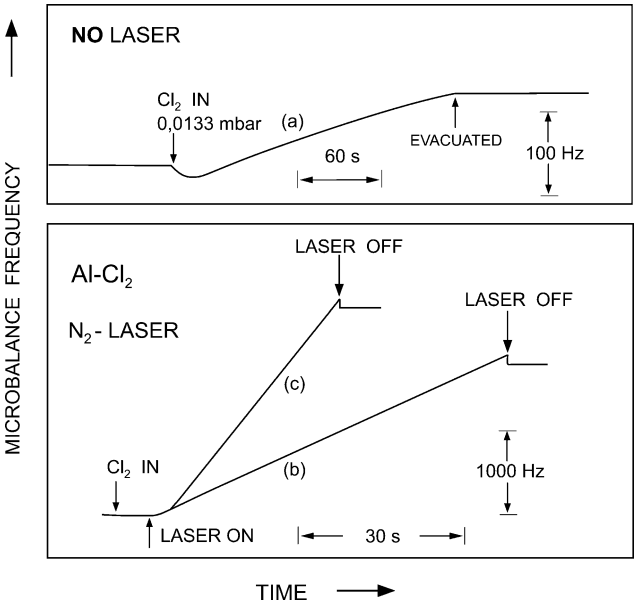

Fig. 14.3.1 Frequency responses of a quartz crystal microbalance (QCM) covered with a thin film of Al exposed to a Cl_2 atmosphere. (a) *Dark* etching, $p(Cl_2) = 0.013\,\mathrm{mbar}$. (b) N_2-laser irradiation ($0.12\,\mathrm{J/cm^2}$, $\tau_\ell = 10\,\mathrm{ns}, 30\,\mathrm{pps}$), $p(Cl_2) = 0.013\,\mathrm{mbar}$. (c) As in (b) but with $p(Cl_2) = 0.13\,\mathrm{mbar}$ [*Sesselmann* and *Chuang* 1985]

14.3.2 Diffusive Etching Systems

Diffusive etching systems are characterized by strong physisorption or chemisorption of the reactant *and* by the diffusion of corresponding radicals into the bulk. The main difference to spontaneous etching systems is related to the low vapor pressure of products. Among the model systems investigated are Ag and Cu in a Cl_2 atmosphere. The degree of chlorination of the metal surface, $MeCl_x$, depends on the Cl_2 pressure, the time of exposure, and the distance from the surface. This has been evaluated from Auger depth profiles which were calibrated by means of X-ray photoemission spectroscopy (XPS) [*Sesselmann* and *Chuang* 1987]. For Cl_2 exposures lower than 10^7 L (1 L = 1 Langmuir = 10^{-6} Torr s) the Cl concentration decreases rapidly with depth. In this regime, the chlorine uptake increases logarithmically with exposure time. This behavior can be explained on the basis of field-enhanced diffusion, as described by Cabrera and Mott (Chap. 26). The strongly electronegative chlorine atoms adsorbed on the Ag surface become negatively charged by electron transfer from the metal. The resulting electric field across the surface layer causes diffusion of Cl^- ions into the metal and of Ag^+ ions towards the surface. Because of the smaller radius of Ag^+ ($\approx$ 1.26 Å) compared to Cl^- ($\approx$ 1.81 Å), Ag diffusion to the surface is dominant. In this surface-chlorination reaction, dissociative chemisorption of chlorine seems to be rate limiting. For exposures $> 10^7$ L, the chlorinated layer becomes quite thick, up to 50 Å, and has a composition close to stoichiometric AgCl ($x > 0.8$). In this regime, bulk diffusion of ions becomes rate limiting and the chlorine uptake increases with $t^{1/2}$. Because both silver and copper chlorides have a very low volatility, no spontaneous etching occurs.

Laser-light irradiation removes the chlorinated layer. Figure 14.3.2 shows the behavior of Cu, Ag, and Au in Cl_2 under N_2-laser radiation. No etching is observed with Au, and Cu etches faster than Ag ($W_E \approx 0.3$ Å/pulse). The desorption yields, as well as the mass and velocity distributions of species (Me, Cl, and Me_yCl_x) for VIS and UV laser pulses, were determined by time-of-flight (TOF) mass spectrometry [*Sesselmann* et al. 1986a, b; *van Veen* et al. 1988]. The type and relative concentration of species desorbed from the surface depends on the laser parameters and differs significantly from that observed in standard thermal desorption experiments. The influence of gas-phase excitations of chlorine and of thermal and electronic excitations of the $MeCl_x$ layer has been studied by *Brannon* and *Brannon* (1989).

14.3.3 Passivating Reaction Systems

The class of passivating reaction systems investigated includes: Fe, Mo, Ni, W, and Ni_xFe_y alloys in a Cl_2 atmosphere, and Ti in Br_2 and CCl_3Br. The situation is similar to surface passivation by native oxide formation (Chap. 26). The etchant chemisorbs on the metal surface and forms a stable and dense metal–halide layer which suppresses any further reaction. The layer is, typically, 10−30 Å thick and can be estimated from QCM measurements. The decrease in microbalance frequency

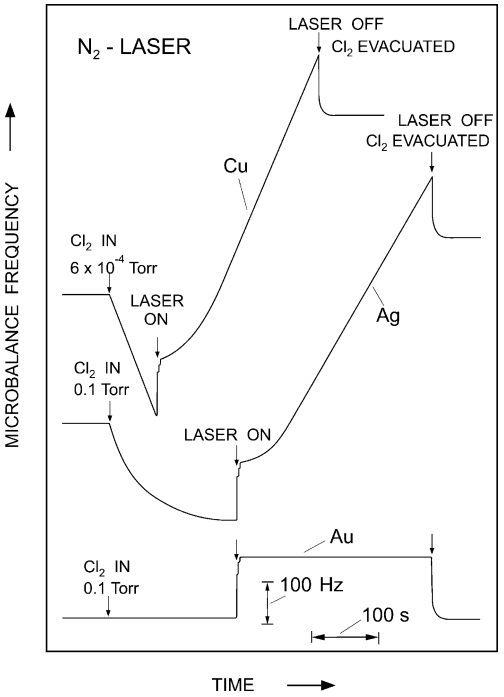

Fig. 14.3.2 Frequency response of QCM with evaporated Cu, Ag and Au films after exposure to Cl_2 and N_2-laser irradiation ($\phi = 0.12\,\mathrm{J/cm^2}$, $\tau_\ell = 10\,\mathrm{ns}$, $30\,\mathrm{Hz}$). The step-like frequency change observed when the laser is switched on and off are caused by temperature changes and *not* by desorption or adsorption of species [*Sesselmann* et al. 1986a]

observed directly after Cl_2 exposure of Ni, Fe, and Ni_xFe_y alloys can be seen in Fig. 14.3.3. In contrast to diffusive etching systems, no diffusion of the halogen into the bulk metal takes place.

Laser-light irradiation yields a local temperature rise, which results in a step-like increase in QCM frequency. Subsequently, a continuous increase in QCM frequency due to laser-induced desorption of the metal–halide layer is observed. While the etch rate is almost negligible for pure Ni, it increases strongly with Fe alloying. With the parameters employed, the rates were $W_E(\mathrm{Ni}) < 0.01\,\mathring{\mathrm{A}}/\mathrm{pulse}$, $W_E(\mathrm{Fe_{0.53}Ni_{0.47}}) \approx 0.2\,\mathring{\mathrm{A}}/\mathrm{pulse}$, and $W_E(\mathrm{Fe}) \approx 0.5\,\mathring{\mathrm{A}}/\mathrm{pulse}$. The differences in etch rates can be related to the volatilities of reaction products. $FeCl_3$ has a relatively high vapor pressure, while Ni chlorides are essentially non-volatile below about 500 K.

Localized etching by means of focused cw-Ar^+-laser radiation in a Cl_2 atmosphere was investigated for Ti, and for thin films of Mo and W on glass substrates. Figure 14.3.4 shows etch-rate measurements for Mo films and various Cl_2 pressures. The solid curves have been calculated on the basis of a thermally activated process. The good agreement with experimental data suggests that etching at medium-to-high laser powers can be interpreted by (mainly) thermal desorption of reaction products. The influence of non-thermal effects is still under discussion.

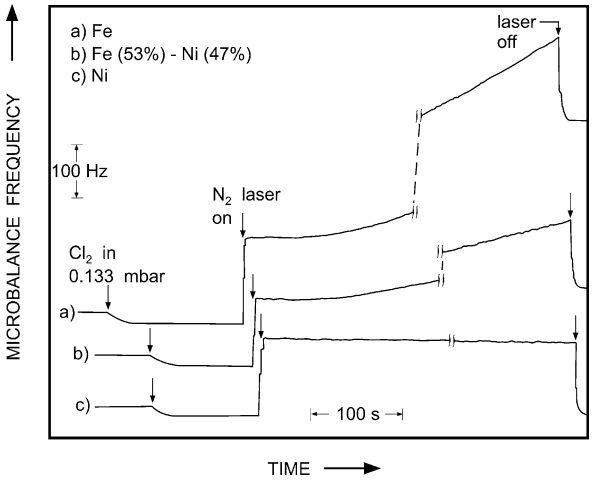

Fig. 14.3.3 Frequency response of QCM covered with metal films exposed to a 0.13 mbar Cl_2 atmosphere and N_2-laser radiation ($0.12\,J/cm^2$, $\tau_\ell = 10$ ns, 30 Hz) [*Chuang* et al. 1984]

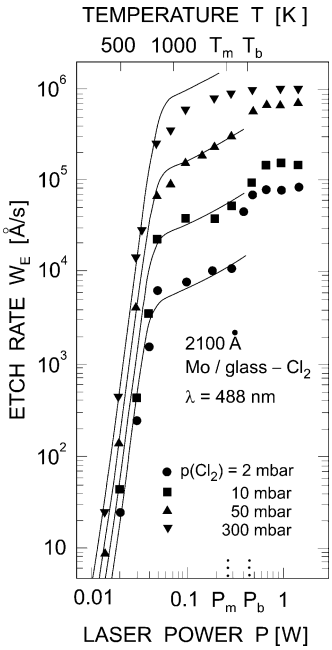

Fig. 14.3.4 Laser-induced etch rate for 2100 Å Mo films on glass as a function of 488 nm Ar^+-laser power ($w_0 \approx 5.7\,\mu$m) and for various Cl_2 pressures. $T_m(P_m)$ and $T_b(P_b)$ indicate the temperatures (laser powers) for melting and boiling of Mo, respectively. The solid curves have been calculated [*Mogyorosi* et al. 1989a]

Arrays of etched holes in W films on a-SiO_2 substrates using a 2D-lattice of a-SiO_2 microspheres and a WF_6 atmosphere have been fabricated by means of Ar^+-laser radiation [*Denk* et al. 2003].

14.4 Dry-Etching of Inorganic Insulators

Laser-induced dry-etching of inorganic insulators has been investigated for fused quartz, for various glasses of complex composition, for different ceramic, poly-, and single-crystalline oxides and nitrides, and for some other materials. The precursor molecules employed are mainly halides and halogen compounds and, with oxides, also H_2. In this section we include some materials which are neither real insulators nor classified as semiconductors.

14.4.1 SiO_2 Glasses

Photochemical dry-etching of fused quartz (a-SiO_2) and of SiO_2-rich glasses has been investigated mainly with hydrogen and various halide radicals. The latter have been produced by both electronic and vibrational excitations of precursor molecules. Spontaneous etching can be ignored.

ArF- and KrF-laser radiation has been used to photodissociate molecules like CF_2Cl_2, CF_2Br_2 and CF_3Br, CF_3I, CF_3NO, and $CO(CF_3)_2$ [*Brannon* 1984; *Loper* and *Tabat* 1984]. Etching was very efficient for CF_2Cl_2 and CF_2Br_2, where etch rates of, typically, 0.2–0.5 Å/pulse have been achieved. With the other compounds, which mainly form CF_3 as photoproduct, etching was either inefficient or else did not take place at all. Apparently, CF_2 radicals interact with SiO_2 more strongly than CF_3 radicals – the reason for this observation remains unexplained. Experiments carried out under similar conditions but with Br_2 and SF_6 did not etch SiO_2 significantly.

Etching of SiO_2 in a Cl_2 atmosphere by visible Ar^+-laser radiation has been investigated by *Chuang* (1982). Because SiO_2 is transparent within the visible spectral region, laser-induced heating of the substrate is of little importance. In fact, the etch rate has been found to be correlated to the concentration of chlorine radicals produced within the gas phase. For 457.9-nm radiation and a chlorine pressure of $p(Cl_2) = 133$ mbar, an etch rate of up to 3 Å/s was achieved. With the 514.5 nm laser line, under otherwise identical conditions, the etch rate was significantly lower. The lateral dimensions of etched features were much larger than the focal-spot size. For example, for $2w_0 \approx 7\,\mu$m the diameter of etched holes was 50–80 μm, depending on laser-beam illumination time. This can be explained by the diffusion of Cl radicals produced within the gas phase.

Large-area etching of SiO_2 activated by *multiphoton* vibrational dissociation (MPD) of CF_3Br and CDF_3 by means of pulsed CO_2-laser radiation has been reported by *Harradine* et al. (1981). Because of the high laser-light intensities, such

experiments can only be performed with parallel laser-beam incidence. The etch rates achieved were around 0.3 Å/pulse.

Projection patterning of SiO_2-rich glasses by transient heating in a H_2 atmosphere has been demonstrated with ArF-laser radiation. Gratings with a resolution of about 0.4 μm have been produced. The etch rates achieved were, typically, of the order of 0.1 μm/pulse, with $\phi \approx 1\,\mathrm{J/cm^2}$ and $p(H_2) \approx 500\,\mathrm{mbar}$ [*Ehrlich* et al. 1985].

14.4.2 Oxides

Laser-induced dry-etching of various oxides and nitrides in ceramic, polycrystalline, and single-crystalline forms has been studied for different ambient media. Among the materials investigated in most detail are oxidic perovskites and ferrites.

Oxidic Perovskites

With short, high-intensity UV-laser pulses whose photon energies exceed the bandgap energy of the perovskite ($h\nu > E_g \approx 3\,\mathrm{eV}$), surface patterning is based on ablation, and the results of such investigations are incorporated in Chap. 12.

Well-defined dry-etching with visible laser light ($h\nu < E_g$) of low-to-moderate intensity requires a reducing atmosphere. Here, laser-induced heating (initiated by an absorbing paint, defects, or by trapped radiation within ceramic samples) results in the formation of oxygen vacancies and quasi-free electrons (Sect. 26.6). With increasing laser power, metallization and, finally, etching occurs. The most detailed investigations have been performed for crystalline $BaTiO_3$ and $SrTiO_3$, and for ceramic $BaTiO_3$ and $PbTi_{1-x}Zr_xO_3$ (PZT) in a H_2 atmosphere [*Eyett* et al. 1986]. The role of H_2 is interpreted by efficient local reduction of the material. This has two consequences:

- The formation of oxygen vacancies, color centers, and quasi-free electrons strongly increases the optical absorption within the laser-heated zone.
- With increasing oxygen-vacancy concentration, a local collapse of the perovskite lattice occurs.

Temperature measurements using visual and photoelectric pyrometry revealed an Arrhenius-type behavior of the average etch rate. For laser-induced temperatures $T_s \leq 1600\,\mathrm{K}$, an apparent activation energy of $\Delta E = 41 \pm 8\,\mathrm{kcal/mol}$ was derived. In connection to this it seems interesting to note that the evaporation enthalpies for pure PbO [*JANAF Thermochemical Tables*] and for PbO in $PbTi_{1-x}Zr_xO_3$ ($x = 0.65$) [*Northrop* 1968] are 56 and 39 kcal/mol, respectively. The evaporation enthalpies for pure TiO_2 and ZrO_2 are 137 and 170 kcal/mol, respectively. Thus, evaporation of PbO seems to be important in the etching process. This conclusion is supported by SEM and electron-beam-induced X-ray fluorescence studies. In a region of about 30−50 μm around groove edges, morphology

changes due to a depletion of Pb, and sometimes even cracks are observed. Beyond this region, the morphology and chemical composition corresponds to that of bulk PZT. The thickness of the damaged zone depends on the incident laser power and the scanning velocity. The etch rates achieved are, typically, between a few μm/s and some hundred μm/s. The results were quite similar for the other perovskites investigated. Note that patterning of PZT by ablation can be achieved without significant material damage (Chap. 12).

Ferrites

The most detailed investigations on (pyrolytic) laser-induced etching of single-crystalline (100) Mn-Zn ferrites ($MnO:ZnO:Fe_2O_3 = 31:17:52$) were performed by *Takai* et al. (1988a). The experiments employed Ar^+-laser radiation and gaseous CCl_4 or CCl_2F_2 as etchant. Crack-free etching with high aspect ratio and rates of up to 68 μm/s was achieved (Fig. 14.4.1).

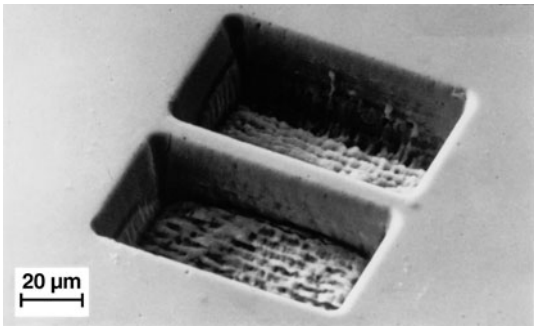

Fig. 14.4.1 Magnetic head structure in $MnO:ZnO:Fe_2O_3$ etched by CCl_4 using a scanned Ar^+-laser beam ($P \approx 0.35$ W, $w_0 \approx 1.3$ μm, $v_s \approx 30$ μm/s, $p(CCl_4) \approx 30$ mbar) [*Takai* et al. 1988a]

Similar experiments have been performed in aqueous solutions of KOH and H_3PO_4. With Fe:Al:Si (Sendust) etch rates up to 400 μm/s, and aspect ratios of 40 have been achieved [*Takai* et al. 1994]. The technique is employed for the fabrication of magnetic head structures for computer, audio, and video recording applications. Single-sided MIG (metal-indium-gap) heads fabricated by LCP show a performance higher than those fabricated by conventional machining.

14.5 Wet-Etching

Laser-enhanced wet-etching has been studied for metals in the form of thin films, foils, and slabs. For transparent materials, in particular dielectrics, both front-side etching and backside etching has been investigated. The microscopic mechanisms involved in liquid-phase *chemical* reactions are described in Chap. 21.

14.5.1 Front-Side Etching

Among the metals studied in most detail are Au, Cu, Fe (including steel), Ni, and Ti. The etchants employed mainly were aqueous solutions of acids like HCl, HNO_3, H_3PO_4, etc., lyes like NaOH and KOH, and neutral salt solutions of NaCl, KBr, $NaNO_3$, K_2SO_4, etc. Most of the experiments were performed by means of Ar^+- and Nd:YAG-laser radiation. In the absence of an external voltage, the etch rates achieved were, typically, between 1 μm/s and more than 10 μm/s. Such rates exceed the corresponding rates for dark etching by many orders of magnitude. Spatial resolutions of better than 2 μm have been demonstrated. With most systems, laser-induced wet etching is thermally activated. Here, an exponential increase in etch rate is followed by a mass-transport-limited regime, which starts around the melting point of the metal [*Nowak* and *Metev* 1996].

Laser-enhanced electrochemical etching (LEE) is achieved by simply reversing the polarity of the cathode and anode in the experiments described for laser-enhanced plating (Sect. 21.2). LEE has been used to produce 50 μm diameter holes in stainless steel using aqueous $NiCl_2$ as an electrolyte and Ar^+-laser radiation [*von Gutfeld* 1984]. Etch rates of up to 10 μm/s have been obtained. Large-area LEE of metal oxides has been demonstrated by *Yavas* et al. (1996).

Dielectrics

Laser-enhanced etching of photosensitive glass ceramics (Foturan) in aqueous HF has been studied by means of ns $Nd:YVO_4$ laser radiation at $\lambda = 266$ nm and $\lambda = 355$ nm [*Livingston* et al. 2008]. Etch rate ratios of more than a factor of 30 have been achieved.

Laser-assisted machining of pyrex glass in water is described in [*Chung* et al. 2009].

14.5.2 Backside Etching

Laser-induced backside processing of transparent materials in an ambient medium was described by *Bäuerle* 1996. The irradiation geometry is shown in Fig. 9.5.1b. The laser light penetrates the transparent workpiece to be processed and excites the adjacent medium which should be strongly absorbing. Estimations on laser-induced temperature distributions and the effects of convection and temperature jumps, are discussed in previous chapters. With fs-pulses, however, backside processing does *not* require a linearly absorbing medium, as discussed in Sects. 9.5 and 13.6.

Most of the experiments on so-called *l*aser-*i*nduced *b*ackside *w*et *e*tching (LIBWE) do *not* employ an etchant. Thus, as already mentioned in the introduction to this chapter, the term etching is misleading, but well established in the literature. In the experiments under consideration, material removal is based on both rapid local heating, softening, melting or even boiling of the material via the absorbing liquid that is in contact to the workpiece and, depending on the fluence, on

microcavitation effects (Sect. 30.5). First experiments of this type have been performed by *Wang* et al. (1999). In these studies, well-defined micropatterning of a quartz plate in contact with a solution of pyrene dissolved in acetone has been demonstrated. By using KrF-laser-light projection, gratings with sharp edges and smooth surfaces have been fabricated without any indication of cracks. The etch rate increases with increasing absorption of the solution, i.e., the concentration of pyrene. With 0.4 mol/dm^3 solutions and $\phi \approx 1.3\,\mathrm{J/cm^2}$, etch rates of about 25 nm/pulse have been achieved. In this regime, the surface roughness is, typically, 10–30 nm.

Backside material removal has meanwhile been demonstrated for various different substrates and liquids. Among the structures fabricated are deep microholes (Fig. 14.5.1a) and trenches [*Kawaguchi* et al. 2007], gratings [*Vass* et al. 2007] in a-SiO_2, microlenses in a-SiO_2 and BaF_2 (Fig. 14.5.1b) [*Kopitkovas* et al. 2007], different types of patterns in Al_2O_3 , CaF_2 and MgF_2 [*Böhme* et al. 2002], microfluidic channels, etc. Backside etching using solid and molten metal as absorbers has been described by *Hopp* et al. (2009).

Investigations on the physical and chemical processes involved in LIBWE have been performed by a number of different groups. For *low* laser fluences the organic solution is thermally decomposed and generates an adherent carbon film on the substrate surface. The film thickness, and thereby the absorption of the laser light increases with the number of laser pulses. The enhanced absorption results in an enhanced temperature rise at the rear-side surface. After a certain number of 'incubation' pulses, typically 10^2–10^3, depending on the laser fluence, defect formation and depletion of single components of the material, e.g. the loss of oxygen in a-SiO_2, takes place. This enhances absorption and results in softening/melting, and material removal [*Kopitkovas* et al. 2008]. For intermediate to higher laser fluences material removal takes place after a single or a few laser pulses. In this regime, carbon depo-

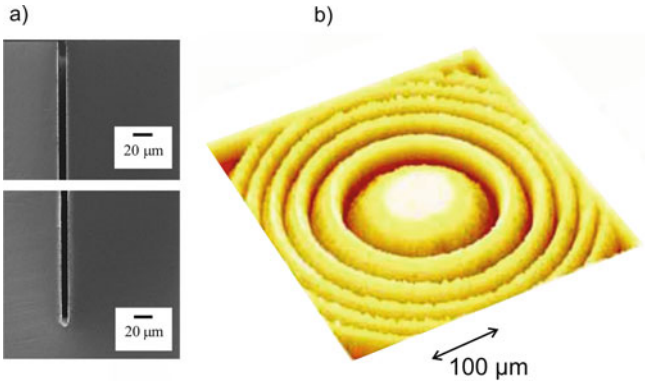

Fig. 14.5.1 Laser-induced backside wet-etching (**a**) 986 µm deep and 9.7 µm wide hole in a-SiO_2 using KrF-laser radiation and a saturated solution of pyrene in acetone [*Kawaguchi* et al. 2007] (**b**) Fresnel lens fabricated in BaF_2 by means of XeCl-laser radiation using 1.4 M pyrene in tetrahydrofuran [*Kopitkovas* et al. 2007]

sition and heating/melting/boiling of the substrate via the superheated liquid takes place. The formation/collapse of microbubbles and transient shock waves result in rapid material removal [*Niino* et al. 2007]. This is discussed in further detail in Sect. 30.5.

Liquid-assisted femtosecond laser patterning by rear-side material illumination was demonstrated by *Hwang* et al. (2009c, 2004). By this means, well-defined 3D-microchannels in glass substrates have been fabricated. The process is probably based on multiphoton- and avalanche ionization, optical breakdown, the formation of a plasma, shock waves, and the generation of micro-/nanobubbles at the liquid–solid interface (Sects. 13.6 and 30.5). This interpretation of the ablation mechanism is supported by experiments using pyrene solutions, as discussed above. While the processing rates achieved with ns-pulses strongly depend on pyrene concentration, they are independent of it for sub-ps-laser pulses [*Böhme* et al. 2007].

Chapter 15
Etching of Semiconductors

This chapter deals with laser-induced etching of element and compound semiconductors. The most detailed investigations on dry-etching have been performed for Si, GaAs, and InP. The precursor molecules mainly employed include halides and halogen compounds such as Cl_2, HCl, XeF_2, NF_3, CCl_4, CF_3Br, CF_3I, and SF_6. Laser-induced wet-etching has been studied mainly for compound semiconductors in aqueous solutions of H_2SO_4/H_2O_2, HNO_3, and KOH.

In *photothermal* dry-etching the rates typically achieved are between 0.01 μm/s and several μm/s, and about ten times higher in wet-etching.

Photochemical etching is based on the interaction between radicals and carriers within the semiconductor surface. Radicals can be formed spontaneously by molecule–surface interactions (Si–XeF_2 system), by selective electronic excitation (Si–Cl_2 system), or by vibrational excitation (Si–SF_6 system) of the etchant. The carriers can be incorporated into the semiconductor by doping or they can only be generated by photo-excitation. Thus, photochemical etch rates depend on the concentration of active species within the ambient medium, including the adsorbate, on the optical penetration depth of the laser light in the semiconductor surface, carrier lifetimes, recombination processes, surface band bending, and the concentration of impurities. The etch rates are typically between several Å/s and some 0.1 μm/s.

15.1 Dark Etching

Before discussing the mechanisms involved in light-enhanced etching of silicon in a halogen atmosphere, it is useful to first consider some basic interactions between halogen radicals, X ≡ F, Cl, Br, . . . , and silicon in the dark.

Chlorine molecules become dissociatively chemisorbed on clean Si surfaces. This process is mediated by charge (electron) transfer from silicon to physisorbed chlorine molecules (Fig. 15.1.1a). Clearly, the number of electrons and holes increases with temperature. Charge transfer results in the formation of a passivating $SiCl_x$ layer which suppresses any further reaction. This process is similar to the initial phase of surface oxidation.

The situation is different with fluorine, which can etch Si *spontaneously*. The main differences to chlorine result from the higher electronegativity and the smaller

D. Bäuerle, *Laser Processing and Chemistry,* 4th ed.,
DOI 10.1007/978-3-642-17613-5_15, © Springer-Verlag Berlin Heidelberg 2011

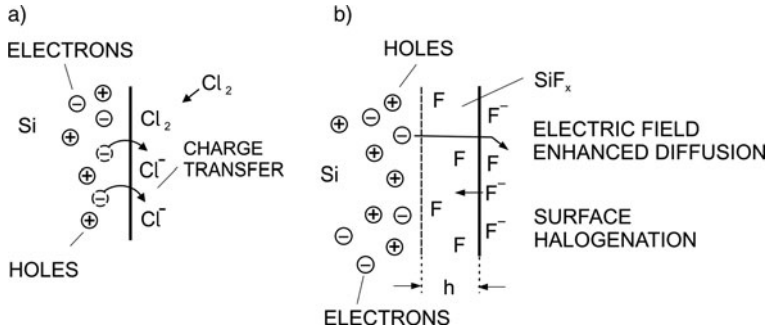

Fig. 15.1.1a, b Schematic showing charge (electron) transfer and the generation of a surface electric field for Si in halogen atmosphere. (**a**) Chlorine molecules dissociatively chemisorb on clean Si surfaces. This process is mediated by electron transfer. (**b**) Fluorine chemisorbs on Si and diffuses into the surface. Diffusion is enhanced by the surface electric field

radius of fluorine [atomic radius $r_a(F) \approx 0.64$ Å; (Pauling) ionic radius $r_i(F^-) \approx 1.36$ Å], compared to chlorine [$r_a(Cl) \approx 0.97$ Å; $r_i(Cl^-) \approx 1.81$ Å]. As a consequence, fluorine not only chemisorbs on Si but diffuses into the surface and forms a thick fluorosilyl layer (Fig. 15.1.1b). This becomes plausible from the inter-atomic distances for silicon (100), (110) and (111) surfaces. The Si radius in tetrahedral coordination is 1.17 Å. Thus, one finds, together with the lattice constants, that the radius of the 'hole' between Si atoms is about 1.54 Å for (100), 1.36 Å for (110) and 1.04 Å for (111) surfaces. It has in fact been confirmed by both model calculations [*Seel* and *Bagus* 1983] and experiments [*McFeely* et al. 1986; *Winters* and *Plumb* 1991] that fluorine can penetrate into all of the different Si surfaces. The fluorosilyl layer has a thickness of, typically, 10–30 Å and is dominated by SiF_3 groups. Spontaneous etching occurs from this fluorosilyl layer by desorption of SiF_x. The main volatile product at 300 K is SiF_4. Si_2F_6 and Si_3F_8 are observed to a minor extent as well. Heating of Si to temperatures up to about 600 K does not change the distribution of reaction products, but only increases the overall reaction rate. The situation changes at higher temperatures. For example, thermal desorption studies of fluorinated Si have shown that at 800 K the primary etch product is SiF_2. The distribution of reaction products depends also on the orientation of the Si surface.

The main aspects of surface fluorination can be qualitatively understood along the lines of the Cabrera–Mott mechanism (Chap. 26). Consider the schematic shown in Fig. 15.1.1b. With stationary conditions, the thickness of the fluorosilyl layer remains constant. Thus, for compensation of desorbed SiF_x, transport of Si to the surface, or of F to the SiF_x-Si interface, is required. Because of the difference in radius, diffusion of fluorine through the SiF_x layer is expected to be dominant. The picture is similar to that of Fig. 26.3.1. The main difference to surface oxidation is that many saturated halides are volatile, while most oxides are not.

To achieve further insight, we consider the simple band model in Fig. 15.1.2. It schematically shows the highest valence band and the lowest conduction band of

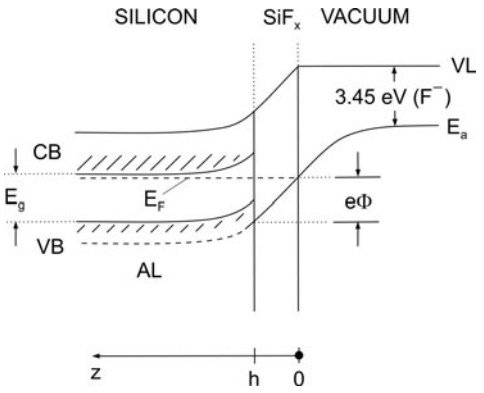

Fig. 15.1.2 Schematic band model which describes the influence of an electric field caused by chemisorbed F^- ions on a silicon surface. CB stands for conduction band, VB for valence band, AL for affinity level, and VL for vacuum level [adapted from *Winters* and *Haarer* 1987]

Si, the SiF_x layer, and the vacuum level. At infinite distance, the affinity level of fluorine atoms is about 3.45 eV below the vacuum level. As fluorine approaches the surface, this value increases, mainly because of the image-charge attraction from the (bulk) Si and the SiF_x layer. There are indications that the affinity level for fluorine is situated below the valence band of Si. When fluorine atoms become adsorbed, electrons will be transferred to them as long as the affinity level at the surface $z = 0$ is below the Fermi level. The electric field generated by F^- ions on the surface of the SiF_x layer and the (positive) space charge within the Si near the interface (Fig. 15.1.1b), causes the bands to bend upward. The degree of band bending is a measure of the field strength. The surface concentration of F^- ions and the field strength are determined by the energy difference between the Fermi level, E_F, and the affinity level, E_a, at the Si–SiF_x interface. This difference is denoted by $(E_F - E_a)_{z=h} = e\Phi$. The equilibrium (number) density of F^- ions at the surface is, according to Gauss's law

$$N_{F^-} = \varepsilon_{SiF_x} \frac{\Phi}{eh} , \tag{15.1.1}$$

where ε_{SiF_x} is the dielectric constant of the SiF_x layer. h is the thickness of the SiF_x layer, which is assumed to be an insulator. The space charge accumulated within the bulk Si near the Si–SiF_x interface must be equal (but of opposite sign) to the charge of F^- ions at the SiF_x surface (note that for a capacitor $C = \varepsilon F/h = Q/\Phi$ and $Q/F = eN_{F^-}$). This, together with (15.1.1), determines the potential difference, Φ, and the number density, N_{F^-}, for a given SiF_x-layer thickness. From qualitative arguments one finds that N_{F^-} increases with dopant concentration only with heavily doped (degenerate) n-type Si, and remains almost unaffected otherwise. With increasing layer thickness, h, the density, N_{F^-}, decreases. Dark etching of doped (111) Si in a XeF_2 atmosphere is consistent with this model; the measured etch rates are directly correlated with the surface concentration of fluorine ions, N_{F^-}. In

a quantitative treatment of the problem, N_{F^-}, Φ, and h must be determined self-consistently from (15.1.1), the Poisson–Boltzmann equation, and a kinetic equation of the type (28.3.4) for $h = h(N_{F^-}, \Phi)$. The problem is, however, that the detailed surface chemistry and the corresponding kinetic coefficients are unknown.

15.2 Laser-Induced Etching of Si in Cl_2

The most detailed investigations on laser-induced dry-etching of element semiconductors have been performed for Si. Only a few papers have been published on Ge.

15.2.1 Surface Patterning

High-resolution etching of Si in a Cl_2 atmosphere has been demonstrated mainly by direct writing. Here, feature sizes of well below 100 nm have been achieved [*Müllenborn* et al. 1995]. The chlorine-gas pressures employed range from about 1 mbar to several hundred mbar.

Figure 15.2.1a shows a SEM of deep grooves obtained by Ar^+-laser direct writing. Here, the laser-beam intensity was adjusted in such a way that melting occurred only in the center of the laser-induced temperature profile. The increase in resolution with respect to the diffraction-limited diameter of the laser beam is based on the much higher reactivity of liquid Si with respect to crystalline Si (Sect. 5.3.6; Fig. 15.2.2).

Figure 15.2.1b shows another example of three-dimensional patterning. Here, the laser beam was swept in a circular scan. The technique permits computer-aided design (CAD) or manufacturing (CAM) of silicon-based micro-electromechanical devices.

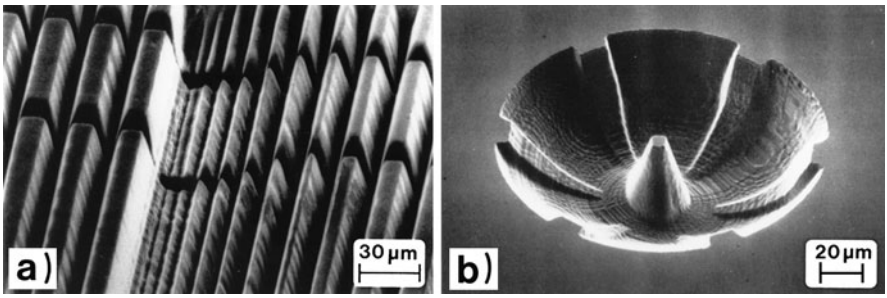

Fig. 15.2.1a, b SEM pictures of patterns fabricated in c-Si by 488 nm Ar^+-laser direct writing in a Cl_2 atmosphere. (**a**) Trenches ($P = 3$ W, $v_s = 1$ mm/s, 10 scans per line; $p(Cl_2) = 140$ mbar) [*Müllenborn* et al. 1995]. (**b**) Hollow with cone. The microscope objective was lowered in 1 µm increments after each plane was scanned at $v_s = 7.5$ mm/s ($2w_0 \approx 1$ µm, $p(Cl_2) = 133$ mbar) [*Ehrlich* 1993]

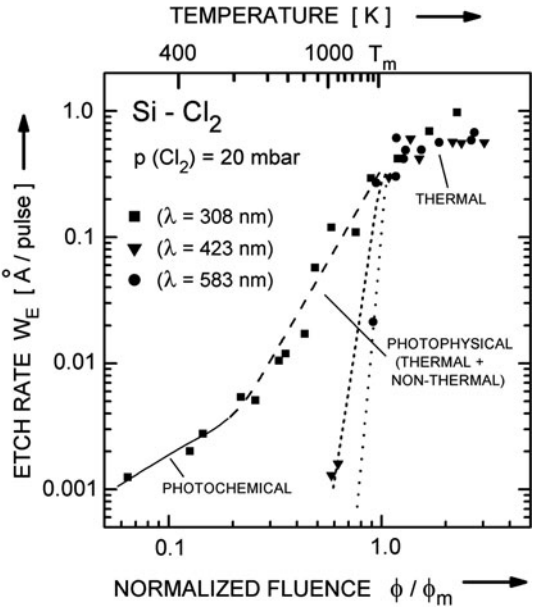

Fig. 15.2.2 Etch rate of (100)Si (slightly p-doped with $\approx 10^{14}$B atoms/cm^3, $\varrho = 100$ to 150 Ωcm) as a function of (normalized) laser fluence, and for three different wavelengths (the 423 nm and 583 nm lines were obtained from a XeCl-laser-pumped dye laser) [*Kullmer* and *Bäuerle* 1987]

Nanopatterning by means of a SNOM-type setup has been demonstrated by *Wysocki* et al. (2004). This is discussed in Sect. 15.2.6.

Laser-induced dry-etching permits the micropatterning of planar and non-planar substrates and 3D-micromachining. Real and potential applications include the following:

- Deep and surface patterning of Si, including thin films and membranes [*Müllenborn* et al. 1996a].
- Rapid prototyping.
- Fabrication of micromechanical devices such as tweezers, knives, positioning tools, etc. [*Larsen* et al. 1997].
- Micro-electromechanical systems (MEMS) for applications as sensors and biochemical devices.
- Free-standing tunnels and micro-structures in SiO_2-covered Si for applications as microfluidic devices or as parts of MEMS [*Allard* et al. 1997].
- Optical devices such as microlenses, gratings, etc. [*Müllenborn* et al. 1996a].
- THz waveguide components and feedhorns [*Lubecke* et al. 1998].

15.2.2 Photochemical and Thermal Etching

Silicon is quite inert to a Cl_2 atmosphere at 300 K. Etching is observed only at higher temperatures, or in the presence of light.

Laser-induced etching of Si in a Cl_2 atmosphere has been investigated by various groups. For *low* light intensities the molecule–surface interactions can be qualitatively explained on the basis of Figs. 15.1.1 and 15.1.2. The exact position of the chlorine affinity level is unknown – it is probably situated near the valence-band edge. At higher laser-light intensities, thermal activation of the etching reaction is expected.

Figure 15.2.2 shows the etch rate achieved with pulsed irradiation at three different wavelengths and constant Cl_2 pressure. The fluences $\phi(\lambda)$ were normalized to the fluences $\phi_m(\lambda)$ required for surface melting, $\phi^* = \phi/\phi_m$. The results obtained with 308 nm XeCl-laser radiation show three characteristic regimes:

- For low laser fluences which cause negligible surface heating ($\phi^*(308\,\text{nm}) < 0.2$), the etch rate increases linearly with ϕ^* (solid line). Within this regime, etching is purely *photochemical* and based on both chlorine radicals produced within the gas phase and electron–hole pairs generated within the Si surface.
- At medium energy densities, i.e., $0.2\,(\approx 150\,\text{mJ/cm}^2) < \phi^*(308\,\text{nm}) < 1\,(\approx 440\,\text{mJ/cm}^2)$, the etch rate increases non-linearly with laser fluence. In this regime, thermal processes become important, but photogenerated Cl radicals are still required.
- At laser fluences that cause surface melting, i.e., with $\phi^* > 1$, the etch rate levels off. Such behavior can be caused by the latent heat of melting, the step-like increase in reflectivity at the melting point, or mass transport limitations. With the Cl_2 pressures employed in this experiment, the latter mechanism should be irrelevant. This could be proved by studying the dependence of the etch rate on the diameter of the laser focus. In any case, within this regime, etching is mainly *thermally* activated.

Figure 15.2.2 shows that for $\phi^* > 1$ the etch rate depends only slightly on laser wavelength, while for $\phi^* < 1$ a strong decrease with increasing wavelength is observed. This wavelength dependence suggests that without surface melting, etching of Si requires the presence of Cl radicals, which are only generated at wavelengths $\lambda \leq 500\,\text{nm}$ (Sect. 14.1). Photocarriers, on the other hand, are generated with all of the wavelengths investigated, and their role cannot be revealed from these experiments because any changes in laser power or wavelength cause simultaneous changes in both the chlorine-atom concentration within the gas phase *and* the concentration of photoelectrons within the Si surface.

To separate the influence of chlorine radicals and electron–hole pairs, one can use a *combined* irradiation scheme, as shown in Fig. 30.1.1a. Such experiments have been performed for the Si–Cl_2 system by using 308 nm XeCl excimer-laser radiation at parallel incidence to the Si surface and 647.1 nm cw-Kr^+-laser radiation at perpendicular incidence. By this means, the concentrations of Cl radicals within the gas phase and electron–hole pairs within the Si surface can be controlled *independently* via the XeCl-laser fluence, ϕ, and the Kr^+-laser power, P, respectively. In brief, the main observation is as follows: significant etching of (p-doped) Si with or without negligible surface heating is observed only if both lasers are switched

on. Thus, etching of p-type Si at laser powers that cause negligible surface heating requires both chlorine radicals *and* electrons.

15.2.3 Chlorine Radicals

The data points in Fig. 15.2.3a represent the etch rate measured as a function of XeCl-laser fluence. Both the chlorine-gas pressure, and the Kr^+-laser power, were kept constant. The measured etch rate can be compared with the reaction flux of chlorine atoms onto the Si surface

$$J_{Cl}(r, z_s) = kN_{Cl}(r, z_s) \approx \frac{1}{4}\eta_{Si}(r)\,\langle v_{Cl}\rangle\, N_{Cl}(r, z_s)\ . \qquad (15.2.1)$$

The etch probability, $\eta_{Si}(r)$, includes the sticking probability of Cl radicals, the conversion of Si to $SiCl_x$, and the desorption of $SiCl_x$ from the surface. Within the area of the (Gaussian) Kr^+-laser spot, it can be described by $\eta_{Si}(r) = \eta_{Si}(0)\exp(-r^2/l_c^2)$, where l_c is of the order of the free-carrier diffusion length. $\langle v_{Cl}\rangle$ is the average Cl-atom velocity.

The concentration of Cl atoms on the Si surface can be calculated as outlined in Sect. 14.2 (z_s is the distance of the Si surface from the center of the XeCl-laser beam; Fig. 30.1.1a). With $N_{Cl}(0, z_s)$ calculated for the reaction chamber employed in the experiments, and parameters $\eta'_{Si} = 0$ and $\eta_w = 0.01$ (η'_{Si} refers to non-irradiated Si

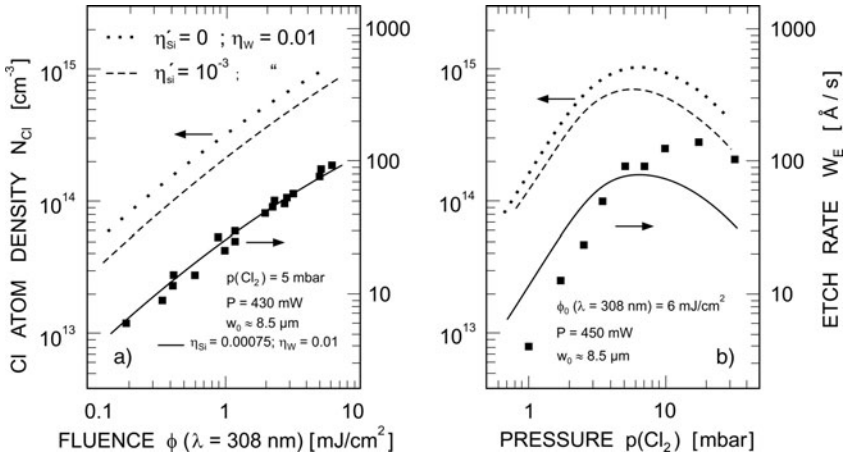

Fig. 15.2.3a, b Data points show the measured etch rate, W_E (*right-hand scale*), at constant Kr^+-laser power ($\lambda = 647$ nm; $P = 430$ mW; $w_0 \approx 8.5\,\mu$m). The pulse-repetition rate of the XeCl laser was 100 Hz. The calculated chlorine-atom density, N_{Cl}, on the Si surface within the center of the Kr^+-laser beam (*dotted* and *dashed curves*) are shown (*left-hand scale*). The etch rates calculated with $\eta'_{Si} = 0$, $\eta_w = 0.01$ and $\eta_{Si}(r = 0) \equiv \eta_{Si} = 0.0075$ are also shown (*solid curves*). $SiCl_2$ was assumed to be the main reaction product. (**a**) Dependence on XeCl-laser fluence. (**b**) Dependence on chlorine pressure [*Kullmer* and *Bäuerle* 1988a]

and η_w to the walls of the reaction chamber; Sect. 14.2.3), the measured etch rate, $W_E(0)$, can be fitted with $\eta_{Si}(0) = 0.0075$ (this value is in good agreement with that reported by *Mogyorosi* et al. (1988); note that $W_E(0) = Zm_{Si}J_{Cl}(0)/\varrho_{Si}$, where $Z = 1$, $1/2$ and $1/4$ with reaction products SiCl, $SiCl_2$, and $SiCl_4$, respectively). With pulsed UV- and VIS-laser radiation the main desorption products are SiCl and $SiCl_2$ [*Aliouchouche* et al. 1993; *Paulsen-Boaz* et al. 1992]. The result of the fit, which assumes $SiCl_2$ as the reaction product, is shown in Fig. 15.2.3a by the solid curve. The figure demonstrates that the observed dependence $W \propto \phi^{0.79}$ agrees very well with the calculated reaction flux of chlorine atoms. With the parameters employed, the reaction is *kinetically* controlled ($D_{Cl}/\eta_{Si}\langle v_{Cl}\rangle w_0 \gg 1$; Chap. 3). The data can also be compared with chemiluminescence measurements (Fig. 30.1.1b), from which we find $N_{Cl}(0,0) \propto \phi^{0.73}$. The consistency of results shows that the etch rate depends linearly on chlorine-atom concentration

$$W_E \propto N_{Cl} \,. \tag{15.2.2}$$

The dependence of the etch rate on chlorine-gas pressure (Fig. 15.2.3b) can be described by

$$W_E \propto p^{\gamma}(Cl_2) \,, \tag{15.2.3}$$

where $\gamma \approx 2$ with pressures ≤ 3 mbar. The quadratic dependence of the etch rate on Cl_2 pressure can qualitatively be described by the solid curve, which was calculated by using $\eta'_{Si} = 0$ and $\eta_{Si} = 0.0075$, as in Fig. 15.2.3a. The discrepancies may originate from XeCl-laser-induced gas-phase heating which is most pronounced in the regime of high Cl_2-gas pressures, additional mass transport by convection, other reaction products, in particular SiCl, etc. Such effects could explain the higher etch rates observed in the high-pressure regime.

15.2.4 Electron–Hole Pairs

Figure 15.2.4 shows the etch rate versus Kr^+-laser power for two different sizes of the laser focus and two chlorine-atom concentrations. The change in N_{Cl} was achieved by changing the distance between the excimer-laser beam and the silicon substrate (Fig. 30.1.1a). The solid lines have equal slopes with $W_E \propto P^{0.7}$. The dashed curves are guides for the eye. The etch rate increases with Kr^+-laser power, and thus with the concentration of electron–hole pairs within the Si surface. This observation can be described in (15.2.1) via the etch probability, $\eta_{Si}(r)$. The simplest ansatz is

$$\eta_{Si}(r) \propto N_e(r, P) \propto P^{\beta}(\lambda = 647\,\text{nm}) \,. \tag{15.2.4}$$

The concentration of photoelectrons, N_e, calculated from (2.4.1) is shown in Fig. 15.2.5 for different laser wavelengths. The parameters employed refer to

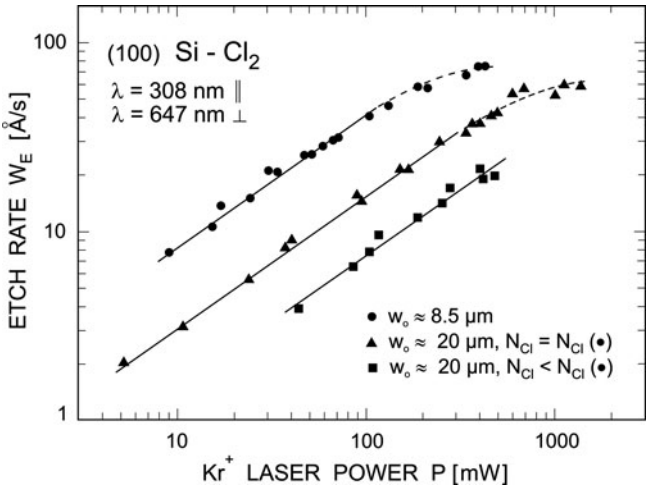

Fig. 15.2.4 Etch rate W_E versus Kr^+-laser power, P, for two different laser-spot sizes $w_0(1/e)$. The Cl atoms were generated by a XeCl-laser at parallel incidence to the Si substrate. The parameters employed were $p(Cl_2) = 5$ mbar and $\phi(308\,\text{nm}) = 4\,\text{mJ/cm}^2$. *Solid lines* are fitted with equal slopes of 0.70 [*Kullmer* and *Bäuerle* 1988a]

undoped c-Si with $D_e = 18.2\ \text{cm}^2/\text{s}$. Any surface recombination of electron–hole pairs or depletion of electrons at the surface due to surface reactions were ignored. With the wavelengths considered, N_e increases almost linearly up to $P \approx 300\,\text{mW}$ $[I(r = 0) \approx 10^5\ \text{W/cm}^2]$. Only for $N_e > 5 \times 10^{18}\ \text{cm}^{-3}$ does Auger recombination become effective and decrease the slope of the curves.

From Fig. 15.2.5 and the ansatz (15.2.4) one would expect $\beta = 1$ and thus $\eta_{Si}(r) \propto P$ as long as $P < 300\,\text{mW}$. This is in contrast to the measured power dependence of the etch rate, $W_E \propto \eta_{Si}(r) \propto P^{0.7}$. This discrepancy can be explained by surface effects which diminish the photoelectron concentration:

- Structural damages and, possibly, surface chlorination near the etched hole cause recombination and/or trapping centers for electrons.
- Chemisorbed Cl^- ions produce a space charge layer at the silicon surface and thereby influence the carrier concentration within it, see Fig. 15.1.1a and *Morrison* (1977).

The bending indicated by the dashed lines in the upper two curves of Fig. 15.2.4 is unexplained. From the model calculations on N_{Cl}, we expect mass-transport limitations to become effective only with etch rates that are one order of magnitude higher than those observed in Fig. 15.2.4. In principle, such a bending could indicate the onset of Auger recombination.

The calculated diameters of the photoelectron distribution, FWHM(N_e), and the measured diameters of holes, $2w$, defined by the hole depth at FWHM, are in good agreement and significantly larger than the spot size of the Kr^+-laser beam [see *Kullmer* and *Bäuerle* (1988a)]. This loss in resolution produced by the diffusion of

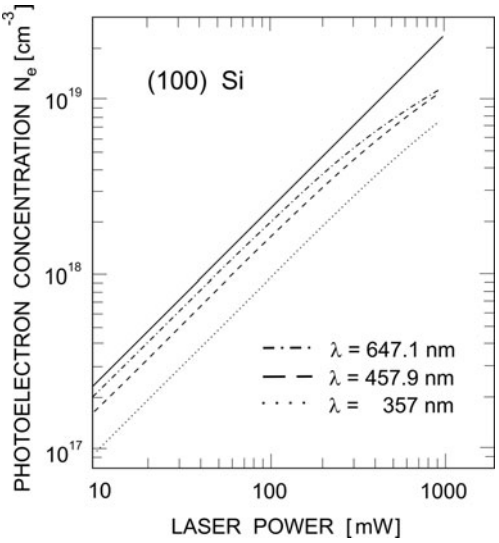

Fig. 15.2.5 Concentration of photo-electrons generated within a (100) Si surface as a function of laser power for different cw-laser wavelengths and $w_0 \approx 10.6\,\mu m$. The solid line has been calculated for 514.5 nm radiation assuming $\alpha \rightarrow \infty$ and no Auger recombination [*Mogyorosi* et al. 1988]

both photogenerated carriers within the Si surface and Cl atoms within the gas is a problem frequently encountered in photolytic processing (Sect. 5.3).

Calculations on the photochemical etching of Si in Cl_2 atmosphere have been performed by *Sytov* (1992, 1995).

15.2.5 Crystal Orientation and Doping

The etch rate of single-crystalline Si depends on crystal orientation. With low laser powers, corresponding to temperatures well below the melting point, the etch rate for (100) surfaces exceeds that for (111) surfaces by at least two orders of magnitude. The crystallographic orientation influences the etch rate via specific properties such as the degree of band bending, Fermi-level pinning, the geometrical arrangement of atoms, etc. The latter will strongly determine the diffusion of halogen ions into the Si surface (Sect. 15.1).

Because of the important role of electrons, photochemical etch rates in n-type Si exceed those in p-type Si. Clearly, the effect of doping can be observed only if the number of photoelectrons is small or comparable to the number of electrons originating from the dopant.

In heavily doped (degenerate) n-type Si, also denoted as n^+-type Si, the etch rate becomes almost independent of the irradiation geometry and spontaneous etching by chlorine radicals is observed [*Horiike* et al. 1987].

15.2.6 Nanopatterning

Laser-induced etching of Si in Cl_2 by means of a SNOM-type setup has been demonstrated by *Wysocki* et al. (2004). Figure 15.2.6 summarizes the results. Within the purely photochemical regime (Fig. 15.2.6a), the microscopic processes involved in the reaction are linear and the width of the etched hole corresponds, approximately, to the diameter of the tip of the glass fiber employed in the setup. Within the photophysical regime (Fig. 15.2.6b) nonlinearities in the interaction processes significantly increase the spatial confinement. This can be easily understood. For thermally activated processes, the reaction rate depends exponentially on temperature as described by Eq. (3.1.1). From the heat equation, we obtain for the case of a Gaussian beam and surface absorption, the *linearized* center temperature [Eq. (7.1.4)]

$$\theta_c \equiv \theta_c^G\,(\alpha^* \to \infty) = \sqrt{\pi}\, I_a w_o\,/(2\,\kappa) = P\,(1-R)/(2\,\sqrt{\pi}\,\kappa\, w_o) \qquad (15.2.5)$$

For non-metals, the temperature dependence of the heat conductivity can be described by Eq. (7.3.1), i.e. by $\kappa(T) \approx \kappa(T(\infty))/T^{*m}$ where $T^* = T/T(\infty)$. For Si, the exponent is $m \approx 1.22$. With the approximation $m = 1$, the Kirchhoff transform yields the analytical expression $T(\theta) \approx T(\infty)\,\exp\{\theta/T(\infty)\}$. Thus, we find for the rate W a *double* exponential dependence on laser beam intensity. This explains the strong confinement observed in Fig. 15.2.6b.

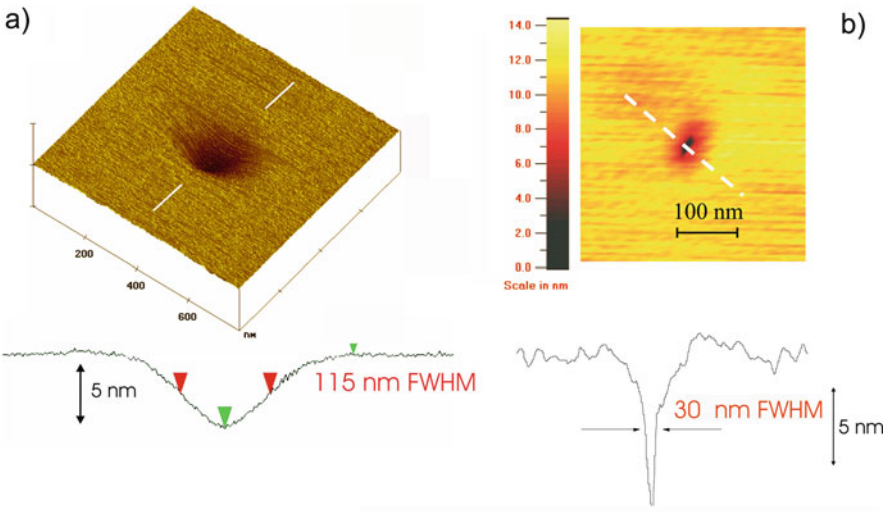

Fig. 15.2.6 AFM pictures and cross-sectional views of holes in (001) Si etched in Cl_2 atmosphere by using a tapered fiber tip (*left*: $\lambda = 351\,\text{nm}$, $P_{\text{tip}} \approx 10\,\mu\text{W}$, $\tau_\ell = 5\,\text{s}$, *right*: $\lambda = 514.5\,\text{nm}$, $P_{\text{tip}} \approx 2.5\,\text{mW}$, $\tau_\ell = 10\,\text{s}$) [*Wysocki* et al. 2004]

15.3 Si in Halogen Compounds

Light-enhanced etching of Si in XeF_2, NF_3, and SF_6 atmospheres has been investigated mainly by means of Ar^+- and CO_2-laser radiation.

15.3.1 Si in XeF_2

XeF_2 etches Si spontaneously (Sect. 15.1). Neither Ar^+- nor CO_2-laser radiation can excite gaseous XeF_2 in a single-photon process.

Band-gap excitation of Si with Ar^+-laser-light intensities $< 20\,W/cm^2$ changes the population of product species desorbing from the surface, but has almost no influence on the etch rate. For higher intensities, $W_E \propto I^n$, where $1 \leq n \leq 2$. The etch rate observed with low laser powers is somewhat higher with n-type Si than with p-type Si.

Qualitatively, the enhancement in W_E can be understood, at least in part, from the preceding outline. Band-gap excitation increases the potential difference, Φ, in (15.1.1). Additionally, laser-enhanced desorption of the etch products, SiF_x, decreases the thickness of the fluorosilyl layer below its equilibrium value. Both effects will increase the ratio Φ/h and thus W_E.

Figure 15.3.1 shows the (normalized) desorption fluxes $J(SiF_3)$ and $J(SiF_4)$ as a function of Ar^+-laser power. The figure suggests that only SiF_3 is a photoproduct. The selective nature of the etching reaction has been explained by F^- ions that preferentially break those Si bonds to which the desorbing SiF_3 group is bound. Such a process can be described, symbolically, by *Houle* (1989)

$$-Si^+-SiF_3 + F^- \rightarrow Si-F + SiF_3(\uparrow)\,. \tag{15.3.1}$$

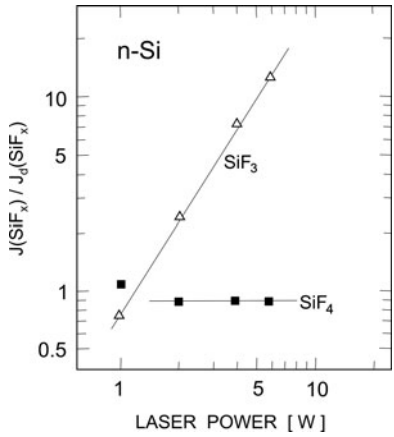

Fig. 15.3.1 514.5 nm Ar^+-laser-induced desorption fluxes of SiF_3 and SiF_4 normalized to the respective dark fluxes [*Houle* 1989]

For pulsed irradiation, the interaction mechanisms seem to be different from those involved in low-power cw-Ar^+-laser-enhanced etching. For example, irradiation with 532 nm frequency-doubled Nd:YAG-laser pulses results in the desorption of SiF_x ($x \leq 3$) fragments and Si atoms [*Chuang* et al. 1984]. The yield for less F-coordinated species and Si atoms was found to increase with increasing light intensity. Similarly, with sub-bandgap irradiation using pulsed CO_2 lasers, the dominant species were also SiF_x with $x \leq 3$. It was speculated that transient thermal electrons generated by single- or multiphoton processes create transient electric fields within the Si surface and thereby enhance the etch rate. However, with the fluences employed, the process may be entirely thermal in nature, as discussed already with the Si–Cl_2 system. The estimated laser-induced temperatures are high enough to expect changes in the type of species desorbed from the surface (see also Sect. 15.1).

Ar^+-laser-enhanced etching of Si in a CF_4/O_2 plasma has been investigated by *Holber* et al. (1985).

15.3.2 Si in SF_6

A model system in which vibrational excitation has been demonstrated to enhance the molecule–surface reactivity is the etching of Si in a SF_6 atmosphere (Sects. 2.3 and 14.1).

Silicon is almost inert against ground-state SF_6 at 300 K. However, pulsed-CO_2-laser excitation of SF_6 induces high etch rates, particularly at normal incidence. The major volatile reaction products observed are SiF_4 and SF_4. It has been suggested that gaseous or physisorbed SF_6 molecules are excited into higher vibrational states via coherent multiphoton excitation according to (14.1.8). In contrast to ground-state SF_6, vibrationally excited SF_6^* can dissociatively chemisorb on Si surfaces:

$$SF_6^* \rightarrow 2F^- + SF_4(\uparrow) \; . \tag{15.3.2}$$

Part of the chemisorbed F^- ions penetrate into the Si and form a fluorosilyl layer (Sect. 15.1). Via a number of subsequent surface processes, SiF_4 is formed and desorbs from the surface.

The importance of selective non-dissociative multiphoton vibrational excitation of SF_6 in the low intensity range has been derived from a number of observations: the etch rate shows a pronounced wavelength dependence, with a maximum that is much broader and lower in frequency than the single-photon absorption spectrum of the ν_3 mode of SF_6 at 948 cm^{-1} (Fig. 15.3.2a). The dependence of the etch rate on laser fluence can be described by $W_E \propto \phi^{3.5}$ (Fig. 15.3.2b). This may indicate that the overall rate-limiting step is based on selective three- or four-photon excitations. The reaction yield increases monotonically with SF_6-gas pressure and saturates at about 2 mbar. However, in the intensity range considered, substantial substrate heating and, with the pressures employed, (non-selective) gas-phase heating is expected. In fact, gas-phase heating can also cause a broadening of the absorption spectrum

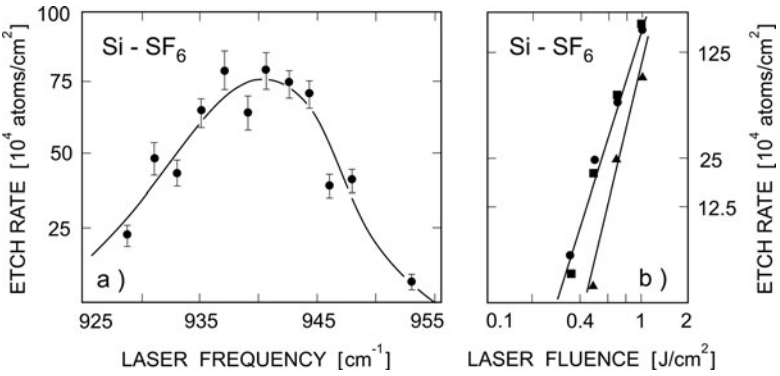

Fig. 15.3.2a, b Etch rate for Si in SF_6 achieved with CO_2-laser radiation at perpendicular incidence. (**a**) Frequency dependence ($\phi = 0.9\,\mathrm{J/cm^2}$, $p(SF_6) = 3.3\,\mathrm{mbar}$). (**b**) Fluence dependence ($\lambda = 10.6\,\mu\mathrm{m}$, $\tilde{\nu} = 942.4\,\mathrm{cm^{-1}}$): ▲ $p(SF_6) = 1.1\,\mathrm{mbar}$; • 2.7 mbar; ■ 6.7 mbar [adapted from *Chuang* 1981]

and a shift to lower wavenumbers (longer wavelengths). Clearly, perpendicular IR radiation will result in additional (indirect) gas-phase heating (Sects. 3.5 and 9.5).

With very high fluences and *parallel* incidence of the CO_2-laser beam, SF_6 molecules were decomposed into SF_5 and F atoms. This process was suggested to involve coherent and sequential multiphoton absorption resulting in the dissociation (MPD) of the molecule (Sect. 14.1.2). Unstable SF_5 decomposes into SF_4 and another F atom. The product species, SF_4 and F, diffuse to the Si surface and react to form SiF_4.

Similar experiments have been reported for the Si-NF_3 system [*Brannon* 1988]. Here, it was suggested that CO_2-laser radiation dissociates gaseous NF_3 via a collisionally enhanced multiphoton process generating NF_2 and F radicals which diffuse to the surface and cause etching. With the high pressures used in these experiments, up to $p(NF_3) > 300\,\mathrm{mbar}$, the formation of a fluorinated surface layer consisting of mainly SiF_3 and SiF_4 has been observed.

Due to the high laser-light intensities involved, material processing based on MPD can be applied only with parallel laser-beam incidence. Thus, the technique can be employed for large-area etching, unless a mask is used. This technique seems to be promising, since many halogen-containing molecules, such as COF_2, CF_3X, CF_2X_2 (X ≡ Cl, Br, I), N_2F_4, etc, can be readily decomposed by MPD to produce reactive radicals for surface reactions not only with Si but with many other materials as well.

15.4 Microscopic Mechanisms

In this section we will complete and summarize the microscopic mechanisms involved in the laser-induced etching of silicon in a halogen atmosphere.

15.4.1 Photochemical Etching

Photochemical etching of silicon in halogen atmosphere is consistent with a model in which the interaction of halogen radicals and carriers within the silicon surface plays a fundamental role. The different steps consist of the generation of halogen radicals, the formation of reaction products, and their desorption from the surface:

- Halogen radicals are formed spontaneously by molecule–surface collisions (Si–XeF_2 system), or by selective electronic (Si–Cl_2 system) or vibrational excitation (Si–SF_6 system) of the etchant.
- The radicals become adsorbed and, because of their strong electronegativity, capture an electron from the Si. Electron transfer is promoted by donator doping or by interband photo-excitation. With the formation of a *thin* SiX_x (X ≡ F, Cl, Br, . . .) layer, tunneling of electrons through this layer will become important. This process is similar to surface oxidation (Chap. 26).
- X^- ions on the surface and positive holes within the silicon generate a surface electric field. This field causes a change in surface band bending and thus in charge transfer to the adsorbate. The strength of the surface electric field is proportional to the number of X^- ions adsorbed on the surface. However, even without charge transfer, laser irradiation of a semiconductor surface causes a surface electric field as high as 0.0001–0.1 V/Å. This field is related to the different mobilities of electrons and holes [*Gauthier* and *Guittard* 1976]. With localized irradiation, a separation of charges will also take place in the radial direction (Dember effect; see Fig. 15.6.4b). Clearly, any heating of the surface will generate additional electron–hole pairs.
- The surface electric field and the noble-gas character of X^- ions favor their diffusion into the Si. This mechanism is discussed in detail for surface oxidation (Chap. 26).
- With undoped, lightly doped, and strongly p-doped materials, bandgap excitation will shift the Fermi level towards the conduction band and thereby increase the potential difference, Φ, in (15.1.1).
- Laser-light irradiation may change the thickness of the halogenated surface layer, h (Sect. 15.1).
- The etch rate depends on the density of X^- ions on the Si surface.
- The etch rate depends on the concentration of free carriers. This concentration is determined by the doping level, interband photo-excitation, electron–hole pair recombination, and electron trapping. In the Si–Cl_2 system, the sublinear increase in etch rate with Kr^+-laser power is related to electron traps or to modified recombination kinetics caused by structural and chemical defects produced by the etching process itself.
- Defects influence the concentration of free carriers. Shorter lifetimes of free carriers in impure or heavily doped Si will diminish the etch rate but enhance the ultimate resolution via the decrease in carrier diffusion length.
- Adsorption of halogen radicals, charge transfer, and the penetration of species depend on the morphology, microstructure, and orientation of the Si surface.

- Reaction products must desorb from the surface. Desorption can take place spontaneously or it can be activated by the laser light. The composition of product species depends on the particular system and the parameters employed.

15.4.2 Combined Photochemical and Thermal Etching

For laser-light intensities that generate high electron densities, a substantial amount of the light energy absorbed is directly converted into heat via Auger recombination (Sect. 2.4). In this intermediate regime (Fig. 15.2.2), surface etching is caused by both photochemical *and* thermal mechanisms. For the Si–Cl_2 system, chlorine radicals are still necessary to cause significant etching within this regime.

15.4.3 Thermal Etching

With laser-light intensities that cause surface melting, or which are close to those, etching is mainly thermally activated. In this regime, photogenerated radicals play no, or only a minor role, at least, in the Si–Cl_2 system.

15.5 Dry-Etching of Compound Semiconductors

Laser-induced dry- and wet-etching of compound semiconductors has been investigated for the III–V compounds GaAs, GaN, InP, InSb, and the II–VI compounds CdS and CdSe. The microscopic etching mechanisms are similar to those described for silicon. Because of the lower thermal and chemical stability of compound semiconductors, photochemical etching is of particular importance. Surface patterning was demonstrated by direct writing, laser-beam interference, and projection. The precursor molecules most commonly used were Cl_2, Br_2, HCl, HBr, CCl_4, CH_3X, and CF_3X, with $X \equiv$ Cl, Br, I.

15.5.1 III–V Compounds

Thermal etching of GaAs, InP, and InSb in a CCl_4 atmosphere using focused Ar^+-laser radiation has been studied by *Takai* et al. (1988b). Figure 15.5.1 shows an Arrhenius plot. The activation energies are quite similar and around 3.7 kcal/mol. The rate-limiting step in the reaction is probably thermal desorption of the respective chlorides. The etch rates are 1–3 orders of magnitude higher than those observed in photochemical etching of these materials [*Brewer* et al. 1984]. The maximum resolution achieved with a 1.2 μm laser focus was about 0.6 μm. Scanning speeds of up to 60 μm/s have been employed. At medium-to-high laser powers, changes in the stoichiometry of the material surrounding the laser-etched groove have been found.

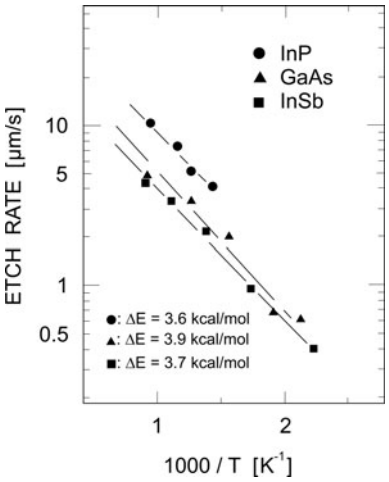

Fig. 15.5.1 Arrhenius plot of Ar^+-laser-induced etch rate achieved in CCl_4 with n-type (100) InP, (100) GaAs, and (111) InSb. Laser-beam scan speeds were 9 μm/s for InP and 3 μm/s for GaAs and InSb. The CCl_4 pressure was about 160 mbar [*Takai* et al. 1988b]

ArF-laser-induced etching of (100) and (111) n-type GaAs and (100) p-type GaAs in CF_3Br and CH_3Br has been investigated by *Brewer* et al. (1984). Surface patterning has been demonstrated by direct masking and laser-light projection. Here, a resolution of about 0.2 μm was achieved.

ArF-laser radiation photodissociates both CF_3Br and CH_3Br. The radicals, Br, CF_3, and CH_3 react with GaAs and form various etch products that have been analyzed by laser-induced fluorescence (LIF). For low fluences, etching is mainly non-thermal. This interpretation is supported by experiments using XeF-laser radiation with otherwise identical experimental conditions. XeF-laser light does *not* photodissociate CF_3Br and CH_3Br but induces about the same surface temperature. No etching was observed in this case. Etch rates achieved with ArF-laser radiation at normal incidence were higher than those for parallel incidence. This difference was interpreted by photocarriers and laser-enhanced thermal desorption of non-volatile products. Blocking of reactive surface sites by non-volatile reaction products can be reduced by uniform substrate heating. As expected, an exponential increase in etch rate with substrate temperature was found. Etching is strongly anisotropic. For (111B), (100), and (111A) orientations, typical etch-rate ratios were 3:2:1. For fluences $\leq$ 35 mJ/cm^2, the surface morphology is relatively smooth. The corresponding etch rates are about 0.01 μm/s. At higher fluences, ablation seems to be the primary mechanism. Then, the surface becomes rough and material damage is observed.

Laser-induced etching of n-type (100) InP has been investigated for excimer-laser radiation with Cl_2, HCl, and HBr as etchants. Figure 15.5.2a shows a microlens of InP fabricated by 248 nm KrF-laser-light projection in a Cl_2 atmosphere. Lenses

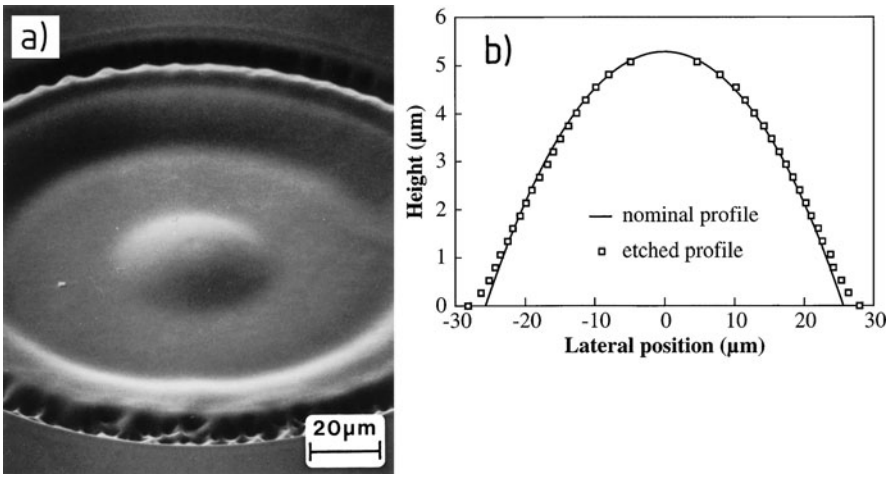

Fig. 15.5.2 (**a**) InP microlens fabricated by KrF-laser-light projection in a Cl_2 atmosphere. (**b**) Nominal and etched lens profiles [after *Matz* et al. 1997]

of this type are employed for the coupling of IR light (1.53 µm) from optoelectronic or optical devices into glass fibers. Deep and smooth patterns were obtained with fluences $0.15\,J/cm^2 \leq \phi \leq 0.28\,J/cm^2$. The deviation of the lens shape from the nominal profile was ≤ 50 nm (Fig. 15.5.2b). With the laser parameters employed, etching seems to be based on the spontaneous reaction of Cl_2 with the molten or almost molten InP surface and the subsequent laser-induced desorption of reaction products. The etch rates were between 1 and 3 nm/pulse. The coupling losses obtained with the laser-etched lenses (4 ± 1dB) were comparable to those obtained with the best lenses fabricated by conventional multiple resist technology. By improving the projection optics for simultaneous etching of whole lens arrays, throughputs of about 10^5 lenses/h can be achieved.

ArF-laser-induced dry-etching of GaN in a HCl atmosphere permits well-defined patterning with smooth surfaces and little material damage [*Leonard* and *Bedair* 1996]. The estimated etch rates were around 0.13 nm/s (≈ 0.04 Å/pulse). The process can be tentatively interpreted by the formation of gallium chlorides and their laser-induced thermal desorption. Very high etch rates have been achieved by KrF-laser irradiation of GaN in a N_2 atmosphere and subsequent removal of the decomposed material in aqueous HCl [*Akane* et al. 1999].

Gratings have been etched in various III–V-compound semiconductors by employing laser-beam interference together with a reactive atmosphere. For GaAs and InP, for example, a mixture of 1% CH_3Br : 99% He has been employed [*Ezaki* et al. 1995]. By a combination of two interference arrangements using the same or different wavelengths or angles of incidence, circular or elliptical dot structures with submicrometer dimensions have been fabricated.

15.5.2 Laser Etching of Atomic Layers

Etching of atomic layers (EAL), also termed *digital* etching, is the inverse of atomic-layer epitaxy (ALE). Layer-by-layer etching requires chemisorption of a monolayer etchant on the substrate surface. Decomposition and product removal can be enhanced or only induced by laser light (Laser-EAL).

Figure 15.5.3 shows the etch rate of InP in a Cl_2 atmosphere as a function of ArF-laser fluence. At $T_s \approx 140\,°C$ and a fluence of about $0.12\,J/cm^2$ the etch rate saturates at about 2.3 Å/pulse, which corresponds to about one monolayer of InP.

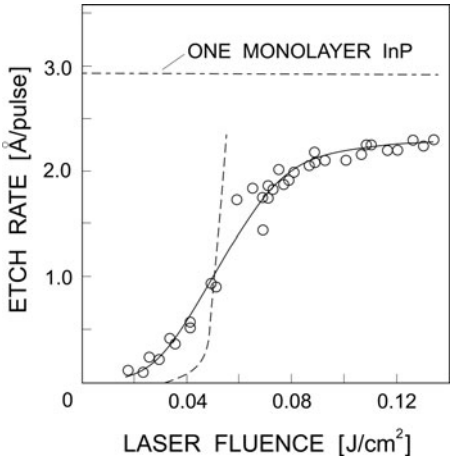

Fig. 15.5.3 InP etch rate as a function of ArF-laser fluence [10 Hz, $p(Cl_2) = 2.5$ mbar, $T_s \approx 140\,°C$]. The calculated etch rate near threshold if etching were limited by sublimation of $InCl_3$ is shown(*dashed curve*) [*Donnelly* and *Hayes* 1990]

15.5.3 Dopants, Impurities, and Defects

Photochemical dry-etching of GaAs can be suppressed by impurities and ion-beam induced defects, which serve as electron traps (Sect. 15.4) [*Ashby* et al. 1990, and references therein; *Houle* 1991]. The combination of ion-beam and laser-beam techniques permits selective high-resolution surface patterning.

15.6 Wet-Etching

Laser-enhanced wet-etching and ablation of semiconductors has been performed in aqueous solutions of acids, lyes, and various mixtures. As already mentioned in the introduction to Chap. 14, laser-induced wet-etching denotes a direct chemical reaction between the etchant and the substrate material. In liquid-phase ablation, the

liquid may cause efficient removal of ablation debris via a chemical reaction and/or enhanced transport of debris out of the interaction zone. The latter mechanisms are important, e.g., in liquid assisted fs-laser ablation of GaN in aq. HCl [*Nakashima* et al. 2009]. Various mechanisms involved in liquid-phase processing are discussed in Chaps. 14, 21, and 30.

15.6.1 Silicon

Laser-induced wet-etching of Si has been investigated in aqueous solutions of HF, NaOH, and KOH using different types of cw- and pulsed lasers.

Figure 15.6.1 shows the volume etch rate as a function of Ar^+-laser power for holes etched in (111) Si wafers immersed in aqueous KOH. Corresponding experiments with ceramic Al_2O_3/TiC are included in the figure. Average (depth) etch rates up to 15 μm/s have been achieved. The influence of the temperature of the etchant, has been studied for Si in KOH and deionized water [*Hong* et al. 2008]. Ultrashort-pulse laser etching of Si coated with a stack of dielectric layers, using NaOH as etchant, has been employed for the fabrication of freestanding micromirrors [*Brodoceanu* et al. 2010].

At low-to medium laser-light intensities non-thermal mechanisms seem to play an important role (Chap. 21). For Si, etch rates in the (100) direction exceed those in the (111) direction by up to more than 2 orders of magnitude.

With increasing intensities, melting, vaporization, and bubble formation become important. Depending on laser parameters, bubble formation may decrease both

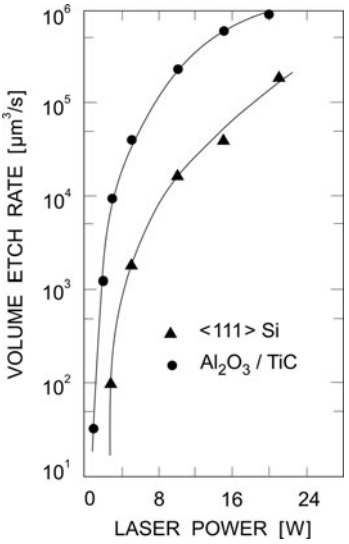

Fig. 15.6.1 Volume etch rate for (111) Si and ceramic Al_2O_3/TiC in KOH as a function of Ar^+-laser power ($\tau_\ell = 5$ s). Solid curves are to guide the eye [*von Gutfeld* and *Hodgson* 1982]

the etch rate and resolution, and may even cause material damages (Sect. 30.5). The situation is quite different to the irradiation geometry employed in LIBWE (Sect. 14.5). The high rates achieved in liquid-phase processing are related to the high density of reactive species within the liquid and the increase in mass transport by microstirring (Chap. 21).

A new cutting technique employs liquid-jet-guided laser radiation [*Hopman* et al. 2009]. Water and aq. KOH were used as carrier liquids. Cutting is based on laser-induced melting together with material expulsion by the liquid jet.

15.6.2 Compound Semiconductors

Laser-enhanced wet-etching of compound semiconductors has been investigated mainly for GaAs, GaN, InP, and InSb.

Figure 15.6.2a shows a SEM picture of a via hole in GaAs. It demonstrates that liquid-phase etching permits one to fabricate deep high-quality holes with perfectly vertical walls. The high aspect ratio achieved can be attributed to waveguiding of the laser light (Sect. 15.6.4). Deep trenches have been produced by translating the substrate with respect to the laser beam. The gratings shown in Fig. 15.6.2b have been etched by using laser-beam interference (Fig. 5.2.1). By varying the angle of incidence, different groove profiles with depth-to-spacing ratios between 0.2 and 0.8 were produced.

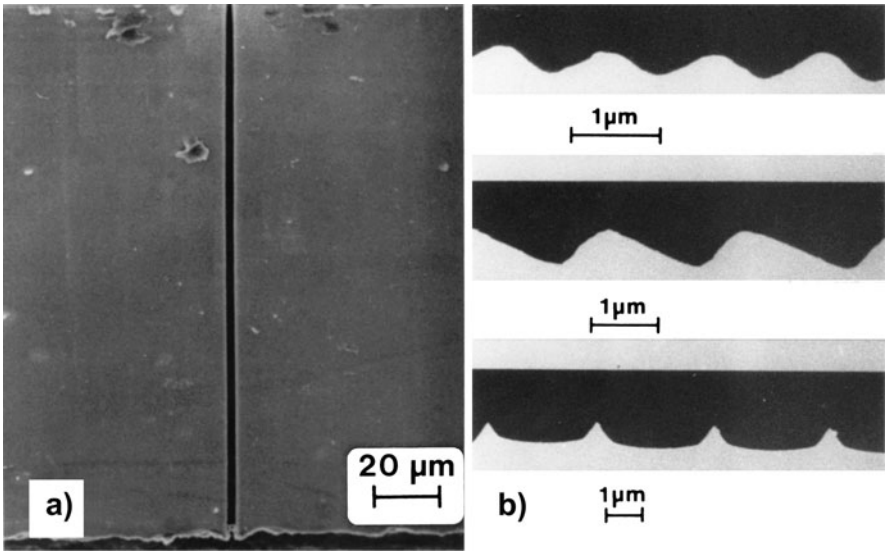

Fig. 15.6.2a, b Ar^+-laser-induced photochemical etching of GaAs in aqueous $H_2SO_4 + H_2O_2$ (volume ratio $H_2SO_4 : H_2O_2 : H_2O = 1 : 1.3 : 25$). (**a**) Via hole, $\lambda(SH\,Ar^+) = 257$ nm [*Podlesnik* et al. 1984]. (**b**) Gratings produced by 514.5 nm Ar^+-laser-light interference. The different profiles were obtained by varying the angle of incidence, Θ [*Podlesnik* et al. 1983]

Figure 15.6.3a shows the etch rate for Si-doped (n-type) GaAs as a function of absorbed photon flux for two laser wavelengths. The HNO_3 solution employed was diluted in such a way that dark etching could be ignored. The etch rates are equal for 514.5 nm and 257 nm radiation. Initially, the rate increases almost linearly and saturates with fluxes above 10^{19} to 10^{20} photons/cm^2 s [$I_a(257\,\text{nm}) \approx 10-10^2\,\text{W/cm}^2$]. The maximum temperature rise was calculated to be < 1 K. The etch rate was independent of crystallographic orientation for UV illumination and only slightly dependent for VIS radiation. Figure 15.6.3b shows the etch rate achieved with 257 nm radiation in GaAs doped with Si, Cr (semi-insulating), and Zn (p-type). The rate increases with increasing n-type character of the material. Etching of p-type material was *not* possible with 514.5 nm laser light.

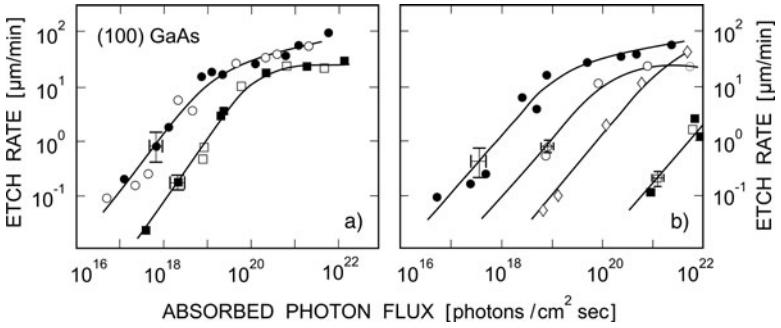

Fig. 15.6.3a, b Ar^+-laser-induced etch rate in GaAs as a function of absorbed photon flux for different types of dopings. The etchant was aqueous HNO_3. (**a**) Si doped with $n = 3 \times 10^{18}$ cm^{-3} (● $\lambda = 515$ nm, ○ $\lambda = 257$ nm) and with $n = 3 \times 10^{16}$ cm^{-3} (■ 515 nm, □ 257 nm). (**b**) Doped with Si (● $n = 3 \times 10^{18}$ cm^{-3}, ○ $n = 10^{16}$ cm^{-3}), Cr (◊ SI, $\varrho > 10^7$ Ωcm), and Zn (□ $p = 10^{16}$ cm^{-3}, ■ $p = 9.5 \times 10^{18}$ cm^{-3}), and $\lambda = 257$ nm [*Ruberto* et al. 1991]

15.6.3 Interpretation of Results

With *low* laser-light intensities, the laser-induced temperature rise can be ignored. In this regime, the enhancement in etch rate can be interpreted by the generation of electron–hole pairs within the semiconductor surface and charge transfer at the liquid–solid interface.

Let us first consider the situation in the dark. The Fermi level in the semiconductor must match the redox level of the liquid. As a consequence, the semiconductor bands bend upwards or downwards, depending on whether the semiconductor is n-type or p-type (Fig. 15.6.4a) [*Gerischer* 1975; *Bockris* and *Reddy* 1977]. The band bending can be easily understood: The oxidizing agent will attract electrons. For n-type material, a negatively charged surface layer within the liquid is thereby formed. This causes an upward band bending resulting in a barrier preventing any further flow of electrons towards the surface. In p-type material, on the other hand, electrons are the minority carriers. In this case, there is a 'transfer of holes' (in

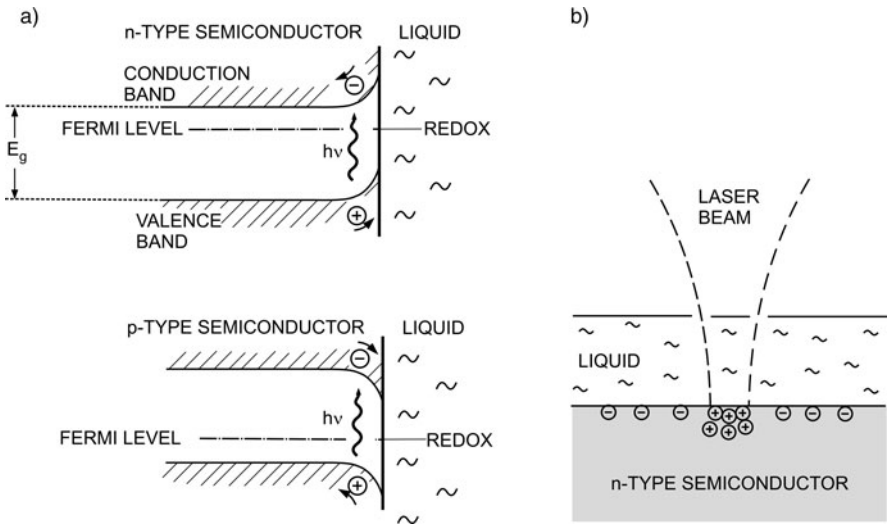

Fig. 15.6.4 (**a**) Band bending of n-type and p-type semiconductors at the interface with a liquid electrolyte. Conditions are similar at gas–semiconductor interfaces. The flow of electrons and holes under illumination with bandgap radiation is indicated. (**b**) Generation of a local EMF by the Dember effect in an n-type semiconductor

reality, this means a transfer of electrons from the liquid side) and the (liquid) surface layer becomes positively charged. This causes downward band bending, and thereby a barrier against any further migration of holes.

Low Light Intensities

Light with a photon energy that exceeds the band gap, $h\nu > E_g$, will generate electron–hole pairs. The different mobilities of electrons and holes cause spatial changes in their concentrations. For GaAs, e.g., the ratio of mobilities for electrons and holes is $\mu_e/\mu_h \approx 8$.

With *uniform* (large-area) irradiation, the changes in carrier concentrations become effective only in the direction perpendicular to the semiconductor surface. In n-type material the holes will drift to the surface, the electrons further into the bulk. The holes can be considered as ionized or broken bonds. The disrupted lattice will strongly interact with the negatively charged surface species. This may result in oxide formation. If the solution contains an acid that dissolves this oxide, the semiconductor will dissolve into positive ions. For p-type material there is a depletion of holes near the surface. Thus, light-induced etching will occur at a slower rate or not at all. For particular liquid–solid interfaces, the process may even be reversed, resulting in material deposition. In this latter case, however, the change in physical properties at the interface will, in general, rapidly terminate the reaction (Chap. 21).

With *localized* irradiation, the different mobilities of carriers will generate a local electromotive force (EMF) in the *radial* direction (Dember effect; Sect. 21.1). This

is schematically shown in Fig. 15.6.4b for n-type material. Holes are enriched within the irradiated area.

n-type GaAs

Etching of n-type GaAs in a dilute acid can be understood as follows: The *anodic* reaction within the irradiated area can be described by

$$\begin{aligned} \mathrm{GaAs} + 2\mathrm{H_2O} + 6\mathrm{h} &\rightarrow \mathrm{Ga^{3+}} + \mathrm{HAsO_2} + 3\mathrm{H^+} \\ &\rightarrow \mathrm{Ga^{3+}} + \mathrm{As^{3+}} + \cdots . \end{aligned} \tag{15.6.1}$$

GaAs first reacts with water and forms an oxide which is subsequently dissolved by the acid. Ga^{3+} and As^{3+} ions go easily into solution. In electroless etching (no external EMF) the overall hole and electron currents must be equal. Thus, the consumption of holes requires the consumption of an equal number of electrons in the *cathodic* reaction outside the illuminated area. Here, electrons are transferred from the GaAs to the oxidizing agent in the solution.

Let us consider a simple estimation of the reaction rate: The bandgap energy of GaAs is $E_g(300\,\mathrm{K}) \approx 1.43\,\mathrm{eV}$ ($\lambda \approx 870\,\mathrm{nm}$). In the absence of an external field and severe band bending, which applies to semi-insulating (SI) material, in good approximation, the concentration of holes within the GaAs surface can be described by (2.4.1). If we consider steady-state conditions and assume at the liquid–solid interface the boundary condition

$$D_\mathrm{h} \left.\frac{\partial N_\mathrm{h}}{\partial z}\right|_{z=0} = k N_\mathrm{h} ,$$

integration of (2.4.1) yields for the 1D case

$$\begin{aligned} N_\mathrm{h}(z) = {} & \frac{\alpha I_\mathrm{a} \tau_\mathrm{rec}}{h\nu \left(\alpha^2 l_\mathrm{c}^2/4 - 1\right)} \\ & \times \left[\frac{k l_\mathrm{c} + \alpha l_\mathrm{c} D_\mathrm{h}}{k l_\mathrm{c} + 2 D_\mathrm{h}} \exp\left(-\frac{2z}{l_\mathrm{c}}\right) - \exp(-\alpha z) \right] , \end{aligned} \tag{15.6.2}$$

where τ_rec is the time for carrier recombination, and $l_\mathrm{c} \approx 2(D_\mathrm{h}\tau_\mathrm{rec})^{1/2}$ the diffusion length of holes. The reaction rate is thus

$$W = D_\mathrm{h} \left.\frac{\partial N_\mathrm{h}}{\partial z}\right|_{z=0} = \frac{\alpha I_\mathrm{a} l_\mathrm{c}}{2h\nu \left(\alpha l_\mathrm{c}/2 + 1\right)\left(1 + 2D_\mathrm{h}/k l_\mathrm{c}\right)} \approx \frac{I_\mathrm{a}}{h\nu} . \tag{15.6.3}$$

The approximation refers to $\alpha l_\mathrm{c} \gg 1$ and $D_\mathrm{h}/k l_\mathrm{c} \ll 1$. The linear increase in etch rate with $I/h\nu$ is consistent with the experimental observations at low-to-medium photon fluxes (Fig. 15.6.3).

The saturation in etch rate observed with higher laser-light intensities can be related to surface defects, impurities, ionic transport limitations within the liquid, etc.

p-type GaAs

With p-type GaAs the influence of VIS-laser light of low-to-medium intensity can be described by

$$\mathrm{GaAs} + 3\mathrm{e} \rightarrow \mathrm{Ga} + \mathrm{As}^{3-} \; . \tag{15.6.4}$$

As^{3-} goes into solution as AsH_3. On the other hand, metallic Ga produced on the surface is not easily dissolved and *passivates* the surface. Within the dark region slow anodic etching as described by (15.6.1) takes place. Thus, the sample is slowly dissolved, except within the illuminated region. The situation is different with UV light, which induces etching also with p-type material, though at smaller rates (Fig. 15.6.3b). This can be explained by the shallow penetration depth of UV light, which generates a much higher concentration of holes at the surface than VIS light [$l_\alpha(257\,\mathrm{nm}) \approx 50\,\mathring{\mathrm{A}}$, $l_\alpha(514.5\,\mathrm{nm}) \approx 1100\,\mathring{\mathrm{A}}$]. Thus, some holes may overcome the potential barrier imposed by the downward band bending.

If a positive voltage is applied to p-type GaAs, the concentration of holes at the interface is increased. Then, it is possible to oxidize and dissolve the Ga layer formed according to (15.6.4) via

$$\mathrm{Ga} + 3\mathrm{h} \rightarrow \mathrm{Ga}^{3+} \; .$$

Thus, by switching the potential between a value at which photoreduction occurs and a value at which oxidation occurs, it becomes possible to also etch p-type GaAs. This type of electrochemical etching has been demonstrated by means of He-Ne- and Ar^+-laser radiation [*Ostermayer* and *Kohl* 1981]. Similar experiments have been performed for InP [*Bowers* et al. 1985]. Further details on electrochemical processes are discussed in Chap. 21.

Thermal Activation

With *high* laser-light intensities, laser-induced heating will generate electron–hole pairs and result in effects similar to those discussed above. For n-type material the thermal EMF and the Dember EMF are oriented in the same direction, while in p-type material they are opposite.

The importance of thermal mechanisms follows from the observation that at high intensities the etch rate becomes independent of laser wavelength and material doping. In this regime, mass-transport limitations may determine the etch rate.

15.6.4 Spatial Resolution, Waveguiding

For *low* laser-light intensities, where the etch rate increases linearly with photon flux, the resolution is determined by carrier diffusion and the intensity distribution of the absorbed laser light. Figure 15.6.5a shows the cross section of a shallow groove etched in n-type GaAs by means of 514.5 nm Ar^+-laser radiation. The carrier diffusion length depends on the number of physical and chemical defects. The dotted curves in Fig. 15.6.6 show measured etch-depth profiles for two doping levels. Here, the etching times were adjusted in such a way that the center etch depths were equal for both samples. With high doping, the etch profile reflects the Gaussian intensity distribution of the laser beam. With lower doping, the profile is bell-shaped and significantly wider. The narrower profile observed with the higher doping is a consequence of both the shorter diffusion length of holes and the smaller width

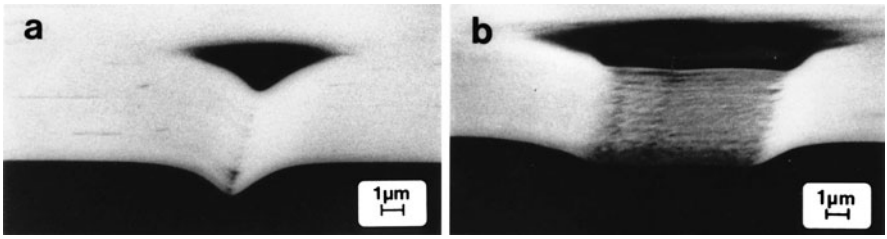

Fig. 15.6.5 SEM pictures showing the relative widths of trenches in n-GaAs (3×10^{18} /cm^2 Si) etched in HNO_3 by Ar^+-laser light ($\lambda = 515$ nm, $w_0 = 1.3\,\mu$m). (**a**) 3 W/cm^2, $v_s = 0.43\,\mu$m/s. (**b**) 150 W/cm^2, $v_s = 2\,\mu$m/s [*Ruberto* et al. 1991]

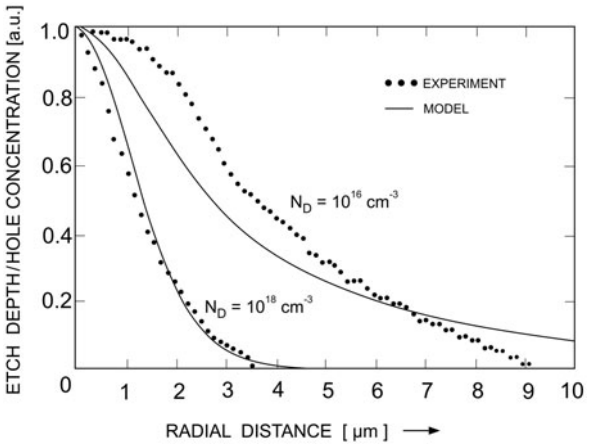

Fig. 15.6.6 Profiles of grooves in n-GaAs. Experimental results achieved in HNO_3 with Ar^+-laser radiation are shown (*dotted curves*). Except for the laser beam dwell time, the parameters employed were the same as in Fig. 15.6.5a. Calculated surface distribution of photogenerated holes is also shown(*solid curves*) [*Ruberto* et al. 1991]

of the depletion layer. The solid curves represent the stationary surface density of photo-generated holes, $N_h(r, 0)$. This has been calculated from an equation of the type (2.4.1) by taking into account band bending.

With *higher* laser-light intensities, changes in etch profiles are observed. The groove shown in Fig. 15.6.5b exhibits a flattened bottom which is related to the saturation in etch rate observed in Fig. 15.6.3. It should be noted that with the laser-light intensities employed, the laser-induced temperature rise can still be ignored.

An estimation of the spatial resolution for grating formation on n-type semiconductors by light-enhanced electrochemical etching has been performed by *Ostermayer* et al. (1985).

Waveguiding

Optical waveguiding is a well-known phenomenon which is described in standard textbooks. A hole, rod, or fiber, for example, in the form of a cylinder, can guide electromagnetic radiation in the axial direction. For waveguides with diameters $d > \lambda$, light guiding is based on multiple reflections and sometimes on total reflections of the radiation.

In laser processing, this effect has been studied in connection with (thermal) laser machining of metals using CO_2-laser or Nd:YAG-laser radiation and with photochemical liquid-phase etching of semiconductors (Fig. 15.6.2). Consider Fig. 15.6.7. The etch velocity, v_E, is perpendicular to the surface being etched. The angle of incidence at the point $M \equiv M(z(t), r(t))$ can be approximated by

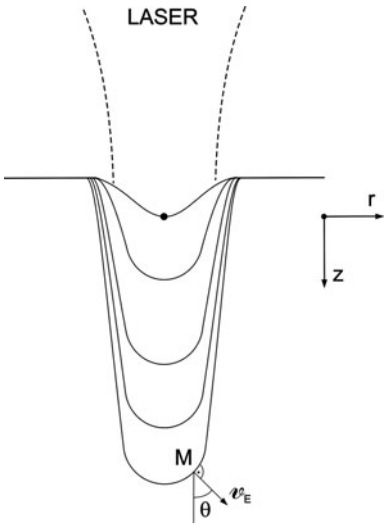

Fig. 15.6.7 Computer simulation of the temporal evolution of a tubular hole, as shown in Fig. 15.6.2a. Adapted from *Ruberto* et al. (1991)

$$\Theta(r, z, t) = \arctan \left| \frac{\mathrm{d}z}{\mathrm{d}r} \right| . \tag{15.6.5}$$

The velocities of a surface element in the axial and lateral directions are then given by

$$\frac{\mathrm{d}z}{\mathrm{d}t} = v_{\mathrm{E}} \cos \Theta \quad \text{and} \quad \frac{\mathrm{d}r}{\mathrm{d}t} = v_{\mathrm{E}} \sin \Theta . \tag{15.6.6}$$

For surface absorption and a purely photochemical process where the etch rate is proportional to the absorbed laser-light intensity, v_{E} can be described by

$$v_{\mathrm{E}} = kI[1 - R(\Theta)] \cos \Theta , \tag{15.6.7}$$

where k is the rate constant and $R(\Theta)$ the reflectivity. The factor $\cos \Theta$ in (15.6.7) describes the change in incident laser power because of the surface tilt. Etch profiles can be calculated by integration of these equations.

For thermally activated reactions, including conventional laser processing of metals (drilling, cutting), the material removal rate depends exponentially on temperature. The temperature distribution, in turn, is a complicated function of the intensity distribution, the geometry of the hole, and the physical properties of the material.

A quantitative treatment must take into account changes in the intensity, I, due to multiple reflections, interference effects, etc. Thus, self-consistent calculations on the basis of Maxwell equations must be performed.

Part IV
Material Deposition

Laser-induced material deposition has been demonstrated from gases and condensed phases (Fig. 1.2.1).

Laser-induced chemical vapor deposition (LCVD) can be employed to fabricate *microstructures* of different types (Chaps. 16, 17, and 18) and to grow large-area *thin films* (Chap. 19). The high cooling rates and/or temperature gradients that can be achieved with certain laser parameters permit to deposit materials with nonequilibrium microstructures and/or to synthesize chemically new compounds that cannot be synthesized by any other technique. Among the latter are materials whose single components are immiscible.

Adsorbates frequently play an important role in LCVD and in deposition techniques using a combination of laser and atomic (molecular) beams (Chap. 20). Material deposition from liquids has been demonstrated with ordinary liquids and with electrolytes with and without an external electromotive force (EMF) (Chap. 21). Thin films can also be fabricated from solid targets by laser-induced evaporation or pulsed-laser ablation and subsequent material condensation onto a substrate. The latter process is denoted as pulsed-laser deposition (PLD). It is discussed in Chap. 22. Laser-induced forward transfer (LIFT) is mainly employed for micropatterning (Chap. 22).

Nucleation, surface coating by laser surface cladding, and surface patterning by solid-phase transformation are discussed in separate chapters.

Chapter 16
Laser-CVD of Microstructures

The decomposition of precursor molecules in laser-induced chemical vapor deposition (LCVD) can be activated thermally (*pyrolytic* LCVD) or non-thermally (*photolytic* LCVD) or by a combination of both (photophysical LCVD). The type of process activation can be verified from the morphology of the deposit and from measurements of the deposition rate as a function of laser power, wavelength, substrate material, etc.; additional information is obtained from the analysis of data on the basis of theoretical models. The subsequent discussion concentrates on examples which were studied in most detail. Nevertheless, this discussion is very general, in the sense that most of the trends, features, and results apply to all of the corresponding systems listed in the previous edition. Applications of LCVD in microfabrication are summarized in Sect. 18.5.

16.1 Precursor Molecules

The application of LCVD in micro-patterning requires proper selection of precursor molecules. An inspection of the bibliography reveals that the precursors most frequently employed are:

- Halogen compounds, hydrocarbons, and silanes.
- Alkyls, carbonyls, and various organometallic coordination complexes.

The first class of molecules possesses electronic transitions in the near to deep UV, where only a few or no adequate laser sources are available. Although the temperatures required for *thermal* decomposition are relatively high, these molecules are frequently used in pyrolytic LCVD because they permit the deposition of materials with high purity.

The second class of molecules possesses electronic transitions in the VIS to near UV. Thus, they facilitate the matching of available laser wavelengths for (high-yield) *photolysis*. On the other hand, utilization of carbonyls and many organic precursors is often linked with the incorporation of large amounts of impurities into the deposit, in particular of carbon. Such impurities cause deterioration of the electrical properties of deposited materials. This problem is less pronounced if these molecules are

D. Bäuerle, *Laser Processing and Chemistry,* 4th ed.,
DOI 10.1007/978-3-642-17613-5_16, © Springer-Verlag Berlin Heidelberg 2011

decomposed either thermally – which is possible at relatively low temperatures – or in a combined pyrolytic–photolytic (photophysical) process.

16.2 Pyrolytic LCVD of Spots

Investigations on the pyrolytic growth of spots allow one to test the adequacy of model calculations for pyrolytic LCVD. In such experiments, the substrate is immersed in a reactive gaseous ambient and perpendicularly irradiated by a focused laser beam. The setup typically employed is shown in Fig. 5.2.2. Both the laser beam and the substrate are at rest.

Henceforth, we assume that the laser light is exclusively absorbed on the substrate surface or on the already deposited material. Transparent substrates are frequently coated with a thin absorbing film or single absorption centers. By this means, latent times for nucleation can almost be avoided (Chap. 4), and a better reproducibility of data can be achieved.

16.2.1 Deposition from Halides

A model system that has been investigated in great detail is the deposition of W from WX_6 ($X \equiv F, Cl$) with or without H_2 or an inert carrier gas, M. In analogy to (3.5.1) the overall reaction can be described by

$$WX_6 + 3H_2 + M \underset{k_2}{\overset{k_1,k_3}{\rightleftharpoons}} W(\downarrow) + 6HX + M \; . \tag{16.2.1}$$

The rate constants k_1 and k_3 describe the decomposition of WX_6 at the surface and in the adjacent gas, respectively; k_2 describes etching of condensed W by HX.

Another practical example is the deposition of Si according to

$$SiCl_4 \underset{k_2}{\overset{k_1,k_3}{\rightleftharpoons}} Si(\downarrow) + 2Cl_2 \; . \tag{16.2.2}$$

Again, H_2 or an inert gas can be added. If the chemical equilibrium is shifted to the other side, this reaction describes the pyrolytic etching of Si in a Cl_2 atmosphere.

Morphology

The morphology of deposits depends mainly on the type of precursor molecules, the gas pressures, the laser-induced temperature distribution, and the illumination time.

Figure 16.2.1a–c shows SEM pictures of W spots deposited from $WF_6 + H_2$ by means of 514.5 nm Ar^+-laser radiation. The substrate employed was fused quartz

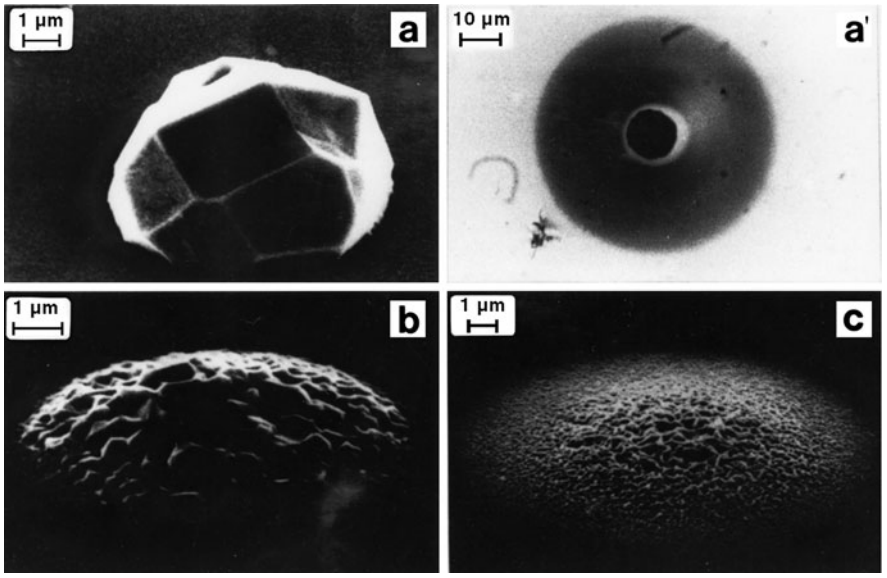

Fig. 16.2.1 SEM pictures (**a–c**) and optical transmission microscope picture (**a'**) of W spots deposited from $WF_6 + H_2$ onto SiO_2 substrates by means of Ar^+-laser radiation [$\lambda \approx 515\,\text{nm}$, $w_0(1/e) \approx 1.1\,\mu\text{m}$]. (**a,a'**) $P = 120\,\text{mW}$, $\tau_\ell = 0.2\,\text{s}$, $\Gamma_\text{p} = 2\,[10/5 \equiv 10\,\text{mbar}\,H_2 + 5\,\text{mbar}\,WF_6]$. (**b**) $P = 110\,\text{mW}$, $\tau_\ell = 0.5\,\text{s}$, $\Gamma_\text{p} = 5\,[25/5]$. (**c**) $P = 120\,\text{mW}$, $\tau_\ell = 0.5\,\text{s}$, $\Gamma_\text{p} = 50\,[250/5]$ [*Toth* et al. 1992]

covered with W absorption centers (radius $r_0 \approx 1.5\,\mu\text{m}$) produced by laser-induced forward transfer (LIFT).

The shape of spots obtained in a particular experiment is determined mainly by the ratio of partial pressures $\Gamma_\text{p} = p(H_2)/p(WF_6)$ *and* the laser-induced temperature distribution. The different types of spots shown in Fig. 16.2.1a–c are henceforth denoted by S_l, S_i, and S_d, respectively.

Spots of type S_l are spatially well *localized*. They consist of only a few single crystallites. The ratio of the spot diameter, d, and height, h, is small and, typically, within the range $2 \leq d/h \leq 3$. Such spots are obtained with small pressure ratios Γ_p, small focus diameters, and low laser powers. The (transparent) SiO_2 substrate permits inspection of the deposit by means of an optical transmission microscope (Fig. 16.2.1a'). This reveals that the spot is surrounded by a smooth, high-reflectance circular film which has a thickness of some 10 Å and which consists of pure W. The spot is separated from the film by a transparent ring which shows the plain SiO_2 surface. These observations are interpreted by a combination of heterogeneous and homogeneous deposition reactions together with etching of condensed W by HF (Sect. 16.3.1).

Spots of type S_d (Fig. 16.2.1c) are fine grain, and very flat with large values of d/h. They are quite *diffuse*, with no well-defined edge, and are also surrounded by a thin film. Spots of this type are obtained with large Γ_p or high laser powers.

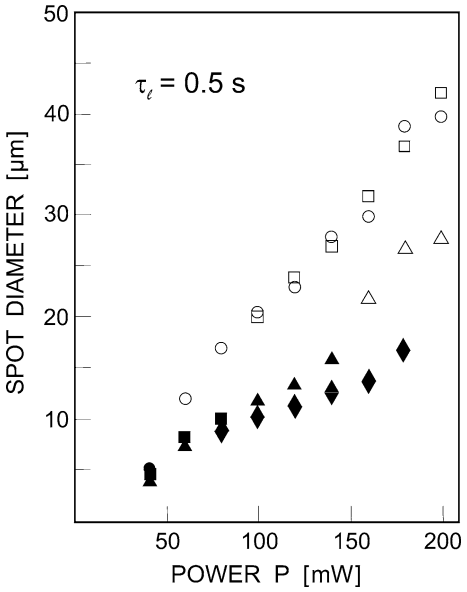

Fig. 16.2.2 Diameter of W spots as a function of laser power for fixed illumination time (τ_ℓ = 0.5 s). Solid symbols refer to well-defined spots of type S_l or S_i (Fig. 16.2.1a, b). Open symbols refer to diffuse spots of type S_d (Fig. 16.2.1c). ♦: Γ_p = 2 (10/5), ▲△: Γ_p = 5 (25/5), ■□: Γ_p = 15 (75/5), ●○: Γ_p = 25 (125/5) [*Toth* et al. 1992]

Spots of type S_i (Fig. 16.2.1b) represent an *intermediate* situation. They are still well defined, have a coarse-grain morphology, and are observed over a broad range of parameters. These spots are again surrounded by a thin film.

The diameter of W spots as a function of laser power is shown in Fig. 16.2.2 for different Γ_p. Besides the change in diameter, a change in surface morphology is observed. This is indicated by full (type S_l or S_i) and open symbols (type S_d). In all cases, deposition starts only above a *threshold* power of about (40±5) mW. Above this threshold, the diameter increases approximately linearly with laser power. With the laser powers investigated and with $1 \leq \Gamma_p \leq 3$, only spots of type S_l are observed. With higher pressure ratios, the shape changes with power. For example, with $\Gamma_p = 5$, spots of type S_i are observed up to powers of about 140 mW. Above about 160 mW, only spots of type S_d are observed. With increasing Γ_p, the transition in shape from type S_i to type S_d is shifted to lower laser powers. Spot shapes obtained with other precursor molecules and experimental parameters are shown in Figs. 16.2.5 and 16.5.2. Deposition of arrays of W spots using a 2D-lattice of a-SiO_2 microspheres has been studied by *Denk* et al. (2003).

In situ monitoring of photophysical growth of Pt dots was demonstrated by coupling the laser radiation via a lensed fiber into a scanning electron microscope [*Hwang* et al. 2008a].

Dependence on Illumination Time

The time-dependent growth of W spots has been investigated with WF_6 and WCl_6 precursors. In such experiments, the laser beam illumination time is increased successively, while all other parameters are kept constant. The growth is characterized by changes in both microstructure and morphology: the grain size, diameter, and maximum height of S_i-type spots increase with illumination time, while the ratio d/h decreases (Fig. 16.2.3a). For very long times τ_ℓ and within certain parameter ranges, the growth of one or several large crystals is observed (Fig. 16.2.5a). Figure 16.2.3b shows similar investigations but for WF_6 and different absorbed laser powers, P_a. Within the parameter range investigated, these spots are of type S_i. Again, spot diameters first increase very rapidly and saturate for longer times, depending on the laser power.

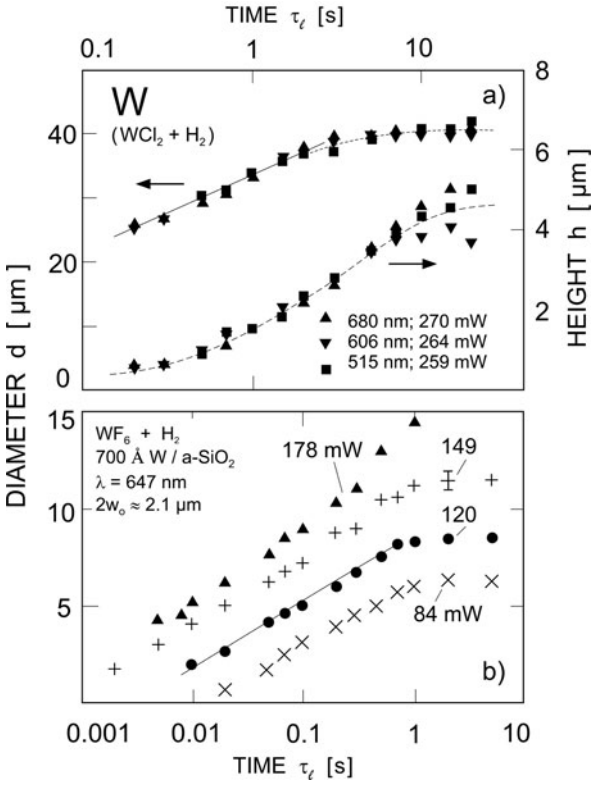

Fig. 16.2.3 a, b Diameter/height of W spots as a function of laser-beam illumination time. The substrate material was SiO_2 covered with a 700 Å thick layer of sputtered W. (**a**) Deposited from 0.49 mbar WCl_6 + 50 mbar H_2 by using different laser wavelengths but constant absorbed laser power $P_a = P(1-R)$ with $2w_0 \approx 15\,\mu m$ [*Kullmer* et al. 1992]. (**b**) Deposited from 5 mbar WF_6 + 500 mbar H_2 at various Kr^+-laser powers ($\lambda \approx 647$ nm; $2w_0 \approx 2.1\,\mu m$) [*Szörenyi* et al. 1988]

Dependence on Wavelength

For pyrolytic deposition, the growth rate is expected to be independent of the laser wavelength as long as the absorbed laser power, $P_a = P(1 - R)$, is kept constant. This is confirmed by the experimental results in Fig. 16.2.3a.

Dependence on Laser Power

The diameter and height of W spots deposited from $WCl_6 + H_2$ is displayed in Fig. 16.2.4 as a function of laser power. Well above the threshold for deposition, the spot diameter increases approximately linearly with power. This can be understood on the basis of (16.4.1). A similar behavior has been found for the WF_6–H_2 system (Fig. 16.2.2) [*Szörenyi* et al. 1988] and for the deposition of Ni from $Ni(CO)_4$ [*Petzoldt* et al. 1984].

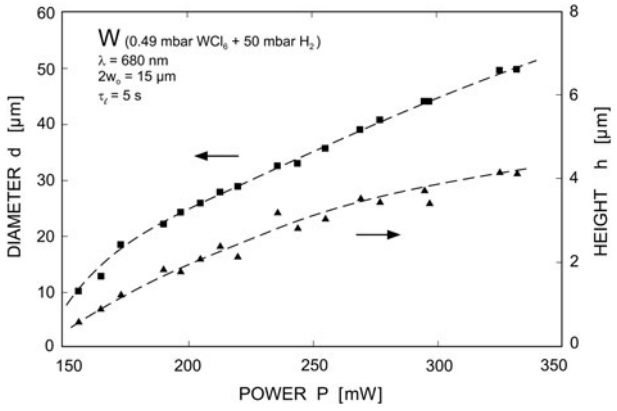

Fig. 16.2.4 Diameter, d, and height, h, of W spots as a function of (dye-) laser power ($\lambda = 680$ nm, $\tau_\ell = 5$ s). The substrate material was 700 Å W/a-SiO_2 [*Kullmer* et al. 1992]

Dependence on Gas Pressure and Composition

The dependence of the growth rate on partial pressures, the pressure ratio Γ_p, and the admixture of noble gases has also been investigated.

The strong influence of Γ_p on the morphology of W spots deposited from $WF_6 + H_2$ has already been discussed. With the admixture of an inert gas such as Ar, the shape of the spots changes from type S_l to type S_i and, with pressures $p(\mathrm{Ar}) > 200$ mbar, to type S_d. With increasing Ar pressure, the ratio d/h increases, while the diameter and the thickness of the thin circular film decrease (Fig. 16.2.1a').

Even when spots are spatially well defined, considerable changes in shape may occur with pressure changes. Examples are illustrated in Fig. 16.2.5 for the WCl_6–H_2 system.

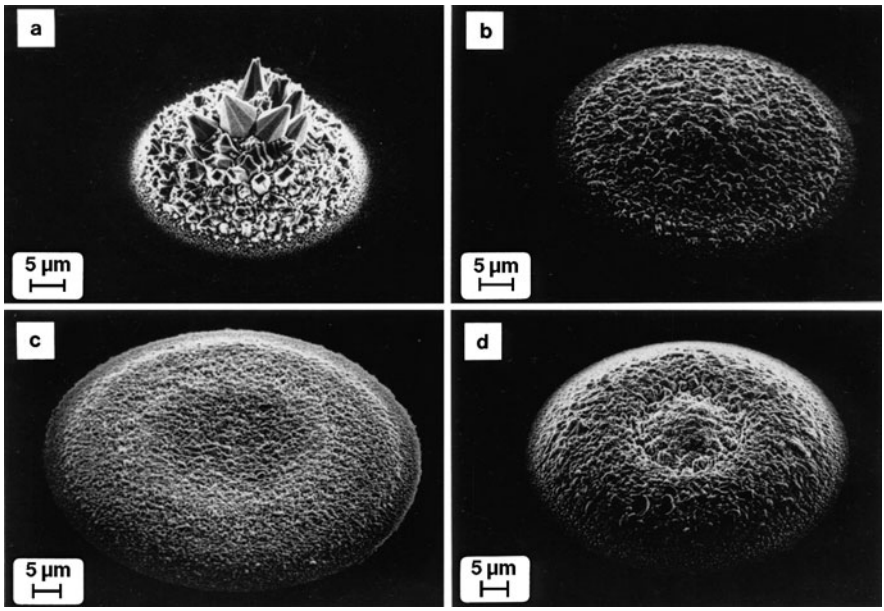

Fig. 16.2.5 a–d SEM pictures of W deposited from WCl_6. (**a**) Pure WCl_6 (0.49 mbar) and 514.5 nm Ar^+-laser radiation ($P = 290$ mW, $\tau_\ell = 20$ s, $w_0 = 7.5\,\mu$m). (**b**) The same conditions as in (**a**) but with an admixture of 50 mbar H_2. (**c**) 0.49 mbarWCl_6 + 400 mbarH_2; 680 nm dye-laser radiation ($P = 300$ mW, $\tau_\ell = 20$ s). Note the dip in the *center*. (**d**) Same as (**c**) but for $P = 240$ mW and $\tau_\ell = 40$ s [*Kullmer* et al. 1992]

16.2.2 Deposition from Carbonyls

Pyrolytic deposition from metal carbonyls was studied in detail for Ni [*Petzoldt* et al. 1984], Cr, Mo, and W [*Singmaster* and *Houle* 1991]. The concentration of carbon and oxygen impurities increases from the spot center towards the (colder) edge but is in total much lower than in photochemically deposited spots.

16.3 Modelling of Pyrolytic LCVD

The spot sizes observed under the conditions usually employed in LCVD can easily be measured and the high growth rates enable a lot of data to be accumulated. Thus, various experimental dependences can be determined with high accuracy. Among those is the shape and size of spots, their axial and lateral growth rates as a function of laser power, gas pressures, etc. From these data, fundamental information on the gas-phase kinetics, the different activation mechanisms, and the influence of the substrate on the growth process can be derived, in principle. Such an analysis requires, however, a *self-consistent* treatment of the various gas-phase processes, the laser-induced temperature distribution, and the growth process itself. Besides the

influence of geometrical effects, axial and lateral growth rates may be determined by *different* apparent activation energies, sticking coefficients, etc. These may originate from the different physico-chemical surface properties of the deposit and the substrate, from temperature gradients on these surfaces, etc. Temperature gradients may influence growth rates via both surface diffusion of species and thermal diffusion within the gas phase. A self-consistent treatment of the general (coupled) problem is very complicated. For this reason, the analysis of data has been performed in two different ways:

- The gas-phase kinetics and transport is studied by assuming the geometry and temperature distribution of the deposit to be *fixed*. The basic equations and the various models employed in such calculations are presented in Chap. 3.
- The shape of the deposit is calculated by assuming a single, thermally activated purely heterogeneous reaction which is kinetically controlled. Here, gas-phase processes are ignored.

These different approaches will now be discussed in further detail.

16.3.1 Gas-Phase Processes

The gas-phase kinetics in pyrolytic LCVD has been investigated by describing the reaction zone either by a hemisphere (Fig. 3.4.1) or by a thin circular film placed on a semi-infinite substrate (Fig. 3.5.1). The hemispherical model is particularly suited for studying different types of transport processes (Sect. 3.4). The cylindrical model, on the other hand, permits one to include, in a simple way, the effect of volume (homogeneous) reactions and to describe qualitatively the influence of gas-phase processes on the shape of deposits. Certainly, this model applies to 'flat' structures only. Nevertheless, it helps in the interpretation of different spot shapes observed experimentally. Subsequently, we shall discuss some essential features of thermally activated reactions of type (3.5.1) which correspond to those described by (16.2.1), (16.2.2), etc. For simplicity, we mainly assume the partial reaction orders $\gamma_i = \gamma_{v,i} = 1$. The flux of species onto the substrate surface $J(r) \equiv J(r, z = 0)$ can be calculated by employing the approximations made in Sect. 3.5. Let us consider different cases.

Case 1: Pure Surface Reaction, $k_1 \neq 0$, $k_2 = k_3 = 0$

The *surface* (heterogeneous) reaction shall take place only in the forward direction. This case applies also to deposition from adsorbed species. Figure 16.3.1a depicts the normalized reaction rate $W^*(r^*) = J(r^*)/J(0)$ for different center temperatures, T_c. At low temperatures, the concentration of reactants AB varies only slightly over the reaction zone and the shape of the deposit is determined mainly by the radial dependence of the rate constant $k_1(T(r, 0))$. The thickness of the deposit decreases

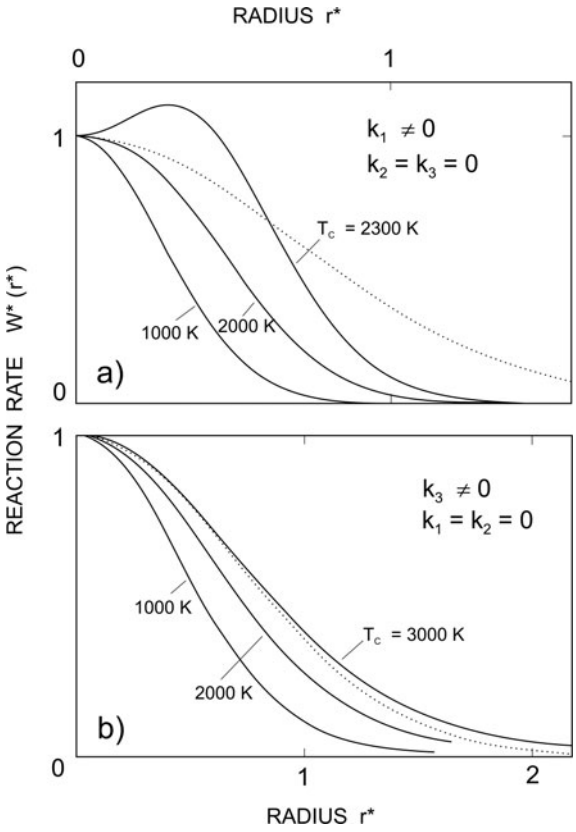

Fig. 16.3.1a, b Normalized reaction rate, W^*, as a function of radius, r^*. Different curves refer to different laser-induced center temperatures, T_c, on the flat deposit/substrate (Fig. 3.5.1). The normalized laser-beam intensity is shown (*dotted curves*). (**a**) Pure surface reaction with $\mathscr{E}_1 = 2 \times 10^4$ K. (**b**) Pure gas-phase reaction with $\mathscr{E}_3 = 8 \times 10^3$ K [*Kirichenko* and *Bäuerle* 1992]

monotonically with distance. At higher temperatures, the top of the deposit becomes flatter. With larger T_c, a dip near the center appears (note that the *absolute* value of $W^*(0)$ increases monotonically with T_c). This dip reflects gas-phase transport limitations of species AB towards the reaction zone. While diffusion is mainly 1D in the center, it becomes almost 3D near the edge; this explains the higher rate for $r^* \approx 0.3$ in the 2300 K curve. For all temperatures, the deposited spot is localized within the area $r \leq r_1$, see (3.5.8). The picture is in qualitative agreement with the spot shapes shown in Fig. 16.2.5b, c.

Case 2: Pure Gas-Phase Decomposition, $k_3 \neq 0$, $k_1 = k_2 = 0$

Figure 16.3.1b exhibits the rate for a pure *gas-phase* reaction. At low temperatures, $W^*(r^*)$ reflects the spatial behavior of the rate constant $k_3(T(r, 0))$ given by (3.5.7b).

At high temperatures, W^* shows long tails. The shape of curves can be interpreted as follows: according to (3.5.8) the gas-phase reaction is localized within a volume of height h_v above the irradiated surface. At low temperatures, h_v is very small and atoms A, generated within this volume, directly diffuse to the surface and form the deposit. At higher temperatures, h_v increases and atoms A diffuse over larger distances. As a consequence, deposition becomes less localized.

Thus, with low laser-induced temperatures, deposition is localized irrespective of whether decomposition of molecules takes place at the surface or within the gas. As a consequence, the growth of spots of type S_l or S_i is observed. With medium and high temperatures, the situation becomes more complicated. In any case, the 'transition' from localized to diffuse deposits (Fig. 16.2.1) can, in principle, be understood by the increasing importance of homogeneous reactions. No new phenomena occur if $k_1 \neq 0$, $k_3 \neq 0$, and $k_2 = 0$.

Case 3: Gas-Phase Decomposition, Etching, $k_2 \neq 0$, $k_3 \neq 0$, $k_1 = 0$

We now consider gas-phase pyrolysis of AB together with surface etching. Figure 16.3.2a shows three characteristic shapes of deposits corresponding to different temperatures T_c where $-J^*(r^*) \propto W^*(r^*)$. At low temperatures, the thickness of the deposit decreases monotonically with the distance r^*. Above a certain temperature, the thickness of the deposit approaches zero at $r^* \approx 1$. At even higher temperatures, etching within a *ring* around the central deposit is observed – here we assume that the substrate consists of material A. At large distances, the reaction rates become small, for both deposition and etching. Here, a thin film is formed via diffusion of atoms A out of the reaction zone. The figure demonstrates an additional phenomenon: an increase in laser-beam intensity, and thus in temperature T_c, results in a *decrease* in the height at $r = 0$. This reflects the competition between deposition and etching.

Case 4: Surface- and Gas-Phase Decomposition, Etching, $k_1 \neq 0$, $k_2 \neq 0$, $k_3 \neq 0$

This is the most general situation, which must, in fact, be considered with reactions of type (16.2.1). Figure 16.3.2b–d depicts different shapes that can be obtained in this case. The profiles shown in (b) are quite similar to those in (a). Figure 16.3.2d demonstrates the strong influence of reaction orders on profiles.

Limits of Validity

In spite of the good agreement between observed and calculated deposition/etch profiles, a direct correlation of results should be considered with care. First, the

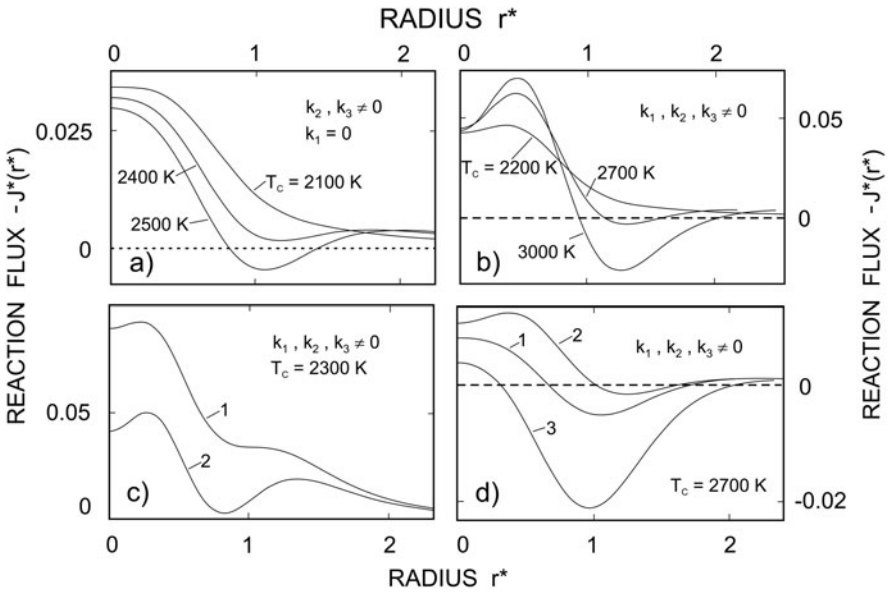

Fig. 16.3.2 a–d Normalized reaction flux $J^*(\mathrm{cm}^{-1}) = J\sqrt{\pi}/2N(\infty)D_{\mathrm{BC}}(\infty)$ as a function of distance, r^*. (**a**) Pure gas-phase reaction and surface etching ($\mathscr{E}_2 = 8 \times 10^3$ K, $\mathscr{E}_3 = 10^4$ K, $D^*_{\mathrm{AB}} = 0.1$). (**b**) Surface and volume decomposition of precursors and surface etching ($\mathscr{E}_1 = 1.5 \times 10^4$ K, $\mathscr{E}_2 = 8 \times 10^3$ K, $\mathscr{E}_3 = 10^4$ K, $D^*_{\mathrm{AB}} = 0.1$). (**c**) Same as (**b**) but for $\mathscr{E}_1 = 2 \times 10^4$ K, $\mathscr{E}_2 = 10^4$ K, $\mathscr{E}_3 = 7 \times 10^3$ K, $T_{\mathrm{c}} = 2,300$ K. Curve 1: $D^*_{\mathrm{AB}} = 0.1$. Curve 2: $D^*_{\mathrm{AB}} = 0.2$. (**d**) Same as (**b**) but for $\mathscr{E}_1 = 1.2 \times 10^4$ K, $\mathscr{E}_2 = 8 \times 10^3$K, $\mathscr{E}_3 = 10^4$ K, $T_{\mathrm{c}} = 2,700$ K, $D^*_{\mathrm{AB}} = 0.1$, $\gamma_{\mathrm{v,AB}} = 1$. Curve 1: $\gamma_{\mathrm{AB}} = \gamma_{\mathrm{BC}} = 1$. Curve 2: $\gamma_{\mathrm{AB}} = 0.5$, $\gamma_{\mathrm{BC}} = 1$. Curve 3: $\gamma_{\mathrm{AB}} = 1$, $\gamma_{\mathrm{BC}} = 0.9$ [*Kirichenko* and *Bäuerle* 1992]

relative contributions of volume and surface reactions are unknown. Second, the model (Fig. 3.5.1) is adequate only for *flat* structures. Third, the assumption of a temperature profile which remains unaffected during deposition is reasonable only if $\kappa_{\mathrm{D}} \approx \kappa_{\mathrm{s}}$.

16.3.2 The Coupling Between $T(x)$ and $h(x)$

In Part II we investigated laser-induced temperature distributions for plane substrates that were infinitely extended in the lateral direction. In some kinds of laser microprocessing, however, these assumptions are invalid. Among the examples are the laser-induced deposition of *microstructures*, the transformation of spun-on metallopolymers, etc. Here, the width of patterns is of similar size as the diameter of the *focused* laser beam. This is schematically shown in Fig. 16.3.3. It is easy to demonstrate that in such cases the laser-induced temperature distribution, $T(\boldsymbol{x})$, depends on the geometry of the pattern, $h(\boldsymbol{x})$. We shall prove this for pyrolytic LCVD by assuming a *kinetically* controlled heterogeneous reaction ($k_2 = k_3 = 0$).

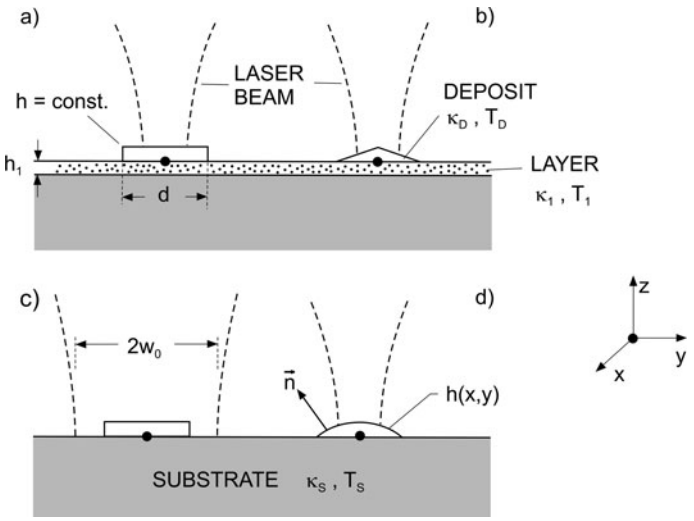

Fig. 16.3.3 a–d Deposits of various shapes with radius $r_D = d/2$ at the substrate surface and height h. In (**d**) the height is described by an arbitrary function $h(x, y)$. The intermediate layer has a thickness h_1. The radius r_D can be either larger or smaller than the radius of the laser focus, w_0. The origin of the coordinate system is indicated by the dot. If the substrate and the laser beam are fixed, these model structures describe the deposition of spots. If the laser beam is scanned, e.g., perpendicularly to the plane of the paper, these structures describe laser direct writing of lines with different shapes

In the kinetically controlled regime, the growth rate depends exponentially on the temperature distribution induced by the absorbed laser light on the substrate or the already deposited material. This temperature distribution, in turn, depends on the geometry of the deposit and thereby changes during the growth process. This can be demonstrated by considering, for example, laser-induced temperature distributions for the (fixed) model structures depicted in Fig. 16.3.3a–d. Thus, even when gas-phase processes are ignored, any quantitative or semi-quantitative calculations on the shape of deposits require a *self-consistent* treatment of the laser-induced temperature distribution and the equation of growth.

In photolytic processing the situation is different. Here, the precursor molecules are decomposed within the ambient gas and the profile of patterns depends on the concentration of product species reaching the surface (Chaps. 14, 15 and 19).

Let us consider a deposit of arbitrary shape $h(x, y)$ within the region $0 < z < h(x, y)$ (Fig. 16.3.3d). The temperatures of the deposit and the substrate are denoted by T_D and T_s, respectively. The notations for the other quantities are analogous. The temperature distribution induced by the absorbed laser light can then be calculated from the boundary-value problem

$$c_{\mathrm{D}}\varrho_{\mathrm{D}}\frac{\partial T_{\mathrm{D}}}{\partial t} - \nabla[\kappa_{\mathrm{D}}(T_{\mathrm{D}})\nabla T_{\mathrm{D}}] = Q(x, y, z, t) \,, \tag{16.3.1}$$

$$\kappa_{\mathrm{D}}(T_{\mathrm{D}}) \left.\frac{\partial T_{\mathrm{D}}}{\partial z}\right|_{z=0} = J_{\mathrm{loss}}(z = 0) \,,$$

$$-\kappa_{\mathrm{D}}(T_{\mathrm{D}}) \left.\frac{\partial T_{\mathrm{D}}}{\partial \hat{\boldsymbol{n}}}\right|_{z=h} = J_{\mathrm{loss}}(z = h) \,.$$

Here, c_{D} is the specific heat and ϱ_{D} the mass density of the deposit. The unit vector $\hat{\boldsymbol{n}} = \boldsymbol{n}/|\boldsymbol{n}|$ is directed perpendicular to the surface $z = h(x, y)$ so that $\boldsymbol{n}$ has the components $(-\partial h/\partial x, -\partial h/\partial y, 1)$. Equation (16.3.1) and the corresponding equations for the substrate and, if present, for the thin layer are coupled via the heat flux from the deposit, $J_{\mathrm{loss}}(z = 0)$. These equations can be directly solved numerically.

For the simulation of deposition profiles, (16.3.1) must be solved self-consistently together with the equation of growth. In a coordinate system that is fixed with the laser beam, the shape of the deposit is given by

$$\frac{\partial h}{\partial t} = W(T_{\mathrm{D}}) \times |\boldsymbol{n}| + v_{\mathrm{s}}\frac{\partial h}{\partial x} \,. \tag{16.3.2}$$

The factor $|\boldsymbol{n}| = [1 + (\nabla_2 h)^2]^{1/2}$ takes into account that growth takes place perpendicularly to the surface $h(x, y)$ (∇_2 is the gradient in the xy-plane). If $v_{\mathrm{s}} \neq 0$, scanning of the laser beam is performed exclusively in the x-direction (Fig. 16.3.3). The growth rate can be described by

$$W(T_{\mathrm{D}}) = k_0 \exp\left(-\frac{\mathscr{E}}{T_{\mathrm{D}}}\right)\left[1 + \exp\left(\frac{T_{\mathrm{th}} - T_{\mathrm{D}}}{\delta T_{\mathrm{th}}}\right)\right]^{-1} \,, \tag{16.3.3}$$

where $\mathscr{E} \equiv \Delta E/k_{\mathrm{B}}$. According to our assumptions, the growth process shall be characterized by a *single* apparent activation energy, ΔE. The additional factor in the Arrhenius-type law shall account for the 'threshold' behavior observed with certain systems. Depending on the type of precursor molecules employed, the deposition rate either drops off very sharply for $T_{\mathrm{D}} \approx T_{\mathrm{th}}$ or it shows a smooth behavior. This 'width' of the threshold is denoted by δT_{th}. In the *absence* of a threshold we set the last factor in (16.3.3) equal to unity. The boundary and initial conditions are usually characterized by $h = 0$. For the simulation of growth we can frequently employ the assumption $\partial T_{\mathrm{D}}/\partial t = 0$. This is a good approximation if thermal equilibrium is reached within a time $\tau_{\mathrm{T}} \ll [\partial \ln h/\partial t]^{-1}$. Usually we can also ignore heat losses to the gas phase and set $J_{\mathrm{loss}}(z = h) = 0$.

Before we present self-consistent calculations, we consider temperature distributions induced on model structures of fixed geometry.

16.4 Temperature Distributions on Circular Deposits

In the present section we discuss *stationary* temperature distributions that have been calculated for combined structures consisting of a circular deposit, a plane semi-infinite substrate, and a layer of thickness h_1 in between (Fig. 16.3.3). The geometry of the deposit is kept fixed. This is usually a good approximation, as the temperature becomes quasi-stationary within a time $t_{st} = l^2/D$, where l characterizes the size of the microstructure. In most cases of micropatterning, this time is very short compared to the time of material deposition. Thus, temporal changes in temperature are mainly due to changes in the geometry of the deposit. Henceforth, we consider cw-laser irradiation of Gaussian shape, if not otherwise noted. For circular spots, the maximum temperature occurs in the beam center. The source term in (16.3.1) can be written as

$$Q = \frac{P_a}{\pi w_0^2} \exp\left(-\frac{r^2}{w_0^2}\right) f(z) \ ,$$

where $P_a = P(1 - R)$ (Sect. 6.1; note the different definitions of the z-direction). With the geometries under consideration, the solution of the heat equation is most conveniently performed by employing finite element techniques.

The laser-induced temperature distribution is mainly characterized by the thermal conductivities κ_D, κ_1, and κ_s, by the radius of the deposited spot, $r_D = d/2$, and by the radius of the laser focus, w_0.

In the following, we discuss only a few important features of such temperature distributions.

Case 1: Cylinders with $r_D > w_0 = \text{const.}$, $\alpha_D \to \infty$, $h_1 = 0$

In this case we approximate the deposit by a *circular cylinder* of (fixed) diameter d and height h (Fig. 16.3.3a). We set $h_1 = 0$ (this is identical to $h_1 \neq 0$ and $\kappa_1 = \kappa_s$). The normalized surface temperature rise is indicated in Fig. 16.4.1 as a function of the distance from the center. For $\kappa^* \equiv \kappa_D/\kappa_s = 1$, the temperature distribution approximates that of the plane substrate (dashed curve). Here, significant differences occur only near r_D. The center-temperature rise strongly decreases with increasing κ^*. In the limit $\kappa^* \gg 1$, the temperature is almost uniform over the surface of the cylinder. This latter case applies to metal deposits on thermally insulating substrates. The temperature distribution for radii $r \gg r_D$ is only slightly influenced by κ^*. A detailed analysis shows that the temperature at the edge of the deposit, $T(r_D)$, depends strongly on the diameter of the spot, but much less on its exact height and shape [*Bäuerle* 1986]. If $\kappa^* \gg 1$, the temperature rise $\Delta T(r_D, h)$ scales approximately inversely with d. This can easily be understood. With $w_0 < r_D$, the temperature gradient in the substrate is

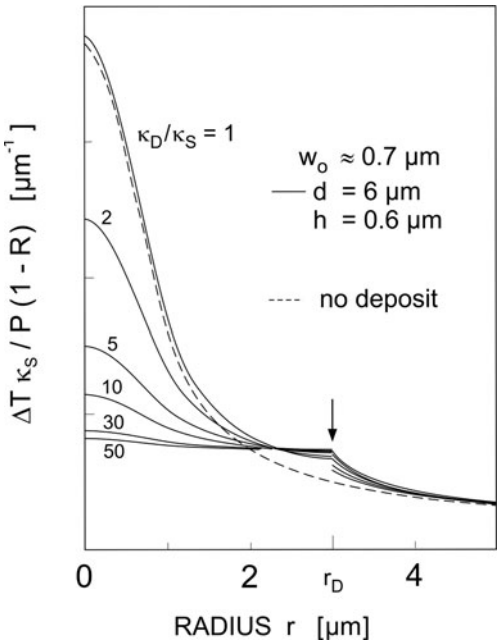

Fig. 16.4.1 Normalized laser-induced surface temperature rise calculated for a circular cylinder of radius $r_D = d/2$ and height h placed on a semi-infinite substrate. The edge of the cylinder is shown (*arrow*). The temperature distribution calculated for a plane semi-infinite substrate is also shown (*dashed curve*) [*Piglmayer* et al. 1984]

$\nabla T \approx \Delta T/r_D$. The energy balance yields $P_a \approx \pi r_D^2 \kappa_s \nabla T$. Thus, we obtain the simple relation $\Delta T(r_D, h) \approx P(1-R_D)/\pi r_D \kappa_s$. An exact analytical solution yields for $\kappa^* \to \infty$

$$\Delta T(r < r_D, h) = \frac{P(1-R_D)}{4 r_D \kappa_s} \,. \tag{16.4.1}$$

This temperature rise is not very sensitive to changes in κ_D as long as $\kappa^* w_0/r_D \gg 1$. For example, if κ^* is doubled, numerical calculations yield a decrease in $\Delta T(r_D, h)$ by a few percent only. Furthermore, it can be verified that (16.4.1) describes quite well the temperature rise at the deposit substrate interface, i.e., $\Delta T(r < r_D, 0)$, even for *thermally thick* deposits.

Figure 16.4.2 shows the normalized center-temperature rise on the top of parabolic spots as a function of r_D/w_0 and h/w_0 for three different values of κ^*. With $r_D = \text{const.}$ and $\kappa^* \gg 1$, the temperature $\Delta T(0, h)$ first decreases with increasing h and then increases when $h/r_D \approx 1$. This increase in $\Delta T(0, h)$ can result in 'explosive' growth and the occurrence of instabilities (Sect. 28.3.6).

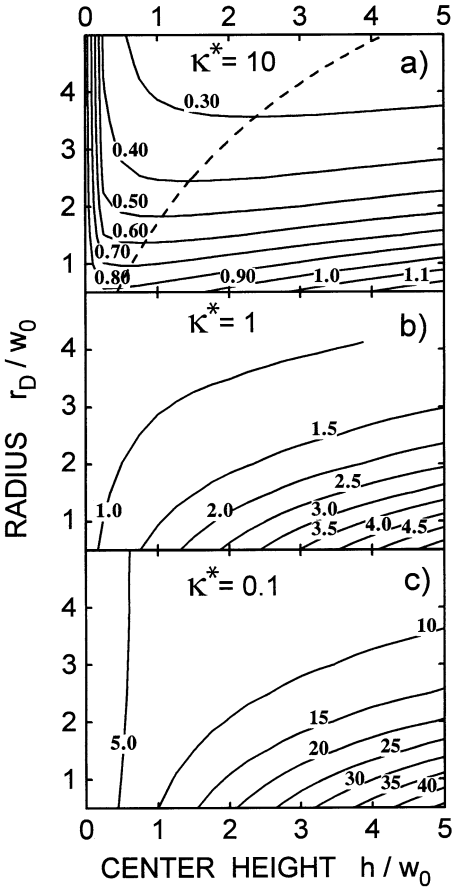

Fig. 16.4.2 a–c Normalized center-temperature rise at the top of the deposit $\Delta T(0, h)\kappa_s / I_0 A w_0$ as a function of the normalized height h/w_0 and radius r_D/w_0 for parabolic spots and for different κ^*. The geometry of the spot and the meaning of r_D and $h \equiv h_{max} = h(0, 0)$ are illustrated in Fig. 16.3.3d. Surface absorption within the deposit has been assumed. The position of *minima* in $\Delta T(0, h)$ for $r_D = \text{const.}$ (*dashed curve*) is shown [*Arnold* 1996]

Case 2: Influence of a Thin Layer and the Laser Focus: Cylinders with $r_D > w_0$, $\alpha_D \to \infty$, $h_1 \neq 0$

The *solid* curves in Fig. 16.4.3 show temperature distributions for a cylinder of radius r_D and height $h = r_D/10$, $h_1 \neq 0$, and $w_0 = r_D/3$ (Fig. 16.3.3a). In Fig. 16.4.3a, c, the intermediate layer has no influence on the temperature distribution. In Fig. 16.4.3b the layer h_1 is thermally insulating. The parameters employed are appropriate to a situation where a metal spot is deposited onto a metal or a Si substrate that is covered with an oxide layer. The curves were calculated for equal center temperatures which require *different* absorbed laser powers.

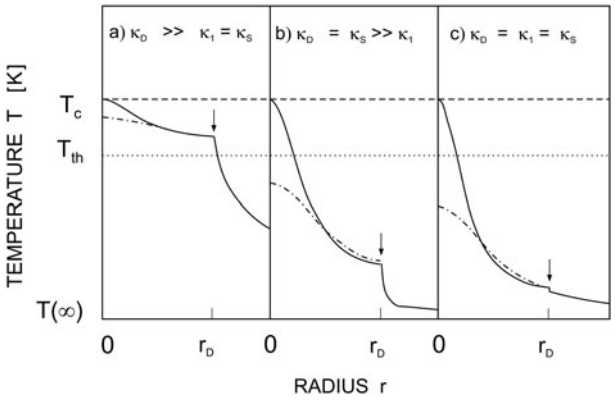

Fig. 16.4.3 a–c Temperature profiles calculated for the model structure depicted in Fig. 16.3.3a. Three different ratios of thermal conductivities and two different radii of the laser focus have been considered. The *solid curves* have been calculated for equal center temperature $T_c = 530\,\mathrm{K}$, with $h_D = r_D/10$ and $w_0 = r_D/3$, and $T(\infty) = 300\,\mathrm{K}$. T_{th} schematically indicates a threshold temperature. (**a**) $\kappa_D = 0.7\,\mathrm{W/cm\,K}$, $\kappa_1 = \kappa_s = 1.3 \times 10^{-2}\,\mathrm{W/cm\,K}$. (**b**) $\kappa_D = \kappa_s = 0.7\,\mathrm{W/cm\,K}$, $\kappa_1 = 1.3 \times 10^{-2}\,\mathrm{W/cm\,K}$, $h_1 = 4000\,\text{Å}$. (**c**) $\kappa_D = \kappa_1 = \kappa_s = 0.7\,\mathrm{W/cm\,K}$. *Dash-dotted curves*: $h = r_D/10$ and $w_0 = 2r_D/3$. All other parameters are the same as with the *solid curves* [*Bäuerle* 1984]

Temperature profiles calculated for the same parameter sets, but with twice the diameter of the laser focus, $w_0 = 2r_D/3$, are presented by *dash-dotted* curves. The change in center temperature is more pronounced in Fig. 16.4.3b, c than in Fig. 16.4.3a. As long as $r_D > w_0$, the temperature at the edge of spots, $\Delta T(r_D, h)$, remains almost unaffected.

Temperature distributions calculated for the case shown in Fig. 16.3.3c were given in *Piglmayer* and *Bäuerle* (1986).

16.5 Simulation of Pyrolytic Growth

We now consider the 2D model (Fig. 16.3.3d) with $h = h(x, y)$. The problem is then described by (16.3.1–3) with $v_s = 0$. Let us first assume $\alpha_D \to \infty$ and a *flat* deposit with $\partial h/\partial x, \partial h/\partial y \ll 1$.

Because changes in the laser-induced temperature distribution related to the geometry of the deposit are the more pronounced the more the ratio of thermal conductivities differs from unity, we consider $\kappa^* \equiv \kappa_D/\kappa_s \gg 1$. For flat structures we can write

$$\frac{\partial T_D}{\partial \hat{\boldsymbol{n}}} = \frac{\partial T_D}{\partial z} - \nabla_2 h \times \nabla_2 T_D \,. \tag{16.5.1}$$

Furthermore, we assume $T_D = T_D(x, y, z, t) \approx T_D(x, y, 0, t)$, which holds if $h/(r_D\kappa^*) \ll 1$ (this follows from $\kappa_D \partial T_D/\partial z = \kappa_s \partial T_s/\partial z$ and $\partial T_s/\partial z \approx [T_s(z = 0) - T(\infty)]/r_D$). In this case we can expand T_D in a Taylor series and take into account only the first term

$$T_D(z) = T_D(z = 0) + \mathcal{O}(z) \; . \tag{16.5.2}$$

With these additional approximations the original boundary-value problem (16.3.1) can be written as [*Arnold* and *Bäuerle* 1993]

$$\theta_s = \theta_s^0 + \frac{\kappa^*(T(\infty))}{2\pi} \left[\nabla_2 (h \nabla_2 \theta_D) * \frac{1}{|\boldsymbol{r}|} \right] , \tag{16.5.3}$$

where

$$\theta_s^0 = \frac{1}{2\pi\kappa_s(T(\infty))} \left(I_a * \frac{1}{|\boldsymbol{r}|} \right)$$

is the (linearized) temperature distribution without the deposit (Chap. 2). $\boldsymbol{r}$ is a 2D radius vector within the xy-plane, and $*$ denotes the convolution integral

$$f * g \equiv \int_{-\infty}^{+\infty} \int_{-\infty}^{+\infty} f(\boldsymbol{r}') g(\boldsymbol{r} - \boldsymbol{r}') \, \mathrm{d}x' \, \mathrm{d}y' \; .$$

θ_s^0 remains unchanged during growth as long as the reflectivity, R, stays constant. If R changes (16.5.3) is still valid. In this case, however, the computational time will increase significantly. At $z = 0$, the temperatures θ_s and θ_D are related via the condition

$$T_D(\theta_D) = T_s(\theta_s) \; , \tag{16.5.4}$$

i.e., $\theta_s = \theta_s(\theta_D)$. This dependence can be fitted by the polynomial

$$\theta_s = \theta_D + \beta\theta_D^2 + \ldots \; .$$

With this substitution, (16.5.3) becomes a non-linear integro-differential equation for the determination of θ_D. The real temperature is obtained from the inverse Kirchhoff transform $T(x, y) = T_D(\theta_D)$. The advantages of solving (16.5.3) instead of (16.3.1) are:

- The problem is 2D, but describes the temperature distribution in three dimensions.
- No boundary conditions need to be considered; they are included implicitly in θ_s and θ_D.
- Any temperature dependences in κ_D and κ_s can easily be taken into account.
- It is sufficient to calculate the convolution integrals within regions $h \neq 0$ and $I_a \neq 0$.

With (16.5.3) the shape of the deposits can be calculated from (16.3.2) with $v_s = 0$. The results of such calculations shall now be discussed for W and Ni spots deposited onto SiO_2 substrates. For convenience, we normalize h, x, y, and k_0 to the radius of the (Gaussian) laser beam, w_0. Temperatures and activation energies are normalized to $T(\infty)$. The normalized intensity is $I_0^* = I_0 w_0 / T(\infty)\kappa_s$.

Figure 16.5.1a shows the evolution of W spots together with surface temperature profiles. The kinetic data $k_0^* = 2.14$ and $\mathscr{E}^* = 5.68$ were taken from experimental investigations on the deposition of W from $WCl_6 + H_2$ [*Kullmer* et al. 1992]. The other parameters are $T_{th}^* = 2.71$, $\delta T_{th}^* = 0.01$, $T(\infty) = 443\,\mathrm{K}$, $\kappa^*(T(\infty)) = 50.56$ and $AI_0^* = 10.3$. The thermal conductivities were approximated by $\kappa_D(\mathrm{W}) = c_1 + c_2/T - c_3/T^2$, with $c_1 = 42.65\,\mathrm{W/mK}$, $c_2 = 1.898 \times 10^4\,\mathrm{W/m}$ and $c_3 =$

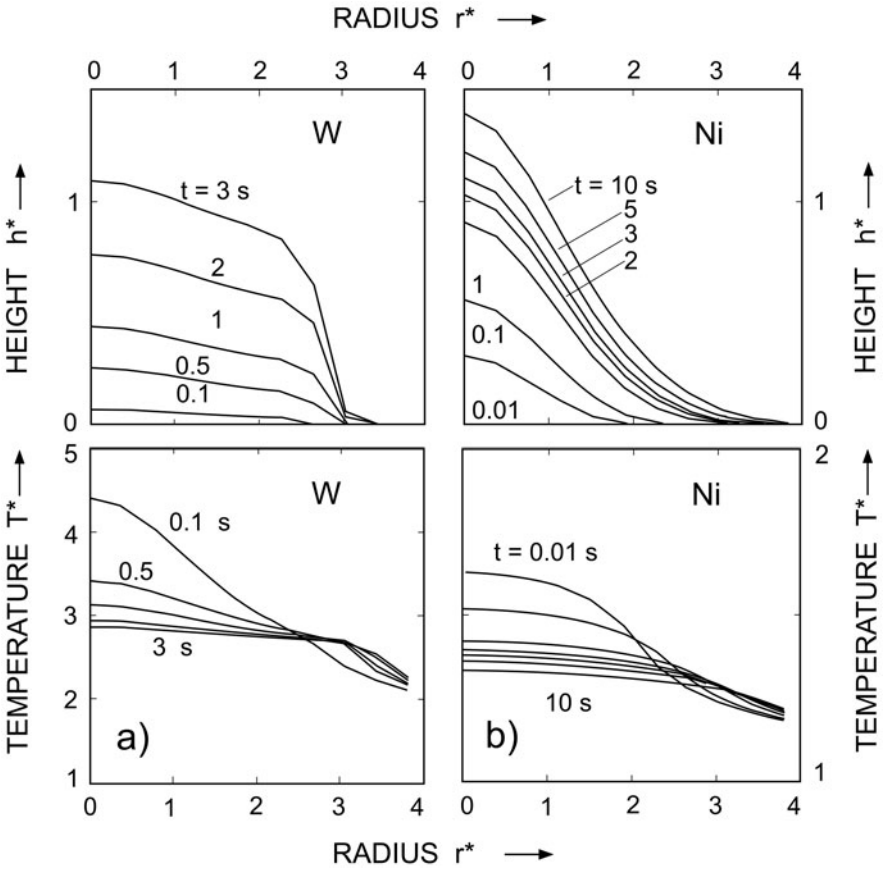

Fig. 16.5.1 Normalized height of spots calculated for various stages of growth as a function of the (normalized) distance from the laser-beam center. The parameters employed are typical for LCVD. The lower part of the picture shows the evolution of the (normalized) surface temperature distribution. (**a**) Deposition of W from $WCl_6 + H_2$. (**b**) Deposition of Ni from $Ni(CO)_4$ [*Arnold* and *Bäuerle* 1993]

$1.498 \times 10^6\,\mathrm{WK/m}$, and by $\kappa_s(SiO_2) = a_1 + a_2 T$, with $a_1 = 0.9094\,\mathrm{W/mK}$ and $a_2 = 1.422 \times 10^{-3}\,\mathrm{W/m\,K^2}$ [*Heraeus* 1979]. The Kirchhoff transform permits one to find the approximations

$$\theta_s^* \approx \theta_D^* + 0.46\theta_D^{*2} \quad \text{and} \quad T_D^* \approx 1 + \theta_D^* + 0.12\theta_D^{*2}\,.$$

The saturation in width is reached faster than in height, mainly due to the small value of δT_{th}. This is in agreement with experimental observations (Fig. 16.2.3a). Within a short time, the temperature becomes almost uniform over the surface of the spot, as expected from the simple model developed in the previous section.

Figure 16.5.1b displays growth profiles for Ni spots. Here, no threshold was assumed and the thermal conductivities were kept constant [$\kappa^*(T(\infty) = 300\,\mathrm{K}) = 30$]. The kinetic data, $k_0^* = 1.1 \times 10^{13}$ and $\mathscr{E}^* = 45(27\,\mathrm{kcal/mol})$, correspond to pyrolytic decomposition of $Ni(CO)_4$. The other parameters employed were $T(\infty) = 300\,\mathrm{K}$ and $AI_0^* = 1.33$. Due to the absence of a threshold, there is *no* abrupt saturation in width. Furthermore, the aspect ratio $\Gamma = h/d$ is bigger than for W. This is related to the higher activation energy which causes faster growth in the center than near the edge. The calculated shape is in qualitative agreement with experimental observations (Fig. 16.5.2).

When the deposit grows in height and becomes thermally *thick*, the temperature gradient in z-direction cannot be ignored any further. When the height h/w_0, at constant width r_D/w_0, crosses the dashed line in Fig. 16.4.2a, the temperature at the top of the spot *increases* and explosive growth resulting in the formation of a fiber is observed (Chap. 17, Sect. 28.3.6). The onset of this regime can be seen in Fig. 16.5.2.

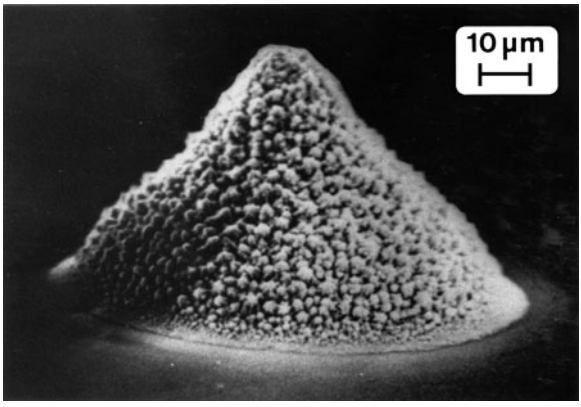

Fig. 16.5.2 SEM picture of a Ni spot deposited from $Ni(CO)_4$ onto a 1,000 Å a-Si/glass substrate [*Piglmayer* and *Bäuerle* 1986]

16.6 Photolytic LCVD

Photolytic LCVD is based on *selective* excitations of precursor molecules. In many systems, decomposition of molecules takes place in the gas phase within the total volume of the laser beam (Fig. 1.2.2). The product species diffuse and condense, in part, on the substrate surface. Photolytic LCVD can therefore be employed for *thin-film* formation at relatively low substrate temperatures. Today, this is its main application (Chap. 19).

Single-step production of *microstructures* based on photolytic LCVD has also been demonstrated. With the systems investigated, the spatial confinement of deposits is closely related to physisorbed layers of parent molecules, and to nucleation processes. Here, adsorbed-layer photolysis significantly contributes or even dominates the deposition process. In systems where physisorption is weak, spatially well-defined direct patterning by photolytic LCVD is impossible.

Fabrication of microstructures based on selective *electronic* excitations has been studied mainly for metal-alkyls and metal-carbonyls. These compounds are readily available, have a relatively high vapor pressure at ambient or slightly elevated temperatures, and can be decomposed by single-photon or sequential multiphoton excitation in the near to medium UV. This spectral range can easily be reached by frequency doubling of cw-Ar^+- or Kr^+-laser lines, by excimer lasers, or by higher harmonics of Nd:YAG lasers. Other precursors frequently employed are organic coordination complexes, in particular, various acetylacetonates, which can be designed for particular applications.

Photolysis by coherent multiphoton electronic excitations is only of limited value for controlled deposition of micrometer-sized patterns, mainly because of the high laser-light intensities required.

At present, there is *no* clear example for the deposition of microstructures based on selective multiphoton vibrational excitations using IR radiation. This is quite understandable from Sect. 2.3.2. In any case, this excitation mechanism would not permit one to achieve the resolution obtained with VIS or UV radiation.

It should be noted that in many of the experiments reported, the laser- light intensities employed are high enough to induce a significant temperature rise. Thus, much of the experimental data should be analyzed on the basis of a combined photochemical–photothermal (photophysical) model.

16.6.1 Metals

Photolytic LCVD of metals from *alkyls* has been most thoroughly studied for $Cd(CH_3)_2$ and $Al_2(CH_3)_6$. These (model) compounds can be dissociated by single-photon excitation in the near UV and their photochemistry is well known [*Price* 1972]. Dissociation of $Cd(CH_3)_2$ by single-photon excitation with 257 nm Ar^+-laser radiation can be described by

$$Cd(CH_3)_2 + h\nu(257\,\text{nm}) \rightarrow Cd(^1S_0) + 2CH_3\ . \qquad (16.6.1)$$

The free methyl radicals subsequently react and form volatile hydrocarbons such as ethane. Photolysis can take place within the gas and on the surface. The latter mechanism requires adsorbed $Cd(CH_3)_2$ molecules. Adsorbed-layer photolysis determines the confinement of the deposition process. In other words, metal atoms generated within the gas condense, preferentially, within the irradiated area (see also Chaps. 4, 5, and 20).

Figure 16.6.1 shows the (thickness) deposition rate for Cd spots versus laser-light intensity. The linear increase reflects single-photon dissociation. At very low laser fluences, the threshold for surface nucleation prevents deposition. At much higher fluences than those shown in the figure, the deposition rate saturates due to mass-transport limitations. This effect is more pronounced when a buffer gas is used. Mass transport could be increased by employing a gas flow. Deposition rates for Cd of up to 0.1 μm/s have been measured at UV intensities of about 10^4 W/cm^2. Direct writing of lines with widths as small as 0.7 μm has also been demonstrated.

Thermal and photochemical decomposition of $Al_2(CH_3)_6$ has been investigated by *Suzuki* et al. (1986), and others. Direct writing of Al lines with widths of 2–3 μm was demonstrated for different substrate materials. Deposition rates up to 0.1 μm/s and scanning speeds up to a few μm/s have been achieved.

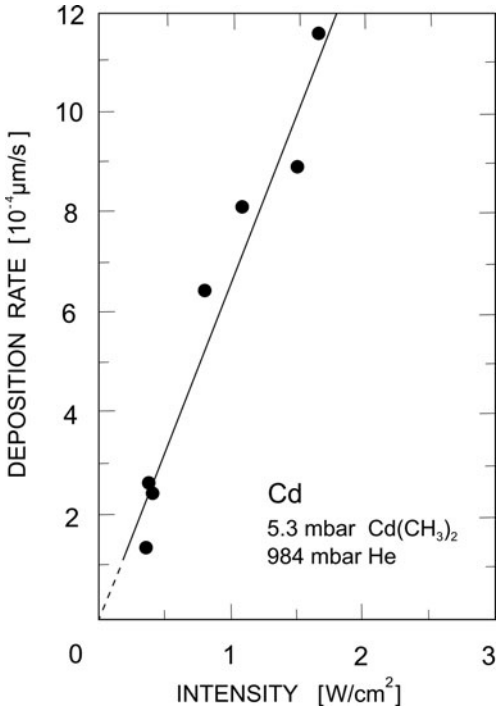

Fig. 16.6.1 Deposition rate for Cd spots versus Ar^+-laser light intensity ($\lambda = 257$ nm). Helium was used as buffer gas [*Ehrlich* et al. 1982]

Photolytic deposition was also studied with other precursors, such as $Ga(CH_3)_3$, $In(CH_3)_3$, $Te_2(CH_3)_2$, $Zn(CH_3)_2$, $Zn(C_2H_5)_2$ [*Eden* 1991 and references therein].

Deposition from Carbonyls

Metal carbonyls such as $Ni(CO)_4$, $Fe(CO)_5$, $Cr(CO)_6$, $Mo(CO)_6$, and $W(CO)_6$ are used for metal deposition in the form of microstructures and extended thin films. For many metal carbonyls, molecular fragmentation begins to occur in the near UV at wavelengths $\lambda < 350\,\text{nm}$. For cw- and pulsed-laser irradiation at low power densities, decomposition seems to be based on *sequential* elimination of CO ligands by single-photon processes:

$$\begin{array}{lll} \text{Me(CO)}_m & + h\nu \rightarrow \text{Me(CO)}^*_{m-1} & + \text{CO}\,, \\ \text{Me(CO)}^*_{m-1} & + h\nu \rightarrow \text{Me(CO)}^*_{m-2} & + \text{CO}\,, \\ \vdots & \vdots \quad \vdots & \vdots \\ \text{Me(CO)}^* & + h\nu \rightarrow \text{Me}^* & + \text{CO}\,, \end{array} \tag{16.6.2}$$

where the asterisk indicates internal vibrational and possibly electronic excitations. Due to the high gas pressures employed in LCVD, or due to molecule–substrate interactions, stripping of the remaining ligands, for example, after absorption of one or two photons, can also occur via collisions. Focused high-power pulsed-laser excitation may favor *coherent* multiphoton photochemistry rather than sequential single-photon photochemistry.

Laser-induced deposition of metals by photolysis of carbonyls has been studied by many researchers. The literature on the most important investigations is included in *Bäuerle* (2000). Investigations on the deposition of Cr, Mo, and W were performed by *Singmaster* et al. (1990). These experiments employed 257 nm Ar^+-laser radiation and Si substrates. With the laser powers employed, the estimated temperature rise on the substrate was $< 50\,\text{K}$. The intrinsic compositions of deposits, as determined by scanning Auger microscopy, were found to be independent of the laser power. Auger analysis of deposits provides information on surface photodissociation and dissociative chemisorption of species. Chemical differences are observed only for the Cr system where the laser-light forces additional desorption of CO. Thus, metal-carbonyl fragments adsorbed on the spot surface lose CO groups spontaneously. The remaining CO forms metal-oxycarbide in the case of Mo and W, and an oxide mixed with amorphous or graphitic carbon in the case of Cr.

The deposits show columnar structure and, in the case of Mo and W, many cracks. For all three materials, deep ripples are observed (Sect. 28.2). Addition of N_2 buffer gas results in a delocalization of the deposit. This situation is quite similar to that described for pyrolytic deposition of W from $WF_6 + H_2$ in the presence of Ar (Sect. 16.2). The initial deposition rates achieved with laser-light intensities of $3 \times 10^3\,\text{W/cm}^2$ are around 0.2–0.4 μm/s for Cr and Mo, and about one order of magnitude smaller for W. Without window purge, the rates decrease rapidly due to

attenuation of the laser-light intensity by material deposited on the windows of the reaction chamber.

Organo-Metallic Coordination Complexes

Various organic coordination complexes, and, in particular, different acetylacetonates, have been used to deposit Au, Cu, Ir, Pt, etc. *Baum* et al. (1991) demonstrated substrate patterning with Au by direct writing and laser-light projection. Typical deposition rates were a few Å/s. Feature sizes as small as about 2 μm were achieved.

16.6.2 Other Materials

There are only very few investigations on photolytic LCVD of semiconductors and insulators as microstructures. Among them is the projection printing of 10 μm wide SiO_2 patterns by ArF-laser photolysis of $Si_2H_6+N_2O/N_2$ [*Hiura* et al. 1991]. However, the real decomposition mechanism has not yet been investigated.

16.6.3 Process Limitations

Deposition rates that are attractive for applications can only be achieved when the laser wavelength matches a transition which results in efficient decomposition of the molecule. For many molecules which would be suitable for photolytic LCVD, such transitions are located in the medium-to-far UV, where, at present, only a few powerful lasers are available. There are, however, more fundamental and thus more severe limitations: one is the tendency for homogeneous cluster formation at higher laser-light intensities or partial pressures of reactants. Clusters may condense everywhere on the substrate and on the walls of the reaction chamber, including entrance windows. Then, controlled deposition becomes impossible. For these reasons, deposition rates achieved in photolytic LCVD will always be lower than those in pyrolytic LCVD. Another limitation concerns the purity of deposits. Photoproducts, including incompletely decomposed precursors, are often incorporated into the deposit with high concentrations. These can only be reduced by substrate heating.

Controlled growth in UV-laser photodeposition of metals is observed for laser-beam intensities of, typically, $1-10^4\ W/cm^2$, and for gas pressures between 0.1 and 100 mbar. Typical deposition rates are 0.001 to some 0.1 μm/s. These rates are by a factor of 10^2-10^4 smaller than those in pyrolytic LCVD. The lateral resolution achieved in photolytic deposition of stripes was of the order of 0.1 μm. It should be emphasized, however, that for the aforementioned reasons broad tails, thin films, or big clusters of material are frequently observed around the deposit. The main advantage of photolytic LCVD is the lower local processing temperature and the smaller influence of the physical properties of the substrate. On the other hand, without uniform substrate heating, the microstructure and purity of photodeposited materials, and thus their electrical properties, are unsatisfactory.

Chapter 17
Growth of Fibers

As demonstrated in the preceding chapter, lateral growth of photothermally deposited spots saturates for long laser-beam illumination times, τ_ℓ. With certain systems and within certain parameter ranges, this saturation is accompanied by an increase in axial growth and the formation of a fiber along the axis of the laser beam. A typical fiber is shown in Fig. 17.0.1 with the example of Si. Two phases of growth can be observed. Near the onset, the deposition rate depends strongly on the physical properties of the substrate. Under quasi-stationary conditions, as characterized by a constant fiber diameter, the temperature in the tip becomes independent of substrate material and time. For this reason, the temperature can be measured in situ with high precision.

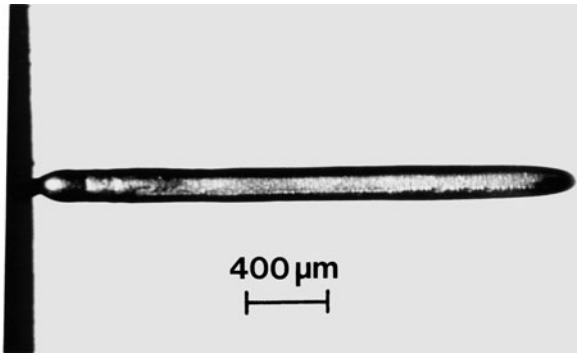

Fig. 17.0.1 Silicon fiber grown from SiH_4 by means of 488 nm Ar^+-laser radiation ($P = 400$ mW, $p \equiv p(SiH_4) = 133$ mbar) [*Bäuerle* et al. 1983a]

The maximum growth rate occurs at the center of the tip, and it is equal to the axial growth velocity, v_a. Therefore, the deposition rate can be defined as the growth in length of the fiber per unit time

$$W_D(T) = v_a(T) \equiv v(r = 0, T) = \frac{\Delta h(r = 0, T)}{\Delta t} \,. \qquad (17.0.1)$$

D. Bäuerle, *Laser Processing and Chemistry,* 4th ed.,
DOI 10.1007/978-3-642-17613-5_17, © Springer-Verlag Berlin Heidelberg 2011

With partial pressures of precursor gases of up to 1 bar, the axial growth rates are, typically, 10−100 μm/s. With higher pressures, growth rates up to 10^3 μm/s have been achieved.

Because of the high deposition rates and the possibility of in situ temperature measurements, the growth of fibers is a *unique* technique for both rapid determination of apparent chemical activation energies and investigations of gas-phase processes. Due to the localization of the laser-induced temperature distribution, such investigations can be performed up to temperature regimes and gas pressures that cannot be reached by any standard technique. Furthermore, materials can be grown under strong nonequilibrium conditions and in strong external magnetic or electric fields. Cooling rates in excess of 10^{12} K/s that can be achieved with pulsed lasers permit to deposit materials with nonequilibrium microscopic structures (arrangement of atoms) or chemically new compositions that cannot be synthesized by any other technique.

17.1 In Situ Temperature Measurements

An experimental setup employed for *in situ* temperature measurements during steady growth of fibers is schematically depicted in Fig. 17.1.1. The beam is focused onto the tip of the growing fiber.

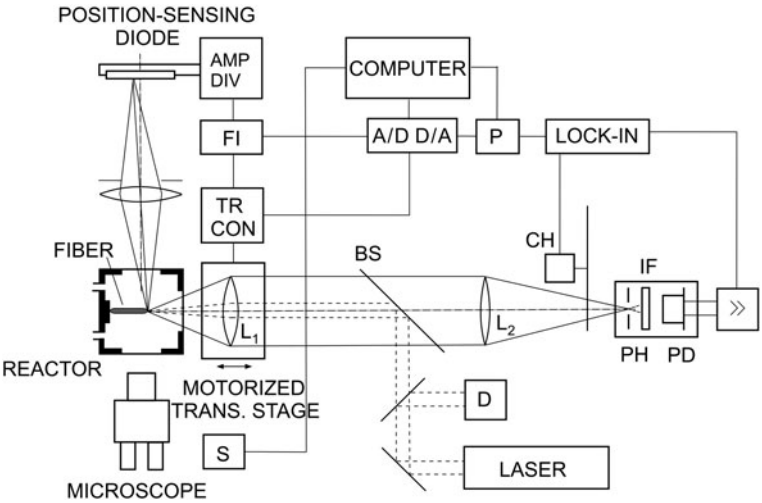

Fig. 17.1.1 Experimental setup employed for in situ temperature measurements during LCVD of fibers. AMP DIV: amplifier and analog divider, BS: beamsplitter, CH: light chopper, D: power meter, FI: electronic filter, P: peak detector, PD: Si photodiode, PH: pinhole, S: switch, TR CON: translation control [*Doppelbauer* and *Bäuerle* 1986]

To achieve quasi-stationary conditions, the lens L_1 is moved with the velocity v_a as defined by (17.0.1). Thus, the tip of the fiber is always located within the focal plane.

For *monochromatic* pyrometry the thermal radiation emitted from the hot tip of the fiber is collected by the focusing lens L_1, transmitted through the beam-splitter (BS) and focused with a lens, L_2, onto a pinhole (PH). The spatial resolution of the measurements is, typically, a few microns. The light transmitted by the pinhole and the interference filter (IF) is detected.

During deposition of pyrolytic carbon by means of 488 nm cw Ar^+-laser radiation, temperature measurements between 2000 and 3000 K were performed at a center wavelength of 700 nm. With silicon fibers grown between 1100 and 1700 K, the center wavelength was 1000 nm. In both cases, a bandpass of 10 nm was employed. The radiation was detected by a high-quality silicon photodiode whose output was measured by means of a lock-in amplifier. A tungsten band lamp was employed to calibrate the response of the detection system. From the measured spectral intensity of the thermal radiation, the local temperature was evaluated by using Planck's law (Sect. 29.4). The angular dependence of the emissivity was ignored. Because the radiation flux depends non-linearly on temperature, the temperature evaluated in these measurements essentially represents the *maximum* temperature in the center of the fiber tip, i.e., $T \equiv T_D(r = 0)$.

For measurements on carbon fibers, a constant emissivity, $\varepsilon = 0.85$, was used. For silicon, the linear relation $\varepsilon(T) = 0.946 - (2.76 \times 10^{-4})T$ was employed within the range $1000\,\mathrm{K} < T < 1688\,\mathrm{K}$ [*Lampert* et al. 1981; *Sato* 1967; *Allen* 1957].

The standard deviations in temperatures evaluated were, typically, about 10 K for C fibers and about 5 K for Si fibers.

For temperatures $T > 2300\,\mathrm{K}$, the axial growth rate of C fibers was measured by imaging the thermal radiation emitted from the hot tip of the fiber onto a position-sensing photodiode placed perpendicular to the fiber axis. The output of this diode was simultaneously used to control the distance between the focusing lens and the fiber tip. In this way, quasi-stationary conditions are achieved. For temperatures below 2300 K, the growth rate could be measured more precisely by means of a microscope.

17.2 Microstructure and Physical Properties

The morphology and microstructure of fibers depend on the laser-induced temperature and on the gas pressure. They have been studied mainly by optical microscopy, scanning electron microscopy, X-ray diffraction, and Raman scattering. Fibers of various different metals, metal alloys, semiconductors, and insulators have been grown in amorphous, polycrystalline, and single-crystalline forms. Among the materials studied in most detail are: amorphous B [*Boman* and *Bäuerle* 1995; *Wallenberger* et al. 1994], B_xC_y [*Maxwell* et al. 2007], C [*Maxwell* et al. 2005], Al_xO_y [*Wanke* et al. 1997], SiO_x and SiO_2 [*Szikora* et al. 1984], etc.; polycrystalline

fibers of Ni and Ni/Fe alloys [*Maxwell* et al. 1996, *Kräuter* et al. 1983, *Bäuerle* 1983], C [*Goduguchinta* and *Pegna* 2007; *Maxwell* et al. 2006; *Doppelbauer* 1987, *Leyendecker* et al. 1983b, 1981], Si [*Kargl* et al. 1997; *Bäuerle* et al. 1982a, b], SiC and Si_XN_y [*Wallenberger* et al. 1994]; single crystalline fibers of B [*Boman* and *Bäuerle* 1995], Cr_2O_3 [*Arnone* et al. 1986], Si [*Bäuerle* et al. 1983], and W [*Boman* and *Bäuerle* 1987].

The growth of fibers *within* a photocurable organic-inorganic resin (ORMOCER) was studied by *Hidai* et al. (2008). With 523 nm fiber-laser radiation ($\tau_\ell < 500$ fs; 10^6 pps) growth rates of up to 2 mm/s have been achieved. The process is based on 2-photon photopolymerization (Sect. 27.2).

Figure 17.2.1 shows SEM pictures of single-crystal fibers of Si and W. The Si fiber was grown from SiH_4 at 1650 K with 530.9 nm Kr^+-laser radiation. The orientation of the fiber axis was found to be close to either [100] or [110], which are the fastest directions of growth in crystalline Si. With a silane pressure of $p \equiv p(SiH_4) = 133$ mbar, single-crystal growth was observed only above 1560 K. In this context, it is interesting to recall the microstructure of Si films grown on single-crystal Si substrates by standard CVD. Here, the regime of polycrystalline growth is separated from the regime of single-crystal growth by a border line (dashed line in Fig. 17.2.2). This line is determined by the flux of Si atoms giving rise to the observed growth rate, and the time for surface diffusion needed to arrange the arriving atoms on proper lattice sites. Linear extrapolation of this border line to higher temperatures yields an intersection point with the LCVD curve at about 1555 K. This value is in remarkably good agreement with the temperature limit found for single-crystal growth of Si fibers. The orientation of the W fiber shown in Fig. 17.2.1b is [001] with [110] facets.

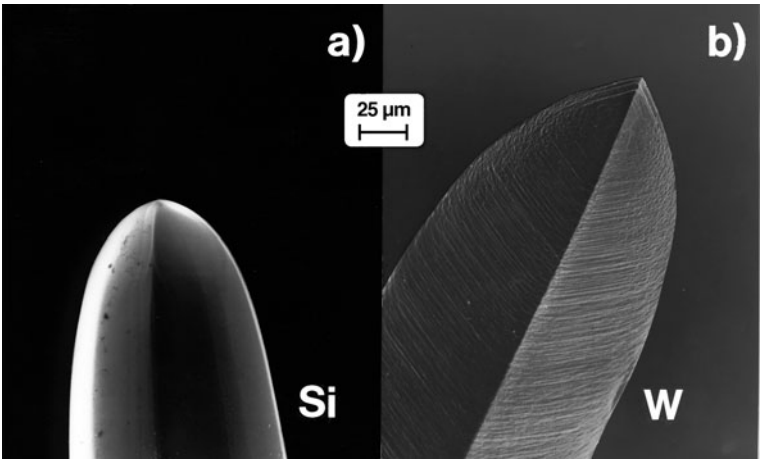

Fig. 17.2.1 a, b SEM pictures of the tip of laser-grown single-crystalline fibers. (**a**) Si grown from SiH_4 [*Bäuerle* et al. 1983]; (**b**) W grown from $WF_6 + H_2$ (*Boman* and *Bäuerle* 1987, unpublished)

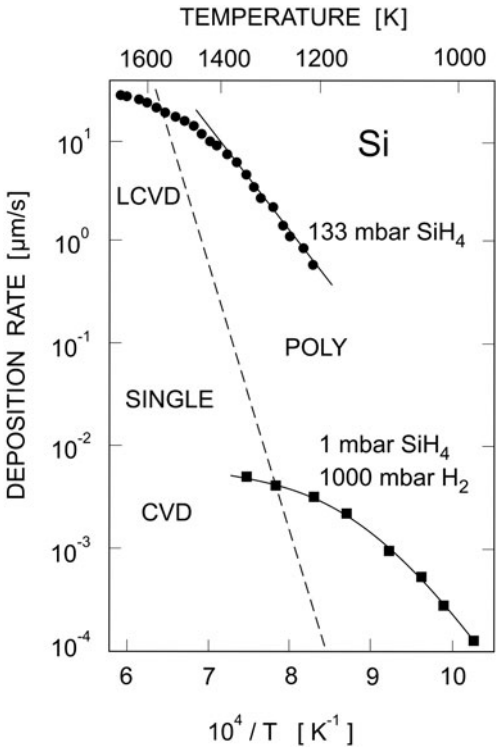

Fig. 17.2.2 Arrhenius plot for the growth of Si from SiH_4 by LCVD and standard CVD. Regions of single-crystal and polycrystalline growth are shown (separated by *dashed line*); the intersection points of the LCVD and CVD curves are at 1555 K and 1262 K, respectively [*Bäuerle* 1983b]

With gas pressures up to several bars (Table 17.3.1) fiber growth rates up to several 10^3 µm/s have been achieved. The tensile strengths of fibers with diameters of approximately 25 µm were up to 7.6 GPa for B, 3 GPa for C, and about 2 GPa for SiC [*Wallenberger* et al. 1994]. The Vickers hardness of B_xC_y fibers was up to 43.5 ± 1.5 GPa [*Maxwell* et al. 2007]. Carbon fibers have been grown with different types of microstructures, including DLC, nc-graphite, and glassy carbon [*Maxwell* et al. 2006, 2005].

Potential applications of 3D objects grown by LCVD are discussed in Sect. 18.5.

17.3 Kinetic Studies

Investigations on the steady growth of fibers yield accurate information on the chemical kinetics in pyrolytic LCVD. The systems investigated in most detail are listed in Table 17.3.1. Non-integral reaction orders indicate that the decomposition of precursor molecules includes different reaction channels, and that the activation energy depends on temperature (Sect. 3.1).

Table 17.3.1 Activation energies and reaction orders derived from steady growth of fibers

Material	Precursor	Temp. range (10^3 K)	Pressure range (bar)	Activation energy (kcal/mol)	Reaction orders	Reference
B	BCl_3+ H_2	1.1–2.3	(0.05–0.4)+ (0.05–0.8)	26.5 ± 1	< 1	*Boman* and *Bäuerle* (1995)
B_xC_y	B_2H_6+ C_5H_{20}+ He	2.7–3.8	2.1–2.9	47.1±6.5		*Maxwell* et al. (2007)
C	CH_4	2.85–3.1	0.5–1	119 ± 2	1.25	*Leyendecker* et al. (1983b)
		2.4–2.75	0.5–1	43.5±1.4	2.2	
	C_2H_2	1.9–2.45	0.05–1	47.3±0.6	0.8	*Leyendecker* et al. (1981, 1983b)
	C_2H_4	2.0–2.25	0.3–1	58.3±1.3	0.8	*Doppelbauer* (1987)
	C_2H_6	2.2–2.65	0.3–1	78.9 ± 4	2	*Doppelbauer* (1987)
C	C_nH_{2n}	1.3–3.3	1.5–4		1.45–1.9	*Maxwell* et al. (2006)
	C_nH_{2n-2}	1.5–2.5	1.5–4		3.07–4.51	*Maxwell* et al. (2006)
	C_6H_6		1.5–4		2.25	*Maxwell* et al. (2006)
Si	SiH_4	1.15–1.35	0.03–0.3	43.5 ± 1	0.6	*Bäuerle* et al. (1982a, b)
	Si_2H_6	1.3–1.4	0.05	40		*Kargl* et al. (1997)
W	$WF_6 + H_2$		(0.005) + (0.01)			*Boman* and *Bäuerle* (1987)

17.3.1 Silicon

Figure 17.2.2 shows an Arrhenius plot for the growth of Si from SiH_4. The upper curve refers to data obtained for pyrolytic LCVD of Si fibers. The temperature was measured in situ (Sect. 17.1). In the kinetically controlled regime, which reaches up to about 1400 K, the deposition rate increases exponentially with temperature and is characterized by an apparent chemical activation energy $\Delta E = 44 \pm 4$ kcal/mol (this value is not corrected for the temperature dependence of the pre-exponential factor [*Leyendecker* et al. 1983b]). The decrease in slope observed above 1400 K is probably due to mass transport limitation. The lower part of the figure shows the deposition rate obtained by standard CVD of Si from SiH_4 with H_2 as carrier gas [*v.d. Brekel* 1978]. A comparison of curves shows remarkable differences between localized and large-area CVD: the localization of the temperature distribution permits one to study the deposition process up to higher temperatures and much higher pressures of reactant molecules.

17.3.2 Carbon

The precursors employed for the growth of carbon fibers are C_2H_2, C_2H_4, C_2H_6 and CH_4. Figure 17.3.1a displays an Arrhenius plot of the axial growth rate for various pressures of C_2H_2. The diameter of fibers, $d = 2r_D$, increases almost linearly with laser power (Fig. 17.3.1b).

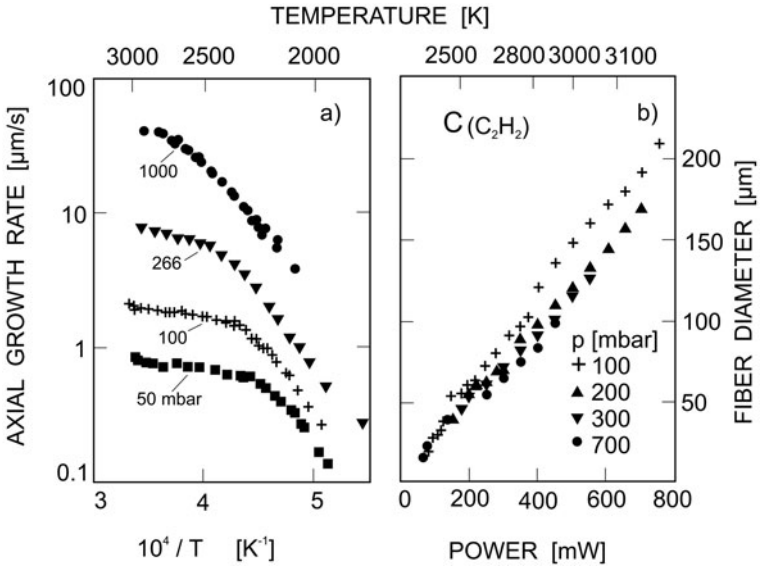

Fig. 17.3.1 a, b Ar^+-laser-induced growth of C fibers from (pure) C_2H_2 at various pressures. (**a**) Arrhenius plot ($\lambda = 488\,\text{nm}$, $w_0 \approx 10\,\mu\text{m}$), adapted from [*Leyendecker* et al. 1983b and *Doppelbauer* 1987]. (**b**) Diameter of fibers. Here, the temperature scale refers to the 300 mbar data only; adapted from *Doppelbauer* (1987)

The activation energies derived from these investigations are also relevant to CVD and gas-phase epitaxy. The determination of ΔE via the standard techniques is very time-consuming and problematic because a number of parameters, such as the substrate temperature, gas velocity, and gas mixture must be kept constant over long time periods; for this reason, only a small number of data points can be obtained. However, because of the strong temperature gradients in LCVD, the activation energies are *not* necessarily equal to those derived from CVD experiments. Nevertheless, the deviations are probably small and below the inaccuracies in measurements.

17.4 Gas-Phase Transport

Investigations of the steady growth of fibers permit one to analyze contributions of different transport mechanisms to the growth rate. Because growth takes place mainly at the tip of fibers, the reaction zone can be described by a hemisphere (Sect. 3.4). In order to avoid confusion, we denote the temperature within the gas by T and the temperature in the tip of the fiber by T_S.

17.4.1 The Coupling of Fluxes

In pyrolytic LCVD, strong temperature gradients near the deposit may strongly influence the gas-phase transport of species. Such temperature gradients together

with temperature and concentration dependences of the transport coefficients result in a coupling of fluxes. Let us consider a first-order non-equimolecular purely heterogeneous reaction of type (3.4.2) with $q = 1$, $\kappa = \text{const.}$, and $D_{AB} \propto T^n$ (Sect. 3.3). From (3.4.3) and (3.4.7) we obtain for the average velocity of the gas

$$v^*(r^*) = \frac{b x_{AB}(1)}{r^{*2}} \frac{T^*}{T_s^*} \exp\left(-\frac{\mathscr{E}^*}{T_s^*}\right) . \tag{17.4.1}$$

For an equimolecular reaction ($b = 0$) chemical convection is absent and $v^* = 0$. The temperature distribution within the gas is obtained from (3.4.5) and (3.4.8):

$$T^*(r^*) = 1 + \frac{T_s^* - 1}{1 - \exp(-\zeta)} \left[1 - \exp\left(-\frac{\zeta}{r^*}\right)\right] , \tag{17.4.2}$$

where

$$\zeta = \frac{b\gamma k_0^* x_{AB}(1)}{T_s^*} \xi \exp\left(-\frac{\mathscr{E}^*}{T_s^*}\right) , \tag{17.4.3}$$

where $\gamma \equiv c_p/c_v$. Henceforth, we set $\xi = c_v D_{AB}(\infty) N(\infty)/\kappa = 1$. Figure 17.4.1 shows the gas-phase temperature calculated for $T_s^* = 10$, and for various values of b and the (normalized) thermal diffusion coefficient $\alpha_T^* = k_T/x_{AB}$. The parameter values employed for $\mathscr{E}^*$ and k_0^* describe, approximately, the deposition kinetics of carbon from various hydrocarbons of the type C_xH_y, and of silicon from SiH_4. Carrier gases that have been investigated are mainly H_2, He, and Ar. For $b = 0$ (dotted curve), T is independent of α_T^*. The full and dashed curves, calculated for $b = 3$ and 5, refer to values of $\alpha_T^* = -0.3$ and $\alpha_T^* = +0.3$, respectively. In both cases, $\alpha_T^* > 0$ and $\alpha_T^* < 0$, chemical convection increases the heat flux to regions outside of the reaction zone. If $\alpha_T^* < 0$, the temperature distribution even changes shape, in particular for large values of b. If $b < 0$, the curve is slightly below that for $b = 0$. The effect of additional gas-phase heating by chemical convection with $b > 0$ becomes more pronounced with decreasing values of α_T^*. This originates from the coupling between thermal diffusion and chemical convection. Negative values of α_T^* result in an enrichment of reactant molecules at the surface $r = r_D$ and, thereby, in an enhancement of the reaction rate, which, in turn, increases the flux of product molecules away from this surface. With decreasing temperature T_s^*, these phenomena become less important. With the same parameter values but temperatures $T_s^* \leq 5$, the temperature distribution becomes almost independent of b and α_T^* and close to the form $T^*(r^*) = 1 + (T_s^* - 1)/r^*$, which is obtained with $b = 0$.

Figure 17.4.2 exhibits the normalized ratio $x_{AB}^*(1) = x_{AB}(1)/x_{AB}(\infty)$ as a function of b for various values of α_T^*, $T_s^* = 10$ and $n = 3/2$. With a fixed value of b, $x_{AB}^*(1)$ increases with decreasing α_T^*. This is a consequence of thermal diffusion. The dependence of $x_{AB}^*(1)$ on b is more complex. Here, $x_{AB}^*(1)$ can decrease or increase with increasing b, depending on α_T^*. Thus, the chemical convection can decrease or increase the reaction rate. This behavior is by no means obvious. In any

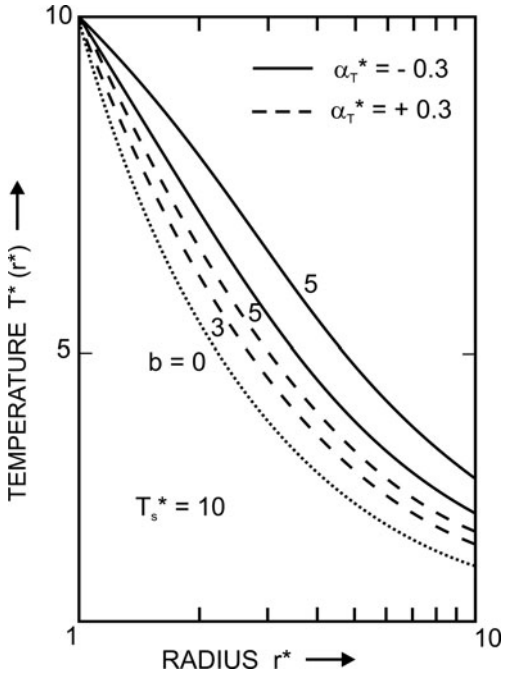

Fig. 17.4.1 Distribution of gas-phase temperature for $T_s^* = T_s/T(\infty) = 10$ with $T(\infty) = 300\,\mathrm{K}$ and various values of b. For $b = 0$, the curvature is independent of α_T^* (*dotted curve*). The other parameters employed were $\mathscr{E}^* = 90\,(54\,\mathrm{kcal/mol})$, $k_0^* = 5 \times 10^6$, $x_{AB}(\infty) = 0.1$, and $\gamma = 5/3$ [*Luk'yanchuk* et al. 1992]

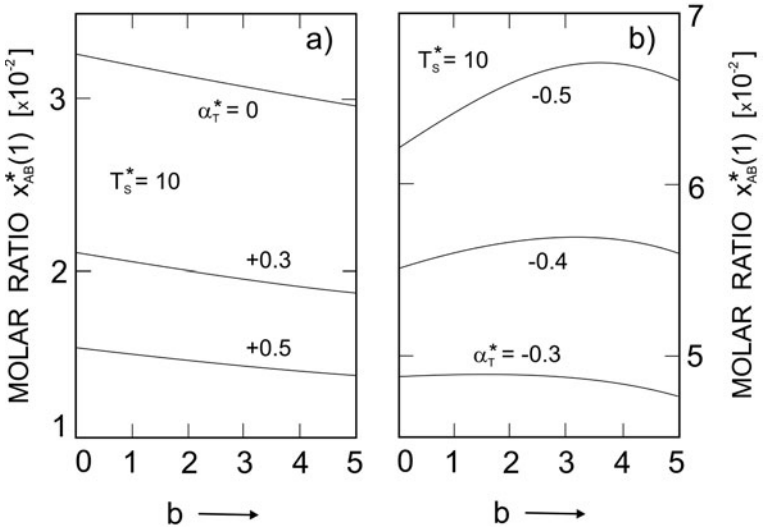

Fig. 17.4.2 a, b Molar ratio at the surface of the reaction zone, $x_{AB}^*(1)$, as a function of b for $T_s^* = 10$ and various values of α_T^* [*Luk'yanchuk* et al. 1992]

case, the effect of chemical convection is diminished by the coupling of fluxes. From a practical point of view the results demonstrate that for *high* substrate temperatures the influence of chemical convection is small for both $\alpha_T^* > 0$ and $\alpha_T^* < 0$. In other words, with molecules like C_2H_6, WF_6, $Mo(CO)_6$, etc., high deposition rates can be obtained in spite of strong chemical convection. The inverted behavior of $x_{AB}^*(1)$ observed for values $\alpha_T^* < 0$ is quite interesting. Here, chemical convection *increases* the reaction rate. This is a consequence of the spatial extension of the temperature profile and the temperature dependence of the molecular diffusion coefficient, D_{AB}. This effect strongly increases with decreasing (more negative) values of α_T^* and increasing exponents n, which, in certain cases, can exceed the value 3/2. For values of n close to 2 inversion exists even for $\alpha_T^* = 0$. In other words, for gas mixtures where the mass of carrier-gas molecules, m_M, exceeds the mass of reactant molecules, m_{AB}, chemical convection can even increase the reaction rate. A practical example of such a situation is the deposition of C from mixtures of C_xH_y with Ar, Xe, etc. Thus, the coupling of ordinary non-isothermal diffusion, thermal diffusion, and chemical convection can result in non-trivial dependences of the temperature and concentration profiles. In particular, this coupling can result in inversion effects in the process kinetics.

17.4.2 Thermal Diffusion (Soret Effect)

The influence of thermal diffusion on the gas-phase distribution of constituents can most easily be studied for an equimolecular reaction ($b = 0$). The model employed is the same as in Sect. 3.4. The main features of the solution of the boundary-value problem are summarized in Figs. 17.4.3 and 17.4.4. Details of the calculations are presented in *Bäuerle* et al. (1990) and *Kirichenko* et al. (1990).

Figure 17.4.3a shows the molar ratio $x_{AB}(r_D)$ as a function of the normalized temperature T_s^* with $x_{AB}(\infty) = 0.1$. The case $k_0^* \to 0$ characterizes the kinetically controlled regime where

$$x_{AB}(r_D) \approx \left(1 + \frac{1 - x_{AB}(\infty)}{x_{AB}(\infty)} T_s^{*\alpha_T}\right)^{-1} . \tag{17.4.4}$$

Comparison with the solid curves shows that (17.4.4) is a good approximation for $T_s^* \leq 5$. Figure 17.4.3b depicts the normalized molar ratio $x_{AB}^*(r_D)$ as a function of T_s^* for various values of $x_{AB}(\infty)$.

The figure demonstrates to what extent the thermal diffusion flux $J_T \propto -\alpha_T \nabla T$ changes the surface concentration $x_{AB}(r_D)$. It is evident that with $\alpha_T < 0$ this concentration increases, while with $\alpha_T > 0$ it decreases. In other words, addition of a carrier gas, M, will increase the surface concentration of species AB if $m_M > m_{AB}$, and it will decrease it if $m_M < m_{AB}$. The latter situation is also possible with B ≡ M. From Fig. 17.4.3b it becomes evident that the effect of thermal diffusion becomes more pronounced with decreasing concentration $x_{AB}(\infty)$.

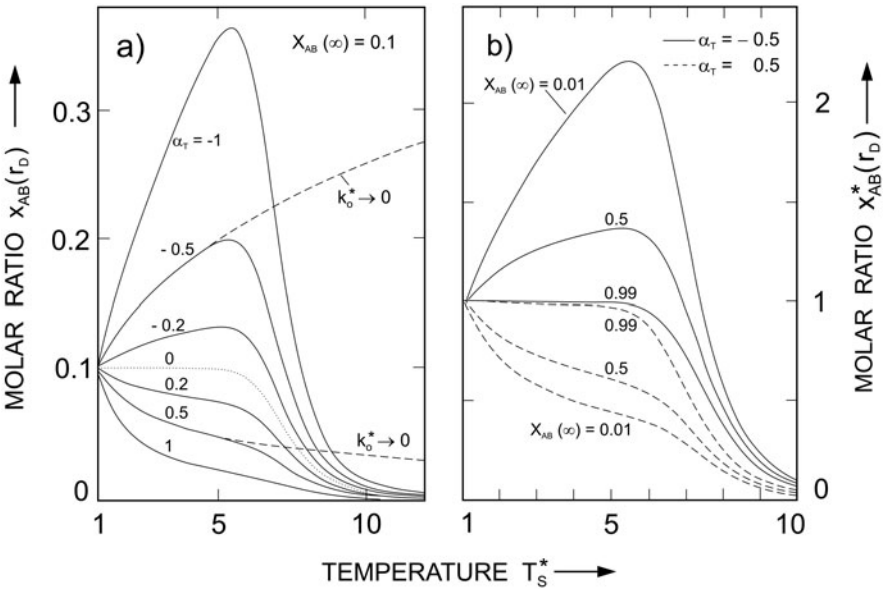

Fig. 17.4.3 a, b Influence of thermal diffusion on the concentration of species AB at the surface of the reaction zone as a function of surface temperature T_s^* for $b = 0$, $n = 2$, $\mathscr{E}^* = 90$, and $k_0^* = 5 \times 10^6$. (**a**) $x_{AB}(\infty) = 0.1$. Various values of α_T are shown (*solid curves*). $\alpha_T \to 0$ (*dotted curve*) and $k_0^* \to 0$ (*dashed curves*) are also shown. (**b**) Different curves refer to different values $x_{AB}(\infty)$ with $\alpha_T = -0.5$ (*solid curves*) and $\alpha_T = +0.5$ (*dashed curves*) [*Bäuerle* et al. 1990]

The influence of thermal diffusion on the reaction rate is shown in Fig. 17.4.4 for $x_{AB}(\infty) = 0.1$ and the values $\alpha_T = -1$, 0, and $+1$. Thermal diffusion influences *both* the kinetically controlled regime *and* the transport-limited regime. With respect to the case $\alpha_T = 0$, the reaction rate is increased if $\alpha_T < 0$, and decreased in the opposite case.

The experimental results presented in Fig. 17.4.5 can tentatively be interpreted along these lines. The decomposition reaction

$$C_2H_2 + M \to 2C(\downarrow) + H_2(\uparrow) + M$$

is equimolecular. For the lighter carrier gases, M $\equiv$ He or H_2, we have $\alpha_T = \alpha_0(m_{C_2H_2} - m_M)/(m_{C_2H_2} + m_M) > 0$. Thus, He and H_2 will accumulate near the hot tip of the fiber. As a consequence, the partial pressure of the reactant, and thereby the deposition rate, is lowered. For M $\equiv$ Ar, the mass exceeds that of C_2H_2 and α_T becomes negative. Thus, Ar will be depleted near the hot surface. Therefore, the partial pressure of C_2H_2 near the surface of the reaction zone is increased and, consequently, so is the deposition rate. This behavior is in *qualitative* agreement with the theoretical results represented by the solid curves in Fig. 17.4.4. However, these curves have been calculated for r_D = const., while the radius of fibers increases with T_s (Fig. 17.3.1b). In any case, the experiments demonstrate that the

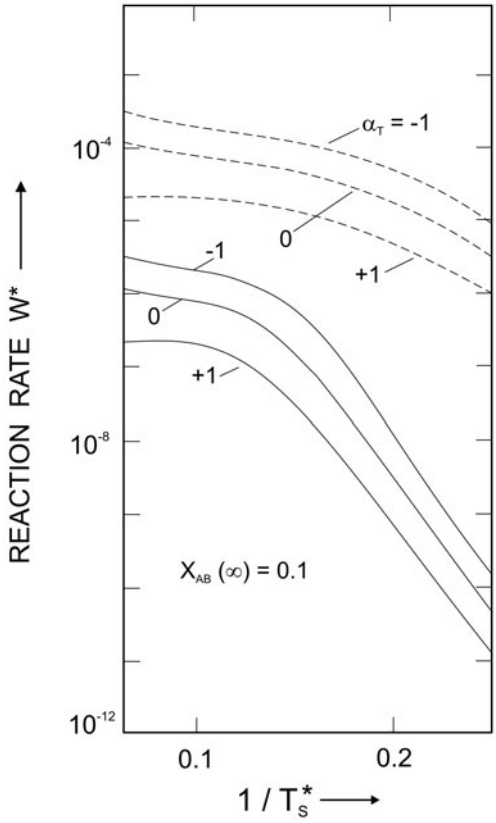

Fig. 17.4.4 Influence of thermal diffusion on the reaction rate W^* for $x_{AB}(\infty) = 0.1$, $b = 0$, and $\alpha_T = -1, 0$, and $+1$. $T_s^* \equiv T_s/T(\infty)$ with $T(\infty) = 300\,\mathrm{K}$. Solid curves: $\mathscr{E}^* = 90\,(54\,\mathrm{kcal/mol})$, $k_0^* = 5 \times 10^6$. Dashed curves: $\mathscr{E}^* = 45$, $k_0^* = 5 \times 10^4$ [*Bäuerle* et al. 1990]

selection of carrier gases has an important influence on the maximum deposition rates achieved in LCVD.

The spatial distributions of C_2H_4 and H_2 mol fractions and the effect of thermal diffusion during steady growth of C rods was simulated in simplified numerical calculations by *Yu* and *Camarero* (2009). The results are in qualitative agreement with the experimental and theoretical findings discussed above.

Gas-Phase Nucleation

The ultimate limit of controlled growth is set by gas-phase nucleation above the tip of the fiber (Chap. 4). This appears in Fig. 17.4.5 for temperatures above about 3000 K, where the slope of curves starts to increase again. This limit decreases with increasing C_2H_2 pressure. Homogeneous gas-phase decomposition and nucleation can also result in spontaneous breakdowns due to autocatalyzation of the reaction. This has been observed during LCVD of Ni from $Ni(CO)_4$.

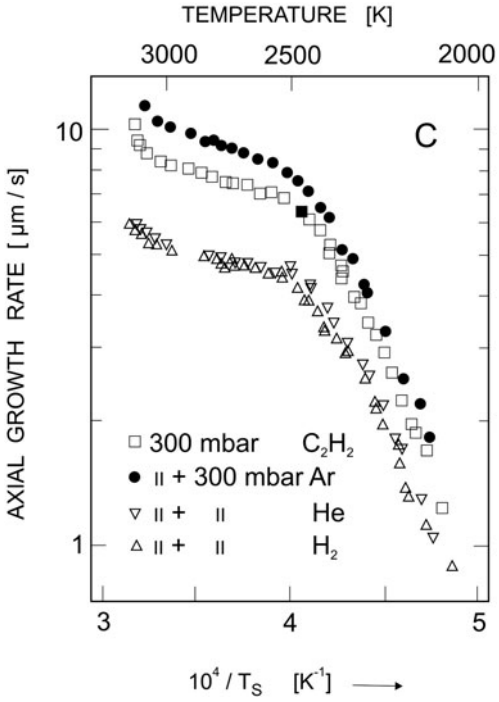

Fig. 17.4.5 Arrhenius plot for laser-induced deposition of carbon from pure C_2H_2 and from gas mixtures of C_2H_2 with H_2, He and Ar [*Doppelbauer* and *Bäuerle* 1986]

17.5 Simulation of Growth

In a simple 1D model, quasi-stationary growth of fibers can be described by the energy balance and the Arrhenius law. Let us assume cylindrical symmetry. The laser-induced temperature can then be determined from the energy balance

$$\kappa_D \frac{\partial}{\partial z}\left[\pi r_D^2(z)\frac{\partial \theta_D}{\partial z}\right] - 2\pi r_D(z)\kappa_G \left.\frac{\partial \theta_G}{\partial r}\right|_{r_D} = 0\,, \tag{17.5.1}$$

and the boundary condition

$$\pi r_D^2 \kappa_D \left.\frac{\partial \theta_D}{\partial z}\right|_{z=0} = P_a\,,$$

where z denotes the fiber axis. θ_D and θ_G are the linearized temperatures for the fiber and gas, respectively; κ_D and κ_G are the corresponding heat conductivities. We substitute $\partial\theta_G/\partial r|_{r_D} \approx \eta\theta_D/r_D$, where η is of the order of unity. In the simplest approximation we can calculate the temperature distribution from (17.5.1) and integrate the growth rate (normal to the surface) as given by the Arrhenius law. The radius of the fiber then becomes

$$r_{\mathrm{D}} \approx \frac{P_{\mathrm{a}}}{4\eta\kappa_{\mathrm{G}}\mathscr{E}} , \tag{17.5.2}$$

where $\mathscr{E}$ is the activation temperature. κ_{D} does not enter (17.5.2) because $\kappa_{\mathrm{D}} \gg \kappa_{\mathrm{G}}$. Both the linear increase in r_{D} with laser power and its only slight dependence on gas pressure are in agreement with the experimental results presented in Fig. 17.3.1b (in the elementary kinetic theory of gases, κ_{G} is independent of pressure). For a more detailed treatment see *Arnold* et al. (1996).

Chapter 18
Direct Writing

Laser direct writing by pyrolytic or photolytic decomposition of gas-phase precursors permits single-step surface patterning of planar and non-planar substrates. The process can most easily be studied by translating the substrate in one dimension perpendicular to the focused laser beam. By this means one obtains stripes (lines). The literature on such investigations is included in *Bäuerle* (2000).

18.1 Characteristics of Pyrolytic Direct Writing

The *morphology* and *geometry* of stripes strongly vary with laser power. This quite general phenomenon is illustrated in Fig. 18.1.1 with the example of Si deposited from SiH_4 onto Si wafers. At laser powers corresponding to center temperatures well below the melting point, a convex cross section is observed. When the laser power is increased, the cross section becomes mesa-type, and, at even higher powers, a dip in the middle of the stripe occurs. This dip becomes more pronounced the higher the laser power. Such changes in surface morphology can be understood from the laser-induced temperature distribution and the transport of species. The latter includes both the transport of reactant and product molecules within the gas phase and surface diffusion of species. Surface diffusion increases exponentially with temperature. Near melting, the surface tension strongly decreases, in general, and pulls off the soft or liquefied material from the center of the lines (Sect. 10.5).

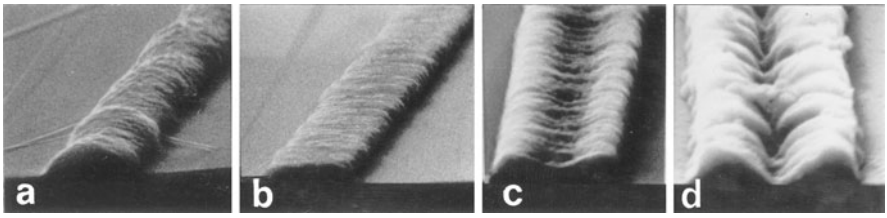

Fig. 18.1.1 a–d Si lines deposited onto Si wafers by Ar^+-laser pyrolysis of SiH_4 ($\lambda = 488$ nm, $v_s = 10\,\mu$m/s, $p(SiH_4) \approx 40$ mbar). The laser-beam intensity increases from *left* to *right* [*D. Bäuerle, G. Leyendecker, S. Szikora*, 1982, unpublished]

D. Bäuerle, *Laser Processing and Chemistry,* 4th ed.,
DOI 10.1007/978-3-642-17613-5_18, © Springer-Verlag Berlin Heidelberg 2011

Additionally, high laser powers may induce gas-phase reactions (Sect. 3.5). The reaction products, such as polysilanes in the SiH_4 system, condense in the neighborhood of the stripe. Furthermore, coherent and non-coherent structure formation is frequently observed within certain ranges (Chap. 28).

The influence of melting and changes in the morphology of stripes complicate the understanding of the deposition process. The following analysis of direct writing will therefore be confined to laser powers where *no* dramatic changes in the shape of the cross section occur and where an unequivocal definition of the stripe width d and height h is possible.

Figure 18.1.2 shows SEM pictures of W lines deposited on a 1200 Å a-Si/SiO_2 substrate from $WF_6 + H_2$. The microstructure of the lines is polycrystalline. The grain size depends on the laser power and gas pressures. With this system, a thin tungsten film is initially formed by silicon reduction according to

$$2WF_6 + 3Si \rightarrow 2W + 3SiF_4(\uparrow) \; . \tag{18.1.1}$$

This reaction is self-terminating at a film thickness of about 100–1000 Å [*Liu* 1986]. The slight deepening observed near the edges of lines is considered an indication for this process. Nevertheless, etching by HF may be important as well (Sect. 16.3.1). After the initial step of silicon reduction, deposition continues via hydrogen reduction of WF_6, as described by (16.2.1).

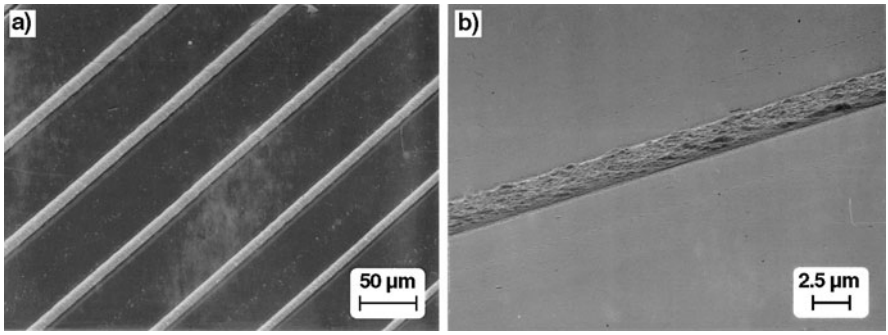

Fig. 18.1.2 a, b SEM pictures of W stripes deposited from $WF_6 + H_2$ with Kr^+-laser light ($\lambda = 647$ nm, $w_0(1/e) \approx 1.3\,\mu$m, $v_s = 100\,\mu$m/s). (**a**) $p(WF_6) = 5$ mbar, $p(H_2) = 400$ mbar, $P = 146, 132, 120, 107, 97$, and 83 mW (*left to right*). (**b**) $p(WF_6) = 5$ mbar, $p(H_2) = 100$ mbar, P = 135 mW [*Zhang* et al. 1987]

18.1.1 Dependence on Laser Parameters and Substrate Material

Figure 18.1.3 shows the height and width of lines as a function of laser power for two different substrate materials and various pressures of WF_6 and H_2.

For the thermally insulating substrate (Fig. 18.1.3a) both d and h increase almost linearly with laser power. The width is independent of both the WF_6 and H_2 partial

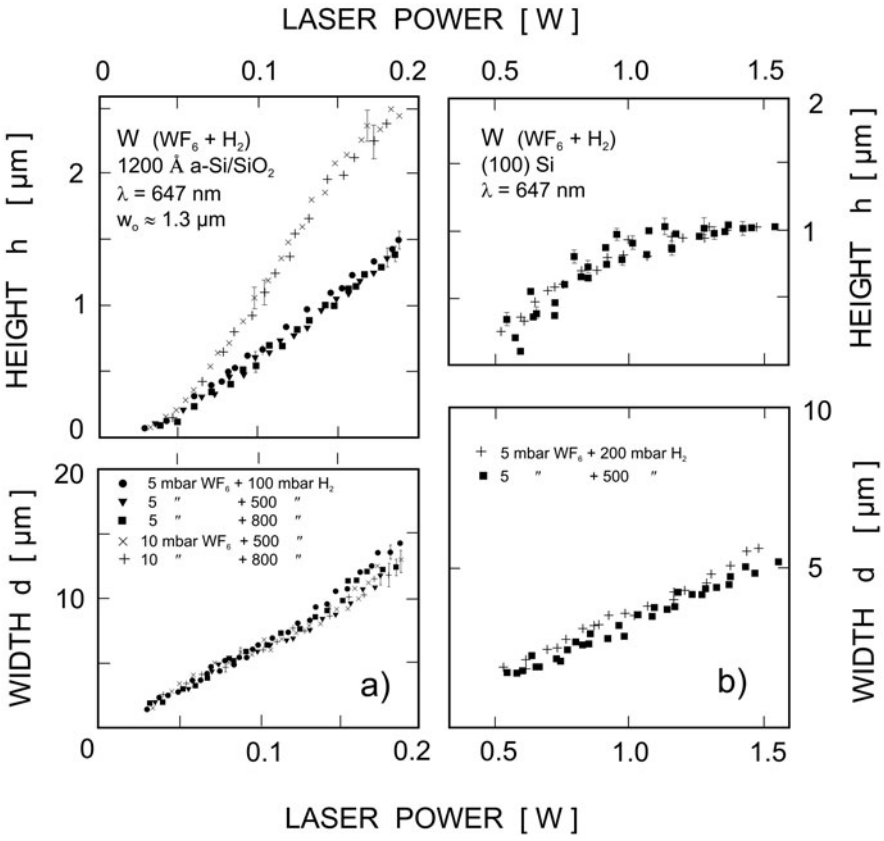

Fig. 18.1.3 a, b Height and width of W stripes as a function of Kr^+-laser power for two substrate materials ($\lambda = 647\,\text{nm}$, $v_s = 100\,\mu\text{m/s}$). (**a**) Fused quartz substrate covered with 1200 Å amorphous silicon. The laser focus was $w_0(1/e) \approx 1.3\,\mu\text{m}$ [*Zhang* et al. 1987]. (**b**) (100) Si-wafer substrate [*Zhang* et al. 1987, unpublished]

pressures. The height increases with WF_6 pressure but is independent of $p(H_2)$. The ratios d/h are approximately 10 and 5 for WF_6 pressures of 5 and 10 mbar, respectively. The mesa-type cross section (almost perfectly rectangular) observed with 5 mbar WF_6 changes to convex-type with 10 mbar WF_6. With $p(WF_6) > 5$ mbar, thin wings of W are frequently observed. Significant deposition takes place only above a certain threshold $\propto P/w_0$, which is related to the laser-induced temperature rise [see (7.1.4)]. From Fig. 18.1.3a we derive $P_{th} \approx 30\,\text{mW}$; within the ranges investigated, this value is independent of the partial pressures of gases. Another feature is the increase in resolution which is observed for the lowest laser powers. Here, the width of lines is about half the diffraction-limited diameter of the laser focus. This effect originates mainly from the exponential dependence of the deposition rate on temperature (Sect. 5.3.6).

The situation is different with W lines deposited onto (100) Si wafers. Here, the laser beam was focused a few micrometers below the Si surface. In this way, the formation of periodic structures can be suppressed and the reproducibility of data improved. The laser powers required for direct writing are more than a factor of ten higher compared to SiO_2 substrates. This is mainly related to the high heat conductivity of Si [$\kappa(\mathrm{c-Si};300\,\mathrm{K}) \approx 1.5\,\mathrm{W/cm\,K}$; $\kappa(\mathrm{a-Si/SiO_2};300\,\mathrm{K}) \approx \kappa(\mathrm{SiO_2};300\,\mathrm{K}) = 0.014\,\mathrm{W/cm\,K}$]. The height of lines rapidly saturates with increasing power.

Similar experiments have been performed on the deposition of Ni from $Ni(CO)_4$ [*Kräuter* et al. 1983]. The laser wavelength has no or only little influence on the width and thickness of lines as long as the absorbed power remains constant. For thermally insulating substrates and medium-to-high powers, the width of metal lines is much larger than the laser focus ($d \gg 2w_0$) and independent of w_0. This is expected from Fig. 16.4.2a, where it has been shown that the temperature rise at the edge of the deposit remains almost unaffected if the laser focus is increased at constant power. On the other hand, deposition continues to lower laser powers as the diameter of the laser focus becomes smaller. Thus, the *smallest* widths of lines are obtained with the smallest focus. If the thermal conductivities of the deposit and the substrate are comparable, as in the case of the c-Si substrate, the width of lines remains of the order of the focus diameter.

The range of parameters and the maximum scanning velocities that can be employed in laser direct writing strongly depend on both the physical properties of the deposit *and* the substrate. While the possible range of variation in the width of stripes is very large for $\kappa_D \gg \kappa_s$, it is very small if $\kappa_D \approx \kappa_s$. The upper limit is essentially based on the maximum center temperature at which *controlled* deposition is possible, i.e., where no dramatic changes in the geometry of the deposit, no damaging of the substrate, and no triggering of a (uncontrolled) homogeneous gas-phase reaction above the surface of the deposit occur. Furthermore, small changes in w_0, or in the positioning of the substrate, will have a much stronger influence on systems where $\kappa_D \approx \kappa_s$ than on systems where $\kappa_D \gg \kappa_s$.

18.1.2 Electrical Properties

The electrical properties of W lines have been investigated for the same parameters and substrate as in Fig. 18.1.3a. Figure 18.1.4 shows the resistance of stripes per unit length and their resistivity, normalized to the bulk value of W, as a function of laser power and $p(WF_6) = 5\,\mathrm{mbar}$. No influence on H_2 pressure was observed. The strong decrease in resistance with increasing laser power is mainly due to the increase in cross section of stripes. The increase in resistivity with increasing laser power is ascribed to changes in the morphology and texture. Stripes deposited at low laser-induced temperatures are microcrystalline and have smooth surfaces. At higher temperatures, but otherwise identical experimental conditions, the surface becomes rougher and larger crystallites – up to several tenths of a micrometer – are formed. The larger grains may result in higher inter-grain resistances. Nevertheless,

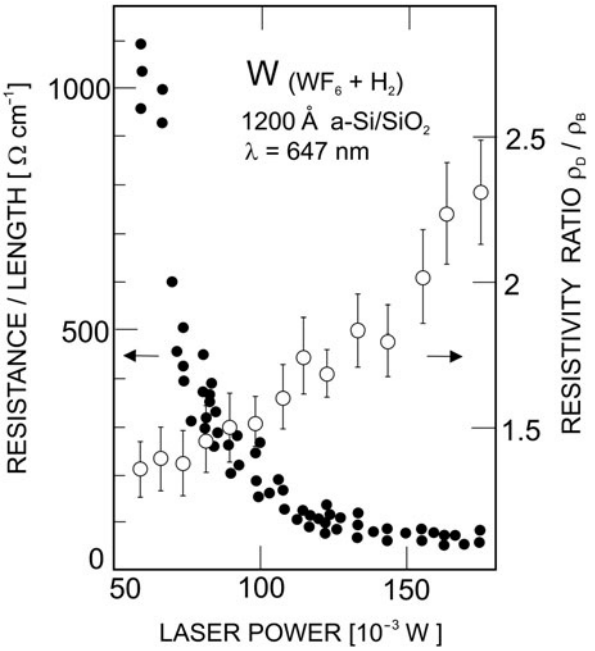

Fig. 18.1.4 Electrical resistance (*left scale*) and resistivity ratio (*right scale*) of W stripes as a function of laser power (647 nm Kr^+, $w_0 = 1.3\,\mu m$). The partial pressures of WF_6 and H_2 were $p(WF_6) = 5$ mbar and 100 mbar $\leq p(H_2) \leq$ 800 mbar. For normalization we used $\varrho_B(W) = 5.33 \times 10^{-6}\,\Omega$ cm [*Zhang* et al. 1987]

the resistivity values are only a factor of 1.5−2.5 larger than those of bulk W. Similar results have been achieved with Au and Cu (see previous editions).

18.2 Temperature Distributions in Direct Writing

The model employed in the calculations is depicted in Fig. 18.2.1. Scanning of the laser beam is performed in the x direction with velocity v_s. We consider quasi-stationary conditions with the coordinate system fixed to the laser beam. In this system, the geometry of the stripe remains unchanged. The precise temperature distribution induced within the deposited stripe can only be calculated numerically. For many applications, however, a rough estimation of this distribution, or even of the center temperature only, is useful.

18.2.1 Center-Temperature Rise

The simplest estimation of the temperature rise is based on the energy balance. Assume a stripe of rectangular cross section and uniform height within the region $-\infty < x \leq a$.

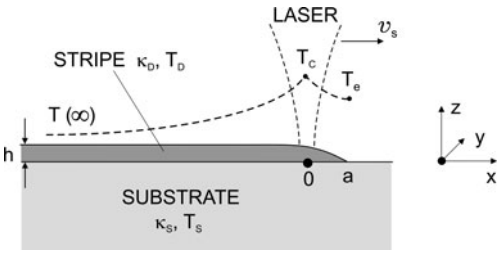

Fig. 18.2.1 Model for laser direct writing of stripes. The origin of the coordinate system (indicated by *the dot*) is fixed with the center of the laser beam. The forward edge of the stripe is at $x = a$. T_c and T_e are the temperatures at $x = 0$ and $x = a$, respectively. The temperature profile calculated analytically is schematically indicated (*dotted curve*). The width of the stripe is $d = 2r_D$ and its height is h

If $\kappa_D \leq \kappa_s$, the width of deposited stripes is comparable to the width of the laser spot, i.e., $w \approx r_D = d/2$. From simple energy considerations the center-temperature rise is

$$\Delta T_c \equiv \Delta T(\boldsymbol{x} = 0) \approx \frac{P_a}{\pi w \kappa_s} \left(1 + \frac{v_s w}{D_s} + \frac{\kappa_D - \kappa_s}{\kappa_s} \frac{hd}{\pi w^2}\right)^{-1} , \quad (18.2.1)$$

where $P_a = I_0 A \pi w^2$ is the absorbed laser power, and D_s the heat diffusivity of the substrate. The influence of scanning can be neglected as long as $v_s^* = v_s w/D_s \ll 1$. Because this estimation ignores temperature gradients in z-direction, it can be applied only if $h \ll d$.

If $\kappa^* \equiv \kappa_D/\kappa_s \gg 1$, the width of stripes can become large compared to the laser spot so that $w \ll r_D$. With the approximation $v_s^* = 0$, the energy balance for the tip of a stripe with cross section F can be written as

$$P_a \approx \pi r_D^2 \kappa_s \nabla T_s(\boldsymbol{x} = 0) + F \kappa_D \nabla T_D(\boldsymbol{x} = 0) . \quad (18.2.2)$$

The temperature gradient within the substrate surface can be approximated by $\nabla T_s(\boldsymbol{x} = 0) \approx \Delta T(\boldsymbol{x} = 0)/r_D \equiv \Delta T_c/r_D$. For an estimation of $\nabla T_D(\boldsymbol{x} = 0)$ we consider the energy balance for a stripe element between x and $x + \mathrm{d}x$. If we ignore the source term, this yields $\nabla T_D(\boldsymbol{x} = 0) \approx \Delta T_c/l$, where $l = (F\kappa^*/\eta)^{1/2}$. l characterizes the drop in the laser-induced temperature rise in the x-direction. If we set $\eta = 2$ and substitute $\nabla T_s(\boldsymbol{x} = 0)$ and $\nabla T_D(\boldsymbol{x} = 0)$ in (18.2.2), we obtain

$$\Delta T_c \approx \frac{P_a}{\pi r_D \kappa_s} \left[1 + \frac{1}{\pi r_D} \left(2F \frac{\kappa_D}{\kappa_s}\right)^{1/2}\right]^{-1} . \quad (18.2.3)$$

With $F = 2r_D h = dh$, this yields

$$\Delta T_c \approx \frac{P_a}{\pi r_D \kappa_s}\left[1+\frac{2}{\pi}\left(\frac{h}{r_D}\frac{\kappa_D}{\kappa_s}\right)^{1/2}\right]^{-1} .$$

From the comparison of terms $v_s \nabla T$ and $D_s \nabla^2 T$ in the heat equation (2.2.1) we find that the influence of scanning can be ignored as long as $v_s^* \equiv v_s r_D^2 / D_s l \ll 1$. It is clear that the previous equations represent only crude approximations. Nevertheless, they permit one to *qualitatively* understand some basic features observed in laser direct writing.

18.2.2 1D Approach, $\kappa^* \gg 1$

With the 1D model shown in Fig. 18.2.1 the laser-induced temperature distribution can also be calculated in a more sophisticated way from the energy balance:

$$c_D \varrho_D F \frac{\partial T_D}{\partial t} = \frac{\partial}{\partial x}\left(F \kappa_D \frac{\partial T_D}{\partial x}\right) - \int_{-r_D}^{r_D} \kappa_s \frac{\partial T_s}{\partial z}\bigg|_{z=0} \mathrm{d}y + \mathscr{P}_a . \quad (18.2.4)$$

Here, the influence of scanning is again ignored. c_D is the specific heat, and ϱ_D the mass density of the deposit. $\mathscr{P}_a \equiv \mathscr{P}_a(x)$ is the absorbed laser power per unit length of the stripe. The cross section, F, is assumed to be constant, because the heat loss along the stripe is dominated by the region where h and r_D are constant. This approximation is in good agreement with the exact solution of (18.2.4) with $F \equiv F(x)$. All material parameters have been assumed to be constants. If $\kappa^* \gg 1$, we can employ the approximation $T_s(z=0) \approx T_D$. We also approximate the integral in (18.2.4) by $\eta \kappa_s \Delta T_D$, where η is a dimensionless geometrical parameter which describes the heat flux from the deposit into the substrate by an effective (linear) heat exchange (Sect. 6.1.2). The value of η is near 2, because $\partial T_s/\partial z \approx \Delta T_D / r_D$, where $\Delta T_D = T_D - T(\infty)$. If $w < r_D$, we can replace $\mathscr{P}_a$ by $P_a \delta(x) = PA\delta(x)$, where A is the absorptivity.

With these simplifications and under stationary conditions, (18.2.4) yields

$$l^2 \frac{\partial^2 T_D}{\partial x^2} - [T_D - T(\infty)] + \frac{P_a}{\eta \kappa_s}\delta(x) = 0 , \quad (18.2.5)$$

where $l^2 = F\kappa^*/\eta$. The boundary conditions employed are

$$\frac{\partial T_D}{\partial x}\bigg|_{x=a} = 0 \quad \text{and} \quad T_D(x=-\infty) = T(\infty) .$$

The solution of this problem with $x < 0$ is

$$T_D(x) = T(\infty) + \Delta T_c \exp\left(\frac{x}{l}\right) , \quad (18.2.6)$$

where

$$\Delta T_c \equiv \Delta T(x=0) = \frac{P_a}{2\eta l \kappa_s}\left[1+\exp\left(-\frac{2a}{l}\right)\right] .$$

This relation coincides with (18.2.3) if we use expansions with respect to $a/l \ll 1$ and ignore coefficients of the order of unity.

With $0 < x < a$, we obtain

$$T_D(x) = T(\infty) + \Delta T_e \cosh\left(\frac{x-a}{l}\right) , \tag{18.2.7}$$

where

$$\Delta T_e \equiv \Delta T(x=a) = \frac{P_a}{\eta l \kappa_s}\exp\left(-\frac{a}{l}\right) .$$

To model direct writing, the unknown quantities ΔT_c, ΔT_e, a, F, l, h, and r_D must be calculated self-consistently together with the equation of growth.

18.2.3 Numerical Solutions

Numerical calculations of the laser-induced temperature distribution were performed for *rectangular* stripes of *uniform* thickness within the region $-\infty < x \le a$ (Fig. 18.2.1). Heat losses to the ambient medium were ignored. The results obtained by employing the finite difference technique are presented in Fig. 18.2.2. If $\kappa_D = \kappa_s$,

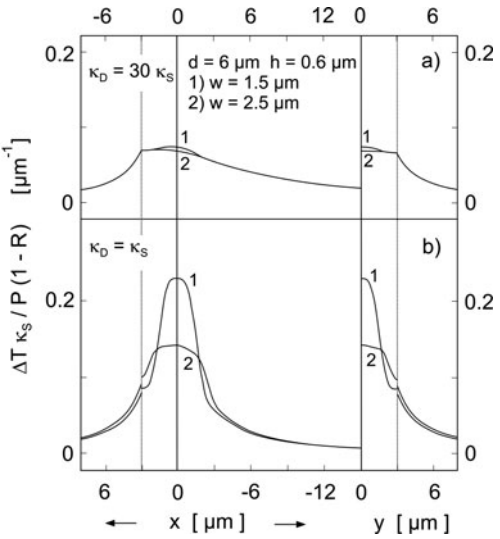

Fig. 18.2.2 a, b Calculated temperature distributions for stripes with rectangular cross sections. The choice of coordinates is the same as in Fig. 18.2.1 [adapted from *Piglmayer* et al. 1984]

the temperature distribution remains essentially unaffected by the deposit and is almost symmetric. If, however, $\kappa_D \gg \kappa_s$, the general trend is the same as for the spots.

For realistic parameters, the temperature profiles are almost independent of scanning velocity. The temperature profiles shown in Fig. 18.2.2 are therefore very similar to those in Fig. 16.4.3. The main differences result from the heat transport along the stripe, which yields a reduction of the center temperature with increasing cross section (Fig. 18.2.3). This effect is important in particular if $\kappa_D \gg \kappa_s$.

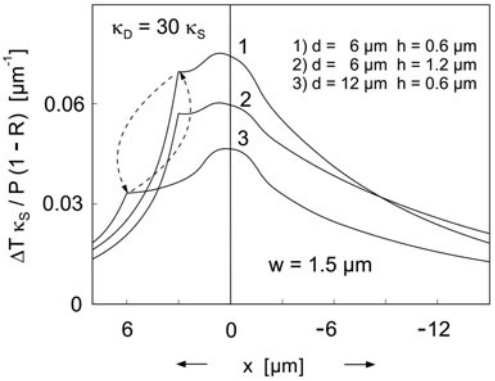

Fig. 18.2.3 Influence of the width and height of stripes on the temperature profile [*Piglmayer* et al. 1984]

For *arbitrary* cross sections with $h \ll \kappa^* r_D$ and $\kappa^* \gg 1$, the temperature distribution can be calculated numerically from (16.5.3).

Semi-analytical calculations of the center-temperature rise on the top of stripes with parabolic cross sections have been performed by *Arnold* (1996) (see also Sect. 16.4).

18.3 Simulation of Direct Writing

In this section we discuss self-consistent model calculations of pyrolytic direct writing for $\kappa^* \gg 1$. The theoretical results are compared with experimental data.

18.3.1 1D Model

In a coordinate system that is fixed with the laser beam, the height of the stripe is given by (16.3.2), where $h = h(x, t)$. The stationary conditions are expressed by $\partial h/\partial t = 0$. The growth rate shall be described by the Arrhenius-type law (16.3.3). If we use the approximation $\partial h/\partial x \approx -h/(\gamma a)$ for the position $x = 0$, where h is the (constant) height behind the laser beam (Fig. 18.2.1), we obtain, for lines with $|\boldsymbol{n}| \approx 1$,

$$W(T_c) - v_s \frac{h}{\gamma a} = 0 \,, \tag{18.3.1}$$

where γ is of the order of unity. To determine the unknown quantities, we need three additional equations: The cross section of the stripe is

$$F \approx \zeta h r_D \,, \tag{18.3.2}$$

where ζ is a dimensionless geometrical coefficient (for a rectangular stripe $\zeta \approx 2$, for a parabolic cross section $\zeta \approx 4/3$, etc.). The position of the laser beam with respect to the front edge of the stripe (Fig. 18.2.1) is characterized by

$$a \approx r_D/\xi \,. \tag{18.3.3}$$

ξ is again dimensionless and of the order of unity. Ansatz (18.3.3) implies that the temperature distribution has almost axial symmetry near the position of the laser beam. This is confirmed by both experimental observations and numerical simulations of the growth process. Depending on the type of precursor molecule, we consider laser-induced deposition with or without a threshold temperature [see (16.3.3)]. *With* a threshold, T_{th} must be reached at the same distance from the center in both the x and y directions. The temperatures at $x = a$ and $y = r_D$ shall then be approximated by

$$T_e \approx T_{th} \,. \tag{18.3.4a}$$

Without a threshold, we ignore deposition for temperatures $T < T_e$, where T_e is given by $W(T_e)/W(T_c) = \exp(-\beta)$, with $\beta \approx 1$. This yields

$$T_e = \frac{\mathscr{E} T_c}{\mathscr{E} + \beta T_c} \approx T_c \left(1 - \frac{\beta T_c}{\mathscr{E}}\right) \,. \tag{18.3.4b}$$

From (18.2.6) and (18.2.7) we obtain

$$\mu = \frac{a}{l} = \operatorname{arccosh}\left(\frac{\Delta T_c}{\Delta T_e}\right) \,, \tag{18.3.5}$$

where $\Delta T_e = T_e - T(\infty)$. From (18.2.7) we find

$$l = \frac{P_a}{\eta \kappa_s \Delta T_e} \exp(-\mu) \,. \tag{18.3.6}$$

Equations (18.2.6), (18.2.7), and (18.3.1, 18.3.2, 18.3.3, 18.3.4, 18.3.5 and 18.3.6) permit one to calculate all relevant dependences. If $v_s = \text{const.}$, T_c is independent of P_a while r_D, h, a, and l scale *linearly* with P_a. The dependence of these quantities on v_s is more complex. With (18.3.5) and (18.3.6) we can write (18.3.3) as

$$r_D = \xi a = \xi l \mu = \frac{\xi P_a}{\eta \kappa_s \Delta T_c} \mu \exp(-\mu) \ . \tag{18.3.7}$$

From (18.3.2) and (18.3.7) we obtain, with $l^2 = F\kappa^*/\eta$,

$$h = \frac{\eta}{\zeta \xi \kappa^*} \frac{a}{\mu^2} = \frac{P_a}{\zeta \xi \kappa_D \Delta T_e} \mu^{-1} \exp(-\mu) \ . \tag{18.3.8}$$

Equation (18.3.1) yields

$$v_s = \frac{\gamma \zeta \xi}{\eta} \kappa^* \mu^2 W(T_c) \ . \tag{18.3.9}$$

Equations (18.3.7, 18.3.8 and 18.3.9) are a parametric representation [with respect to T_c or μ in (18.3.5)] of the determination of h and $r_D = d/2$ as a function of v_s. Both T_c and μ increase with v_s. r_D depends only on κ_s, while h depends on κ_D. The ratio h/r_D does *not* depend on P_a.

With very *low* laser powers, the width of stripes can become comparable to the laser focus, so that $r_D \approx w_0$. Then, the point-source approximation (18.2.5) becomes invalid. Heuristically, we can take into account the *finite* diameter of the laser focus by substituting $a = l\mu + \chi w_0$, where $\chi \approx 1$. Consideration of w_0 changes the power dependence of r_D and h within the range $r_D \approx w_0$ [*Arnold* et al. 1995a].

18.3.2 Comparison with Experimental Data

With constant scanning velocity, the temperature T_c and thereby the rate $W(T_c)$ and $\mu(T_c)$ in (18.3.9) do not vary with laser power. Thus, according to (18.3.7) and (18.3.8), d and h increase *linearly* with laser power. This is in agreement with experimental data on pyrolytic direct writing for systems with $\kappa^* \gg 1$ (Fig. 18.1.3a). The constant value of T_c can be easily understood: with increasing power P_a, the height and width of stripes increase, and thereby so does the heat flow along the stripe.

Figure 18.3.1 shows the dependence of the normalized height, $h^* \equiv h\kappa_D T(\infty)/P_a$, the width $r_D^* \equiv r_D \kappa_s T(\infty)/P_a$ and the temperature $T_c^* \equiv T_c/T(\infty)$ on scanning velocity. The curves were calculated from (18.3.7, 18.3.8 and 18.3.9) together with (18.3.5). The height of lines decreases monotonically with increasing v_s because of the decrease in laser-beam dwell time $\tau_\ell \propto 1/v_s$. The increase in T_c with v_s can be understood from the overall decrease in the cross section, F. The width of lines shows a more complex behavior:

For materials with *no* or low deposition threshold, where T_e is given by (18.3.4b), r_D decreases monotonically with increasing v_s. The parameter set employed in Fig. 18.3.1a refers, approximately, to pyrolytic LCVD of Si from SiH_4. A similar dependence is found for the deposition of Ni from $Ni(CO)_4$ (Fig. 18.3.2).

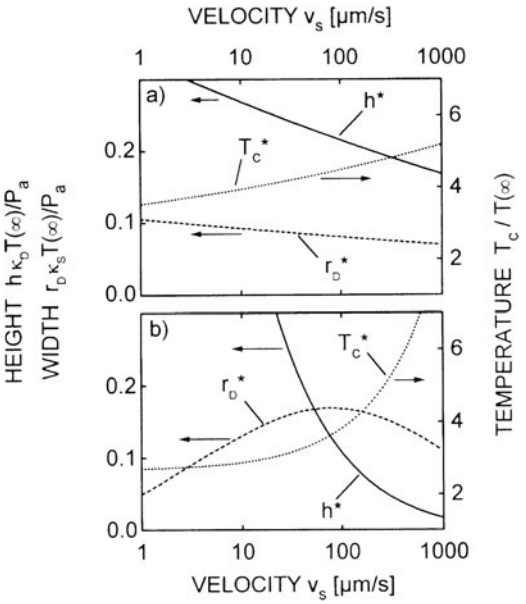

Fig. 18.3.1 a, b Normalized height, width, and center temperature for direct writing of stripes as a function of scanning velocity. The parameters employed correspond to SiO_2 substrates and deposits of: (**a**) Si from SiH_4 with $k_0 = 3 \times 10^8\,\mu$m/s, $\mathscr{E}^* = 73$, $T(\infty) = 300\,$K, $\kappa^* = 10$, $\eta = 1.6$, $\zeta = 4/3$, $\xi = 1.25$, $\gamma = 1.3$, $\beta = 1.8$; (b) W from $WCl_6 + H_2$ with $k_0 = 16\,\mu$m/s, $\mathscr{E}^* = 5.7$, $T(\infty) = 443\,$K, $T^*_{\rm th} = 2.7$, $\kappa^* = 17$. η, ζ, ξ, γ are the same as in (**a**) [adapted from *Arnold* et al. 1995a]

In the *presence* of a threshold, where T_e is given by (18.3.4a), the situation is different (Fig. 18.3.1b). The width first increases up to a maximum value $r_D^{\max}$ at $v_s^{\max}$, and then decreases for $v_s > v_s^{\max}$. This behavior can be understood from the maximum in $r_D(v_s)$ at $\mu = 1$. For this point, we obtain

$$T_c^{\max} = T(\infty) + \Delta T_{\rm th}\cosh(1) \approx T(\infty) + 1.5\Delta T_{\rm th}\,, \tag{18.3.10a}$$

$$r_D^{\max} = \xi a = \xi l = \frac{\xi P_a}{\eta\kappa_s \Delta T_{\rm th}}\,{\rm e}^{-1}\,, \tag{18.3.10b}$$

$$h^{\max} = \frac{P_a}{\zeta\xi\kappa_D \Delta T_{\rm th}}\,{\rm e}^{-1}\,, \tag{18.3.10c}$$

$$v_s^{\max} = \frac{\gamma\zeta\xi}{\eta}\kappa^* W(T_c^{\max})\,. \tag{18.3.10d}$$

The maximum in $r_D(v_s)$ is related to the threshold temperature. The increase in T_c is due to the decrease in heat flux along the stripe. Among the experimental examples that refer to this case is the deposition of W from $WCl_6 + H_2$.

Figure 18.3.3 shows the height and width of W stripes as a function of scanning velocity for two different WCl_6 pressures. The effective incident laser power

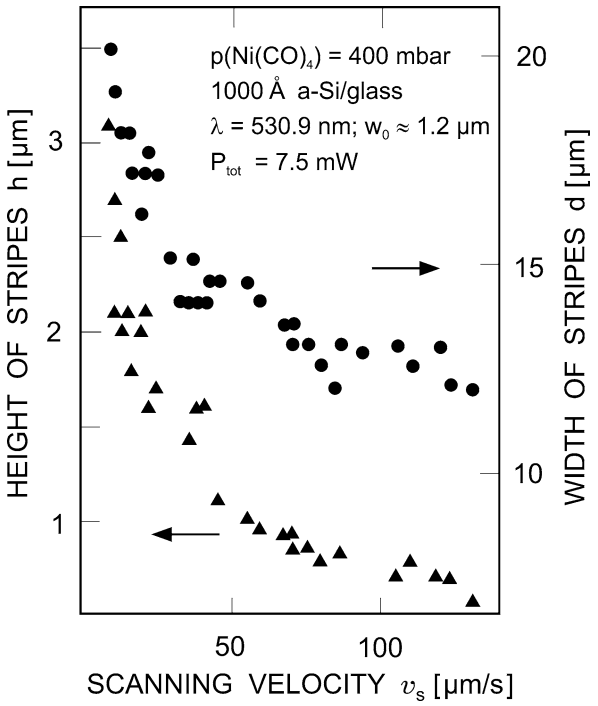

Fig. 18.3.2 Dependence of the height and width of Ni stripes on scanning velocity [*Kräuter* et al. 1983]

was the same in both cases. The substrate was fused quartz (SiO_2) covered with a $h_1 \approx 700$ Å-thick layer of sputtered W. Solid and dashed curves were calculated from (18.3.7, 18.3.8 and 18.3.9). The value $\xi = 1.25$ was derived from experimental data. The sputtered W layer has been ignored in the calculations; this is a good approximation if $\kappa^* h_1 / r_D \ll 1$. The figure shows almost quantitative agreement between experimental data and theoretical curves. The maximum in d shifts to higher velocities with increasing WCl_6 pressure. This is expected from (18.3.10d) because of the pre-exponential factor k_0 in $W(T)$. For a partial reaction order of unity with respect to WCl_6, we expect $k_0 \propto p(WCl_6)$. From the figure we derive for the ratio of velocities $v_s(d^{max})$ a factor 2.5, which is in excellent agreement with the ratio of WCl_6 pressures employed, i.e., 2.25.

Figure 18.3.4 shows the width of W stripes as a function of scanning velocity for different laser powers. The width increases more or less linearly with laser power; the position of the maximum width, however, remains unchanged. The dashed curves have been calculated by employing the same parameters as in Fig. 18.3.3a.

Equations (18.3.10b, c) suggest that d^{max} and h^{max} depend only on the threshold temperature and increase linearly with laser power. This is confirmed by experiments which show, for example, that in the WCl_6–H_2 system d^{max} and h^{max} are almost independent of pressure [*Arnold* et al. 1993].

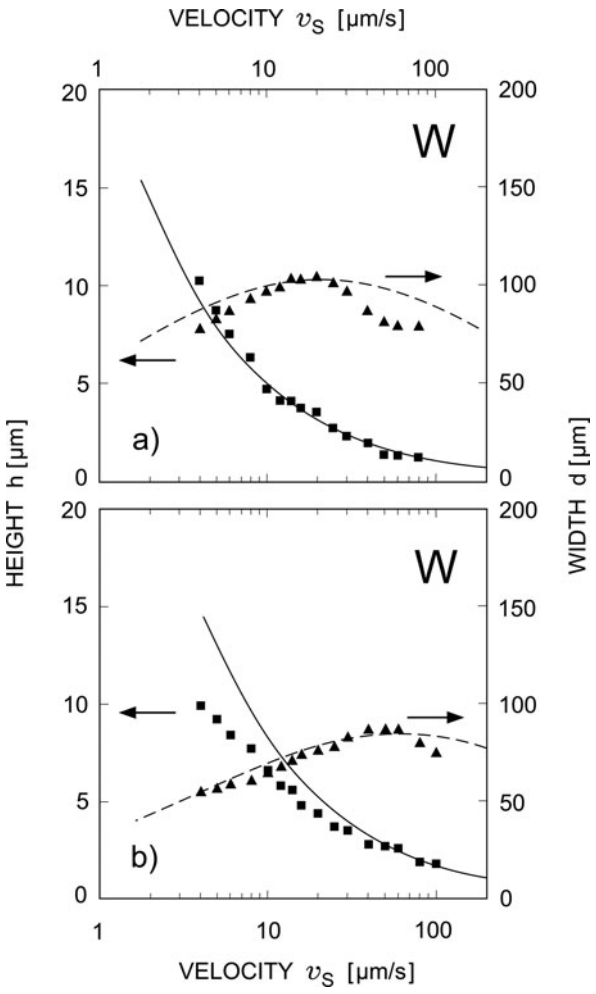

Fig. 18.3.3 a, b Height and width of Ar^+-laser-deposited W stripes as a function of scanning velocity for two mixtures of $WCl_6 + H_2$ [$\lambda = 514.5\,\text{nm}$, $P = 645\,\text{mW}$, $w_0(1/e) = 7.5\,\mu\text{m}$; $p(H_2) = 50\,\text{mbar}$] [*Kullmer* et al. 1992]. The *solid* and *dashed curves* were calculated as described in the text. The parameters were $A = 0.55$, $T(\infty) = 443\,\text{K}$, $\mathscr{E}^* = 5.7$, $\kappa^* = 17$, $\kappa_s = 0.032\,\text{W/cm K}$; $\eta = 1.6$, $\zeta = 4/3$, $\xi = 1.25$, $\gamma = 1.3$. (**a**) $p(WCl_6) = 0.49\,\text{mbar}$, $k_0 = 7.15\,\mu\text{m/s}$, $T^*_{th} = 2.4$. (**b**) $p(WCl_6) = 1.1\,\text{mbar}$, $k_0 = 16.05\,\mu\text{m/s}$, $T^*_{th} = 2.7$ [*Arnold* et al. 1993]

Within the approximations made, the agreement between theoretical predictions and experimental data is quite satisfactory. One should keep in mind that important parameters such as k_0, $\mathscr{E}$, T_{th}, and the reaction orders can only be estimated from experimental investigations.

The temperature dependences of κ_D, κ_s, and A can easily be taken into account. Even in this case a *linear* dependence of r_D, h, a, and l on absorbed laser power

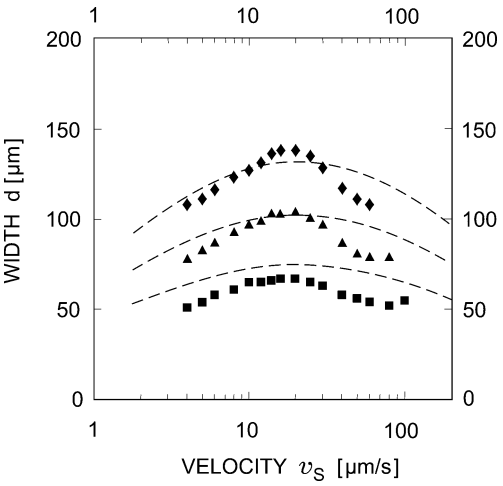

Fig. 18.3.4 Width of W stripes as a function of scanning velocity for three different laser powers. The precursors employed were 0.49 mbar $WCl_6 + 50$ mbar H_2. The parameters were the same as in Fig. 18.3.3a except for the laser power: ♦ P = 825 mW; ▲ P = 645 mW; ■ P = 475 mW [*Arnold* et al. 1993]

is obtained; the maximum center temperature, T_c^{max}, will still depend only on T_{th} and the materials' properties. With realistic parameters, the changes in quantities are below 30%.

18.3.3 2D Model

Equations (16.3.1, 16.3.2 and 16.3.3) permit a self-consistent calculation of line shapes and laser-induced temperature distributions. Here, one can ignore the time derivative in the heat equation and use the same approximations and normalizations as in Sect. 16.5.

Contour lines and isotherms have been calculated for various stages of direct writing of W lines onto SiO_2 [*Arnold* and *Bäuerle* 1993]. They reveal that stationary conditions are achieved only after a relatively long time. The larger width of stripes observed with short times is related to the fact that energy losses due to heat conduction along the stripe are not yet effective. The results are in agreement with experimental observations.

Within the parameter range investigated, the calculated shape of W lines always remains uniform, i.e., it shows *no* oscillations in height or width (Sect. 28.3.5). The calculations also permit one to derive the parameter $\xi = r_D/a$ for different scanning velocities [see (18.3.3)]. Here, we find $1.2 < \xi < 1.5$. The experimental value for the WCl_6–H_2 system is $\xi \approx 1.25$. The discrepancy between the 1D and the 2D model is, for realistic parameters, about 30%.

Different morphologies of Cu lines including volcano shapes have been modelled by *Han* and *Jensen* (1994).

18.4 Photophysical LCVD

Up to now we have concentrated on pyrolytic direct writing. There are several reasons for this:

- *Pyrolytic* LCVD permits surface patterning with submicrometer dimensions. The deposition rates exceed those in photolytic LCVD by several orders of magnitude. Consequently, pyrolytic LCVD permits much higher scanning velocities in direct writing and also the production of 3D structures. The microstructure and the electrical properties of pyrolytically deposited materials are superior to those of materials deposited by photolysis. Pyrolytic reaction rates depend only slightly on the exact wavelength of the laser light. For this reason, a great variety of materials can be deposited with the same experimental setup. Disadvantageous are the high local laser-induced temperatures and their dependence on substrate material.
- The basic advantage of *photolytic* LCVD is the lower local processing temperature and the lower sensitivity to the physical properties of the substrate (Sect. 16.6). Therefore, direct writing of patterns onto heat-sensitive materials and more uniform writing onto combined materials with variations in thermal properties can be performed. Disadvantageous is the lower purity of the deposited material and, last but not least, the unsatisfactory localization of the deposit. For these reasons, purely photolytic LCVD *cannot* be applied in micropatterning, in general.

A possibility that makes the best of the advantages and disadvantages of pyrolytic and photolytic LCVD is a twin-beam or a single-beam *combined* pyrolytic–photolytic reaction. This technique is also termed photophysical- or hybrid-LCVD. It should be emphasized, however, that in many systems classified as pyrolytic or photolytic both mechanisms are important, at least during the phase of nucleation. Initial investigations of this type have been performed for the deposition of Ni from $Ni(CO)_4$ [*Kräuter* et al. 1983]. Here, it was demonstrated that for (visible) Ar^+- or Kr^+-laser radiation that is absorbed neither within gaseous $Ni(CO)_4$ nor by the substrate the latent times for nucleation are significantly diminished when the UV plasma radiation of the laser tube, which is absorbed by $Ni(CO)_4$, is *not* blocked but focused onto the substrate together with the laser light. Short latent times have also been observed when using 356 nm Kr^+-laser light without the plasma radiation. This wavelength is slightly absorbed by $Ni(CO)_4$, but not by quartz substrates. When nucleation is started, deposition proceeds mainly thermally and depends only on the absorbed laser power and not on the presence of the plasma radiation. This can be understood from the strong absorption of the deposited Ni, which is approximately constant within this spectral range.

Photophysical LCVD has been investigated in further detail for Mo, W, and Pt [*Gilgen* et al. 1987]. Here, the UV multiline Ar^+-laser output between 351 and 364 nm was used together with $Mo(CO)_6$, $W(CO)_6$ and Pt (hfacac) as parent molecules. With transparent substrates such as glass or sapphire, deposition is

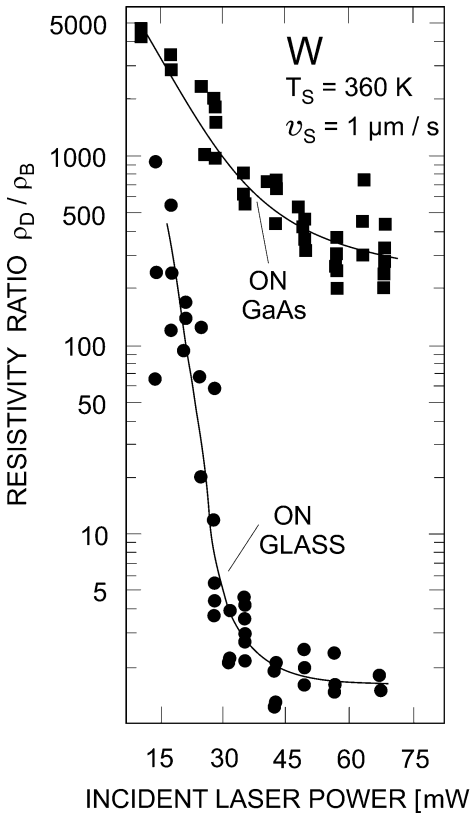

Fig. 18.4.1 Resistivities of laser-deposited W lines normalized to bulk values as a function of laser power (351–364 nm Ar^+-laser output). The pressure of the $W(CO)_6$ was 0.05 mbar. No buffer gas was used [*Gilgen* et al. 1987]

initiated by photolytic decomposition of the precursors. No delay or latent times were observed. After this initial step, absorption is determined by the deposited film and growth becomes dominated by pyrolysis. The deposition rates were, typically, $0.1-0.3\,\mu m/s$ and the writing speeds a few $\mu m/s$.

Figure 18.4.1 shows, for the example of W and two different substrates, the (normalized) resistivities of stripes versus laser power. The precursor was $W(CO)_6$ without any buffer gas. The most remarkable feature is the difference in resistivities of W stripes deposited on GaAs and glass substrates. This behavior originates from differences in the optical and thermal properties of these substrates. The thermal conductivity of GaAs exceeds that of glass by a factor of 10−30, depending on temperature. Therefore, the local temperature at a certain laser power will be considerably lower on GaAs than on glass. Consequently, the relative importance of pyrolytic and photolytic mechanisms will be quite different for these substrates. The lower laser-induced temperature on GaAs favors incorporation of photofragments such as C, O, CO, or CO_2 into the W films. The situation may even be more

complicated. The higher film resistivities measured on GaAs substrates may also originate, in part, from the different metallurgical phases of W. Even in bulk W, the electrical conductivity of the α-phase, which is formed between 300 and 650 °C, exceeds that of the β-phase, which is formed at lower temperatures, by a factor of 100−300.

The examples for combined photolytic–pyrolytic LCVD mentioned in this section are by no means unique. In particular, with transparent substrates, the initial phase of growth is quite frequently based on photolysis of gaseous or adsorbed precursors (Sects. 4.2 and 20.2). Photophysical LCVD with single or dual laser beams thus permits one to pattern transparent substrates at technically relevant deposition rates.

18.5 Applications of LCVD in Microfabrication

From a technological point of view, the experimental results presented throughout Chaps. 16, 17 and 18 demonstrate that LCVD enables one to fabricate smooth microstructures of good morphology and well-defined height-to-diameter ratio in a single-step maskless process. In the following, we summarize some of the real and potential applications of the technique in planar and non-planar materials processing (Sect. 1.2).

18.5.1 Planar Substrates

In microelectronic fabrication, LCVD has been found to be an invaluable technique for increasing product yields and testing early engineering designs. Among the present-day applications are ohmic contacts, interconnects for circuit and mask repair, device restructuring and customization, design and fault correction, etc. [see, e.g., *Baum* et al. 1991; *Nassuphis* et al. 1994]. Another interesting application is the fabrication of microlenses of SiO_2 on flat quartz substrates [*Kubo* and *Hanabusa* 1990].

Contacts

Spot-like deposits can be used for the fabrication of contacts. As demonstrated in Sect. 16.2, the smallest diameters of well-defined W spots produced from $WF_6 + H_2$ on 700 Å W/a-SiO_2 substrates were around 0.6 µm. The fabrication of a similar feature by standard CVD or plasma CVD (PCVD) in combination with photolithographic techniques would require many production steps. The sticking of W spots on amorphous SiO_2 substrates (with or without the 700 ÅW layer) has been studied by the Scotch-tape test. The different types of spots have all passed this test.

The fabrication of Schottky contacts has been demonstrated for W on GaAs [*Tabbal* et al. 1997] and for Cd on InP and $In_{0.53}Ga_{0.47}As$ [*Licata* et al. 1991].

Circuit Repair

The requirements for the repair of electrical open-circuits in microelectronic applications are quite strict: the repair must be of good electrical integrity, be reliable to electrical and environmental stressing, withstand subsequent chemical and physical treatments, and match the dimensions of the existing circuit. All these requirements are fulfilled by LCVD of gold using $Au(CH_3)_2$ (tfacac) and Ar^+-laser radiation. Figure 18.5.1 shows a SEM picture of a copper circuit on a polyimide substrate after repair by LCVD of gold. The repaired defect was about 250 μm long, 15 μm wide, and 5−10 μm high. The electrical resistivity was, typically, between 3 and 10 times higher than for bulk gold (2.4 μΩ cm).

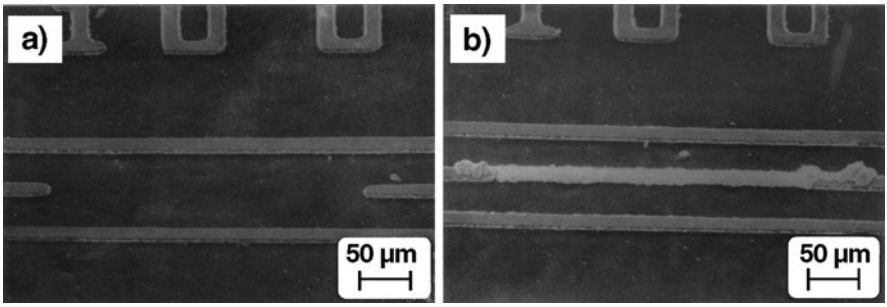

Fig. 18.5.1 a, b SEM picture demonstrating the repair of a defective copper circuit on a polyimide substrate. (**a**) Defect prior to repair ($d \approx 15\,\mu m$). (**b**) Similar feature after repair by LCVD of gold [*Baum* et al. 1991]

Interconnects

Similarly to in circuit repair, LCVD can be used to interconnect discrete regions on modules or integrated circuits (IC). The process has been used to rewire defective regions of a circuit, to customize components for specific designs or applications, to form interconnects on IC gate arrays, to interconnect inter-level metal planes by filling vertical vias, etc. The materials mainly employed were Ni, Pt, and W.

Mask Repair

Pyrolytic and photolytic LCVD has been employed to repair clear defects on lithographic masks, e.g., chrome-on-glass masks, where the metal is missing. Here, the only demands are to match the resolution and to completely block any light transmission.

18.5.2 Non-planar Substrates, 3D Objects

LCVD offers unique possibilities for the coating, patterning, and fabrication of non-planar 3D objects.

For example, it is possible to produce uniform protective coatings on mechanical workpieces of complex geometry, or to *selectively* increase the thickness of protective coatings (produced by standard techniques) on the edges or sides of tools or devices where mechanical or chemical requirements are particularly severe [*Hopfe* et al. 1996].

One can also conceive of many applications in chemical technology. For example, for catalytic purposes, production of metal coatings on cheap substrates, such as glass wool, could become of importance. Here, high-porosity sponge-like deposition would be possible by appropriate control of processing parameters.

LCVD makes it possible to directly write virtually any pattern onto 3D devices. An example is shown in Fig. 18.5.2a for the case of a W helix deposited by means of a focused Ar^+-laser beam on a (rotating) Si core. Here, patterning by mechanical masking or lithographic techniques together with large-area processing would be extremely difficult and in most cases even impossible. LCVD also enables one to fabricate free-standing 3D patterns by dissolving the substrate after the direct-write process (Fig. 18.5.2b).

Millimeter-high wall-like patterns with lateral dimensions of only a few micrometers can be fabricated for various different materials by repetitive direct writing. LCVD can also be used to fill up deep grooves or holes with almost any type of material.

Fibers of almost any length can be grown, even as single crystals, without any crucible and in an otherwise completely cold atmosphere. This technique not only

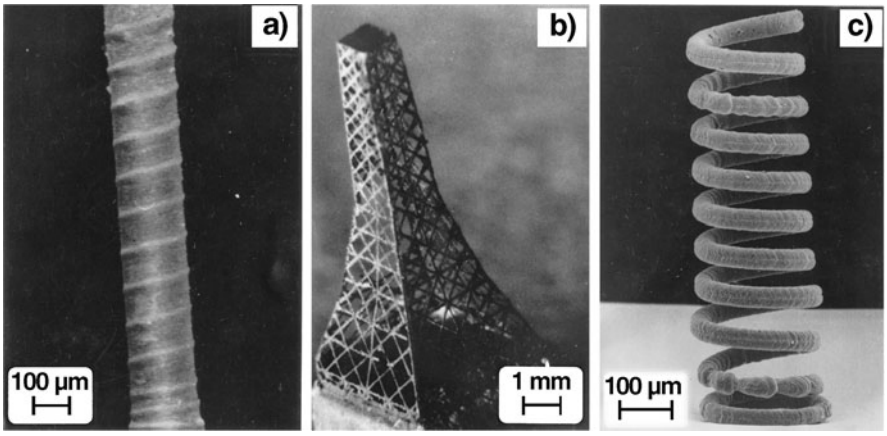

Fig. 18.5.2 a–c Examples of non-planar processing and fabrication of 3D objects by LCVD. (**a**) Microsolenoid with silicon core and tungsten helix [*Westberg* et al. 1993]. (**b**) Al-grid structure fabricated by laser direct writing onto poly-carbonate which was dissolved after LCVD [*Lehmann* and *Stuke* 1991]. (**c**) Free-standing boron microspring [*Johansson* et al. 1992]

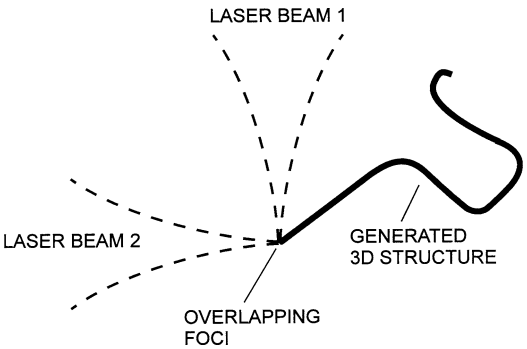

Fig. 18.5.3 Setup for 3D microfabrication of free-standing objects. The two laser beams are attenuated in such a way that almost no growth is observed for either beam alone, but only in the area of overlapping foci [*Lehmann* and *Stuke* 1995]

permits one to grow materials with higher purity, but also to grow new materials, quite possibly under extreme physical conditions, for example, at very high temperatures, pressures, or within electric or magnetic fields. Here, applications can only be speculated on.

Laser-CVD allows also *direct* 3D fabrication of microscopic objects. An example is the free-standing boron microspring shown in Fig. 18.5.2c. Here, the spring was moved in such a way that the laser focus was always positioned at its end. A more sophisticated setup that permits one to grow 3D microstructures of almost arbitrary shapes is shown in Fig. 18.5.3. Here, the intensities of the two laser beams are tuned in such a way that no significant growth takes place for either beam alone. Typical 'writing' speeds are some $10\,\mu m/s$. This setup has been used for rapid prototyping of micromechanical actuators such as microtweezers, micromotors, etc. [*Lehmann* and *Stuke* 1995], and for the fabrication of photonic bandgap structures [*Wanke* et al. 1997].

Chapter 19
Thin-Film Formation by Laser-CVD

Light-assisted CVD, and in particular laser-CVD, opens up new possibilities in thin-film fabrication. Laser light permits one to *selectively* generate high concentrations of atomic or molecular intermediate species that are present either not at all or only in small equilibrium concentrations in standard CVD using the same precursor molecules. Thus, LCVD enables one to study *new* reaction pathways and altered kinetics in thin-film growth. Lasers are often preferred over high-intensity lamps, at least in fundamental investigations, because of their high experimental versatility related to their intensity, monochromaticity, tunability, and directionability. In particular, at parallel incidence to the substrate surface, lasers permit pure gas-phase excitation. With perpendicular laser-beam irradiation, well-defined gas *and/or* surface excitations become possible. These include adsorbed layer photochemical and/or photothermal decomposition of precursor molecules, localized substrate heating which widely avoids homogeneous gas-phase processes, etc. The different irradiation geometries employed in large-area LCVD have been described together with Fig. 5.2.4.

From a practical point of view, light-assisted film growth is mainly studied with the intention of fabricating high-quality films at either *lower* substrate temperatures or under conditions of well-localized substrate heating. LCVD based on gas-phase heating (parallel incidence only; Fig. 1.2.2b) or laser-induced photolysis of gas- or adsorbed-phase precursors (Fig. 1.2.2a, b) permits one to deposit thin films without significant substrate heating. In such cases, elevated substrate temperatures are employed only, if at all, for improving film morphologies. This is one of the main advantages over conventional CVD. Furthermore, in contrast to plasma-CVD, there are no problems with VUV radiation or particle bombardment (Sect. 1.2). LCVD also permits monolayer control of film thicknesses. This is a requirement for the well-defined fabrication of heterostructures consisting of multiple thin-film layers with different material properties. The fact that gas-phase pyrolysis can be widely avoided by pulsed-laser irradiation of the substrate permits one to grow thin sponge-like "films" of single-wall carbon nanotubes (SWNT; Sect. 4.3.3).

As before, we concentrate on model systems for which the most complete data are available. For additional information and a list of systems investigated in the past, the reader is referred to the Appendices in previous editions of the book. These Appendices also include results on thin-film formation using lamps for either direct

D. Bäuerle, *Laser Processing and Chemistry,* 4th ed.,
DOI 10.1007/978-3-642-17613-5_19, © Springer-Verlag Berlin Heidelberg 2011

or indirect (via photosensitization) decomposition of parent molecules. Systems for which adsorbed-layer decomposition has been proved to be important, are discussed in Chap. 20.

19.1 Direct Heating

In the following, we consider systems where gas-phase molecules *directly* absorb the laser light. The excitation energy shall be locally randomized via collisions within a time that is short compared to any non-thermal reaction step. The laser beam shall propagate *parallel* to the substrate surface and thermally activate a (purely) homogeneous reaction (Figs. 19.1.1 and 1.2.2b). This situation applies to many types of large-area LCVD but also to some types of laser-induced etching.

The temperature distribution induced within the ambient medium can be calculated from the heat equation (2.2.1). In the case of uniform substrate heating, the temperature T_s enters the problem via the boundary condition $T(h_s) = T_s$. General solutions of (2.2.1) have been presented in Sect. 6.2. For the present problem, we can directly employ the specific solutions given in Chap. 7. Here, the window of the reaction chamber (at $z = 0$) can be taken into account by employing either $\eta \approx \kappa_w/w$ ('semi-infinite' windows) or $\eta \to \infty$ ('cold' windows). Solutions with $\eta = 0$ ignore the influence of the window; nevertheless, such solutions can be employed for $z > z_0 \approx \kappa/\eta \approx w\kappa/\kappa_w$ and weak absorption with $\alpha^* \ll 1$ and $z_0 < l_\alpha \times \kappa$ and κ_w are the heat conductivities of the gas and the window, respectively.

19.1.1 Stationary Solutions

For many estimations it is appropriate to find stationary solutions of the heat equation. For a laser beam with cylindrical symmetry, this can be written as

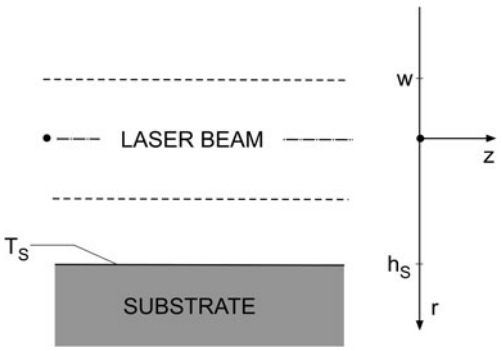

Fig. 19.1.1 Direct heating of an ambient medium by laser-light irradiation at parallel incidence to the substrate. The origin of the coordinate system, indicated by a *dot*, is in the *center* of the laser beam on the *left-hand* side. The laser beam has a radius w and propagates in z direction. The distance from the beam center to the substrate surface is h_s

$$\frac{1}{r}\frac{\partial}{\partial r}\left(r\frac{\partial T}{\partial r}\right)+\frac{\partial^2 T}{\partial z^2}+\frac{\alpha I_0}{\kappa}g(r)\exp(-\alpha z)=0\,, \tag{19.1.1}$$

where α and κ are constants, $r \geq 0$, $z > 0$ and $T = T(r, z)$. In the *absence* of the substrate, the boundary conditions are

$$T(z\to\infty)=T(r\to\infty)=T(\infty)\,,\qquad \left.\frac{\partial T}{\partial r}\right|_{r=0}=0\,, \tag{19.1.2a}$$

and

$$\left.\frac{\partial T}{\partial z}\right|_{z=0}=0\,. \tag{19.1.2b}$$

The boundary condition for $z = 0$ ignores the influence of the chamber window. In many cases it is more realistic to instead use

$$T(z=0)=T(\infty)\,. \tag{19.1.2c}$$

In any case, by employing Hankel transforms, the solution of the problem yields the temperature rise

$$\Delta T(r,z)=\frac{\alpha I_0}{\kappa}\int_0^\infty \mathrm{d}q\mathbf{J}_0(qr)g(q)\frac{q\exp(-\alpha z)-\xi\exp(-qz)}{q^2-\alpha^2}\,, \tag{19.1.3}$$

where $\xi \equiv \alpha$ with (19.1.2b) and $\xi \equiv q$ with (19.1.2c). $\mathbf{J}_0$ is the Bessel function of order zero and $g(q)$ is given by

$$g(q)=\int_0^\infty r\mathbf{J}_0(rq)g(r)\,\mathrm{d}r\,. \tag{19.1.4}$$

In the following, we consider only solutions for $\xi \equiv \alpha$ and for various intensity distributions [*Arnold* and *Bäuerle* 1994].

Case 1: Gaussian Laser Beam

For a Gaussian laser beam $g(r) = \exp(-r^2/w_0^2)$ we obtain

$$g(q)=\frac{1}{2}w_0^2\exp\left(-\frac{q^2w_0^2}{4}\right)\,. \tag{19.1.5}$$

Substituting (19.1.5) into (19.1.3) yields the temperature rise $\Delta T(r, z)$ whose maximum is given by

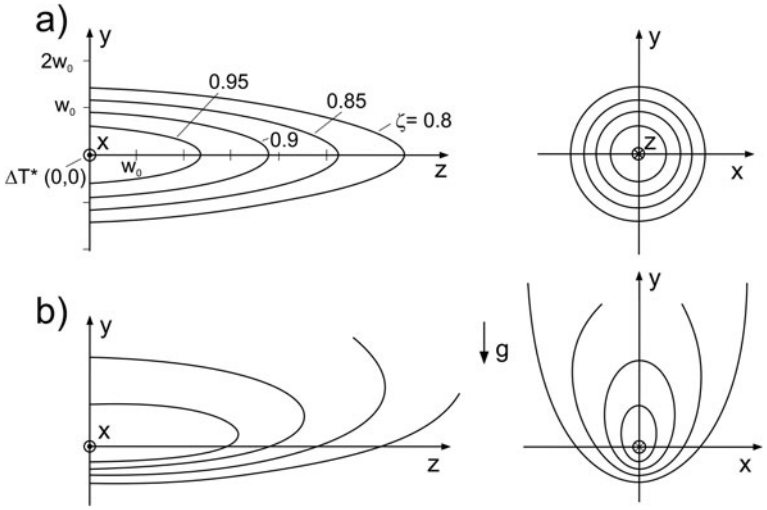

Fig. 19.1.2 a, **b** Isotherms $\Delta T^*(r, z) = \zeta \Delta T^*(0, 0)$ plotted in planes $x = 0$ and $z = 0$. (**a**) Gaussian beam, no convection. (**b**) Qualitative influence of free convection; $\boldsymbol{g}$ is the vector of gravity

$$\Delta T(0, 0) = \frac{\alpha I_0 w_0^2}{2\kappa} \int_0^\infty \frac{\mathrm{d}q}{\alpha + q} \exp\left(-\frac{w_0^2 q^2}{4}\right) . \tag{19.1.6}$$

We introduce the same normalization as in (7.2.8). The dependence of $\Delta T^*(0, 0)$ on α^* is identical to that shown in Fig. 7.2.2. Isotherms $\Delta T^*(r, z) = \text{const.} = \zeta \Delta T^*(0, 0)$ within planes $x = 0$ and $z = 0$ are plotted in Fig. 19.1.2a.

Case 2: Rectangular (Top Hat) Intensity Distribution

A circular beam with constant intensity over its cross section is described by $g(r) = \mathscr{H}(w - r)$, where $\mathscr{H}$ is the Heaviside function. With (19.1.4) we obtain

$$g(q) = \int_0^w r \mathbf{J}_0(qr)\,\mathrm{d}r = \frac{w}{q}\mathbf{J}_1(qw) . \tag{19.1.7}$$

If we still ignore the substrate, the temperature distribution $T(r, z)$ can be calculated by substituting (19.1.7) into (19.1.3). The maximum temperature rise is

$$\Delta T(0, 0) = \frac{\alpha I_0 w}{\kappa} \int_0^\infty \frac{\mathbf{J}_1(qw)}{q(q + \alpha)}\,\mathrm{d}q . \tag{19.1.8}$$

The dependences $\Delta T(0, 0) = f(\alpha)$ and $\Delta T(r, z) = \text{const.}$ are qualitatively similar to those plotted in Figs. 7.2.2 and 19.1.2, respectively.

Case 3: Influence of the Substrate

If we assume *cylindrical* symmetry, where the substrate has the form of a tube, the condition $T(r \to \infty) = T(\infty)$ in (19.1.2a) must be replaced by $T(r = h_s) = T_s$, where T_s is the temperature, and h_s the radius of the tube (Fig. 19.1.1). This geometry can be used for coating the insides of tubes by LCVD. For a weakly absorbing medium we can set $\partial T/\partial z \approx 0$ and $\exp(-\alpha z) \approx 1$. The solution of (19.1.1) is then

$$T(r) = T_s + \frac{\alpha I_0}{\kappa} \int_r^{h_s} \frac{dr'}{r'} \int_0^{r'} g(r'')r''\,dr'' \,. \tag{19.1.9}$$

For a *Gaussian* beam we obtain

$$T(r) = T_s + \frac{\alpha I_0 w_0^2}{4\kappa} \left[\mathrm{Ei}\left(-\frac{r^2}{w_0^2}\right) - \mathrm{Ei}\left(-\frac{h_s^2}{w_0^2}\right) + 2\ln\left(\frac{h_s}{r}\right) \right] , \tag{19.1.10}$$

where Ei denotes the exponential integral (Appendix B). This equation can be applied only if $h_s < (w_0 l_\alpha)^{1/2}$ or $h_s < \kappa/\eta$. If both h_s and the length of the reactor become very large, the temperature distribution is given by (19.1.3).

For a circular beam with constant intensity distribution, (19.1.9) can be written for $r < w$ as

$$T(r < w) = T_s + \frac{\alpha I_0 w^2}{2\kappa} \left[\ln\left(\frac{h_s}{w}\right) + \frac{1}{2}\left(1 - \frac{r^2}{w^2}\right) \right] , \tag{19.1.11a}$$

and for $r > w$ as

$$T(r > w) = T_s + \frac{\alpha I_0 w^2}{2\kappa} \ln\left(\frac{h_s}{r}\right) \,. \tag{19.1.11b}$$

The range of validity is similar to (19.1.10).

In pyrolytic laser-chemical processing with *plane* substrates, the assumption of cylindrical symmetry is certainly a crude approximation. This is true, however, even in the absence of a substrate or reaction chamber, because of convection (Fig. 19.1.2b). In gases, convection can be reduced by decreasing the pressure [note that $\mathscr{R}a \propto p^2 \Delta T/T$; see (9.5.12)] or by changes in the geometry of the reaction chamber. In some cases, the homogeneity of surface processes can be improved by increasing the laser power so that convective flows become turbulent.

At medium-to-high gas pressures and $\Delta T_c \geq T_s$, convection becomes very important. The characteristic length in (9.5.9) is of the order $l \leq h_s$. Typical flow velocities, v_c, are 0.2−5 cm/s. In the case of turbulence, v_c can exceed these values by several orders of magnitude.

19.1.2 Non-stationary Solutions

For a Gaussian beam, the center-temperature rise derived from (2.2.1) and (19.1.2), and the initial condition $T(t = 0) = T(\infty)$ is given by (7.5.1). For very short pulses where $t \ll w^2/D$, one can employ the energy balance and obtain for weak absorption, in analogy to (7.5.6),

$$T(r, t) = T(r, 0) + \frac{\alpha I(r)}{\varrho c_\mathrm{p}} t \ . \tag{19.1.12}$$

Influence of the Substrate

For cylindrical symmetry we can use the solution (19.1.12) in the initial phase and (19.1.9) for $t > h_\mathrm{s}^2/D$.

For a *plane* substrate with $T_\mathrm{s} \equiv T(y = 0) = T(t = 0)$ (Fig. 19.2.1), weak absorption, and a Gaussian beam with $w_0 < h_\mathrm{s}$, the center-temperature rise is

$$\Delta T(0, 0, t) = \frac{\alpha I_0 w_0^2}{4\kappa} \left[\ln(1 + 4t^*) + \mathrm{Ei}\left(-\frac{4h_\mathrm{s}^{*2}}{1 + 4t^*} \right) - \mathrm{Ei}\left(-4h_\mathrm{s}^{*2} \right) \right] , \tag{19.1.13}$$

where $t^* = tD/w_0^2$ and $h_\mathrm{s}^* = h_\mathrm{s}/w_0$. This solution can be applied only if $l_\alpha \gg h_\mathrm{s}$. For $t^* \to \infty$, we obtain

$$\Delta T(0, 0) = \frac{\alpha I_0 w_0^2}{4\kappa} \left[\mathrm{C} - \mathrm{Ei}\left(-4h_\mathrm{s}^{*2} \right) + \ln\left(4h_\mathrm{s}^{*2} \right) \right] , \tag{19.1.14}$$

where $\mathrm{C} = 0.577$ is Euler's constant.

19.2 Pyrolytic Processing Rates

We now calculate the reaction flux of product species, and thereby the processing rate, for homogeneous pyrolysis of precursor molecules. The laser beam shall have either cylindrical symmetry with the radius $w \equiv w_\mathrm{y}$ or rectangular symmetry with the widths $2w_\mathrm{x}$ and $2w_\mathrm{y}$ (Fig. 19.2.1). The latter situation applies to many cases of excimer-laser processing. For a first-order reaction of the type

$$\mathrm{AB} \to \mathrm{A}(\downarrow) + \mathrm{B}(\uparrow) \ , \tag{19.2.1}$$

the number density, $N_\mathrm{A} \equiv N_\mathrm{A}(\boldsymbol{x}, t)$, can be calculated from (14.2.1). Henceforth, we assume $N_\mathrm{AB} \gg N_\mathrm{A}, N_\mathrm{B}$. The generation of species A within the *volume* heated by the laser beam can be described by

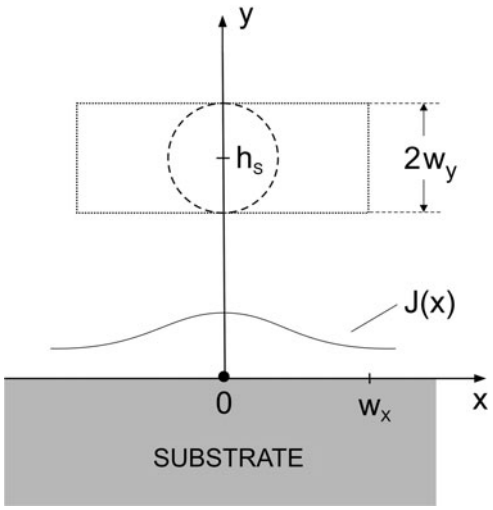

Fig. 19.2.1 Laser-chemical processing by means of a parallel laser beam propagating in the z direction (normal to the plane of the paper) at height h_s above the substrate surface ($y = 0$). The beam profile is either circular (*dashed line*) or rectangular (*dotted line*). The flux profile of species is shown (*solid curve*)

$$Q_{v,A} = k(T)N_{AB} = k_0 N_{AB} \exp\left(-\frac{\mathscr{E}}{T}\right) \equiv W_v(T) \,, \tag{19.2.2}$$

where $T \equiv T(\boldsymbol{x}, t) = T(\infty) + \Delta T(\boldsymbol{x}, t)$ is the temperature within the medium *above* the substrate (Sect. 19.1). With stationary conditions and a number of additional assumptions, analytic solutions of (14.2.1) can be found.

19.2.1 Diffusion

We consider AB and B as ideal gases and set $D_A \propto T$, so that $N(T)D_A(T) = N(\infty)D_A(\infty)$, with $N \approx N_{AB}$. Gas-phase recombination shall be ignored. Molecules impinging onto the surface shall stick on it with unit probability, i.e., $N_A(x, 0, z) = 0$. All quantities shall be independent of z. With these assumptions, (14.2.1) can be written as

$$N_{AB}(\infty)D_A(\infty)\nabla^2 x_A + W_v(T) = 0 \,. \tag{19.2.3}$$

The flux of species A at the surface $y = 0$ is

$$J_A(x) = -N_{AB}(\infty)D_A(\infty)\nabla x_A\Big|_{y=0} \,. \tag{19.2.4}$$

By employing the Green's function technique, we obtain

$$-J_{\mathrm{A}}(x) = \frac{1}{\pi}\int_{-\infty}^{\infty}\int_{0}^{\infty} W_{\mathrm{v}}(T)\frac{y'}{(x-x')^2+y'^2}\,\mathrm{d}y'\,\mathrm{d}x' = W_{\mathrm{s}}(x)\,, \quad (19.2.5)$$

where $W_{\mathrm{s}}(x)$ is the surface reaction rate. Note that $T = T(x', y')$. Let us consider various cases.

Case 1: w or w_{x}, $w_{\mathrm{y}} \ll h_{\mathrm{s}}$

The laser beam is circular or rectangular and concentrated near $x = 0$, $y = h_{\mathrm{s}}$. Substitution of $x' = 0$ and $y' = h_{\mathrm{s}}$ in (19.2.5) yields

$$W_{\mathrm{s}}(x) = -J_{\mathrm{A}}(x) \approx \frac{1}{\pi}\frac{h_{\mathrm{s}}}{x^2+h_{\mathrm{s}}^2}\Phi\,. \quad (19.2.6)$$

The function Φ describes the total number of species A produced within the volume heated by the laser beam (per unit time and length in the z direction)

$$\Phi = \iint W_{\mathrm{v}}(T(x', y'))\,\mathrm{d}x'\,\mathrm{d}y' \approx F\,W_{\mathrm{v}}(T_{\mathrm{c}})\,. \quad (19.2.7)$$

F is the cross section of the reaction zone. We then obtain

$$W_{\mathrm{s}}(x) = \frac{1}{\pi}\frac{h_{\mathrm{s}}F}{x^2+h_{\mathrm{s}}^2}W_{\mathrm{v}}(T_{\mathrm{c}})\,. \quad (19.2.8)$$

If we introduce the width of the temperature distribution, w_{T} (Sect. 6.5), we can make the approximation $F \approx \pi w_{\mathrm{T}}^2 T_{\mathrm{c}}/\mathscr{E}$. The normalized *film thickness* is

$$h^*(x^*) = \frac{h(x)}{h(0)} = \frac{W_{\mathrm{s}}(x)}{W_{\mathrm{s}}(0)} = \frac{1}{1+x^{*2}}\,, \quad (19.2.9)$$

where $x^* = x/h_{\mathrm{s}}$. This profile can be compared with experimental data obtained for a-Si:H films deposited from SiH_4 by means of CO_2-laser radiation. The data points in Fig. 19.2.2 represent average values obtained for distances $h_{\mathrm{s}} = 6, 7, 8$ and 9 mm and a reaction zone radius $w' \approx w_{\mathrm{T}}(T_{\mathrm{c}}/\mathscr{E})^{1/2} \leq 0.5\,\mathrm{mm} \ll h_{\mathrm{s}}$. The solid curve represents the (average) thickness profile calculated for a point source from (19.2.9).

Case 2: $w_{\mathrm{y}} \ll h_{\mathrm{s}}$

With the approximation $W_{\mathrm{v}}(x', y') = 2w'_{\mathrm{y}}W_{\mathrm{v}}(T(x'))\delta(y' - h_{\mathrm{s}})$, integration over y' in (19.2.5) yields

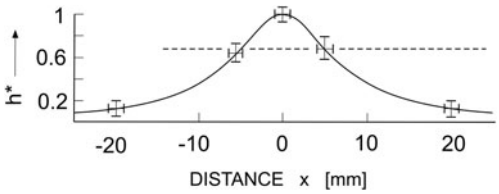

Fig. 19.2.2 Data represent the (average) thickness profile of an a-Si:H film deposited from SiH_4 by means of a CO_2-laser beam at parallel incidence to a vertical substrate [$w(1/e) \approx 5$ mm; $T_s \approx 350$°C] [*Golusda* et al. 1992]. The *solid curve* was calculated

$$-J_A(x) = \frac{2w_y}{\pi} \int_{-\infty}^{\infty} W_v(T(x')) \frac{h_s}{(x-x')^2 + h_s^2} \, dx' \, .$$

If we assume $W_v(T(x')) = W_v(T_c)$ with $|x'| \leq w_x$ and $W_v(T(x')) = 0$ with $|x'| > w_x$, we obtain

$$W_s(x) = \frac{\Phi}{2\pi w_x} \left[\arctan\left(\frac{w_x - x}{h_s}\right) + \arctan\left(\frac{w_x + x}{h_s}\right) \right] , \quad (19.2.10)$$

with $\Phi = F W_v(T_c) \approx 4 w_x w_y W_v(T_c)$, where w_x and w_y characterize the width of the reaction zone in the x and y directions. With $w_x \to 0$, we obtain (19.2.6). The normalized film thickness can be calculated in analogy to (19.2.9).

Case 3: $w_y \ll h_s$, $w_x \to \infty$

If we introduce the total number of species produced within the heated volume per unit length in the z and x directions, $\tilde{\Phi} = \Phi / 2w_x$ (species/cm^2 s), we obtain from (19.2.10)

$$-J_A(x) \approx \tilde{\Phi} \, . \quad (19.2.11)$$

In this approximation all species condense on the substrate.

19.2.2 Recombination

We now estimate the influence of recombination with

$$f(N_A, N_B) = -\frac{N_A(\infty)}{\tau_A^{rec}} x_A = -k_A^{rec} N_A(\infty) x_A = -C x_A \, , \quad (19.2.12)$$

where $C = \text{const}$. In the absence of gas-phase heating, this ansatz coincides with (14.2.15). Together with (19.2.3) and $x_A(y = 0) = 0$, we obtain for a point source instead of (19.2.6)

$$-J_{\mathrm{A}}(x) = \frac{2\Phi}{\pi}\frac{h_{\mathrm{s}}}{l l_{\mathrm{A}}^{\mathrm{rec}}}\mathbf{K}_1\left(\frac{2l}{l_{\mathrm{A}}^{\mathrm{rec}}}\right) , \tag{19.2.13}$$

where $l_{\mathrm{A}}^{\mathrm{rec}} = 2(D_{\mathrm{A}}\tau_{\mathrm{A}}^{\mathrm{rec}})^{1/2}$ is the recombination length, $l = (h_{\mathrm{s}}^2 + x^2)^{1/2}$, and $\mathbf{K}_1$ the modified Bessel function. The (normalized) thickness profile is

$$h^*(x^*) = \frac{1}{l^*}\frac{\mathbf{K}_1(2\beta l^*)}{\mathbf{K}_1(2\beta)} , \tag{19.2.14}$$

where $l^* = l/h_{\mathrm{s}} = (1 + x^{*2})^{1/2}$ and $\beta = h_{\mathrm{s}}/l_{\mathrm{A}}^{\mathrm{rec}}$. Comparison of (19.2.9) and (19.2.14) shows that recombination leads to a better localization of the deposit (Fig. 19.2.3). The analysis of the shape of the deposit permits one to experimentally investigate the recombination length, $l_{\mathrm{A}}^{\mathrm{rec}}$, from β. For a point source, the *total* flux to the surface is

$$J_{\mathrm{tot}} = \frac{2\Phi}{\pi}\int_0^\infty \frac{2\beta}{l^*}\mathbf{K}_1(2\beta l^*)\,\mathrm{d}x^* . \tag{19.2.15}$$

If $\beta \gg 1$, this yields

$$J_{\mathrm{tot}} = \Phi\exp(-2\beta) . \tag{19.2.16}$$

With $\beta \ll 1$, the flux is $J_{\mathrm{tot}} = \Phi$. For $w_{\mathrm{x}} \to \infty$, we obtain (19.2.15), except that Φ must be replaced by $\tilde{\Phi} = \Phi/2w_{\mathrm{x}}$.

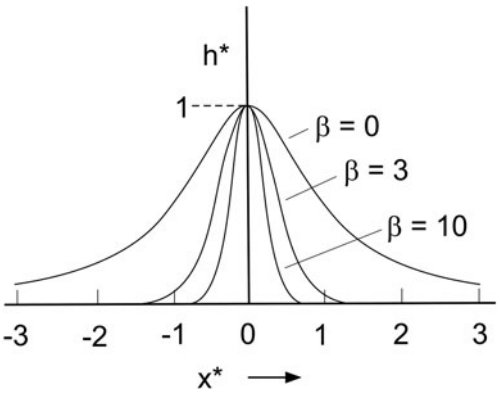

Fig. 19.2.3 Influence of recombination ($\beta > 0$) on the (normalized) thickness profile of the deposit

19.3 Photolytic Processing Rates

The density of product species $N_{\mathrm{A}}(\boldsymbol{x}, t)$ generated in a photochemical reaction

$$\mathrm{AB} + h\nu \to \mathrm{A}(\downarrow) + \mathrm{B}(\uparrow) \tag{19.3.1}$$

can be calculated from (14.2.1) and (14.2.2), together with the appropriate boundary conditions.

In the following, we discuss analytical solutions for the simple reaction (19.3.1) and the irradiation geometry in Fig. 19.2.1. With the assumptions made in Sect. 19.2.1 and *continuous* irradiation, the reaction rate on the surface can be described by (19.2.5). If w or w_x, $w_y \ll h_s$, we can use the approximate solution (19.2.6). The only difference is that W_v in (19.2.7) is now the *photolytic* decomposition rate:

$$W_v(I) = \sigma_{AB} N_{AB} \frac{I}{h\nu} ,$$

where σ_{AB} is the excitation/dissociation cross section. With $\Phi \approx F W_v(I)$, we obtain

$$W_s(x) = -J_A(x) = \frac{1}{\pi} \frac{h_s F}{x^2 + h_s^2} W_v(I) , \tag{19.3.2}$$

where F is now the cross section of the laser beam. The other cases discussed in Sect. 19.2 can be employed in analogy. For *pulsed* irradiation, the average rate is

$$\langle W_s(x) \rangle \approx \frac{1}{\pi \tau_i} \frac{h_s F}{x^2 + h_s^2} \sigma_{AB} N_{AB} \frac{\phi}{h\nu} , \tag{19.3.3}$$

where $1/\tau_i$ is the pulse repetition rate, and ϕ the laser fluence per pulse. The normalized thickness profiles are equal to (19.2.9). The effect of recombination can be taken into account as in Sect. 19.2.2.

19.4 Metals

Extended thin films of metals have been fabricated with areas up to about $10\,cm^2$. The precursors mainly employed were metal halides, metal alkyls, and metal carbonyls (see previous editions). The preferred light sources are excimer lasers and harmonics of Nd:YAG lasers. In many systems, decomposition of precursors is mainly photolytic at low laser-light intensities and mainly pyrolytic at higher intensities.

19.4.1 Deposition from Metal Halides

Detailed investigations on large-area film deposition have been performed in particular for W using mixtures of WF_6 and H_2 [*Deutsch* 1984; *van Maaren* et al. 1991]. Here, ArF-laser radiation at *parallel* incidence has been employed. The substrates, mainly silicon wafers with and without a thermally grown SiO_2 layer, were

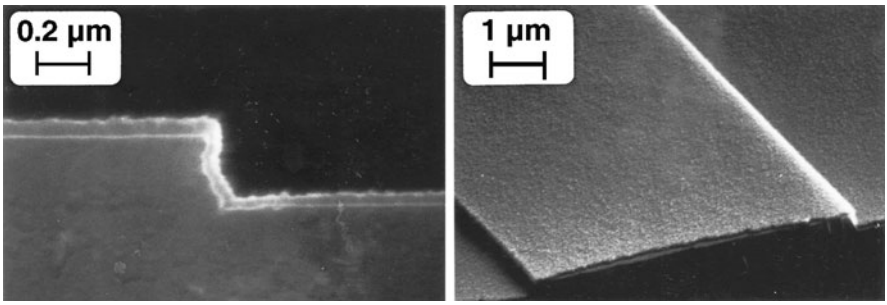

Fig. 19.4.1 SEM pictures showing a side and a top view of a W film over a SiO_2 step on a Si substrate. Deposition was performed with ArF-laser radiation from $WF_6 + H_2$ with $T_s = 285°C$ [*Deutsch* 1984]

preheated to a certain temperature, T_s. The surface morphology of films, and in particular the conformal coverage of the substrate, is excellent (Fig. 19.4.1).

Figure 19.4.2 shows an Arrhenius plot of the deposition rate. T_s is the (uniform) substrate temperature. No experimental information on the laser-induced gas-phase temperature exists. For comparison, corresponding results obtained by standard CVD are included in the figure. Here, it should be noted that with the present systems and the parameters under consideration standard CVD is *selective*, i.e., W deposition is observed only on Si and not on SiO_2. LCVD is *non-selective* and permits deposition at temperatures $T_s < 600\,K$. With many applications, however, selective substrate coating is desirable. Another important feature seen in the figure is the strong decrease in the apparent chemical activation energy, which is characterized by the slope of the dashed line. This may demonstrate that the laser light changes the chemical reaction pathways involved in the deposition process. There are, however, uncertainties in this interpretation because of laser-induced gas-phase heating.

The overall decomposition of WF_6 in the presence of H_2 is described by (16.2.1). With Si substrates, film growth may be initiated by thermally activated reduction of WF_6 according to (18.1.1).

Photochemical activation by ArF-laser radiation ($\lambda = 193\,nm$; $6.4\,eV$) produces radicals, probably via the reaction

$$WF_6 + h\nu(ArF) \rightarrow WF_x + (6 - x)F\,, \tag{19.4.1}$$

with $x = 4$ or 5. This process is followed by reactions with H_2 and, in the case of Si substrates, with Si. The latter reaction channel seems to be of minor importance (Figs. 19.4.1 and 19.4.2). Fluorine atoms can react with H_2 in a strongly exothermic reaction,

$$H_2 + F \rightarrow HF + H\,. \tag{19.4.2}$$

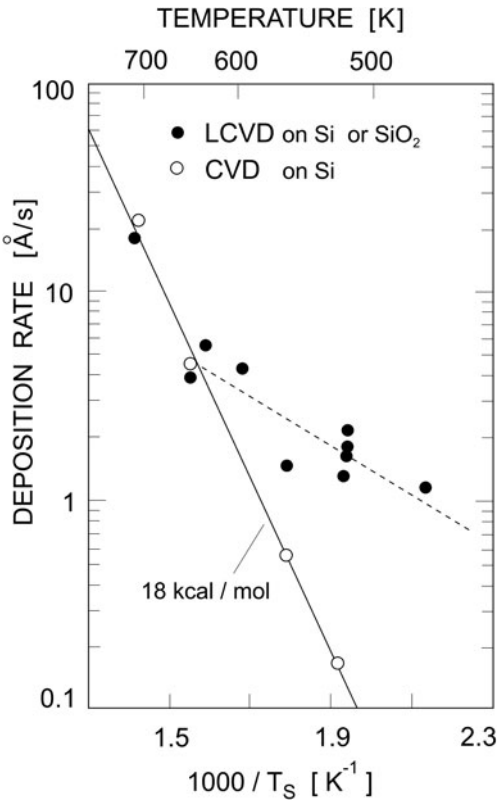

Fig. 19.4.2 Arrhenius plot of the (*thickness*) deposition rate of W films. The precursor was WF_6 diluted in H_2. ●: Deposition by ArF-laser radiation on Si and SiO_2/Si substrates. ○: Deposition by standard CVD on Si substrates [adapted from *Deutsch* 1984]

Atomic H formed in the gas can react with WF_6 and with WF_x radicals via a complex series of reactions that result in W deposition and in gaseous HF. Such a reaction pathway could qualitatively explain the strong change in activation energy with respect to standard CVD, where the rate-limiting step in the kinetically controlled region is probably determined by the formation of atomic H via dissociative adsorption of H_2 on the W surface [*Hitchman* et al. 1989]. It should be emphasized that these mechanisms are still under discussion.

Laser-deposited W films are of high purity, with a concentration of $F < 1\%$. Good adherence and low electrical resistivity of films was achieved only at elevated substrate temperatures. At $T_s = 400°C$, the electrical (sheet) resistivity of LCVD films exceeds that of pure bulk W by less than a factor of two. While this T_s seems to be rather high, standard CVD of W is frequently performed at even higher temperatures. In particular, with SiO_2 substrates, reasonable deposition rates are only obtained with $T_s \geq 700\,°C$.

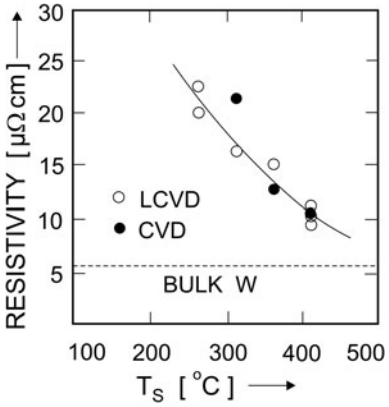

Fig. 19.4.3 Resistivity of W films deposited from a mixture of WF_6 and H_2 on Si substrates by LCVD (○) and standard CVD (●) at various substrate temperatures, T_s [adapted from *van Maaren* et al. 1989]

Figure 19.4.3 compares electrical resistivities of films deposited by LCVD and standard CVD on Si substrates at various temperatures, T_s. The film resistivity decreases strongly with increasing T_s. This behavior is mainly ascribed to the grain size of films, which increases with T_s. With temperatures as low as 250°C, the resistivity of laser-deposited films is only 20 μΩ cm. At this temperature, films produced by standard CVD are strongly non-uniform. Laser-deposited films show, in general, significantly smaller thickness variations than standard CVD films. This was revealed from Rutherford back-scattering (RBS) [*van Maaren* et al. 1989, 1991].

LCVD of circular Ti films with diameters of a few mm has been studied both experimentally [*Chou* et al. 1989] and theoretically [*Kar* et al. 1991]. Here, CO_2-laser radiation at perpendicular incidence has been used to thermally decompose $TiBr_4$. The substrate was stainless steel and the deposition rate about 0.05 μm/s.

19.4.2 Deposition from Alkyls and Carbonyls

Intense investigations have been performed on the deposition of Al from $Al_2(CH_3)_6$ and of Cr, Mo, and W from the hexacarbonyls on Pyrex, SiO_2 and Si substrates. Most of these experiments were performed with ArF and KrF lasers.

With *perpendicular* laser-beam incidence, bright silvery metallic films of reasonable quality were obtained. Typical deposition rates are between a few Å/s and some 10 Å/s. The adhesion of films depends strongly on the type and cleaning of the substrate material and on the laser power and wavelength. With SiO_2 substrates good film adhesion has been achieved ($> 5 \times 10^8$ dynes/cm^2). The tensile stresses were between 10^9 and 7×10^9 dynes/cm^2. Films of Cr and Mo deposited at room temperature had a tendency to peel when exposed to air. This could be avoided by

heating the substrate to about 150°C either during deposition or prior to removal from the cell.

With *parallel* laser-beam irradiation and low substrate temperatures, grey or black particulate films with high impurity contents were obtained.

Films deposited photolytically without significant substrate heating have resistivities that exceed the corresponding bulk values by a factor of 10–10^4. This large variation in ϱ originates from differences in grain sizes and, more importantly, in impurity concentrations which strongly depend on surface temperature. The concentrations of C_xH_y or C_xO_y fragments incorporated decrease with increasing T_s. This explains the superior electrical properties of films deposited with perpendicular incidence [ϱ(Cr, Mo, W) $\approx 20\varrho_B$(Cr, Mo, W)]. With Al the resistivity ratio was significantly lower.

There are several possible ways to improve the morphology and physical properties of photodeposited films. Among these are:

- Uniform substrate heating to temperatures where no significant dark reactions take place.
- Combined twin-beam or single-beam photophysical LCVD (Sect. 18.4) using irradiation geometries as shown in Fig. 5.2.3b, c.
- Post-deposition treatment. For example, in Al films deposited from $Al_2(CH_3)_6$ the contamination with CH_3 can be significantly diminished by subsequent ArF-laser irradiation in a vacuum [*Higashi* and *Rothberg* 1985]. By using pulsed optoacoustic IR spectroscopy, it has been demonstrated that high-yield non-thermal photodesorption of CH_3 groups incorporated in the films can be achieved with ArF-laser radiation, but not with KrF-laser radiation. Such post-treated films had electrical and optical properties similar to those deposited at elevated substrate temperatures. If these observations hold more generally, this technique would be a unique tool to improve the quality of both photolytically and pyrolytically deposited films. It would also be relevant in high-resolution pyrolytic patterning, where low (local) laser-induced temperatures are employed. The improvement of other laser-deposited materials, such as Al_2O_3, by UV-laser irradiation, can eventually be explained, at least in part, along similar lines. Inhomogeneous laser-beam illumination and structure formation (Chap. 28) can result in inhomogeneous impurity incorporation [*Houle* et al. 1986].

19.5 Semiconductors

Light-enhanced/induced growth of thin films of semiconductors has been studied mainly with excimer lasers, frequency-doubled Nd:YAG lasers, cw- or pulsed-CO_2 lasers, and with lamps. A tabular presentation of the various different investigations is given in *Bäuerle* (2000). When lamps are used, the precursor molecules are excited either directly or indirectly via Hg photosensitization.

19.5.1 Photodecomposition of Silanes

Amorphous, polycrystalline, and epitaxial films of Si and Ge have been deposited mainly from SiH_4, Si_2H_6 and GeH_4. The photodecomposition channels can most easily be understood from the UV absorption spectra and energy-level diagrams shown in Fig. 19.5.1 for SiH_4 and Si_2H_6. Arrows indicate various optical transitions induced by lasers, lamps, or photosensitization. Single-photon decomposition of SiH_4 and Si_2H_6 can be achieved only with energies $h\nu \geq 8$ eV when $\lambda \leq 155$ nm and ≥ 6.2 eV when $\lambda \leq 200$ nm. Thus, decomposition of SiH_4 by 193 nm (6.4 eV) ArF- or 248 nm (5 eV) KrF-excimer-laser radiation requires coherent absorption of at least two photons. This process is quite efficient, even with relatively low intensities ($< 10^6$ W/cm^2). Si_2H_6 can be decomposed by single-photon absorption of either ArF- or 157 nm F_2-laser radiation. This is the reason why Si_2H_6 is the preferred precursor for selective photochemical LCVD. With high laser-light intensities, two-photon absorption and optical activation of photofragments also seems to become important with Si_2H_6.

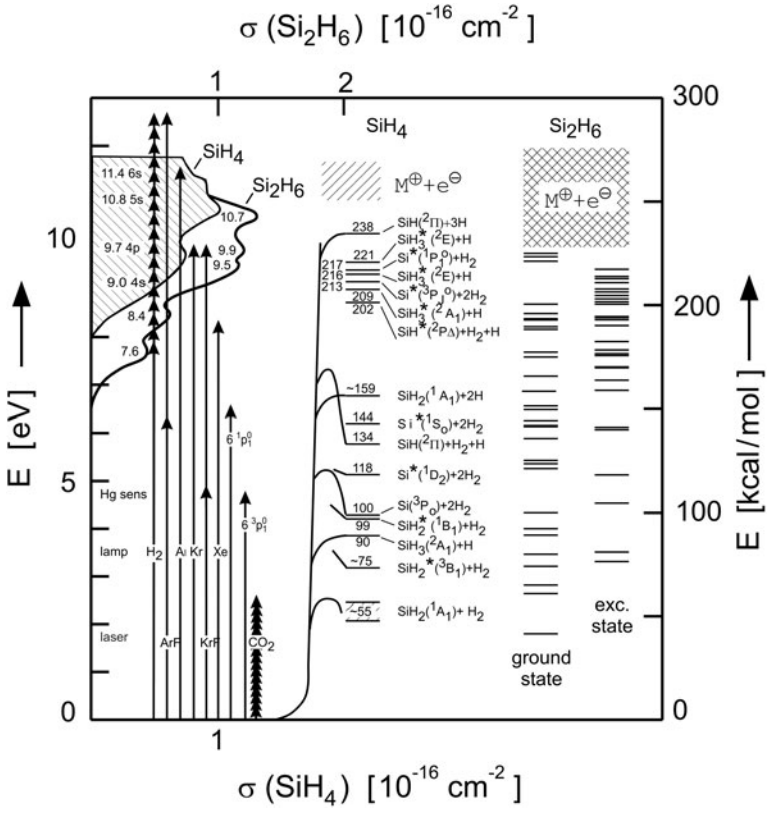

Fig. 19.5.1 Energy level diagrams of SiH_4 and Si_2H_6 including absorption spectra, optical excitation processes, and primary decomposition pathways [adapted from *Stafast* 1988]

The primary *photochemical* decomposition processes of SiH_4 and Si_2H_6 have been investigated by means of a 147 nm Xe lamp [*Perkins* et al. 1979]. The main reaction steps with SiH_4 can be described by

$$SiH_4 + h\nu \rightarrow SiH_2 + 2H \tag{19.5.1a}$$

and

$$SiH_4 + h\nu \rightarrow SiH_3 + H\,, \tag{19.5.1b}$$

where the relative quantum yield of (19.5.1a) is by about a factor of 5 larger than that of (19.5.1b). Corresponding experiments with Si_2H_6 have revealed three primary reaction channels,

$$Si_2H_6 + h\nu \rightarrow SiH_2 + SiH_3 + H\,, \tag{19.5.2a}$$
$$Si_2H_6 + h\nu \rightarrow Si_2H_4 + 2H\,, \text{ and} \tag{19.5.2b}$$
$$Si_2H_6 + h\nu \rightarrow Si_2H_5 + H\,, \tag{19.5.2c}$$

with relative quantum yields 0.61:0.18:0.21.

Mercury-photosensitized decomposition of SiH_4 and Si_2H_6 has also been extensively studied (Sect. 2.3.1). The most probable channel for fragmentation due to energy transfer from $Hg(^3P_1)$ to SiH_4 can be described by

$$Hg(^3P_1) + SiH_4 \rightarrow Hg(^1S_0) + SiH_3 + H\,. \tag{19.5.3}$$

Thermal activation by either standard heating or by IR-laser radiation permits decomposition along the most *energetically* favorable pathway,

$$SiH_4 \rightarrow SiH_2 + H_2\,. \tag{19.5.4}$$

Other decomposition pathways are characterized by higher activation energies and primary fragments such as SiH_3, SiH_2, and SiH radicals, or diradicals and Si atoms.

With Si_2H_6, the lowest activation energy is required for the fragmentation reaction

$$Si_2H_6 \rightarrow SiH_4 + SiH_2\,, \tag{19.5.5}$$

while the thermodynamically most stable products are formed according to

$$Si_2H_6 \rightarrow Si_2H_4 + H_2\,. \tag{19.5.6}$$

For further details on the photochemistry of SiH_4 and Si_2H_6, see, e.g., *Stafast* (1988) and references therein.

The amount of hydrogen incorporated in deposited films depends on the type and density of precursor molecules, on the particular decomposition channel involved, and on the substrate temperature.

19.5.2 Crystalline Ge and Si

The growth of Si and Ge films has been investigated for various substrate materials by employing excimer-laser radiation and mixtures of SiH_4/N_2 and GeH_4/He [*Eden* 1991]. With *parallel* laser-beam incidence, the growth rates were, typically, between 0.1 and 1 Å/s, depending on the (uniform) substrate temperature and gas pressure. These rates are 10−100 times lower than those achieved at normal laser-beam incidence. The average grain sizes of deposited films depend on the specific parameter set employed.

Epitaxial growth of Si on (100) Si wafers at (moderate) temperatures ($600°C \leq T_s \leq 650°C$) has been demonstrated with ArF- and XeF-laser radiation at perpendicular incidence using Si_2H_6 diluted in H_2 [*Yamada* et al. 1989]. The good crystallinity and electrical properties of films were interpreted by laser-enhanced surface migration of Si atoms.

Epitaxial growth of Ge onto (100) GaAs has been demonstrated with ArF-laser radiation at parallel incidence and substrate temperatures $T_s \geq 285°C$ [*Kiely* et al. 1989]. In the absence of laser light, films are amorphous ($T_s \approx 305°C$) or polycrystalline ($T_s \approx 415°C$). This clearly demonstrates the change in deposition kinetics due to the excitation of GeH_4. The initial step is ascribed to photochemically generated GeH_2 and GeH_3 radicals that are transformed into Ge_2H_6 via collisions. These species diffuse to the substrate surface, where they subsequently pyrolyse.

19.5.3 Amorphous Hydrogenated Silicon (a-Si:H)

The enormous interest in a-Si:H arises from various applications of this material. Among these are low-cost solar cells, electrophotographic plates, thin-film transistors, optical sensors, etc. [*Fritzsche* 1984; *LeComber* et al. 1981; *Takahashi* and *Konagai* 1986]. Hydrogen incorporation into a-Si is necessary because it saturates Si dangling bonds and relieves strains, resulting in a reduced defect level and the ability to modulate the Fermi level by substitutional doping. Currently, the preferred technique of producing a-Si:H films is plasma-CVD (PCVD) using SiH_4 as a precursor. Structurally superior amorphous films are produced by standard CVD. However, to obtain reasonable deposition rates, CVD requires substrate temperatures of at least 600°C. With such high temperatures, the films contain an insufficient amount of hydrogen (< 1 at. %) to achieve good electronic properties.

Photoenhanced deposition of thin films of a-Si:H has been demonstrated with lasers, lamps [*Redondas* et al. 1998], and by Hg photosensitization [*Kamimura* and

Hirose 1986]. The precursors most commonly used are SiH_4, Si_2H_6, and Si_3H_8 diluted in appropriate buffer gases.

Excimer-Laser-Induced Deposition

Thin films of a-Si:H can be deposited efficiently from Si_2H_6 with ArF-laser light (Fig. 19.5.1). Deposition from SiH_4 was observed only if significant substrate heating takes place [*Murahara* and *Toyoda* 1984].

Figure 19.5.2 compares film growth rates obtained by conventional CVD using Si_2H_6 diluted in H_2 and He with those obtained under otherwise identical conditions in the presence of an ArF-laser beam at *parallel* incidence. For conventional CVD the apparent activation energy is $\Delta E \approx 35 \pm 2$ kcal/mol. With LCVD and temperatures $T_s < 400\,°C$, this energy is only $\Delta E = 2.1 \pm 0.5$ kcal/mol. This weak dependence on T_s suggests that deposition is dominated by gas-phase photolysis. The small increase in slope observed near 450°C reflects the increasing importance of thermal activation. At a laser-pulse repetition rate of 20 Hz, growth rates between

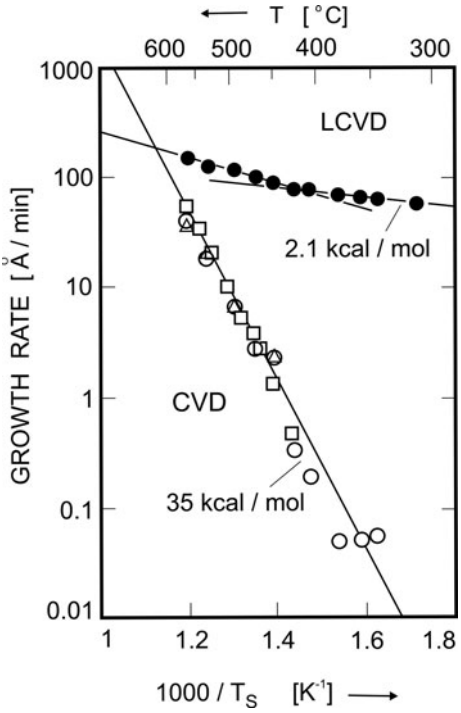

Fig. 19.5.2 Arrhenius plot for the deposition of a-Si:H films on thermally oxidized (100) Si ($p =$ 5 Torr; 40 sccm of 10% Si_2H_6/90% H_2 and 390 sccm of He window flush). T_s is the (uniform) substrate temperature. Open symbols refer to standard CVD and solid symbols to LCVD (ArF laser at parallel incidence; 20 Hz, 750 mW/cm^2) [*Eres* et al. 1988]

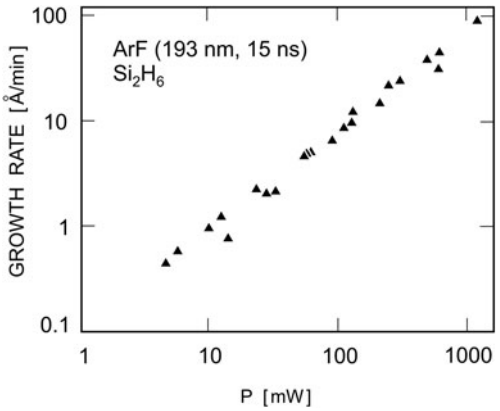

Fig. 19.5.3 Growth rate of a-Si:H films as a function of ArF-laser power [*Eres* et al. 1988]

1 and 3 Å/s have been obtained. The high deposition rates achieved at relatively low temperatures enable one to optimize the physical properties of films with each substrate material.

The film-growth rate increases linearly with laser power (Fig. 19.5.3). Thus, with the laser powers employed, disilane photolysis is dominated by a single-photon process. No film growth was observed with KrF-laser radiation.

The influence of buffer gases (H_2, He, and Ar) was studied in detail by *Dietrich* et al. (1989).

Amorphous and microcrystalline silicon films have also been deposited by excimer-laser-assisted RF glow-discharge [*Roca i Cabarrocas* et al. 1998].

CO_2-Laser-Induced Deposition

For CO_2-laser light at *perpendicular* incidence, deposition of Si onto fused quartz is dominated by pyrolysis of precursors at the gas-solid interface (SiO_2 strongly absorbs CO_2-laser light). Nevertheless, *gas-phase* heating can be important as well. This has been demonstrated with SiH_4, for which the wavelength dependence of the deposition rate correlates with the absorption spectrum of gaseous SiH_4. Maximum deposition rates over areas of 1 cm^2 were about 20 Å/s with SiH_4 and 200 Å/s with Si_2H_6 [*Hanabusa* et al. 1984].

Fabrication of high-quality a-Si:H films using *parallel* CO_2-laser-beam incidence requires uniform substrate heating to, typically, 200−400°C. Deposition rates are much lower than for perpendicular incidence, even when significantly higher laser powers are used. With SiH_4, typical growth rates are 2−5 Å/s. However, the uniformity of films is superior to those produced at perpendicular incidence. Films with excellent adherence were deposited over areas up to 80 cm^2 [*Curcio* et al. 1986].

Decomposition of SiH_4 seems to occur in two steps. In the first step, which is considered as the rate-limiting process, SiH_2 radicals and H_2 are produced by

gas-phase heating according to (19.5.4). Here, SiH_4 molecules vibrationally excited in a *single-photon* absorption process (indicated by $*$) transfer their energy among each other via collisions (Sect. 2.3) and decompose according to

$$SiH_4 + h\nu \rightarrow SiH_4^* \rightarrow \cdots \rightarrow SiH_2 + H_2 \,. \tag{19.5.7}$$

This process is most efficient if the CO_2-laser frequency is tuned to a strong vibrational transition of the SiH_4 molecule. The second step depends on SiH_4 pressure and laser fluence. At high pressures and/or high fluences, SiH_2 radicals react homogeneously with other SiH_2 or SiH_4 molecules to produce particulates within the gas. At lower pressures and fluences, diffusion of SiH_2 radicals to the surface dominates and a thin film of a-Si:H will grow, following the reaction

$$SiH_2 \rightarrow SiH_y(\downarrow) + (1 - y/2)H_2(\uparrow) \,, \tag{19.5.8}$$

where y denotes the hydrogen content within the film.

Figure 19.5.4 shows an Arrhenius plot of the film growth rate obtained with different samples, laser powers, substrate temperatures, gas compositions, and gas pressures. T_g is the maximum gas-phase temperature calculated from (19.1.1). Data obtained under different experimental conditions can be described by a single activation energy. This supports the interpretation that deposition is controlled by *single-photon* vibrational absorption of SiH_4 and fast energy relaxation via collisions within the volume of the laser beam. This is in agreement with simple estimations: for typical conditions [an absorbed laser power of 1 W/cm, $p(SiH_4) = 10$ mbar, and $T_g = 10^3$ K] the excitation rate is $W_{exc} \approx 10^3$ /s, and the average time between collisions about 10^{-8} s. The vibrational–translational relaxation rate is $1/\tau_{v\text{-}T} \approx 10^4$ /s. Therefore, (2.3.10) is readily fulfilled. This example shows that even *non-selective* LCVD opens up new possibilities: with parallel laser-beam incidence, high temperatures, and thereby high reaction rates, can be induced in the immediate neighborhood of heat-sensitive substrates.

The composition, morphology, and the optical and electrical properties of a-Si:H films deposited from SiH_4 diluted in Ar has been investigated by *Metzger* et al. (1988), *Meunier* et al. (1987b), and others. The magnitude of the unpaired spin concentration (this is a measure of the concentration of dangling bonds, which should be as low as possible for high-quality films) in LCVD films was about 400 times lower than in conventional CVD films and similar to that of PCVD and HOMOCVD films. The main parameter that determines the physical properties of LCVD films is the substrate temperature, which controls the total concentration of hydrogen. The films have a predominantly Si-H_2 structure, which is similar to HOMOCVD films. Undoped LCVD and HOMOCVD films are almost intrinsic, while PCVD films are usually somewhat n-type, probably due to defects generated by ion bombardment. The high ratio of the photoconductivity, σ_p, to the dark conductivity, σ_d, with values up to some 10^5 is an indication for a low overall defect density.

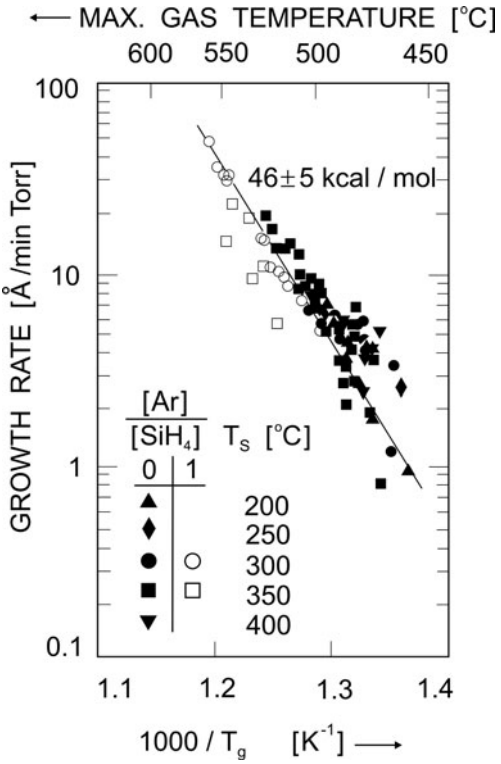

Fig. 19.5.4 Arrhenius plot of the growth rate (Å/min per torr of SiH_4) of a-Si:H films deposited by means of CO_2-laser radiation at parallel incidence. T_g is the calculated maximum laser-induced gas temperature, adapted from [*Meunier* et al. 1987a]

The high hydrogen content of cw-CO_2-laser-deposited films (at $T_s = 300°C$ about 20−25%) is one of the main drawbacks to better film qualities. This problem can be overcome by SF_6 sensitization [*Golusda* et al. 1993]. Contrary to SiH_4, vibrational excitation of the quasi-continuum of SF_6 is possible without intermediate collisions (Sects. 2.3 and 14.1). This is the reason why mixtures of $SiH_4 + SF_6$ permit to deposit a-Si:H films with an optimal hydrogen content ($\approx 10\%$). The photoconductivity of such films is about 10^{-4} $(\Omega cm)^{-1}$. Similar experiments have been performed to fabricate a-Ge:H films [*Barth* et al. 1994]. For further details see *Bäuerle* (2000) and references therein.

19.5.4 Compound Semiconductors

Investigations on photo-enhanced CVD of compound semiconductors have been performed mainly for GaAs, GaP, InP, CdTe, HgTe, and some oxides such as ZnO, In_2O_3, and SnO_2. In the presence of light, films can be grown with lower substrate

temperatures/higher deposition rates. Frequently, the surface morphology of films is significantly improved with respect to those grown by standard metal-organic CVD (MOCVD). Clearly, with lower substrate temperatures, interdiffusion of film and substrate material is reduced. The precursors most frequently employed are alkyls.

For epitaxial growth of CdTe on (100) GaAs substrates, photo-enhancement factors (ratio of growth rates for illuminated and non-illuminated regions) of about 8 have been found for 257 nm Ar^+-laser-light intensities ($0.16 W/cm^2$). Here, the (uniform) substrate temperature was about 300°C. $Cd(CH_3)_2$ and $Te(C_2H_5)_2$ have been employed as precursors [*Irvine* et al. 1989]. At *low* light intensities, different surface processes control the growth kinetics. Among those are: adsorption of Te atoms, photolytic decomposition of adsorbed radicals or undecomposed alkyls, and desorption of C_2H_5 or CH_3 groups. At *higher* intensities, photolytic gas-phase decomposition becomes important as well. For further details see the previous edition of this book and references therein.

19.5.5 Carbon

Classification of carbon is somewhat arbitrary because its electrical and thermal properties depend on whether its microstructure is amorphous, graphitic, or diamond-like. Clearly, the new materials, the fullerenes and graphene are classes by itself.

Amorphous and graphitic carbon films have been deposited by laser-induced photodissociation and/or photothermal decomposition of various different types of precursor molecules. Among the latter are C_2H_3Cl, CCl_4, CH_2I_2, C_2H_2, C_2H_4 and CH_4. Both cw- and pulsed-lasers have been employed.

While films deposited at low substrate temperatures are mainly amorphous, the graphite structure dominates at higher temperatures. For an overview see *Bäuerle* (2000).

Diamond-like carbon (DLC) films were synthesized by employing a stationary CO_2-laser-induced optical discharge (laser plasmatron, Sect. 11.7.1) in a gas mixture of $CH_4/H_2/Xe(Ar)$ at 1 atm. By this means, nanocrystalline- and polycrystalline DLC films were grown with rates up to 50 µm/h [*Konov* et al. 1998]. DLC films fabricated by PLD are discussed in Sect. 22.5.3.

The growth of sponge-like thin 'films' of carbon nanotubes and nanohorns by laser-assisted CVD using both cw- and pulsed-laser irradiation is discussed in Sect. 4.3.3.

19.6 Insulators

Photo-assisted growth of (mainly) insulating films permits one to combine good step coverage, low mechanical stresses and defect concentrations with high deposition rates at low-to-moderate substrate temperatures. The systems investigated up to the year 2000 are listed in the previous edition of this book.

Direct laser-enhanced surface oxidation/nitridation in pure oxygen/nitrogen is described in Chap. 26.

19.6.1 Oxides

The oxidant most frequently employed in photo-assisted CVD of oxide films is N_2O. This molecule can be dissociated within the range $138\,\text{nm} \leq \lambda \leq 210\,\text{nm}$ with almost unit quantum yield. Thus, ArF lasers are the preferred sources in this application. Dissociation can be described by

$$N_2O + h\nu(193\,\text{nm}) \rightarrow N_2 + O(^1D)\,, \tag{19.6.1}$$

where excited *atomic* oxygen is the primary reactive product. Atomic oxygen reacts with the precursor of the other component, or with fragments of it, and forms the oxide.

The physical and chemical properties of Al_2O_3 and SiO_2 films deposited by means of ArF-laser radiation from mixtures of $Al_2(CH_3)_6 + N_2O$ and $SiH_4 + N_2O$, respectively, are listed in *Bäuerle* (2000).

For *parallel* laser-beam incidence, the deposition rates are, typically, between 10 and 50 Å/s. The mechanical, optical and electrical properties of LCVD films can be further improved by using *combined parallel / perpendicular* laser-beam irradiation.

Photo-assisted growth of SiO_2 layers by means of different types of lamps have been performed by *Boyd* (1995), *Inushima* et al. (1988), and others.

19.6.2 Nitrides

Large-area LCVD of nitrides has been investigated mainly for Si_3N_4 and TiN. Here, NH_2 radicals generated by photodissociation via

$$NH_3 + h\nu(193\,\text{nm}) \rightarrow NH_2 + H \tag{19.6.2}$$

play a similar role as atomic oxygen in oxide formation. With ArF-laser light ground-state NH_2 is formed with nearly unit efficiency. The absorption cross section of NH_3 [$\sigma(193\,\text{nm}) \approx 10^{-17}\,\text{cm}^2$] exceeds that of N_2O by a factor 10^2. For this reason, the partial pressure of NH_3 generally employed is much lower than that of N_2O used for the deposition of oxides.

Si_3N_4 films were deposited by means of ArF lasers using mixtures of SiH_4 or Si_2H_6 with NH_3 / N_2 or He [*Sugii* et al. 1988]. The substrates, mainly Si, thermally oxidized Si wafers, and ZnSe, were uniformly heated ($50°C \leq T_s \leq 600°C$). With combined parallel / perpendicular incidence ($\phi_\parallel \approx 10\,\phi_\perp$), deposition rates of up to 12 Å/s were achieved.

Low-temperature photodeposition of silicon nitride by means of Hg lamps [*Petitjean* et al. 1992] has also been demonstrated. For further details see *Bäuerle* (2000) and references therein.

19.7 Heterostructures

LCVD with *parallel-beam* incidence has several advantages in low-temperature fabrication of amorphous multilayer structures. Among those are:

- High-resolution control of the film thickness. At moderate laser fluences less than one monolayer can be deposited per pulse.
- High deposition rates.
- Well-defined layer boundaries with minimal impurity or dopant diffusion.

These advantages have been demonstrated for heterostructures of a-Si/a-Ge and a-Si/a-Si_3N_4 [*Lowndes* et al. 1988]. The precursors (Si_2H_6, GeH_4, and mixtures of $Si_2H_6 + NH_3$) were photochemically decomposed by ArF-laser radiation. Figure 19.7.1 shows a laser-deposited heterostructure of a-Si/a-Ge. The respective layer thicknesses were 10.7 ± 0.4 nm and 5.4 ± 0.2 nm.

Similar experiments have been performed to fabricate heterostructures of a-Si:H/a-$Al_{1-x}O_x$ from Si_2H_6 diluted in H_2, and $Al_2(CH_3)_6 + O_2$ [*Uwasawa* et al. 1991]. The growth rates of a-Si:H and a-$Al_{1-x}O_x$ layers were around 0.3 Å/s and 0.8 Å/s, respectively [$\phi_{\|}(\mathrm{ArF}) \approx 35\,\mathrm{mJ/cm^2}$, $\tau_\ell \approx 17$ ns, 40 Hz], and almost independent of substrate temperature (200°C $\leq T_s \leq$ 350°C). The film properties were analyzed by SIMS, TEM, XPS, and optical spectroscopy. Good thickness uniformity and sharp interfaces have been obtained.

The low substrate temperatures that can be employed in photo-assisted CVD permit one to fabricate well-defined heterostructures of heat-sensitive materials such as II–VI compounds. This has been demonstrated by means of Hg/Xe-arc-lamps for HgTe/CdTe [*Ahlgren* et al. 1988].

The fabrication of heterostructures by pulsed-laser deposition (PLD) is described in Chap. 22.

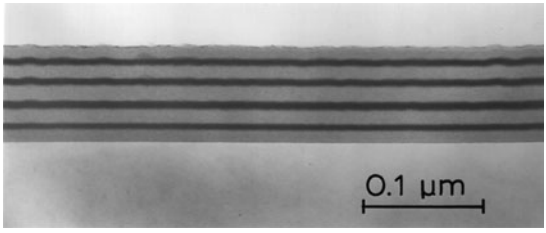

Fig. 19.7.1 TEM cross-section of a a-Si/a-Ge (*dark*) heterostructure deposited on (100) Si by ArF-laser photolysis at $T_s = 250$°C [*Lowndes* et al. 1988]

19.8 Comparison of LCVD and Standard Techniques

While standard CVD requires *uniform* substrate heating, typically, between 400 and 1500°C, LCVD can be performed at considerably lower temperatures, and in some cases even at room temperature. Thus, LCVD permits deposition on temperature-sensitive materials such as polymer foils, ceramics and compound semiconductors. These materials would melt, crack or decompose at the temperatures required for many conventional CVD systems. Even without such problems, lower temperatures can be desirable because they avoid or reduce material warpage, heat-induced mechanical stresses, diffusion or mixing between materials, and side reactions of the material surface with the ambient medium. An example where elimination or reduction of diffusion is a requirement is the coating and patterning of prefabricated Si surfaces. Here, lower processing temperatures can increase the yields achieved in device fabrication, both in microelectronics and micromechanics. There are many materials that can be deposited with high quality only at relatively low substrate temperatures. Among these are compound semiconductors and hydrogenated amorphous Si. With other materials, the purity, morphology and crystallinity may deteriorate with decreasing film/substrate temperature and one has to strike a balance between the film quality and the heat sensitivity of the substrate. Another advantage of LCVD is the excellent step coverage. The process enables one to uniformly coat irregularly shaped substrates.

In plasma-CVD (PCVD), a plasma is used to generate reactive species. The processing temperatures for thin-film deposition can thus be significantly lower than those used in standard CVD. However, plasma techniques have a number of other inherent properties which may be disadvantageous or even make the technique inadequate for a particular application. Among these are heavy ion bombardment, vacuum ultraviolet (VUV) irradiation of the substrate, loading effects, and contamination of the deposit by impurities originating directly from the reactant, or from carrier gases, or from sputtering of the reaction chamber. Further problems arise from the difficulty to control processing parameters. The RF power and frequency, the discharge geometry, electrode configuration, gas flow, total pressure, substrate temperature, etc., are all interrelated; thus, it is almost impossible to control and characterize effects due to *single* parameter variations. Above all, a stable discharge can be maintained only for a very narrow range of operating parameters, and this limits the versatility of the technique even further. However, PCVD is cheap, relatively simple, and permits large-area processing with high throughputs.

In LCVD, radiation damage, impurity sputtering, loading effects, etc., are absent or cause only minor problems. LCVD also allows one to vary the laser power and wavelength, the spatial location, gas flow, total pressure, substrate temperatures, etc., *independently*, i.e., without affecting any one of the other parameters. Lasers permit selective processing. For example, it is conceivable that alternating layers of elements or compounds can be deposited from admixtures of gases by simply changing the laser wavelength and thereby the decomposition yield of particular species.

The deposition rates achieved in LCVD are comparable to, or even higher than, those achieved in PCVD, at least for areas up to about $10\,cm^2$. The maximum deposition rates can be determined by the available laser power or the mismatch of the laser wavelength and the maxima in the absorption cross section of reactant molecules, by transport limitations or gas-phase nucleation. The physical and chemical properties of laser-deposited films are already satisfactory in many respects.

Photochemical processing with lamps is often disadvantageous because large-volume irradiation produces photofragments in regions which do not contribute to film growth. Consequently, reactants are not only lost, but they may also lead to unwanted reactions on reactor walls, etc. The deposition rates achieved with lamps are up to a few Å/s.

Among the most serious disadvantages of LCVD is the low throughput that can be achieved in production lines (Sect. 1.2).

Chapter 20
Adsorbed Layers, Laser–MBE

Adsorbed precursor molecules, reaction products, or impurities play an important role in various types of laser surface processing. They may control reaction rates, the spatial resolution in surface patterning, nucleation times in material deposition or synthesis, concentration profiles in surface doping, etc. Adsorbates are of importance also in new techniques that use a combination of laser *and* molecular/atomic beams.

Static and dynamic interactions between molecules/atoms and solid surfaces have been studied extensively. Most of the experimental investigations were performed under ultrahigh-vacuum (UHV) conditions at pressures below 10^{-10} mbar. Here, molecule–surface interactions are studied for low surface coverages or for particle beams and physically well-defined solid surfaces.

The number of molecules being adsorbed depends on their binding energy to the surface, on the interactions between them (e.g., dipole–dipole or direct Coulomb interactions), on the microstructure, roughness and temperature of the surface, and on the density of species within the ambient medium. The strength of these interactions also determines the extent of changes in the electronic and vibrational properties of adsorbed molecules with respect to free molecules. Adsorption may result in shifts and broadenings of electronic and vibrational energy levels and in the relaxation of selection rules for the interaction with light. As a consequence, the cross section for photo-excitation at a particular wavelength may differ significantly for adsorbed molecules and free gas-phase molecules. Contrary to investigations on basic molecule–surface interactions, laser-induced chemical processing (LCP) is, in general, performed only in high-vacuum (HV) reaction chambers that can be pumped out to, typically, 10^{-6} mbar. Therefore, substrate surfaces are covered by rest-gas molecules. Additionally, the substrates are, in most cases, only chemically cleaned according to standard procedures; such surfaces may be contaminated with water molecules, organic molecules, etc.

Laser light changes the adsorption behavior via substrate heating, and via selective electronic or vibrational excitations of gas-phase molecules, the solid surface, or the adsorbate–adsorbent complex. Due to interactions with light, adsorbed molecules may desorb from the surface, migrate across the surface, change the nature of bonding to the surface (e.g., from physical to chemical), diffuse into the bulk, or decompose at or react with the solid surface (Fig. 1.2.1a, b).

D. Bäuerle, *Laser Processing and Chemistry,* 4th ed.,
DOI 10.1007/978-3-642-17613-5_20, © Springer-Verlag Berlin Heidelberg 2011

The various systems investigated up to the year 2000 are listed in the previous edition. This list contains also materials that have been deposited by laser-MBE (molecular-beam epitaxy) or laser-ALE (atomic-layer epitaxy).

20.1 Fundamental Aspects

Molecules on solid surfaces may be adsorbed either physically or chemically. *Physical adsorption* (physisorption) is, in general, a non-activated process with binding energies of, typically, 0.05 to 0.5 eV (1−10 kcal/mol). The adsorption process is reversible, i.e., the adsorbate can be removed without any chemical changes by increasing the temperature or by lowering the (number) density of species within the ambient medium.

Chemisorption is, in general, an activated process. The binding energies are similar to those of intramolecular bonds, typically, 0.5 to 5 eV (10−100 kcal/mol). Thus, chemisorbed species cannot be desorbed from the surface without chemical changes.

If we assume a surface coverage of at most one monolayer, only *one* type of species, AB, and first-order kinetics, the density of adsorbed species $N_{\mathrm{AB}}^{\mathrm{ad}}$ (molecules per unit area), can be described by

$$\frac{\partial N_{\mathrm{AB}}^{\mathrm{ad}}}{\partial t} = k^{\mathrm{ad}} \left(1 - \frac{N_{\mathrm{AB}}^{\mathrm{ad}}}{N_{\mathrm{as}}}\right) N_{\mathrm{AB}} - k^{\mathrm{des}} N_{\mathrm{AB}}^{\mathrm{ad}} - W + \nabla_2 \left(D_{\mathrm{AB}}^{\mathrm{ad}} \nabla_2 N_{\mathrm{AB}}^{\mathrm{ad}}\right) - J_{\mathrm{s}} \,, \tag{20.1.1}$$

with

$$J_{\mathrm{s}} = -D_{\mathrm{AB}} \left.\frac{\partial N_{\mathrm{AB}}^{\mathrm{s}}}{\partial z}\right|_{z=0} \,,$$

where $N_{\mathrm{AB}}^{\mathrm{s}}$ (species/cm^3) is the number density of species within the substrate ($z > 0$). In the most general case, the various quantities depend on surface coordinates and time, for instance, $N_{\mathrm{AB}}^{\mathrm{ad}} \equiv N_{\mathrm{AB}}^{\mathrm{ad}}(\boldsymbol{x}_{\mathrm{s}}, t)$ and, if relevant, on laser parameters. The first three terms on the right-hand side describe changes in $N_{\mathrm{AB}}^{\mathrm{ad}}$ due to adsorption, desorption, and surface reactions. Note that N_{AB} (first term) is the density of molecules within the gas. The fourth term describes (ordinary) diffusion of species along the surface, and J_{s} the flux of species into the bulk substrate. Thermal diffusion has been ignored. $N_{\mathrm{AB}}^{\mathrm{ad}}$ must be calculated self-consistently together with the 3D-diffusion equation for $N_{\mathrm{AB}}^{\mathrm{s}}$, and the boundary conditions $N_{\mathrm{AB}}^{\mathrm{s}}(z = 0) = N_{\mathrm{AB}}^{\mathrm{ad}}/h_l$ and $N_{\mathrm{AB}}^{\mathrm{s}}(z \to \infty) = 0$. h_l is the thickness of the adlayer. Single terms will now be discussed in further detail.

According to the Langmuir theory, adsorption occurs at active adsorption sites whose density, N_{as}, is, in general, smaller than the total atom density of the substrate surface, N_s. The number of species adsorbed is

$$N_{AB}^{ad} \leq N_{as} \leq N_s \ . \tag{20.1.2}$$

The limiting case $N_{AB}^{ad} = N_{as}$ characterizes a monolayer coverage. The rate constant k^{ad} can often be described by the Arrhenius law

$$k^{ad}(T) = k_0^{ad} \exp\left(-\frac{\Delta E^{ad}}{k_B T_g}\right) \ , \tag{20.1.3}$$

where ΔE^{ad} is the activation energy for adsorption. T_g is the temperature of gas-phase molecules, which shall be equal to the substrate temperature, $T_g = T_s$. For physical adsorption we can set $\Delta E^{ad} \approx 0$. A typical potential energy curve for this case is shown in Fig. 20.1.1a. It is often described by a Lennard–Jones potential. *Chemical* adsorption is described by the potential energy curve (Fig. 20.1.1b). It can be constructed by assuming, for example, a Lennard–Jones potential for physisorbed species and, for example, a Morse potential for chemisorbed species. In the case of *molecular* adsorption, the intersection of potential curves occurs at energies $E \leq 0$. *Dissociative* adsorption is activated with $\Delta E^{ad} > 0$ (it results from an energy separation between the two potentials for $z \to \infty$ which corresponds to the dissociation

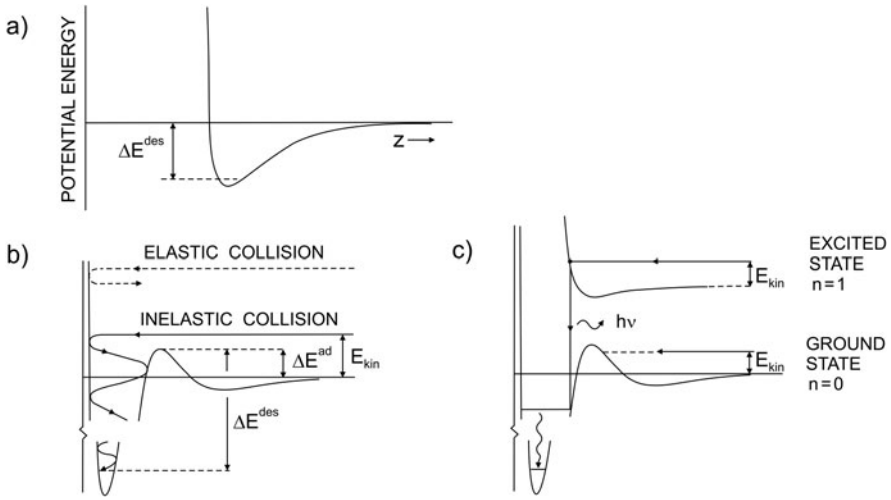

Fig. 20.1.1 a–c Molecule–surface interaction potentials for simple demonstration of adsorption processes. z is the distance from the surface. (**a**) Physical adsorption. (**b**) Activated chemical adsorption; the break in scale is to indicate that ΔE^{des} is much larger than in case (**a**). (**c**) Chemical adsorption via an electronically excited molecule. Energy dissipation by emission of a photon is only one of the various possible mechanisms

energy of the gas-phase species). ΔE^{ad} can be as high as several tenths of an eV [for GaAs we find $\Delta E^{\mathrm{ad}}(\mathrm{N_2O}) \approx 0.15\,\mathrm{eV}$ and $\Delta E^{\mathrm{ad}}(\mathrm{O_2}) \approx 0.47\,\mathrm{eV}$]. If we describe adsorption by 'active collisions', the kinetic energy of species impinging onto the surface with velocity component v_z must exceed the activation energy, i.e., $E_{\mathrm{kin}} = mv_z^2/2 > \Delta E^{\mathrm{ad}}$. For a Maxwell distribution we can write

$$k_0^{\mathrm{ad}} \approx \frac{1}{4} \langle v_{\mathrm{AB}} \rangle \ , \tag{20.1.4}$$

where $\langle v_{\mathrm{AB}} \rangle = (8k_{\mathrm{B}}T_{\mathrm{g}}/\pi m_{\mathrm{AB}})^{1/2}$ is the arithmetic mean velocity of gas molecules. However, even if $E_{\mathrm{kin}} > \Delta E^{\mathrm{ad}}$, species may be reflected from the surface. This process is indicated in Fig. 20.1.1b by the broken trajectory. For adsorption to take place, collisions between incoming species and the surface must be inelastic (full trajectory). Among the mechanisms for inelastic molecule–surface interactions are the transfer of kinetic energy (excitation of phonons), the transformation of translational energy into vibrational/rotational energy of the molecule (excitation of internal degrees of freedom), etc. If the probability of energy conversion is small during the molecule–surface interactions, the adsorption rate is small.

The second term in (20.1.1) describes desorption of molecules from the surface. The rate constant for *thermally* activated desorption can be described by

$$k^{\mathrm{des}}(T) = k_0^{\mathrm{des}} \exp\left(-\frac{\Delta E^{\mathrm{des}}}{k_{\mathrm{B}}T_{\mathrm{s}}}\right) \ . \tag{20.1.5}$$

ΔE^{des} is the activation energy for desorption. k_0^{des} is sometimes termed the attempt frequency with which adsorbed species try to escape from the surface. This frequency is of the order of molecular vibrational frequencies, typically some $10^{11}-10^{14}$ /s. Because of anharmonicity, k_0^{des} depends on temperature and can be described, approximately, by $k_0^{\mathrm{des}} \propto T_{\mathrm{s}}$. In the presence of an atmosphere, k_0^{des} may become dependent on gas pressure, mainly due to 'sputtering' of adspecies via impinging molecules. From (20.1.3) and (20.1.5) it follows that the enthalpy of adsorption

$$\Delta H^{\mathrm{ad}} = \Delta E^{\mathrm{ad}} - \Delta E^{\mathrm{des}} \tag{20.1.6}$$

is negative if $\Delta E^{\mathrm{des}} > \Delta E^{\mathrm{ad}}$ (exothermal process) and positive if $\Delta E^{\mathrm{des}} < \Delta E^{\mathrm{ad}}$ (endothermal process). The latter case requires an interaction potential with a metastable state. Parameters that characterize adsorption/desorption processes can be found for various systems, e.g., in *Kreuzer* and *Gortel* (1986).

The third term in (20.1.1) describes the change in the density of adsorbed species due to surface reactions. If the reaction of adsorbed molecules AB is of the first order,

$$W = kN_{\mathrm{AB}}^{\mathrm{ad}} \ . \tag{20.1.7}$$

The fourth term in (20.1.1) describes ordinary diffusion of adsorbed molecules along the surface with

$$D_{\mathrm{AB}}^{\mathrm{ad}}(T_{\mathrm{s}}) = D_0^{\mathrm{ad}} \exp\left(-\frac{\Delta E_{\mathrm{d}}^{\mathrm{ad}}}{k_{\mathrm{B}} T_{\mathrm{s}}}\right) \tag{20.1.8}$$

and $T_{\mathrm{s}} \equiv T_{\mathrm{s}}(\boldsymbol{x}_{\mathrm{s}}, t)$ [for Xe on (110) W, $D_{\mathrm{AB}}^{\mathrm{ad}}(T_{\mathrm{s}} = 400\,\mathrm{K}) \approx 10^{-7}\,\mathrm{cm}^2/\mathrm{s}$ and $\Delta E_{\mathrm{d}}^{\mathrm{ad}} \approx 0.05\,\mathrm{eV} \approx \Delta E^{\mathrm{des}}/4$]. The surface diffusion length can be estimated from

$$l_{\mathrm{AB}}^{\mathrm{ad}} \approx 2\left(D_{\mathrm{AB}}^{\mathrm{ad}}\tau\right)^{1/2} , \tag{20.1.9}$$

where τ is the average lifetime of species on the surface, which, in general, is mainly determined by the desorption process. Because $\Delta E_{\mathrm{d}}^{\mathrm{ad}} < \Delta E^{\mathrm{des}}$, $l_{\mathrm{AB}}^{\mathrm{ad}}$ decreases with increasing temperature, T_{s}.

The last term in (20.1.1) describes ordinary diffusion of adsorbed species *into* the bulk substrate with

$$D_{\mathrm{AB}}(T_{\mathrm{s}}) = D_0 \exp\left(-\frac{\Delta E_{\mathrm{d}}}{k_{\mathrm{B}} T_{\mathrm{s}}}\right) \tag{20.1.10}$$

and $T_{\mathrm{s}} \equiv T_{\mathrm{s}}(z, t)$. ΔE_{d} is the activation energy for (bulk) diffusion (for B in solid Si, for example, $\Delta E_{\mathrm{d}} = 3.69\,\mathrm{eV}$). This term is important in surface doping from adsorbed layers, and in surface oxidation, mainly of semiconductors.

The surface density of adsorbed molecules is often written as

$$N_{\mathrm{AB}}^{\mathrm{ad}}(\boldsymbol{x}_{\mathrm{s}}, t) = \Theta_{\mathrm{AB}}(\boldsymbol{x}_{\mathrm{s}}, t) N_{\mathrm{as}} , \tag{20.1.11}$$

where Θ_{AB} is the coverage. The number density within *one* monolayer can be estimated, if we assume that the mass density of the adsorbed film is equal to that of a liquid, i.e.,

$$\begin{aligned} N_{\mathrm{AB}}^{\mathrm{ad}}(\Theta_{\mathrm{AB}} = 1) = N_{\mathrm{as}} &\approx \left(\frac{\varrho}{m_{\mathrm{AB}}}\right)^{2/3} \\ &\approx 10^{14}\text{–}10^{15}\,(\mathrm{species/cm}^2) , \end{aligned} \tag{20.1.12}$$

where ϱ is the mass density of liquid AB, and m_{AB} the mass of molecules.

The preceding discussion simplifies the real situation considerably. In reality

- The assumption of first-order kinetics does not hold in many cases.
- Activation energies often change with coverage. The simplest ansatz is $E^{\mathrm{ad}}(\Theta) = E^{\mathrm{ad}}(\Theta = 0) + \zeta\Theta$.
- Adsorption processes strongly depend on the distribution function of gas-phase species. This holds also for desorption, mainly due to 'sputtering'. For this

reason, molecular/atomic beams are frequently employed for adlayer formation or the cleaning of surfaces from adsorbed molecules.
- Surface defects may play an important or even dominant role in adsorption/ desorption processes.

20.1.1 Influence of Laser Light

Laser light may thermally or non-thermally excite the solid surface, the incoming molecules, and the adsorbate–adsorbent system. The influence of laser-induced heating on the adsorption process is quite clear from the preceding equations. Additionally, laser light can increase or decrease the number of active adsorption sites, for example, by the generation of vacancies, electron–hole pairs, etc.

Selective electronic excitations of molecules change the molecule–surface interaction potential. For the example depicted in Fig. 20.1.1c the kinetic energy of incoming species in the electronic ground state is smaller than the activation energy for chemical adsorption, $E_{\mathrm{kin}} < \Delta E^{\mathrm{ad}}(n = 0)$. Thus, ground-state molecules will mainly be physisorbed (trapped by the shallow minimum in the potential curve). For electronically excited molecules ($n = 1$) there is no such barrier and they can directly chemisorb via transitions $n = 1$ to $n = 0$. Among the various mechanisms for energy conversion is the emission of photons. This process is extremely fast and one of the simplest to explain the increase in sticking coefficients frequently observed with excited species.

Changes in the adsorption behavior originating from *vibrational* excitations of molecules can be based on various mechanisms [*Benedek* 1987]. For example, vibrational excitation can change or only generate a dipole moment of a molecule, which, in turn, can directly interact with the solid surface via electrostatic forces. A strong increase in the sticking coefficient has been observed with vibrationally excited SF_6^* on semiconductor surfaces (Sect. 15.3) and with BCl_3^* on metals.

Laser light can directly excite adsorbed species (intramolecular bonds or adsorptive bonds), cause charge-transfer reactions within adsorbate–adsorbent complexes, enhance diffusion of adspecies along the surface and into the bulk of the substrate, etc. [*Kröner* et al. 2007].

In total, laser light increases or decreases adsorption/desorption rates, causes an inhomogeneous distribution of adspecies on the surface and, eventually, causes thermal or non-thermal decomposition of species.

The situation is, however, even more complex. For a particular species, the excitation probability is determined not only by the type of substrate material, but also by its surface properties, e.g., its microscopic structure (amorphous, crystalline), roughness, degree of contamination, oxidation, etc. For example, the optical excitation cross section may strongly increase when a molecular resonance overlaps with optically active surface resonances such as surface plasmons [*Nitzan* and *Brus* 1981]. The influence of the surface morphology on light–molecule–surface interactions has been clearly demonstrated, e.g., in surface-enhanced Raman scattering (SERS).

20.2 Deposition from Adsorbed Layers

Physisorbed or chemisorbed molecules strongly influence laser-induced reaction rates on substrate surfaces, in particular, in cases where the light is absorbed neither by the substrate nor by the gaseous or liquid ambient medium. Among the effects that result in rate changes are:

- The high concentration of molecules within adsorbed layers.
- Spectral shifts which change absorption cross sections.
- Electric field enhancements at the solid surface.

Photodecomposition of adlayers has been investigated in experiments performed in a vacuum (Fig. 1.2.1a) and in atmospheres consisting of the gaseous form of the adspecies (Fig. 1.2.1b).

Some systems for which the role of adsorbed layers has been investigated, in particular, with respect to material deposition, are listed in the previous edition. It should be emphasized, however, that adsorbed layers may play an important or even decisive role in nucleation (Chap. 4) and in many of the other systems employed in LCVD (Chaps. 16–19). The extent to which adlayers contribute to laser-induced material deposition can be discovered most unambiguously by investigating deposition rates as a function of surface temperature and reactant-gas pressure; the dependence on laser-beam spot size does *not* permit unique conclusions (Chap. 14).

From a practical point of view, adsorbed-layer processing permits high-resolution patterning because it avoids pattern smearing by diffusion of gas-phase species. Photodissociation of adsorbed layers can be used to *prenucleate* condensation areas that are filled up later by large-area standard CVD, pyrolytic LCVD, etc. Such combined techniques permit maskless formation of microstructures and higher overall throughputs in production lines.

20.2.1 Vacuum

Laser processing with adsorbates in a vacuum is possible only if the molecules are strongly physisorbed or chemisorbed on the substrate surface. In such investigations the substrate is first cleaned, for example, by a single or a few UV-laser pulses, and then exposed to the gas AB. During exposure, an adsorbate is formed. After exposure, the gas AB is pumped off. Even when multilayers have been formed, only the *first* layer, which is most strongly bound to the surface, remains, in general. Thus, besides a few exceptions, the surface coverage in a vacuum is $\Theta_{AB} \leq 1$.

Langmuir Equation

Let us first consider the exposure cycle and a system where the equilibrium coverage (in the presence of the gas AB) is $\Theta_{AB} \leq 1$. If we consider only adsorption and desorption processes in (20.1.1), the change in coverage is

$$\frac{\mathrm{d}\Theta_{\mathrm{AB}}}{\mathrm{d}t} = k^{\mathrm{ad}}\left(1-\Theta_{\mathrm{AB}}\right)\frac{N_{\mathrm{AB}}}{N_{\mathrm{as}}} - k\Theta_{\mathrm{AB}}$$
$$= s\frac{J_{\mathrm{AB}}}{N_{\mathrm{as}}}\left(1-\Theta_{\mathrm{AB}}\right) - k\Theta_{\mathrm{AB}}\ , \qquad (20.2.1)$$

with $k \equiv k^{\mathrm{des}} \times J_{\mathrm{AB}}$ is the flux of molecules AB onto the surface. The sticking coefficient, s, is assumed to be a constant. In reality, s depends on Θ. The fraction $(1-s)$ of impinging molecules is directly reflected from the surface. In the simplest kinetic theory, the flux of impinging molecules is

$$J_{\mathrm{AB}} = \frac{1}{4}\langle v_{\mathrm{AB}}\rangle N_{\mathrm{AB}} = \frac{p_{\mathrm{AB}}}{(2\pi m_{\mathrm{AB}} k_{\mathrm{B}} T_{\mathrm{g}})^{1/2}}\ , \qquad (20.2.2)$$

where $p_{\mathrm{AB}} = N_{\mathrm{AB}} k_{\mathrm{B}} T_{\mathrm{g}}$. The steady-state coverage obtained from (20.2.1) yields the *Langmuir isotherm*

$$\Theta_{\mathrm{L}} \equiv \Theta_{\mathrm{AB}}(t\to\infty) = \frac{1}{1+\Gamma_{\mathrm{AB}}^{\mathrm{ad}}} = \frac{bp_{\mathrm{AB}}}{1+bp_{\mathrm{AB}}}\ , \qquad (20.2.3)$$

with $\Gamma_{\mathrm{AB}}^{\mathrm{ad}} = \tau_{\mathrm{AB}}^{\mathrm{ad}}/\tau_{\mathrm{AB}}^{\mathrm{des}}$. Here, $\tau_{\mathrm{AB}}^{\mathrm{ad}} = N_{\mathrm{as}}/k^{\mathrm{ad}}N_{\mathrm{AB}} = N_{\mathrm{as}}/sJ_{\mathrm{AB}}$ and $\tau_{\mathrm{AB}}^{\mathrm{des}} = 1/k^{\mathrm{des}}$ are the time constants for adsorption and desorption, respectively. The adsorption coefficient is given by

$$b = \frac{s\tau_{\mathrm{AB}}^{\mathrm{des}}}{N_{\mathrm{as}}\,(2\pi m_{\mathrm{AB}} k_{\mathrm{B}} T_{\mathrm{s}})^{1/2}} = \frac{\exp(-\Delta H^{\mathrm{ad}}/k_{\mathrm{B}}T_{\mathrm{s}})}{k_0^{\mathrm{des}} N_{\mathrm{as}}\,(2\pi m_{\mathrm{AB}} k_{\mathrm{B}} T_{\mathrm{s}})^{1/2}}\ , \qquad (20.2.4)$$

where $T_{\mathrm{s}} = T_{\mathrm{g}} \times 1/b$ is sometimes denoted as the adsorption pressure, which, at room temperature, has typical values of the order of 10^{-6} bar. We obtain $\Theta_{\mathrm{L}} = bp_{\mathrm{AB}}$ if $bp_{\mathrm{AB}} \ll 1$ and $\Theta_{\mathrm{L}} = 1$ if $bp_{\mathrm{AB}} \gg 1$. With (20.2.1) and the initial condition $\Theta_{\mathrm{AB}}(t=0) = 0$, the coverage increases as

$$\Theta_{\mathrm{AB}}(t) = \Theta_{\mathrm{L}}\left[1-\exp\left(-\frac{t}{\tau_{\mathrm{AB}}}\right)\right] \approx 1-\exp\left(-\frac{t}{\tau_{\mathrm{AB}}^{\mathrm{ad}}}\right)\ . \qquad (20.2.5)$$

$\tau_{\mathrm{AB}} = \tau_{\mathrm{AB}}^{\mathrm{ad}}\Theta_{\mathrm{L}}$ is the characteristic time for surface coverage, which decreases with increasing temperature. The approximation in (20.2.5) assumes $\tau_{\mathrm{AB}}^{\mathrm{ad}} \ll \tau_{\mathrm{AB}}^{\mathrm{des}}$ and thus $\Theta_{\mathrm{L}} \approx 1$.

Desorption, Laser Irradiation

In the next step of the (idealized) experiment, the gas pressure is reduced to zero, i.e., $p_{\mathrm{AB}} \propto N_{\mathrm{AB}} = 0$, and the laser is switched on. For simplicity, we assume that this takes place at time $t = 0$. The coverage will now decrease due to both desorption *and* laser-induced decomposition of species. If we assume first-order kinetics, the change in Θ is still given by (20.2.1), with $J_{\mathrm{AB}} = 0$ and $k = k^{\mathrm{des}} + k^{\mathrm{dec}}$, where k^{dec}

is still the rate constant for laser-induced adlayer decomposition. The coverage then decreases as

$$\Theta_{\mathrm{AB}}(t) = \Theta_{\mathrm{AB}}(0)\exp(-kt)\ , \tag{20.2.6}$$

where the initial value is $\Theta_{\mathrm{AB}}(0) = \Theta_{\mathrm{L}}$. If, during exposure, a multilayer coverage is formed and reduced to a monolayer due to pumping, we can still employ this equation, but with $\Theta_{\mathrm{AB}}(0) = 1$.

Let us now consider the reaction rate for adlayer decomposition. For a focused laser beam with intensity $I(\boldsymbol{x}_{\mathrm{s}}, t)$ the coverage, and thereby the rate, becomes dependent on surface coordinate

$$W(\boldsymbol{x}_{\mathrm{s}}, t) \approx k^{\mathrm{dec}}(T_{\mathrm{s}})N^{\mathrm{ad}}_{\mathrm{AB}}(\boldsymbol{x}_{\mathrm{s}}, t) = k^{\mathrm{dec}}N_{\mathrm{as}}\Theta_{\mathrm{AB}}(\boldsymbol{x}_{\mathrm{s}}, t)\ . \tag{20.2.7}$$

For *pyrolytic* activation k^{dec} is given by (3.1.2). For single-photon *photolytic* activation, k^{dec} is given by (3.2.4a), where $\sigma^{\mathrm{ad}}_{\mathrm{AB}}$ is the dissociation cross section of the adspecies. In many systems, both thermal and non-thermal contributions will determine the processing rate.

Qualitatively, the kinetics for adlayer decomposition under the action of *focused* laser light can be described as follows: Initially, the laser light simply decomposes the adlayer. If molecules AB can diffuse into the sink produced by photodecomposition, a localized surface reaction can be sustained. This reaction is initially *kinetically* controlled. At later times, molecules must diffuse over larger distances and the reaction becomes *transport limited* and, finally, tends to zero [*Freeman* and *Doll* 1983; *Zeiger* et al. 1989].

Experimental Examples

In the experiments described here, the number of molecules adsorbed on the surface is, in general, of the order of one monolayer, i.e., $10^{14}-10^{15}$ molecules/cm^2. Therefore, the amount of deposited, etched, or doped material is very small, and decreases even further with increasing temperature.

Direct (photochemical) breaking of SiH bonds on hydrogenated (111)Si surfaces was demonstrated by electronic excitation with 157 nm F_2-laser radiation [*Pusel* et al. 1999].

Laser-induced adlayer photolysis has been investigated mainly for $Ni(CO)_4$, $Cd(CH_3)_2$, and $Al_2(CH_3)_6$ adsorbed on glass, SiO_2, and Al_2O_3 substrates. For example, for the deposition of nickel, the glass or quartz substrate was first exposed to a $Ni(CO)_4$ atmosphere of some millibars for several minutes. Then, after several cycles of pumping and purging with He or H_2, the substrate was irradiated with 476 nm or 356 nm Kr^+-laser light. As expected from the optical absorption spectra of $Ni(CO)_4$, the latent time for photodecomposition was much shorter for 356 nm than for 476 nm radiation. Experiments on adsorbed $Cd(CH_3)_2$ and $Al_2(CH_3)_6$ were

mainly performed with 193 nm ArF-, 257 nm frequency-doubled Ar^+-, and 356 nm Kr^+-laser radiation.

The metal deposits are less than a monolayer thick. They can be used as nucleation centers for subsequent film growth by standard techniques.

20.2.2 Gaseous Ambient

The role of adsorbed layers is quite different in gas-phase LCP, which is usually performed at reactant (partial) pressures ranging from 10^{-4} mbar up to more than 1 bar. In this case, the adsorbed layer is in a *dynamic equilibrium* with the surrounding atmosphere and its thickness is determined by the pressure p_{AB}. Laser radiation may interact with the adsorbate–adsorbent system and with gas-phase species, and thereby increase or decrease the sticking coefficient of species and thus the thickness of the adlayer (note that s may also change due to laser-induced material deposition, etching, etc.; Sect. 4.2.1).

Low Coverages

At low pressures, p_{AB}, where $\Theta_{AB} \leq 1$, the change in coverage for a first-order reaction can be calculated from (20.2.1), with $k = k^{des} + k^{dec}$. The steady-state reaction rate is

$$W = k^{dec} N_{as} \frac{\Theta'_L}{1 + \Gamma \Theta'_L} \,. \tag{20.2.8}$$

Due to the modified sticking coefficient, $s = s(I)$, Θ'_L can differ from Θ_L in (20.2.3). $\Gamma = k^{dec} N_{as} / k^{ad} N_{AB} = k^{dec} N_{as} / s J_{AB}$. If $\Gamma \Theta'_L \ll 1$, the rate is

$$W = k^{dec} N_{as} \Theta'_L \,. \tag{20.2.9a}$$

In this regime W changes *non-linearly* with pressure p_{AB} as in (20.2.3). If $\Gamma \Theta'_L \gg 1$

$$W = k^{dec} N_{as} \frac{1}{\Gamma} \propto p_{AB} \tag{20.2.9b}$$

and the rate becomes *linearly* dependent on p_{AB}.

Multilayer Coverages

At *high* pressures, p_{AB}, multilayer molecular films may be formed. The upper layers are weakly bound by van der Waals forces to the more strongly bound first monolayers. The total number of adsorbed molecules depends on the strength of bonding, the temperature, and the gas pressure. Figure 20.2.1 shows isotherms for adsorbed

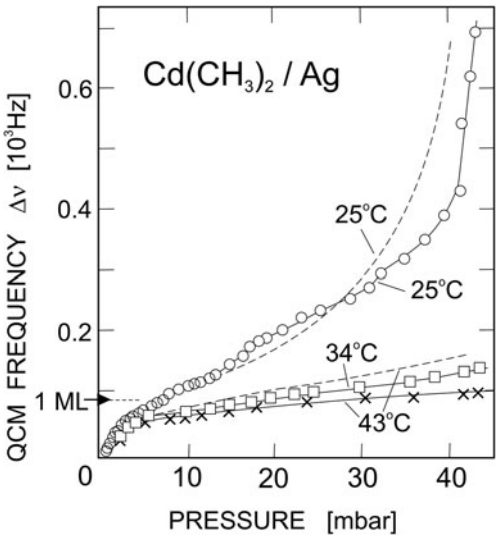

Fig. 20.2.1 Isotherms of $Cd(CH_3)_2$ adsorbed on an Ag film evaporated on a quartz-crystal microbalance (QCM) as a function of $Cd(CH_3)_2$ gas pressure. Curves calculated from the BET theory ($E_{ms} \approx 0.44\,eV$, $E_{mm} \approx 0.37\,eV$) are shown (*dashed curves*) [*Ehrlich* et al. 1982]

$Cd(CH_3)_2$ as a function of pressure. The low-pressure knee occurs at a coverage of about one monolayer. The curves measured at 34 and 43°C almost saturate at this coverage. Only the 25°C curve shows two further steps related to the second and third monolayer. When $p_{AB} \equiv p[Cd(CH_3)_2]$ approaches the vapor pressure, p_v, the coverage can become very high, 10 monolayers or more. This can be seen from the strong decrease in QCM frequency.

A good fit to the isotherms of many physisorbed systems is provided by the BET theory [*Brunauer*, *Emmett* and *Teller* 1938]:

$$\Theta_{BET} \equiv \Theta(p_{AB}, T) = \frac{C p_{AB}}{(p_v - p_{AB})[1 + (C-1)p_{AB}/p_v]} \approx \frac{C p_{AB}}{p_v} , \quad (20.2.10)$$

where Θ_{BET} describes the amount of adsorbed species with respect to one monolayer, and may therefore become *larger* than unity. The latter approximation refers to systems with $(C-1)p_{AB}/p_v \ll 1$. The coefficient C characterizes the particular adsorbate–adsorbent system, and its temperature dependence is approximately given by $\exp[(E_{ms} - E_{mm})/k_B T]$; E_{ms} and E_{mm} are molecule–surface and molecule–molecule interaction energies, respectively. The total (equilibrium) number density of adsorbed species is

$$N_{AB}^{ad}(p_{AB}, T) = \Theta_{BET} N_{as} . \quad (20.2.11)$$

The surface coverage Θ_{BET} varies *non-linearly* with pressure. This can be seen from the dashed curves in Fig. 20.2.1. The theoretical curve reproduces the first

knee in the isotherms, which is due to the strongly bound first monolayer. The additional steps observed in the 25°C curve at integral multiples of a monolayer are not reproduced; this is expected because the BET theory assumes a common binding energy for all the upper layers. The BET theory becomes inaccurate with pressures $p_{AB}/p_v > 0.5$. Θ_{BET} is sensitive to changes in temperature, primarily via the Arrhenius factor in p_v. The change in Θ_{AB} with even slight changes in temperature is a consequence of the (weak) van der Waals binding forces of the upper layers. This can be seen from the isotherms measured at higher temperatures (Fig. 20.2.1). Only the first strongly bound layer remains. In fact, this layer could not be removed even after 1 hour of pumping at room temperature. Similar results have been obtained with $Al_2(CH_3)_6$ and with Au and oxidized Si-layer substrates.

If we ignore the role of reaction products and surface diffusion of species, the coverage in the *presence* of *light* can be described by

$$\frac{d\Theta_{AB}}{dt} = \frac{1}{\tau'_{AB}}(\Theta'_{BET} - \Theta_{AB}) - k^{dec}\Theta_{AB} \ . \tag{20.2.12}$$

Note that all quantities refer to *multilayer* molecular films. τ'_{AB} is the (pressure-dependent) relaxation time in the BET theory. Θ'_{BET} takes into account the change in coverage caused by the change in sticking coefficient due to the laser light [in (20.2.10) s is included in the coefficient C]. The steady-state coverage becomes

$$\Theta_{AB}(\infty) = \frac{\Theta'_{BET}}{1 + \Gamma'} \ , \tag{20.2.13}$$

where $\Gamma' = \tau'_{AB}k^{dec}$. The reaction rate is then

$$W = k^{dec}N_{as}\Theta_{AB}(\infty) \ . \tag{20.2.14}$$

Experimental Examples, Separation of Mechanisms

Adsorbates that are in a dynamic equilibrium with the corresponding gas-phase molecules contain a high density of relevant species. Their influence on reaction rates in LCP may thereby become important or even dominant. Decomposed adlayer molecules are continuously replenished by gas-phase molecules, and this permits rapid growth of films that are thick compared to a monolayer.

The variation of the substrate temperature is the most simple and transparent way to investigate the relative importance of adsorbed-phase, gas-phase, and solid-surface excitations. Figure 20.2.2 shows the thickness of Zn lines deposited from $Zn(C_2H_5)_2$ by means of 257 nm Ar^+-laser radiation. The deposition rate *decreases* almost exponentially with temperature – between 20 and 60°C by about a factor of 100. This reflects the strong decrease in coverage with temperature – mainly via the

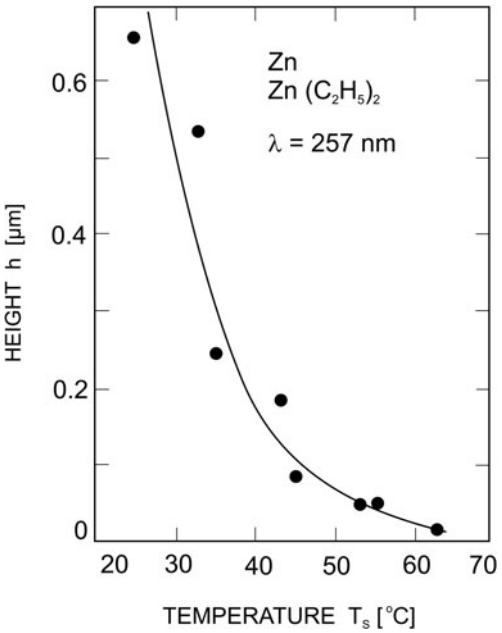

Fig. 20.2.2 Height of Zn lines photodeposited from $Zn(C_2H_5)_2$ on glass by means of 257 nm Ar^+-laser radiation ($v_s = 1.4\,\mu m/s$). The strong dependence on substrate temperature, T_s, is a clear indication of adsorbed-layer photolysis [*Krchnavek* et al. 1987]

increase in p_v. This is a clear indication of adsorbed-layer-controlled deposition. For higher substrate temperatures, gas-phase deposition becomes dominant. The situation is, however, more complicated. A change in surface temperature alters not only the surface coverage but also the surface mobility of species, recombination efficiencies of photoproducts, etc. The interrelation between such mechanisms may explain why the photodeposition rate of Al observed with $Al_2(CH_3)_6$ on quartz substrates first increases and then decreases with increasing substrate temperatures [*Tsao* and *Ehrlich* 1984].

The relative importance of adsorbed-phase and gas-phase photodecomposition can also be studied via the dependence of the reaction rate on pressure p_{AB}. In *gas-phase* processing the reaction rate is $W \propto p_{AB}^{\gamma}$, where, for first-order kinetics, $\gamma \approx 1$. For *adsorbed-layer* photolysis we have $W \propto \Theta_{AB}$. Furthermore, the reaction zone in *photolytic* gas-phase processing is, in general, much wider than the laser-beam spot size. In adsorbed-phase photolysis the profile of the deposit is similar to the intensity distribution of the laser beam. Further insight into excitation mechanisms can often also be obtained from the different wavelength dependences of gas-, adsorbed-, and solid-phase excitations (Sect. 2.1).

A clear demonstration of the application of adsorbed-layer photolysis is given in Fig. 20.2.3: excimer-laser-light projection has been used to photolyze adlayers of $Al(C_4H_9)_3$ on substrate materials such as Al_2O_3, SiO_2, GaAs, and Si. The

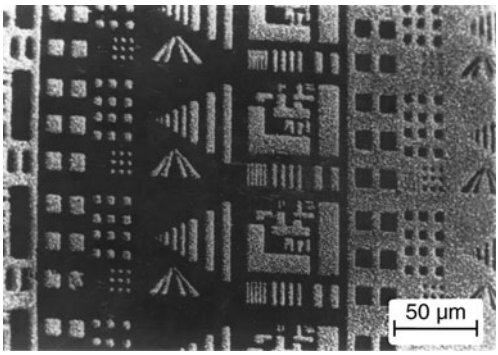

Fig. 20.2.3 SEM picture of an Al pattern produced by photolysis of adsorbed $Al(C_4H_9)_3$ by KrF-laser light projection and subsequent standard CVD [*Higashi* 1989]

reactive Al sites produced in this way act as nucleation centers for (spatially) selective growth by standard CVD. The figure demonstrates that 4 µm holes are accurately reproduced at pressures where the mean free path of (gas-phase) species is $\lambda_m \approx 100\,\mu m$. Features of this type would be difficult to reproduce if gas-phase photoreactions dominated. In adsorbed-layer processing, the resolution of features is controlled mainly by the laser wavelength and the imaging optics. With ArF-laser radiation and optimized imaging, it should be possible to improve the resolution achieved in Fig. 20.2.3 by more than a factor of 20. The electrical resistivity of features exceeds that of bulk Al by only a factor of two, although the deposits were very rough.

Adsorbed-layer photolysis often plays an important role in the initiation of the deposition process (Chap. 4). A few nuclei or monolayers of photo-deposited material may already absorb enough light to cause significant laser-induced heating; film growth then continues thermally.

The influence of local electric field enhancements on adsorbed-layer photodecomposition yields has been studied for $Cd(CH_3)_2$ adlayers in dynamic equilibrium with gaseous $Cd(CH_3)_2$ and Ar [*Chen* and *Osgood* 1983]. The substrate was a C film with predeposited Cd spheres. Cd possesses a plasmon resonance which can be excited with 257 nm laser light. The observed growth kinetics is modified by the plasmon excitation and is in agreement with model calculations.

20.3 Combined Laser and Molecular/Atomic Beams

There is considerable interest in the growth of epitaxial layers, mainly of semiconductors, by molecular-beam epitaxy (MBE) and atomic-layer epitaxy (ALE). Lasers have been incorporated in these techniques to enhance surface diffusion and photodecomposition of adsorbed species, to replace standard effusion cells, to generate species of variable kinetic energies for surface doping, etc.

20.3.1 Laser-MBE

The term laser-assisted MBE (in short, laser-MBE) shall henceforth be used to describe *all* cases of MBE where lasers have been incorporated in the deposition process.

Standard MBE with Substrate Illumination

Laser-assisted growth of p-type CdTe:Sb films has been reported by *Bicknell* et al. (1986). Here, a standard MBE apparatus was used together with an Ar^+-laser for substrate illumination (Fig. 20.3.1). Films grown under similar conditions in the absence of light were insulating. The same technique has been used to grow n-type layers of $Cd_{1-x}Mn_xTe$.

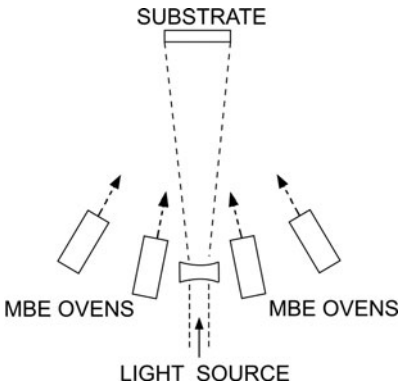

Fig. 20.3.1 Apparatus for film growth by light-assisted molecular-beam epitaxy (MBE). Single material components are provided from MBE ovens (effusion cells)

Laser-Assisted Gas-Source MBE

In gas-source MBE (also denoted as chemical-beam epitaxy, CBE) a molecular beam is used instead of a standard effusion cell.

Laser-assisted MOMBE (metal-organic-MBE) of GaAs using $Ga(C_2H_5)_3$ and elemental As_2 and As_y [formed by standard pyrolysis from $As(CH_3)_3$ or $As(C_2H_5)_3$] has been demonstrated by *Donnelly* et al. (1988). With ArF-laser radiation and substrate temperatures $T_s < 450°C$ very smooth films can be grown selectively (Fig. 20.3.2). The measured deposition rates cannot be explained on the basis of gas-phase photodecomposition, mainly because of the low (gas-phase) density of precursor molecules ($\approx 10^{-6}$ mbar) and the low laser pulse repetition rate (20 Hz). The observations can be understood, however, by adlayer decomposition of $Ga(C_2H_5)_3$, if desorption of species between laser pulses is ignored. Decomposition of the $Ga(C_2H_5)_3$ adlayer can be based on direct (non-thermal) photodissociation of molecules, on interactions with electron–hole pairs generated within the GaAs

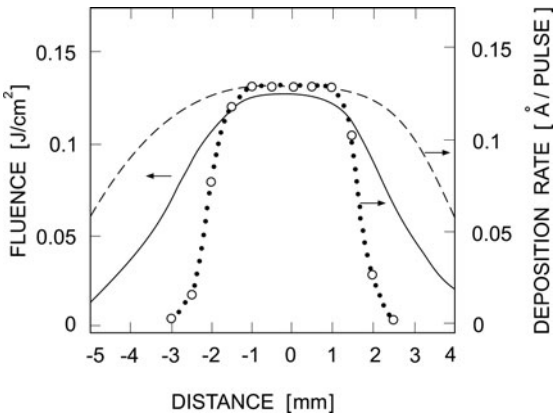

Fig. 20.3.2 ArF-laser-induced deposition rate of GaAs as a function of distance from the beam center (data and *dotted curve*; $T_s = 400°C$). The laser-beam intensity ($\phi_{max} \approx 0.12\,J/cm^2$, $\tau_\ell = 15\,ns$, 20 Hz) (*solid curve*) and the deposition rate expected for adsorbed-layer photolysis (*dashed curve*) are also shown [*Donnelly* et al. 1988]

surface, and on transient heating. The comparison of the measured film profile (dotted curve) with the laser-light intensity (full curve) suggests a strongly nonlinear decomposition mechanism. Both adsorbed-layer photolysis (dashed curve) and charge-transfer mechanisms cannot explain the rapid drop-off in deposition rate. Therefore, laser-enhanced growth has been ascribed to transient heating and thermal decomposition of *adsorbed* $Ga(C_2H_5)_3$. The analysis of data on the basis of calculated temperature distributions yields reasonable agreement with the measured deposition profile ($\Delta E[Ga(C_2H_5)_3] \approx 18-25\,kcal/mol$). This interpretation is supported by XPS studies which show that adsorbed $Ga(C_2H_5)_3$ is not efficiently photolyzed at 193 nm [*McCaulley* et al. 1989]. By means of excimer-laser-light projection, selective-area growth of GaAs has been demonstrated [*Donnelly* and *McCaulley* 1989].

MBE Using Laser-Induced Material Ablation

In another type of laser-assisted MBE, one or several standard MBE ovens (effusion cells) are replaced by solid or liquid sources (targets) from which the material is ablated under the action of laser light (Chaps. 11–13). The technique has been employed for the fabrication of thin films and for bandgap engineering (Sect. 22.5).

20.3.2 Laser-ALE

Atomic-layer epitaxy (ALE) and atomic-layer etching require self-limiting surface processes. Here, the binding energy of the first monolayer adsorbed on the substrate should considerably exceed that of subsequent layers, if existent. This can be

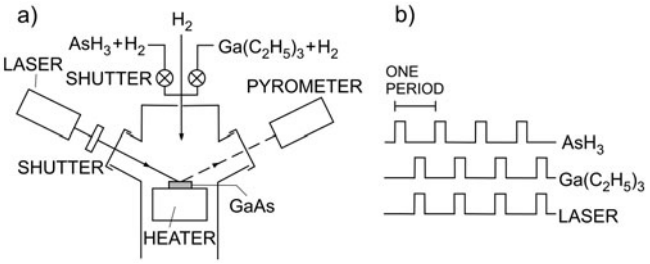

Fig. 20.3.3 (**a**) Setup employed in laser-ALE. (**b**) Typical time sequences of gas flow and laser irradiation [adapted from *Aoyagi* et al. 1987]

controlled by proper selection of the substrate temperature or by laser-light irradiation. Light can enhance the decomposition of these strongly adsorbed species or it can desorb reaction products.

Laser-assisted ALE (laser-ALE) has been demonstrated for semiconductors, and in particular for GaAs [*Isshiki* et al. 1993]. A typical setup is shown in Fig. 20.3.3. The precursors, AsH_3 and $Ga(C_2H_5)_3$ or $Ga(CH_3)_3$, are introduced into the reaction chamber in alternating 'pulses'. These pulses are synchronized with the laser pulses, as shown in Fig. 20.3.3b. Ideal ALE has been observed with 355 nm or 515 nm pulsed-Ar^+-laser radiation but not with 1.064 μm Nd:YAG-laser radiation [*Meguro* et al. 1988]. This wavelength dependence was ascribed to the photolysis of adsorbed $Ga(C_2H_5)_3$. Photodecomposition seems to be self-limiting. If $Ga(C_2H_5)_3$ is adsorbed on the As layer of the GaAs surface, it is decomposed by Ar^+-laser radiation. If, however, $Ga(C_2H_5)_3$ is adsorbed on a Ga layer, no significant decomposition takes place.

Figure 20.3.4 shows the growth rate in monolayers per cycle as a function of substrate temperature, T_s. The solid curves were calculated by assuming different ratios of decomposition rates of $Ga(C_2H_5)_3$ on As and Ga layers. Without laser light, the growth rate increases continuously (open symbols, enhancement factor = 1). In the presence of laser light, the growth rate shows a plateau at one monolayer per cycle and only increases at higher temperatures. The fabricated films are of high quality. The same technique has been employed for the fabrication of AlAs and $Ga_{1-x}Al_xAs$ films.

20.3.3 Laser-OMBD

Organic molecular-beam deposition (OMBD) is one of the most promising techniques for the fabrication of ordered organic films. By combining OMBD with KrF-laser photoisomerization, well-oriented crystalline films of trans,trans-BESB [Bis(ethynylstyryl) benzene] have been grown on KBr substrates [*Fuchigami* et al. 1998]. The experimental arrangement was similar to that shown in Fig. 20.3.1.

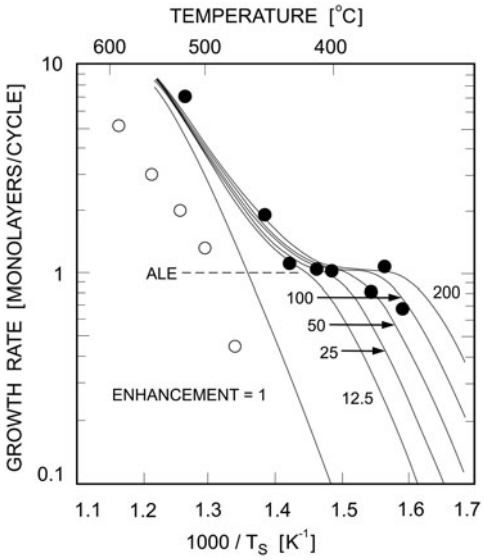

Fig. 20.3.4 Arrhenius plot for the growth of GaAs. ●: Ar^+-laser irradiation (laser-ALE). ○: Standard growth (no light). Curves calculated for various ratios of decomposition rates of $Ga(C_2H_5)_3$ on As and Ga layers (*solid curves*) are shown [*Aoyagi* et al. 1990]

20.3.4 Laser-Focused Atomic Deposition

Laser focusing of neutral atoms is a viable form of nanofabrication. In this technique, a highly collimated beam of atoms passes through a standing-wave laser field tuned near an electonic transition in the atom (Fig. 20.3.5). The resulting dipole force focuses the atoms into the nodes of the interference pattern. By this means, an array of lines separated by $\lambda/2$ is formed. This is shown in Fig. 20.3.6 for the example of Cr. The (uncorrected) line width measured with an AFM is $d_{\mathrm{FWHM}} \approx 38\,\mathrm{nm}$ (see also *Anderson* et al. 1999). Exposure of such patterns to a reactive ion etch

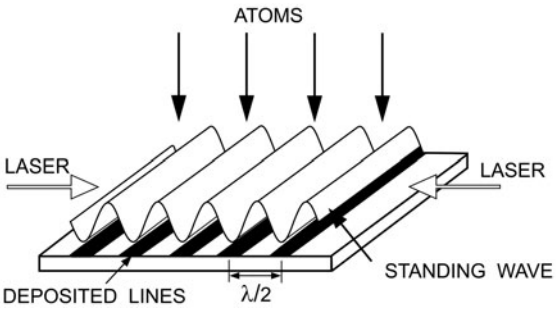

Fig. 20.3.5 Focused deposition of atoms in a standing wave laser field [*McClelland* et al. 1998]

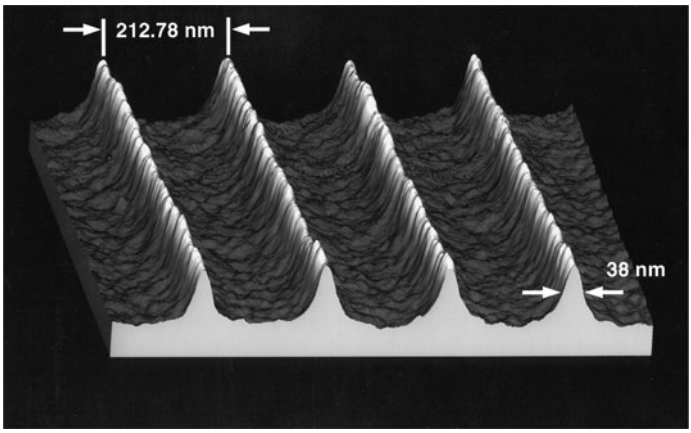

Fig. 20.3.6 Atomic force microscope image of Cr lines formed by laser-focused atomic deposition. The lines have a height of 8 ± 1 nm (the vertical scale has been expanded to enhance visibility) [*McClelland* et al. 1996]

yields Cr wires with (total) widths down to $d = 2r_D \approx 64$ nm. By using the Cr wires as a 'mask', trenches in Si substrates with widths as small as 85 nm have been etched. In a similar way, dot structures have been fabricated by using two standing waves, e.g., in orthogonal directions. By subsequent reactive ion etching (RIE), such patterns can again be transferred into the substrate.

Chapter 21
Liquid-Phase Deposition, Electroplating

Laser-enhanced/induced liquid-phase processing is mainly applied for material deposition and etching. Both electrolytic solutions and, to a smaller extent, ordinary liquids (non-electrolytes) are employed. The precursor molecules are dissolved in the liquid (solvent) and possibly dissociate. The dipoles or ions formed in this way interact with each other, with the solvent, and with the substrate. Thus, electrochemical effects will often play an important or even decisive role. They may arise from the illumination of the liquid–solid interface, or from an external electromotive force (EMF).

The high number densities of species involved in liquid-phase processing cause significant changes in transport properties with respect to gases. These rely on both changes in transport coefficients and additional transport mechanisms. For example, the shorter mean free path of molecules makes diffusion in liquids much slower than in gases (Sect. 3.3.2). Therefore, convection, turbulence, and bubbling related to strong temperature gradients in pyrolytic liquid-phase processing can exceed the transport of species by diffusion by several orders of magnitude.

Laser-induced processes in electrolytes are quite different for metals, semiconductors, and insulators. Some of these differences have already been discussed in connection with laser-induced wet etching (Chaps. 14 and 15).

21.1 Liquid-Phase Processing Without an External EMF

In the absence of an external EMF, the fundamental mechanisms in laser-induced liquid-phase processing are based on thermal, electrothermal, or electrochemical effects.

21.1.1 Thermal Decomposition

In the simplest case, electrical interactions can be ignored and the precursor molecules are just thermally decomposed at the liquid–solid interface. This situation frequently applies to laser processing using ordinary liquids. Because of strong

D. Bäuerle, *Laser Processing and Chemistry,* 4th ed.,
DOI 10.1007/978-3-642-17613-5_21, © Springer-Verlag Berlin Heidelberg 2011

changes in optical properties and boiling, processing can be performed in a relatively small temperature interval only. The difficulty with quantitative calculations arises from the paucity of information on kinetic constants and hydrodynamic effects. From the reaction rates achieved in pyrolytic liquid-phase processing, (normalized) activation energies $\mathscr{E}^* \equiv \Delta E/k_B T(\infty)$ in the range 10−30 can be estimated. Let us consider a reaction of the type

$$AB_\mu + M \rightarrow A(\downarrow) + \mu B(\uparrow) + M\,,$$

where M now denotes the liquid solvent. Here, the total particle number density, N, can be considered to be independent of temperature so that $q = 0$ in (3.3.11).

To demonstrate some essential features, we consider transport by (ordinary) diffusion only. In this case we can directly calculate the (normalized) density, N^*_{AB}, and the reaction rate, W^*, from the equations given in Chap. 3. Here, we assume a spherical reaction zone (Fig. 3.4.1) and $\mathscr{E}^* = 10$. The dashed curves in Fig. 21.1.1a have been calculated for temperature-independent transport coefficients, i.e., $n = 0$ and $m = 0$ (Sect. 3.3.2). The results show that transport limitations start with relatively low temperatures. An Arrhenius plot of the normalized reaction rate is shown in Fig. 21.1.1b for various values of $k_0^* \equiv k_0 r_D/D_{AB}(\infty)$. The dashed curves apply to $n = 0$ and $m = 0$. As in the case of gases, N^*_{AB} and $W^* \equiv W/k_0 N(\infty) x_{AB}(\infty)$ are strongly affected by the temperature dependence of D_{AB} but not by the heat conductivity κ (compare full and dotted curves). The temperature distribution does not depend on q and n.

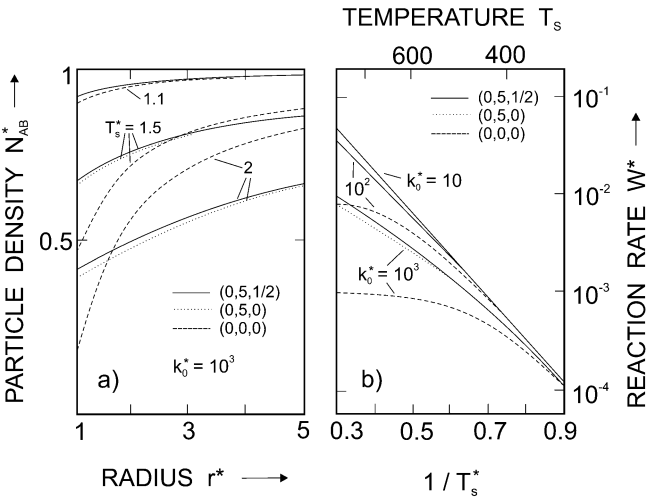

Fig. 21.1.1 a, b Normalized concentration of species AB and reaction rate in *liquid*-phase processing. Different curves belong to various parameter sets ($q = 0, n, m$) with $T_s^* \equiv T_s/T(\infty)$ and $\mathscr{E}^* = 10$. q, n, m describe the respective temperature dependences on particle number density, molecular diffusion coefficient, and heat conductivity [*Bäuerle* et al. 1990]

Convection and Bubble Formation

Convective flows are of particular importance in liquid-phase processing. Even at moderate laser-light intensities, Rayleigh numbers $\mathscr{R}a \approx 10^3$ to 10^4 are obtained. In many systems, convection determines the transport of species and the temperature distribution near the reaction zone. In the simplest approximation, the convective flux can be estimated from

$$J_c \approx v_c N_{AB} \ . \tag{21.1.1}$$

For a spherical reaction zone with radius r_D, the diffusion flux can be estimated from (3.4.17):

$$J_d \approx \frac{D_{AB} N_{AB}}{r_D} = v_d N_{AB} \ , \tag{21.1.2}$$

where v_d is the diffusion 'velocity'. The ratio of fluxes is

$$\frac{J_c}{J_d} = \frac{v_c r_D}{D_{AB}} = \frac{v_c}{v_d} \ . \tag{21.1.3}$$

With $v_c = 1\,\mathrm{cm/s}$, $r_D = 10\,\mu\mathrm{m}$, and $D_{AB} = 10^{-5}\,\mathrm{cm^2/s}$, we obtain $J_c/J_d = v_c/v_d \approx 10^2$. The influence of convection on the processing rate can be estimated from the (modified) Smoluchowski equation (3.4.14), with $k^* = k/(v_c + D_{AB}/r_D) \approx k/v_c$. The latter approximation refers to strong convection. In this case, reaction rates within the transport-limited regime may be enhanced by several orders of magnitude. Additionally, convective flows increase the temperature further away from the laser-heated area and thereby favor homogeneous reactions and cluster formation within the liquid. The clusters may absorb the laser radiation and, in turn, further heat the liquid. Such a positive feedback may cause instabilities and structure formation (Chap. 28). Cluster formation may result in porous deposits with weak adhesion to the substrate. Convective flows can be diminished or even avoided by using short laser-beam dwell times [see (9.5.15)].

With higher laser-light intensities, bubble formation above the irradiated surface may occur [*Yavas* et al. 1994]. In this regime, controlled surface processing becomes very difficult, or even impossible.

Pyrolytic laser-induced metal deposition has also been demonstrated with organic solutions containing compounds with zero (metal) valency. Among those are triphenyl-phosphine complexes of Au and complexes of Cr, Fe, Mo, and W [*Brook* et al. 1991 and references therein]. Materials such as C, Si, etc., can be deposited from liquid hydrocarbons [*Lu* et al. 1999; *Lyalin* et al. 1999], silanes, etc. Clearly, this process permits deposition onto both conducting and insulating substrates. Figure 21.1.2 shows an array of Pd-dots that have been deposited from a solution of $PdCl_2/NH_3$ by using a 2D lattice of a-SiO_2 microspheres and KrF-laser radiation.

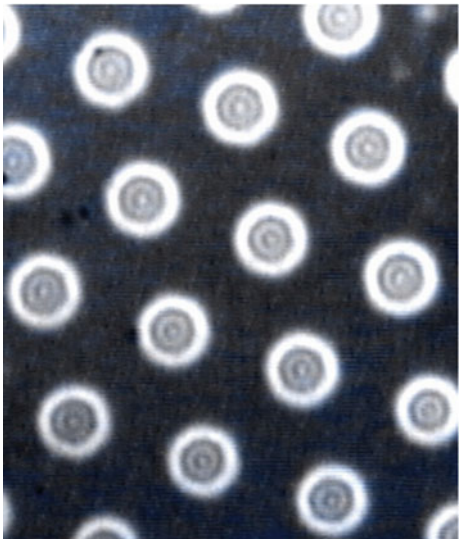

Fig. 21.1.2 Optical microscope picture of Pd dots deposited from an aqueous solution of 0.1 mol $PdCl_2$ in 1 mol NH_3 using a-SiO_2 microspheres of diameter $d = 6.6\,\mu m$ and 350 nm Ar^+-laser radiation ($\phi = 25\,J/cm^2$, $\tau_\ell = 10\,ms$, $N_\ell = 90$). The substrate was PI [*Bäuerle* et al. 2004]

Metal oxide films have been deposited from strongly absorbing liquids onto transparent substrates by laser irradiation of the liquid–solid interface (Fig. 9.5.1b). Among the materials studied in detail are thin films of Cr_2O_3, Fe_2O_3, and MnO_2 [*Dolgaev* et al. 1999 and references therein].

21.1.2 Electroless Plating

In electroless plating the charge balance is maintained via a reducing agent, Re, incorporated into the solution. Thus, plating can be performed without simultaneous etching. The process can be described by the redox equations

$$Re^{z_0+} \rightarrow Re^{(z_0+z)+} + z\,e^-$$

and

$$Me^{z+} + z\,e^- \rightarrow Me\,, \tag{21.1.4}$$

where Me^{z+} stands for z-fold charged metal ions within the solution. The metal ions are reduced by capturing electrons from the reducing agent, Re, which itself becomes oxidized. Laser light can thermally or non-thermally enhance or initiate this process. When the reaction has been started, the deposited metal may act as a catalyst and the reaction becomes self-sustaining. Laser-induced/enhanced

electroless plating has been employed for fast localized deposition of metals. In general, virtually no plating takes place outside the laser-illuminated region. The technique can be applied also to electrically insulating substrates. Among the experimental examples is the electroless plating of premetallized glass substrates with Ni from solutions containing sodium hypophosphate (I) as reducing agent. With Ar^+-laser radiation local deposition rates up to 0.1 μm/s have been achieved. The background plating rates were about 5 Å/s [*von Gutfeld* 1984].

Other types of electroless plating have been demonstrated for laser pretreated surfaces. Among the examples are Au films on n-doped GaAs [*Sugioka* and *Toyoda* 1992], Cu, Ni, Pd and Pt films on ablated dielectrics such as Al_2O_3, $PbTi_{1-x}Zr_xO_3$ (PZT), SiC, $LiNbO_3$, etc. [*Shafeev* 1998; *J.Y. Zhang* et al. 1997], Cu and Ni films on modified [*Niino* and *Yabe* 1993a] or ablated [*Niino* and *Yabe* 1993b] polymer surfaces, etc.

21.1.3 Metal–Liquid Interfaces

Reactions at interfaces between metals and electrolytic solutions may be enhanced or initiated by laser light via changes in the electrochemical (Nernst) potential or via the external photoeffect. For this latter mechanism there is, up to now, no experimental evidence.

The (equilibrium) electrochemical potential of a metal with respect to the electrolyte can be described by

$$\Phi_e(T, N_i) = \Phi_0(T) + \frac{R_G T}{zF} \ln\left(\frac{a_i}{a_{Me}}\right) , \tag{21.1.5}$$

where $F = eL$ is the Faraday constant, and L the Avogadro number. a_i and a_{Me} are the activities of ions i within the solvent and the metal, respectively. For low ion concentrations $x_i = N_i/N \ll 1$, we have $a_i \propto x_i$. For pure metals, the activity is $a_{Me} = 1$, per definition. The potentials Φ_e and Φ_0 cannot be measured directly. The potential difference between a metal in an electrolyte with $a_i = 1$ and a standard hydrogen electrode, measured at $T = 25\,°C$, is called the standard electrode potential [*Bockris* and *Reddy* 1977].

Laser-Induced Changes in the Nernst Potential

Laser-light irradiation of a metal generates a local electric cell via changes in the potential (21.1.5). If this change in Φ_e is based on a local laser-induced temperature difference, $\Delta T = T_c - T(r)$, a *thermobattery* with an EMF

$$U_{EMF}(\Delta T) \leq [\Phi_e(T_c) - \Phi_e(T(r))]_{N_i=\text{const.}} \tag{21.1.6}$$

is generated. $T_c \equiv T(r = 0)$ is the laser-induced center temperature, and $T(r)$ the temperature at distance r. The EMF originates mainly from the temperature

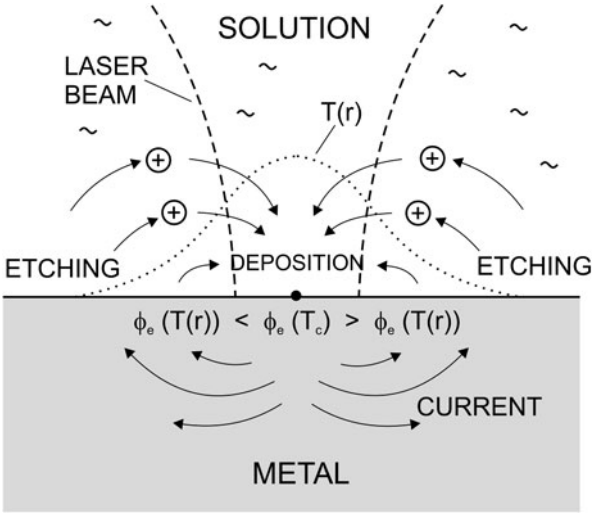

Fig. 21.1.3 Laser-induced thermobattery on a metal surface

dependence of $\Phi_0(T)$. For most metals, $\partial\Phi_0/\partial T \approx$ const. > 0 and has typical values of some 10^{-3} V/K. The situation is schematically shown in Fig. 21.1.3. The potential at the center of the laser beam (anode) will be higher than outside (cathode). For a temperature rise of $\Delta T = 100$ K an EMF of some 0.1 V is generated. While these voltages are very small, the electric field strengths are very high due to the small dimensions of the battery. Because the metal itself acts like an external load resistance in a standard Galvanic element, the current within the metal flows from the center to peripheral regions. In order to maintain the overall charge neutrality, the (positive ion) current within the solution must flow towards the center. Thus, we observe deposition (plating) in the heated center and simultaneous etching outside. This situation is exactly opposite to that in standard electroplating using an *external* battery. If $\partial\Phi_0/\partial T < 0$, etching occurs in the center and deposition outside. Because of the finite current, the real EMF, (21.1.6), is below the value estimated from the right side of the formula. The current $j(\xi)$ and the overpotentials $\xi(T_c)$ and $\xi(T(r))$ can be estimated from equations of the type (21.2.1) and Ohm's law for the microgalvanic element in Fig. 21.1.3. The plating rate is proportional to the normal component of the current at the electrolyte–metal interface. Because etching (plating) takes place on a large area outside the laser focus, the change in film thickness can be ignored, in general. This type of liquid-phase processing which is related to a laser-generated thermobattery is also termed *laser-enhanced exchange plating* (etching).

According to (21.1.5) an EMF can also be generated via a local laser-induced change in concentration, N_i:

$$U_{EMF}(\Delta N_i) = [\Phi_e(N_i(0)) - \Phi_e(N_i(r))]_{T=\text{const.}} \tag{21.1.7}$$

This is referred to as a *concentration battery*. The change in N_i can be related to the reaction itself (this is important within the transport-limited regime only), to thermal diffusion of species, etc. In general, the thermobattery effect exceeds the concentration battery effect, although the two effects cannot be separated.

Up to now we have considered a situation where both the metal surface and the metal ions in solution are of the same nobility as, for example, with a Cu substrate immersed in aqueous $CuSO_4$. Laser-induced exchange plating enables one, however, to plate a less noble metal, Me_2, onto a more noble metal, Me_1. For a uniform temperature T_0 we have $\Phi_{e2}(T_0) < \Phi_{e1}(T_0)$, and no plating takes place. With a focused laser beam, however, we can generate a local thermobattery so that $\Phi_{e2}(T_c) > \Phi_{e1}(T(r))$. Thus, plating becomes possible above a certain threshold intensity (temperature).

Laser-enhanced exchange plating has been studied for premetallized substrates (glasses etc.) and for bulk metals such as Cu, Ni, W, etc. These substrates have been plated with Cu from aqueous $CuSO_4$, and with Au from various solutions (see 3rd ed.). At constant laser-light intensity, the deposition rate for Cu spots was found to decrease with increasing thickness of the metal film covering the glass substrate. This is in agreement with the corresponding decrease in temperature rise.

21.1.4 Semiconductor–Liquid Interfaces

Laser-light with photon energies $h\nu > E_g$ generates electron–hole pairs (Fig. 2.1.1). Because of the different mobilities of electrons and holes (for most semiconductors $\mu_e > \mu_h$), spatial changes in carrier concentrations take place (Dember effect). These, in turn, alter the charge-transfer rates at the semiconductor–electrolyte interface. This (non-thermal) mechanism is of particular importance in wet-etching of semiconductors at low laser-light intensities (Sect. 15.6). Nevertheless, this mechanism is also important within the *initial* phase of plating. With localized irradiation, the Dember effect generates a local EMF. If we consider an n-type semiconductor, a depletion of electrons within the irradiated area and an enrichment of them outside will take place (Fig. 15.6.4b). Thus, the laser-irradiated surface acts like an *external* battery. Positive ions within the solution move from illuminated to dark regions, exactly opposite to the situation shown in Fig. 21.1.3. As a consequence, etching within the center and ring-shaped (metal) plating outside is observed. For an estimation of the current, electrical conductivities are required. For a 1-molar electrolyte solution the conductivity is, typically, about $10^{-1}\ (\Omega\,\mathrm{cm})^{-1}$; for an n-type semiconductor, it is between 10^4 and $10^{-2}\ (\Omega\ \mathrm{cm})^{-1}$, depending on the degree of doping.

Electron–hole pairs are also generated if the absorbed laser light just heats the surface. A local temperature rise results in a depletion of the major carriers (Sect. 15.6.3). The thermal EMF for semiconductors is about 10^3 times higher than for metals.

21.1.5 Further Experimental Examples

In most cases of laser-induced/enhanced liquid-phase processing, different effects will simultaneously contribute to the overall reaction rate and the dominating mechanism may even change during the reaction.

Pt, Au, and Ni have been deposited from aqueous solutions of H_2PtCl_6, $HAuCl_4$ (also used as methanolic solution) and $NiSO_4$ by means of pulsed-dye-laser radiation ($580\,\text{nm} \leq \lambda \leq 720\,\text{nm}$; within this range, the solutions are transparent) [*Karlicek* et al. 1982]. The substrates employed were mainly doped and undoped InP. In the initial phase, a thermally activated chemical reaction between the InP and the metal salt leads to the formation of PtP_2, NiP or similar compounds within the interfacial layer. Deposition seems to proceed via thermal decomposition of precursors at the metal–liquid interface. Smooth platinum films up to a thickness of $0.5\,\mu\text{m}$ were deposited. Within the platinum deposits, no solution contaminants were found. Deposits of Pt and Au on undoped InP exhibited ohmic behavior. Pt has also been successfully deposited on n-type GaAs, but not on Si.

21.2 Electrochemical Plating

In laser-enhanced electrochemical plating, an *external* battery is applied in such a way that, in general, the substrate is negatively biased with respect to a counter-electrode. The applied voltages are, typically, $1-2\,\text{V}$. Detailed experiments have shown that the enhancement of the reaction rate is based on local laser-induced heating [*von Gutfeld* 1984]. By reversing the polarity of the electrodes, the same process can be employed to *etch* material surfaces (Chaps. 14 and 15). With the systems investigated, photochemical effects within the liquid have been excluded. We shall therefore concentrate on the effect of local heating on charge- and mass-transfer rates within an electrochemical system. Here, we have to consider the temperature dependence of the current density. In the kinetically controlled regime, i.e., at low overpotentials, the current density j (A/cm^2) is given by the Butler–Volmer equation [*Bockris* and *Reddy* 1977]:

$$j = j_0 \left[\exp\left(\frac{\beta' \xi z F}{R_\text{G} T} \right) - \exp\left(-\frac{\beta \xi z F}{R_\text{G} T} \right) \right] , \tag{21.2.1}$$

where j is directed from the electrode to the electrolyte. β and β' are the so-called symmetry factors (transfer coefficients). In general, $\beta' \approx 1 - \beta$ and $\beta \approx 1/2$. $\xi = \Phi - \Phi_\text{e}$ is the overpotential. If $\xi < 0$, we obtain plating with $j < 0$, and we obtain etching if $\xi > 0$ ($j > 0$). Equation (21.2.1) can be derived in analogy to the Frenkel–Wilson law (10.1.9) by taking into account the distortion of the potential barrier by the external electric field. The exchange current density j_0 (also termed the charge-transfer rate) is given by

$$j_0 = zN_c F k_c \exp\left(-\frac{\beta z F \Phi_e}{R_G T}\right) . \tag{21.2.2}$$

j_0 describes the equilibrium flux of charges through the interface in one direction. Clearly, in equilibrium the total flux is zero. N_c (mol/cm^2) is the ion concentration near the electrode; $N_c L$ is the number of ions per square centimeter. For concentrated solutions we must introduce, instead of N_c, the molar activity per cm^2 which takes into account ion–ion interactions. The rate constant is given by

$$k_c = \frac{k_B T}{h} \exp\left(-\frac{\Delta E}{R_G T}\right) . \tag{21.2.3}$$

ΔE is the activation energy for ions within the solution to become incorporated into the metal in the absence of an external field. The temperature dependence of j_0 is dominated by the Arrhenius term in (21.2.3), since $\Delta E > \beta z F |\Phi_e|$. Even when the temperature dependence of Φ_e is taken into account, the rate always increases with temperature.

At higher overpotentials, transport of ions becomes rate limiting. In addition to diffusion and forced convection, transport due to gradients in the potential Φ must be taken into account. According to *W. Nernst* and *M. Planck*, the flux of ions i within the solution can be written in the form

$$J_i = -D_i \nabla N_i + N_i v_c - \frac{z_i F}{R_G T} D_i N_i \nabla \Phi . \tag{21.2.4}$$

Forced convection (second term) has been estimated for liquid-phase processing by solving the 3D Navier–Stokes equations. In the general case one has to solve the total magnetohydrodynamic problem. The influence of *focused* laser-light irradiation in electrochemical plating (etching) can be summarized as follows:

- Localized heating causes a positive shift in the rest potential and thereby permits localized plating on large-area electrodes. Because there is no background plating, the technique can be employed for single-step fabrication of microstructures.
- Localized heating results in 3D diffusion of ions and, at higher laser-light intensities, in convection. In any case, the rate achieved within the transport-limited range is increased; with tight focusing, the current density increases as $j \propto w_0^{-1}$. This has been verified experimentally [*Puippe* et al. 1981].

Laser-enhanced electrochemical plating (etching) has been studied most extensively with Ar^+- and Kr^+-lasers. The power densities employed were between 10^2 and 10^6 W/cm^2. Both continuous and pulsed plating (etching) were demonstrated by modulating the external voltage source, the laser output power, or both synchronously. Plating has been studied in detail for Au, Cu and Ni. The substrates were glass and c-Al_2O_3, both covered with 0.1 μm thick films of Au, Cu, Ni, Mo, or W. The resolution achieved in these experiments was a few micrometers.

The plating mechanism was investigated by illuminating the metallized glass surface with Ar^+-laser radiation either from the front through the solution or from the back through the optically transparent glass. In the latter geometry, no photons reach the electrolyte. The deposition rate was found to be equal in both cases. This is expected for a thermally activated reaction. Hence, photochemical processes cannot play an important role. Further support for the thermal character of the process was obtained from the comparison of plating rates achieved with premetallized c-Al_2O_3 ($\kappa \approx 0.2\,\mathrm{W/cm\,K}$) and glass ($\kappa \approx 0.01\,\mathrm{W/cm\,K}$) substrates. Under otherwise identical experimental conditions, the rates on c-Al_2O_3 substrates were found to be much lower than on glass, as expected from the lower laser-induced center temperature.

Detailed investigations on electrochemical Au plating have revealed that dense, small-grained, crack-free, and uniform deposits of good adhesion are formed at elevated temperatures and high concentrations of gold within the electrolyte. Here, the operating potential should be *below* the mass-transport limit. Near this limit, Au of good morphology was deposited over areas of 500 μm in diameter with rates of up to 1 μm/s. Direct writing of Cu lines on premetallized glass substrates was possible with widths of $\geq 2\,\mu\mathrm{m}$.

21.2.1 Jet-Plating

Laser-enhanced jet-plating permits one to achieve significantly higher deposition rates. Here, the mass transport to the substrate is increased by a jet (Fig. 21.2.1; the flow velocities are, typically, 10^3 cm/s). The laser beam is focused on the center

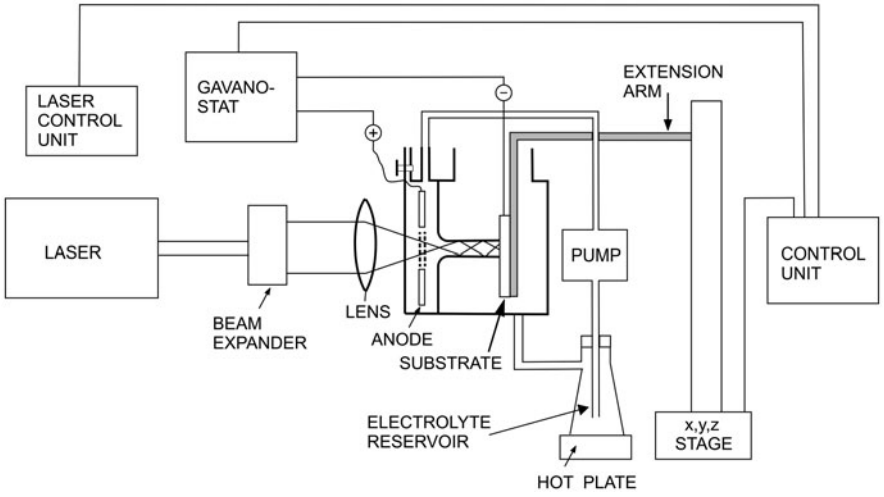

Fig. 21.2.1 Experimental setup for laser-induced electrochemical jet-plating. The laser beam is focused to the center of the jet orifice. The substrate can be moved via the extension arm [*von Gutfeld* 1984]

of the orifice of the jet and is maintained within the liquid column by total internal reflection until impingement on the cathode occurs. The potentiostat is set to deliver constant current, i.e., to plate galvanostatically.

Jet plating permits high-quality, rapid, localized plating. The electrochemical and hydrodynamical parameters determining the mechanical and metallurgical properties of deposits have been investigated, in particular, for Au. Here, plating rates of up to $12\,\mu m/s$ have been achieved. The surface smoothness of Au films increases with laser-light intensity. Simultaneously, their nodularity decreases and voids disappear. The Knoop hardness of films was between 20 and $90\,kg/mm^2$, which is characteristic for soft gold.

Laser-enhanced plating can be applied for circuit and mask repair [*Jacobs* and *Nillesen* 1990], the fabrication of interconnects, in customization and ohmic contact formation, etc. (Sect. 18.5).

Chapter 22
Thin-Film Formation by Pulsed-Laser Deposition and Laser-Induced Evaporation

Lasers can be used to fabricate thin extended films by condensing on a substrate surface the material that is ablated from a target under the action of laser light. Depending on the specific laser and material parameters, ablation takes place under quasi-equilibrium conditions, as in laser-induced thermal vaporization (Chap. 11), or far from equilibrium, as in many cases of pulsed-laser ablation (PLA) (Chaps. 12 and 13). Thin-film formation based on PLA is termed pulsed-laser deposition (PLD). Instead of PLD, terms such as laser-sputter deposition (LSD), pulsed-laser evaporation (PLE), and others, are also used in the literature. PLD is of particular interest because it enables one to fabricate multicomponent stoichiometric films from a *single* target.

From the aspect of film formation, the detailed ablation mechanisms are of minor relevance. It is only important that ablation of the target takes place on a time scale that is short enough to suppress the dissipation of the excitation energy beyond the volume ablated during the pulse. Only with this condition, can damage of the remaining target and its segregation into different components be largely avoided. In this regime of interactions, the relative concentrations of species within the plasma plume remain almost unchanged for successive laser pulses and almost equal to those within the target material. This is the main reason why PLD has been found to be useful, in particular, for the deposition of epitaxial or large-grain oriented films with complex stoichiometry. A list of materials studied in detail up to the year 2000 is given in the previous edition of this book.

PLD is a very reliable technique. It offers great experimental versatility, it is fairly simple, and fast – as long as films of up to several square-centimeters are to be fabricated. The use of corrosive and/or hazardous chemicals employed in material synthesis by standard techniques can widely be avoided. The short turn-around times enable one to efficiently study a great variety of different compounds and film dopings. For these reasons, PLD is particularly suitable in materials research and development. There are, however, some additional aspects. The short interaction times and the strong non-equilibrium conditions in PLD open up some new and *unique* possibilities in thin film synthesis. Among those are:

D. Bäuerle, *Laser Processing and Chemistry,* 4th ed.,
DOI 10.1007/978-3-642-17613-5_22, © Springer-Verlag Berlin Heidelberg 2011

- The synthesis of metastable materials that cannot be produced by any standard technique.
- Single-step deposition of complex multicomponent materials as, e.g., different types of oxides, fluorides, nitrides, etc.
- Synthesis of films from species that are generated only during PLA. With certain systems, the physical properties of such films are superior to those fabricated by standard evaporation, electron-beam evaporation, etc.
- Atomic-layer control on deposits.
- Formation of heterostructures and composite films consisting of different materials.
- Nanocrystalline and nanocomposite films.
- Synthesis of films in reactive atmospheres up to several mbar.
- Development of functional materials.
- Thin film formation from organic targets, including biomaterials.

The major disadvantage of PLD is the relatively low throughput that can be achieved. Another problem, in particular with thin epitaxial films, can be the particulates that frequently occur on the substrate and film surface. Clearly, other thin-film techniques have their peculiarities as well. For example, RF sputtering enables one to produce large-area films with good thickness uniformity and small surface roughness (typically < 100 Å with 1000 Å thick films). Here, the control over the correct stoichiometry is, however, much more problematic. Furthermore, sputtering requires large targets and longer preparation cycles, and it affords less experimental versatility.

In the present chapter we put special emphasis on the deposition of thin films of various different types, including nanostructured materials and biomaterials. The last section deals with thin film deposition and pattern formation by laser-induced forward transfer (LIFT). The diagnostics and the expansion dynamics of laser-induced vapor/plasma plumes is outlined in Chaps. 29 and 30. Pulsed-laser plasma chemistry (PLPC) where reactive species within the plasma directly react with the substrate (target) surface and thereby form a chemically modified layer is discussed in Sect. 26.2.3.

22.1 Experimental Requirements

A typical setup employed for film deposition is schematically shown in Fig. 22.1.1. It essentially consists of a laser, a reaction chamber, a target, and a substrate. The material ablated from the target is condensed on the substrate and forms a thin film. Ablation can take place either in a vacuum or in an inert or reactive atmosphere. The latter technique is termed reactive laser ablation (reactive laser sputtering).

It is evident that the setup depicted in Fig. 22.1.1 is considerably simplified and shows only the main components. The proper choice of the laser depends on the physical properties of the target, which, in any case, should strongly absorb the laser light. With transparent materials, absorption may be based on multiphoton and

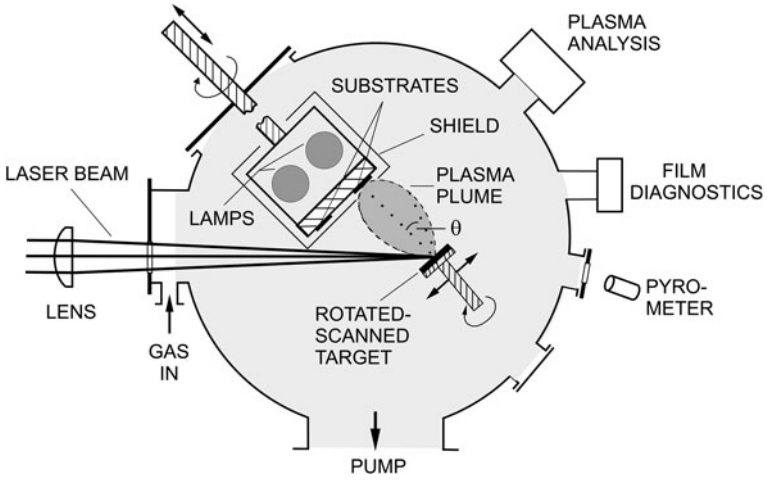

Fig. 22.1.1 Schematic of an experimental setup employed in PLD

avalanche ionization processes, which become important or even dominant with ultrashort pulses (Sect. 13.6). The attenuation of the incident laser beam by ablated material that condenses on the entrance window of the chamber may become a problem, in particular when deposition is performed in a vacuum. This can be reduced by a rotating disc, by a light pipe, or by flushing the window with an appropriate gas. The fluences typically employed in PLD, $\phi \approx 0.1-10\,\mathrm{J/cm^2}$, generate a vapor/plasma plume in front of the target. Typical deposition rates are between a monolayer and several ten Å per pulse.

Targets are mainly used in the form of discs or cylinders. Disc-shaped targets are rotated and symmetrically scanned with respect to the laser beam (Fig. 22.1.2). By this means, surface roughening and structure formation can be significantly suppressed (Fig. 22.1.3). As a consequence, the density of particulates and dis-

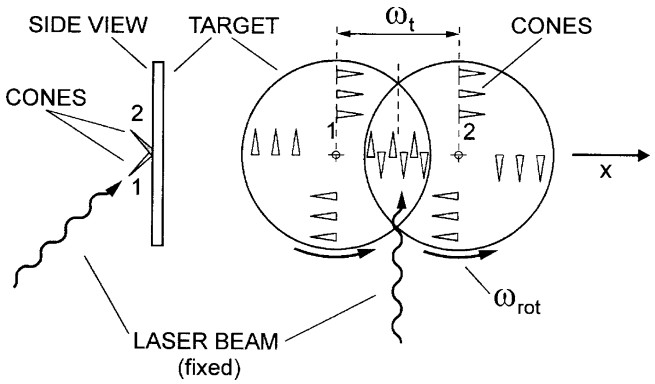

Fig. 22.1.2 Surface structures which align with the incident laser beam, e.g., cones, can be suppressed by simultaneous rotation and translation of the substrate with incommensurate frequencies ω_{rot} and ω_{t}, respectively. By this means, each target site is ablated from opposing incident angles

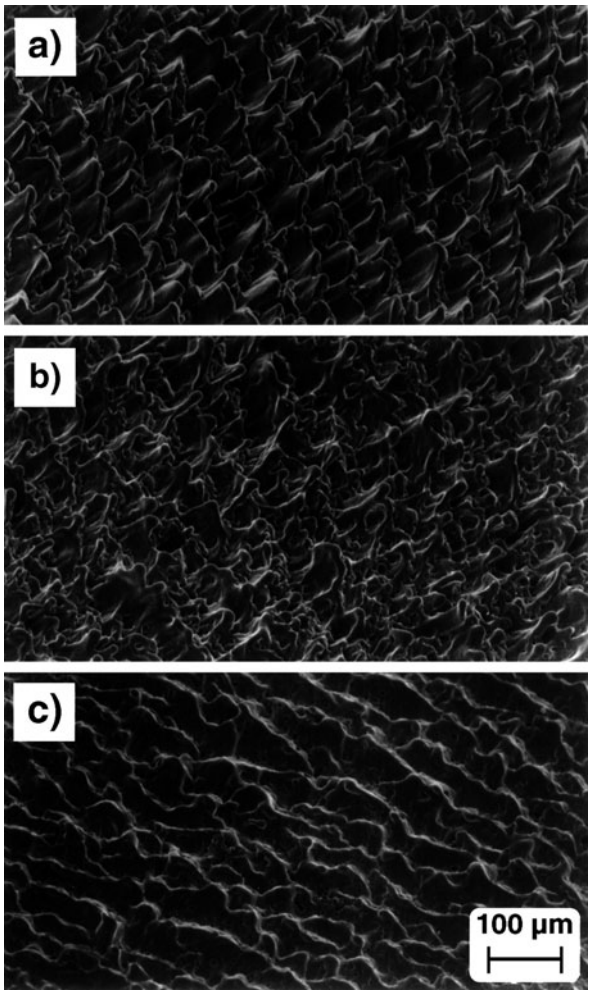

Fig. 22.1.3 a–c Influence of fluence and scanning mode on the surface morphology of ceramic $YBa_2Cu_3O_7$. (**a**) $\omega_{rot} \neq 0$, $\omega_t = 0$, $\phi = 1.2\,J/cm^2$, $N_\ell = 350$ pulses/site, (**b**) same as (**a**) but with $\phi = 3.25\,J/cm^2$, (**c**) same as (**b**) but with $\omega_{rot} \neq 0$ and $\omega_t \neq 0$ [*Stangl* and *Proyer* 1995]

placements of the plasma-plume direction are minimized and the ablation rates and the profiles of deposited films remain almost constant with respect to the number of laser pulses. Cylindrical targets are mainly employed in cross-beam PLD (Sect. 22.1.4).

The distance between the target and the substrate should match, approximately, the length of the visible plasma plume (Chap. 30) and this is, typically, $l \approx 3-8$ cm. The uniformity in film thickness can be improved by moving the substrate relative to the plasma plume, for example, by excentric rotation of the substrate holder. With some materials, the throughput in film preparation can be enhanced by mounting several substrates. *Large-area* films can be grown by rotation and/or translation of

the substrate and/or the target and/or by controlled deflection of the laser beam. The fabrication of thin films of oxides, in particular of high-temperature superconductors, has been demonstrated on 12.5 cm (5 inch) Si-wafers, on sheet-like substrates, and on metal ribbons [*Miura* et al. 2010; *Kakimoto* et al. 2010; *Fuji* et al. 2008; *Greer* 2007; Sect. 22.4.6].

The substrate temperature determines, to a large extent, the morphology and microstructure of films. Proper temperature control requires shielding of the sample holder, thermometers mounted on the substrate surface and the sample holder and, if possible, pyrometric measurements. Special optical arrangements permit laser-induced substrate cleaning prior to film deposition and in situ laser annealing of the deposited film. For stoichiometric deposition and the suppression of particulates, different types of shutters, masks, and apertures are introduced in the chamber. Additional windows/load locks on the deposition chamber are used for plasma-plume-analysis and in situ film diagnostics, e.g. by RHEED [*Rijnders* and *Blank* 2007; Chaps. 29 and 30). Further experimental aspects are outlined throughout this chapter.

22.1.1 Congruent and Incongruent Ablation

The proper choice of laser parameters is of great importance, since they determine the type and the relative concentrations, the degree of ionization, and the spatial and temporal distribution of species leaving the target surface.

Congruent Ablation

High laser-power densities and short pulses (dwell times) cause short interaction cycles resulting in (almost) congruent ablation of small material volumes. If the thickness of the ablated layer per pulse fulfils the condition (12.0.1), heat loading of the target and material segregation remain small. Both can be further suppressed by target scanning (Fig. 22.1.2) and/or laser-beam deflection. With these conditions, the ablated material has essentially the same composition as the original target, even after many laser pulses. The angular distribution of ablated products is strongly forward-directed and can be fitted by a $\cos^n \Theta$ law, where Θ is the angle between the surface normal and the direction of propagation of species within the plasma plume. The forward orientation of the plume becomes more pronounced with increasing laser fluence and spot size. With the laser parameters typically employed in this regime, the exponent has values $n \geq 10$ (Sect. 22.2.5). Congruent ablation is a prerequisite for the synthesis of thin films of multicomponent materials from *single* targets. High-intensity laser pulses also permit one to partially or completely dissociate materials that ordinarily evaporate in molecular form only.

Incongruent Ablation

In the case of equilibrium or quasi-equilibrium laser heating, the target surface is melted and vaporized in a similar way as in conventional thermal evaporation

(Chap. 11). Here, the relative concentrations of species leaving the surface, in general, differ significantly from those of the original target. Components with high vapor pressure leave the target before those with low vapor pressure. The angular distribution of species can be described by a $\cos\Theta$ law, as expected for thermal (equilibrium) evaporation. This parameter range is not appropriate for stoichiometric deposition of compounds from *single* targets.

With materials that consist of a *single* component, the terms congruent and incongruent ablation become meaningless. However, the type of ablated species (atoms, molecules, clusters), their density, degree of ionization, and velocity are all dependent on the specific laser parameters employed. These properties of species strongly influence the microstructure, morphology, and quality of films.

Simple Estimations

With strongly absorbing inorganic materials, the requirements for congruent laser ablation are reasonably well fulfilled with nanosecond laser pulses and fluences of, typically, $1-10\,\mathrm{J/cm^2}$. This becomes plausible from a simple estimation of the characteristic times involved in the process. Let us assume purely thermal ablation and 1D heat flow. The time to reach the stationary vaporization temperature on the target surface, t_v, can be estimated from (11.2.22). From Fig. 11.2.4 we find, with $\phi \approx 1\,\mathrm{J/cm^2}$ and $\tau_\ell \approx 10\,\mathrm{ns}$, that $t_\mathrm{v} \approx 5\times10^{-8}\,\mathrm{s}$ for a Cu target, about $5\times10^{-10}\,\mathrm{s}$ for a ceramic target of a high temperature superconductor (YBCO), and about $5\times10^{-12}\,\mathrm{s}$ for PET with surface absorption. Clearly, these estimations ignore laser–plasma interactions. At least for non-metals, these heating times are too short for significant material segregation. With certain materials and laser parameters, stoichiometric ablation can even be achieved with rapidly scanned cw-lasers or fast rotating targets. In this case τ_ℓ corresponds to the dwell time of the laser beam.

If (12.0.1) is fulfilled, the heat load of the target is minimized. Thin-film formation, however, requires multiple-pulse irradiation. In this case, target heating can become significant, and it can be estimated from the average absorbed intensity (Sect. 6.3). In any case, one has to compromise between the pulse-repetition rate, which determines the overall growth rate of the film, and the maximum tolerated temperature of the target. Consideration of these conditions is very important because material segregation may also take place *between* laser pulses.

22.1.2 Targets

The targets mainly employed in PLD are ceramics and, in special cases, liquids. To a lower extent, targets in single-crystalline, polycrystalline, powdery, or amorphous form, and also frozen liquids [*Dygert* et al. 2007; *Yoshida* et al. 2007] are used as well. Frozen solutions with low concentrations of precursor molecules, typically 0.1 up to several wt %, are used in matrix-assisted pulsed-laser evaporation (MAPLE; Sect. 22.9) and in matrix-assisted laser desorption and ionization (MALDI; Sect. 30.1.3).

With single-crystalline and coarse-grain-polycrystalline targets uniform deposition and low concentrations of particulates within the film can frequently be achieved only during the first few laser pulses. Subsequent fracturing of the target material due to thermal shocks can result in the ejection of large fragments which deteriorate the uniformity and quality of the deposited film.

Small-grained *dense* ceramic targets permit more uniform conditions during longer sputtering times. An additional advantage of such targets is the enhanced extinction due to radiation trapping. This is of particular importance with materials that are otherwise transparent at the laser wavelength under consideration. The diminished thermal conductivity originating from thermal barriers between grains is also an advantage. Both properties considerably enhance the surface temperature with respect to that induced in single-crystalline or polycrystalline material.

With low-to-moderate energy densities, liquid or surface-molten targets remain smooth at all times and permit one to efficiently reduce or almost avoid particulates on the film surface. Clearly, with fluid targets it is neither necessary to rotate the target nor to scan the laser beam. Liquid targets, however, can only be applied with homogeneous liquids or with compounds that melt congruently. With high heating rates, superheating of the liquid may result in bubble formation and explosive vaporization.

For the fabrication of doped films or heterostructures, multiple targets consisting of the individual elements, compounds, or various types of mixtures are used.

Multiple targets are also used for the synthesis of compounds for which the requirements for stoichiometric ablation cannot be fulfilled, or if single stoichiometric targets are not available, or if the sticking coefficients of single constituents on the film surface are very different. Here, ablation can be achieved by sequential or simultaneous exposure of the individual targets. In any case, ablation from multiple targets is more difficult to handle because the rate of ablation will vary with each source. The composition of the film can then be controlled via the dwell time or the power of the laser beam on each source. Nevertheless, such arrangements are used in laser molecular beam epitaxy (LMBE) and the fabrication of nanocomposite materials.

22.1.3 Uniform Ablation

The deposition of uniform films requires a good surface morphology and smooth ablation of the target. Independent of the angle of incidence, the preferred direction of the vapor plume is perpendicular to the target surface. With an uneven surface, however, the direction of plume expansion will continuously change. With the development of any surface structures, e.g., cones (Fig. 22.1.3; Sect. 28.4), which align with the beam, the ablation rate decreases, and the number of particulates increases with the number of laser pulses. Additionally, such structures cause a bending of the plasma plume towards the incident laser beam, resulting in non-uniform

material deposition (it should be noted that with very high fluences, which are rarely employed in PLD, the plume also bends towards the incident laser beam, but for other reasons). These problems can be suppressed or even avoided if the target is simultaneously rotated *and* translated during ablation (Fig. 22.1.2). In this way, each target site will be ablated from opposing directions. For optimal conditions, the translational motion must be symmetric with respect to the position of the laser beam. The frequencies of rotation, ω_{rot}, translation, ω_{t}, and laser-pulse repetition, ω_{r}, must all be incommensurate. Uniform ablation is achieved if the average exposure provided by the laser beam is the same for all target points. If the radius of the laser beam is very small compared to the radius of the target, i.e., if $w \ll R_{\mathrm{t}}$, the temporal dependence of the translational motion along the diameter of the target in the x direction must follow a square-root dependence at each quarter cycle, as shown in Fig. 22.1.4a. It can be described by

$$x = \sqrt{2} R_{\mathrm{t}} \left(\left| 2t^* - \left[2t^* \right] \right| \right)^{1/2} \operatorname{sign} \left(t^* - \left[t^* \right] \right) \ , \tag{22.1.1}$$

with $t^* = t/T_{\mathrm{t}}$. The square brackets indicate that the round value, i.e., the integer closest to a given value, should be taken. Figure 22.1.4b shows the average exposure as a function of the normalized distance from the target center, ϱ/R_{t}, for four different beam shapes. The most uniform exposure of targets is achieved with top-hat circular beams of radii $w \lesssim 0.1 R_{\mathrm{t}}$ (*solid curve*). A non-linear dependence of the ablation rate on intensity will *sharpen* the interaction zone and thereby diminish non-uniformities in ablation related to the finite size of the laser beam. The results have been verified by experiments using $YBa_2Cu_3O_{7-\delta}$ targets [*Broser* 2008; *Stangl* and *Proyer* 1995].

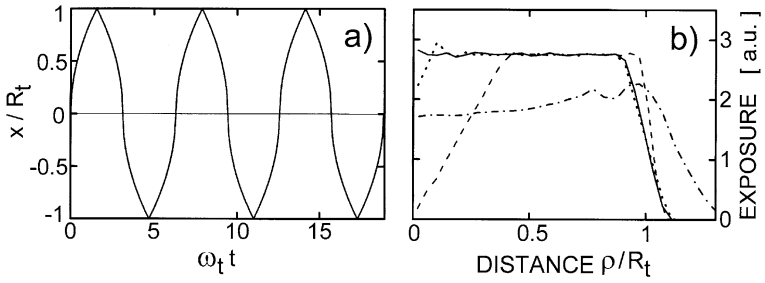

Fig. 22.1.4a, b Uniform ablation of targets. (**a**) Vibration of the beam center in the x direction as described by (22.1.1). (**b**) Dependence of the (average) target exposure on the (dimensionless) distance from the target center, ϱ/R_{t}. In all cases, the ratio of frequencies is $\omega_{\mathrm{r}}{:}\omega_{\mathrm{rot}}{:}\omega_{\mathrm{t}} = 10\mathrm{e}{:}\pi{:}1$. The different beam shapes employed have the *same* total power. *Solid curve*: top-hat circular beam with $w_{\mathrm{x}} = w_{\mathrm{y}} = 0.1 R_{\mathrm{t}}$. *Dotted curve*: top-hat square beam with $w_{\mathrm{x}} = 0.1 R_{\mathrm{t}}$, $w_{\mathrm{y}} = 0.1 R_{\mathrm{t}}$. *Dashed curve*: top-hat rectangular beam with $w_{\mathrm{x}} = 0.01 R_{\mathrm{t}}$, $w_{\mathrm{y}} = 0.2 R_{\mathrm{t}}$. *Dash-dotted curve*: top-hat rectangular beam with $w_{\mathrm{x}} = 0.1 R_{\mathrm{t}}$, $w_{\mathrm{y}} = 0.4 R_{\mathrm{t}}$ and *sinusoidal* translational motion [*Arnold* and *Bäuerle* 1999]

22.1.4 Cross-Beam PLD

In cross-beam PLD, two intersecting plasma plumes are generated by ablating cylindrical targets by means of two (synchronized) laser beams [*Gorbunov* 2007; *Basillais* et al. 2005]. Due to the interaction of plumes and the inertia of particulates, including droplets, the deposited films are often smoother and contain less particulates. Clearly, droplet formation due to further vapor cooling after plume collisions and/or nucleation on the substrate surface cannot be avoided (Sect. 30.4). Cross-beam PLD seems to be advantageous in particular for the synthesis of metal alloys and heterostructures. However, the costs and complexity of the setup in comparison to that shown in Fig. 22.1.1 does not pay off in most cases. Additionally, the fabrication of cylindrical targets is much more expensive or not at all possible with many materials. With further complexity of the apparatus, disc-shaped targets could be employed as well.

22.2 Volume and Surface Processes, Film Growth

Figure 22.2.1 shows, schematically, different volume and surface processes in reactive PLD. The laser-induced plasma plume consists of UV radiation, electrons, ionized or neutral atoms, molecules, clusters, and fragments (Chap. 30). The different species may react with each other or with a background atmosphere and impinge onto the film/substrate surface. Adsorbed species diffuse on the surface and contribute to film growth or they desorb. If the grown film does *not* require any post-deposition treatment, the process is termed in situ fabrication.

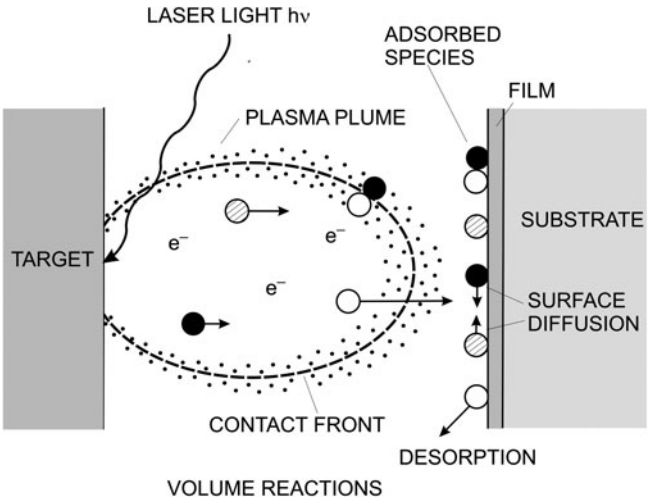

Fig. 22.2.1 Volume and surface processes relevant in thin-film formation by PLD. Reactions (collisions) between ablated species and the ambient atmosphere take place, in particular, near the contact front. However, with certain systems and experimental conditions, mixing between ablated species and the ambient atmosphere may take place within a larger volume (Chap. 30)

22.2.1 Plasma and Gas-Phase Reactions

On their way from the target to the substrate, reactive and non-reactive collisions of ablated species take place within the plasma plume, at the contact front between the plume and the ambient gas, and near the substrate surface. Such volume reactions are strongly influenced by the UV plasma radiation, by free electrons within the plasma, and, near the target, by the laser radiation itself. In the absence of an ambient atmosphere, the number of collisions between species is largest close to the target. In any case, the type, energy, and flux of species at the substrate surface are determined by the laser fluence/energy and by collisions and chemical reactions of species within the volume between the target and the substrate.

Reactive ambient atmospheres frequently employed are oxidizing gases such as O_2, O_3, N_2O, or NO_2. They allow one to fabricate stoichiometric oxide films by ablation of single-component or multicomponent targets. Here, the exact oxygen content within the film can be tuned via the background gas pressure. Similarly, nitride films are frequently grown in an N_2 background atmosphere. The much lower reactivity of N_2 in comparison to O_2 is often compensated by an additional RF-plasma source within the PLD chamber.

Volume excitation/dissociation of species can be thermally or non-thermally activated. Comparison of bond dissociation energies shows that the formation of atomic oxygen from O_2 requires about 5.11 eV, while with O_3 only 1.05 eV and with N_2O about 1.67 eV is needed.

Thermal activation is most pronounced near the target and substrate surface. Non-thermal processes take place, in particular, within the plasma plume. Laser-induced volume excitations play a significant role only near the target because of the oblique beam incidence. The photochemistry of the oxidizing gases mentioned above can be described by

$$\mathrm{XO} + h\nu \rightarrow \mathrm{X} + \mathrm{O}(^1\mathrm{D}, ^3\mathrm{P}) \,, \tag{22.2.1}$$

where $\mathrm{X} \equiv \mathrm{O}, \mathrm{O_2}, \mathrm{NO}, \mathrm{N_2}$. Thus, oxygen atoms are mainly in either the ground state (^{3}P) or the first excited state (^{1}D), depending on the precursor molecule, the laser wavelength, and the spectral intensity distribution of the plasma radiation. The absorption cross sections for different wavelengths can be found in Table V. At very high laser fluences, multiphoton dissociation of species near the target surface may become important.

Electronic excitation and dissociation of species can also be mediated via energetic electrons within the vapor/plasma plume (Sect. 11.6.2). For example,

$$\mathrm{O_2} + \mathrm{e} \rightarrow \mathrm{O_2}^* + \mathrm{e} \rightarrow 2\mathrm{O}(^1\mathrm{D}, ^3\mathrm{P}) + \mathrm{e} \,, \tag{22.2.2}$$

or

$$\mathrm{N_2O} + \mathrm{e} \rightarrow [\mathrm{N_2O}]^* + \mathrm{e} \rightarrow \mathrm{N_2} + \mathrm{O}(^3\mathrm{P}) + \mathrm{e} \,, \tag{22.2.3}$$

and

$$O(^3P) + e \rightarrow O(^1D) + e \ . \tag{22.2.4}$$

Similar processes can take place with the other precursors mentioned above. With the laser fluences typically employed in PLD, the average energy of electrons is between 2 and 4 eV. The rate constants for these processes are then $k(O_2) \leq 5 \times 10^{-11}\,\mathrm{cm}^3/(\mathrm{electron} \times \mathrm{s})$ and $k(O_3) \approx k(N_2O) \approx 10^{-8}-10^{-9}\,\mathrm{cm}^3/(\mathrm{electron} \times \mathrm{s})$ [*Kline* et al. 1991].

Energetic neutrals, ions, and clusters cause similar excitation/dissociation processes. Unfortunately, very little is known about the yield related to such collisions. In any case, with the background gases under consideration, the species ablated from the target will react with oxygen and form oxide molecules.

Dissociation of species i by UV radiation and electron impact is particularly strong near the target surface where the flux $J_i(0)$ is generated. For *low* densities of background species, N_j, and strong forward direction (1D propagation) the flux at the substrate at distance l can be written as

$$J_i(l) = J_i(0)\exp(-\sigma_i N_j l) \ , \tag{22.2.5}$$

where σ_i is the cross section for both non-reactive and reactive collisions; any electromagnetic interactions are ignored. Within this approximation, the film growth rate should exponentially decrease with increasing background pressure. If, however, species i are only generated from gas-phase molecules j, for example, by photodissociation or reactive collisions with ablated species, the flux J_i will *increase* with increasing pressure p_j, at least close to the target surface. The validity of (22.2.5) has been proved for PLA of Y-Ba-Cu-O targets in O_2 and Ar atmospheres [$10^{-5}\,\mathrm{mbar} \leq p_j(O_2, \mathrm{Ar}) \leq 0.4\,\mathrm{mbar}$] by means of ion-probe measurements [*Geohegan* 1992]. The scattering cross sections derived from these experiments were around $2.5 \times 10^{-16}\,\mathrm{cm}^2$. For *high* number densities, a hydrodynamic description of the problem is required.

22.2.2 Substrate Temperature, Laser-Pulse-Repetition Rate

Species impinging onto the substrate need a certain time for surface diffusion and incorporation at proper lattice sites. Surface diffusion is a thermally activated process which increases with increasing temperature. This is the reason why high-quality crystalline films can be deposited at reasonable growth rates only at elevated temperatures. The time necessary for surface diffusion is also the reason why laser-pulse-repetition rates must be adapted to the particular material under investigation, the substrate temperature, and the flux of species onto the surface. Due to the dissipated kinetic and internal energy of impinging species and their heat of condensation and desorption, the temperature on the substrate/film surface changes during and between laser pulses. Such (rapid) changes in temperature

which significantly influence surface processes cannot, at present, be detected with the setups employed in PLD. The total (additional) energy input by the impinging species depends on the laser parameters, and in particular on the laser fluence and pulse-repetition rate, and on the distance between the target and the substrate. Thus, there is a complex interrelation between the laser parameters, the properties of the target, the volume expansion and reaction of ablated species, and the different processes on the substrate surface. For such reasons, film growth during PLD is quite different from that in standard techniques.

A problem related to high laser-pulse-repetition rates is the *overall* increase in target temperature, which favors material segregation. If, on the other hand, the laser-pulse-repetition rate is too low, the relative importance of thermal desorption of volatile components from the film increases. Additionally, in the case of non-reactive deposition, incorporation of gas-phase impurities takes place at a higher relative rate.

22.2.3 Energy of Species

The kinetic energy of species in pulsed-laser ablation is up to several 10 eV and up to several 10^3 eV for nanosecond and femtosecond pulses, respectively. Clearly, it depends also on the intensity and/or the spot size of the laser beam. In PLD, energetic species can improve or deteriorate the overall morphology, stoichiometry, and microstructure of the growing film. This is well known from ion-beam techniques. High-energy species may break atomic bonds, generate subsurface vacancies and displacements of atoms, induce recoil implantation and self-sputtering, cause thermal spikes, etc. [*Perea* et al. 2008]. However, energetic species also improve film adhesion to the substrate and enhance surface diffusion of adsorbed atoms/molecules. The latter mechanism permits to grow films at lower (average) substrate temperatures and/or with improved crystallinity. Clearly, the film quality achieved with a certain deposition technique, depends on the type of material to be deposited.

As already discussed, the energy of species leaving the target can be tuned via the laser fluence only within a limited region, simply because of the requirements for stoichiometric ablation. The energy of species impinging onto the substrate can, however, be controlled via the distance between the substrate and the target, and via the pressure of the background atmosphere. By this means, a broad range of energies that are not available with standard techniques such as thermal evaporation (average kinetic energy of species < 0.5 eV) or sputtering (5–10 eV) can be covered. However, tuning of the energy of species via the background pressure is limited as well. High background pressures favor the formation of clusters/particulates within the gas phase. Such particulates may condense on the film surface, which is not desirable for most applications. The interrelation between these quite different parameters is the reason why ns-PLD is, with a few exceptions, superior to fs-PLD (see also Chaps. 4, 13 and 30).

22.2.4 Particulates

Different types of mechanisms that result in the appearance of particulates in pulsed-laser ablation are discussed in Sects. 4.2 and 30.4. With the laser parameters and the experimental conditions (homogeneous target ablation, etc.) typically employed in PLD, some of these mechanisms are irrelevant. Subsequently, we describe particulates and various other features that appear on films deposited by PLD. These particulates can be classified according to the following main types:

- Clusters formed in the vapor phase. The size of these clusters depends on the type of material and the experimental conditions, but they are at most 20 nm in diameter (Sect. 4.2). In most cases, PLD is performed at 'low' gas pressures with $p \lesssim 1$ mbar. With these conditions, and the laser parameters typically employed, cluster sizes are a few nanometers and below. Bigger clusters *may* form near and/or on the *substrate* by further growth and coalescence. However, with heated substrates, thermophoretic forces inhibit deposition of clusters (Sect. 4.1.3). This has, in fact, been observed experimentally [*Geohegan* et al. 1999].
- Solidified melt drops with diameters between about 0.1 and 3 μm (Fig. 22.2.2). These *droplets* are mainly related to hydrodynamic instabilities at the target surface (Sect. 28.5). The size of these droplets does not, or only slightly, depend on the pressure of the background atmosphere. During film growth, droplets may change their shape due to crystallization, coverage by the ablated material, etc.
- Irregularly shaped solid grains with diameters between 1 μm and more than 10 μm. These grains are directly ejected from the target, e.g., due to thermal stresses.
- Solidified splash drops with diameters of up to more than 10 μm, originating from superheating and liquid-phase expulsion (Sect. 11.4).
- With organic polymers and biological materials high-molecular-weight fragments are frequently observed (Sect. 12.8.1).

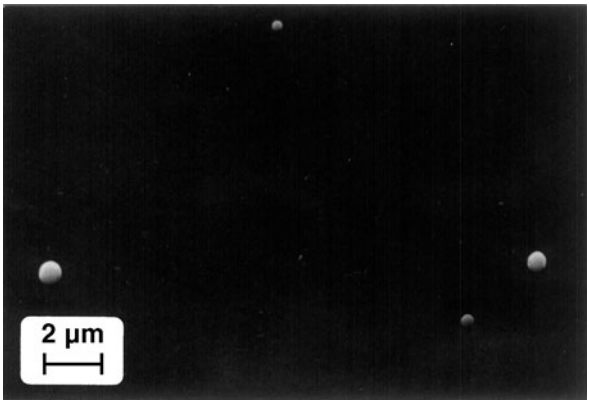

Fig. 22.2.2 $YBa_2Cu_3O_7$ film deposited on (100) MgO using KrF-laser radiation and optimized experimental conditions. The remaining particulates are mainly droplets

- Particulates that are specific to the particular material. Among those are outgrowths, needles, platelets, etc. [*Proyer* et al. 1996]. Some of these features are formed at the substrate surface only, and they are also frequently observed on films deposited by other techniques. The outgrowths, e.g., are related to different crystallographic orientations. Subsequently, the term 'particulates' shall include all types of these additional features.

Particulates diminish the film quality in many respects. They locally destroy the microstructure, increase the surface roughness, reduce the minimum width of features in microfabrication, degrade the electrical properties, etc. For these reasons, great efforts have been made to eliminate the particulates or, at least, reduce their size and density. In fact, with proper experimental handling, the density of the *coarse* particulates can be drastically reduced. This can be achieved by:

- Selecting the proper target material (Sect. 22.1.2). With molten/liquid targets solid particulates can be completely avoided. This is not the case for droplets [*Hopp* et al. 2004].
- Outgassing of the target prior to ablation. In particular with pressed-powder targets or ceramic targets of low density, rapid expansion of trapped gas bubbles beneath the target surface may result in explosive-type ejection of large particulates.
- Employing smooth targets and uniform target ablation by combined rotation and scanning with respect to the laser beam (Fig. 22.1.2). By this means, the ablation conditions remain almost independent of the number of laser pulses, N_ℓ (Sect. 22.1.3).
- Optimization of the laser parameters (Chaps. 12 and 13). Material damages such as microcracks, exfoliation, etc., result in loosely attached fragments which can be ejected from the target during multiple-pulse irradiation. In the case of laser-induced evaporation, where a molten surface layer is important, optimization of the laser parameters is necessary even with single-component material, because of droplet formation due to hydrodynamic instabilities or splashing of the melt due to overheating. With finite absorption, subsurface superheating may result in explosive-type ablation of large fragments. The optimal laser parameters depend on the particular material under investigation. With metals, for example, the number density of droplets observed on the film surface decreases with increasing laser fluence [*van Riet* et al. 1993], while with other materials the situation may be just opposite as, e.g., with carbon [*Rode* et al. 1999]. For $YBa_2Cu_3O_7$ the density of particulates first decreases, reaches a minimum, and then increases with fluence (Fig. 22.4.1). With amorphous carbon and silicon films, the density of particulates can be significantly lowered when using ps or fs instead of ns laser pulses for ablation. The laser parameters that are optimized with respect to the density of particulates are, however, not necessarily equal to those that yield films with the best chemical and physical properties.
- Increasing the aspect ratio (length to width) of the plume, Γ. This can be achieved with larger laser spot sizes and/or higher fluences. If we assume that particulates that originate from the target are homogeneously distributed, their

number density, for a given film thickness, decreases with increasing Γ. Thus, a strongly forward-directed plume would be favorable. An almost spherical distribution of particulates is, however, only observed with certain systems and laser parameters.

There are a number of experimental techniques which suppress the flux of particulates to the substrate. These include the following:

- Variation of the substrate orientation with respect to the (main) direction of plasma-plume expansion, and off-axis deposition [*Inoue* et al. 1997; *Holzapfel* et al. 1992].
- Multiple vane wheels [*Barr* 1969], choppers [*Pechen* et al. 1995], electromagnetic shutters [*Lubben* et al. 1985], etc., which are placed between the target and the substrate and which deflect or filter the (slower) particulates but transmit the fast-moving atoms and molecules.
- Shadow masks [*Pang* et al. 2004].
- Ablation from the edge of disc-shaped targets rotating at high speed.
- Fragmentation of particulates by means of an additional laser beam propagating in parallel to the substrate surface.
- Dual-laser ablation from a single target [*Mukherjee* et al. 2002], or cross-beam PLD from two targets [*Gorbunov* 2007].
- Deflection of particulates by means of a supersonic gas jet [*Murakami* 1992].

Most of these techniques increase the complexity of the experimental setup and reduce the deposition rate. While a particular technique, e.g., off-axis deposition, permits one to suppress some types of particulates, it may favor the formation of others, e.g., outgrowths in HTS films, or it may cause the film stoichiometry to deteriorate, lead to thickness inhomogeneities, etc. For these reasons, the conditions can be optimized only for each particular system and the specific requirements. For HTS films, the particle density can be diminished by up to a factor of 10^2 by post-deposition chemical-mechanical polishing [*Pedarnig* et al. 2010] or by ion-beam polishing [*Hatzistergos* et al. 2004]. With subsequent oxygen annealing, both techniques do *not* affect the critical temperature and current density.

Droplets

While the coarse particulates can be largely avoided by selecting the proper experimental conditions and, if necessary, by employing the additional techniques described, the finer particulates, the droplets, are more difficult to suppress. They seem to be inherently linked with PLD. Figure 22.2.2 shows a typical example of a thin film on which only the droplets can be seen. The formation of droplets may have different origins.

If ablation is performed in a vacuum, vapor cooling due to the expansion of the plasma plume results in gas-phase condensation (Sect. 30.4.3). This effect is particularly important for large adiabatic exponents, γ. However, further growth of clusters is quenched, just because of the lack of collisions at later stages of plume

expansion. A background atmosphere favors cluster formation within the vapor plume (Sect. 4.2). Droplets may also form near or at the substrate via interactions with species desorbing from the substrate, or by coalescence of clusters. In any case, with the parameters typically employed, the size of such droplets should be in the submicrometer region.

Droplet formation can also be related to superheating of the target, to the recoil pressure onto the liquefied surface layer (Sect. 11.4), and to hydrodynamic instabilities (Sect. 28.5). There is, in fact, experimental evidence that droplets originate from Kelvin–Helmholtz and/or Rayleigh–Taylor instabilities at the target surface [*X. Zhang* et al. 1997; *Proyer* et al. 1996; *Bennett* et al. 1995].

22.2.5 Chemical Composition and Thickness of Films

With certain compounds, PLD can result in films which are sub-stoichiometric with respect to a particular constituent, even when ablation is, in total, congruent. There can be various reasons for this:

- Differences in the transport of species between the target and the substrate. Among these are differences in hydrodynamic expansion and in the number and efficiencies of collisions of species within the plasma plume. In other words, in spite of the collisions, the differences in masses and/or charges may cause differences in the angular distribution of species.
- The sticking coefficients of different species impinging onto the substrate surface are not equal, and also depend on the energy of species and the angle of incidence.
- The desorption enthalpies of adspecies differ from each other.
- Differences in binding energies, outdiffusion, and desorption of species that were already built-in on proper lattice sites.

Compensation can be achieved in various ways, depending on the particular material:

- A uniform background pressure yields an additional reactive flux onto the substrate surface. Furthermore, ablated species may react with gas-phase molecules *before* they condense onto the substrate.
- Via a continuous or pulsed gas stream which directs precursor molecules, e.g. via a nozzle, onto the substrate surface.
- By means of another source, for example, an ion gun.
- By using a target that contains an excess of the particular constituent.

Thickness Profiles

If the target and substrate are mounted on an axis, as shown in Fig. 22.1.1, the deposited film is non-uniform because of the strong forward direction of the plasma plume [*Toftmann* et al. 2003; *Svendsen* et al. 1998; see Chap. 30]. If PLD is performed in a vacuum, or at a low gas pressure, the film profile can be approximated by [*Anisimov* et al. 1993]

$$h(\theta) = \frac{M_\mathrm{p}\Gamma^2}{2\pi\varrho l^2}\left(1+\Gamma^2\tan^2\theta\right)^{-3/2} \propto \cos^n\theta\ , \qquad (22.2.6)$$

where M_p is the total ablated mass, ϱ the density of the deposited film, l the target-substrate distance, and $\Gamma \equiv Z/X$ the aspect ratio where Z is the length and $2X$ the (average) width of the plume. The latter proportionality refers to small angles with $n \approx 3\Gamma^2$. The ratio Γ decreases with decreasing spot size. Thus, the uniformity in film thickness becomes better with decreasing focus. The dependence of Γ on laser fluence is more complicated. With many systems, Γ first increases and then becomes constant with higher fluences.

Patterned Films

Single-step growth of isolated structures can be achieved by using PLD in combination with a mechanical mask. The influence of deposition parameters on the resolution of patterns has been investigated for the case of oxide films by *Riele* et al. (2007). Possible contaminations of films by species sputtered from the mask have not been investigated.

22.3 Overview of Materials and Film Properties

PLD permits thin epitaxial or large-grain oriented films, heterostructures, and films with 'step-like' morphology to grow. It also allows metastable materials to be synthesized, small grain and even nanocrystalline films to be deposited, and composite materials consisting of different constituents to be fabricated.

Epitaxial and *large-grain* oriented films have been studied for a great variety of different compounds and film dopings. Among those are different types of high-temperature superconductors (HTS), metals, semiconductors, dielectrics, ferroelectrics, electro-optic and giant magnetoresistance oxides, and organic materials, mainly polymers. The precise and fast control of the material composition achieved in PLD is of particular importance for the synthesis of stoichiometric high-quality films for bandgap engineering and the fabrication of heterostructures.

Nanocrystalline films have been fabricated by either condensing the clusters formed from ablation products on a substrate in a background atmosphere (Sect. 4.1.4), or by embedding clusters formed on the surface in a host material. The size of clusters can be controlled, in the first case, via the pressure of the background gas and, in the second case, by the relative number of laser pulses on each target, the laser fluence, repetition rate, etc.

The lasers mainly employed in film fabrication are excimer lasers, Nd:YAG lasers and Nd:glass lasers. Some experiments have been performed with pulsed CO_2 lasers and scanned cw-lasers.

Films deposited by laser ablation are amorphous, polycrystalline, or single crystalline. Higher substrate temperatures favor, in general, crystalline growth. With

multiphase materials, the particular crystalline phase formed during deposition is determined by both the substrate temperature and the gas pressure. The film growth rates achieved range from a few Å/s to some ten μm/s.

With substrates that do not match the lattice spacing of the film or which favor strong interdiffusion of species, a buffer layer becomes necessary. The buffer layer can be fabricated by standard techniques or it is laser-deposited prior to the film by employing an additional target. The (uniform) substrate temperatures used during film deposition are between 20 and 1200°C. In most publications, the temperatures quoted were measured at the substrate holder. The most important techniques for in situ and post-deposition characterization of films are summarized in Chaps. 29 and 30.

In the following section we discuss in further detail the peculiarities, possibilities, and limitations of PLD for the *example* of high-temperature superconductors.

22.4 High-Temperature Superconductors

Thin films of high-temperature superconductors (HTS) have been fabricated by PLD in both reactive and non-reactive atmospheres. The material studied in most detail is $YBa_2Cu_3O_{7-\delta}$ (YBCO, Y-123). Among the other materials investigated are different RE-123 (RE = rare earth) compounds, and different phases of $Bi_2Sr_2Ca_{n-1}Cu_nO_{2(n+2)\pm\delta}$ [$T_{c0} \lesssim 10\,\mathrm{K}$ ($n = 1$), $T_{c0} \approx 86\,\mathrm{K}$ ($n = 2$), and $T_{c0} \approx 110\,\mathrm{K}$ ($n = 3$)], $Tl_2Ba_2Ca_{n-1}Cu_nO_{2(n+2)\pm\delta}$ [$T_{c0} = 95\,\mathrm{K}$ ($n = 1$), 110 K ($n = 2$), 125 K ($n = 3$)], $HgBa_2Ca_{n-1}Cu_nO_{2(n+1)\pm\delta}$ [$T_{c0} = 95\,\mathrm{K}$ ($n = 1$), 124 K ($n = 2$), 134 K ($n = 3$)], and $(C_xCu_{1-x})Ba_2Ca_{n-1}Cu_nO_{2n+3}$ [$T_{c0} \lesssim 78\,\mathrm{K}$($n \approx 4$)].

Among the *new* materials studied since 2000 are MgB_2 ($T_{co} \approx 34.2\,\mathrm{K}$) [*Wu* et al. 2008; *Lucarelli* et al. 2007] and iron-based compounds such as $Ba(Fe_{1-x}Co_x)_2As_2$ [*Iida* et al. 2009] and $LaO_{1-x}F_xFeAs$. With the latter, an onset to superconductivity at 11 K has been observed [*Backen* et al. 2008]. This temperature is, however, much lower than that obtained in *ceramics* (up to 43 K) [*Takahashi* et al. 2008].

In most of the experiments, UV excimer-laser radiation and high-density ceramic targets are used. The preference for excimer lasers is related to their short wavelengths, high pulse energies, and short pulse lengths, typically, 10−40 ns (Table I). These properties favor strong light absorption and congruent target ablation. In this parameter regime, the depth of laser energy deposition can be estimated from the heat-diffusion length, since $l_T \gg l_\alpha$. For YBCO and KrF-laser radiation, e.g., $l_T \approx 0.6\,\mu\mathrm{m}$ [$D(T_b) \approx 0.05\,\mathrm{cm}^2/\mathrm{s}$, $\tau_\ell = 20\,\mathrm{ns}$] while $l_\alpha \approx 0.04\,\mu\mathrm{m}$.

Stoichiometric laser ablation of (ceramic) targets requires energy densities of, typically, $1-5\,\mathrm{J/cm}^2$ (Fig. 12.4.1). With low-energy short pulses and high-energy long pulses, compositional changes have been observed in the targets, and thus in deposited films [*Auciello* et al. 1988; *Heitz* et al. 1990]. Stoichiometric target ablation can still result in films that are sub-stoichiometric with respect to a particular constituent. Surface desorption and outdiffusion from the bulk are responsible for the loss of Bi, Tl, and Pb in the respective HTS systems.

Among the substrate materials investigated for thin-film deposition were $SrTiO_3$, $LaAlO_3$, MgO, YSZ, ZrO_2, Al_2O_3, $LiNbO_3$, $NdGaO_3$, GaAs, Si, thermally oxidized Si, and different metal sheets such as Ag foils and stainless steel.

22.4.1 Non-reactive Deposition

Non-reactive deposition was mainly performed in a vacuum. In order to form the desired superconducting phase with the correct oxygen concentration, films must be post-annealed in an O_2 atmosphere [*Venkatesan* et al. 1988]. Post-annealing is time consuming and, more importantly, it damages the surface morphology and the film–substrate interface, mainly due to material interdiffusion. The high annealing temperatures, typically 800–950°C, limit the choice of substrate materials and are incompatible with many potential applications, e.g., in semiconductor device technology, the fabrication of multilayer structures, etc.

With $YBa_2Cu_3O_{7-\delta}$ ($0 \leq \delta \leq 0.2$) films the transition to the superconducting state is around $T_{c0} \approx 91$ K (zero-resistance temperature in the absence of a magnetic field; the criterion typically employed is $1-10\,\mu V/cm$, with bridges of several μm in width). Mainly due to grain boundaries, the critical current densities are by about a factor of 10 smaller than those found with in-situ-fabricated films.

The synthesis of stoichiometric single-phase films of Bi-Sr-Ca-Cu-O is more complicated because of the multiphase behavior of this material. With Tl-Ba-Ca-Cu-O and Hg-Ba-Ca-Cu-O an additional problem is the incorporation of the correct amount of Tl and Hg, respectively. This has been achieved by sputtering sequential layers, e.g., of Ba-Ca-Cu-O and HgO, and/or post-annealing of films in the presence of precursor pellets.

22.4.2 Reactive Deposition

Reactive deposition in O_2, O_3, N_2O, or NO_2 permits in situ fabrication of high-quality superconducting films. An ambient atmosphere attenuates the propagation of the plasma plume (Sect. 30.3). For this reason, the laser fluences are somewhat higher than those employed in vacuum deposition, typically between 3 and $10\,J/cm^2$. The background pressure of the oxidant is, typically, between 0.01 and a few mbar. Subsequent to deposition, films are cooled to room temperature in a well-defined way. This is essential for incorporating the correct oxygen content, because oxygen out-/indiffusion is significant at temperatures $T_s > 300$°C. Deposition rates for high-quality films are between 1 and 150 Å/s (about $0.1-6$ Å/pulse).

RE-123

In-situ-deposited $YBa_2Cu_3O_7$ films are black with a smooth mirror-like appearance, good surface hardness, good chemical stability in air, and metallic resistance

behavior within the normal conductive state [$\varrho(100\,\mathrm{K}) \approx 60\,\mu\Omega\,\mathrm{cm}$ on $SrTiO_3$]. Films with thicknesses between 300 Å and 1 μm have been fabricated on wafers up to 12.5 cm (5 inches) in diameter. Film-thickness variations can be diminished by moving the substrate holder. The microstructure of films is crystalline.

The best-quality films with respect to the transition temperature, T_{c0}, and the critical current density, $j_c(T)$, have been obtained with (100) $SrTiO_3$ substrates (the mismatch with the *b*-axis of orthorhombic $YBa_2Cu_3O_7$ is $<1\%$). At temperatures $T_s \approx 750°C$, epitaxial *c*-axis-oriented ($c \approx 11.68$ Å $\perp$ to substrate surface) films have been grown with $T_{c0} \approx 92\,\mathrm{K}$ and $j_c(77\,\mathrm{K}) \approx 2 \times 10^7\,\mathrm{A/cm^2}$.

With other crystallographic orientations of $SrTiO_3$ and other substrate materials, lower values of both T_{c0} and $j_c(T)$ have been obtained. For example, with (100) MgO substrates the best films with respect to both the superconducting properties ($T_{c0} \approx 89\,\mathrm{K}$; $j_c(77\,\mathrm{K}) \approx 4 \times 10^6\,\mathrm{A/cm^2}$) and the density of particulates have been obtained with KrF-laser fluences $\phi \approx 3$ to $3.5\,\mathrm{J/cm^2}$, $T_s = 750°C$, and $p(O_2) = 0.7\,\mathrm{mbar}$. This is shown in Fig. 22.4.1. With higher laser fluences, the deposition rate and the density of particulates both increase, while T_{c0} and j_c remain constant.

The superconducting properties of different $REBa_2Cu_3O_7$ and $REBaSrCu_3O_7$ (REBSCO) compounds fabricated by PLD on various substrate materials are listed in *Bäuerle* (1998). Figure 22.4.2 shows the temperature dependences of the resistivities and the critical current densities of $GdBa_2Cu_3O_7$ and $GdBaSrCu_3O_7$ films.

Deposition of $YBa_2Cu_3O_7$ in an N_2O Atmosphere

Figure 22.4.3 demonstrates the influence of the type of background atmosphere on film properties. For substrate temperatures *below* about 650°C, the superconducting properties of $YBa_2Cu_3O_7$ films deposited in N_2O are superior to those achieved in O_2. Samples prepared in O_2 at temperatures $T_s \leq 570°C$ are semiconductors.

The advantage of N_2O is ascribed to atomic oxygen generated by *thermal* dissociation of N_2O at the film surface. This becomes plausible from the lower dissociation energy of N_2O with respect to O_2 (Sect. 22.2.1). Nevertheless, higher concentrations of atomic oxygen generated within the plasma plume, and a higher reactivity near the contact surface (Fig. 22.2.1), can also contribute to this behavior.

22.4.3 Heterostructures

Heterostructures are grown by using multiple targets consisting of the individual elements, compounds, or various types of mixtures. Other possibilities include the exchange of the background atmosphere, or the integration of an additional source into the PLD chamber, e.g., a Knudsen cell or an ion gun.

Heterostructures allow one to study coupling mechanisms across layered planes of varying compositions, thicknesses, etc. Among the different material combinations studied up to now are the following:

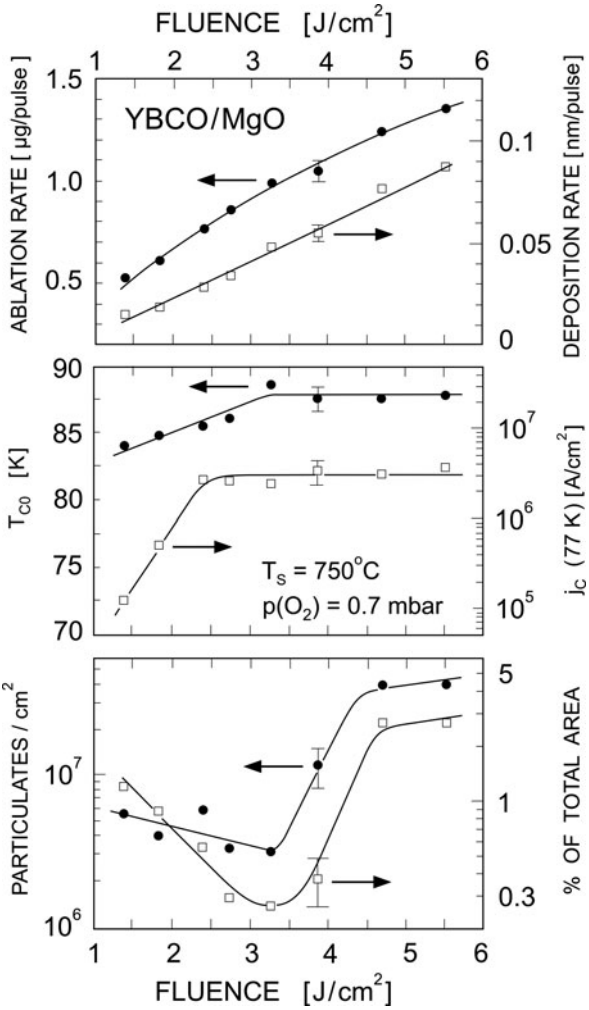

Fig. 22.4.1 Dependence of the ablation rate of ceramic $YBa_2Cu_3O_7$ targets and the deposition rate of films on KrF-laser fluence (laser spot size 2.3 mm^2, $N_\ell = 6000$). The behavior of the transition temperature, T_c(77 K), and the critical current density, j_c(77 K), of films, and the number density of particulates/fraction of total area covered by particulates is also shown [adapted from *Proyer* et al. 1996]

- Superlattices of $YBa_2Cu_3O_7/Y_{1-x}Pr_xBa_2Cu_3O_7$ with $0 \leq x \leq 1$ [*Venkatesan* et al. 1990; *Lowndes* et al. 1992]. *c*-axis-oriented layers with periodicities between some 10 Å and several 100 Å were grown on MgO, $SrTiO_3$ and $LaAlO_3$ substrates. AES depth profiles and cross-sectional TEM indicate abrupt Pr–Y interfaces within one unit cell and virtually no disruptions of layers at interfaces. For device applications the demands on the crystallinity and interface properties are quite stringent. This is related to the short coherence length in HTS

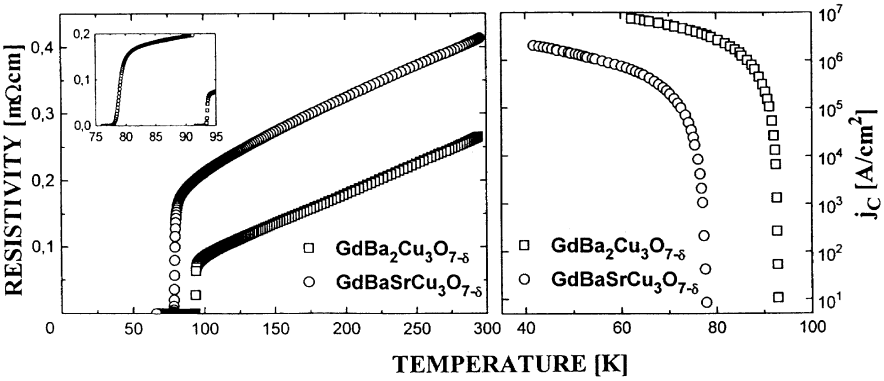

Fig. 22.4.2 Temperature dependences of the resistivities (*left*) and the critical current densities (*right*) of GdBCO and GdBSCO films deposited on (100) MgO by KrF-laser radiation [*Stangl* et al. 1996b]

(typically a few Å along the *c*-axis and 20 Å within *ab*-planes). Among the various materials under consideration, $Y_{1-x}Pr_xBa_2Cu_3O_7$ is particularly suitable. First, the orthorhombic structure is maintained with only small changes in lattice constants ($< 1.5\%$ for all axes), and second, this system is a superconductor for $x < 0.6$ and a semiconductor otherwise.

- Superconducting heterostructures of $(BaCuO_{2+\delta})_2/(CaCuO_2)_2$. Note that $BaCuO_{2+\delta}$ and $CaCuO_2$ films alone are *not* superconducting. The occurrence of superconductivity is related to the charge transfer between layers containing different alkaline earth ions [*Tebano* et al. 2006].
- HTS/ferromagnetic bilayers consisting of $YBa_2Cu_3O_{7-\delta}/La_{2/3}Ca_{1/3}MnO_3$ or $SrRuO_3$ [*Habermeier* et al. 2004] and multilayers of $YBa_2Cu_3O_7/SrTiO_3/La_xSr_{1-x}MnO_3$. Such structures permit the injection of spin-polarized electrons into HTS films. This can produce a local reduction in the superconductivity-order parameter. This phenomenon can be used to fabricate unique high-voltage- and high-current-gain superconducting transistors [*Horwitz* et al. 1998].
- Ferroelectric/HTS structures are discussed in Sect. 22.5.5.

22.4.4 Metastable Compounds, Mixed Systems

PLD permits one to synthesize compounds that can be prepared either not in single-phase or not at all by solid-state reactions or by standard evaporation techniques. This unique possibility is related to the lower substrate temperatures that can be employed in PLD, to the type and energy of species involved in this process, and to the short turn-around times. Synthesis can be achieved by ablation of either multiple targets or a single target consisting of non-reacted or multiphase *mixtures* of the individual components. Among the systems investigated are the following:

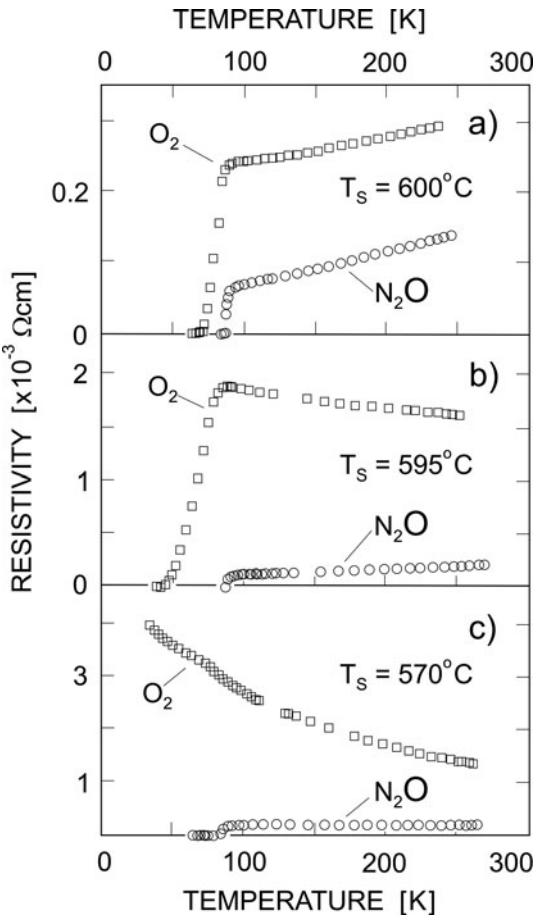

Fig. 22.4.3 a–c Temperature dependence of the resistivity of $YBa_2Cu_3O_7$ films deposited by means of KrF-laser radiation onto (100) MgO substrates ($\phi \approx 4\,\mathrm{J/cm^2}$, $\tau_\ell \approx 34\,\mathrm{ns}$, 10 Hz). The gas pressures were equal in all cases, $p(N_2O) = p(O_2) = 0.4$ mbar [*Schwab* and *Bäuerle* 1991]

$YBa_{2-x}Sr_xCu_3O_{7-\delta}$

This example demonstrates that PLD enables the extension of the solid-solution range for substitutions in HTS compounds. Standard ceramic techniques permit one to stabilize the pure 123-phase only for Sr contents $x < 1.2$. With PLD this range was extended up to $x = 1.8$ [*Schwab* et al. 1993]. The chemical composition of films was equal to that of the targets, as proved by electron microprobe (EDX) analysis.

$REBa_2Cu_3O_{7-\delta}$, $REBaSrCu_3O_{7-\delta}$

For small rare earth ions (RE = Lu, Tm, Er) single-phase $REBa_2Cu_3O_{7-\delta}$ and $REBaSrCu_3O_{7-\delta}$ have not been successfully fabricated by standard techniques.

High quality single-phase $LuBa_2Cu_3O_7$ films have been synthesized by PLD using (100) MgO, $SrTiO_3$, and $LaAlO_3$ substrates, an O_2 atmosphere, and stoichiometric multiphase ceramic targets [*Gnanasekar* et al. 1996; *Schwab* et al. 1992b]. The films were *c*-axis oriented with $T_{c0} \approx 90\,\mathrm{K}$, a transition width $\Delta T_c < 1\,\mathrm{K}$, and a critical current density $j_c(83\,\mathrm{K}) \approx 10^6\,\mathrm{A/cm^2}$.

$TmBaSrCu_3O_7$ films with $T_{c0} \approx 72\,\mathrm{K}$ and $j_c(57\,\mathrm{K}) \approx 10^6\,\mathrm{A/cm^2}$ have been fabricated in an O_2 atmosphere [*Stangl* et al. 1995]. $LuBaSrCu_3O_7$ can only be synthesized at $T_s \approx 600°\mathrm{C}$ in N_2O ($T_{c0} \approx 54\,\mathrm{K}$).

22.4.5 Films with Step-Like Morphology

The physical properties of many materials are strongly anisotropic and cannot be fully determined from epitaxial films. Such materials are often not available as single crystals as well. This situation applies, for example, to many HTS materials. In such cases, it has been found useful to fabricate films on off-axis-oriented substrates (Fig. 22.4.4). Such films show a step-like morphology. This has been demonstrated for YBCO [*Pedarnig* et al. 2002; *Markowitsch* et al. 1997], Bi-2212 [*Rössler* et al. 2000], and Hg-1212 [*Yun* et al. 2000] films deposited on vicinal (100) $SrTiO_3$ and MgO substrates. The *c*-axis of such films is tilted by $0 \leq \theta_f \leq 2°$ with respect to the (001) direction of the substrate, which itself forms an angle θ_s with the surface normal $\hat{n}$. The height of steps is, typically, 6–20 nm, and their width 20–100 nm, depending on θ_s. Because of the step-like structure, the anisotropic material properties can be determined from measurements performed in different

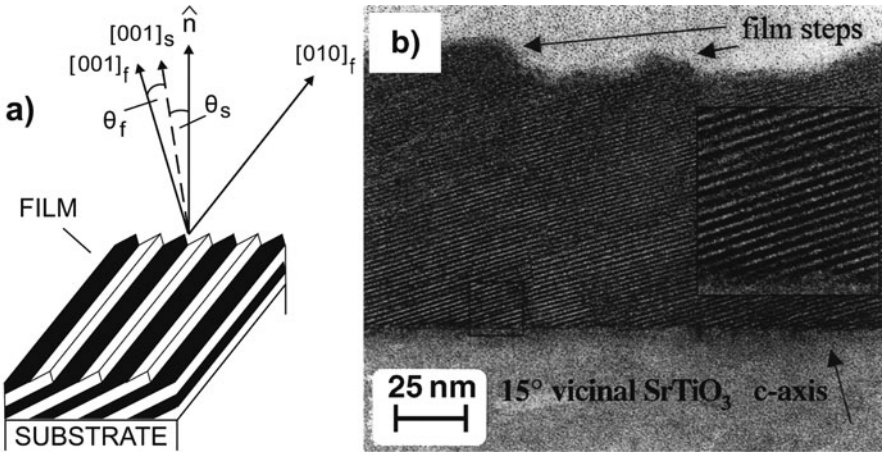

Fig. 22.4.4 (**a**) Schematic picture which shows an off-*c*-axis oriented (001) $SrTiO_3$ or MgO substrate (surface normal $\hat{n}$) and a step-like grown film. The angle between $\hat{n}$ and the (001) direction of the substrate is θ_s. The angle between $(001)_s$ and the *c*-axis of the film is $0 \leq \theta_f \leq 2°$. (**b**) TEM picture of a Bi-2212 film on a $SrTiO_3$ substrate with $\theta_s = 15°$

film directions. For example, the resistance along the projection of the c-axis onto the film surface is given by

$$R_{\mathrm{o}} \approx \frac{l_{\mathrm{b}}}{A}\left(\rho_{\mathrm{ab}}\cos^2\theta_{\mathrm{s}} + \rho_{\mathrm{c}}\sin^2\theta_{\mathrm{s}}\right) \tag{22.4.1}$$

In the perpendicular direction we have

$$R_{\mathrm{p}} = \frac{l_{\mathrm{b}}}{A}\rho_{\mathrm{ab}} \tag{22.4.2}$$

where l_{b} is the length and A the cross section of the bridge-type sample geometry employed in the measurements. For oxygen-depleted $YBa_2Cu_3O_x$ ($x \approx 6.6$) and 300 K we find for a tilt angle $\theta_{\mathrm{s}} = 10°$ a ratio $\varrho_{\mathrm{c}}/\varrho_{ab} = 110$. This value is in excellent agreement with that obtained for *single* crystals. Figure 22.4.5 shows ϱ_{c} and ϱ_{ab} for Bi-2212 films for various tilt angles and film thicknesses. With $\theta_{\mathrm{s}} > 15°$, the quality of films starts to deteriorate due to mixed growth in the c and ab directions. This is reflected in the drop-off in ϱ_{c}. With $\theta_{\mathrm{s}} \leq 15°$ the values of ϱ_{c} and ϱ_{ab} are *independent* of h_1. Initial results obtained with Hg-1212 films grown on vicinal (001) $SrTiO_3$ substrates with $\theta_{\mathrm{s}} = 10°$ yield an electrical resistivity ratio $\varrho_{\mathrm{c}}/\varrho_{ab}(300\,\mathrm{K}) \approx 405$ [*Yun* et al. 2000]. As well as these fundamental aspects, there are also practical applications. HTS films with step-like morphology show a large transverse *Seebeck effect*, which can be employed for the fabrication of broad-band radiation detectors [*Zahner* et al. 1997].

22.4.6 Buffer Layers, Applications

While $SrTiO_3$ is an almost ideal substrate for the growth of high-quality $YBa_2Cu_3O_7$ films, it is not very practical. Single-crystalline $SrTiO_3$ is, by far, too expensive and its RF and/or mechanical properties are inadequate for most applications presently under consideration. With MgO, cubic YSZ, and $LaAlO_3$ substrates, the transition temperatures and critical current densities achieved are somewhat lower. However, these substrates, in particular, MgO and YSZ, are much cheaper and have significantly lower RF losses. However, for the main application of HTS films which include microelectronics, sensor and microwave technology, and electric energy transport, all of these substrates are inadequate.

In microelectronics and sensor technology, the important substrate materials are Si, SiO_2, Si_3N_4, etc. For energy transport using so-called coated conductors, metallic substrates, mainly ribbons of different types of steel or Ni-alloys, are employed. All of these materials, however, do *not* fulfil the requirements necessary for high-quality film growth. Besides of the mismatches in lattice constants and thermal-expansion coefficients, some of these materials even react with YBCO at elevated temperatures. These problems can be overcome, in part, by employing a buffer layer (Sect. 5.2.4). Here, YSZ and bilayers consisting of CeO_2 and some other

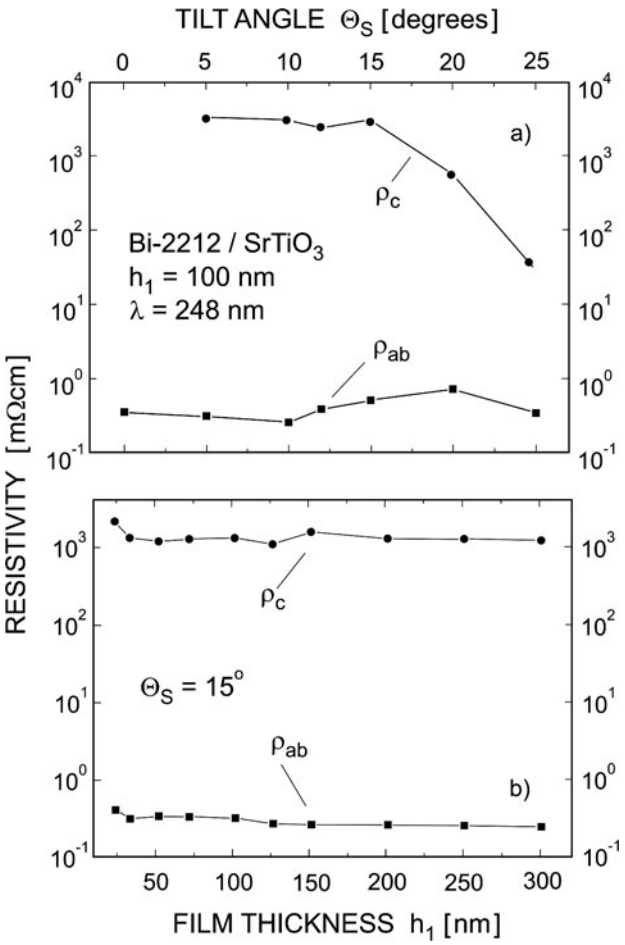

Fig. 22.4.5 a, **b** Electrical resistivities ϱ_{ab} and ϱ_c of Bi-2212 films deposited by PLD on vicinal (001) $SrTiO_3$ substrates ($\lambda = 248$ nm, $\phi \approx 3.5$ J/cm^2, $\tau_\ell \approx 25$ ns, $p(O_2) \approx 2.5$ mbar). (**a**) Dependence on tilt angle, θ_s. $N_\ell = 800$. (**b**) Dependence on film thickness. $N_\ell = 170$ to 2,500 [*Rössler* et al. 2000]

oxide are the best choices. Oriented uniform buffer layers of YSZ (200–1500 Å thick) have been fabricated by PLD on large Si wafers (10 cm diameter) [*Pryds* et al. 2007]. For YBCO films transition temperatures up to $T_{c0} \approx 90$ K and critical current densities up to 10^6 A/cm^2 have been achieved. YSZ has also been used for growing YBCO films on silicon on sapphire (SOS) substrates and on steel ribbons [*Usoskin* et al. 2009]. Coated conductors using $GdBa_2Cu_3O_{7-\delta}$ have been fabricated up to a kilometer in length on Ni-alloy ribbons. Here, buffer layers consisting of CeO_2 and MgO deposited by PLD and IBAD, respectively, have been employed. The critical current at 77 K was $I_c \gtrsim 300$ A ($J_c \gtrsim 3 \times 10^6$ A/cm^2) [*Hanyu* et al. 2010].

22.5 Metals, Semiconductors, and Insulators

Thin films of compound materials are synthesized by using either a reactive atmosphere, or multiple targets for the individual elements, or mixed or single stoichiometric targets. In the latter case, additional sources must frequently be employed to obtain stoichiometric films (Sect. 22.2.5).

22.5.1 Metals

Non-reactive PLD from metal targets results in the formation of metallic films. Detailed investigations have been performed for a large number of single element and alloy films, including metastable phases, giant magnetoresistance materials [*Krebs* 2007; *Krebs* et al. 2003; *Svendsen* et al. 1996] and superlattices of various different material combinations [*Fähler* et al. 1999]. Investigations on the growth of *ultrathin* films of Fe on (111) and (100) Cu, and on vicinal Cu surfaces, have revealed that the phase of nucleation, the thickness range of metastable fcc Fe, and the magnetic properties of PLD films may significantly differ from those fabricated by standard thermal evaporation [*Klaua* et al. 1999].

Reactive PLD from metal targets in oxygen or oxygen containing atmospheres yields semiconducting or insulating metal oxides (see, e.g., *Xu* and *Shen* 2009). In a similar way, metal nitrides, halides and other metal compounds have been synthesized [*O'Mahony* and *Lunney* 2007; *Mah* et al. 2002; *Willmott* et al. 2000]. In some cases, the film quality can be improved by using an additional plasma source (Sect. 22.2).

22.5.2 Semiconductors

The fabrication of thin films of element and compound semiconductors by means of CVD, PCVD, MBE, etc. is studied since decades. Here, PLD cannot compete with these standard techniques, apart from a few exceptions. Among those are the synthesis of metastable materials, special types of heterostructures, and developments of other, new materials. Subsequently, we briefly summarize the various different activities in this field. Further details on earlier investigations can be found in the previous editions of this book.

Pure and hydrogenated Si films have been fabricated by ablation of Si targets in vacuum and H_2 atmosphere, respectively [*Hanabusa* et al. 1983]. Ge films have been deposited by using molten Ge targets and pulsed CO_2-laser radiation [*Cheung* and *Sankur* 1992].

Among the compound semiconductors deposited as thin films are AlN, GaN, InN, ZnO, and different types of alloys consisting of $Me_xMe_{1-x}X$ with X ≡ O, N. Here, solid compound targets or solid or liquid metallic targets together with a reactive atmosphere have been employed (see above). Wide band gap materials,

in particular GaN and ZnO, have many real and potential applications in optoelectronics within the blue and UV spectral regions. Besides of its direct band gap, ZnO and its alloys exhibit a large exciton binding energy of 60 meV, in comparison to 25 meV of GaN.

Epitaxial films of GaN have been fabricated by ablation of liquid or solid Ga targets in N_2 or NH_3 atmosphere [*O'Mahony* and *Lunney* 2007; *Kobayashi* et al. 2007; *Zhou* et al. 2003; *Schröder* and *Rupp* 2002].

High-quality films of ZnO [*Rogers* et al. 2007; *Johne* et al. 2007; *Pedarnig* et al. 2005b] have been fabricated by PLD using ceramic targets. Figure 22.5.1 shows a micrograph of a high resolution TEM cross section of an epitaxial ZnO film on a 25° vicinal (100) $SrTiO_3$ substrate. Films of $Mg_xZn_{1-x}O$ with hexagonal structure (x = 0.15, 0.28) and cubic structure (x = 0.85) and optical band gaps of $E_g \approx 3.52$, 4, and 6.42 eV [*Hullavarad* et al. 2008] have been synthesized mainly by KrF-laser ablation of ceramic targets. The high solubility of MgO in ZnO achieved in such films is a consequence of the strong non-equilibrium conditions in PLD.

With GaAs, even congruent ablation results in As-deficient films. This originates from the lower sticking coefficient of As with respect to Ga. Similar observations have been made with $Hg_{1-x}Cd_xTe$. Here, the loss of Hg was compensated by an additional Hg source or an Hg background pressure. The dependence of film properties on laser fluence and dwell time has been investigated for different materials. Further details are outlined in the previous edition.

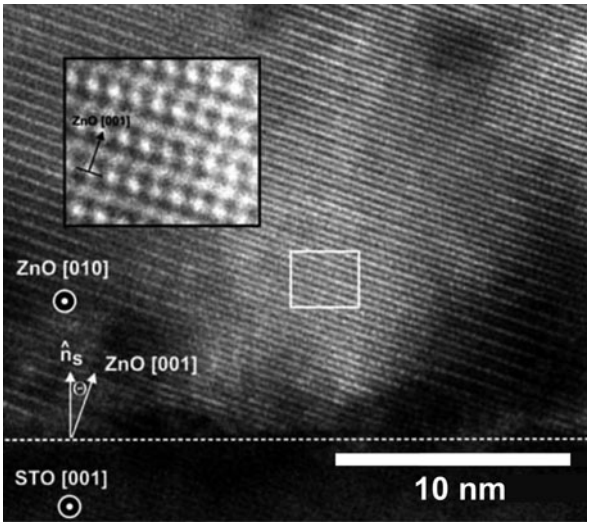

Fig. 22.5.1 High resolution TEM cross-section of epitaxial ZnO grown on 25° vicinal (100) $SrTiO_3$ by KrF-laser ablation of a ceramic target. The ZnO [001] direction is inclined by an angle $\theta \approx 20°$ with respect to the substrate normal (*inset*). The *bright white lines* are oriented parallel to the *a,b* plane of the ZnO unit cell. The interface between film and substrate is indicated by the *dashed line* [*Peruzzi* et al. 2004]

Heterostructures, Bandgap Engineering

Heterostructures are of increasing interest for both fundamental investigations and materials device engineering. They permit one to study carrier transport across layered planes, quantum-size effects, etc. Among the systems fabricated by PLD are:

- $InGaZn_6O_{9-\delta}$/SiC [*Sahu* et al. 2009].
- CdTe/$Cd_{1-x}Hg_xTe$, CdTe/$Cd_{1-x}Mn_xTe$, ZnS/ZnSe, and ZnO/$Me_{1-x}Zn_xO$ with Me ≡ Al, Li, Mg [*Vlad* et al. 2009; *Heitsch* et al. 2007; *Pedarnig* et al. 2005].

The material composition, and thereby the bandgap, can be *modulated* in an almost arbitrary way. This can be achieved by employing different targets and variable laser-pulse-repetition rates, by using two or several lasers for ablation, or by combining laser ablation with MBE (Sect. 20.3). By such techniques, tailored band-gap profiles can be fabricated. This is known as band-gap engineering. Here, the instantaneousness of the laser ablation process enables one to precisely change the stoichiometry over monolayer distances.

Superlattices grown by PLD show excellent interfacial abruptness, uniformity, and electrical characteristics. By band-gap engineering, multiple quantum wells with triangular, trapezoidal, and sawtooth-shaped composition profiles have been grown.

Heterostructures are important components in a number of applications. Apart from laser diodes, there are novel applications, e.g., in staircase solid-state photomultipliers, optical modulators, and second-harmonic generators for long-wavelength radiation.

Heterostructures of dielectric/semiconducting $SrTiO_3$/$SrTiO_{3-\delta}$ are discussed in Sect. 22.5.5.

22.5.3 Carbon Films

Amorphous carbon, hydrogenated amorphous carbon (a-C:H), and diamond-like carbon (DLC) films have been grown by both LCVD (Sect. 19.5.5) and PLD. The synthesis of carbon nanotubes and nanohorns by laser ablation is discussed in Chap. 4.

In a-C:H, the C atoms are mainly sp^2-bonded. The microstructure of DLC is mainly amorphous as well, but contains both sp^3 (diamond) and sp^2 (graphite) bonds. Furthermore, in contrast to a-C:H, diamond-like carbon contains no or only a small amount of H, depending on the technique employed in film synthesis. DLC is of increasing interest for many technical and medical applications. Its hardness and chemical inertness are attractive for coatings of specific tools, including medical instruments and prosthesis [*Nelea* et al. 2007]. Its high thermal conductivity and its insulating properties are interesting in semiconductor device technology. Subsequently, we concentrate on DLC films fabricated by PLD using graphite targets.

In DLC films fabricated by PLD, the relative concentration of sp^3 and sp^2 bonds depends on the type and energy of impinging species during film growth,

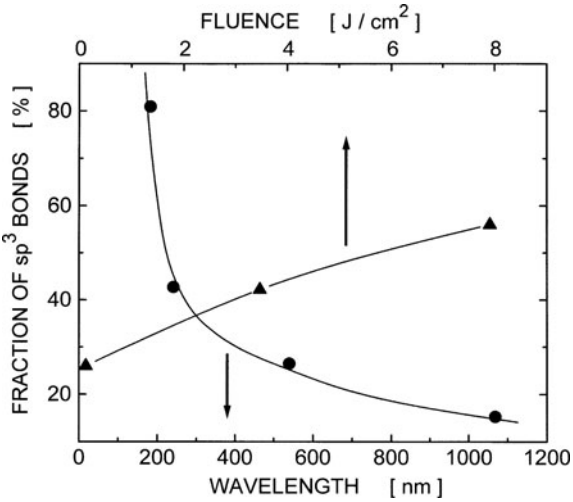

Fig. 22.5.2 Fraction of sp^3 (*diamond*) bonds in DLC as a function of KrF-laser fluence (*upper scale*; $\tau_\ell = 23\,\text{ns}$, $\nu_\text{r} = 30\,\text{Hz}$) and for different laser wavelengths [adapted from *Yamamoto* et al. 1997, 1998]

and thereby on the laser parameters. Figure 22.5.2 reveals that the number of sp^3 bonds increases with decreasing wavelength and increasing laser fluence. This suggests that the formation of sp^3 bonds is favored by a plasma that contains mainly C atoms and C^+ ions of high kinetic energy. In other words, the fraction of sp^3 bonds can be controlled by the laser wavelength and/or its fluence/intensity. With excimer lasers, high quality DLC films can be produced with fluences of only 1–3 J/cm^2 ($\sim 10^8$ W/cm^2). With 532 nm Nd:YAG laser radiation and similar pulse lengths, the fluences required are about 10–100 times higher. With 1064 Nd:YAG laser radiation and fluences of up to 10^4 J/cm^2 [$(1 - 10) \times 10^{11}$ W/cm^2], nanoparticle films with a hardness of up to 77 GPa have been fabricated [*Davonloo* et al. 1992]. With ultrashort-pulse lasers, mainly Ti:sapphire lasers, no films with a quality similar to that obtained with ns-lasers have been synthesized (Sect. 22.2.3).

In most of the experiments performed in vacuum, the substrate is kept at room temperature. Substrate temperatures $T_\text{S} \gtrsim 150°\text{C}$ favor cluster formation and graphitization of films. Average growth rates of DLC films achieved with ArF-laser radiation and a fluence of $\phi \approx 10\,\text{J/cm}^2$ are around 0.45 Å/pulse. High-quality films (fraction of sp^3 bonds $\gtrsim 90$ %) have a hardness of 60–70 GPa, a (Tauc) band gap up to 2 eV and a refractive index of n (633 nm) $= 2.2 \pm 0.2$. Such films are essentially chemically inert below 800°C and cannot be dissolved in solutions of $HF + HNO_3$. For comparison, real diamond has a hardness of 80–105 GPa, a (direct) band gap of $E_\text{g} \approx 6\,\text{eV}$ (the indirect band gap is $\approx 5.5\,\text{eV}$), and a refractive index of $n = 2.42$ (see Tables).

An inert gas atmosphere favors cluster formation and thereby deteriorates the quality of DLC films [*Ossi* et al. 2005]. This is expected from the preceding

discussion. The situation is different with O_2 and H_2 atmospheres. It is well known that O_2 and atomic H preferentially etch graphite, i.e. sp^2 carbon. This promotes an increase in sp^3 bonds. Such films show an optical band-gap up to energies of about $E_g \lesssim 2.5\,\text{eV}$ [*Yoshitake* et al. 2004; *Nakajima* et al. 2002].

Further details on the growth of DLC films, their mechanical, optical, and electrical properties, including those of doped films, can be found in overviews by *Narayan* (2007), and *Szörényi* (2006) and in recent publications by *Sikora* et al. (2009), *Hanyecz* et al. (2010), and others.

22.5.4 Insulators

This section summarized experimental investigations on mainly electrically insulating materials. Among those are dielectric and ferroelectric materials, and magnetic oxides. Various different types of heterostructures consisting of wide-band gap oxides, show completely new physical phenomena.

Among the dielectric materials deposited as thin films are oxides like SiO_2, ZrO_2, Al_2O_3, piezoelectric $GaPO_4$ [*Pedarnig* et al. 2006], etc., and fluorides such as MgF_2, CaF_2, SrF_2, etc. For further details and references see the previous editions of this book. The loss of oxygen observed with many oxides can be compensated by reactive ablation in O_2 at pressures between 10^{-4} and 1 mbar. The deposition rates achieved with these materials are, typically, between 0.5 and 50 Å/s. Hybrid techniques using, for example, PLD in combination with an RF source or an ion beam have been employed as well [*Bae* and *Cho* 1999; Sect. 22.2].

Ferroelectric Materials

Ferroelectric films fabricated by PLD include oxidic perovskites such as $BaTiO_3$, $KTa_{1-x}Nb_xO_3$ (KTN), $PbTi_{1-x}Zr_xO_3$ (PZT), $Pb_{1-y}La_yTi_{1-x}Zr_xO_3$ (PLZT), and $Sr_xBa_{1-x}TiO_3$ (SBT), incipient ferroelectrics [*Migoni* et al. 1976] such as $SrTiO_3$ and $KTaO_3$, and perovskite-like materials such as $Bi_4Ti_3O_{12}$ (BTO), $LiNbO_3$, $Pb(Mg_{1/3}Nb_{2/3})O_3$ (PMN), $SrBi_2Ta_2O_9$ (SBiT), etc.

Epitaxial and oriented *polycrystalline* films of these materials have been grown on different types of substrates, such as $SrTiO_3$, $LaAlO_3$, MgO, fused quartz (a-SiO_2), Si, etc. With Si substrates, buffer layers, mainly of YSZ and a-SiO_2 are employed. The structural, morphological, and ferroelectric properties of films depend strongly on the laser parameters, the type of substrate material, and the substrate temperature. For example, with crystalline films of $PbTi_{1-x}Zr_xO_3$ ($0.48 \leq x \leq 0.55$) deposited by means of 248 nm KrF-laser radiation on bare and Pt- or Au-coated Si substrates at temperatures $T_s \approx 600°C$, one finds a dielectric constant $\varepsilon' \approx 850$, a remanent polarization $P_r \approx 22\,\mu C/cm^2$, a coercive field $E_c \approx 40\,kV/cm$, and a resistivity $\varrho \approx 10^{13}\,\Omega\,cm$ [*Roy* et al. 1992]. With the *same* material and substrate, but with Nd:YAG laser radiation and $T_s \approx 375°C$, the values are $\varepsilon' \approx 500$, $P_r \approx 15\,\mu C/cm^2$, $E_c \approx 100\,kV/cm$ [*Verardi* et al. 1997b].

Among the materials investigated most recently are PZT [*Goh* et al. 2005], $(Bi_{4-x}Ln_x)Ti_3O_{12}$ with Ln ≡ La, Nd, Sm [*Adachi* et al. 2005], nitrogen-doped $SrTiO_3$ [*Marozau* et al. 2007], $LiNbO_3$ [*Chaos* et al. 2000a], and $GaFeO_3$ [*Sun* et al. 2008]. Of particular interest is the ferroic material $BiFeO_3$ [*Zelezny* et al. 2010].

An enhancement of ferroelectricity revealed in both a higher transition temperature and a higher remanent polarization is observed in *strained* films. Among the materials investigated are $BaTiO_3$ [*Choi* et al. 2004], $SrTiO_3$ [*Haeni* et al. 2004], PZT [*Vrejoiu* et al. 2006], $BiFeO_3$ [*Zeches* et al. 2009]. Overviews on PLD of ferroelectric and (only) piezoelectric[1] thin films are given by *Chen* and *Horwitz* (2007) and *Craciun* and *Dinescu* (2007).

Magnetic Films

The physical properties of manganese perovskites of the type $RE_{1-x}Me_xMnO_3$ with RE ≡ La, Pr, Nd and Me ≡ Ca, Sr, Ba are closely related to the coupling between structural, electrical, and magnetic degrees of freedom. This coupling of physical properties leads to new fascinating effects. For example, these materials show a giant (colossal) negative magnetoresistance (GMR, CMR) near the ferromagnetic ordering temperature, T_c. With the onset of magnetic ordering, a sharp drop in the electrical resistivity occurs for $T < T_c$. The electron and oxygen vacancy transport properties are potentially useful for applications in solid oxide fuel cells (SOFC). The effect of interfacial stress on transport properties was studied for films of $La_{1/2}Sr_{1/2}MnO_3$ and $La_{2/3}Ca_{1/3}MnO_3$. Thin epitaxial films of these materials have been deposited mainly on (100) $SrTiO_3$, (100) $NdGaO_3$, (100) $SrRuO_3$, and (100) $LaAlO_3$ substrates by excimer-laser ablation of stoichiometric ceramic targets [*Lussier* et al. 2008].

Electrochemical Materials

Oxidic perovskites, spinels, etc. are also studied for applications as electrode materials in batteries and fuel cells (SOFC). Besides of the materials already mentioned in the previous paragraph, $La_{1-x}Ca_xCoO_{3-\delta}$ [*Lippert* et al. 2007], $LiCo_{1-x}Al_xO_2$ [*Perkins* et al. 1999], $LiMn_2O_4$ [*Singh* et al. 2002] have been studied in most detail. An overview is given by *Montenegro* and *Lippert* (2007).

Biocompatible Materials

Besides of DLC and carbon-based materials (Sect. 22.5.3), calcium phosphates belong to the most important materials for the coating of prosthesis etc. In particular, the chemical composition of hydroxylapatite, $Ca_{10}(PO_4)_6(OH)_2$, is quite similar to

[1] Note that all ferroelectric materials are also piezoelectric, but not vice versa.

that of the mineral parts of bones and teeth. An overview on biocompatible materials is given by *Nelea* et al. (2007).

22.5.5 Heterostructures

The fabrication of multilayer structures has been demonstrated for many material combinations:

- Dielectric/dielectric structures consisting of (insulating) perovskites such as $LaAlO_3/SrTiO_3$. Here, new phenomena have been observed. The interface is electrically conducting. It shows a magnetic state [*Brinkman* et al. 2007] and a 2D superconducting condensate. By tuning the carrier density via an electrostatic field, switching between the 2D superconducting state and an insulating state has been demonstrated [*Caviglia* et al. 2008].
- Ferroelectric/dielectric structures such as $PZT/SrTiO_3/Si$ [*Ma* et al. 2005], $SrBi_2Ta_2O_9/Bi_2O_3$ [*Dinu* et al. 1999].
- Superlattices consisting of $BaTiO_3/SrTiO_3/CaTiO_3$ on $SrRuO_3$ show an enhanced polarization with respect to pure $BaTiO_3$ [*Lee* et al. 2005].
- Ferroelectric/giant magneto-resistive (GMR) structures like $PZT/La_xCa_{1-x}MnO_3$ [*Grishin* et al. 1999].
- Ferroelectric/ferromagnetic structures of $PZT/CoFe_2O_4$ [*Zhou* et al. 2007].
- Ferromagnetic/antiferromagnetic superlattices of $La_{0.6}Sr_{0.4}MnO_3/La_{0.6}Sr_{0.4}FeO_3$ [*Kawasaki* et al. 1999].
- Dielectric/semiconducting structures consisting of alternating layers of (fully oxidized) $SrTiO_3$ and oxygen deficient $SrTiO_{3-\delta}$ have been grown by varying the oxygen pressure during deposition. Sharp doping profiles over subnanometer distances have been achieved [*Muller* et al. 2004]. These observations open up completely new possibilities in semiconductor device fabrication.
- Ferroelectric/high-temperature superconductor structures, such as, e.g., BTO/$YBa_2Cu_3O_7$ (YBCO) [*Maffei* and *Krupanidhi* 1992], PZT/YBCO [*Z.G. Liu* et al. 1999], YBCO/PZT/YBCO [*Verardi* et al. 1997b; *Ramesh* et al. 1992].

Heterostructures of these various different types are of great interest for both fundamental investigations and several different applications. Among the latter are microwave signal processing devices, magneto-sensitive memory cells, high-density dynamic random access memories (DRAMs), non-volatile ferroelectric RAMs, different types of sensors, the wide field of oxide electronics, etc.

22.6 Nanostructured Materials

Up to now, we have considered PLD of thin uniform films that are synthesized primarily from a flux of atoms/ions and small molecules impinging onto the surface of a substrate, including an already deposited layer. During the *initial* phase of growth,

and for certain systems, laser parameters, and deposition temperatures, islands or non-uniform films of nanocrystals may be formed on the *substrate* by nucleation, growth, and coalescence of clusters. This phenomenon is well known from standard thin film growth techniques. It is widely discussed in the literature as the so-called Vollmar-Weber nucleation mechanism (Sect. 4.3).

The situation changes significantly when higher ambient gas pressures, typically several mbar to several hundred mbar, are employed. Such conditions favor the formation of clusters and nanocrystals within the *gas-phase* (Chap. 4). The latter have diameters of about 1–20 nm and contain 10^2–10^6 atoms. By condensing the clusters/nanocrystals onto a substrate, so-called nanoparticle films can be fabricated. If, on the other hand, materials are ablated from mixed or, alternately, from different types of targets, atoms, molecules or nanoclusters can be embedded in a matrix either stochastically or periodically. This permits material doping or the synthesis of different types of nanocomposites. The (average) size of nanoparticles can be controlled via the laser parameters, background pressure, substrate temperature, etc. Thin sponge-like films of nanowires, nanotubes, and nanohorns are discussed in Chap. 4.

22.6.1 Nanoparticle films

Nanoparticle (NP) films may consist of crystalline or/and amorphous particles. Such films have physical properties that are quite different from those of uniform films. They may show quantum confinement effects, or may consist of entirely new compounds formed, e.g., in a reactive atmosphere. Such films are promising materials for applications in photonics, optoelectronics requiring room-temperature photoluminescence (PL), gas-sensor technology, etc. Among the materials investigated are films of nanocrystalline Si and silicon-rich silicon oxide (SRSO) [*Meunier* et al. 2008; *Marine* et al. 1998] , ZnO [*Late* et al. 2009, *Kawasaki* et al. 1998], WO_3, $W_{18}O_{49}$ [*Lethy* et al. 2008], etc. In the latter investigations, the increase in particle sizes/roughness of W_xO_y films with increasing O_2 pressure has been studied. Shape tailoring of NP films by excitation of surface plasmon resonances (SPR) is discussed in Sect. 4.3.4.

22.6.2 Nanocomposites

Nanostructured materials consisting of nanoparticles embedded in a matrix are often denoted as nanocomposites. They can be fabricated by employing a composite target, or by sequential or simultaneous ablation of different targets. Depending on the specific experimental conditions, atoms/molecules or clusters can be embedded in a matrix either stochastically or in a well-defined periodic arrangement. In the latter case, a layer of “host” material is deposited and, subsequently, the nanocrystals are implanted into the surface of the matrix layer and/or they are formed on its

surface (Vollmer-Weber nucleation). The crystallite sizes can be controlled via the laser fluence, the number of laser pulses on each target, the gas-pressure within the chamber and/or the substrate temperature.

Among the composites investigated in detail are Bi nanocrystals embedded in a-Ge [*Serna* et al. 1998], Ag, Au, Bi, and Cu in a-Al_2O_3 [*Haro-Poniatowski* et al. 2008; *Gonzalo* et al. 2005, *Suarez-Garcia* et al. 2003, *Barnes* et al. 2002, *Afonso* et al. 1999], Pt in TiO_2 [*Beck* et al. 1999], Si in a-SiO_2 [*Makimura* et al. 1998], Ge in a-Lu_2O_3 [*Yuan* et al. 2006], CdTe in a-SiO_2 [*Ohtsuka* et al. 1993], etc. Films of $YBa_2Cu_3O_{7-\delta}$ containing nanocrystalline regions of the Me-2411 phase (Me $\equiv$ Ag, Nb, Ru, Zr) have been deposited from mixed targets [*Siraj* et al. 2008]. Here, the embedded nanocrystals serve as artificial pinning centers that increase the critical current density by a factor of 3 to 4 with respect to undoped films. Similar effects have been found in YBCO films doped with $BaZrO_3$ [*Maiorov* et al. 2009]. A number of experiments have also been performed for metal clusters that have been embedded in polymers. Among the examples are clusters of Ag, Au, Pd and Cu in PC or PMMA [*Röder* et al. 2008]. Giant magnetoresistance (GMR) effects were observed in composite Co-PTFE granular films [*Kwong* et al. 2006].

Alternate deposition from different targets permits a high flexibility and good control of various different parameters. The distribution of NPs within the host can be controlled via the number of pulses on the host target. The concentration and size of NPs depends on the number of pulses on the 'dopant' target.

Depending on laser fluence, the number of laser pulses, and the type of materials employed, several competing processes have been identified. Detailed investigations have been performed for Au NPs embedded in a-Al_2O_3. For *low* laser fluences and *low* concentrations of Au atoms (small number of pulses on the Au target), small nanoclusters are formed and *implanted* into the surface of the (host) a-Al_2O_3 layer [*Gonzalo* et al. 2005]. The position of the embedded layer with respect to the a-Al_2O_3 surface increases with increasing fluence i.e. with the kinetic energy of impinging Au species. With increasing concentrations of Au atoms, large clusters of Au are formed on the *surface* of the a-Al_2O_3 layer. While the size of implanted Au clusters does neither depend on the concentration of Au nor on the laser fluence, the size of large clusters increases with both, the concentration of Au and the laser fluence. Above a certain threshold, the size of 'surface' NPs decreases with increasing fluence due to 'self-sputtering'. This phenomenon is again related to the increase in kinetic energy of impinging species (Sect. 22.2.3).

The size distributions of embedded crystallites are quite small and narrower than those achieved with other techniques as, e.g., ion implantation or sol-gel methods. Size distributions and orientations of nanoclusters are characterized mainly by TEM, HREM, Raman scattering [*Bachelier* et al. 2007], etc.

Periodic Structures

Thin films of a-Al_2O_3 doped with Er and Yb in alternating parallel layers show improved PL for layer separations up to about 3 nm. The increase in PL intensity is related to the energy transfer between Yb^{3+} and Er^{3+} ions [*Suarez-Garcia*

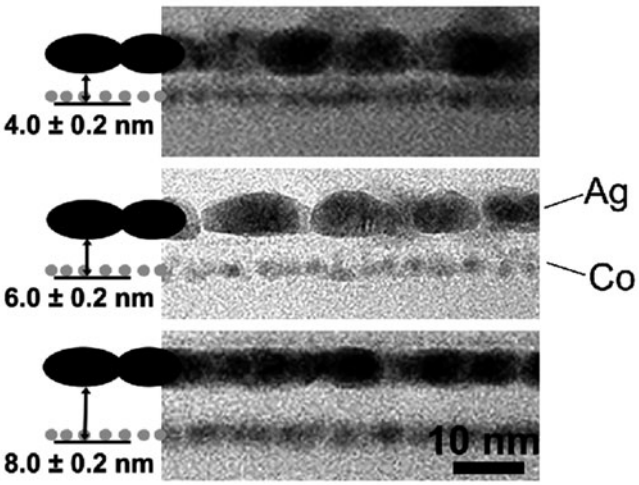

Fig. 22.6.1 TEM pictures and schematics of cross sections of a-Al_2O_3 containing Co–Ag bilayers with different spacings [*Margueritat* et al. 2008]

et al. 2004]. Similar investigations have been performed for codoped Er/Tm films [*Xiao* et al. 2007].

Nanoparticles of Co and Ag arranged in parallel layers within an a-Al_2O_3 matrix have been fabricated by alternate ArF-laser ablation of Al_2O_3, Co, and Ag targets. The spacing between layers has been controlled through the number of laser pulses on the Al_2O_3 target (Fig. 22.6.1). When the separation of Co and Ag particles becomes smaller than a critical distance, the excitation of surface plasmon resonances (SPR) of Ag NPs causes enhanced Raman scattering of (spherical) Co NPs [*Margueritat* et al. 2008].

Alternate PLD has also been employed to grow self-assembled nanocolumns of polycrystalline Ag embedded in a-Al_2O_3 [*Margueritat* et al. 2006]. The nanocolumns have diameters of about 3 nm and heights up to 7 nm. Their electronic and dynamic behavior has been studied by *Burgin* et al. (2008).

Free-standing arrays of aligned nanorods grown by nanoparticle assisted PLD are discussed in Sect. 4.3.

22.7 Organic Materials

Thin films of organic materials fabricated by PLD include various organic polymers, liquid crystals, and proteins. In contrast to standard techniques such as spin-coating, dip-coating, etc., PLD is a solvent-free technique. Thus, it circumvents difficulties that are associated with solvent incompatibilities in many types of device fabrication processes and in sophisticated medical and pharmaceutical technologies. PLD permits, for example, sequential deposition of multiple thin film coatings consisting

of different materials. Such coatings are desirable in sensor technology, the fabrication of multiple-layer polymer light-emitting diodes (PLEDs), etc. Protective coatings are also desirable on many tools employed in biotechnology and medicine, but also for drug-delivery [*Talton* et al. 2007], etc. Additionally, PLD permits to fabricate thin films of materials and composites that cannot be fabricated by any other technique. Among the examples are thin films of PTFE (Teflon). In matrix assisted pulsed-laser evaporation (MAPLE) thermally or/and photochemically sensitive molecules to be deposited are embedded in a matrix.

PLD of organic materials has been demonstrated, in particular, with nanosecond UV-, and IR-laser radiation and with ultrashort-laser-pulses.

The most detailed investigations using mainly UV-excimer laser radiation, were performed for polytetrafluoroethylene (PTFE). The good mechanical, thermal, and chemical stability of PTFE (Teflon) together with its low surface adhesion, low frictional resistance, and low dielectric constant, makes this material unique for numerous applications in mechanics, microelectronics, chemistry, medicine, and bioscience. For certain applications, thin PTFE films are desirable. With bulk PTFE targets, UV-laser irradiation results in rapid depolymerization and ejection of low-molecular-weight fragments that, to some extent, repolymerize on the substrate. The deposition rates achieved are a few Å/pulse. The deposits consist of both amorphous and crystalline components, they are quite rough, show many particulates, and are opaque to visible light. Their electrical properties are quite poor. Figure 22.7.1a shows an optical micrograph of such a film. For some applications, the good hydrophobicity of films that is, in part, also related to their surface roughness is advantageous [*Kwong* et al. 2007; *Li* et al. 1998; *Norton* et al. 1996; *Blanchet* and *Shah* 1993].

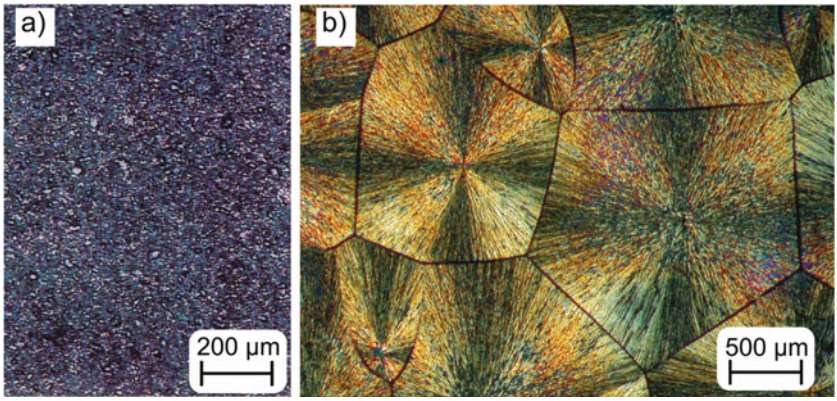

Fig. 22.7.1 a, **b** Optical polarization micrographs of PTFE-Teflon films deposited by KrF-laser radiation on 100 nm PdAu/(100) Si. (**a**) Bulk Teflon target; (**b**) pressed and sintered powder target. The parameters employed were $\phi(KrF) \approx 3\,\mathrm{J/cm^2}$, $\tau_\ell \approx 20\,\mathrm{ns}$, $T_s \approx 360°\mathrm{C}$, $p(\mathrm{Ar}) \approx 0.3\,\mathrm{mbar}$ [*Li* et al. 1998]

With pressed powder targets, deposition rates of up to 40 Å/pulse have been achieved (Fig. 22.7.1b). At substrate temperatures $T_s \approx$ 360–490°C, films are formed via melting and crystallization of laser-transferred PTFE grains. From IR spectroscopy, X-ray diffraction, and XPS measurements it has been found that such films have a chemical composition similar to that of the source material [*Hopp* et al. 2007; *Li* et al. 1998]. The films are crystalline with a smooth surface and high transparency to non-polarized visible light, and they pass the Scotch-tape test. Post-annealing improves the morphology of films, and favors spherulitic growth up to lateral dimensions of several 100 μm. The dielectric constant of films is 1−5; their dielectric strength $(1-3) \times 10^5$ V/cm. Their resistivity is up to 10^{14} Ω cm. The charge stability of these films is comparable or even superior to that of PTFE foils (Fig. 22.7.2).

Among the other organic materials deposited are doped films of poly-methyl-methacrylate (PMMA) and polystyrene (PS) [*Rebollar* et al. 2007], polyvinylidene fluoride (PVDF) [*Norton* et al. 1996], polyacrylonitrile (PAN) [*Nishio* et al. 1996], electroluminescent copper-phthalocyanine (CuPc) [*Matsumoto* et al. 1997], the polymer electrolyte polyethylene oxide (PEO) [*Manoravi* et al. 1998], liquid crystals [*Gonzalo* et al. 1999], ceramic films from human tooth, pepsin [*Hopp* et al. 2007] and proteins [*Tsuboi* et al. 1998].

Thin film deposition by vibrationally selective (resonant) IR-laser ablation has been demonstrated for several types of polymers [*Haglund* et al. 2007; *Dygert* et al. 2007]. In these experiments bulk material, liquids, and frozen solutions have been employed as target materials (see below). Ablation was performed by employing *tunable* free-electron laser (FEL) radiation. In contrast to many cases

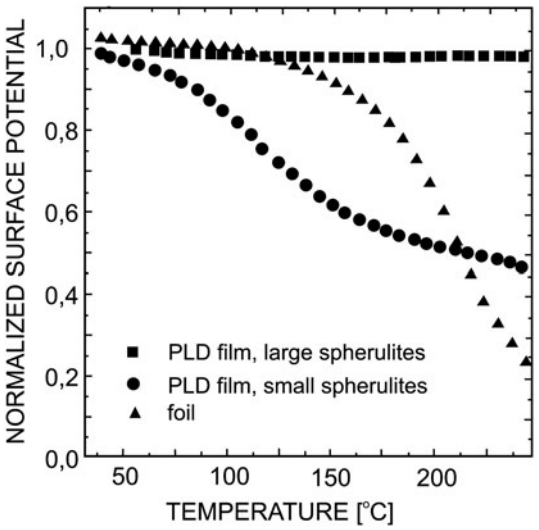

Fig. 22.7.2 Thermally stimulated surface potential decay for positively and negatively charged foils and PLD films of PTFE [*Schwödiauer* et al. 1998]

of UV-laser ablation, the technique permits to deposit films with low or even no detectable chain fragmentation (Sect. 12.6.1).

22.7.1 MAPLE

Matrix assisted pulsed-laser evaporation (MAPLE) permits to deposit sensitive molecules with minimum photothermal or photochemical damage. In this technique, the target is fabricated by dissolving the material to be deposited in a volatile solvent (matrix). The concentration of dissolved molecules is, typically, between 0.1 and several wt %. The dilute solution is then frozen and placed into a PLD chamber. The frozen solvent should readily absorb the laser light. Pulsed-laser irradiation results in a collective ablation of matrix and dissolved molecules. In MAPLE, the ejected molecules are deposited onto the substrate, while in MALDI (Sect. 30.1.3) the matrix-isolated molecules are directed into a mass spectrometer. In both cases, most of the volatile solvent molecules are pumped off from the chamber. Since the ablation threshold is determined by the thermodynamic properties of the volatile solvent rather than the dissolved material, deposition can proceed at very low laser fluences, thereby minimizing decomposition of matrix-isolated molecules.

MAPLE has been employed to deposit polymers [*Toftmann* et al. 2004] and various different types of biomolecules [*Purice* et al. 2007]. However, the fabrication of smooth homogeneous films is difficult, mainly due to incomplete evaporation of matrix molecules during the transfer process. A further problem are incubation processes which change the absorptivity of the matrix with successive laser pulses. This may result in uncontrolled material ejection [*Kokkinaki* and *Georgiou* 2008]. Typical thicknesses of deposits are within the range of 10–100 nm. An overview on experimental setups and materials is given by *Piqué* (2007).

The physical mechanisms involved in MAPLE were investigated by molecular dynamics (MD) simulations (*Sellinger* et al. 2008; *Leveugle* and *Zhigilei* 2007; see also Sect. 13.4). The results obtained for matrix-isolated polymer molecules can be summarized as follows: in contrast to PLD, MAPLE permits to deposit polymer molecules without significant photothermal bond scission. However, overheating of the target results in 'phase explosion' and the formation of a foamy transient structure of interconnected liquid regions (see Fig. 13.4.1). This structure subsequently decomposes into a mixture of matrix-polymer clusters and gaseous matrix molecules. The large clusters have much lower ejection velocities compared to the smaller ones and either reach the substrate or they condense on the target. In the former case, the clusters cause a rough film surface or even 'deflated balloon-type' features via internal boiling of matrix molecules, or elongated 'nanofibers' that result from the expansion and freezing of droplet-type products. On the other hand, the clusters that condense on the target lead to an undefined morphology of the surface which, with subsequent pulses, results in an undefined ablation behavior. For all of these reasons, the fabrication of smooth films by MAPLE is difficult or even impossible to achieve.

22.8 Laser-Induced Forward Transfer

Patterning by laser-induced forward transfer (LIFT) employs laser radiation to transfer parts of a target film initially precoated on an optically transparent support onto a substrate (Fig. 22.8.1). With certain systems, good results can also be achieved by laser irradiation of the target film via the (transparent) substrate. The same technique can be employed for the patterning of target films. Patterning is achieved by direct writing, projection, laser-beam interference, or by means of microlens arrays (Fig. 5.2.1).

Among the prerequisites for depositing material with good morphology, spatial resolution, and adherence are the following:

- The laser fluence employed should just exceed the threshold fluence for removal of the target-film from the support.
- Target films should not be too thick; with metals, typically, less than a few 100 nm. The fluence necessary for material transfer increases with increasing film thickness.
- The target film should be in close contact with the substrate.
- The absorption of the target film should be high and that of the support as low as possible.
- Transfer of target films with *low* absorptivity and/or low mechanical, thermal or photochemical stability, can be achieved by incorporating an absorbing film (transfer film) in between the support and the target film.

The mechanisms of film removal depend on the laser parameters and the type of target/support materials. Let us first consider target films with high absorptivity. Near threshold, elastic forces related to thermal expansion of the heated film are important. With some materials, e.g. with metal films of low adherence, this may result in material pop-off. With increasing fluence, the formation of a vapor or a

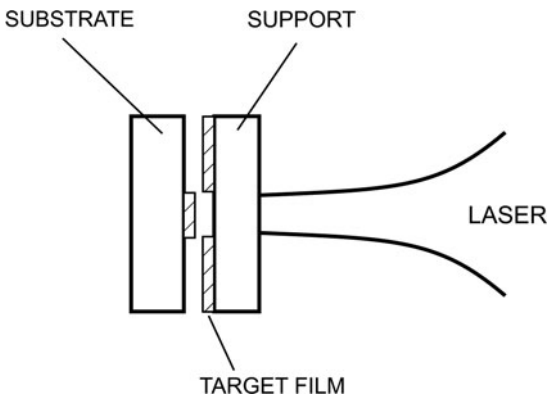

Fig. 22.8.1 Schematic demonstrating the LIFT technique. The target film which is precoated onto a transparent support is brought into close proximity to the substrate. In some cases, a transfer film in between the support and the target film is employed

plasma at the target–support interface dominates the transfer process. Laser-induced modification of the material can proceed after its transfer onto the substrate.

The LIFT technique is simple and can be employed with a wide variety of target materials. The film thickness on the substrate can be controlled by repetitive transfer of thin films. Depending on laser fluence, repetitive transfer can also be employed for the fabrication of multilayer structures or alloys. Problems may occur with the uniformity, morphology and adhesion of films, and with material implantation into the substrate surface. At low laser fluences transfer may be incomplete, while at high fluences droplet formation or substrate doping/alloying is observed. Additionally, plasma formation at the film-support interface may result in surface ablation of the support. This introduces impurities into the transferred material and, eventually, into the substrate. This can be overcome, at least in part, by employing a transfer film.

Pattern formation by LIFT has been demonstrated for various metals [*Kim* et al. 2009; *Klini* et al. 2008; *Banks* et al. 2006; *Landström* et al. 2004; *Zergioti* et al. 1998a; *Toth* et al. 1993], high-temperature superconductors [*Fogarassy* 1990], semiconductors [*Wong* et al. 1999; *Zergioti* et al. 1998a], dielectrics [*Kim* et al. 2004], and for various organic [*Banks* et al. 2008] and biological materials. Among the latter are DNA, proteins, different types of cells, fungal spores, etc. [*Dinca* et al. 2008; *C.B. Arnold* et al. 2007; *Kattamis* et al. 2007; *Hopp* et al. 2005a, b]. Film supports frequently employed are standard glass, SiO_2, Al_2O_3, $SrTiO_3$, etc. Substrate materials employed include various metals, semiconductors, ceramics, glasses, and polymers.

For the generation of *metal* patterns, practical film thicknesses are between 10 and 300 nm. The corresponding fluences employed with ns pulses (dwell times) are typically 0.01–10 J/cm^2. The smallest pattern sizes achieved with metal films and ns laser pulses are several 100 nm wide. This increase in resolution with respect to the laser foci employed, can be achieved by using a laser fluence that is just slightly above the threshold for material transfer (Sect. 5.3). The confinement of features can be further improved by means of fs pulses. Here, lateral heat conduction within the target film can be widely avoided. Nanoscale deposits, e.g. of Cr [*Banks* et al. 2006] have been generated in this way.

Material transfer from targets consisting of stacked layers of elements has also been demonstrated. By tuning the laser fluence, multilayer deposits with low interlayer mixing or, with higher fluences, metal alloy patterns can be produced.

Single-step printing of periodic patterns by means of microlens arrays has been demonstrated by *Landström* et al. (2004). Here, an unfocused or defocused laser beam is used to generate on a substrate surface and/or on the target film thousands, millions, or even billions of single micron-sized features by means of a single laser shot. The method employs a target film which is directly evaporated onto a regular two-dimensional (2D) lattice of microspheres formed by self-assembly on a transparent support (Fig. 5.2.1d). During transfer, the substrate is in close contact to the (coated) microspheres. The diameter of dots on the substrate depends on the laser fluence. Figure 22.8.2 shows an example for the case of Au dots. Clearly, the material transferred to the substrate produces ‘windows’ on the coated microspheres. Thus, the technique can be employed to produce micron- or even

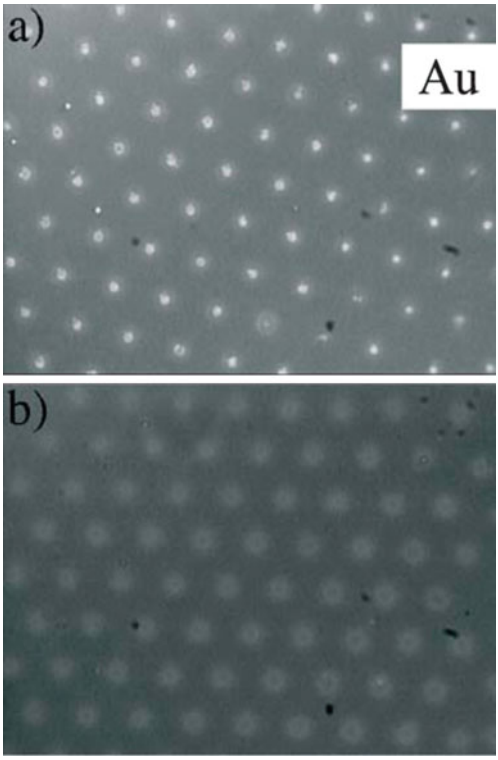

Fig. 22.8.2 Hexagonal lattices of Au dots fabricated on mica substrates by LIFT using 248 nm KrF-laser radiation ($\tau_\ell \approx 28$ ns) and 100 nm Au films on 2D lattices of 6 μm a-SiO_2 microspheres. The laser fluences employed were (**a**) 20 mJ/cm^2 and (**b**) 30 mJ/cm^2 and the corresponding dot sizes 4 and 8.5 μm, respectively [*Landström* et al. 2004]

nano-sized apertures on lens arrays. An example is shown in Fig. 22.8.3. In order to produce *circular* deposits/apertures, proper selection of the Mie parameters is essential. In other words, the intensity should have a *single* central maximum, as shown in Fig. 5.3.4a.

Microlenses have been also employed to print periodic arrays of metal dots by using a thin metal foil in between the microspheres and the substrate [*Bäuerle* et al. 2003]. Simultaneously, regular holes within the metal foil are generated.

22.8.1 Transfer films

LIFT of target films that are transparent or have low absorptivity has been achieved by using a transfer film. The transfer film should consist of a well absorbing highly volatile material (with the latter requirement contamination of the transferred film is widely avoided) [*Nagel* et al. 2008; *Fardel* et al. 2007; *Kattamis* et al. 2007].

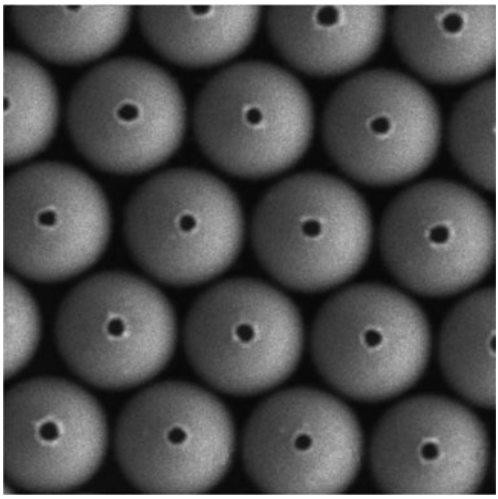

Fig. 22.8.3 Apertures fabricated by single-pulse Ti :sapphire laser radiation ($\lambda \approx 797\,\text{nm}$, $\phi \approx 35 \pm 7\,\text{mJ/cm}^2$; $\tau_\ell = 130 \pm 15\,\text{fs}$) on a monolayer of a-$SiO_2$ microspheres ($r_{sp} = 2\,\mu\text{m}$) coated with a $h \approx 40\,\text{nm}$ thick Au film. The radius of apertures $r_a \cong 0.2\,\mu\text{m}$ is well below the caustic radius $\rho_c \cong 0.66\,\mu\text{m}$. Laser-light irradiation was performed from the rear side [*Langer* et al. 2006]

Transfer films are also employed for 'gentle' LIFT of thermally or/and photochemically or/and mechanically instable materials. Among those are sensitive multiple layer structures, biological materials, etc. Transfer films most frequently employed are polymers, in particular PI and triazene [*Doraiswamy* et al. 2006]. In contrast to inorganic transfer films, a photodecomposing volatile polymer minimizes contamination during the transfer process.

For thermally and/or photochemically sensitive systems, the thickness of the transfer film should exceed the thermal/optical penetration depth in order to avoid (target) film damage. The technique permits, e.g., contamination-free deposition of viable embryonic stem cells [*Kattamis* et al. 2007].

Part V
Material Transformations, Synthesis and Structure Formation

Laser-induced material modifications can be classified into physical, chemical, and physicochemical transformations. *Physical* transformations can be performed in an inert atmosphere and they take place without any changes in the overall chemical composition of the material. Here, no real chemical reaction between the different constituents, if present, is activated. *Chemical* transformations are characterized by an overall change in the chemical composition of the material or the activation of a real chemical reaction. This shall include material synthesis, decomposition, and some types of surface modifications. The latter can take place either in a chemically reactive ambient medium, by adding a new material to the surface, or by depleting a certain constituent of the material. With *physicochemical* transformations both physical and chemical processes are important.

Large-area surface modifications are performed with excimer lasers, Nd:YAG or Nd:glass lasers, and with high-power CO_2 lasers. For localized processing, low-power cw lasers such as Ar^+-, Kr^+- or Nd:YAG-lasers are employed.

Chapter 23
Material Transformations, Laser Cleaning

Laser-induced structural transformations such as transformation hardening, annealing, recrystallization, glazing, shock hardening, polishing (planarization), etc., are based on the high processing temperatures that can be reached during *short* heating and cooling cycles under high-power pulsed-laser or rapidly scanned cw-laser irradiation. Short processing cycles permit material transformations within thin films and surfaces without significant influence on the substrate or the underlying bulk material. In the case of surface absorption, which is a good approximation with many applications, the thickness of the heated zone is approximately described by the heat-diffusion length, l_T. The time for heating the material to a certain temperature and depth, and the time for cooling can both be calculated from the equations given in Chaps. 6, 7, 8 and 9. The thickness of the modified layer, $\Delta h \approx l_T$, decreases with decreasing pulse length. With ultrashort laser pulses, Δh becomes so small that cooling rates up to more than 10^{12} K/s can be achieved (Chap. 13). With such cooling rates, it is possible to freeze *non-equilibrium* phases, suppress nucleation, etc. There is, however, a limitation. The transformation temperature must be sustained for a time which is longer or at least comparable to the time required for the phase transformation to take place. Furthermore, with many systems, successful laser processing is related to strong temperature gradients, which induce internal stresses, redistributions of defects, different types of transport phenomena, etc.

23.1 Transformation Hardening

Transformation hardening involves laser heating of the material above a certain transformation temperature and subsequent rapid cooling. The transformation temperature is, in general, *below* the melting temperature. This type of heat treatment permits one to freeze non-equilibrium phases with modified physical properties within a thin layer. Thus, the technique permits hardening within a well-defined surface layer *without* affecting the elastic properties of the bulk material. For the same reason, material distortions are significantly diminished or even absent. These are the great advantages of laser hardening in comparison to standard techniques. Laser hardening is meanwhile a well established technique with a wide range of

D. Bäuerle, *Laser Processing and Chemistry,* 4th ed.,
DOI 10.1007/978-3-642-17613-5_23, © Springer-Verlag Berlin Heidelberg 2011

applications, including the hardening of gears, clutches, and cylinder liners in automotive industry.

The material studied most intensively is steel. With carbon steel the austenitizing temperature is above 723°C (eutectic), depending on the carbon content. At this temperature, the (soft) pearlite phase with non-dissolved carbon transforms into austenite, which is a solid solution of carbon in γ-Fe. Rapid cooling at rates $> 10^3$ K/s results in the formation of a (hard) metastable martensite. Frozen-in thermal stresses, micro-cracks, segregation phenomena, etc., are often of importance in hardening processes as well.

Experiments were mainly performed with CO_2 lasers at powers exceeding 10^3 W. Because CO_2-laser radiation is strongly reflected by metals [Fig. 7.2.4; for steel and perpendicular incidence $A(\Theta = 0) \leq 0.2$] surfaces are often coated with absorbing layers consisting of graphite, sulfides such as MoS_2 or Fe_2S_3, metal oxides, or black inks. Absorption can also be increased by employing the Brewster effect. With metals for which $A(\Theta = 0) \ll 1$, irradiation with π-polarized light under the Brewster angle,

$$\Theta_B \approx \frac{\pi}{2} - \frac{A(\Theta = 0)}{2\sqrt{2}} ,$$

yields an absorptivity $A(\Theta_B) \approx 2/(1 + \sqrt{2}) \approx 0.83$ which is *independent* of the specific material.

In a typical experiment, a laser beam with an intensity of about 10^4 W/cm^2 is scanned over the surface with a dwell time $\tau_\ell = 2w/v_s$ of 0.01 to 1 s. The transformed layer thickness (HAZ) scales approximately with $l_T \sim (D\tau_\ell)^{1/2} \sim (Dw/v_s)^{1/2}$. Laser-hardened surface layers are, typically, some 0.1 to a few mm thick, depending on the material properties and the laser parameters employed. Because of the shorter cooling cycles with respect to standard processes (induction heating, flames, arcs, etc.) the martensite formed in laser hardening is finer and the residual stress more compressive. Thus, laser-treated surfaces have improved fatigue and wear properties with reduced friction coefficients. For steel, the (Vickers) hardness is, typically, increased by a factor of 3–5. Because the absorptivity of most metals increases with decreasing wavelength, Nd:YAG- and excimer-lasers have meanwhile become reliable and economic alternatives to CO_2 lasers. In any case, the depth of the hardened zone can be estimated in the simplest form from the heat-penetration depth, or from the laser-induced temperature distribution together with the phase diagram of the material and the related kinetic constants.

For materials in which solid-phase diffusion is *not* fast enough to obtain complete solution of the relevant species, laser transformation hardening can be achieved by melting and resolidification (Chap. 10). In such cases, surface roughening and subsequent machining are, in many cases, inevitable. However, by using optimized laser parameters, hardening by nitrogen doping together with surface polishing in a single step process has been demonstrated (Sect. 26.2).

Laser *shock hardening* is based on quite different mechanisms (Sect. 23.4).

The criteria for the several different types of laser hardening and the depth of the hardened zone have been investigated experimentally and theoretically for various types of metal alloys, and in particular for steel [*Bergmann* 2004; *Steen* 2003; *Ready* 1997; *Wissenbach* et al. 1985].

23.2 Laser Annealing, Recrystallization

Laser annealing shall denote the epitaxial regrowth of thin defective or amorphous layers which are formed during a particular processing step on otherwise crystalline bulk material. The term laser-induced recrystallization often refers to the transformation of small-grain polycrystalline or amorphous films or slabs into large-grain crystalline material. This includes the crystallization of films deposited on substrates by standard evaporation, electron-beam evaporation or other techniques. In the literature, the terms laser annealing and laser recrystallization are often used as synonyms.

The advantages of laser annealing and recrystallization over standard (oven) annealing are related to the short processing cycles that can be achieved with lasers. The good surface crystallinity of laser-annealed/recrystallized materials is often related to laser-induced melting and regrowth of the material. Here, solidification velocities can reach several meters per second (Chap. 10). Solid-phase transformations where the laser-induced surface temperature stays *below* the melting temperature have been demonstrated as well. In any case, preheating of the substrate is advantageous in most of these applications because it allows processing at lower laser-light intensities and better process control. Most of the investigations on laser annealing have concentrated on ion-implanted silicon surfaces. Laser-induced recrystallization of films has been demonstrated for a large number of materials. Laser- and electron-beam remelting of ion-implanted metal surfaces has been demonstrated for Al, Cu, Ni, etc. [*Picraux* and *Follstaedt* 1983; *Buene* et al. 1981]. The motivation for such experiments is the improvement of surfaces against corrosion and wear.

Recently, laser-annealing has been employed for spatially selective intermixing of quantum well (QW) and barrier materials. The feasibility of the technique has been demonstrated for InGaAsP/InP QW microstructures [*Stanowski* and *Dubowski* 2009].

23.2.1 Ion-Implanted Semiconductors

One of the transformations studied in most detail is the recrystallization of amorphous and polycrystalline semiconductor surfaces, and in particular of Si [*Cullis* 1985; *Celler* 1984]. Thin amorphous films are generated on single-crystal Si wafers during the surface doping by ion implantation which is widely used for the fabrication of thin p- or n-type layers in semiconductor device technology. The amorphized surface layers, which are typically some 0.1 μm thick, must be

recrystallized in order to restore the physical properties of crystalline Si and to electrically activate the dopant atoms by incorporating them into proper (substitutional) lattice positions.

Pulsed-Laser Annealing

Pulsed-laser annealing offers new possibilities in comparison to oven annealing. With laser-beam dwell times of, typically, some ps to some 100 ns, diffusion broadening or redistribution of dopant profiles, or the precipitation of dopants, can widely be suppressed. This permits one to generate very high concentrations of *active* dopants. Figure 23.2.1 demonstrates some of the main features for the example of ion-implanted As and B in (100) Si. Similar results have been obtained with In, Ga, P, Sb, etc. The solid solubility limit in Si can be exceeded by a factor of up to 100. More than 95% of the implanted dopant atoms can be (electrically) activated. Pulsed-laser annealing involves, in general, surface melting (Chap. 10). Almost defect-free crystallization of the melt on pure (100) Si has been found for solid–liquid interface velocities, v_{sl}, of up to about 15 m/s (Fig. 23.2.2). The maximum interface velocities for *defect-free* crystal growth on pure Si lie in the order (001) > (011) > (112) > (111).

Pulsed lasers are the superior sources for the fabrication of very steep and ultrashallow pn junctions, good ohmic contacts or regions with very low sheet resistivity. The lasers most commonly employed are excimer lasers and Q-switched Nd:YAG lasers. In any case, the photon energy should exceed the bandgap energy,

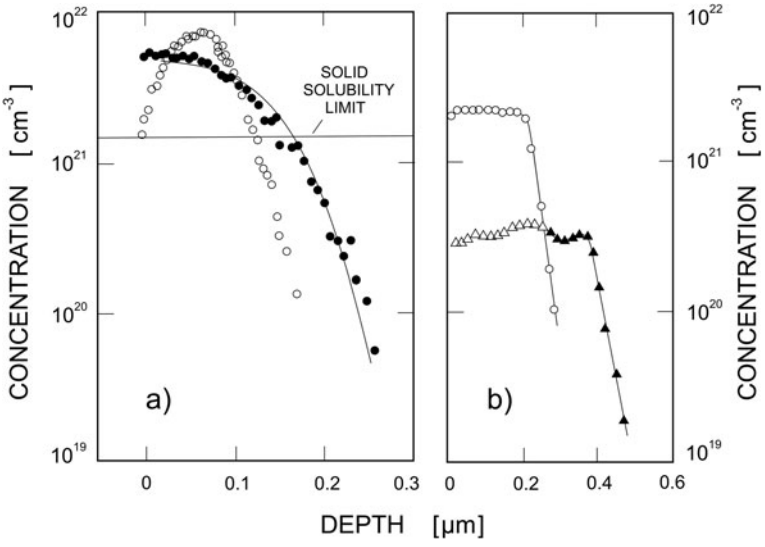

Fig. 23.2.1 a, b Dopant profiles generated in (100) Si. (**a**) ○ after implantation with 100 keV As^+ ions ($6.4 \times 10^{16}/cm^2$). ● after laser annealing. Adapted from *White* et al. (1980). (**b**) Implantation of B^+ (△, ▲) and As^+ (○) ions followed by multiple-pulse laser annealing [*Hill* et al. 1982]

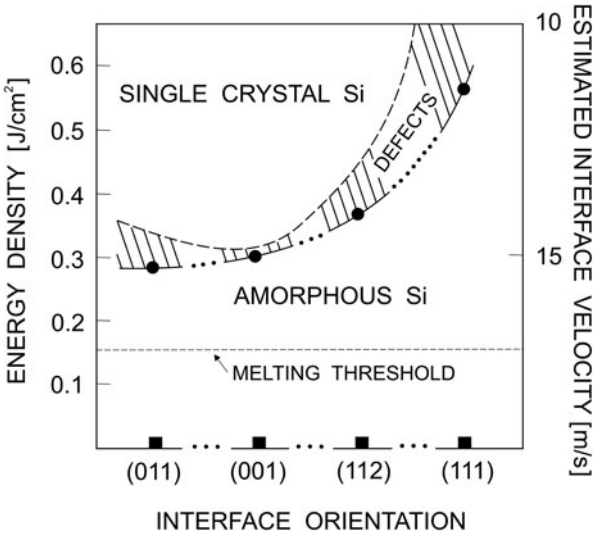

Fig. 23.2.2 Maximum (estimated) interface velocities for defect-free crystalline growth (*dashed curve*) and amorphization on Si for 347 nm frequency-doubled ruby-laser irradiation ($\tau_\ell \approx 2.5$ ns) and for different crystallographic orientations [*Cullis* 1985]

i.e., $h\nu > E_g$. Otherwise, process control becomes very difficult due to the strong feedbacks in the absorption process (Sect. 7.6). All of the experimental results achieved with ns and ps laser pulses can be explained on the basis of purely thermal processes [*Malvezzi* et al. 1985].

Solid-phase XeCl-laser annealing of Al^+ ion implanted SiC using 200 ns pluses has been studied by *Dutto* et al. (2003). The increase in infrared absorption of S^+-ion implanted n-type (111) Si after XeCl-laser-induced surface melting and solidification was investigated by *Kim* et al. (2006).

Cw-Laser Annealing

Cw-laser annealing does *not* involve surface melting, in general. Here, the laser-beam dwell times are, typically, some ms. Today, surface annealing of ion-implanted Si is mainly performed with intense lamps. Widely used techniques are rapid thermal annealing (RTA) and flash annealing.

Recently it has been demonstrated that submelt millisecond laser annealing in 45 nm CMOS technology enhances dopant activation without detrimental diffusion of ion-implanted Ge and B in the p-Si gate [*Colin* et al. 2011, 2008]. The cooling rates are, typically, 10^6 K/s. A problem arises from the non-uniformities in optical absorption and heat transport related to the patterned surface of the device. While optical inhomogeneities can be widely diminished by means of an absorbing layer, thermal inhomogeneities can be controlled only via the laser parameters.

While laser annealing of ion-implanted semiconductors in real device fabrication processes is, up to now, not widely used, these investigations have stimulated

rapid annealing with lamps and also revealed many fascinating fundamental aspects. Among the latter are rapid solidification processes with liquid-solid interface velocities of several meters per second. Such investigations provide insights into a new regime of crystallization. Time-resolved measurements using both X-ray and ps or fs laser pulses open up new regimes of photon-electron-phonon interactions (Sect. 29.3). Studies on dopant segregation, supercooling, the formation of metastable phases, instabilities, and structure formation have elucidated many new phenomena at liquid–solid and solid–solid interfaces.

23.2.2 Thin Films

Large-area crystallization of thin films on low-cost glass or plastic substrates is a key technology for many applications. Among those are integrated active-matrix-based displays, system-on-panel products, thin-film solar cells, etc. For example, large-panel thin-film transistors (TFT) are required to switch the pixels in liquid-crystal displays (LCD).

For the fabrication of crystalline Si films one often starts out with a 30–100 nm thick (TFTs) or several μm thick (solar cells) amorphous silicon (a-Si) layer. This layer is deposited by standard techniques, e.g. CVD, PECVD, or EBE.

The cheapest crystallization process is solid-phase crystallization at about 600°C, which is compatible with glass substrates. After several hours, the a-Si layer converts into c-Si with grain sizes of about 1 μm. Similar grain sizes are obtained by KrF-laser crystallization of a-Si. Both techniques are industrially employed for the fabrication of TFTs in flat panel displays. Recently, it has been demonstrated that in thin films grains with widths of several 10 μm and lengths exceeding 100 μm can be produced by overlapping scans of cw-laser radiation. Most appropriate is 514.5 nm Ar^+ and 532 nm Nd:YAG laser radiation whose penetration depth in a-Si is of the order of the film thickness [*Andrä* and *Falk* 2008]. TFTs fabricated by Ar^+-laser crystallization showed carrier mobilities of up to 690 cm^2/Vs. From an economic point of view it would be more appropriate to use arrays of diode lasers. These would permit to generate a long line focus and avoid overlapping. For the fabrication of solar cells, laser-crystallized layers can be employed as seed layers for subsequent epitaxial thickening by standard techniques or by so-called layered laser crystallization (LLC). In the latter technique, single KrF-laser pulses are employed *during* Si deposition, e.g. by EBE. The laser pulses melt the newly deposited Si and favor epitaxial growth of the film [*Sinh* et al. 2002].

Localized crystallization of a-Si films has been demonstrated by laser direct writing, projection, interference, and by SNOM techniques (Sect. 5.2.1). Here, patterns with sizes of several 10 μm down to less than 100 nm have been fabricated [*Andrä* and *Falk* 2008; *M. Lee* et al. 2000; *Nebel* et al. 1998]. New phenomena may occur when the heat of crystallization becomes comparable to the absorbed laser power. In this regime, explosive crystallization in laser direct writing gives rise to the formation of periodic structures (Chap. 28).

Among the other semiconductors for which laser-induced crystallization has been studied are thin films of a-Ge [*Siegel* et al. 1999a], a-SiC [*Hedler* et al. 2003; *Urban* and *Falk* 2001], GeSb [*Siegel* et al. 1999b] and CdSe [*Shaffer* et al. 2008] etc. Laser-induced structural transformations have also been studied for DLC films [Sect. 23.5; *Mechler* et al. 1998], for C_{60} [*Käsmaier* et al. 1996], in connection with the fabrication of micron-sized magnetic domains in amorphous TbFe [*Suits* et al. 1986], the formation of nanocrystalline $LiCoO_2$ films used as high-power density cathode material for Li-ion batteries [*Ketterer* et al. 2008], etc.

23.3 Glazing

Just as amorphous materials can be crystallized under the action of laser light, crystalline materials can often be transformed into the amorphous state. This is achieved if the cooling rate exceeds a critical velocity, v_{ls}^{cr}, which strongly depends on the type of material. v_{ls}^{cr} can vary over many orders of magnitude. Glazing of material surfaces and thin layers has many applications. These are based on the quite different physical and chemical properties of amorphous and crystalline phases.

Amorphization of Si takes place above interface velocities of 11-15 m/s, depending on crystal orientation (Fig. 23.2.2). With 50 nm a-Ge films, amorphization velocities of only 1.7–4 m/s have been measured [*Siegel* et al. 1998]. With high dopant concentrations, amorphization thresholds can significantly change [*Campisano* et al. 1984].

Of particular interest are thin films of so-called phase change materials such as AgInSbTe and GeTe-Sb_2Te_3. These compounds are presently employed in rewritable (RW) optical discs (CD-/DVD-RW principle). For recording one starts out with the highly reflecting polycrystalline film that is embedded between dielectric layers, in most cases a polymer. During writing, the intensity within the focus of the laser beam is so high that it locally melts the film. The amorphous (liquid) phase is frozen-in due to rapid heat transport into the surrounding material. Thus, by switching the laser-beam on and off, amorphous regions within the crystalline layer are produced. For reading, one can use the same laser, but with a lower intensity. The *changes* in the reflected light intensity at transitions from amorphous to crystalline regions, and vice versa, correspond to those between pits and lands in standard CDs/DVDs. The information can be erased by heating and 'slow' cooling of the film so that amorphous regions crystallize. If this step is done with the laser, longer dwell times and lower intensities, typically one third of those for recording, are used. Thus, with the materials employed, recrystallization does *not* require melting.

Storage devices that are based on the strong differences in *electrical* properties between crystalline and amorphous phases are under development.

Within the last 20 years significant progress in optical data storage capacity (blu-ray disc) and archival lifetimes have been achieved. This is by no means the case with respect to data transfer rates. At present, the laser pulse times that can be employed are too long, typically 30 ns. These pulse times, and thus the data transfer rates are limited by the lack of cheap, compact ps-lasers that trigger the

phase transition and, additionally, by the response time of the phase change material. For the latter reason, the amorphization/crystallization dynamics of many different materials are presently investigated. Among those is $Ge_2Sb_2Te_5$. In this compound, laser pulses shorter than 10 ns can switch the material between amorphous and crystalline phases. As expected from the model calculations presented in Sect. 9.4, the transient temperature profile, and thereby the dynamics of phase transformations, depends on the thermal properties of the substrate and the wavelength and duration of laser pulses [*Siegel* et al. 2008; *Wiggins* et al. 2005; *Siegel* et al. 2004a].

Laser treatment of (crystalline) *metals* often results in the formation of fine-grain poly-crystalline material and not in real metallic glasses. Glass formation requires cooling rates in excess of 10^6–10^{12} K/s. The critical interface velocities are, typically, 10^2–10^3 m/s. Molecular dynamics (MD) simulations of cooling rates and the recrystallization kinetics in ultrashort-pulse laser quenching of metal targets have been performed by *Duff* and *Zhigilei* (2007), *Lin* and *Zhigilei* (2006), and others.

With *insulators*, liquid phases can be frozen-in with cooling rates of only 10^{-4} to 10^2 K/s.

Laser-induced surface modification/glass formation of metals and insulators is applied for improved corrosion resistance and surface hardening. Problems may arise with crack formation, recrystallization, etc.

23.4 Shock Hardening

In contrast to the structural transformations discussed in the preceding sections, laser-induced shock hardening is performed at laser-light intensities of $I > 10^8$ W/cm^2 (Sect. 11.7.2). With such intensities, pressures up to several 10^3 bar are generated. The compressive shock mechanically densifies the material surface [*Bergmann* 2004; *Fairand* et al. 1974]. An example is the transformation of some fourfold coordinated non-metals into more densely packed metallic phases. Shock hardening can also be related to the generation of very high densities of non-equilibrium defects (vacancies, dislocations, etc.).

23.5 Surface Polishing

Laser polishing (planarization) is a viable technique to diminish the roughness of materials surfaces. The materials studied in most detail are DLC (Sect. 22.5.3) and cast iron (Sect. 26.2.4). DLC films are polycrystalline with great surface roughness (Fig. 23.5.1a). Because of the extreme hardness of DLC, traditional polishing techniques are very time consuming and expensive. Laser polishing, on the other hand, is very fast and can also be applied to *non-planar* surfaces. For DLC, the underlying mechanism seems to be quite simple: the rough surface is irradiated with laser light that is strongly absorbed by the material. This is schematically shown in Fig. 23.5.2. Material heating is stronger within the hills, just because heat transport

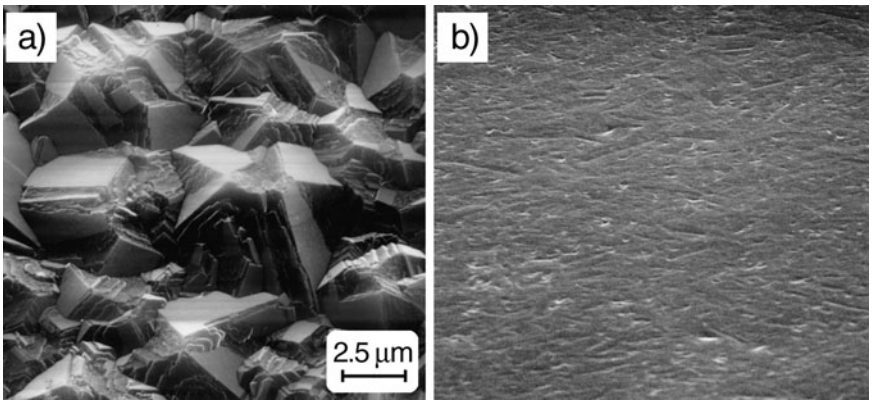

Fig. 23.5.1 a, b SEM pictures of diamond-like carbon. (**a**) Film grown by plasma-enhanced CVD. (**b**) ArF-laser polished film ($\phi \lesssim 10\,\mathrm{J/cm^2}$, $\tau_\ell \approx 20\,\mathrm{ns}$, $\nu_\mathrm{r} = 20\,\mathrm{Hz}$, $\theta_\mathrm{i} \approx 80°$). The ambient atmosphere was air [*Tosin* et al. 1996]

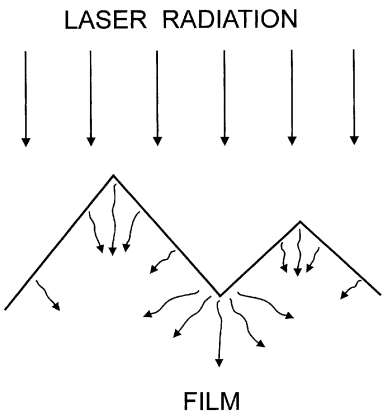

Fig. 23.5.2 Schematic picture illustrating laser polishing. The absorbed laser light heats the top of crystallites more efficiently than the valleys where heat diffusion is more effective, as indicated by *arrows*. This results in surface planarization by material removal at the hills or via melting/softening and surface tension effects

is more efficient, i.e. more 3D-type, around the valleys. With grazing incidence ($\theta_\mathrm{i} = 80°$ to 85°) this effect is enhanced because the valleys are shadowed by the hills. The surface quality is further improved if the sample is rotated. By this means, different facets are illuminated from different sides and, additionally, ripple formation is suppressed [*Gloor* et al. 1997].

DLC transforms into graphite at around 1200 K and sublimates at around 3900 K. Strong absorption starts for wavelength $\lambda \lesssim 230\,\mathrm{nm}$. Polishing is most efficient if the thermal penetration depth is comparable to the size of crystallites, d. If $l_\mathrm{T} \ll d$, only the very top of crystallites is overheated and removed. If, on the

other hand, $l_T \gg d$, the temperature difference between hills and valleys decreases. With the crystallite sizes in Fig. 23.5.1a, optimal polishing conditions are achieved with 193 nm ArF-laser radiation and pulse lengths around 20 ns ($l_T \approx 4\,\mu m$). Figure 23.5.1b shows the result. With a laser-pulse energy $E_\ell \approx 0.5$ J, a laser-beam spot size of 0.05 cm^2, a repetition rate $\nu_r = 20$ Hz, and crystallite sizes around 5 μm, polishing requires about 20 minutes/cm^2. This is about 1500 times faster than mechanical polishing. With industrial ArF lasers, this time can be further reduced. If the laser-polished surface does not match the requirements of a special application, subsequent mechanical polishing can be applied. Such a combined technique yields very smooth surfaces within relatively short processing times [*Pimenov* et al. 1999].

Laser polishing of metals has been demonstrated mainly for steel and cast iron. The latter has gained great importance in the automotive industry, in particular in the fabrication of Diesel engines (Sect. 26.2.4). Laser planarization has been studied also for films of Si [*Wang* et al. 2003], GaN [*Duboswski* et al. 2001], and $(Y_{1-x}Eu_x)_2O_3$ [*McKittrick* et al. 1998]. F_2-laser polishing of organic materials has been demonstrated for PTFE [*Gumpenberger* et al. 2005a].

With these materials, a mechanism similar to that shown in Fig. 23.5.2 may become effective. If the laser light causes melting/softening on the top of "hills" *only*, viscous flows due to surface tension effects will cause a smoothening of the surface (Chap. 10). If, on the other hand, the laser-light intensities are too high, they melt/soften a thin surface layer. This may result in ripple formation and thereby in surface roughening (Chap. 28). This explanation seems to be in agreement with the experimental observations. With compounds, material decomposition may become important.

23.6 Transformations Within Bulk Materials

Laser-induced physical and/or chemical transformations within the *volume* of transparent materials permit unique applications. Among those is the 3D-patterning for erasable or non-erasable marking, the fabrication of diffractive optical elements, e.g., Bragg gratings in optical fibers, the fabrication of waveguides, 3D optical storage, etc.

Physical material transformations may be based on structural phase transitions, material crystallization, amorphization, etc. Chemical transformations based on thermal, photophysical, or photochemical reactions result in material conversion, degradation, or decomposition. Both, physical and chemical transformations may cause local changes in optical absorption, scattering, and refractive index. The latter may be related to changes in the material density or composition, or to laser-induced birefringence. *Periodic* changes in (bulk) material properties due to (coherent) laser-induced instabilities are discussed in Chap. 28. Material decomposition may result in the formation of bubbles or extended cavities. For *high-resolution* modification of material properties, ultrashort-pulse lasers together with pulse shaping are required [*Mermillod-Blondin* et al. 2008a]. The mechanisms

for nanosecond and ultrashort-pulse laser-material interactions are discussed in Chaps. 12 and 13, respectively.

Subsequently, we give a brief overview on applications of material transformations for the fabrication of 3D-buried structures. In these applications, material modifications may be reversible or non-reversible, depending on the type of material and the laser parameters employed. With increasing laser-light intensities, a transition from structural changes to void formation is observed. In this regime, the material density changes dramatically. This transition and devices based on *hollow* embedded structures are mainly discussed in Sect. 13.6.3.

23.6.1 Non-erasable Marking

Laser marking of materials and devices has become an important technique in many different fields. *Surface* markings are based on structural or chemical modifications, foaming, material evaporation/ablation, etching, etc. (Sect. 11.8.3). Clearly, in many cases, such markings can be easily polished off. Laser-induced permanent transformations within the *bulk* of (linearly) transparent materials are non-erasable. An example is shown in Fig. 23.6.1 (see also Fig. 13.6.4). Such transformations are mainly based on the local degradation or decomposition of the material. With ultrashort-pulse lasers, feature sizes of a few 100 nm have been achieved (Chap. 13). Among the applications are the inscription of logos or trade marks, the identification of components, devices, gems, etc.

23.6.2 Gratings

Fiber Bragg gratings (FBGs) are widely used in optical telecommunication, sensor technology, fiber-based laser processing, etc. A FBG is based on an equidistant

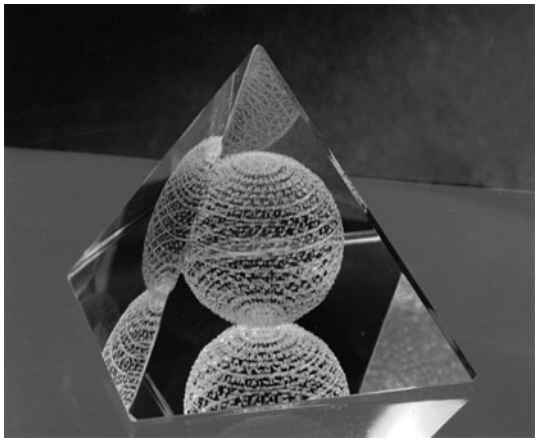

Fig. 23.6.1 3D non-erasable volume marking of glass by means of Nd:YAG-laser radiation ($P = 2\,\mathrm{W}$, $\tau_\ell = 20\,\mathrm{ns}$, $\nu_\mathrm{r} = 1\,\mathrm{kHz}$) [ILT, Aachen, Germany, 1999]

variation of the index of refraction in the fiber core. Such gratings permit one to manipulate the optical transmission spectrum through fibers. For both optical telecommunication systems and high-power applications, fused quartz fibers are most commonly used.

Femtosecond lasers are an ideal tool for high-precision localized inscription of Bragg gratings in (linearly) transparent non-photosensitive materials such as a-SiO_2 (Sect. 13.6). Depending on laser parameters, changes in refractive index, Δn, within the range of 10^{-5} to 10^{-2} have been observed. These index changes seem to be related to local heating/melting and rapid quenching of a-SiO_2 within the focal volume of the laser beam. This results in a densification of the material and thereby in an increase in refractive index. For higher laser-light intensities, however, other mechanisms become important. Refractive index changes related to stress-induced birefringence, depletion of oxygen, and the generation of periodic structures with alternating higher and lower material density, corresponding to $\Delta n > 0$ and $\Delta n < 0$, respectively, are observed. The latter are discussed in Sect. 28.2. Patterning has been performed by both pulse-to-pulse modification [*Martinez* et al. 2004] and by phase-mask techniques [*Thomas* et al. 2007a].

Different types of (amplitude) gratings with 1D, 2D, and concentric structure have been fabricated within silicone films by fs-laser direct writing [*Kuna* et al. 2008]. The process is based on laser-induced chemical decomposition and carbonization of the silicone. Embedded structures of this type can be integrated into encapsulation layers of high power light-emitting diodes (LEDs). They permit to homogenize and to control the light emitted from such devices.

23.6.3 Waveguides

The fabrication of waveguides within the surface or the bulk of solid materials is of great importance for applications in integrated optics, for the fabrication of compact lasers, etc. In contrast to the standard techniques, lasers permit direct writing of waveguides into or onto the surface of almost any material by a single-step process. Waveguiding may be based on local physical or chemical modifications of the surface, on ablation, etching, or material deposition. These different possibilities are discussed throughout various chapters. However, lasers permit one to generate also 3D *buried* waveguides. Good confinement of the laser-induced material modification can be achieved with ultrashort laser pulses. There are essentially two geometries for laser direct writing. So-called longitudinal and transverse waveguides are fabricated by scanning the laser focus $\boldsymbol{v}_s \parallel \boldsymbol{k}$ and $\boldsymbol{v}_s \perp \boldsymbol{k}$, respectively. $\boldsymbol{k}$ is the wavevector. Longitudinal waveguides are circular in shape. A problem are wavefront distortions generated at the air-dielectric-interface. These limit the writing length of waveguides. This problem can be overcome, in part, by using adaptive spatial tailoring of laser pulses [*Mauclair* et al. 2008]. Transverse writing offers greater flexibility, but yields elliptically-shaped waveguide cross sections. This can be overcome by beam shaping as well.

Most of the experiments have been performed with fused silica (a-SiO_2) [*Szameit* et al. 2007; *Diez-Blanco* et al. 2007; *Nolte* et al. 2003], $LiNbO_3$ [*Osellame* et al. 2007; *Thomas* et al. 2007], and PMMA [*Sowa* et al. 2006]. $LiNbO_3$ is the preferred material for applications that require a high optical nonlinearity. There are essentially two methods for fabricating transverse waveguides:

- Laser direct writing using single or multiple scans at low to medium laser fluences. This causes changes in the refractive index by nonlinear absorption of the material within the laser focus. In such cases, waveguiding takes place *within* this trace of the laser-modified material. Waveguides fabricated by using multiple scans have superior properties. These include the better control of cross-sectional shapes and mode profiles, and a better (temporal) stability of the refractive index changes. This has several reasons: first, the lower pulse energies that can be employed with multiple scans diminish the extension of damages. Second, subsequent scans cause an annealing of irradiated regions and thereby increase the uniformity of the waveguide. Third, almost arbitrary cross-sectional shapes can be generated [*Osellame* et al. 2007]. For example, by using an elliptical focus for writing, waveguides with a circular cross section have been fabricated.
- Higher laser fluences cause irreversible material damages and stress-induced refractive index changes in the surrounding region. By laser direct writing of *pairs* of traces with appropriate distance, light can be guided *in between* such traces. By this means, symmetric and thermally stable waveguides have been fabricated in periodically poled $LiNbO_3$. The damping losses of such waveguides were about 1 dB/cm and the conversion efficiency for SHG of 1064 nm Nd:YAG-laser radiation up to 58% [*Thomas* et al. 2007b; *Burghoff* et al. 2007].

Image reconstruction using segmented waveguide arrays fabricated by fs-laser direct writing in a-SiO_2 has been demonstrated by *Szameit* et al. (2008).

23.6.4 3D-Optical Storage

Three-dimensional data storage offers the possibility to increase the recording density from some 10^9 bit/cm^2 for conventional laser- and magneto-optical discs to more than 10^{14} bit/cm^3. Among the materials investigated are the following:

- *Photopolymers*, where the data are recorded as local refractive index changes. These index changes are related to photopolymerization and/or to mass densification. Isolated voxels with widths below 100 nm have been fabricated. In any case, these processes are irreversible and can be employed for read-only memories (ROMs). The refractive index changes are, typically, $\Delta n \approx 10^{-2}$ to 10^{-3}. For further details see Chap. 27.
- *Photorefractive* materials where, within certain laser parameters, index changes are reversible as, e.g., in $LiNbO_3$ and $LiTaO_3$ (see above). Typical values for $LiNbO_3$ are $\Delta n \approx 10^{-6}$ to 5×10^{-4} [*Juodkazis* et al. 2008; *Ueki* et al. 1996].
- *Photochromic* materials. For recording, an isomer, A, is irradiated with a wavelength λ_A that transforms A into B (Fig. 23.6.2). Illumination with λ_B induces the

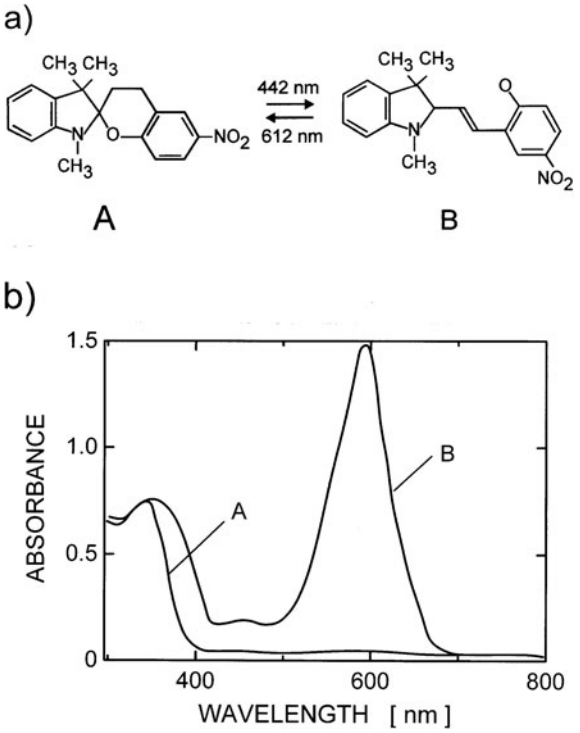

Fig. 23.6.2 a, b Photochromic reaction of NSP (1,3,3-trimethylindolino-6′-nitrobenzopyrylospiran). (**a**) A and B are isomers of NSP. (**b**) Absorption spectra of a polystyrene film containing NSP before irradiation (isomer A) and after irradiation with 442 nm light (isomer B) [adapted from *Toriumi* et al. (1997)

reverse photochemical reaction B → A. This type of readout, however, erases the recorded information. To overcome this problem, photochromic materials with 'stable' isomers, B, that are not transformed into A at 'low' light intensities are developed. Alternatively, one can use a wavelength that is *not* absorbed by the photochromic material, and thereby does not stimulate the reaction B → A. This has been demonstrated for NSP where small differences in the refractive index in the near infrared (NIR), related to isomers A and B, can be used for reading without erasing recorded data [*Toriumi* et al. 1997; *Dvornikov* and *Rentzepis* 1997].

- ROMs based on PMMA doped with a colourless dye precursor and a light-sensitive photoacid generator. Storage is based on two-photon absorption within two overlapping laser beams [*Walker* and *Rentzepis* 2008]. Here, 3D storage is achieved by changing the focusing position of the writing beam within the medium. By this means, hundreds of layers within a 1.5 mm thick DVD-type disc can be addressed. Terabyte recording using 532 nm Nd:YAG laser pulses ($\phi \approx 7$ nJ, $\tau_\ell \approx 6.5$ ps, $\nu_r = 75$ MHz) has been demonstrated. The recording rate was 25 Mbit/s.

Clearly, with many of these materials the underlying interaction mechanisms are similar to those discussed above.

23.7 Laser Cleaning

The term laser cleaning denotes the removal of *particulates* or thin extended *contamination layers* from solid surfaces. The latter application includes such different areas as cleaning stainless steel of scale or organic impurities, the removal of paint from metal surfaces, the cleaning of semiconductor surfaces and microelectronic or micromechanical devices, the removal of contamination layers from mechanical or electrical contacts, switches, etc., the pretreatment of glass substrates for liquid-crystal displays (LCD) or adhesion surface areas, etc. An important field is also the restoration of ancient metal artwork, coins, medieval stained glass, historical paper, textiles, paintings, frescos, and whole buildings (Chap. 32). On a wider scope, one can also include processes where a thin surface layer is 'cleaned' by *outdiffusion of impurities* under the action of laser light (see, e.g., Sects. 19.5.4 and 26.5). Review articles and original papers including the various types of laser cleaning and its applications can be found in [*Phipps* et al. 2007; *Kane* 2006; *Delaporte* and *Oltra* 2006; *Luk'yanchuk* 2002].

The removal of contamination layers from solid surfaces can be understood on the basis of the mechanisms discussed throughout Chaps. 11, 12 and 13. Thus, these mechanisms will not be discussed any further. *New* aspects arise with the cleaning of surfaces from particulates with sizes (diameters) in the range below several μm to several 10 nm. For these reasons, we will concentrate the further discussion on the problem of particle removal.

Efficient techniques to clean off smaller and smaller particulates from solid surfaces, heat-sensitive coatings, devices, etc. become increasingly important in lithography, semiconductor device fabrication, micromechanics, optics, telecommunication, etc. Conventional techniques such as ultrasonic and megasonic cleaning, wiping and scrubbing, high-pressure jet spraying, CO_2 snow cleaning, etching, plasma cleaning etc. are often inadequate for the removal of particulate contaminations of micron and submicron size. The reason is that small particulates adhere on substrates or devices with relatively strong forces that are difficult to overcome with these traditional cleaning techniques. As a consequence, these techniques are often ineffective, result in the addition of contaminations, the damaging of prefabricated parts, etc. It has been demonstrated that, under certain conditions, laser-cleaning can be used to efficiently remove micron and submicron particles from solid surfaces. Laser cleaning related to pulsed-laser heating of the surface and/or the particulates themselves is denoted as *dry laser cleaning* (DLC). If the removal of particulates is assisted by the evaporation of a thin liquid film, the technique is denoted as *steam laser cleaning* (SLC). If laser cleaning is performed in an atmosphere of high relative humidity, e.g. in water vapor, we use the term *wet laser cleaning* (WLC). Matrix laser cleaning (MLC) employs a thin solid film that is condensed on the contaminated surface.

In all of these different techniques, the cleaning efficiency for single-pulse laser irradiation is defined by $\eta = 1 - N_f/N_i$ where N_i and N_f are the respective surface densities of particulates before and after laser-light irradiation. η depends on the material and laser parameters, the ambient medium, and the size of particulates. Because of the latter reason, *spherical* particles with relatively narrow size distributions are often used as model contaminants. Such particulates are commercially available as colloidal solutions which are spun-on onto the substrate. For well-defined cleaning experiments, one has to avoid coalescence of particles and the formation of aggregates.

A fundamental problem in laser cleaning of surfaces from particulates is related to the local enhancement of the electromagnetic field caused by the particulates themselves (Sect. 5.3.7). Depending on the material properties of particulates and substrate, and the laser parameters, this field enhancement may cause local structural damages or even local ablation of the surface. This problem strongly limits applications of the technique. Laser cleaning based on substrate absorption is problematic with heat sensitive and/or inhomogeneous substrates. Among the latter are porous materials or substrates that are covered in part by another material as, e.g., in semiconductor device fabrication, etc. In such cases, the absorbed laser power and, as a consequence, the cleaning efficiency varies over the substrate surface.

23.7.1 Adhesion Forces

The mechanisms that cause strong adhesion of tiny particulates on solid surfaces are illustrated in Fig. 23.7.1.

The (non-retarded) *Van der Waals* force between two flat surfaces of contact area F is

$$K_{VdW} = \zeta \frac{F}{8\pi^2 a^3} \tag{23.7.1}$$

where ζ is the material-dependent Lifshitz-Van der Waals constant; it is related to the Hamaker constant, H, via $\zeta = (4\pi/3)H$. For details see *Israelachvili* (1992).

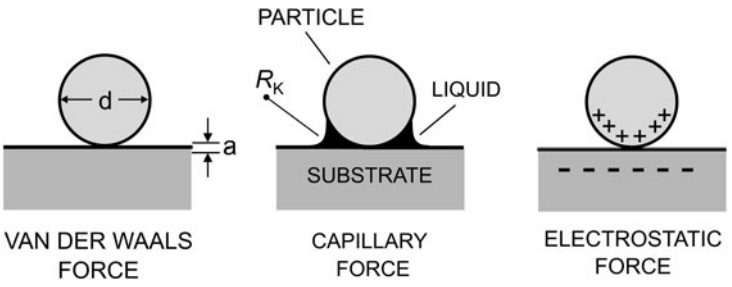

Fig. 23.7.1 Schematic picture illustrating the main adhesion forces for a particle of size (diameter) $d = 2r$ on a substrate. R_K is the Kelvin radius. The electrostatic image force is not shown

Typical values of ζ range from about 0.5 eV for polymer-polymer to about 10 eV for metal-metal interactions. The (microscopic) distance a at the contact is, typically, between 4 and 10 Å. For a spherical particle of radius r and a *point* contact, the *effective* area is $F \approx \pi\, a\, r$. We then obtain

$$K_{\mathrm{VdW}} = \zeta \frac{r}{8\pi a^2} \,. \tag{23.7.1a}$$

Thus, for a 1 µm particle, K_{VdW} may exceed the gravitational force by a factor of 10^7. This force may cause surface deformations and thereby change the point contact into a contact area of radius r_{d}. In this case the force is given by

$$K_{\mathrm{VdW}} = \zeta \frac{r_{\mathrm{d}}^2}{8\pi a^3} \,, \tag{23.7.1b}$$

where $r_{\mathrm{d}} \propto r^{\mathrm{n}}$, with $n = 2/3$ and 1/2 for elastic and plastic deformations, respectively [*Schrems* et al. 2003; *Rimai* et al. 1995].

The *capillary* adhesion force due to a thin liquid layer, that is typically the atmospheric moisture condensed between the particle and the surface, is

$$K_{\mathrm{c}} = 2\pi\sigma r(\cos\ \varphi_1{}' + \cos\varphi_2{}') \tag{23.7.2}$$

where σ is the surface tension coefficient of the liquid. $\varphi_1{}'$ and $\varphi_2{}'$ are the wetting angles for the substrate *and* the particle, respectively (Fig. 23.7.1; Sect. 4.2). K_{c} can exceed K_{VdW} by more than a factor of 10.

There are two types of *electrostatic* forces [*Bowling* 1995]. The electrostatic *double-layer* force is

$$K_{\mathrm{e}} \approx \pi\varepsilon_0 \frac{rU^2}{a} \,, \tag{23.7.3}$$

where ε_0 is the dielectric constant in a vacuum and U the contact potential difference. For short distances, this force is weaker than K_{VdW} as $K_{\mathrm{e}} \propto 1/a$. If the particle bears a net charge, an electrostatic *image* force also exists. For a homogeneous charge distribution we have

$$K_{\mathrm{ei}} = \frac{q^2}{16\pi\varepsilon_0 r^2} \frac{\varepsilon_{\mathrm{S}} - \varepsilon_{\mathrm{M}}}{\varepsilon_{\mathrm{M}}(\varepsilon_{\mathrm{S}} + \varepsilon_{\mathrm{M}})} \,, \tag{23.7.4a}$$

where ε_{M} and ε_{S} are the dielectric constants of the ambient medium and the substrate, respectively. If the charge is homogeneously distributed over the surface with density N_{e}, and if $\varepsilon_{\mathrm{M}} = 1$, we can write, with $q = 4\pi r^2 e N_{\mathrm{e}}$,

$$K_{\mathrm{ei}} = \frac{\pi}{\varepsilon_0} r^2 e^2 N_{\mathrm{e}}^2 \frac{\varepsilon_{\mathrm{S}} - 1}{\varepsilon_{\mathrm{S}} + 1} \,. \tag{23.7.4b}$$

Thus, the electrostatic image force plays an important role only for particulates larger than a few ten μm, as $K_{ei} \propto r^2$. Here, it is assumed that $N_e = \text{const}$.

In reality the adhesion forces depend not only on the type of particle and substrate material, but also on the real shape of particulates, on the properties of the surface, i.e., its roughness, hardness, etc., and on the ambient medium.

23.7.2 Dry Cleaning

Dry laser cleaning (DLC) can be classified into two extreme cases where particle removal relies on strong absorption of the laser light by either the substrate *or* the particulate.

Substrate Absorption

Consider a non-absorbing rigid (non-elastic) particulate on an absorbing substrate and uniform pulsed-laser irradiation (Fig. 23.7.2). The quasi-stationary 1D-thermal expansion of the surface due to laser-light absorption is, in the simplest case,

$$z(t) \approx \beta_T \frac{A\phi(t)}{\rho c_p}, \tag{23.7.5}$$

where β_T is the coefficient of linear thermal expansion. This result can be obtained by spatial integration of the heat equation. Due to the Grüneisen law, $\beta_T/c_p \approx$ const., Eq. (23.7.5) holds even with temperature-dependent parameters. A more sophisticated treatment yields the additional factor $2(1+\mu)$, where μ is the Poisson ratio. With $\phi = 0.3\,\text{J/cm}^2$, $A = 0.5$, $\beta_T = 10^{-6}\,\text{K}^{-1}$, $\rho = 3\text{g/cm}^3$, $c_p = 0.5\,\text{J/gK}$

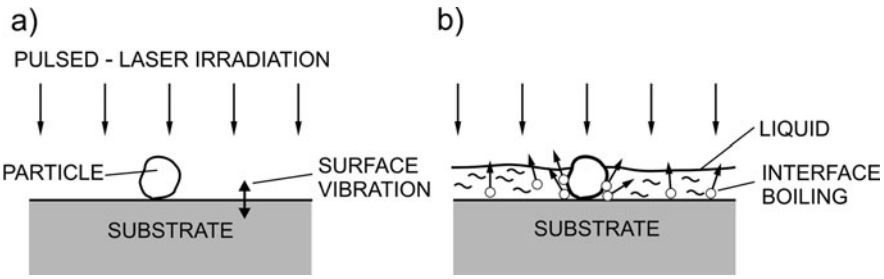

Fig. 23.7.2 a, b Laser cleaning based on strong substrate absorption. (**a**) Dry cleaning. The absorbed laser-light causes rapid vertical expansion of the substrate surface and thereby a strong acceleration of the particulate. Subsequently, the substrate surface relaxes rapidly. Local field enhancement effects cause local three-dimensional (3D) thermal expansion and/or substrate ablation below the particle. (**b**) Steam cleaning using a transparent liquid film. Superheating of the liquid film at the liquid/solid interface causes explosive ablation of the liquid and removal of particulates. As liquid, mainly water with a few percents of alcohol is employed

we obtain $z \approx 10^{-7}$ cm. Thermal expansion takes place during the laser pulse. The velocity normal to the surface is

$$\dot{z}(t) \equiv v = \beta_{\mathrm{T}} \frac{A\, I(t)}{\rho c_{\mathrm{p}}} \tag{23.7.6}$$

and the acceleration

$$\ddot{z} \approx \beta_{\mathrm{T}} \frac{A\dot{I}(t)}{\rho\, c_{\mathrm{p}}} \approx \beta_{\mathrm{T}} \frac{A\phi}{\rho\, c_{\mathrm{p}} \tau_\ell^2} \approx 2.5 \cdot 10^8\ \mathrm{cm/s^2}. \tag{23.7.7}$$

The calculated value refers to the aforementioned parameters and $\tau_\ell \approx 20$ ns. This value exceeds the acceleration due to gravity by more than a factor of 10^5. The *maximum* acceleration that can be achieved with lasers, can be estimated from $\ddot{z}_{\max} \approx l_\alpha / t_0^2$ with $t_0 \approx 1/\alpha v_0$, where l_α is the optical penetration depth and v_0 the sound velocity. Thus, $\ddot{z}_{\max} \approx \alpha v_0^2 \approx 10^{16}\,\mathrm{cm/s^2}$. This value exceeds the acceleration achieved by conventional techniques by many orders of magnitude. Clearly, damage of the material or of prefabricated device structures limits the maximum fluence and thereby the maximum acceleration that can be employed in reality.

Particle *removal* requires a certain 'external' force. From Newton's law we can calculate with $m \propto r^3$ the acceleration required to overcome the forces K_{e}, K_{c} and K_{VdW} (for a point contact and for plastic deformations). With dry laser cleaning we find with $K_{\mathrm{c}} = K_{\mathrm{e}} = 0$ and (23.7.7) the threshold fluence for cleaning

$$\phi_{th} \approx \frac{\xi\, c_p}{8\,\pi^2\, a^3\, \beta_T\, A} \frac{\tau_\ell^2}{r^q} \propto \frac{\tau_\ell^2}{r^q}, \tag{23.7.8}$$

where the exponent is within the range $1 \le q \le 2$. This simple one-dimensional (1D) model already shows that surface cleaning becomes increasingly difficult with decreasing particle size. For pulsed-laser irradiation, the time of interaction may become so short that the acceleration (23.7.7) is *not* high enough to remove a particle *during* the pulse. This becomes relevant for pulse durations shorter than some 10^2 ns. An *upper* limit of the intensity/fluence that can be employed is set by material damage due to fracture, melting, and ablation. More sophisticated 1D models take into account elastic deformations, the influence of pulse shapes, etc.

While such 1D models *qualitatively* describe some trends in laser cleaning, the calculated threshold fluences ϕ_{th}, wavelength dependences, etc. often disagree from the experimental results by up to several orders of magnitude. This has several reasons. Among those is the enhancement of the electromagnetic field underneath particulates. This field enhancement can be related to the focusing of the incident light by the particle itself, if $r \gg \lambda$, or to Mie scattering, if $r \lesssim \lambda$ (Sect. 5.3.7). In any case, local field enhancements cause a *local* temperature rise in addition to the uniform temperature rise related to the uniform laser-light irradiation. The local temperature rise causes local 3D-thermal expansion and may even cause local

damage/ablation of the substrate material. Such 3D model calculations have been performed by *Arnold* et al. (2004), *Luk'yanchuk* et al. (2004), and others.

Detailed *experimental* investigations have been performed on the laser cleaning of Al_2O_3, SiO_2, Si_3N_4, polysterene (PS) particulates, mainly from Si [*Graf* et al. 2005; *Schrems* et al. 2003; *Mosbacher* et al. 2002], glass [*Pleasants* and *Kane* 2003], and polyimid (PI) substrates [*Fourrier* et al. 2001]. Cleaning efficiencies were evaluated by either counting the particle densities before and after cleaning by means of an optical microscope in combination with special computer software, or by measuring the changes in scattered light from a HeNe probe beam illuminating the area under consideration [*Chaoui* et al. 2003]. Cleaning of surfaces is performed by using either a single laser pulse or multiple-pulse irradiation. In the latter case cleaning efficiencies can be described by

$$\eta(N_\ell) \approx 1 - (1 - \eta)^{N_\ell} \tag{23.7.9}$$

where $\eta \equiv \eta(N_\ell = 1)$ is the single-pulse cleaning efficiency. The number of laser pulses typically employed in laser cleaning is between 1 and 10.

Figure 23.7.3 shows the typical behavior of the cleaning efficiency as a function of fluence for two different particle sizes. η strongly increases above a certain threshold fluence and then remains almost constant. With decreasing particle size, ϕ_{th} increases. This is in *qualitative* agreement with (23.7.8). However, a detailed analysis reveals that experimental data on ϕ_{th} as a function of particle size cannot be explained in this way, and even not on the basis of 3D thermal

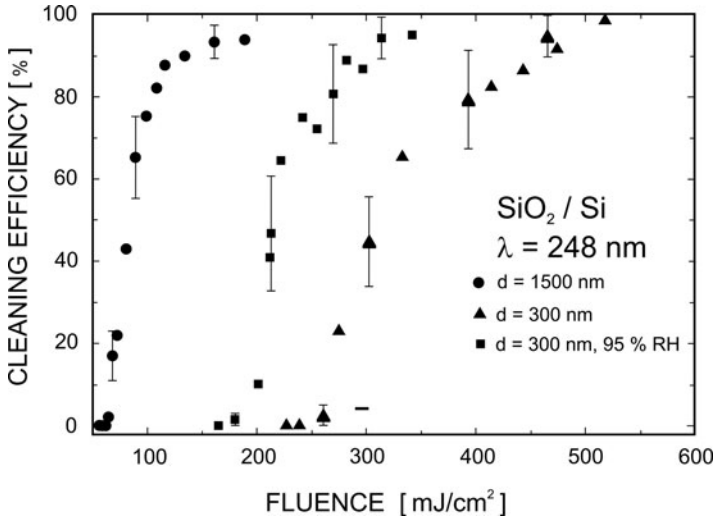

Fig. 23.7.3 Cleaning efficiencies achieved with single-pulse KrF-laser radiation. The substrate was (100) Si contaminated with spherical particles of SiO_2. Experiments were performed in vacuum (● $d = 1500\,\text{nm}$, ▲ $d = 300\,\text{nm}$, $p < 10^{-4}\,\text{mbar}$) and water atmosphere of relative humidity RH ≈ 95% ($T \approx 27°\text{C}$); ■ $d = 300\,\text{nm}$, $p = 35.7\,\text{mbar}$) [*Bäuerle* et al. 2006]

expansion. This is quite understandable from experimental observations. With many systems investigated so far, local substrate damage and the formation of craters is observed - even with fluences $\phi \lesssim \phi_{th}^{a}$ where ϕ_{th}^{a} is the fluence for *uniform* substrate damage/ablation. Thus, for such systems, DLC is *not*, or not only, based on thermal expansion. Apparently, local substrate ablation plays an important or even dominating role. Clearly, due to local field enhancement, the fluence underneath the particle, ϕ(local), exceeds the incident uniform fluence ϕ(uniform). Thus, ϕ_{th} (cleaning) $< \phi_{th}^{a}$. Figure 23.7.4 shows the threshold fluence for cleaning of Si substrates from SiO_2 particles together with the cleaning threshold calculated on the basis of particle removal by local ablation. There is still no quantitative agreement with the experimental data. However, these calculations yield a more consistent description of the dependence of ϕ_{th} (cleaning) on particle size. The situation may be even more complicated. As investigated by *Schrems* et al. (2003), cleaning thresholds may increase with storage time due to plastic deformations of particulates. Detailed measurements have been performed for SiO_2 particulates on Si substrates.

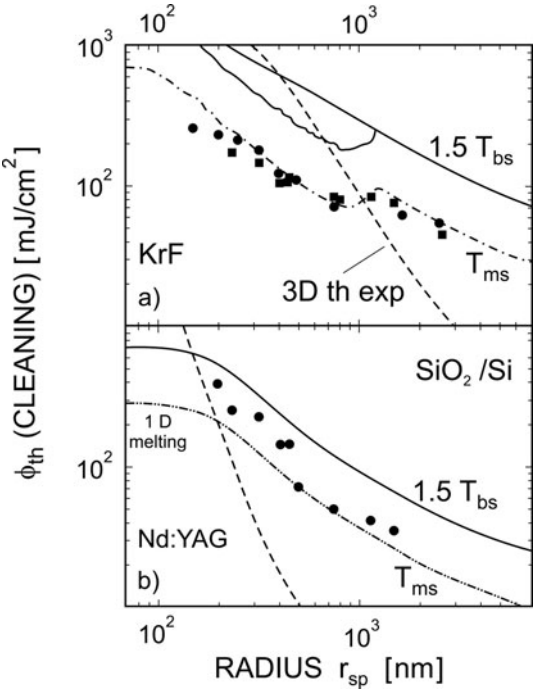

Fig. 23.7.4 Calculated and measured dependences of cleaning thresholds for SiO_2 particles on Si for two different wavelengths. *Dashed curve* – threshold based on 3D thermal expansion of the substrate and particle. *Dash-dotted* curves refer to local melting of the substrate at T_{ms}. *Solid curves* – threshold based on the evaporation of the substrate at T_{bs}. (**a**) $\lambda = 248$ nm. *Thin solid curve* uses exact averaged Mie results. (**b**) Same as (**a**) but for $\lambda = 532$ nm [after *Arnold* et al. 2004]

Particulate Absorption

Experimental investigations using strongly absorbing particulates on transparent or almost transparent substrates have been performed, e.g., for Cu and Al particles on SiO_2 substrates [*Lu* et al. 1998b] and for PI particles on PMMA [*Fourrier* et al. 2001]. In both cases, KrF-laser radiation has been employed.

Here, the situation is often quite similar to that described before. However, with strong particulate absorption, cleaning may become determined by *vaporization/ablation* of the particle, in particular when its thermal contact to the substrate is weak and/or if this substrate is a thermal insulator. This mechanism differs significantly from that described above. The fluence that causes vaporization of the particulate can be estimated from the energy balance and is given by

$$\phi_{\mathrm{th}} \approx \frac{\rho}{A} r \left[c_p T_{\mathrm{v}} + \Delta H_{\mathrm{v}} \right] \tag{23.7.10}$$

The physical parameters for the particulate, mainly A, which enter this equation make this process very selective with respect to the type of particulates. It is evident, however, that all of these quantities change during evaporation.

In all cases of dry cleaning, recondensation of particulates on the cleaned substrate can be drastically reduced by employing vacuum conditions or a laminar flow of H_2 or He and an appropriate geometry of the setup with $\hat{\boldsymbol{n}} \parallel \boldsymbol{g}$ or $\hat{\boldsymbol{n}} \perp \boldsymbol{g}$ ($\hat{\boldsymbol{n}}$ is the surface normal and $\boldsymbol{g}$ the acceleration due to gravity).

Particulate and Substrate Absorption

The removal of metallic particles such as Au, Cu, and W from Si [*Curran* et al. 2002] and metal surfaces has been studied by using the fundamental and harmonics of Nd:YAG-laser radiation. Here, it has been found that substrate damage can be often reduced by using instead of perpendicular laser-light incidence glancing angles [*J. Lee* et al. 2000]. In this case, field enhancement effects are diminished. Inclined laser irradiation at photon energies that excite surface plasmons for cleaning of Si from 40 nm Au particles however, was not possible without surface damages [*Luk'yanchuk* et al. 2007b].

Cleaning was also demonstrated by exciting surface acoustic waves (SAW) by means of a *focused* laser beam [*Kolomenskii* et al. 1998]. In this technique, *nonlocal* cleaning within the region of the propagating SAW can be achieved. Cleaning covers an area of only several millimeters around the laser-irradiated spot and causes substrate damage as well.

Acoustic Laser Cleaning

A possibility to avoid local substrate damages due to the enhancement of the laser fluence by the optical near field of particulates, is acoustic laser cleaning (ALC). Here, a laser-induced plasma generated at the rear side of the sample excites an acoustic wave which propagates through the sample and may 'kick off' the

particulates from the surface. Thus, the mechanism of particle detachment is quite similar to that expected for front side illumination of the substrate and thermal expansion only. ALC has been studied for Si substrates contaminated with PS (polystyrene) particulates [*Geldhauser* et al. 2007].

23.7.3 Steam Cleaning

Laser cleaning can be significantly enhanced by a liquid film that is deposited, e.g. via a nozzle, onto the particle-contaminated surface prior to pulsed-laser irradiation. This technique is denoted as steam laser cleaning (SLC). High cleaning efficiencies have been achieved with strongly *absorbing substrates* and liquid films that are transparent at the incident laser wavelength. For example, with KrF- and Nd:YAG-laser radiation, particulates of Au, Cu, Al_2O_3, Fe_2O_3, Si, PS, etc. have been efficiently cleaned off from different metal substrates and, in particular, from Si wafers and Si membranes [*Lang* et al. 2003; *Leiderer* et al. 2002; *Neves* et al. 2002; *Allen* et al. 1997; *Tam* et al. 1992]. In most experiments, the liquid film is typically a few tenths to several μm thick and consists of water mixed with 10–20% alcohol. The alcohol improves substrate wetting. Figure 23.7.5 shows, for Si substrates, the dependence of the cleaning efficiency on laser fluence for particles of different materials (Al_2O_3, SiO_2, PS) and *different* sizes (60–800 nm) and geometries (spherical SiO_2 and PS and arbitrarily shaped Al_2O_3). In contrast to the situation in DLC, there seems to be the *same* cleaning threshold for *all* types and sizes of particles. This permits one to use lower laser fluences. This is particularly important in connection

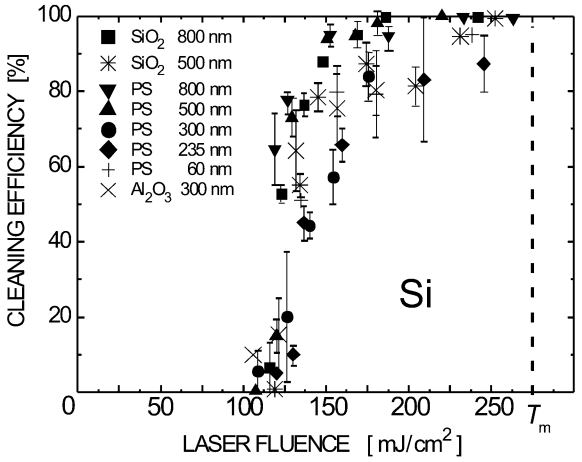

Fig. 23.7.5 Steam laser cleaning (SLC) efficiency achieved on Si wafers contaminated with various colloidal particles. Here, 20 pulses of 532 nm Nd:YAG-laser radiation have been employed (τ_ℓ (FWHM) = 7 ns). T_m is the melting threshold for a clean Si surface. The sprayed-on liquid film did consist of a mixture of water and 10% isopropanol. Note that the cleaning threshold is the same for all types of particles [*Leiderer* et al. 2002]

with substrate damage or/and in situations where particles melt or/and react or form an alloy with the substrate material. For other laser wavelengths and other types of substrate materials and liquid films, this threshold fluence may change significantly.

Steam laser cleaning is based on the momentum transfer during explosive evaporation of the liquid. With water films very high transient pressures caused by superheated water at the liquid-solid interface can be achieved (Fig. 23.7.2b). With superheating to 370°C [$T_{cr}(H_2O) \approx 375°C$] the peak pressure would be about 200 atm [$p_{cr}(H_2O) \approx 220$ atm]. The analysis of the results presented in Fig. 23.7.5 may, however, indicate that the detachment of particulates is not related to this pressure but to the pressure wave which results from fast-growing bubbles at temperatures $T > T_b$. This pressure was measured to be 5–10 atm [*Leiderer* et al. 2002, 1998; *Park* et al. 1996a, b]. For micron-sized particles, this would correspond to maximum accelerations of 10^{10}–10^{11} cm/s^2. Thus, although the adhesion forces for the different types of particles vary by more than an order of magnitude, the cleaning forces are so high that they exceed by far the adhesion forces for *all* particulates. Systematic investigations on the problem of substrate damage in SLC and the influence of cavitation effects are still lacking.

Absorbing Liquid Films

Steam laser cleaning using a strongly absorbing liquid film widely avoids substrate absorption. Thus, it can be employed also with heat sensitive and/or inhomogeneous substrates. The most detailed experiments have been performed with 1 μm thick water films and infrared light tuned to the absorption maximum of a line at $\lambda \approx 2.94$ μm. The samples did consist of polystyrene (PS) particles placed on (transparent) glass or Si substrates [*Frank* et al. 2008]. The cleaning thresholds for both substrates did increase with decreasing particle sizes between 1 μm and 300 nm. This is in agreement with what is expected from Eq. (23.7.8). It is, however, in contrast to the situation shown in Fig. 23.7.5. Apparently, superheating of the liquid film from the top is less efficient for cleaning than superheating and bubble formation at the substrate-liquid interface. This is supported by experiments using front side and rear side illumination. In the latter case, the corresponding threshold fluences are significantly smaller. The experiments prove that heating of the liquid volume underneath the particle plays a dominant role.

Cleaning experiments using water films, 10.6 μm CO_2-laser radiation and Si substrates covered with different types of particles with sizes ranging from about 0.1 to 10 μm were less efficient, as expected, but are in qualitative agreement with the above findings [*Boughaba* et al. 1999; *Allen* et al. 1997].

23.7.4 Wet Cleaning

A technique which combines some of the advantages of DLC and SLC and which avoids some of their disadvantages is wet laser cleaning (WLC). In WLC, the substrate is immersed in an atmosphere of high relative humidity (RH) of water with, typically, RH $\gtrsim$ 95%. The technique is advantageous for small particulates

whose mass is comparable to the mass of the explosively evaporated water in the interstice between the particulate and the substrate. With this condition, the threshold for cleaning is well below that for DLC in vacuum. For SiO_2 on Si substrates this effect becomes significant for particle sizes $d \lesssim 700\,\text{nm}$ [*Schrems* et al. 2003]. Figure 23.7.3 shows this influence for 300 nm particles. For complete wetting, the mass of capillary condensed water is $m_\ell \approx 4\pi r \rho_\ell \; {R_\text{K}}^2$ where $R_\text{K} \approx 0.52\,\text{nm/ln}\,(\text{RH}^{-1})$ is the Kelvin radius. With RH = 95% we find $R_\text{K} = 10\,\text{nm}$. Further investigations in this field, in particular for particle sizes $d \lesssim 100\,\text{nm}$ and humidities RH > 95%, would be valuable. In any case, in comparison to SLC, the technique does not require synchronization between (liquid) film deposition and the laser pulse. Overall surface contamination is also widely avoided. By using an irradiation scheme that causes optical breakdown near the meniscus of the liquid, removal of 50 nm PS particles from Si has been demonstrated without evidence for substrate damage [*Luk'yanchuk* et al. 2007b].

23.7.5 Matrix Cleaning

In matrix-assisted laser cleaning (MLC) the contaminant particles are embedded in a solid layer which is condensed on the substrate surface. The technique has some similarities to MALDI (Sect. 30.1). Experiments have been performed with dry ice (CO_2) [*Luk'yanchuk* et al. 2007b; *Graf* et al. 2005]. Sublimation of the CO_2 layer by the laser pulse cleans off the particles. Cleaning of Si wafers from PS particles with diameters down to 50 nm has been demonstrated. Further experimental investigations must clarify whether substrate damage can really be avoided by this technique.

Chapter 24
Doping

As with laser-induced structural transformations, laser-induced surface doping takes advantage of the high heating and cooling rates that can be achieved with lasers. The short temperature cycles enable one to produce very shallow, heavily doped layers within solid surfaces. Pulsed lasers are mainly used for both large-area doping and local doping by projection. Cw lasers allow local doping by direct writing. In any case, the absorbed light intensity must be high enough to substantially heat or even melt the sample surface in order to allow dopant incorporation by high-temperature diffusion or liquid-phase transport. The dopant source may be an adsorbate, a gas, a liquid, or an evaporated film.

Doping from *gas-phase* precursors requires thermal or photochemical decomposition of parent molecules. With surface melting, gas-phase transport of species is usually rate-limiting, in particular if convective fluxes within the molten layer become effective. Efficient surface doping based on solid-phase diffusion of species has been observed for some types of polycrystalline materials, and for III–V semiconductors with dopants such as Cd, S, Se, and Zn.

The *thickness* of the doped layer can be controlled via the laser-beam dwell time. With fixed dwell time, the dopant density within the solid can be tuned via the concentration of precursors within the gas or liquid, via the thickness of the evaporated film, etc.

This chapter deals with the incorporation of *electrically active* dopants into semiconductor surfaces and, in particular, with Si. This is based on the special importance of Si and also on its excellent stability, which allows one to study wide parameter ranges.

The deposition of doped films is discussed in Chaps. 19, 20, and 22. Surface doping by ion implantation in combination with laser annealing is described in Chap. 23. Sheet doping in connection with thin-film coating has been studied for metals, particularly for stainless steel. This is included in Chap. 25.

D. Bäuerle, *Laser Processing and Chemistry,* 4th ed.,
DOI 10.1007/978-3-642-17613-5_24, © Springer-Verlag Berlin Heidelberg 2011

24.1 Solid-Phase Diffusion

Surface doping by solid-phase diffusion is schematically shown in Fig. 24.1.1. The starting material shall consist of a semi-infinite substrate, S, that is covered with a layer of the dopant, A. Due to laser heating, species A will diffuse into S and vice versa. In the 1D case, the density profile of A in S can be described by $N_\mathrm{A} \equiv N_\mathrm{A}(z,t)$. Because of the temperature gradients in the z direction, N_A must be calculated by solving the diffusion equation

$$\frac{\partial N_\mathrm{A}(z,t)}{\partial t} = \frac{\partial}{\partial z}\left(D_\mathrm{s}(T(z,t))\frac{\partial N_\mathrm{A}(z,t)}{\partial z}\right) \tag{24.1.1}$$

simultaneously with the heat equation. $D_\mathrm{s}(T(z,t))$ is the diffusion coefficient for species A in S (we denote the coefficient for solid-phase diffusion by D_s and for liquid-phase diffusion by D_l). The temperature dependence of D_s can be approximated by

$$D_\mathrm{s}(T(z,t)) = D_0 \exp\left(-\frac{\mathscr{E}_\mathrm{d}}{T(z,t)}\right) . \tag{24.1.2}$$

The initial condition shall be characterized by

$$N_\mathrm{A}(z, t=0) = 0 \quad \text{with } z > 0 . \tag{24.1.3}$$

The concentration of species A at the interface $z = 0$ shall be constant, and it shall vanish far away from the surface, i.e.,

$$N_\mathrm{A}(0,t) = N_\mathrm{A}^0 \quad \text{and} \quad N_\mathrm{A}(\infty,t) = 0 . \tag{24.1.4}$$

The heat equation can be written in analogy to (2.2.1).

Let us consider surface doping where we can set $h_1 \approx 0$. Because the heat-diffusion length, l_T, or the optical penetration depth, l_α, is much larger than the

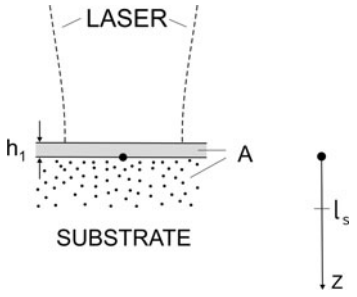

Fig. 24.1.1 Surface doping by laser-induced solid-phase diffusion. The semi-infinite substrate is covered with a dopant layer, A

effective diffusion length of dopants, i.e., $l_s \ll \max\{l_\alpha, l_T\}$, the temperature within the depth l_s can be assumed to be uniform and the diffusion coefficient becomes independent of coordinate z. The solution of the boundary-value problem is then

$$N_A(z,t) = N_A^0 \operatorname{erfc}\left(\frac{z}{l_s}\right) . \tag{24.1.5}$$

The spatial variation of N_A is schematically shown in Fig. 24.1.2 by the solid curve. The effective diffusion length can be approximated by $l_s \approx 2(\langle D_s \rangle)^{1/2}$, where $\langle\rangle$ denotes the time-average, i.e.,

$$\langle D_s \rangle = \frac{1}{t} \int_0^t D_s(T(0,t'))\,dt' . \tag{24.1.6}$$

For pulsed-laser irradiation with uniform intensity and constant absorptivity, the diffusion length l_s at time t can be estimated from [*Libenson* and *Nikitin* 1973]

$$l_s \approx 2\left[\frac{[\Delta T(t)]^2}{\mathscr{E}_d \dot{T}(t)} D_s(T(t))\right]^{1/2} . \tag{24.1.7}$$

For *surface absorption* this yields

$$l_s \approx 2\left[\frac{2\Delta T(0)}{\mathscr{E}_d} D_s(T(0))t\right]^{1/2} , \tag{24.1.8a}$$

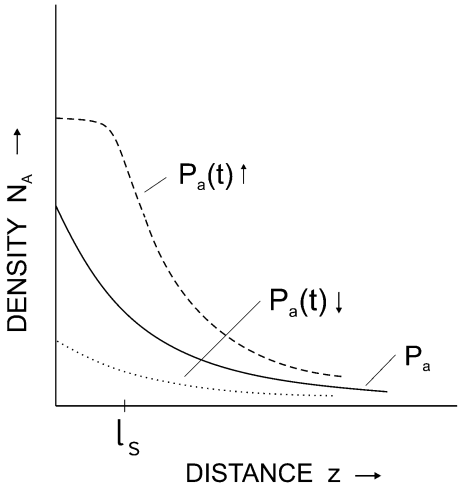

Fig. 24.1.2 Concentration profiles observed in laser-enhanced solid-phase diffusion; z is the distance from the substrate surface (Fig. 24.1.1). The absorbed laser power, P_a, can be constant during the laser-beam dwell time, τ_ℓ (*solid curve*); it can increase (*dashed curve*) or decrease (*dotted curve*)

where $T(0) \approx \Delta T(0) = I_0 A l_T/\sqrt{\pi}\kappa$ and $l_T \approx 2(Dt)^{1/2}$. For *finite absorption* with $l_\alpha \gg l_s$, we obtain

$$l_s \approx 2\left[\frac{\alpha I}{\mathscr{E}_d \varrho c_p} D_s(T(t))t^2\right]^{1/2} . \tag{24.1.8b}$$

For Si and dopant atoms such as B, Bi, Ga, In, P, and Sb, typical values of D_s at temperatures well below melting are within $10^{-12}\,\mathrm{cm}^2/\mathrm{s} < D_s(T \ll T_m) < 10^{-10}\,\mathrm{cm}^2/\mathrm{s}$. For temperatures near T_m typical values are $10^{-6}\,\mathrm{cm}^2/\mathrm{s} \leq D_s(T \leq T_m) \leq 10^{-5}\,\mathrm{cm}^2/\mathrm{s}$ [*Kimerling* and *Benton* 1980]. With $\Delta T(0) = 10^3\,\mathrm{K}$, $D_s = 10^{-6}\,\mathrm{cm}^2/\mathrm{s}$, $\mathscr{E}_d = 10^4\,\mathrm{K}$ and $\tau_\ell = 10^{-3}\,\mathrm{s}$, we obtain $l_s \approx 0.3\,\mu\mathrm{m}$.

The preceding treatment *ignores* a number of important effects:

- The rate of dopant diffusion through the surface $z = 0$ is, in reality, finite. Thus, (24.1.4) must be replaced by a boundary condition which depends on temperature.
- Interdiffusion of A and S and temperature dependences in R, α, etc., change the optical properties of the solid. Thus, depending on the particular system, the absorbed laser power will increase (positive feedback) or decrease (negative feedback) during the laser-beam dwell time. Changes in absorbed laser power result in changes in the temperature distribution and thereby in the diffusion profile of species. This is schematically shown in Fig. 24.1.2 by dashed and dotted curves for positive and negative feedback, respectively.
- Stress gradients related to thermal expansion increase, in general, solid-phase diffusion [*Shewmon* 1963]. They can be estimated by solving the problem of thermoelasticity. Stress gradients can also decrease the activation energy for diffusion, change the optical properties of the material, etc.
- Defects such as vacancies, dislocations, microcracks, etc., may significantly enhance solid-phase diffusion of dopants. Defects can be generated by laser-induced heating, stresses, shock waves, etc. Thermally induced defects are localized near the solid surface. Near melting, the concentration of vacancies can be very high, in metals and semiconductors up to 10^{19} or $10^{20}\,\mathrm{cm}^{-3}$. Due to thermal diffusion and stress effects, the real concentration of vacancies can be much higher than their equilibrium concentration. The diffusion coefficient can then be approximated by

$$D_s^{ne} = D_s \frac{N^{ne}}{N} ,$$

  where N^{ne} and N denote non-equilibrium and equilibrium concentrations of defects, respectively. N^{ne}/N can be of the order of 10^5–10^6. When the density of vacancies exceeds a critical value, condensation and droplet formation may occur. This is well known from radiation damage caused by particle bombardment. It is often termed *cold melting*.
- Laser-induced shock waves can produce a high density of defects within a *large* volume of the solid.

- Electronic or vibrational excitations can induce charge-transfer effects, generate electron–hole pairs, vacancies, etc., and may thereby enhance diffusion of host or impurity atoms/ions.
- Compound formation in laser alloying and synthesis can result in the formation of various kinds of defects which also enhance diffusion.

Because of the numerous contributions to solid-phase diffusion, an estimate of the density N_A as presented at the beginning of this section cannot be thought of as quantitative.

24.2 Liquid-Phase Transport

Surface melting considerably increases processing rates in surface doping and alloying. This is due to enhanced transport by both diffusion and convection (Chap. 10). For surface alloying from thin evaporated layers, the melt depth, h_l, must exceed h_1.

The diffusion length of species within the melt can be estimated from $l_l \approx 2(D_l/\Delta t_m)^{1/2}$, where Δt_m is the time during which the surface stays molten.

The laser fluences commonly employed in these processing applications are between 0.1 and 10 J/cm^2. In the simplest approximation, h_l can be estimated from (10.1.3), and Δt_m from (10.2.1).

Liquid-phase diffusion coefficients exceed solid-phase diffusion coefficients near melting by one to three orders of magnitude. In molten metals, typical values of D_l are between 10^{-5} and 10^{-4} cm^2/s. In Si, liquid-phase diffusion coefficients for dopant atoms such as B [D_l(B) $\approx 2.5 \times 10^{-4}$ cm^2/s], Bi, Ga, In, P [D_l(P) $\approx D_l$(B)] and Sb are almost equal and typically in the range $10^{-4}\,\text{cm}^2/\text{s} \leq D_l \leq 10^{-3}\,\text{cm}^2/\text{s}$.

Experimental investigations have demonstrated, however, that in surface doping and alloying species A and S are often well mixed within the *total* melt depth. This fast mixing can only be explained by convective fluxes or surface instabilities within the liquid layer. Remnants of convective fluxes and instabilities frequently appear as cellular structures on the resolidified surface [*Fogarassy* et al. 1985]. The flow velocities, v_c, are between 1 cm/s and a few m/s (Sect. 10.4). For a homogeneous distribution of A in S, convective mixing must take place within a depth $l_c \approx v_c \Delta t_m \approx h_l$.

24.3 Sheet Doping

Large-area thin-layer doping (sheet doping) has mainly been performed with (pulsed) UV-laser radiation, which is strongly absorbed in semiconductors and also photodissociates most of the relevant precursor molecules.

24.3.1 Silicon

Surface doping of Si has been demonstrated with adsorbed layers, gases, liquids, and solid films. For fs-laser doping using above threshold fluences see Sect. 28.7.

Adsorbed Layers, No Ambient Medium

Adsorbed layers provide a finite source of dopant and permit extremely shallow doping profiles to be generated. Because the precursor gas is pumped off prior to laser-light irradiation, efficient adlayer doping requires strong adsorption of parent molecules (Sect. 20.2.1). Most of the experiments were performed with excimer lasers, using BCl_3, B_2H_6, BF_3, and PCl_3 as precursors [*Deutsch* 1984].

Gaseous Ambient

Gas-phase doping of Si from AsH_3, BCl_3, BF_3, B_2H_6, PCl_3, and PH_3 has been demonstrated mainly with ArF-laser radiation. BF_3, which does not absorb 193 nm radiation, is thermally decomposed at the gas–solid interface. The other molecules are directly photodissociated by ArF-laser radiation [*Slaoui* et al. 1990].

Figure 24.3.1a exhibits SIMS profiles of the B concentration obtained with (100) n-type Si wafers. With the laser parameters employed, the Si surface is melted [$\phi_m(193\,\text{nm}) \approx 0.25\,\text{J/cm}^2$]. From Fig. 24.3.1a we estimate $h_l^{max} \approx 0.4\,\mu\text{m}$. This value is close to that calculated from (10.1.3c) with $\phi_a \rightarrow (\phi - \phi_m)(1 - R)$ and $R = 0.7$. From (10.2.6b) we find the solidification time $\tau_s \approx 60\,\text{ns}$. The time during which the surface is molten is $\Delta t_m \approx \tau_\ell + \tau_s \approx 80\,\text{ns}$. The estimated diffusion length within the liquid, $l_l \approx 2(D_l \Delta t_m)^{1/2} \approx 0.08\,\mu\text{m}$, is in good agreement with

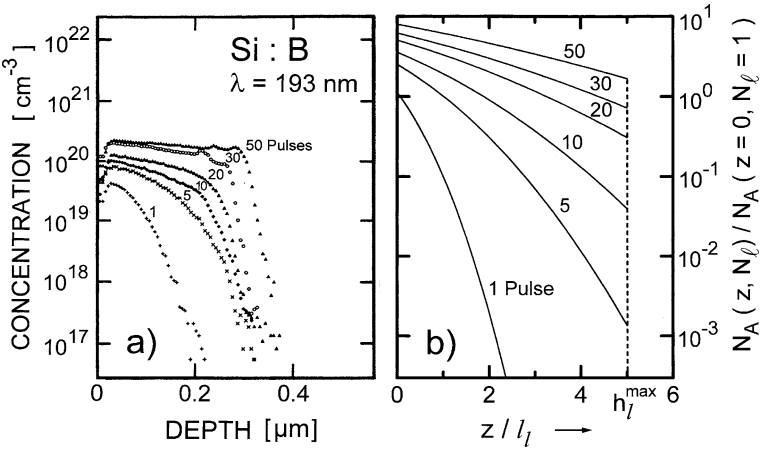

Fig. 24.3.1 a, b ArF-laser-induced doping of (100) Si with B. (**a**) SIMS profiles of the B concentration [$\phi \approx 1\,\text{J/cm}^2$, $\tau_\ell \approx 21\,\text{ns}$, $\nu_r = 2\,\text{Hz}$, $p(BCl_3) \approx 6.7\,\text{mbar}$] [*Slaoui* et al. 1990]. (**b**) Normalized concentration profile of B calculated from (24.3.3) [*Arnold* and *Bäuerle* 1994]

the doping depth derived from the single-pulse data. Because the observed doping depth agrees well with l_l but not with $h_l^{\max}$, convection seems to be unimportant in these experiments. Thus, we can calculate the doping profile in a similar way as in Sect. 24.1. With a gaseous ambient, however, it is more reasonable to assume instead of (24.1.4) a constant surface *flux* of species A, i.e.,

$$J_{\mathrm{A}}(0,t) = J_{\mathrm{A}}^0 \,. \tag{24.3.1}$$

The solution is then

$$J_{\mathrm{A}}(z,t) = -D_l \frac{\partial N_{\mathrm{A}}(z,t)}{\partial z} = J_{\mathrm{A}}^0 \,\mathrm{erfc}\left(\frac{z}{l_l}\right) \tag{24.3.2}$$

and

$$N_{\mathrm{A}}(z,t) = \frac{J_{\mathrm{A}}^0 l_l}{D_l(0,t)} \mathrm{i\,erfc}\left(\frac{z}{l_l}\right) \,. \tag{24.3.3}$$

This function is shown in Fig. 24.3.1b. It is in excellent agreement with the experimental data for a single pulse. For *multiple-pulse* irradiation we estimate $\Delta t_{\mathrm{m}}(N_\ell) \approx N_\ell \Delta t_{\mathrm{m}}$. As a consequence, dopant atoms further diffuse into the molten layer and we can set $l_l(N_\ell) \approx l_l\sqrt{N_\ell}$. Thus, in contrast to (24.1.5), the concentration of dopants at the surface, $N_{\mathrm{A}}(0,t) \equiv J_{\mathrm{A}}^0 l_l(N_\ell)/D_l \approx J_{\mathrm{A}}^0 l_l\sqrt{N_\ell}/D_l$, *increases* with pulse number. This result is also in agreement with the experimental data. With a large number of laser pulses, the concentration of dopants becomes almost uniform within the molten layer and drops off sharply beyond it because $D_l \gg D_{\mathrm{s}}$. This transition is observed when $l_l\sqrt{N_\ell} \approx h_l^{\max}$, i.e., with $N_\ell \approx 25$ pulses. Due to the cut-off in diffusion with $z \approx h_l^{\max}$, the theoretical curves become meaningless for $z > h_l^{\max}$.

Figure 24.3.2 shows the sheet resistance of (100) Si versus the number of ArF-laser pulses for BF_3 and B_2H_6. The initial drop-off in sheet resistance is much slower for BF_3 compared to B_2H_6, in spite of the much higher pressure employed. This demonstrates that photolysis of B_2H_6 substantially enhances the doping efficiency. With B_2H_6 the surface carrier concentration saturates at about 10^{21} B atoms/cm^3. This value exceeds the equilibrium solubility of B in Si at 1,300°C by about a factor of two. From electrical measurements and SIMS profiles, it was estimated that about 70% of the B atoms incorporated are electrically active. With very high doping densities, the mobility of carriers is reduced due to scattering.

Adsorbed molecules play an important role in systems such as Si:BCl_3. This follows from the pressure dependence of the sheet resistance, which was found to be in qualitative agreement with adsorption isotherms [*Deutsch* 1984].

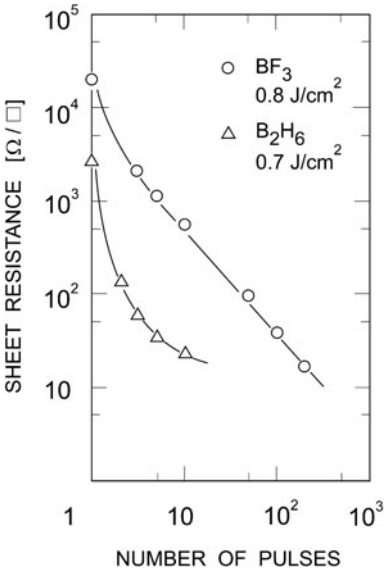

Fig. 24.3.2 Sheet resistance versus number of laser pulses. The partial pressures of BF_3 and B_2H_6 precursors were about 67 and 6.7 mbar, respectively [*Matsumoto* et al. 1990]

Liquid Ambient

Liquid-phase doping of Si with P and Sb has been demonstrated by *Stuck* et al. (1981). The doping solutions were either tributyl-phosphate ($C_{12}H_{27}O_4P$) with 2.5×10^{21} P atoms/cm^3, or $SbCl_3$ with 1.5×10^{21} Sb atoms/cm^3 in ethanol. Irradiation was performed with Q-switched ruby laser light ($\phi \approx 1-2\,\mathrm{J/cm^2}$, $\tau_\ell \approx 20\,\mathrm{ns}$), which is either only very slightly or else not at all absorbed by these liquids. The sheet resistances of P and Sb doped layers were $120\,\Omega/\square$ and $60-80\,\Omega/\square$, respectively.

Solid Films

Doping of Si with Al, B, Bi, Ga, In, P, Sb and Se has also been performed by laser-induced heating of spun-on or evaporated dopant films [*Tabbal* et al. 2010; *X. Zhang* et al. 1996]. Some of the experimental results are in reasonable agreement with model calculations and similar to those obtained by laser annealing of ion-implanted Si surfaces.

Applications

Laser-induced sheet doping of Si can be used to produce very shallow junctions [*Bollmann* et al. 1993; *Kramer* et al. 1993; *Matsumoto* et al. 1990]. The I–V characteristics of pn-junction diodes fabricated by ArF-laser doping from B_2H_6 is depicted in Fig. 24.3.3.

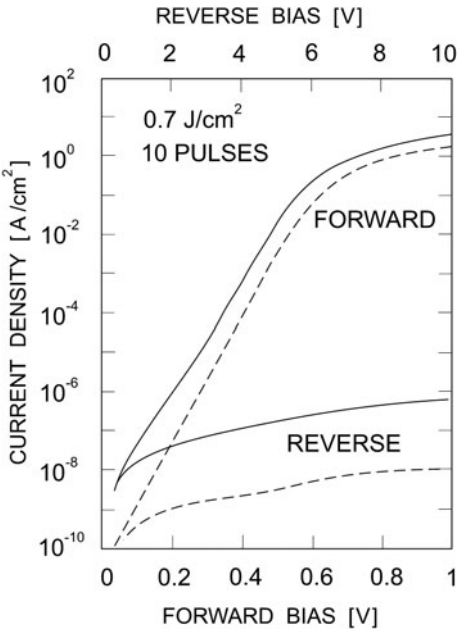

Fig. 24.3.3 I–V characteristics of pn-junction diodes fabricated by ArF-laser doping of Si in B_2H_6. The surface carrier concentration is $\approx 10^{21}\,cm^{-3}$ and the junction depth $\approx 0.1\,\mu m$. Non-annealed (*solid curves*) and annealed (800°C, 30 min, *dashed curves*) samples are shown [*Matsumoto* et al. 1990]

24.3.2 Compound Semiconductors

Laser-induced sheet doping of compound semiconductors is more problematic. With the laser fluences necessary for efficient in-diffusion of dopants, the surface may decompose via selective evaporation of the more volatile component. Additionally, laser-induced heating can introduce slip planes and other defects which degrade the electrical properties of these materials. Doping has mainly been studied for GaAs and InP by employing gas-phase precursors.

Doping of GaAs has been performed with frequency-doubled Nd:YAG lasers (with and without blocking the fundamental line) and excimer lasers.

The formation of n-type layers has been demonstrated with dopants such as Si [*Sugioka* and *Toyoda* 1994], Se [*Kräutle* et al. 1985], S [*S.K. Zhang* et al. 1994], and Ge [*Garcia* et al. 1988]. The Se doping source was gaseous H_2Se diluted in $H_2 + AsH_3$. During the 3 ns Nd:YAG-laser pulse employed in these experiments, the surface is heated to temperatures near melting. H_2Se molecules adsorbed on the GaAs wafer thermally decompose and Se diffuses into the surface. The loss of As during heating is compensated by the supply of As from adsorbed AsH_3. With 532 nm radiation, surface layers with a thickness less than 0.02 μm and with more than 10^{20} Se atoms/cm^3 have been produced. Thicker dopant profiles have been

obtained by simultaneous illumination with the 1064 nm fundamental line. Similar experiments have been performed with $Zn(C_2H_5)_2$.

Acceptor doping of GaAs has been demonstrated for C [*Sugioka* et al. 1989] and Zn [*Beneking* 1984]. KrF-laser-induced doping from gaseous CH_4 yielded a sheet resistance as low as $165\,\Omega/\square$ and a surface carrier density of $8 \times 10^{14}\,\mathrm{cm}^{-2}$. The doped layer was about $0.05\,\mu\mathrm{m}$ thick and had a surface concentration of about 10^{21} atoms/cm^3. The maximum efficiency of active dopants was 69%. In this way, non-alloyed ohmic contacts can be produced. No significant deterioration of the GaAs surface was observed. Similar results have been obtained for Si doping from SiH_4.

Formation of p-type layers in InP was demonstrated by ArF-laser photolysis of $Cd(CH_3)_2$ [*Deutsch* 1984].

24.4 Local Doping

Local doping of semiconductors by cw-Ar^+-laser direct writing has been demonstrated for lateral dimensions down to submicrometer levels. Boron doping patterns in (111) and (100) Si have been produced by local pyrolysis or photolysis of BCl_3 at gas pressures of about 10^2 mbar [*Ehrlich* and *Tsao* 1982]. For 515 nm Ar^+-laser radiation *below* the melting intensity, the doped region was about $0.6\,\mu\mathrm{m}$ wide. This width is considerably smaller than the laser focus employed, $2w_0 \approx 1.8\,\mu\mathrm{m}$. The increase in spatial resolution is consistent with the exponential dependence of the diffusion coefficient on temperature (Sect. 5.3.6; the activation energy for isothermal diffusion of B in Si is $\Delta E_\mathrm{d} \approx 3.69\,\mathrm{eV}$). A depth profile of the B density determined by SIMS analysis is shown in Fig. 24.4.1.

Direct cw-laser doping of InP with Cd and Zn has also been demonstrated [*Ehrlich* et al. 1980]. In these experiments 257 nm frequency-doubled Ar^+-laser radiation was used collinearly with the 515 nm fundamental output. By controlling the individual beam intensities, it was possible to vary independently the flux of Cd atoms produced by photodissociation of $Cd(CH_3)_2$ at or near the gas–solid interface, and the surface temperature. In fact, electrical measurements have revealed a linear increase in dopant concentration (up to $> 10^{19}$ Cd atoms/cm^3) with the 257 nm light flux. The 515 nm radiation controls the surface temperature and thereby the spatial width of the doped region. The dominant mechanism for dopant incorporation seems to be *solid-phase* diffusion due to thermal, stress, and concentration gradients.

Local doping of GaAs with Si has been demonstrated by KrF-laser light projection [*Sugioka* and *Toyoda* 1990] and with Zn by Ar^+-laser direct writing [*Licata* et al. 1990]. Linewidths between about 0.3 and $3\,\mu\mathrm{m}$ have been achieved. Local doping of Si was simulated by *Fell* and *Willeke* (2010). Their calculations are in good agreement with concentration profiles of P doped Si samples ($\lambda = 355\,\mathrm{nm}$ Nd:YAG, $\phi = 1\mathrm{J/cm}^2$, $\tau_\ell = 40\,\mathrm{ns}$) measured by SIMS.

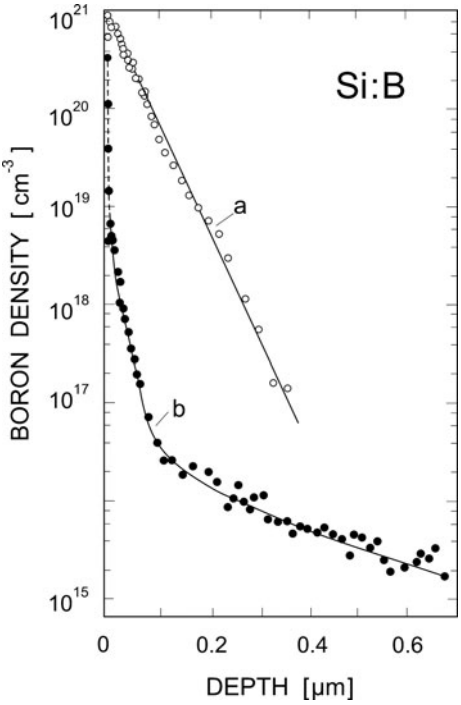

Fig. 24.4.1 Boron depth profiles determined by SIMS analysis of a raster-scanned 2000 Ω cm (111) Si sample. Scan speeds were 19 μm/s (*a*), 440 μm/s (*b*) [*Ehrlich* and *Tsao* 1982]

24.5 Laser Implantation

Laser implantation (LI) denotes a technique where a substrate is doped with material ablated from a target in close proximity. The experimental arrangement is the same as in laser-induced forward transfer (Fig. 22.8.1). This technique has been demonstrated for various organic substrate and target (source) films, including photochromic molecules [*Fukumura* et al. 1998]. High-resolution local doping has been achieved by using, instead of a target film, a hollow fiber filled at the tip with solution of the organic dopant (Fig. 5.2.1d). Injection of organic compounds into biological tissues [*Goto* et al. 1999] and of nanoparticles into single animal cells [*Yamaguchi* et al. 2008] has been demonstrated as well.

Chapter 25
Cladding, Alloying, and Synthesis

The emphasis of this chapter is on laser-assisted cladding, alloying, and synthesis of stoichiometric compounds. The main objective of laser-assisted cladding is the coating of substrates with thick films of metals or alloys. Laser-assisted alloying is applied for both surface modification and compound formation.

In the experiments discussed throughout this chapter, the material to be added to the substrate, or the starting material, is mainly in *solid* form. It can be a powder, a single layer, a stack of several layers, a solid solution, etc. In most of these applications, the laser powers employed cause surface melting. With cw-laser irradiation and long laser-beam dwell times, materials alloying and synthesis may take place via solid-phase diffusion.

25.1 Laser-Assisted Cladding and Sintering

Laser-assisted cladding denotes the coating of a substrate with a thick metal or alloy film (clad). The coating material is either predeposited on the substrate surface in the form of a powder or a solid layer or is only fed in during the process. An arrangement for the latter technique is schematically shown in Fig. 25.1.1a. The technique is based on laser-induced melting of both the coating material and a *shallow* layer of the substrate surface. Fusion bonding guarantees good adhesion of the clad to the substrate. In contrast to surface alloying, intermixing of materials is minimized in order to avoid degradation of the physical and chemical properties of the clad and the substrate. The lasers mainly employed are CO_2 and Nd:YAG lasers with powers up to 4×10^3 W and beam radii between 0.5 and 3 mm. Substrate velocities are between 0.5 and 5 cm/s. Figure 25.1.1b shows the cladding rate, W_c (cm^2/s), for stainless steel on a mild steel substrate as a function of laser power. The linear behavior can be directly understood from the energy balance (11.1.1), which yields $W_c = 2wv_s = AP/h(\varrho c_p \Delta T_m + \Delta H_m) \propto P$. Typical thicknesses of the clad are between 0.1 and 2 mm. Thicker layers can be built up by repetitive scans. Among the cladding materials most frequently used are alloys of B, C, Co, Cr, Ni, Fe, Si, and W.

D. Bäuerle, *Laser Processing and Chemistry,* 4th ed.,
DOI 10.1007/978-3-642-17613-5_25, © Springer-Verlag Berlin Heidelberg 2011

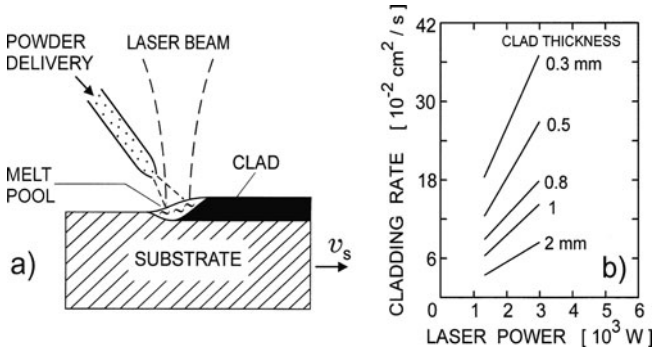

Fig. 25.1.1 (**a**) Laser cladding using powder delivery. (**b**) Cladding rate, W_c, for stainless steel (316 L) on a mild steel substrate as a function of CO_2-laser power ($w = 2.5$ mm) and for various thicknesses of the clad. The coating material was fed in as powder (powder flow ≈ 0.2 g/s, particle velocity ≈ 1.4 m/s) [*Weerasinghe* and *Steen* 1984]

If the coating material is predeposited in the form of a solid layer, the temperature rise induced by a Gaussian laser beam and $v_s w_0/D \ll 1$ can be estimated from (9.4.2) and (9.4.3), or from Fig. 9.4.2. With $v_s w/D \geq 1$ and arbitrary beam shapes, the Green's function given by *Burgener* and *Reedy* (1982) can be used.

Besides of the advantages already mentioned, laser cladding causes low thermal damage to the substrate material, including low material distortions and cracking. It also permits simple automation. The technique can be employed for applications involving wear, erosion, abrasion, corrosion, impact, etc. For further details see *Kim* and *Kweon* (2007), *Steen* (2003), *Schuöcker* (1999), etc. Laser cladding competes with other techniques such as plasma spraying, plasma-CVD (PCVD), and electrochemical plating.

A similar technique is *laser sintering*. Here, the laser light is used to densify a coating – either without melting, or with partial or total melting of the layer. Among the examples are dense films of $La_{0.8}Sr_{0.2}CoO_3$ on a-SiO_2 fabricated from (La, Sr)CoO_3 sol gel coatings [*Zergioti* et al. 1999], electrically conducting thin films and microstructures generated from solution-deposited ZnO [*Pan* et al. 2009] or ink-jet printed metal [*Ko* et al. 2008] nanoparticles. The advantage of using nanoparticles for laser sintering is related to their low melting temperature (Chap. 4). For example, while the melting temperature of (bulk) Au is about 1064°C, nanoparticles of Au with sizes of 2–3 nm start to melt already at 130–140°C. Thus, laser sintering becomes compatible with heat sensitive substrates as, e.g., organic polymers. In combination with laser ablation and/or advanced illumination techniques, using, e.g., digital micromirror devices (DMDs), this process may become attractive for lithography-free fabrication of low cost large-area electronics on flexible substrates [*Pan* et al. 2010].

25.1.1 3D Rapid Prototyping

Laser cladding and laser sintering can be applied for rapid prototyping and rapid manufacturing of three-dimensional (3D) devices. By repetitive scans together with a CAD-program (computer aided design), almost any type of component or device can be built up. By process optimization, the porosity in metal deposits has been diminished to below 0.1% [*Ng* et al. 2009].

25.2 Alloying

Laser alloying can be applied to modify the physical and chemical properties of solid surfaces and to fabricate new metastable materials.

25.2.1 Laser–Surface Alloying

The objective in laser–surface alloying (LSA) is the complete mixing of the added material within the *molten* substrate surface. This is an important difference to laser cladding. Within the alloyed layer, the concentrations of added material and substrate material are of the same order of magnitude – in contrast to surface doping. Most of the investigations have concentrated on the alloying of steel with C, Cr, Mn, Ni, V, and W. Of increasing interest, in particular for automotive and aerospace applications, is the improvement of the wear and corrosion resistances of light metals like Al and Mg. This can be achieved by alloying Al with Ni or Si, and Mg with Al and Ni [*Galun* and *Mordike* 1999]. Improved resistance of Al-alloys against abrasive wear and corrosion can also be achieved by surface nitriding (Sect. 26.2).

LSA enables one to modify surface properties of materials within depths of, typically, 1–2000 μm without affecting the bulk. In order to achieve uniform mixing of the added and the substrate material, the time during which the surface layer remains molten, Δt_m, must be sufficiently long (Chap. 10). Only by this means, can uniform material mixing, which is frequently based on hydrodynamic convective fluxes, take place (Sects. 10.4 and 10.5). The scanning velocities employed are up to some 10 cm/s. With the high cooling rates that can be achieved, material segregation can be widely suppressed. Surface alloying with expensive precursor elements is considerably cheaper than bulk alloying.

High-concentration doping and coating of stainless steel (SUS 304) with Si by KrF-laser irradiation in an SiH_4 atmosphere has been studied by *Jyumonji* et al. (1995a). The hardness and chemical stability of the surface with respect to etching in aqueous HCl and H_2SO_4 was significantly improved.

New fields of LSA include the alloying and coating of ceramics, mainly with metals, and the synthesis of Si_xGe_{1-x} layers. The latter have been fabricated by KrF-laser-induced melting of a-Ge on (100) Si [*Larciprete* et al. 1998].

25.2.2 Formation of Metastable Materials

The formation of metastable materials is mainly based on the high heating and cooling rates achieved with lasers. For scanned cw-laser-heated surfaces, the cooling rates are comparable to those achieved in standard splat cooling or melt spinning techniques (about 10^6 K/s). With Q-switched and mode-locked pulsed lasers, rates of $10^{10}-10^{12}$ K/s can be obtained. Such cooling rates make it possible to produce glassy alloys which have never before been available. Detailed investigations have been performed for binary alloys consisting of two transition metals, and for combinations of metals with group-IV elements. Among the binary transition metal systems, glasses of Au–Ti, Cu–Ti, Co–Ti, Cr–Ti, V–Ti and Ag–Cu have been produced [*von Allmen* and *Blatter* 1995]. Glass formation seems to fail if single-phase crystallization is possible from the melt, or if the glass is unstable at ambient temperatures. The most extensive investigations on binary alloys consisting of metals and group-IV elements have been performed for silicides.

25.2.3 Silicides

Lasers enable one to synthesize silicides with various compositions, simply by varying the laser fluence. This is quite different to conventional synthesis within a furnace, where sequential phase formation is observed. Most of the experiments start out with a metal film deposited on the Si substrate.

Silicide formation by means of scanned *cw lasers* has been demonstrated for Co, Nb, Pd, and Pt. Uniform layers of MeSi, Me_2Si, or $MeSi_2$ (Me = metal) consisting of essentially a single phase, have been produced [*Shibata* et al. 1980]. The process seems to be dominated by solid-phase diffusion.

Silicide formation using *pulsed-laser* irradiation has been investigated for Au, Co, Cr, Mo, Ni, Pd, Pt, Ti, and W. Excimer, ruby, Nd:YAG, and Nd:glass lasers were mainly employed in these experiments. Here, silicide formation is mainly based on surface melting and liquid-phase mixing of the metal and Si. Due to rapid solidification, amorphous films, or films with different Me_xSi_y precipitates surrounded by Si, are formed. Suitable variation of the laser fluence, pulse length, and thickness of the metal film makes it possible to produce uniform layers with a predetermined single phase or average composition $x{:}y$ [*Bohac* et al. 1993; *D'Anna* et al. 1988; *Baeri* et al. 1985]. An example for which both multiphase and single-phase silicide formation has been demonstrated is the Ni–Si system. With relatively thick metal layers, typically 0.1 μm, evaporated on a Si wafer, the quantity of material liquefied by the laser fluences employed was so large that nucleation and growth of different phases took place during solidification. Simultaneous formation of Ni_2Si, NiSi, $NiSi_2$, and $NiSi_3$ was observed [*Bentini* et al. 1982]. On the other hand, with thin evaporated metal layers ($h_1 < 0.02\,\mu$m) and with certain processing conditions, single-phase $NiSi_2$ can be grown even epitaxially onto (100) and (111) Si wafers [*Grimaldi* et al. 1983]. The physical

properties of these films are very similar to those produced by standard furnace annealing.

The results obtained by different groups can be summarized as follows: depending on the laser fluence and dwell time, the film thickness, and the optical and thermal properties of the system, it is possible to

- synthesize different silicides
- completely react the metal film with Si
- react only part of the film at the Me–Si interface
- produce *single-phase* silicides, e.g., Me_2Si if Me is a noble metal (Pt, Pd, etc.) and $MeSi_2$ if Me is a refractory metal (Cr, Mo, Ti, W). Here, the reaction starts when the interface temperature, T_i, and the eutectic temperature, T_e, of the Me/Si system are equal, i.e., $T_i = T_e$. Single-phase silicide formation is observed if $T_e < T_i < T_m(\mathrm{Me})$
- simultaneously form silicides with complex composition. This situation is observed with *thick* Me layers and high fluences that cause deep melting
- widely suppress surface instabilities (Chap. 28).

25.3 Synthesis

Lasers have been used to synthesize stoichiometric compounds, mainly in the form of thin films and fibers. In the experiments described in the following, the starting material consisted of a single layer, a stack of several layers, or a rod. Laser-induced synthesis of organic polymers from monomers is included in Chap. 27.

25.3.1 Thin Films

Laser-induced synthesis of thin crystalline films has been investigated in particular for compound semiconductors [*Laude* et al. 1986]. The systems studied in detail include binary compounds such as III–V (AlSb, AlAs), II–VI (CdTe, CdSe, ZnSe), IV–VI ($GeSe_2$, GeSe) and IV–IV ($Si_{1-x}Ge_x$) semiconductors, and even ternary compounds, for example, $CuInSe_2$. Synthesis has been achieved by irradiating solid solutions or alternating multiple layers consisting of appropriate proportions of the elements. In order to avoid oxidation or other contaminations during processing in air, films were often encapsulated between SiO_x layers.

Cw-Laser Synthesis

Cw-laser synthesis has been demonstrated for AlSb, $GeSe_2$, and $CuInSe_2$. The size of crystallites formed is, typically, in the μm range. Both free-standing films and films on glass or NaCl substrates exhibit good stoichiometry and optical properties comparable to those of single crystals. For the Ge–Se system different compositions and scanning velocities ranging from 1 cm/s to 20 m/s, have been investigated.

Well-defined periodic structures were observed within certain parameter ranges (Sect. 28.3.4). Films of microcrystalline SiC have been synthesized by cw Ar^+- and 532 Nd:YAG-laser irradiation of mixtures of Si and C on glass substrates. In similar experiments using KrF laser pulses, nanocrystalline SiC is formed [*Hobert* et al. 2002].

Pulsed-Laser Synthesis

Synthesis by pulsed-laser radiation requires melting, or at least partial melting, of the elemental constituents. The dependence of the threshold fluence on pulse duration and substrate temperature has been investigated for AlSb.

An interesting point is the possibility of selecting particular phases by changing the laser-beam illumination time. For example, with dye-laser pulses of $\tau_\ell = 10^{-6}$ s, irradiation of Cd–Te and Cd–Se free-standing films yielded a mixture of hexagonal and cubic CdTe and hexagonal CdSe, respectively. Chopped Ar^+-laser irradiation with pulse durations of $\tau_\ell = 3.6 \times 10^{-2}$ s, on the other hand, revealed films of *cubic* structure only. Thus either type of phase can be produced by proper control of the laser beam dwell time (note that II–VI single crystals are cubic if grown at low temperatures and hexagonal if grown at high temperatures). The physical properties of CdTe films are very similar to those of single crystals grown by standard techniques. In particular, the laser-grown material is very pure, with electrical impurity concentrations ranging from 10^{15} to 10^{17} defects/cm^3 only. The deviation from the correct stoichiometry is 1−2%.

Microcrystalline films of semiconducting $Ge_{1-x}Sn_x$ ($x \approx 0.22$) have been synthesized from amorphous RF-sputtered films by means of ArF- and KrF-laser radiation [*Oguz* et al. 1983].

Films of $CaTiO_3$ doped with a phosphor such as Pr^{3+} have been synthesized by KrF-laser irradiation of spin-coated precursor films on several different glass substrates [*Nakajima* et al. 2008].

25.3.2 Fibers

Lasers permit one to synthesize polycrystalline and single-crystalline fibers, some of which cannot be fabricated by conventional techniques. This has been demonstrated for various materials by the float-zone technique (Fig. 25.3.1). Here, in contrast to the technique described in Chap. 17, the source material is solid, frequently a ceramic in the form of a rod. Fiber growth is achieved by moving the source rod and the fiber through the laser-heated zone. CO_2 lasers are most commonly employed. If the fiber diameter is smaller than the diameter of the source rod, the technique is also termed laser-heated pedestal growth (LHPG) [*Feigelson* 1988]. Similar to the growth of fibers by LCVD, the technique does not require any crucibles and therefore avoids contaminations and frozen-in stresses. The composition of fibers can easily be controlled via the starting material. With the fiber diameters under consideration and focused laser-beam irradiation, strong temperature

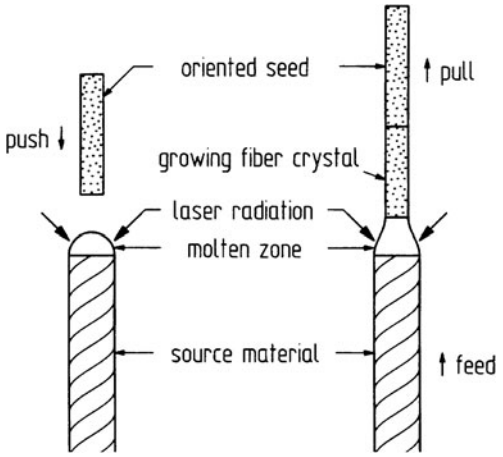

Fig. 25.3.1 Growth of fibers by pedestal growth [adapted from *Feigelson* 1988]

gradients, and hence rapid pulling rates, typically $10-100\,\mu m/s$, can be achieved. The heat source in pedestal growth must have dimensions comparable to the diameter of the fiber and source rod. This requirement is hard to realize with resistance heating. Induction heating would require either a conducting sample or a susceptor. Electron-beam (EB) techniques can only be applied in a vacuum. Thus, with many systems, lasers are the ideal sources. Laser light can be tightly focused, can readily melt any known material, and can be applied in conjunction with inert or reactive atmospheres. With appropriate optics, uniform ring-shaped illumination of the molten zone is possible. The temperature distibution within the laser-heated zone can be calculated in a similar way as described in Sects. 17.5, 18.2.2, and 18.3.1.

Laser-heated pedestal growth has been employed to grow single-crystal fibers of halides, oxides, borides, carbides, metals, semiconductors, and high-temperature superconductors. Most of the materials so far investigated are listed in *Bäuerle* (2000).

Chapter 26
Oxidation, Nitridation, and Reduction

Surface oxidation of metals and semiconductors in an oxidizing agent is a well-known phenomenon. Clean surfaces of many materials such as Al, Nb, Si, etc., *spontaneously* react in air, even at room temperature, to form thin native oxide layers. With the materials under consideration the native oxide layer is very dense and terminates further oxidation. Native oxide layers are, typically, $10-100$ Å thick.

For many applications such as local hardening, chemical passivation, electrical insulation, etc., it is desirable to increase the thickness of the oxide layer, or to stimulate oxidation on material surfaces that do *not* spontaneously oxidize in an oxygen-containing environment. In many cases, the reoxidation of oxygen-deficient oxide layers and the transformation of oxides, for example, of M_xO_y into $M_{x\pm\varepsilon}O_{y\pm\delta}$ is desirable as well. The latter includes the depletion of oxygen in a reducing ambient medium.

Among the many techniques investigated for surface oxidation, the most commonly used ones are thermal oxidation by uniform substrate heating in an oxygen-rich atmosphere and plasma oxidation. Both techniques have their characteristic advantages and disadvantages (Chap. 1).

Light-enhanced and in particular laser-enhanced material oxidation is based on thermal or non-thermal molecule–surface excitations. Single-photon dissociation of O_2 starts at around 5.1 eV ($\lambda \leq 240$ nm). Nitridation of solid surfaces is generating increasing interest as an alternative to oxidation. The fundamental aspects and the techniques employed are similar to those for surface oxidation. Photodissociation of gaseous N_2 starts at around 9.8 eV. Laser-induced reduction of oxides has been performed in a vacuum and in different types of inert or reducing atmospheres.

Among the advantages of laser-enhanced material oxidation, nitridation, and reduction are the lower substrate temperatures, the short processing times, the possibility of localized processing, and the formation of *new* types of oxides/nitrides. The main disadvantages are the low total throughput, the roughness of modified surfaces, and the tendency for crack formation.

Laser-enhanced surface oxidation has been mainly performed in air and O_2 atmosphere while nitridation has been demonstrated in both gaseous *and* liquid N_2, and in NH_3. An overview on the various systems investigated until the year 2000 is given in the previous edition. Laser-induced chemical vapor deposition of oxides

D. Bäuerle, *Laser Processing and Chemistry,* 4th ed.,
DOI 10.1007/978-3-642-17613-5_26, © Springer-Verlag Berlin Heidelberg 2011

and nitrides is included in Chaps. 16, 17, 18 and 19. Thermochemical instabilities observed during laser-enhanced oxide formation are discussed in Chap. 28.

26.1 Basic Mechanisms

Native oxide formation involves a number of consecutive steps:

- Transport of oxygen from the ambient medium to the solid surface.
- Adsorption of molecular oxygen.
- Electron transfer to adsorbed O_2.
- Electric-field-enhanced diffusion of species through the oxide layer.

Adsorption of (strongly electronegative) O_2 on a metal or semiconductor surface favors electron transfer. The situation is similar to that shown in Fig. 15.1.1a. Dissociative chemisorption is enhanced for O_2^- because it requires only 3.8 eV, compared to 5.1 eV for O_2. Chemisorbed oxygen reacts with surface ions/atoms and forms an ultrathin oxide layer. Further oxide growth can proceed via electron tunneling and diffusion of species through the growing layer. This process is self-terminating, because it becomes less likely with increasing layer thickness. Clearly, the surface morphology, the microstructure of the substrate material, the concentration of physical and chemical defects, etc., will strongly influence this *initial* phase of oxide growth. While the fine details certainly depend on the particular system under consideration, the main aspects of this scenario can be applied to many materials.

Oxide growth beyond a single or a few monolayers is controlled by the transport of electrons, ions, atoms, or molecules through the oxide layer (Fig. 26.1.1). With *thin films* and charged species, this transport is enhanced/suppressed by the electric field which builds up within the oxide due to electron transfer from the metal to oxygen. This process takes place until a quasi-equilibrium state is reached. The related potential difference across the oxide layer is, typically, of the order of

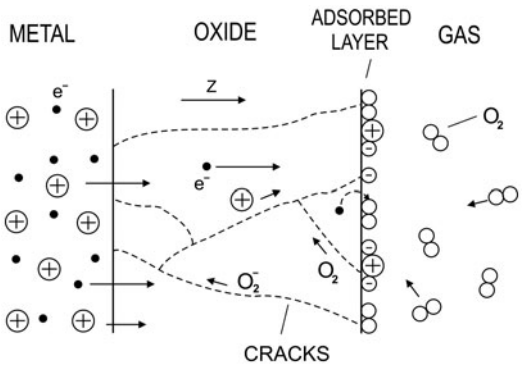

Fig. 26.1.1 Model for surface oxidation of metals. With most metals, the metal ions diffuse to the surface to react with oxygen. Diffusion is enhanced if cracks within the oxide layer are formed

$\Phi \approx 1\,\mathrm{V}$ and almost independent of layer thickness. With *thick films*, the transport of species becomes dominated by ordinary diffusion. For most metal oxides, such as those of Cu, Fe, Pb, Zn, etc., diffusion of metal cations dominates. The metal ions reaching the surface react with adsorbed oxygen. Thus, oxide growth takes place at or near the interface between the gas and the oxide surface. For the oxides of Hf, Nb, Ta, W, and Zr, diffusion of oxygen seems to dominate and growth takes place mainly at the metal–oxide interface [*Roberts* and *McKee* 1978]. With some systems, the species which predominantly diffuses even changes with temperature.

The growth in oxide layer thickness can often be described by the Cabrera–Mott theory, which was originally developed for metal oxidation only. Here, three different regimes of oxidation are distinguished:

26.1.1 Very Thin Films

In the initial phase of growth the oxide layer is very thin and the electric field set up by electron tunneling, $E \approx \Phi/h$, is of the order of $10^7\,\mathrm{V/cm}$ or more. In this regime the transport of ions is dominated by this strong surface electric field and can be described by a Butler–Volmer type equation (Sect. 21.2), which leads to the kinetic law

$$\frac{\partial h}{\partial t} = k_0' \exp\left(-\frac{\mathscr{E}}{T}\right) \exp\left(\frac{h_\mathrm{M}}{h}\right) , \tag{26.1.1}$$

where $k_0' \approx 10^4\,\mathrm{cm/s}$. This equation holds for $h \approx (20\text{–}100\,\text{Å}) \ll h_\mathrm{M} = qa\Phi/k_\mathrm{B}T \approx 100\text{–}1000\,\text{Å}$. q is the ionic charge, and a the distance between ion jumps, which is of the order of the oxide lattice constant. Henceforth, we assume $q = e$.

26.1.2 Thin Films

After the initial phase of oxidation, i.e., for film thicknesses $h_\mathrm{M} < h \leq h_\mathrm{D}$, the (very mobile) electrons can still pass easily through the oxide layer. However, the drift of ions can now be assumed to be proportional to the electric field $E = \Phi/h$, as with Ohm's law. The oxidation behavior can then be described by the transport equations and the Poisson equation. The flux of electrons is given by

$$J_\mathrm{e} = -D_\mathrm{e}\frac{\mathrm{d}N_\mathrm{e}}{\mathrm{d}z} - N_\mathrm{e}\mu_\mathrm{e}E \ . \tag{26.1.2}$$

The ion flux is

$$J_\mathrm{i} = -D_\mathrm{i}\frac{\mathrm{d}N_\mathrm{i}}{\mathrm{d}z} + N_\mathrm{i}\mu_\mathrm{i}E \ . \tag{26.1.3}$$

N_e and N_i are the number densities of electrons and ions within the oxide layer. μ_e and μ_i are the respective mobilities, where $\mu_e \gg \mu_i$. The Poisson equation can be written as

$$\frac{d^2\Phi}{dz^2} = -\frac{4\pi e}{\varepsilon}[N_i(z) - N_e(z)] , \tag{26.1.4}$$

where ε is the dielectric constant. From these equations and the appropriate boundary conditions one can derive the stationary ion flux

$$J_i = J_i(h) \propto N_i E \propto \frac{N_i \Phi}{h} . \tag{26.1.5}$$

With $\partial h/\partial t \propto J_i$, we find the kinetic law

$$\frac{\partial h}{\partial t} = \frac{k_{0n}}{h^n} \exp\left(-\frac{\mathscr{E}_{ox}}{T}\right) = \frac{k_n}{h^n} , \tag{26.1.6}$$

where k_{0n} is a constant and $\mathscr{E}_{ox} \equiv \Delta E_{ox}/k_B$. Here ΔE_{ox} includes the activation energy for diffusion of species through the oxide layer and some energies which characterize interface processes. The exponent n has values 0, 1, 2, etc., depending on the material and the regime of surface oxidation. Let us consider the following three different systems:

- For *interstitial* diffusion, which is typical for oxidation of metals such as Al, Zn, etc., $N_i = \text{const}$. From (26.1.5) we find $\dot{h} \propto h^{-1}$, which corresponds to $n = 1$ in (26.1.6). This yields the parabolic law

$$h^2 = 2k_1 t . \tag{26.1.7}$$

- For *substitutional* diffusion, which is typical for oxidation of Cu, Fe, etc., the density $N_i \propto \Phi/h$ [note that the oxide layer can be considered as a capacitor with fixed potential difference Φ; see also (15.1.1)]. This yields $\dot{h} \propto h^{-2}$, which corresponds to $n = 2$ in (26.1.6). Integration results in the cubic law

$$h^3 = 3k_2 t . \tag{26.1.8}$$

- For a *non-compact* layer, or the case where k_1 increases with h, one often observes an 'apparent' linear behavior,

$$h = k_0 t . \tag{26.1.9}$$

  This situation is typical for the oxidation of Mg.

26.1.3 Thick Films

The surface electric field drops off within the distance $h_D \approx (\varepsilon k_B T/8\pi N_e e^2)^{1/2}$, which is the thickness of the double layer related to the space charge built up near the oxide surface or near the oxide–metal interface, depending on the particular system under consideration (h_D is also known as the screening or Debye length). Thus, for thick films with $h \approx 10^4$ Å $\gg h_D$, the electric field can be ignored and ordinary diffusion of species determines the rate. Then, $J_i \propto dN_i/dz \approx N_i/h$ so that $\dot{h} \propto h^{-1}$. This again yields a parabolic law (Wagner relationship),

$$h^2 = 2k_1' t \ , \tag{26.1.10}$$

where $k_1' = k_{01}' \exp(-\mathscr{E}_d/T) \propto D$. Note that the physical origin of this law is quite different from (26.1.7).

Parameters derived from oxidation experiments performed in furnaces can be found for various materials in the Oxide Handbook [*Samsonov* 1973]. For example, the growth kinetics of Cu_2O can be described by this parabolic law with $k_{01}' = 4.38 \times 10^{-5}\,cm^2/s$ and $\mathscr{E}_d = 9645\,K$.

In the preceding treatment a single chemically uniform oxide layer has been assumed. With many materials, however, the concentration of oxygen within the layer is *not* constant but varies with depth. Such chemical inhomogeneities can be described by multilayer structures as schematically shown in Fig. 26.1.2 for Cu and Fe. In such situations, the oxidation kinetics becomes much more complex. For example, for two-layer systems, such as $CuO/Cu_2O/Cu$, the kinetics of thick films can be described by the Wagner–Valency theory.

26.1.4 Influence of Laser Light

Laser-enhanced *pyrolytic* (photothermal) oxidation can be understood along similar lines as ordinary thermal oxidation. The influence of the oxide-layer thickness, h,

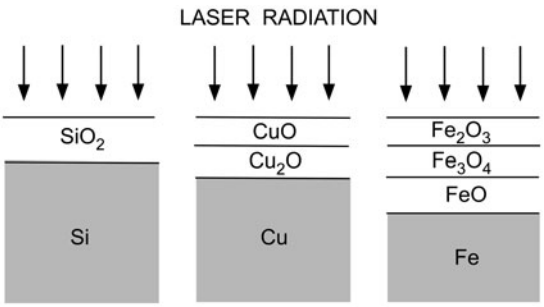

Fig. 26.1.2 Laser-induced oxide formation on different material surfaces. The change in oxygen concentration with depth can be described by multiple layers. The composition and thickness of these layers depends on the laser parameters

on the laser-induced temperature rise, ΔT, is related to changes in the thermal and optical properties of the irradiated material (Chap. 9). Changes in the absorptivity due to laser-beam interferences yield oscillations in the laser-induced temperature distribution and thus in the oxidation rate. Instead of considering single well-defined layers, one can solve the Maxwell equations for (smoothly) varying concentrations of oxygen in the z direction. In any case, because of the temporal changes in temperature, and therefore in coefficients k_n in (26.1.6), laser-enhanced oxidation can be modelled by means of the kinetic laws in their differential form only.

The laser-induced temperature rise enhances the diffusion flux and the reaction rate of species within the irradiated area. This enhancement is based on various different mechanisms: the temperature dependence of ordinary diffusion, the thermal generation of defects such as vacancies, etc., and the thermal excitation of electrons. The latter increases the rate of electron transfer to oxygen and thereby the electric field which enhances the diffusion flux. Furthermore, strong temperature gradients induced by the laser light will enhance the transport of species via thermal diffusion and via the formation of stresses, strains, cracks, and other defects (Fig. 26.1.1). Finally, with the dwell times involved, in particular in pulsed-laser oxidation, thermodynamically unstable phases may remain, while other phases cannot nucleate or form larger crystallites within such short times. It is evident that the formation of different oxides follows different kinetic laws and that optical excitations can modify activation energies, etc. Thus, it is not very astonishing that, in spite of the thermal character of the interaction mechanisms, the growth rate, composition, thickness, morphology, and microstructure of laser-fabricated oxide layers differ significantly from those observed with films fabricated under equilibrium conditions in an oven. For example, CO_2-laser-induced surface oxidation of Cu slabs in air results in the formation of CuO and Cu_2O, as shown in Fig. 26.1.2. On the other hand, the oxidation of thin Cu films on glass or sapphire substrates under the action of visible Ar^+-laser radiation yields mainly Cu_2O.

Photolytic (photochemical) mechanisms have been proved to be important, in particular in cases where the photon energy matches the energy for selective excitation of a particular transition:

- Far-UV radiation results in gas-phase formation of atomic oxygen and ozone, which can efficiently react with many material surfaces. The mechanisms are similar when, instead of molecular oxygen, other oxygen containing species are employed.
- If $h\nu$ exceeds the bandgap energy, E_g, electron–hole pairs are generated within the oxide layer or within the (non-metallic) substrate. Photoelectrons and holes can modify oxygen adsorption on the surface, its reaction with surface atoms, or its migration into the surface, etc. UV-laser light may directly excite adsorbed oxygen and thus promote its dissociation.
- UV- and far-UV-laser light can generate high concentrations of (mainly) oxygen vacancies within the oxide layer. These vacancies increase the mobility of species, lower the temperature for surface melting, etc.
- For both metals and non-metals, photoelectrons may directly be ejected into the oxide layer and modify the electric field.

- In cases where $h\nu < E_g$, excitation of bandgap states may become important. These states are related to impurities, lattice imperfections, surface states, localized states at the substrate–oxide interface, etc. Even if the density of such localized states is low, they may efficiently contribute to the overall oxidation process because of their long lifetimes.

At high intensities, laser light initiates a breakdown at or near the solid surface. This is the regime of *pulsed-laser plasma chemistry* (Sect. 26.2.3).

26.2 Metals

Investigations of laser-enhanced oxidation of metals have been performed with essentially two types of samples: metal plates and thin metal films. With plate-like samples, the laser-oxidized surface layer is very thin in comparison to the sample thickness. This case will be termed laser-induced surface oxidation. Here, the oxidized layer contains, in general, various types of oxides that can be described by Me_xO_y, where Me stands for metal (Fig. 26.1.2). With thin metal films, having thicknesses of, typically, $h \leq 0.1\,\mu m$, oxidation can succeed throughout the whole film. In this case, oxidation often results in the synthesis of a single stoichiometric oxide. Very thin metal-oxide layers have been produced by PLPC.

26.2.1 Photothermal Oxidation

Photothermal oxidation of metal plates and thin metal films has been studied mainly with CO_2 lasers, Nd:YAG lasers, Nd:glass lasers, and Ar^+ lasers. Many of the systems investigated are listed in the previous edition. With most metals, laser-enhanced surface oxidation can be described along the lines of the Cabrera–Mott theory [*Cabrera* and *Mott* 1949].

Among the systems so far investigated in detail is the oxidation of thin Cu films on sapphire substrates by means of cw Ar^+-laser radiation. The laser-grown oxide consists mainly of Cu_2O. Figure 26.2.1a depicts the time-resolved reflectivity measured in situ with a HeNe-laser probe beam for different Ar^+-laser powers. The reflected light intensity shows damped oscillations due to interference. The decrease in time between oscillations observed with increasing incident laser power is due to the increase in film growth rate. However, even with constant laser power, the absorbed power increases with film thickness (Fig. 9.2.2). For a quantitative description of the results, the oscillations in the absorbed Ar^+-laser power are of relevance. Figure 26.2.1b displays the oxide-layer thickness as a function of irradiation time for constant incident laser power. The stepwise growth is related to the oscillations in absorbed laser power.

For an analysis of results, the exothermal energy release during oxidation can be ignored. The additional source term can be approximated by $I_{ox} \approx \Delta H_{ox} v$,

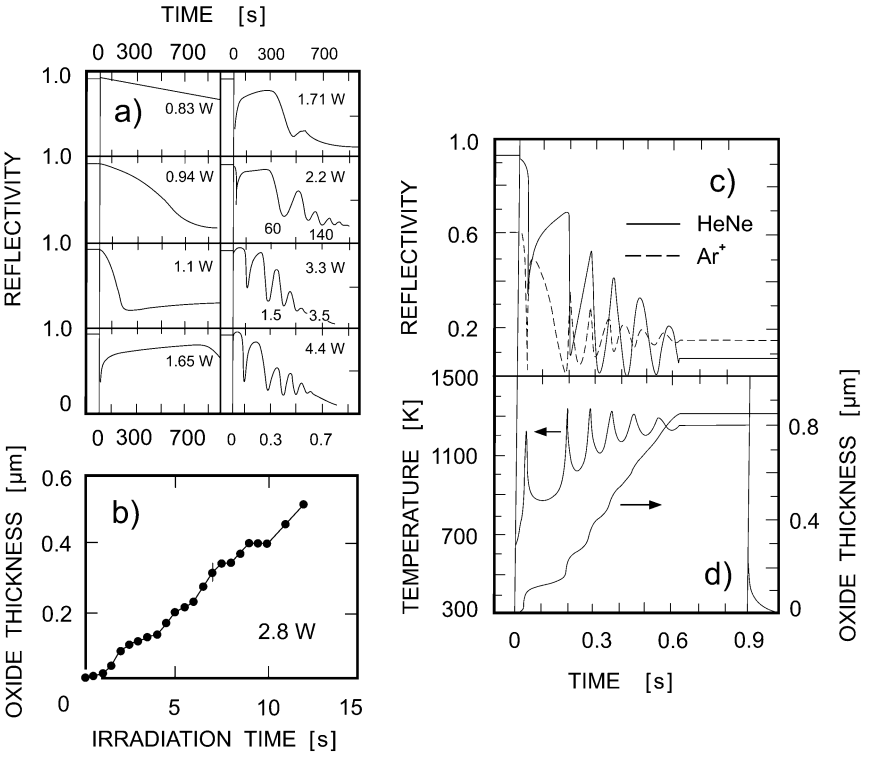

Fig. 26.2.1 a, b Ar^+-laser-induced oxidation of 0.05 μm thick Cu films on sapphire [$\lambda = 514.5$ nm, $w_0 \approx 80\,\mu$m, $p(O_2) \approx 200$ mbar]. (**a**) Time-resolved reflectance measured by HeNe-laser probe beam. *Vertical lines* indicate beginning of Ar^+-laser irradiation. Note changes in time scales with 2.2, 3.3, and 4.4 W curves (lower scales). (**b**) Oxide-layer thickness as a function of irradiation time. (**c,d**) *Calculated* temporal dependence of the reflectivity of HeNe- and Ar^+-laser beams, of the film thickness, and of the temperature for $P = 4.4$ W. Oscillations end when the film is oxidized over the whole thickness [adapted from *Baufay* et al. 1987]

with $\Delta H_{ox} \approx 7 \times 10^3$ J/cm^3. For an average oxidation velocity $v \approx 10^3$ Å/10 ms (corresponding to a laser power of about 4.4 W), we have $I_{ox} \approx 10^{-3} I_0$.

The experimental data presented in Fig. 26.2.1a, b were simulated using different models [*Baufay* et al. 1987]. Figure 26.2.1c, d exhibits the results of calculations where the thermally strongly-conducting copper film is placed on a semi-infinite (sapphire) substrate. The main features observed in the experiments are reproduced by the calculations. If the thermal properties of the sapphire substrate are adapted, almost quantitative agreement with the experimental data is achieved.

The good agreement between experimental and theoretical results achieved for the preceding example does *not* mean that laser-enhanced metal oxidation can, in general, be described on the basis of such a simple model with similar success. There are many different reasons for this:

- For *surface* oxidation, the measurement and definition of the oxide-layer thickness is by no means trivial, especially when the surface oxide is chemically inhomogeneous.
- There are no reliable measurements of the laser-induced temperature distribution within the oxide layer. Thus, the temperature that enters the kinetic equations can only be estimated from model calculations. Such calculations require, however, accurate knowledge of the optical and thermal material parameters and their spatial and temporal changes during the oxidation process.

A more sophisticated model also has to account for the following:

- The transport of oxygen or oxygen-containing species from the gas-phase to the solid surface and the adsorption kinetics of these species on the surface.
- Non-thermal oxidation mechanisms.
- The transport of metal ions and oxygen through the oxide layer with highly non-uniform properties related to strong temperature gradients.
- Diffusion of species along grain boundaries and cracks within the oxide (Fig. 26.1.1).
- Nucleation and growth of crystallites.
- Effects due to macroscopic non-equilibrium in the system when temperature variations are faster than the chemical relaxation of the medium, the relaxation of the charge distribution, etc.
- Laser-induced thermal or non-thermal decomposition, transformation or ablation of oxides that have already been formed.

Some of these effects and their relative influence on the laser-induced temperature distribution and the transport of species have been considered [*Karlov* et al. 1992; *Wautelet* 1990]. The oxidation kinetics is sensitive to the specific material and laser parameters. This is the reason for the significant differences in apparent kinetic constants reported by different groups for similar materials.

The influence of an *external* electric field on oxide formation has been investigated for cw CO_2-laser enhanced oxidation of Cu and V in air [*Nanai* et al. 1993].

Oxide layers with periodic thickness profiles have been generated on Al surfaces by laser-beam interference (355 nm Nd:YAG, $\tau_\ell \approx 10\,\text{ns}$, $\nu_\text{r} = 10\,\text{Hz}$) [*Alessandria* and *Mücklich* 2010]. As expected, the oxide layer thickness at interference maxima exceeds that at the minima.

26.2.2 Photochemical Contributions

Whether there are systems where *non-thermal* effects during laser-enhanced oxidation have been observed is still an open question. For example, the increase in oxidation rate of Ni in an O_2 atmosphere with decreasing wavelength between 1064 and 308 nm was interpreted by the photoexcitation of molecularly adsorbed oxygen at the NiO surface [*Mesarwi* and *Ignatiev* 1989]. However, the fact that the experimental data cannot, or only poorly, be described by (26.1.6) does not mean that

non-thermal effects play an important role. The discrepancies may be simply related to the difficulties in the measurements and analysis of data, as mentioned above. Additionally, the absorptivity of the surface changes because of both the dependence of the reflectivity on wavelength (Table III) and the growth of the oxide film (see, e.g., Figs. 26.2.1 and 9.3.1). Thus, a clarification of the microscopic mechanisms requires more detailed investigations.

26.2.3 Oxidation by Pulsed-Laser Plasma Chemistry

Pulsed-laser plasma chemistry (PLPC) is based on laser-induced breakdown at or near the solid surface. In the literature, the same technique is also termed laser-pulse plasma chemistry and abbreviated by LPPC. In any case, the laser-generated plasma contains reactive species which may react with the substrate surface and thereby form a chemically modified layer. At higher laser-light intensities, ablation and cluster formation within the plasma takes place (Chap. 4). The clusters may or may not react with the ambient medium. At high gas pressures, the clusters condense on the surface and form an overlayer of aggregated nanoparticles (NPs). Surface oxidation based on PLPC was studied in detail for Nb films ($\approx 130\,\mu$m thick) in O_2 atmosphere and pulsed-CO_2-laser radiation [*Marks* et al. 1983]. Single-pulse laser-activated oxidation was found to produce thicker films than multiple-pulse irradiation. For a single pulse with a fluence of $\phi = 0.75\,\mathrm{J/cm^2}$, the thickness of the native oxide consisting of $Nb_2O_{5-\delta}$ was increased by 18 Å, while 3 pulses, each having a comparable fluence, yielded a net increase of only 11 Å. This is interpreted in terms of competing mechanisms: oxidation by PLPC and oxide ablation due to absorption of CO_2-laser radiation within the oxide layer. As revealed by XPS, the valence defect, δ, decreases monotonically with increasing layer thickness. A similar behavior has been found for films produced by standard plasma oxidation. However, for a given layer thickness, δ is 3–5 times smaller for PLPC oxides ($0.02 \leq \delta \leq 0.04$) than for plasma oxides ($0.1 \leq \delta \leq 0.2$). In other words, PLPC yields more complete oxidation. Furthermore, in comparison with laser-enhanced photothermal oxidation or conventional oxidation, PLPC reduces the formation of suboxides. Niobium oxide layers ($18-40$ Å with $0.24-0.79\,\mathrm{J/cm^2}$) produced by PLPC may be applied for the fabrication of tunnel barriers in tunneling devices. It is difficult to produce such well-defined dielectric layers with comparable thickness control and quality by standard techniques.

PLPC has been also employed for the formation of porous nanostructured ZnO layers on Zn targets. The synthesized ZnO-based material consisting of well-packed nanospheres with diameters between 20 and 40 nm shows efficient random lasing [*Kabashin* et al. 2007]. Another example is the surface modification of steel targets. Here, condensed iron-oxide nanoparticles change the surface properties with respect to adhesion, corrosion, etc. The size of NPs can be controlled via the laser parameters and the pressure and composition of the background atmosphere [*Pereira* et al. 2004; see also Chap. 4].

26.2.4 Nitridation

Nitridation of metal surfaces has been studied in detail for Al, Ti, Fe, and steel. Pulsed- and cw-CO_2 lasers, Nd:YAG lasers, and excimer lasers were employed. The ambient media were gaseous or liquid N_2, and NH_3. Nitridation is extremely sensitive to traces of O_2, simply because of the higher reactivity of oxygen (Sect. 22.2.1).

Thick TiN overlayers have been fabricated by CO_2-laser-induced surface melting in combination with an N_2/Ar-gas jet. With laser-beam dwell times $\tau_\ell < 1$ s, layer thicknesses of 50−500 μm have been produced (oxide layers have been fabricated in a similar way; *Gasser* et al. 1989).

Detailed investigations on the nitridation of Ti using 532 nm Nd:YAG-laser radiation and N_2 atmosphere have been performed by *Höche* et al. (2008). The influence of the laser and scanning parameters on the size and orientation of TiN_x grains and the related microstrains were studied by X-ray diffraction. Nd:YAG-laser-induced nitridation of Ti in *liquid* N_2 was studied by *Takada* et al. (2007). This technique permits formation of very shallow nitrided layers with almost no oxygen contamination.

Nitridation of Al-alloys has been demonstrated by means of excimer-laser radiation in gaseous N_2 [*Bergmann* 2004; *Carpene* et al. 2002]. A reduction of the wear rate of up to 30% has been achieved. Hard and adherent layers of TiN have been produced also by multiple-pulse XeCl-laser irradiation of Ti in N_2 and NH_3 atmospheres [*D'Anna* et al. 1991].

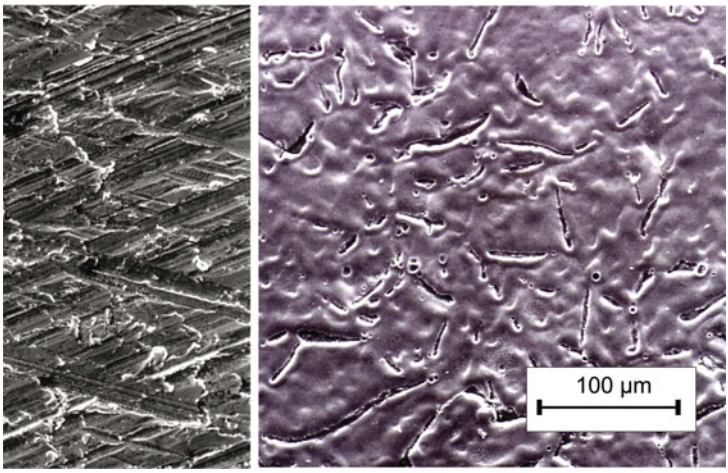

Fig. 26.2.2 Scanning electron microscope pictures of the surface of an engine cylinder liner after mechanical honing (*left*) and laser treatment (308 nm XeCl, $\tau_\ell = 25$ ns) (*right*). Mechanical honing leaves grooves along which oil flows. Laser treatment with optimized parameters smoothens the surface and opens microcavities in the cast iron where oil can collect. Within the same process, a few micron thick superplastic nanocrystalline surface which contains about 17% N is formed [courtesy of H. Lindner, Audi AG]

Among the most spectacular recent developments is the laser-induced modification of cylinder surfaces in the automotive industry. Here, laser irradiation of superfinish-bored cylinder surfaces permits polishing, the opening of microcavities and surface nitridation in a *single* production step. Figure 26.2.2 show the results. In comparison to the superfinish-bored surface, the laser-irradiated surface is much smoother. Simultaneously, laser-irradiation burns out segregated carbon inclusions in the cast iron and thereby opens microcavities (1–5 μm width) which collect the motor oil. In N_2 atmosphere and with the fluences employed, surface doping with atomic nitrogen ($\approx$ 17%) causes a nanocrystalline ceramic-type surface layer with superplastic properties. This surface layer is only a few micrometers thick. Laser treatment diminishes oil consumption by about 80% and wear from piston rings by about 90%. The higher combustion pressures that can be employed with such engines increase their efficiency and thereby decrease fuel consumption and pollution. The process is employed in series production of Diesel engines since 2004.

26.3 Elemental Semiconductors

Surface oxidation and nitridation of elemental semiconductors is of basic importance in semiconductor device technology. The investigations have concentrated on silicon and, to a smaller extent, on germanium.

Surface oxidation of crystalline and amorphous silicon has been investigated with cw and pulsed lasers and various atmospheres. Air and O_2 have been most commonly employed, sometimes with admixtures of other species that catalyze the overall oxidation process. Oxide formation by annealing of oxygen-ion (O^+)-implanted Si surfaces has also been demonstrated. In many experiments, the Si substrate was preheated to several hundred degrees. For photon energies $h\nu < E_g$, the enhancement in oxidation rate is primarily due to laser-induced surface heating (Sect. 7.6). The bandgap energy [$E_g(\mathrm{Si}, 300\,\mathrm{K}) \approx 1.12\,\mathrm{eV} \mathrel{\widehat{=}} 1107\,\mathrm{nm}$] decreases with increasing temperature. Excitation by visible and ultraviolet laser radiation results in the emission of electrons from Si into the SiO_2 layer. These electrons enhance the dissociation of molecular oxygen and thus the oxidation rate (Fig. 26.3.1).

26.3.1 Photothermal Oxidation of Si

During thermal oxidation of Si in an O_2 atmosphere the oxide-layer thickness increases linearly for short oxidation times (thin layers) and follows a parabolic law for longer times [*Deal* and *Grove* 1965]. These growth regimes can be described by (26.1.6) with $n = 0$ and $n = 1$, respectively.

Within the *linear* regime and for temperatures above 600°C, activation energies between 1.7 and 2 eV have been measured. These activation energies are close to the

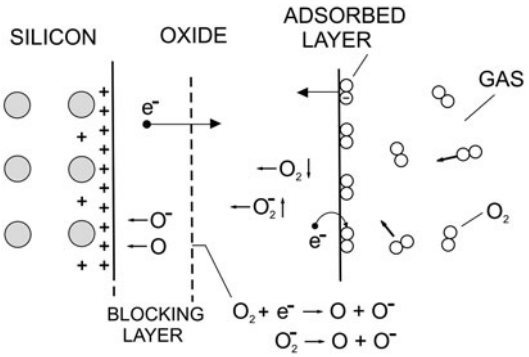

Fig. 26.3.1 Model for laser-induced surface oxidation of Si. ↑ and ↓ denote increasing and decreasing concentrations, respectively

Si–Si-bond-breaking energy, which is around 1.8 eV. Thus, the oxidation rate within this regime can be related to the formation of Si radicals.

The *parabolic* regime can be described along similar lines as metal oxidation. With Si – and this holds also for Ge – mainly oxygen diffuses through the oxide layer. Thus, oxide growth takes place at the interface between the semiconductor and the oxide. With Si, the activation energy measured within this regime is around 1.23 eV. This compares favorably with activated diffusion of O_2 through SiO_2 for which $\Delta E_d \approx 1.17\,\text{eV}$ ($\mathscr{E}_d \approx 13600\,K$).

The microscopic mechanisms considered are schematically depicted in Fig. 26.3.1. Native-oxide formation proceeds as described in Sect. 26.1. Electrons are transferred from Si to adsorbed O_2. Thus, physisorbed O_2 becomes chemisorbed and forms an ultrathin oxide layer. Up to a thickness of about 10 Å, rapid oxide growth due to electron tunneling and oxygen diffusion through the thin oxide layer is observed.

A further increase in oxide-layer thickness requires both the diffusion of adsorbed oxygen into the oxide and the ejection of 'hot electrons' from the Si. Activated diffusion of oxygen is possible because the free volume within the SiO_2 lattice is about 45 Å^3 and thus of a size similar to that of the O_2 molecule. On its way towards the Si–SiO_2 interface, oxygen will pick up electrons which are trapped in the oxide; thus, the concentration of O_2 decreases, while that of O_2^- increases. Diffusion of O_2^- ions is enhanced by the electric field related to the positively charged holes ('broken bonds') at the Si surface. At distances of 10−20 Å from the interface, diffusion of O_2^- and O_2 becomes blocked. This is related to the reduction in lattice parameters caused by the mismatch between the (smaller) lattice constant of Si and that of SiO_2. However, *hot* electrons emitted into the SiO_2 conduction band can easily penetrate the blocking layer. These hot electrons promote dissociation of oxygen into O and O^-. Atomic oxygen has a volume of only about 5 Å^3 and can easily diffuse through the blocking layer to the Si–SiO_2 interface, react with silicon and increase the oxide-layer thickness. Clearly, the oxidation rate can be

limited by diffusion of oxygen towards the blocking layer or by dissociation of oxygen molecules near the blocking layer. The latter is related to the flux of electrons penetrating the blocking layer.

The enhancement of the oxidation rate by CO_2-laser radiation is due to the heating of both the oxide and silicon. SiO_2 strongly absorbs CO_2-laser radiation via vibrational excitations (Si–O stretching mode at around 1000–1100 cm^{-1}; see also Fig. 7.2.4). Heating of the oxide layer, in turn, favors oxygen diffusion. CO_2-laser heating of Si occurs via free-carrier excitations (Sect. 7.6). This increases the density of hot electrons and thereby favors oxygen dissociation. Clearly, preheating of the substrate has the same effect.

With CO_2-laser radiation, films up to a thickness of about 0.2 μm have been grown at an average rate of about 3×10^{-5} μm/s. Films with thicknesses > 0.04 μm exhibited an average dielectric breakdown of about 6.5×10^6 V/cm; for further details see *Boyd* (1987).

A sharp increase in oxide formation is observed with laser fluences that cause surface melting. In this regime, however, strong surface degradation and structural damage is observed.

26.3.2 Photochemically Enhanced Oxidation of Si

The enhancement of the oxidation rate by VIS or UV laser light can be qualitatively understood with the same model (Fig. 26.3.1). Besides thermal stimulation, direct bandgap excitation increases the density and average energy of electrons emitted into the oxide. Thus, electron capture and dissociation of oxygen molecules becomes more likely and takes place further away from the Si–SiO_2 interface.

The enhancement in oxide growth rate in the presence of Ar^+-laser radiation (about 40% with $I = 10^2$ W/cm^2) was found to be *linearly* proportional to the photon flux [*Young* 1988],

$$J = \frac{I_a}{h\nu} = \frac{I_a}{hc}\lambda \,, \tag{26.3.1}$$

and only slightly dependent on crystal orientation [*Massoud* and *Plummer* 1987]. According to (26.3.1), the enhancement increases with laser wavelength – as long as I_a stays constant and the oxidation mechanism remains unchanged. When the photon energy exceeds 3.15 eV, a step-like increase in oxidation rate is observed. This is related to direct electronic transitions from the Si conduction band into the SiO_2 conduction band. For example, with 308 nm (4.03 eV) XeCl-laser radiation, an enhancement with respect to visible laser light by a factor of 10 was obtained. For photon energies above 4.25 eV, electrons can be directly excited from the Si valence band into the SiO_2 conduction band. This gives an additional 20% increase in oxidation rate. When the photon energy is increased to above 5.1 eV, photodissociation

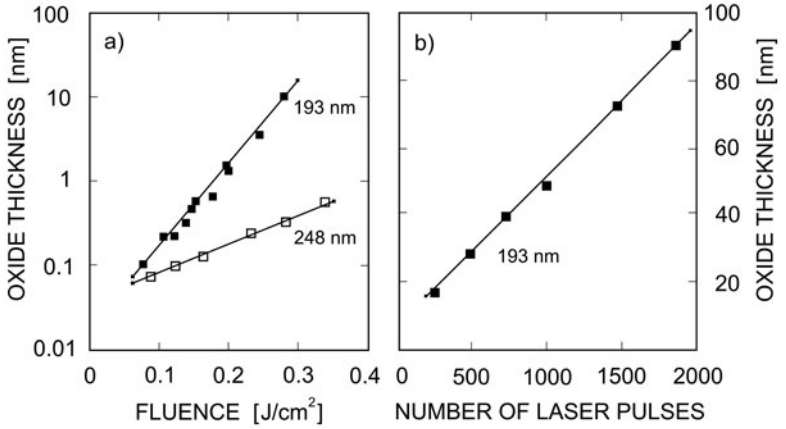

Fig. 26.3.2 a, b Thickness of oxide layer formed on (100) Si ($T_s = 300\,K$) in an oxygen atmosphere. (**a**) 20 ArF- or KrF-laser pulses, $p(O_2) \approx 13\,mbar$. (**b**) $\phi(ArF) \approx 0.16\,J/cm^2$, $p(O_2) \approx 366\,mbar$ [adapted from *Orlowski* and *Mantell* 1988]

of molecular oxygen begins. The effect of atomic oxygen can be directly seen in Fig. 26.3.2a, which shows the oxide-layer thickness as a function of fluence for 193 nm (6.42 eV) ArF- and 248 nm (5 eV) KrF-laser light. The maximum fluence employed is just below the melting threshold ($\approx 0.35\,J/cm^2$). The high oxidation rate observed with ArF-laser radiation is mainly ascribed to direct photodissociation of O_2 (Table V). With respect to visible laser light, the enhancement observed with ArF-laser radiation is about a factor of 300. Figure 26.3.2b shows the dependence of the oxide-layer thickness on the number of laser pulses.

Surface oxidation of Si has also been demonstrated with twin-beam irradiation, where, for example, Ar^+-laser light produces excess free carriers in the conduction band so that CO_2-laser radiation can be absorbed more efficiently. This technique permits localized surface oxidation.

Surface oxidation of Si and $Si_{0.8}Ge_{0.2}/Si$ enhanced by Hg-lamp ($\lambda = 254\,nm$, 185 nm) irradiation has been studied by *Boyd* et al. (1993). At 550°C enhancements in growth rates of up to 50 times have been observed.

Film Properties

Characterization of oxide films has been performed by IR spectroscopy, XPS, and capacitance–voltage (CV) measurements. The latter experiments revealed fixed oxide charge densities of $(3-8) \times 10^{11}/cm^2$ and surface state densities of the same magnitude. A considerable improvement in the electrical quality of as-grown films can be achieved by means of a short (about 20 min) anneal at 900°C in 1000 mbar O_2. The fixed charge density is then about $6 \times 10^{10}/cm^2$, and the breakdown voltage $> 5 \times 10^5\,V/cm$.

26.3.3 Nitridation of Silicon

Surface nitridation of Si has been investigated mainly for N_2 and NH_3 atmospheres and excimer-laser radiation. Efficient nitridation was observed only in NH_3. With ArF-laser radiation, nitridation is characterized by an initial phase of rapid growth (for about 2000 pulses with $\tau_\ell = 12\,\text{ns}$ and $\phi \approx 15\,\text{mJ/cm}^2$) followed by inhibited growth similar to thermal nitridation [*Sugii* et al. 1988]. The maximum film thickness achieved was $\approx 25\,\text{Å}$. On the basis of AES studies, laser-grown films are very similar to those thermally grown at $T_s \approx 1000°\text{C}$. Nitridation seems to be related to photogenerated NH_2 radicals, which easily react with Si. Nitridation may proceed in a similar way to oxidation.

26.4 Compound Semiconductors

The oxidation of compound semiconductors and its photon enhancement has been studied extensively. The most detailed experiments have been performed for the III–V compounds GaAs, InAs, and InP. With these materials, surface oxidation proceeds in three successive steps [*Mönch* 1986] as follows:

- Oxygen adsorption at cleavage-induced defects.
- Activated adsorption and dissociation of oxygen followed by breaking of adjacent III–V surface bonds.
- Field-assisted diffusion of oxygen and film growth.

Laser-enhanced oxidation of compound semiconductors, in particular of GaAs and InP, has been demonstrated with VIS- and UV-laser light. The experiments were mainly performed in O_2 and NO_2 atmospheres. An overview is given in the previous edition.

The (dark) sticking coefficient of O_2 on GaAs depends on coverage and has values in the range $10^{-5} \leq s \leq 10^{-9}$. Light with photon energies $h\nu \geq E_g(\text{GaAs}, 300\,\text{K}) \approx 1.43\,\text{eV} \mathrel{\widehat{=}} 867\,\text{nm}$ increases s by about a factor of 10^3. This is related to the increase in electron transfer, which favors chemisorption of O_2. With VIS and near-UV light, the enhancement in oxidation rate saturates at around 1 ML (monolayer) [*Z. Lu* et al. 1990; *Bertness* et al. 1987].

At a photon energy of about 4.1 eV ($\approx 302\,\text{nm}$), a sharp increase in oxidation rate due to photoemission of electrons into the GaAs oxide has been observed. Another increase in rate observed with 193 nm ArF-laser radiation is related to photodissociated O_2.

The stoichiometry of oxides depends on the laser parameters. After laser irradiation, the oxide layer mainly consists of Ga_2O_3 and variable amounts of As_2O_3 and As_2O_5. These amorphous oxide mixtures may crystallize and form stable Ga_2O_3 and $GaAsO_4$ [*Schwartz* 1975].

X-ray-induced low-temperature oxidation of (110) GaAs in N_2O has been studied by *Seo* et al. (1990).

Laser-enhanced oxidation of compound semiconductors can be described along similar lines as silicon oxidation. Important differences are related to the differences in bandgap energy and the type of surface oxides. To elucidate finer details, more experimental data are required.

26.4.1 Summary

Semiconductor oxidation takes place mainly at the semiconductor–oxide interface, while metal oxidation frequently proceeds at the oxide surface. In semiconductors, the oxidation rate depends *strongly* on wavelength, mainly due to electron–hole pair generation for photon energies $h\nu > E_g$. Laser radiation may generate defects within the oxide layer and at the oxide–substrate interface. Defects such as oxygen vacancies, cracks, etc., significantly enhance the transport of species.

Laser-induced surface oxidation and nitridation of metals and semiconductors results in the formation of films with thicknesses of, typically, 10 Å to 1 μm. Such films can be produced either by single-step direct writing or over extended areas. The technique is *complementary* to LCVD, which permits the growth of films with typical thicknesses of $1-100\,\mu m$.

26.5 Oxide Transformation, Reoxidation

Laser irradiation of an oxide M_xO_y in oxygen or an oxygen-containing atmosphere can result in a new oxide of composition $M_{x\pm\varepsilon}O_{y\pm\delta}$. Experiments of this type have been performed, in particular, for metal oxides.

Laser-induced reoxidation permits direct writing of superconducting $YBa_2Cu_3O_7$ lines into semiconducting $YBa_2Cu_3O_6$ [*Sobolewski* et al. 1994; *Shen* et al. 1991; *Liberts* et al. 1988a]. Experiments have been performed with both ceramic pellets and thin films. The oxygen uptake within the material is induced by cw Ar^+- or Kr^+-laser heating in an O_2 atmosphere. The electrical properties of lines depend on the laser-beam intensity, the scanning velocity, and the oxygen pressure. The temperature dependence of the line resistance per unit length is shown in Fig. 26.5.1 for various scanning velocities. For $v_s = 2\,\mu m/s$ the onset to superconductivity occurs at around 88 K. The large transition width of about 10 K is probably related to chemical inhomogeneities within such lines. Similar experiments have been performed for oxidic perovskites [*Bäuerle* 1985; *Otto* et al. 1984].

26.5.1 Silicon Oxide

Another type of oxide transformation is the dehydroxylation of silicon oxide surfaces including those on Si wafers. It is well known that OH-groups on solid surfaces provide reactive sites that permit atoms/molecules, functional groups,

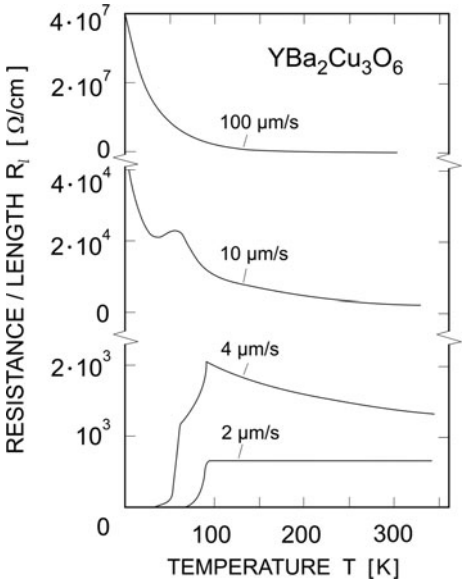

Fig. 26.5.1 Temperature dependence of the resistance R_l (Ω/cm) of Ar^+-laser fabricated lines in ceramic $YBa_2Cu_3O_6$ for various scanning velocities ($P = 500\,\text{mW}$, $\lambda = 488\,\text{nm}$, $2w_0 = 35\,\mu\text{m}$, $p(O_2) = 1800\,\text{mbar}$) [*Liberts* et al. 1988a]

particulates, and even biological cells to attach (Sect. 27.1). The reduction of the density of OH transforms the hydrophilic surface into hydrophobic. Laser direct writing using 514.5 nm Ar^+-laser radiation causes a dehydroxylation of both native oxide (Sect. 26.3.1) and thermally grown oxide layers on Si-wafers [*Hartmann* et al. 2009]. The process is thermally activated with an activation energy of $\Delta E = 342 \pm 27\,\text{kJ/mol}$. Thus, laser direct writing results in a strong confinement of the reaction (Sect. 5.3). The technique permits subwavelength patterning of reactive templates. As expected for a thermally activated process and the laser parameters employed, corresponding experiments on quartz plates have failed. On the other hand, dehydroxylation of a-SiO_2 plates by means of KrF-laser radiation was successful [*Fernandes* et al. 2006]. In these latter investigations, the decrease in particulate adhesion due to laser treatment was studied.

26.6 Reduction and Metallization of Oxides

Just as laser-induced heating of certain materials in an oxygen-rich atmosphere permits one to incorporate oxygen into the lattice or to form a surface oxide layer, specific materials can give up their oxygen to a reducing environment under the appropriate laser-heating conditions. This has been demonstrated for different metal and semiconductor oxides, for oxidic perovskites and perovskite-related oxides such as

$BaTiO_3$, $PbTiO_3$, $PbTi_{1-x}Zr_xO_3$ (PZT), $Pb_{1-3y/2}La_yTi_{1-x}Zr_xO_3$ (PLZT), $SrTiO_3$, and $LiNbO_3$, and for high-temperature superconductors.

26.6.1 Qualitative Description

The laser-induced depletion of species from a solid material, and in particular of oxygen from oxides, can be described by the diffusion equation. The situation is similar to solid-phase doping. The main difference is that (24.1.3) and (24.1.4) must be replaced by

$$N_A(z, t = 0) = N_A^0 ; \quad N_A(0, t) = 0 ; \quad N_A(\infty, t) = N_A^0 , \tag{26.6.1}$$

where N_A^0 is the initial concentration of the species that are depleted. When species A reach the surface it is assumed that they immediately desorb. Otherwise, more complicated boundary conditions at $z = 0$ must be employed. With (26.6.1), the solution of (24.1.1) becomes

$$N_A(z, t) = N_A^0 \left[1 - \mathrm{erfc} \left(\frac{z}{l_s} \right) \right] = N_A^0 \, \mathrm{erf} \left(\frac{z}{l_s} \right) , \tag{26.6.2}$$

where the effective diffusion length is given by $l_s \approx 2(\langle D_s \rangle t)^{1/2}$. Thus, the spatial variation (26.6.2) can be obtained from the solid curve in Fig. 24.1.2. Equations (24.1.7) and (24.1.8) can be employed without any changes.

Metallization

Let us now consider a somewhat different situation where a metal oxide in the form of a slab with area F and thickness h_s is reduced according to the reaction

$$Me_xO_y + yH_2 \rightarrow xMe + yH_2O + \Delta H . \tag{26.6.3}$$

In the simplest approximation, this process can be described by the energy balance

$$\varrho c_p F h_s \dot{T} = P A(h_1) - P_{loss}(T) - \Delta H \dot{h}_1 F , \tag{26.6.4}$$

and the equation for the growing metal film

$$\dot{h}_1 = v_0 \exp \left(-\frac{\mathscr{E}}{T} \right) , \tag{26.6.5}$$

where $h_1 \ll h_s$. In general, the absorptivity of an oxide covered with a thin metal film is lower than that of the oxide, i.e., $A_{Me} < A_{ox}$ (Fig. 7.2.4), and decreases further with increasing film thickness, h_1. This results in a *negative* feedback.

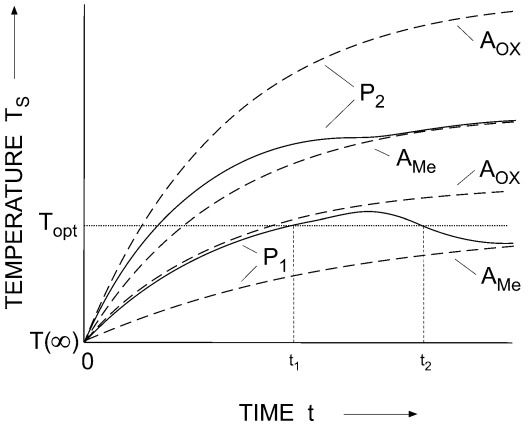

Fig. 26.6.1 Qualitative behavior of surface temperature T_s (*solid curves*) during laser-induced metallization of a metal oxide. The laser is switched on at $t = 0$ (power $P_1 < P_2$). The behavior of T_s for a pure oxide with absorptivity A_{ox} and an oxide covered with a metal film with $A_{Me} < A_{ox}$ is shown (*dashed curves*). For P_1, metallization takes place only during the time interval $t_1 < t < t_2$

Let us first ignore the reaction enthalpy, ΔH. Figure 26.6.1 shows, qualitatively, the temporal behavior of the surface temperature (solid curves) for two different laser powers P_1 and P_2, with $P_1 < P_2$. Initially, the *absorbed* laser power is determined by the absorptivity of the oxide and a rapid rise in surface temperature is observed. With the formation of a metal film, the absorptivity decreases. When $h_1 > l_\alpha$ (metal), the absorbed laser power is determined by the absorptivity of the metal and T_s increases more slowly, or it may even decrease. Figure 26.6.1 reveals another interesting feature. For low laser powers, P_1, the surface temperature shows a maximum and exceeds the optimal temperature, T_{opt}, for controlled surface reduction only within a time interval $t_1 < t < t_2$. The final layer thickness is then almost independent of the total illumination time. This self-stabilization permits efficient and reproducible surface processing (without crack formation, etc.) by selecting the optimal laser power.

If ΔH cannot be ignored, the additional source term in (26.6.4) may cause strong transient changes in temperature and uncontrolled processing. An example would be the reduction of Cu_2O according to (26.6.3) by CO_2-laser light, where $A_{ox} \equiv A(Cu_2O, 10.6\,\mu m) \approx 0.82$ and $A_{Me} \equiv A(Cu, 10.6\,\mu m) \approx 0.02$, and $\Delta H \approx -73.5\,kJ/mol$ (Fig. 3.1.1).

26.6.2 Oxidic Perovskites and Related Materials

Oxidic perovskites are insulators with a band gap of, typically, 3 eV. Most of them are ferroelectric and thereby piezoelectric. It is well known that the physical properties of these materials can be dramatically changed by reducing the bulk material at elevated temperatures, e.g., in an H_2 atmosphere at 500–1500 K. This treatment

results in the formation of oxygen vacancies and free or quasi-free electrons. The concentration of oxygen vacancies and free electrons increases with increasing temperature and with decreasing oxygen partial pressure. The oxygen vacancies act as shallow donor levels and the insulating material becomes an n-type semiconductor. The originally transparent material changes to blue or black, depending on the concentration of vacancies. Because of the fundamental role of the oxygen ion in connection with the dynamic properties of perovskites, oxygen vacancies strongly influence the structural phase transitions (ferroelectric and nonferroelectric) observed in these materials [*Migoni* et al. 1976; *Wagner* et al. 1980; *Bäuerle* et al. 1980].

Laser-light irradiation of oxidic perovskites in a reducing atmosphere can result in *local* reduction of the material surface. While for sub-bandgap radiation ($h\nu < E_g$) the reduction mechanism is mainly thermal, UV and far-UV radiation ($h\nu > E_g$) directly generates quasi-free electrons and oxygen vacancies. The reduction process is reversible, i.e., on heating of the material in an O_2 atmosphere or air, the reduced (blue to black) regions vanish and only small changes in surface morphology remain. With increasing laser-light intensity, the degree of reduction increases and the electrical properties of laser-treated regions change from semiconducting to metallic. Beyond a certain threshold intensity, etching or cutting of the material is observed.

Laser-induced reduction and metallization of oxidic perovskites allows single-step conductive patterning of the otherwise insulating material surface. Metallization has been studied in detail for hot-pressed optically transparent ferroelectric PLZT ceramics. The electrical resistivity of the bulk material was $> 10^{14}\,\Omega\,\mathrm{cm}$. Figure 26.6.2a shows the resistance per unit length, R, of lines produced by UV-laser direct writing as a function of laser power in an H_2 atmosphere. The decrease in slope observed with $P > 120\,\mathrm{mW}$, can be explained, in part, by Fig. 26.6.1. Metallization decreases the laser-induced temperature rise and the process becomes less efficient. Above about 180 mW, microcracks are occasionally observed in the region adjacent to the metal line. These cracks have no influence on the electrical conductivity of lines. However, with $P > 250\,\mathrm{mW}$, cracks penetrate deep into the bulk material. The resistance of lines as a function of scanning velocity shows a pronounced minimum between about 10 and 100 $\mu\mathrm{m/s}$ (Fig. 26.6.2b). Very slow scanning velocities favor evaporation of Pb and the formation of cracks. For high velocities, the laser-beam dwell time is too short for oxygen out-diffusion. The location of the minimum and the overall change in R depend on the laser parameters and the H_2 pressure. For the dependence of R on H_2 pressure a similar behavior has been found.

The experiments show that there are ranges of optimal parameters where metallic lines with $R < 10^3\,\Omega/\mathrm{cm}$ ($\varrho \approx 10^{-4}\,\Omega\,\mathrm{cm}$) can be fabricated with good reproducibility.

The conductivity of metallized regions within PLZT surfaces produced by *UV-laser* radiation in an H_2 atmosphere is essentially determined by the reduction of the material to metallic Pb, Ti, and Zr, the evaporation of Pb and, for certain parameters, the cracking of lines. The evaporation of Pb results in the occurrence of

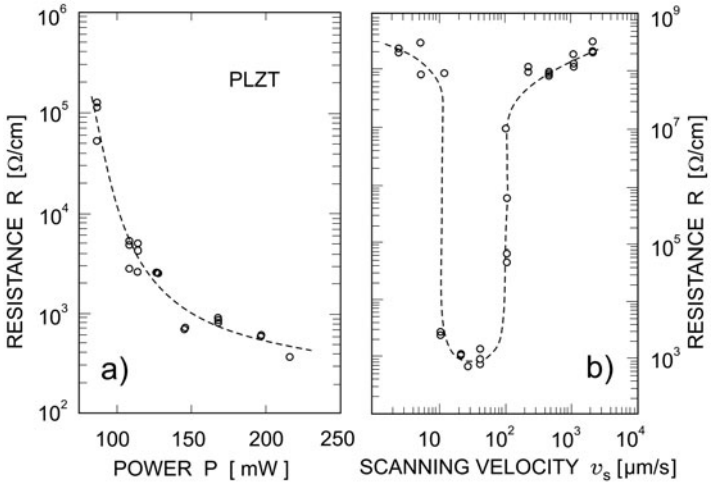

Fig. 26.6.2 (**a**) Resistance per unit length of lines produced by laser-direct writing on ceramic PLZT as a function of laser power [337–356 nm cw Kr^+ laser, $w_0 \approx 0.9\,\mu m$, $v_s = 25\,\mu m/s$; $p(H_2) = 500$ mbar]. (**b**) Same as (**a**) but for constant laser power and different scanning velocities [$P = 190$ mW, $p(H_2) = 500$ mbar] [*Kapenieks* et al. 1986a]

a shallow groove in the middle of the metal line. Local depletion of Pb is consistent with X-ray microanalysis and similar investigations performed on $PbTi_{1-x}Zr_xO_3$.

Electrodes of areas up to $0.5 \times 0.5\,cm^2$ have been fabricated on PLZT surfaces in a similar way [*Kapenieks* et al. 1986b]. They were characterized by temperature-dependent dielectric measurements on samples with different thicknesses (0.1−2 mm) at frequencies between 10 kHz and 10 MHz. Below 400 K, laser-fabricated contacts led to higher dielectric constants than conventional evaporated Au electrodes. The difference is most pronounced for small sample thicknesses. In combination with the observed increase in adherence, laser-processed electrodes, which can eventually be thickened by electrochemical plating, can be superior to conventional electrodes in microprocessing.

26.6.3 Superconductors

The physical properties of high-temperature superconductors (HTS) are sensitive to the oxygen content.

The depletion of oxygen under laser-light irradiation has been investigated for ceramic platelets and thin films of $YBa_2Cu_3O_{7-\delta}$ [*Shen* et al. 1991; *Liberts* et al. 1988b]. Here, the oxygen content within the material surface is reduced by local heating under cw Ar^+- or Kr^+-laser irradiation in a vacuum or an H_2 or N_2 atmosphere. This technique permits one to locally reduce the transition temperature from the normal to the superconducting state, or to direct write semiconducting ($\delta > 0.5$) or metallic patterns into the otherwise superconducting material

($0 \leq \delta < 0.5$). Figure 26.6.3 shows the temperature-dependent resistance of a strip line before laser treatment. It shows a clear transition from the normal to the superconducting state. After laser-induced reduction in N_2, the strip line is semiconducting. Local oxygen depletion has also been achieved by using a SNOM-type setup [*Pedarnig* et al. 1998] or an array of microspheres (Sect. 5.2). Figure 26.6.4 shows a hexagonal pattern on a thin film of $YBa_2Cu_3O_{7-\delta}$ generated by means of a 2D lattice of a-SiO_2 microlenses and a single KrF-laser pulse. The dark dots consist of small humps with a maximum height of 5–8 nm. Such a structure yields additional

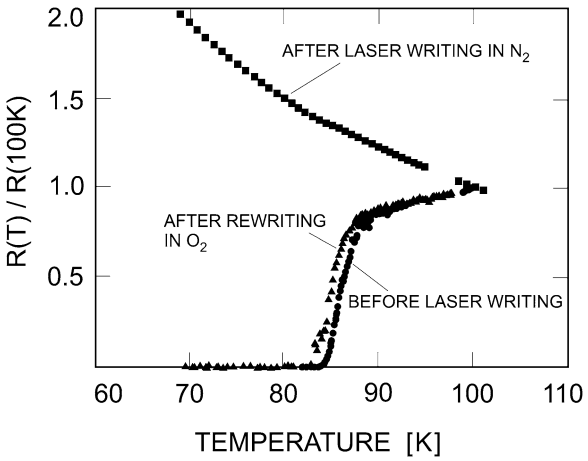

Fig. 26.6.3 Normalized resistance of a strip line in $YBa_2Cu_3O_{7-\delta}$, as a function of temperature. After Ar^+-laser-induced reduction in an N_2 atmosphere, the material is semiconducting ($I = 6 \times 10^5\,W/cm^2$, $v_s = 5\,\mu m/s$, 48 scans, $p(N_2) = 1$ bar). Superconductivity can be recovered with 2 scans in an O_2 atmosphere. For the three data sets $R(100\,K)$ was 62 Ω, 1850 Ω, and 85 Ω [*Shen* et al. 1991]

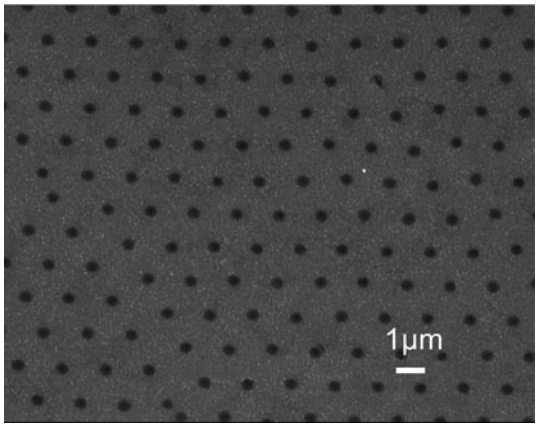

Fig. 26.6.4 $YBa_2Cu_3O_{7-\delta}$ film on (100) MgO patterned by means of 248 nm KrF-laser radiation ($\tau_\ell \approx 24$ ns) using a 2D lattice of a-SiO_2 microspheres ($d = 1.5\,\mu m$) [after *Bäuerle* et al. 2006]

well-defined periodic pinning centers for the superconducting flux. With a higher density of *periodic* pinning centers, new effects are expected.

Oxygen depletion is reversible, i.e., reoxidation recovers the superconducting state.

Laser-induced local oxidation or depletion of oxygen can be employed for surface patterning, trimming, tuning of critical currents, the fabrication of weak links for SQUIDs (superconducting quantum interference devices), etc.

Chapter 27
Transformation and Functionalization of Organic Materials

This chapter deals with laser-induced surface modifications and chemical transformations of *mainly* organic materials. It includes cases where a solid surface or a thin film is decomposed so that only a single component or a mixture of components of the original material remains. Photochemical transformations of organic resins are the basis of laser lithography and 3D-microfabrication. Laser-induced decomposition and/or ablation of organic compounds is frequently used for material patterning.

27.1 Surface Modification of Polymers

The properties of polymer surfaces can be modified by light that is strongly absorbed within a thin layer, l_α. Similar to the examples already discussed for inorganic materials, laser light permits the surface morphology, crystallinity, chemical composition, reactivity, electrical resistivity, mechanical stability, etc. of polymers to be changed *without* affecting their bulk properties. Such surface modifications change the adhesion of polymers for coatings, their optical properties, their surface wetting for liquids, etc.

Many chemical aspects of light-induced effects in organic materials have been outlined by *Lippert* 2005.

27.1.1 Laser-Enhanced Adhesion

Successful material coating and bonding is closely related to the adhesion forces between the materials under consideration. With many materials, adhesion must be increased by modifying the surfaces prior to the coating or bonding process. Besides standard chemical and physical (e.g., RF plasma) techniques, UV-laser light has been proved to be a powerful tool that opens up new possibilities. Laser-enhanced adhesion may be based on different types of surface roughening, the scission of surface chemical bonds and their saturation with other atoms/radicals,

D. Bäuerle, *Laser Processing and Chemistry,* 4th ed.,
DOI 10.1007/978-3-642-17613-5_27, © Springer-Verlag Berlin Heidelberg 2011

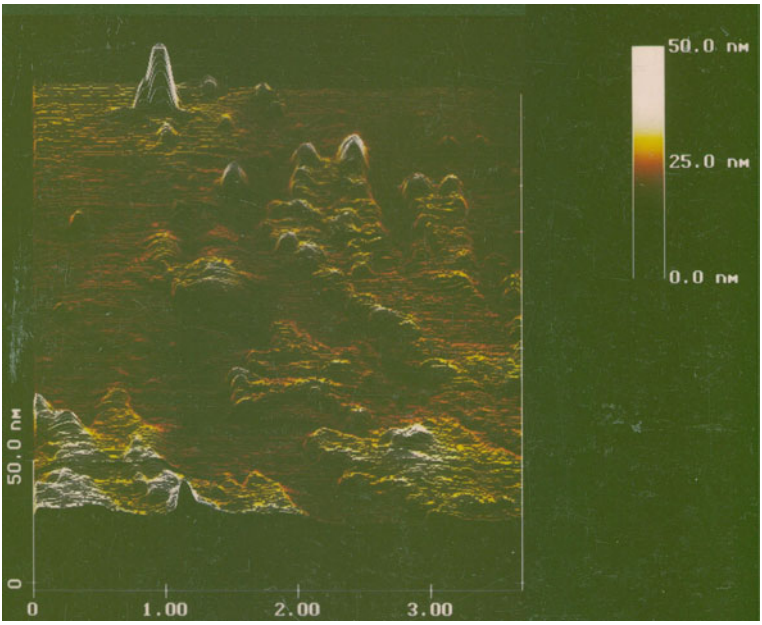

Fig. 27.1.1 AFM picture showing the surface roughening of an ultraflat PET foil after single-pulse KrF-laser irradiation ($\phi \approx 41\,\mathrm{mJ/cm^2}$). The lower length scale is in μm

etc. Systematic investigations of this type have been performed for many organic materials, in particular for polymers. Laser-enhanced adhesion between organic and organic-inorganic materials is often denoted as *photochemical welding*.

Figure 27.1.1 shows the surface of a PET foil after single-pulse KrF-laser irradiation. While the initial roughness of this (ultra-flat) foil was $\leq \pm 2.5$ nm the roughness of the irradiated area due to dendrite formation was between ± 5 and ± 30 nm (Sect. 4.3.2). The adhesion of metal films on such foils irradiated with UV light prior to film deposition is significantly increased with respect to non-irradiated foils. This is shown in Fig. 27.1.2 for a 200 nm thick CoNi film deposited by means of electron-beam evaporation. The adhesion force was measured by a standard peel test (EAA test) [*De Puydt* et al. 1988] and a modified test [*Hagemeyer* et al. 1994]. The peel strength rapidly increases with laser fluence and reaches the limit of the standard test ($\approx 4\,\mathrm{N/cm}$) at about $15\,\mathrm{mJ/cm^2}$. This fluence is considerably *below* the threshold fluence for ablation [$\phi_{\mathrm{th}}(\mathrm{PET}) \approx 40\,\mathrm{mJ/cm^2}$]. Similar results have been achieved with other Co alloys, e.g., CoCr or CoNi-oxide. Such metal coatings are applied for different types of devices. Here, the adhesion of the metal film on the polymer foil determines, to a large extent, the lifetime of the product. Another example for laser-enhanced adhesion is the "photochemical welding" of silicone rubber $[\mathrm{SiO(CH_3)_2}]_n$ with a-$\mathrm{SiO_2}$ [*Okoshi* et al. 2007] (see also Sect. 27.1.3).

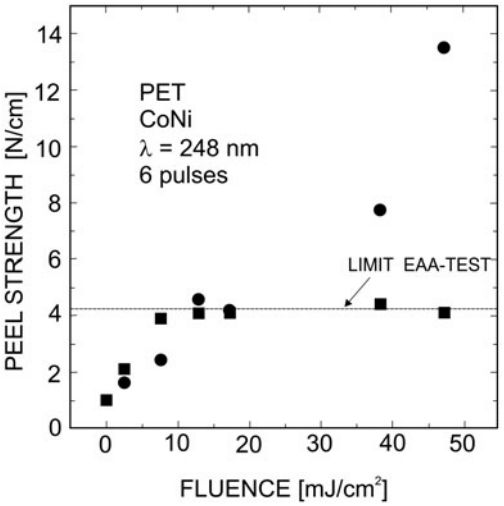

Fig. 27.1.2 Adhesion force of 200 nm thick $Co_{80}Ni_{20}$ films on PET foils (thickness $\approx$ 50 μm) irradiated with 248 nm KrF-laser light prior to film deposition. Two different types of peel tests have been employed (■ EAA test, ● modified test). The threshold fluence for ablation is $\phi_{th} \approx 40\,mJ/cm^2$ [*Hagemeyer* et al. 1994]

27.1.2 Swelling, Amorphization, Crystallization

Laser-light irradiation of polymer surfaces with fluences $\phi \leq \phi_{th}$ can significantly change the mass density of the material. An example that has already been discussed, is the volume increase observed on semicrystalline PI after single-pulse 302 nm Ar^+-laser irradiation (Sect. 12.4). This volume increase (swelling) has been ascribed to both the amorphization of crystalline domains and to polymer fragments trapped within the interaction volume. Another example is the swelling of DPT (diphenyltriazene)-doped PMMA observed after 308 nm XeCl-laser irradiation. Here, volume expansion is related to nitrogen elimination during dissociation of DPT and, possibly, to other species generated in subsequent reactions. Laser-induced swelling has been employed for well-defined surface roughening. Figure 27.1.3 shows small humps on a PEN foil irradiated by a single 500 fs KrF-laser pulse through a 2D lattice of a-SiO_2 microspheres (Fig. 5.2.1d). The distance between humps is much smaller than the diameter of microspheres. Thus, patterning is related to intensity maxima caused by higher order interference of the radiation behind the foci of neighbouring spheres (Sect. 5.2.1). Depending on laser fluence, the height of humps is between 3 and 15 nm.

Laser-induced amorphization and subsequent recrystallization may also play an important role during the growth of dendrites on PET surfaces (Sect. 4.3.2). Physical and chemical surface modifications are also responsible for laser-induced changes in the refractive index of polymers. Such index changes are used for the fabrication of waveguides, gratings, etc. (Sect. 23.6). For example, illumination of PMMA with

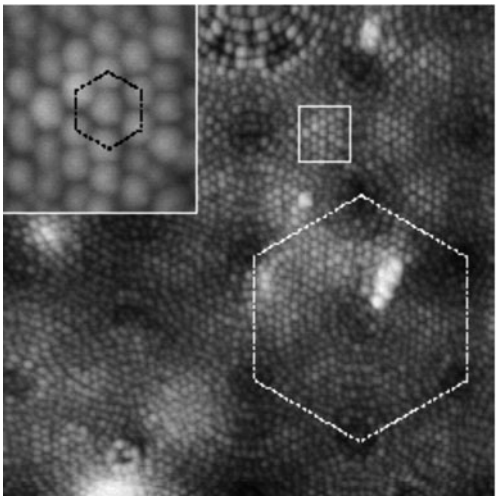

Fig. 27.1.3 Higher order subpatterns (humps) obtained on a PEN foil irradiated through a 2D lattice of a-SiO_2 microspheres with a single pulse of a 500 fs KrF-laser ($\phi \approx 900\,\mathrm{mJ/cm^2}$, $r_{sp} = 3\,\mu\mathrm{m}$, $z = f + \varepsilon$). The big hexagon connects the positions of microspheres [*Bäuerle* et al. 2003]

UV lasers or lamps and wavelengths $\lesssim 250\,\mathrm{nm}$ results in main chain scissions and the formation of C = C double bonds. This process is accompanied by an increase in mass density and refractive index. With 248 nm KrF-laser radiation an increase in refractive index of $\Delta n \approx 9 \times 10^{-3}$ has been found [*Pfleging* et al. 2003a; *Bityurin* et al. 1997]. Transient changes in the optical properties of PI induced by ArF-laser pulses have been studied by *Ball* et al. (1995a, b).

27.1.3 Photochemical Exchange of Species

Photochemical transformations of polymer surfaces is a field of extensive investigations. Here, UV-laser or lamp irradiation in a reactive ambient medium causes photochemical bond breaking and substitution of atoms/molecules in the polymer surface by radicals of the precursor molecules. The material studied in most detail is PTFE (Teflon). Irradiation of PTFE in a reactive medium may result in defluorination of the surface and substitution of F atoms by different functional groups. An example is the photochemical reaction

$$\begin{array}{c} \mathrm{F\ F} \\ \mathrm{|\ \ |} \\ \mathrm{[–C–C–]}_n \\ \mathrm{|\ \ |} \\ \mathrm{F\ F} \end{array} + \mathrm{NH_3} + h\nu(193\,\mathrm{nm}) \rightarrow \begin{array}{c} \mathrm{NH_2\ NH_2} \\ \mathrm{|\ \ \ \ |} \\ \mathrm{[–C–C–]}_n \\ \mathrm{|\ \ \ \ |} \\ \mathrm{F\ \ F} \end{array} + \mathrm{HF} \qquad (27.1.1)$$

The laser fluences employed in this processing mode are well below the ablation threshold and, typically, $\phi < 50\,\mathrm{mJ/cm^2}$. Because PTFE has negligible absorption at 193 nm, direct breaking of C–F bonds by ArF-laser radiation ($h\nu \approx 6.4\,\mathrm{eV}$) seems to be unlikely. Photochemical exchange seems to be enhanced by the reaction of H atoms with F [bond energy $\Delta E_\mathrm{D}(\mathrm{HF}) \approx 5.7\,\mathrm{eV}$; $\Delta E_\mathrm{D}(\mathrm{CF}) \approx 5.1\,\mathrm{eV}$] [*Gumpenberger* et al. 2005; *Heitz* et al. 2002, 1996; *Bäuerle* et al. 2000]. In a similar way, ArF-laser irradiation in N_2H_4 atmosphere photolyses the hydrazine. The photoproducts, mainly H, NH_2, N_2H_3, and NH, react with the PTFE surface and also substitute F by NH_2 radicals [*Niino* and *Yabe* 1996b]. ArF-laser irradiation in $B(CH_3)_3$ results in the substitution of F radicals by CH_3 groups [$\Delta E_\mathrm{D}(\mathrm{BF}) \approx 7.9\,\mathrm{eV}$; *Murahara* and *Toyoda* 1995]. In similar investigations using an aqueous solution of $B(OH)_3$, F atoms are substituted by OH. KrF-laser irradiation of PTFE in an aqueous solution of phenylhydrazine promotes abstraction of F atoms by H radicals and incorporation of NH_2 and OH groups into PTFE chains [*Niino* and *Yabe* 1998]. All of these surface transformations have been performed also with UV-radiation from 172 nm $Xe_2{}^*$- and 146 nm $Kr_2{}^*$-lamps.

In any case, reactions of this type turn the originally hydrophobic/lipophobic PTFE surface into hydrophilic/lipophilic. Such transformed surfaces show good adherence to metal coatings and they are biocompatible. Because of its low dielectric constant, metallization of PTFE is attractive with respect to different applications, e.g. for printed wiring boards. Epoxy bonding to steel is increased, typically, from 20 to $1280\,\mathrm{N/cm^2}$ [*Niino* et al. 1997; *Murahara* and *Toyoda* 1995]. The biocompatibility of transformed PTFE surfaces has been proved via the adhesion and growth of biological cells, e.g. endothelial cells [*Heitz* et al. 2005; *Gumpenberger* et al. 2005, 2003]. Similar investigations have been performed for other material/cell combinations [*Hanada* et al. 2009b; *Pfleging* et al. 2009; *Olbrich* et al. 2008; *Hopp* et al. 2008]. Irradiation of the surface via a contact mask permits the fabrication of living micro-cell arrays for high throughput analysis of gene functions, pharmacological testings, cell multiplexing, etc. [*Mikulikova* et al. 2005].

Photochemical exchange of species was also studied for PC, PE (polyethylene), PET, and PP (polypropylene).

27.1.4 Chemical Degradation

UV-laser radiation with fluences $\phi \approx \phi_\mathrm{th}$ may cause drastic changes in the composition of polymer surfaces.

Multiple-pulse UV-laser irradiation of PI significantly decreases the surface concentration of oxygen and nitrogen with respect to carbon (Fig. 12.1.3). This process results in a dramatic increase in surface conductivity (Fig. 27.1.4). After about 500 laser pulses, the sheet conductance (Sect. 30.4.3) is increased by about 15 orders of magnitude. This effect is ascribed to the formation of a carbon-rich layer on the polymer surface. If irradiation is performed in O_2, the conductance is lowered, while in Ar or N_2 it is enhanced with respect to air. The maximum conductance

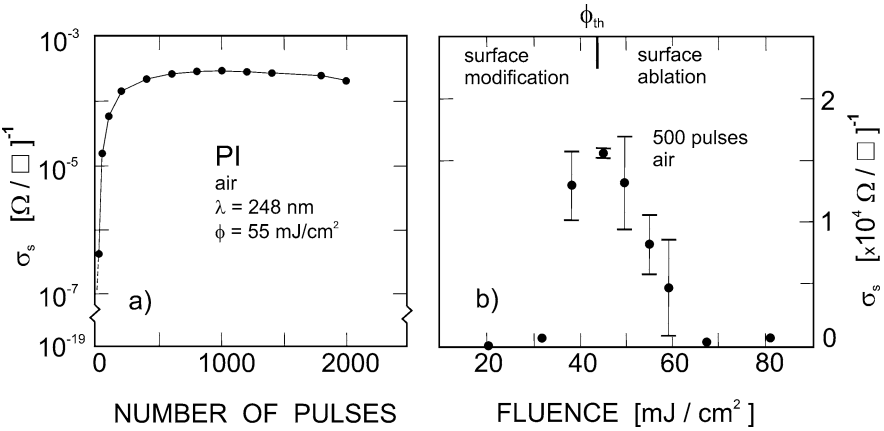

Fig. 27.1.4 a, **b** Dependence of the sheet conductance of PI (Upilex R) foils on KrF-laser treatment in air ($\tau_\ell \approx 28$ ns, 5 Hz, $w_x \times w_y \approx 2 \times 20\,\mathrm{mm}^2$). The threshold fluence for ablation is $\phi_{th}(\mathrm{PI}, 248\,\mathrm{nm}) \approx 44 \pm 3\,\mathrm{mJ/cm}^2$ [*Arenholz* et al. 1993]

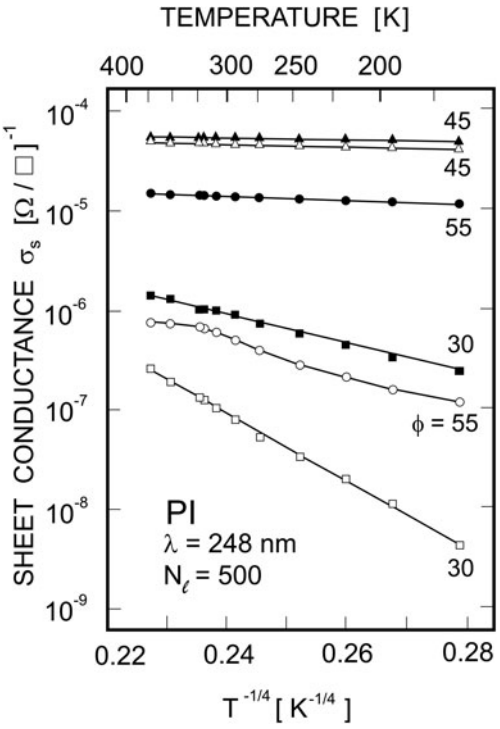

Fig. 27.1.5 Temperature dependence of the sheet conductance for PI irradiated with KrF-laser light at different fluences (*solid symbols*: after irradiation; *open symbols*: after irradiation and treatment in aqueous HCl) [*Bäuerle* et al. 1995a]

appears for fluences near ϕ_{th} (Fig. 27.1.4b). The conducting layer is highly porous and has a thickness of around 0.5 µm, depending on the experimental conditions. By using laser-beam interference (Fig. 5.2.1c), line patterns with widths of 0.5 µm and periods of 0.9 µm have been fabricated [*Phillips* et al. 1993b].

The temperature dependence of σ_s is shown in Fig. 27.1.5 for different laser fluences. Open symbols refer to samples which were exposed to aqueous HCl subsequent to irradiation. This treatment destroys carbon–carbon double bonds formed at the surface. With fluences both below and above the ablation threshold, the conductivity can be described by variable range hopping [*Mott* and *Davis* 1979],

$$\sigma = \sigma_0 \exp\left[-\left(\frac{T_0}{T}\right)^{1/4}\right] . \qquad (27.1.2)$$

For $\phi \approx \phi_{th}$, the temperature dependence of the conductivity shows 'metal-like' behavior. XRD studies indicate that the conducting layer consists of amorphous carbon with a small amount of carbon-rich clusters [*Qin* et al. 1998]. Laser-beam interference has been employed for the fabrication of line patterns with variable resistance in (conducting) polyanliline (PANI) [*Lasagni* et al. 2008]. These investigations are of particular interest for electrochemical sensor technology.

27.2 Chemical Transformations Within Thin Films and Bulk Materials

Light-induced transformations within organic materials are widely studied in connection with photochromic reactions (Sect. 23.6), photodecomposition, and polymerization. Photopolymerization has become an important field in polymer science and technology. Here, UV or VIS radiation is used for converting monomers or prepolymers into crosslinked networks. An example is the transformation of MMA (methylmethacrylate) into PMMA (poly-MMA). Lasers permit *localized* polymerization by direct writing, laser-light projection and interference (Sect. 5.2.1). Photopolymerization based on multiple-photon absorption opens up new possibilities in 3D-photoprocessing.

For *surface* patterning mainly excimer lasers and frequency-multiplied Nd:YAG lasers, are employed.

The most important applications of *laser-induced* chemical transformations include the following:

- *Laser lithography*. Since about 1996 Hg-lamps employed in optical lithography for microelectronic chip fabrication ($\lambda = 436$ nm or 365 nm) are substituted by UV lasers, mainly KrF- and ArF-excimer lasers (Sect. 27.2.1). For special applications maskless techniques gain increasing importance, e.g. for customization, or the direct fabrication of low-resolution patterns (Sect. 27.2.2).

- *Decomposition* of precursor and template films for direct surface patterning of materials, surface marking, etc. (Sect. 27.2.3).
- *Photopolymerization* for the fabrication of optical waveguides, 3D optical data storage, photonic bandgap structures, etc. (Sect. 27.2.4).

The fabrication of microstructures by laser-induced transformation and decomposition of thin solid films is shown schematically in Fig. 27.2.1. In the first step, the substrate is coated with a photoresist (Fig. 27.2.1a) or a thin film which already contains the precursor molecules (Fig. 27.2.1b). Frequently, such films are fabricated by spin-on, spray-on, paint-on and other techniques with a thickness of 0.1 to 10 μm, depending on the particular application. In the second step, the film is selectively transformed by laser-light projection, direct writing, laser-beam interference, etc. (Sect. 5.2). With precursor films, this step frequently causes a strong

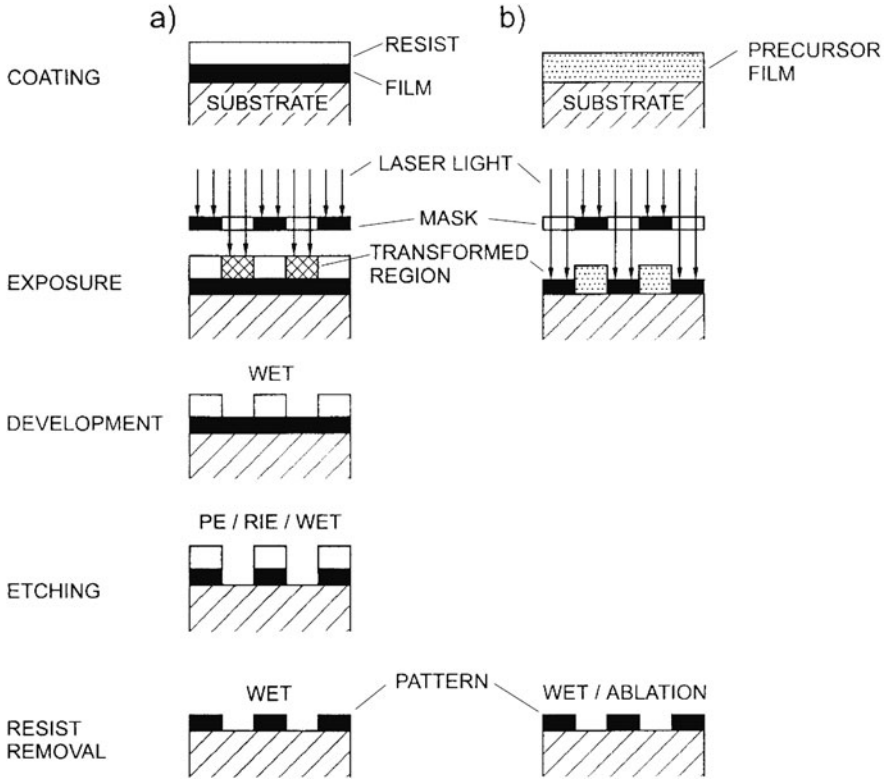

Fig. 27.2.1 a, **b** Main steps of pattern formation by laser-induced solid-phase transformation. (**a**) Laser lithography by 'standard' (positive) photoresist technique (layer thickness ~ 0.5 μm). (**b**) Decomposition of a precursor film. Note the difference in height between the precursor film and the resulting pattern

shrinkage in height (Fig. 27.2.1b). In the third step, illuminated or non-illuminated resist/precursor film material is dissolved.

By far the most important application of light-induced chemical transformations within thin (resist) films is projection photolithography (Fig. 27.2.1a). It should be noted, however, that the term laser lithography is used throughout the literature also for other, quite different techniques of thin film or substrate patterning. Among those are the following:

- Single-step patterning by *direct* laser-induced ablation of the photoresist.
- Direct laser-induced ablation or etching of the film/substrate without employing any photoresist.
- Selective area gas- or liquid-phase deposition.
- Structural or chemical modifications of surfaces by direct writing, interference, etc.

These techniques have been described in previous chapters.

27.2.1 Laser Lithography

Projection photolithography is the main high-throughput patterning technology in microelectronic circuit fabrication. The main steps of this process are shown in Fig. 27.2.1a: a prepatterned transparent mask with opaque features is imaged in reduction onto a photoresist-covered substate. The optical arrangement is, in principle, similar to that schematically shown in Fig. 5.2.1b. In reality, however, distortion-free and chromatic-aberration-free flat-field imaging over the field of interest requires a large number of complex optical elements and a narrow-band (spectral) line source for illumination. A large number of identical features, in particular ICs on Si wafers, are produced by exposing a small substrate area, stepping the substrate to a new location, and then repeating the exposure process. As a result of exposure, the resist undergoes chemical changes. During development, the photoresist is dissolved within illuminated (positive resist) or non-illuminated (negative resist) areas. The remaining resist protects regions from subsequent processing steps such as etching, doping, and metallization. This sequence is iterated up to more than 30 times to produce a typical chip. The smallest feature or linewidth that a lithographic optical system can produce is determined by the wavelength of the light source and the numerical aperture of the projection optics, as discussed together with (5.2.1). Because the depth of focus, DOF, decreases with the second power of *NA* (5.2.2), smaller feature sizes can be achieved mainly by reducing the laser wavelength. At present, the only lasers that fulfill the requirements for high-resolution lithography, in particular with respect to wavelength, spectral band width, intensity, etc., are excimer lasers. While lithography with 248 nm KrF- and 193 nm ArF-lasers are already on line, the application of 157 nm F_2-laser radiation is still questionable, mainly due to the photo-induced degradation of the imaging optics.

193 nm ArF-Laser Lithography

Suitable *materials* for the design of 193 nm projection optics are high-purity a-SiO_2 and crystalline CaF_2. These materials have a relatively low absorption coefficient at 193 nm (Table III), they can be fabricated with a good optical homogeneity with respect to the index of refraction and low stress birefringence, and they have a reasonable stability to 193 nm radiation. With both a-SiO_2 and CaF_2, the absorption coefficient increases with the number of laser pulses, mainly due to the generation of color centers. For high-quality a-SiO_2 with $0.001 \leq \alpha \leq 0.004$, a laser fluence of $\phi \approx 1\,\mathrm{mJ/cm^2}$, and $N_\ell = 2 \times 10^9$ pulses, the increase in α is almost zero to a factor of two. The trend is similar in CaF_2. In contrast to CaF_2, irradiation of a-SiO_2 causes compaction, i.e., a volumetric reduction (densification), which is accompanied by an increase in refraction index within the exposed volume and by stress birefringence around it.

The development of *photoresists* with optimal absorptivity, photosensitivity, intrinsic resolution, and stability to subsequent processing steps, e.g., plasma etching (PE), is another challenge in 193 nm lithography. Among the photoresists investigated are aliphatic acrylic polymers, and resists with alicyclic groups (cyclic configurations with single C–C bonds). A different resist process that has been studied is top surface imaging (TSI) in polyvinylphenol (this is cross-linked by 193 nm radiation) and subsequent vapor-phase silylation and oxygen reactive ion etching (RIE) [*Rothschild* 1998; *Ohfuji* et al. 1996].

A large field ($32.5 \times 22\,\mathrm{mm^2}$) step-and-scan system that utilizes catadioptric projection optics (refractive parts made out of a-SiO_2) with $NA = 0.5$ was developed by *Rothschild* and coworkers. Together with a combination of different resist techniques, fully scaled MOSFETs on SOI wafers were fabricated with a minimum feature size of 200 nm.

Several optical techniques have been developed to further increase the spatial resolution, i.e., to lower the limits set by (5.2.1) and (5.2.2) by decreasing ξ_1 and increasing ξ_2. This is denoted as *wavefront engineering* or *resolution enhancing techniques* (RET). Among those are off-axis illumination, phase-shifting masks, and optical proximity correction. For example, through the use of phase-shifting masks instead of traditional binary (opaque/transparent) masks the edges of contours become sharper due to destructive interference. By this means, 110 nm features with a DOF of about 1 µm have been produced (Fig. 27.2.2). With ArF immersion-lithography feature sizes of only 45 nm have been achieved.

157 nm F_2-Laser Lithography

At present, CaF_2 is the only practical optical material for 157 nm lithography. Its absorption coefficient at 157 nm is significantly higher than that of high-quality a-SiO_2 at 193 nm (Table III). However, the laser-induced temperature rise in CaF_2 is smaller, because of its higher thermal conductivity (Table II). Additionally, the temperature dependence of the refractive index of CaF_2 is significantly weaker, so that the overall optical effect due to absorption is smaller than that of 193 nm radiation in a-SiO_2.

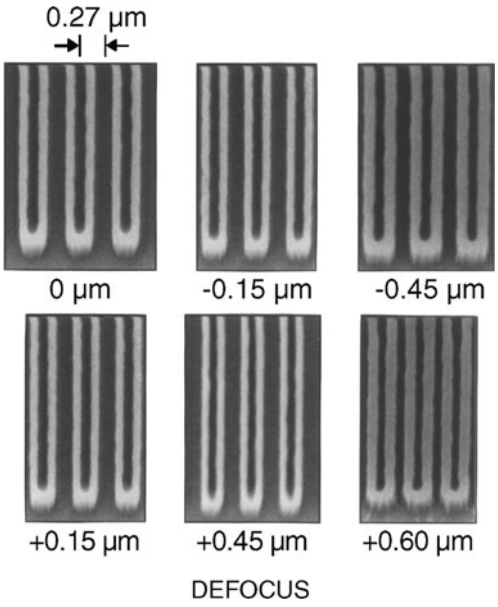

Fig. 27.2.2 Scanning electron micrographs of 110 nm lines produced by means of 193 nm ArF-laser radiation, a chromeless phase edge photomask and $NA \approx 0.5$. The images show the change in feature size as the focus is varied [*Rothschild* 1998]

With 157 nm laser radiation, absorption of O_2 and H_2O is so strong that the beam path must be purged with dry N_2. By using a 200 Hz, 40 mJ/pulse F_2-laser, a chromeless phase-shifting CaF_2 mask, a Schwarzschild microscope objective for projection, and the TSI method, lines with 80 nm width have been fabricated. This resolution corresponds to the limit $\xi_1' = 0.25$ in (5.2.1).

Nevertheless, the degradation of the expensive imaging optics due to photo-induced formation of defects, in particular of color centers, has prevented large-scale industrial applications.

Plasmon-Polariton Waveguides

Dielectric-loaded surface plasmon-polariton waveguides (DLSPPWs) consist of dielectric ridges, in most cases a polymer, on a smooth metal film, mainly Au, supported by a substrate, mainly glass [*Holmgaard* et al. 2008]. In comparison to direct writing of DLSPPWs based on two-photon polymerization (see below), UV-laser lithography is more appropriate for mass production.

EUV Lithography

For the next generation of optical lithography, light sources that emit extreme ultraviolet (EUV) radiation at 13.5 nm are under development. The efforts are concentrated on essentially two competing technologies based on a laser-produced plasmas

(LPP) and gas discharge-produced plasmas (GDPP) [*Stamm* 2004]. For the latter, the major challenges are related to the thermal load and lifetime of the discharge electrodes. For LPP sources further developments of several ten kW pulsed lasers are necessary. With both GDPP and LPP sources, the debris-related lifetime of the collector optics is a problem. The most promising sources based on LPPs use Sn targets together with Q-switched Nd:YAG- or CO_2-lasers [*Nakamura* et al. 2008].

For industrial applications of EUV lithography in nanoelectronic chip fabrication, an average EUV power of 100–200 W within a bandwidth of around 2% at 13.5 nm is required.

27.2.2 Maskless Techniques

Lithography using direct writing, near-field optical techniques, and laser-beam interference permits surface patterning with subwavelength resolution. The various experimental techniques are based on quite different physical mechanisms. Among those are thermal and nonlinear optical processes that result in a strong confinement of the interaction volume, as discussed in Chap. 5 and throughout different parts of the book. For example, by direct writing using fs-laser two photon polymerization of a resin, feature sizes below 25 nm have been achieved [*Tan* et al. 2007; see also Sect. 27.3]. Nanolithography has been demonstrated also by near-field optical techniques using, e.g., a SNOM-type-setup (Fig. 5.2.1d) [*Riehn* et al. 2003; *Zeisel* et al. 1997], by *single* optically trapped microlenses [*Fardel* et al. 2010; *McLeod* and *Arnold* 2009], or arrays of microlenses [*Lim* et al. 2007; *Bäuerle* et al. 2002; *Denk* et al. 2002], by surface-plasmon assisted techniques, by combining laser-direct writing with STED (stimulated emission depletion) [*Fischer* et al. 2010], etc. The resolution achieved in many of these experiments is well below 100 nm. However, these processes are very slow and permit applications only in very special cases. In direct writing, the scanning speeds are between 0.1 μm/s and a few cm/s, depending on the particular technique employed.

Laser interference lithography in combination with thermal annealing has been used for maskless fabrication of large-area periodic structures. By this technique Au nanodots on a-SiO_2 substrates have been fabricated [*Ma* et al. 2008].

Low-Resolution Patterns

For applications that do not require submicrometer resolution, one or several of the processing steps shown in Fig. 27.2.1a can be replaced by laser techniques as well. For example, two time-consuming wet chemical processes, namely development and resist removal can be eliminated by *direct* laser ablation of the photoresist. This process shall be denoted by laser-ablation lithography (LAL). Other terms like excimer-laser ablation lithography (EAL) are found in the literature as well. The application of LAL has been investigated in connection with the fabrication of

thin-film transistors (TFT; Sect. 23.2.2) [*Suzuki* et al. 1998] and solar cells [*Glunz* et al. 2000]. In these experiments, mainly KrF-laser radiation has been employed. Typical lateral dimensions of the patterns are several ten μm.

For rapid maskless processing, liquid crystal devices (LCDs) and digital micromirror devices (DMDs) have been employed as electrically controllable spatial light modulators. With LCDs line patterns with widths of around 10 μm have been fabricated [*Hayashi* et al. 2008]. By combining a DMD and near-field optics, feature sizes even down to 100 nm have been achieved [*Pan* et al. 2010].

27.2.3 Decomposition of Precursor Films

Substrate patterning by laser-induced decomposition of a precursor film is used for the fabrication of a mask or a reactive template, for the formation of 'seed' layers, or the direct fabrication of metallic, semiconducting or insulating patterns. Some types of surface marking are based on thermal or photochemical decomposition of coating layers as well (Sect. 11.8.3).

In most applications, the precursor is dissolved in an adequate solvent, coated onto the substrate, and dried or baked for excess solvent removal. Precursor films are between a monolayer and several micrometers thick. For thick films, and many materials, a strong shrinkage in height due to laser-induced material decomposition and vaporization of product species takes place. Patterning by direct writing has been performed with scanning speeds up to 10 cm/s. Presently the main drawbacks for applications in microfabrication are related to the low throughput or/and the porosity of the resultant material, or/and the incorporation of impurities originating from non-volatile decomposition products, or/and the tendency for (non-coherent) structure formation, etc.

Extended thin films can be fabricated by using high-power unfocused or defocused laser beams, or a line focus. The thickness of deposits can subsequently be increased by employing standard techniques, e.g., CVD, electrochemical plating, etc.

Among the precursor films investigated in most detail are organometallic compounds, metal acetates, organosilicates, and composites.

Examples for Pattern Formation

For the fabrication of *metal* patterns, one of the most interesting classes of precursor compounds are metallopolymers that are stable at room temperature. In the first detailed experiments in this area, Au and Pd patterns were produced on SiO_2 and Si substrates by using Ar^+-laser radiation for (overall exothermal) material transformation [*Gross* et al. 1987]. Subsequent to laser direct writing, non-transformed parts of the precursor film were dissolved in CH_2Cl_2. Figure 27.2.3a displays the average width of Au lines as a function of Ar^+-laser power for two scanning velocities. The

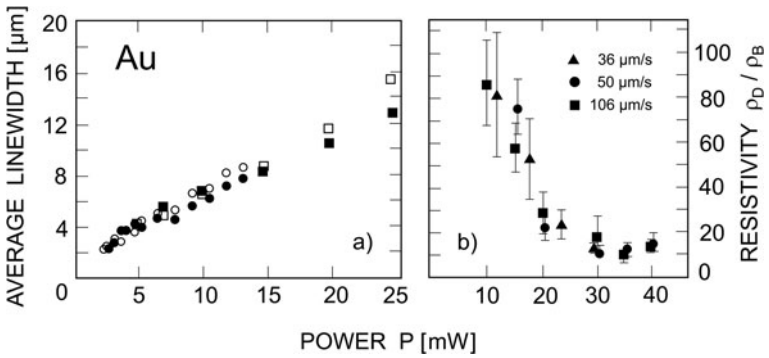

Fig. 27.2.3 a, **b** Properties of Au lines fabricated by 514.5 nm Ar^+-laser-induced decomposition of a metallopolymer film (thickness after pre-baking $\approx$ 1.7 μm). (**a**) Average width. ●, ■: v_s = 36 μm/s, ○, □: v_s = 206 μm/s (different symbols designate data from different samples) [*Fisanick* et al. 1985]. (**b**) Electrical resistivity of lines normalized to the resistivity of bulk Au ($\varrho_B \approx 2.44\,\Omega$ cm) [*Fennell* et al. 1985]

width of lines increases approximately linearly, as in LCVD. Lines produced with powers < 10 mW were incompletely reacted. The (normalized) electrical resistivity of Au lines is shown in Fig. 27.2.3b as a function of laser power. For $P > 25$ mW, the resistivity is about five times that of evaporated Au films. The large error bars in the low power range are related to periodic non-coherent structures (Sect. 28.3.4). The same technique has been used for a variety of other materials (see previous edition).

The fabrication of metal patterns by excimer-laser light projection or by means of a contact mask has also been demonstrated [*Esrom* and *Wahl* 1989]. For example, Pd patterns were fabricated from palladium (II) acetate films ($\approx$ 0.1 μm thick) which were spin-coated onto SiO_2 or ceramic Al_2O_3 substrates, illuminated by excimer-laser light, and developed in CCl_4. Subsequently, the thin Pd patterns ($\approx$ 60 Å thick) were electroless plated with Cu ($h_1 \approx$ 0.1 to 6 μm; plating rate about 15 Å/s). With ceramic Al_2O_3 substrates, the film adhesion was typically $\geq$ 30 N/mm^2. Contact metallization of laser-drilled via-holes using the same process has also been demonstrated. Decomposition of Pd-acetate films is thermally activated.

Another example of solid-phase transformation is the generation of *SiO_2 patterns* by laser pyrolysis of organosilicate films produced by spin-coating from $Si(OR)_x(OH)_{4-x}$ [*Krchnavek* et al. 1984]. Smooth, continuous lines were fabricated on Si-wafers by employing 514.5 nm Ar^+-laser radiation and scanning speeds up to 100 μm/s. Linewidths as small as 1 μm were obtained.

Patterning of alkylsiloxane monolayers on surface-oxidized silicon substrates by 514.5 nm Ar^+-laser-induced thermal decomposition was reported by *Balgar* et al. (2006). At scanning speeds of up to 2.5 cm/s, linewidths down to 200 nm have been achieved. These subwavelength linewidths can be explained by the strong nonlinearity of the process (Sect. 5.3). Similar experiments have been performed with

fs-laser pulses on a-SiO_2 substrates [*Hartmann* et al. 2008]. Here, the excitation of the (linearly) transparent layer/substrate is based on multiphoton absorption, as described in Sect. 13.6.

27.2.4 3-D Photopolymerization

Photopolymerization can be employed for 3D-fabrication by stereolithography. This technique uses a CAD (computer aided design) program that controls scanning of either the laser beam or an *xyz*-positioning stage for the model to be fabricated. In *single-photon* stereolithography using UV or VIS radiation, the 3D-structure is built up by photopolymerization of the resin in a layer-by-layer process. Today, this technique is widely employed for the fabrication of 3D-model structures and devices. By using laser-beam interference for layer-by-layer polymerization, 3D periodic structures have been fabricated [*Lai* et al. 2010].

Fabrication of 3D-structures based on *multiphoton* polymerization employs ultrashort-pulse lasers. In this case, the laser light is focused into the *volume* of the photosensitive material and initiates polymerization by *nonlinear* absorption within the focal spot. The small volume in which polymerization takes place, is often denoted as voxel. The resins employed for multiphoton polymerization are various types of viscous liquids such as acrylates, epoxys, hybrid organic-inorganic

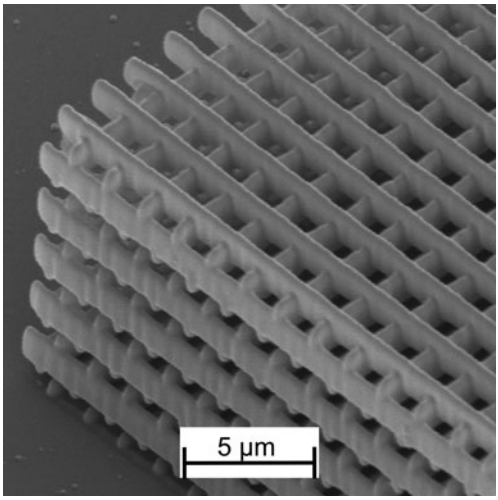

Fig. 27.2.4 SEM picture showing a detail of a photonic crystal structure generated by two-photon polymerization from a mixture of a silica sol-gel and a nonlinear optical chromophore (780 nm Ti:sapphire laser, $\phi \approx 44\,\mathrm{mJ/cm^2}$, $v_s = 20\,\mu\mathrm{m/s}$, $\tau_\ell \approx 60\,\mathrm{fs}$, $\nu_r = 90\,\mathrm{MHz}$). The total side length of the quadratic structure is about 35 µm. Since the contrast in refractive index to air is only about 0.5, the structure shows no real photonic bandgap, but a NIR stop-gap in certain directions [*Farsari* et al. 2008]

polymers, e.g., ORMOCER (organically modified ceramic), silica sol-gels, etc. In most cases, these materials are mixed with a photoinitiator. With fs-Ti:sapphire laser radiation, polymerization in these materials is, in most systems, based on two-photon absorption (Sect. 3.2). After polymerization the unexposed material is dissolved in an organic liquid (ethanol, THF, etc.). The minimum feature sizes achieved are well below 100 nm [*Haske* et al. 2007; *Tan* et al. 2007]. The technique has been employed for the growth of fibers (Sect. 17.2), the fabrication of different types of microscopic models and mechanical devices [*Mizeikis* et al. 2006; *Straub* et al. 2004; *Sun* et al. 2001], distributed feedback (DFB) resonators [*C.F. Li* et al. 2007], photonic crystal templates [*Deubel* et al. 2004], and dielectric-loaded surface plasmon-polariton waveguides (DLSPPWs), splitters, couplers, etc. [*Luo* et al. 2009; *Reinhardt* et al. 2007; *Kiyan* et al. 2007]. While mass fabrication of DLSPPWs is certainly cheaper by using UV-laser lithography (Sect. 27.2.1), laser direct writing permits rapid prototyping of different types of patterns. Of particular interest is the fabrication of 3D photonic crystal structures [*Farsari* et al. 2008; *Haske* et al. 2007; *Mizeikis* et al. 2006; *Straub* et al. 2004; *Deubel* et al. 2004]. Figure 27.2.4 shows an example of a photonic structure generated in a mixture consisting of a photosensitive silica sol-gel and a nonlinear optical chromophore.

27.3 Laser-LIGA, LAN

Laser-LIGA provides a fast and flexible technique for the fabrication of masters which are subsequently used for economic replication by standard techniques. The main steps of this technique are shown in Fig. 27.3.1. The polymer coating is patterned by excimer-laser ablation (Chaps. 12 and 13). Subsequently, a thin metallic film, e.g. Ni, is evaporated onto the patterned surface. This film is thickened, e.g.,

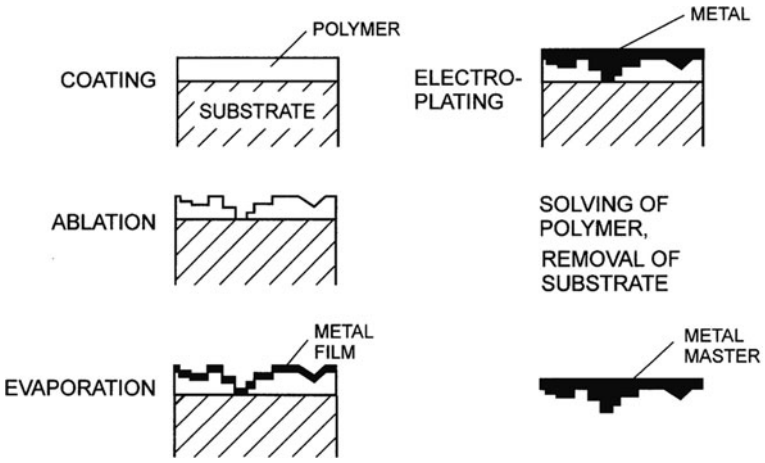

Fig. 27.3.1 Main steps during the fabrication of a master tool by laser-LIGA

by electroplating. If necessary, the resulting metal surface is planarized. Finally, the polymer film is dissolved and the substrate released. Sometimes, this step involves shock-freezing in liquid N_2. The master can then be used for pattern formation by imprinting, injection molding, etc.

While standard LIGA, which employs X-ray lithography, permits a higher resolution and the fabrication of deeper patterns, laser-LIGA permits real 3D-pattern formation with arbitrary heights of patterns, inclined walls, etc. Finally, laser-LIGA is much faster and cheaper than standard LIGA.

LAN

Laser-assisted nanoimprint lithography (LAN) is a technique which uses a transparent master fabricated, e.g. from a-SiO_2, together with a laser. The master (mold) is pressed onto the polymer/resist-coated substrate. Laser exposure *through* the transparent mold softens/melts the resist layer and thereby facilitates imprinting. By using single-pulse 308 nm XeCl-laser radiation, regular 100 nm wide grating lines have been fabricated. Self-perfection by laser-assisted liquefaction (SPEL) is a new technique in nanofabrication which diminishes defects and improves the quality of structure profiles [*Xia* and *Chou* 2010].

Chapter 28
Instabilities and Structure Formation

Instabilities are observed in many different types of laser processing. They are related to positive feedbacks between different characteristics (degrees of freedom) in laser–matter interactions. The appearance of an instability means that a small perturbation of the system initially grows exponentially with time. Its further development can lead to different self-organization phenomena, such as spontaneous formation of periodic or stochastic dissipative structures, spiral waves, and many other structures with broken or unbroken symmetry ('unbroken' refers to transformations from an unstable structure to a stable or metastable structure without changes in initial symmetry).

From a *scientific* point of view, the analysis of instabilities yields fundamental information on laser–matter interactions. From a *technical* point of view, many applications of laser materials processing require spontaneous structure formation to be suppressed or even avoided altogether.

28.1 Coherent and Non-coherent Structures

Structures that develop on solid or liquid surfaces under the action of laser light can be classified into coherent structures and non-coherent structures.

Coherent structures are *directly* related to the coherence, the wavelength, and the polarization of the laser light. For non-coherent structures such a direct relation to these laser parameters is absent.[1]

The feedback that causes coherent or non-coherent structure formation can originate from different mechanisms such as local thermal expansion, changes in optical or thermal properties, surface tension effects, surface acoustic waves (SAW), capillary waves, melting, vaporization, transformation energies, chemical reactions, etc.

Coherent structures have a common origin: the oscillating radiation field on the material surface which is generated by the *interference* between the incident laser

[1] In the traditional theory of self-organization (synergetics) the term 'coherent' is sometimes used in a different way. It denotes cooperative structure formation with an 'internal' period that does *not* depend on the initial and boundary conditions, any external disturbances, etc.

D. Bäuerle, *Laser Processing and Chemistry,* 4th ed.,
DOI 10.1007/978-3-642-17613-5_28, © Springer-Verlag Berlin Heidelberg 2011

beam and scattered/excited surface waves. The spatial periods of such structures are therefore proportional to the laser wavelength.

Non-coherent structures are *not* directly related to any spatial periodicity of the energy input caused by interference phenomena. Here, the feedback results in either spontaneous symmetry breaking or a non-trivial spatio-temporal ordering of the (whole) system [*Gaponov-Grekhov* et al. 1989; *Haken* 1983; *Nicolis* and *Prigogine* 1977].

An example where coherent *and* non-coherent structure formation can be seen *simultaneously* is shown in Fig. 28.1.1a. The slow oscillation (long spatial period) is not related to the laser wavelength and polarization. It depends only on the laser-beam intensity, scanning velocity, and the gas pressure. Superimposed on these slow oscillations are fine periodic structures. The distance between these ripples is proportional to the laser wavelength. Their orientation is perpendicular to the electric vector of the incident light. Non-coherent structure formation can be suppressed by changing the experimental conditions. This is demonstrated in Fig. 28.1.1b. The ripples are still present. Their orientation can be changed by changing the polarization of the incident light (Fig. 28.1.1c). Ripple formation can also be suppressed, to a large extent, by an appropriate selection of experimental parameters. Within the literature, ripples are often denoted as LIPSS (laser-induced periodic surface structures).

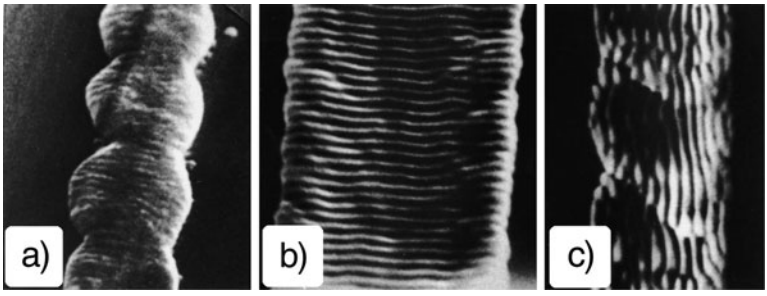

Fig. 28.1.1a–c Coherent and non-coherent structures observed during 488 nm Ar^+-laser direct writing of Si lines (from SiH_4) on Si wafers. The slow oscillation in (**a**) is superimposed by ripples whose periods are of the order of the laser wavelength. The orientation of ripples depends on the polarization of the electric vector of the radiation. This was parallel to the scanning direction in (**b**) and perpendicular to it in (**c**) [*Bäuerle* 1984]

28.1.1 Equations

A theoretical description of coherent and non-coherent structure formation is quite complex. It requires one to solve the electrodynamic, heat, and kinetic equations simultaneously in three dimensions by taking into account the different *feedback* mechanisms involved. The (partial) differential equations have an infinite number of degrees of freedom (here, this term is used in a way different to classical mechanics).

Therefore, simplified models which provide further insight into the problem are very useful. Following synergetic methods, one can restrict the problem to the 'most important' degrees of freedom which are termed *order parameters*, $\mathscr{O}_i$. Their choice is sometimes a question of physical intuition.

From a mathematical point of view, the evolution of order parameters can be described by differential equations of the type

$$\left(\frac{\partial}{\partial t} + \boldsymbol{v}_\mathrm{s}\nabla\right)\mathscr{O}_i = \sum_j \nabla(\mathscr{D}_{ij}\nabla\mathscr{O}_j) + \mathscr{F}_i \tag{28.1.1}$$

with $i = 1, 2, \ldots, n$, where n is the number of order parameters. $\mathscr{D}_{ij} \equiv \mathscr{D}_{ij}(\boldsymbol{O})$ are 'diffusion' coefficients and $\boldsymbol{O} \equiv \{\mathscr{O}_1, \mathscr{O}_2, \ldots, \mathscr{O}_n\}$. $\boldsymbol{v}_\mathrm{s}$ is the velocity of the moving medium as, for example, the moving ablation front, the scanning velocity of the laser beam, etc. For non-autonomous systems the source term depends explicitly on time, so that $\mathscr{F}_i = \mathscr{F}_i(\boldsymbol{O}; \boldsymbol{x}, t)$. For autonomous non-homogeneous systems $\mathscr{F}_i$ depends on the (spatial) coordinates $\boldsymbol{x}$ only, i.e., $\mathscr{F}_i = \mathscr{F}_i(\boldsymbol{O}; \boldsymbol{x})$. If $\mathscr{F}_i = \mathscr{F}_i(\boldsymbol{O})$, the system is termed homogeneous and autonomous.

In some cases, (28.1.1) can be reduced to a set of *ordinary* differential equations. Some examples will be discussed in Sect. 28.3.

28.1.2 Stability

There are different approaches to investigate the stability of solutions [*Haken* 1983]. Let us consider *small* perturbations, $\mathscr{O}_i^\mathrm{p}(\boldsymbol{x}, t)$, of the stationary solution $\mathscr{O}_i = \mathscr{O}_i^\mathrm{s}(\boldsymbol{x})$ so that

$$\mathscr{O}_i(\boldsymbol{x}, t) = \mathscr{O}_i^\mathrm{s}(\boldsymbol{x}) + \mathscr{O}_i^\mathrm{p}(\boldsymbol{x}, t) \; .$$

The relevant equations can then be linearized with respect to $\mathscr{O}_i^\mathrm{p}$ by the ansatz

$$\mathscr{O}_i^\mathrm{p}(\boldsymbol{x}, t) = \mathscr{O}_i(\boldsymbol{x}) \exp(\Gamma t) \; . \tag{28.1.2}$$

This ansatz enables one to determine the eigenvectors $\boldsymbol{O}^{(j)}(\boldsymbol{x}) = \{\mathscr{O}_1^{(j)}, \ldots, \mathscr{O}_n^{(j)}\}$ and the dispersion relations for the increments $\Gamma^{(j)} = \gamma^{(j)} - i\Omega^{(j)}$, where $j = 1, 2, \ldots, n$.

For distributed systems, only a part of the spatial coordinates $\boldsymbol{x}$ explicitly enter the linearized equations. These coordinates shall be denoted by $\boldsymbol{x}_1$. $\boldsymbol{x}_2$ stands for all other coordinates, i.e., the linearized problem is *homogeneous* with respect to $\boldsymbol{x}_2$. Then, $\mathscr{O}_i^{(j)}(\boldsymbol{x})$ can often be written in the form

$$\mathscr{O}_i^{(j)}(\boldsymbol{x}) = \mathscr{O}_i^{(j)}(\boldsymbol{x}_1) \exp(\mathrm{i}\boldsymbol{q}\boldsymbol{x}_2) \; .$$

All $\Gamma^{(j)}$, $\gamma^{(j)}$ and $\Omega^{(j)}$ are functions of $\boldsymbol{q}$. If for some value of $\boldsymbol{q}$ one of the $\gamma^{(j)}(\boldsymbol{q}) > 0$, the particular stationary solution $\mathscr{O}_i^{\mathrm{s}}(\boldsymbol{x})$ is unstable. If for all values of $\boldsymbol{q}$ all $\gamma^{(j)}(\boldsymbol{q}) < 0$, the solution is stable.

28.1.3 Coherent Structures

For coherent structures, the source term depends on order parameters in such a way that it becomes a periodic function of some coordinates, for example,

$$\mathscr{F}_i \propto \mathscr{R}e[\exp(\mathrm{i}\boldsymbol{q}\boldsymbol{x})] = \cos \boldsymbol{q}\boldsymbol{x} \ , \tag{28.1.3}$$

where $\boldsymbol{q}$ is the wavevector of the surface corrugation. The dispersion relation has the form

$$\Gamma = \Gamma(\boldsymbol{q}, \boldsymbol{k}_{\mathrm{i}}, \varepsilon) \ , \tag{28.1.4}$$

where $\boldsymbol{k}_{\mathrm{i}}$ is the wavevector of the incident laser light, and ε the permittivity of the material. Additionally, Γ depends also on other parameters which influence the feedback. The orientation and dominant period of the structure that develops most rapidly is given by the maximum value of the increment, $\gamma_{\max}$.

28.1.4 Non-coherent Structures

For non-coherent structures, $\mathscr{F}$ is *not* periodic in $\boldsymbol{x}$ and sometimes even independent of $\mathscr{O}_i$. Nevertheless, the increment Γ depends on some internal period, $\boldsymbol{q}_{\mathrm{nc}}$. The $\boldsymbol{q}_{\mathrm{nc}}$ related to the maximum increment $\gamma_{\max}(\boldsymbol{q}_{\mathrm{nc}})$ determines the period of the structure in the initial phase.

With increasing amplitude of the (coherent or non-coherent) structure, nonlinearities become important. In this regime, the generation and coupling of different harmonics, the interference of surface electromagnetic waves oriented in different directions, etc., make the problem more complex.

28.2 Ripple Formation

Frequently observed coherent structures in laser-surface processing are ripples. These are spatially periodic structures, also denoted as LIPSS (laser-induced periodic surface structures; Figs. 28.1.1 and 28.2.1).

Ripple formation was first observed by *Birnbaum* (1965) after ruby-laser irradiation of various semiconductor surfaces. Further investigations have shown that ripple formation is a quite general phenomenon which is practically always observed on solid or liquid surfaces within certain ranges of laser parameters. Ripples originate from the interference of the incident and reflected/refracted laser light with the scattered (diffracted) light near the interface.

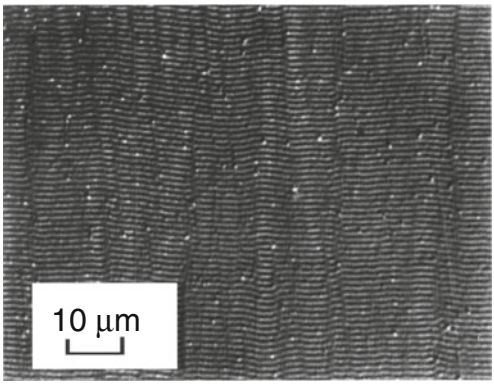

Fig. 28.2.1 Ripples (LIPPS) generated on Ge with linearly polarized 1.06 µm Nd:YAG-laser radiation at perpendicular incidence ($\boldsymbol{q} \parallel \boldsymbol{E}_\mathrm{i}$) [*Driel* et al. 1985]

Scattering of the incident light can be caused by microscopic roughnesses of the surface, by defects, spatial variations in the dielectric constant, etc. The interference between the different waves leads to an inhomogeneous energy input which, together with positive feedback mechanisms, can cause surface instabilities.

The intensity of the scattered waves depends on the laser parameters and the type of material. If the material under consideration possesses an optically active mode near the laser frequency, the scattered light can directly excite a real surface electromagnetic wave (SEW). Such SEWs or surface polaritons are waves travelling along the interface between two media. If, on the other hand, there is *no* optically active mode near the laser frequency, ν_ℓ, ripples can form if one of the diffracted waves propagates close to the surface. These 'waves' are sometimes denoted as radiation remnants. In any case, the *period* of the emerging structure (distance between ripples) depends on the wavelength ($\Lambda \propto \lambda$), the angle of incidence, Θ_i, and the polarization of the laser beam. The *orientation* of ripples is determined by the polarization of the incident light and, in some cases, by Θ_i. With metals and semiconductors, the ripples are mainly oriented perpendicularly to the electric vector of the incident light. With dielectrics, both perpendicular and parallel orientations are observed.

28.2.1 Interference Pattern

A laser beam that hits a *plane* transparent substrate surface is partially reflected and partially transmitted. The amplitudes of reflected and transmitted waves are given by the Fresnel formulas. If, however, the surface is *rough*, diffracted waves will also appear. These diffracted waves interfere with the incident wave $\boldsymbol{k}_\mathrm{i}$, the reflected wave $\boldsymbol{k}_\mathrm{r}$, and the transmitted wave $\boldsymbol{k}_\mathrm{t}$. This results in a periodic intensity distribution near the substrate surface.

The solid shall be characterized by a uniform dielectric constant $\varepsilon = \varepsilon' + \mathrm{i}\varepsilon''$. Let us start with transparent materials where $\varepsilon' > 1$ and $\varepsilon'' \approx 0$. For the linear

problem it is sufficient to study the diffraction of the incident laser light, $\boldsymbol{E}_\mathrm{i} = \mathscr{R}e\{\boldsymbol{E}_0 \exp[\mathrm{i}(\boldsymbol{k}_\mathrm{i}\boldsymbol{r} - \omega t)]\}$, by the Fourier component of the surface roughness, which shall be characterized by the wave vector $\boldsymbol{q}$ and frequency Ω_q. We define the plane of incidence as the xz-plane, as shown in Fig. 28.2.2. In general, the vector $\boldsymbol{q}$ is oriented in arbitrary directions within the xy-plane. In the figure, $\boldsymbol{q}$ shall be oriented, for simplicity, in the x-direction. The corrugation of the surface is described by

$$z(\boldsymbol{r}) = \frac{1}{2}\left(\tilde{\xi}\exp(\mathrm{i}\boldsymbol{q}\boldsymbol{r}) + \mathrm{c.c.}\right) = \xi\cos(\boldsymbol{q}\boldsymbol{r} + \delta)\ , \tag{28.2.1}$$

where $\tilde{\xi}$ is a complex amplitude and $q = 2\pi/\Lambda$. With σ-polarization $\boldsymbol{E}_\mathrm{i} \parallel y$ (TE wave) and with π-polarization $\boldsymbol{H}_\mathrm{i} \parallel y$ (TM wave) (instead of σ and π one sometimes uses the letters s and p, respectively). Due to diffraction, we obtain

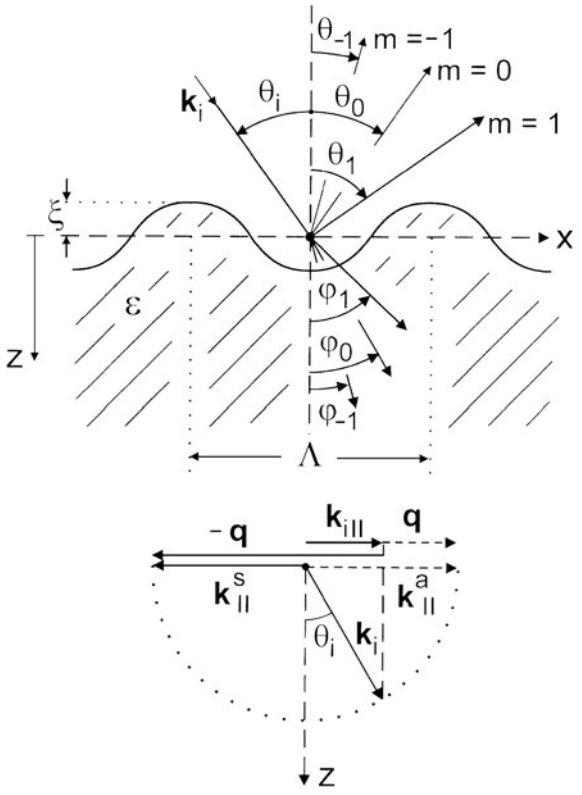

Fig. 28.2.2 Reflection and refraction at a corrugated surface. The lower part illustrates a wavevector diagram for the diffracted reflected wave along the surface. $\boldsymbol{k}_\mathrm{i}$ is the wave vector of the incident laser light and $\boldsymbol{k}_{\mathrm{i}\parallel}$ its projection onto the surface. $\boldsymbol{q}$ is the grating vector which characterizes the surface corrugation. The scattered waves can have wavevectors $\boldsymbol{k}^\mathrm{s}_\parallel = \boldsymbol{k}_{\mathrm{i}\parallel} - \boldsymbol{q}$ (Stokes wave; *solid arrows*) or $\boldsymbol{k}^\mathrm{a}_\parallel = \boldsymbol{k}_{\mathrm{i}\parallel} + \boldsymbol{q}$ (anti-Stokes wave; *dashed arrows*)

a set of reflected and refracted waves. The diffracted (scattered) waves within the vacuum ($z < 0$) and within the medium ($z > 0$) are given by the grating equation

$$\boldsymbol{k}_{\parallel}^{\mathrm{s,a}} = \boldsymbol{k}_{\mathrm{i}\parallel} \mp m\boldsymbol{q} \tag{28.2.2}$$

or, for the simplified case $\boldsymbol{q} \parallel \boldsymbol{k}_{\mathrm{i}\parallel}$, as shown in Fig. 28.2.2,

$$k_{\mathrm{i}} \sin\Theta_m = k \sin\varphi_m = k_{\mathrm{i}} \sin\Theta_{\mathrm{i}} \mp mq \ ,$$

where $\boldsymbol{k}_{\parallel}^{\mathrm{s,a}} \equiv \boldsymbol{k}_{\mathrm{r}\parallel}^{\mathrm{s,a}} = \boldsymbol{k}_{\mathrm{t}\parallel}^{\mathrm{s,a}}$ are surface components of the wavevectors of the Stokes ($-$sign) and anti-Stokes ($+$sign) diffracted (scattered) waves. The indices r and t indicate that these diffracted waves are related to either the reflected or the transmitted light. Θ_m and φ_m are, respectively, the angles of the reflected and refracted (transmitted) waves of order m with $m = 0, 1, 2, \ldots$. Henceforth, we shall restrict the analysis to the first order diffracted waves, i.e., $m = 1$. If the medium with $z < 0$ is a vacuum, the wave vector of the laser light is given by $k_{\mathrm{i}} = \omega/c = 2\pi/\lambda$. In the medium, $z > 0$, we have $k = n\omega/c$, where $n = \sqrt{\varepsilon}$ is the refractive index. The z-components can be obtained from the Helmholtz equations, $k_{\parallel}^2 + k_z^2 = \varepsilon k_{\mathrm{i}}^2$, for the corresponding media, which yield

$$k_{\mathrm{rz}}^{\mathrm{s,a}} = \left(k_{\mathrm{i}}^2 - k_{\parallel}^{\mathrm{s,a}2}\right)^{1/2} \quad \text{and} \tag{28.2.3a}$$

$$k_{\mathrm{tz}}^{\mathrm{s,a}} = \left(\varepsilon k_{\mathrm{i}}^2 - k_{\parallel}^{\mathrm{s,a}2}\right)^{1/2} \ . \tag{28.2.3b}$$

These equations are quite general and even hold for arbitrary values of ε' and ε''. Ripple formation is most pronounced when either $\boldsymbol{k}_{\mathrm{r}}^{\mathrm{s,a}}$ or $\boldsymbol{k}_{\mathrm{t}}^{\mathrm{s,a}}$ is parallel to the surface, i.e., if $\boldsymbol{k}_{\mathrm{rz}}^{\mathrm{s,a}}$ or $\boldsymbol{k}_{\mathrm{tz}}^{\mathrm{s,a}}$ are close to zero. Thus, we obtain with (28.2.3) and (28.2.2) for the (first-order) *reflected* waves

$$k_{\mathrm{i}} = k_{\parallel}^{\mathrm{s,a}} = \left|\boldsymbol{k}_{\mathrm{i}\parallel} \mp \boldsymbol{q}\right| \ , \tag{28.2.4a}$$

and for the *transmitted* waves

$$\varepsilon^{1/2} k_{\mathrm{i}} = k_{\parallel}^{\mathrm{s,a}} = \left|\boldsymbol{k}_{\mathrm{i}\parallel} \mp \boldsymbol{q}\right| \ . \tag{28.2.4b}$$

We now consider the situation where the first-order scattered (reflected or transmitted) waves are either along the x-axis (Fig. 28.2.2) or along the y-axis (Fig. 28.2.3). These two cases are, in fact, the most important ones. This is discussed in more detail together with SEWs. For the *reflected* waves we obtain from (28.2.4a)

$$q = k_{\mathrm{i}}(1 \pm \sin\Theta_{\mathrm{i}}) \qquad \text{for } \boldsymbol{q} \parallel x \tag{28.2.5a}$$

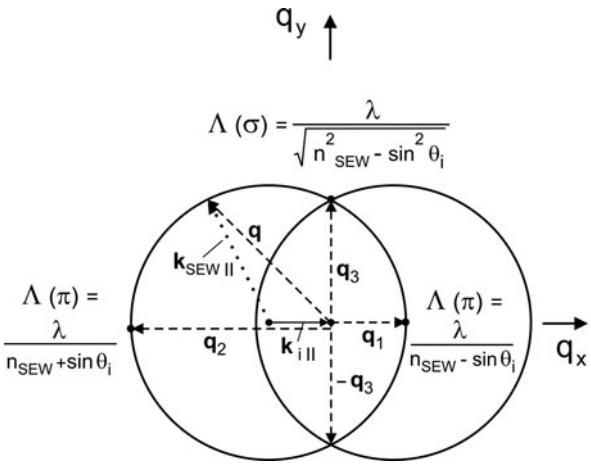

Fig. 28.2.3 Schematic showing the projection of wavevectors onto the xy-plane. The radius of circles is $k_{\mathrm{SEW}\|}$ as given by (28.2.7)

and

$$q = k_i(1 - \sin^2 \Theta_i)^{1/2} \qquad \text{for } \boldsymbol{q} \parallel y \,. \tag{28.2.5b}$$

With $q = 2\pi/\Lambda$, the spatial period of the interference pattern becomes

$$\Lambda = \frac{\lambda}{1 \pm \sin \Theta_i} \qquad \text{for } \boldsymbol{q} \parallel \boldsymbol{k}_{i\|} \parallel x \tag{28.2.5c}$$

and

$$\Lambda = \frac{\lambda}{\cos \Theta_i} \qquad \text{for } \boldsymbol{q} \perp \boldsymbol{k}_{i\|}\,, \text{ i.e., } \boldsymbol{q} \parallel y \,. \tag{28.2.5d}$$

For the *transmitted* wave we obtain in analogy to (28.2.4b)

$$q = k_i(n \pm \sin \Theta_i) \qquad \text{for } \boldsymbol{q} \parallel x \tag{28.2.6a}$$

and

$$q = k_i(n^2 - \sin^2 \Theta_i)^{1/2} \qquad \text{for } \boldsymbol{q} \parallel y \,. \tag{28.2.6b}$$

The period of the interference is then

$$\Lambda = \frac{\lambda}{n \pm \sin \Theta_i} \qquad \text{for } \boldsymbol{q} \parallel \boldsymbol{k}_{i\|} \parallel x \tag{28.2.6c}$$

and

$$\Lambda = \frac{\lambda}{(n^2 - \sin^2 \Theta_\mathrm{i})^{1/2}} \qquad \text{for } \boldsymbol{q} \perp \boldsymbol{k}_{\mathrm{i}\parallel}\,, \text{ i.e., } \boldsymbol{q} \parallel y\,. \tag{28.2.6d}$$

Ripples with periods equal to (28.2.5) and (28.2.6) have been observed experimentally.

Ripple Formation due to SEW

With materials that possess an optically active mode near ν_ℓ, surface electromagnetic waves can be excited if $\varepsilon'(\nu_\ell) < -1$. Their wavevector within the xy-plane is

$$k_{\mathrm{SEW}\parallel} = \left(\frac{\varepsilon'}{\varepsilon' + 1}\right)^{1/2} k_\mathrm{i} \equiv n_\mathrm{SEW} k_\mathrm{i}\,. \tag{28.2.7}$$

The field of SEWs decays exponentially into both the substrate and the ambient medium. The different types of SEWs include surface phonon-polaritons observed in insulators and semiconductors, surface plasmon-polaritons in metals, etc.

Ripple formation is most pronounced if one of the scattered waves is in resonance with a SEW, i.e., if

$$\boldsymbol{k}_\parallel^{\mathrm{s,a}} = \boldsymbol{k}_{\mathrm{i}\parallel} \mp \boldsymbol{q} = \boldsymbol{k}_{\mathrm{SEW}\parallel}\,, \tag{28.2.8a}$$

therefore

$$\left|\boldsymbol{q} \pm \boldsymbol{k}_{\mathrm{i}\parallel}\right| = n_\mathrm{SEW} k_\mathrm{i}\,. \tag{28.2.8b}$$

Thus, all possible wavevectors $\boldsymbol{q}$ that match this condition can be described within the $\boldsymbol{q}$-plane by two circles of radius $n_\mathrm{SEW} k_\mathrm{i}$ that are shifted by $\pm\boldsymbol{k}_{\mathrm{i}\parallel}$ with respect to the origin $\boldsymbol{q} = 0$. This is shown in Fig. 28.2.3. SEWs are π-polarized with respect to the plane fixed by $k_{\mathrm{SEW}\parallel}$ and z.

If the incident light is π-polarized, i.e., if $\boldsymbol{E}_\mathrm{i}$ is within the xz-plane, the SEWs that are most efficiently excited propagate in $\pm x$-direction. Thus, the strongest ripples will have wave vectors $\boldsymbol{q}_1$ and $\boldsymbol{q}_2$, as shown in Fig. 28.2.3. Simple calculations result in an equation similar to (28.2.5c), except that n has to be substituted by n_SEW:

$$\Lambda(\pi) = \frac{\lambda}{n_\mathrm{SEW} \pm \sin \Theta_\mathrm{i}} \approx \frac{\lambda}{1 \pm \sin \Theta_\mathrm{i}} \qquad \text{for } \boldsymbol{q} \parallel \boldsymbol{k}_{\mathrm{i}\parallel} \parallel x\,. \tag{28.2.9}$$

The approximation refers to the case where $|\varepsilon| \gg 1$ and thus $n_\mathrm{SEW} \approx 1$. This situation refers, e.g., to metals and semiconductors (Sect. 11.6.2).

The situation is more complicated if the incident light is σ-polarized, i.e., if $\boldsymbol{E}_\mathrm{i} \parallel y$. In this case the most prominent grating vectors are $\pm\boldsymbol{q}_3$ (Fig. 28.2.3).

Because both $+\boldsymbol{q}_3$ *and* $-\boldsymbol{q}_3$ fulfill the resonant condition (28.2.8), and because both belong to the *same* corrugation, two SEWs are created. This enhances the interference. The period Λ is then, in analogy to (28.2.6d), given by

$$\Lambda(\sigma) = \frac{\lambda}{(n_{\mathrm{SEW}}^2 - \sin^2\Theta_\mathrm{i})^{1/2}} \approx \frac{\lambda}{\cos\Theta_\mathrm{i}} \quad \text{for } \boldsymbol{q} \perp \boldsymbol{k}_{\mathrm{i}\parallel}\,, \text{ i.e., } \boldsymbol{q} \parallel y\,. \tag{28.2.10}$$

The approximation refers again to $n_{\mathrm{SEW}} \approx 1$.

28.2.2 Distribution of Energy

We now consider the distribution of the absorbed energy. In the general case, the diffracted fields can be calculated from the Maxwell equations and the boundary conditions on the corrugated surface. Here, we take into account only terms of first order in the corrugation ξ/λ, and $m = 1$. For arbitrary polarization, the electric vector of the anti-Stokes diffracted wave in the medium at $z = 0$ can be written as [*Agarwal* 1977; *Akhmanov* et al. 1985]:

$$\boldsymbol{E}_\mathrm{t}^\mathrm{a} = \mathrm{i}\frac{\tilde{\xi}}{2}\left(\check{k}_\mathrm{rz}^\mathrm{a} - k_\mathrm{tz}^\mathrm{a}\right)\frac{\left[\boldsymbol{k}_\mathrm{t}^\mathrm{a} \times \left(\boldsymbol{E}_\mathrm{t} \times \check{\boldsymbol{k}}_\mathrm{r}^\mathrm{a}\right)\right]}{\boldsymbol{k}_\mathrm{t}^\mathrm{a}\boldsymbol{k}_\mathrm{t}^\mathrm{a}}\,, \tag{28.2.11}$$

where $\check{\boldsymbol{k}}_\mathrm{r}^\mathrm{a} \equiv (\boldsymbol{k}_\parallel^\mathrm{a}, -k_\mathrm{rz}^\mathrm{a})$. $\boldsymbol{E}_\mathrm{t}$ is the amplitude of the refracted wave, given by the Fresnel formulas. The decay of waves is described by the imaginary part of wave vectors. The analogous equation for the Stokes wave is obtained with the substitution $\tilde{\xi} \to \tilde{\xi}^*$, where the asterisk indicates the complex-conjugated value.

From the transmitted (Fresnel) wave, and the anti-Stokes and Stokes waves *inside* the medium, one can calculate the source term Q as in Sect. 2.2.1. With $z = 0$, we obtain

$$\begin{aligned} Q &\propto \boldsymbol{E}\boldsymbol{E}^* \propto \left[\boldsymbol{E}_\mathrm{t}\exp(\mathrm{i}\boldsymbol{k}_\mathrm{t}\boldsymbol{r}) + \boldsymbol{E}_\mathrm{t}^\mathrm{a}\exp(\mathrm{i}\boldsymbol{k}_\mathrm{t}^\mathrm{a}\boldsymbol{r}) + \boldsymbol{E}_\mathrm{t}^\mathrm{s}\exp(\mathrm{i}\boldsymbol{k}_\mathrm{t}^\mathrm{s}\boldsymbol{r})\right]\cdot(\mathrm{c.c.}) \\ &\propto \boldsymbol{E}_\mathrm{t}\boldsymbol{E}_\mathrm{t}^* + \left[(\boldsymbol{E}_\mathrm{t}^\mathrm{a}\boldsymbol{E}_\mathrm{t}^* + \boldsymbol{E}_\mathrm{t}\boldsymbol{E}_\mathrm{t}^{\mathrm{s}*})\exp(\mathrm{i}\boldsymbol{q}\boldsymbol{r}) + \mathrm{c.c.}\right] \\ &= Q_0\left[1 + \left(\frac{\tilde{\xi}}{2}k_\mathrm{i}\tilde{F}\exp(\mathrm{i}\boldsymbol{q}\boldsymbol{r}) + \mathrm{c.c.}\right)\right] = Q_0\left[1 + \mu\cos(\boldsymbol{q}\boldsymbol{r} + \delta + \psi)\right]\,, \end{aligned} \tag{28.2.12}$$

where the complex modulation coefficient

$$\tilde{\mu} \equiv \tilde{\xi}k_\mathrm{i}\tilde{F} = 2\frac{\boldsymbol{E}_\mathrm{t}^\mathrm{a}\boldsymbol{E}_\mathrm{t}^* + \boldsymbol{E}_\mathrm{t}\boldsymbol{E}_\mathrm{t}^{\mathrm{s}*}}{\boldsymbol{E}_\mathrm{t}\boldsymbol{E}_\mathrm{t}^*} \tag{28.2.13}$$

has been introduced. Substituting (28.2.11) into (28.2.13), $\boldsymbol{E}_\mathrm{t}$, ξ, and λ cancel in the expression for $\tilde{F}$. The result can then be written in terms of a 3D polarization vector of the transmitted wave, $\hat{\boldsymbol{e}}_\mathrm{t}$, as

$$\tilde{F} \equiv F\exp(\mathrm{i}\psi) = \mathrm{i}\frac{\breve{k}_{\mathrm{rz}}^{\mathrm{a}} - k_{\mathrm{tz}}^{\mathrm{a}}}{k_{\mathrm{i}}} \cdot \frac{\hat{\boldsymbol{e}}_{\mathrm{t}}^{*}\left[\boldsymbol{k}_{\mathrm{t}}^{\mathrm{a}} \times \left(\hat{\boldsymbol{e}}_{\mathrm{t}} \times \breve{\boldsymbol{k}}_{\mathrm{r}}^{\mathrm{a}}\right)\right]}{\breve{\boldsymbol{k}}_{\mathrm{r}}^{\mathrm{a}}\boldsymbol{k}_{\mathrm{t}}^{\mathrm{a}}} + \left(\mathrm{i}\frac{\breve{k}_{\mathrm{rz}}^{\mathrm{s}} - k_{\mathrm{tz}}^{\mathrm{s}}}{k_{\mathrm{i}}} \cdot \frac{\hat{\boldsymbol{e}}_{\mathrm{t}}^{*}\left[\boldsymbol{k}_{\mathrm{t}}^{\mathrm{s}} \times \left(\hat{\boldsymbol{e}}_{\mathrm{t}} \times \breve{\boldsymbol{k}}_{\mathrm{r}}^{\mathrm{s}}\right)\right]}{\breve{\boldsymbol{k}}_{\mathrm{r}}^{\mathrm{s}}\boldsymbol{k}_{\mathrm{t}}^{\mathrm{s}}}\right)^{*} . \quad (28.2.14)$$

In this form, $\tilde{F}$ depends only on the polarization of the incident wave, the angle of incidence, and the complex dielectric constant of the medium.

The inhomogeneous part in the absorbed energy distribution (28.2.12) can generate a modulation of thermal and non-thermal surface processes. In the simplest approximation, the surface temperature rise is

$$\Delta T(\boldsymbol{r}) = \Delta T_{\mathrm{av}} + \delta T(\boldsymbol{r}) \propto Q_0\left[1 + \xi k_{\mathrm{i}} F\cos(\boldsymbol{q}\boldsymbol{r} + \delta + \psi)\right] , \quad (28.2.15)$$

where ΔT_{av} is the uniform temperature rise and $\delta T(\boldsymbol{r})$ the temperature modulation. If, for example, $\psi = 0$, the amount of energy absorbed within the valleys of ripples is larger than that on the hills (Fig. 28.2.4a). If, however, $\psi = \pi$, the situation is opposite (Fig. 28.2.4c).

The expressions for $\boldsymbol{E}_{\mathrm{t}}^{\mathrm{a}}$ or $\boldsymbol{E}_{\mathrm{t}}^{\mathrm{s}}$, and therefore for $\tilde{F}$, have typical resonant denominators

$$\Delta \propto \breve{\boldsymbol{k}}_{\mathrm{r}}^{\mathrm{s,a}}\boldsymbol{k}_{\mathrm{t}}^{\mathrm{s,a}} \propto \varepsilon k_{\mathrm{rz}}^{\mathrm{s,a}} - k_{\mathrm{tz}}^{\mathrm{s,a}} . \quad (28.2.16)$$

The latter proportionality can be obtained from (28.2.3). Inspection of (28.2.11) shows that Δ influences mainly the component of the scattered (diffracted) field $\boldsymbol{E}_{\mathrm{t}}^{\mathrm{s,a}}$ that lies in the plane of propagation of this wave defined by $\boldsymbol{k}_{\parallel}^{\mathrm{s,a}}$. The condition $\Delta = 0$ is equivalent to $k_{\parallel}^{\mathrm{s,a}} = k_{\mathrm{SEW}\parallel}$. In reality, as $k_{\parallel}^{\mathrm{s,a}}$ is *real* [see (28.2.2)] and $k_{\mathrm{SEW}\parallel}$ is complex, Δ can never become zero.

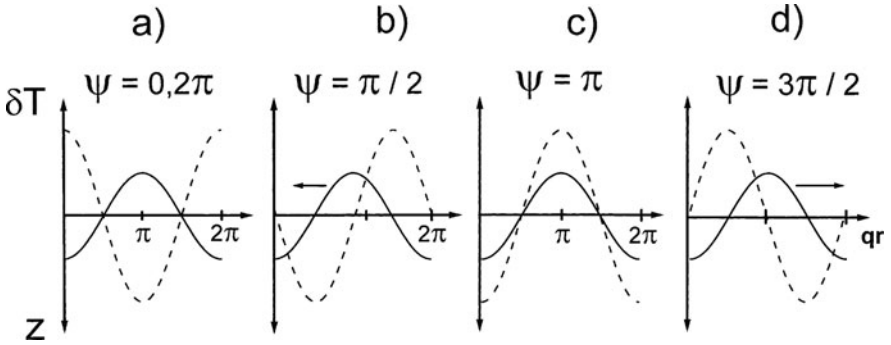

Fig. 28.2.4 a–d Modulation of temperature (*dashed curves*) and surface profile (*solid curves*) for different values of the phase ψ. The direction of ripple movement applies, e.g., to a feedback mechanism based on evaporation

For SEWs and $|\varepsilon'| \gg |\varepsilon''|$, $|\varepsilon'| \gg 1$, the *amplitude* F in (28.2.14) is of the order of [*Akhmanov* et al. 1985]

$$F \approx \left| \frac{k_\mathrm{i}(\varepsilon - 1)}{\varepsilon k_\mathrm{rz}^{\mathrm{s,a}} - k_\mathrm{tz}^{\mathrm{s,a}}} \right| \approx \frac{k_\mathrm{i}}{|\varepsilon'|^{1/2} \cdot \left| (\Delta k_\parallel^{\mathrm{s,a}} - \mathrm{i}\Pi) \right|} \,, \tag{28.2.17}$$

where $\Delta k_\parallel^{\mathrm{s,a}}$ is given by

$$\Delta k_\parallel^{\mathrm{s,a}} \equiv k_\parallel^{\mathrm{s,a}} - k_{\mathrm{SEW}\parallel} \approx k_\parallel^{\mathrm{s,a}} - \left(\frac{\varepsilon'}{\varepsilon' + 1} \right)^{1/2} k_\mathrm{i} \,. \tag{28.2.18}$$

Π describes the damping of the SEW, which is given by

$$\Pi \approx \frac{k_\mathrm{i} \varepsilon''}{2\,|\varepsilon'|^2} \ll k_\mathrm{i} \,. \tag{28.2.19}$$

This determines the width of the resonance and the maximum modulation.

A similar analysis can be carried out for $\varepsilon' > 0$. In this case Δ may become small when the diffracted reflected/transmitted wave propagates close to the surface, in agreement with the results (28.2.4). Here, the resonance is much weaker, less pronounced, and less sensitive to the polarization of the incident light.

28.2.3 Feedback

We now discuss the mechanisms for the change in surface corrugation. The phase shift ψ is given by (28.2.14). It depends on Θ_i and $\boldsymbol{q}$. Let us consider, qualitatively, some typical cases as depicted in Fig. 28.2.4. The solid curves represent the surface profile $z(\boldsymbol{qr})$ and the dashed curves the temperature modulation $\delta T(\boldsymbol{qr})$. With $\psi = 0$, the profiles z and δT are in phase, and with $\psi = \pi$ in opposite phase. Note, that the axes for z and δT are oriented in opposite directions. The response depends on the particular feedback mechanism:

- If thermal expansion dominates, the feedback is positive with $\psi = \pi$. The maximum temperature occurs on the hills and increases the amplitude $\xi \propto \delta T$; the increase in ξ yields an increase in $\delta T \propto \mu \propto \xi$, etc.
- If material evaporation dominates, the feedback becomes positive with $\psi = 0$.
- For surface capillary waves, which arise from a thermal modulation of the surface tension coefficient, the feedback is positive for $\psi = 0$ if $\mathrm{d}\sigma/\mathrm{d}T < 0$ (Sect. 10.4).
- Temperature modulations cause a modulation in the dielectric permittivity which, in principle, can cause ripple formation on its own [*Guosheng* et al. 1982].

There is a large number of other feedback mechanisms which may be related to different types of phase transitions, the generation of defects, or electron–hole pairs in semiconductors, to plasma formation, changes in surface chemistry, etc.

Ripple Movement

For phase shifts $0 < \psi < \pi$, the right side of hills in Fig. 28.2.4b, and for $\pi < \psi < 2\pi$, the left side of hills in Fig. 28.2.4d are heated to higher temperatures. With certain types of feedbacks, this may result in ripple movement along the $\boldsymbol{q}$-direction, i.e.,

$$z(\boldsymbol{r}) = \mathscr{R}e\left[\tilde{\xi}\exp(\Gamma t + \mathrm{i}\boldsymbol{q}\boldsymbol{r})\right] , \tag{28.2.20}$$

with $\Gamma = \gamma - \mathrm{i}\Omega_{\boldsymbol{q}}$, where γ is the increment of instability. With a scanned laser beam, positive feedback may occur at a particular velocity, v_s. Here, an intense amplification of surface acoustic waves may be observed [*Dykhne* and *Rysev* 1986].

The preceding examples show the importance of the phase ψ and the type of feedback mechanism. Ripple formation will be most pronounced with optimal values $\mu = \mu_\mathrm{opt}$ and $\psi = \psi_\mathrm{opt}$, which correspond to $\gamma_\mathrm{max} > 0$. Here, μ and ψ depend differently on $\boldsymbol{q}$, Θ_i, and the polarization. Thus, the optimal conditions cannot be obtained in a simple form.

28.2.4 Comparison of Experimental and Theoretical Results

The orientation and period of ripples for *arbitrary* wave vectors $\boldsymbol{k}_\mathrm{i}$ and $\boldsymbol{q}$ can be found from the dispersion equation (28.1.4). They are summarized in Table 28.2.1 for ripples caused by evaporation of materials with $|\varepsilon'| \gg \varepsilon''$. Similar considerations can be carried out for other feedback mechanisms. Terms 'normal' and 'anomalous' refer to ripples with $\boldsymbol{q} \parallel \boldsymbol{E}_{\mathrm{i}\parallel}$ and $\boldsymbol{q} \perp \boldsymbol{E}_{\mathrm{i}\parallel}$, respectively. Thus, ripples related to SEWs are, in general, normal ripples. The table illustrates that there are many coherent structures with different orientations and periods. The majority of them can be understood on the basis of the previous equations. For

Table 28.2.1 Orientation and period, Λ, of ripples as a function of Θ_i and $\varepsilon = \varepsilon' + \mathrm{i}\varepsilon''$, with $|\varepsilon'| \gg \varepsilon''$. $\Lambda(\sigma)$ and $\Lambda(\pi)$ refer to σ- and π-polarization, respectively. The mechanism considered is based on laser-induced evaporation, adapted from *Akhmanov* et al. (1985)

$\mathscr{R}e\,\varepsilon$	$\varepsilon' < -1$	$-1 < \varepsilon' < 0$	$0 < \varepsilon' < 1$	$\varepsilon' > 1$
Type	Normal	Anomalous	Anomalous	Normal
Orientation	$\boldsymbol{q} \parallel E_{\mathrm{i}y}$	$\boldsymbol{q} \perp E_{\mathrm{i}y}$	$\boldsymbol{q} \perp E_{\mathrm{i}y}$	$\boldsymbol{q} \parallel E_{\mathrm{i}y}$
$\Lambda(\sigma)$	$\dfrac{\lambda}{[n_\mathrm{SEW}^2 - \sin^2\Theta_\mathrm{i}]^{1/2}}$	$0 < q < k_\mathrm{i}$	$\dfrac{\lambda}{\left\|\sqrt{\varepsilon'} \pm \sin\Theta_\mathrm{i}\right\|}$	$\dfrac{\lambda}{[n'^2 - \sin^2\Theta_\mathrm{i}]^{1/2}}$
Orientation	$\boldsymbol{q} \parallel E_{\mathrm{i}x}$	$\boldsymbol{q} \perp E_{\mathrm{i}x}$	$\boldsymbol{q} \perp E_{\mathrm{i}x}$	$\boldsymbol{q} \parallel E_{\mathrm{i}x}$
$\Lambda(\pi)$	$\dfrac{\lambda}{n_\mathrm{SEW} \pm \sin\Theta_\mathrm{i}}$	$0 < q < k_\mathrm{i}$	$\dfrac{\lambda}{[\varepsilon' - \sin^2\Theta_\mathrm{i}]^{1/2}}$	$\dfrac{\lambda}{n' \pm \sin\Theta_\mathrm{i}}$

The following values for n' and n_SEW are used:
$n'^2 = 1 + (n+\kappa)^2/(n^2+\kappa^2)^2$ for $|\varepsilon| \gg 1$ with $\sqrt{\varepsilon} = n + \mathrm{i}\kappa$
$n_\mathrm{SEW}^2 = |\varepsilon'|/(|\varepsilon'| - 1) \approx 1$ for $\varepsilon' < -1$ (SEW)

example, (28.2.9) and (28.2.10) coincide with the periods given for $\varepsilon' < -1$ with π- and σ-polarization, respectively. The periods (28.2.5) approximately correspond to those obtained for $\varepsilon' > 1$. The periods (28.2.6) correspond to those listed for $0 < \varepsilon' < 1$. Let us now consider the orientation and period of ripples found *experimentally*.

Metals

For metals and linearly polarized light, ripples are perpendicular to the projection of the electric vector $\boldsymbol{E}_\mathrm{i}$ onto the surface $z = 0$. In other words, the orientation of the grating vector is $\boldsymbol{q} \parallel \boldsymbol{E}_{\mathrm{i}\parallel}$. The periods observed were $\Lambda \approx \lambda/\cos\Theta_\mathrm{i}$ with σ-polarization and $\Lambda \approx \lambda/(1 \pm \sin\Theta_\mathrm{i})$ with π-polarization [*Isenor* 1977; *Jain* et al. 1981]. This is in agreement with the periods found for SEWs in (28.2.9) and (28.2.10).

Semiconductors

For semiconductors, the situation is similar to metals and the ripples are mainly oriented with $\boldsymbol{q} \parallel \boldsymbol{E}_{\mathrm{i}\parallel}$ (Figs. 28.1.1 and 28.2.1). However, n_SEW in (28.2.9) or (28.2.10) may differ from unity. Additionally, ripples of the type (28.2.5) and (28.2.6) may appear as well.

With 'low' laser fluences, ripple formation observed on Si, is certainly consistent with the previous discussion and can be attributed to periodic surface softening/melting.

With 'high' fluences that result in surface melting and evaporation/ablation, surface corrugations on metal and semiconductor surfaces can be due to surface capillary waves (Sect. 28.5 and Chap. 10).

Dielectrics

Ripple formation has also been studied for dielectric materials. For example, ripples generated on fused and crystalline quartz by $10.6\,\mu\mathrm{m}$ ($\tilde{\nu} = 943.3\,\mathrm{cm}^{-1}$) CO_2-laser radiation show the 'normal' orientation $\boldsymbol{q} \parallel \boldsymbol{E}_{\mathrm{i}\parallel}$. With σ- and π-polarization a single period and two periods, respectively, have been observed [*Keilmann* 1983 and references therein]. If, however, $9.33\,\mu\mathrm{m}$ ($\tilde{\nu} = 1072\,\mathrm{cm}^{-1}$) radiation is used, the situation changes. For all angles $\Theta_\mathrm{i} > 0$, gratings with 'anomalous' orientation $\boldsymbol{q} \perp \boldsymbol{E}_{\mathrm{i}\parallel}$ occur. In this case two spacings were found with σ-polarization and a single spacing with π-polarization. An inspection of the dielectric function of quartz reveals that $\left|\varepsilon'(10.6\,\mu\mathrm{m})\right| > 1$ while $\left|\varepsilon'(9.33\,\mu\mathrm{m})\right| < 1$. Thus, the normal and anomalous behavior observed in these experiments is consistent with the results listed in Table 28.2.1. This is not surprising, as feedbacks based on surface capillary waves and surface acoustic waves also result in anomalous ripples if $\left|\varepsilon'\right| < 1$ and $\left|\varepsilon'\right| \gg \varepsilon''$.

On *polymers*, ripple formation under the action of UV excimer-laser radiation has been observed for fluences well below and well above the threshold for ablation, ϕ_th

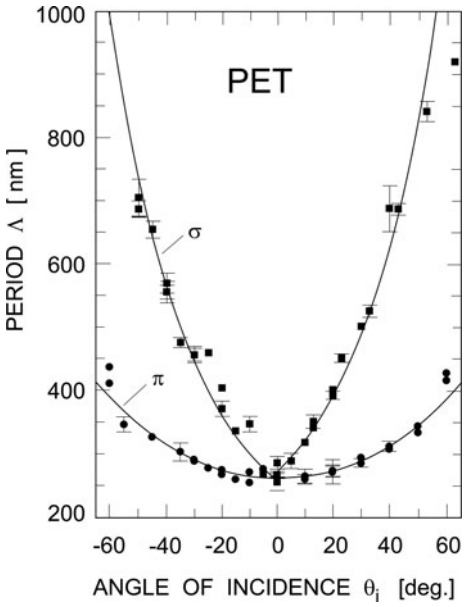

Fig. 28.2.5 Period of ripples observed on PET versus angle of laser-beam incidence, Θ_i (308 nm XeCl laser, $\phi < \phi_{th}$). Different branches refer to π- and σ-polarization. The grating vector of ripples, is $\boldsymbol{q} \perp \boldsymbol{E}_i$. Solid curves have been calculated [*Bäuerle* et al. 1995b]

[*Bäuerle* et al. 1995b; *Bolle* and *Lazare* 1993; *Dyer* and *Farley* 1990]. Figure 28.2.5 shows experimental data for PET and 308 nm laser radiation with $\phi \approx 26\,\mathrm{mJ/cm^2} < \phi_{th} \approx 170\,\mathrm{mJ/cm^2}$. For σ-polarization the data can be fitted by $\Lambda = \lambda/(n' \pm \sin\Theta_i)$ and for π-polarization by $\Lambda = \lambda/(n'^2 - \sin^2\Theta_i)^{1/2}$ with $n' = 1.17 \pm 0.01$ (solid curves), where n' is defined in Table 28.2.1. For 248 nm KrF-laser radiation, a fit to the experimental curves yields $n' \approx 1.22$ (for untreated PET, $n \approx 1.6$). Thus, these ripples are described by (28.2.5), except that 1 has be to substituted by $n' \gtrsim 1$. In other words, this situation corresponds to that in the table, except that the orientation of ripples behaves anomalously, which is probably related to the different feedback mechanisms. With polymers, a possible feedback can be related to similar mechanisms as those described in Sect. 12.4 for hump formation [*Himmelbauer* et al. 1997].

It is interesting to note that ripple formation extends over areas that greatly exceed the spatial coherence area of the laser. This can be related to repeated scattering during multiple-pulse irradiation, which can act to propagate the pattern. Here, local spatial coherence must exist, at least over distances of the order of Λ.

Ambient Medium with $\varepsilon_M \neq 1$

Up to now we have assumed that the laser light is incident from a vacuum. If the permittivity of the ambient medium is $\varepsilon_M \neq 1$, the previous equations must be

modified. In particular, the denominator (28.2.16) becomes (in the general case) proportional to

$$\Delta \propto \varepsilon \left(k_{\parallel}^{\mathrm{s,a}2} - \varepsilon_{\mathrm{M}} k_{\mathrm{i}}^2\right)^{1/2} + \varepsilon_{\mathrm{M}} \left(k_{\parallel}^{\mathrm{s,a}2} - \varepsilon k_{\mathrm{i}}^2\right)^{1/2} , \tag{28.2.21}$$

where k_{i} is the wavevector of the incident light in a vacuum. In the following we consider the case $\varepsilon''_{\mathrm{M}}, \varepsilon'' < \varepsilon'_{\mathrm{M}}, \varepsilon'$. For non-radiative modes with $|\varepsilon'| \gg |\varepsilon'_{\mathrm{M}}|$ and $|\varepsilon'| \gg 1$, the denominator Δ becomes small for $k_{\parallel}^{\mathrm{s,a}} \approx \varepsilon_{\mathrm{M}}'^{1/2} k_{\mathrm{i}}$. Thus, for materials like Si ($\varepsilon' \approx 12$) or Ge ($\varepsilon' \approx 16$) in air, the ripple period is given by (28.2.5c, d), where λ must be substituted by $\lambda_{\mathrm{M}} = \lambda/\sqrt{\varepsilon'_{\mathrm{M}}}$. Θ_{i} is the angle of incidence within the ambient medium. On the other hand, with dielectrics, such as NaCl, MgF_2, etc., where $\varepsilon' \gtrsim \varepsilon'_{\mathrm{M}}$, components with $k_{\parallel}^{\mathrm{s,a}} = \sqrt{\varepsilon'} k_{\mathrm{i}}$ can have a large amplitude. The period is then given by (28.2.6c, d) with the substitutions $\lambda \to \lambda/\sqrt{\varepsilon'_{\mathrm{M}}}$ and $n \to \sqrt{\varepsilon'/\varepsilon'_{\mathrm{M}}}$.

If $\varepsilon'_{\mathrm{M}}$ and ε' are of different sign and $|\varepsilon'| > \varepsilon'_{\mathrm{M}} > 0$ or $|\varepsilon'_{\mathrm{M}}| > \varepsilon' > 0$, SEWs can be excited. Their wavevector is given by

$$k_{\mathrm{SEW}\parallel} = \left(\frac{\varepsilon'_{\mathrm{M}} \varepsilon'}{\varepsilon'_{\mathrm{M}} + \varepsilon'}\right)^{1/2} k_{\mathrm{i}} = n_{\mathrm{SEW}} k_{\mathrm{i}} \, . \tag{28.2.22}$$

This situation may be relevant for liquid-phase processing, where $\varepsilon'_{\mathrm{M}}$ and ε' may become comparable. In this case, the periods are given by (28.2.9) and (28.2.10), where n_{SEW} must be taken from (28.2.22); λ and Θ_{i} refer then to a *vacuum*.

The preceding discussion has shown that most of the features observed with coherent structures can be quantitatively described by theoretical models.

28.2.5 Ripples Generated by Ultrashort-Laser Pulses

While the formation of ripples (LIPSS) for laser pulse durations longer than about 10 ps can be well described on the basis of the equations discussed in the preceding sections, new phenomena are observed with ultashort-laser pulses. Qualitatively speaking, this is not astonishing. With ultrashort-laser pulses, nonlinear optical phenomena, nonequilibrium effects, etc. become important or even dominating (Chap. 13). Thermal equilibration between electrons and the lattice, the development of hydrodynamic effects, ablation, etc., take place only after the pulse.

A quite general phenomenon observed with multiple-pulse fs-laser irradiation are different types of ripples with *different* spatial characteristics. For *perpendicular* laser-beam incidence, ripples with periods comparable to λ and λ/n are found (Sect. 28.2.4). These ripples, whose behavior is similar to those already discussed, are henceforth denoted as low spatial frequency (LSF) ripples. In the literature they are also denoted as LSF LIPSS (LSFL). With certain materials, mainly non-metals, and certain ranges of laser parameters, ripples with a period significantly smaller

than the laser wavelength are observed. These ripples are henceforth denoted as high spatial frequency (HSF) ripples, or HSFL. HSF ripples are observed upon irradiation with several ten to several thousand laser pulses at fluences typically *below* the single-pulse ablation threshold. In contrast to the 'normal' ripples that are rather insensitive to the laser pulse duration, the HSF ripples are observed only for ultrashort laser pulses. To our present understanding, the peculiarities of ripple formation on semiconductor and insulator surfaces upon fs-laser irradiation can be understood on the basis of nonlinear interaction processes, in particular multiphoton- and impact-ionization (Sect. 13.6) and second harmonic generation (SHG). The former process results in the generation of quasifree electrons within the conduction band of the material. Nevertheless, other mechanisms based on self-organization of long-lived surface perturbations cannot be ruled out and may become important within certain parameter regions [*Reif* et al. 2008].

Subsequently, we discuss experimental results and tentative explanations of the characteristics of fs-laser ripple formation. Roughly speaking, for a wide variety of dielectrics and semiconductors, the appearance of HSF ripples can be attributed to the second harmonic of the incident laser radiation [*Dufft* et al. 2009; *Jia* et al. 2005; *Bonse* et al. 2005; *Borowiec* and *Haugen* 2003]. Thus, for 'weakly' absorbing materials, the period of ripples related to the second harmonic should be of the order $\lambda/2n$. Clearly, with ultrashort laser pulses, we cannot employ the linear index of refraction. Thus, the analysis of ripple periods, for both HSF and LSF ripples, requires consideration of transient changes in dielectric properties of the material. Let us discuss the situation in further detail for the example of ZnO [*Dufft* et al. 2009; *Guo* et al. 2009]. Figure 28.2.6a shows the well-known LSF ripples after 800 nm Ti:sapphire-laser irradiation. They are oriented perpendicularly to the polarization of the laser beam. The fluence employed is significantly lower than the single-pulse damage threshold $\phi_{\text{th}} \approx 1.07\,\text{J/cm}^2$ of ZnO. At the edge of the spot,

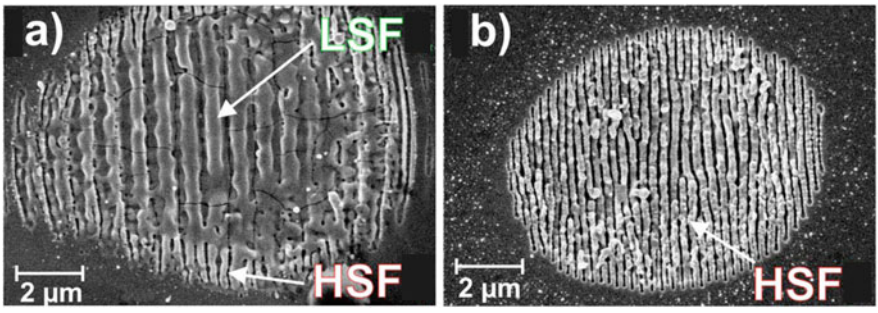

Fig. 28.2.6 SEM images of ripples formed during multiple-pulse 800 nm fs-laser radiation on a single-crystalline ZnO (c-cut) surface. The laser beam was linearly polarized and at perpendicular incidence to the ZnO surface. The pulse length was $\tau_\ell = 200\,\text{fs}$. (**a**) LSF ripples ($\phi = 0.62\,\text{J/cm}^2$; $N_\ell = 10$, $\nu_\text{r} = 100\,\text{Hz}$). Their grating vector is $\boldsymbol{q} \parallel \boldsymbol{E}_\text{i}$. At the edge of the spot, ripples with a higher periodicity appear. These are the HSF ripples. (**b**) With a lower fluence and a higher number of laser pulses ($\phi = 0.48\,\text{J/cm}^2$; $N_\ell = 50$, $\nu_\text{r} = 100\,\text{Hz}$) only HSF ripples are observed [adapted from *Dufft* et al. 2009]

where the laser fluence is lower, ripples with a much higher periodicity are observed. These are the HSF ripples. When decreasing the fluence to $\phi \approx 0.48\,\mathrm{J/cm^2}$ and increasing the number of pulses to $N_\ell = 50$, a relatively sharp transition occurs and only HSF ripples are observed (Fig. 28.2.6b). They are also oriented perpendicularly to the polarization of the laser beam. Depending on the laser fluence and number of pulses, the periodicity of LSF ripples varies between 630 and 730 nm while that of HSF ripples is between 200 and 280 nm.

For a semiquantitative description of the observations, let us consider the transient changes in material properties, and in particular in the dielectric function [*Dufft* et al. 2009; *Jia* et al. 2005; *Wu* et al. 2003]. The (complex) refractive index of the excited material can be estimated from

$$\tilde{n} = (\varepsilon + \Delta\varepsilon'_K + \Delta\varepsilon_D)^{1/2} \tag{28.2.23}$$

where ε is the dielectric function and $\Delta\varepsilon'_K$ the change of its real part due to the Kerr effect. $\Delta\varepsilon_D$ describes the change in ε due to the generation of quasifree electrons in the conduction band (Sect. 11.6.2). The change in refractive index due to the Kerr effect can be approximated by $n = n_o + n_2 I = n_o + \Delta n_K$. With $\varepsilon' + \Delta\varepsilon_K = (n_o + \Delta n_K)^2$ we obtain

$$\Delta\varepsilon'_K = 2n_o n_2 I + (n_2 I)^2 \tag{28.2.24}$$

The change in dielectric function due to electrons generated by multiphoton- and avalanche-ionization, $\Delta\varepsilon_D$, can be described by the Drude formula (11.6.3). In a solid, we have to substitute the free electron mass, m_e, by an effective mass $m_\mathrm{eff} = \xi m_\mathrm{e}$, with $\xi < 1$, while ω_c is given by the time of collisions of conduction band electrons (Sect. 2.1). With the laser parameters employed in the experiments in Fig. 28.2.6, we find that $\Delta\varepsilon_K$ can be ignored in comparison to $\Delta\varepsilon_D$. Fig. 28.2.7 shows the real and imaginary part of the refractive index for ZnO calculated from (28.2.23) and (11.6.3) as a function of the density of laser-generated conduction band electrons for $\lambda = 800$ nm and 400 nm radiation. The parameters employed in the Drude formula were $\xi = 0.27$ and $\tau_\mathrm{c} = 1$ fs. The reflectivity has been calculated from $R = \mid (\tilde{n}-1)/(\tilde{n}+1) \mid^2$. The figure reveals that changes in refractive index and reflectivity for electron densities N_e between some 10^{20} and $10^{23}\,\mathrm{cm^{-3}}$ cannot be ignored. Thus, from the equations presented in Sect. 28.2.1, and the previous considerations about SHG, it becomes evident that laser-induced generation of conduction band electrons changes the period of both LSF and HSF ripples. The interpretation that the HSF ripples are related to SHG at the ZnO surface, are supported by the following results:

- An analysis of the radiation scattered from the ZnO surface shows a pronounced maximum near 395 nm [*Dufft* et al. 2009; *Shih* et al. 2009].
- For carrier densities between 10^{21} and $10^{22}/\mathrm{cm^3}$ the penetration depth of 400 nm radiation is significantly longer (the absorption lower) than for 800 nm radiation. Thus, 400 nm radiation can still strongly interact with the highly excited ZnO.

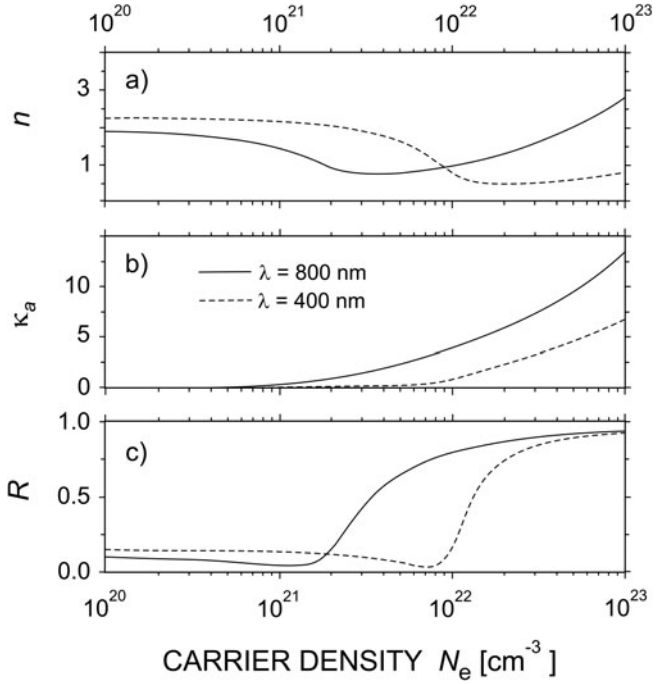

Fig. 28.2.7 Optical properties of single-crystalline ZnO as a function of the density of 'free' (conduction band) electrons, N_e, generated by fs-laser pulses. *Solid* and *dashed curves* refer to wavelengths of 800 and 400 nm, respectively. (**a, b**) Show the dependence of the real and imaginary part of the refractive index $\tilde{n} = n + i\kappa_a$. (**c**) Reflectivity $R = R(N_e)$ calculated for normal incidence [adapted from *Dufft* et al. 2009]

- For the second harmonic we expect a period $\Lambda \approx \lambda/2n = 400\,\text{nm/n}$. From Fig. 28.2.7 we obtain for the carrier concentrations under consideration for the refractive index $n(400) \approx 2$. Thus, we find $\Lambda \approx 200$. This is in reasonable agreement with the HSF periods found experimentally.
- The transition to a "metal-like" behavior with high reflectivity occurs with 800 nm radiation at electron densities that are about a factor of 10 lower than those for 400 nm radiation. This may explain the 'sharp' transition from HSF to LSF ripples observed at somewhat higher fluences.

A similar analysis for LSF ripples observed for Si, yields evidence that scattered surface waves couple to coherent oscillations of conduction band electrons, i.e., it seems that surface plasmon-polaritons (SPPs) play a dominant role in the interaction processes [*Bonse* et al. 2009b]. This is quite plausible. Formation of LSF ripples requires a much lower number of laser pulses and thereby causes less surface damage. With the fluences employed, the electron concentrations can reach those of a metal.

In spite of the consistency of these results, it is by no means evident that the Drude model can be applied to the carrier concentrations under consideration. In particular, upon fs-laser irradiation of semiconductors, feedback effects may cause nonequilibrium electron-hole pair concentrations that are so high that the band gap collapses. Then, the penetration depth of the incident laser light shrinks to the skin depth of a metal. Transport of non-equilibrium electrons into the bulk and emission of hot electrons from the metallized surface may result in a quite complex behavior of ε (Sect. 13.5). For dielectrics, transient free electron densities have been calculated on the basis of both a multiple rate equation (MRE) which includes fast electron recombination, and a kinetic model [*Rethfeld* et al. 2010]. However, with all types of materials, and in particular with semiconductors and dielectrics, multiple-pulse irradiation and, in particular, the big number of laser pulses necessary for the development of HSF ripples, destroys the crystallinity of the surface. Thus, strictly speaking, it is questionable to talk about 'conduction band' electrons. With compounds, also chemical defects related to the depletion of one or several elements of the material must be considered. Addtionally, most experiments were performed in air and the influence of chemical reactions, in particular surface oxidation, has not been clarified. There are indications that on Si surfaces and with high fluences the SiO_x layer becomes so thick that the orientation of ripples changes from $\mathbf{q} \parallel \mathbf{E}_i$ to $\mathbf{q} \perp \mathbf{E}_i$ [*Martsinovskii* et al. 2008]. In any case, physical and chemical defects, surface oxidation, etc. deteriorate the crystallinity, change the material properties, trap electrons, etc. This may also explain why ripple formation becomes insensitive to crystal orientations.

For further investigations, detailed experiments on the dependence of ripple periods on laser fluence, and thereby on the density of electrons, would be desirable. Variations in ripple periods should be particularly pronounced at excitation levels close to the critical carrier density when $\mathrm{Re}\{\varepsilon\} \equiv \varepsilon'$ in (11.6.3) vanishes, i.e., with $\varepsilon' = 0$. Depending on the effective mass of electrons, m_{eff}, and the electron collision time, τ_c, this critical electron density is between $N_e^{cr} \approx 10^{21}$ and $10^{22}\,\mathrm{cm}^{-3}$. Additionally, any influence of a local temperature rise related to laser pulse repetition rates should be excluded via variations of ν_r (Sect. 6.3). This should be considered in particular with dielectrics where, in some of the experiments, pulse repetition rates of 10^3 Hz and more have been employed.

Detailed experiments on the influence of the ellipticity of the incident radiation and of surface defects, e.g. scratches, on the shape and orientation of ripples have been reported for CaF_2 and MgF_2 [*Reif* et al. 2008]. The typical length of ripples decreases with decreasing ellipticity. For circular polarization, the structure transforms to spherical dots. On the other hand, by coherent linking of HSF ripples, 'large-size' nanogratings can be generated. This has been demonstrated for ZnO [*Guo* et al. 2009].

Subwavelength periodic structures have also been observed for a few metals such as Cu [*Weck* et al. 2007] and stainless steel [*Römer* et al. 2009]. Whether these ripples are related to interference effects or to melting instabilities is still under discussion.

28.2.6 Embedded Periodic Structures

Self-organized nanogratings (Fig. 28.2.8a) and arrays of nanostructures (Fig. 28.2.8b) have been generated *inside* silica glass after focused fs-laser irradiation. In both cases, the grating vector of structures is in parallel to the polarization of the laser beam. It seems also quite evident that the initial interaction mechanisms are the same: multiphoton- and impact-ionization followed by avalanche ionization and plasma formation within the a-SiO_2 (Sect. 13.6). The most important differences observed are related to the period of structures.

The period of nanogratings can be varied between 140 and 320 nm via the pulse energy and number of laser pulses. This can be interpreted by the interference between the electric field of the incident laser beam and the field of the electron plasma wave. The interference pattern increases the coupling to the incident radiation and thereby causes a positive feedback in structure formation. The stripe-like dark regions in Fig. 28.2.8a have a lower density compared to the surrounding material. This is related to local oxygen depletion. The increase in grating period with pulse energy has been explained via the increase in plasma temperature.

The planes of nanostructures, on the other hand, are spaced at about $\lambda/2$ for both 800 and 400 nm radiation. Here, structure formation has been discussed on the basis of a nanoplasmonic model where local field enhancements that occur during dielectric breakdown play an important role. The structure period, which scales with λ, is imposed by the modes related to planar waveguides and depends *not* on pulse energy. Deep periodic *surface* structures observed in GaP [*Hsu* et al. 2008] have some features in common to those shown in Fig. 28.2.8b.

An overview on the formation of self-organized periodic nanostructures inside transparent materials is given by *Kazansky* 2006.

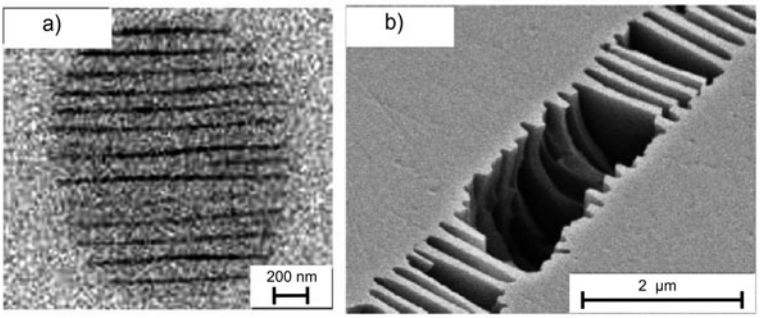

Fig. 28.2.8 (**a**) Backscattering electron image of a silica glass surface polished close to the depth of the focal spot [*Shimotsuma* et al. 2003]. (**b**) High resolution SEM image of an etched structure (20 min in 1% HF) written with $\mathbf{E}_i \parallel \boldsymbol{v}_s$, where $\boldsymbol{v}_s$ is the scanning velocity of the laser beam [*Bhardwaj* et al. 2006; courtesy of National Research Council, Ottawa, Canada]

28.3 Spatio-Temporal Oscillations

The formation of non-coherent structures due to spatio-temporal ordering is observed with laser-induced oxidation, explosive crystallization, exothermal reactions, direct writing, etc. They are related to changes in absorptivity, the release of latent heat, spatial inhomogeneities induced by localized laser-beam irradiation, etc.

Order parameters most commonly used in such problems are:

- The temperature near the position of the laser beam.
- The temperature at the crystallization or reaction front.
- The velocity of a moving front.
- The width or height of the deposit near the laser beam.
- The concentration of species in the reaction zone.
- The width of the temperature or concentration distribution.

For the problems under consideration, the evolution of these order parameters can be described by ordinary differential equations.

From a physical point of view, the volume around the laser beam where transformations and reactions take place can often be described by a 'chemical reactor'. If such a reactor is closed with respect to mass and energy transfer, undamped oscillations are forbidden. This follows directly from the second law of thermodynamics. In laser processing, however, this reactor is an *open* system. The input of energy is provided by the laser light and, if relevant, by the latent heat of chemicals supplied to the reaction zone from outside. The energy output includes heat transport into the surrounding medium, enthalpy changes in endothermal processes, etc. The input and output of matter (precursor molecules, reaction products, transformed materials, etc.) can take place via diffusion, convection, laser-beam scanning, etc.

The appearance of oscillations requires, in general, *at least* two degrees of freedom. To demonstrate the situation in further detail, let us assume a system where these two degrees of freedom are the temperature, T, and a variable, h, which describes the thickness of a transformed layer or the height of a deposit or the concentration of a particular species, etc. In any case, T shall be the fast variable and h the slow variable. The fast variable shall reach its equilibrium value for each value of h very quickly. Qualitatively, such a system can be described by

$$\begin{aligned} c_\mathrm{p}\varrho\dot{T} &= P_\mathrm{input}(T, h; P_\mathrm{a}, v_\mathrm{s}, \ldots) - P_\mathrm{loss}(T, h; v_\mathrm{s}, \ldots) \\ &\equiv f(T, h; P_\mathrm{a}, v_\mathrm{s}, \ldots) \end{aligned} \tag{28.3.1}$$

and

$$\dot{h} = g(h, T; P_\mathrm{a}, v_\mathrm{s}, \ldots) \,. \tag{28.3.2}$$

The behavior of the system can most conveniently be understood from the shape of zero isoclines.

28.3.1 Zero Isoclines

The zero isocline of a particular variable is given by the condition that the time derivative of this variable is zero. The zero isocline for the temperature, $f(T, h; P_a, v_s, \ldots) = 0$, is shown schematically in Fig. 28.3.1 by the solid curve. The branches which attract adjacent trajectories are drawn by thick lines and the branch which repels them by the thin line. The dashed curves represent zero isoclines for the slow variable for different values of parameters. The intersection points of the zero isoclines for T and h characterize stationary states of the system.

Oscillatory behavior of systems where a clear separation into fast and slow variables is possible requires the zero isocline of the fast variable to be non-monotonic, as drawn in the figure. Such a behavior is obtained if, within a certain temperature range, the supply of energy [first term in (28.3.1)] increases more rapidly than the heat losses. Oscillations will take place only if the zero isocline of the slow variable varies as shown by curve 2. The stationary state (intersection point 0) is unstable. The limit cycle indicated by the dotted trajectory *abcd* represents (stable) oscillatory behavior.

The case of curve 1 corresponds to the *latent regime*. If the intersection point is close to the minimum of the solid curve, a small deviation from equilibrium may result in a large *single* (non-oscillatory) response.

If the zero isocline of h behaves as shown by curve 3, the system is bistable.

If a clear separation into 'fast' and 'slow' variables is *not* possible, oscillations can occur for almost all shapes of zero isoclines.

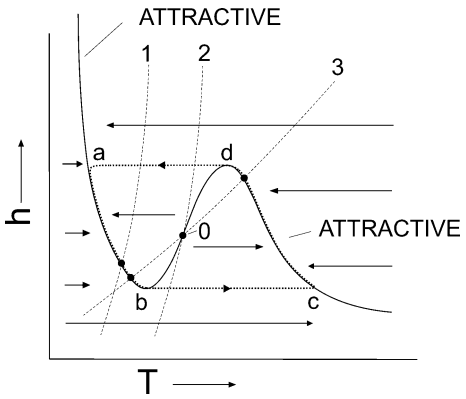

Fig. 28.3.1 Typical shape of zero isocline for the fast variable, T (*solid curve*; *thick lines* indicate attractive branches, the *thin line* the repulsive branch). Three different cases of zero isoclines for the slow variable, h, are shown (*dashed curves*). Curve 1 is characteristic for the latent regime, curve 2 for the oscillatory regime, and curve 3 for the regime of bistability. The *dotted trajectory* shall demonstrate oscillations (limit cycle). *Arrows* indicate the evolution of the system as a result of disturbances

28.3.2 Instabilities in Laser-Induced Oxidation

As an example of a thermochemical instability we consider laser-induced surface oxidation of a metallic slab of thickness h_s. If $h_s \ll l_T$, the temperature in the z-direction can be considered to be uniform. The heat conduction problem can then be described by

$$h_s \varrho c_p \frac{\partial T}{\partial t} = h_s \kappa \nabla^2 T + I_a + \frac{k_0}{h} \Delta H_{ox} \exp\left(-\frac{\Delta E_{ox}}{k_B T}\right) - \Delta H_v v_0 \exp\left(-\frac{\Delta E_v}{k_B T}\right) - \eta[T - T(\infty)] \,, \tag{28.3.3}$$

where h is the thickness of the oxide layer, $I_a = I_a(x, y)$, and $T = T(x, y)$. The third term on the right-hand side describes the heat release due to oxidation and the fourth term the heat loss due to evaporation (sublimation) of the oxide. ΔH_{ox} and ΔH_v are the corresponding enthalpies. The last term represents heat losses by ordinary convection. The change in oxide-layer thickness is given by

$$\frac{dh}{dt} = \frac{k_0}{h} \exp\left(-\frac{\Delta E_{ox}}{k_B T}\right) - v_0 \exp\left(-\frac{\Delta E_v}{k_B T}\right) \,. \tag{28.3.4}$$

Even with *uniform* laser-beam irradiation [first term on the right-hand side of (28.3.3) equal to zero] the growth in oxide-layer thickness can be stationary or it can oscillate, depending on the parameter values and the laser-beam intensity. In this case, the behavior of the system is described by two ordinary differential equations, the modified equation (28.3.3) and (28.3.4). Thus, the system possesses two degrees of freedom and the situation is similar to that described in Fig. 28.3.1. Oscillations of this type have been observed within certain parameter ranges during (large-area) CO_2-laser-induced oxidation of metals, e.g., Mo and W. Figure 28.3.2

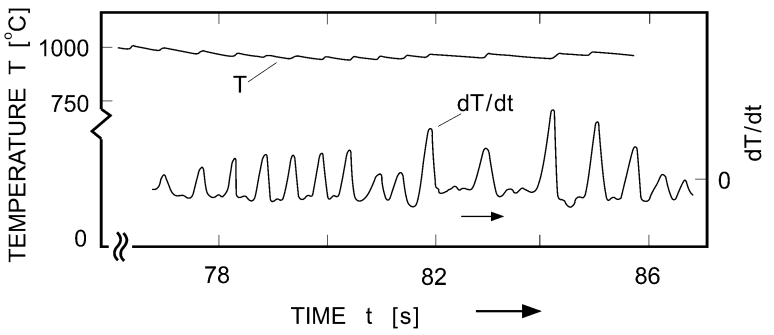

Fig. 28.3.2 Temporal dependence of temperature, T, and derivative dT/dt during CO_2-laser-induced oxidation/evaporation of Mo/Mo_xO_y. The disturbances of the periodicity reflect experimental difficulties, mainly related to the liquid-oxide layer [adapted from *Karlov* et al. 2000]

shows such oscillations in the laser-induced temperature for Mo. The temporal dependence becomes more evident from the derivative dT/dt. These oscillations are *not* related to interference effects. The main oxidation product, (liquid) MoO_3, strongly absorbs CO_2-laser radiation so that $l_\alpha \leq \lambda \ll h$.

Besides these homogeneous stationary and oscillating structures, *inhomogeneous* stationary,[2] oscillating, and spatio-temporal structures (autowaves such as rotating spiral waves, circular waves [pacemakers, leading centers], etc.) can be observed. For *non-uniform* irradiation, different spatiotemporal behaviors may coexist within different areas. For instance, with a Gaussian beam, the period of structures varies with radius r.

28.3.3 Explosive Crystallization

Explosive crystallization is observed during laser-induced crystallization of amorphous Si and Ge films on thermally insulating substrates [*Chapman* et al. 1980]. In these systems, the latent heat release related to the (structural) transformation from amorphous to crystalline exceeds the absorbed laser power and crystallization becomes self-promoting. If the laser beam is scanned with respect to the substrate, large-grained, crescent-like periodic structures are observed within certain ranges of scanning velocities, v_s. This is shown in Fig. 28.3.3 for plasma-deposited Si on Si_3N_4-coated-glass substrates. The period of the structure increases with scan speed; it also depends on the type of material, the layer thickness, the laser power, and the ambient temperature.

Explosive crystallization can be understood along similar lines as discussed in the previous two subsections. Let us first consider explosive crystallization in the absence of the laser beam. In this case, our 'chemical reactor' is the area near the crystallization front. It can be characterized by two dynamic variables, the velocity of the crystalline–amorphous interface, v_{ca}, and the corresponding temperature, T_i. Here, T_i is not necessarily the fast variable; in some cases, it may even be v_{ca}.

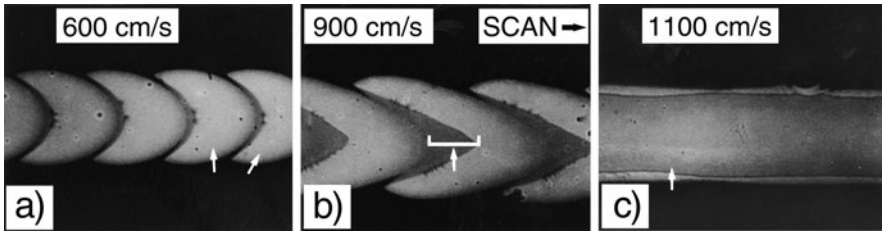

Fig. 28.3.3 a–c Optical transmission photographs of laser-crystallized Si lines for different scanning velocities, v_s. With the parameters employed, explosive crystallization takes place without melting. The pictures are similar when melting takes place [*Nguyen* et al. 1984]

[2] The situation is somewhat similar to the formation of Benard cells.

The zero isocline for v_{ca} is given by the Frenkel–Wilson law (Sect. 10.1.1) which describes the equilibrium front propagation,

$$v_{ca} = v_0 \left[1 - \exp\left(\frac{\Delta \mathscr{H}_c^a}{T_m} \frac{\Delta T_i}{T_i} \right) \right] \exp\left(-\frac{\mathscr{E}_{ac}}{T_i} \right) , \tag{28.3.5}$$

where $\mathscr{E}_{ac} = \Delta E_{ac}/k_B$ is the activation temperature for the transformation; $\Delta \mathscr{H}_c^a = \Delta H_c^a(T_m)/k_B < 0$ is the normalized heat of crystallization per atom at the melting temperature, T_m (for the definitions of ΔE_{ac}^a and ΔH_c^a see Fig. 10.1.5).

Another relation between T_i and v_{ca} follows from the heat balance. Consider a film of thickness h on a semi-infinite substrate. In the simplest model we can assume the propagation of the crystallization front to be stationary. The temperature T_i is then determined only by the heat of crystallization and the heat losses. The latter are mainly due to heat conduction into the crystallized film and the substrate. With these approximations, the zero isocline for T_i has the form [*Shklovskii* and *Kuz'menko* 1989]

$$T_i = T(\infty) + \frac{\Delta H_c}{c_p} \Psi(v_{ca}^*) , \tag{28.3.6}$$

with $v_{ca}^* = v_{ca} h/D$, where D is the thermal diffusivity of the film. Ψ is a monotonically increasing function which depends on the particular experimental conditions. The rate of relaxation of T_i to the equilibrium value is determined by the heat conductivity.

The zero isocline (28.3.5) is strongly non-monotonic and the system can become bistable. This corresponds to a situation where the intersection of the two isoclines is of the type displayed in Fig. 28.3.1 (case 3). Thus, within a certain range of parameters, D, h, and $T(\infty)$, there are *two* stable velocities of the propagation front.

In *laser* direct writing, the absorbed power ignites the crystallization process whenever it has stopped, and a new cycle starts near the edge of the crystallized material. If $v_s < v_{ca}$, periodic structures are observed. If, however, $v_s > v_{ca}$, the line of crystallized material becomes uniform (Fig. 28.3.3c).

28.3.4 Exothermal Reactions

Non-coherent structure formation can also be related to latent heats in laser-induced chemical reactions. Examples are periodic structures observed during laser direct writing of metal lines, mainly of Au and Pd from metallopolymer films (Sect. 27.2) or of Fe lines from $Fe(CO)_5$ [*Jackman* et al. 1986], or during rapid-scan synthesis of Ge_xSe_{1-x} films from sandwich layers of Ge and Se [*Laude* et al. 1986], etc. In all of these examples, the spatial periods of structures are much larger than the laser wavelength.

If the overall exothermal energy exceeds the absorbed laser-light energy, the periodic structures observed in chemically reactive systems can be described in analogy

to explosive crystallization. If, however, the latent heat release is of comparable size only, a description in analogy to that outlined in Sect. 28.3.5 is more adequate. Here, a term proportional to $\exp(-\Delta\mathscr{H}/T)$, where $\Delta\mathscr{H} = \Delta H/k_B$ is the exothermal energy release, must be added in (28.3.7). The important point is that the overall energy input must be large enough to produce a non-monotonic shape of the zero isocline for the temperature (solid curve in Fig. 28.3.1).

28.3.5 Instabilities in Direct Writing

Stable oscillations with (spatial) periods much longer than the ripples have been observed in different LCVD systems during pyrolytic direct writing (Figs. 28.1.1a and 28.3.4). These oscillations are neither related to the wavelength and polarization of the laser light nor to latent heat effects. Their period has been found to increase with laser power, scanning velocity, size of focus, and pressure of the reactant gas.

Figure 28.3.5 shows the dependence of Λ on laser power and scanning velocity for W. It should be noted that in this system periodic structures were observed only in the presence of small amounts of O_2 and only within a certain range of laser powers and scanning velocities (shaded area in Fig. 28.3.6). The concentrations of tungsten oxychlorides related to these traces of O_2 cannot, however, contribute significantly to the total W deposition rate. Additionally, on the basis of available thermodynamic data, the heat of chemical reaction can be ignored in comparison to the absorbed laser power. An important point seems to be the oscillating behavior observed in the surface absorptivity, A. A change in absorbed laser power changes the surface temperature and thus the growth rate, which, in turn, changes the surface morphology, and thereby A.

Interpretation of Oscillations

A phenomenological description of the oscillations has to consider the interdependence between the geometry of stripes, the laser-induced temperature distribution which depends on the absorptivity, and the kinetics of the growth process. Let us consider the most simple model. The width of the deposited line shall be $d = 2r_D$ and the reaction shall take place only in a region of radius r_D around the center of the laser beam. Our 'chemical reactor' is then determined by the area πr_D^2, the height of the deposit, h, at the position of the laser beam, and the average temperature at this position, T. For certain systems, for example, for W deposited from $WCl_6 + H_2$, the radius r_D saturates much faster than the height h (Fig. 16.5.1a). We choose as order parameters the (fast) variable T and the slow variable h. The energy balance yields

$$c_p \varrho \pi r_D^2 h \dot{T} = PA(T) - P_{loss} \; . \tag{28.3.7}$$

$PA(T) = P(1 - R)$ is the energy input. If $\kappa_D \gg \kappa_s$, the heat losses can be approximated by

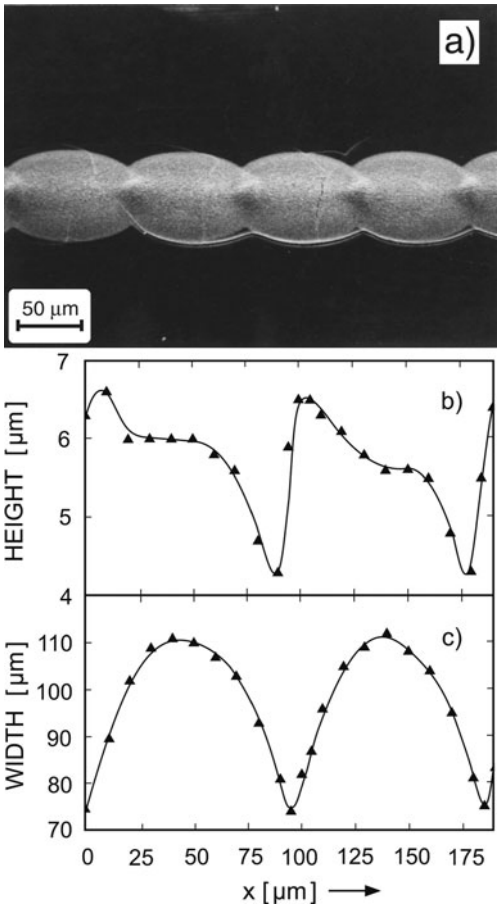

Fig. 28.3.4 (**a**) Periodic structure observed for a W line deposited from 1.1 mbar WCl_6 + 50 mbar H_2 + 15 µbar O_2 by cw-Ar^+-laser direct writing ($\lambda = 514.5$ nm, $P = 650$ mW, $2w_0 = 15$ µm, $v_s = 15$ µm/s; the SEM picture was taken under an angle of 45°). (**b**) and (**c**) show the height and width along the scanning direction [*Kargl* et al. 1993a]

$$P_{\text{loss}} \approx (\pi r_D^2 \kappa_s + h r_D \kappa_D) \frac{\Delta T}{r_D} = \kappa_s \Delta T \left(\pi r_D + h \frac{\kappa_D}{\kappa_s} \right) , \qquad (28.3.8)$$

where $\Delta T = T - T(\infty)$. The first term describes heat losses to the substrate, and the second term the losses due to heat transport along the stripe. h is given by the equation of growth (16.3.2)

$$\dot{h} = v_0 \exp\left(-\frac{\mathscr{E}}{T} \right) - v_s \frac{h}{r_D} . \qquad (28.3.9)$$

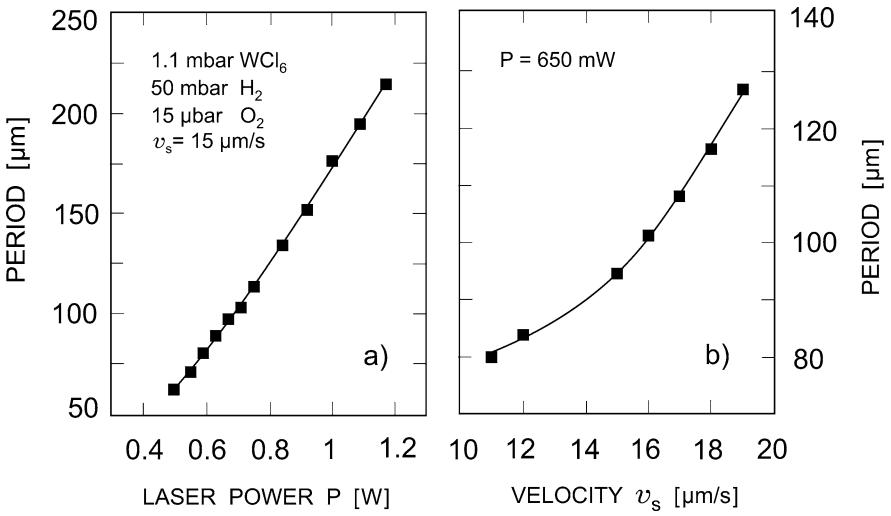

Fig. 28.3.5a, b Period of oscillations observed in direct writing of W lines. (**a**) Dependence on laser power for a fixed scanning velocity, v_s. (**b**) Dependence on v_s at a fixed laser power [*Kargl* et al. 1993a]

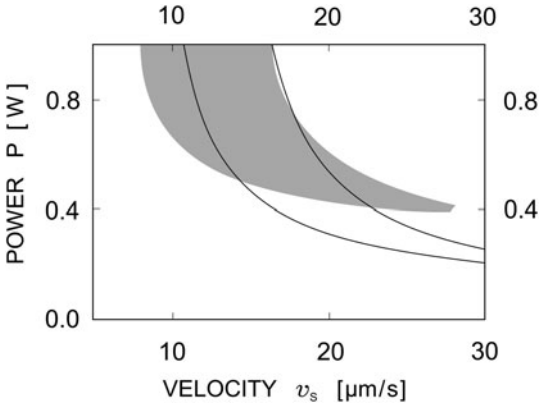

Fig. 28.3.6 The shaded area indicates the range of laser powers and scanning velocities where oscillations in Ar^+-laser direct writing of W have been experimentally observed [$p(WCl_6) = 1.1$ mbar, $p(H_2) = 50$ mbar, $p(O_2) = 15\,\mu$bar]. The *solid curves* have been calculated [*N. Arnold* et al. 1995b]

Here, the 'removal' of material from the reactor due to scanning has been approximated by $v_s \partial h/\partial x \approx -v_s h/r_D$. If the increase in absorptivity with temperature is sufficiently strong, the zero isoclines are similar to those shown in Fig. 28.3.1 by the solid curve and the dashed curve 2. Thus, oscillations are expected.

It is evident that this model oversimplifies the real situation. However, it outlines the essential features and explains the main relationships. For example, this model

predicts that oscillations will exist only within a certain range of scanning velocities and laser powers.

Self-consistent calculations based on the 1D model discussed in Chap. 18 have been performed by taking into account the temperature-dependent absorptivity. They describe the main features observed in the experiments, as, for example, the range of oscillations in Fig. 28.3.6 (solid curves). These results are confirmed by detailed 3D numerical calculations [*Arnold* et al. 1997].

The growth of even isolated islands observed within certain parameter ranges during direct writing of Ni 'lines' (Fig. 28.3.7a) can be tentatively understood in the following way: the laser light absorbed within the a-Si layer induces a temperature distribution with a center temperature barely exceeding the threshold for deposition. This results in Ni deposition and a concomitant decrease in temperature. Once deposition has ceased, it cannot start again until the overlap of the laser focus with the spot-like, well-reflecting heat sink has decreased sufficiently for the threshold temperature to be attained again.

Figure 28.3.7b shows *damped* oscillations which start at the edge between the covered and uncovered substrate.

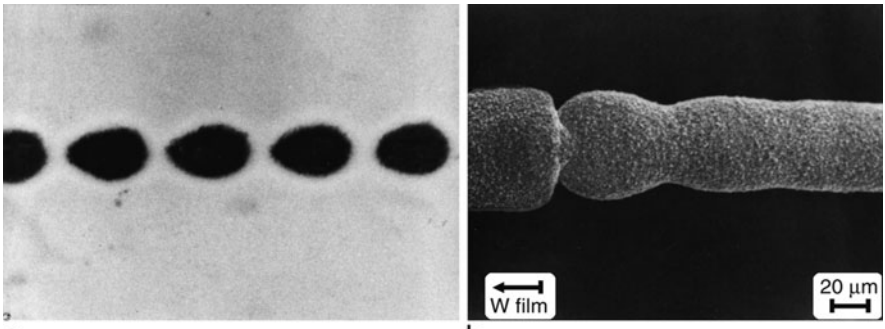

Fig. 28.3.7 (**a**) Periodic structures observed in pyrolytic direct writing of Ni deposited from $Ni(CO_4)$ onto 1,000 Å a-Si/glass substrates [*Kräuter and Bäuerle* 1982, unpublished]. (**b**) Strongly damped oscillations observed during Ar^+-laser direct writing (from left to right) of W (WCl_6+H_2). The substrate was quartz which, in part, was covered with a 700 Å W film [*Kargl* et al. 1993a]

28.3.6 Discontinuous Deposition and Bistabilities

The first clear observation of discontinuous growth was made during pyrolytic direct writing of Si lines. Figure 28.3.8a demonstrates the essential features. In the lower part of the figure the laser power was continuously increased when scanning from left to right. The scanning velocity and the gas pressure were kept constant. For low laser powers a uniform line with a height of, typically, a few µm is observed. When a certain laser power is reached, the line becomes non-uniform and consists of single tiny rods which are in close contact to each other. When the power is

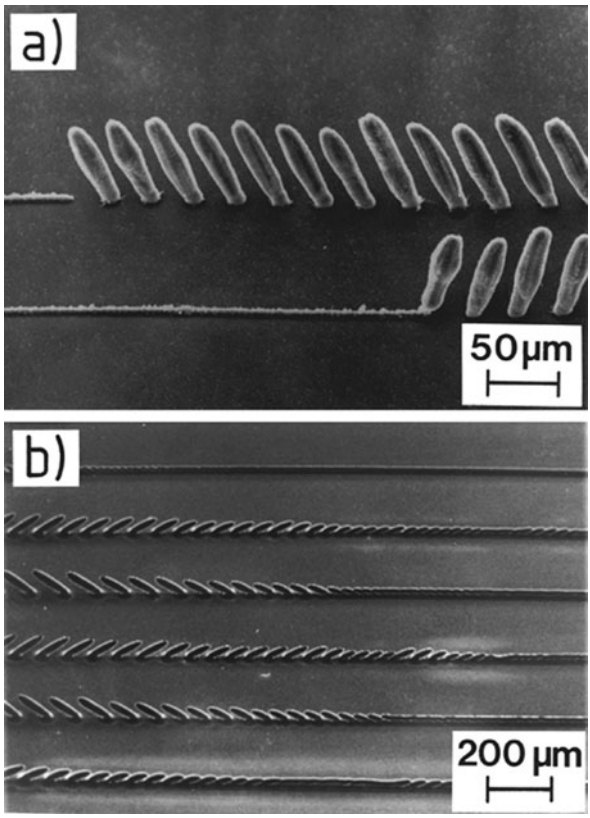

Fig. 28.3.8a, b SEM picture of Si and C deposits fabricated by Ar^+-laser direct writing ($\lambda = 514.5$ nm, $2w_0 = 3\,\mu$m). (**a**) Si deposited from SiH_4 with $p(SiH_4) = 500$ mbar. *Lower trace*: constant scanning ($v_s = 15\,\mu$m/s) from left to right with continuously increasing laser power from 53 mW to 63 mW. *Upper trace*: scanning from right to left with decreasing laser power [*Kargl* et al. 1993b]. (**b**) C deposited from 1000 mbar C_2H_2. Here, the laser power was kept constant at P = 150 mW and the scanning velocity was increased/decreased [*Kargl* et al. 1997]

further increased, a discontinuous change occurs. The deposit consists now of single, almost equidistant rods tilted into the scanning direction. The height of these rods increases continuously with laser power. The upper part of the figure shows the result of a similar experiment where the laser power was decreased with scanning from right to left. Here, a transition from rod-type to line-type growth is observed.

Figure 28.3.9a exhibits the height of deposits as a function of laser power. Solid triangles and solid circles refer to data obtained with increasing and decreasing laser powers, respectively. It becomes evident that there is a well-pronounced hysteresis (bistability). With increasing power, the transition occurs at about 59 mW, and with decreasing power at about 55 mW. The *critical* power P^{cr} increases with v_s. A similar behavior has been observed when the scanning velocity is varied at otherwise constant parameters (Fig. 28.3.9b).

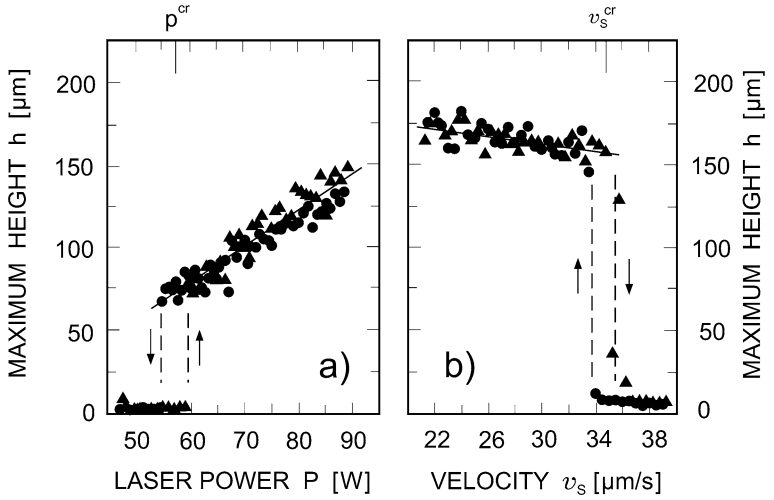

Fig. 28.3.9 Maximum height of deposits as a function of (**a**) laser power at constant scanning velocity $v_s = 15\,\mu m/s$ and (**b**) scanning velocity at constant laser power (136 mW; the other parameters are the same as in Fig. 28.3.8). ▲ and ● refer to increasing and decreasing laser power/scanning velocity [*Kargl* et al. 1993b]

Such transitions from line-type to rod-type growth are a quite general phenomenon that has also been observed for the deposition of C from C_2H_2, C_2H_4, and CH_4 on various thermally insulating substrates [*Kargl* et al. 1997]. For the example shown in Fig. 28.3.8b, the transition is almost continuous.

The experimental results can be interpreted, qualitatively, along the lines of the 1D model in Chap. 18. For 'thick' deposits, however, the temperature gradient in the z-direction (Fig. 18.2.1) cannot be ignored any further. In the simplest approximation we can estimate this gradient by employing a Taylor expansion

$$T_D(z = h) \approx T_D(z = 0) + h \left.\frac{\partial T_D}{\partial z}\right|_{z=0} . \tag{28.3.10}$$

From the continuity of the heat flux at $z = 0$ and the approximation $\partial T_s/\partial z|_{z=0} \approx \theta_s/r_D$, with $\theta_s = T_s(x = 0, z = 0) - T(\infty)$, we obtain for the *center*-temperature rise at the top of the deposit

$$\theta_c(z = h) \approx \left(1 + \frac{h}{\kappa^* r_D}\right) \theta_c(z = 0) . \tag{28.3.11}$$

$\theta_c(z = 0)$ must be calculated numerically. For lines one can use the approximation (18.2.6). The situation is simpler for spot-like deposits, where $\theta_c(z = 0)$ can be approximated by (16.4.1). The estimation (28.3.11) agrees well with the results shown in Fig. 16.4.2a for $h/r_D \gtrsim 1$ (the region on the right side of the dashed curve). The deposition behavior can then be understood as follows (Fig. 18.2.1):

If v_s decreases, $T_c(z = 0)$ decreases because of the increasing cross section of the stripe. On the other hand, with increasing h/r_D, the difference $T_c(z = h) - T_c(z = 0)$ also increases. If the latter effect dominates, the exponential increase of the growth rate with temperature results in a dramatic increase in deposition rate. In the case of direct writing, a continuous stripe of thickness $h \lesssim r_D$ is deposited, as long as the scanning velocity is fast enough. If, however, v_s falls below a critical value, $v_s < v_s^{cr}$, the thickness h increases 'explosively' and a transition to rod-type growth takes place. The growth of a rod ceases when its height becomes comparable to the Rayleigh length, z_R (Sects. 5.1 and 17.5). The laser beam then directly hits the substrate and another rod growths from a spot. The hysteresis observed in Fig. 28.3.9 is related to the somewhat lower temperature $T_c(h)$ of lines with respect to spots of the same height, h, and width, r_D. Numerical solutions of this process support this qualitative picture [*Arnold* et al. 1997].

28.4 Instabilities and Structure Formation in Laser Ablation

For some types of non-coherent instabilities, the picture of the 'chemical reactor' described in Sect. 28.3 is inadequate. A typical example is the instability of the ablation front which is related to temperature gradients at the material surface (Sect. 28.4.1). Of increasing interest is the formation of conical and columnar structures that are formed within certain ranges of laser parameters around and above the ablation threshold. The occurrence and shape of these structures may also depend on the type of ambient medium (Sect. 28.4.2).

28.4.1 Fundamental Aspects

Consider a planar surface from which material is ablated under the action of laser light (Fig. 28.4.1). Here, small perturbations of the surface may give rise to instabilities which result in spontaneous symmetry breakings and structure formation [*Anisimov* and *Khokhlov* 1995]. The laser-induced temperature distribution with $z \geq 0$ is given by the heat equation

$$\varrho c_p \frac{\partial T}{\partial t} - \kappa \nabla^2 T = Q \,, \tag{28.4.1}$$

with

$$Q = \alpha I_0 (1 - R) \exp\{-\alpha [z - Z(x, y, t)]\} \,, \tag{28.4.2}$$

where $Z = Z(x, y, t)$ describes the (moving) surface. We assume $I_0(1 - R) =$ const. The boundary conditions can be written as

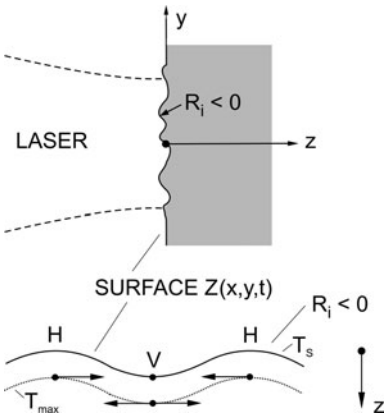

Fig. 28.4.1 Schematic of a surface $Z(x, y, t)$ irradiated by a laser beam. The *lower part* demonstrates how a surface deformation in the z-direction generates a heat flux in the x, y-directions. H and V stand for 'hills' and 'valleys', respectively. R_i denote the principal radii

$$\kappa \left.\frac{\partial T}{\partial z}\right|_{z=Z} = \varrho \Delta H_\mathrm{v} \dot{Z} \quad \text{and} \quad T(z \to \infty) = T(\infty) \,, \tag{28.4.3}$$

where ΔH_v (J/g) is the enthalpy of vaporization and $\dot{Z} \equiv \mathrm{d}Z/\mathrm{d}t$. The curvature of the surface shall be described, at a given point, by the principal radii R_1 and R_2. The sign of R_i is defined in the picture. This yields

$$\dot{Z} = v_0 \exp\left[-\frac{\Delta E_\mathrm{v}(\infty)}{k_\mathrm{B} T_\mathrm{s}} - \frac{\sigma}{N_0 k_\mathrm{B} T_\mathrm{s}} \left(\frac{1}{R_1} + \frac{1}{R_2}\right)\right] , \tag{28.4.4}$$

where $T_\mathrm{s} = T(z = Z)$ and σ is the surface tension coefficient. $\Delta E_\mathrm{v}(\infty) \approx \Delta H_\mathrm{v}^\mathrm{a}$ is the enthalpy of vaporization per atom/molecule from a *plane* surface, and $N_0 \equiv V_\mathrm{n}^{-1}$ the number density of atoms/molecules within the surface of the material. The second term in the exponent describes the change in activation energy due to the surface corrugation [see also (4.1.13)]. Equations (28.4.1) to (28.4.4) have a stationary solution in the form of a plane ablation front (Sect. 11.2.1). Here, z in (11.2.13) must be substituted by $z^* = z - vt$. The maximum temperature, T_max, occurs at a distance $z^* = z_0$ *below* the surface [see (11.2.15)]. Thus, the temperature gradient at the surface is positive, $\partial T/\partial z|_{z=Z} > 0$. Due to the inhomogeneity in the temperature distribution, a small deformation of the surface will generate heat fluxes *perpendicular* to the z-direction. For *long* wave perturbations with $q < q_\mathrm{min}$ (Fig. 28.4.2), the overall heat flux will decrease the temperature within the valleys, V (Fig. 28.4.1). Thus, material evaporation will be slower in the valleys than on the hills, i.e., the feedback is negative and $\gamma < 0$.

For *short* wave perturbations with $q > q_\mathrm{min}$, the situation is opposite. This is schematically shown in the lower part of Fig. 28.4.1. The resultant heat flux to the valleys, V, is positive and the surface corrugation is increased. With $q > q_1 \approx$

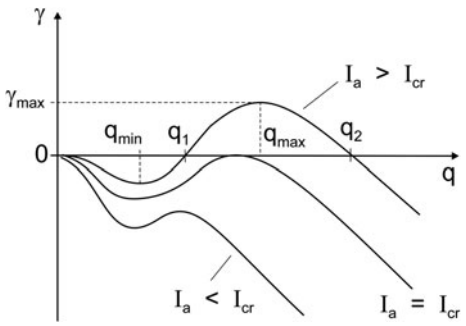

Fig. 28.4.2 Dependence of the increment γ on the wavevector of the surface perturbation, q. With $\gamma < 0$, surface perturbations are damped out. The instability which develops most rapidly is characterized by $\gamma_{\max}$ and $q_{\max}$. The decrease in γ for $q > q_{\max}$ is due to surface tension effects

$2\pi/z_0$, $\gamma > 0$ and the surface becomes unstable. However, this positive feedback competes with a negative feedback related to the change in vaporization energy with curvature [see exponent in (28.4.4)]. This negative feedback increases with an increasing wavevector of the perturbation.

Let us now continue the calculations and assume $\boldsymbol{q} \parallel y$. The perturbation in the temperature distribution can then be described by

$$T = T_0(z^*) + T_1(z^*)\mathscr{R}e[\exp(\mathrm{i}qy + \gamma t)] \,, \tag{28.4.5}$$

where $T_0(z^*)$ corresponds to the stationary solution (11.2.13). The shape of the surface shall be described by

$$Z = vt + \xi \,,$$

where v is the stationary velocity of the ablation front and

$$\xi = \xi_0 \mathscr{R}e[\exp(\mathrm{i}qy + \gamma t)] \,. \tag{28.4.6}$$

With the approximation $R_1^{-1} \approx -\partial^2 Z/\partial y^2$, which holds for $\xi/\Lambda \ll 1$, the boundary-value problem can be solved. Figure 28.4.2 displays, qualitatively, the dependence of γ versus q. If the absorbed laser-light intensity is smaller than some critical intensity, i.e., $I_\mathrm{a} < I_\mathrm{cr}$, surface perturbations will be damped out because $\gamma < 0$. If, however, $I_\mathrm{a} > I_\mathrm{cr}$, there exists a region $q_1 < q < q_2$ in which $\gamma = \gamma(q) > 0$. Perturbations with such wavenumbers grow exponentially with time and the surface becomes unstable. For wavevectors $q > q_2$ the surface is stabilized again due to surface tension effects.

The threshold for the appearance of an instability is determined by the dimensionless parameter

$$\Xi \equiv \frac{\alpha\sigma}{\Delta E_\mathrm{v}(\infty) N_0} \approx \alpha N_0^{-1/3} \,. \tag{28.4.7}$$

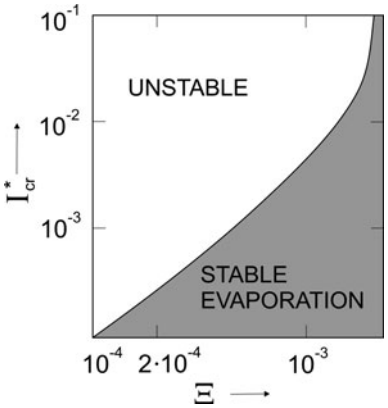

Fig. 28.4.3 Stability boundary. Within the shaded region evaporation is stable [*Anisimov* et al. 1980]

The dependence $I^*_{\rm cr} = I_{\rm cr}/I_{\rm k} = I_{\rm cr}(1-R)/v_0\varrho\Delta H_{\rm v}$ is shown in Fig. 28.4.3 as a function of Ξ. Vaporization is stable only within the shaded region. For a material with an absorption coefficient $\alpha = 10^3\,{\rm cm}^{-1}$, the characteristic value $I_{\rm cr}$ is $10^6 - 10^8\,{\rm W/cm}^2$.

The period of the structure which develops most rapidly is given by

$$q_{\max} \approx \left(\frac{\alpha I_0(1-R)N_0}{2\sigma\kappa}\,\frac{\Delta E_{\rm v}(\infty)}{T_{\rm s}}\right)^{1/3} . \tag{28.4.8}$$

Note that $q_{\max}$ is *not* directly related to the laser wavelength, except via the absorption coefficient α. Typical values of $q_{\max}$ are between a few μm and some ten μm. The time for the development of this instability is

$$\gamma_{\max}^{-1} \approx \frac{D}{v^2}\left(\frac{k_{\rm B}T_{\rm s}}{\Delta E_{\rm v}(\infty)}\right)^2 . \tag{28.4.9}$$

For a metal, e.g., with $D = 1\,{\rm cm}^2/{\rm s}$, $v = 0.1\,\mu{\rm m/pulse}$, $\tau_\ell \approx 10^{-8}\,{\rm s}$ and $[k_{\rm B}T_{\rm s}/\Delta E_{\rm v}(\infty)] \approx 0.1$, we obtain $\gamma^{-1} \approx 10^{-8}\,{\rm s}$. Thus, in metals this type of instability can develop during ns pulses but not during ps and fs pulses. From the preceding discussion it becomes evident that, with the mechanism under consideration, a positive feedback arises only if $\partial T/\partial z|_{z^*=0} > 0$, where $z^* = 0$ denotes the position of the (plane) ablation front.

Similar considerations for UV-laser (photophysical) ablation of dielectrics, and in particular of organic polymers, show that the ablation velocity is a function of temperature, the concentration of excited species, $N_{\rm A^*}$ (Sect. 13.3), and some other parameters, Ψ_i, if relevant. The necessary condition for the development of a surface instability is then

$$\frac{\partial v}{\partial z} = \frac{\partial v}{\partial T}\frac{\partial T}{\partial z} + \frac{\partial v}{\partial N_{A^*}}\frac{\partial N_{A^*}}{\partial z} + \sum_i \frac{\partial v}{\partial \Psi_i}\frac{\partial \Psi_i}{\partial z} > 0 \,, \qquad (28.4.10)$$

where all derivatives with respect to z should be taken at $z^* = 0$. The second term originates from activated desorption of excited species. The third term describes the influence of mass density changes, stresses, shielding by impurities, debris, etc. Let us first ignore Ψ_i. Because $\mathrm{d}N_{A^*}/\mathrm{d}z|_{z^*=0} < 0$, the second term *stabilizes* the ablation front [*Luk'yanchuk* et al. 1993b]. This stabilization becomes more pronounced with increasing thermal relaxation time, τ_T. For many polymers, the surface is stable if $\tau_T > 10^{-11}$ s. The typical length of structures calculated for the unstable regime is of the order of 10^3 Å.

These considerations allow one to understand why it is difficult to obtain smooth surfaces during ns UV-laser ablation of metals or during IR-laser ablation of polymers. Instabilities will *not* develop during laser pulses with $\tau_\ell \ll \gamma_{max}^{-1}$. This is one of the reasons why polymer surfaces ablated by ps or fs laser pulses are smoother than those ablated by ns laser pulses [*Küper* and *Stuke* 1989].

A different type of surface instability occurs if the temperature $T_{max}(z_0)$ becomes so high that liquid or gaseous bubbles are formed *below* the surface. In such cases, explosive-type ablation will be observed. For metals, this mechanism seems to be unimportant because the time for bubble formation is very long compared to γ_{max}^{-1} in (28.4.9). The situation may, however, be different with non-metals.

28.4.2 Conical and Columnar Structures

The development of conical or columnar structures during repetitive laser pulses with fluences around and above the ablation threshold is observed for many materials, such as organic polymers, semiconductors, metals, and different types of ceramics [*Dyer* et al. 2009; *Conde* et al. 2009; *Oliveira* and *Vilar* 2008; *Urech* et al. 2006; *Silvain* et al. 1999; *Heitz* et al. 1997; *Krajnovich* and *Vazquez* 1993]. The formation and shape of such structures depend on the laser parameters and the type of ambient medium and, with gases, on gas pressure. Structure formation is *not* necessarily related to surface melting. This can be seen from Fig. 28.4.4 for the example of PI which only sublimates. The cone axes are oriented along the direction of the incident laser beam. The number density of cones increases with the number of laser pulses and decreases with increasing laser fluence.

To our present understanding, formation of conical/columnar structures can be based on different physical and/or chemical mechanisms. Among those are shielding effects, the depletion of single species in compound materials, interference effects, hydrodynamic instabilities, etc.

The formation of conical structures has often been explained by *shielding* effects related to local enrichments of photofragments or material impurities, to debris condensing on the surface between laser pulses, etc. At least within the initial phase, structure formation may also be ascribed to spontaneous symmetry breakage which

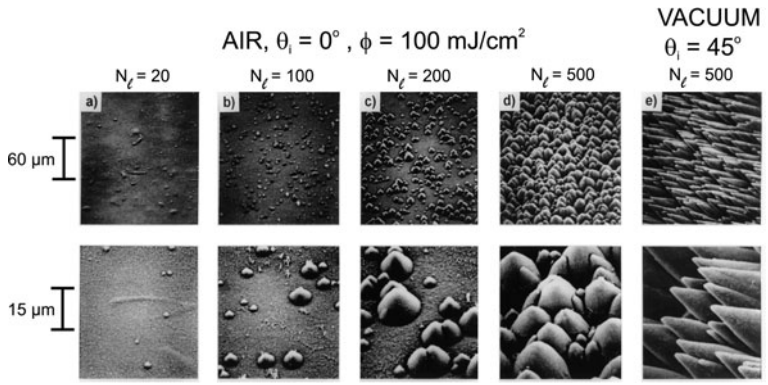

Fig. 28.4.4 (**a–d**) SEM photographs of polyimide ablated in air at $\phi = 100\,\mathrm{mJ/cm^2}$ for different numbers of pulses, N_ℓ. The laser beam was normally incident on the sample. (**e**) Same as (**d**) but irradiated in a vacuum under $\Theta_\mathrm{i} = 45°$ [*Krajnovich* and *Vazquez* 1993]

develops within the plain ablation front and which can be described in analogy to (28.4.10) with $\Psi_i \neq 0$.

Let us consider PI where laser irradiation results in an enrichment of carbon within the surface (Sect. 27.2). If we denote the density of carbon atoms by $\Psi \equiv N_\mathrm{c}$ and if $\partial v/\partial N_\mathrm{c} < 0$, the third term in (28.4.10) is positive because $\partial N_\mathrm{c}/\partial z|_{z^*=0} < 0$. Such a mechanism would *destabilize* the surface. Instabilities of this type can be described, in principle, by localized perturbations of the form (28.1.2) with $\Omega = 0$ and $\mathscr{O}_i(\boldsymbol{r}) \equiv \mathbf{J}_0(qr)$, where $\mathbf{J}_0$ is the Bessel function so that

$$\mathscr{O}^\mathrm{p}(\boldsymbol{r}, t) \propto \mathbf{J}_0(qr)\exp[\gamma(q)t]\,. \tag{28.4.11}$$

Figure 28.4.5 shows the formation of cones on ceramic Si_3N_4. The dependence of the surface morphology on laser fluence and pulse number is exhibited in Fig. 28.4.6. With KrF-laser radiation and $\phi = \text{const.}$, the height of cones, h_con, and their number density increases with N_ℓ, while their opening angle decreases. When the surface is totally covered with cones, ablation ceases. With $N_\ell = \text{const.}$, h_con increases with the laser fluence, while the total number of cones decreases. With ArF-laser radiation and $\phi < 2.5\,\mathrm{J/cm^2}$, the situation is quite similar. However, with $2.5\,\mathrm{J/cm^2} \leq \phi \leq 4\,\mathrm{J/cm^2}$, only a few cones with large opening angles and heights $h_\mathrm{con} \ll h$ are observed.

The cones formed on Si_3N_4 may be related to a Si-rich surface layer which changes the optical properties during the first few laser pulses. With fluences $\phi(\mathrm{ArF, KrF}) \gtrsim 4\,\mathrm{J/cm^2}$, smooth flat surfaces without cones are obtained (Fig. 28.4.5b).

It is important to note that with the various conical structures discussed in this subsection, the tips of cones are below or at most within the original substrate surface. Thus, the height of cones is always smaller or equal to the ablated layer thickness, i.e., $h_\mathrm{con} \lesssim h$.

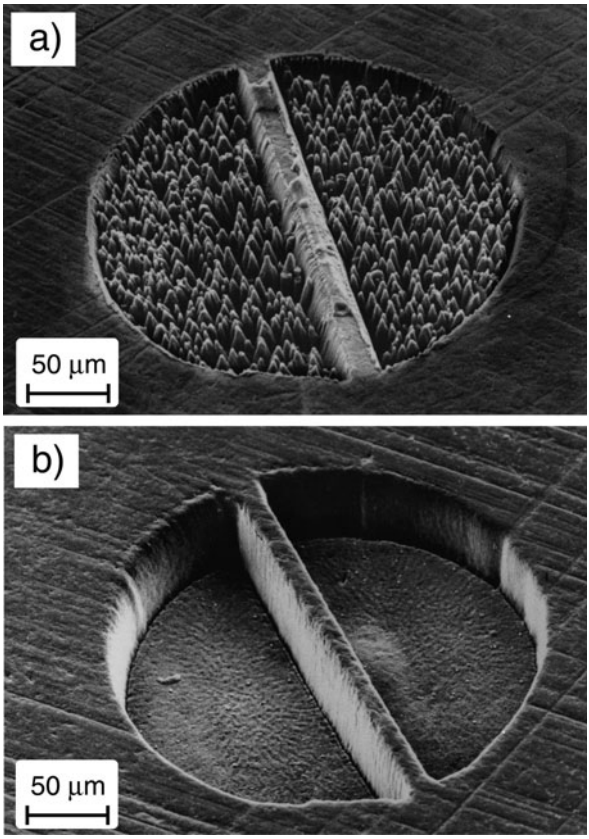

Fig. 28.4.5 a, b Ablation of ceramic Si_3N_4 by ArF-laser-light projection. (**a**) Cone formation. The laser parameters were $\phi = 1.2\,\mathrm{J/cm^2}$, $N_\ell = 500$, and $\nu_\mathrm{r} = 3\,\mathrm{Hz}$. The maximum height of cones, h_con, is smaller or at most equal to the ablated depth, i.e., $h_\mathrm{con} \lesssim h$. (**b**) Same as (**a**) but for $\phi = 5.3\,\mathrm{J/cm^2}$ [*Heitz* et al. 1997]

Around cones generated on polycarbonate (PC) by 157 nm F_2-laser ablation, interference fringes have been observed [*Dyer* et al. 2009]. They originate from interferences between the incident beam and reflections from the cone walls. The analysis of fringes yields the spatial coherence length of the F_2-laser radiation. For the wide and narrow dimension of the rectangular aperture employed in the experiments, values of 21–24 and 54 µm, respectively, have been derived.

Influence of Ambient Medium

The ambient medium strongly affects both the formation and shape of columnar and conical structures. By far, the influence of reactive ambient media on structure formation has been studied most intensively for Si. Among the gases employed were

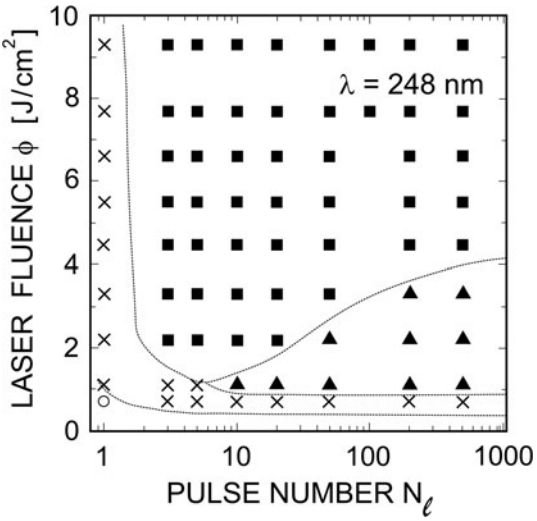

Fig. 28.4.6 Dependence of the surface morphology of Si_3N_4 on the number of laser pulses and the laser fluence for KrF-laser irradiation. (○) No visible change of surface; (×) change in color without significant ablation; (▲) ablation with remaining cones whose height, h_{con}, is comparable to h; (■) ablation resulting in flat surfaces [*Heitz* et al. 1997]

SF_6, Cl_2, inert gases with and without traces of O_2, and air [*Her* et al. 1998; *Zorba* et al. 2008a; *Pedraza* et al. 1999].

Irradiation of Si wafers immersed in SF_6 or Cl_2 (660 mbar) with 800 nm Ti-sapphire-laser pulses ($\phi \approx 1\,J/cm^2$, $\tau_\ell = 100$ fs, $N_\ell = 500$) results in the formation of sharp conical structures. Their tops are approximately at the *same* level as the surrounding Si surface, i.e. $h_{con} \lesssim h$ with heights up to $h_{con} \approx 40\,\mu m$. On the top of cones spherical caps with a diameter of, typically, 1.5 μm are observed. In vacuum, N_2, and He, blunt cones are formed. Virtually no difference in cone formation was observed with 400 nm pulses [*Her* et al. 1998]. Similar experiments using 248 nm KrF-laser radiation and pulse lengths of 15 ns, 5 ps, and 500 fs and SF_6 atmosphere have been performed by *Zorba* et al. (2008a, b). The heights and widths of cones has been found to decrease with decreasing laser pulse lengths while their density increases. For ns-pulses, the cones grow tens of microns *above* the initial surface, i.e. $h_{con} > h$. With ps- and fs-pusles $h_{con} \approx h$ for low fluences, and $h_{con} < h$ for high fluences. The core of cones is single crystalline with the same orientation as the substrate. Their surface is covered with a layer of nanocrystalline Si which contains S. The thickness of this layer is a few 100 nm. For ns-laser pulses, spherical caps on the top of cones have been observed for all fluences that result in cone formation. For fs-pulses spherical caps have been observed only for very high fluences (see also Sect. 28.7).

In other investigations, using 25 ns KrF-laser radiation ($\phi \approx 2.7$ to $3.3\,J/cm^2$, $N_\ell = 1000$) and air, structures that are more columnar than conical were found. The height of these columns grow *above* the original substrate surface, i.e. $h_{col} > h$

[*Pedraza* et al. 1999]. With the same laser parameters, but with ambient atmospheres of N_2, Ar, or Ar + 4%H_2, all at 1000 mbar pressure, *no* columnar growth was observed. With N_2+5%O_2, the columns have almost vertical sides, with a molten tip at a height of about 2 μm. The height of these columns increases with the number of laser pulses. The growth process is tentatively explained by laser-induced vaporization and the condensation of the Si-rich vapor on the molten tips of the columns. As in conventional vapor–liquid–solid (VLS) growth, the liquid tips may act as preferred sites for Si deposition, because of their larger accomodation coefficient. Oxygen is considered as an 'etchant' that enhances the flux of Si-rich vapor from the valleys between columns. The growth process is enhanced by the high gas pressure which keeps the vapor long enough around the columns. These are probably the reasons, why columns have a different shape and grow to heights above the Si surface. Additionally, halogenated gases employed by *Her* et al. and *Zorba* et al. can etch the Si. For example, high intensity fs-laser pulses can dissociate SF_6. The resulting F radicals react with Si by forming volatile SiF_4 (Chap. 15). The absence of cone formation in inert atmospheres as observed by *Pedraza* et al. can be related to the higher fluences, longer pulse length, and the higher gas pressure employed in these experiments. However, cone formation observed in vacuum and inert atmospheres could also be related to small traces of oxygen.

The mechanisms of cone formation in single element materials such as Si, are still under discussion. In any case, at least in experiments using halogenated gases, shielding by debris seems to be unlikely. A possible scenario of cone formation could be described as follows: Defects or surface roughnesses cause inhomogeneous absorption of the incident radiation. The inhomogeneous temperature distribution results in inhomogeneous surface melting. For Si, this effect is further enhanced by the *nonlinear* dependence of the laser-induced temperature rise on absorbed laser-light intensity (Sect. 15.2.6). Because of the exponential increase in chemical reaction rates, there is a strong feedback between chemical etching and enhanced absorption of the radiation within the etched valleys. Self-organization may result in the quasiperiodic structure observed. Clearly, the roughening of the surface can also be initiated by the incident radiation via formation of ripples or, with higher fluences, via capillary waves on the molten surface (Sect. 28.5). During multiple-pulse irradiation, a cone-/columnar-like structure evolves (Fig. 28.5.1). In a reactive atmosphere, the feedback is significantly enhanced by the etching process. An estimation of the quasiperiod of cones, Λ_c, on the basis of capillary waves for the case of 'shallow melting', which applies to the typical fluences employed in the experiments, is given in Sect. 28.5.3. This estimation yields a period $\Lambda_c \approx 1\,\mu m$. Interferences and instabilities of waves result in a bead-like quasiperiodic structure of cones/columns. The increase in average distance between cones observed with increasing pulse energy is consistent with Eq. (28.5.11). It is related to the increase in melt depth, h_l, and thereby the lifetime of the liquid layer, Δt_m. In fact, this scenario is supported by experiments of *Shen* et al. (2003), who investigated cone formation by fs-laser irradiation through a mask. In this case, *periodic* arrays of cones have been observed. The symmetry of cone arrangement, can be related to Fresnel diffraction of the light at the mask boundaries (see also Fig. 12.1.2).

Formation of columnar structures upon ultrashort-pulse laser ablation of Si within *liquids*, mainly water or alcohol, has been studied by *Stolee* et al. (2010), *Shen* et al. (2004), and others. With ns-pulses and certain ranges of laser parameters, hexagonal patterns, possibly related to Rayleigh-Taylor instabilities, are observed [*Chen* et al. 2009; Sect. 28.5].

In summary, the formation of conical/columnar structures can be related to quite different physical/chemical mechanisms, some of which may be initiated by physical or chemical defects, surface roughnesses, etc. Among those are:

- Shielding by debris condensed on the surface during the first few laser pulses.
- In compounds, the depletion of single elements/molecules can locally enhance the threshold fluence for ablation. An example may be PI where local carbonization causes shielding.
- Interferences of wavelike features around defects.
- Hydrodynamic instabilities as discussed in Sect. 28.5.

Clearly, combinations of these different mechanisms are possible as well. This makes classification quite difficult. Furthermore, the experimental situation is unsatisfactory. Results obtained by different groups are sometimes even contradictory. Some technological aspects related to conical/columnar structures are summarized in Sect. 28.7.

28.5 Hydrodynamic Instabilities

Hydrodynamic motions within laser-molten surfaces and/or liquid or gaseous ambient media are of fundamental importance in many types of laser processing. Such motions, and their mutual interactions, can result in the development of instabilities. The most important hydrodynamic instabilities can be classified according to Kelvin–Helmholtz- and Rayleigh–Taylor-type instabilities [*Chandrasekhar* 1961]. These have already been mentioned in various chapters.

28.5.1 Kelvin–Helmholtz Instabilities

KH instabilities are excited, under certain conditions, at interfaces of heterogeneous or even homogeneous liquids when different layers are in relative *tangential* motion. In laser processing this can be related to the following:

- The lateral expansion of the vapor/plasma plume (Sect. 30.3.1).
- The motion of the liquid layer due to the recoil pressure in laser ablation (Sect. 11.3).
- The gas jet in liquid-phase expulsion (Sect. 10.7).
- Surface tension effects (Sect. 10.4) etc.

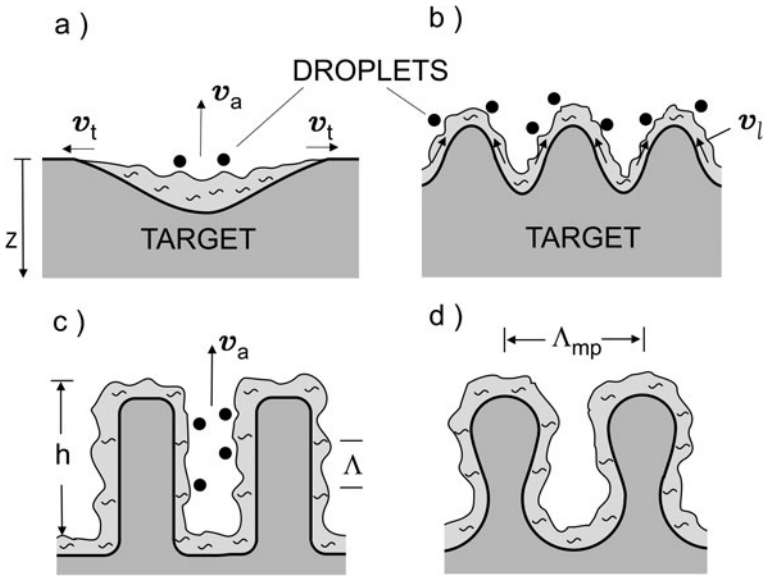

Fig. 28.5.1a–d Droplet formation due to hydrodynamic instabilities generated during laser-induced melting and ablation. For simplicity, the laser beam and vapor plume are not drawn (Fig. 11.0.1). (**a**) The expansion velocity, v_t, of the vapor/plasma plume excites surface capillary waves. (**b**) With multiple-pulse irradiation, the motion of the liquid from the valleys of capillary waves increases the corrugation. Centrifugal forces near the hills may cause Rayleigh–Taylor instabilities. (**c**) Shear flow (Kelvin–Helmholtz) instability. (**d**) Necking and formation of solid particulates

Let us discuss KH instabilities in further detail for the example of vapor/plasma-plume expansion. The tangential component of the expansion velocity, v_t, excites *capillary* waves within the molten substrate surface (Fig. 28.5.1a). With moderate laser fluences, the mass density of the vapor, ϱ_v, is small compared to that of the liquid, i.e., $\varrho_v \ll \varrho_l$. In this case, we can approximate the increment by

$$\Gamma \approx \pm\left(\frac{\varrho_v}{\varrho_l} v_t^2 q^2 - gq - \frac{\sigma}{\varrho_l} q^3\right)^{1/2} - \mathrm{i}\frac{\varrho_v}{\varrho_l} v_t q \equiv \gamma - \mathrm{i}\Omega \ . \qquad (28.5.1)$$

The first term in the parentheses describes the transfer of momentum from the gas to the liquid surface. This term destabilizes the plane surface. The second and third terms stabilize the instability via gravity and surface tension, respectively. The influence of a finite but small viscosity can be estimated by adding the term $-2\nu_k q^2$. Note that g can refer to normal gravity or to an artificial gravity. Unstable perturbations exist, if the velocity exceeds some critical value,

$$v_t > v_c \approx \left(\frac{4\sigma g \varrho_l}{\varrho_v^2}\right)^{1/4} \ . \qquad (28.5.2)$$

In this case, the square root in (28.5.1) is real within certain intervals of $\Lambda \equiv 2\pi/q$. Here, one branch of γ is always positive. The imaginary part in (28.5.1) then describes the (slow) movement of the (unstable) waves along the surface. If we assume that damping is dominated by surface tension, the wavevector that corresponds to the *maximum* increment is given by

$$q_{\max} \approx \frac{2}{3}\frac{\varrho_{\mathrm{v}} v_{\mathrm{t}}^2}{\sigma} \quad \text{with} \quad \gamma_{\max} \approx \left(\frac{\sigma q_{\max}^3}{2\varrho_l}\right)^{1/2} . \tag{28.5.3}$$

The maximum wavevector and increment in the presence of damping due to an artificial gravity can also be obtained from (28.5.1). For a finite thickness of the molten layer, these formulas hold only as long as $h_l >> \Lambda$. With $v_{\mathrm{t}} = 0$, no KH-instabilities are excited. In this limit, Eq. (28.5.1) becomes identical to the equation for gravity-capillary waves.

If, however, $h_l \lesssim \Lambda$, all increments are reduced due to the stabilizing influence of the solid bottom. Thus, even with $v_{\mathrm{t}} \neq 0$, KH instabilities may be suppressed.

Instability of Evaporation Front

Consider the flux of species through a plane liquid–gas interface, where $\varrho_l v_{\mathrm{v}l} = \varrho_{\mathrm{v}} v_{\mathrm{v}}$. A disturbance of this interface will cause the pressure to increase within valleys with respect to hills. By this means, an instability may develop which can be described by equations similar to (28.5.1), (28.5.2) and (28.5.3). The main difference is that this wave does *not* move, i.e., the imaginary part in (28.5.1) vanishes; the lateral velocity v_{t} must be substituted by the velocity of the vapor flow *normal* to the surface, v_{a}.

28.5.2 Rayleigh–Taylor Instabilities

RT instabilities arise at interfaces between fluids (liquids or gases) of different densities that are superimposed over one another and which are in an external field (gravity, centrifugal forces, etc.). Here, the force must be directed from the fluid with the high density, ϱ_l, towards the fluid with the low density, ϱ_{v}. In laser processing, such instabilities can cause the following:

- Different types of surface structures.
- Droplets in laser-surface melting and vaporization (Sects. 4.2, 12.6.5 and 22.2.4).
- Fast mixing of gases at the contact front between the plasma plume and the ambient medium in laser ablation (Sect. 30.4.4).

In a linear approximation and for negligible viscosity, the increment for RT instabilities is given by [*Kull* 1991]

$$\Gamma \equiv \gamma = \left(\frac{\varrho_l - \varrho_\mathrm{v}}{\varrho_l + \varrho_\mathrm{v}} g_\mathrm{RT} q - \frac{\sigma}{\varrho_l + \varrho_\mathrm{v}} q^3 \right)^{1/2}$$
$$\approx \left(g_\mathrm{RT} q - \frac{\sigma}{\varrho_l} q^3 \right)^{1/2} . \tag{28.5.4}$$

The last equality implies $\varrho_l \gg \varrho_\mathrm{v}$, and the equation becomes equal to (28.5.1) with $v_\mathrm{t} = 0$ and negative (artificial) gravity, g_RT. The wavevector and the increment of the dominating structure are given by

$$q_\mathrm{max} = \left(\frac{g_\mathrm{RT}(\varrho_l - \varrho_\mathrm{v})}{3\sigma} \right)^{1/2} \approx \left(\frac{g_\mathrm{RT} \varrho_l}{3\sigma} \right)^{1/2}$$

with (28.5.5)

$$\gamma_\mathrm{max} = \left(\frac{2}{3} g_\mathrm{RT} q_\mathrm{max} \frac{\varrho_l - \varrho_\mathrm{v}}{\rho_l + \varrho_\mathrm{v}} \right)^{1/2} \approx \left(\frac{2}{3} g_\mathrm{RT} q_\mathrm{max} \right)^{1/2} .$$

In the absence of surface tension, the influence of a finite but small viscosity can be estimated again by adding the term $-2\nu' q^2$ to (28.5.4). Here, ν' is the average viscosity, $\nu' \approx (\varrho_l \nu_l + \varrho_\mathrm{v} \nu_\mathrm{v})/(\varrho_l + \varrho_\mathrm{v}) \approx \nu_l$. This expression becomes invalid for large values of q, because viscosity alone *cannot* completely stabilize an RT instability.

The influence of finite compressibility on RT instabilities is discussed in *Anisimov* and *Khokhlov* (1995).

For RT instabilities, terms in (28.1.1) which are *non-linear* in the perturbation $\mathscr{O}_i^\mathrm{p}(\boldsymbol{x}, t)$ become important even with small values of $\xi/\Lambda \sim 0.1$ to 0.4. In this non-linear stage, bubbles of the fluid with the lower density, ϱ_v, ascend in the direction opposite to g_RT, while spikes of the fluid ϱ_l penetrate into ϱ_v ($+g_\mathrm{RT}$-direction). The motion of bubbles can be described by the Taylor–Davies formula:

$$v \approx \frac{2}{3} \left(\frac{\varrho_l - \varrho_\mathrm{v}}{\varrho_l + \varrho_\mathrm{v}} g_\mathrm{RT} r_\mathrm{b} \right)^{1/2} \approx \frac{2}{3} (g_\mathrm{RT} r_\mathrm{b})^{1/2} , \tag{28.5.6}$$

where r_b is the radius of (isolated) bubbles. Further development of the instability results in turbulent mixing. In the absence of damping, the thickness of the mixing region is

$$\xi_\mathrm{mix} \approx \zeta \frac{\varrho_l - \varrho_\mathrm{v}}{\varrho_l + \varrho_\mathrm{v}} g_\mathrm{RT} t^2 \approx \zeta g_\mathrm{RT} t^2 . \tag{28.5.7}$$

For the 3D case, ζ is within the range 0.07–0.08.

28.5.3 Surface Corrugations, Droplets

The different hydrodynamic instabilities discussed in the preceding sections can result in the formation of surface corrugations, the ejection of droplets from the laser-irradiated surface, the development of conical and columnar structures, etc.

Droplets

Figure 28.5.1a shows the formation of droplets due to a *KH instability* related to the lateral expansion of the vapor/plasma plume. The typical radius of such droplets can be estimated from (28.5.3), which yields

$$r_{\mathrm{KH}} \approx \frac{\Lambda_{\max}}{4} \approx \frac{2\sigma}{\varrho_{\mathrm{v}} v_{\mathrm{t}}^2} \approx \frac{3\sigma}{p_{\mathrm{rec}}} \approx \frac{2\sigma \Delta H_{\mathrm{v}}}{v_{\mathrm{v}} \varrho_l I_{\mathrm{a}}} \,. \tag{28.5.8}$$

Because v_{t} is related to the laser parameters in a non-trivial way, we have to make further assumptions. If the laser beam is well focused we can set $v_{\mathrm{t}} \approx v_{\mathrm{a}} \approx v_{\mathrm{v}}$. Together with (11.3.1) and (11.3.5b), we then obtain the two latter approximations in (28.5.8).

From measurements one finds $v_{\mathrm{v}} \approx 10^5\,\mathrm{cm/s}$. As material parameters we use $\sigma = 10^{-4}\,\mathrm{J/cm^2}$, $\Delta H_{\mathrm{v}} = 3.5 \times 10^4\,\mathrm{J/cm^3}$ and $\varrho_l = 5\,\mathrm{g/cm^3}$. The laser parameters typically employed in ns pulsed-laser ablation/deposition are $\phi = 3\,\mathrm{J/cm^2}$ and $\tau_\ell = 20\,\mathrm{ns}$. Because of screening, we assume that the laser fluence that is absorbed on the substrate is $\phi_{\mathrm{a}} \approx 0.7\,\mathrm{J/cm^2}$. With these parameters, the recoil pressure is of the order of 700 atm. The radius of droplets formed during single-pulse irradiation is then $r_{\mathrm{KH}} \approx 0.05\,\mu\mathrm{m}$. For larger laser spot diameters, however, v_{t} may be significantly smaller and correspondingly r_{KH} may become larger.

The instability of the evaporation front (EF) will result in droplets of radius r_{EF}, which can also be estimated from (28.5.8), if we substitute v_{t} by v_{a}. In this case, the approximation $v_{\mathrm{a}} \approx v_{\mathrm{v}}$ is more appropriate and almost independent of laser spot size. In this way, we obtain $r_{\mathrm{EF}} \approx 0.05\,\mu\mathrm{m}$, which is the same as r_{KH} estimated for a tightly focused beam.

The characteristic time for droplet formation can be estimated from the condition that the amplitude of the corrugation, ξ, becomes comparable to $\Lambda_{\max}$. This yields $t_{\mathrm{drop}} \approx \gamma_{\max}^{-1} \ln(\Lambda_{\max}/4\xi_0)$. With (28.5.3) and the initial corrugation $\xi_0 \approx 1\,\mathrm{nm}$, one finds with $v_{\mathrm{t}} \approx v_{\mathrm{v}}$ the time $t_{\mathrm{drop}}(\mathrm{KH}) \approx t_{\mathrm{drop}}(\mathrm{EF}) \approx 2\,\mathrm{ns}$. With $v_{\mathrm{t}} \approx v_{\mathrm{a}}/10$, one obtains, however, $t_{\mathrm{drop}}(\mathrm{KH}) \approx 4\,\mu\mathrm{s}$ and $r_{\mathrm{KH}} \approx 5\,\mu\mathrm{m}$.

The typical radius of droplets caused by *RT instabilities* is given by (28.5.5):

$$r_{\mathrm{RT}} \approx \frac{\Lambda_{\max}}{4} \approx 3 \left(\frac{\sigma}{g_{\mathrm{RT}} \varrho_l} \right)^{1/2} . \tag{28.5.9}$$

Here, the artificial gravity g_{RT} can have the following different origins:

- The *recoil pressure* in laser ablation accelerates the vapor–liquid interface in the z-direction. In a reference frame fixed with this interface, this is described by an artificial gravity in the $-z$-direction, which can be estimated from (11.4.4):

$$g_{\mathrm{RT}} \approx \frac{\kappa_{\mathrm{s}} v_{\mathrm{v}} T_{\mathrm{b}}}{w^2 \Delta H_{\mathrm{v}}} \,. \tag{28.5.10a}$$

  Together with (28.5.9) and the same parameters as those employed above, we obtain with $\kappa_{\mathrm{s}} = D\varrho_l c_{\mathrm{p}}$, $D = 0.5\,\mathrm{cm}^2/\mathrm{s}$, $c_{\mathrm{p}} = 0.5\,\mathrm{J/gK}$, $T_{\mathrm{b}} \approx T_{\mathrm{s}} = 4000\,\mathrm{K}$, and $w(\mathrm{PLD}) = 10^3\,\mu\mathrm{m}$ for $g_{\mathrm{RT}} \approx 1.5 \times 10^6\,\mathrm{cm/s}^2$ and for the radius of droplets $r_{\mathrm{RT}} \approx 300\,\mu\mathrm{m}$. The time of formation is $t_{\mathrm{drop}}(\mathrm{RT}) \approx 2\,\mathrm{ms}$. Thus, this mechanism is irrelevant for PLD using ns and shorter pulses.
- The (normal) *thermal expansion* of the material. For a plane surface this is described by (23.7.9):

$$g_{\mathrm{RT}} \approx \beta_{\mathrm{T}} \frac{\phi_{\mathrm{a}}}{c_{\mathrm{p}} \varrho_l \tau_\ell^2} \,. \tag{28.5.10b}$$

  With $\beta_{\mathrm{T}} = 10^{-5}\,\mathrm{K}^{-1}$ and the same parameters as before, we obtain $g_{\mathrm{RT}} \approx 7 \times 10^9\,\mathrm{cm/s}^2$, $r_{\mathrm{RT}} \approx 5\,\mu\mathrm{m}$, and $t_{\mathrm{drop}}(\mathrm{RT}) \approx 2\,\mu\mathrm{s}$.
- The *different densities* of the liquid and the solid. This yields

$$g_{\mathrm{RT}} \approx \pm \frac{\varrho_l - \varrho_{\mathrm{s}}}{\varrho_l} \left(\frac{D}{\tau_\ell^3} \right)^{1/2} \,. \tag{28.5.10c}$$

  If $\varrho_l < \varrho_{\mathrm{s}}$, the acceleration g_{RT} destabilizes the surface when the velocity v_{ls} slows down (Chap. 10). With $\varrho_{\mathrm{s}} = 1.1\varrho_l$ and otherwise the same parameters, we obtain from (28.5.10c) and (28.5.9) the values $g_{\mathrm{RT}} \approx 3 \times 10^9\,\mathrm{cm/s}^2$, $r_{\mathrm{RT}} \approx 2\,\mu\mathrm{m}$, and $t_{\mathrm{drop}}(\mathrm{RT}) \approx 1\,\mu\mathrm{s}$.

The formation of droplets ascribed to this instability is shown in Fig. 28.5.2. For Au and the parameters employed in these experiments, one obtains $r_{\mathrm{RT}} \approx 1.2\,\mu\mathrm{m}$. This size is in reasonable agreement with the size of droplets shown in the figure. The time of droplet formation is $t_{\mathrm{drop}}(\mathrm{RT}) \approx 0.45\,\mu\mathrm{s}$. Because of this long time, such droplets can develop only in multiple-pulse experiments.

Surface corrugations formed due to KH instabilities and/or instabilities of the evaporation front solidify between successive laser pulses. With *multiple-pulse* irradiation and low-to-medium laser fluences, only a thin layer of the corrugated surface becomes molten during each pulse (Fig. 28.5.1b). This liquid moves out of the valleys, due to the higher pressure or due to other reasons, and thereby increases the amplitude of the corrugation. Near the hills, this motion results in centrifugal accelerations $g_{\mathrm{RT}} \approx v_l^2/R_1 \approx v_l^2 \xi q_{\max}^2$, where R_1 is the curvature and ξ the amplitude of the corrugation. $q_{\max}$ is given by (28.5.3) or the analogous expression for the evaporation front instability. The velocity at the end of each pulse can be estimated from the balance of forces. If we assume $\xi \approx \Lambda_{\max}/4 \approx \pi/2q_{\max}$, we

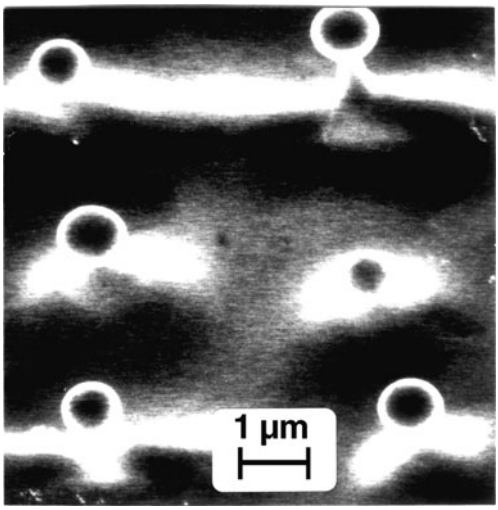

Fig. 28.5.2 SEM picture of Au surface after multiple-pulse KrF-laser irradiation ($\phi = 1\,\mathrm{J/cm^2}$, $\Theta_\mathrm{i} = 5°$) [*Bennett* et al. 1995]

obtain $v_l \approx p_\mathrm{rec} q_\mathrm{max} \tau_\ell / \varrho_l \approx \delta v_\mathrm{v} I_\mathrm{a} q_\mathrm{max} \tau_\ell / \Delta H_\mathrm{v}$, where $\delta \ll 1$ corrects for different factors that may significantly decrease v_l and ξq_max. These centrifugal forces yield an artificial acceleration

$$g_\mathrm{RT} \approx \frac{\delta^2}{8} \frac{\varrho_l^3 \tau_\ell^3}{\sigma^3} \left(\frac{v_\mathrm{v} I_\mathrm{a}}{\Delta H_\mathrm{v}} \right)^5 , \qquad (28.5.10\mathrm{d})$$

which may again cause a RT instability and the formation of droplets. With the parameters employed before and $\delta \approx 0.1$, we obtain $g_\mathrm{RT} \approx 7 \times 10^{13}\,\mathrm{cm/s^2}$, $r_\mathrm{RT} \approx 0.05\,\mu\mathrm{m}$, and $t_\mathrm{drop}(\mathrm{RT}) \approx 1\,\mathrm{ns}$.

If the amplitude of the corrugation becomes very large (Fig. 28.5.1c), the velocity of the vapor along the walls, v_t, may cause shear-flow KH instabilities. In this case, we can substitute $v_\mathrm{t} \approx v_\mathrm{a} \approx v_\mathrm{v}$ even with uniform irradiation. Correspondingly, the droplets will have radii of $r_\mathrm{KH} \approx 0.05\,\mu\mathrm{m}$. The time of formation is again $t_\mathrm{drop}(\mathrm{KH}) \approx 2\,\mathrm{ns}$. If some of the Λ_a become comparable to h and if the corresponding amplitudes are large enough, this mechanism may cause necking and the formation of particulates with radii of 1 µm to several µm (Fig. 28.5.1d).

Cones, Columnar Structures

With some materials and laser parameters, the formation of cones and columnar structures, as discussed in Sect. 28.4.2, can be related to hydrodynamic instabilities as well. In particular for single element materials and reactive ambient media, alternative formation mechanisms such as shielding by debris or depletion of single elements can be excluded. With very high fluences exceeding the melting and ablation

threshold, capillary waves on the molten surface may develop. Depending on the boundary conditions, interferences between waves may result in different types of surface corrugations and quasiperiodic formation of conical/columnar structures. However, cone formation has also been observed with fluences $\phi \gtrsim \phi_m$ that cause only shallow melting. In this case the period of surface capillary waves can be estimated from the dispersion relation derived in [*Landau* and *Lifshitz*: *Fluid Mechanics VI*, 1974]. For shallow melting we can ignore gravity and use the approximation $\tanh x \approx x$. We then obtain

$$\Lambda_C \approx (2\pi\, \Delta t_m)^{1/2} \left(\frac{\sigma h_l}{\rho_l}\right)^{1/4} \tag{28.5.11}$$

where we have introduced the duration of the molten phase, Δt_m (Chap. 10).

As discussed in Sect. 28.4.2 most of the experiments have been performed for Si. Thus, for those experiments where fluences $\phi \gtrsim \phi_m$ have been employed, we obtain from Eq. (10.1.3c) a maximum melt depth of $h_l^{max} \lesssim 0.8\,\mu m$. Here, we have assumed $\phi = 1\,J/cm^2$, a reflectivity $R \approx 0.34$, and $\Delta H \approx \Delta H_m$. If we approximate the duration of the melt, Δt_m, by the time of solidification, Eq. (10.2.6b) yields $\tau_s \approx 10\,ns$. With $\sigma \approx 0.85 \times 10^3\,g/s^2$ we obtain for the period $\Lambda_C \approx 1\,\mu m$. This estimation yields, at least, the right order of magnitude for the separation of cones/columns. The increase in average distance between cones observed with increasing pulse energy is consistent with Eq. (28.5.11). An increase in ϕ increases the melt depth and thereby the lifetime of the liquid layer. This is supported by experimental observations (Sect. 28.4.2).

Hexagonal patterns formed on Si by nanosecond laser-induced surface melting in water were ascribed to RT instabilities [*Chen* et al. 2009]. The period of patterns was analysed on the basis of Eq. (28.5.5). A value of $g_{RT} \approx 10^{11}\,cm/s^2$ was derived. The development of such patterns may initiate the formation of cones/columns as well.

28.6 Stress-Related Instabilities

Spontaneous breakings in axial symmetry imposed by laser beams can result in instabilities, as shown in Fig. 28.6.1. With low laser-light intensities, etching of regular holes in Mo films immersed in a Cl_2 atmosphere is observed (Sect. 14.3). With medium intensities, a 'star-like' structure develops. The number of 'rays' increases with intensity. The formation of stars is probably related to built-up stresses caused by laser-induced heating. Beyond a certain laser-light intensity, the stresses become so high that a large area of the film pops off. This area has about the same diameter as the ring surrounding the holes. This behavior has only been observed with films which were not strongly adherent to the substrate surface. From a mathematical point of view, the appearance of these stars can be described by a perturbation

$$\mathcal{O}_i^p \propto \exp[im\varphi + \gamma(m)t]\,. \tag{28.6.1}$$

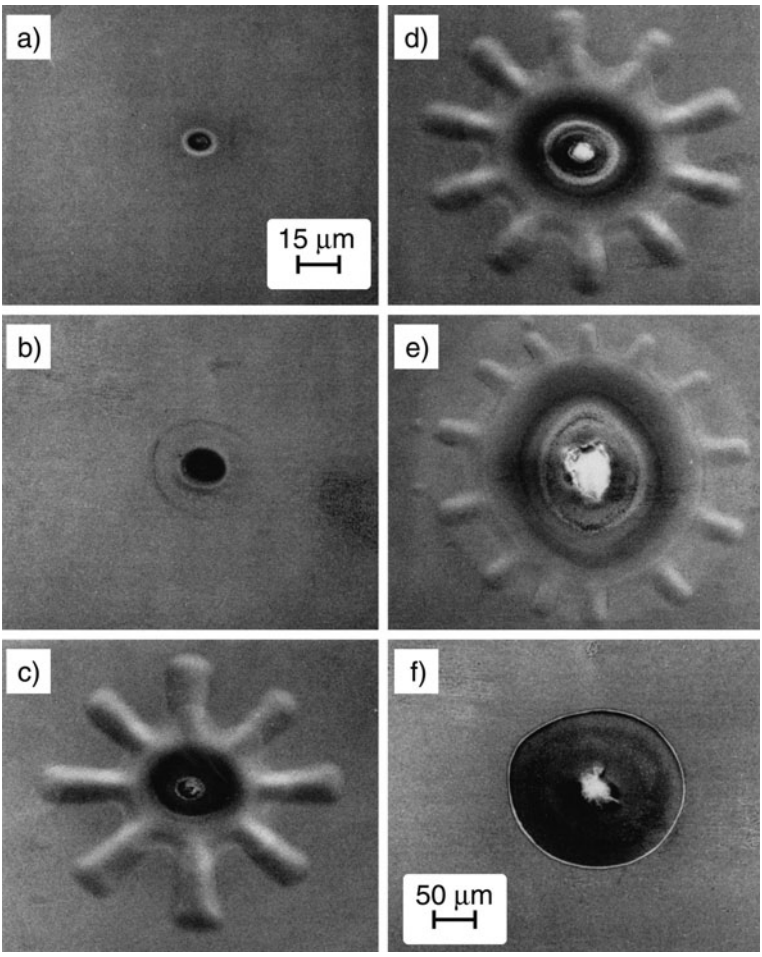

Fig. 28.6.1a–f SEM pictures of holes and stars formed in 2,500 Å Mo–glass films during Ar^+-laser-induced etching in a Cl_2 atmosphere ($\lambda = 488nm$, $w_0(1/e) \approx 5.7\,\mu m$, $p(Cl_2) = 50\,mbar$). The laser powers employed were $P =$(**a**) 10 mW, (**b**) 20 mW, (**c**) 50 mW, (**d**) 100 mW, (**e**) 500 mW, and (**f**) 150 mW [*Mogyorosi* et al. 1989a]

The number of rays is given by the particular m for which the increment ($\gamma > 0$) becomes maximum.

Wall- and Nap-type Structures

Polymer surfaces ablated with UV-laser light frequently show wall- or nap-type structures, as shown for PI in Fig. 28.6.2. These (non-coherent) structures are related to internal stresses within the polymer foil.

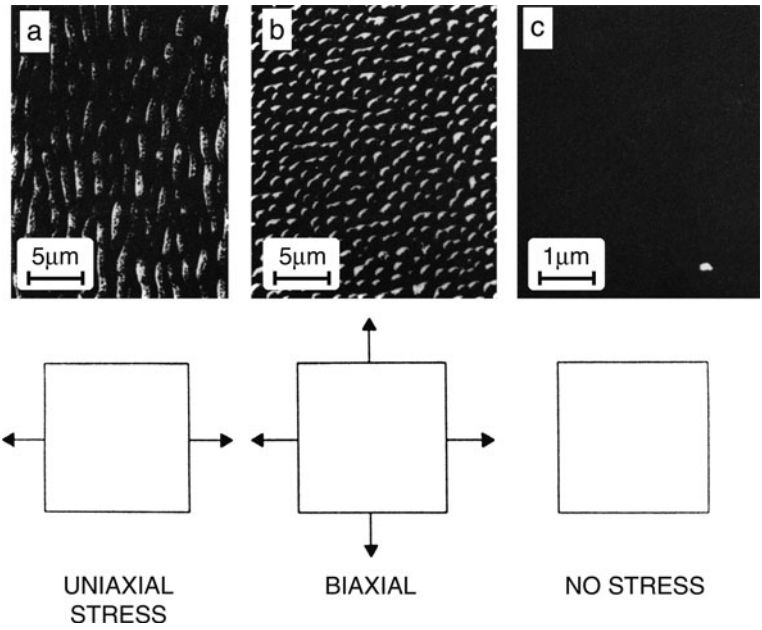

Fig. 28.6.2a–c SEM micrographs of different types of structures observed on PI foils after ablation with KrF-laser radiation. (**a**) Foil was uniaxially stretched before ablation ($\phi \approx 136\,\mathrm{mJ/cm^2}$, 30 pulses). (**b**) Foil was biaxially stretched before ablation ($\phi \approx 115\,\mathrm{mJ/cm^2}$, 50 pulses). (**c**) Annealed foil ($\phi \approx 120\,\mathrm{mJ/cm^2}$, 50 pulses) [*Arenholz* et al. 1992]

Uniaxial stretching prior to laser-light irradiation results in wall-type structures, while biaxial stretching gives rise to nap-type structures. The surface of foils that have been annealed (stress released) prior to laser-light irradiation remains smooth. Naps seem to be formed by 'superposition' of walls aligned perpendicularly to the respective stresses [*Arenholz* et al. 1991]. The average distance between walls or naps, Λ, increases with the number of laser pulses (Fig. 28.6.3), the laser fluence, and wavelength (optical penetration depth). Depending on these parameters, Λ is within the range of about 0.5–50 μm. No influence of the laser pulse repetition rate on Λ was observed within the range 1–50 Hz. The dependence of the period Λ on the number of laser pulses N_ℓ remains unchanged for nanosecond (28 ns) and subpicosecond (500 fs) KrF-laser pulses. The increase in Λ with N_ℓ becomes less pronounced with an increasing angle of laser-beam incidence.

A tentative explanation for the formation of these structures is based on a stress-release model. Here, craze formation is considered to be due to an externally applied or frozen-in stress, S, parallel to the surface (Fig. 28.6.4). Formation of a craze reduces the stress, but increases the surface energy.

In the simplest approximation, stress release takes place within a volume $V_{el} \propto (aF/\Lambda) \min\{a, \Lambda\}$, where a is the depth of the craze, F the irradiated area, and Λ the spatial period. This result is based on the notion that with $a \gg \Lambda$ the stress between the crazes relaxes almost completely, while, in the opposite case, $a \ll \Lambda$,

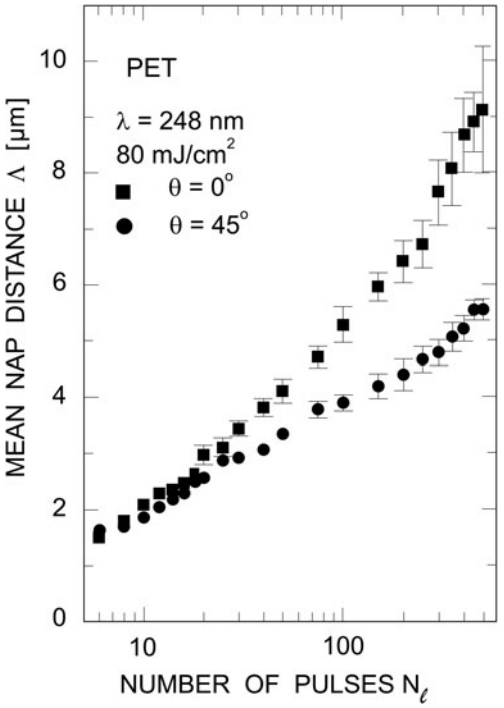

Fig. 28.6.3 Mean nap distance versus number of laser pulses observed on untreated PET foils [*Arenholz* et al. 1994]

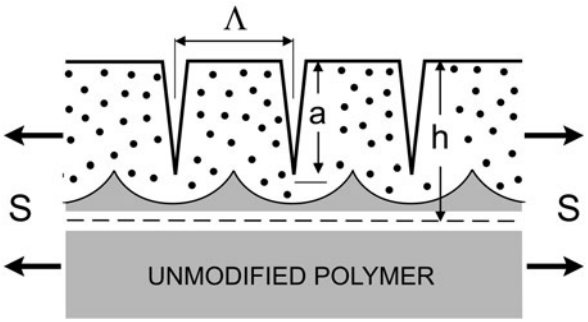

Fig. 28.6.4 Schematic of quasiperiodic structures originating from craze formation in materials with frozen-in or externally applied stress fields. *h* is the thickness of the laser-modified surface layer. The *dotted* regions indicate the volume in which the stress is relaxed

only the volume around each craze $\propto a^2$ is relaxed. Craze formation *increases* the surface by $2aF/\Lambda$, and thereby increases the surface energy. The combination of the elastic and surface energy yields the total energy change per unit area:

$$\Delta E = \Delta E_{\mathrm{el}} + \Delta E_{\mathrm{surf}} \approx -\frac{a}{\Lambda} \min\{a, \Lambda\} \frac{S^2}{Y} + \frac{a\sigma}{\Lambda} , \tag{28.6.2}$$

where Y is Young's modulus and σ the surface tension coefficient. For a finite period Λ and $a < \Lambda$, the depth of crazes grows if $\Delta E < 0$, i.e., for

$$a \geq a_{\mathrm{c}} = \frac{\sigma Y}{S^2} . \tag{28.6.3}$$

Here, it is assumed that crazes of depth $a \geq a_{\mathrm{c}}$ already exist on the surface of the stretched material. Within the simplest picture, the *optimal* period is $\Lambda \approx a$. This is due to the fact that for a given a the total energy (28.6.2) increases with both $\Lambda > a$ and $\Lambda < a$. With $\Lambda \approx a$, the energy is

$$\Delta E \approx -a\frac{S^2}{Y} + \sigma . \tag{28.6.4}$$

This energy release increases with a. If we assume that the crazes can grow only within the laser-modified layer, h, we have $a \approx \Lambda \approx h$. For a thermal process and single-pulse irradiation, h can be estimated in a similar way as h_l in Sect. 10.1. Correspondingly, one can introduce an effective temperature $T_{\mathrm{a}}^{\mathrm{eff}} = T_{\mathrm{a}} + \Delta H_{\mathrm{a}}/c_{\mathrm{p}}$, where ΔH_{a} is the enthalpy for surface modification, e.g., by thermal bond breaking. For a non-thermal process, one can assume, in analogy, that surface modification requires a certain number of photochemically broken bonds. Then, the situation is similar to that described in Sect. 12.8.

For polymers, Y depends strongly on temperature and has values of about $10^5\,\mathrm{N/cm^2}$ for 20°C and $10^2\,\mathrm{N/cm^2}$ for 150°C. Typical values of σ are between $0.02\,\mathrm{J/cm^2}$ (PMMA) and $0.15\,\mathrm{J/cm^2}$ (PS). Frozen-in stresses in polymers which are related to the fabrication process are of the order of 10^2 to $10^4\,\mathrm{N/cm^2}$.

The dependence of Λ on the number of laser pulses (Fig. 28.6.3) and on the absorption coefficient of the polymer may tentatively be understood on the basis of the dependence of h on these parameters. Irradiation of a quasiperiodic structure leads to preferential ablation of top layers where the stress fields are relaxed. At the bottom, both ablation and further extension of the craze increase the depth of the structure. When the crazes become very deep, naps or walls drop over in random directions so that, for example, a new nap is formed out of two. By this means, the average period increases with N_ℓ. A more sophisticated treatment of this problem is presented by *Bityurin* et al. (2007).

28.7 Technological Aspects

For applications it is often desirable to suppress structure formation because it influences the smoothness of the surface, limits the ultimate resolution in micropatterning, laser lithography, etc. On the other hand, surface roughening during the initial phase of structure formation can be employed for surface functionalization with respect to adhesion, wetting, tribological properties etc. An increase in surface area is also advantageous for some types of catalytic, chemical and gas sensing applications. Additionally, for Si visible photoluminescence (PL) was observed from both, ripple-type [*Kumar* and *Soni* 2008] and cone-type structures [*Wu* et al. 2002] (Sect. 23.5).

Ripple formation can be suppressed by reducing the correlation time of the polarization, for example, by using circularly polarized light, and by avoiding good spatial coherence. Another possibility is to use fluences which result in plasma formation – as long as this is compatible with the particular processing application. With the generation of a plasma, interference effects on the surface are significantly reduced.

Ripple formation can be applied for the fabrication of gratings for well-defined orientation of molecules, e.g., for aligned growth of biological cells [*Rebollar* et al. 2008], etc. The combination of different techniques opens up a great variety of possibilities. Among the examples are periodic submicrometer gratings and dot structures generated by ripple formation together with laser-beam interference [*Nakata* and *Miyanaga* 2010; *Kumagai* et al. 1992, see also previous edition].

Non-coherent structure formation can be suppressed for certain ranges of process parameters which must be determined experimentally for every system of interest. Here, even simple theoretical models, as discussed in the preceding sections, can help to find these ranges. With some systems, and in particular with stress-related instabilities, structure formation can be diminished or even avoided altogether by proper pretreatment of the sample.

Nevertheless, there are a number of real and potential applications of some types of non-coherent structures. Figure 28.7.1 shows arrays of conical structures fabricated on Si in SF_6 using 800 nm Ti:sapphire laser radiation (Sect. 28.4). Single cones show nodules with sizes up to several 100 nm. These dual-scale structures are, in fact, quite similar to the dual-scale structures on lotus leaves. The latter consist of cone-type papillose epidermal cells with sizes of 5–10 μm and surface densities of about $4.2 \times 10^5\,\mathrm{cm}^{-2}$ and, additionally, a layer of epicuticular waxes with nodules of about 150 nm in size. Thus, it is not astonishing that the artificial structure shown in Figure 28.7.1 shows almost the same water repellency and self-cleaning effects as natural lotus leaves. Additionally, laser-induced conical and columnar structures on Si surfaces are also investigated for applications as cold cathode electron emitters [*Zorba* et al. 2006] and photodetectors. The latter application is based on the fact that such structures fabricated in SF_6 atmosphere absorb radiation over a spectral region between 200 nm and 2.5 μm with a (constant) absorptivity of about $A \approx 0.9$ [*Wu* et al. 2001]. For this reason, the material is sometimes termed 'black silicon'. Note that c-Si is almost transparent for wavelengths $\lambda \gtrsim 1.1\,\mu\mathrm{m}$. Furthermore, such

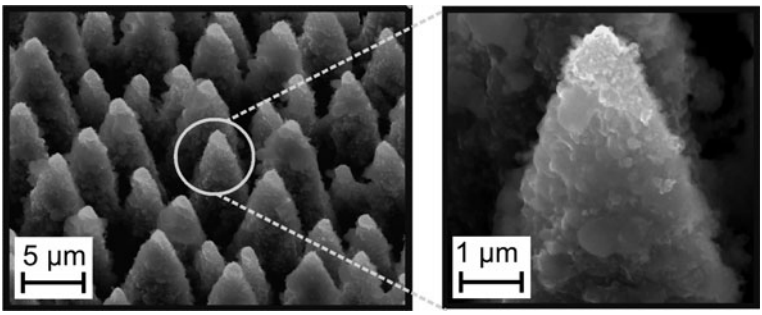

Fig. 28.7.1 SEM images of conical structures fabricated on Si by 800 nm Ti:sapphire-laser radiation ($\phi \approx 2.5\,\mathrm{J/cm^2}$; $\tau_\ell \approx 180\,\mathrm{fs}$, $N_\ell = 500$, $\nu_\mathrm{r} = 10^3\,\mathrm{Hz}$) in 667 mbar SF_6. The average height of cones is about 10 µm, their surface density about $10^6\ \mathrm{cm^{-2}}$. The magnification shows nodules with sizes up to few hundred nanometers on the slopes of cones [*Zorba* et al. 2008a; courtesy of IESL-Forth, Greece]

structures seem to be quite useful for applications in laser desorption ionization of biomolecules [*Stolee* et al. 2010]. In contrast to MALDI (Sect. 30.1) such structures facilitate fragmentation, ionization, and desorption without the necessity of a matrix. Thus, ion production for mass-spectroscopical analysis is considerably simplified. The ionization mechanism in this process is probably related to the electric field enhancement at the tip of columns (Sect. 5.3.7).

Part VI
Diagnostic Techniques, Plasmas

The next chapter gives an overview on some experimental tools, on techniques for *in situ* measurements of processing rates and laser-induced temperatures, and on the analysis of laser-processed materials. Such measurements are of great importance for both an understanding of fundamental laser-matter interactions and process optimization.

Chapter 30 deals with precursor and product species that are relevant in various different types of laser processing. It also summarizes some fundamental aspects and observations on the expansion of laser-induced vapor/plasma plumes in vacuum, and in gaseous or liquid ambient media.

Chapter 29
Diagnostic Techniques

29.1 Characterization of Laser-Beam Profiles

The intensity distribution of laser beams with diameters in the range 0.1−5 cm can conveniently be measured in real time by employing a linear or a 2D array of photodiodes, a vidicon (a semiconductor or pyroelectric detector array), or a CCD camera. Further details, in particular on the characterization of excimer-laser-beams, have been outlined by *Mann* (2005).

For *focused* laser beams with spot sizes of a few tenths of a micrometer to a few micrometers, a simple and cheap method is the scanning knife-edge technique [*Suzaki* and *Tachibana* 1975]. Here, the transmitted (reflected) laser power P_T is measured during scanning a sharp edge, e.g., a razor blade, across the laser spot. For a Gaussian laser beam P_T is given by

$$P_T(x) = \frac{P}{\pi^{1/2} w_0} \int_x^\infty \exp\left(-\frac{x'^2}{w_0^2}\right) dx' = \frac{P}{2} \operatorname{erfc}\left(\frac{x}{w_0}\right) , \qquad (29.1.1)$$

where P is the total power. The fit of the experimental curve $P_T(x)/P$ yields the beam radius, w_0.

29.2 Homogenization of Laser Beams

The production of a spatially uniform energy density in a plane perpendicular to the optical axis of the laser beam is termed beam homogenization. Here, single rays of the incident beam which propagate along different paths are superimposed in the exit plane.

Homogenization of highly coherent lasers which have a Gaussian or Gaussian-like beam profile is mainly performed by diffractive methods.

Highly non-coherent lasers, such as excimer lasers, have a top-hat profile. Here, beam homogenization is frequently based on a combination of reflective and refractive (catadioptric) optics. The beam profile of excimer lasers is often optimized

D. Bäuerle, *Laser Processing and Chemistry,* 4th ed.,
DOI 10.1007/978-3-642-17613-5_29, © Springer-Verlag Berlin Heidelberg 2011

inside the resonator, for example, by X-ray pre-ionization of the laser-active gases or by special geometries of the electrodes.

Other requirements on homogenizers include: low energy losses, transmission of high energy densities, compact design for applications with small working distances, and long lifetimes.

Many techniques employed for laser-beam homogenization are also suitable for other light sources such as lamps.

29.2.1 Diffractive Methods

Laser beams with Gaussian or Gaussian-like profiles can be homogenized by diffractive methods employing metallic grids, optical gratings, phase plates, or holographic techniques [*Jain* et al. 1984; *Possin* et al. 1983; *Veldkamp* 1982; *Han* et al. 1983]. The application of these methods requires long-term stability of the position, the (resonator) mode, and, with pulsed lasers, of subsequent pulses of the incident beam.

29.2.2 Reflective Methods

Homogenization by multiple reflections is achieved by focusing the laser beam into a light guide of rectangular or circular cross section. This is schematically shown in Fig. 29.2.1a. The light guide can consist of highly reflecting mirrors, a quartz rod, or a fiber inside which the light is totally reflected. High energy densities at the entrance plane can cause material damages. For a given length of the light guide

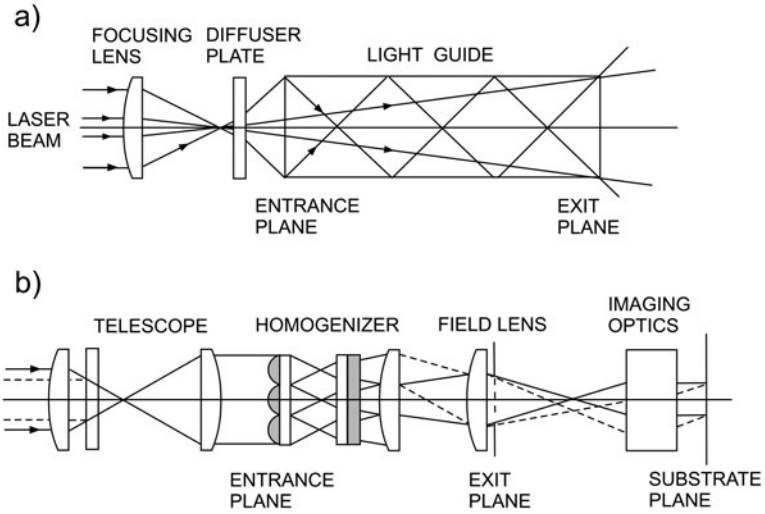

Fig. 29.2.1 Laser-beam homogenization by means of (**a**) multiple reflections within a light guide and (**b**) a fly's eye homogenizer. The crossed lens arrays are indicated by a grey tone

the number of reflections is determined by the beam divergence in the entrance plane. Single rays which undergo a different number of reflections inside the light guide, are superimposed at the exit plane. The homogeneity can be improved by inserting a diffuser plate in front of the light guide. By means of imaging optics, the homogenized beam can be concentrated onto a mask for substrate patterning (Fig. 5.2.1).

Other arrangements for beam homogenization use a *curved* quartz rod [*Cullis* et al. 1979] or multifaceted mirrors which divide the laser beam into rectangular segments that are superimposed at the image plane by means of an imaging mirror [*Dickey* and *O'Neil* 1988].

29.2.3 Refractive Methods

Particularly suitable for homogenization of large-area, high-power laser beams, for example, excimer-laser beams, is the fly's eye homogenizer, which is frequently used in lithography (Fig. 29.2.1b). It consists mainly of *crossed* anamorphic-lens arrays, in most cases cylinder lenses, and an imaging lens. The telescope is used to match the diameter of the (excimer) laser beam to the size of the homogenizer entrance aperture. The size of the homogenized beam in the exit plane is determined by the width of the anamorphic lenses, by the focal lengths of the second lens array, and the image formation lens. For projection patterning, a mask is positioned at the exit plane. The field lens in front of the mask reduces vignetting. The imaging optics transfers the image produced by the mask onto the substrate. The fly's eye homogenizer permits one to employ relatively large cross sections of optical components (quartz or glass) and thereby high energy throughputs. For further details see *Oesterlin* and *Koch* (2006) and *Mann* (2006).

29.3 Deposition, Etch, and Ablation Rates

This section deals with the most commonly used optical and non-optical techniques employed for *in situ* measurements of processing rates in laser-induced material deposition, etching, and ablation.

29.3.1 Optical Techniques

Speckles

When irradiating a substrate with a cw-laser beam, a characteristic speckle pattern is observed, in general. With a fixed laser beam and substrate, the beginning of deposition or etching can be detected by the onset of uniform speckle movement. The observation of the speckles is a qualitative but very sensitive method and it is mainly used in gas-phase processing.

Interference Fringes

The growth of thin films can be monitored from the interference pattern of a probe beam, for example, a HeNe-laser beam. The distance between subsequent maxima in the oscillations of the reflected beam intensity (perpendicular incidence) corresponds to a change in layer thickness, $\Delta h = \lambda/2n$, where n is the refractive index of the layer. The detailed equations that apply to different cases are given in Sect. 9.2. Interference fringes are also used for in situ measurements of etch depths and of ablation thresholds.

Reflection and Transmission Measurements

Deposition and etch rates can sometimes be estimated from the intensity of either the laser beam employed in processing, or of a probe beam transmitted through/reflected from the deposited or etched film. An estimation of film thicknesses, however, requires a knowledge of the optical constants of the film and the substrate, if present. For thin metal films whose thickness is comparable to the optical penetration depth ($l_\alpha = \alpha^{-1}$) the optical behavior is dominated by surface effects. The optical constants of thin films may differ significantly from the bulk values and, additionally, they change with film thickness. As a consequence, estimations of film thicknesses from transmitted/reflected light intensities often involve tremendous inaccuracies. If we ignore these effects, the film thickness can be estimated from the reflectivity/transmittivity which is given for different cases in Sect. 9.2.

Real time reflectivity, transmission, and scattering experiments have been employed to study laser-induced changes in surface morphologies of organic polymers [*Ball* et al. 1995a, b], and chemical reactions, e.g. during LCVD of Au [*Comita* et al. 1992]. Raman microprobe experiments are included in Sect. 29.4.2.

Photoelectric Methods, Laser-Beam Deflection/Scattering

Deposition rates achieved during steady growth of fibers can be measured by imaging the hot tip of the fiber onto a position-sensing diode (Fig. 17.1.1; *Doppelbauer* and *Bäuerle* 1986).

In PLA, the *deflection/scattering/absorption* of a probe beam propagating in parallel to the substrate surface can be used to detect ablation thresholds, different types of particles ejected from the target, etc. [*Petkovšek* et al. 2008; *Hunger* et al. 1992]. The experimental setup is similar to that shown in Fig. 30.1.1a. The beam at perpendicular incidence to the substrate, e.g., an excimer-laser beam, causes ablation. The probe beam, propagating in parallel to the target surface, becomes deflected due to transient changes in refractive index above the laser heated surface or scattered/absorbed by the ablated species [*König* et al. 2005]. Shadowgraph and Schlieren images are obtained with similar experimental arrangements using either pulsed white-light discharge lamps or (visible) laser radiation together with fiber optics for illumination [*Vogel* et al. 2006; Sect. 30.4.3].

Ultrafast Optical Techniques

With the development of ultrashort-pulse lasers, fast optical techniques for investigating transient laser-induced phenomena have become of increasing importance. Clearly, the classification between 'quasistationary' diagnostic techniques and 'ultrafast' optical techniques is somewhat arbitrary. Subsequently we mention some investigations where transient laser-induced phenomena such as temporal evolutions of surface reflectivities, surface deformations, melting and ablation thresholds have been investigated with temporal resolutions of a few femtoseconds to a few nanoseconds. Among those are:

- Time resolved microscopy (TRM). A schematic picture of an experimental setup is shown in Fig. 29.3.1. The sample surface is excited by a pump pulse and imaged for variable time delays of a (low intensity) probe pulse onto a CCD camera. For surface (low penetration) testing, the probe pulse is frequency doubled. With the fs-lasers employed, time delays of up to about 10 ns could be investigated [*Bonse* et al. 2006; *Sokolowski-Tinten* et al. 1998]. A similar setup has been employed for imaging transient electronic plasmas in dielectrics [*Gawelda* et al. 2008; Sect. 13.6].
- Optical reflection interferometry uses a Michelson-type setup as shown in Fig. 29.3.2. The 'movable' mirror in a standard Michelson interferometer is substituted by the sample. The pump pulse causes a deformation of the sample surface. The probe beam that enters the interferometer is split into an 'object' pulse and a reference pulse. The interference between these two reflected pulses is measured by means of a CCD camera. The temporal resolution is determined by the duration of the probe pulse [*Agranat* et al. 2007; *Temnov* et al. 2006].

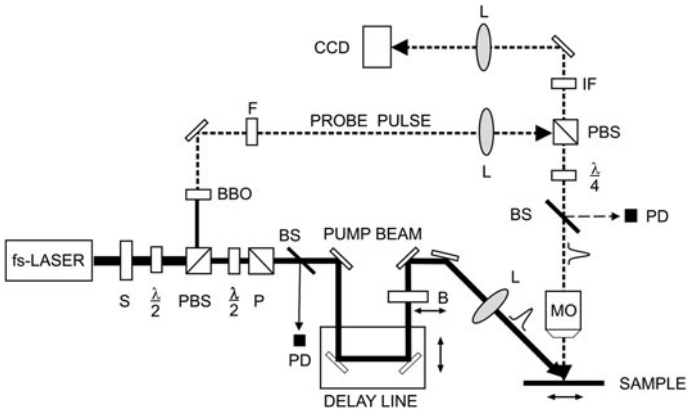

Fig. 29.3.1 Schematic picture of an experimental setup employed for fs-time-resolved microscopy. Part of the fs-laser beam is used as a probe beam which is frequency doubled (BBO crystal). The signal reflected from the sample surface is imaged onto a CCD camera. S: electromechanical shutter; PBS: polarizing beam splitter; P: polarizer; BS: beam splitter; L: lens; F: bandpass filter; PD: photodiode; MO: microscope objective; IF: interference filter [adapted from *Bonse* et al. 2006]

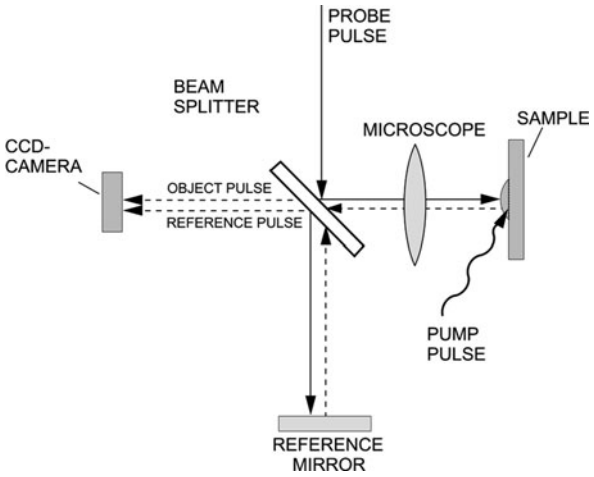

Fig. 29.3.2 Setup employed in microinterferometry. The pump pulse causes a surface deformation. This results in different path lengths of the probe pulse reflected from the sample (object pulse) and the reference mirror (reference pulse). The surface deformation shown is strongly exaggerated

- Real-time pump/reflectivity (RTR) measurements permit to study reflectivity changes over longer times. The experimental setup is similar to that shown in Fig. 29.3.1. Here, the probe beam is substituted, e.g., by Ar^+-laser pulses, and the CCD camera by a streak camera. RTR measurements have been used to study transient electron temperatures during/after ultrashort-pulse laser irradiation of metals and semiconductors, laser-induced melting and ablation, optical breakdown in transparent materials, etc. [*Bonse* et al. 2006; *Chaoui* et al. 2001].
- Coherent anti-Stokes Raman spectroscopy (CARS) has been used to investigate on a ps time scale the ablation dynamics of PMMA [*Hare* and *Dlott* 1994].
- Time-resolved phase-contrast microscopy has been used for investigating the temporal evolution of void formation [*Mermillod-Blondin* et al. 2009; Sect. 13.7].
- Ultrafast dynamic ellipsometry permits to study time-resolved changes in refractive indices [*Bolme* and *Funk* 2008].
- *In situ* time-resolved electron diffraction [*Siwick* et al. 2003] and X-ray diffraction [*Seres* et al. 2009; *Woerner* et al. 2009] have been employed for studying the dynamics of *atoms* under fs-laser irradiation of materials. In such experiments, laser-generated X-rays are of particular advantage (Sect. 30.2).

29.3.2 Other Techiques

Microbalances

A very sensitive method for measuring mass deposition, etch, and ablation rates over larger areas (several mm^2) involves the use of a microbalance. This is a piezoelectric slab-shaped crystal or ceramic with metal electrodes. The materials most commonly

used for microbalances are crystalline quartz and ceramic PZT($PbTi_{1-x}Zr_xO_3$). For etch- and ablation-rate measurements the material to be investigated must first be evaporated as a thin film or bonded as a thin platelet onto the microbalance surface. Detailed investigations on quartz-crystal microbalances (QCM) including different mass load ranges and measurement techniques have been described extensively in the literature [*Chang* et al. 2000; *Benes* 1984]. When the electrodes of the microbalance are attached to an oscillating circuit, resonance occurs at a (fundamental) frequency ν. For *small* mass changes originating from laser-induced deposition ($\Delta m > 0$) or material removal ($\Delta m < 0$), the frequency change can be approximated by

$$\Delta\nu \approx -\frac{\nu^2 \Delta m}{C\varrho F} \ , \tag{29.3.1}$$

where C denotes a frequency constant, ϱ is the mass density of the piezoelectric slab and F its *active* area, on which material is deposited or from which it is removed. For AT-cut quartz crystals $C \approx 1.668 \times 10^5$ cm/s and $\varrho \approx 2.648\,\mathrm{g/cm^3}$. Equation (29.3.1) is valid for mass changes $\Delta m/m \leq 2\%$. Since the resonant frequency can be monitored continuously, material deposition or removal rates can be measured directly. Microbalances are commercially available and can routinely measure mass-load changes of $10^{-9}\,\mathrm{g/cm^2}$ and, if special care is taken, changes down to $10^{-12}\,\mathrm{g/cm^2}$.

A typical frequency response of a QCM covered with a thin evaporated Si film to pulsed CO_2-laser radiation is illustrated in Fig. 29.3.3. The microbalance was positioned with the active area perpendicular to the unfocused laser beam. The momentary increase in microbalance frequency during each laser pulse is due to the

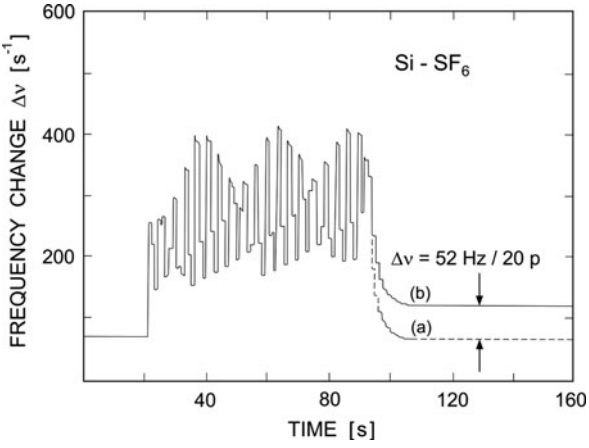

Fig. 29.3.3 a, b Frequency response of a quartz-crystal microbalance (QCM) covered with a Si film, to pulsed CO_2-laser radiation ($\lambda = 942.4\,\mathrm{cm^{-1}}$; $\phi = 1\,\mathrm{J/cm^2}$). (**a**) Vacuum. (**b**) $p(SF_6) = 2.7$ mbar [*Chuang* 1981]

temporary temperature rise caused by the absorbed laser light. In the absence of any reactive gas, and for (low) laser fluences that do not cause ablation, the microbalance returns to its original frequency (curve a). In a reactive gaseous atmosphere, e.g., in SF_6, the microbalance frequency increases (curve b). The detected frequency change of $\Delta v = 52\,\text{Hz}$ after 20 pulses corresponds to an *etch* rate of 4.4×10^{14} Si atoms/pulse. The same technique has been used for measuring deposition rates in LCVD [*Jackson* and *Tyndall* 1988], and ablation rates for both inorganic [*Toftmann* et al. 2003; *Svendsen* et al. 1998; *X. Zhang* et al. 1997] and organic materials [*Dumont* et al. 2005; *Küper* et al. 1993; *Lazare* and *Granier* 1989].

The angular distribution of species can be monitored by using an array of QCMs, as shown in Fig. 29.3.4. Such a setup can also be employed for measuring the angular dependence of overall deposition rates as a function of laser parameters, and for investigations on the dynamics of vapor/plasma-plumes (Chap. 30) [*Toftmann* et al. 2003]. In the case of ablation of multicomponent targets together with a chemical analysis of deposits on single QCMs, the angular distribution of single elements can be determined. This information is of importance for both the expansion dynamics of single elements/molecules and the chemical homogeneity of thin films fabricated by pulsed-laser deposition (PLD).

Finally, it should be noted that (*mass*) deposition, etch and ablation rates and the corresponding threshold intensities measured by QCMs can differ significantly from those determined by means of optical techniques, mechanical profilometers, etc. In material deposition, these differences can be related to the incorporation of

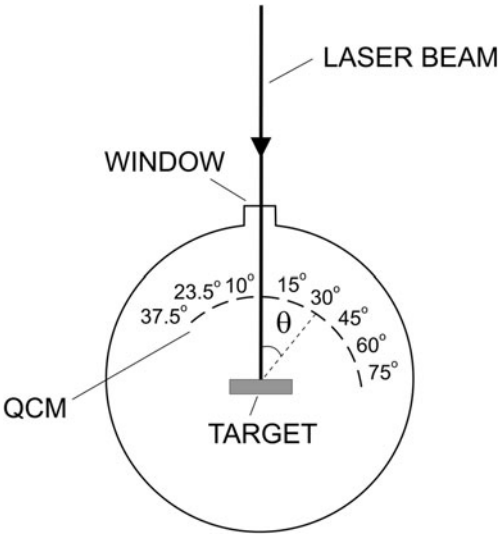

Fig. 29.3.4 Experimental setup for measuring the angular distribution of the (overall) mass flux of ablated species by means of a circular array of QCMs [adapted from *Toftmann* et al. 2003]. A similar setup is used for measuring electron-/ion-fluxes. Here, the QCMs are substituted by Langmuir probes

impurities, porosities, etc. On the other hand, mass losses related to the depletion of single species can take place without significant material etching or ablation (Chap. 12).

Acoustic and Pyroelectric Monitors

For detection of elastic (acoustic) waves emitted from the laser-processed region, one frequently uses, instead of discs of crystalline quartz or ceramic PZT [*Melcher* 1984], piezoelectric materials in the form of films or foils. Ideal for this application are foils of (ferroelectric) PVDF (polyvinylidene fluoride). Here, the sample to be investigated is either bonded or, in the case of thin films, directly evaporated onto the PVDF foil.

Piezoelectric materials that possess a unique polar axis (dipole moment) in the absence of a stress are also pyroelectric. Pyroelectric materials develop a polarization charge that is proportional to the (uniform) temperature rise. (Note that a piezoelectric material that is *not* pyroelectric can generate an electric charge if it is *non*-uniformly heated; this is simply due to piezoelectric stresses created by thermal expansion.) Because all ferroelectric materials are piezoelectric *and* pyroelectric, PVDF foils can also be used as pyroelectric detectors.

Acoustic and pyroelectric monitors have been employed to measure threshold fluences and pressures associated with pulsed-laser ablation of various materials [*Krüger* et al. 2002; *Grad* and *Mozina* 1993; *Dyer* et al. 1992a].

29.4 Temperature Measurements

Knowledge of the laser-induced temperature distribution, or at least of the maximum temperature rise, is of great importance for fundamental investigations, and for process control and optimization.

Temperature measurements can be classified according to optical techniques (photoelectric pyrometry, Raman spectroscopy, photothermal deflection, etc.) and other techniques such as pyroelectric calorimetry, acoustic methods, time-of-flight techniques, etc.

29.4.1 Photoelectric Pyrometry

In photoelectric pyrometry the local temperature is derived from the optical radiation emitted from the laser-heated surface. The spectral radiance emitted from a solid depends on temperature and is given by

$$L(\nu, T) = \varepsilon(\nu, T) L_{b0}(\nu, T) \ , \tag{29.4.1}$$

where $\varepsilon(\nu, T)$ is the spectral emissivity and

$$L_{b0}(\nu, T) = \frac{2h\nu^3}{c^2} \frac{1}{\exp\left(\frac{h\nu}{k_B T}\right) - 1} = \frac{2h\nu^3}{c^2} \langle n \rangle$$

the spectral radiance of the blackbody radiation in a vacuum (radiant power of the non-polarized radiation emitted per unit projected area of the surface per unit solid angle within the interval between ν and $\nu + \mathrm{d}\nu$). If ε is known, measurements of $L(\nu, T)$ permit direct determination of the temperature. The situation is more complicated if the material is irradiated with a focused laser beam, which results in spatially localized heating. In this case, the total emitted radiation is a mixture of radiation emitted from different elements at different temperatures. This has led to the concept of apparent emissivities, ε_a [*Zeldovich* and *Raizer* 1966]. For the (simpler) case of large-area laser-beam irradiation (1D problem), the apparent emissivity is approximately equal to the emissivity of a uniformly heated solid only if the variation in temperature is small over the distance $l_{\alpha e} = \alpha_e^{-1}$ (α_e is the absorption coefficient at the wavelength employed in the pyrometric measurements).

The main advantages of photoelectric pyrometry are the high temperature sensitivity, the relatively low sensitivity to surface properties – as compared to other techniques – and the suitability for in situ measurements. The spatial resolution is limited by diffraction and, at low temperatures, by the sensitivity of the detection system. The temperature can be derived from the emitted radiation in various ways:

- From its intensity at a certain wavelength $\lambda_1 \equiv \lambda_e$ (monochromatic pyrometry).
- From its intensity integrated over a broader spectral region.
- From its spectral dependence, including temperature determination from the ratio of the radiances at two wavelengths.

For *monochromatic* pyrometry, from the law of error propagation in Wien's approximation we obtain

$$\delta T = \frac{\lambda_1 T^2}{C_2} \left[\left(\frac{\delta I}{I} \right)^2 + \left(\frac{\delta \varepsilon}{\varepsilon} \right)^2 \right]^{1/2} , \tag{29.4.2}$$

where δT is the uncertainty in temperature. $C_2 = hc/k_B = 1.4388 \times 10^7$ nm K is the second radiation constant, and I the measured intensity. A similar expression applies to broadband pyrometry.

If the temperature is evaluated from the ratio of radiances at *two wavelengths*, we obtain

$$\delta T = \frac{\lambda_{eff} T^2}{C_2} \frac{\delta R_i}{R_i} , \tag{29.4.3}$$

with $\lambda_{eff} = (1/\lambda_2 - 1/\lambda_1)^{-1}$ and $R_i = (I_1/\varepsilon_1)/(I_2/\varepsilon_2)$, where I_1 and I_2 are the intensities, and ε_1 and ε_2 the emissivities at wavelengths λ_1 and λ_2, respectively. In large-area pyrometry of uniformly heated materials, the error in temperature

measurements is mainly determined by uncertainties in the emissivity, so that two-wavelength pyrometry gives the best results [*Battuello* and *Ricolfi* 1980]. The situation is different in laser *microprocessing*, where temperature distributions are strongly localized. Here, the light fluxes to be measured are rather small and the uncertainties in the measured intensities can exceed those in the emissivities. If inaccuracies in the intensity measurements dominate, we find from (29.4.2) and (29.4.3) that, irrespective of the difference between the two wavelengths, the evaluation of the temperature from the radiance at the smaller of the two wavelengths yields a smaller error than the evaluation from the ratio of radiances. Additionally, chromatic errors in the imaging system become more serious for small spot sizes. Monochromatic pyrometry is therefore the superior technique in most cases of laser microchemical processing. Additional advantages are the simplicity of the experimental setup and calibration (via a radiance standard such as a tungsten band lamp). However, in many cases sufficient accuracy can only be achieved if the influence of the laser-induced temperature distribution on the apparent emissivity is known.

The sensitivity of the detector required for photoelectric pyrometry can be estimated from the spectral radiance of the blackbody in the temperature range under consideration. Figure 29.4.1 exhibits the wavelength dependence of the spectral radiance ($\mathrm{W/nm\,\mu m^2\,sr}$) of the blackbody radiation for various temperatures; the range of applicability for different detectors has also been included. The intensities that can be measured in a real experiment are reduced by a factor of $10-10^2$ with respect to the ideal values, mainly due to the lower emissivity, $\varepsilon < 1$, the detected

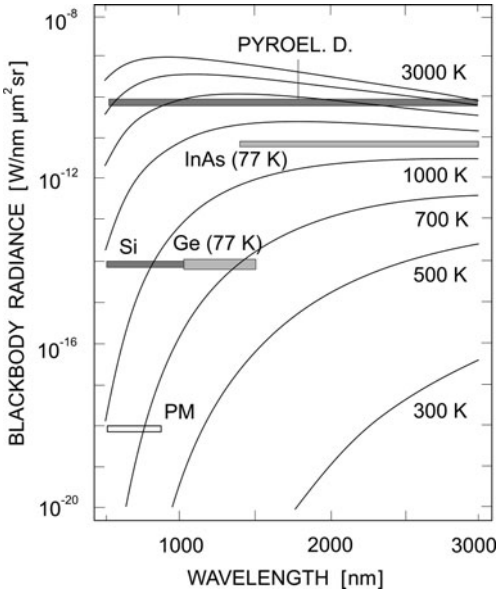

Fig. 29.4.1 Blackbody radiances that can be measured with various detectors in photoelectric pyrometry. Isotherms for various temperatures are shown (*solid curves*). The bars indicate the noise equivalent power (NEP) in $\mathrm{Ws^{1/2}}$ and the range of spectral sensitivity. PM: photomultiplier

solid angle, which is often < 1 sr, and losses in the optical components. At temperatures above 1000 K, high-quality silicon photodiodes (noise equivalent power, NEP $\approx 10^{-14}$ W/Hz$^{1/2}$) can often be employed. Lower temperatures, down to about 700 K, can be measured by using cooled Ge diodes and a spectral bandwidth of several nanometers.

An Experimental Example

Typical spectra of the emitted radiation measured during steady growth of silicon fibers are shown in Fig. 29.4.2a for various laser powers. The experimental arrangement employed was similar to that in Fig. 17.1.1. The depth of the temperature distribution along the axis of the glowing fiber was estimated to be larger than about 100 μm, even when the reactor was filled with H_2. Since the energy of the bandgap of Si decreases with increasing temperature, the condition $w_T^a \gg l_{\alpha e}$ (Sect. 6.5) is satisfied over the spectral range investigated. The fit of the spectra by Planck's law (Wien's approximation; Fig. 29.4.2b) permits one to derive the corresponding temperatures. The results are quite consistent and demonstrate that the influence of excess carriers at temperatures above 900 K can be ignored. The agreement with measured spectra can even be improved if we take into account the (extrapolated) emissivity of Si, $\varepsilon(\nu, T)$ [*Jellison* and *Modine* 1983].

Time-resolved photoelectric pyrometry has been demonstrated by *Chen* and *Grigoropoulos* (1997).

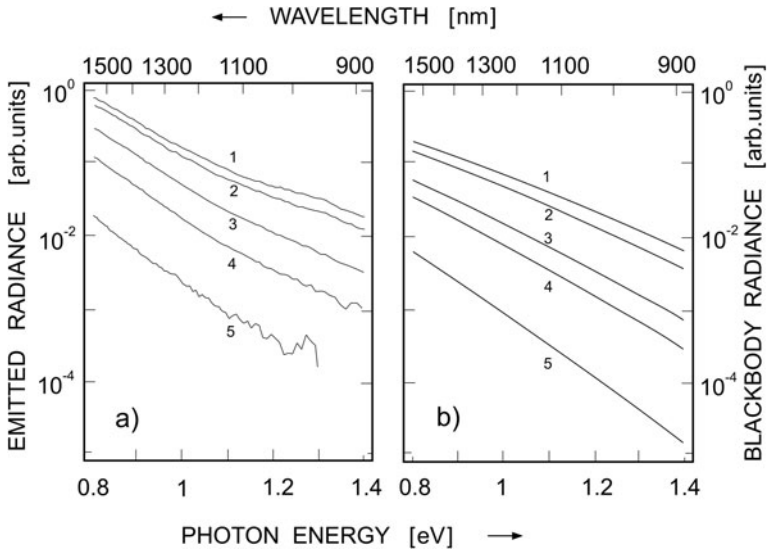

Fig. 29.4.2 (**a**) Spectral dependence of the radiation emitted from laser-heated tips of Si fibers grown by LCVD from SiH_4 at various laser powers, P. *Curve* 1: $P = 150$ mW (1360 K); 2: 140 mW (1300 K); 3: 120 mW (1150 K); 4: 100 mW (1080 K); 5: 80 mW (900 K). The temperature values given in parentheses were derived from fits to Planck's law (Wien's approximation) (**b**) Blackbody radiances for the temperature values given in (**a**) [*Doppelbauer* and *Bäuerle* 1987]

29.4.2 Other Optical Techniques

Raman spectroscopy allows one to determine temperatures from the relative intensities of Stokes and anti-Stokes components, which are given by

$$\frac{I_\mathrm{s}}{I_\mathrm{as}} = f(\alpha_\mathrm{i}, \nu_\mathrm{i}) \frac{\langle n \rangle + 1}{\langle n \rangle} \,, \tag{29.4.4}$$

where $\langle n \rangle \equiv \langle n(\nu_\mathrm{M}) \rangle$ is the Bose–Einstein factor for the particular (vibrational, rotational, etc.) mode under consideration, and $f(\alpha_\mathrm{i}, \nu_\mathrm{i})$ a factor which corrects the measured Raman intensities for the actual absorption coefficients, the frequency dependence of Raman efficiencies, the spectral sensitivity of the experimental setup, etc. In a crude approximation, $f(\alpha_\mathrm{i}, \nu_\mathrm{i}) \approx 1$. Alternatively, the temperature can also be derived by analyzing the shifts and shapes of Stokes Raman lines only. The accuracy achieved in such measurements with Si at 1200 K is about $\pm$ 100 K [*Tang* and *Herman* 1991; *Compaan* 1985]. With strongly inhomogeneous temperature distributions, similar problems as in photoelectric pyrometry arise. Local laser-induced temperature distributions were derived from Raman spectra during cw-laser heating of Si [*Pazionis* et al. 1989] and LCVD of Si from SiH_4 [*Magnotta* and *Herman* 1986]. A clear disadvantage of the Raman technique is the high cost of the experimental setup.

Laser-induced temperatures have also been derived from time-resolved *reflectivity* and *transmittivity* measurements [*Park* et al. 1996a] and from changes in optical *absorbance* [*Lee* et al. 1992].

Photothermal Deflection

Localized heating causes thermal expansion of the sample surface. The surface deformation can be measured via the deflection of a probe beam. For modulated or pulsed-laser irradiation, the deflection angle is, within a certain range [*von Gutfeld* et al. 1986; *Melcher* 1984], given by

$$\varphi \propto \frac{\beta_\mathrm{T} P_\mathrm{a} \tau_\ell}{\kappa} \,, \tag{29.4.5}$$

where β_T is the thermal expansion coefficient [*Vicanek* et al. 1994]. Because of the difference in the thermal and elastic (acoustic) response, the deformation is *not* a direct indicator of the temperature. Furthermore, the technique can be employed only in very special types of laser processing.

29.4.3 Other Techniques

Thin foils (10−30 μm) of PVDF (Sect. 29.3) have been employed to measure average surface temperatures [*Emmerich* et al. 1992] and phase changes [*Coufal* 1984]

in thin evaporated films. Similarly, non-invasive real-time measurements of thermoelastic pressure amplitudes, calibrated to temperature changes, have been performed during laser treatments at the retina [*Kandulla* and *Brinkmann* 2008]. Here, an ultrasonic transducer, embedded in the contact lens used during irradiation, has been employed.

Time of Flight

Time-of-flight (TOF) techniques permit one to estimate the surface temperature from the velocity of desorbed/ablated species. This technique has been used during pulsed-laser annealing [*Stritzker* et al. 1981] and laser-induced deposition, ablation, and etching [*Cavalleri* et al. 1999; *Baller* 1990]. Because the evaluated temperature depends on the model employed in the analysis of the TOF spectra, the temperature values are not very accurate (Sect. 30.1.2).

Thermistors

Thin-film thermistors of NiSi placed between thin polymer foils and quartz substrates have been used to directly measure laser-induced temperature profiles with ns resolution [*Brunco* et al. 1992].

29.5 Analysis of Surfaces and Thin Films

Among the techniques most commonly employed for the diagnostics of laser-processed surfaces and thin films are various optical methods, including X-ray diffraction (XRD), electrical measurements, and many of the 'standard' techniques employed in surface science. For details see, e.g., *Lüth* (2001) and *Ertl* and *Küppers* (1985). In the following, we list some applications of these techniques with special emphasis on their use as diagnostic tools for laser-processed surfaces. Clearly, some of these investigations could be equally well incorporated into Sect. 29.3.

29.5.1 Surface Topologies, Microstructures

Various different techniques are employed for investigating the morphology and topology of laser-processed surfaces. Among those are:

- Microscopy and optical reflection interferometry for investigating (permanent) surface deformations, the shape of deposits or of etch/ablation craters, etc.
- Different types of scanning-probe microscopes (SXM) are employed to measure laser-induced topological changes (AFM, STM) and/or reflectivity changes (SNOM) with a spatial resolution down to below 10 nm (Sect. 5.2).

- Raman microprobe spectroscopy has been applied for measuring stress variations across laser-processed surfaces with submicrometer resolution [*Murphy* and *Brueck* 1983].
- Photoacoustic techniques have been employed for non-destructive detection of defects like microcracks at sample surfaces and/or bulk defects such as bubbles, voids, etc. [*Kozhushko* and *Hess* 2007].
- High-resolution scanning AES together with XPS has been employed for chemical analysis of the heat affected zone (HAZ) after pulsed laser ablation, e.g. of TiN [*Bonse* and *Krüger* 2010].
- High-pressure RHEED has also been employed for in situ characterization of thin films *during* PLD [*Rijnders* and *Blank* 2007; Chap. 22].

29.5.2 Transport Measurements

The resistance of a rectangularly shaped film of length l, width d, and height h is given by

$$R = \frac{\varrho}{h}\frac{l}{d} = \frac{\varrho}{h} \equiv \mathscr{R}(\Omega/\square) \; .$$

The latter equality holds for one *square* of the film, i.e., for $l = d$. $\mathscr{R}$ is termed the *sheet resistance* and depends only on the resistivity and thickness of the film but not on its size. The sheet conductance is defined by $\sigma_s = 1/\mathscr{R}$. Sheet resistances are most commonly measured by means of *four-point-probe* methods.

In the configuration shown in Fig. 29.5.1a the resistivity of a semi-infinite substrate ($h_1 = 0$) is given by

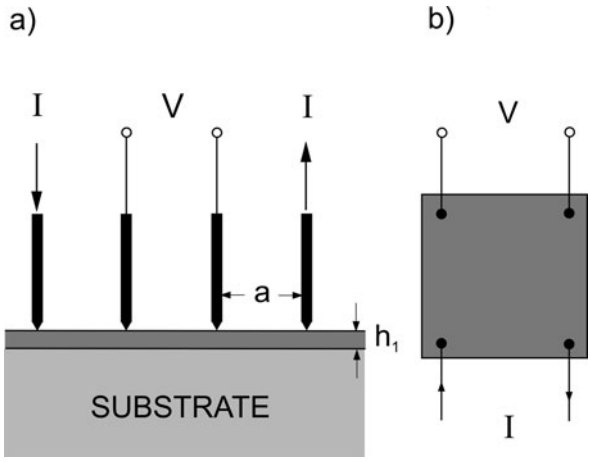

Fig. 29.5.1 a, **b** Four-point-probe methods for sheet-resistance measurements. I and V denote the current and voltage, respectively

$$\varrho_s = 2\pi \frac{V}{I} a \ , \tag{29.5.1}$$

where a is the distance between the *equidistant* electrodes. Probe spacings typically employed lie between $a = 200\,\mu\text{m}$ and several mm. If a film of resistivity ϱ is placed on an insulating substrate so that $\varrho \ll \varrho_s$, the sheet resistance is

$$\mathscr{R} = \frac{\varrho}{h_1} = \frac{\pi}{\ln 2} \frac{V}{I} = 4.532 \frac{V}{I} \ . \tag{29.5.2}$$

Higher spatial resolution can be achieved with the configuration depicted in Fig. 29.5.1b. The sheet resistance is then

$$\mathscr{R} = \frac{2\pi}{\ln 2} \frac{V}{I} \tag{29.5.3}$$

For further details see, e.g., *Maissel* and *Glang* (1970) and references therein.

Chapter 30
Analysis of Species and Plasmas

30.1 Precursor and Product Species

Optical and mass spectroscopy have been applied to analyze product species in laser annealing, ablation, etching, and LCVD.

30.1.1 Optical Spectroscopy

The analysis of fundamental interaction mechanisms in laser processing (LP) requires one to separate excitations within the ambient medium from those at the substrate surface. Among the different optical techniques are laser-induced fluorescence (LIF), optical emission spectroscopy, Raman spectroscopy, UV-, VIS-, and IR-absorption spectroscopy, and combinations of these techniques.

Figure 30.1.1a illustrates an optical setup which uses combined laser-beam irradiation. The beam at perpendicular incidence excites the substrate. The beam propagating parallel to the substrate surface is used for thermal or non-thermal excitation of the ambient medium, or as a probe beam, as, for example, in laser ablation. This irradiation geometry has been applied, for example, in investigations on photolytic *etching* of Si in a Cl_2 atmosphere (Sect. 15.2). Here, XeCl-laser radiation at parallel incidence has been used to photodissociate Cl_2 molecules, while Kr^+-laser radiation at perpendicular incidence has been employed to *only* generate electron–hole pairs within the Si surface. The number density of Cl atoms can be derived from the measured chemiluminescence intensity (Sect. 14.1.1). This is shown in Fig. 30.1.1b together with the Cl density calculated from (14.2.1).

LIF has been employed to study species desorbed from Si and Al surfaces during laser-induced etching [*Herman* et al. 1991], and during LCVD of W from WF_6 [*Heszler* et al. 1993].

An experimental setup similar to that shown in Fig. 30.1.1a, with or without a second (parallel) laser beam is used for the analysis of laser-induced vapor/plasma plumes. Here, the beam at normal incidence is used for ablation. For large-area irradiation and thin samples or foils, the beam that ablates the material can be employed simultaneously for measurements of both the time delay between plume

D. Bäuerle, *Laser Processing and Chemistry,* 4th ed.,
DOI 10.1007/978-3-642-17613-5_30, © Springer-Verlag Berlin Heidelberg 2011

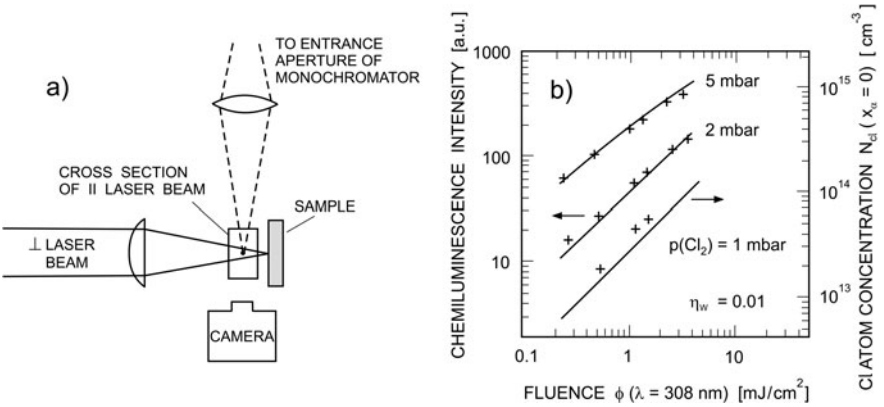

Fig. 30.1.1 (**a**) Schematic of an experimental setup used for in situ measurements during LP. The optical emission of species is analyzed by means of a spectrometer. Spatially or temporally resolved measurements can be performed by imaging different volumes onto the entrance slit of the monochromator or by using a polychromator together with a CCD camera. (**b**) Chemiluminescence intensity measured *during* etching of Si in a Cl_2 atmosphere as a function of XeCl-laser fluence [parallel incidence to sample surface in (**a**)]. The solid curves (*right-hand scale*) have been calculated. For details see Sect. 15.2.3 and *Kullmer* and *Bäuerle* (1988a)

formation and the beginning of the laser pulse, and the (dynamic) attenuation (screening; Chap. 12) of the incident laser light by the plume. This can be achieved by detecting the intensity transmitted through a small hole in the sample [*Schmidt* et al. 1998]. A modified arrangement using an Ag target with an array of holes has been employed to measure UV-/VIS- absorption spectra of Ag plasmas [*Donnelly* and *Lunney* 2008]. For further analysis, the plasma plume is viewed perpendicularly to the axis of expansion and investigated by means of a spectrometer, or a polychromator in combination with a CCD camera, a streak camera, etc. The detected species are excited during the ablation process itself, or via inelastic collisions or chemical reactions within the plume, or via a second (parallel) laser beam. In the latter case a tunable laser beam can excite transitions within specific species.

The *spatial* and *temporal* distribution of species can be investigated by imaging different volumes of the plume; here, the spatial resolution achieved along the target normal is, typically, 100 μm. By time-resolved detection of single emission lines, the velocities of species can be deduced as well. LIF permits 3D-mapping of species with high spatial and spectral resolution. The latter enables high-precision Doppler shift measurements. The type of product species observed in such experiments are classified in Sect. 30.2. For further experimental investigations of vapor/plasma plumes see also Sect. 30.4.4.

Pulsed-laser ablation is also used for *chemical* analysis of materials. It is sometimes denoted as laser-induced breakdown spectroscopy (LIBS) or as laser-induced plasma spectroscopy (LIPS). Because PLA preserves the stoichiometry of the target during ablation (Chaps. 12 and 13), LIBS permits one to detect low concentrations of impurities and/or changes in material composition. A significant enhancement

of the emission intensity can be obtained by cross-beam PLA [*Sobral* et al. 2008]. In combination with SNOM, a spatial resolution of the order of a few micrometers has been achieved [*Hwang* et al. 2009a]. Today, LIBS is applied in different areas of research, technology, and biosciences [*Rehse* et al. 2007; *Miziolek* et al. 2006; *Gruber* et al. 2004].

Irrespective of the particular technique employed, spatially and/or temporally resolved optical emission, absorption, or Raman spectra yield information on the species relevant in different types of laser processing. These species can originate from laser-induced photochemical or thermal reactions within the ambient medium and/or the substrate surface. In the case of PLA, such measurements permit to study also the expansion dynamics of the plasma plume [*Camacho* et al. 2009; *König* et al. 2005; *Siegel* et al. 2004b; *Chaos* et al. 2000b].

30.1.2 Mass Spectrometry

An experimental setup that permits in situ identification of species taking part in laser-driven surface reactions is shown in Fig. 30.1.2. Here, the surface reaction is modulated via the laser-light intensity. The modulation causes transients in the concentrations of gas-phase precursor and product species. These species are sampled through an orifice in the center of the reaction zone and identified by phase-sensitive detection using a mass spectrometer. Thus, product species can be differentiated from those formed by ionization and fragmentation of precursor molecules. This and similar setups have been used for gas-phase analysis during LCVD of Au from dimethyl-gold-hfacac [*Kodas* and *Comita* 1989], W from WF_6 [*van Maaren* et al. 1990], a-Si:H from SiH_4 and Si_2H_6 [*Golusda* et al. 1991], etc.

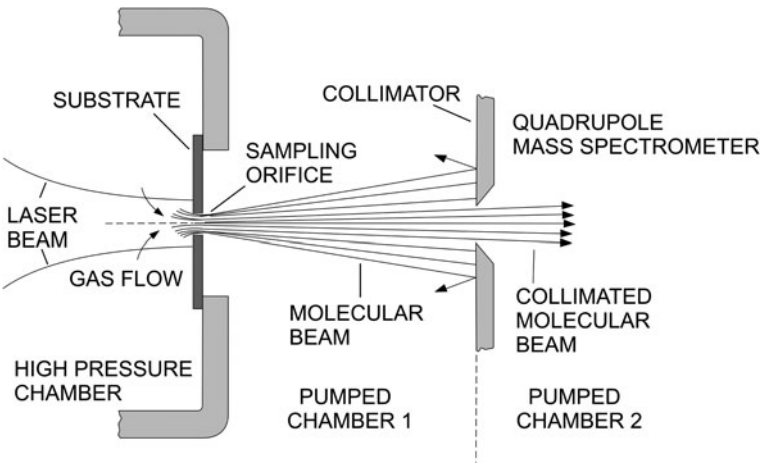

Fig. 30.1.2 Experimental setup employed for the diagnosis of species. The diameter of the orifice is, typically, ten to several ten micrometers [adapted from *Kodas* and *Comita* 1989]

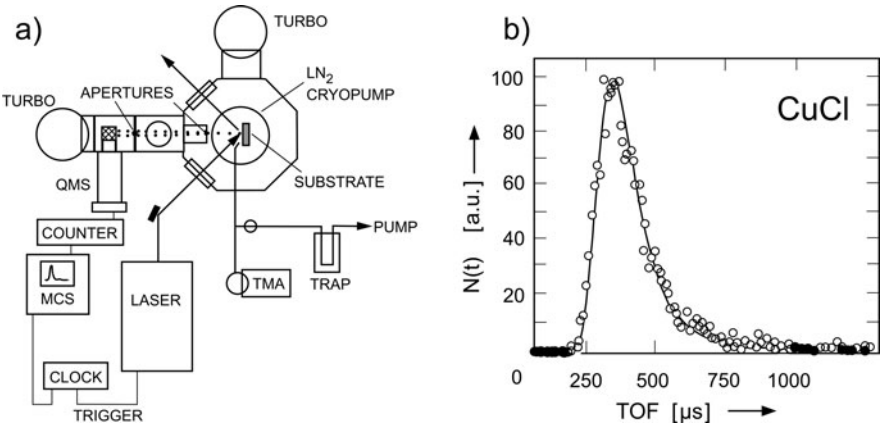

Fig. 30.1.3 (**a**) Schematic of an apparatus to measure photoproducts, here of $Al(CH_3)_3$ (TMA), by TOF-MS [*Orlowski* and *Mantell* 1989]. (**b**) TOF distribution for XeCl-laser-induced etching of (100) Cu in a Cl_2 atmosphere ($\lambda = 308$ nm, $E_\ell = 90$ mJ/pulse, $\nu_r = 1$ Hz). The mass spectrometer setting was $m/e = 98$ [*Kools* et al. 1992]

Mass spectrometers coupled with time-of-flight (TOF) techniques permit one to determine the chemical nature of product species and their desorption dynamics and energy distribution (Fig. 30.1.3). The experimental apparatus shown in the figure contains two stages of differential pumping which separate the quadrupole mass spectrometer (QMS) from the sample chamber. The QMS is mounted with its axis perpendicular to the molecular flight path. The sample is aligned with its surface normal in the direction of observation. Illumination of the substrate occurs at an angle of 45°. TOF data are collected by setting the QMS to a desired mass and recording the number of counts during a certain integration time. Such setups have been used for the *in situ* diagnosis of species generated during laser-induced decomposition of $Al(CH_3)_3$ [*Orlowski* and *Mantell* 1989], $Ga(CH_3)_3$ and $Ga(C_2H_5)_3$ [*Donnelly* 1991], during etching of Cu and Si in Cl_2 [*Kools* et al. 1992; *Baller* 1990; *van Veen* et al. 1988], and during ablation of a large variety of inorganic and organic materials. During laser ablation, the velocity distribution of ions ejected from the target depends strongly on laser parameters (Sect. 30.2). Care must be taken that the observed fragments actually originate from the sample surface, since larger mass fragments can also create smaller fragments within the QMS ionizer. This can be accomplished by investigating correlations in the transit times of species.

An example of a typical TOF distribution is shown in Fig. 30.1.3b. The full curve is a fit to experimental data by an elliptical Maxwell–Boltzmann distribution,

$$N(t) = \frac{\zeta}{t^3} \exp\left\{-\frac{m}{2k_B T_{xy}}\left[\left(\frac{x}{t}\right)^2 + \left(\frac{y}{t}\right)^2\right] - \frac{m}{2k_B T_z}\left(\frac{z}{t} - u\right)^2\right\}, \qquad (30.1.1)$$

where t is the flight time, ζ a scaling factor, m the fragment mass, and u the stream velocity. The values of the fit parameters derived were $T_{xy} = 1400$ K, $T_z = 2400$ K,

and $u = 1200\,\mathrm{m/s}$. From T_{xy} and T_z the (thermodynamic) temperature at the surface has been calculated by assuming *isothermal* expansion [*Kools* et al. 1992].

It should be noted that TOF spectra can be fitted equally well by *adiabatic* solutions of the gas-dynamic equations [*Anisimov* et al. 1996]. The temperatures derived in these two ways may differ significantly.

Laser ablation combined with inductively coupled plasma mass spectrometry (ICP-MS) is a powerful technique for both chemical analysis of substrate/target materials and of product species formed during ablation [*Durrant* and *Ward* 2005; *Durrant* 1999; *Russo* et al. 2000]. The effect of cluster formation on the ionization efficiency in the ICP and a device for particle separation, which is mainly based on centrifugal forces in a thin coiled tube, was described by *Guillong* et al. (2003). Here, the cut-off in particle sizes can be changed via the inner diameter of the tube, the number of turns, and the diameter of the coil.

30.1.3 MALDI, LAESI

Matrix-assisted laser desorption and ionization (MALDI) in combination with mass spectrometry is a technique which is successfully applied to analyze large biomolecules, polymer fragments, and clusters in the mass range from about 10^3 to some 10^5 amu [*Miller* and *Haglund* 1998]. Sample preparation and ablation is almost the same as in MAPLE (Sect. 22.9). The molecules to be analyzed are usually embedded in a solid matrix consisting of highly absorbant volatile species. During pulsed-laser ablation the molecules embedded in the matrix are directed into a mass spectrometer while the (small) volatile solvent molecules are pumped off. Here, ultrashort laser pulses cause a lower internal energy transfer in comparison to ns pulses [*Luo* et al. 2008].

The expansion dynamics of the 'heavy' and 'light' vapor/plasma-plume components has been described by MD simulations (Sect. 13.4) and special solutions of the gas-dynamic equations [*Sellinger* et al. 2008; *Leveugle* and *Zhigilei* 2007; *Zhigilei* et al. 2003].

Matrix-free laser desorption/ionization mass spectrometry using microcolumnar arrays has been discussed in Sect. 28.7.

A new development is laser ablation electrospray ionization (LAESI) in combination with mass spectrometry. It is based on the discovery that 'native water' in plant and animal tissues is an efficient *natural* matrix for IR laser ablation. Here, the O-H vibrational mode of water molecules is excited by means of $2.94\,\mu\mathrm{m}$ laser pulses from a Nd:YAG-laser driven parametric oscillator. The ablated material is electrosprayed and the resulting ions are analysed by time-of-flight mass spectrometry (TOF-MS). In contrast to 'conventional' MALDI, ablation can be performed at atmospheric pressure. This technique permits in vivo investigations of biomolecules and biological processes [*Nemes* et al. 2009; *Vertes* et al. 2008; *Y. Li* et al. 2007]. 3D imaging permits to correlate molecular compositions with the morphology of tissues.

30.2 Species in Vapor and Plasma Plumes

The analysis of laser-induced vapor/plasma plumes is of great importance for both, the elucidation of fundamental interaction processes in laser ablation and for many applications. In particular with applications, including chemical analysis by LIBS or/and mass spectrometry, PLD, etc., the knowledge of the type of species, their angular distribution, and their velocities is essential for the design of experiments and a correct interpretation of data. Let us just mention a single example. The understoichiometric content of Li ions in $LiNbO_3$ films prepared by PLD from $LiNbO_3$ targets can be directly related to the delayed release of Li ions and their expansion dynamics derived from vapor-phase optical absorption spectra (Sect. 30.1, *Chaos* et al. 2000b).

The types of species observed by different techniques can be classified into atomic and molecular neutrals in ground or excited states, ions, electrons, photons, large molecular fragments, and clusters. Here, we do *not* consider macroscopic particulates (Chaps. 4 and 22). Atomic and molecular neutrals, and large molecular fragments are the dominating species observed with laser fluences below and around the ablation threshold, ϕ_{th}. With increasing fluence, the number of electronically excited species, ions, and lower-molecular-weight species increases. Changes in the type of ablated species with laser parameters can originate from changes in the ablation mechanism, from secondary photolysis (Sect. 12.6.4) or from reactions with the ambient medium, if present. With ultrashort laser pulses and high intensities, the situation changes and the different types of ablation mechanisms such as spallation, phase explosion, Coulomb explosion, etc. (Chap. 13) result in different types of product species and fragments.

30.2.1 Species at Subthreshold Fluences

The ejection of electrons, atoms, ions, and molecular species from different material surfaces has been detected for laser fluences well below ϕ_{th}. Among the different techniques employed are optical methods, mass-loss and acoustic measurements,

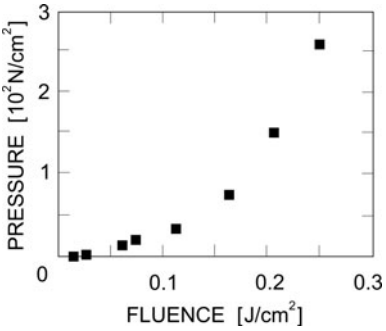

Fig. 30.2.1 Peak surface pressure measured by means of a PVDF foil during KrF-laser irradiation of $YBa_2Cu_3O_7$ [adapted from *Dyer* et al. (1992b)]

TOF-MS techniques, Langmuir probes, etc. Figure 30.2.1 demonstrates that for YBCO irradiated by KrF-laser light. The desorption of species is already observed for fluences $\phi < \phi_{th} \approx 0.75\,J/cm^2$. This is consistent with the results presented in Sect. 12.4. Similar observations have been made with Si and Ge, various compound semiconductors [*Alvarez* et al. 2008; *Bialkowski* et al. 1991], different types of dielectrics [*Dickinson* 2008; *John* et al. 2007; *Miller* and *Haglund* 1998; Sects. 12.4 and 12.8], including organic polymers such as PMMA, PET, PI, etc. [*Kuhnke* et al. 2007; Sects. 12.4, 27.1].

30.2.2 Atomic and Molecular Neutrals

Even for *quasi-equilibrium* evaporation using cw lasers or long laser pulses, the species within the vapor may significantly differ from those in standard evaporation. This is based, in most cases, on the higher temperatures involved in laser ablation and on the interactions between the laser light and the plume.

For example, the vapor-phase species observed in standard evaporation of compound semiconductors are mainly atoms for group-II and -III elements and mainly molecules and clusters for group-V and -VI elements. With appropriate parameters, lasers enable one also to produce the latter in atomic form only. This can significantly modify the growth kinetics and properties of films in PLD (Chaps. 4 and 22).

With *short* laser pulses, the differences in the evaporation characteristics become more pronounced (Sect. 22.1.1). The most prominent features are the congruent (stoichiometric) ablation of multicomponent targets and the forward direction of the vapor plume. With moderate laser fluences which, however, well exceed the threshold for stoichiometric ablation, the ablated species consist of ground-state and electronically excited neutrals and a *small* fraction of ions, depending on the fluence. This is the regime employed in many cases of PLD. Here, optical spectroscopy permits one to directly correlate emission spectra with excited neutrals and ionized species (Sect. 30.1).

Atomic and molecular neutrals and ions have been analyzed during ns- and fs-laser ablation of metals [*Toftmann* et al. 2003, 2000; *Ye* and *Grigoropoulos* 2001, *Bennett* et al. 1995, *Saenger* 1989], high-temperature superconductors [*Geohegan* et al. 1999; *Otis* and *Goodwin* 1993; *Dyer* et al. 1992b], silicon [*Bulgakov* et al. 2004], graphite [*Camacho* et al. 2009; *Kokai* 1997; *Krajnovich* 1995], and a large number of dielectrics [*Chaos* et al. 2000a; *Varel* et al. 1998, *Kreitschitz* et al. 1994; *Mitzner* et al. 1993] including organic polymers [*Johnson* et al. 2009a; *Lippert* 2005; *Hansen* 1989; *Dyer* et al. 1988].

Vapor–plasma plumes generated by excimer-laser ablation of Y-Ba-Cu-O in a *vacuum* contain neutral and ionized atomic Y, Ba, and Cu, molecular O_2 ions, and diatomic molecules of BaO, CuO, and YO. The fractional ionization of ablated species for fluences $\phi \leq 4\,J/cm^2$ is $\leq 4\%$. At $1\,J/cm^2$, typical velocities of species derived from optical emission spectra were around 10^6 cm/s and somewhat smaller than those measured with an ion probe. The plume temperature has been estimated to be 5×10^3 to 10^4 K. With an O_2 background pressure, the optical emission intensity increases. This is mainly related to inelastic collisions between elemental

species and electronically excited oxygen atoms, to collisions between electrons and ions, and to the recombination of species (Sect. 22.2.1).

With many materials and a broad range of laser parameters, the velocity of neutral atoms and molecules can be fitted by a Maxwell–Boltzmann distribution. The kinetic energy of species in nanosecond excimer-laser ablation is, typically, in the range of a few eV to several tens of eV. The hyperthermal neutrals and ions corresponding to the 'hot' tail of the distribution function can significantly influence the properties of thin films synthesized by PLD (Sect. 22.2.3). With fs-laser irradiation at even moderate energy densities, neutrals and ions have energies of a few to several keV (velocities of 10^6 to several 10^7 cm/s).

The angular distribution of the (overall) mass-flux of ablated species has been measured by means of QCMs (Fig. 29.3.4). The results are in agreement with thickness profiles of thin films fabricated by PLD (Sects. 22.2) and with model calculations (Sects. 30.3 and 30.4).

30.2.3 Electrons and Ions

With increasing light intensities, the fraction of ions within the vapor/plasma plume increases. Above a certain threshold, avalanche ionization is observed and the fraction of ions becomes almost 100%. This threshold for optical breakdown depends on the target material, the ambient medium, and the laser parameters (Chaps. 11, 12 and 13). If photochemical ablation mechanisms are important, this threshold is one to two orders of magnitude *lower* than with purely thermal ablation. In any case, with laser-beam intensities exceeding some $10^9\,\mathrm{W/cm^2}$, electrons and ions are the dominant species. With inorganic materials, the ions are mainly positively charged and consist of atoms, molecules, and clusters. The fragmentation and degree of ionization of species increases with laser fluence.

Angular Distribution

The kinetic energy and angular distribution of electrons and ions as a function of laser parameters have been investigated for different systems, mainly by TOF-mass spectrometry [*Kaplan* et al. 2008; *Kobayashi* et al. 2008; *Ye* and *Grigoropoulos* 2001; *Toftmann* et al. 2000; *Hansen* et al. 1998]. Subsequently, we summarize the most important results obtained for Ag targets ablated with 355 nm Nd:YAG-laser radiation ($\phi \approx 0.8 - 1.3\,\mathrm{J/cm^2}$, $\tau_\ell = 6\,\mathrm{ns}$) using Langmuir probes for electron and ion detection (Fig. 29.3.4):

- With the laser parameters employed, the degree of ionization within the plasma is low.
- The flux and energy of ions is strongly peaked in the direction of the target normal [*Toftmann* et al. 2000].
- The flux of electrons and the electron temperature T_e/average velocity of electrons, is only *weakly* dependent on angle θ. The electron energy is about two

orders of magnitude lower than the energy of the ions. With the laser parameters employed, one finds $0.1\,\text{eV} \lesssim T_e \lesssim 0.5\,\text{eV}$ [*Toftmann* et al. 2000].
- The angular variation of the plasma density and ion energy is consistent with the model of self-similar isentropic adiabatic expansion of the plume (Sect. 30.3).

Some of the results achieved in vacuum and a gaseous atmosphere are discussed in further detail in Sects. 30.3 and 30.4, respecively.

With *multicomponent* targets the TOF spectra show a multiple peak structure. This is related to different ion velocities. The faster ions are more concentrated around the centerline of the plume.

The possibility of generating ion beams with specific energies by means of temporally tailored fs-laser pulses has been discussed for the case of Si targets by *Spyridaki* et al. (2003). Fast ion emission related to Coulomb explosion is discussed in Sect. 13.6.

30.2.4 Plasma Radiation, X-Rays

Plasma radiation is related to the emission of excited neutrals, the recombination of electrons with ions, and to Bremsstrahlung. This has been discussed throughout various chapters. With the laser-light intensities employed in standard laser machining, the highest photon energies within the plasma are, typically, up to several 10 eV. With laser light intensities exceeding $10^{12}\,\text{W/cm}^2$, extreme ultraviolet (EUV) radiation related to field ionization and collisional heating is generated. The photon energies are then within the range of about 10^2–10^3 eV, corresponding to wavelengths of about 10 nm to 1 nm. Laser-light intensities exceeding $10^{16}\,\text{W/cm}^2$ generate X-rays. These are related to electron transitions to K-shell holes within atoms (line spectrum) and to (continuous) Bremsstrahlung from inelastic scattering of energetic electrons with atoms. Typical photon energies are $(5\text{–}30) \times 10^3$ eV (K_α radiation). With laser-light intensities exceeding $10^{20}\,\text{W/cm}^2$, MeV Bremsstrahlung and γ-radiation is observed [*Gibbon* et al. 2009; *Horn* et al. 2007; *Schwoerer* 2004]. Laser-generated EUV and X-ray pulses have a very high intensity and they are emitted from a very small volume. Thus, they are ideal sources for dynamical studies of atoms in molecules and solids [*Silies* et al. 2009; *Zamponi* et al. 2009] and they gain increasing importance for applications in nanomachinig, lithography, medical imaging etc. [*Makimura* et al. 2007; *Hatanaka* and *Fukumura* 2006; *Schwoerer* 2004].

30.2.5 Clusters and Fragments

High-molecular-weight fragments, clusters and droplets observed during laser ablation can have different origins. They can be *directly* ejected from the target and/or only formed during expansion of the vapor/plasma plume. This has been discussed throughout Chaps. 4, 11, 12, and 22 mainly for nanosecond PLA of inorganic and organic targets. The particle size distribution depends on laser parameters, the type

of target material, the ambient medium, and the distance between the target and the position of particle detection (Chap. 4). The type of fragments observed in polymer ablation with ns-pulses is discussed in Chap. 12. An overview is given in *Bäuerle* (2000).

With fs-pulses, additional mechanisms become important (Chap. 13). The break up of the spallation layer may generate macroscopic fragments (Fig. 13.4.1). With high intensities, phase explosion results in a broad distribution of droplets. Particles with a very broad size distribution and large angular divergence have been observed after ultrashort-pulse laser ablation of Si. In contrast to the fast ions and neutrals, the (slow) particles have a very broad velocity distribution (10^2–10^4 cm/s) and a large angular divergence. Light emission from these particles can be described by black-body radiators [*Amoruso* et al. 2006].

30.3 Plume Expansion in Vacuum

In this section we briefly discuss some theoretical and experimental investigations on the expansion of laser-induced vapor-/plasma-plumes in vacuum. Here, the emphasis is put on general trends and on those experimental observations that permit a direct comparison with the model calculations. For further details, the reader is referred to the original literature.

In a vacuum, the plume undergoes free expansion and ultimately reaches some final constant velocity. This process can be considered, in good approximation, to be *adiabatic*. A broad class of self-similar solutions of the hydrodynamic equations can be obtained under the assumption that the expansion velocity of the plasma $\boldsymbol{v}_\mathrm{p}(\boldsymbol{r}, t)$ is a *linear* vector function of $\boldsymbol{r}$.

30.3.1 Spherical Plume

With *spherical* symmetry, the velocity of a volume element located at a distance r from the center of the plume is given by

$$v_\mathrm{p} = \dot{R}\frac{r}{R} \,, \tag{30.3.1}$$

where R is the radius of the plume and $\dot{R}$ the expansion velocity at the leading edge, i.e., $\dot{R} \equiv v_\mathrm{p}(r = R)$. The density and pressure within the plume can be described by

$$\varrho_\mathrm{p} = \varrho_\mathrm{c}\left(1 - \frac{r^2}{R^2}\right)^k \qquad \text{and} \qquad p_\mathrm{p} = p_\mathrm{c}\left(1 - \frac{r^2}{R^2}\right)^{k+1} \,, \tag{30.3.2}$$

where $\varrho_\mathrm{c} = \xi M_\mathrm{p}/R^3(t)$ and $p_\mathrm{c} = (\xi' E/R_0^3)[R_0/R(t)]^{3\gamma_\mathrm{p}}$ are the time-dependent density and pressure, respectively, in the plume center. ξ and ξ' are constants of the order of unity; their values can be obtained by spatial integration. k describes the

spatial shape of the density distribution. For an isentropic plume $k = 1/(\gamma_\mathrm{p} - 1)$, where γ_p is the adiabatic coefficient of the plume. The profiles ϱ_p and p_p in (30.3.2) satisfy the gas-dynamic equations.

The total energy of the plume, consisting of the thermal energy, E_T, and the kinetic energy, E_kin, can be described by

$$E = E_\mathrm{T} + E_\mathrm{kin} = \left(\frac{R_0}{R}\right)^{3(\gamma_\mathrm{p}-1)} E + \zeta M_\mathrm{p} \dot{R}^2 \,, \tag{30.3.3}$$

where $R_0 \approx (w^2 Z_0)^{1/3}$ is the initial radius of the plume, w is the radius of the laser focus, and $Z_0 \approx v_0^\mathrm{p} \tau_\ell$, where v_0^p is the sound velocity within the (hot) vapor. M_p is the total mass within the plume. The coefficient ζ is due to spatial integration, and it is given by $\zeta = 3/(4k + 10)$. Equation (30.3.3) assumes $\dot{R}(t = 0) = 0$. Thus, initially the total energy is purely thermal, i.e., $E_\mathrm{T}(t = 0) = E$. Note that E and M_p correspond to *twice* the energy and mass of a *hemispherical* plume. E_T in (30.3.3) can be understood from mass conservation and the adiabatic law. The expansion dynamics of the plume, $R = R(t)$, is determined by the energy conservation $E = \text{const}$. When the plume expands and R becomes of the order of several R_0, the thermal energy is transformed almost totally into kinetic energy, and further expansion proceeds with the final constant velocity

$$v_\mathrm{p}^\mathrm{max} \equiv v_\mathrm{p}(t \gg t_\mathrm{f}) \equiv \dot{R}(t \gg t_\mathrm{f}) = \left(\frac{E}{\zeta M_\mathrm{p}}\right)^{1/2} \,, \tag{30.3.4}$$

where $t_\mathrm{f} \approx R_0 / v_\mathrm{p}^\mathrm{max} \approx R_0 (M_\mathrm{p}/E)^{1/2}$. The radius of the plume is

$$R \approx \left(\frac{E}{\zeta M_\mathrm{p}}\right)^{1/2} t \,. \tag{30.3.5}$$

With $R_0 = 10\,\mu\mathrm{m}$ and $v_\mathrm{p}^\mathrm{max} \approx 10^6\,\mathrm{cm/s}$, one obtains $t_\mathrm{f} \approx 10^{-9}\,\mathrm{s}$.

30.3.2 Elliptical Plume

For *elliptical* adiabatic expansion, the total energy of the plume can be obtained in analogy to (30.3.3) [*Anisimov* et al. 1993]

$$E = \left(\frac{X_0 Y_0 Z_0}{X Y Z}\right)^{\gamma_\mathrm{p}-1} E + \frac{\zeta}{3} M_\mathrm{p} \left(\dot{X}^2 + \dot{Y}^2 + \dot{Z}^2\right) \,, \tag{30.3.6}$$

where X_0, Y_0, and Z_0 are the initial values of the plume boundary $X(t)$, $Y(t)$, and $Z(t)$. These latter functions can be obtained with (30.3.6) from the Hamilton equations. For typical experimental conditions with $X_0/Z_0 = 100$, the final expansion

velocity in the *shortest* direction of the initial plume is $\dot{Z}_{\max} = \sqrt{3} v_{\mathrm{p}}^{\max}$. $\dot{X}_{\max}$ and $\dot{Y}_{\max}$ are by a factor of 3−10 smaller. The final velocity in each direction is reached after times $t_{\mathrm{f}}(X) \approx X_0 / v_{\mathrm{p}}^{\max}$ etc. For example, with $X_0 \equiv w = 10^3\,\mu\mathrm{m}$, $v_{\mathrm{p}}^{\max} = 10^6\,\mathrm{cm/s}$, $v_0^{\mathrm{p}} = 10^5\,\mathrm{cm/s}$, and $\tau_\ell = 10\,\mathrm{ns}$, one obtains $t_{\mathrm{f}}(X) = 100\,\mathrm{ns}$, $Z_0 = 10\,\mu\mathrm{m}$, and $t_{\mathrm{f}}(Z) = 1\,\mathrm{ns}$. The approximation $Z_0 \approx v_0^{\mathrm{p}} \tau_\ell$ takes into account that the initial plume gains energy during the laser pulse.

30.3.3 Mass- and Ion-Flux Measurements

Different experimental techniques that have been employed for investigating the dynamical behavior of vapor-/plasma-plumes in vacuum have been discussed in the preceding sections. In connection with the verification of the models outlined above, measurements on the angular dependences of mass- and ion-fluxes on laser parameters are of particular interest. In fact, the mass density distribution in the elliptical plume is in good agreement with the thickness profile of PLD films deposited without substrate movement, Eq. (22.2.6). Furthermore, measurements on the angular distribution of the mass- and ion-fluxes using a set of quartz crystal microbalances and Langmuir probes, respectively, are in excellent agreement with the model of self-similar isentropic adiabatic expansion of the plume. This has been demonstrated for Ag targets ablated with nanosecond 355 nm Nd:YAG-laser radiation (Sect. 30.2; Fig. 29.3.4). Even the dependence of the plume shape on the ellipticity of the laser spot has been confirmed. The value of the adiabatic coefficient derived from the mass-flux measurements is $\gamma_{\mathrm{p}} \approx 1.4$ [*Toftmann* et al. 2003]. For the ionic component, derived from the Langmuir probe experiments, a value of $\gamma_{\mathrm{p}} \approx 1.25$ has been obtained [*Hansen* et al. 1999]. The model is also consistent with the experiments on the influence of the laser spot diameter on the ablation rate (Sect. 12.6).

The dynamics of the initial stage of ultrashort-pulse laser ablation has been discussed in Chap. 13. Shell formation and the onset of its hydrodynamic motion is described by *Anisimov* et al. (2007). Shock formation and material expansion at later stages is included in Sect. 30.4.

Numerical simulations on clusters observed during nanosecond and femtosecond pulsed-laser ablation of solid or liquid targets have been performed for quite different physical mechanisms and within the frame of different numerical techniques. In many cases, both ablation into vacuum and the influence of a background atmosphere has been considered. For these reasons, the corresponding literature is included into Sect. 30.4.

30.4 Plume Expansion in Gases, Shock Waves

In the presence of an ambient gas with a pressure of, typically, $p_g > 0.1$ mbar, the expansion dynamics of the plasma changes significantly. Here, the species ejected from the target act like a piston which compresses and thereby heats the ambient

gas. This causes an *external* shock wave (SW) *ahead* of the contact surface. This is drawn, schematically, in Fig. 30.4.1. Figure 30.4.2 shows the real experimental situation for Nd:YAG-laser ablation of pyrolytic carbon in an Ar atmosphere.

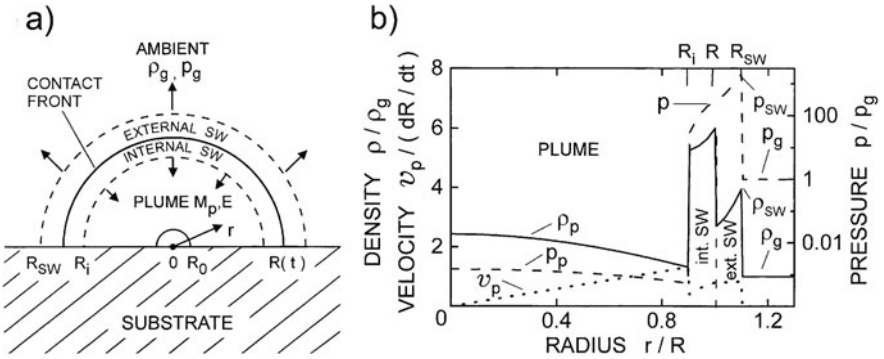

Fig. 30.4.1 Schematics showing the expansion of a *spherical* vapor-plasma plume in an ambient medium. (**a**) R_0 is the initial radius of the plume. The velocity of the contact front is $\dot{R}(t)$. The internal shock wave (SW) with inner radius R_i propagates towards the plume center. R_{sw} denotes the shock front. (**b**) The central part of the plume obeys the free-expansion laws. Mass density within the plume, ϱ_p, the external shock wave, ϱ_{sw}, and the ambient gas, ϱ_g, (*solid curves*) and corresponding pressures (*dashed curves*) are shown. Velocity profile within the plume and SWs is also shown (*dotted curves*). Parameters are similar to those used in Fig. 30.4.3 with $t = 0.3t_{fS}$ [adapted from *Arnold* et al. 1999b]

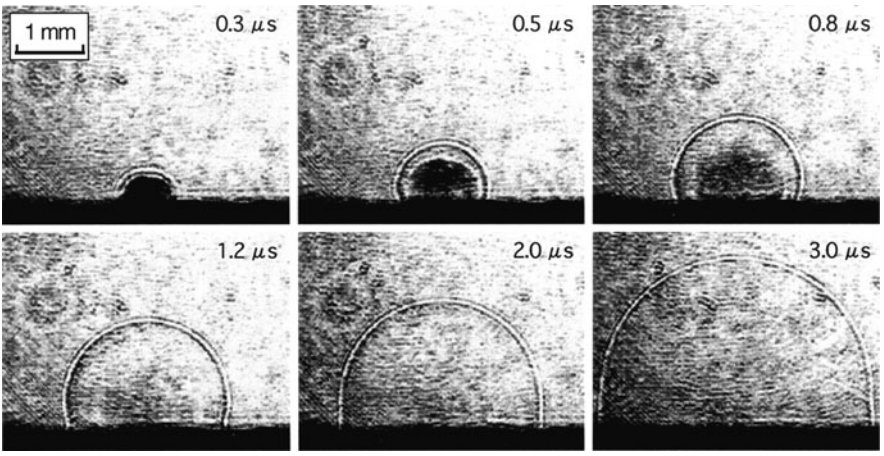

Fig. 30.4.2 Shadowgraph images of carbon species and the shock wave at various delay times following Nd:YAG-laser ablation of graphite in an Ar atmosphere [$\lambda = 1064\,\text{nm}$, $\phi = 12\,\text{J/cm}^2$, $E_\ell \approx 34\,\text{mJ}$, $\tau_\ell = 8\,\text{ns}$, $w = 300\,\mu\text{m}$; $p(\text{Ar}) = 737\,\text{mbar}$] [*Kokai* et al. 1999]

30.4.1 Point Blast Model

Let us first ignore the ablated material and consider the propagation of the SW alone. In the simplest approximation, the SW can be described by the model for strong explosion. In this model, one assumes an uniform (ambient) medium and an instantaneous release of energy, E, at $\boldsymbol{r} = 0$ and $t = 0$. The radius of the shock front is then given by [*Zeldovich* and *Raizer* 1966; *Sedov* 1959]

$$R_{\mathrm{sw}} \approx \xi_{\mathrm{S}} \left(\frac{E}{\varrho_{\mathrm{g}}} t^2 \right)^n , \tag{30.4.1}$$

where $\xi_{\mathrm{S}} \equiv \xi_{\mathrm{S}}(\gamma_{\mathrm{g}}) \approx 1$. Here, γ_{g} refers to the ambient medium (for air $\gamma_{\mathrm{g}} \equiv c_{\mathrm{p}}/c_{\mathrm{v}} = 7/5$). ξ_{S} and n depend on the symmetry of the shock front. For spherical expansion $n = 1/5$ [$\xi_{\mathrm{S}}(\gamma_{\mathrm{g}} = 7/5) = 1.033$], for cylindrical symmetry $n = 1/4$, and for a plane SW $n = 1/3$. $\varrho_{\mathrm{g}} \equiv \varrho_{\mathrm{g}}(\infty)$ is the undisturbed density of the atmosphere. For strong SWs, where $p_{\mathrm{sw}} \gg p_{\mathrm{g}}(\infty) \equiv p_{\mathrm{g}}$, the density and temperature at the shock front are [*Landau* and *Lifshitz*: Fluid Mechanics 1974]

$$\varrho_{\mathrm{sw}} = \varrho_{\mathrm{g}} \frac{\gamma_{\mathrm{g}} + 1}{\gamma_{\mathrm{g}} - 1} \quad \text{and} \quad T_{\mathrm{sw}} = T_{\mathrm{g}} \frac{\gamma_{\mathrm{g}} - 1}{\gamma_{\mathrm{g}} + 1} \frac{p_{\mathrm{sw}}}{p_{\mathrm{g}}} . \tag{30.4.2}$$

For spherical symmetry, the (time-dependent) pressure is given by

$$p_{\mathrm{sw}} = 2 \left(\frac{2\xi_{\mathrm{S}}}{5} \right)^2 \left(\frac{E^2 \varrho_{\mathrm{g}}^3}{t^6} \right)^{1/5} \gg p_{\mathrm{g}} . \tag{30.4.3}$$

The thickness of the shell which contains most of the mass of the compressed ambient gas follows from (30.4.2) and the mass conservation $(4\pi/3) R_{\mathrm{sw}}^3 \varrho_{\mathrm{g}} \approx 4\pi R_{\mathrm{sw}}^2 \Delta R_{\mathrm{sw}} \varrho_{\mathrm{sw}}$, so that

$$\Delta R_{\mathrm{sw}} \approx R_{\mathrm{sw}} \frac{\gamma_{\mathrm{g}} - 1}{3(\gamma_{\mathrm{g}} + 1)} . \tag{30.4.4}$$

During the propagation of the SW, the density, temperature, pressure, and velocity drop off. The degeneration of the SW into a sound wave occurs when the velocity of the SW, $\dot{R}_{\mathrm{sw}}$, becomes comparable to the velocity of sound in the ambient medium, i.e., $\dot{R}_{\mathrm{sw}} \approx v_0^{\mathrm{g}} = (\gamma_{\mathrm{g}} p_{\mathrm{g}}/\varrho_{\mathrm{g}})^{1/2}$.

Let us now apply this model to PLA. In this case, the energy E can be approximated by $E/2 \approx A\phi F - E_{\mathrm{loss}} - F\Delta h \Delta H_{\mathrm{v}}$, where A is the absorptivity of the material, F the irradiated area, E_{loss} the energy loss due to heat conduction into the solid and ΔH_{v} the enthalpy of vaporization.

For high laser fluences and pulse durations that are long compared to the formation of the SW, a laser-supported detonation wave can develop (Sect. 11.7).

30.4.2 Combined Propagation of Plume and SW

A proper description of PLA requires *simultaneous* consideration of both the propagation of the SW *and* the ablated material. The situation is schematically shown in Figs. 30.4.1 and 30.4.3.

In the very initial phase, the propagation of the plume is similar to that observed in a vacuum. This is quite evident. During this stage, the internal pressure that drives the plume is, typically, of the order of 10^3 bar, depending on laser parameters. Thus, under normal conditions, any background pressure can be ignored. As the plume expands, the internal pressure rapidly decreases and expansion slows down. The transition from free plume expansion to the Sedov regime (30.4.1) is given by the condition that the mass of the plume, M_p, becomes comparable to the mass of the displaced (ambient) gas, i.e., $M_p \approx \rho_g R_{fS}^3$ – the factor $(2\pi/3)$ has been ignored. R_fS is the radius of the shock wave where this transition takes place. This condition yields

$$R_\mathrm{fS} \approx (M_\mathrm{p}/\varrho_\mathrm{g})^{1/3} \tag{30.4.5a}$$

Thus, with increasing pressure or higher atomic/molecular mass of the ambient gas, the shock wave starts closer to the target. The corresponding time is

$$t_\mathrm{fS} \approx R_\mathrm{fS}/v_\mathrm{p}^\mathrm{max} \approx \left(M_\mathrm{p}^5/\varrho_\mathrm{g}^2 E^3\right)^{1/6} . \tag{30.4.5b}$$

During further expansion, the compression and acceleration of the ambient gas by the expanding plume reduces the velocity of ablated species, just because of

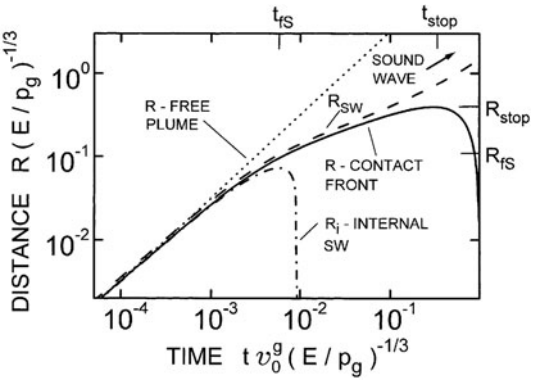

Fig. 30.4.3 Expansion dynamics of (*spherical*) plume and shock wave (SW) in dimensionless variables. *Dotted line*: Radius R for free plume expansion in a vacuum with velocity $(v_\mathrm{p}^\mathrm{max}/v_0^\mathrm{g})^2 = 10^3$. All other curves refer to the expansion dynamics in an ambient medium. *Dash-dotted curve*: Radius of internal SW, R_i. *Solid curve*: Plume radius (contact front), R. *Dashed curve*: Radius of external SW, R_sw. For longer times, the SW degenerates into a sound wave. Parameters: $\gamma_\mathrm{p} = \gamma_\mathrm{g} = 5/3$, $k = 3/2$

energy conservation. This deceleration starts near the contact front where the ablated species heavily collide with molecules of the ambient gas, so that they are even partially reflected. As a consequence of these processes, the plume is compressed and heated near its leading edge. This results in an *internal* SW which propagates back towards the target. As plume expansion slows down, the internal SW reaches the plume center on the substrate and, in turn, becomes reflected. This interaction between the internal SW and the flow of ablated material homogenizes the temperature and mass density within the ablation plume. For such a homogenized plume and with spherical symmetry and the assumption that the *external* SW is located close to the contact surface (Fig. 30.4.2, $t = 0.3\,\mu\text{s}$), the energy conservation can be written, approximately, as

$$\frac{3}{10} M_\text{p} \dot{R}^2 + \frac{4\pi}{3} R^3 \frac{p}{\gamma_\text{p} - 1} + \frac{4\pi}{3} R^3 \varrho_\text{g} \frac{\dot{R}^2}{2} = E \,. \tag{30.4.6}$$

The first and second terms describe, respectively, the kinetic and thermal energy of the (homogeneous) plume. The third term is the kinetic energy of the SW. Note that the mass of the external SW is equal to the mass of the ambient gas displaced and compressed by the expanding plume. The pressure at the contact surface, p, can be found from Newton's law for the external SW

$$\frac{\mathrm{d}}{\mathrm{d}t} \left(\frac{4\pi}{3} R^3 \varrho_\text{g} \dot{R} \right) = 4\pi R^2 (p - p_\text{g}) \,. \tag{30.4.7}$$

From (30.4.6) and (30.4.7) we can eliminate the pressure p and obtain an equation for R. If the thermal energy of the SW and the unperturbed gas and the fact that, in reality, $R_\text{sw} \approx R + \Delta R_\text{sw}$ are taken into account, we obtain

$$(\xi_1 M_\text{p} + \xi_2 \varrho_\text{g} R^3) \dot{R}^2 + \xi_3 \varrho_\text{g} R \frac{\mathrm{d}}{\mathrm{d}t} (R^3 \dot{R}) + \xi_4 p_\text{g} R^3 = E \,, \tag{30.4.8}$$

where ξ_i are coefficients of the order of unity; these coefficients depend on the real spatial distributions of variables ϱ_p, p_p, v_p, v_g, etc. (Fig. 30.4.1b). Numerical calculations of these profiles have been performed by *Brode* (1959). If the first term in parentheses and the last term are ignored, and if we assume $R \propto t^n$, (30.4.8) becomes equal to (30.4.1), except for the value of the factor ξ.

During further expansion, the pressure within the plume and the external SW decreases and approaches the pressure of the ambient gas. This transition is given by $p \approx p_\text{sw} \approx p_\text{g}$, which yields, with (30.4.3), the time

$$t_\text{stop} \approx (E^2 \varrho_\text{g}^3 / p_\text{g}^5)^{1/6} \approx R_\text{stop} / v_0^\text{g} \tag{30.4.9a}$$

and, together with (30.4.1), the radius

$$R_\text{stop} \approx (E / p_\text{g})^{1/3} \,. \tag{30.4.9b}$$

During the time interval between t_{fS} and t_{stop}, the SW detaches from the expanding plume and weakens. This transition can be seen in Fig. 30.4.2 for times $\gtrsim 0.5\,\mu s$. Finally, the (weak) SW propagates with the velocity of sound, v_0^g. With typical conditions employed in PLA/PLD we estimate, with $E = 0.1\,J$ and $M_p = 5 \times 10^{-7}\,g$, a velocity $v_p^{max} \approx 1.4 \times 10^6\,cm/s$. Together with $v_0^g = 3 \times 10^4\,cm/s$ and $p_g = 10^3\,mbar\,/\,1\,mbar$, we obtain $R_{SW} \approx 0.08\,cm/0.8\,cm$ and $t_{SW} \approx 60\,ns/0.6\,\mu s$; $R_{stop} \approx 1\,cm/10\,cm$ and $t_{stop} \approx 3\,\mu s/30\,\mu s$.

Drag Model

A simple model that is frequently employed for the description of plume expansion within an ambient medium is the drag model. Here, it is assumed that the plume initially propagates with the free-expansion velocity v_p^{max}, and that it slows down due to a (viscous) drag force $\propto \eta_n \dot{R}^n$, where η_n is a fitting parameter; the value of n frequently employed is $n = 1$ or 2. This ansatz results in the linear dependence $R(t) = v_p^{max} t$ in the initial phase of expansion, and, with $n < 2$, in a finite radius $R_{stop} = R_{stop}(\eta_n, n) \equiv R(t \to \infty)$ for long times. In comparison to (30.4.8), the drag model has a number of disadvantages:

- It is based on the assumption that the deceleration of the plume is related to the viscosity, and not to the mass of the external SW and the counter pressure.
- It yields a finite radius R_{stop} only with $t \to \infty$.
- R_{stop} is determined by an empirical parameter η_n.
- It does *not* describe the dependence $R \propto t^{2/5}$ frequently observed within the intermediate region (Fig. 30.4.4).

For further details the reader is referred to the large number of more sophisticated theoretical models on shock waves and the expansion of vapor/plasma plumes. These calculations are mainly based on kinetic models, on hydrodynamic (macroscopic) approaches, or on combinations of both [*Volkov* et al. 2008; *Gusarov* et al. 2000; *Yabe* et al. 1999; *Bulgakov* and *Bulgakova* 1998, and many others]. For the interpretation of fs-laser processing of metals, the influence of multiphoton absorption and optical breakdown within the ambient gas has been considered (Sects. 13.1 and 11.6.3). The enhancement of the coupling of thermal energy to the sample, related to the laser-induced gas-dynamic motion in the plasma, has been estimated by *Bulgakova* et al. 2008. Subsequently, we briefly discuss some investigations on the expansion of vapor/plasma plumes together with the formation of particulates.

30.4.3 Formation of Nanoparticles

Clusters and fragments observed during pulsed-laser ablation may have quite different origins. Roughly speaking, they may be *directly* ejected from the target, or they may only be formed during expansion of the vapor/plasma plume, or originate

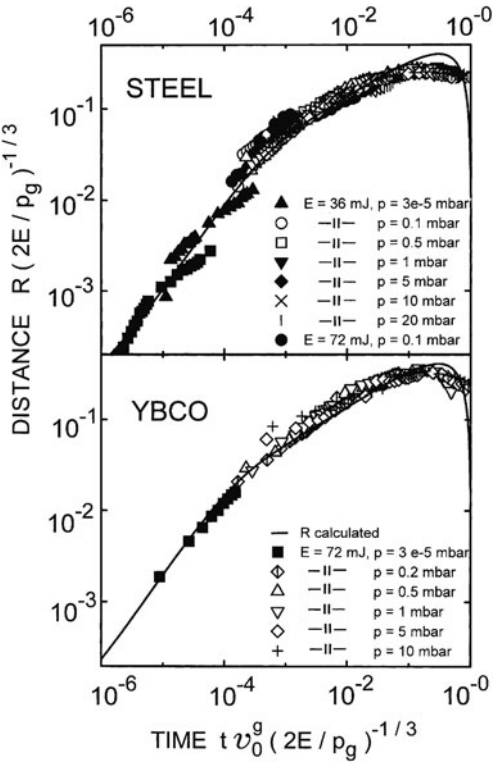

Fig. 30.4.4 Normalized temporal dependence of the distance of the luminous front from the target during KrF-laser ablation of steel and YBCO in an Ar atmosphere ($\tau_\ell \approx 30\,\text{ns}$, $w = 0.5\,\text{mm}$) [*Gruber* 1999]. The solid curves are calculated with $v_p^{max}/v_0^g = 100$ for steel and $v_p^{max}/v_0^g = 200$ for YBCO. The other parameters are the same as in Fig. 30.4.3 [*Arnold* et al. 1999b]

from a combination of both. Various different mechanisms have been discussed throughout the book, in particular in Chaps. 4, 10, 11, 12, 13, 22, and 28. Subsequently, we give a brief overview on a few of the many calculations dealing with the condensation and cluster formation during expansion of vapor/plasma plumes into vacuum and into background atmospheres, and on the direct ejection of clusters from targets.

- The expansion of vapor/plasma plumes generated by ns-laser pulses and the formation of clusters have been studied within the frame of a generalized Zeldovich-Raizer theory of condensation. Both ablation into vacuum and the influence of a background atmosphere has been considered [*Ohkubo* et al. 2003; *Luk'yanchuk* et al. 1999; *Callies* et al. 1998]. During plume expansion into vacuum, cooling rates of up to 10^{11} K/s can be reached. These cooling rates and the density of vapor-phase species are strongly non-uniform. As a consequence, the rates of nucleation and growth of clusters vary strongly within the plume. This is the reason why PLA in *vacuum* does *not* permit one to fabricate clusters with a narrow size distribution. Roughly speaking, large clusters are formed in the center of the

plume and smaller ones near the edge. By taking into account the influence of a background atmosphere, the dependence of the cluster size on gas pressure was simulated [*Ohkubo* et al. 2003]. This has been discussed in Sect. 4.2.

- Calculations based on a combination of multiple-elastic scattering and hydrodynamic approaches permit a consistent explanation of plume splitting during expansion into *low* pressure gases. The fast component propagates with the 'vacuum velocity'. The velocity of the slow component depends on the pressure of the ambient atmosphere, as observed experimentally. The differences in expansion dynamics of ablated species in different background gases can be explained on the basis of the conservation laws via (non-reactive) collisions with atoms/molecules of different masses [*Wood* et al. 1998]. Good agreement with experimental data on the expansion of Si in He and Ar atmospheres and the observed differences in cluster formation is obtained (Sect. 4.2).
- A combination of molecular dynamics (MD) and Monte Carlo (MC) simulations has been used to study *direct* particle ejection from the target due to explosive-type decomposition phenomena during ultrashort-pulse laser ablation [*Itina* and *Zhigilei* 2007]. In the absence of clusters, the plume of atoms/molecules evolves from pancake-type to almost spherical, and to an oval elongated along the target normal. In the presence of clusters, plume splitting into two components occurs. An oval cloud of atoms/molecules with a very high velocity and a second cloud that remains in the vicinity of the target. Interestingly, when changing the pulse length from 15 ps to 150 ps, corresponding to the regimes of stress confinement and thermal confinement, respectively, the two cloud structure remains almost the same. The clusters ejected from the target are important for the further development and composition of the plume. In particular, they facilitate collisional condensation and evaporation processes during plume expansion. This has been modelled by direct simulation MC techniques [*Itina* 2007]. The segregation of clusters within the plume results in a plume structure with several components. Their average axial velocity decreases with increasing mass of clusters. This is in agreement with experimental observations (see below).

30.4.4 Comparison with Experimental Investigations

The propagation of laser-induced vapor/plasma plumes and shock waves in gaseous atmospheres has been investigated by time-integrated and time-resolved photography including Schlieren arrangements, by interferometry, electron-, ion-, and mass-flux measurements, mass spectrometry, etc. The formation of nanoparticles by laser ablation in gaseous ambient media and the dependence of their size on laser parameters, gas pressure, etc. is discussed in Chap. 4.

Photography

The *overall* expansion and shape of the luminous plasma plume in vacuum and different background gases has been investigated by time-integrated photography and spectroscopy [*Proyer* and *Stangl* 1995; *Dyer* et al. 1992b]. Time-resolved

measurements have been performed by *Ursu* et al. 2010, *Park* et al. 2005, *Holzapfel* et al. 1996 and others.

Figure 30.4.4 shows experimental results for KrF-laser ablation of steel and YBCO for various laser-beam energies and pressures of the Ar background gas. The boundary of the visible plume in z-direction was measured by means of a gated ICCD camera. Here, $R \equiv Z$ was determined from the criterion that the maximum intensity of the luminous plume decreased to 10%. The solid curves have been calculated on the basis of an equation similar to (30.4.8). The experimental data are in excellent agreement with the theoretical analysis. In particular, the transitions from free expansion to the strong SW, and the slowing down (stopping) of the plume are clearly revealed. The positions of these transitions are well reproduced by the (refined) estimations (30.4.5) and (30.4.9). The remaining discrepancies may be due to non-spherical expansion of the real plume, energy losses, etc. The deviations observed for steel at low pressures are also due to difficulties in the determination of the plume boundary.

For laser parameters that result in a strongly forward-directed plume, (30.4.8) becomes less adequate. Figure 30.4.5 shows the length of a plume generated by KrF-laser ablation of YBCO in an O_2 atmosphere. For $p(O_2) = 1$ mbar, the aspect ratio of the plume is $\Gamma \equiv Z/X \approx 5$ and it becomes about unity for 100 mbar. The solid curve is calculated on the basis of (30.4.9b), which yields a slope $\beta = 1/3$. For low pressures one can use the model for adiabatic expansion of an elliptical plume instead [see (30.3.6)]. This yields $Z_{\mathrm{stop}} \equiv \max\left\{z, p_{\mathrm{p}}(z) = p_{\mathrm{g}}\right\} = X_0 f(\gamma_{\mathrm{p}}, \zeta_0, \eta_0)(p_{\mathrm{g}} X_0^3/E)^{-\beta}$, where $X_0 \approx w_{\mathrm{x}}$, and $\beta = \beta(\gamma_{\mathrm{p}}, \zeta_0, \eta_0) \approx 1/3\gamma_{\mathrm{p}}$. $\zeta_0 \approx Z_0/w_{\mathrm{x}}$ and $\eta_0 \approx w_{\mathrm{y}}/w_{\mathrm{x}}$ characterize the 'initial' geometry of the plume. This dependence describes the data in Fig. 30.4.5 equally well. With this approach, one

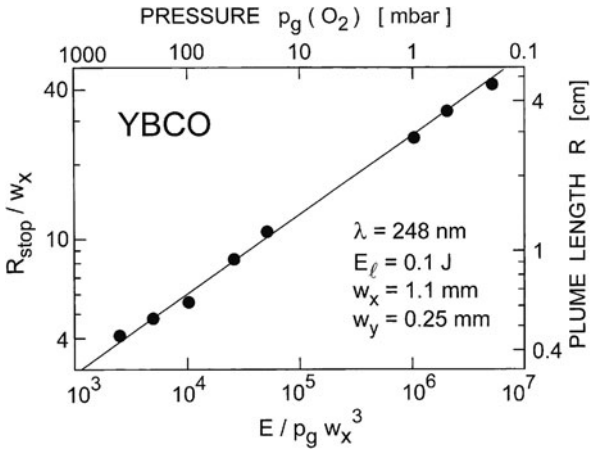

Fig. 30.4.5 Data show the length of the visible plume for KrF-laser ablation ($E_\ell = 0.1$ J, $\tau_\ell \approx 20$ ns, $w_{\mathrm{x}} = 1.1$ mm, $w_{\mathrm{y}} = 0.25$ mm) of YBCO in O_2 atmosphere (*right-hand scale*) measured for different gas pressures (*upper scale*). The *solid curve* represents a fit in dimensionless quantities with the slope $\beta = 1/3$. Here, $E = E_\ell$ was assumed (adapted from *Stangl* et al. 1994)

can also study the *shape* of the stationary plume. For $p_g w_x^3/E < 10^{-7}$, the length of the visible plume was found to become almost independent of p_g [*Proyer* and *Stangl* 1995].

Schlieren Techniques

Schlieren arrangements [*Vogel* et al. 2006; *Kokai* et al. 1999; *Geohegan* et al. 1998; *Srinivasan* et al. 1990a, b] permit a direct visualization of the external and internal shock waves and of the ablation plume. High-resolution Schlieren techniques have been employed to study nanosecond PLA of water targets. Indications for phase explosion characterized by a mixture of vapor and droplets (Sect. 13.4) and a subsurface stress wave have been visualized [*Vogel* et al. 2006]. The internal shock wave travels back towards the target, becomes reflected and can move back and forth inside the plume. This leads to the formation of a 'uniform' plasma inside the contact front (Fig. 30.4.1a).

Mass- and Ion-Flux Measurements

Mass- and ion-flux measurements using arrays of quartz-crystal microbalances (QCMs) and Langmuir probes, respectively, have been employed also for investigating the influence of the pressure and the type of background gases on the plume dynamics (Fig. 29.3.4). Detailed experiments have been performed for Ag targets ablated in Ar, Xe, and O_2 atmospheres by nanosecond 355 nm Nd:YAG laser pulses [*Amoruso* et al. 2008; *Schou* et al. 2007]. For very low background pressures the TOF spectra show a single peak that can be related to the fast expansion of species in vacuum, as described by Eq. (30.3.5). This is in agreement with the results outlined above. With increasing pressure, a double peak structure is revealed. The second peak that is observed at later times, corresponds to the 'slow' component of the plume. This component, which generates the shock wave, can be described by Eq. (30.4.1) with $n = 1/5$, corresponding to spherical expansion. As expected, background gases consisting of atoms/molecules with higher masses stop plume expansion at a lower pressure. Possible chemical reactions between Ag species and oxygen as well as cluster formation have been ignored in the analysis.

Ultrashort Laser Pulses

With ultrashort laser pulses, the ablation mechanisms are quite different to those for nanosecond and longer pulses. Thus, the term 'vapor-/plasma-plume' has some different meaning. Some of these aspects are discussed in Chap. 13. Nevertheless, ablation by fs-laser pulses has been analyzed at 'later' stages by using mainly the same experimental techniques and models outlined in the previous sections. The most important results can be summarized as follows:

- With fs-laser pulses the interaction of the incident laser light with the 'plume' is irrelevant, simply because the pulse duration is short in comparison to the motion of atoms.

- In the initial phase of laser-material interaction, the target surface locally expands. The observation of Newton fringes is related to the formation of a 'shell' (Fig. 13.4.1).
- Long after the laser pulse, i.e. on a ns time scale, shadowgraphy reveals in addition to the "hemispherical" shock wave and an ablation plume, as observed with ns-pulses (Fig. 30.4.2), a *primary conically-shaped* SW, at least for metal targets [*Horn* et al. 2010, *Breitling* et al. 2004b]. This may be caused by the initial, strongly forward directed burst of electrons and ions originating from target ablation of a thin layer of the order of the skin depth. Alternative explanations are given in the literature.
- Even at atmospheric pressure, the initial propagation of the "hemispherical" (secondary) shock wave can be described by the *linear* law, Eq. (30.3.5), similar to vacuum expansion of the plume. This has been verified in experiments using steel targets and 200 fs-laser pulses ($\lambda \approx 800\,\text{nm}$; $\nu_r = 1\,\text{kHz}$) [*J. König* et al. 2005]. With these laser parameters, one can fit the data by $R(t) \propto t$, up to delay times of 30 ns. This is consistent with the high internal pressure in plasma plumes generated by fs-laser pulses. For times $t > 30\,\text{ns}$, the expansion of the shock wave can be described by Eq. (30.4.1) with $n = 1/5$, i.e. by $R_{sw}(t) \propto t^{2/5}$.
- During further expansion of the plume, segregation of clusters consisting of different numbers of atoms/molecules results in the formation of a complex multicomponent plume structure, as described in 30.4.3 [*Itina* et al. 2007]. These results agree with experimental observations of ultrashort pulse laser ablation of Au, Cu and Si targets where very slow particles with a broad distribution in particle size and velocities have been observed (Sect. 30.2.5) [*Noël* et al. 2007; *Amoruso* et al. 2006].
- Time-resolved measurements of plasmas and of particle ejections from metals using pump-probe photography have been performed by *Mingareev* and *Horn* (2008).
- For fs-pulses the 'mushroom-type' ablation plume observed with ns- and longer pulses is washed out due to strong turbulences caused by (nonlinear) wave-front disturbances.
- With high laser-light intensities, nonlinear interactions with the *ambient gas* lead to conical emission, beam profile disruption, and increased beam divergence (Chaps. 9 and 13).

Mixing and Chemical Reactions

With certain systems, the ablated material reacts with the ambient medium. Such reactions are particularly strong near the *contact surface*. Here, the reaction rate is enhanced by the external SW. The width of the reaction zone may be increased by turbulent mixing.

The high temperatures generated by the SW can thermally enhance reactions or radical formation from gas- or liquid-phase molecules which, in turn, may strongly react with each other or with ablation products. Such reactions are of great importance for the synthesis of nanoparticles (Chap. 4), the suppression of debris in

surface patterning (Chaps. 12 and 13) and, in particular, in many cases of PLD (Chap. 22).

At pressures of, typically, $p_g > 1$ mbar, mixing between ablation products and the hot ambient gas within the SW is enhanced by Rayleigh–Taylor instabilities (Sect. 28.5). The deceleration of the expanding plume causes an artificial gravity directed outwards from the plume center (in the reference frame fixed with the contact surface; Fig. 30.4.1). Its value can be estimated from $g_{RT} \approx v_p^{max}/t_{fS} \approx v_p^{max\,2}/R_{fS}$. With the parameters used with (30.4.9), this yields $g_{RT} \approx 2\times10^{13}$ cm/s^2 for 10^3 mbar and 2×10^{12} cm/s^2 for 1 mbar. In the nonlinear stage, this acceleration causes turbulent mixing within a zone of width $\Delta R \approx \zeta g_{RT} t^2$, which is given by (28.5.7). As a consequence, plume material penetrates deeply into the shock-compressed ambient gas. This explains why the radius of the *visible* plume observed experimentally often follows the SW-like laws (30.4.1) or (30.4.8). In other words, reactions can take place *far away* from the target, at a distance $R \approx R_{sw} \propto t^{0.4}$.

At later times $t > t_{stop}$, mixing between ablated species and the ambient is caused by diffusion, i.e. $\Delta R \propto t^{1/2}$. Furthermore, for certain systems oscillations of the contact surface $R(t \gtrsim t_{stop})$ have been observed [*Bulgakov* and *Bulgakova* 1998]. Such oscillations may increase the mixing of species as well. Plume confinement and mixing of species within the plasma plume are the reasons why clusters with a relatively small size distribution are formed only in the presence of a background atmosphere (Chap. 4).

With very low pressures, when the mean free path of species becomes very large, so that $\lambda_m > \Delta R_{sw}$, gas dynamics does *not* apply and ballistic effects become dominant.

30.5 Optical Breakdown in Liquids, Cavitation

Laser-induced optical breakdown at liquid-solid interfaces and within the volume of liquids is accompanied by the generation of SWs and bubble formation. Both play an important role in many cases of *liquid-phase* laser processing. Among the examples are laser ablation for particle formation and surface patterning, some cases of liquid-phase deposition, etching, laser cleaning, etc. This has been discussed in previous chapters. Henceforth, we will concentrate on model systems that are of particular interest for laser applications in medicine and biotechnology. Among those are soft materials including biological tissues immersed in liquids, pure liquids, in particular water, and synthetic materials that contain a high amount of liquid.

The detailed interaction mechanisms depend on the laser parameters and the system under consideration. Optical excitation, breakdown and plasma formation may be based on *linear* absorption and/or on *non-linear* absorption. For pure water and materials that contain a high amount of water, optical breakdown for VIS- and NIR-laser radiation occurs at threshold intensities of, typically, several 10^{11} W/cm^2. This corresponds to fluences of several 10^3 J/cm^2 to several J/cm^2 for 10 ns- and 10 ps-pulses, respectively. Within the regime of 10 ps to 10 fs pulses, the threshold

intensity increases up to several 10^{13} W/cm^2, corresponding to fluences of several 100 mJ/cm^2 for 10 fs-pulses. These threshold intensities/fluences have been estimated from Eq. (13.6.1) for a critical electron concentration $N_e^{cr} \approx 10^{21}$ cm^{-3} [*Vogel* et al. 2007b]. Multiphoton absorption is of particular importance with (linearly) transparent materials and ultrashort laser pulses (Chap. 13). In any case, in this regime of laser parameters, the response of the materials under consideration is strongly affected by the (partial) conversion of the laser-light energy into mechanical energy of SWs and cavitation bubbles.

30.5.1 Absorbing Targets

With μs *laser pulses* and energies of, typically, some 100 mJ the (primary) SW induced by the expansion of the ablated material in front of an absorbing target, e.g., a stone, plays a *minor* role in the fragmentation process. More important seems to be the (secondary) shock, which is related to the collapse of the cavitation bubble [*Rink* et al. 1992; *Ihler* 1992]. The formation of large cavitation bubbles observed with these laser parameters is probably related to the large amount of material ablated from the surface. This is important in the application of lasers in lithotripsy.

With ns *laser pulses* and energies of a few mJ, the primary shock significantly exceeds the secondary shock. Figure 30.5.1 shows the peak pressures of (primary) SWs induced during XeCl-laser ablation of PI [*Zweig* and *Deutsch* 1992]. Here, the velocities of SWs, v_{sw}, have been determined by HeNe-laser probe beams parallel to the PI target. The pressure is then estimated from Newton's law

$$p_{sw} = \varrho_l v_{sw} v \tag{30.5.1}$$

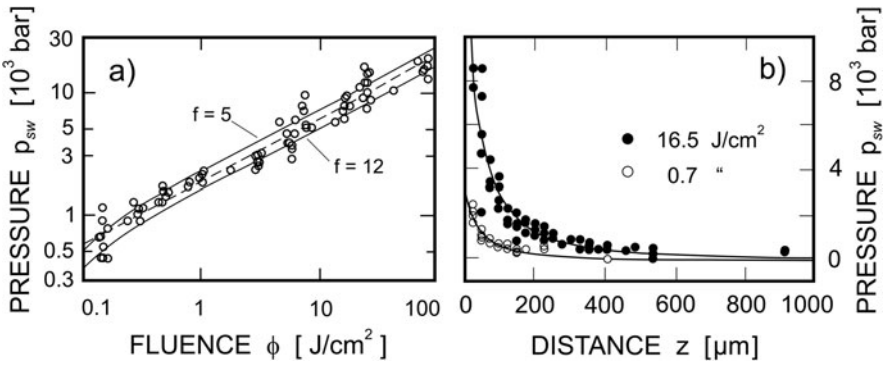

Fig. 30.5.1a, **b** Pressures of (primary) shock waves, p_{sw}, transmitted into water at the *rear* surface of a 25 μm-thick PI foil irradiated with XeCl-laser light. (**a**) p_{sw} (measured at a distance $z = 25$ μm away from the rear surface) as a function of fluence, ϕ. The dashed line is a least-squares fit to data with a slope of 0.52. The *solid curves* have been calculated from (30.5.3). (**b**) p_{sw} versus distance z for two laser fluences. *Solid curves* are fits to (30.5.4) [*Zweig* and *Deutsch* 1992]

and the relation

$$v_{\mathrm{sw}} = v_0^l + \xi v \ , \tag{30.5.2}$$

where $\varrho_l \equiv \varrho_l(\infty)$ and v_0^l is the velocity of sound within the liquid. v is the mass velocity of the liquid behind the SW. Equation (30.5.2) is a good approximation for 'weak' SWs. For water, the (undisturbed) density is $\varrho_l(20°\mathrm{C}) \approx 0.987\,\mathrm{g/cm^3}$, $v_0^l = 1.483 \times 10^5\,\mathrm{cm/s}$, and $\xi = 2.07$. The dependence of the shock pressure on laser fluence and pulse length can be calculated from

$$p_{\mathrm{sw}} \approx \zeta \left(\frac{\phi - \phi_{\mathrm{th}}}{\tau_\ell} \right)^{1/2} \tag{30.5.3}$$

with $\zeta = \zeta(\rho\, v_0^i,\, f)$ where v_0^i is the sound velocity within the medium i. f is given by $f = 2c_{\mathrm{v}}/R_{\mathrm{G}}$, where the (molar) specific heat, c_{v}, depends on the number of (molecular) degrees of freedom.

At large enough distances from the irradiated zone, the SW propagates spherically. Because of momentum conservation, the pressure, p_{sw}, varies inversely with the square of the distance from the shock center, i.e.,

$$p_{\mathrm{sw}} \propto \frac{1}{(R_{\mathrm{sw}} - R_0)^2} \ , \tag{30.5.4}$$

where R_0 is a fit parameter. This simple relation describes the data in Fig. 30.5.1b quite well.

The dependence given by Eq. (30.5.3), is in good agreement with the data in Fig. 30.5.1a. The equation may also explain why primary SWs play a more important role with short laser pulses. The formation of SWs and microbubbles has been studied also in connection with liquid-phase backside ablation of materials (Sect. 14.5.2).

30.5.2 Transparent Media

Laser-induced energy deposition and breakdown *inside* linearly transparent media offers a unique possibility for localized processing within the *volume* of liquid or solid media. The latter application was already discussed in connection with the fabrication of embedded structures (Sect. 13.6) and structural/chemical transformations inside bulk materials (Sects. 23.6, 28.2.6). Optical breakdown has also been studied for pure liquids and materials that contain a high amount of liquid, mainly water. As expected from the discussions in previous chapters, and in particular in Chaps. 12 and 13, the fundamental interaction processes in such systems are quite different for nanosecond and femtosecond laser pulses. With nanosecond and longer pulses, optical breakdown and plasma formation is mainly related to "seed" electrons, impurities, and defects, including incubation centers that are only generated by the

laser light. With ultrashort laser pulses, generation of "free" electrons is initiated by multiphoton ionization. In any case, with the generation of absorption centers and/or electrons, strong feedback effects cause optical breakdown and plasma formation with a rapid rise in temperature and pressure within the interaction volume. Clearly, the threshold for optical breakdown is much sharper for fs-pulses than for ns-pulses. Simply, with ns-pulses the generation of absorption centers takes more time and depends – even within the same material – on sample purity, history, etc.

Nanosecond Pulses

The most detailed experiments on optical breakdown, SW emission and cavitation bubble formation have been performed for pure water and a (transparent) polyacrylamide (PAA) gel immersed in water [*Brujan* and *Vogel* 2006]. The PAA gel can be considered as a tissue phantom whose elastic properties can be varied over a wide range via its water content. The experiments were performed with 6 ns Nd:YAG laser pulses. The results can be summarized as follows: Breakdown in water causes a purely compressive stress wave similar to that shown in Fig. 30.5.2 for 30 ps pulses. Together with the rapid expansion of the plasma, a cavitation bubble is formed. Well above the threshold for breakdown, the maximum radius of bubbles for both water and PAA, scales with the laser-pulse energy as $R_{\text{bub}} \propto E_\ell^{1/3}$. Bubble "collapse" to a bubble with smaller size causes a secondary shock. This is revealed in the figure in the acoustic signal for water. Subsequently, the compressed gas within the bubble causes reexpansion until a second collapse takes place. This causes a third stress wave, etc. Thus, the bubble radius oscillates with decreasing amplitude due to shock wave emission. A similar behavior is observed with PAA only for high water content ($\approx$ 95 %) and high laser pulse energies. With both pure water and PAA, the maximum pressure is generated during optical breakdown. The dependence of pressure on laser pulse energy within the range 1 mJ $\lesssim E_\ell \lesssim$ 10 mJ is consistent

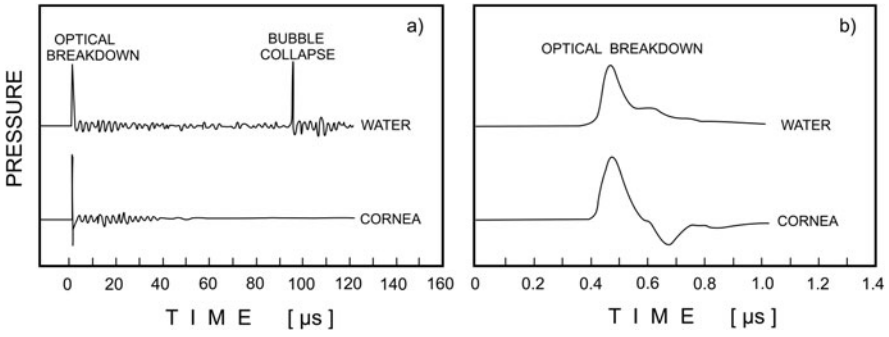

Fig. 30.5.2 Acoustic signals after a 30 ps laser pulse focused into physiological saline and cornea ($E_\ell = 300\,\mu$J) (**a**) overview (**b**) detailed view of the breakdown pulse. Measurements were performed at 10 mm distance from the breakdown site. The compressive stress amplitude at this distance was 24 bar and the tensile stress amplitude about 1 bar [adapted from *Brujan* and *Vogel* 2006]

with (30.5.3). Subsequent shocks related to bubble collapse are weaker. The situation changes for PAA samples with lower water content (higher elastic modulus): the maximum radius of bubbles shrinks and the amplitudes of bubble oscillations decrease. As a consequence, the stress wave related to bubble collapse becomes weaker and vanishes for strong damping. For sufficiently high laser-pulse energies, however, samples with low water content show in addition to the compression wave a tensile wave, similar to that observed with cornea (Fig. 30.5.2).

Femtosecond Pulses

For ultrashort laser pulses the interaction with transparent liquids, gels, different types of resins, etc. is based on multiphoton absorption followed by either impact ionization and plasma formation, or by direct (photochemical) breaking/cross-linking of chemical bonds. The latter mechanism is of particular importance in photopolymerization of viscous liquids (Sect. 27.2.4). With water-rich materials considered in this section, plasma formation together with local heating, thermomechanical effects, and chemical changes are the relevant mechanisms. Under the condition of stress confinement, as defined by Eq. (13.2.1), isochoric heating and subsequent stress relaxation causes very high pressures and the formation of bubbles/voids (Chap. 13). For water and water rich materials compressive pressures of up to several 10^3 bar at temperatures below 200°C within volumes of submicrometer dimensions and stress transient times of less than 300 ps have been found. For fs-pulses, the conversion of absorbed laser-light energy into mechanical energy is, typically, below 0.1%, while for ns-pulses it is between several percents and several 10%, depending on laser parameters. Thus, for fs-pulses the situation is quite different to ns and longer pulses where high pressures are always related to high temperatures and SW transient times of several 10 ns. Furthermore, the radii of cavitation bubbles with ns-pulses, are, typically, between several 10 µm and several 100 µm. For fs-pulses, typical radii of bubbles are between a few 100 nm and several µm, depending on laser-pulse energy, E_ℓ, and wavelength. Experiments using 1040 nm Yb:glass-laser pulses ($\tau_\ell = 340$ fs, $\nu_r = 1$ kHz) and higher harmonics at 520 nm and 347 nm have revealed that the increase in the maximum bubble radius with E_ℓ is slowest with the shortest wavelength, 347 nm [*Vogel* et al. 2008]. This is of great importance for the confinement achieved in micro-/nanosurgery (Chap. 31). Theoretical considerations predict a threshold temperature of about 170°C. For $T > 300$°C phase explosion and a rapid increase in R_{bub} with E_ℓ is observed. Model calculations have been performed on the basis of equations similar to (13.6.1) [*Vogel* et al. 2007a, b; *C.L. Arnold* et al. 2007; *Lubatschowski* and *Heisterkamp* 2004a; *Schaffer* et al. 2002]. Here, the same restrictions as those discussed in Sect. 13.6, hold as well.

Part VII
Lasers in Medicine, Biotechnology and Arts

The following chapters on lasers in medicine and biotechnology and on restoration and art conservation shall summarize those applications of lasers, whose underlying fundamental interaction mechanisms have been discussed throughout this book. These chapters have been added to give readers a quick and comprehensive overview on the various different applications in these fields and direct them to the original literature of a particular area of interest.

Chapter 31
Lasers in Medicine and Biotechnology

The use of lasers in various different areas of medicine and biotechnology has been described in a number of books [*Bäuerle* 2009; *Bille* and *Schlegel* 2005; *Niemz* 2004; *Greulich* 1999] and a large number of review articles [*Vogel* et al. 2007a, b; *Lubatschowski* and *Heisterkamp* 2004a, b; *Minet* et al. 2004]. Several remarks related to medical and biological applications of lasers have been made also throughout the text. Among those are the synthesis of nanoparticles for bioanalysis, bioimaging, tumor treatment, drug delivery, etc. (Sect. 4.2), the fabrication of different kinds of prosthesis (Sects. 13.1, 25.1 and 27.3), the formation of biocompatible or protective coatings (Sects. 22.5 and 22.7), the formation of viable cell patterns for bioengineering and biosensor technology using laser-induced forward transfer (Sect. 22.8), the injection of organic and inorganic compounds or particles into biological tissues (Sect. 24.5), modifications of polymer surfaces for cell adhesion (Sect. 27.1), etc. Subsequently, we give a brief overview on further applications that are related to laser-material-interactions that have been discussed throughout this book. Among those are laser-induced modifications, coagulation, decomposition, evaporation and ablation of soft and hard biological tissues. The numerous applications of laser-based diagnostic techniques are not included in this chapter.

The type of lasers employed for tissue treatments depend on the particular application. Here, laser-beam irradiation times reach from several seconds to several ten femtoseconds. For *low* laser-light intensities, the laser wavelength determines the (linear) optical penetration depth $\ell_\alpha = \beta^{-1}$ where $\beta = \alpha + \alpha_S$ is the extinction coefficient (Sect. 2.2). For biological tissues, the attenuation of the radiation by scattering cannot be ignored in most cases. The thickness of the laser-affected zone is $h \approx \max\{\ell_T, \ell_\alpha\}$ where ℓ_T is the thermal penetration depth (Chap. 12). Clearly, due to the heterogeneity of most biological tissues, the optical and thermal properties refer to *average* values. In medical and biotechnological applications where short- or even ultrashort-laser pulses are used, strongly nonlinear optical effects, the generation of a plasma, shock waves, and the formation of cavitation bubbles become important (Chaps. 12, 13 and 30). In addition to the spatial and temporal energy localization that are the basis for many applications of laser-materials processing, applications in medicine and biotechnology take advantage of lasers as a 'massless' and absolutely sterile tool.

D. Bäuerle, *Laser Processing and Chemistry,* 4th ed.,
DOI 10.1007/978-3-642-17613-5_31, © Springer-Verlag Berlin Heidelberg 2011

31.1 Medical Applications

The most established applications of lasers in medicine include ophthalmology, dermatology, and surgery.

31.1.1 Ophthalmology

In ophthalmology different types of lasers are used as diagnostic tools, e.g. for the detection of retinal alterations, early stages of glaucoma, etc. Laser treatments are often classified into those at the posterior part of the eye, in particular the retina, and those at the anterior part, in particular the cornea [*LeHarzic* et al. 2009; *Bäuerle* 2009; *Lubatschowski* and *Heisterkamp* 2004b; *König* et al. 2002; *Niemz* 2004; *Deutsch* 1997].

A routine treatment is the 'point welding' of the *retina* to the underlying choroidea. This suppresses further retinal detachment. Here, in most cases, Ar^+-lasers are employed. Such lasers have an excellent beam pointing stability and the 514.5 nm line is well absorbed by the melanin of the epithelial tissue and the choroidea. The intensity at the focus of the laser beam is tuned in such a way that the local temperature rise is around 100°C. This results in a local coagulation ('welding') of the tissue. Typical laser parameters employed are: $100\,\mathrm{mW} \lesssim P \lesssim 300\,\mathrm{mW}$; $100\,\mu\mathrm{m} \lesssim 2w_\mathrm{o} \lesssim 300\,\mu\mathrm{m}$; $0.1\,\mathrm{s} \lesssim \tau_\ell \lesssim 0.3\,\mathrm{s}$. This process is repeated to generate a pearl-type chain around the detached zone. The attachment of the coagulated tissue is strong enough to avoid further tearing.

The most established treatment of the anterior part of the eye is the ablation of the *cornea* for visual correction. Here, the standard technique employed is laser in situ keratomileusis (LASIK). In the first step, a corneal flap is cut by using either a scalpel (microkeratom) or fs-laser pulses. This flap is opened like a book cover. Subsequently, intrastromal tissue is ablated by computer-controlled scanning of nanosecond ArF-laser pulses. Finally, the flap is pulled down. It sticks on the ablated tissue due to adhesion. In the case of shortsightedness (myopia) the refraction of the cornea is too strong in comparison to the axial length of the eye. Thus, the curvature of the cornea must be decreased by ablating its central part. For longsightedness (hyperopia) the situation is just opposite. Thus, by ring-shaped ablation around the center of the cornea, refraction is increased. The ArF-laser fluences typically employed for intrastromal ablation are 1–5 J/cm^2. The ablated thickness/pulse is then 0.1–1 μm which corresponds to a change of refraction of 0.01–0.1 diopters.

31.1.2 Dermatology and Surgery

In dermatology and surgery the lasers most frequently employed are Ar^+-, dye-, Nd:YAG-, diode-, Er:YAG-, CO_2-, and, for the treatment of psoriasis, XeCl-lasers. With cw-lasers and long laser pulses, tissue treatment is based on local heating that

causes coagulation or evaporation/ablation related to material decomposition and optical breakdown (Sect. 31.3). Lasers permit evaporation/ablation of skin tumors, warts, hair, etc. Unique applications in surgery include the resection/destruction of bronchial tumors, excision/coagulation of brain tumors, liver resection , etc. In contrast to resections by means of a scalpel, lasers permit almost 'dry cutting' due to simultaneous vessel closing by (thermal) coagulation. The application of fs-laser pulses in neurosurgery is under investigation [*Götz* 2004].

31.1.3 Photodynamical Therapy

Photodynamical therapy (PDT) uses a photosensibilisator which is injected into the tissue prior to laser treatment. Subsequent photochemical dissociation of the sensibilisator initiates chemical reactions between the photoradicals and the surrounding tissue.

31.1.4 Prosthesis

Laser fabrication of prosthesis is an important field by its own. Examples are metallic stents fabricated by laser machining (Fig. 13.1.4), implants or models produced by laser sintering (Sect. 25.1) or 3D-photopolymerization (Sect. 27.3), or laser shaping [*Weigl* et al. 2004; *Niemz* 2004]. There is also a rapid development in the fabrication of biochips [*Obata* et al. 2006] and 'lab-on-a-chip' devices (Fig. 13.6.2).

31.2 Biotechnology

There are numerous applications of lasers in biotechnology ranging from the handling of single cells by laser tweezers, different types of laser microscopy, including STED-nanoscopy, etc. A new field of applications is biophotonics [*Popp* and *Strehle* 2006; *Greulich* 1999]. Subsequently, we will briefly discuss some applications of lasers in microdissection, in micro- and nanosurgery and the manipulation of cells. A few comments on biopolymers are added.

31.2.1 Laser Microdissection

Laser microdissection permits rapid and contamination-free preparation of small specimens from organic tissues for subsequent investigations in different areas of molecular biology and medicine [*Vogel* et al. 2007c; *Elvers* et al. 2005; *Schütze* and *Lahr* 1998; *Meier-Ruge* et al. 1976]. In this technique, an optical microscope is used together with a laser for inspection of large-area samples and subsequent dissection of histological specimens, so-called dissectats. The dissectats are collected in vials for proteomic and genomic analysis, cell surgery, etc. The samples typically

employed consist of a microtome cut of the biological tissue placed on a supporting polymer foil or a glass substrate. In microdissection instruments mainly nanosecond N_2-lasers are employed.

31.2.2 Micro-/Nanosurgery and Manipulation

Femtosecond-laser surgery permits to study the function of single cells *without* damaging neighboring cells. Even single organelles of cells inside tissues have been ablated/dissected without collateral damage. Cuts with widths below 200 nm (FWHM) have been demonstrated. Among the examples are cell organelles such as mitochondria, membranes or chromosomes [*K. König* et al. 2005; *Riemann* et al. 2005; *König* et al. 2002; *Sacconi* et al. 2005; *Watanabe* et al. 2004; *Heisterkamp* et al. 2005]. The dissection of axons, e.g., in living C. elegans worms, permits to identify neuronal functions and to study the regeneration of neuronal networks [*Chung* and *Mazur* 2009; *Hosokawa* et al. 2008; *Bourgeois* and *Ben-Yakar* 2007; *Yanik* et al. 2004]. Ablation of the zona pellicula (outer egg membrane) permits fertilization or hatching [*Mantoudis* et al. 2001], etc.

Laser-induced cell lysis and transfer into a micropipet is employed for time-resolved capillary electrophoresis. Transient perforation of cell membranes is applied for transfection of genes and/or transfer of other substances, e.g. green fluorescent proteins (GFPs), into specific cell types [*Paterson* et al. 2005; *Tirlapur* and *König* 2002]. GFPs permit visualization of the transport of attached molecules, e.g. drugs and, in the case of ablation, better characterization of species within the vapor-/plasma-plume.

Laser polymerization of actin enhances neuronal growth. That has been demonstrated for rat/mouse hybrid neuroblastoma cells. The enhancement of growth rates was equal for 780 nm diode laser and 1064 nm fiber laser radiation [*Stevenson* et al. 2006]. With the light intensities employed, the temperature rise is only a few degrees and insufficient to explain thermal enhancement in actin polymerization.

31.2.3 Biopolymers

Chemical changes such as depletion of species or single components, seem to be important also in laser treatments of *soft* and *hard biological tissues*. As with 'standard' organic polymers, laser irradiation of biopolymers results in material swelling, depletion of species, modification on the surface or within the bulk, etc. (Chaps. 12, 13 and 27). An interesting phenomenon is the observation of a microfoam. For example, KrF-laser irradiation of collagen, chitosan, gelatine, etc. results in bubble formation and the generation of a microfoam. This effect cannot be explained by the laser-induced temperature rise. It is rather ascribed to the laser-induced pressure wave which generates a tensile stress and fast 'cold' boiling and expulsion of liquid constituents (Sect. 13.4). Microfoams can be employed to

improve cell attachment, manipulation and implantation in tissue repair, etc. [*Lazare* et al. 2009, 2007; *Gaspard* et al. 2008]. 3D micropatterning of biopolymers by fs-laser pulses has been demonstrated by *Oujja* et al. (2009).

31.3 Interaction Mechanisms

The mechanisms involved in laser ablation of biological tissues depend on the laser parameters and the type of tissue. Two regimes of laser-material interactions are of particular importance: the regime of 'low' and the regime of 'high' laser-light intensities. The latter shall be defined by laser light intensities that cause optical breakdown and plasma formation.

'Low' intensity UV radiation from nanosecond N_2- or excimer-lasers is well absorbed within biomolecules such as proteins, melanin (the primary pigment in skin), DNA, etc. *Visible* laser radiation is mainly absorbed by haemoglobin in vascularized tissues and by melanin in pigmented tissues such as skin, ocular tissues, etc. Nevertheless, apart from these exceptions, absorption of VIS-radiation is much lower than for UV- and IR-radiation. Thus, visible radiation requires for most types of biological tissues higher fluences for ablation. This is illustrated in Fig. 31.3.1. On the length scale under consideration, nanosecond UV-laser radiation results in well-defined ablation and sharp cuts, in contrast to visible radiation at even shorter pulse length. In some cases, more well-defined ablation with VIS radiation is achieved by staining the tissue [*Sacconi* et al. 2005]. Infrared radiation from Er:YAG and CO_2 lasers is strongly absorbed by water. The quality of cuts, the degree of fragmentation, etc., depend on the type of tissue, in particular its water content, and on the laser wavelength and intensity. Clearly, shorter wavelengths permit tighter focusing and thereby a better spatial localization of the interaction process. In some types of tissues longer wavelengths have a higher penetration depth and thereby permit

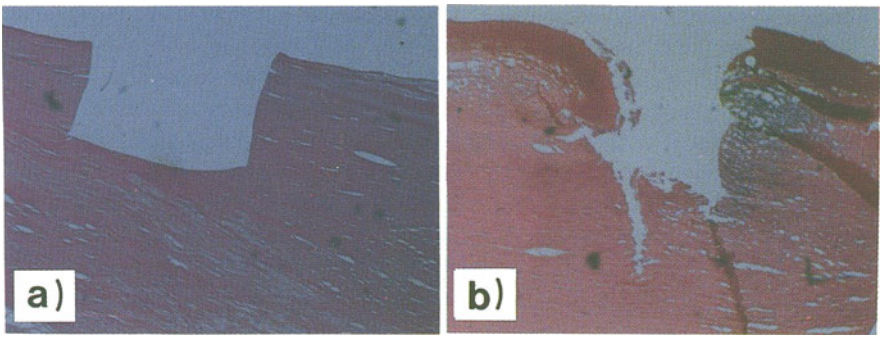

Fig. 31.3.1 Cross section of the luminal side of an aortic wall. (**a**) Trench (0.35 mm) produced by ArF-laser radiation ($\phi \approx 0.25\,\mathrm{J/cm^2}$, $\tau_\ell \approx 14\,\mathrm{ns}$). (**b**) Crater (0.4 mm) produced by 532 nm Nd:YAG-laser radiation ($\phi \approx 1.0\,\mathrm{J/cm^2}$, $\tau_\ell \approx 5\,\mathrm{ns}$). The absorption coefficients of the material at the two wavelengths differ by about a factor of 10^3 [*Srinivasan* 1986]

subsurface treatment or to achieve higher ablation rates. Whether *linear* absorption by seed electrons and the formation of a low density plasma is of importance with the fluences under consideration, is an open question.

In any case, absorption and energy dissipation result in material heating. Depending on the laser parameters and the type of tissue, this can cause internal pressures due to thermal expansion, mechanical tearing of the tissue matrix, thermal dissociation of biomolecules, boiling, bubble formation, explosive vaporization, and the generation of a shock wave (Sect. 30.5). For soft tissues such as liver, secondary material expulsion has been observed with 70 ns Er:YAG-laser pulses and fluences $\phi \gtrsim 5\ J/cm^2$ by *Apitz* and *Vogel* (2005). Thus, thermomechanical mechanisms play an important and often decisive role in laser ablation of biological materials using ns or longer pulses.

For laser-light intensities exceeding some $10^{11}\,\mathrm{W/cm^2}$, optical breakdown, plasma formation, the generation of SWs and cavitation bubbles become important. The situation seems to be similar to that discussed for PAA and ns-pulses (Sect. 30.5). The collapse of large bubbles, the long transient shocks, and the high conversion of absorbed laser-light energy into mechanical energy, causes extended disruptions of the tissue. For these reasons, such laser parameters do not permit *micro-* and *nanosurgery* of cells and tissues.

As expected from the investigations with water and PAA, the situation is quite different with fs-laser pulses. Here, strongly nonlinear optical absorption results in low threshold fluences for optical breakdown and a low energy load, typically only a few nJ per pulse. The short stress transient times caused by fs-laser pulses together with the very low conversion of absorbed energy into mechanical energy, permits strong confinement of the interaction down to a width of a few 100 nm or less. The laser pulse repetition rates employed are either in the MHz range using fs-oscillator pulses, or in the kHz range, using amplified pulses.

Experiments using MHz repetition rates, typically within the range of 10–100 MHz, are performed with fluences *below* the threshold for optical breakdown, i.e. with $\phi < \phi_{\mathrm{th}}$. In this case, the deposited laser energy is accumulated. This results in local heating. A reliable estimation of the local temperature rise, however, is difficult, because there are too many unknown parameters. In particular, with the great number of pulses, the optical and thermal properties within the interaction volume change *during* multiple-pulse irradiation. Thus, it is not yet clear, whether cell damage/dissection is caused by thermal decomposition. Other mechanisms, in particular photochemical bond breaking within biomolecules together with subsequent chemical reactions have been suggested as well. This is discussed below. With higher fluences, bubble formation, probably related to thermal and/or photochemical decomposition of molecules, is observed.

Surgery with repetition rates between 1 and 100 kHz is performed, in the majority of cases, with fluences causing optical breakdown. The typical pulse energies employed are 1–50 nJ. If $\phi \approx \phi_{\mathrm{th}}$, thermal and photochemical effects seem to dominate. With kHz repetition rates, the time *between* pulses is long enough for the diffusion of heat out of the interaction volume. Thus, regardless of the number of pulses, thermal and photochemical damages remain confined to the

interaction volume. Fluences $\phi > \phi_{th}$ cause thermoelastic stresses, shock waves, and transient bubbles. In this regime, surgery is probably based on the mechanisms discussed in Sect. 30.5. The tensile stresses associated with optical breakdown (Fig. 30.5.2), are believed to affect biological tissues more efficiently compared to the compressive stresses. With fluences $\phi >> \phi_{th}$ phase explosion will take place (Chap. 13).

31.3.1 Chemical Effects

The gases inside cavitation bubbles have been analyzed for a few systems. For water they consist of atomic/molecular hydrogen and oxygen. For corneal tissue, nitrogen, CO, and CH_4 have been detected as well [*Lubatschowski* and *Heisterkamp* 2004]. The origin of these molecules/radicals can be attributed to thermal and/or photochemical dissociation. Irrespective of the particular type of biological tissue, and the repetition rate of laser pulses, photodissociation of biomolecules and/or water can be attributed to *direct* single- or multiphoton absorption and dissociation or to electron-mediated processes as described, e.g., in Sect. 22.2. [*Vogel* et al. 2007b; *Garrett* et al. 2005]. The atomic/molecular radicals and quasifree electrons can react with biomolecules, decompose them and thereby cause photochemical damage. Such 'defects' may act like incubation centers as discussed in several different chapters and in particular in Sects. 12.5 and 13.6. This will result in avalanche-type thermal or photophysical processes. Investigations on the dependence of damage thresholds as a function of the number of laser pulses during nanoaxotomy in C.elegans worms supports the importance of incubation centers [*Bourgeois* and *Ben-Yakar* 2007].

Chapter 32
Restoration and Conservation of Artworks

The application of lasers in restoration and conservation of artworks covers a wide field ranging from the cleaning of stone and metal statues and reliefs, cleaning of coins, pottery, medieval stained glass, paintings, frescos, textiles, parchments, and whole buildings. Of increasing importance is the analysis of artworks using, e.g., pulsed-laser ablation together with optical spectroscopy or mass spectrometry. The latter also permits the dating of organic materials via the carbon ^{14}C method.

Numerous conference proceedings, special issues of regular journals and review articles have been published in this field [LACONA (Lasers in the Conservation of Artworks) conference proceedings; *Casadio* et al. 2010; *Kautek* 2010, 2008; *Chiari* et al. 2008; *Zafiropulos* 2002]. Subsequently, we give a very brief overview on various different aspects and applications.

32.1 Cultural Heritages

The cleaning of the cathedrals Notre Dame in Paris and St. Stephan in Vienna, or the town hall in Rotterdam are only a few of the numerous examples where laser cleaning has been applied for the removal of contamination layers from whole buildings. These are formed on sandstone by acid rain according to the reactions

$$CaCO_3 + 2\,H^+ \rightarrow Ca^{2+} + CO_2 + H_2O$$

and

$$Ca^{2+} + {SO_4}^{2-} + 2H_2O \rightarrow CaSO_4\ (\text{plaster}) + 2\,H_2O \qquad (32.1.1)$$

Thus, the binding agent in sandstone, lime, is dissolved and transformed into plaster. The plaster, together with soot and other atmospheric contaminants forms the grey/black layer on sandstone buildings, sculptures and reliefs, including those

D. Bäuerle, *Laser Processing and Chemistry,* 4th ed.,
DOI 10.1007/978-3-642-17613-5_32, © Springer-Verlag Berlin Heidelberg 2011

made from marble. Laser ablation permits to clean off such contamination layers in a quite well defined and gentle way. In most cases, 1064 nm Nd:YAG-laser radiation is employed. While sandblasting *increases* the porosity on the stone surface and thus enhances recontamination, laser cleaning decreases the surface porosity. Laser cleaning of stone is mainly based on thermomechanical ablation, as discussed in Sect. 12.10.

32.1.1 Metal Artworks

Sculptures, reliefs, jewelry, coins, etc. made from copper, bronze or other metal alloys, can be cleaned from physical and chemical contamination layers. Among the latter are oxides, carbonates, sulfates, chlorides, etc. Depending on the particular type of contamination, cleaning is based on laser-induced vaporization or ablation (Chaps. 11, 12 and 13). In both cases, the cleaning process is self-terminated. When using the correct laser parameters, the process stops when the metal surface is reached. The absorbed laser fluence is then too low to evaporate/ablate the (highly reflecting) metal surface. While the threshold fluence for organic contaminants and soot is very low, for excimer laser radiation typically a few mJ/cm^2, metal carbonates and oxides are much more stable. Because of the high heat diffusivity of metals and/or the low absorptivity of contamination layers, most well-defined material removal is achieved with ultrashort-pulse lasers (Chap. 13). For example, for copper and bronze, the threshold fluence for 780 nm 150 fs-laser pulses is 2–3 J/cm^2. For copper oxides ϕ_{th} is more than a factor of two and for carbonates more than a factor of three times lower [*Barcikowski* et al. 2006].

32.1.2 Oil-paintings, Frescos

Lasers permit to clean frescos and oil-paintings from contamination layers and/or to remove overpaints. Figure 32.1.1 shows an ikon that has been cleaned from a contamination layer by means of KrF-laser radiation. By using optimized laser parameters, gentle and well-defined successive ablation of contamination layers, overpaintings, degraded varnish layers, etc. with an accuracy of a few nanometers or even better can be achieved. None of these applications requires mechanical and/or chemical treatments. For the removal of varnish layers, excimer-lasers are almost ideal sources [*Bounos* et al. 2007]. The UV radiation of excimer lasers is well absorbed by most types of contaminants and varnishes, and the pulse length, typically 20 ns, is short enough to avoid thermal damage of the remaining material (Chap. 12). Thus, the original oil colors are neither photochemically nor thermally damaged.

Fig. 32.1.1 Ikon that has been cleaned using KrF excimer laser radiation (FORTH Group: C. Fotakis, S. Georgiou, V. Zafiropulos)

32.2 Analysis and Origin of Artworks

Destruction-free chemical analysis of artwork is of particular interest for clarifying the composition of oil colors as, e.g., the famous bright Tizian colors, or the composition of the lacquer of a Stradivari-violin, etc. Additionally, the exact chemical composition of lacquers, paints and varnishes is like a fingerprint. It is unique. Thus, such an analysis can be used to examine the authenticity of artwork. In all of these cases, laser ablation in combination with LIBS [*Anglos* and *Miller* 2006] and/or mass spectrometry is particularly suitable. Because ablation is stoichiometric, it can be used for any material, and it requires only tiny amounts of material, typically a few μm^3. Prehistorical artwork that consists in part or in total of organic material can be dated via the isotope ratio $^{14}C/^{12}C$ by using laser ablation together with mass spectrometry.

32.3 Architecture, Modern Artwork

Lasers are increasingly applied for the design and prototyping in architecture, sculpture, and in different types of modern art. Material removal is based on melting and/or vaporization, or ablation (Chaps. 10, 11, 12 and 13). Together with CAD

techniques, lasers permit 3D-cutting and shaping of any material including thin foils. Additionally, laser techniques open up completely *new* possibilities for artists. Among those are holographic techniques, the fabrication of 3D structures by laser-induced transformations within the volume of transparent materials (Sect. 23.6), by laser sintering (Sect. 25.1), stereolithography (Sect. 27.2), etc.

Appendix A
Definitions and Symbols

A.1 Symbols and Conversion Factors

A	absorptivity
a	distance
	aperture
b	net increase in number of molecules per formula unit; $b = \mu - 1$
C	constant
C	Euler's constant; C = 0.577
C_p	heat capacity
c	speed of light; $c = 2.998 \times 10^{10}$ cm/s
c_p	specific heat at constant pressure [J/gK, J/molK]
c_v	specific heat at constant volume [J/gK, J/molK]
D	heat diffusivity [cm^2/s]
	transmittivity
D_i	molecular diffusion coefficient of species i [cm^2/s]
d	lateral width of laser-processed features [μm, cm]
	diameter
E	electric field [V/cm]
	energy [J]
	$k_\mathrm{B}T\,(T = 273.15\,\mathrm{K}) = 2.354 \times 10^{-2}\,\mathrm{eV}$
	$1\,\mathrm{kcal/mol} \mathrel{\widehat{=}} 0.043\,\mathrm{eV} \mathrel{\widehat{=}} 5.035 \times 10^2\,\mathrm{K}$
	$1\,\mathrm{eV} \mathrel{\widehat{=}} 1.1604 \times 10^4\,\mathrm{K} \mathrel{\widehat{=}} 1.602 \times 10^{-19}\,\mathrm{J}$
	$1\,\mathrm{kcal} \mathrel{\widehat{=}} 4.187 \times 10^3\,\mathrm{J}$
	$1\,\mathrm{cm}^{-1} \mathrel{\widehat{=}} 1.24 \times 10^{-4}\,\mathrm{eV} \mathrel{\widehat{=}} 1.439\,\mathrm{K}$
	$1\,\mathrm{J} \mathrel{\widehat{=}} 2.39 \times 10^{-4}\,\mathrm{kcal}$
E_F	Fermi energy
$\mathscr{E}$	activation temperature [K]; $\mathscr{E} = \Delta E / k_\mathrm{B}$
$\mathscr{E}^*$	normalized activation temperature; $\mathscr{E}^* = \mathscr{E} / T(\infty)$
ΔE	activation energy [eV; kcal/mol]
ΔE_m	activation energy for melting
ΔE_v	activation energy for vaporization at T_b

D. Bäuerle, *Laser Processing and Chemistry,* 4th ed.,
DOI 10.1007/978-3-642-17613-5, © Springer-Verlag Berlin Heidelberg 2011

E_g	bandgap energy = energy distance between (lowest) conduction and (highest) valence bands
E_ℓ	laser-pulse energy [J]
e	elementary charge; $e = 1.602 \times 10^{-19}$ C
e	$e \approx 2.718$
eV	electron Volt 1 eV/particle = 23.04 kcal/mol
F	area Faraday constant; $F = 96485$ C/mol
f	focal length [cm]
$\mathscr{G}_r$	Grashof number
ΔG	Gibbs free energy
$\boldsymbol{g}$	acceleration due to gravity
g_T	temperature discontinuity coefficient
ΔH	total enthalpy [J/cm^3, J/g, J/mol] reaction enthalpy ΔH^a [J/atom] $= \Delta H$ [J/cm^3] $\cdot\, M/\rho L$ $= \Delta H$ [J/g] $\cdot\, M/L = \Delta H$ [J/mol]$/L$
ΔH_v	heat of vaporization at T_b
ΔH_m	heat of melting
ΔH_t	total latent heat $\Delta H_t = \Delta H_m + \Delta H_v$
h	Planck's constant; $h = 6.626 \times 10^{-34}$ Js height, thickness or depth of laser-processed patterns [Å, μm]
h_1	thickness of single evaporated or sputtered layer on a substrate
h_i	thickness of layer i on a substrate
h_l	thickness of a liquid layer, or an adsorbate
h_s	thickness of slab or substrate
Δh	change in layer thickness ablated layer thickness per pulse [Å/pulse]
$h\nu$	photon energy $h\nu$[eV] $\approx 1240/\lambda$[nm]
I	intensity [W/cm^2]
I_a	absorbed laser-light intensity
I_{th}	threshold intensity
I_v	evaporation intensity
J	flux
J_i	flux of species i [species/cm^{2}s]
j	current density
K	force
k	kinetic (rate) constant
k_0	pre-exponential factor
k_B	Boltzmann constant; $k_B = 1.381 \times 10^{-23}$ Ws/K
k_i^{rec}	recombination constant for species i
k_ℓ	wavevector of laser radiation
k_T	thermal diffusion ratio

L Avogadro number (Loschmidt number); $L = 6.022 \times 10^{23}$ /mol
L Langmuir [$1\,\mathrm{L} = 10^{-6}$ Torr s]
l characteristic length, depth [μm]
l_T heat-diffusion length [μm]
l_α optical penetration depth [μm]; $l_\alpha = \alpha^{-1}$
M molar mass [g/mol]
m mass
exponent, e.g., in $\kappa(T)$
N total number of species (atoms, molecules, electrons, holes, etc.) per volume [cm^{-3}] or per area [cm^{-2}]
N_i number of species i per volume [cm^{-3}] or per area [cm^{-2}]
N_ℓ number of laser pulses
n refractive index (real part)
exponent, e.g., in $D_i(T)$
$\boldsymbol{n}$ normal vector
$\hat{\boldsymbol{n}}$ unit vector
$\tilde{n}$ complex refractive index; $\tilde{n} = \sqrt{\varepsilon} = n + \mathrm{i}\kappa_a \equiv n(1 + \mathrm{i}\kappa_0)$
P laser power [W]
P_a absorbed laser power [W]
p total gas pressure [mbar]
$1\,\mathrm{mbar} \mathrel{\widehat{=}} 10^2\,\mathrm{N/m^2} \mathrel{\widehat{=}} 10^2\,\mathrm{Pa} \approx 0.750\,\mathrm{Torr} \mathrel{\widehat{=}} 1.02 \times 10^{-3}\,\mathrm{at[kp/cm^2]}$
$\mathrel{\widehat{=}} 9.87 \times 10^{-4}\,\mathrm{atm}$
$1\,\mathrm{atm} \mathrel{\widehat{=}} 2.688 \times 10^{19}\mathrm{[species/cm^3]}$
p_i partial pressure of species i [mbar]
Q source term
q exponent, e.g., in equation of state
$\boldsymbol{q}$ wavevector
R optical (power) reflectivity
electrical resistance [Ω]
$\mathscr{R}$ sheet resistance [$\Omega/\square$]
R_D optical reflection coefficient of deposited material
R_G gas constant; $R_\mathrm{G} = 8.314\,\mathrm{J/Kmol} \mathrel{\widehat{=}} 1.987\,\mathrm{cal/K\,mol}$
$\mathscr{R}a$ Rayleigh number
r radial distance
r_D radius of deposit
S stress
oversaturation
$\boldsymbol{S}$ Poynting vector
energy flux [$\mathrm{J/cm^2 s}$]
s sticking coefficient
T temperature [K]
T_b boiling temperature
T_c center temperature

T_g	gas-phase temperature
T_l	temperature within liquid
T_M	temperature within medium
T_m	melting temperature
T_s	substrate temperature
	surface temperature
T_{st}	stationary temperature
T_{th}	threshold temperature
T_v	temperature of vapor
$T(\infty)$	temperature far away from irradiated zone
ΔT	temperature rise
T^*	normalized temperature, e.g., $T/T(\infty)$
t	time
t_v	time to reach T_{st} (Fig. 11.2.2)
Δt	time interval
Δt_m	time of existence of melt on surface
V	volume [cm^3]
V_n	volume per molecule/atom
v	velocity [cm/s]
	mass average velocity
v_{ls}	velocity of liquid–solid interface
v_{vl}	velocity of vapor–liquid interface
v_0	sound velocity
v_s	scanning velocity of laser beam or substrate [μm/s]
$\langle v \rangle$	thermal velocity of gas molecules
W	reaction rate
	heterogeneous reactions [number of species/s cm^2]
	homogeneous reactions [number of species/s cm^3]
W_A	ablation rate [μm/s; Å/pulse]
W_D	deposition rate [μm/s; Å/pulse]
W_E	etch rate [μm/s; Å/pulse]
W_{ex}	excitation rate
w	radius of laser focus with constant intensity distribution [μm]
	radius of laser focus at FWHM
w_e	radius of laser focus ($1/e^2$ intensity); $w_e = \sqrt{2} w_0$
w_0	radius of laser focus of Gaussian beam ($1/e$ intensity) [μm]
w'	probability
	width of reaction zone
x_i	molar ratio of species i; $x_i = N_i/N$
$\boldsymbol{x}$, x_α	set of space coordinates with $\alpha = 1, 2, 3$, e.g., x, y, z
Y	Young's modulus
Z	number of condensed atoms per molecule
z	charge of ions in units of e
z_R	Rayleigh length of laser focus [μm]

α	optical absorption coefficient [cm^{-1}]
α_T	thermal diffusion constant
β	exchange coefficient
	exponent
	parameter
	symmetry factor
	factor
β_T	coefficient of thermal expansion
Γ	increment
	parameter
	ratio
	aspect ratio [ratio of depth or height to width]; $\Gamma = h/d$
γ	exponent
	total reaction order
	adiabatic index; $\gamma = c_\mathrm{p}/c_\mathrm{v}$; $1 < \gamma \leq 5/3$
	real part of increment
γ_i	reaction order with respect to species i
Δ	difference
δ	delta function
	parameter
ε	dielectric constant
	permittivity
	spectral emissivity
ε_a	apparent emissivity
ε_0	dielectric constant in vacuum; $\varepsilon_0 = 8.854 \times 10^{-12}\,\mathrm{As/Vm}$
ε_t	total emissivity
ζ	parameter
	integer
	factor
ζ_i	stoichiometric coefficient of species i
η	dissociation yield
	dynamic viscosity [g/cm s]; $\eta = \rho\nu_\mathrm{k}$
	reaction probability
	surface conductance [coefficient of surface heat transfer] [$\mathrm{W/cm^2K}$]
Θ	angle
θ	linearized temperature
θ_c	center-temperature rise for Gaussian beam; $\theta_\mathrm{c} = \sqrt{\pi}\, I_\mathrm{a} w_0/2\kappa$, see (7.1.4)
Θ_i	coverage by species i
ϑ	angle
κ	thermal conductivity [W/cm K]; $1\,\mathrm{W/m\,K} \mathrel{\widehat{=}} 2.39 \times 10^{-3}\,\mathrm{cal/cm\,K\,s}$
κ_a	absorption index $\kappa_\mathrm{a} = n\kappa_0$
κ_D	thermal conductivity of deposit
κ_L, κ_1	thermal conductivity of thin layer

κ_M	thermal conductivity of medium
κ_s	thermal conductivity of substrate
κ_0	attenuation index
Λ	parameter
	spacing
	function
λ	wavelength of electromagnetic radiation [nm, μm]
	λ[nm] $\approx 1240/h\nu$ [eV]
λ_m	mean free path of molecules [cm]
μ	factor
	index
	integer
	chemical potential
	Poisson ratio
	$\mu = b + 1$
μ_e, μ_h	mobility of electrons and holes [cm^2/Vs]
ν	frequency [s^{-1}]
	index
ν_k	kinematic viscosity [cm^2/s]
ν_r	laser-pulse-repetition rate [Hz]
ξ	overpotential
	parameter
$\prod$	product
	parameter
π	3.14159
ρ	electrical resistivity [Ω cm]
	mass density [g/cm^3]
$\sum$	summation sign
$\sum_{\pm}$	e.g., $a \pm b \mp c \equiv (a + b - c) + (a - b + c)$
σ	electrical conductivity [Ω cm]$^{-1}$
	surface tension [J/cm^2]
	excitation cross section of species [cm^2]
σ_r	Stefan–Boltzmann constant; $\sigma_r = 5.67 \times 10^{-12}$ W/cm^2K^4
τ	relaxation time [s]
τ_ℓ	laser-pulse duration [s]
	laser-beam dwell time [s]; $\tau_\ell = 2w/v_s$
τ_m	time for surface melting
τ_T	thermal relaxation time [s]
Φ	electrical potential
ϕ	laser fluence [J/cm^2]
	angle
ϕ_{th}	threshold fluence
φ	angle

χ	magnetic susceptibility
	parameter
Ψ	function
ψ	wave function
Ω	total solid angle; $\Omega = 4\pi$
	Ohm
$d\Omega$	solid angle [sr]
ω	angular frequency [s^{-1}]; $\omega = 2\pi\nu$
$\perp$	normal (perpendicular)
$\parallel$	parallel
∇^2	Laplace operator
∇	Nabla operator

A.2 Abbreviations, Acronyms

acac	$[CH_3COCHCOCH_3]^-$ = acetylacetonate anion
AdGC	allyl-diglycol-carbonate
AES	Auger electron spectroscopy
ALE	atomic layer epitaxy
AM1	sunlight illumination
APD	ablative photodecomposition
BBS	barium aluminum borosilicate
BK7	boron crown glass
CAD	computer-aided design
CAM	computer-aided manufacturing
CARS	coherent anti-Stokes Raman scattering
CBE	chemical beam epitaxy
CCD	charge-coupled device
CMR	colossal magnetoresistance, same as GMR
CPA	chirped-pulse amplification
CVD	chemical vapor deposition
DLC	diamond-like carbon; dry laser cleaning
EAL	etching of atomic layers; excimer-laser ablation lithography
EB	electron beam
EBCVD	electron-beam-induced chemical vapor deposition
EBE	electron-beam evaporation
EDX	energy-dispersive X-ray analysis
EELS	electron-energy-loss spectroscopy
EMF	electromotive force
ESCA	electron spectroscopy for chemical analysis
ESR	electron spin resonance
FEP	tetrafluoroethylene-hexafluoropropylene
FH	fourth harmonic
Foturan	lithium aluminosilicate glass doped with (photoactive) Ce

FWHM	full width at half maximum
GMR	giant magnetoresistance
HAZ	heat-affected zone
hfacac	$[CF_3COCHCOCF_3]^-$ = hexafluoroacetylacetonate anion
HPDS	hexaphenyldisilane
HTS	high-temperature superconductors
HV	high vacuum ($10^{-7} < p < 10^{-3}$ mbar)
IBAD	ion-beam assisted deposition
IC	integrated circuit
IR	infrared radiation
ITO	indium tin oxide
Kapton	polyimide (Du Pont)
LA	laser annealing
LAL	laser-ablation lithography
LC	laser cleaning; liquid crystal
LCP	laser-induced chemical processing
LCVD	laser-induced CVD
LEC	laser-enhanced electrochemistry
LEE	laser-enhanced electrochemical etching
LEED	low-energy electron diffraction
LEP	laser-enhanced electrochemical plating
LI	laser implantation
LID	laser-induced desorption
LIF	laser-induced fluorescence
LIFT	laser-induced forward transfer
LIS	laser isotope separation
LMBE	laser molecular beam epitaxy
LPCVD	laser-enhanced PCVD
LPE	laser-enhanced plasma etching
LPPC	laser-pulsed plasma chemistry
LSA	laser-surface alloying
LSAW	laser-supported absorption wave
LSCW	laser-supported combustion wave
LSD	laser-sputter deposition
LSDW	laser-supported detonation wave
MALDI	matrix-assisted laser desorption ionization
MBE	molecular beam epitaxy
ME	metal
ML	multiline operation of laser monolayer
MMA	methylmethacrylate
MOCVD	metal-organic CVD
MP	multiphoton
MPA	multiphoton absorption
MPD	multiphoton dissociation

MPI	multiphoton ionization
Mylar	same as PET
NC	nitrocellulose
NEP	noise equivalent power
NIR	near IR
OMA	optical multichannel analyzer
PA	polyamide
PAN	polyacrylonitrile
PC	polycarbonate
PCVD	plasma CVD
PE	plasma etching
	polyethylene
PEEK	polyetheretherketone
PEO	polyethylene oxide
PES	polyethersulfone
PET	polyethylene-terephthalate (same as Mylar)
PI	polyimide [Kapton, Upilex]
PL	photoluminescence
PLA	pulsed-laser annealing
PLD	pulsed-laser deposition
PLE	pulsed-laser evaporation
PLPC	pulsed-laser plasma chemistry
PLZT	lanthanum-doped PZT, i.e., $Pb_{1-3y/2}La_yTi_{1-x}Zr_xO_3$
PMMA	polymethyl-methacrylate (Plexiglas)
PP	polypropylene
PPQ	poly(phenyl-quinoxaline)
pps	pulses per second
PS	polystyrene
PSL	polystyrene latex
PSUL	polysulfone
PTFE	polytetrafluoroethylene (Teflon)
PU	polyurethane
PVAC	polyvinylacetate
PVC	polyvinyl chloride
PVDF	polyvinylidene fluoride
PXE	same as PZT ($PbTi_{1-x}Zr_xO_3$)
Pyrex	borosilicate glass (80% SiO_2, 12% B_2O_3, 3% Al_2O_3, 4% Na_2O)
PZT	lead titanate zirconate $PbTi_{1-x}Zr_xO_3$
QCM	quartz-crystal microbalance
QMS	quadrupole mass spectrometer
RBS	Rutherford backscattering spectroscopy
RF	radio frequency
RHEED	reflection high-energy electron diffraction
RIE	reactive ion etching
rms	root mean square

RTA	rapid thermal annealing
SAW	surface acoustic wave
SEM	scanning electron microscopy
SERS	surface-enhanced Raman scattering
SEW	surface electromagnetic wave
SH	second harmonic
SI	semi-insulating
SIMS	secondary ion mass spectroscopy
SLC	steam laser cleaning
SNOM	scanning near-field optical microscopy
SOI	silicon on insulator
SOS	silicon on sapphire
SQUID	superconducting quantum interference device
SRR	split ring resonator
STE	self-trapped exciton
STED	stimulated emission depletion
SXM	scanning-probe microscopy
TEM	transmission electron microscopy
TEOS	tetraethylorthosilicate
TFT	thin-film transistor
TG	thermogravimetry
TH	third harmonic
TiBAl	$Al(C_4H_9)_3$
TM	trade mark
TMVS	trimethylvinylsilane
TOF	time-of-flight
UHV	ultrahigh-vacuum ($p < 10^{-7}$ mbar)
ULSI	ultra-large-scale integrated systems
UPS	ultraviolet photo-spectroscopy
UV	ultraviolet radiation
VIS	visible radiation
VLSI	very-large-scale integrated systems
VUV	vacuum UV
XAFS	X-ray absorption fine structure spectroscopy
XPS	X-ray photoemission spectroscopy
XRD	X-ray diffraction
YBCO	$YBa_2Cu_3O_{7-\delta}$
YSZ	8 mol % Y_2O_3 stabilized ZrO_2

Appendix B
Mathematical Functions and Relations

Bessel Function

$$\mathbf{J}_n(x) = \frac{1}{\pi}\int_0^{\pi} \cos(x\cos\zeta - n\zeta)\,\mathrm{d}\zeta = \frac{\mathrm{i}^{-n}}{\pi}\int_0^{\pi} \exp(\mathrm{i}x\cos\zeta)\cos n\zeta\,\mathrm{d}\zeta$$

$$\mathbf{J}_n(x \ll 1) \approx x^n\left(\frac{1}{2^n n!} - \frac{x^2}{2^{n+2}(n+1)!} + \frac{x^4}{2^{n+4}(n+2)!} + \cdots\right)$$

$$\mathbf{J}_n(x \gg 1) \approx \left(\frac{2}{\pi x}\right)^{1/2}\left\{\cos\left[\left(\frac{n}{2}+\frac{1}{4}\right)\pi - x\right] + \cdots\right\}$$

Modified Bessel function $\mathbf{I}_n(x)$ of order n

$$\mathbf{I}_n(x) = (-1)^n\mathbf{I}_n(-x) = \frac{1}{\pi}\int_0^{\pi} \exp(x\cos\zeta)\cos n\zeta\,\mathrm{d}\zeta$$

$$\mathbf{I}_0(x \ll 1) \approx 1 + \frac{x^2}{4} + \frac{x^4}{64} + \cdots$$

$$\mathbf{I}_0(x \gg 1) \approx \frac{1}{(2\pi x)^{1/2}}\left(1 + \frac{1}{8x} + \frac{9}{128x^2} + \cdots\right)\exp x$$

Modified Bessel function $\mathbf{K}_n(x)$ of order n

$$\mathbf{K}_n(x > 0) = \int_0^{\infty} \exp(-x\cosh\zeta)\cosh n\zeta\,\mathrm{d}\zeta$$

$$\mathbf{K}_0(x \ll 1) = -\ln\left(\frac{x}{2}\right) - \mathrm{C} - \frac{x^2}{4}\ln x + \cdots$$

$$\mathbf{K}_1(x \ll 1) = \frac{1}{x} + \frac{x}{2}\ln\left(\frac{x}{2}\right) + \frac{x}{2}\left(\mathrm{C} - \frac{1}{2}\right) + \cdots$$

$$\mathbf{K}_n(x \gg 1) = \left(\frac{\pi}{2x}\right)^{1/2}\left(1 + \frac{4n^2-1}{8x} + \frac{(4n^2-1)(4n^2-9)}{128x^2} + \cdots\right)\exp(-x)$$

$\mathrm{C} = 0.577$ is Euler's constant

Error Function

$$\operatorname{erf} x = -\operatorname{erf}(-x) = \frac{2}{\sqrt{\pi}} \int_0^x \exp(-\zeta^2)\, \mathrm{d}\zeta$$

$$\operatorname{erf}(x \ll 1) \approx \frac{2x}{\pi^{1/2}} - \frac{2x^3}{3\pi^{1/2}} + \frac{x^5}{5\pi^{1/2}} + \cdots$$

$$\operatorname{erf}(x \gg 1) \approx 1 + \left(-\frac{1}{\pi^{1/2} x} + \frac{1}{2\pi^{1/2} x^3} - \cdots \right) \exp(-x^2)$$

Complementary error function

$$\operatorname{erfc} x = 1 - \operatorname{erf} x = \frac{2}{\pi^{1/2}} \int_x^\infty \exp(-\zeta^2)\, \mathrm{d}\zeta$$

$$\operatorname{erfc}(x \ll 1) \approx 1 - \frac{2x}{\pi^{1/2}} - \frac{2x^3}{3\pi^{1/2}} - \cdots$$

$$\operatorname{erfc}(x \gg 1) \approx \left(\frac{1}{\pi^{1/2} x} - \frac{1}{2\pi^{1/2} x^3} + \frac{3}{4\pi^{1/2} x^5} - \cdots \right) \exp(-x^2)$$

$$\mathrm{i}^{-1} \operatorname{erfc} x = \frac{2}{\pi^{1/2}} \exp(-x^2)$$

$$\mathrm{i}^{0} \operatorname{erfc} x = \operatorname{erfc} x$$

$$\mathrm{i} \operatorname{erfc} x = \frac{\exp(-x^2)}{\pi^{1/2}} - x \operatorname{erfc} x$$

$$\mathrm{i}^{2} \operatorname{erfc} x = \frac{1}{4} (\operatorname{erfc} x - 2x \,\mathrm{i} \operatorname{erfc} x)$$

$$\mathrm{i}^{n} \operatorname{erfc} x = \int_x^\infty \mathrm{i}^{n-1} \operatorname{erfc} \zeta \, \mathrm{d}\zeta = -\frac{x}{n} \mathrm{i}^{n-1} \operatorname{erfc} x + \frac{1}{2n} \mathrm{i}^{n-2} \operatorname{erfc} x$$

Exponential Integral Function

$$\operatorname{Ei}(x < 0) = -\int_{-x}^\infty \zeta^{-1} \exp(-\zeta)\, \mathrm{d}\zeta$$

$$\operatorname{Ei}(x > 0) = -\mathscr{P} \int_{-x}^\infty \zeta^{-1} \exp(-\zeta)\, \mathrm{d}\zeta \quad (\mathscr{P} \text{ stands for principal value})$$

$$\operatorname{Ei}(x \ll 1) \approx \mathrm{C} + \ln|x| + x + \cdots$$

$$\operatorname{Ei}(x \gg 1) \approx \left(\frac{1}{x} + \frac{1}{x^2} + \frac{2}{x^3} + \cdots \right) \exp(x)$$

Gamma Function

$$\Gamma(x) = \int_0^\infty \zeta^{x-1} \exp(-\zeta)\,\mathrm{d}\zeta$$
$$\Gamma(n) = (n-1)!\,, \quad \Gamma(x+1) = x\Gamma(x)$$
$$\Gamma(1) = 0! = 1$$
$$\Gamma(x \ll 1) \approx \frac{1}{x} - \mathrm{C} + \left(\frac{\mathrm{C}^2}{2} + \frac{\pi^2}{12}\right) x + \cdots$$
$$\Gamma(x \gg 1) \approx \left(\frac{x}{\mathrm{e}}\right)^x \left(\frac{2\pi}{x}\right)^{1/2} \left(1 + \frac{1}{12x} + \cdots\right)$$

Heaviside Function

$$\mathscr{H}(x) = \begin{cases} 0 \text{ if } x \le 0 \\ 1 \text{ if } x > 0 \end{cases}$$

Jacobian Theta Function

$$\theta_3^{\mathrm{J}}[u|\exp(-\beta)] = \theta_3^{\mathrm{J}}(u) = 1 + 2\sum_{n=1}^{\infty} \cos(2nu)\exp(-\beta n^2)$$
$$= \left(\frac{\pi}{\beta}\right)^{1/2} \sum_{n=-\infty}^{+\infty} \exp\left(-\frac{(u - n\pi)^2}{\beta}\right)$$

$$\theta_3^{\mathrm{J}}(u|\beta \gg 1) \approx 1 + 2\exp(-\beta)\cos(2u) + \cdots$$

The $\mathscr{F}$-Function

The temperature distribution along the axis of laser-beam propagation (z-direction) is determined by the $\mathscr{F}$-function only. This function depends on the absorption coefficient α^*, the heat loss described by η^*, and the thickness of the substrate (Fig. 6.1.1). Interference effects are ignored (Chap. 8). The $\mathscr{F}$-function can be written in the form

$$\mathscr{F}(z^*, t_1^*) = \alpha^* \sum_{n=-\infty}^{\infty} \mathrm{F}_n(z^*, t_1^*)$$
$$= \alpha^* \left(\mathrm{F}_0(z^*, t_1^*) + 2 \sum_{n=1}^{\infty} \mathrm{F}_n(z^*, t_1^*) \right) \tag{B.1}$$

with

$$\mathrm{F}_n(z^*, t_1^*) = A_n f_n(z^*, t_1^*) \,, \tag{B.2}$$
$$f_n(z^*, t_1^*) = B_n Z_n(z^*) \exp(-\nu_n^2 t_1^*)$$
$$= B_n \left(\cos(\nu_n z^*) + \frac{\eta^*}{\nu_n} \sin(\nu_n z^*) \right) \exp(-\nu_n^2 t_1^*) \,, \tag{B.3}$$

$$B_n = \frac{\nu_n^2}{h_\mathrm{s}^*(\nu_n^{*2} + \eta^{*2}) + 2\eta^*} \,.$$

ν_n are the roots of

$$\tan(h_\mathrm{s}^* \nu_n) = \frac{2\eta^* \nu_n}{\nu_n^2 - \eta^{*2}} \,. \tag{B.4}$$

The coefficients A_n in (B.2) are given by

$$A_n = \int_0^{h_\mathrm{s}^*} Z_n(z_1^*) \exp(-\alpha^* z_1^*) \, \mathrm{d}z_1^*$$
$$= \frac{1}{\alpha^{*2} + \nu_n^2} \Big[(\alpha^* + \eta^*)(1 - \cos(\nu_n h_\mathrm{s}^*) \exp(-\alpha^* h_\mathrm{s}^*))$$
$$+ \frac{\nu_n^2 - \alpha^* \eta^*}{\nu_n} \sin(\nu_n h_\mathrm{s}^*) \exp(-\alpha^* h_\mathrm{s}^*) \Big] \,. \tag{B.5}$$

In the following, we discuss some limiting cases for infinite slabs and semi-infinite substrates.

Axial Temperature Distribution for Infinite Slabs

Case 1: $\alpha^* \neq \infty$, $\eta^* = 0$

For finite absorption we obtain from (B.4) in the absence of heat losses for a slab of thickness h_s

$$\tan(\nu_n h_\mathrm{s}^*) = 0 \quad \text{or} \quad \nu_n h_\mathrm{s}^* = n\pi \quad \text{with} \quad n = 0, \pm 1, \pm 2, \ldots$$

Thus, (B.3) and (B.5) yield

$$f_n(z^*, t_1^*) = \frac{1}{h_s^*} \cos\left(n\pi \frac{z^*}{h_s^*}\right) \exp\left(-\frac{n^2\pi^2}{h_s^{*2}} t_1^*\right) ,$$
$$A_n = \frac{\alpha^* h_s^{*2}}{\alpha^{*2} h_s^{*2} + n^2\pi^2} [1 - (-1)^n \exp(-\alpha^* h_s^*)] .$$

The $\mathscr{F}$-function can then be written as

$$\mathscr{F}(z^*, t_1^*) = \frac{1}{h_s^*}\Bigg[[1 - \exp(-\alpha^* h_s^*)] + 2\sum_{n=1}^{\infty} \frac{\alpha^{*2} h_s^{*2}}{\alpha^{*2} h_s^{*2} + n^2\pi^2} [1 - (-1)^n \exp(-\alpha^* h_s^*)] \times \cos\left(n\pi \frac{z^*}{h_s^*}\right) \exp\left(-\frac{n^2\pi^2}{h_s^{*2}} t_1^*\right)\Bigg] . \tag{B.6}$$

In the limit $t_1^* \to \infty$ ($t_1^* \gg h_s^{*2}/\pi^2$), we obtain

$$\mathscr{F}(z^*, t_1^*) \to \mathscr{F} = \frac{1}{h_s^*} [1 - \exp(-\alpha^* h_s^*)] .$$

Case 2: $\alpha^* \to \infty, \eta^* \neq 0$

For surface absorption and finite heat losses, we obtain from (B.5) $\lim_{\alpha^* \to \infty} [\alpha^* A_n] = 1$ and thus

$$\mathscr{F}(z^*, t_1^*) = \sum_{n=-\infty}^{\infty} f_n(z^*, t_1^*) , \tag{B.7}$$

where f_n is given by (B.3).

Case 3: $\alpha^* \to \infty, \eta^* = 0$

With surface absorption and no heat losses, the $\mathscr{F}$-function becomes

$$\mathscr{F}(z^*, t_1^*) = \frac{1}{h_s^*} \boldsymbol{\theta}_3^{\mathrm{J}} \left[\frac{\pi z^*}{2h_s^*} | \exp\left(-\frac{\pi^2 t_1^*}{h_s^{*2}}\right)\right] , \tag{B.8}$$

where $\boldsymbol{\theta}_3^{\mathrm{J}}$ is the Jacobian theta function.

Axial Temperature Distribution for Semi-infinite Substrates

To obtain the temperature distribution along the z-axis for semi-infinite substrates, we have to consider the $\mathscr{F}$-function (B.1) in the limit $h_s^* \to \infty$. This yields

$$\begin{aligned}\mathscr{F}(z^*, t_1^*) = \frac{1}{2}\alpha^* \exp(\alpha^{*2} t_1^*) \Bigg[& \exp(\alpha^* z^*)\ \operatorname{erfc}\left(\alpha^* t_1^{*1/2} + \frac{z^*}{2t_1^{*1/2}}\right) \\ & + \exp(-\alpha^* z^*)\ \operatorname{erfc}\left(\alpha^* t_1^{*1/2} - \frac{z^*}{2t_1^{*1/2}}\right)\Bigg] \\ & - \frac{\alpha^* \eta^*}{\sqrt{\pi}(\eta^* - \alpha^*)} \int_0^{t_1^*} \frac{\mathrm{d}t_2^*}{(t_1^* - t_2^*)^{1/2}} \exp\left(-\frac{z^{*2}}{4(t_1^* - t_2^*)}\right) \\ & \times [\eta^* \exp(\eta^{*2} t_2^*)\ \operatorname{erfc}(\eta^* t_2^{*1/2}) \\ & - \alpha^* \exp(\alpha^{*2} t_2^*)\ \operatorname{erfc}(\alpha^* t_2^{*1/2})] \,. \end{aligned} \tag{B.9}$$

We now discuss some special cases of (B.9).

Case 1: $\eta^* = 0$

In the absence of heat losses, (B.9) yields

$$\begin{aligned}\mathscr{F}(z^*, t_1^*) = \frac{1}{2}\alpha^* \exp(\alpha^{*2} t_1^*) \Bigg[& \exp(\alpha^* z^*)\ \operatorname{erfc}\left(\alpha^* t_1^{*1/2} + \frac{z^*}{2t_1^{*1/2}}\right) \\ & + \exp(-\alpha^* z^*)\ \operatorname{erfc}\left(\alpha^* t_1^{*1/2} - \frac{z^*}{2t_1^{*1/2}}\right)\Bigg] \,. \end{aligned} \tag{B.10}$$

Case 2: $\alpha^* \to \infty$, $\eta^* \neq 0$

With surface absorption and finite heat losses (B.9) yields

$$\begin{aligned}\mathscr{F}(z^*, t_1^*) = & \frac{1}{(\pi t_1^*)^{1/2}} \exp\left(-\frac{z^{*2}}{4t_1^*}\right) \\ & - \frac{\eta^*}{\sqrt{\pi}} \int_0^{t_1^*} \mathrm{d}t_2^* \frac{1}{(t_1^* - t_2^*)^{1/2}} \exp\left(-\frac{z^{*2}}{4(t_1^* - t_2^*)}\right) \\ & \times \left(\frac{1}{(\pi t_2^*)^{1/2}} - \eta^* \exp(\eta^{*2} t_2^*)\ \operatorname{erfc}(\eta^* t_2^{*1/2})\right) \,, \end{aligned} \tag{B.11}$$

where we have used the approximation for $\operatorname{erfc}(x \gg 1)$.

Case 3: $\alpha^* \to \infty, \eta^* = 0$

With surface absorption, one obtains from (B.11) in the absence of heat losses

$$\mathscr{F}(z^*, t_1^*) = \frac{1}{(\pi t_1^*)^{1/2}} \exp\left(-\frac{z^{*2}}{4t_1^*}\right) . \tag{B.12}$$

This equation can also be obtained from (B.8) with $h_s^* \to \infty$. All terms in the Jacobian theta function vanish, except that for $n = 0$.

Appendix C
Tables

Table I Commercial lasers most commonly used in materials processing. Only the strongest lines are listed. The wavelengths are given in nanometers, if not otherwise indicated. The corresponding (rounded) photon energies are given in parentheses; the conversion is λ (nm) $= 1240/h\nu$ (eV). Wavelengths of higher harmonics are given in italics. Within the text, both laser wavelengths and photon energies are sometimes rounded

Laser	Wavelength, λ (nm) (Energy eV)
Gas Lasers	
F_2	157 (7.9)
ArF	193 (6.42)
KrCl	222 (5.58)
KrF	248 (5)
XeCl	308 (4.03)
XeF	351 (3.53)
N_2	337 (3.68)
HeCd	441.6 (2.81)
Ar^+	275–306 (4.51–4.05)
	334–364
	458–515
	457.9
	229
	476.5
	488.0 (2.54)
	244
	496.5
	501.7
	514.5 (2.41)
	257
	528.7
Kr^+	337−356
	413.1
	476.2
	520.8
	530.9
	568.2
	647.1 (1.92)
	676.4
	752.5

Table I (continued)

HeNe	632.8 (1.96)
Cu vapor	511 nm (2.43)
	578 nm (2.15)
	255.3
CO	5−7 μm (0.248−0.18)
CO_2	9−11 μm (0.14−0.11)
Semiconductor Lasers	
GaN	376 (3.30)
	402
	417
$Al_xGa_yIn_{1-x-y}P$	630−680 (1.97−1.82)
$Al_{1-x}Ga_xAs$	780−880 (1.59−1.41)
	430
$In_{1-x}Ga_xAs$	915–1060
	470–490
$In_{1-x}Ga_xAs_{1-y}P_y$	1150–1650 (1.08−0.75)
$Pb_{1-x}Eu_xSe$	3.5−8 μm
PbSe	8 μm (0.155)
$Pb_{1-x}Sn_xSe$	8−12.5 μm (0.155−0.10)
Other Solid-State Lasers	
Ruby[a]	694.3 (1.79)
Alexandrite[b]	701−820 (1.77−1.51)
Ti:sapphire[c]	670–1080 (1.85−1.15)
	780 (1.59)
Nd:glass	1062.3
Nd:YAG	1064.1 (1.17)
	532 (2.33)
	355 (3.50)
	266 (4.66)
	213 (5.82)
Nd:YLF[d]	1.047 μm (1.18)
	1.053 μm (1.18)
Ho:YAG	2.1 μm (0.59)
Er:YAG	2.94 μm (0.42)

[a] $Al_2O_3:Cr^{3+}$.
[b] $BeAl_2O_4:Cr^{3+}$.
[c] Al_2O_3:Ti.
[d] YLF yttrium lithium fluoride.

Table II Thermophysical properties of materials: ρ mass density; T_g glass temperature; T_m melting/decomposition temperature; T_b (at 1013 mbar) boiling temperature; c_p specific heat; κ thermal conductivity; D thermal diffusivity. If not otherwise indicated in parentheses, values of ρ, c_p, κ, and D refer to $T \approx 300\,\mathrm{K}$

Material	ϱ (g/cm^3)	T_m (K)	T_b (K)	c_p (J/gK)	$\kappa(T[\mathrm{K}])$ (W/cm K)	$D(T[\mathrm{K}])$ (cm^2/s)
Ag	10.5	1234	2483	0.23	4.28	1.72
					4.12 (500)	1.61 (500)
					3.75 (1000)	1.3 (1000)
					1.97 (2000)	
					1.91 (3000)	
Al	2.7	933	2730	0.90	2.37	1.03
				1.00 (1000)	2.35 (500)	0.88 (500)
				1.70 (1500)	0.96 (1500)	
AlAs	4.22	1323				
AlN	3.22	2673		0.78	2.5	0.83
Al_2O_3	4.0	2324		0.75	0.30	0.10
Al_2O_3 (cer.)	3.89	2340	3800	0.9	0.30	0.09
p-Al_2O_3					0.40	1.0
					0.20 (500)	0.048 (500)
					0.078 (1000)	0.016 (1000)
					0.06 (2000)	0.012 (2000)
AlP	3.81	>1873			1.3	
AlSb	6.1				0.57	
As_2S_3	3.43	579	980	0.50		
Au	19.3	1338	3080	0.13	3.17	1.22
					3.09 (500)	1.19 (500)
					2.78 (1000)	0.93 (1000)
					2.44 (1500)	
					1.20 (2000)	
					1.25 (3000)	

Table II (continued)

Material	ϱ (g/cm^3)	T_m (K)	T_b (K)	c_p (J/gK)	$\kappa(T\,[\mathrm{K}])$ (W/cm K)	$D(T\,[\mathrm{K}])$ (cm^2/s)
$BaTiO_3$	6.02	1891		0.49	0.062	0.023
Be	1.85	1556	2753	1.8	2.2 (273)	
					2.01	0.42
					0.96 (1000)	
BeO	3.03	2828	4173	1	3.0	0.99
Bi	9.8	544	1833	0.12	0.09	0.08
Bi-Sr-Ca-Cu-O		1160				≈ 0.5
BK7	2.51 ($T_g \approx 830$)			0.86		
BN	2.25	subl. 3273		0.81	1.80	0.99
C (graph.)	2.24	subl. 4098		0.71	20	12.58
					22.3 $\parallel$	
					0.11 $\perp$	
					11.3 (500) $\parallel$	
					0.05 $\perp$	
					5.3 (1000) $\parallel$	
					0.03 $\perp$	
					2.5 (2000) $\parallel$	
					0.01 $\perp$	
C (diam.)	3.52	>3822		0.50	20	11.36
Ca	1.55	1112	1735	0.65	2.01	2.00
CaF_2	3.18	1694	2723	0.85		
Cd	8.65	594	1038	0.23	0.95 (273)	0.47
CdS	4.82	1653		0.35	0.16	0.09
CdSe	5.81	1623		0.26		
CdTe	5.9	1354		0.21	0.06	0.05
Co	8.9	1768	3172	0.43	1.05 (273)	
					1.02	0.27
					0.74 (500)	

Table II (continued)

Material	ϱ (g/cm^3)	T_m (K)	T_b (K)	c_p (J/gK)	$\kappa(T[K])$ (W/cm K)	$D(T[K])$ (cm^2/s)
$CoSi_2$	4.9	1550		0.65		
Cr	7.2	2130	2945	0.46	0.97 (273)	
					0.95	0.29
					0.85 (500)	0.23 (500)
					0.65 (1000)	0.16 (1000)
					0.67 (1300)	
$CrSi_2$	5.0	1833		0.7		
Cu	8.94	1357	2840	0.39	4.0 (273)	1.14
				0.41 (500)	3.97	
				0.47 (1000)	3.88 (500)	1.04 (500)
					3.56 (1000)	0.85 (1000)
					1.82 (2000)	
					1.80 (3000)	
Brass (70% Cu; 30% Zn)	8.5			0.38	1.05	0.33
Fe	7.86	1808	3023	0.46	0.84 (273)	
					0.80	0.23
					0.62 (500)	0.15 (500)
					0.33 (1000)	
					0.32 (1500)	
					0.43 (2000)	
					0.46 (3000)	
Cast iron	7.4			0.57	0.56	0.12
Mild steel (0.1% C)	7.85			0.49	0.46	0.12
Stainless steel (304)	8.03	1712	3273	0.5	0.15	0.04
					0.16 (500)	
					0.25 (1000)	
$FeSi_2$	4.9	1485		0.67		

Table II (continued)

Material	ϱ (g/cm^3)	T_m (K)	T_b (K)	c_p (J/gK)	$\kappa(T[K])$ (W/cm K)	$D(T[K])$ (cm^2/s)
Ga	5.91	303	2676	0.36		
GaAs	5.32	1511		0.35	0.47	0.24
GaN	4.09	1738		0.88	1.7	
GaP	4.13	1681			1.0	
GaSb	4.79	1328			0.39	
Ge	5.34	1210	3104	0.32	0.6	0.36
GeO_2	4.7	1347	2625	0.72		
Glass						
Crown	2.4			0.89	0.01	0.0058
BK7	2.51			0.86	0.011	0.0052
Hf	13.3	2506	4876	0.14	0.23	
l-H_2O	1	273	373	4.19	0.06	0.014
HgSe	8.25	1073		0.18		
HgTe	8.27	943		0.15		
In	7.31	429	2340	0.23	0.85	0.51
				0.26 (500)		
InAs	5.78	796			0.27	
InP	4.79	1337			0.68	
InSb	5.77	798			0.17	
KCl	1.99	1045	1773	0.65		
$LaAlO_3$		2373				
LiF	2.62	1121	1949	1.9		
$LiNbO_3$	4.46	1526		0.64	0.042	0.015
Mg	1.74	923	1380	1.03	1.56	0.87
MgO	3.62	3100	3873	1.0	0.36	0.10
					0.27 (500)	0.065 (500)
					0.10 (1000)	0.022 (1000)
						0.159 (1500)
					0.09 (2000)	0.02 (2000)

Table II (continued)

Material	ϱ (g/cm^3)	T_m (K)	T_b (K)	c_p (J/gK)	$\kappa(T[K])$ (W/cm K)	$D(T[K])$ (cm^2/s)
Mn	7.2	1517	2235	0.48	0.077	0.022
Mo	10.2	2887	5442	0.26	1.37	0.52
					1.30 (500)	0.49 (500)
					1.12 (1000)	0.38 (1000)
					0.98 (1500)	0.29 (1500)
					0.88 (2000)	0.22 (2000)
						0.17 (2500)
						0.13 (3000)
Mo_2C	9.1	2902		0.62	0.07	0.012
NaCl	2.16	1074	1686	0.83		
Nb	8.5	2741	5209	0.27	0.52 (273)	
					0.54	0.24
					0.60 (1000)	
				0.44 (3000)	0.65 (3000)	
NbC	7.7	3773		0.47	0.14	0.039
NbN	7.85	2448		0.47	0.03	0.008
Ni	8.90	1727	3095	0.44	0.91 (273)	
					0.89	0.24
					0.72 (500)	0.17 (500)
					0.72 (1000)	0.14 (1000)
$NiSi_2$	4.8	1263		0.65		
Os	22.5	2973	>5573	0.13	0.88	0.25
Pb	11.3	601	2018	0.13	0.35	0.24
					0.33 (500)	0.21 (500)
					0.22 (1000)	

Table II (continued)

Material	ϱ (g/cm^3)	T_m (K)	T_b (K)	c_p (J/gK)	$\kappa(T[K])$ (W/cm K)	$D(T[K])$ (cm^2/s)
PbS	7.5	1390		0.21	0.024	0.015
PbSe	8.1	1344		0.17	0.017	0.012
PbTe	8.16	1192		0.15	0.022	0.018
Pd	12.1	1826	3328	0.24	0.76 (273)	0.24
					0.71	
a-PE	0.852	($T_g \approx 252$)		1.55	0.0039	
c-PE	1.004	415		2.2		
PEN	1.36	539 ($T_g \approx 395$)				
a-PET	1.33	($T_g \approx 340$)				
c-PET	1.45	540	0	2.1	0.0015	0.001
PI (Kapton)	1.42	subl.		2.2	0.0012	0.0008
		($T_g \approx 508$)		1.28 (400)	0.0017 (400)	
				1.55 (500)	0.0018 (500)	
PMMA	1.18	($T_g \approx 377$)		1.41	0.002	0.001
PS				1.6 J/cm^{3}K		0.001
Pt	21.5	2045	4100	0.13	0.71 (273)	
					0.72	0.25
					0.73 (500)	0.24 (500)
					0.79 (1000)	0.24 (1000)
					0.90 (1500)	0.25 (1500)
						0.27 (2000)
a-PTFE	2.15	($T_g \approx 240$)		0.9	0.004	0.0021
c-PTFE	2.89	605		1.03		
PtSi	12.4	2046		0.23		
PVC	1.39	546		0.95	0.0016	0.0012
		($T_g \approx 354$)				
PZT	7.6	1660		0.38	0.012	0.0042
Re	20.5	3453	5873	0.14	0.48	0.17

Table II (continued)

Material	ϱ (g/cm^3)	T_m (K)	T_b (K)	c_p (J/gK)	$\kappa(T[K])$ (W/cm K)	$D(T[K])$ (cm^2/s)
Rh	12.4	2240	4000 ± 100	0.24	1.51	0.51
					1.40 (500)	
					1.21 (1000)	
Ru					1.17	
Sb	6.69	904	2012	0.21	0.25	0.18
Se	4.82	490	958	0.32	0.005	0.0032
a-Si	2.28	1420		0.8	0.018	0.0097
				1.15 (1000)	0.010 (1000)	
c-Si	2.32	1690	2654	0.71	1.5	0.85
				0.99 (1500)	0.23 (1500)	0.10 (1500)
l-Si	2.52			0.91	0.53 (1800)	0.29 (1800)
					0.6 (2000)	
a-Si_3N_4	3.1					
SiO	2.13	>1975	2153	0.94	0.015	0.007
a-SiO_2	2.2	1873	2503	0.72	0.014	0.009
				1.1 (500)	0.021 (500)	0.009 (500)
				1.22 (1000)	0.033 (1000)	0.013 (1000)
					0.076 (1500)	
SiO_2	2.5	1970	2503	0.74	0.14	0.086
SiC	3.22	3093		1.24	4.9	1.23
Si_3N_4	3.0	2173		1.1		
Sn	7.30	505	2705	0.23	0.67 (273)	
					0.65	0.38
					0.60 (500)	
					0.41 (1000)	
SnO_2	6.95	1898		0.35	0.032	
Sr	2.6	1041	1655	0.30	0.35	0.45
$SrTiO_3$	5.11	2183		0.69		

Table II (continued)

Material	ϱ (g/cm^3)	T_m (K)	T_b (K)	c_p (J/gK)	$\kappa(T[K])$ (W/cm K)	$D(T[K])$ (cm^2/s)
Ta	16.6	3270	5700	0.14	0.56 (273)	
					0.56	0.24
					0.58 (500)	0.24 (500)
					0.61 (1000)	0.235 (1000)
						0.23 (1500)
					0.64 (2000)	0.22 (2000)
						0.20 (2500)
					0.665 (3000)	0.17 (3000)
TaC	14.2	4153	5773	0.26	0.22	0.060
Ta_2N	14.1	3363		0.20	0.05	0.018
$TaSi_2$	9.1	2573		0.32		
Te	6.25	722	1263	0.2	0.04	0.032
ThO_2	9.8	3493 ± 50	4673	0.23	0.15	0.07
					0.06 (500)	0.02 (500)
					0.03 (1000)	0.01 (1000)
Ti	4.52	1937	3560	0.52	0.22	0.094
					0.20 (500)	0.075 (500)
					0.21 (1000)	0.062 (1000)
TiC	4.9	3423	5093	0.84	0.24	0.058
TiN	5.33	3203		0.81	0.2	0.046
TiO_2 (rutile)	4.26	2113	2773−3273	0.93	0.089 (273)	0.031 (273)
					0.065	0.016
					0.059 (500)	0.017 (500)
					0.035 (1000)	0.009 (1000)
$TiSi_2$	4.0	1813		0.73		

Table II (continued)

Material	ϱ (g/cm^3)	T_m (K)	T_b (K)	c_p (J/gK)	$\kappa(T[\mathrm{K}])$ (W/cm K)	$D(T[\mathrm{K}])$ (cm^2/s)
V	5.96	2166	3662	0.49	0.30 (273)	
					0.31	0.11
					0.33 (500)	0.11 (500)
					0.39 (1000)	0.10 (1000)
					0.51 (2000)	0.10 (2000)
VC	5.8	3093	4173	0.79	0.25	0.055
VN	6.1	2593		0.77	0.18	0.038
VSi_2	4.5	2023		0.70		
W	19.35	3660	5882	0.13	1.82 (273)	
					1.78	0.65
					1.49 (500)	0.56 (500)
					1.20 (1000)	0.41 (1000)
					1.08 (1500)	0.35 (1500)
					1.0 (2000)	0.30 (2000)
						0.26 (2500)
					0.91 (3000)	0.23 (3000)
WC	15.7	3143	6273	0.25	0.29	0.073
WSi_2	9.7	2323		0.31		
Y	4.5	1795	3611	0.30	0.172	0.13
YBCO	6.4	subl. 2173		1.43	0.12 $\perp c$	0.006 $\parallel c$
						0.03 $\perp c$
Zn	7.14	693	1180	0.39	1.17 (273)	
					1.16	0.43
					1.11 (500)	0.36 (500)
					0.67 (1000)	
ZnO	5.68	2247	2310	0.49	0.29	0.010
				0.65 (1000)	0.13 (500)	
					0.04 (>1300)	

Table II (continued)

Material	ϱ (g/cm^3)	T_m (K)	T_b (K)	c_p (J/gK)	$\kappa(T[K])$ (W/cm K)	$D(T[K])$ (cm^2/s)
ZnS	4.1	1973		0.49		
ZnS (α)	3.98		1458			
ZnS (β)	4.09		1293			
ZnSe	5.42	1781		0.35		
ZnTe	6.03	1511		0.26		
Zr	6.5	2127	4672	0.28	0.22 (273)	
					0.23	0.12
					0.21 (500)	0.10 (500)
					0.24 (1000)	0.10 (1000)
					0.31 (2000)	
ZrC	6.57	3813	5373	0.48	0.20	0.063
ZrN	7.22	3253		0.48	0.17	0.049
ZrO_2	5.82	2950	5273	0.61	0.02	0.0074
					0.02 (500)	0.0063 (500)
					0.02 (1000)	0.0053 (1000)
$ZrSi_2$	4.9	1973		0.51		

Table III Optical band-gap energy E_g^a, Fermi energy E_F for metals, normal-incidence reflectivity $R(\lambda)$ (mainly for polished surfaces), and optical absorption coefficient $\alpha(\lambda)$ (cm^{-1}), at $T \approx 300$ K

Material	E_g, E_F(eV)	R	$\alpha(cm^{-1})$	$\lambda(\mu m)$
Ag	5.51	0.25		0.2
		0.30	5 E5	0.25
		0.34		0.251
		0.09		0.305
		0.75		0.357
		0.91	7.14 E5	0.5
		0.95	7.75 E5	0.59
			8.1 E5	0.532
		0.95		0.7
		0.97		1
		0.99	8.33 E5	1.064
		0.98		5
		0.99		9
		0.99	8.33 E5	10.6
Al	11.7	0.93	1 E6	0.248
		0.92	1.49 E6	0.25
		0.86		0.305
		0.90	1.43 E6	0.5
		0.92	1.5 E6	0.532
		0.87		0.7
		0.87	1.3 E6	0.8
		0.91		1
		0.94	1.23 E6	1.064
		0.98	1.22 E6	5
		0.98		9
		0.98	1.12 E6	10.6
Al_2O_3	8.7	0.9	30–70	0.694
		0.3 (3800 K)		0.694
Au	5.52	0.22		0.193
		0.33	5.6 E5	0.25
		0.39		0.251
		0.28		0.357
		0.39	6.1 E5	0.4
		0.47	4.6 E5	0.5
		0.84		0.6
		0.92		0.7
		0.96	7.5 E5	0.8
		0.98	7.7 E5	1.064
		0.97		5
		0.98		9
		0.98	7.1 E5	10.6
$BaTiO_3$	3.5	0.29	3.6 E5	0.308
		0.26	3 E4	0.35
		0.16	< 10	0.647
		0.27	1.6 E4	10.6
BBS	4			
$BiFeO_3$	2.75			
BK7			21	0.248
BN	5.5			

Table III (continued)

Material	E_g, E_F(eV)	R	$\alpha(cm^{-1})$	$\lambda(\mu m)$
C (diam.)	5.5			
C (graph.)		0.21	1.5 E5	1.064
		0.19 (1000 K)		
		0.16 (2000 K)		
		0.11 (4000 K)		
CaF_2	10		0.004	0.157
			0.002	0.193
CdTe	1.52		0.002	10.6
Co		0.56	8.77 E5	0.400
Cornea			2.7 E3	0.193
Cr		0.69	1.12 E6	0.4
		0.55		0.6
		0.55		0.7
		0.56		0.8
		0.56		0.9
		0.56		1
		0.63		2
		0.7		3
		0.75		4
		0.8		5
Cu	7.03	0.1[b]	8 E5	0.25
		0.23	7.8 E5	0.266
		0.26		0.3
		0.4	6.9 E5	0.4
		0.43	7.14 E5	0.5
		0.73		0.6
		0.83		0.7
		0.83	7.8 E5	0.8
		0.89		0.9
		0.89	8.3 E5	1
		0.98−0.71	7.7 E5	1.06
		0.95		2
		0.96		3
		0.96		4
		0.97	6.7 E5	5
		0.98	7.7 E5	10.6
Fe			9.4 E5	0.25
		0.57		0.6
		0.59		0.7
		0.61	5.8 E5	0.8
		0.62		0.9
		0.64	5.2 E5	1
		0.77		2
		0.84		3
		0.87		4
		0.91	3.6 E5	5
		0.95	3.8 E5	10.6
Fe(Steel)		0.7		10.6

Table III (continued)

Material	E_g, E_F(eV)	R	$\alpha(cm^{-1})$	$\lambda(\mu m)$
GaAs	1.43	0.6	1.67 E6	0.25
		0.39	1 E5	0.5
		0.31	143	1.06
		0.28	0.02	10.6
GaN	3.4		1.6	0.248
GaP	2.26			
$GaPO_4$	7.1		4.1 E5	0.157
a-Ge		0.48	1 E6	0.25
		0.47	2 E5	0.5
		0.42	1 E4	1.06
		0.34	0.032	10.6
c-Ge	0.67	0.42	1.43 E6	0.25
		0.49	6.7 E5	0.5
		0.38	50	1.06
		0.36	0.032	10.6
Hf			4.3 E5	0.8
l -H_2O	6.5	0.03	0.1	0.193
		0.02	0.1	0.5
		0.02		1.0
			1.2 E4	2.94
		0.01	8.6 E2	10.6
In		0.84	1.2 E6	0.248
		0.57 (500 K)		
		0.37 (1000 K)		
a-InP		0.39	0.55	
c-InP	1.35	0.33	0.55	
InAs	0.35			
KCl	8.1	0.05	< 1	0.25
		0.04	< 1	0.5
		0.04	< 1	1.06
		0.03	0.001	10.6
$LiNbO_3$	4.0	0.20	280	0.308
		0.18	< 1	0.35
		0.16	< 1	0.647
		0.01	890	10.6
MgO	7.8			
Mo		0.63		0.248
		0.55	1 E6	0.4
		0.58−0.66		0.633
		0.61−0.7		1.064
NaCl	8.5		0.002	10.6
Nb		0.75	5 E5	1.064
		0.68 (1500 K)		
		0.56 (2800 K)		
		0.19 (4000 K)		
Ni		0.44		0.2
		0.15[b]	1.25 E6	0.25
		0.49		0.357

Table III (continued)

Material	E_g, E_F(eV)	R	$\alpha(cm^{-1})$	$\lambda(\mu m)$
		0.48	7.4 E5	0.4
		0.62	8.33 E5	0.5
		0.7	7.5 E5	0.532
		0.65		0.6
		0.69		0.7
		0.70		0.8
		0.72		1
		0.67	6.7 E5	1.06
		0.94		5
		0.96		9
		0.97	2.7 E5	10.6
PC			1.14 E5	0.157
			5.5 E5	0.193
			1 E4	0.248
			22	0.308
			4	0.351
PE			630	0.193
			<10	0.248
			<10	0.308
			<10	0.351
PET			3 E5	0.193
			1.6 E5	0.248
			1.3 E5	0.254
			4 E3	0.308
			1.1 E4	0.3
		0.1	3 E3	9
PI (Kapton)		0.08	4 E5	0.193
		0.12−0.06	2.6 E5	0.248
		0.11−0.06	0.86 E5–1 E5	0.308
		0.1	0.34 E5	0.351
PMMA			1 E6	0.157
PMMA			2 E3	0.193
		0.05	400	0.248
			<20	0.308
			<10	0.351
PP			530	0.193
			<10	0.248
			<10	0.308
			<10	0.351
PS			8 E5	0.193
			6.5 E3	0.248
			80	0.308
			≈ 10	0.351
PSUL			4 E5	0.193
			1.5 E5	0.248
			810	0.308
			≈ 10	0.351

Table III (continued)

Material	E_g, E_F(eV)	R	$\alpha(cm^{-1})$	$\lambda(\mu m)$
Pt		0.46		0.248
		0.34		0.251
		0.40		0.305
		0.43		0.357
		0.56	8.9 E5	0.4
		0.58		0.5
		0.64		0.6
		0.69		0.7
		0.70		0.8
		0.73		1
		0.94		5
		0.95		9
PTFE			260	0.193
			< 160	0.248
			< 10	0.308
			< 10	0.351
PU			1 E5	0.248
PVAC			1 E3	0.193
			< 100	0.248
			< 10	0.308
			< 10	0.351
Re		0.56		0.248
Ru		0.71	1.45 E6	0.4
a-Si		0.55	1.5 E6	0.193
		0.75	1 E6	0.25
		0.48	1 E5	0.5
		0.44	7 E4	0.694
		0.35	1 E4	1.06
		0.32	< 1	10.6
c-Si[c]	1.12	0.59	1 E6	0.193
		0.61	1.67 E6	0.25
		0.730	2.09 E6	0.276
		0.60	1.48 E6	0.308
		0.591	1.38 E6	0.31
		0.56	1.12 E6	0.337
		0.571	1 E6	0.354
		0.58	1.07 E6	0.355
		0.591		0.37
		0.48	9.01 E4	0.405
		0.467	7.11 E4	0.413
		0.42	2.64 E4	0.458
		0.39	1.71 E4	0.485
		0.39	1.56 E4	0.488
		0.392	1.39 E4	0.496
		0.36	2 E4	0.5
		0.38	1.12 E4	0.514
		0.37	9 E3	0.53
		0.348	3.8 E3	0.62
		0.35	3.6 E3	0.633
		0.34−0.44	2.5 E3–7 E4	0.694

Table III (continued)

Material	E_g, E_F(eV)	R	$\alpha(cm^{-1})$	$\lambda(\mu m)$
		0.33	1.1 E3	0.8
		0.33	50	1.06
		0.30		1.064
		0.30	10	10.6
l-Si		0.68	1.67 E6	0.193
		0.69	1.46 E6	0.308
				0.532
		0.72	1.25 E6	0.5
		0.72	7.69 E5	1.064
a-SiO_2	8.5		0.003	0.193
		0.06	< 1	0.25
		0.04	< 1	0.5
				0.8
		0.04	< 1	1.064
		0.2	250	10.6
a-Si_3N_4	5.0		1.5 E5	0.193
W		0.51	1.43 E6	0.248
		0.51	1.43 E6	0.25
		0.49	7.69 E5	0.5
		0.58	4.35 E5	1.064
		0.98	5 E5	10.6
Ti			5.2 E5	0.8
YBCO		0.2	2.3 E5	0.248
		0.15	5E4	1.064
ZnO	3.37	0.2	3.3 E5	0.248
				0.4
				0.532
				0.8
Zr			1.9 E5	0.8

[a] For amorphous materials and (real) liquids this energy refers to the 'edge' of strong absorption.
[b] Unpolished.
[c] See Table 7.6.1.

Table IV Melting and vaporization enthalpies. The values listed in the table have been obtained by averaging 'most reliable' results reported in the literature. Values in parentheses are often not exactly equal to those obtained by simple conversion

Material	ΔH_m 10^3 J/g (10^3 J/mol)	ΔH_v 10^3 J/g (10^3 J/mol)
Ag	0.11 (12)	2.48 (250)
Al	0.40 (11)	10.75 (290)
Al_2O_3 (cer.)	1.1 (110)	4.76 (486)
AlSb	0.55 (82)	
As_2S_3	0.12 (29)	
Au	0.07 (12)	1.72 (335)
Be	1.3 (12)	32.2 (290)
BeO	3.24 (81)	
Bi	0.05 (11)	0.81 (170)
C (graph.)		(719)[a]
C (diam.)	8.3 (100)	
CaF_2	0.38 (30)	
Cd	0.06 (6.2)	0.89 (100)
Co	0.27 (16)	6.52 (380)
Cr	0.29 (15)	5.96 (310)
Cu	0.20 (13)	4.7 (300)
Fe	0.27 (15)	6.3 (350)
Stainless steel (304)	0.3	6.5
Ge	0.51 (37)	4.13 (300)
GeO_2	0.42 (44)	
H_2O		2.26
s-H_2O	0.33	
Hg		0.29
In	0.03 (3.3)	2.0 (230)
InAs	0.41 (77)	
InP	0.51 (75)	
KCl	0.36 (27)	1.61 (120)
LiF	1.04 (27)	
Mg	0.35 (8.5)	5.35 (130)
MgO	1.91 (77)	
Mn	0.27 (15)	4.19 (230)
Mo	0.29 (28)	6.15 (590)
NaCl	0.5 (28)	
Nb	0.28 (26)	7.32 (680)
Nb		(723)[a]
Ni	0.31 (18)	6.4 (370)
Os	0.14 (27)	4.10 (780)
Pb	0.02 (4.8)	0.87 (180)
PbS	0.15 (36)	
PbSe	0.17 (49)	
PbTe	0.17 (57)	
Pd	0.16 (17)	3.4 (360)
PET	0.017 (3.32)	
PI		air 0.35 (133)[b] vac. 0.81 (310)[b]
PMMA		0.97 (98)
Pt	0.10 (20)	2.61 (510)
PTFE	0.068 (3.42)	2.64 (132)

Table IV (continued)

Material	ΔH_m 10^3 J/g (10^3 J/mol)	ΔH_v 10^3 J/g (10^3 J/mol)
Sb	0.16 (20)	1.6 (190)
a-Si	1.25 (35)	
c-Si	1.78 (50)	15.0 (420)
c-SiO_2	0.14 (8.5)	12.3[c]
Sn	0.06 (7.0)	1.94 (230)
Ta	0.17 (31)	3.87 (700)
Te	0.14 (18)	0.38 (49)
Ti	0.41 (19)	8.8 (420)
TiO_2	0.84 (67)	
V	0.41 (21)	
W	0.19 (35)	3.86 (710)
YBCO		(430)[c]
Zn	0.11 (7.4)	1.8 (120)
ZnO	0.97	7.66
Zr	0.19 (17)	5.5 (500)
ZrO_2	0.71 (87)	

[a] Includes ΔH_m.
[b] Enthalpy for decomposition.
[c] Calculated.

Table V Absorption/dissociation cross sections, σ, for precursor molecules commonly used in LCP. The values listed in the table have been obtained by averaging 'most reliable' results reported by different authors

Molecule	σ (10^{-18} cm^2)	λ (nm)
$Al(CH_3)_3$	20 ± 3	193
	0.011	248
	3 E–3	257
$Al(C_2H_5)_3$	4.7 ± 1.4	193
$Al_2(CH_3)_6$	20	193
	2 E–3	257
$As(CH_3)_3$	45	193
$As(C_2H_5)_3$	18	193
AsH_3	18	193
$B(C_2H_5)_3$	0.44	193
BCl_3	0.045	193
B_2H_6	0.13 ± 0.09	193
Br_2	$<$E–4	193
	$<$E–4	248
	$<$E–4	266
	3.8 E–4	308
	0.034	351
$Cd(CH_3)_2$	7 ± 3	193
	3 ± 1	248
	1.3 ± 0.4	257
	0.45	266
CCl_4	0.7 ± 0.3	193
	2.3 E–3	248
CF_2Br_2	1.1	193
	0.63 ± 0.03	248
	0.24	257
CF_3Br	0.073 ± 0.01	193
	(5 ± 3) E–3	248
	4.5 E–4	257
C_2F_5Br	0.14 ± 0.04	193
	4.2 E–3	248
	E–3	257
1,2-$C_2F_4Br_2$	1.1	193
	0.051	248
	0.016	257
CF_2Cl_2	0.32	193
CF_3Cl	(1.4 ± 0.6) E–3	193
C_2F_5Cl	1.9 E–3	193
l,2-$C_2F_4Cl_2$	0.044	193
CF_3I	3.8 E–3	193
	0.27 ± 0.01	248
	0.034	308
	$<$E–3	351
C_2F_5I	$<$E–3	193
	0.33	248
	0.64	268
	0.058	308

Table V (continued)

Molecule	σ (10^{-18} cm^2)	λ (nm)
1,2-$C_2F_4I_2$	0.97	248
	1.5	257
	2.1	266
	0.10	308
CH_2Br_2	0.36	248
	0.11	257
CH_3Br	0.55 ± 0.03	193
	0.016 ± 0.003	248
	(3.7 ± 0.6) E–3	257
CH_2Cl_2	0.37 ± 0.02	193
$CHCl_3$	0.89 ± 0.02	193
CH_3Cl	0.062 ± 0.008	193
CH_4	<E–3	193
C_2H_4	0.015	193
C_2H_3Cl	6	193
C_2H_5Cl	0.035	193
CH_2FCl	0.010	193
CHF_2Cl	1.2 E–3	193
$CHFCl_2$	0.20	193
CH_2I_2	29	193
	1.6	248
	1.3	257
	1.7 ± 0.3	266
	3.3	308
	0.25	351
CH_3I	0.82	248
	1.1	257
	0.95	266
	8.4 E–3	308
Cl_2	2.5 E–3	193
	<E–3	248
	0.010	266
	0.19	308
	0.14 ± 0.03	351
	0.25 E–2	458
	6 E–4	488
	1.5 E–4	515
$Cr(CO)_6$	19 ± 7	193
	47 ± 10	248
	25	257
	25	266
	5.3 ± 0.2	308
CrO_2Cl_2	3.0	248
	3.1	257
	5.5	266
	5.1	308
F_2	<E3	193
	0.013	248
	0.015	266
	0.019	308
	5.7 E–3	351

Table V (continued)

Molecule	σ (10^{-18} cm^2)	λ (nm)
$Fe(CO)_5$	57	193
	27	248
	14 ± 5	257
	13	266
	2.4	308
	1.3	355
$Ga(CH_3)_3$	20 ± 6	193
	2.1	248
	1.8	257
$Ga(C_2H_5)_3$	7.4 ± 1.6	193
GeH_4	0.025	193
HBr	1.7	193
HCl	0.89	193
HF	<E–3	193
HNO_3	12 ± 1	193
	0.020	248
	0.019	257
	0.017 ± 1	266
	(1.1 ± 0.1) E–3	308
H_2O_2	0.60	193
	0.08 ± 0.003	248
	0.061 ± 0.004	257
	0.04 ± 0.003	266
	4.2 E–3	308
H_2S	6.4 ± 0.6	193
	0.048 ± 0.023	248
$Hg(CH_3)_2$	26 ± 1	193
	0.2 ± 0.12	248
	0.05	257
HI	0.56 ± 0.02	193
	0.51	248
	0.18	266
I_2	6.1	193
	0.027	248
	0.054	266
$In(CH_3)_3$	12 ± 2	193
	2 ± 0.8	248
	1.5	257
	1.5	266
InI	<7	193
$Mo(CO)_6$	56 ± 5	193
	51 ± 7	248
	20	257
	17	266
	13	308
	0.5	350−360
MoF_6	4.9	193
	0.20	248
	0.14	257
	0.090	266
	<E–3	308

Table V (continued)

Molecule	σ (10^{-18} cm^2)	λ (nm)
NF_3	(5.7 ± 0.4) E–3	193
NH_3	9 ± 3	193
NO	0.020	193
NO_2	0.6 ± 0.19	193
	0.03 ± 0.01	248
	0.03 ± 0.012	257
	0.035 ± 0.01	266
	0.16	308
N_2O	0.09 ± 0.007	193
	2 E–6	248
$Ni(CO)_4$	30	248
	2.4	308
O_2	(7.5 ± 7) E–4	193
	4 E–6	248
O_3	0.4	193
	5	248
PET (Mylar)	20[a]	193
PH_3	27 ± 14	193
$P(CH_3)_3$	34	193
$P(C_2H_5)_3$	8.5	193
$Pb(CH_3)_4$	0.37	257
	0.062	266
$Pt(PF_3)_4$	0.19	248
Pt(hfacac)	100	
ReF_6	7.3	193
SO_2	9.3	193
	0.075	248
	0.19	257
	0.45	266
	0.63	308
SF_6	6.8 E–4	193
$Si(CH_3)_4$	< E–3	193
$Si_2(CH_3)_6$	46	193
$SiH_3(C_6H_5)$	170 ± 130	193
SiH_4	1.1 E–3	193
Si_2H_6	2	193
$Sn(CH_3)_4$	40	193
$SnCl_4$	38	193
	8.3	248
	5.2	257
	1.3	266
$Te(CH_3)_2$	5.2 ± 1.4	193
	7 ± 3	248
	1.7 ± 0.6	257
$Te(C_2H_5)_2$	15	193
	8 ± 2	248
	1.4 ± 0.5	257
	1	266
$TiBr_4$	20	248
	23	257
	30	266
	1.2	308

Table V (continued)

Molecule	σ (10^{-18} cm^2)	λ (nm)
$TiCl_4$	30	193
	11	248
	5.5	257
	10	266
	2.3	308
TlBr	22	193
TlI	24	193
	2.6	248
VCl_4	10	248
	9.6	257
	8.9	266
	11	308
$VOCl_3$	18	248
	13	257
	8.9	266
	5.0	308
$W(CO)_6$	12	193
	4.5	248
	2.4	308
	0.5	350–360
WF_6	0.35	193
$Zn(CH_3)_2$	15	193

[a] Per monomer unit.

References

Abdolvand A., R.W. Lloyd, M.J.J. Schmidt, D.J. Whitehead, Z. Liu, L. Li: Formation of highly organised, periodic microstructures on steel surfaces upon pulsed laser irradiation, Appl. Phys. A **95**, 447 (2009)

Abdolvand A., S.Z. Khan, Y. Yuan, P.L. Crouse, M.J.J. Schmidt, M. Sharp, Z. Liu, L. Li: Generation of titanium-oxide nanoparticles in liquid using a high-power, high-brightness continuous-wave fiber laser, Appl. Phys. A **91**, 365 (2008)

Abraham F.F.: *Homogeneous Nucleation Theory*, (Academic Press, London 1978)

Adachi Y., D. Su, P. Muralt, N. Setter: Ferroeletric and piezoelectric properties of lanthanoid-substituted $Bi_4Ti_3O_{12}$ thin films grown on (111) Pt and (100) IrO_2 electrodes, Appl. Phys. Lett. **86**, 172904 (2005)

Afonso C.N., J. Solís, R. Serna, J. Gonzalo, J.M. Ballesteros, J.C.G. de Sande: PLD of nanocomposite thin films for photonic applications. In *Laser Applications in Microelectronic and Optoelectronic Manufacturing IV*, ed. by J. Dubowski et al. SPIE Proceedings **3618**, 453 (1999)

Agarwal G.S.: Interaction of electromagnetic waves at rough dielectric surfaces, Phys. Rev. B **15**, 2371 (1977)

Agranat M.B., S.I. Ashitkov, S.I. Anisimov, A.V. Ovchinnikov, A.B. Shvartsburg, D.S. Sitnikov, V.E. Fortov: Formation of absorbing heterogeneous plasma layer by fs laser-induced melting and ablation of silicon, Appl. Phys. A **94**, 879 (2009)

Agranat M.B., S.I. Anisimov, S.I. Ashitkov, V.V. Zhakhovskii, N.A. Inogamov, K. Nishihara, Yu.V. Petrov, V.E. Fortov, V.A. Khokhlov: Dynamics of plume and crater formation after action of femtosecond laser pulse, Appl. Surf. Sci. **253**, 6276 (2007)

Ahlgren W.L., E.J. Smith, J.B. James, T.W. James, R.P. Ruth, E.A. Patten: Photo-MOCVD growth of HgTe-CdTe superlattices, J. Cryst. Growth **86**, 198 (1988)

Akane T., K. Sugioka, K. Midorikawa: High-speed etching of hexagonal GaN by laser ablation and successive chemical treatment, Appl. Phys. A **69** [Suppl.], S309 (1999)

Akhmanov S.A., V.I. Emel'yanov, N.I. Koroteev, V.N. Seminogov: Interaction of powerful laser radiation with the surfaces of semiconductors and metals: Nonlinear optical effects and nonlinear optical diagnostics, Sov. Phys. Usp. **28**, 1084 (1985)

Akin J.E.: *Finite elements for analysis and design* (Academic Press, London 1998)

Aliouchouche A., J. Boulmer, B. Bourguignon, J.P. Budin, D. Débarre, A. Desmur: Laser etching of silicon by chlorine: Effect of post-desorption collisions and chlorine in-diffusion on the laser desorption yield, Appl. Surf. Sci. **69**, 52 (1993)

Allard M., S. Boughaba, M. Meunier: Laser micromachining of free-standing structures in SiO_2-covered silicon, Appl. Surf. Sci. **109–110**, 189 (1997)

Allen F.G.: Emissivity at 0.65 micron of silicon and germanium at high temperatures, J. Appl. Phys. **28**, 1510 (1957)

Allen S.D., A.S. Miller, S.J. Lee: Laser assisted particle removal 'dry' cleaning of critical surfaces, Materials Science and Engineering B **49**, 85 (1997)

Allmen M. von, A. Blatter: *Laser-Beam Interactions with Materials*, 2nd ed., Springer Ser. Mater. Sci. Vol. 2 (Springer, Berlin, Heidelberg 1995)

Alvarez J., M. Lopez-Arias, R.de Nalda, M. Martín: CdS plume composition and dynamics of neutral species upon ablation with 532 nm laser light, Appl. Phys. A **92**, 831 (2008)

Amoruso S., J. Schou, J.G. Lunney: Influence of the atomic mass of the background gas on laser ablation plume propation, Appl. Phys. A **92**, 907 (2008)

Amoruso S., G. Ausanio, R. Bruzzese, L. Gragnaniello., L. Lanotte, M. Vitiello, X. Wang: Characterization of laser ablation of solid targets with NIR pulses of 100 fs and 1 ps duration, Appl. Surf. Sci. **252**, 4863 (2006)

Ancona A., D. Nodop, J. Limpert, S. Nolte, A. Tünnermann: Microdrilling of metals with an inexpensive and compact ultra-short-pulse fiber amplified microchip laser, Appl. Phys. A **94**, 19 (2009)

Ancona A., F. Röser, K. Rademaker, J. Limpert, S. Nolte, A. Tünnermann: High speed laser drilling of metals using a high repetition rate, high average power ultrafast fiber CPA system, Optics Express **16**, 8958 (2008)

Anderson W.R., C.C. Bradley, J.J. McClelland, R.J. Celotta: Minimizing feature width in atom optically fabricated chromium nanostructures, Phys. Rev. A **59**, 2476 (1999)

Andrä G., F. Falk: Multicrystalline silicon films with large grains on glass: preparation and applications, phys. stat. sol. (c) **5**, No. 10, 3221 (2008)

Anglos D., J.C. Miller: Cultural heritage applications of LIBS, in *Laser–induced breakdown spectroscopy (LIBS)* – Fundamentals and Applications, ed. by A.W., Miziolek, V. Palleschi, I. Schechter (Cambridge University Press 2006), p. 332

Anisimov S.I., N.A. Inogamov, Yu.V. Petrov, V.V. Zhakhovskii, K. Nishihara: Numerical simulation of the expansion into vacuum of a crystal heated by an ultrashort laser pulse, in *Laser Ablation and its Applications*, ed. by C. R. Phipps (Springer 2007) p. 1

Anisimov S.I., B. Rethfeld: On the theory of ultrashort laser pulse interaction with a metal, SPIE **3093**, 192 (1997)

Anisimov S.I., B.S. Luk'yanchuk, A. Luches: An analytical model for 3D laser plume expansion into vacuum in hydrodynamic regime, Appl. Surf. Sci. **96–98**, 24 (1996)

Anisimov S.I., V.A. Khokhlov: *Instabilities in Laser-Matter Interaction* (CRC Press, Boca Raton 1995)

Anisimov S.I., D. Bäuerle, B.S. Luk'yanchuk: Gas dynamics and film profiles in pulsed-laser deposition of materials, Phys. Rev. B **48**, 12076 (1993)

Anisimov S.I., M.I. Tribel'skii, Ya.G. Epelbaum: Instability of plane evaporation front in interaction of laser radiation with a medium, Sov. Phys. JETP. **51**, 802 (1980)

Anisimov S.I., B.L. Kapeliovich, T.L. Perel'man: Electron emission from metal surface exposed to ultrashort laser pulse, Zh. Eksp. Teor. Fiz. **66**, 776 (1974) [Sov. Phys. JETP **39**, 375 (1974)]

Anisimov S.I., Y.A. Imas, G.S. Romanov, Y.V. Khodyko*: Action of High-Power Radiation on Metals* (Consult. Bureau, Springfield, VA 1971)

Aoyagi Y., T. Meguro, S. Iwai: Beam assisted layer-by-layer processes and the mechanism in III-V compounds, 1st. Int'l. Symp. on Atomic Layer Epitaxy, ed. L. Niinistö, Acta Polytechnica Scandinavica, Chemical Technology and Metallurgy Series No. 195, Helsinki (1990), p. 55

Aoyagi Y., A. Doi, S. Iwai, S. Namba: Atomic-layer growth of GaAs by modulated-continuous-wave laser metal-organic vapor-phase epitaxy, J. Vac. Sci. Technol. B **5**, 1460 (1987)

Apitz I., A. Vogel: Material ejection in ns Er:YAG laser ablation of water, liver, and skin, Appl. Phys. A **81**, 329 (2005)

Arenholz E., A. Kirchebner, S. Klose, J. Heitz, D. Bäuerle: Deposition of ablation products from UV-laser irradiated polymer surfaces, Mater. Res. Soc. Symp. Proc. Vol. **526**, 385 (1998)

Arenholz E., J. Heitz, V. Svorcik, D. Bäuerle: Non-coherent structure formation on UV-laser irradiated polymers, in *Excimer Lasers*, ed. by L.D. Laude, NATO ASI Series (Kluwer, Dordrecht 1994), p. 237

Arenholz E., J. Heitz, M. Wagner, D. Bäuerle, H. Hibst, A. Hagemeyer: Laser-induced surface modification and structure formation of polymers, Appl. Surf. Sci. **69**, 16 (1993)

Arenholz E., M. Wagner, J. Heitz, D. Bäuerle: Structure formation in UV-laser-ablated polyimide foils, Appl. Phys. A **55**, 119 (1992)
Arenholz E., V. Svorcik, T. Kefer, J. Heitz, D. Bäuerle: Structure formation in UV-laser ablated poly-ethylene-terephthalate (PET), Appl. Phys. A **53**, 330 (1991)
Armstrong D.A., J.L. Holmes: Decomposition of halides and derivatives, in *Decomposition of Inorganic and Organometallic Compounds*, ed. by C.H. Bamford, C.F.H. Tipper, Chem. Kinetics, Vol. 4 (Elsevier, Amsterdam 1972) p. 143
Arnold C.B., P. Serra, A. Piqué: Laser direct-write techniques for printing of complex materials, MRS. Bulletin **32**, 23 (2007)
Arnold C.L., A. Heisterkamp, W. Ertmer, H. Lubatschowski: Computational model for nonlinear plasma formation in high NA micromachining of transparent materials and biological cells, Opt. Express **15**, 10303 (2007)
Arnold N., G. Schrems, D. Bäuerle: Ablative thresholds in laser cleaning of substrates from particulates, Appl. Phys. A **79**, 729 (2004)
Arnold N., D. Bäuerle: Uniform target ablation in pulsed-laser deposition, Appl. Phys. A **68**, 363 (1999)
Arnold N., J. Gruber, J. Heitz: Spherical expansion of the vapor plume into ambient gas: an analytical model, Appl. Phys. A **69** [Suppl.], S87 (1999)
Arnold N., B. Luk'yanchuk, N. Bityurin: A fast quantitative modeling of ns laser ablation based on non-stationary averaging technique, Appl. Surf. Sci. **127–129**, 184 (1998)
Arnold N., D. Bäuerle: 1998, unpublished
Arnold N., P.B. Kargl, D. Bäuerle: Modeling of pyrolytic laser direct writing: noncoherent structures and instabilities, J. Appl. Phys. **82**, 1018 (1997)
Arnold N., E. Thor, N. Kirichenko, D. Bäuerle: Pyrolytic LCVD of fibers: A theoretical description, Appl. Phys. A **62**, 503 (1996)
Arnold N., P.B. Kargl, D. Bäuerle: Laser direct writing and instabilities: A one-dimensional approach, Appl. Surf. Sci. **86**, 457 (1995a)
Arnold N., P.B. Kargl, R. Kullmer, D. Bäuerle: Oscillations in laser direct writing of W from WCl_6 and H_2: A theoretical analysis, Appl. Phys. A **61**, 347 (1995b)
Arnold N., D. Bäuerle: 1994, unpublished
Arnold N., R. Kullmer, D. Bäuerle: Simulation of growth in pyrolytic laser-CVD of Microstructures: I. One-dimensional approach, Microelectronic Eng. **20**, 31 (1993)
Arnold N., D. Bäuerle: Simulation of growth in pyrolytic laser-CVD of microstructures: II. Two-dimensional approach, Microelectronic Eng. **20**, 43 (1993)
Arnone C., M. Rothschild, J.G. Black, D.J. Ehrlich: Visible-laser photodeposition of chromium oxide films and single crystals, Appl. Phys. Lett. **48**, 1018 (1986)
Ashby C.I.H., D.R. Myers, G.A. Vawter, R.M. Biefeld, A.K. Datye: Selective suppression of photochemical dry etching using elevated surface impurity concentrations: A new technique for self-aligned etching, J. Appl. Phys. **68**, 2406 (1990)
Ashcroft N.W., N.D. Mermin: *Solid State Physics* (Holt-Saunders, New York 1976)
Ashkenasi D., H. Varel, A. Rosenfeld, S. Henz, J. Herrmann, E.E.B. Campbell: Application of self-focusing of ps laser pulses for 3D microstructuring of transparent materials, Appl. Phys. Lett. **72**, 1442 (1998)
Auciello O., A.R. Krauss, J. Santiago-Aviles, A.F. Schreiner, D.M. Gruen: Surface com positional and topographical changes resulting from excimer laser impacting on $YBa_2Cu_3O_7$ single phase superconductors, Appl. Phys. Lett. **52**, 239 (1988)
Aussenegg F.R., A. Leitner, M.E. Lippitsch eds.: *Surface Studies with Lasers*, Springer Ser. Chem. Phys., Vol. 33 (Springer, Berlin, Heidelberg 1983)
Auston D.H., J.A. Golovchenko, A.L. Simons, R.E. Slusher, P.R. Smith, C.M. Surko, T.N.C. Venkatesan: Dynamics of laser annealing, in *Laser-Solid Interactions and Laser Processing*, ed. by S.D. Ferris, H.J. Leamy, J.M. Poate (AIP, New York 1979) p. 11
Avouris P., W.M. Gelbart, M.A. El-Sayed: Nonradiative electronic relaxation under collision-free conditions, Chem. Rev. **77**, 793 (1977)

Bachelier G., J. Margueritat, A. Mlayah, J. Gonzalo, C.N. Afonso: Size dispersion effects on the low-frequency Raman scattering of quasispherical silver nanoparticles: Experiment and theory, Phys. Rev. B **76**, 235419 (2007)

Bachmann F., P. Loosen, R: Poprawe: High Power Diode Lasers – Technology and Applications, Springer Ser. Opt. Sci. 128 (Springer, Berlin, Heidelberg 2007)

Backen E., S. Haindl, T. Niemeier, R. Hühne, T. Freudenberg, J. Werner, G. Behr, L. Schultz, B. Holzapfel: Growth and anisotropy of La(O,F)FeAs thin films deposited by PLD, Supercond. Sci. Technol. **21**, 122001 (2008)

Bae J.H., J. Cho: Structural, morphological, and mechanical properties of amorphous carbon and carbon nitride thin films deposited by reactive and ion beam assisted laser ablation, J. Mat. Sci **34**, 1093 (1999)

Baeri P., S.U. Campisano, F. Priolo, E. Rimini: Transient temperature measurement by thin film thermocouple during nanosecond laser-induced mixing of Ni-Si Layers, *in Energy Beam-Solid Interactions and Transient Thermal Processing*, ed. by V.T. Nguyen and A.G. Cullis (Physique, Les Ulis 1985) p. 237

Bäuerle D.: Laser chemical processing: An overview to the 30th anniversary, Appl. Phys. A **101**, 447 (2010)

Bäuerle D.: *LASER Grundlagen und Anwendungen in Photonik, Technik, Medizin und Kunst*, (Wiley-VCH, Weinheim 2009)

Bäuerle D., T. Gumpenberger, D. Brodoceanu, G. Langer, J. Kofler, J. Heitz, K. Piglmayer: Laser cleaning and surface modifications: Applications in nano- and biotechnology, in "Laser Cleaning II", Chap. 1, p. 1–28, ed. D.M.Kane (World Scientific, Singapore, 2006)

Bäuerle D., L. Landström, J. Kofler, N. Arnold, K. Piglmayer: Laser-processing with colloid monolayers, Proc. SPIE. **5339**, 20 (2004)

Bäuerle D., G. Wysocki, L. Landström, J. Klimstein, K. Piglmayer, J. Heitz: Laser-induced single step micro/nanopatterning, SPIE. **5063**, 8 (2003)

Bäuerle D., K. Piglmayer, R. Denk, N. Arnold: Laser-induced surface patterning by means of microspheres, Lambda Physik Highlights, 60, (July 2002), p.1–3

Bäuerle D.: *Laser Processing and Chemistry*, 3rd ed. (Springer-Verlag, Berlin, Heidelberg, New York 2000)

Bäuerle D., J. Heitz, E. Arenholz: *Fluorpolymer-Beschichtungen mit guter Haftung und guter Abriebfestigkeit für den Einsatz in der Medizin sowie ein Verfahren zu ihrer Herstellung*, Austrian Patent AT 406.756 B (2000)

Bäuerle D.: Pulsed-laser deposition and characterization of high-temperature superconductors, Supercond. Sci. Technol. **11**, 968 (1998)

Bäuerle D.: *Laser Processing and Chemistry*, 2nd ed. (Springer-Verlag, Berlin, Heidelberg, New York 1996)

Bäuerle D., E. Arenholz, V. Svorcik, J. Heitz, B. Luk'yanchuk, N. Bityurin: Laser-induced surface modifications, structure formation, and ablation of organic polymers, SPIE. Proc. **2403**, 312 (1995a)

Bäuerle D., E. Arenholz, J. Heitz, S. Proyer, E. Stangl, B. Luk'yanchuk: Surface patterning and thin-film formation by pulsed-laser ablation, in *Semiconductor Processing and Characterization with Lasers – Applications in Photovoltaics*, ed. by M. Brieger, H. Dittrich, M. Klose, H.W. Schock, J. Werner, Mater. Sci. Forum. **173–174**, 41 (1995b)

Bäuerle D., B. Luk'yanchuk, K. Piglmayer: On the reaction kinetics in laser-induced pyrolytic chemical processing, Appl. Phys. A **50**, 385 (1990)

Bäuerle D.: *Chemical Processing with Lasers*, Springer Ser. Mater. Sci., Vol. 1 (Springer, Berlin, Heidelberg 1986)

Bäuerle D.: Materialbearbeitung mit Laserlicht, Laser und Optoelektronik **1**, 29 (1985)

Bäuerle D.: Laser induced chemical vapor deposition, in *Laser Processing and Diagnostics*, ed. by D. Bäuerle, Springer Ser. Chem. Phys., Vol. 39 (Springer, Berlin, Heidelberg 1984) p. 166

Bäuerle D.: Production of microstructures by laser pyrolysis, in *Laser Diagnostics and Photochemical Processing for Semiconductor Devices*, ed. by R.M. Osgood, S.R.J. Brueck, H.R. Schlossberg, MRS Proc. **17**, 19 (1983*a*)

Bäuerle D.: Laser induced chemical vapor deposition, in *Surface Studies with Lasers*, ed. by F.R. Aussenegg, A. Leitner, M.E. Lippitsch, Springer Ser. Chem. Phys., Vol. 33 (Springer, Berlin, Heidelberg 1983*b*) p. 178

Bäuerle D., G. Leyendecker, D. Wagner, E. Bauser, Y.C. Lu: Laser grown single crystals of silicon, Appl. Phys. A **30**, 147 (1983)

Bäuerle D., G. Leyendecker, S. Szikora: 1982, unpublished

Bäuerle D., P. Irsigler, G. Leyendecker, H. Noll, D Wagner: Ar^+ laser-induced chemical vapor deposition of Si from SiH_4, Appl. Phys. Lett. **40**, 819 (1982a)

Bäuerle D., G. Leyendecker, P. Geittner, H. Lydtin: Laser induced chemical vapor deposition of C and Si, Appl. Phys. B **28**, 267 (1982b)

Bäuerle D., D. Wagner, M. Wöhlecke, B. Dorner, H. Kraxenberger: Soft modes in semi-conducting $SrTiO_3$: II. The ferroelectric mode; Z. Phys. B **38**, 335 (1980)

Bagratashvili V.N., V.N. Doljikov, V.S. Letokhov, E.A. Ryabov: Isotopically-selective dissociation of the CF_3I molecules at high pressure under the action of the pulse radiation of CO_2 laser, Zh. Tekh. Phys. Letters (Pis'ma Red.) **4**, 1181 (1978)

Bagratashvili V.N., I.N. Knyazev, V.S. Letokhov, V.V. Lobko: Optoacoustic detection of multiple photon molecular absorption in a strong IR field, Opt. Commun. **18**, 525 (1976)

Balgar T., S. Franzka, N. Hartmann: Laser-assisted decomposition of alkylsiloxane monolayers at ambient conditions: rapid patterning below the diffraction limit, Appl. Phys. A **82**, 689 (2006)

Ball Z., B. Hopp, M. Csete, F. Ignácz, B. Rácz, R. Sauerbrey, G. Szabó: Transient optical properties of excimer-laser-irradiated polyimide. I. Refractive index, Appl. Phys. A **61**, 547 (1995a)

Ball Z., B. Hopp, M. Csete, F. Ignácz, B. Rácz, G. Szabó, R. Sauerbrey: Transient optical properties of excimer-laser-irradiated polyimide. II. Carbon-cluster scattering, Appl. Phys. A **61**, 575 (1995b)

Baller T.: Chemical etching induced by a pulsed laser beam, PhD Thesis, University of Twente, Holland (1990)

Balling P., J. Esberg, K. Kirsebom, D.Q.S. Le, U.I. Uggerhøj, S.H. Connell, J. Härtwig, F. Masiello, A. Rommeveaux: Bending diamonds by fs laser ablation, Nucl. Instrum. Methods. Phys. Res B **267**, 2952 (2009)

Banks D.P., K. Kaur, R. Gazia, R. Fardel, M. Nagel, T. Lippert, R.W. Eason: Triazene photopolymer dynamic release layer-assisted femtosecond laser-induced forward transfer with an active carrier substrate, EPL **83**, 38003 (2008)

Banks D.P., C. Grivas, J.D. Mills, R.W. Eason, I. Zergioti: Nanodroplets deposited in microarrays by femtosecond Ti:sapphire laser-induced forward transfer, Appl. Phys. Lett. **89**, 193107 (2006)

Barcikowski S., A. Hahn, A.V. Kabashin, B.N. Chichkov: Properties of nanoparticles generated during fs laser machining in air and water, Appl. Phys. A **87**, 47 (2007)

Barcikowski S., N. Bärsch, T. Burmester, J. Bunte, J. Ulrich, A. Gervais, M. Meier: Femtosecond laser cleaning of metallic antique artworks – advantages, limits and economic aspects, in *Laser Cleaning II*, Kane D.M. ed., (World Scientific, Singapore, 2006) p. 209

Barnes J.-P., A.K. Petford-Long, R.C. Doole, R. Serna, J. Gonzalo, A. Suarez-Garcia, C.N. Afonso, D. Hole: Structural studies of Ag nanocrystals embedded in amorphous Al_2O_3 grown by pulsed laser deposition, Nanotechnol **13**, 465 (2002)

Barr W.P.: The production of low scattering dielectric mirrors using rotating vane particle filtration, J. Phys. E **2**, 2 (1969)

Barth M., P. Hess, G. Mollekopf, H. Stafast: SF_6 sensitized CO_2-laser chemical vapor deposition of a-Ge:H, Thin Solid Films **241**, 61 (1994)

Basillais A., R. Benzerga, H. Sanchez, E. Le Menn, C. Boulmer-Leborgne, J. Perrière: Improvement of the PLD process assisted by RF plasma for AlN growth, Appl. Phys. A **80**, 851 (2005)

Basting D., G. Marowsky eds.: *Excimer Laser Technology* (Springer-Verlag, Berlin 2005)

Battuello M., T. Ricolfi: Effect of the emissivity of real bodies on pyrometer readings, High Temperatures – High Pressures **12**, 247 (1980)

Baufay L., F.A. Houle, R.J. Wilson: Optical self-regulation during laser-induced oxidation of copper, J. Appl. Phys. **61**, 4640 (1987)

Baum T.H., P.B. Comita, T.T. Kodas: Laser-induced gold deposition for thin-film circuit repair, SPIE. Proc. **1598**, 122 (1991)

Beck K.M., T. Sasaki, N. Koshizaki: Characterization of nanocomposite materials prepared via laser ablation of Pt/TiO_2 bi-combinant targets, Chem. Phys. Lett. **301**, 336 (1999)

Beinhorn F., J. Ihlemann, K. Luther, J. Troe: Plasma effects in picosecond-femtosecond UV laser ablation of polymers, Appl. Phys. A **79**, 869 (2004)

Bekesi J., J. Meinertz, J. Ihlemann, P. Simon: Fabrication of large-area grating structures through laser ablation, Appl. Phys. A **93**, 27 (2008)

Benedek G.: Molecule-surface interaction: Vibrational excitations, in *Interfaces under Laser Irradiation*, ed. by L.D. Laude, D. Bäuerle, M. Wautelet, Nato ASI Series (Nijhoff, Dordrecht 1987) p. 27

Benes E.: Improved quartz crystal microbalance technique, J. Appl. Phys. **56**, 608 (1984)

Bennett T.D., D.J. Krajnovich, C.P. Grigoropoulos: Separating thermal, electronic, and topographic effects in pulsed laser melting and sputtering of gold, Phys. Rev. Lett. **76**, 1659 (1996)

Bennett T.D., C.P. Grigoropoulos, D.J. Krajnovich: Near-threshold laser sputtering of gold, J. Appl. Phys. **77**, 849 (1995)

Ben-Shaul A., Y. Haas, K.L. Kompa, R.D. Levine: *Lasers and Chemical Change*, Springer Ser. Chem. Phys., Vol. 10 (Springer, Berlin, Heidelberg 1981)

Bentini G.G., M. Servidori, C. Cohen, R. Nipoti, A.V. Drigo: Titanium and nickel silicide formation after Q-Switched laser and multiscanning electron beam irradiation, J. Appl. Phys. **53**, 1525 (1982)

Bergmann H.W.: Surface Treatment, in Landolt-Börnstein – Numerical Data and Functional Relationships in Science and Technology, New Series, Group VIII/1C (Group VIII: Advanced Materials and Technologies, Vol. 1 Laser Physics and Applications, Subvolume C: Laser Applications, edited by R. Poprawe, H. Weber, G. Herziger (Springer Berlin, Heidelberg, New York 2004), p. 75

Bertness K.A., T.T. Chiang, C.E. McCants, P.H. Mahowald, A.K. Wahi, T. Kendelewicz, I. Lindau, W.E. Spicer: Comparative uptake kinetics of N_2O and O_2 chemisorption on GaAs (110), Surf. Sci. **185**, 544 (1987)

Besner S., A.V. Kabashin, F.M. Winnik, M. Meunier: Ultrafast laser based "green" synthesis of non-toxic nanoparticles in aqueous solutions, Appl. Phys. A **93**, 955 (2008)

Beuermann Th., H.J. Brinkmann, T. Damm, M. Stuke: Picosecond UV excimer laser ablation of $LiNbO_3$, MRS Proc. **191**, 37 (1990)

Bhardwaj V.R, E. Simova, P.P. Rajeev, C. Hnatovsky, R.S. Taylor, D.M. Rayner, P.B. Corkum: Optically produced arrays of planar nanostructures inside fused silica, Phys. Rev. Lett. **96**, 057404 (2006)

Bhattacharyya A., B.G. Streetman: Theoretical considerations regarding pulsed CO_2 laser annealing of silicon, Solid. State. Commun. **36**, 671 (1980)

Bialkowski M.M., G.S. Hurst, J.E. Parks, D.H. Lowndes, G.E. Jellison: Charge emission from silicon and germanium surfaces irradiated with KrF excimer laser pulses, in *Laser Ablation - Mechanisms and Applications*, ed. by J.C. Miller, R.F. Haglund, Lecture Notes Phys., Vol. 389 (Springer, Berlin, Heidelberg 1991) p. 265

Bicknell R.N., N.C. Giles, J.F. Schetzina: p-Type CdTe epilayers grown by photoassisted molecular beam epitaxy, Appl. Phys. Lett. **49**, 1735 (1986)

Bille J., W. Schlegel eds.: *Medizische Physik 3*, *Medizinische Laserphysik*, Springer 2005

Bird R.B., W.E. Stewart, E.N. Lightfoot: *Transport Phenomena* (Wiley, New York 1960)

Birnbaum M.: Semiconductor surface damage produced by ruby lasers, J. Appl. Phys. **36**, 3688 (1965)

Bityurin N.: 2011, private communications

Bityurin N., E. Arenholz, N. Arnold, D. Bäuerle: Laser-induced structure formation on stretched polymer foils, Phys. Rev. E **75**, 041603 (2007)

Bityurin N., B.S. Luk'yanchuk, M.H. Hong, T.C. Chong: Models for laser ablation of polymers, Chem. Rev. **103**, 519 (2003)

Bityurin N., N. Arnold, B. Luk'yanchuk, D. Bäuerle: Bulk model of laser ablation of polymers, Appl. Surf. Sci. **127–129**, 164 (1998)
Bityurin N., S. Muraviov, A. Alexandrov, A. Malyshev: UV laser modifications and etching of polymer films (PMMA) below the ablation threshold, Appl. Surf. Sci. **109–110**, 270 (1997)
Bixon M., J. Jortner: Intramolecular radiationless transitions, J. Chem. Phys. **48**, 715 (1968)
Blanchet G.B., S. I. Shah: Deposition of polytetrafluoroethylene films by laser ablation, Appl. Phys. Lett. **62**, 1026 (1993)
Bockris J.O.M., A.K.N. Reddy: *Modern Electrochemistry* I and II (Plenum, New York 1977)
Böhm H.R., S. Gigan, F. Blaser, A. Zeilinger, M. Aspelmeyer, G. Langer, D. Bäuerle, J. B. Hertzberg, K. C. Schwab: High reflectivity high-Q micromechanical Bragg mirror, Appl. Phys. Lett. **89**, 223101 (2006)
Böhme R., S. Pissadakis, M. Ehrhardt, T. Rudolph, D. Ruthe, K. Zimmer: Backside etching of fused silica with ultra-short laser pulses at the interface to absorbing liquid, J. Phys. Conf. Ser. **59**, 173 (2007)
Böhme R., A. Braun, K. Zimmer: Backside etching of UV-transparent materials at the interface to liquids, Appl. Surf. Sci. **186**, 276 (2002)
Bohac V., E. D'Anna, G. Leggieri, S. Luby, A. Luches, E. Majkova, M. Martino: Tungsten silicide formation by XeCl excimer-laser irradiation of W/Si samples, Appl. Phys. A **56**, 391 (1993)
Bolle M., S. Lazare: Large scale excimer laser production of submicron periodic structures on polymer surfaces, Appl. Surf. Sci. **69**, 31 (1993)
Bollmann D., G. Neumayer, R. Buchner, K. Haberger: Shallow p-n junctions produced by laser doping with boron silicate glass, Appl. Surf. Sci. **69**, 249 (1993)
Bolme C.A., D.J.: Funk: Ultrafast dynamic ellipsometry measurements of early time laser ablation of titanium thin films, Appl. Phys. A **92**, 761 (2008)
Boman M., D. Bäuerle: Laser-assisted chemical vapor deposition of boron, J. Chinese Chem. Soc. **42**, 405 (1995)
Boman M, D. Bäuerle: 1987, unpublished
Boneberg J., J. König-Birk, H.J Münzer, P. Leiderer, K. Shuford, G.C. Schatz: Optical near-fields of triangular nanostructures, Appl. Phys. A **89**, 299 (2007)
Bonn M., D.N. Denzler, S. Funk, M. Wolf, S.-Svante Wellershoff, J. Hohlfeld: Ultrafast electron dynamics at metal surfaces: Competition between electron-phonon coupling and hot-electron transport, Phys. Rev. B **61**, 1101 (2000)
Bonse J., J. Krüger: Probing the heat affected zone by chemical modifications in fs pulse laser ablation of titanium nitride films in air, J. Appl. Phys. **107**, 054902 (2010)
Bonse J., A. Rosenfeld, C. Grebing, G. Steinmeyer, N. Mailman, G.A. Botton, H.K. Haugen: Ablation and structural changes induced in InP surfaces by single 10 fs laser pulses in air, J. Appl. Phys. **106**, 074907 (2009a)
Bonse J., A. Rosenfeld, J. Krüger: On the role of surface plasmon polaritons in the formation of laser-induced periodic surface structures upon irradiation of silicon by femtosecond-laser pulses, J. Appl. Phys. **106**, 104910 (2009b)
Bonse J., G. Bachelier, J. Siegel, J. Solis, H. Sturm: Time- and space-resolved dynamics of ablation and optical breakdown induced by fs laser pulses in indium phosphide, J. Appl. Phys. **103**, 054910 (2008)
Bonse J., G. Bachelier, J. Siegel, J. Solis: Time- and space-resolved dynamics of melting, ablation and solidification phenomena induced by fs laser pulses in germanium, Phys. Rev. B **74**, 134106 (2006)
Bonse J., M. Munz, H. Sturm: Structure formation on the surface of indium phosphide irradiated by fs-laser pulses, J. Appl. Phys. **97**, 013538 (2005)
Born M., E. Wolf: *Principles of Optics* (Pergamon, Oxford 1980)
Borowiec A., H.K. Haugen: Subwavelength ripple formation on the surfaces of compound semiconductors irradiated with femtosecond laser pulses, Appl. Phys. Lett. **82**, 4462 (2003)
Borsella E., S. Botti, R. Giorgi, S. Martelli, S. Turtu, G. Zappa: Laser-driven synthesis of nanocrystalline alumina powders from gas-phase precursors, Appl. Phys. Lett. **63**, 1345 (1993*a*)

Borsella E., S. Botti, R. Alexandrescu, I. Morjan, T. Dikonimos-Makris, R. Giorgi, S. Martelli: Nanocomposite ceramic powder production by laser-induced gas-phase reactions, Mater. Sci. Eng. **A 168**, 177 (1993*b*)

Boughaba S., J.B. Héroux, M. Curcio, E. Sacher, M. Meunier: Removal of particulate contamination from silicon surfaces with laser-based cleaning technology. Particles on Surfaces **5 & 6**: Detection, Adhesion and Removal, 297 (1999)

Bounos G., A. Nevin, S. Georgiou, C. Fotakis: Laser restoration of painted artworks, in *Laser Ablation and its Applications*, ed. by C. R. Phipps (Springer 2007) p. 549

Bourgeois F., A. Ben-Yakar: Femtosecond laser nanoaxotomy properties and their effect on axonal recovery in C. elegans, Opt. Express **15**, 8521 (2007)

Bovatsek J., A. Tamhankar, R.S. Patel, N.M. Bulgakova, J. Bonse: Thin film removal mechanisms in ns-laser processing of photovoltaic materials, Thin Solid Films **518**, 2897 (2010)

Bowers J.E., B.R. Hemenway, D.P. Wilt: Etching of deep grooves for the precise positioning of cleaves in semiconductor lasers, Appl. Phys. Lett. **46**, 453 (1985)

Bowling R.A.: A theoretical review of particle adhesion. In *Particles on Surfaces*. In *Particles on Surfaces: Detection, Adhesion, and Removal*. ed. by K.L. Mittal, Marcel Dekker Inc. (New York, Basel, Hong Kong 1995)

Boyd I.W.: ULSI dielectrics: Low-temperature silicon dioxides, Mater. Chem. and Phys. **41**, 266 (1995)

Boyd I.W., V. Craciun, A. Kazor: Vacuum-ultra-violet and ozone induced oxidation of silicon and silicon-germanium, Jpn. J. Appl. Phys. **32**, 6141 (1993)

Boyd I.W.: *Laser Processing of Thin Films and Microstructures*, Springer Ser. Mater. Sci., Vol.3 (Springer, Berlin, Heidelberg 1987)

Brannon J.H., K.W. Brannon: UV photoetching of copper, J. Vac. Sci. Technol. B**7**, 1275 (1989)

Brannon J.H.: Chemical Etching of Silicon by CO_2-Laser-induced Dissociation of NF_3, Appl. Phys. A **46**, 39 (1988)

Brannon J.H.: Excimer Laser Induced Photochemical Etching of Glass, in *Laser Chemical Processing of Semiconductor Devices*, ed. by F.A. Houle, T.F. Deutsch, R.M. Osgood (Materials Research Society, Boston 1984) Extended Abstracts, p. 112

Breitling D., C. Föhl, F. Dausinger, T. Kononenko, V. Konov: Drilling of metals, in *Femtosecond Technology for Technical and Medical Applications*, ed. by F. Dausinger, F. Lichtner, H. Lubatschowski, Springer Series Topics in Applied Physics **96**, Springer Verlag 2004a, p. 131

Breitling D., S. Klimentov, F. Dausinger: Interaction with Atmosphere, in *Femtosecond Technology for Technical and Medical Applications*, ed. by F. Dausinger, F. Lichtner, H. Lubatschowski, Springer Series Topics in Applied Physics **96**, Springer Verlag 2004b, p. 75

Brekel C.H.J. van der: Mass transport and morphology in chemical vapour deposition Processes, Dissertation, University of Nijmegen (1978)

Brewer P., S. Halle, R.M. Osgood: Photon-Assisted Dry Etching of GaAs, Appl. Phys. Lett. **45**, 475 (1984)

Brinkman A., M. Huijben, M.van Zalk, J. Huijben, U. Zeitler, J.C. Maan, W.G. van der Wiel, G. Rijnders, D.H.A. Blank, H. Hilgemkamp: Magnetic effects at the interface between non-magnetic oxides, Nature Materials; Letters, Advance Online Publication, Published online 3 June 2007, doi: 10.1038/nmat1931

Brode H.L.: Blast wave from a spherical charge. The Physics of Fluids **2**, 217 (1959)

Brodoceanu D., G.D. Cole, N. Kiesel, M. Aspelmeyer, D. Bäuerle: Femtosecond laser fabrication of high reflectivity micromirrors, Appl. Phys. Lett. **97**, 041104 (2010)

Brodoceanu D., L. Landström, D. Bäuerle: Laser-induced nanopatterning of silicon with colloidal monolayers, Appl. Phys. A **86**, 313 (2007)

Brook M.R., K.I. Grandberg, G.A. Shafeev: Kinetics of Laser-induced Au Pyrolytic Deposition from the Liquid Phase, Appl. Phys. A **52**, 78 (1991)

Broser R.M.: Homogene Laserablation von Keramiken und gepulste Laserabscheidung von hochtemperatursupraleitenden $YBa_2Cu_3O_{7-\delta}$ Schichten, Thesis, Johannes-Kepler-Universität Linz, August 2008

Bruines J.J.P., R.P.M. van Hal, H.M.J. Boots, W. Sinke, F.W. Saris: Direct Observation of Resolidification from the Surface upon Pulsed-Laser Melting of Amorphous Silicon, Appl. Phys. Lett. **48**, 1252 (1986)

Brujan E.-A., A. Vogel: Stress wave emission and cavitation bubble dynamics by ns optical breakdown in a tissue phantom, J. Fluid Mech. **558**, 281 (2006)

Brunauer S., P.H. Emmett, E. Teller: Adsorption of Gases in Multimolecular Layers, J. Am. Chem. Soc. **60**, 309 (1938)

Brunco D.P., M.O. Thompson, C.E. Otis, P.M. Goodwin: Temperature Measurements of Polyimide during KrF Excimer Laser Ablation, J. Appl. Phys. **72**, 4344 (1992)

Buene L., D.C. Jacobson, S. Nakahara, J.M. Poate, C.W. Draper, J.K. Hirvonen: Laser Irradiation of Nickel: Defect Structures and Surface Alloying, in *Laser and Electron-Beam Solid Interactions and Materials Processing*, MRS Proc. **1**, 583 (1981)

Bulgakov A.V., I. Ozerov, W. Marine: Silicon clusters produced by fs laser ablation: non-thermal emission and gas-phase condensation, Appl. Phys. A 79, 1591 (2004)

Bulgakov A.V., N.M. Bulgakova: Gas-dynamic effects of the interaction between a pulsed laser-ablation plume and the ambient gas: analogy with an underexpanded jet, J. Phys. D: Appl. Phys. 31, 693 (1998)

Bulgakova N.M., V.P. Zhukov, A.Y. Vorobyev, Ch. Guo: Modeling of residual thermal effect in femtosecond laser ablation of metals: role of a gas environment, Appl. Phys. A **92**, 883 (2008)

Bulgakova N.M., R. Stoian, A. Rosenfeld, I.V. Hertel, E.B. Campbell: Fast electronic transport and Coulomb explosion in materials irradiated with ultrashort laser pulses, Chapter 2 in *Laser Ablation and its Applications*, ed. by C. R. Phipps (Springer 2007) p. 17

Bulgakova N.M., R. Stoian, A. Rosenfeld, I.V. Hertel, W. Marine, E.E.B. Campbell: A general continuum approach to describe fast electronic transport in pulsed laser irradiated materials: The problem of Coulomb explosion, Appl. Phys. A **81**, 345 (2005)

Bulgakova N.M, A.V. Bulgakov: Pulsed laser ablation of solids: transition from normal vaporization to phase explosion, Appl. Phys. A **73**, 199 (2001)

Bunkin F.V., A.K. Dmitriyev, B.S. Luk'yanchuk, G.A. Shafeev: Thermo-diffusional Instability and Potential Distribution in Laser-Heated Absorbing Electrolytes, Appl. Phys. A **40**, 159 (1986)

Bunkin F.V., N.A. Kirichenko, B.S. Luk'yanchuk: *Optimal Regimes of Material Heating by Laser Radiation*, Preprint FIAN, No. 146 (P.N. Lebedev Phys. Inst., Moscow 1978) (in Russian)

Burgener M.L., R.E. Reedy: Temperature Distributions Produced in a Two-Layer Structure by a Scanning cw Laser or Electron Beam, J. Appl. Phys. **53**, 4357 (1982)

Burghoff J., C. Grebing, S. Nolte, A. Tünnermann: Waveguides in lithium niobate fabricated by focused ultrashort laser pulses, Appl. Surf. Sci. **253**, 7899 (2007)

Burgin J., P. Langot, A. Arbouet, J. Margueritat, J. Gonzalo, C.N. Afono, F. Vallée, A. Mlayah, M.D. Rossell, G. Van Tendeloo: Acoustic vibration modes and electron-lattice coupling in self-assembled silver nanocolumns, Nano Letters **8**, 1296 (2008)

Burns F.C., S.R. Cain: The effect of pulse repetition rate on laser ablation of polyimide and polymethylmethacrylate-based polymers, J. Phys. D: Appl. Phys. **29**, 1349 (1996)

Byskov-Nielsen J., J.-M. Savolainen, M.S. Christensen, P. Balling: Ultra-short pulse laser ablation of metals: threshold fluence, incubation coefficient and ablation rates, Appl. Phys. A **101**, 97 (2010)

Cabrera N., N.F. Mott: Theory of the Oxidation of Metals, Rep. Prog. Phys. **12**, 163 (1949)

Calder I.D., R. Sue: Modeling of cw Laser Annealing of Multilayer Structures, J. Appl. Phys. **53**, 7545 (1982)

Callies G., H. Schittenhelm, P. Berger, H. Hügel: Modeling of the expansion of laser-evaporated matter in argon, helium and nitrogen and the condensation of clusters, Appl. Surf. Sci. **127-129**, 134 (1998)

Calvert J.G., J.N. Pitts: *Photochemistry* (Wiley, New York 1966)

Camacho J.J., M. Santos, L. Diaz, J.M.L. Poyato: Spatial characterization of the laser-induced plasma plumes generated by IR CO_2 pulsed laser on carbon targets, Appl. Phys. A **94**, 373 (2009)

Campbell E.E.B., D. Ashkenasi, A. Rosenfeld: Ultra-short-pulse laser irradiation and ablation of dielectrics. Chap. 5 in "*Lasers in Materials*" ed. by R.P. Agarnala (Trans.Tech. Pub. 1999)

Campbell E.E.B., G. Ulmer, B. Hasselberger, H.-G. Busmann, I.V. Hertel: An Intense, Simple Carbon Cluster Source, J. Chem. Phys. **93**, 6900 (1990)

Campisano S.U., D.C. Jacobson, J.M. Poate, A.G. Cullis, N.G. Chew: Impurity and Interfacial Effects on the Formation of Amorphous Si from the Melt, Appl. Phys. Lett. **45**, 1216 (1984)

Carpene E.: Ultrafast laser irradiation of metals: Beyond the two-temperature model, Phys. Rev. B **74**, 024301 (2006)

Carpene E., P. Schaaf, M. Han, K.P. Lieb, M. Shinn: Reactive surface processing by irradiation with excimer laser, Nd:YAG laser, free electron laser and Ti:sapphire laser in nitrogen atmosphere, Appl. Surf. Sci. **186**, 195 (2002)

Carslaw H.S., J.C. Jaeger: *Conduction of Heat in Solids* (Clarendon Press, Oxford 1988)

Casadio F., C. Fotakis, M. Menu, G. Padeletti, M. Stuke (Guest Eds.): Special Issue "*Precise Processing, Diagnostics, Characterization and Identification of Materials for Restoration of Art*", Appl. Phys. A **100**, 3 (2010)

Cavalleri A., K. Sokolowski-Tinten, J. Bialkowski, M. Schreiner, D.V.D. Linde: Fs melting and ablation of semiconductors studied with time of flight mass spectroscopy, J. Appl. Phys. **85**, 3301 (1999)

Caviglia A.D., S. Gariglio, N. Reyren, D. Jaccard, T. Schneider, M. Gabay, S. Thiel, G. Hammerl, J. Mannhart, J.-M. Triscone: Electric field control of the $LaAlO_3/SrTiO_3$ interface ground state, Nature **456**, 624 (2008)

Celler G.K.: Modification of Silicon properties with lasers, Electron beams, and incoherent light, CRC Crit. Rev. Solid State and Mater. Sci. **12**, 193 (1984)

Chan C.L., J. Mazumder: One-Dimensional Steady-State Model for Damage by Vaporization and Liquid Expulsion due to Laser-Material Interaction, J. Appl. Phys. **62**, 4579 (1987)

Chan W.-L., R.S. Averback, D.G. Cahill: Nonlinear energy absorption of fs laser pulses in noble metals, Appl. Phys. A **97**, 287 (2009)

Chandrasekhar S.: *Hydrodynamic and Hydromagnetic Stability* (Clarendon, Oxford 1961)

Chang S.-M., H. Muramatsu, C. Nakamura, J. Miyake: The principle and applications of piezoelectric crystal sensors, Materials Science and Engineering C **12**, 111 (2000)

Chaos J.A., V. Pruneri, J. Gonzalo, C.N. Afonso: Second-harmonic generation in highly textured $LiNbO_3$ films prepared by pulsed laser deposition, J. Appl. Phys. **88**, 3768 (2000a)

Chaos J.A., R.W. Dreyfus, A. Perea, R. Serna, J. Gonzalo, C.N. Afonso: Delayed release of Li atoms from laser ablated lithium niobate, Appl. Phys. Lett. **76**, 649 (2000b)

Chaoui N., J. Solis, C.N. Afonso, T. Fourrier, T. Mühlberger, G. Schrems, M. Mosbacher, D. Bäuerle, M. Bertsch, P. Leiderer: A high sensitivity in-situ optical diagnostic technique for laser cleaning of transparent substrates, Appl. Phys. A **76**, 767 (2003)

Chaoui N., J. Siegel, J. Solis, C.N. Afonso: Reflectivity of crystalline Ge and Si at the melting temperature measured in real time with sub-ns temporal resolution, J. Appl. Phys. **89**, 3763 (2001)

Chapman R.L., J.C.C. Fan, H.J. Zeiger, R.P. Gale: Crystallization-Front Velocity during Scanned Laser Crystallization of Amorphous Ge Films, Appl. Phys. Lett. **37**, 292 (1980)

Chen C., J.S. Horwitz: Ferroelectric thin films for microwave device applications, in *Pulsed Laser Deposition of Thin Films: Applications-Led Growth of Functional Materials*, ed. R. Eason (Wiley 2007) p. 533

Chen C.J., R.M. Osgood: Direct Observation of the Local-Field-Enhanced Surface Photochemical Reactions, Phys. Rev. Lett. **50**, 1705 (1983); ibid.: Surface-Catalyzed Photochemical Reactions of Physisorbed Molecules, Appl. Phys. A **31**, 171 (1983)

Chen S., C.P. Grigoropoulos: Noncontact ns-time-resolution temperature measurements in excimer laser heating of Ni-P disk substrates, Appl. Phys. Lett. **71**, 3191 (1997)

Chen X.Y., J. Lin, J.M. Liu, Z.G. Liu: Formation and evolution of self-organized hexagonal patterns on silicon surface by laser irradiation in water, Appl. Phys. A **94**, 649 (2009)

Chen Z.C., M.H. Hong, H. Dong, Y.D. Gong, C.S. Lim, L.P. Shi, T.C. Chong: Parallel laser microfabrication of terahertz metamaterials and its polarization-dependent transmission property, Appl. Phys. A **101**, 33 (2010)

Chiari G., C. Fotakis, M. Menu, G. Padeletti, M. Stuke eds.: "*Science and Technology of Cultural Heritage Materials: Art Conservation and Restoration*", Appl. Phys. A **92**, 1 (2008)

Chiashi S., M. Kohno, Y. Takata, S. Maruyama: Localized synthesis of single-walled carbon nanotubes on silicon substrates by a laser heating catalytic CVD, J. Phys. Conf. Ser. **59**, 155 (2007)

Chimmalgi A., C.P. Grigoropoulos, K. Komvopoulos: Surface nanostructuring by ns-/fs laser-assisted scanning force microscopy, J. Appl. Phys. **97**, 104319 (2005)

Choi J.H., D. Lucas, C.P. Koshland: Laser ablation of nanoscale particles with 193 nm light, J Phys: Conf. Ser. **59**, 54 (2007)

Choi K.J., M. Biegalski, Y.L. Li, A. Sharan, J. Schubert, R. Uecker, P. Reiche, Y.B. Chen, X.Q. Pan, V. Gopalan, L.Q. Chen, D.G. Schlom, C.B. Eom: Enhancement of ferroelectricity in strained $BaTiO_3$ thin films, Science **306**, 1005 (2004)

Choi T.Y., C. P. Grigoropoulos: Observation of femtosecond laser-induced ablation in crystalline silicon, J. Heat Trans. **126**, 723 (2004)

Chou W.B., M.N. Azer, J. Mazumder: Laser Chemical Vapor Deposition of Ti from $TiBr_4$, J. Appl. Phys. **66**, 191 (1989)

Christensen B.H., P. Balling: Modeling ultrashort-pulse laser ablation of dielectric materials, Phys. Rev. B **79**, 155424 (2009)

Christensen M.N., J. Byskov-Nielsen, B.H. Christensen, P. Balling: Single-shot ablation of sapphire by ultrashort laser pulses, Appl. Phys. A **101**, 279 (2010)

Chuang T.J., H. Hiraoka, A. Mödl: Laser-Photoetching Characteristics of Polymers with Dopants, Appl. Phys. A **45**, 277 (1988)

Chuang T.J., I. Hussla, W. Sesselmann: Laser-Assisted Chemical Etching of Inorganic Materials: Mechanistic Studies, in *Laser Processing and Diagnostics*, ed. by D. Bäuerle, Springer Ser. Chem. Phys., Vol. 39 (Springer, Berlin, Heidelberg 1984) p. 300

Chuang T.J.: Laser-Enhanced Chemical Etching of Solid Surfaces, IBM J. Res. Dev. **26**, 145 (1982)

Chuang T.J.: Multiple Photon Excited SF_6 Interaction with Silicon Surfaces, J. Chem. Phys. **74**, 1453 (1981)

Chung C.K., Y.C. Sung, G.R. Huang, E.J. Hsiao, W.H. Lin, S.L. Lin: Crackless linear through-wafer etching of Pyrex glass using *liquid-assisted* CO_2 laser processing, Appl. Phys. A **94**, 927 (2009)

Chung S.H., E. Mazur: Fs laser ablation of neurons in *C. elegans* for behavioral studies, Appl. Phys. A **96**, 335 (2009)

Cillessen J.F.M., R.M. Wolf, D.M. de Leeuw: Pulsed Laser Deposition of Hetero-epitaxial Thin Pt Films on MgO (100), Thin Solid Films **226**, 53 (1993a)

Cillessen J.F.M., R.M. Wolf, A.E.M. De Veirman: Hetero-Epitaxial Oxidic Conductor $La_{1-x}Sr_xCoO_3$ Prepared by Pulsed Laser Deposition, Appl. Surf. Sci. **69**, 212 (1993b)

Clyne M.A.A., D.H. Stedman: Recombination of Ground-State Halogen Atoms, Part 1 – Radiative Recombination of Chlorine Atoms, Trans. Faraday Soc. **64**, 1816 (1968); ibid. Part 2 – Kinetics of the Overall Recombination of Chlorine Atoms, Trans. Faraday Soc. **64**, 2698 (1968)

Colin A., P. Morin, R. Beneyton, Luc Pinzelli, D. Mathiot, E. Fogarassy: Dopant diffusion and activation induced by sub-melt laser anneal within the co-implanted p+ polycrystalline silicon gate used in CMOS technologies, Thin Solid Films **518**, 2390 (2011)

Colin A., P. Morin, F. Cacho, H. Bono, R. Beneyton, D. Mathiot, E. Fogarassy: Optical-thermal simulation applied to the study of the pattern effects induced by the sub-melt laser anneal process in advanced CMOS technologies, Appl. Phys. A **104**, 517 (2011)

Colin A., P. Morin, F. Cacho, H. Bono, R. Beneyton, M. Bidaud, D. Mathiot, E. Fogarassy: Simulation of the sub-melt laser anneal process in 45 CMOS technology – application to the thermal pattern effects, Mater. Sci. Eng. B **154–155**, 31 (2008)

Comita P.B., P.E. Price, T.T. Kodas: Time-Resolvec Reflectance Studies of Surface Melting during Laser-Assisted Deposition with a Modulated Laser Source, J. Appl. Phys. **71**, 221 (1992)

Compaan A.: Phonon populations during pulsed laser annealing, J. Luminesc. **30**, 425 (1985)

Conde J.C., P. González, F. Lusquinos, B. León: Analysis of the formation and evolution of oriented microstructures on laser ablated silicon, Appl. Phys. A **95**, 465 (2009)
Conforti P.F., M. Prasad, B.J. Garrison: The impact of point thermal absorbers in ablation of PMMA, Appl. Phys. A **92**, 1037 (2008)
Coufal H.: Photothermal spectroscopy using a pyroelectric thin-film detector, Appl. Phys. Lett. **44**, 59 (1984)
Craciun F., M. Dinescu: Piezoelectrics, in *Pulsed Laser Deposition of Thin Films: Applications-Led Growth of Functional Materials*, ed. R. Eason (Wiley 2007) p. 487
Craciun V., A.H. Reader, D.E.W. Vandenhoudt, S.P. Best, R.S. Hutton, A. Andrei, I.W. Boyd: Low temperature UV oxidation of SiGe for preparation of Ge nanocrystals in SiO_2 Thin Solid Films **255**, 290 (1995a)
Craciun V., S. Amirhaghi, D. Craciun, J. Elders, J.G.E. Gardeniers, I.W. Boyd: Effects of Laser Wavelength and Fluence on the Growth of ZnO Thin Films by Pulsed Laser Deposition, Appl. Surf. Sci. **86**, 99 (1995b)
Cramer L.P., S.C. Langford, J.T. Dickinson: The formation of metallic nanoparticles in single crystal CaF_2 under 157 nm excimer laser irradiation, J. Appl. Phys. **99**, 054305 (2006)
Crank J.: *Free and Moving Boundary Problems* (Clarendon Press, Oxford 1988)
Cullis A.G.: Transient Annealing of Semiconductors by Laser, Electron Beam and Radiant Heating Techniques, Rep. Prog. Phys. **48**, 1155 (1985)
Cullis A.G., H.C. Webber, P. Bailey: A Device for Laser Beam Diffusion and Homo-genisation, J. Phys. E **12**, 688 (1979)
Curran C., J.M. Lee, K.G. Watkins: UV laser removal of small metallic particles from silicon wafers, Optics and Lasers in Engineering **38**, 405 (2002)
D'Alessandria M., F. Mücklich: Tailoring the chemical behavior of aluminum for selective etching by laser interference metallurgy, Appl. Phys. A **98**, 311 (2010)
Daminelli G., S. Pentzien, A. Hertwig, J. Krüger: Influence of film thickness on laser ablation of hydrogenated amorphous carbon films, Appl. Phys. A **83**, 89 (2006)
D'Anna E., G. Leggieri, A. Luches, M. Martino, A.V. Drigo, I.N. Mihailescu, S. Ganatsios: Synthesis of Pure Titanium Nitride Layers by Multipulse Excimer Laser Irradiation of Titanium Foils in a Nitrogen-Containing Atmosphere, J. Appl. Phys. **69**, 1687 (1991)
D'Anna E., G. Leggieri, A. Luches: Laser Synthesis of Metal Silicides, Appl. Phys. A **45**, 325 (1988)
Davanloo F., T.J. Lee, D.R. Jander, H. Park, J.H. You, C.B. Collins: Adhesion and mechanical properties of amorphic diamond films prepared by a laser plasma discharge source, J. Appl. Phys. **71**, 1446 (1992)
Deal B.E., A.S. Grove: General Relationship for the Thermal Oxidation of Silicon, J. Appl. Phys. **36**, 3770 (1965)
Delaporte Ph., R. Oltra: Laser Cleaning: State of the Art, Chapter 13 in *Recent Advances in Laser processing of Materials*, J. Perriere, E. Millon, E. Fogarassy eds., p. 411 (Elsevier 2006)
Demtröder W.: *Laser Spectroscopy*, 2nd ed. (Springer, Berlin, Heidelberg 1996)
Denk R., K. Piglmayer, D. Bäuerle: Laser-induced etching and deposition of W using a-SiO_2 microspheres, Applied Physics A **76**, 549 (2003)
Denk R., K. Piglmayer, D. Bäuerle: Laser-induced nanopatterning of PET using a-SiO_2 microspheres, Appl. Phys. A **74**, 825 (2002)
De Puydt Y., P. Bertrand, P. Lutgen: Study of the Al/PET Interface in Relation with Adhesion, Surf. Interface Anal. **12**, 486 (1988)
Deubel M., G.v. Freymann, M. Wegener, S. Pereira, K. Busch, C.M. Soukoulis: Direct laser writing of 3D photonic-crystal templates for telecommunications, Nature **3**, 444 (2004)
Deutsch T.F.: Lasers and optics in health care, Proc. of the IEEE **85**, 1797 (1997)
Deutsch T.F.: Applications of Excimer Lasers to Semiconductor Processing: in *Laser Processing and Diagnostics*, ed. by D. Bäuerle, Springer Ser. Chem. Phys., Vol. 39 (Springer, Berlin, Heidelberg 1984) p. 239
Dickey F.M., B.D. O'Neil: Multifaceted Laser Beam Integraters: General Formulation and Design Concepts, Opt. Eng. **27**, 999 (1988)

Dickinson J.T.: Observation of negative alkali ions from alkali halides during 248-nm laser irradiation, Appl. Phys. A **92**, 1025 (2008)

Dickinson J.T.: Low fluence laser desorption and plume formation from wide bandgap crystalline materials. In Miller J.C., R.F. Haglund eds.: *Laser Ablation and Desorption*. Vol 30: Experimental Methods in the Physical Sciences. Academic Press 1998, p. 139

Dickinson J.T., S.C. Langford, L.C. Jensen: Simultaneous Bombardment of Wide Bandgap Materials with UV Excimer Irradiation and keV Electrons, *in Laser Ablation - Mechanisms and Applications*, ed. by J.C. Miller, R.F. Haglund, Lecture Notes Phys., Vol. 389 (Springer, Berlin, Heidelberg 1991) p. 301

Diez-Blanco V., J. Siegel, A. Ferrer, A. Ruiz de la Cruz, J. Solis: Deep subsurface waveguides with circular cross section produced by femtosecond laser writing, Appl. Phys. Lett. **91**, 051104 (2007)

Dinca V., A. Ranella, M. Farsari, D. Kafetzopoulos, M. Dinescu, A Popescu, C. Fotakis: Quantification of the activity of biomolecules in microarrays obtained by direct laser transfer, Biomed. Microdevices **10**, 719 (2008)

Dolgaev S.I., N.A. Kirichenko, G.A. Shafeev: Deposition of nanostructured Cr_2O_3 on amorphous substrates under laser irradiation of the solid-liquid interface, Appl. Surf. Sci.**138–139**, 449 (1999)

Donnelly T., J.G. Lunney: Optical absorption in early stage low temperature laser produced plasma, Appl. Phys. A **92**, 951 (2008)

Donnelly V.M.: Products of Pulsed Laser Induced Thermal Decomposition of Triethylgallium and Trimethylgallium Adsorbed on GaAs (100), J.Vac. Sci. Technol. A **9**, 2887 (1991)

Donnelly V.M., T.R. Hayes: Excimer Laser Induced Etching of InP, Appl. Phys. Lett. **57**, 701 (1990)

Donnelly V.M., J.A. McCaulley: Selected Area Growth of GaAs by Laser-Induced Pyrolysis of Adsorbed Triethylgallium, Appl. Phys. Lett. **54**, 2458 (1989)

Donnelly V.M., C.W. Tu, J.C. Beggy, V.R. McCrary, M.G. Lamont, T.D. Harris, F.A. Baiocchi, R.C. Farrow: Laser-Assisted Metalorganic Molecular Beam Epitaxy of GaAs, Appl. Phys. Lett. **52**, 1065 (1988)

Doppelbauer J., D. Bäuerle: Kinetics of Laser-induced Pyrolytic Chemical Processes and the Problem of Temperature Measurements, in *Interfaces under Laser Irradiation*, ed. by L.D. Laude, D. Bäuerle, M. Wautelet, NATO ASI Series (Nijhoff, Dordrecht 1987) p. 277

Doppelbauer J.: Kinetische Untersuchungen an Laserinduzierten Pyrolytischen Prozessen, Thesis, Universität Linz, Austria (1987)

Doppelbauer J., D. Bäuerle: Kinetic Studies of Pyrolytic Laser-induced Chemical Processes, in *Laser Processing and Diagnostics II*, ed. by D. Bäuerle, K.L. Kompa, L.D. Laude (Les Editions de Physique, Les Ulis 1986) p. 53

Doraiswamy A., R.J. Narayan, T. Lippert, L. Urech, A. Wokaun, M. Nagel, B. Hopp. M. Dinescu, R. Modi, R.C.Y. Auyeung, D.B. Chrisey: Excimer laser forward transfer of mammalian cells using a novel triazene absorbing layer, Appl. Surf. Sci. **252**, 4743 (2006)

Dou J., J. Li, P.R. Herman, J.S. Aitchison, T. Fricke-Begemann, J. Ihlemann, G. Marowsky: Laser machining of micro-lenses on the end face of single-mode optical fibers, Appl. Phys. A **91**, 591 (2008)

Driel H.M. van, J.E. Sipe, J.F. Young: Laser-induced coherent modulation of solid and liquid surfaces, J. Luminesc. **30**, 446 (1985)

Dubowski J.J., S. Moisa, B. Komorowski, H. Tan, J.B. Webb: Laser polishing of GaN, Proc. SPIE Vol. **4274**, 442 (2001)

Dubowski J.J., P.J. Poole, G.I. Sproule, G. Marshall, S. Moisa, C. Lacelle, M. Buchanan: Enhanced quantum well photoluminescence in InGaAs/InGaAsP heterostructures following excimer-laser-assisted surface processing, Appl. Phys. A **69** [Suppl.], S299 (1999)

Duff W.H., L.V. Zhigilei: Computational study of cooling rates and recrystallization kinetics in short pulse laser quenching of metal targets, J. Phys. Conf. Ser. **59**, 413 (2007)

Dufft D., A. Rosenfeld, S.K. Das, R. Grunwald, J. Bonse: Femtosecond laser-induced periodic surface structures revisited: A comparative study on ZnO, J. Appl. Phys. **105**, 034908 (2009)

Duffy D.M., A.M. Rutherford: Including the effects of electronic stopping and electron–ion interactions in radiation damage simulations, J. Phys. Condens. Matter **19**, 016207 (2007)
Duley W.W.: *Laser Processing and Analysis of Materials* (Plenum, New York 1983)
Duley W.W.: *CO_2 Lasers - Effects and Applications*, (Academic Press, London 1976)
Dumont Th., R. Bischofberger, T. Lippert, A. Wokaun: Gravimetric and profilometric measurements of the ablation rates of photosensitive polymers at different wavelengths, Appl. Surf. Sci. **247**, 115 (2005)
Durrant S.F., N.I. Ward: Recent biological and environmental applications of laser ablation inductively coupled plasma mass spectrometry (LA-ICP-MS), J. Anal. At. Spectrom. **20**, 821 (2005)
Durrant S.F.: Laser ablation inductively coupled plasma mass spectrometry: achievements, problems, prospects, J. Anal. At. Spectrom. **14**, 1385 (1999)
Dutto C., E. Fogarassy, D. Mathiot, D. Muller, P. Kern, D. Ballutaud: Long-pulse duration excimer laser annealing of Al^+ ion implanted 4H-SiC for pn junction formation, Appl. Surf. Sci. **208–209**, 292 (2003)
Dvornikov A.S, P.M. Rentzepis: Novel organic ROM materials for optical 3D memory devices, Opt. Comm. **136**, 1 (1997)
Dyer P.E., C.D. Walton, R. Zakaria: Interference effects in 157 nm laser ablated cones in polycarbonate and application to spatial coherence measurement, Appl. Phys. A **95**, 319 (2009)
Dyer P.E., S.R. Farrar, P.H. Key: Fast time-response photoacoustic studies and modelling of KrF laser ablated $YBa_2Cu_3O_7$, Appl. Surf. Sci. **54**, 255 (1992a)
Dyer P.E., S.R. Farrar, A. Issa, P.H. Key: Laser Ablation Dynamics of Superconductors: Photoacoustic and Spectroscopic Studies, in *Laser Ablation of Electronic Materials*, ed. by E. Fogarassy and S. Lazare (Elsevier, Amsterdam 1992b) p. 101
Dyer P.E., G.A. Oldershaw, J. Sidhu: Ultraviolet-Laser-induced Ablation of Poly(ethylene terephthalate), J. Phys. Chem. **95**, 10004 (1991)
Dyer P.E., R.J. Farley: Periodic surface structures in the excimer laser ablative etching of polymers, Appl. Phys. Lett. **57**, 765 (1990)
Dyer P.E., R.D. Greenough, A. Issa, P.H. Key: Spectroscopic and ion probe measurements of KrF laser ablated Y-Ba-Cu-O bulk samples, Appl. Phys. Lett. **53**, 534 (1988)
Dygert N.L., A.P. Gies, K.E. Schriver, R.F. Haglund: Deposition of polyimide precursor by resonant infrared laser ablation, Appl. Phys. A **89**, 481 (2007)
Dykhne A.M., B.P. Rysev: On the simultaneous excitation of surface acoustic and electromagnetic waves under the thermoelastic action of laser radiation, Bull. USSR Acad. Sci., Ser. Phys, **50** (3), 609 (1986)
Eaton S.M., H. Zhang, P.R. Herman, F. Yoshino, L. Shah, J. Bovatsek, A.Y. Arai: Heat accumulation effects in femtosecond laser-written waveguides with variable repetition rate, Optics Express **13**, 4708 (2005)
Eden J.G.: Photochemical Vapor Deposition, in *Thin Film Processes II* (Academic, London 1991)
Egitto F.D., C.R. Davis: Dopant-Induced Excimer Laser Ablation of Poly(tetrafluoroethylene) II. Effect of Dopant Concentration, Appl. Phys. B **55**, 488 (1992)
Ehrlich D.J.: Critical issues for single-chamber manufacturing: The role of laser technology, Appl. Surf. Sci. **69**, 115 (1993)
Ehrlich D.J., J.Y. Tsao, C.O. Bozler: Submicrometer patterning by projected excimer-laser-beam induced chemistry, J. Vac. Sci. Technol. B **3**, 1 (1985)
Ehrlich D.J., R.M. Osgood, Jr., T.F. Deutsch: Photodeposition of metal films with UV laser light, J. Vac. Sci. Technol. **21**, 23 (1982)
Ehrlich D.J., J.Y. Tsao: Submicrometer-linewidth doping and relief definition in silicon by laser-controlled diffusion, Appl. Phys. Lett **41**, 297 (1982)
Ehrlich D.J., R.M. Osgood, T.F. Deutsch: Direct writing of regions of high doping on semiconductors by UV-laser photodeposition, Appl. Phys. Lett. **36**, 916 (1980)
Elaboudi I., S. Lazare, C. Belin, D. Talaga, C. Labrugère: From polymer films to organic nanoparticles suspensions by means of excimer laser ablation in water, Appl. Phys. A **93**, 827 (2008)
Elvers D., L. Remer, N. Arnold, D. Bäuerle: Laser-microdissection of biological tissues: Process optimization, Appl. Phys. A **80**, 55 (2005)

Emmerich R., S. Bauer, B. Ploss: Temperature distribution in a film heated with a laser spot: Theory and measurement, Appl. Phys. A **54**, 334 (1992)
Endert H., M. Kauf, R. Pätzel: Excimerlaser-technologie: Stand der technik und perspektiven (Excimer laser technology: industry trends and future perspectives) LaserOpto, 31(4) (1999), p. 46
Endert H., R. Pätzel, D. Basting: in optical and quantum electronics **27**, 1319 (1995)
Englert L., M. Wollenhaupt, L. Haag, C. Sarpe-Tudoran, B. Rethfeld, T. Baumert: Material processing of dielectrics with temporally asymmetric shaped fs laser pulses on the nm scale, Appl. Phys. A **92**, 749 (2008)
Eres D., D.H. Lowndes, D.B. Geohegan, D.M. Mashburn: Laser photochemical growth of amorphous silicon at low temperatures and comparison with thermal chemical vapor deposition, MRS Proc. **101**, 355 (1988)
Ertl G., J. Küppers: *Low Energy Electrons and Surface Chemistry*, (VCH, Weinheim 1985)
Esrom H., G. Wahl: UV Excimer laser-induced pre-nucleation of surfaces followed by electroless metallization, Chemtronics **4**, 216 (1989)
Eversole D., B. Luk'yanchuk, A. Ben-Yakar: Plasmonic laser nanoablation of silicon by the scattering of femtosecond pulses near gold nanospheres, Appl. Phys. A **89**, 283 (2007)
Eyett M., D. Bäuerle: Influence of the beam spot size on ablation rates in pulsed-laser processing, Appl. Phys. Lett. **51**, 2054 (1987)
Eyett M., D. Bäuerle, W. Wersing, H. Thomann: Excimer laser-induced etching of ceramic $PbTi_{1-x}Zr_xO_3$, J. Appl. Phys. **62**, 1511 (1987)
Eyett M., D. Bäuerle, W. Wersing, K. Lubitz, H. Thomann: Laser-induced chemical etching of ceramic $PbTi_{1-x}Zr_xO_3$, Appl. Phys. A **40**, 235 (1986)
Eyring H., S.H. Lin, S.M. Lin: *Basic Chemical Kinetics* (Wiley, New York 1980)
Ezaki M., H. Kumagai, K. Toyoda, M. Obara: Surface modification of III-V compound semiconductors using surface electromagnetic wave etching induced by UV lasers, IEEE J. Select.Top. Quant.Elect. **1**, 841 (1995)
Fähler S., M. Weisheit, K. Sturm, H.U. Krebs: PLD of metallic multilayers: The interface of laser-deposited Fe/Ag multilayers: Evidence for the 'subsurface growth mode' during PLD and examination of the bcc-fcc transformation, Appl. Phys. A **69** [Suppl.], S459 (1999)
Fairand B.P., A.H. Clauer, R.G. Jung, B.A. Wilcox: Quantitative assessment of laser-induced stress waves generated at confined surfaces, Appl. Phys. Lett. **25**, 431 (1974)
Faißt B.: *Laser Marking on Plastics* (Photonik International 2008/1, p. 20)
Falkovsky L.A., E.G. Mishchenko: Electron-lattice kinetics of metals heated by ultrashort laser pulses, J. Exp. Theor. Phys **88**, 84 (1999)
Fardel R., E. McLeod, Y.-C. Tsai, C.B. Arnold: Nanoscale ablation through optically trapped microspheres, Appl. Phys. A **101**, 41 (2010)
Fardel R., L. Urech, T. Lippert, C. Phipps, J.M. Fitz-Gerald, A. Wokaun: Laser ablation of energetic polymer solutions: effect of viscosity and fluence on the splashing behavior, Appl. Phys. A **94**, 657 (2009)
Fardel R., M. Nagel, T. Lippert, F. Nüesch, A. Wokaun, B.S. Luk'yanchuk: Influence of thermal diffusion on the laser ablation of thin polymer films, Appl. Phys. A **90**, 661 (2008)
Fardel R., M. Nagel, F. Nüesch, T. Lippert, A. Wokaun: Fabrication of organic light-emitting diode pixels by laser-assisted forward transfer, Appl. Phys. Lett. **91**, 061103 (2007)
Farsari M., A. Ovsianikov, M. Vamvakaki, I. Sakellari, D. Gray, B.N. Chichkov, C. Fotakis: Fabrication of 3D photonic crystal structures containing an active nonlinear optical chromophore, Appl. Phys. A **93**, 11 (2008)
Feigelson R.S.: Opportunities for Research on Single-Crystal Fibers, Mater. Sci. Eng. B **1**, 67 (1988)
Feit M.D., A.M. Komashko, A.M. Rubenchik: Ultra-short pulse laser interaction with transparent dielectrics, Appl. Phys. A **79**, 1657 (2004)
Fell A., G.P. Willeke: Fast simulation code for heating, phase changes and dopant diffusion in silicon laser processing using the alternating direction explicit (ADE) method, Appl. Phys. A **98**, 435 (2010)

Fell A., D. Kray, G.P. Willeke: Transient 3D/2D simulation of laser-induced ablation of silicon, Appl. Phys. A **92**, 987 (2008)

Fennell M.D., G.J. Fisanick, D.K. Atwood: Electrical Characterization of Au Lines Produced by Laser-Direct-Writing of Metallopolymer Films, in *Beam Induced Chemical Processes*, ed. by R.J.von Gutfeld, J.E.Greene, H.Schlossberg (Materials Research Society, Boston 1985) Extended Abstracts p. 39

Fernandes A.J., D.M. Kane, B. Gong, R.N. Lamb: UV Laser-induced dehydroxylation of UV fused silica surfaces, in "*Laser Cleaning II*", Chap. 6, p. 147, ed. D.M.Kane (World Scientific, Singapore, 2006)

Ferziger J.H., H.G. Kaper: *Mathematical Theory of Transport Processes in Gases* (North Holland, Amsterdam 1972)

Fisanick G.J., M.E. Gross, J.B. Hopkins, M.D. Fennell, K.J. Schnoes, A. Katzir: Laser-initiated microchemistry in thin films: Development of new types of periodic structures, J. Appl. Phys. **57**, 1139 (1985)

Fischer J., G.v. Freymann, M. Wegener: The materials challenge in diffraction-unlimited direct-laser-writing optical lithography, Adv. Mater. **22**, 3578 (2010)

Fisher V.I., V.M. Kharash: Fast gas-ionization wave in a laser beam, Sov. Phys. – JETP, **56** (5), 1004 (1982)

Fogarassy E., S.de Unamuno, B. Prevot, P. Boher, M. Stehle, D. Pribat: Super-lateral-growth regime analysis in long-pulse-duration excimer-laser crystallization of a-Si films on SiO_2, Appl. Phys. A **68**, 631 (1999)

Fogarassy E., A. Grob, J. Grob, D. Muller, B. Prévot, S. Unamuno, P. Boher, M. Stehle: Growth of pseudomorphic $Si_{1-y}C_y$ and $Si_{1-x-y}Ge_xC_y$ alloy layers on <100> Si by ion implantaion and pulsed excimer laser induced epitaxy, Mater. Chem. Phys **54**, 153 (1998)

Fogarassy E.: Basic mechanisms and applications of the laser-induced forward transfer for high T_c superconducting thin film deposition, SPIE Proc. **1394**, 169 (1990)

Fogarassy E., D.H. Lowndes, R. Narayan, C.W. White: UV laser incorporation of dopants into silicon: Comparison of two processes, J. Appl. Phys. **58**, 2167 (1985)

Fotakis C., V. Zorba, E. Stratakis, A. Athanassiou, P. Tzanetakis, I. Zergioti, D.G. Papagoglou, K. Sambani, G. Filippidis, M. Farsari, V. Pouli, G. Bounos, S. Georgiou: Novel aspects of materials processing by ultrafast lasers: From electronic to biological and cultural heritage applications, J. Phys. Conf. Ser. **59**, 59, 266 (2007)

Fourrier T., G. Schrems, T. Mühlberger, J. Heitz, N. Arnold, D. Bäuerle, M. Mosbacher, J. Boneberg, P. Leiderer: Laser cleaning of polymer surfaces, Appl. Phys. A **72**, 1 (2001)

Frank P., F. Lang, M. Mosbacher, J. Boneberg, P. Leiderer: Infrared steam laser cleaning, Appl. Phys. A **93**, 1 (2008)

Freeman D.L., J.D. Doll: The influence of diffusion on surface reaction kinetics, J. Chem. Phys. **78**, 6002 (1983)

Fritzsche H.: Noncrystalline Semiconductors, Physics Today **37**, 34 (October 1984)

Fuchigami H., Y. Nakao, S. Tanimura, Y. Uehara, T. Kurata, S. Tsunoda, H. Niino, A. Yabe: Organic molecular beam deposition combined with a laser-induced chemical reaction, Appl. Phys. A **67**, 277 (1998)

Fuji H., M. Igarashi, Y. Hanada, T. Miura, S. Hanyu, K. Kakimoto, Y. Iijima, T. Saitoh: Long Gd-123 coated conductor by PLD method, Physica C **468**, 1510 (2008)

Fukumura H., H. Uji-i, H. Banjo, H. Masuhara, D.M. Karnakis, N. Ichinose, S. Kawanishi, K. Uchida, M. Irie: Laser implantation of photochromic molecules into polymer films: a new approach towards molecular device fabrication, Appl. Surf. Sci. **127–129**, 761 (1998)

Furmanski J., A.M Rubenchik, M.D. Shirk, B.C. Stuart: Deterministic processing of alumina with ultrashort laser pulses, J. Appl. Phys. **102**, 073112 (2007)

Fuss W., T.P. Cotter: Energy and pressure dependence of the CO_2 laser-induced dissociation of sulfur hexafluoride, Appl. Phys. **12**, 265 (1977)

Gaižauskas E.: Filamentation vs. optical breakdown in bulk transparent media, in *3D Laser Microfabriation. Principles and Applications*, ed. by H. Misawa, S. Juodkazis (Wiley-VCH, Weinheim, 2006) p. 109

Gallardo I., K. Hoffmann, J.W. Keto: CdSe & ZnS core/shell nanoparticles generated by laser ablation of microparticles, Appl. Phys. A **94**, 65 (2009)
Gaponov S.V., B.M. Luskin, N.N. Salashenko: Synthesis of a superlattice structure by laser deposition, Sov. Phys. Tech. Phys. **5**, 210 (1979)
Gaponov-Grekhov A.V., A.S. Lomov, G.V. Osipov, M.I. Rabinovich: Pattern formation and dynamics of two-dimensional structures in non-equilibrium dissipative media, in *Nonlinear Waves 1 – Dynamics and Evolution*, ed. by A.V. Gaponov-Grekhov, M.I. Rabinovich, J. Engelbrecht (Springer, Berlin, Heidelberg 1989)
Garcia B.J., J. Martinez, J. Piqueras: Ge diffusion into GaAs by pulsed laser irradiation, Appl. Phys. A **46**, 191 (1988)
Garrett B.C. et al.: Role of water in electron-initiated processes and radical chemistry: Issues and scientific advances, Chem. Rev. **105**, 355 (2005)
Gaspard S., M. Forster, C. Huber, C. Zafiu, G. Trettenhahn, W. Kautek, M. Castillejo: Fs laser processing of biopolymers at high repetition rate, Phys. Chem. Chem. Phys. **10**, 6174 (2008)
Gasser A., E.W. Kreutz, K. Wissenbach: Beschichten mit CO_2-laserstrahlung, (cladding with CO_2-laser radiation) oberflächentechnik, SURTEC Berlin'89, (Hanser, München 1989) p. 545
Gauthier R., C. Guittard: Mechanism investigations of a pulsed laser light induced desorption, Phys. Status. Solidi (a) **38**, 477 (1976)
Gawelda W., D. Puerto, J. Siegel, A. Ferrer, A. Ruiz de la Cruz, H. Fernandez, J. Solis: Ultrafast imaging of transient electronic plasmas produced in conditions of fs waveguide writing in dielectrics, Appl. Phys. Lett. **93**, 121109 (2008)
Geldhauser T., S. Ikegaya, A. Kolloch, N. Murazawa, K. Ueno, J. Boneberg, P. Leiderer, E. Scheer, H. Misawa: Visualization of near-field enhancements of gold triangles by nonlinear photopolymerization, Plasmonics **6**, 207 (2011)
Geldhauser T., F. Ziese, F. Merkt, A. Erbe, J. Boneberg, P. Leiderer: Acoustic laser cleaning of silicon surfaces, Appl. Phys. A **89**, 109 (2007)
Geohegan D.B., A.A. Puretzky, D.J. Rader: Gas-phase nanoparticle formation and transport during PLD of $Y_1Ba_2Cu_3O_{7-d}$, Appl. Phys. Lett. **74**, 3788 (1999)
Geohegan D.B., A.A. Puretzky, G. Duscher, S.J. Pennycook: Time-resolved imaging of gas phase nanoparticle synthesis by laser ablation, Appl. Phys. Lett. **72**, 2987 (1998)
Geohegan D.B.: Physics and diagnostics of laser ablation plume propagation for High-T_c superconductor film growth, Thin Solid Films **220**, 138 (1992)
Gerischer H.: Electrochemical photo and solar cells - principles and some experiments, electroanal. Chem. Interfacial. Electrochem. **58**, 263 (1975)
Gibbon P., M. Maşek, U. Teubner, W. Lu, M. Nicoul, U. Shymanovich, A. Tarasevitch, P. Zhou, K. Sokolowski-Tinten, D.v.d. Linde: Modelling and optimisation of fs laser-produced K_α sources, Appl. Phys. A **96**, 23 (2009)
Gigan S., H. R. Böhm, M. Paternostro, F. Blaser, G. Langer, J.B. Hertzberg, K.C. Schwab, D. Bäuerle, M. Aspelmeyer, A. Zeilinger: Self-cooling of a micromirror by radiation pressure, Nature **444**, 67 (2006)
Gilgen H.H., T. Cacouris, P.S. Shaw, R.R. Krchnavek, R.M. Osgood: Direct Writing of Metal Conductors with Near UV-Light, Appl. Phys. B **42**, 55 (1987)
Gloor S., W. Lüthy, H.P. Weber: Laser polishing of extended diamond films. Diamond Films and Technol 7, 233 (1997)
Glunz S.W., R. Preu, S. Schaefer, E. Schneiderlöchner, W. Pfleging, R. Lüdemann, G. Willeke: New simplified methods for patterning the rear contact of RP-PERC high-efficiency solar cells, Photovoltaic Specialists Conference, 2000. Conference Record of the Twenty-Eighth IEEE, 15–22 Sept. 2000 Page(s):168–171 IEEE
Gnanasekar K.I., M. Sharon, R. Pinto, S.P. Pai, M.S.R. Rao, P.R. Apte, A.S. Tamhane, S.C. Purandare, L.C. Gupta, R. Vijayaraghavan: Pulsed laser ablation: A new route to synthesize novel superconducting compounds as oriented films, J. Appl. Phys. **79**, 1082 (1996)
Goduguchinta R., J. Pegna: Variational analysis of LCVD rod growth, Appl. Phys. A **88**, 191 (2007)

Götz M.: Neurosurgical applications, in *Femtosecond Technology for Technical and Medical Applications*, ed. by F. Dausinger, F. Lichtner, H. Lubatschowski, Springer Series Topics in Applied Physics **96** (Springer Verlag 2004) p. 203

Goh W.C., K. Yao, C.K. Ong: Pseudo-epitaxial lead zirconate titanate thin film on silicon substrate with enhanced ferroelectric polarization, Appl. Phys. Lett. **87**, 072906 (2005)

Golusda E., P. Hessenthaler, G. Mollekopf, H. Stafast: SF_6 Sensitized CO_2 laser CVD of amorphous silicon, Appl. Surf. Sci. **69**, 258 (1993)

Golusda E., R. Lange, K.-D. Lühmann, G. Mollekopf, M. Wacker, H. Stafast: CW CO_2 laser CVD of amorphous hydrogenated silicon (a-Si:H): Influence of the deposition geometry, Appl. Surf. Sci. **54**, 30 (1992)

Golusda E., K.D. Lühmann, G. Mollekopf, H. Stafast, M. Wacker: CO_2 laser chemical vapor deposition of amorphous silicon: Gas phase processes and thin film properties, Ber. Bunsenges. Phys. Chem. **95**, 1414 (1991)

Gonzalo J., A. Perea, D. Babonneau, C.N. Afonso, N. Beer, J.P. Barnes, A.K. Petford-Long, D. E. Hole, P.D. Townsend: Competing processes during the production of metal nanoparticles by pulsed laser deposition, Phys. Rev. B **71**, 125420 (2005)

Gonzalo J., P.E. Dyer, H.V. Snelling, J. Hird: Liquid crystal films grown by PLD, Appl. Surf. Sci. **138–139**, 179 (1999)

Gorbunov A.: Cross-beam PLD: Metastable film structures from intersecting plumes, in *Pulsed Laser Deposition of Thin Films: Applications-Led Growth of Functional Materials*, ed. R. Eason (Wiley 2007) p. 131

Gorbunov A., O. Jost: Laser ablation synthesis of single-wall carbon nanotubes: The SLS model, in *Pulsed Laser Deposition of Thin Films: Applications-Led Growth of Functional Materials*, ed. R. Eason (Wiley 2007) p. 613

Gorbunov A.A., R. Friedlein, O. Jost, M.S. Golden, J. Fink, W. Pompe: Gas-dynamic consideration of the laser evaporation synthesis of single-wall carbon nanotubes, Appl. Phys. A **69** [Suppl.], S593 (1999)

Gorbunov A.A., W. Pompe, A. Sewing, S.V. Gaponov, A.D. Akhsakhalyan, I.G. Zabrodin, I.A. Kas'kov, E.B. Klyenkov, A.P. Morozov, N.N. Salaschenko, R. Dietsch, H. Mai, S. Völlmar: Ultrathin film deposition by pulsed laser ablation using crossed beams, Appl. Surf. Sci. **96–98**, 649 (1996)

Goto M., J. Hobley, S. Kawanishi, H. Fukumura: Laser-induced implantation of organic molecules into sub-micrometer regions of polymer surfaces, Appl. Phys. A **69** [Suppl.], S257 (1999)

Grad L., J. Mozina: Acoustic in situ monitoring of excimer laser ablation of different ceramics, Appl. Surf. Sci. **69**, 370 (1993)

Graf J., F. Lang, M. Mosbacher, P. Leiderer: Laser cleaning of particles from silicon wafers: Capabilities and mechanisms, Solid State Phenomena **103–104**, 185 (2005)

Green M.A.: Polycrystalline silicon on glass for thin-film solar cells, Appl. Phys. A **96**, 153 (2009)

Greer J.: Large-area commercial pulsed laser deposition, in *Pulsed Laser Deposition of Thin Films: Applications-Led Growth of Functional Materials*, ed. R. Eason (Wiley 2007) p. 191

Greulich K.-O.: *Micromanipulation by Light in Biology and Medicine: The Laser Microbeam and Optical Tweezers (Methods in Bioengineering)* (Birkhäuser Boston 1999)

Grigoropoulos C.P., D.J. Hwang, A. Chimmalgi: Nanometer-scale laser direct-write using near-field optics, MRS Bulletin **32**, January 2007, p. 16

Grigoropoulos C.P., S. Moon, M. Lee, M. Hatano, K. Suzuki: Thermal transport in melting and recrystallization of amorphous and polycrystalline Si thin films, Appl. Phys. A **69** [Suppl.], S295 (1999)

Grimaldi M.G., P. Baeri, E. Rimini, G. Celotti: Epitaxial $NiSi_2$ formation by pulsed laser irradiation of thin Ni layers deposited on Si substrates, Appl. Phys. Lett. **43**, 244 (1983)

Grishin A.M., S.I. Khartsev, P. Johnsson: Epitaxial ferroelectric/giant magnetoresistive heterostructures for magnetosensitive memory cell, Appl. Phys. Lett. **74**, 1015 (1999)

Groeneveld R.H.M., R. Sprik, A. Lagendijk: Femtosecond spectroscopy of electron-electron and electron-phonon energy relaxation in Ag and Au, Phys. Rev. B **51**, 11433 (1995)

Gross M.E., A. Appelbaum, P.K. Gallagher: Laser direct-write metallization in thin palladium acetate films, J. Appl. Phys. **61**, 1628 (1987)
Gruber J., J. Heitz, N. Arnold, D. Bäuerle, N. Ramaseder, W. Meyer, J. Hochörtler, F. Koch: *In-situ* analysis of metal melts in metallurgic vacuum devices by laser-induced breakdown spectroscopy, Appl. Spectrosc **58**, 457 (2004)
Gruber J.: Liquid steel analysis by laser-induced plasma spectroscopy, PhD Thesis, Johannes-Kepler-Universität Linz, Nov. (2002)
Gruber J.: Temporally resolved photographic and spectroscopic investigation of the plasma plume created by laser ablation, Diploma Thesis, Johannes-Kepler-Universität Linz (April 1999)
Guillemot F., F. Prima, V.N. Tokarev, C. Belin, M.C. Porté-Durrieu, T. Gloriant, C. Baquey, S. Lazare: Single-pulse KrF laser ablation and nanopatterning in vacuum of β-titanium alloys used in biomedical applications, Appl. Phys. A **79**, 811 (2004)
Guillong M., H. Kuhn, D. Günther: Application of a particle separation device to reduce inductively coupled plasma-enhanced elemental fractionation in laser ablation-inductively coupled plasma-mass spectrometry, Spectrochimica. Acta Part B **58**, 211 (2003)
Gumpenberger T., J. Heitz, D. Bäuerle, T.C. Rosenmayer: F_2-laser polishing of polytetrafluoroethylene surfaces, Europhys. Lett. **70** (6), 831 (2005a)
Gumpenberger T., J.Heitz, D.Bäuerle, T.Rosenmayer (GORE): Modification of expanded polytetrafluoroethylene by UV irradiation in reactive and inert atmosphere, Appl. Phys. A **80**, 27 (2005b)
Gumpenberger T., J. Heitz, D. Bäuerle, H. Kahr, I. Graz, C. Romanin, V. Svorcik, F. Leisch: Adhesion and proliferation of human endothelial cells on photochemically modified polytetrafluoroethylene, Biomaterials **24**, 5139 (2003)
Gunton J.D., M. San Miguel, P.S. Sahni: The Dynamics of First-Order phase transitions. In *Phase Transitions and Critical Phenomena*, ed. by C. Domb, J.L. Lebowitz (Academic, London 1983)
Guo R.Q., J. Nishimura, M. Matsumoto, D. Nakamura, T. Okada: Catalyst-free synthesis of vertically-aligned ZnO nanowires by nanoparticle-assisted pulsed laser deposition, Appl. Phys. A **93**, 843 (2008)
Guo W., Z.B. Wang, L. Li, D.J. Whitehead, B.S. Luk'yanchuk, Z. Liu: Near-field laser parallel nanofabrication of arbitrary-shaped patterns, Appl. Phys. Lett. **90**, 243101 (2007)
Guo X.D., R.X. Li, Y. Hang, Z.Z. Xu, B.K. Yu, Y. Dai, B. Lu, X.W. Sun: Coherent linking of periodic nano-ripples on a ZnO crystal surface induced by femtosecond laser pulses, Appl. Phys. A **94**, 423 (2009)
Guosheng Z., P.M. Fauchet, A.E. Siegmann: Growth of spontaneous periodic surface structures on solids during laser illumination, Phys. Rev. B **26**, 5366 (1982)
Gusarov A.V., A.G. Gnedovets, I. Smurov: Gas dynamics of laser ablation: influence of ambient atmosphere, J. Appl. Phys. **88**, 4352 (2000)
Gutfeld R.J. von, F.A. McDonald, R.W. Dreyfus: Surface Deformation Measurements Following Excimer Laser Irradiation of Insulators, Appl. Phys. Lett. **49**, 1059 (1986)
Gutfeld R.J. von: Laser Enhanced Plating and Etching: A Review, in *Laser Processing and Diagnostics*, ed. by D. Bäuerle, Springer Ser. Chem. Phys., Vol. 39 (Springer, Berlin, Heidelberg 1984) p. 323
Gutfeld R.J. von, R.T. Hodgson: Laser enhanced etching in KOH, Appl. Phys. Lett. **40**, 352 (1982)
Haas S., G. Schöpe, C. Zahren, H. Stiebig: Analysis of the laser ablation processes for thin-film silicon solar cells, Appl. Phys. A **92**, 755 (2008)
Habermeier H.-U., J. Albrecht, S. Soltan: The enhancement of flux-line pinning in all-oxide superconductor/ferromagnet heterostructures, Supercond. Sci. Technol. **17**, S140 (2004)
Hänggi P., P. Talkner, M. Borkovec: Reaction-rate Theory: Fifty years after kramers, Rev. Mod. Phys. **62**, 251 (1990)
Haeni J.H., P. Irvin, W. Chang, R. Uecker, P. Reiche, Y.L. Li, S. Choudhury, W. Tian, M.E. Hawley, B. Craigo, A.K. Tagantsev, X.Q. Pan, S.K. Streiffer, L.Q. Chen, S.W. Kirchoefer, J. Levy, D.G. Schlom: Room-temperature ferroelectricity in strained $SrTiO_3$, Nature **430**, 758 (2004)
Hagemeyer A., H. Hibst, J. Heitz, D. Bäuerle: Improvements of the Peel Test for Adhesion Evaluation of Thin Metallic Films on Polymeric Substrates, J. Adhesion Sci. Technol. **8**, 29 (1994)

Haglund R.F., S. L. Johnson, H.K. Park: Electronic and optical properties of polymer thin films deposited by resonant infrared laser ablation, J. Laser. Micro/Nanoengineering **2**, 234 (2007)

Haglund R.F.: Mechanisms of laser-induced desorption and ablation. In Miller J.C., R.F. Haglund (eds.: *Laser Ablation and Desorption*. Vol 30: Experimental Methods in the Physical Sciences. Academic Press 1998, p. 15

Haken H.: *Synergetics, An Introduction*, Springer Ser. Syn., Vol. 1, 3rd ed. (Springer, Berlin, Heidelberg 1983)

Han C.H., Y. Ishii, K. Murata: Reshaping Collimated Laser Beams with Gaussian Profile to Uniform Profiles, Appl. Opt. **22**, 3644 (1983)

Han J., K.F. Jensen: Combined experimental and modeling studies of laser-assisted chemical vapor deposition of copper from copper(I)-Hexafluoro-acetylacetonate trimethylvinylsilane, J. Appl. Phys. **75**, 2240 (1994)

Hanabusa M., H. Kikuchi, T. Iwanaga, K. Sugai: IR Laser Photo-Assisted Deposition of Silicon Films, in *Laser Processing and Diagnostics*, ed. by D. Bäuerle, Springer Ser. Chem. Phys., Vol. 39 (Springer, Berlin, Heidelberg 1984) p. 197

Hanabusa M., S. Moriyama, H. Kikuchi: Laser-induced deposition of silicon films, Thin Solid Films **107**, 227 (1983)

Hanada Y., K. Sugioka, H. Kawano, I. Shihira Ishikawa, A. Miyawaki, K. Midorikawa: Nano-aquarium with microfluidic structures fo dynamic analysis of *Cryptomonas* and *Phormidium* fabricated by fs laser direct writing of photostructurable glass, Appl. Surf. Sci. **255**, 9893 (2009a)

Hanada Y., K. Sugioka, H. Kawano, T. Tsuchimoto, I. Miyamoto, A. Miyawaki, K. Midorikawa: Selective cell culture on UV transparent polymer by F_2 laser surface modification, Appl. Surf. Sci. **255**, 9885 (2009b)

Hanada Y., K. Sugioka, Y. Gomi, H. Yamaoka, O. Otsuki, I. Miyamoto, K. Midorikawa: Development of practical system for laser-induced plasma-assisted ablation (LIPAA) for micromachining of glass materials, Appl. Phys. A **79**, 1001 (2004)

Hansen S.G.: Velocity profiles of species ejected in UV laser ablation of several polymers examined by time-of-flight mass spectroscopy, J. Appl. Phys. **66**, 3329 (1989)

Hansen T.N., B. Toftmann, J. Schou, J.G. Lunney: Langmuir probe study of plasma expansion in pulsed laser ablation, Appl. Phys. A **69**, S601 (1999)

Hansen T.N., J. Schou, J.G. Lunney: Angle-resolved energy distributions of laser ablated silver ions in vacuum, Appl. Phys. Lett. **72**, 1829 (1998)

Hanyecz I., J. Budai, A. Oszko, E. Szilagyi, Z. Toth: Room temperature pulsed laser deposition of Si_xC thin films in different compositions, Appl. Phys. A **100**, 1115 (2010)

Hanyu S., C. Tashita, Y. Hanada, T. Hayashida, K. Morita, Y. Sutoh, M. Igarashi, K. Kakimoto, H. Kutami, Y. Iijima, T. Saitoh: Fabrication of km-length IBAD-MgO substrates at a production rate of km h^{-1}, Supercond. Sci. Technol. **23**, 014017 (2010)

Hare D.E., D.D. Dlott: Picosecond coherent raman study of solid-state chemical reactions during laser polymer ablation, Appl. Phys. Lett. **64**, 715 (1994)

Haro-Poniatowski E., R. Serna, M. Jimenez de Castro, A. Suarez-Garcia, C.N. Afonso, I. Vickridge: Size-dependent thermo-optical properties of embedded Bi nanostructures, Nanotech **19**, 485708 (2008)

Harradine D., F.R. McFeely, B. Roop, J.I. Steinfeld, D. Denison, L. Hartsough, J.R. Hollahan: Reactive etching of semiconductor surfaces by laser-generated free radicals, SPIE Proc. **270**, 52 (1981)

Hartmann N., B. Klingebiel, T. Balgar, S. Franzka, E. Hasselbrink: Laser-induced local dehydroxylation on surface-oxidized silicon substrates: mechanistic aspects and prospects in nanofabricaiton, Appl. Phys. A **94**, 95 (2009)

Hartmann N., S. Franzka, J. Koch, A. Ostendorf, B.N. Chichkov: Subwavelength patterning of alkylsiloxane monolayers via nonlinear processing with single fs laser pulses, Appl. Phys. Lett. **92**, 223111 (2008)

Haske W., V.W. Chen, J.M. Hales, W. Dong, S. Barlow, S.R. Marder, J.W. Perry: 65 nm feature sizes using visible wavelength 3-D multiphoton lithography, Optics. Express **15**, 3426 (2007)

Hatanaka K., H. Fukumura: X-ray generation from optical transparent materials by focusing ultrashort laser pulses, in *3D Laser Microfabriation. Principles and Applications*, ed. by H. Misawa, S. Juodkazis (Wiley-VCH, Weinheim, 2006) p. 199

Hatzistergos M.S., H. Efstathiadis, J.L. Reeves, V. Selvamanickam, L.P. Allen, E. Lifshin, P. Haldar: Microstructural and compositional analysis of $YBa_2Cu_3O_{7-\delta}$ films grown by MOCVD before and after GCIB smoothing, Physica C **405**, 179 (2004)

Hayashi T., T. Shibata, T. Kawashima, E. Makino, T. Mineta, T. Masuzawa: Photolithography system with liquid crystal display as active gray-tone mask for 3D structuring of photoresist, Sensors and Actuators A **144**, 381 (2008)

Heaven M.C., M.A.A. Clyne: Interpretation of the spontaneous predissociation of $Cl_2[B^3II(O_u^+)]$, J. Chem. Soc., Faraday. Trans. 2, **78**, 1339 (1982)

Hedler A., S. Urban, F. Falk, H. Hobert, W. Wesch: Excimer laser crystallization of amorphous silicon carbide produced by ion implantation, Appl. Surf. Sci. **205**, 240 (2003)

Heisterkamp A., I. Z. Maxwell, E. Mazur, J. M. Underwood, J. A. Nickerson, S. Kumar, D. E. Ingber: Pulse energy dependence of subcellular dissection by fs-laser pulses, Opt. Express **13**, 3690 (2005)

Heitsch S., G. Benndorf, G. Zimmermann, C. Schulz, D. Spemann, H. Hochmuth, H. Schmidt, T. Nobis, M. Lorenz, M. Grundmann: Optical and structural properties of MgZnO/ZnO hetero- and double heterostructures grown by pulsed laser deposition, Appl. Phys. A **88**, 99 (2007)

Heitz J., M. Olbrich, S. Moritz, C. Romanin, V. Svorcik, D. Bäuerle: Surface modification of polymers by UV-irradiation: Applications in micro- and biotechnology, Proc. SPIE **5958**, 466 (2005)

Heitz J., T. Gumpenberger, N. Huber, D. Bäuerle, J. Pühringer, V. Svorcik, K. Walachova: *Optical method for improving the adhesion of biological cells on polymer surfaces.* European Patent EP 1 234 588 A2 (2002)

Heitz J., E. Arenholz, D. Bäuerle: Patent AT 406.756 (2000)

Heitz J., J.T. Dickinson: Characterization of particulates accompanying laser ablation of pressed polytetrafluoroethylene (PTFE) targets, Appl. Phys. A 68, 515 (1999)

Heitz J., J.D. Pedarnig, D. Bäuerle, G. Petzow: Excimer-laser ablation and micro-patterning of ceramic Si_3N_4, Appl. Phys. A 65, 259 (1997)

Heitz J., H. Niino, A. Yabe: Chemical surface modification on polytetrafluoroethylene films by vacuum ultraviolet excimer lamp irradiation in ammonia gas atmosphere, Appl. Phys. Lett. **68**, 2648 (1996)

Heitz J., X.Z. Wang, P. Schwab, D. Bäuerle, L. Schultz: KrF Laser-induced ablation and patterning of Y-Ba-Cu-O films, J. Appl. Phys. **68**, 2512 (1990)

Her T., R.J. Finlay, C. Wu, S. Deliwala, E. Mazur: Microstructuring of silicon with fs laser pulses, Appl. Phys. Lett. **73**, 1673 (1998)

Heraeus Inc., Germany: Data sheet Q-A 1/112 (1979)

Herman I.P., H. Tang, P.P. Leong: Real time optical diagnostics in laser etching and deposition, MRS Proc. **201**, 563 (1991)

Herziger G., E.W. Kreutz: Fundamentals of laser microprocessing of metals, Physica Scripta T **13**, 139 (1986)

Herziger G., E.W. Kreutz: Fundamentals of Laser Micromachining of Metals, *in Laser Processing and Diagnostics*, ed. by D. Bäuerle, Springer Ser. Chem. Phys., Vol. 39 (Springer, Berlin, Heidelberg 1984) p. 90

Hess W.P., P. Herman, D. Bäuerle, H. Koinuma eds.: The 8th International Conference on Laser Ablation (COLA'05), Banff, Canada, Sept. 11–16, 2005, J. Phys.Confer. Ser. Vol. **59**, 2007 (ISSN: 1742-6588) (IOP)

Heszler P., P. Mogyorosi, J.O. Carlsson: Time resolved spectroscopy of the emission of fluorescent light upon UV laser assisted CVD of W from WF_6, Appl. Surf. Sci. **69**, 376 (1993)

Hidai H., D.J. Hwang, C.P. Grigoropoulos: Self-grown fiber fabrication by two-photon photopolymerization, Appl. Phys. A **93**, 443 (2008)

Higashi G.S.: Excimer laser projection-patterned deposition of aluminium using alkyl-aluminium precursor molecules, Chemtronics **4**, 123 (1989)

Higashi G.S., L.J. Rothberg: Surface photochemical phenomena in laser chemical vapor deposition, J. Vac. Sci. Technol. B **3**, 1460 (1985)

Hill C., A.L. Butler, J.A. Daly: Shaping of Dopang Concentration Profiles in Silicon by Multiple-Pulse Laser Processing, in *Laser and Electron-Beam Interactions with Solids*, ed. by B.R. Appleton, G.K. Celler, MRS Proc. **4**, 579 (1982)

Hillyard P.B., K.J. Gaffney, A.M. Lindenberg, S. Engemann, R.A. Akre, J. Arthur, C. Blome, P.H. Bucksbaum, A.L. Cavalieri, A. Deb, R.W. Falcone, D.M. Fritz, P.H. Fuoss, J. Hajdu, P. Krejcik, J. Larsson, S.H. Lee, D.A. Meyer, A.J. Nelson, R. Pahl, D.A. Reis, J. Rudati, D.P. Siddons, K. Sokolowski-Tinten, D. von der Linde, J.B. Hastings: Carrier-density-dependent lattice stability in InSb, Phys. Rev. Lett. **98**, 125501 (2007)

Himmelbauer M., N. Arnold, N. Bityurin, E. Arenholz, D. Bäuerle: UV-laser-induced periodic surface structures on polyimide, Appl. Phys. A **64**, 451 (1997)

Himmelbauer M., E. Arenholz, D. Bäuerle: Single-shot UV-laser ablation of polyimide with variable pulse lengths, Appl. Phys. A **63**, 87 (1996a)

Himmelbauer M., E. Arenholz, D. Bäuerle, K. Schilcher: UV-laser-induced surface topology changes in polyimide, Appl. Phys. A **63**, 337 (1996b)

Himmelbauer M.: Ablation von organischen Polymeren unter dem Einfluß variabler UV-Laserpulse. Dissertation, Universität Linz, Austria (1996)

Hiramatsu H., T. Kamiya, M. Hirano, H. Hosono: Heteroepitaxial film growth of layered compounds with the ZrCuSiAs-type and $ThCr_2Si_2$-type structures: From Cu-based semiconductors to Fe-based superconductors, Physica C **469**, 657 (2009)

Hiramatsu H., T. Katase, T. Kamiya, M. Hirano, H. Hosono: Heteroepitaxial growth and optoelectronic properties of layered iron oxyarsenide, LaFeAsO, Appl. Phys. Lett. **93**, 162504 (2008)

Hiromatsu K., D.J. Hwang, C.P. Grigoropoulos: Active glass nanoparticles by ultrafast laser pulses, Micro. Nano. Lett. **3**, 121 (2008)

Hirschfelder J.O., C.F. Curtiss, R.B. Bird: *Molecular Theory of Gases and Liquids*, (Wiley, New York 1964)

Hitchman M.L., A.D. Jobson, L.F.T. Kwakman: Some considerations of the thermodynamics and kinetics of the chemical vapour deposition of tungsten, Appl. Surf. Sci. **38**, 312 (1989)

Hiura Y., Y. Morishige, S. Kishida: laser chemical vapor deposition direct patterning of insulating film, J. Appl. Phys. **69**, 1744 (1991)

Ho C.Y., R.W. Powell, P.E. Liley: Thermal conductivity of the elements: A comprehensive review, J. Phys. Chem. Ref. Data. **3**, Suppl. 1, 588 (1974)

Hobert H., H.H. Dunken, S. Urban, F. Falk, H. Stafast: Laser-induced changes of silicon carbon films studied by vibrational spectroscopy, Vibrat. Spectr. **29**, 177 (2002)

Höche D., H. Schikora, H. Zutz, R. Queitsch, A. Emmel, P. Schaaf: Microstructure of TiN coatings synthesized by direct pulsed Nd:YAG laser nitriding of Ti: Development of grain size, microstrain, and grain orientation, Appl. Phys. A **91**, 305 (2008)

Hohlfeld J., S. Wellershoff, J. Güdde, U. Conrad, V. Jähnke, E. Matthias: Electron and lattice dynamics following optical excitation of metals, Chem. Phys. **251**, 237 (2000)

Holber W., G. Reksten, R.M. Osgood: Laser-enhanced plasma etching of Silicon, Appl. Phys. Lett. **46**, 201 (1985)

Holmgaard T., Z. Chen, S.I. Bozhevolnyi, L. Markey, A. Dereux, A.V. Krasavin, A.V. Zayats: Bend- and splitting loss of dielectric-loaded surface plasmon-polariton waveguides, Opt. Exp. **16**, 13585 (2008)

Holzapfel B., K. Kämmer, L. Schultz: PLD plume diagnostics by high-speed ICCD photography, Lambda Physik Science Report No. 7, August 1996, p. 1–3

Holzapfel B., B. Roas, L. Schultz, P. Bauer, G. Saemann-ischenko: Off-axis laser deposition of $YBa_2Cu_3O_{7-\delta}$ thin films, Appl. Phys. Lett. **61**, 3178 (1992)

Hong M.H., K.Y. Ng, Q. Xie, L.P. Shi, T.C. Chong: Pulsed laser ablation in a cooled liquid environment, Appl. Phys. A **93**, 153 (2008)

Hong M.H., Y. Lin, G.X. Chen, L.S. Tan, Q. Xie, B. Luk'yanchuk, L.P. Shi, T.C. Chong: Nanopatterning by pulsed laser irradiation in near field, J. Phys. Conf. Ser. **59**, 64 (2007)

Hopfe V., R. Jäckel, K. Schönfeld: Laser based coating and modification of carbon fibres: application of industrial lasers to manufacturing of composite materials, Appl. Surf. Sci. **106**, 60 (1996)

Hopkins P. E., P.M. Norris: Substrate influence in electron–phonon coupling measurements in thin Au films, Appl. Surf. Sci. **253**, 6289 (2007)

Hopman S., A. Fell, K. Mayer, M. Mesec, A. Rodofili, D. Kray: Comparison of laser chemical processing and laser microjet for structuring and cutting silicon substrates, Appl. Phys. A **95**, 857 (2009)

Hopp B., T. Smausz, C. Vass, G. Szabó, R. Böhme, D. Hirsch, K. Zimmer: Laser-induced backside dry and wet etching of transparent materials using solid and molten tin as absorbers, Appl. Phys. A **94**, 899 (2009)

Hopp B., T. Smausz, B. Papdi, Z. Bor, A. Szabó, L. Kolozsvári, C. Fotakis, A. Nógrádi: Laser-based techniques for living cell pattern formation, Appl. Phys. A **93**, 45 (2008)

Hopp B., T. Smausz, G. Kecskeméti, A. Klini, Zs. Bor: Femtosecond pulsed laser deposition of biological and biocompatible thin layers, Appl. Surf. Sci. **253**, 7806 (2007)

Hopp B., T. Smausz, N. Kresz, N. Barna, Z. Bor, L. Kolozsvari, D.B. Chrisey, A. Szabo, A. Nogradi: Survival and proliferative ability of various living cell types after laser-induced forward transfer, Tiss. Eng. **11**, 1817 (2005*a*)

Hopp B., T. Smausz, N. Barna, Cs. Vass, Zs. Antal, L. Kredics, D. Chrisey: Time-resolved study of absorbing film assisted laser induced forward transfer of *Trichoderma longibrachiatum* conidia, J. Phys. D: Appl. Phys. **38**, 1 (2005*b*)

Hopp B., R. Hegedüs, C. Vass, T. Smausz, Z. Bor: 3D photography and reconstruction of jets and droplets ejected from the surface of excimer laser ablated molten polyethylene-glycol 1000, Appl. Phys. A **79**, 779 (2004)

Hopp B., T. Smausz, N. Kresz, P.M. Nagy, A. Juhasz, F. Ignacz, Z. Marton: Production of biologically inert teflon thin layers on the surface of allergenic metal objects by pulsed laser deposition technology, Appl. Phys. A **76**, 731 (2003)

Horiike Y., N. Hayasaka, M. Sekine, T. Arikado, M. Nakase, H. Okano: Excimer-laser etching on Silicon, Appl. Phys. A **44**, 313 (1987)

Horn A., D. Wortmann, A. Brand, I. Mingareev: Development of a time-resolved white-light interference microscope for optical phase measurements during fs-laser material processing, Appl. Phys. A **101**, 231 (2010)

Horn A., I. Mingareev, A. Werth, M. Kachel, U. Brenk: Investigations on ultrafast welding of glass-glass and glass-silicon, Appl. Pyhs. A **93**, 171 (2008)

Horn A., C. Kaiser, R. Ritschel, T. Mans, P. Russbüldt, H.D. Hoffmann, R. Poprawe: Si-K_α radiation generated by the interaction of fs laser radiation with silicon, J. Phys. Conf. Ser. **59**, 159 (2007)

Horwitz J.S., D.B. Chrisey, R.M. Stroud, A.C. Carter, J. Kim, W. Chang, J.M. Pond, S.W. Kirchoefer, M.S. Osofsky, D. Koller: Pulsed laser deposition as a materials research tool, Appl. Surf. Sci. **127–129**, 507 (1998)

Hosokawa C., S. N. Kudoh, A. Kiyohara, Y. Hosokawa, K. Okano, H. Masuhara, T. Taguchi: Femtosecond laser modification of living neuronal network, Appl. Phys. A **93**, 57 (2008)

Houle F.A.: Doping effects on the etching chemistry of GaAs and Si, MRS Proc. **204**, 25 (1991)

Houle F.A.: Photochemical etching of Silicon: The influence of photogenerated charge carriers, Phys. Rev. B **39**, 10120 (1989)

Houle F.A., R.J. Wilson, T.H. Baum: Surface processes leading to carbon contamination of photochemically deposited copper films, J. Vac. Sci. Technol. A **4**, 2452 (1986)

Hsu E.M., T.H.R. Crawford, C. Maunders, G.A. Botton, H.K. Haugen: Cross-sectional study of periodic surface structures on gallium phosphide induced by ultrashort laser pulse irradiation, Appl. Phys. Lett. **92**, 221112 (2008)

Huang S.M., Z.A. Wang, Z. Sun, Z.B. Wang, B. Luk'yanchuk: Theoretical and experimental investigation of the near field under ordered silica spheres on substrate, Appl. Phys. A **96**, 459 (2009)

Huang S.M., M.H. Hong, Y.F. Lu, B.S. Luk'yanchuk, W.D. Song, T.C. Chong: Pulsed-laser assisted nanopatterning of metallic layers combined with atomic force microscopy, J. Appl. Phys. **91**, 3268 (2002)

Hubenthal F.: Nanoparticles and their tailoring with laser light, Europ. J. Phys. **30**, S49 (2009)

Hubenthal F.: Ultrafast dephasing time of localized surface plasmon polariton resonance and the involved damping mechanisms in colloidal gold nanoparticles, Prog. Sur. Sci. **82**, 378 (2007)

Hubenthal F., C. Hendrich, J. Ouacha, D. Blázquez Sánchez, F. Träger: Preparation of gold nanoparticles with narrow size distributions and well defined shapes, Inter. J. Mod. Phys. B **19**, Nos. 15, 16 & 17, 2604 (2005)

Hügel H., T. Graf: *Laser in der Fertigung* (Vieweg und Teubner, Wiesbaden 2009)

Hüttner B., G.C. Rohr: On the theory of ps and sub-ps laser pulse interaction with metals. II. Spatial temperature distribution, Appl. Surf. Sci. **126**, 129 (1998)

Hullavarad S.S., N.V. Hullavarad, D. E. Pugel, S. Dhar, T. Venkatesan, R.D. Vispute: Structural and chemical analysis of pulsed laser deposited $Mg_xZn_{1-x}O$ hexagonal ($x = 0.15$,0.28) and cubic ($x = 0.85$) thin films, Opt. Mater. **30**, 993 (2008)

Hunger E., H. Pietsch, S. Petzoldt, E. Matthias: Multishot ablation of polymer and metal films at 248 nm, Appl. Surf. Sci. **54**, 227 (1992)

Hwang D.J., S.G. Ryu, N. Misra, H. Jeon, C.P. Grigoropoulos: Nanoscale laser processing and diagnostics, Appl. Phys. A **96**, 289 (2009a)

Hwang D.J., M. Kim, K. Hiromatsu, H. Jeon, C.P. Grigoropoulos: 3D-opto-fluidic devices fabricated by ultrashort laser pulses for high throughput single cell detection and processing, Appl. Phys. A **96**, 385 (2009b)

Hwang D.J., K. Hiromatsu, H. Hidai, C.P. Grigoropoulos: Self-guided glass drilling by fs laser pulses, Appl. Phys. A **94**, 555 (2009c)

Hwang D.J., N. Misra, C.P. Grigoropoulos, A.M. Minor, S.S. Mao: *In situ* monitoring of material processing by a pulsed laser beam coupled via a lensed fiber into a scanning electron microscope, J. Vac. Sci. Technol. A **26**, 1432 (2008a)

Hwang D.J., H. Jeon, C.P. Grigoropoulos, J. Yoo, R.E. Russo: Laser ablation-induced spectral plasma characteristics in optical far- and near fields, J. Appl. Phys. **104**, 013110 (2008b)

Hwang D.J., A. Chimmalgi, C.P. Grigoropoulos: Ablation of thin metal films by short-pulsed lasers coupled through near-field scanning optical microscopy probes, J. Appl. Phys. **99**, 044905 (2006)

Hwang D.J., T.Y. Choi, C.P. Grigoropoulos: Liquid-assisted femtosecond laser drilling of straight and three-dimensional microchannels in glass, Appl. Phys. A **79**, 605 (2004)

Ihlemann J., J. Békési, J.-H. Klein-Wiele, P. Simon: Processing of dielectric optical coatings by nanosecond and femtosecond UV Laser Ablation, Laser Chemistry Vol. 2008, Article ID 623872, 6 pages (doi:10.1155/2008/623872)

Ihlemann J.: Micro patterning of fused silica by laser ablation mediated by solid coating absorption, Appl. Phys. A **93**, 65 (2008)

Ihlemann J., J.H. Klein-Wiele, J. Bekesi, P. Simon: UV ultrafast laser processing using phase masks, J. Phys.Conf. Ser. **59**, 449 (2007)

Ihlemann J., S. Müller, S. Puschmann, D. Schäfer, M. Wei, J. Li, P.R. Herman: Fabrication of submicron gratings in fused silica by F_2-laser ablation, Appl. Phys. A **76**, 751 (2003)

Ihlemann J., M. Bolle, K. Luther, J. Troe, J. Proc. SPIE **1361**, 1011 (1990)

Ihler B.C.: Laser-Lithotripsie – System und Fragmentierungsprozesse unter der Lupe (Laser Lithotripsy – System and Fragmentation Processes Closely Examined), Lase. Optoelek. **24**, 76 (1992)

Iida K., J. Hänisch, R. Hühne, F. Kurth, M. Kidszun, S. Haindl, J. Werner, L. Schultz, B. Holzapfel: Strong T_c dependence for strained epitaxial $Ba(Fe_{1-x}Co_x)_2As_2$ thin films, Appl. Phys. Lett. **95**, 192501 (2009)

Im J.S., M.A. Crowder, R.S. Sposili, J.P. Leonard, H.J. Kim, J.H. Yoon, V.V. Gupta, H. Jin Song, H.S. Cho: Controlled super-lateral growth of Si films for microstructural manipulation and optimization, phys. stat. sol. (a) **166**, 603 (1998)

Industrial Laser Annual Handbook (Penwell Books, Tulsa 1990)
Inogamov N.A., V.V. Zhakhovskii, S.I. Ashitkov, Yu. V. Petrov., M.B. Agranat, S.I. Anisimov, K. Nishihara, V.E. Fortov: Nanospallation induced by an ultrashort laser pulse, J. Exp. Theoret. Phys. **107**, 1 (2008)
Inogamov N.A., Yu.V. Petrov, S.I. Anisimov, A.M. Oparin, N.V. Shaposhnikov, D.von der Linde, J. Meyer-ter-Vehn: Expansion of matter heated by an ultrashort laser pulse, JETP. Lett. **69**, 310 (1999)
Inoue N., T. Ozaki, T. Monnaka, S. Kashiwabara, R. Fujimoto: A new pulsed laser deposition method using an aperture plate, Jpn. J. Appl. Phys. **36**, 704 (1997)
Irvine S.J.C., H. Hill, G.T. Brown, S.J. Barnett, J.E. Hails, O.D. Dosser, J.B. Mullin: Selected area epitaxy in II-VI compounds by Laser-induced Photo-metalorganic vapor phase epitaxy, J. Vac. Sci. Technol. B **7**, 1191 (1989)
Irvine S.J.C., J.B. Mullin, J. Tunnicliffe: Low Temperature Growth of HgTe by a UV Photosensitisation Method, in *Laser Processing and Diagnostics*, ed. by D. Bäuerle, Springer Ser. Chem. Phys., Vol. 39 (Springer, Berlin, Heidelberg 1984) p. 234
Isenor N.R.: CO_2 Laser-Produced Ripple Patterns on Ni_xP_{1-x} Surfaces, Appl. Phys. Lett. **31**, 148 (1977)
Israelachvili J.N.: *Intermolecular and Surface Forces*, 2nd edition, Academic Press (San Diego San Francisco New York) 1992
Isshiki H., Y. Aoyagi, T. Sugano, S. Iwai, T. Meguro: Formation of Low-dimensional structures by atomic layer epitaxy, Optoelect. Dev. Tech. **8**, 509 (1993)
Itina T.E., L.V. Zhigilei: Generation of nanoparticles by laser ablation: Combined MD-DSMC computational study, J. Phys. Conf. Ser. **59**, 44 (2007)
Itina T.E., K. Gouriet, L.V. Zhigilei, S. Noel, J. Hermann, M. Sentis: Mechanisms of small clusters production by short and ultra-short laser ablation, Appl. Surf. Sci. **253**, 7656 (2007)
Itina T.E., A.A. Katassonov, W. Marine, M. Autric: Numerical study of the role of a background gas and system geometry in PLD, J Appl. Phys. **83**, 6050 (1998)
Itoh N., K. Hattori, Y. Nakai, J. Kanasaki, A. Okano, R.F. Haglund: Laser-induced Particle Emission from Surfaces of Non-Metallic Solids: A Search for Primary Processes of Laser Ablation, in *Laser Ablation – Mechanisms and Applications*, ed. by J.C. Miller, R.F. Haglund, Lecture Notes Phys., Vol. 389 (Springer, Berlin, Heidelberg 1991) p. 213
Ivanov D.S., B. Rethfeld, G. M. O'Connor, T. J. Glynn, A.N. Volkov, L.V. Zhigilei: The mechanism of nanobump formation in femtosecond pulse laser nanostructuring of thin metal films, Appl. Phys. A **92**, 791 (2008)
Ivanov D.S., L.V. Zhigilei: Kinetic limit of heterogeneous melting in metals, Phys. Rev. Lett. **98**, 195701 (2007)
Ivanov D.S, L.V. Zhigilei: Effect of pressure relaxation on the mechanisms of short-pulse laser melting, Phys. Rev. Lett. **91**, 105701 (2003)
Jackman R.B., J.S. Foord, A.E. Adams, M.L. Lloyd: LCVD of patterned Fe on Silica Glass: Observation and origins of periodic ripple structures, J. Appl. Phys. **59**, 2031 (1986)
Jackson R.L., G.W. Tyndall: Quartz crystal microbalance determination of laser photochemical deposition rates: Mechanism of laser photochemical deposition from the group 6 Hexacarbonyls, MRS Proc. **101**, 207 (1988)
Jacobs J.W.M., C.J.C.M. Nillesen: Repair of transparent defects on photomasks by Laser-induced metal deposition from an Aqueous solution, J.Vac. Sci. Technol. B **8**, 635 (1990)
Jain A.K., V.N. Kulkarni, D.K. Sood, J.S. Uppal: Periodic surface ripples in laser-treated Aluminum and their use to determine absorbed power, J. Appl. Phys. **52**, 4882 (1981)
Jain K., M.R. Latta, G.T. Sincerbox: Holographic method and apparatus for transforming of a light beam into a line source of required curvature and finite numerical aperture, U.S. patent nos. 4,444,456 and 4,516,832 (1984)
JANAF Thermochemical Tables (National Bureau of Standards, Washington, DC 1970)
Jegenyes N., J. Etchepare, B. Reynier, D. Scuderi, A. Dos-Santos, Z. Tóth: Time-resolved dynamics analysis of nanoparticles applying dual fs laser pulses, Appl. Phys. A **91**, 385 (2008)

Jellison G.E., F.A. Modine: Optical functions of Silicon between 1.7 and 4.7 eV at elevated temperatures, Phys. Rev. B **27**, 7466 (1983)

Jersch J., F. Demming, K. Dickmann: Nanostructuring with laser radiation in the nearfield of a tip from a scanning force microscope, Appl. Phys. A **64**, 29 (1997)

Jeschke H.O., M.S. Diakhate, M.E. Garcia: Molecular dynamics simulations of laser-induced damage of nanostructures and solids, Appl. Phys. A **96**, 33 (2009)

Jia T.Q, H.X. Chen, M. Huang, F.L. Zhao, J.R. Qiu, R. X. Li, Z.Z. Xu, X.K. He, J. Zhang, H. Kuroda: Formation of nanogratings on the surface of a ZnSe crystal irradiated by femtosecond laser pulses, Phys. Rev. B **72**, 125429 (2005)

Johansson S., J. Schweitz, H. Westberg, M. Boman: Microfabrication of three-dimensional Boron structures by laser chemical processing, J. Appl. Phys. **72**, 5956 (1992)

John S.R., S.C. Langford, J.T. Dickinson: Ablation mechanism of PTFE under 157 nm irradiation, Appl. Phys. A **92**, 981 (2008)

John S.R., J.A. Leraas, S.C. Langford, J.T. Dickinson: Ion emission from fused silica under 157-nm irradiation, J. Phys. Conf. Ser. **59**, 736 (2007)

Johne R., M. Lorenz, H. Hochmuth, J. Lenzner, H.v. Wenckstern, G. Zimmermann, H. Schmidt, R. Schmidt-Grund, M. Grundmann: Cathodoluminescence of large-area PLD grown ZnO thin films measured in transmission and reflection, Appl. Phys. A **88**, 89 (2007)

Johnson S.L., K.E. Schriver, R.F. Haglund, D.M. Bubb: Effects of the absorption coefficient on resonant infrared laser ablation of poly(ethylene glycol), J. Appl. Phys. **105**, 024901 (2009a)

Johnson S.L., D.M. Bubb, R.F. Haglund: Phase explostion and recoil-induced ejectrion in resonant-infrared laser ablation of polystyrene, Appl. Phys. A **96**, 627 (2009b)

Juodkazis S., V. Mizeikis, M. Sudzius, H. Misawa, K. Kitamura, S. Takekawa, E.G. Gamaly, W.Z. Krolikowski, A.V. Rode: Laser induced memory bits in photorefractive $LiNbO_3$ and $LiTaO_3$, Appl. Phys. A **93**, 129 (2008)

Jyumonji M., K. Sugioka, H. Takai, H. Tashiro, K. Toyoda: Mechanism of Silicon implant-deposition for surface modification of stainless steel 304 using KrF-excimer laser, Appl. Phys. A **60**, 41 (1995a)

Jyumonji M., K. Sugioka, H. Takai, K. Toyoda: Rapid formation of Arsenic-doped layer more than 1.0 μm deep in Si using two KrF excimer lasers, Jpn. J. Appl. Phys. **34**, 6878 (1995b)

Kabashin A.V., A. Trudeau, W. Marine, M.Meunier: Synthesis of efficient ZnO-based random lasing medium using laser-induced air breakdown processing, Appl. Phys. Lett. **91**, 201101 (2007)

Käsmaier R., S. Lätsch, H. Hiraoka: Irradiation of solid C_{60} films with pulsed UV-laser-light: Fabrication of a periodic submicron C_{60} structure and transformation of C_{60} into a different carbon phase, Appl. Phys. A **63**, 305 (1996)

Kakimoto K., M. Igarashi, Y. Hanada, T. Hayashida, C. Tashita, K. Morita, S. Hanyu, Y. Sutoh, H. Kutami, Y. Iijima, T. Saitoh: High-speed deposition of high-quality RE123 films by a PLD system with hot-wall heating, Super. Sci. Technol. **23**, 014016 (2010)

Kamimura T., M. Hirose: Effect of Hydrogen dilution of Silane in Hydrogenated Amorphous Silicon films prepared by Photochemical Vapor Deposition, Jpn. J. Appl. Phys. **25**, 1778 (1986)

Kandulla J., R. Brinkmann: Non invasive real-time temperature determination during laser treatments at the retina, Photonik international 2008/1, p. 42

Kane D.M. ed.: "*Laser Cleaning II*" (World Scientific, Singapore, 2006)

Kantorowitz Z., J.D.B. Featherstone, D. Fried: Caries prevention by CO_2 laser treatment: dependency on the number of pulses used, JADA **129**, 585 (1998)

Kapenieks A., M. Eyett, D. Bäuerle: Laser-induced surface metallization of ceramic PLZT, Appl. Phys. A **41**, 331 (1986a)

Kapenieks A., M. Eyett, R. Stumpe, D. Bäuerle: Laser Direct Writing of Electrodes on PLZT Ceramics, in *Laser Processing and Diagnostics II*, ed. by D. Bäuerle, K.L. Kompa, L.D. Laude (Physique, Les Ulis 1986b) p. 165

Kaplan A., M. Lenner, C. Huchon, R.E. Palmer: Nonlinearity and time-resolved studies of ion emission in ultrafast laser ablation of graphite, Appl. Phys. A **92**, 999 (2008)

Kar A., M.N. Azer, J. Mazumder: Three-dimensional transient mass transfer model for laser chemical vapor deposition of titanium on stationary finite slabs, J. Appl. Phys. **69**, 757 (1991)
Kargl P.B., N. Arnold, D. Bäuerle: Bistabilities in pyrolytic laser-CVD of silicon and carbon, Appl. Surf. Sci. **108**, 257 (1997)
Kargl P.B., R. Kullmer, D. Bäuerle: Periodic Structures in Pyrolytic Laser-CVD of W from WCl_6, Appl. Phys. A 57, 175 (1993a)
Kargl P.B., R. Kullmer, D. Bäuerle: Bistable growth in laser chemical vapor deposition, Appl. Phys. A **57**, 577 (1993b)
Karlicek R.F., V.M. Donnelly, G.J. Collins: Laser-induced metal deposition on InP, J. Appl. Phys. **53**, 1084 (1982)
Karlov N., N.A. Kirichenko, B.S. Luk'yanchuk: *Laser Thermochemistry. Fundamentals and applications* (Cambridge International Science Publishing, 2000)
Karlov N.V., N. Kirichenko, B. Luk'yanchuk: *Laser Thermochemistry* (Nauka, Moscow 1992) (in Russian)
Karlov N.V., B.S. Luk'yanchuk, E.V. Sisakyan, G.A. Shafeev: Etching of semiconductors by products of laser thermal dissociation of molecular gases, Sov. J. Quantum Electron. **15**, 522 (1985)
Kasuya K., K. Nagato, Y. Jin, H. Morii, T. Ooi, M. Nakao: Rapid and localized synthesis of single-walled carbon nanotubes on flat surface by laser-assisted chemical vapor deposition, Jpn. J. Appl. Phys. **46**, L333 (2007)
Kattamis N.T., P. E. Purnick, R. Weiss, C.B. Arnold: Thick film laser induced forward transfer for deposition of thermally and mechanically sensitive materials, Appl. Phys. Lett. **91**, 171120 (2007)
Kautek W.: Lasers in cultural heritage: the non-contact intervention, in *Laser-Surface Interactions for New Materials Production: Tailoring Structure and Properties*, A. Miotello, P.M. Ossi eds., Springer Series in Materials Science **130** (2010), p. 313
Kautek W.: *Handbook on the Use of Lasers in Conservation and Conservation Science*: Chapt. 2.4, in M. Schreiner, M. Strlič, R. Salimbeni eds., COST office, Brussels 2008 (http://www.science4heritage.org/COSTG7/booklet/)
Kawaguchi Y., H. Niino, T. Sato, A. Narazaki, R. Kurosaki: A deep micro-trench on silica glass fabricated by laser-induced backside wet etching (LIBWE), J. Phys: Conf. Ser. **59**, 380 (2007)
Kawasaki M., M. Izumi, Y. Konishi, T. Manako, Y. Tokura: Perfect epitaxy of perovskite manganite for oxide spin-electronics, Mater. Sci. Eng. B **63**, 49 (1999)
Kawasaki M., A. Ohtomo, I. Ohkubo, H. Koinuma, Z.K. Tang, P. Yu, G.K.L. Wong, B.P. Zhang, Y. Segawa: Excitonic UV laser emission at room temperature from naturally made cavity in ZnO nanocrystal films, Mater. Sci. Eng. B **56**, 239 (1998)
Kawata S., T. Tanaka, Y. Hashimoto, Y. Kawata: Three-dimensional confocal optical memory using photorefractive materials, Proc. SPIE **2042**, 314 (1994)
Kazansky P.G.: Formation of sub-wavelength periodic structures inside transparent materials, Chap. 8 in *3D Laser Microfabriation. Principles and Applications*, ed. by H. Misawa, S. Juodkazis (Wiley-VCH, Weinheim, 2006) p. 181
Keilmann F.: Laser-Driven Corrugation Instability of Liquid Metal Surfaces, Phys. Rev. Lett. **51**, 2097 (1983)
Keldysh L.V.: Ionization in the field of a strong electromagnetic wave, Soviet Physics Jetp **20**, Number 5, p. 1307, May 1965 (J. Exptl. Theoret. Phys. (USSR) **47**, 1945 (Nov. 1964)
Ketterer B., H. Vasilchina, K. Seemann, S. Ulrich, H. Besser, W. Pfleging, T. Kaiser, C. Adelhelm: Development of high power density cathode materials for Li-ion batteries, Int. J. Mat. Res. (formerly Z. Metallkd.) **99** (2008) 10 (p. 1171)
Kiely C.J., V. Tavitian, J.G. Eden: Microstructural studies of epitaxial Ge films grown on [100] GaAs by laser photochemical vapor deposition, J. Appl. Phys. **65**, 3883 (1989)
Kim H., R.C.Y. Auyeung, S.H. Lee, A.L. Huston, A. Piqué: Laser forward transfer of silver electrodes for organic thin-film transistors, Appl. Phys. A **96**, 441 (2009)
Kim H., G.P. Kushto, C.B. Arnold, Z.H. Kafafi, A. Piqué: Laser processing of nanocrystalline TiO_2 films for dye-sensitized solar cells, Appl. Phys. Lett. **85**, 464 (2004)
Kim J.-D., J.-W. Kweon: CO_2 laser cladding of VERSAlloy^{TM} on carbon steel with powder feeding, J. Phys. Conf. Ser. **59**, 36 (2007)

Kim T.G., J.M. Warrender, M.J. Aziz: Strong sub-band-gap IR absorption in silicon supersaturated with sulfur, Appl. Phys. Lett. **88**, 241902 (2006)

Kimerling L.C., J.L. Benton: Defects in Laser Processed Semiconductors, in *Laser and Electron Beam Processing of Materials*, ed. by C.W. White, P.S. Peercy (Academic, London 1980) p. 385

Kirichenko N., D. Bäuerle: The Influence of Heterogeneous and Homogeneous Reactions in Laser-Chemical Processing, Thin Solid Films **218**, 1 (1992)

Kirichenko N., K. Piglmayer, D. Bäuerle: On the kinetics of Non-equimolecular reactions in laser chemical processing, Appl. Phys. A **51**, 498 (1990)

Kitai M.S., V.L. Popkov, V.A. Semchishen: Dynamics of UV-laser Ablation of PMMA, caused by mechanical stresses. theory and experiment, Macromol. Chem. Macromol. Symp. **37**, 257 (1990)

Kittel C.: *Introduction to Solid State Physics*, 8th ed. (Wiley, 2005)

Kiyan R., C. Reinhardt, S. Passinger, A.L. Stepanov, A. Hohenau, J.R. Krenn, B.N. Chichkov: Rapid prototyping of optical components for surface plasmon polaritons, Opt. Exp. **15**, 4205 (2007)

Klaua M. J. Shen, P. Ohresser, C.V. Mohan, S. Manoharan, J. Barthel, J. Kirschner: Comparative studies of morphology, structure and magnetism of ultrathin Fe films on Cu(111) and Cu(100) grown by thermal and pulsed laser deposition. 5th International Conference on laser ablation COLA, Göttingen, Germany, July 19–23 (1999) Abstracts, p. 23

Kleinbauer J., R. Knappe, R. Wallenstein: Ultrashort pulse lasers and amplifiers based on Nd:YVO_4 and Yb:YAG bulk crystals, in *Femtosecond Technology for Technical and Medical Applications*, ed. by F. Dausinger, F. Lichtner, H. Lubatschowski, Springer Series Topics in Applied Physics **96**, Springer Verlag 2004, p. 17

Klein-Wiele J.H., P. Simon: Fabrication of periodic nanostructures by phase-controlled multiple-beam interference, Appl. Phys. Lett. **83**, 4707 (2003)

Kline L.E., W.D. Partlow, R.M. Young, R.R. Mitchell, T.V. Congedo: Diagnostics and modeling of RF discharge dissociation in N_2O, IEEE Trans. PS.-**19**, 278 (1991)

Klini A., P.A. Loukakos, D. Gray, A. Manousaki, C. Fotakis: Laser induced forward transfer of metals by temporally shaped femtosecond laser pulses, Opt. Exp. **16**, 11300 (2008)

Klose, S., E. Arenholz, A. Kirchebner, J. Heitz, D. Bäuerle: Laser-induced dendritic structures on PET: the importance of redeposited ablation products, Appl. Phys. A **69** [Suppl.], S487 (1999)

Ko S.H., H. Pan, C.P. Grigoropoulos, J.M.J. Fréchet, C.K. Luscombe, D. Poulikakos: Lithography-free high-resolution organic transistor arrays on polymer substrate by low energy selective laser ablation of inkjet-printed nanoparticle film, Appl. Phys. A **92**, 579 (2008)

Kobayashi A., S. Kawano, Y. Kawaguchi, J. Ohta, H. Fujioka: Room temperature epitaxial growth of *m*-plane GaN on lattice-matched ZnO substrates, Appl. Phys. Lett. **90**, 041908 (2007)

Kobayashi T., T. Kato, Y. Matsuo, M. Kurata-Nishimura, Y. Hayashizaki, J. Kawai: Temporal pulsewidth and the wavelength dependences of the product ions obtained by laser ablation of solid C_{60}, Appl. Phys. A **92**, 777 (2008)

Koch J., T. Bauer, C. Reinhardt, B.N. Chichkov: Recent progress in direct write 2D and 3D photo-fabrication techniques with fs laser pulses, Chapter 8 in *Recent Advances in Laser processing of Materials*, J. Perriere, E. Millon, E. Fogarassy (eds.), p. 243 (Elsevier 2006)

Koch J., F. Korte, T. Bauer, C. Fallnich, A. Ostendorf, B.N. Chichkov: Nanotexturing of gold films by femtosecond laser-induced melt dynamcis, Appl. Phys. A **81**, 325 (2005)

Kodas T.T., P.B. Comita: A diffusive transport relaxation technique for studying Laser-induced chemical vapor deposition reactions at high pressures, J. Appl. Phys. **65**, 2513 (1989)

König J., S. Nolte, A. Tünnermann: Plasma evolution during metal ablation with ultrashort laser pulses, Opt. Exp. **13**, 10597 (2005)

König K., I. Riemann, F. Stracke, R. LeHarzic: Nanoprocessing with nanojuoule NIR fs laser pulses, Med. Laser Appl. **20**, 169 (2005)

König K., O. Krauss, I. Riemann: Intratissue surgery with 80 MHz nanojoule fs laser pulses in the near infrared, Opt. Exp. **10**, 171 (2002)

König K., I. Riemann, W. Fritzsche: Nanodissection of human chromosomes with near-infrared fs laser pulses, Opt. Lett. **26**, 819 (2001)

Kofler J., N. Arnold: Axially symmetric focusing as a cuspoid diffraction catastrophe: scalar and vector cases and comparison with the theory of Mie, Phys. Rev. B **73**, 235401 (2006)

Kofler, J: Focusing of light in axially symmetric systems with the wave optics approximation, Diploma Thesis, Linz, 2004

Kokai F., K. Takahashi, D. Kasuya, M. Yudasaka, S. Iijima: Growth dynamics of single-wall carbon nanotubes and nanohorn aggregates by CO_2 laser vaporization at room temperature, Appl. Surf. Sci, **197–198**, 650 (2002)

Kokai F., K. Takahashi, K. Shimizu, M. Yudasaka, S. Iijima: Shadowgraphic and emission imaging spectroscopic studies of the laser ablation of graphite in an Ar gas atmosphere, Appl. Phys. A **69** [Suppl.], S223 (1999)

Kokai F.: Optical emission spectra from laser ablation of graphite at 266 nm and 1064 nm under a magnetic field, Jpn. J. Appl. Phys. **36**, 3504 (1997)

Kokkinaki O., S. Georgiou: Incubation in the UV irradiation of condensed $CHCl_3$ solids, Appl. Phys. A **92**, 1013 (2008)

Kolomenskii A.A., H.A. Schuessler, V.G. Mikhalevich, A.A. Maznev: Interaction of laser-generated surface acoustic pulses with fine particles: surface cleaning and adhesion studies, J. Appl. Phys. **84**, 2404 (1998)

Konov V.I., A.M. Prokhorov, S.A. Uglov, A.P. Bolshakov, I.A. Leontiev, Dausinger, F., Hügel, H., Angstenberger, B., Sepold, G., Metev, S.: CO_2 laser-induced plasma CVD synthesis of diamond, Appl. Phys. A **66**, 575 (1998)

Kools J.C.S., T.S. Baller, S.T.De Zwart, J. Dieleman: Gas flow dynamics in laser ablation deposition, J. Appl. Phys. **71**, 4547 (1992)

Kopitkovas G., V. Deckert, T. Lippert, F. Raimondi, C.W. Schneider, A. Wokaun: Chemical and structural changes of quartz surfaces due to structuring by laser induced backside wet etching, Phys. Chem. Chem. Phys. **10**, 3195 (2008)

Kopitkovas G., T. Lippert, J. Venturini, C. David, A. Wokaun: Laser induced backside wet etching: Mechanisms and fabrication of micro-optical elements, J. Phys. Conf. Ser. **59**, 526 (2007)

Korytin A.I., N.M. Bityurin, A.P. Alexandrov, N.A. Babina, L.A. Smirnova, A.M. Sergeev: High-contrast bitwise 3-D optical data storage in doped polymers, Opt. Memo. Neu. Net. **7**, 11 (1998)

Kosalathip V., A. Dauscher, B. Lenoir, S. Migot, T. Kumpeerapun: Preparation of conventional thermoelectric nanopowders by pulsed laser fracture in water: application to the fabrication of a pn hetero-junction, Appl. Phys. A **93**, 235 (2008)

Kostrykin V., M. Nießen, W. Schulz, E.W. Kreutz, R. Poprawe: Heat and mass transfer induced by ps laser pulses, SPIE **3343**, 971 (1998)

Kozhushko V.V., P. Hess: Nondestructive evaluation of microcracks by laser-induced focused ultrasound, Appl. Phys. Lett. **91**, 224107 (2007)

Kräuter W., D. Bäuerle, F. Fimberger: Laser-induced chemical vapor deposition of Ni by decomposition of $Ni(CO)_4$, Appl. Phys. A **31**, 13 (1983)

Kräutle H., P. Roentgen, M. Maier, H. Beneking: Laser-induced doping of GaAs, Appl. Phys. A **38**, 49 (1985)

Krajnovich D.J.: Laser sputtering of highly oriented Pyrolytic Graphite at 248 nm, J. Chem. Phys. **102**, 726 (1995)

Krajnovich D.J., J.E. Vázquez: Formation of "Intrinsic" surface defects during 248 nm photoablation of polyimide, J. Appl. Phys. **73**, 3001 (1993)

Kramer K.J., S. Talwar, P.G. Carey, E. Ishida, D. Ashkenas, K.H. Weiner, T.W. Sigmon: Impurity distribution and electrical characteristics of Boron-Doped $Si_{1-x}Ge_x$/Si p^+/N Heterojunction Diodes produced using pulsed UV-laser -induced epitaxy and Gas-immersion laser doping, Appl. Phys. A **57**, 91 (1993)

Krchnavek R.R., H.H. Gilgen, J.C. Chen, P.S. Shaw, T.J. Licata, R.M. Osgood: Photodeposition rates of metal from metal alkyls, J. Vac. Sci. Technol. B **5**, 20 (1987)

Krchnavek R.R., H.H. Gilgen, R.M. Osgood, Jr.: Maskless laser writing of Silicon Dioxide, J. Vac. Sci. Technol. B **2**, 641 (1984)

Krebs H.-U.: Pulsed laser deposition of metals, in *Pulsed Laser Deposition of Thin Films: Applications-Led Growth of Functional Materials*, ed. R. Eason (Wiley 2007) p. 363

Krebs H.-U., M. Weisheit, J. Faupel, E. Süske, T. Scharf, C. Fuhse, M. Störmer, K. Sturm, M. Seibt, H. Kijewski, D. Nelke, E. Panchenko, M. Buback: Pulsed laser deposition (PLD) – a versatile thin film technique, in *Adv. in Solid State Phys*., B. Kramer ed. Vol. **43**, 505 (Springer, Berlin, Heidelberg 2003)

Kreitschitz O., W. Husinsky, G. Betz, N.H. Tolk: Time-of-flight investigation of the intensity dependence of laser-desorbed positive ions from SrF_2, Appl. Phys. A **58**, 563 (1994)

Kreuzer H.J., Z.W. Gortel: *Physisorption Kinetics*, Springer Ser. Surf. Sci., Vol. 1 (Springer, Berlin, Heidelberg 1986)

Kröner D., T. Klamroth, M. Nest, P. Saalfrank: Laser-induced charge transfer and photodesorption of Cs at Cu(111): quantum dynamical model simulations, Appl. Phys. A **88**, 535 (2007)

Krokhin O.N.: Generation of high-temperature vapors and plasmas by laser radiation. In laser handbook, Vol. 2, ed. by F.T. Arecchi and E.O. Schulz-Dubois (North-Holland, Amsterdam 1972) Part E: Physical Applications, p. 1371

Krüger J., D. Dufft, R. Koter, A. Hertwig: Femtosecond laser-induced damage of gold films, Appl. Surf. Sci. **253**, 7815 (2007)

Krüger J., W. Kautek: Ultrashort pulse laser interaction with dielectrics and polymers, Adv. Polym. Sci. **168**, 247 (2004)

Krüger J., M. Lenzner, S. Martin, M. Lenner, C. Spielmann, A. Fiedler, W. Kautek: Single-and multi-pulse femtosecond laser ablation of optical filter materials, Appl. Surf. Sci. **208–209**, 233 (2003)

Krüger J., H. Niino, A. Yabe: Investigation of excimer laser ablation threshold of polymers using a microphone, Appl. Surf. Sci. **197–198**, 800 (2002)

Krüger J., W. Kautek, M. Lenzner, S. Sartania, C. Spielmann, F. Krausz: Structuring of dielectric and metallic materials with ultrashort laser pulses between 20 fs and 3 ps, SPIE **2991**, 40 (1997)

Krüger O., G. Schöne, T. Wernicke, W. John, J. Würfl, G. Tränkle: UV laser drilling of SiC for semiconductor device fabrication, J. Phys. Conf. Ser. **59**, 740 (2007)

Kubo M., M. Hanabusa: Fabrication of microlenses by laser chemical vapor deposition, Appl. Optics **29**, 2755 (1990)

Kuehn T.H., R.J. Goldstein: Numerical solution to the navier-stokes equations for laminar natural convection about a horizontal isothermal circular cylinder, Int. J. Heat Mass Transfer **23**, 971 (1980)

Küper S., J. Brannon, K. Brannon: Threshold behavior in polyimide Photo-ablation single-shot rate measurements and surface-temperature modeling, Appl. Phys. A **56**, 43 (1993)

Küper S., J. Brannon: Ambient Gas effects on debris formed during KrF laser ablation of polyimide, Appl. Phys. Lett. **60**, 1633 (1992)

Küper S., M. Stuke: Ablation of UV-transparent materials with femtosecond UV excimer laser pulses, Microelect. Eng. **9**, 475 (1989)

Kuhnke M., L. Cramer, P.E. Dyer, J.T. Dickinson, T. Lippert, H. Niino, M. Pervolaraki, C.D. Walton, A. Wokaun: F_2 excimer laser (157 nm) ablation of polymers: relation of neutral and ionic fragment detection and absorption, J. Phys. Conf. Ser. **59**, 625 (2007)

Kull H.J.: Theory of the rayleigh-taylor instability, Phys. Rep. **206**, No. 5, 197 (1991)

Kullmer R.: Heat transfer from small tungsten spheres into an ambient H_2 atmosphere, Appl. Phys. B **62**, 191 (1996)

Kullmer R., B. Kargl, D. Bäuerle: Laser-induced deposition of tungsten from tungsten Hexachloride, Thin. Solid. Film. **218**, 122 (1992)

Kullmer R., D. Bäuerle: Laser-induced chemical etching of Silicon in Chlorine atmosphere: III. Combined cw- and pulsed-irradiation, Appl. Phys. A **47**, 377 (1988a)

Kullmer R., D. Bäuerle: Excimer-laser-induced ablation of the high T_c superconductor Bi-Ca-Sr-Cu-O, Appl. Phys. A **47**, 103 (1988b)

Kullmer R., D. Bäuerle: Laser-induced chemical etching of Silicon in Chlorine atmosphere: I. Pulsed-Irradiation, Appl. Phys. A **43**, 227 (1987)

Kumagai H., M. Ezaki, K. Toyoda, M. Obara: Fabrication of periodic submicron dot structures of N-InP by laser-induced surface electromagnetic wave etching, Jpn. J. Appl. Phys. **31**, L928 (1992)

Kumar B., R.K. Soni: Luminescent nanoclusters array fabricated by pulsed laser beam irradiation, Nuc. Instr. Met. Phys. Res. B **266**, 2576 (2008)
Kuna L., C. Sommer, E. Zinterl, J.R. Krenn, P. Pachler, P. Hartmann, S. Tasch, G. Leising, F.P. Wenzl: Volume structuring of high power LED encapsulates by fs laser direct writing, Appl. Phys. A **93**, 421 (2008)
Kurosawa K., W. Sasaki, Y. Takigawa, M. Ohmukai, M. Katto, M. Okuda: Growth of Silicon microcrystals in thin surface layers of quartz glass with Vacuum Ultraviolet laser processing, Appl. Surf. Sci. **70–71**, 712 (1993)
Kurtze D.A., W.v. Saarloos, J.D. Weeks: Front propagation in self-sustained and laser-driven explosive crystal growth: Stability analysis and morphological aspects, Phys. Rev. B **30**, 1398 (1984)
Kuznetsov A.I., J. Koch, B.N. Chichkov: Nanostructuring of thin gold films by femtosecond lasers, Appl. Phys. A **94**, 221 (2009)
Kwong D.L., D.M. Kim: Pulsed laser heating of Silicon: The coupling of optical absorption and thermal conduction during irradiation, J. Appl. Phys. **54**, 366 (1983)
Kwong H.Y., M.H. Wong, Y.W. Hong, K.H. Wong: Superhydrophobicity of polytetrafluoroethylene thin film fabricated by pulsed laser deposition, Appl. Surf. Sci. **253**, 8841 (2007)
Kwong H.Y., M.H. Wong, Y.W. Wong, K.H. Wong: Magnetoresistivity of cobalt-PTFE granular composites, Appl. Phys. Lett. **89**, 173109 (2006)
Lai N.D., T.S. Zheng, D.B. Do, J.H. Lin, C.C. Hsu: Fabrication of desired 3-D structures by holographic assembly technique, Appl. Phys. A. **100**, 171 (2010)
Lambda Industrial Report No. 8: The key to advanced technology (Lambda Physik, Göttingen, November 1994)
Lampert M.O., J.M. Koebel, P. Siffert: Temperature dependence of the reflectance of solid and liquid Silicon, J. Appl. Phys. **52**, 4975 (1981)
Landau L.D., E.M. Lifshitz: *Statistical Physics V*, Pt. 1 (Pergamon, Oxford 1980)
Landau L.D., E.M. Lifshitz: *Theory of Elasticity VII* (Pergamon, Oxford 1976)
Landau L.D., E.M. Lifshitz: *Fluid Mechanics VI* (Pergamon, Oxford 1974)
Landau L.D., E.M. Lifshitz: *Physical Kinetics X* (Pergamon, Oxford 1974)
Landolt-Börnstein – Group VIII/1C Laser Physics and Applications, edited by R. Poprawe, H. Weber, G. Herziger (Springer Berlin, Heidelberg, New York 2004)
Landström L., J. Klimstein, G. Schrems, K. Piglmayer, D. Bäuerle: Single-step patterning and the fabrication of contact masks by laser-induced forward transfer, Appl. Phys. A **78**, 537 (2004)
Lang F., M. Mosbacher, P. Leiderer: Near field induced defects and influence of the liquid layer thickness in steam laser cleaning of silicon wafers, Appl. Phys. A **77**, 117 (2003)
Langer G., D. Brodoceanu, D. Bäuerle: Femtosecond laser fabrication of apertures on two-dimensional microlens arrays, Appl. Phys. Lett. **89**, 261104 (2006)
Larciprete R., M.G. Grimaldi, E. Borsella, S. Cozzi, S. Martelli, S. Pieretti, I. Vianey: KrF laser epitaxy of silicon germanium alloy layers by irradiation of $Si_{(1-x)}Ge_x$/Si (100) structures, J.Vac. Sci. Technol. B **16**, 1589 (1998)
Larsen U.D., O. Sigmund, S: Bouwstra: Design and fabrication of compliant micro-mechanisms and structures with negative Poisson's ratio, J. Micro. Sys. **6**, 99 (1997)
Lasagni A.F., D.F. Acevedo, C.A. Barbero, F. Mücklich: Advanced design of conductive polymeric arrays with controlled electrical resistance using direct laser interference patterning, Appl. Phys. A **91**, 369 (2008)
Late D.J., P. Misra, B.N. Singh, L.M. Kukreja, D.S. Joag, M.A. More: Enhanced field emission from pulsed laser deposited nanocrystalline ZnO thin films on Re and W, Appl. Phys. A **95**, 613 (2009)
Laude L.D. ed.: *Excimer Lasers*, NATO ASI Series – Applied Sciences, Vol. 265 (Kluwer, Dordrecht 1994)
Laude L.D., M. Wautelet, R. Andrew: Laser-induced synthesis of compound semi-conducting films, Appl. Phys. A **40**, 133 (1986)

Lazare S., R. Bonneau, S. Gaspard, M. Oujja, R. DeNalda, M. Castillejo, A. Sionkowska: Modeling the dynamcis of one laser pulse surface nanofoaming of biopolymers, Appl. Phys. A **94**, 719 (2009)

Lazare S., V.N. Tokarev, A. Sionkowska, M. Wisniewski: Negative pressure model for surface foaming of collagen and other biopolymer films by KrF laser ablation, J. Phys. Conf. Ser. **59**, 543 (2007)

Lazare S., W. Guan, D. Drilhole: High sensitivity quadrupole mass spectrometry of neutrals sputtered by UV-laser ablation of polymers, Appl. Surf. Sci **96–98**, 605 (1996)

Lazare S., V. Granier: Mechanism of Polymer Photoablation Explored with a Quartz Crystal Microbalance, in *Polymers in Microlithography: Materials and Processes*, ed. by E. Reichmanis, S.A.MacDonald, T. Iwayanagi, ACS Symp. Ser. **412**, 411 (Am. Chem. Soc., Washington, DC 1989)

LeComber P.G., A.J. Snell, K.D. Mackenzie, W.E. Spear: Applications of a-Si field effect transistors in liquid Crystal displays and in integrated logic circuits, J. Phys. Paris. C-**4**, 423 (1981)

Lee J.M., K.G. Watkins, W.M. Steen: Angular laser cleaning for effective removal of particles from a solid surface, Appl. Phys. A **71**, 671 (2000)

Lee M., S. Moon, M. Hatano, K. Suzuki, C.P. Grigoropoulos: Relationship between fluence gradient and lateral grain growth in spatially controlled excimer laser crystallization of amorphous silicon films, J. Appl. Phys. **88**, 4994 (2000)

Lee N.N., H.M. Christen, M.F. Chisholm, C.M. Rouleau, D.H. Lowndes: Strong polarization enhancement in asymmetric 3-component ferroelectric superlattices, Nature **433**, 395 (2005)

Lee S., X. Wen, W.A. Tolbert, D.D. Dlott, M. Doxtader, D.R. Arnold: Direct measurement of polymer temperature during laser ablation using a molecular thermometer, J. Appl. Phys. **72**, 2440 (1992)

Leech P.W., A.S. Holland, S. Sriram, M. Bhaskaran: Patterning of PLZT and PSZT thin films by excimer laser, Appl. Phys. A **91**, 679 (2008)

Le Harzic R., K. König, C. Wüllner, K. Vogler, C. Donitzky: UV fs laser creation of corneal flap, J. Refr. Sur. **25**, 383 (2009)

Lehmann O., M. Stuke: Laser-driven movement of 3D microstructures generated by laser rapid prototyping, Science **270**, 1644 (1995)

Lehmann O., M. Stuke: Generation of three-dimensional free-standing metal micro-objects by laser chemical processing, Appl. Phys. A **53**, 343 (1991)

Leiderer P., C. Bartels, J. König-Birk, M. Mosbacher, J. Boneberg: Imaging optical near-fields of nanostructures, Appl. Phys. Lett. **85**, 5370 (2004)

Leiderer P., M. Mosbacher, V. Dobler, A. Schilling, O. Yavas, S.B. Luk'yanchuk, J. Boneberg: Steam laser cleaning of silicon surfaces: Laser-induced gas bubble nucleation and efficiency measurements, Chap. 6 in "Laser Cleaning", Luk'yanchuk B.S. ed.: (World Scientific, Singapore, 2002) p. 255

Leiderer P., J. Boneberg, M. Mosbacher, A. Schilling, O. Yavas: Laser cleaning of silicon surfaces, SPIE **3274**, 68 (1998)

Lenzner M., J. Krüger, W. Kautek, F. Krausz: Incubation of laser ablation in fused silica with 5-fs pulses, Appl. Phys. A **69**, 465 (1999a)

Lenzner M., J. Krüger, W. Kautek, F. Krausz: Precision laser ablation of dielectrics in the 10-fs regime, Appl. Phys. A **68**, 369 (1999b)

Lenzner M., J. Krüger, S. Sartania, Z. Cheng, C. Spielmann, G. Mourou, W. Kautek, F. Krausz: Femtosecond optical breakdown in dielectrics, Phys. Rev. Lett. **80**, 4076 (1998)

Leonard R.T., S.M. Bedair: Photoassisted dry etching of GaN, Appl. Phys. Lett. **68**, 794 (1996)

Lethy K.J., D. Beena, R. Vinod Kumar, V.P. Mahadevan Pillai, V. Ganesan, V. Sathe, D.M. Phase: Nanostructured tungsten oxide thin films by the reactive pulsed laser deposition technique, Appl. Phys. A **91**, 637 (2008)

Letokhov V.S.: Laser-induced chemistry – basic nonlinear processes and applications, Appl. Phys. B **46**, 237 (1988)

Letokhov V.S.: *Nonlinear Laser Chemistry, Multiple Photon Excitation*, Springer Ser. Chem. Phys., Vol. 22 (Springer, Berlin, Heidelberg 1983)

Leveugle E., L. V. Zhigilei: Molecular dynamics simulation study of the ejection and transport of polymer molecules in matrix-assisted pulsed laser evaporation, J. Appl. Phys. **102**, 074914 (2007)

Levich V.G.: *Physicochemical Hydrodynamics* (Prentice Hall, Englewood Cliffs, NJ 1962)

Levine R.D., R.B. Bernstein: *Molecular Reaction Dynamics and Chemical Reactivity* (Oxford University Press, New York 1987)

Leyendecker G., J. Doppelbauer, D. Bäuerle, P. Geittner, H. Lydtin: Raman diagnostics of CVD systems: Determination of local temperatures, Appl. Phys. A **30**, 237 (1983a)

Leyendecker G., H. Noll, D. Bäuerle, P. Geittner, H. Lydtin: Rapid determination of apparent activation energies in chemical vapor deposition, J. Electr. Soc. **130**, 157 (1983b)

Leyendecker G., D. Bäuerle, P. Geittner, H. Lydtin: Laser induced chemical vapor deposition of carbon, Appl. Phys. Lett. **39**, 921 (1981)

Li C.-F., X.-Z.Dong, F. Jin, W. Jin, W.-Q. Chen, Z.-S. Zhao, X.-M. Duan: Polymeric distributed-feedback resonator with sub-micrometer fibers fabricated by two-photon induced photopolymerization, Appl. Phys. A **89**, 145 (2007)

Li H., K. Iga eds.: *Vertical-cavity Surface-emitting Laser Devices*, Springer, Heidelberg 2003

Li J., J. Dou, P.R. Herman, T. Fricke-Begemann, J. Ihlemann, G. Marowsky: Deep ultraviolet laser micromachining of novel fibre optic devices, J. Phys. Conf. Ser. **59**, 691 (2007)

Li S.T., E. Arenholz, J. Heitz, D. Bäuerle: Pulsed-laser deposition of crystalline Teflon (PTFE) films, Appl. Surf. Sci. **125**, 17 (1998)

Li S.T., A. Ritzer, S. Proyer, E. Stangl, D. Bäuerle: Anisotropic resistivity in pulsed-laser deposited $Bi_2Sr_2CaCu_2O_{8+}$ films, Appl. Surf. Sci. **96–98**, 713 (1996)

Li Y., B. Shrestha, A. Vertes: Atmospheric pressure molecular imaging by infrared MALDI mass spectrometry, Anal. Chem. **79**, 523 (2007)

Libenson M.N., M.N. Nikitin: On the Diffusion of Film Atoms into the Substrate under the Action of Laser Radiation, Fiz. i Khim. Obrabotki Materialov (Physics and Chemistry of Material Processing), **1**, 9 (1973) (In Russian)

Liberts G., M. Eyett, D. Bäuerle: Direct laser writing of superconducting patterns into semiconducting ceramic Y-Ba-Cu-O, Appl. Phys. A **46**, 331 (1988a)

Liberts G., M. Eyett, D. Bäuerle: Laser-induced surface reduction of the high T_c superconductor $YBa_2Cu_3O_{7-x}$, Appl. Phys. A **45**, 313 (1988b)

Licata T.J., M.T. Schmidt, R.M. Osgood, W.K. Chan, R. Bhat: Application of photodeposited Cd to schottky barrier Diode and Transistor Fabrication on InP and $In_{0.53}Ga_{0.47}As$ substrates, Appl. Phys. Lett. **58**, 845 (1991)

Licata T.J., D.V. Podlesnik, H. Tang, I.P. Herman, R.M. Osgood, S.A. Schwarz: Continuous-wave laser doping of micrometer-sized features in gallium arsenide using a dimethylzinc ambient, J. Vac. Sci. Technol. A **8**, 1618 (1990)

Lim C.S., M.H. Hong, Y. Lin, G.X. Chen, A. Senthil Kumar, M. Rahman, L.S. Tan, J.Y.H. Fuh, G.C. Lim: Sub-micron surface patterning by laser irradiation through microlens arrays, J. Mater. Proc. Tech. **192–193**, 328 (2007)

Lin C.H., L. Jiang, Y.H. Chai, H. Xiao, S.J. Chen, H.L. Tsai: Fabrication of microlens arrays in photosensitive glass by fs laser direct writing, Appl. Phys. A **97**, 751 (2009)

Lin Z., R.A. Johnson, L.V. Zhigilei: Computational study of the generation of crystal defects in a bcc metal target irradiated by short laser pulses, Phys. Rev. B **77**, 214108 (2008a)

Lin Z., L.V. Zhigilei, V. Celli: Electron-phonon coupling and electron heat capacity of metals under conditions of strong electron-phonon nonequilibrium, Phys. Rev. B **77**, 075133 (2008b)

Lin Z., L.V. Zhigilei: Time-resolved diffraction profiles and atomic dynamics in short-pulse laser-induced structural transformations: Molecular dynamics study, Phys. Rev. B **73**, 184113 (2006)

Lindenberg A.M., J. Larsson, K. Sokolowski-Tinten, K.J. Gaffney, C. Blome, O. Synnergren, J. Sheppard, C. Caleman, A.G. MacPhee, D. Weinstein, D.P. Lowney, T.K. Allison, T. Matthews, R.W. Falcone, A.L. Cavalieri, D.M. Fritz, S.H. Lee, P.H. Bucksbaum, D.A. Reis, J. Rudati, P.H. Fuoss, C.C. Kao, D.P. Siddons, R. Pahl, J. Als-Nielsen, S. Duesterer, R. Ischebeck, H. Schlarb, H. Schulte-Schrepping, Th. Tschentscher, J. Schneider, D. von der Linde, O. Hignette, F. Sette, H.N. Chapman, R.W. Lee, T.N. Hansen, S. Techert, J.S. Wark, M. Bergh, G. Huldt, D. van der Spoel, N. Timneanu, J. Hajdu, R.A. Akre, E. Bong, P. Krejcik,

J. Arthur, S. Brennan, K. Luening, J.B. Hastings: Atomic-scale visualization of inertial dynamics, Science **308**, 392 (2005)

Lippert T., M.J. Montenegro, M. Döbeli, A. Weidenkaff, S. Müller, P.R. Willmott, A. Wokaun: Perovskite thin films deposited by pulsed laser ablation as model systems for electrochemical applications, Prog. Sol. Stat. Chem. **35**, 221 (2007)

Lippert T.: Interaction of photons with polymers: From surface modification to ablation, Plasma processes and polymers **2**, 525 (2005)

Lippert T., J.T. Dickinson: Chemical and spectroscopic aspects of polymer ablation: special features and novel directions, Chem. Rev. **103**, 453 (2003)

Liu B., Z. Hu, Y. Che, Y. Chen, X. Pan: Nanoparticle generation in ultrafast pulsed laser ablation of nickel, Appl. Phys. Lett. **90**, 044103 (2007)

Liu Y.S.: Laser Direct Writing of Tungsten Lines for VLSI Applications, in *Tungsten and Other Refractory Metals for VLSI Applications I*, ed. by R.S. Blewer (Materials Research Society, Pittsburgh, PA 1986) p. 43

Liu Z., D.J. Styers-Barnett, A.A. Puretzky, C.M. Rouleau, D. Yuan, I.N. Ivanov, K. Xiao, J. Liu, D.B. Geohegan: Pulsed laser CVD investigations of single-wall carbon nanotube growth dynamics, Appl. Phys. A **93**, 987 (2008)

Liu Z.G., J. Yin, Z.C. Wu.: PLD of Ta-doped PZT ferroelectric films for memory applications using conductive oxide $La_{0.25}Sr_{0.75}CoO_3$ and $SrRuO_3$ electrodes, Appl. Phys. A **69** [Suppl.], S659 (1999)

Liu Z-W., Q.H. Wei, X. Zhang: Surface plasmon interference nanolithography, Nano Lett. **5**, 957 (2005)

Livingston F.E., L.F. Steffeney, H. Helvajian: Genotype-inspired laser material processing: a new experimental approach and potential applications to protean materials, Appl. Phys. A **93**, 75 (2008)

Livingston F.E., H. Helvajian: Photophysical processes that lead to ablation-free microfabrication, in: *Glass-Ceramic Materials*, in: *3D Laser Microfabriation*, ed. by H. Misawa, S. Juodkazis (Wiley-VCH, Weinheim, 2006) and references therein

Loper G.L., M.D. Tabat: UV Laser-induced radical-etching for Micro-electronic Processing, in *Laser Assisted Deposition, Etching, and Doping*, ed. by S.D. Allen, SPIE Proc. **459**, 121 (1984)

Lowndes D.H., C.M. Rouleau, T. Thundat, G. Duscher, E.A. Kenik, S.J. Pennycook: Silicon and zinc telluride nanoparticles synthesized by pulsed laser ablation: size distributions and nanoscale structure, Appl. Surf. Sci. **127–129**, 355 (1998)

Lowndes D.H., D.P. Norton, S. Zhu, X.Y. Zheng: Laser ablation synthesis and properties of epitaxial $YBa_2Cu_3O_{7-}$/$PrBa_2Cu_3O_{7-}$ superconducting superlattices, in *Laser Ablation of Electronic Materials*, ed. by E. Fogarassy, S. Lazare, (Elsevier, Amsterdam 1992) p. 265

Lu Y.F., S.M. Huang, C.H.A. Huan, X.F. Luo: Amorphous hydrogenated carbon synthesized by pulsed laser deposition from cyclohexane, Appl. Phys. A **68**, 647 (1999)

Lu Y.F., S.M. Huang, X.B. Wang, Z.X. Shen: Laser-assisted growth of diamond particulates on a silicon surface from a cyclohexane liquid, Appl. Phys. A **66**, 543 (1998a)

Lu Y.F., W.D. Song, C.K. Tee, D.S.H. Chan, T.S. Low: Wavelength effects in the laser cleaning process, Jpn. J. Appl. Phys. **37**, 840 (1998b)

Lu Y.F., W.D. Song, B.W. Ang, M.H. Hong, D.S.H. Chan, T.S. Low: A theoretical model for laser removal of particles from solid surfaces, Appl. Phys. A **65**, 9 (1997)

Lu Z., M.T. Schmidt, D.V. Podlesnik, C.F. Yu, R.M. Osgood: Ultraviolet-light-induced oxide formation on GaAs surfaces, J. Chem. Phys. **93**, 7951 (1990)

Lubatschowski H., A. Heisterkamp: Interaction with Biological Tissue, in *Femtosecond Technology for Technical and Medical Applications*, ed. by F. Dausinger, F. Lichtner, H. Lubatschowski, Springer Series Topics in Applied Physics **96**, Springer Verlag 2004a, p. 91

Lubatschowski H., A. Heisterkamp: Ophthalmic applications, in *Femtosecond Technology for Technical and Medical Applications*, ed. by F. Dausinger, F. Lichtner, H. Lubatschowski, Springer Series Topics in Applied Physics **96**, Springer Verlag 2004b, p. 187

Lubben D., S.A. Barnett, K. Suzuki, S. Gorbatkin, J.E. Greene: Laser-induced plasmas for primary Ion deposition of epitaxial Ge and Si films, J. Vac. Sci. Techn. B **3**, 968 (1985)

Lubecke V.M., K. Mizuno, G.M. Rebeiz: in IEEE transactions on microwave theory and techniques, Vol. 46 (11), Nov. 1998

Lucarelli A., S. Hümmert, A. Chaney, G. Lüpke, B. Moeckly, Y. Zhao, S.X. Dou: Kinetic roughening of magnetic flux penetration in MgB_2 thin films, Appl. Phys. Lett. **91**, 222505 (2007)

Lüth H.: *Surface and Interfaces of Solids*, 4th ed. (Springer, Berlin, Heidelberg 2001)

Luk'yanchuk B.S., Z.B. Wang, M. Tribelsky, V. Ternovsky, M.H. Hong, T.C. Chong: Peculiarities of light scattering by nanoparticles and nanowires near plasmon resonance frequencies, J. Phys. Conf. Ser. **59**, 234 (2007a)

Luk'yanchuk B.S., W.D. Song, Z.B. Wang, M.H. Hong, T.C. Chong, J. Graf, M. Mosbacher, P. Leiderer: New methods for laser cleaning of nanoparticles, Chapter 3 in *Laser Ablation and its Applications*, ed. by C. R. Phipps (Springer 2007b) p. 37

Luk'yanchuk B.S., Z.B. Wang, W.D. Song, M.H. Hong: Particle on surface: 3D-effects in dry laser cleaning, Appl. Phys. A **79**, 747 (2004)

Luk'yanchuk B.S. ed.: "*Laser Cleaning*" (World Scientific, Singapore, 2002)

Luk'yanchuk B.S., W. Marine, S. I. Anisimov, G.A. Simakina: Condensation of vapor and nanoclusters formation within the vapor plume, produced by ns-laser ablation of Si, Ge and C. In "*Laser Applications in Microelectronic and Optoelectronic Manufacturing*", ed. by J. Dubovsky, SPIE Proc. **3618**, 434 (1999)

Luk'yanchuk B., D. Bäuerle: 1999, unpublished

Luk'yanchuk B., N. Bityurin, A. Malyshev, S. Anisimov, N. Arnold, D. Bäuerle: Photophysical Ablation. In High-Power Laser Ablation, ed. by C.R. Phipps, Proc. SPIE **3343**, 58 (1998)

Luk'yanchuk B., N. Arnold, D. Bäuerle: 1997, unpublished

Luk'yanchuk B., D. Bäuerle: 1994, unpublished

Luk'yanchuk B., N. Bityurin, S. Anisimov, D. Bäuerle: Photophysical ablation of organic polymers; in *Excimer Lasers*, ed. by L.D. Laude, NATO ASI Ser. (Kluwer, Dordrecht 1994) p. 59

Luk'yanchuk B., N. Bityurin, S. Anisimov, D. Bäuerle: The role of excited species in UV-laser materials ablation. I. Photo-physical ablation of organic polymers, Appl. Phys. A **57**, 367 (1993a)

Luk'yanchuk B., N. Bityurin, S. Anisimov, D. Bäuerle: The role of excited species in UV-laser materials ablation. II. The stability of the ablation front, Appl. Phys. A **57**, 449 (1993b)

Luk'yanchuk B., K. Piglmayer, N. Kirichenko, D. Bäuerle: Inversion effects in the kinetics of laser-chemical processing, Physica A **180**, 285 (1992)

Luo G., I. Marginean, L. Ye, A. Vertes: Competing ion decomposition channels in matrix-assisted laser desorption ionization, J. Phys. Chem. B **112**, 6952 (2008)

Luo H., Y. Li, H.-B. Cui, H. Yang, Q.-H. Gong: Dielectric-loaded surfae plasmon-polariton nanowaveguides fabricated by two-photon polymerization, Appl. Phys. A **97**, 709 (2009)

Lussier A., J. Dvorak, S. Stadler, J. Holroyd, M. Liberati, E. Arenholz, S.B. Ogale, T. Wu, T. Venkatesan, Y.U. Idzerda: Stress relaxation of $La_{1/2}Sr_{1/2}MnO_3$ and $La_{2/3}Ca_{1/3}MnO_3$ at solid oxide fuel cell interfaces, Thin. Sol. Film. **516**, 880 (2008)

Lyalin A.A., A.V. Simakin, G.A. Shafeev, E.N. Loubnin: Laser deposition of amorphous diamond films from liquid aromatic hydrocarbons, Appl. Phys. A **68**, 373 (1999)

Ma F., M.H. Hong, L.S. Tan: Laser nano-fabrication of large-area plasmonic structures and surface plasmon resonance tuning by thermal effect, Appl. Phys. A **93**, 907 (2008)

Ma Z., F. Zavaliche, L. Chen, J. Ouyang, J. Melngailis, A.L. Roytburd, V. Vaithyanathan, D.G. Schlom, T. Zhao, R. Ramesh: Effect of 90° domain movement on the piezoelectric response of patterned $PbZr_{0.2}Ti_{0.8}O_3/SrTiO_3$/Si heterostructures, Appl. Phys. Lett. **87**, 072907 (2005)

Maaren A.J.P. van, R.L. Krans, W.C. Sinke: HF Formation in Laser-induced CVD of Tungsten, Appl. Surf. Sci. **46**, 138 (1990)

Maaren A.J.P. van, R.L. Krans, E. de Haas, W.C. Sinke: A high vacuum system for laser-induced deposition of tungsten, J. Vac. Sci. Technol. B **9**, 89 (1991); Excimer laser induced deposition of tungsten on Silicon, Appl. Surf. Sci. **38**, 386 (1989)

Madsen N.R., E.G. Gamaly, A.V. Rode, B. Luther-davies: Cluster formation through the action of a single picosecond laser pulse, J. Phys.Conf. Ser. **59**, 762 (2007)

Maffei N., S.B. Krupanidhi: Excimer lated bismuth titanate thin films, Appl. Phys. Lett. **60**, 781 (1992)

Magnotta F., I.P. Herman: Raman microprobe analysis during the direct laser eriting of Silicon microstructures, Appl. Phys. Lett. **48**, 195 (1986)

Mah K.W., J.-P. Mosnier, E. McGlynn, M.O. Henry, D. O'Mahony, J.G. Lunney: Study of photoluminescence at 3.310 and 3.368 eV in GaN/sapphire(0001) and GaN/GaAs(001) grown by liquid-target pulsed-laser deposition, Appl. Phys. Lett. **80**, 3301 (2002)

Maiorov B., S.A. Baily, H. Zhou, O. Ugurlu, J.A. Kennison, P.C. Dowden, T.G. Holesinger, S.R. Foltyn, L. Civale: Synergetic combination of different tyes of defect to optimize pinning landscape using $BaZrO_3$-doped $YBa_2Cu_3O_7$, Nat. Mater. **8**, 398 (2009)

Maissel L.I., R. Glang: *Handbook of Thin Film Technology* (McGraw Hill, New York 1970)

Makimura T., H. Miyamoto, S. Uchida, H. Niino, K. Murakami: Direct nanomachining of inorganic transparent materials using laser plasma soft X-rays, J. Phys. Conf. Ser. **59**, 279 (2007)

Makimura T., Y. Kunii, N. Ono, K. Murakami: Silicon nanoparticles embedded in SiO_2 films with visible photoluminescence, Appl. Surf. Sci. **127–129**, 388 (1998)

Makino T., N. Suzuki, Y. Yamada, T. Yoshida, T. Seto, N. Aya: Size classification of Si nanoparticles formed by pulsed laser ablation in He background gas, Appl. Phys. A **69** [Suppl.], S243 (1999)

Malvezzi A.M., H. Kurz, N. Bloembergen: Nonlinear photoemission from picosecond irradiated Silicon, Appl. Phys. A **36**, 143 (1985)

Mann G., J. Vogel, M. Zoheidi, M. Eberstein, J. Krüger: Breakdown limits of optical multimode fibers for the application of ns laser pulses at 532 nm and 1064 nm wavelength, Appl. Surf. Sci. **255**, 5519 (2009)

Mann K.: Laser beam characterization, Chapter 7 in *Excimer Laser Technology*, D. Basting, G. Marowsky (eds.): (Springer-Verlag, Berlin 2005) p. 105

Manoravi P., M. Joseph, N. Sivakumar: Pulsed laser ablation – thin film deposition of polyethylene oxide, J. Phys. Chem. Solids **59**, 1271 (1998)

Mantoudis E., B.T. Podsiadly, A. Gorgy, G. Venkat, I.L. Craft: A comparison between quarter, partial and total laser assisted hatching in selected infertility patients, Hum. Reprod. **16**, 2182 (2001)

Margueritat J., J. Gonzalo, C.N. Afonso, U. Hörmann, G. Van Tendeloo, A. Mlayah, D.B. Murray, L. Saviot, Y. Zhou, M.H. Hong, B.S. Luk'yanchuk: Surface enhanced Raman scattering of silver sensitized cobalt nanoparticles in metal-dielectric nanocomposites, Nanotechnology **19**, 375701 (2008)

Margueritat J., J. Gonzalo, C.N. Afonso, M. Isabel Ortiz, C. Ballesteros: Production of self-aligned metal nanocolumns embedded in an oxide matrix films, Appl. Phys. Lett. **88**, 093107 (2006)

Marine W., N.M. Bulgakova, L. Patrone, I. Ozerov: Insight into electronic mechanisms of nanosecond-laser ablation of silicon, J. Appl. Phys. **103**, 094902 (2008)

Marine W., B. Luk'yanchuk, M. Sentis: Silicon nanocluster synthesis by conventional laser Ablation. Le VIDE Science, technique et applications, Vol. **2–4**, Nr. 288, 440 (1998)

Markowitsch W., C. Stockinger, W. Lang, K. Bierleutgeb, J.D. Pedarnig, D. Bäuerle: Photoinduced enhancement of the *c*-axis conductivity in oxygen-deficient $YBa_2Cu_3O_x$ thin films, Appl. Phys. Lett. **71**, 1246 (1997)

Marks R.F., R.A. Pollak, P. Avouris, C.T. Lin, Y.J. Théfaine: Laser-Pulsed Plasma Chemistry: Laser-Initiated Plasma Oxidation of Niobium, J. Chem. Phys. **78**, 4270 (1983)

Marozau I., M. Döbeli, T. Lippert, D. Logvinovich, M. Mallepell, A. Shkabko, A. Weidenkaff, A. Wokaun: One-step preparation of N-doped strontium titanate films by pulsed laser deposition, Appl. Phys. A **89**, 933 (2007)

Marsal D.: *Die Numerische Lösung Partieller Differentialgleichungen* (Bibliographisches Institut, Mannheim 1976)

Martinez A., M. Dubov, I. Khrushchev, I. Bennion: Direct writing of fibre Bragg gratings by fs laser, Electronics Lett. **40**, No. 19, p. 1170 (2004)

Martsinovskii G.A., G.D. Shandybina, D.S. Smirnov, S.V. Zabotnov, L.A. Golovan, V. Yu., Timoshenko, P.K. Kashkarov: Ultrashort excitations of surface polaritons and waveguide modes in semiconductors, Optic. Spectr. **105**, 67 (2008)

Masai S. K. Hirata, T. Sakka, Y. H. Ogata: Laser ablation of Ag in water and in nitrogen gas atmosphere: Shift and broadening of emission line profile of ablated Ag atoms, J. Phys: Conf. Ser. **59**, 198 (2007)
Massoud H.Z., J.D. Plummer: Analytical relationship for the oxidation of Silicon in Dry Oxygen in the Thin-Filme Regime, J. Appl. Phys. **62**, 3416 (1987)
Matsumoto N., H. Shima, T. Fujii, F. Kannari: Organic electroluminescence cells based on thin films deposited by UV laser ablation, Appl. Phys. Lett. **71**, 2469 (1997)
Matsumoto S., S. Yoshioka, J. Wada, S. Inui, K. Uwasawa: Boron Doping of Silicon by ArF excimer laser irradiation in B_2H_6, J. Appl. Phys. **67**, 7204 (1990)
Matsuoka Y.: Processing quartz glass by using the second harmonic of picosecond pulse Nd:YVO_4 laser, Appl. Phys. A **89**, 457 (2007)
Matz R., H. Weber, G. Weimann: Laser-induced dry etching of integrated InP microlenses, Appl. Phys. A **65**, 349 (1997)
Mauclair C., A. Mermillod-Blondin, N. Huot, E. Audouard, R. Stoian: Ultrafast laser writing of homogeneous longitudinal waveguides in glasses using dynamic wavefront correction, Opt. Exp. **16**, 5481 (2008)
Maxwell J.L., M.R. Black, C.A. Chavez, K. R. Maskaly, M. Espinosa, M. Boman, L. Landstrom: Growth of normally-immiscible materials (NIMs), binary alloys, and metallic fibers by hyperbaric laser chemical vapor deposition, Appl. Phys. A **91**, 507 (2008)
Maxwell J.L., C.A. Chavez, R. W. Springer, K. R. Maskaly, D. Goodin: Preparation of superhard B_xC_y fibers by microvortex-flow hyperbaric laser chemical vapor deposition, Diamo. Rel. Mater. **16**, 1557 (2007)
Maxwell J.L., M. Boman, R.W. Springer, J. Narayan, S. Gnanavelu: Hyperbaric laser chemical vapor deposition of carbon fibers from the 1-alkenes, 1-alkynes, and benzene, J. Am. Chem. Soc. **128**, 4405 (2006)
Maxwell J.L., M. Boman, R.W. Springer, A. Nobile, K. DeFriend, L. Espada, M. Sandstrom, D. Kommireddy, J. Pegna, D. Goodin: Process-structure map for diamond-like carbon fibers from ethene at hyperbaric pressures, Adv. Funct. Mater. **15**, 1077 (2005)
Maxwell J.L., J. Pegna, D.A. Deangelis, D.V. Messia: Three-dimensional laser chemical vapor deposition of nickel-ion alloys, Mat. Res. Soc. Symp. Proc. Vol. **397**, 601 (1996)
McCaulley J.A., V.R. McCrary, V.M. Donnelly: Laser-induced Decomposition of Triethyl-gallium and Trimethylgallium Adsorbed on GaAs(100), J. Phys. Chem. **93**, 1148 (1989)
McClelland J.J., R. Gupta, R.J. Celotta, G.A. Porkolab: Nanostructure fabrication by reactive-ion etching of laser-focused chromium on silicon, Appl. Phys. B **66**, 95 (1998)
McClelland J.J., R. Gupta, Z.J. Jabbour, R.J. Celotta: Laser focusing of atoms for nanostructure fabrication, Aust. J. Phys. **49**, 555 (1996)
McFeely F.R., J.F. Morar, F.J. Himpsel: Soft X-Ray photoemission study of the Silicon-fluorine etching reaction, Surf. Sci. **165**, 277 (1986)
McKittrick J., G.A. Hirata, C.F. Bacalski, R.Sze, J. Mourant, K.M. Hubbard, S. Pattilo, K.V. Salazar, M. Trkula, T.R. Gosnell: Enhanced photoluminescent emission of thin phosphor films via pulsed excimer laser melting, J. Mater. Res. **13**, 3019 (1998)
McLeod E., C.B. Arnold: Array-based optical nanolitography using optically trapped microlenses, Optics Express **17**, 3640 (2009)
McLeod E., C.B. Arnold: Subwavelength direct-write nanopatterning using optically trapped microspheres, Nature **3**, 413 (2008)
Mechler Á., P. Heszler, Z. Kántor, T. Szörényi, Z. Bor: Diamond-like carbon layer formation on graphite by excimer laser irradiation, Appl. Phys. A **66**, 659 (1998)
Meguro T., T. Suzuki, K. Ozaki, Y. Okano, A. Hirata, Y. Yamamoto, S. Iwai, Y. Aoyagi, S. Namba: Surface processes in Laser-atomic layer epitaxy (Laser-ALE) of GaAs, J. Cryst. Growth **93**, 190 (1988)
Meier-Ruge W., W. Bielser, E. Remy, F. Hillenkamp, R. Nitsche, R. Unsöld: The laser in the Lowry technique for microdissection of freeze-dried tissue slices, Histochem. J. **8**, 387 (1976)
Melcher R.L.: Thermal and Acoustic Techniques for Monitoring Pulsed Laser Processing, in *Laser Processing and Diagnostics*, ed. by D. Bäuerle, Ser. Chem. Phys., Vol. 39 (Springer, Berlin, Heidelberg 1984) p. 418

Mermillod-Blondin A., J. Bonse, A. Rosenfeld, I.V. Hertel, Y.P. Meshcheryakov, N.M. Bulgakova, E. Audouard, R. Stoian: Dynamics of fs laser induced voidlike structures in fused silica, Appl. Phys. Lett. **94**, 041911 (2009)

Mermillod-Blondin A., C. Mauclair, A. Rosenfeld, J. Bonse, I.V. Hertel, E. Audouard, R. Stoian: Size correction in ultrafast laser processing of fused silica by temporal pulse shaping, Appl. Phys. Lett. **93**, 021921 (2008*a*)

Mermillod-Blondin A., I.M. Burakov, Y.P. Meshcheryakov, N.M. Bulgakova, E. Audouard, A. Rosenfeld, A. Husakou, I.V. Hertel, R. Stoian: Flipping the sign of refractive index changes in ultrafast and temporally shaped laser-irradiated borosilicate crown optical glass at high repetition rates, Phys. Rev. B **77**, 104205 (2008b)

Metzger D., K. Hesch, P. Hess: Process Characterization and Mechanism for Laser-induced Chemical Vapor Deposition of a-Si:H from SiH_4, Appl. Phys. A **45**, 345 (1988)

Meunier M., J.-S. Bernier, J.-P. Sylvestre, A.V. Kabashin: Modeling the influence of the porosity of laser-ablated silicon films on their photoluminescence properties, Appl. Surf. Sci. **254**, 2771 (2008)

Meunier M., J.H. Flint, J.S. Haggerty, D. Adler: LCVD of Hydrogenated Amorphous Silicon. I. Gas-Phase Process Model, J. Appl. Phys. **62**, 2812 (1987a)

Meunier M., J.H. Flint, J.S. Haggerty, D. Adler: LCVD of Hydrogenated Amorphous Silicon. II. Film Properties, J. Appl. Phys. **62**, 2822 (1987b)

Mhin S.W., J.H. Ryu, K.M. Kim, G.S. Park, H.W. Ryu, K.B. Shim, T. Sasaki, N. Koshizaki: Simple synthetic route for hydroxyapatite colloidal nanoparticles via a Nd:YAG laser ablation in liquid medium, Appl. Phys. A **96**, 435 (2009)

Migoni R., H. Bilz, D. Bäuerle: Origin of Raman Scattering and Ferroelectricity in Oxidic Perovskites, Phys. Rev. Lett. **37**, 1155 (1976)

Mihailescu I.N., V.S. Teodorescu, E. Gyorgy, A. Luches, A. Perrone, M. Martino: About the nature of particulates covering the surface of thin films obtained by reactive PLD, J. Phys. D: Appl. Phys. **31**, 2236 (1998)

Mikulikova R., S. Moritz, T. Gumpenberger, M. Olbrich, C. Romanin, L. Bacakova, V. Svorcik, J. Heitz: Cell microarrays on photochemically modified polytetrafluoroethylene, Biomaterials **26**, 5572 (2005)

Miller J.C., R.F. Haglund eds.: *Laser Ablation and Desorption. Vol 30: Experimental Methods in the Physical Science.* (Academic Press, London 1998)

Minet O., K. Dörschel, G. Müller: Lasers in biology and medicine, in Landolt-Börnstein – Numerical Data and Functional Relationships in Science and Technology, New Series, Group VIII/1C (Group VIII: Advanced Materials and Technologies, Vol. 1 Laser Physics and Applications, Subvolume C: Laser Applications, edited by R. Poprawe, H. Weber, G. Herziger (Springer Berlin, Heidelberg, New York 2004), p. 279

Mingareev I., A. Horn: Time-resolved investigations of plasma and melt ejections in metals by pump-probe shadowgraphy, Appl. Phys. A **92**, 917 (2008)

Misra N., C.P. Grigoropoulos, D.P. Stumbo, J.N. Miller: Laser activation of dopants for nanowire devices on glass and plastic, Appl. Phys. Lett. **93**, 121116 (2008)

Mitzner R., A. Rosenfeld, R. König: Time-resolved absorption studies of excimer laser ablation of CaF_2, Appl. Surf. Sci. **69**, 180 (1993)

Miura M., M. Yoshizumi, T. Izumi, Y. Shiohara: Increase of the production rate and crystal growth mode of $GdBa_2Cu_3O_y$-coated conductors using an in-plume growth technique for a reel-to-reel pulsed-laser deposition system, Supercond. Sci. Technol. **23**, 014019 (2010)

Miyaji G., K. Miyazaki: Nanoscale ablation on patterned diamondlike carbon film with femtosecond laser pulses, Appl. Phys. Lett. **91**, 123102 (2007)

Mizeikis V., S. Matsuo, S. Juodkazis, H. Misawa: Femtosecond laser microfabrication of photonic crystals, in *3D Laser Microfabriation. Principles and Applications*, ed. by H. Misawa, S. Juodkazis (Wiley-VCH, Weinheim, 2006) p. 239

Miziolek A.W., V. Palleschi, I. Schechter (eds.): *Laser-induced breakdown spectroscopy (LIBS)* – Fundamentals and Applications (Cambridge University Press 2006)

Mönch W.: On the Oxidation of III-V Compound Semiconductors, Surf. Sci. **168**, 577 (1986)

Moening J.P., S.S. Thanawala, D.G. Georgiev: Formation of high-aspect-ratio protrusions on gold films by localized pulsed laser irradiation, Appl. Phys. A **95**, 635 (2009)

Mogyorosi P., K. Piglmayer, D. Bäuerle: Ar^+ Laser-induced chemical etching of Molybdenum in Chlorine atmosphere, Surf. Sci. **208**, 232 (1989a)

Mogyorosi P., T. Szörenyi, K. Bali, Z. Toth, I. Hevesi: Pulsed laser ablative deposition of Thin Metal Films, Appl. Surf. Sci. **36**, 157 (1989b)

Mogyorosi P., K. Piglmayer, R. Kullmer, D. Bäuerle: Laser-induced chemical etching of Silicon in chlorine atmosphere: II. Continuous irradiation, Appl. Phys. A **45**, 293 (1988)

Monreal R., S.P. Apell: Electromagnetic-field-enhanced desorption of atoms, Phys. Rev. B **41**, 7852 (1990)

Montenegro M.J., T. Lippert: Films for electrochemical applications, in *Pulsed Laser Deposition of Thin Films: Applications-Led Growth of Functional Materials*, ed. R. Eason (Wiley 2007) p. 563

Morarescu R., D. Blázquez Sánchez, N. Borg, T.A. Vartanyan, F. Träger, F. Hubenthal: Shape tailoring of hexagonally ordered triangular gold nanoparticles with nanosecond-pulsed laser light, Appl. Surf. Sci. **255**, 9822 (2009)

Morrison S.R.: *The Chemical Physics of Surfaces* (Plenum Press, New York 1977)

Mosbacher M., H.-J. Münzer, M. Bertsch, V. Dobler, N. Chaoui, J. Siegel, R. Oltra, D. Bäuerle, J. Boneberg, P. Leiderer: Laser assisted particle removal from Silicon wafers, in Particles on surfaces 7: detection, adhesion and removal: K.L. Mittal (ed.), VSP Utrecht, 2002, p. 291 (ISBN 978 9067 64372 6)

Mott N.F., E.A. Davis: *Electronic Processes in Non-Crystalline Materials*, 2nd ed. (Clarendon Press, Oxford 1979)

Müllenborn M., H. Dirac, J.W. Petersen, S. Bouwstra: Fast 3-D laser micro-machining of silicon for microsystems, Sensors and Actuators A **52**, 121 (1996a)

Müllenborn, M., Heschel, M., Larsen, U.D., Dirac, H., Bouwstra, S.: Laser direct etching of silicon on oxide for rapid prototyping, J. Micromech. Microeng. **6**, 49 (1996b)

Müllenborn, M., Birkelund, K., Grey, F., Madsen, S.: Laser direct writing of oxide structures on hydrogen-passivated silicon surfaces, Appl. Phys. Lett. **69**, 1 (1996c)

Müllenborn M., H. Dirac, J.W. Petersen: Three-dimensional nanostructures by direct laser etching of Si, Appl. Surf. Sci. **86**, 568 (1995)

Müller F., K. Mann, P. Simon, J.S. Bernstein, G.J. Zaal: A Comparative study of deposition of Thin Film by laser induced PVD with Femtosecond and Nanosecond laser pulses, SPIE Proc. **1858**, 464 (1993)

Münzer H.-J., M. Mosbacher, M. Bertsch, O. Dubbers, F. Burmeister, A. Pack, R. Wannemacher, B.-U. Runge, D. Bäuerle, J. Boneberg, P. Leiderer: Optical near field effects in surface nanostructuring and laser cleaning, Proc. SPIE **4426**, 180 (2002)

Mukherjee P., S. Chen, J.B. Cuff, P. Sakthivel, S. Witanachchi: Evidence for the physical basis and universality of the elimination of particulates using dual-laser ablation. I. Dynamic time-resolved target melt studies, and film growth of Y_2O_3 and ZnO, J. Appl. Phys. **91**, 1828 (2002)

Muller D.A., N. Nakagawa, A. Ohtomo, J.L. Grazul, H.Y. Hwang: Atomic-scale imaging of nano-engineered oxygen vacany profiles in $SrTiO_3$, Nature **430**, 657 (2004)

Murahara M., K. Toyoda: Excimer laser-induced photochemical modification and adhesion improvement of a fluororesin surface, J. Adhesion Sci. Technol. **9**, 1601 (1995)

Murahara M., K. Toyoda: Linear-Focused ArF Excimer Laser Beam for Depositing Hydrogenated Silicon Films, in *Laser Processing and Diagnostics*, ed. by D. Bäuerle, Springer Ser. Chem. Phys., Vol. 39 (Springer, Berlin, Heidelberg 1984) p. 252

Murakami K.: Dynamics of Laser Ablation of High T_c Superconductors and Semiconductors, and a new Method for Growth of Films, in Laser Ablation of Electronic Materials, Basic Mechanisms and Applications, ed. by E. Fogarassy and S. Lazare (Elsevier, Amsterdam 1992) p. 125

Muramoto J., Y. Nakata, T. Okada, M. Maeda: Influences of preparation conditions on laser-ablated Si nano-particle formation processes observed by imaging laser spectroscopy, Appl. Surf. Sci. **127–129**, 373 (1998)

Murphy D.V., S.R.J. Brueck: Optical Microanalysis of small semiconductor structures, in *Laser Diagnostics and Photochemical Processing for Semiconductor Devices*, ed. by R.M. Osgood, S.R.J. Brueck, H.R. Schlossberg, MRS Proc. **17**, 81 (1983)

Murphy-DuBay N., L. Wang, X. Xu: Nanolithography using high transmission nanoscale ridge aperture probe, Appl. Phys. A **93**, 881 (2008)

Nagel M., R. Fardel, P. Feurer, M. Häberli, F.A . Nüesch, T. Lippert, A. Wokaun: Aryltriazene photopolymer thin films as sacrificial release layers for laser-assisted forward transfer systems: study of photoablative decomposition and transfer behavior, Appl. Phys. A **92**, 781 (2008)

Nakajima K., M. Furusawa, T. Yamamoto, J. Tashiro, A. Sasaki, T. Chikyow, P. Ahmet, H. Yamada, M. Yoshimoto: Pulsed laser ablation of graphite in O_2 atmosphere for preparation of diamond films and carbon nanotubes, Diam. Rel. Mater. **11**, 953 (2002)

Nakajima T., T. Tsuchiya, T. Kumagai: Crystal growth of phosphor perovskite titanate thin films under excimer laser irradiation, Appl. Phys. A **93**, 51 (2008)

Nakamura D., K. Tamaru, T. Akiyama, A. Takahashi, T. Okada: Investigation of debris dynamics from laser-produced tin plasma for EUV lithography light source, Appl. Phys. A **92**, 767 (2008)

Nakamura S., K. Midorikawa, H. Kumagai, M. Obara, K. Toyoda: Effect of pulse duration on ablation characteristics of tetrafluoroethylene-hexafluoropropylene copolymer film using Ti: Sapphire laser, Jpn. J. Appl. Phys. **35**, 101(1996)

Nakashima S., K. Sugioka, K. Midorikawa: Fabrication of microchannels in single-crystal GaN by wet-chemical-assisted fs-laser ablation, Appl. Surf. Sci. **255**, 9770 (2009)

Nakashima S., K. Fujita, A. Nakao, K. Tanaka, Y. Shimotsuma, K. Muira, K. Hirao: Enhanced magnetization and ferrimagnetic behavior of normal spinel $ZnFe_2O_4$ thin film irradiated with femtosecond laser, Appl. Phys. A **94**, 83 (2009)

Nakata Y., N. Miyanaga: Effect of interference pattern on fs laser-induced ripple structure, Appl. Phys. A **98**, 401 (2010)

Nanai L., R. Vajtai, I. Hevesi, D.A. Jelski, T.F. George: Metal Oxide layer growth under laser irradiation, Thin. Sol. Film. **227**, 13 (1993)

Narayan R.J.: Diamond-like carbon: Medical and mechanical applications, in *Pulsed Laser Deposition of Thin Films: Applications-Led Growth of Functional Materials*, ed. R. Eason (Wiley 2007) p. 333

Nassuphis N., R.H. Mathews, S.T. Palmacci, D.J. Ehrlich: Three-dimensional laser direct writing: Applications to multichip modules, J. Vac. Sci. Technol. B **12**, 3294 (1994)

Nebel C.E., S. Christiansen, H.P. Strunk, B. Dahlheimer, U. Karrer, M. Stutzmann: Laser-interference crystallization of amorphous silicon: Applications and properties, phys. stat. sol. (a) **166**, 667 (1998)

Nelea V., I.N. Mihailescu, M. Jelinek: Biomaterials: New issues and breakthroughs for biomedical applications, in *Pulsed Laser Deposition of Thin Films: Applications-Led Growth of Functional Materials*, ed. R. Eason (Wiley 2007) p. 421

Nemes P., A.A. Barton, A. Vertes: 3D imaging of metabolites in tissues under ambient conditions by laser ablation electrospray ionization mass spectrometry, Anal. Chem. **81**, 6668 (2009)

Neves P., M. Arronte, R. Vilar, A.M. Botelho do Rego: KrF excimer laser dry and steam cleaning of silicon surfaces with metallic particulate contaminants, Appl. Phys. A **74**, 191 (2002)

Ng G.K.L., A.E.W. Jarfors, G. Bi, H.Y. Zheng: Porosity formation and gas bubble retention in laser metal deposition, Appl. Phys. A **97**, 641 (2009)

Nguyen V.T. and SOI Group: Laser Processing in Silicon on Insulator (SOI) Technologies, in Laser Processing and Diagnostics, ed. D. Bäuerle, Springer Ser. Chem. Phys., 39 (Springer, Berlin, Heidelberg 1984) p. 73

Nicolis G., I. Prigogine: *Self-Organization in Non-Equilibrium Systems* (Wiley, New York 1977)

Niemz M.H.: *Laser-Tissue Interactions – Fundamentals and Applications*, Biological and Medical Physics Series (3rd ed. Springer 2004)

Niino H., Y. Kawaguchi, T. Sato, A. Narazaki, T. Gumpenberger, R. Kurosaki: Laser-induced backside wet etching of silica glass with ns-pulsed DPSS UV laser at the repetition rate of 40 kHz, J. Phys. Conf. Ser. **59**, 539 (2007)

Niino H., A. Yabe: Surface modification of fluorocarbon polymer using phenylhydrazine photolyzed by KrF excimer laser irradiation, J. Photopolym. Sci. Technol. **11**, 357 (1998)
Niino H., H. Okano, K. Inui, A. Yabe: Surface modification of poly(tetrafluoroethylene) by excimer laser processing: enhancement of adhesion, Appl. Surf. Sci. **109–110**, 259 (1997)
Niino H., A. Yabe: Surface chemical reaction of polymer film with reactive intermediates produced by laser ablation of azido compound, Appl. Surf. Sci. **96–98**, 572 (1996a)
Niino H., A. Yabe: Chemical surface modification of fluorocarbon polymers by excimer laser processing, Appl. Surf. Sci. **96–98**, 550 (1996b)
Niino H., A. Yabe: Surface modification and metallization of Fluoro-carbon polymers by excimer laser processing, Appl. Phys. Lett. **63**, 3527 (1993a)
Niino H., A. Yabe: Excimer laser polymer ablation: Formation of positively charged surfaces and its application into the metallization of polymer films, Appl. Surf. Sci. **69**, 1 (1993b)
Nishio S., T. Chiba, A. Matsuzaki, H. Sato, H.: Control of structures of deposited polymer films by ablation laser wavelength: Polyacrylonitrile at 308, 248, and 193 nm, J. Appl. Phys. Lett. **79**, 7198 (1996)
Noack J., D.X. Hammer, G.D. Noojin, B.A. Rockwell, A. Vogel: Influence of pulse duration on mechanical effects after laser-induced breakdown in water, J. Appl. Phys. **83**, 7488 (1998)
Noël S., J. Hermann, T. Itina: Investigation of nanoparticle generation during fs laser ablation of metals, Appl. Surf. Sci. **253**, 6310 (2007)
Nolte S., M. Will, J. Burghoff, A. Tuennermann: Femtosecond waveguide writing: a new avenue to 3-dimensional integrated optics, Appl. Phys. A **77**, 109 (2003)
Nolte S., B.N. Chichkov, H. Welling, Y. Shani, K. Lieberman, H. Terkel: Nanostructuring with spatially localized femtosecond laser pulses, Optics Lett. **24**, 914 (1999a)
Nolte S., C. Momma, G. Kamlage, A. Ostendorf, C. Fallnich, F.von Alvensleben, H. Welling: Polarization effects in ultrashort-pulse laser drilling, Appl. Phys. A **68**, 563 (1999b)
Nolte S., C. Momma, B.N. Chichkov, B. Welling: Mikrostrukturierung mit ultrakurzen Laserpulsen, Physikalische Blätter **55** (6), 41 (1999c)
Nolte S., C. Momma, H. Jacobs, A. Tünnermann, B.N. Chichkov, B. Wellegehausen, H. Welling: Ablation of metals by utralshort laser pulses, J. Opt. Soc. Am. B **14**, 2716 (1997)
Northrop D.A.: Vaporization of lead Zirconate-lead titanate materials: II, Hot-pressed compositions at near theoretical density, J. Am. Ceram. Soc. **51**, 357 (1968)
Norton M.G., W. Jiang, J.T. Dickinson, K.W. Hipps: Pulsed laser ablation and deposition of fluorocarbon polymers, Appl. Surf. Sci. **96–98**, 617 (1996)
Nowak R., S. Metev: Thermochemical laser etching of stainless steel and titanium in liquids, Appl. Phys. A **63**, 133 (1996)
Obata K., K. Sugioka, N. Shimazawa, K. Midorikawa: Fabrication of microchip based on UV transparent polymer for DNA electrophoresis by F_2 laser ablation, Appl. Phys. A **84**, 251 (2006)
Obata K., K. Sugioka, T. Akane, K. Midorikawa, N. Aoki, K. Toyoda: Efficient refractive-index modification of fused silica by a resonance-photoionization-like process using F_2 and KrF excimer lasers, Opt. Lett. **27**, 330 (2002)
Obata K., K. Sugioka, T. Akane, N. Aoki, K. Toyoda, K. Midorikawa: Influence of laser fluence and irradiation timing of F_2 laser on ablation properties of fused silica in F_2 – KrF excimer laser multi-wavelength excitation process, Appl. Phys. A **73**, 755 (2001)
Oesterlin P., A. Koch: Small structures with large excimer lasers, Chapter 9 in *Excimer Laser Technology*, D. Basting, G. Marowsky eds.: (Springer-Verlag, Berlin 2005) p. 127
Oguz S., W. Paul, T.F. Deutsch, B.Y. Tsaur, D.V. Murphy: Synthesis of metastable, Semiconducting Ge-Sn alloys by pulsed UV-laser crystallization, Appl. Phys. Lett. **43**, 848 (1983)
Ohfuji T., T. Ogawa, K. Kuhara, M. Sasago: Prospect and challenges of ArF excimer laser lithography processes and materials, J. Vac. Sci. Technol. B **14**, 4203 (1996)
Ohkubo T., M. Kuwata, B. Luk'yanchuk, T. Yabe: Numerical analysis of nanocluster formation within ns-laser ablation plume, Appl. Phys. A **77**, 271 (2003)
Ohtsuka S., K. Tsunemoto, T. Koyama, S. Tanaka: Ultrafast nonlinear optical effect in CdTE-doped glasses fabricated by the laser evaporiation method, Opt. Mater. **2**, 209 (1993)
Okoshi M., J. Li, P.R. Herman, N. Inoue: Photochemical welding of silica optical components to silicone rubber by F_2 laser, J. Phys. Conf. Ser. **59**, 712 (2007)

Olbrich M., E. Rebollar, J. Heitz, I. Frischauf, C. Romanin: Electroporation chip for adherent cells on photochemically modified polymer surfaces, Appl. Phys. Lett. **92**, 013901 (2008)
Oliveira V., R. Vilar: KrF pulsed laser ablation of polyimide, Appl. Phys. A **92**, 957 (2008)
O'Mahony D., J.G. Lunney: Group III nitride growth, in *Pulsed Laser Deposition of Thin Films: Applications-Led Growth of Functional Materials*, ed. R. Eason (Wiley 2007) p. 291
Orlowski T.E., D. A. Mantell: Aluminum deposition by UV laser photofragmentation of trimethylaluminum on Al:Identification of Photoproducts and Desorption Dynamics, J. Vac. Sci. Technol. A **7**, 2598 (1989)
Orlowski T.E., D.A. Mantell: Ultraviolet laser-induced oxidation of Silicon: The effect of Oxygen photodissociation upon Oxide growth kinetics, J. Appl. Phys. **64**, 4410 (1988)
Osellame R., M. Lobino, N. Chiodo, M. Marangoni, G. Cerullo, R. Ramponi, H.T. Bookey, R.R. Thomson, N.D. Psaila, A.K. Kar: Femtosecond laser writing of waveguides in periodically poled lithium niobate preserving the nonlinear coefficient, Appl. Phys. Lett. **90**, 241107 (2007)
Ossi P.M., C.E. Bottani, A. Miotello: Pulsed-laser deposition of carbon: from DLC to cluster-assembled films, Thin Solid Films **482**, 2 (2005)
Ostendorf A., F. Korte, G. Kamlage, U. Klug, J. Koch, J. Serbin, N. Baersch, T. Bauer, B.N. Chichkov: Applications of fs lasers in 3D machining, in *3D Laser Microfabriation. Principles and Applications*, ed. by H. Misawa, S. Juodkazis (Wiley-VCH, Weinheim, 2006) p. 341
Ostermayer F.W., P.A. Kohl, R.M. Lum: Hole transport equation analysis of photo-electrochemical resolution, J. Appl. Phys. **58**, 4390 (1985)
Ostermayer F.W., P.A. Kohl: Photoelectrochemical etching of p-GaAs, Appl. Phys. Lett. **39**, 76 (1981)
Otis C.E., P.M. Goodwin: Internal energy distributions of laser ablated species from $YBa_2Cu_3O_{7-d}$, J. Appl. Phys. **73**, 1957 (1993)
Otto J., R. Stumpe, D. Bäuerle: Laser induced reduction and etching of Oxidic perovskites, in *Laser Processing and Diagnostics*, ed. D. Bäuerle, Springer Ser. Chem. Phys., 39 (Springer, Berlin, Heidelberg 1984) p. 320
Oujja M., S. Pérez, E. Fadeeva, J. Koch, B.N. Chichkov, M. Castillejo: 3D microstructuring of biopolymers by fs laser irradiation, Appl. Phys. Lett. **95**, 263703 (2009)
Ovsianikov A., S. Passinger, R. Houbertz, B.N. Chichkov: 3D material processing with fs lasers, Chapter 6 in *Laser Ablation and its Applications*, ed. by C. R. Phipps (Springer 2007) p. 121
Pan H., D.J. Hwang, S.H. Ko, T.A. Clem, J.M. Fréchet, D. Bäuerle C.P. Grigoropoulos: High-throughput near-field optical nanoprocessing of solution-deposited nanoparticles, Small **6**, 1812 (2010)
Pan H., N. Misra, S. H. Ko, C.P. Grigoropoulos, N. Miller, E.E. Haller, O. Dubon: Melt-mediated coalescence of solution-deposited ZnO nanoparticles by excimer laser annealing for thin-film transistor fabrication, Appl. Phys. A **94**, 111 (2009)
Pang B.S.H., R.I. Tomov, M.G. Blamire: $La_xA_{1-x}MnO_3$ (A = Sr,Ca)/$YBa_2Cu_3O_{7-\delta}$ superlattices deposited by the "eclipse" pulsed laser deposition technique, Supercond. Sci. Technol. **17**, 624 (2004)
Park H.K., X. Zhang, C.P. Grigoropoulos, C.C. Poon, A.C. Tam: Transient temperature during the vaporization of liquid on a pulsed laser-heated solid surface, J. Heat. Tran. **118**, 702 (1996a)
Park H.K., D. Kim, C. P. Grigoropoulos, A.C. Tam: Pressure generation and measurement in the rapid vaporization of water on a pulsed-laser-heated surface, J. Appl. Phys. **80**, 4072 (1996b)
Park H.S., S.H. Nam, S.M. Park: Time-resolved optical emission studies on the laser ablation of a graphite target: The effects of ambient gases, J. Appl. Phys. **97**, 113103 (2005)
Pászti Z., Z.E. Horváth, G. Peto, A. Karacs, L. Guczi: Pressure dependent formation of small Cu and Ag particles during laser ablation, Appl. Surf. Sci. **109–110**, 67 (1997)
Paterson L., B. Agate, M. Comrie, R. Ferguson, T.K. Lake, J.E. Morris, A.E. Carruthers, C.T.A. Brown, W. Sibbett, P.E. Bryant, F. Gunn-Moore, A.C. Riches, K. Dholakia: Photoporation and cell transfection using a violet diode laser, Opt. Express **13**, 595 (2005)
Patrone L., D. Nelson, V.I. Safarov, M. Sentis, W. Marine, G. Giorgio: Photoluminescence of silicon nanoclusters with reduced size dispersion produced by laser ablation, J. Appl. Phys. **87**, 3829 (2000)

Paulsen-Boaz C., W.L. O'Brien, T. Rhodin: Pulsed Ultraviolet Laser Stimulated Chlorination Mechanisms for Si(111), J. Vac. Sci. Technol. B **10**, 216 (1992)

Pazionis G.D., H. Tang, I.P. Herman: Raman Microprobe Analysis of Temperature Profiles in cw Laser Heated Silicon Microstructures, IEEE J. Quantum Electronics **25**, 976 (1989)

Pechen E.V., A.V. Varlashkin, S.I. Krasnosvobodtsev, B. Brunner, K.F. Renk: PLD of Smooth High-T_c Superconducting Films using a Synchronous Velocity Filter, Appl. Phys. Lett. **66**, 2292 (1995)

Pedarnig J.D., K. Siraj, M.A. Bodea, I. Puica, W. Lang, R. Kolarova, P. Bauer, K. Haselgrübler, C. Hasenfuss, I. Beinik, C. Teichert: Surface planarization and masked ion-beam structuring of $YBa_2Cu_3O_7$ thin films, Thin Solid Films **518**, 7075 (2010)

Pedarnig J.D., S. Roither, M. Peruzzi: Growth and thermal stability of $GaPO_4$ epitaxial thin films, Appl. Phys. Lett. **89**, 241912 (2006)

Pedarnig J.D., M. Peruzzi, H. Salhofer, R. Schwödiauer, W. Reichl, J. Runck: F_2-laser patterning of $GaPO_4$ resonators for humidity sensing, Appl. Phys. A **80**, 1401 (2005a)

Pedarnig J.D., M. Peruzzi, I. Vrejoiu, D.G. Matei, M. Dinescu, D. Bäuerle: Pulsed-laser deposition of inclined ZnO, of $GaPO_4$ and of novel composite thin films, Appl. Phys. A **81**, 339 (2005b)

Pedarnig J.D., R. Rössler, M.P. Delamare, W. Lang, D. Bäuerle, A. Köhler, H.W. Zandbergen: Electrical properties, texture and microstructure of vicinal $YBa_2Cu_3O_{7-\delta}$ thin films, Appl. Phys. Lett. **81**, 2587 (2002)

Pedarnig J.D., H. Göttlich, R. Rössler, W.M. Heckl, D. Bäuerle: Patterning of $YBa_2Cu_3O_{7-\delta}$ films using a near-field optical configuration, Appl. Phys. A **67**, 403 (1998)

Pedraza A.J., J.D. Fowlkes, D.H. Lowndes: Silicon microcolumn arrays grown by ns pulsed-excimer laser irradiation, Appl. Phys. Lett. **74**, 2322 (1999)

Perea A., J. Gonzalo, C. Budtz-Jorgensen, G. Epurescu, J. Siegel, C.N. Afonso, J. Garcia-Lopez: Quantification of self-sputtering and implantation during pulsed laser deposition of gold, J. Appl. Phys. **104**, 084912 (2008)

Pereira A., A. Cros, P. Delaporte, S. Georgiou, A. Manousaki, W. Marine, M. Sentis: Surface nanostructuring of metals by laser irradiation: effects of pulse duration, wavelength and gas atmosphere, Appl. Phys. A **79**, 1433 (2004)

Perkins G.G.A., E.R. Austin, F.W. Lampe: The 147-nm Photolysis of Monosilane, J. Am. Chem. Soc. **101**, 1109 (1979)

Perkins J.D., C.S. Bahn, P.A. Parilla, J. McGraw, M. Fu, M. Duncan, H. Yu, D.S. Ginley: $LiCoO_2$ and $LiCo_{1-x}Al_xO_2$ thin film cathodes grown by pulsed laser ablation, J. Pow. Sour. **81–82**, 675 (1999)

Perry M.D., B.C. Stuart, P.S. Banks, M.D. Feit, V. Yanovsky, A.M. Rubenchik: Ultrashort-pulse laser machining of dielectric materials, J. Appl. Phys. **85**, 6803 (1999)

Peruzzi M., J.D. Pedarnig, H. Sturm, N. Huber, D. Bäuerle: F_2-laser ablation and micro-patterning of $GaPO_4$, Europhys. Lett. **65**, 652 (2004)

Petkovšek R., A. Babnik, J. Diaci, J. Možina: Optodynamik monitoring of laser micro-drilling of glass by using a laser probe, Appl. Phys. A **93**, 141 (2008)

Pettit G.H., R. Sauerbrey: Pulsed UV Laser Ablation, Appl. Phys. A **56**, 51 (1993)

Petzoldt F., K. Piglmayer, W. Kräuter, D. Bäuerle: Lateral Growth Rates in Laser CVD of Microstructures, Appl. Phys. A **35**, 155 (1984)

Pfleging W., M. Torge, M. Bruns, V. Trouillet, A. Welle, S. Wilson: Laser- and UV-assisted modification of polystyrene surfaces for control of protein adsorption and cell adhesion, Appl. Surf. Sci. **255**, 5453 (2009)

Pfleging W., M. Bruns, A. Welle, S. Wilson: Laser-assisted modification of polystyrene surfaces for cell culture applications, Appl. Surf. Sci. **253**, 9177 (2007)

Pfleging W., S. Finke, E. Gaganidze, K. Litfin, L. Steinbock, R. Heidinger: Laser-assisted fabrication of monomode polymer waveguides and their optical characterization, Mat.-wiss. u. Werkstofftech. **34**, 904 (2003a)

Pfleging W., T. Hanemann, M. Torge, W. Bernauer: Rapid fabrication and replication of metal, ceramic and plastic mould inserts for application in microsystem technologies, Proc. Instn. Mech. Engrs. Vol. **217** Part C: J. Mechanical Engineering Science (2003b), Special issue

Pfleging W., A. Ludwig, K. Seemann, R. Preu, H. Mäckel, S.W. Glunz: Laser micromachining for applications in thin films technology, Appl. Surf. Sci. **154-155**, 633 (2000)
Pflügl W., U.M. Titulaer: The Size Distribution of Liquid Droplets during their Growth from a Vapor, Physica A **198**, 410 (1993)
Phillips H.M., D. Sarkar, N.J. Halas, R.H. Hauge, R. Sauerbrey: Excimer-Laser-induced Electric Conductivity in Thin-Film C_{60}, Appl. Phys. A **57**, 105 (1993a)
Phillips H.M., S. Wahl, R. Sauerbrey: Submicron electrically conducting wires produced in polyimide by ultraviolet laser irradiation, Appl. Phys. Lett. **62**, 2572 (1993b)
Picraux S.T., D.M. Follstaedt: Surface modification and alloying: Aluminium, in surface modification and alloying by laser, Ion, and Electron Beams, ed. by J.M. Poate, G. Foti, D.C. Jacobson (Plenum, New York 1983) p. 287
Piglmayer K., E. Arenholz, C. Ortwein, N. Arnold, D. Bäuerle: Single-pulse ultraviolet laser-induced surface modification and ablation of polyimide, Appl. Phys. Lett. **73**, 847 (1998)
Piglmayer K., D. Bäuerle: 1994, unpublished
Piglmayer K., D. Bäuerle: On the reaction Kinetics in Laser-induced photochemical Gas-Phase processing, Appl. Phys. B **48**, 453 (1989)
Piglmayer K., D. Bäuerle: Temperature Distributions in Pyrolytic Laser-induced Chemical Processing, in Laser Processing and Diagnostics II, ed. by D. Bäuerle, K.L. Kompa, L.D. Laude (Les Editions de Physique, Les Ulis 1986) p. 79
Piglmayer K., J. Doppelbauer, D. Bäuerle: Temperature Distributions in CW-Laser Pyrolysis, in laser controlled chemical processing of surfaces, ed. by A.W. Johnson, D.J. Ehrlich, H.R. Schlossberg, Mat. Res. Soc. Symp. Proc. **29**, 47 (1984)
Pimenov S.M., V.V. Kononenko, V.G. Ralchenko, V.I. Konov, S. Gloor, W. Lüthy, H.P. Weber, A.V. Khomich: Laser polishing of diamond plates, Appl. Phys. A **69**, 81 (1999)
Piqué A.: Deposition of polymers and biomaterials using the matrix-assisted pulsed laser evaporation (MAPLE) process, in *Pulsed Laser Deposition of Thin Films: Applications-Led Growth of Functional Materials*, ed. R. Eason (Wiley 2007) p. 63
Pleasants S., D.M. Kane: Laser cleaning of alumina particles on glass and silica substrates – Experiment and quasistatic model, J. Appl. Phys. **93** (2003)
Plech A., P. Leiderer, J. Boneberg: Femtosecond laser near field ablation, Laser & Photon. Rev. **3**, No. 5, 435 (2009)
Podlesnik D.V., H.H. Gilgen, R.M. Osgood: Deep-UV induced Wet Etching of GaAs, Appl. Phys. Lett. **45**, 563 (1984)
Podlesnik D.V., H.H. Gilgen, R.M. Osgood, A. Sanchez: Maskless chemical etching of submicrometer gratings in single-crystalline GaAs, Appl. Phys. Lett. **43**, 1083 (1983)
Popp J., M. Strehle (eds.): *Biophotonics* (Wiley-VCH Weinheim 2006)
Possin G.E., H.G. Parks, S.W. Chiang, Y.S. Liu: The effects of selectively absorbing Dielectric layers and Beam shaping on recrystallization and FET Characteristics in laser recrystallized Silicon on Amorphous substrates, Mat. Res. Soc. Symp. Proc. **13**, 549 (1983)
Prasad M., P.F. Conforti, B.J. Garrison: Influence of photoexcitation pathways on the initiation of ablation in poly (methyl methacrylate), Appl. Phys. A **92**, 877 (2008)
Predtechensky M.R., A.P. Mayorov: Expansion of laser plasma in oxygen at laser deposition of HTSC films: theoretical model, Appl. Supercond. **1**, 2011 (1993)
Press W.H., S.A. Teukolsky, W.T. Vetterling, B.P. Flannery: *Numerical Recipes in FORTRAN – The Art of Scientific Computing* (Cambridge University Press 1992)
Preuss S., M. Späth, Y. Zhang, M. Stuke: Time resolved dynamics of subpico-second laser ablation, Appl. Phys. Lett. **62**, 3049 (1993)
Price S.J.W.: The Decomposition of Metal Alkyls, Aryls, Carbonyls and Nitrosyls, in *Decomposition of Inorganic and Organometallic Compounds*, ed. by C.H. Bamford and C.F.H. Tipper, Chemical Kinetics, 4 (Elsevier, Amsterdam 1972) p. 197
Prokhorov A.M., V.I. Konov, I. Ursu, I.N. Mihailescu: *Laser Heating of Metals* (Adam Hilger Series on Optics and Optoelectronics, New York 1990)

Pronko P.P., S.K. Dutta, J. Squier, J.V. Rudd, D. Du, G. Mourou: Machining of sub-micron holes using a femtosecond laser at 800 nm, Opt. Commun. **114**, 106 (1995)
Proyer S., E. Stangl, M. Borz, B. Hellebrand, D. Bäuerle: Particulates on pulsed-laser deposited Y-Ba-Cu-O films, Physica. C **257**, 1 (1996)
Proyer S., E. Stangl: Time-Integrated photography of laser-induced plasma plumes, Appl. Phys. A **60**, 573 (1995)
Proyer S., E. Stangl, P. Schwab, D. Bäuerle, P. Simon, C. Jordan: Patterning of YBCO films by Excimer-laser ablation, Appl. Phys. A **58**, 471 (1994)
Pryds N., J.Schou, S. Linderoth: Large-area production of yttria-stabilized zirconia by pulsed laser deposition, J. Phys. Conf. Ser. **59**, 140 (2007)
Puippe J.C., R.E. Acosta, R.J. von Gutfeld: Investigation of Laser-enhanced Electroplating mechanisms, J. Electrochem. Soc. **128**, 2539 (1981)
Puretzky A.A., D.J. Styers-Barnett, C.M. Rouleau, H. Hu, B. Zhao, I.N. Ivanov, D.B. Geogehan: Cumulative and continuous laser vaporization synthesis of single wall carbon nanotubes and nanohorns, Appl. Phys. A **93**, 849 (2008)
Puretzky A.A., D.B. Geohegan, X. Fan, S.J. Pennycook: Dynamics of single-wall carbon nanotube synthesis by laser vaporization, Appl. Phys. A **70**, 153 (2000)
Purice A., J. Schou, P. Kingshott, M. Dinescu: Production of active lysozyme films by matrix assisted pulsed laser evaporation at 355 nm, Chem. Phys. Lett. **435**, 350 (2007)
Pusel A., U. Wetterauer, P. Hess: Direkter Bruch der SiH-Oberflächenbindung mittels 157nm-Laserstrahlung (Direct breaking of SiH-surface bonds with 157 nm laser radiation). LaserOpto **31**(5), 48 (Oktober 1999)
Qin Z., T. He, Y. Zhang: Characteristics of the conductive polyimide film surfaces induced by UV laser beam, Appl. Phys. A **66**, 441 (1998)
Rahm A., M. Lorenz, T. Nobis, G. Zimmermann, M. Grundmann, B. Fuhrmann, F. Syrowatka: PLD and characterizaion of ZnO nanowires with regular lateral arrangement, Appl. Phys. A **88**, 31 (2007)
Raizer Y.P.: *Gas Discharge Physics* (Springer-Verlag Berlin, Heidelberg 1991)
Ramesh R., W.K. Chan, B. Wilkens, H. Gilchrist, T. Sands, J.M. Tarascon, V.G. Keramidas, D.K. Fork, J. Lee, A. Safari: Fatigue and retention in ferroelectric Y-Ba-Cu-O/Pb-Zr-Ti-O/Y-Ba-Cu-O heterostructures, Appl. Phys. Lett. **61**, 1537 (1992)
Ready J.F.: *Industrial Applications of Lasers* (2nd ed.) (Academic Press, London 1997)
Rebollar E., I. Frischauf, M. Olbrich, T. Peterbauer, S. Hering, J. Preiner, P. Hinterdorfer, C. Romanin, J. Heitz: Proliferation of aligned mammalian cells on laser-nanostructured polystyrene, Biomaterials **29**, 1796 (2008)
Rebollar E., M.M. Villavieja, S. Gaspard, M. Oujja, T. Corrales, S. Georgiou, C. Domingo, P. Bosch, M. Castillejo: Pulsed laser deposition of polymers doped with fluorescent probes. Application to environmental sensors, J. Phys. Conf. Ser. **59**, 305 (2007)
Redondas X., P. González, B. León, M. Pérez-Amor, J.C: Soares, M.F. da Silva: Structural and compositional studies of a-Si,C:H thin films obtained by excimer lamp chemical vapor deposition from acetylene and silane, J. Vac. Sci. Technol. **A 16**, 660 (1998)
Rehse S.J., J. Diedrich, S. Palchaudhuri: Identification and discrimination of *Pseudomonas aeruginosa* bacteria grown in blood and bile by laser-induced breakdown spectroscopy, Spectrochimica. Acta. Part. B **62**, 1169 (2007)
Reif J., O. Varlamova, F. Costache: Femtosecond laser induced nanostructure formation: Self-organization control parameters, Appl. Phys. A **92**, 1019 (2008)
Reinhardt C., R. Kiyan, S. Passinger, A.L. Stepanov, A. Ostendorf, B.N. Chichkov: Rapid laser prototying of plasmonic components, Appl. Phys. A **89**, 321 (2007)
Rethfeld B., O. Brenk, N. Medvedev, H. Krutsch, D.H.H. Hoffmann: Interaction of dielectrics with fs laser pulses: application of kinetic approach and multiple rate equation, Appl. Phys. A **109**, 19 (2010)
Rethfeld B.: Free-electron generation in laser-irradiated dielectrics, Phys. Rev. B **73**, 035101 (2006)
Rethfeld B.: Unified model for the free-electron avalanche in laser-irradiated dielectrics, Phys. Rev. Lett. **92**, 187401 (2004)

Rethfeld B., A. Kaiser, M. Vicanek, G. Simon: Ultrafast dynamics of nonequilibrium electrons in metals under femtosecond laser irradiation, Phys. Rev. B **65**, 214303 (2002a)

Rethfeld B., K. Sokolowski-Tinten, D. von der Linde, S.I. Anisimov: Ultrafast thermal melting of laser-excited solids by homogeneous nucleation, Phys. Rev. B **65**, 092103 (2002b)

Riehn R., A. Charas, J. Morgado, F. Cacialli: Near-field lithography of a conjugated polymer, Appl. Phys. Lett. **82**, 526 (2003)

Riele P., A. Janssens, G. Rijnders, D.H.A. Blank: Direct patterning of complex oxides by pulsed laser deposition through stencils, J. Phys. Conf. Ser. **59**, 404 (2007)

Riemann I., T. Anhut, F. Stracke, R. Le Harzic, K. König: Multiphoton nanosurgery in cells and tissues, SPIE Vol. **5695**, 216 (2005)

Riet E. van de, Nillesen, C.J.C.M., Dieleman, J.: Reduction of droplet emission and target roughening in laser ablation and deposition of metals, J. Appl. Phys. **74**, 2008 (1993)

Rijnders G., D.H.A. Blank: In situ diagnostics by high-pressure RHEED during PLD, in *Pulsed Laser Deposition of Thin Films: Applications-Led Growth of Functional Materials*, ed. R. Eason (Wiley 2007) p. 85

Rimai D.S., L.P. DeMejo, R. Bowen, J.D. Morris: Particles on surfaces: Adhesion induced deformations. In *Particles on Surfaces: Detection, Adhesion, and Removal*, ed. by K.L. Mittal (Marcel Dekker Inc., New York, Basel, Hong Kong 1995)

Rink K., G. Delacrétaz, R.P. Salathé: Fragmentation process induced by microsecond laser pulses during lithotripsy, Appl. Phys. Lett. **61**, 258 (1992)

Roberts M.W., C.S. McKee: *Chemistry of the Metal-Gas Interface* (Clarendon Press, Oxford 1978)

Roca i Cabarrocas P., N. Layadi, M. Kunst, C. Clerc, H. Bernas: Optical and transport properties of amorphous and microcrystalline silicon films prepared by excimer laser assisted rf glow-discharge deposition, J. Vac. Sci. Technol. A **16**, 436 (1998)

Rode A.V., B. Luther-Davies, E.G. Gamaly: Ultrafast ablation with high-pulse-rate lasers. Part II. Experiments on laser deposition of amorphous carbon films, J. Appl. Phys. **85**, 4222 (1999)

Röder J., J. Faupel, H.-U. Krebs: Growth of polymer-metal nanocomposites by pulsed laser deposition, Appl. Phys. A **93**, 863 (2008)

Römer G.R.B.E., A.J. Huis in't Veld, J. Meijer, M.N.W. Groenendijk: On the formation of laser induced self-organizing nanostructures, CIRP Annals – Manufacturing Technology **58**, 201 (2009)

Rössler R., J.D. Pedarnig, D. Bäuerle, E.J. Connolly, H.W. Zandbergen: Morphology and electrical properties of pulsed-laser deposited $Bi_2Sr_2CaCu_2O_{8+\delta}$ films on vicinal substrates, Appl. Phys. A **71**, 245 (2000)

Rogers D.J., F. Hosseini Teherani, A. Largeteau, G. Demazeau, C. Moisson, D. Turover, J. Nause, G. Garry, R. Kling, T. Gruber, A. Waag, F. Jomard, P. Galtier, A. Lusson, T. Monteiro, M.J. Soares, A. Neves, M.C. Carmo, M. Peres, G. Lerondel, C. Hubert: ZnO homoepitaxy on the O polar face of hydrothermal and melt-grown substrates by pulsed laser deposition, Appl. Phys. A **88**, 49 (2007)

Rosenfeld A., M. Lorenz, R. Stoian, D. Ashkenasi: Ultrashort laser pulse damage threshold of transparent materials and the role of incubation, Appl. Phys. A **69** [Suppl.], S373 (1999)

Rouleau C.M., G. Eres, H. Cui, H.M. Christen, A.A. Puretzky, D.B. Geohegan: Altering the catalytic activity of thin metal catalyst films for controlled growth of chemical vapor deposited vertically aligned carbon nanotube arrays, Appl. Phys. A **93**, 1005 (2008)

Rousse A., C. Rischel, S. Fourmaux, I. Uschmann, S. Sebban, G. Grillon, Ph. Balcou, E. Förster, J.P. Geindre, P. Audebert, J.C. Gauthier, D. Hulin: Non-thermal melting in semiconductors measured at femtosecond resolution, Nature **410**, 65 (2001)

Roy D., S.B. Krupanidhi, J.P. Dougherty: Excimer laser ablation of ferroelectric $Pb(Zr,Ti)O_3$ Thin films with Low pressure direct-current glow discharge, J. Vac. Sci. Technol. A **10**, 1827 (1992)

Ruberto M.N., X. Zhang, R. Scarmozzino, A.E. Willner, D.V. Podlesnik, R.M. Osgood: The laser-controlled Micrometer-scale Photoelectrochemical etching of III-V Semiconductors, J. Electrochem. Soc. **138**, 1174 (1991)

Russo R.E., X.L. Mao, O.V. Borisov, H.C. Liu: Influence of wavelength on fractionation in laser ablation ICP-MS, J. Anal. At. Spectrom. **15**, 1115 (2000)

Sacconi L., I.M. Tolic-Nørrelykke, R. Antolini, F.S. Pavone: Combined intracellular 3-D imaging and selective nanosurgery by a nonlinear microscope, J. Biomed. Opt. **10**, 014002 (2005)

Saenger K.L.: Time-Resolved Optical Emission During Laser Ablation of Cu, CuO, and High-T_c Superconductors: $Bi_{1.7}Sr_{1.3}Ca_2Cu_3O_x$ and $Y_1Ba_{1.7}Cu_{2.7}O_y$, J. Appl. Phys. **66**, 4435 (1989)

Sahu R.K., R.D. Vispute, S. Dhar, D.C. Kundaliya, S. Sundar Manoharan, T. Venkatesan, S.H. Lim, L.G. Salamanca-Riba: Enhanced conductivity of pulsed laser deposited n-$InGaZn_6O_9$ films and its rectifying characteristics with p-SiC, Thin. Sol. Film. **517**, 1829 (2009)

Said A., L. Sajti, S. Giorgio, W. Marine: Synthesis of nanohybrid materials by fs laser ablation in liquid medium, J. Phys. Conf. Ser. **59**, 259 (2007)

Samsonov G.V. ed.: *The Oxide Handbook* (Plenum, New York 1973)

Sasaki T., S. Terauchi, N. Koshizaki, H. Umehara: The preparation of iron complex oxide nanoparticles by pulsed-laser ablation, Appl. Surf. Sci. **127–129**, 398 (1998)

Sato T.: Spectral emissivity of Silicon, Jpn. J. Appl. Phys. **6**, 339 (1967)

Schäfer C., H.M. Urbassek, L.V. Zhigilei: Metal ablation by picosecond laser pulses: A hybrid simulation, Phys. Rev. B **66**, 115404 (2002)

Schaffer C.B., N. Nishimura, E.N. Glezer, A.M.-T. Kim, E. Mazur: Dynamics of fs laser-induced breakdown in water from femtoseconds to microseconds, Opt. Expr. **10**, 196 (2002)

Schey B.: Pulsed-laser deposition of high-temperature superconducting thin films and their applications, in *Pulsed Laser Deposition of Thin Films: Applications-Led Growth of Functional Materials*, ed. R. Eason (Wiley 2007) p. 313

Schey B., W. Biegel, M. Kuhn, B. Stritzker: Large area PLD of YBCO thin films: homogeneity and surface, Appl. Phys. A **69** [Suppl.], S419 (1999)

Schittenhelm H., G. Callies, P. Berger, H. Hügel: Time-resolved interferometric investigations of the KrF-laser-induced interaction zone, Appl. Surf. Sci. **109–110**, 493 (1997)

Schmidt H., J. Ihlemann, B. Wolff-Rottke, K. Luther, J. Troe, J.: UV laser ablation of polymers: spot size, pulse duration, and plume attenuation effects explained, J. Appl. Phys. **83**, 5458 (1998)

Scholz M., W. Fuß, K. Kompa: CVD of Silicon Carbide Powders using Pulsed CO_2 Lasers, Adv. Mater. **5**, 38 (1993)

Schou J., S. Amoruso, J.G. Lunney: Plume dynamics, in *Laser Ablation and its Applications*, ed. by C. R. Phipps (Springer 2007) p. 67

Schrems G., M.P. Delamare, N. Arnold, P. Leiderer, D. Bäuerle: Influence of storage time on laser cleaning of SiO_2 on Si, Appl. Phys. A **76**, 847 (2003)

Schröder H., T. Rupp: Laserinduzierte reaktive Epitaxie (LIRE), Photonik **4**, 6 (2002)

Schröder H., B. Rager, S. Metev, N. Rösch, H. Jörg: Photochemistry of Transition Metal Complexes, in *Interfaces under Laser Irradiation*, ed. by L.D. Laude, D. Bäuerle, M. Wautelet, Nato ASI Series (M. Nijhoff, Dordrecht 1987) p. 255

Schütze K., G. Lahr: Identification of expressed genes by laser-mediated manipulation of single cells, Nat. Biotechnol. **16**, 737 (1998)

Schulz W., V. Kostrykin, M. Nießen, J. Michel, D. Petring, E.W. Kreutz, R. Poprawe: Dynamics of ripple formation and melt flow in laser beam cutting, J. Phys. D. Appl. Phys. **32**, 1219 (1999)

Schuöcker D.: *High power lasers in production engineering* (World Scientific Publishing, Singapore 1999)

Schwab B., D. Hagner, J. Bornemann, R. Heermann: The use of fs technology in otosurgery, in *Femtosecond Technology for Technical and Medical Applications*, ed. by F. Dausinger, F. Lichtner, H. Lubatschowski, Springer Series Topics in Applied Physics **96**, Springer Verlag 2004, p. 211

Schwab P., X.Z.Wang, S. Proyer, A. Kochemasov, D. Bäuerle: Synthesis of $YBa_{2-x}Sr_xCu_3O_{7-d}$ by PLD, Physica. C **214**, 257 (1993)

Schwab P., A. Kochemasov, R. Kullmer, D. Bäuerle: The influence of photodissociated N_2O in PLD of Y-Ba-Cu-O Films, Appl. Phys. A **54**, 166 (1992a)

Schwab P., X.Z. Wang, D. Bäuerle: In Situ Fabrication of superconducting Lu-Ba-Sr-Cu-O films by pulsed-laser deposition, Appl. Phys. Lett. **60**, 2023 (1992b)

Schwab P., D. Bäuerle: Pulsed-Laser Deposition of Y-Ba-Cu-O in O_2 and N_2O Atmospheres, Physica. C **182**, 103 (1991)

Schwartz B.: *GaAs Surface Chemistry – a Review*, CRC critical review in solid state sciences, 5 (CRC Press, Boca Raton 1975) p. 609

Schwödiauer R., S. Bauer-Gogonea, S. Bauer, J. Heitz, E. Arenholz, D. Bäuerle: Charge stability of pulsed-laser deposited polytetrafluoroethylene film electrets, Appl. Phys. Lett. **73**, 2941 (1998)

Schwoerer H.: Generation of X-rays by intense fs lasers, in *Femtosecond Technology for Technical and Medical Applications*, ed. by F. Dausinger, F. Lichtner, H. Lubatschowski, Springer Series Topics in Applied Physics **96**, Springer Verlag 2004, p. 235

Sedov L.I.: *Similarity and Dimensional Methods in Mechanics* (Academic Press, London 1959)

Seel M., P.S. Bagus: Ab initio cluster study of the interaction of fluorine and chlorine with the Si(111) surface, Phys. Rev. B **28**, 2023 (1983)

Sellinger A., E. Leveugle, J.M. Fitz-Gerald, L.V. Zhigilei: Generation of surface features in films deposited by matrix-assisted pulsed laser evaporation: the effects of the stress confinement and droplet landing velocity, Appl. Phys. A **92**, 821 (2008)

Semaltianos N.G., S. Logothetidis, W. Perrie, S. Romani, R.J. Potter, M. Sharp, P. French, G. Dearden, K.G. Watkins: II-VI semiconductor nanoparticles synthesized by laser ablation, Appl. Phys. A **94**, 641 (2009)

Seo J.M., Y.Z. Li, S.G. Anderson, D.J.W. Aastuen, U.S. Ayyala, G.H. Kroll, J.H. Weaver: X-Ray-Induced Low-Temperature Oxidation: N_2O/GaAs(110), Phys. Rev. B **42**, 9080 (1990)

Seres E., J. Seres, C. Spielmann: Time resolved spectroscopy with fs soft-x-ray pulses, Appl. Phys. A **96**, 43 (2009)

Serna R., T. Missana, C.N. Afonso, J.M. Ballesteros, A.K. Petford-Long, R.C. Doole: Bi nanocrystals embedded in an amorphous Ge matrix grown by pulsed laser deposition, Appl. Phys. A **66**, 43 (1998)

Sesselmann W., T.J. Chuang: Reaction of Chlorine with Ag surfaces and radiation effects by X-Ray photons and Ar^+-Ions, Surf. Sci. **184**, 374 (1987)

Sesselmann W., E.E. Marinero, T.J. Chuang: Laser stimulated desorption from Noble Metal surfaces reacted with chlorine, Surf. Sci. **178**, 787 (1986a)

Sesselmann W., E.E. Marinero, T.J. Chuang: Laser-induced desorption and etching processes on chlorinated Cu and Solid CuCl surfaces, Appl. Phys. A **41**, 209 (1986b)

Sesselmann W., T.J. Chuang: Chlorine surface interaction and Laser-induced surface etching reactions, J. Vac. Sci. Technol. B **3**, 1507 (1985)

Seto T., K. Koga, H. Akinaga, F. Takano, T. Orii, M. Hirasawa: Laser ablation synthesis of monodispersed magnetic alloy nanoparticles, J. Nanopart. Res. **8**, 371 (2006)

Shafeev G.A.: Laser assisted activation of dielectrics for electroless metal plating, Appl. Phys. A **67**, 303 (1998)

Shaffer E., A.S. Helmy, D. Drouin, J.J. Dubowski: Excimer laser-induced crystallization of CdSe thin films, Appl. Phys. A **93**, 869 (2008)

Shank C.V., R. Yen, C. Hirlimann: Time-resolved reflectivity measurements of fs-optical-pulse-induced phase transition in silicon, Phys. Rev. Lett. **50**, 454 (1983)

She M., D. Kim, C.P. Grigoropoulos: Liquid-assisted pulsed laser cleaning using near-infrared and ultraviolet radiation, J. Appl. Phys. **86**, 6519 (1999)

Sheehy M.A., B.R. Tull, C.M. Friend, E. Mazur: Chalcogen doping of silicon via intense fs-laser irradiation, Mater. Sci. Eng. B **137**, 289 (2007)

Shen M.Y., C.H. Crouch, J.E. Carey, E. Mazur: Femtosecond laser-induced formation of submicrometer spikes on silicon in water, Appl. Phys. Lett. **85**, 5694 (2004)

Shen M.Y., C.H. Crouch, J.E. Carey, R. Younkin, E. Mazur, J. Sheehy, C.M. Friend: Formation of regular arrays of silicon microspikes by femtosecond laser irradiation through a mask, Appl. Phys. Lett. **82**, 1715 (2003)

Shen Y.Q., T. Freltoft, P. Vase: Laser writing and rewriting on $YBa_2Cu_3O_7$ Films, Appl. Phys. Lett. **59**, 1365 (1991)

Shewmon P.G.: *Diffusion in Solids* (Mc Graw-Hill, New York 1963)

Shibata T., J.F. Gibbons, T.W. Sigmon: Silicide formation using a scanning cw laser beam, Appl. Phys. Lett. **36**, 566 (1980)
Shih T., M.T. Winkler, T. Voss, E. Mazur: Dielectric function dynamics during fs laser excitation of bulk ZnO, Appl. Phys. A **96**, 363 (2009)
Shimotsuma Y., P.G. Kazansky, J. Qiu, K. Hirao: Self-organized nanogratings in glass irradiated by ultrashort light pulses, Phys. Rev. Lett. **91**, 247405 (2003)
Shin J., K. Jang, K.S. Lim, I.B. Sohn , Y.C. Noh, J. Lee: Formation and control of Au and Ag nanoparticles inside borate glasses using fs laser and heat treatment, Appl. Phys. A **93**, 923 (2008)
Shklovskii V.A., V.M. Kuz'menko: Explosive crystallization of amorphous substances, Sov. Phys. Usp. **32**, 163 (1989)
Siegel J., W. Gawelda, D. Puerto, C. Dorronsoro, J. Solis, C.N. Afonso, J.C.G.de Sande, R. Bez, A. Pirovano, C. Wiemer: Amorphization dynamics of $Ge_2Sb_2Te_5$ films upon nano- and femtosecond laser pulse irradiation, J. Appl. Phys. **103**, 023516 (2008)
Siegel J., D. Puerto, W. Gawelda, G. Bachelier, J. Solis, L. Ehrentraut, J. Bonse: Plasma formation and structural modification below the visible ablation threshold in fused silica upon fs laser irradiation, Appl. Phys. Lett. **91**, 082902 (2007)
Siegel J., A. Schropp, J. Solis, C.N. Afonso, W. Wuttig: Rewritable phase-change optical recording in $Ge_2Sb_2Te_5$ films induced by picosecond laser pulses, Appl. Phys. Lett. **84**, 2250 (2004a)
Siegel J., G. Epurescu, A. Perea, F.J. Gordillo-Vázquez, J. Gonzalo, C.N. Afonso: Temporally and spectrally resolved imaging of laser-induced plasmas, Opt. Lett. **29**, 2228 (2004*b*)
Siegel J., J. Solis, C.N. Afonso: Recalescence *after* solidification in Ge films melted by picosecond laser pulses, Appl. Phys. Lett. **75**, 1071 (1999a)
Siegel J., C.N. Afonso, J. Solis: Dynamics of ultrafast reversible phase transitions in GeSb films triggered by picosecond laser pulses, Appl. Phys. Lett. **75**, 3102 (1999b)
Siegel J., J. Solis, C.N. Afonso: Slow interfacial reamorphization of Ge films melted by ps laser pulses, J. Appl. Phys. **84**, 5531 (1998)
Siegman A.E.: *Lasers* (University Science Books, Mill Valley, CA 1986)
Sikora A., A. Berkesse, O. Bourgeois, J.L. Garden, C. Guerret-Piecourt, A.S. Loir, F. Garrelie, C. Donnet: Electrical properties of boron-doped diamond-like carbon thin films deposited by femtosecond pulsed laser ablation, Appl. Phys. A **94**, 105 (2009)
Silies M., H. Witte, S. Linden, J. Kutzner, I. Uschmann, E. Förster, H. Zacharias: Table-top kHz hard X-ray source with ultrashort pulse duration for time-resolved X-ray diffraction, Appl. Phys. A **96**, 59 (2009)
Silvain J.F., H. Niino, S. Ono, S. Nakaoka, A. Yabe: Surface modification of elastomer/carbon composite by Nd+:YAG laser and KrF excimer laser ablation, Appl. Surf. Sci. **141**, 25 (1999)
Singh D., W. Kim, V. Craciun, H. Hofmann, R.K. Singh: Microstructural and electrochemical properties of lithium manganese oxide thin films grown by pulsed laser deposition, Appl. Surf. Sci. **197–198**, 516 (2002)
Singleton D.L., G. Paraskevopoulos, R.S. Irwin: XeCl laser ablation of polyimide:Influence of ambient atmosphere on particulate and Gaseous products, J. Appl. Phys. **66**, 3324 (1989)
Singmaster K.A., F.A. Houle: Effect of laser heating on compositions of films deposited from the Metal Hexacarbonyls, Mat. Res. Soc. Symp. Proc. **201**, 159 (1991)
Singmaster K.A., F.A. Houle, R.J. Wilson: Photochemical deposition of Thin Films from the Metal Hexacarbonyls, J. Phys. Chem. **94**, 6864 (1990)
Sinh N.D., G. Andrä, F. Falk, E. Ose, J. Bermann: Optimization of layered laser crystallization for thin-film crystalline silicon solar cells, Sol. Ener. Mater. Sol. Cell. **74**, 295 (2002)
Sipe J.E., J.F.Young, J.S. Preston, H.M.van Driel: Laser-induced periodic surface structure. I. Theory, Phys. Rev. B. **27**, 1141 (1983)
Siraj K., J.D. Pedarnig, A. Moser, D. Bäuerle, N. Hari Babu, D.A. Cardwell: Europhysics Letters **82**, 57006 (2008)
Siwick B.J., J.R. Dwyer, R.E. Jordan, R.J. Dwayne Miller: An atomic-level view of melting using femtosecond electron diffraction, Science **302**, 1382 (2003)
Slaoui A., F. Foulon, C. Fuchs, E. Fogarassy, P. Siffert: Photoabsorption of BCl_3 Gas under Pulsed ArF Excimer Laser Irradiation, Appl. Phys. A **50**, 317 (1990)

Smoluchowski M.: Zur Theorie der Wärmeleitung in verdünnten Gasen und der dabei auftretenden Druckkräfte, Annalen der Physik **35**, 983 (1911)

Sobol E.N.: *Phase Transformations and Ablation in Laser-Treated Solids* (John Wiley & Sons, New York 1995)

Sobolewski R., W. Xiong, W. Kula, J.R. Gavaler: Laser Patterning of Y-Ba-Cu-O Thin-Film Devices and Circuits, Appl. Phys. Lett. **64**, 643 (1994)

Sobral H., C. Sánchez-Aké, M. Villagrán-Muniz: Intensity enhancement in cross-beam pulsed laser ablation using two orthogonal targets, Spectrochimica Acta Part B **63**, 493 (2008)

Sokolowski-Tinten K., J. Bialkowski, A. Cavalleri, D. von der Linde, A. Oparin, J. Meyer-ter-Vehn, S.I. Anisimov: Transient states of matter during short pulse laser ablation, Phys. Rev. Lett. **81**, 224 (1998)

Sona A.: Metallic Materials Processing: Cutting and Drilling, in *Applied Laser Tooling*, ed. by O.D.D. Soares and M. Perez-Amor (M. Nijhoff, Dordrecht 1987) p. 105

Song J., X. Wang, X. Hu, Y. Dai, J. Qiu, Y. Chen, Z. Xu: Formation mechanism of self-organized voids in dielectrics induced by tightly focused fs laser pulses, Appl. Phys. Lett. **92**, 092904 (2008)

Spyratou E., M. Makropoulou, A.A. Serafetinides: Study of visible and mid-infrared laser ablation mechanism of PMMA and intraocular lenses: experimental and theoretical results, Lasers Med Sci **23**, 179 (2008)

Spyridaki M., E. Koudoumas, P. Tzanetakis, C. Fotakis, R. Stoian, A. Rosenfeld, I.V. Hertel: Temporal pulse manipulation and ion generation in ultrafast laser ablation of silicon, Appl. Phys. Lett. **83**, 1474 (2003)

Srinivasan R.: Interaction of Laser Radiation with Organic Polymers, in Laser Ablation, ed. J.C. Miller, Springer Ser. Mat. Sci., **28** (Springer, Berlin, Heidelberg 1994) p. 107

Srinivasan R.: Ablation of Polyimide (Kapton) Films by Pulsed (ns) Ultraviolet and Infrared (9.17 μm) Lasers; A Comparative Study, Appl. Phys. A **56**, 417 (1993)

Srinivasan R., B. Braren, K.G. Casey: Nature of "Incubation Pulses" in the UV Laser Ablation of Polymethyl Methacrylate, J. Appl. Phys. **68**, 1842 (1990a)

Srinivasan R., K.G. Casey, B. Braren, M. Yeh: The Significance of a Fluence Threshold for UV Laser Ablation and Etching of Polymers, J. Appl. Phys. **67**, 1604 (1990b)

Srinivasan R., B. Braren: Ultraviolet laser ablation of Organic Polymers, Chem. Rev. **89**, 1303 (1989)

Srinivasan R.: Ablation of polymers and Biological Tissue by UV lasers, Science **234**, 559 (1986)

Srinivasan R., B. Braren, R.W. Dreyfus, L. Hadel, D.E. Seeger: Mechanism of the UV Laser ablation of polymethyl methacrylate at 193 and 248 nm: Laser-induced fluorescence analysis, chemical analysis, and Doping studies, J. Opt. Soc. of America **3B**, 785 (1986)

Stafast H.: Initial steps in the photochemical Vapour deposition of amorphous Silicon, Appl. Phys. A **45**, 93 (1988)

Stamm U.: Extreme UV light sources for use in semiconductor lithography – state of the art and future development, J. Phys. D: Appl. Phys. **37**, 3244 (2004)

Stangl E., S. Proyer, B. Hellebrand, D. Bäuerle: Synthesis of RE-Ba-Sr-Cu-O by Pulsed-Laser deposition, Appl. Surf. Sci. **96–98**, 731 (1996a)

Stangl E., S. Proyer, M. Borz, B. Hellebrand, D. Bäuerle: Pulsed-laser deposited $GdBaSrCu_3O_{7-d}$ and $GdBa_2Cu_3O_{7-d}$ films, Physica. C **256**, 245 (1996b)

Stangl E., S. Proyer, B. Hellebrand: Properties of Laser-Deposited $TmBaSrCu_3O_{7-d}$ Thin Films, Physica. C **243**, 69 (1995)

Stangl E., S. Proyer: Pulsed-laser deposition of high-temperature superconducting thin films: Fundamentals and technology. Thesis, Johannes Kepler Universität Linz, 1995

Stangl E., B. Luk'yanchuk, H. Schieche, K. Piglmayer, S. Anisimov, D. Bäuerle: Dynamics of the Vapor Plume in Laser Materials Ablation, in *Excimer Lasers*, ed. L.D. Laude (Kluwer Academic Publishers 1994) p. 79

Stanowski R., J.J. Dubowski: Laser rapid thermal annealing of quantum semiconductor wafers: a one step bandgap engineering technique, Appl. Phys. A **94**, 667 (2009)

Steen W.M.: *Laser Material Processing*, 3rd ed. (Springer, Berlin, Heidelberg 2003)

Steinfeld J.I. ed.: *Laser-induced Chemical Processes* (Plenum, New York 1981)
Stevenson D.J., T.K. Lake, B. Agate, V. Garcés-Chávez, K. Dholakia, F. Gunn-Moore: Optically guided neuronal growth at near infrared wavelengths, Opt. Exp. **14**, 9786 (2006)
Stock D., H.-D. Geiler, K. Hehl: Theoretical evidence for opposite moving phase fronts during ultrafast solidification processes, phys. stat. sol.(a) **87**, K115 (1985)
Stoian R., M. Wollenhaupt, T. Baumert, I.V. Hertel: Temporal pulse tailoring in laser manufacturing technologies, in Laser Precision Microfabrication", eds. K. Sugioka, M. Meunier, A. Pique (Springer Verlag, Heidelberg) 2009
Stoian R., M. Boyle, A. Thoss, A. Rosenfeld, G. Korn, I.V Hertel: Dynamic temporal pulse shaping in advanced ultrafast laser material processing, Appl. Phys. A **77**, 265 (2003)
Stoian R., A. Rosenfeld, D. Ashkenasi, I.V. Hertel, N.M. Bulgakova, E.E.B. Campbell: Surface charging and impulsive ion ejection during ultrashort pulsed laser ablation, Phys. Rev. Lett. **88**, 097603 (2002*a*)
Stoian R., M. Boyle, A. Thoss, A. Rosenfeld, G. Korn, I.V Hertel, E.E.B. Campbell: Laser ablation of dielectrics with temporally shaped femtosecond pulses, Appl. Phys. Lett. **80**, 353 (2002*b*)
Stoian R., D. Ashkenasi, A. Rosenfeld, E.E.B. Campbell: Coulomb explosion in ultrashort pulsed laser ablation of Al_2O_3, Phys. Rev. B **62**, 13167 (2000)
Stolee J.A., Y. Chen, A. Vertes: High-energy fragmentation in nanophotonic ion production by laser-induced silicon microcolumn arrays, J. Phys. Chem. C **114**, 5574 (2010)
Stoneham M., M.M.D. Ramos, R.M. Ribeiro: The mesoscopic modeling of laser ablation, Appl. Phys. A **69** [Suppl.], S81 (1999)
Stralen S. van, R. Cole: *Boiling Phenomena*: *Physicochemical and Engineering Fundamentals and Applications (*Hemisphere Publishing Corporation, McGraw-Hill Book Company, 1979)
Straub M., L.H. Nguyen, A. Fazlic, M. Gu: Complex-shaped 3D microstrucures and photonic crystals generated in a polysiloxane polymer by two-photon microstereolithography, Opt. Mat. **27**, 359 (2004)
Stritzker B., A. Pospieszczyk, J.A. Tagle: Measurement of Lattice temperature of Silicon during Pulsed Laser Annealing, Phys. Rev. Lett. **47**, 356 (1981)
Stuart B.C., M.D. Feit, S. Herman, A.M. Rubenchik, B.W. Shore, M.D. Perry: Optical ablation by high-power short-pulse lasers, J. Opt. Soc. Am. B **13**, 459 (1996)
Stuart B.C., M.D. Feit, A.M. Rubenchik, B.W. Shore, M.D. Perry: Laser-induced damage in dielectrics with ns to sub-ps pulses, Phys. Rev. Lett. **74**, 2248 (1995)
Stuck R., E. Fogarassy, J.C. Muller, M. Hodeau, A. Wattieux, P. Siffert: Laser-induced diffusion by irradiation of Silicon dipped into an Organic solution of the dopant, Appl. Phys. Lett. **38**, 715 (1981)
Suarez-Garcia A., R. Serna, M. Jiménez de Castro, C.N. Afonso, I. Vickridge: Nanostructuring the Er-Yb distribution to improve the photoluminescence response of thin films, Appl. Phys. Lett. **84**, 2151 (2004)
Suarez-Garcia A., R. del Coso, R. Serna, J. Solis, C. N. Afonso: Controlling the transmission at the surface plasmon resonance of nanocomposite films using photonic structures, Appl. Phys. Lett. **83**, 1842 (2003)
Sugii T., T. Ito, H. Ishikawa: Low-temperature fabrication of Silicon Nitride films by ArF excimer laser irradiation, Appl. Phys. A **46**, 249 (1988)
Sugioka K., Y. Cheng and K. Midorikawa: "All-in-One" chip fabrication by 3D fs laser microprocessing for biophotonics, J. Phys. Conf. Ser. **59**, 533 (2007a)
Sugioka K., Y. Hanada, K. Midorikawa: 3D integration of microcomponents in a single glass chip by fs laser direct writing for biochemical analysis, Appl. Surf. Sci. **253**, 6595 (2007b)
Sugioka K., Y. Cheng, K. Midorikawa, F. Takase, H. Takai: Femtosecond laser microprocessing with 3-dimensionally isotropic spatial resolution using crossed-beam irradiation, Opt. Lett. **31**, 208 (2006)
Sugioka K., K. Toyoda: Generation Mechanism and Thermal Stability of High Carrier Concentrations by KrF-Excimer-Laser Doping of Si into GaAs, Appl. Phys. A **59**, 233 (1994)

Sugioka K., K. Toyoda: Selective Deposition of Au Films on GaAs by Projection-Patterned Excimer Laser Doping Combined with Electroless Plating, Appl. Phys. A **54**, 380 (1992)
Sugioka K., K. Toyoda: Self-Aligned Microfabrication of Metal-Semiconductor Contacts by Projection-Patterned Excimer Laser Doping, Jpn. J. Appl. Phys. **29**, 2255 (1990)
Sugioka K., K. Toyoda, K. Tachi, M. Otsuka: Formation of p-Type Layer by KrF Excimer Laser Doping of Carbon into GaAs in CH_4 Gas Ambient, Appl. Phys. A **49**, 723 (1989)
Suits J.C., R.H. Geiss, C.J. Lin, D. Rugar, A.E. Bell: Lorentz Microscopy of Micron-Sized Laser-Written Magnetic Domains in TbFe, Appl. Phys. Lett. **49**, 419 (1986)
Sun H.-B., K. Takada, S. Kawata: Elastic force analysis of functional polymer submicron oscillators, Appl. Phys. Lett. **79**, 3173 (2001)
Sun Z.H., Y.L. Zhou, S.Y. Dai, L.Z. Cao, Z.H. Chen: Preparation and properties of $GaFeO_3$ thin films grown at various oxygen pressures by pulsed laser deposition, Appl. Phys. A **91**, 97 (2008)
Suzaki Y., A. Tachibana: Measurement of the mm Sized Radius of Gaussian Laser Beam Using the Scanning Knife-Edge, Appl. Optics **14**, 2809 (1975)
Suzuki K., M. Matsuda, N. Hayashi: Polymer resist materials for excimer ablation lithography, Appl. Surf. Sci. **127–129**, 905 (1998)
Suzuki N., C. Anayama, K. Masu, K. Tsubouchi, N. Mikoshiba: Pyrolysis and Photolysis of Trimethylaluminum, Jpn. J. Appl. Phys. **25**, 1236 (1986)
Svantesson K.G., N.G. Nilsson: Determination of the absorption and the Free carrier distribution in Silicon at high level photogeneration at 1.06 mm and 294 K, Phys. Scr. **18**, 405 (1978)
Svendsen W., J. Schou, T:N. Hansen, O. Ellegaard: Angular distributions of emitted particles by laser ablation of silver at 355 nm, Appl. Phys. A **66**, 493 (1998)
Svendsen W., O. Ellegaard, J. Schou: Laser ablation deposition measurements from silver and nickel, Appl. Phys. A **63**, 247 (1996)
Sylvestre J.-P., A.V. Kabashin, E. Sacher, M. Meunier, J.H.T. Luong: Stabilization and size control of gold nanoparticles during laser ablation in aqueous cyclodextrins, J. Am. Chem. Soc. **126**, 7176 (2004)
Sytov I.P.: Model of Laser-induced Chemical etching of Silicon in chlorine atmosphere, Appl. Phys. A **53**, 372 (1992); Estimation of the capabilities of maskless micropatterning by Laser-induced Chemical etching, Appl. Phys. A **61**, 75 (1995)
Szameit A., F. Dreisow, M. Heinrich, T. Pertsch, S. Nolte, A. Tünnermann, E. Suran, F. Louradour, A. Barthelemy, S. Longhi: Image reconstruction in segmented femtosecond laser-written waveguide arrays, Appl. Phys. Lett. **93**, 181109 (2008)
Szameit A., F. Dreisow, H. Hartung, S. Nolte, A. Tünnermann, F. Lederer: Quasi-incoherent propagation in waveguide arrays, Appl. Phys. Lett. **90**, 241113 (2007)
Szikora S., W. Kräuter, D. Bäuerle: Laser Induced Deposition of SiO_2, Mat. Lett. **2**, 263 (1984)
Szörényi T: Carbon-based materials by pulsed laser deposition: from thin films to nanostructures, Chapter 3 in *Recent Advances in Laser processing of Materials*, J. Perriere, E. Millon, E. Fogarassy eds. p. 75 (Elsevier 2006)
Szörényi T., K. Piglmayer, G.Q. Zhang, D. Bäuerle: Lateral Growth Rates in Laser CVD of Tungsten Microstructures, Surf. Sci. **202**, 442 (1988)
Tabbal M., T. Kim, D.N. Woolf, B. Shin, M.J. Aziz: Fabrication and sub-band-gap absorption of single-crystal Si supersaturated with Se by pulsed laser mixing, Appl. Phys. A **98**, 589 (2010)
Tabbal M., M. Meunier, R. Izquierdo, B. Beau, A. Yelon: LCVD of W Schottky contacts on GaAs using WF_6 and SiH_4, J. Appl. Phys. **81**, 6607 (1997)
Takada N., T. Sasaki, K. Sasaki: Synthesis of crystalline TiN and Si particles by laser ablation in liquid nitrogen, Appl. Phys. A **93**, 833 (2008)
Takada N., H. Ushida, K. Sasaki: Nitridation of titanium surface by the irradiation of YAG laser pulses in N_2/O_2 gas mixture and liquid nitrogen, J. Phys. Conf. Ser. **59**, 40 (2007)
Takahashi H., K. Igawa, K. Arii, Y. Kamihara, M. Hirano, H. Hosono: Superconductivity at 43 K in an iron-based layered compound $LaO_{1-x}F_xFeAs$, Nature **453**, 376 (2008)
Takahashi K., M. Konagai: *Amorphous Silicon Solar Cells* (Academic Press, London 1986)

Takai M., S. Nagatomo, H. Kohda, C. Yada, H. Sandaiji, F. Takeya: Laser Chemical Processing of Magnetic Materials for Recording-Head Application, Appl. Phys. A **58**, 359 (1994)

Takai M., Y.F. Lu, T. Koizumi, S. Namba, S. Nagatomo: Thermo-chemical Dry Etching of Single-Crystal Ferrite by Laser Irradiation in CCl_4 Gas Atmosphere, Appl. Phys. A **46**, 197 (1988a)

Takai M., J. Tsuchimoto, J. Tokuda, H. Nakai, K. Gamo, S. Namba: Laser-Induced Thermochemical Maskless-Etching of III-V Compound Semiconductors in Chloride Gas atmosphere, Appl. Phys. A **45**, 305 (1988b)

Talton J.D., B. Eppler, M.I. Davis, A.L. Mercado, J.M. Fitz-Gerald: Coating powders for drug delivery systems using PLD, in *Pulsed Laser Deposition of Thin Films: Applications-Led Growth of Functional Materials*, ed. R. Eason (Wiley 2007) p. 217

Tam A.C., W.P. Leung, W. Zapka, W. Ziemlich: Laser-cleaning techniques for removal of surface particulates, J. Appl. Phys. **71**, 3515 (1992)

Tan D., Y. Li, F. Qi, H. Yang, Q. Gong, X. Dong, X. Duan: Reduction in feature size of two-photon polymerization using SCR500, Appl. Phys. Lett. **90**, 071106 (2007)

Tang H., I.P. Herman: Raman Microprobe Scattering of Solid Silicon and Germanium at the Melting Temperature, Phys. Rev. B **43**, 2299 (1991)

Tang H., I.P. Herman: Laser-induced and Room Temperature Etching of Copper Films by Chlorine with Analysis by Raman Spectroscopy, J. Vac. Sci. Technol. **A8**, 1608 (1990)

Tarasenko N.V., A.V. Butsen, A.A. Nevar: Laser ablation of Gd targets in liquids for nanoparticle preparation, Appl. Phys. A **93**, 837 (2008)

Tebano A., C. Aruta, N.G. Boggio, P.G. Medaglia, G. Balestrino: Superconductivity in artifical cuprate structures grown by laser molecular beam epitaxy, Supercond. Sci. Technol. **19**, S45 (2006)

Temnov V.V., K. Sokolowski-Tinten, P. Zhou, D.von der Linde: Ultrafast imaging interferometry at femtosecond-laser-excited surfaces, J. Opt. Soc. Am. B. **23**, 1954 (2006)

Terakawa M., E. Toratani, T. Shirakawa, M. Obara: Fabrication of void array in dielectric materials by fs laser micro-processing for compact photonic devices, Appl. Phys. A **100**, 1041 (2010)

Thomas J., E. Wikszak, T. Clausnitzer, U. Fuchs, U. Zeitner, S. Nolte, A. Tünnermann: Inscription of fiber Bragg gratings with fs pulses using a phase mask scanning technique, Appl. Phys. A **86**, 153 (2007a)

Thomas J., M. Heinrich, J. Burghoff, S. Nolte, A. Ancona, A. Tünnermann: Femtosecond laser-written quasi-phase-matched waveguides in lithium niobate, Appl. Phys. Lett. **91**, 151108 (2007b)

Tirlapur U.K., K. König: Targeted transfection by fs laser, Nature **418**, 290 (2002)

Tode M., Y. Takigawa, M. Ohmukai, K. Kurosawa, M. Muroya: Epitaxially growth of β–$FeSi_2$ thin films on Si(100) substrates from ε–FeSi targets with ArF excimer laser deposition, J. Phys. Conf. Ser. **59**, 376 (2007)

Tönshoff H.K., F.v.Alvensleben, A. Ostendorf, G. Kamlage, S. Nolte: Micromachining of metals using ultrashort laser pulses, Inter. J. Elect. Mach. No. 4, January 1999, p. 1

Toftmann B., M.R. Papantonakis, R.C.Y. Auyeung, W. Kim, S.M. O'Malley, D.M. Bubb, J.S. Horwitz, J. Schou, P.M. Johansen, R.F. Haglund: UV and RIR matrix assisted pulsed laser deposition of organic MEH-PPV films, Thin Solid Films **453–454**, 177 (2004)

Toftmann B., J. Schou, J.G. Lunney: Dynamics of the plume produced by ns ultraviolet laser ablation of metals, Phys. Rev. B **67**, 104101 (2003)

Toftmann B., J. Schou, T.N. Hansen, J.G. Lunney: Angular distribution of electron temperature and density in a laser-ablation plume, Phys. Rev. Lett. **84**, 3998 (2000)

Tokuyama M., Y. Enomoto: Dynamics of Crossover Phenomenon in Phase-Separating Systems, Phys. Rev. Lett. **69**, 312 (1992)

Toriumi A., J.M. Herrmann, S. Kawata: Nondestructive readout of a 3D photochromic optical memory with a near-IR differential phase-contrast microscope, Optics Lett. **22**, 555 (1997)

Tosin P., W. Lüthy, H.P. Weber: Laserbearbeitung von Diamantfilmen, Phys. Blätter **52**, 569 (1996)

Toth Z., T. Szörenyi, A.L. Toth: Ar+-Laser-induced Forward Transfer (LIFT): A Novel Method for Micrometer-Size surface patterning, Appl. Surf. Sci. **69**, 317 (1993)

Toth Z., P. Kargl, C. Grivas, K. Piglmayer, T. Szörenyi, D. Bäuerle: LCVD of Tungsten Microstructures on Quartz, Appl. Phys. B **54**, 189 (1992)

Toulemonde M., S. Unamuno, R. Heddache, M.O. Lampert, M. Hage-Ali, P. Siffert: Time-resolved reflectivity and Melting depth measurements using pulsed ruby laser on Silicon, Appl. Phys. A **36**, 31 (1985)

Trajanovic Z., S. Choopun, R.P. Sharma, T. Venkatesan: Stoichiometry and thickness variation of $YBa_2Cu_3O_{7-x}$ in pulsed laser deposition with a shadow mask, Appl. Phys. Lett. **70**, 3461 (1997)

Trajanovic Z., L. Senapati, R.P. Sharma, T. Venkatesan: Stoichiometry and Thickness Variation of $YBa_2Cu_3O_{7-x}$ in Off-Axis Pulsed Laser Deposition, Appl. Phys. Lett. **66**, 2418 (1995)

Tribelsky M.I., B.S. Luk'yanchuk: Anomalous light scattering by small particles, Phys. Rev. Lett. **97**, 263902 (2006)

Tsuboi Y., M. Goto, A. Itaya: Thin film formation of a protein by laser ablation deposition technique. Chemistry Letters 1998, p. 521 (The Chemical Society of Japan)

Tünnermann A., J. Limpert, S. Nolte: Ultrashort pulse fiber lasers and amplifiers, in *Femtosecond Technology for Technical and Medical Applications*, ed. by F. Dausinger, F. Lichtner, H. Lubatschowski, Springer Series Topics in Applied Physics **96**, Springer Verlag 2004, p. 35

Tyunina M., J. Levoska, A. Sternberg, S. Leppävuori: Dielectric properties of pulsed laser deposited films of $PbMg_{1/3}Nb_{2/3}$-$PbTiO_3$ and $PbSc_{1/2}Nb_{1/2}O_3$-$PbTiO_3$ relaxor ferroelectrics, J. Appl. Phys. **86**, 5179 (1999)

Ueki H., Y. Kawata, S. Kawata: 3D optical bit-memory recording reading with a photorefractive crystal: analysis and experiment, Appl. Opt. **35**, 2457 (1996)

Ullmann M., S.K. Friedlander, A. Schmidt-Ott: Nanoparticle formation by laser ablation, J. Nanoparticle Research **4**, 499 (2002)

Umezu I., H. Minami, H. Senoo, A. Sugimura: Synthesis of photoluminescent colloidal silicon nanoparticles by pulsed laser ablation in liquids, J. Phys. Conf. Ser. **59**, 392 (2007)

Upadhyay A.K., N.A. Inogamov, B. Rethfeld, H.M. Urbassek: Ablation by ultrashort laser pulses: Atomistic and thermodynamic analysis of the processes at the ablation threshold, Phys. Rev. B **78**, 045437 (2008)

Urban S., F. Falk: Laser crystallization of amorphous SiC thin films on glass, Appl. Surf. Sci. **184**, 356 (2001)

Urech L., T. Lippert, A. Wokaun, S. Martin, H. Mädebach, J. Krüger: Removal of doped PMMA from tungsten and titanium substrates by fs- and ns laser cleaning, Appl. Surf. Sci. **252**, 4754 (2006)

Ursu C., O.G. Pompilian, S. Gurlui, P. Nica, M. Agop, M. Dudeck, C. Focsa: Al_2O_3 ceramics under high-fluence irradiation: plasma plume dynamics through space- and time-resolved optical emission spectroscopy, Appl. Phys. A **101**, 153 (2010)

Ursu I., I.N. Mihailescu, L.C. Nistor, V.S. Teodorescu, A.M. Prokhorov, V.I. Konov, S.A. Uglov: Zirconium and Titanium Nitridation by Repeated Action of a Breakdown Plasma Induced in Nitrogen as a Result of Microsecond-Pulsed TEA CO_2 Laser Irradiation, Appl. Optics **25**, 2725 (1986a)

Ursu I., I.N. Mihailescu, L. Nanu, L.C. Nistor, M.Popescu, V.S. Teodorescu, A.M. Prokhorov, V.I. Konov, S.A. Uglov, V.G. Ralchenko: Nitridation of Ti and Zr by Multi-Pulse TEA CO_2 Laser Irradiation in Liquid Nitrogen, J. Phys. D. Appl. Phys. **19**, 1183 (1986b)

Usoskin A., A. Rutt, H.C. Freyhardt, B. Prause, K. Schlenga, J.-M. Saugrain, A. Allais, D. Willen: HTS coated conductors developed for the European super3C cable, IEEE/CSC & ESAS European SuperconductivityNewsForum (ESNF), No. 10, Oct. 2009 (submitted July 29, 2009; accepted Sept. 8, 2009). Reference No. ST129; Category 5

Uwasawa K., F. Ishihara, J. Wada, S. Matsumoto: Fabrication of a-Si:H/a-$Al_{1-x}O_x$ Superlattice by Excimer Laser MOCVD and its Properties, Mat. Res. Soc. Symp. Proc. (Symp. on Surface Chemistry and Beam-Solid Interactions), (MRS Pittsburgh, PA 1991) p. 147

Varel H., M. Wähmer, A. Rosenfeld, D. Ashkenasi, E.E.D. Campbell: Femtosecond laser ablation of sapphire: time-of-flight analysis of ablation plume, Appl. Surf. Sci. **127–129**, 128 (1998)

Vass C., K. Osvay, B. Hopp, Z. Bor: 104 nm period grating fabrication in fused silica by immersion two-beam interferometric laser induced backside wet etching technique, Appl. Phys. A **87**, 611 (2007)

Vedavarz A., K. Mitra, S. Kumar: Hyperbolic temperature profiles for laser surface interactions, J. Appl. Phys. 76, 5014 (1994)

Veen G.N.A van, T.S. Baller, J. Dieleman: A Time-of-Flight Study on the Nanosecond laser induced etching of Cu with Cl_2 at 308 nm, Appl. Phys. A **47**, 183 (1988)

Veldkamp W.B.: Laser Beam profile shaping with interlaced Binary diffraction gratings, Appl. Opt. **21**, 3209 (1982)

Venkatesan T., A. Inam, B. Dutta, R. Ramesh, M.S. Hedge, X.D. Wu, L. Nazar, C.C. Chang, J.B. Barner, D.M. Hwang, C.T. Rogers: Epitaxial $Y_1Ba_2Cu_3O_{7-y}/Y_{1-x}Pr_xBa_2Cu_3O_{7-y}$ Heterostructures, Appl. Phys. Lett. **56**, 391 (1990)

Venkatesan T., C.C. Chang, D. Dijkkamp, S.B. Ogale, E.W. Chase, L.A. Farrow, D.M. Hwang, P.F. Miceli, S.A. Schwarz, J.M. Tarascon, X.D. Wu, A. Inam: Substrate effects on the properties of Y-Ba-Cu-O superconducting films prepared by laser deposition, J. Appl. Phys. **63**, 4591 (1988)

Venugopalan V., A. Guerra III, K. Nahen, A. Vogel: Role of laser-induced plasma formation in pulsed cellular microsurgery and micromanipulation, Phys. Rev. Lett. **88**, 078103 (2002)

Verardi P., M. Dinescu, C. Gerardi, L. Mirenghi, V. Sandu: AlN thin films deposition by laser ablation of Al target in nitrogen reactive atmosphere, Appl. Surf. Sci. **109–110**, 371 (1997a)

Verardi P., M. Dinescu, F. Craciun, V. Sandu: Oriented $PbZr_xTi_{1-.x}O_3$ thin films obtained at low substrate temperature by pulsed laser deposition, Thin. Sol. Film. **311**, 171 (1997b)

Vertes A., P. Nemes, B. Shrestha, A.A. Barton, Z. Chen, Y. Li: Molecular imaging by Mid-IR laser ablation mass spectrometry, Appl. Phys. A **93**, 885 (2008)

Vicanek M., A. Rosch, F. Piron, G. Simon: Thermal Deformation of a Solid Surface under Laser Irradiation, Appl. Phys. A **59**, 407 (1994)

Vlad A., S. Yakunin, E. Kolmhofer, V. Kolotovska, L. Muresan, A. Sonnleitner, D. Bäuerle, J.D. Pedarnig: Deposition, characterization and biological application of epitaxial Li:ZnO/Al:ZnO double-layers, Thin Solid Films **518**, 1350 (2009)

Vogel A., N. Linz, S. Freidank, G. Paltauf: fs-laser-induced nanocavitation in water: implications for optical breakdown threshold and cell surgery, Phys. Rev. Lett. **100**, 038102 (2008)

Vogel A., J. Noack, G. Hüttmann, G. Paltauf: Mechanisms of femtosecond laser nanoprocessing of biological cells and tissues, J. Phys. Conf. Ser. **59**, 249 (2007a)

Vogel A., J. Noack, G. Hüttmann, G. Paltauf: Femtosecond plasma-mediated nanosurgery of cells and tissues, in *Laser Ablation and its Applications*, ed. by C. R. Phipps (Springer 2007b) p. 231

Vogel A., K. Lorenz, V. Horneffer, G. Hüttmann, D.v.Smolinski, A. Gebert: Mechanisms of laser-induced dissection and transport of histologic specimens, Biophys. J. **93**, 4481 (2007c)

Vogel A., I. Apitz, S. Freidank, R. Dijkink: Sensitive high-resolution white-light Schlieren technique with a large dynamic range for the investigation of ablation dynamics, Opt. Lett. **31**, 1812 (2006)

Vogel A., V. Venugopalan: Mechanisms of pulsed laser ablation of biological tissues, Chem. Rev. **103**, 577 (2003)

Vogel A., J. Noack, K. Nahen, D. Theisen, S. Busch, U. Parlitz, D.X. Hammer, G.D. Noojin, B.A. Rockwell, R. Birngruber: Energy balance of optical breakdown in water at ns to fs time scales, Appl. Phys. B **68**, 271 (1999)

Volkov A.N., G.M. O'Connor, T.J. Glynn, G.A. Lukyanov: Expansion of a laser plume from a silicon wafer in a wide range of ambient gas pressures, Appl. Phys. A **92**, 927 (2008)

Vollkommer F., L. Hitzschke: Durchbruch bei der effizienten Erzeugung von Excimer-Strahlung, Phys. Blätter **53**, Nr. 9, 887 (1997)

von der Linde, D., K. Sokolowski-Tinten: The physical mechanisms of short-pulse laser ablation, Appl. Surf. Sci. **154–155**, 1 (2000)

Vorobyev A.Y., C. Guo: Residual thermal effects in laser ablation of metals, J. Phys. Conf. Ser. **59**, 418 (2007)

Vorobyev A.Y., V.A. Petrov, V.E. Titov, A.P. Chernyshov: Experimental Investigation of the Refractory Oxides Vapor Condensation during the Surface Heating of the Target in Air by Laser Radiation, Teplophys. High. Temperat. **29**, 981 (1991)

Vrejoiu I., G.Le Rhun, L. Pintilie, D. Hesse, M. Alexe, U. Gösele: Intrinsic ferroelectric properties of strained tetragonal $PbZr_{0.2}Ti_{0.8}O_3$ obtained on layer-by-layer grown, defect-free single-crystalline films, Adv. Mater. **18**, 1657 (2006)

Wagner D., D. Bäuerle, F. Schwabl, B. Dorner, H. Kraxenberger: Soft Modes in Semiconducting $SrTiO_3$: I. Zone Boundary Mode, Z. Phys. B **37**, 317 (1980)

Walker E., P.M. Rentzepis: Two-photon technology: A new dimension, Nat. Photo. **2**, 406 (2008)

Wallenberger F.T., P.C. Nordine, M. Boman: Inorganic Fibers and Microstructures directly from the Vapor Phase, Compos. Sci. Tech. **51**, 193 (1994)

Wang H.-Y., D. Bourell, J.J. Beaman: Laser polishing of silica slotted rods, Mater. Sci. Tech. **19**, 382 (2003)

Wang J., H. Niino, A. Yabe: One-step microfabrication of fused silica by laser ablation of an organic solution, Appl. Phys. A **68**, 111 (1999)

Wang N., Y.F. Zhang, Y.H. Tang, C.S. Lee, S. T. Lee: SiO_2-enhanced synthesis of Si nanowires by laser ablation, Appl. Phys. Lett. **73**, 3902 (1998)

Wang Z.B., B.S. Luk'yanchuk, L. Li, P.L. Crouse, Z. Liu, G. Dearden, K.G. Watkins: Optical near-field distribution in an asymmetrically illuminated tip-sample system for laser/STM nanopatterning, Appl. Phys. A **89**, 363 (2007)

Wanke M.C., O. Lehmann, K. Müller, Q. Wen, M. Stuke: Laser rapid prototyping of photonic band-gap microstructures, Science **275**, 1284 (1997)

Watanabe W., K. Itoh: 3D-Micromachining with fs laser pulses, Chapter 10 in *Recent Advances in Laser processing of Materials*, J. Perriere, E. Millon, E. Fogarassy eds., p. 299 (Elsevier 2006)

Watanabe W., N. Arakawa, S. Matsunaga, T. Higashi, K. Fukui, K. Isobe, K. Itoh: Fs-laser disruption of subcellular organelles in a living cell, Opt. Exp. **12**, 4203 (2004)

Watanabe W., D. Kuroda, K. Itoh, J. Nishii: Fabrication of Fresnel zone plate embedded in silica glass by fs laser pulses, Opt. Exp. **10**, 978 (2002)

Wautelet M.: Laser-Assisted Reaction of Metals with Oxygen, Appl. Phys. A **50**, 131 (1990)

Weck A., T.H.R. Crawfod, D.S. Wilkinson, H.K. Haugen, J.S. Preston: Ripple formation during deep hole drilling in Cu with ultrashort laser pulses, Appl. Phys. A **89**, 1001 (2007)

Weerasinghe V.M., W.M. Steen: Laser Cladding with Pneumatic Powder Delivery, Proc. 4th Int. Conf. on Lasers in Materials Processing, Los Angeles, Jan. 1983, ed. E.A. Metzbower (Publ. ASM, Ohio 1984) p. 166

Weidman D.: Fiber Bragg gratings enhance real-world applications. Laser Focus World, March 1999, p. 99

Weigl P., A. Kasenbacher, K. Werelius: Dental applications, in *Femtosecond Technology for Technical and Medical Applications*, ed. by F. Dausinger, F. Lichtner, H. Lubatschowski, Springer Series Topics in Applied Physics **96**, Springer Verlag 2004, p. 167

Weikert M., F. Dausinger: Surface Structuring, in *Femtosecond Technology for Technical and Medical Applications*, ed. by F. Dausinger, F. Lichtner, H. Lubatschowski, Springer Series Topics in Applied Physics **96**, Springer Verlag 2004, p. 117

Wellershoff S.S., J. Hohlfeld, J. Güdde, E. Matthias: The role of electron-phonon coupling in femtosecond laser damage of metals, Appl. Phys. A **69** [Suppl.], S99 (1999)

Wendelen W., D. Autrique, A. Bogaerts: Space charge limited electron emission from a Cu surface under ultrashort pulsed laser irradiation, Appl. Phys. Lett. **96**, 051121 (2010)

Westberg H., M. Boman, S. Johansson, J. Schweitz: Free-Standing Silicon Microstructures Fabricated by Laser Chemical Processing, J. Appl. Phys. **73**, 7864 (1993)

White C.W., S.R. Wilson, B.R. Appleton, F.W. Young: Supersaturated Substitutional Alloys formed by Ion Implantation and Pulsed Laser Annealing of Group-III and Group-V Dopants in Silicon, J. Appl. Phys. **51**, 738 (1980)

Wiggins S.M., J. Bonse, J. Solis, C.N. Afonso, K. Sokolowski-Tinten, V.V. Temnov, P. Zhou, D. von der Linde: The influence of wavelength on phase transformations induced by picosecond and femtosecond laser pulses in GeSb thin films, J. Appl. Phys. **98**, 113518 (2005)

Willmott P.R., F. Antoni, M. Döbeli: Kinetic, crystallographic, and optical studies of GaN and $Al_xGa_{1-x}N$ thin films grown on Si(111) by pulsed reactive crossed-beam laser ablation using liquid alloys and N_2 or NH_3, J. Appl. Phys. **88**, 188 (2000)

Winters H.F., I.C. Plumb: Etching Reactions for Silicon with F Atoms: Product Distributions and Ion Enhancement Mechanisms, J. Vac. Sci. Technol. B **9**, 197 (1991)

Winters H.F., D. Haarer: Influence of Doping on the Etching of Si(111), Phys. Rev. B **36**, 6613 (1987)

Wissenbach K., A. Gillner, F. Dausinger: Umwandlungshärten mit CO_2-Laserstrahlung, Las. Optoelekt. **3**, 291 (1985)

Witanachchi S., K. Ahmed, P. Sakthivel, P. Mukherjee: Dual-laser ablation for particulate-free film growth, Appl. Phys. Lett. **66**, 1469 (1995)

Woerner M., C.v. Korff Schmising, M. Bargheer, N. Zhavoronkov, I. Vrejoiu, D. Hesse, M. Alexe, T. Elsaesser: Ultrafast structural dynamics of perovskite superlattices, Appl. Phys. A **96**, 83 (2009)

Wolbold G.E., C.L. Tessler, D.J. Tudryn: Applications of excimer lasers in electronic packaging and manufacturing. Lambda Industrial No. **10** (Lambda Physik GmbH, May 1997) p. 1

Wolff-Rottke B., J.Ihlemann, H.Schmidt, A.Scholl: Influence of the Laser-spot Diameter on Photo-Ablation Rates, Appl. Phys. A **60**, 13 (1995)

Wong W.S., A.B. Wengrow, Y. Cho, A. Salleo, N.J. Quitoriano, K.M. Yu, J. Krüger, F.R. Weber, N.W. Cheung, T. Sands: Integration of GaN thin films with dissimilar substrate materials by metal bonding and laser liftoff. 5th International Conference on Laser Ablation COLA, Göttingen, Germany, July 19–23 (1999), Abstracts, p. 21

Wood R.F., J.N. Leboeuf, K.R. Chen, D.B. Geohegan, A.A. Puretzky: Dynamics of plume propagation, splitting, and nanoparticle formation during pulsed-laser ablation, Appl. Surf. Sci. **127–129**, 151 (1998)

Wood R.F., G.A. Geist: Modeling of Nonequilibrium melting and solidification in laser-irradiated materials, Phys. Rev. B **34**, 2606 (1986)

Wu C., C.H. Crouch, L. Zhao, E. Mazur: Visible luminescence from silicon surfaces microstructured in air, Appl. Phys. Lett. **81**, 1999 (2002)

Wu C., C.H. Crouch, L. Zhao, J.E. Carey, R. Younkin, J.A. Levinson, E. Mazur, R.M. Farrell, P. Gothoskar, A. Karger: Near-unity below-band-gap absorption by microstructured silicon, Appl. Phys. Lett. **78**, 1850 (2001)

Wu Q., Y. Ma, R. Fang, Y. Liao, Q. Yu, X. Chen, K. Wang: fs laser-induced periodic surface structure on diamond film, Appl. Phys. Lett. **82**, 1703 (2003)

Wu X., E. Sacher, M. Meunier: The modeling of excimer laser particle removal from hydrophilic silicon surfaces, J. Appl. Phys. **87**, 3618 (2000)

Wu Y.S., Y. Zhao, D. Wexler, J.H. Kim, S.X. Dou: Optimization of *in situ* annealing conditions for off-axis PLD MgB_2 films, Physica C **468**, 218 (2008)

Wysocki G., J. Heitz, D. Bäuerle: Near-field optical nanopatterning of crystalline silicon, Appl. Phys. Lett. **84**, 2025 (2004)

Wysocki G., R. Denk, K. Piglmayer, N. Arnold, D. Bäuerle: Single-step fabrication of silicon-cone arrays, Appl. Phys. Lett. **82**, 692 (2003)

Wysocki G., S.T. Dai, T. Brandstetter, J. Heitz, D. Bäuerle: Etching of crystalline Si in Cl_2 atmosphere by means of an optical fiber tip, Appl. Phys. Lett. **79**, 159 (2001)

Xia Q., S.Y. Chou: Applications of excimer laser in nanofabrication, Appl. Phys. A **98**, 9 (2010)

Xiao Z., R. Serna, F. Xu, C.N. Afonso: Critical separation for efficient Tm^{3+} – Tm^{3+} energy transfer evidenced in nanostructured Tm^{3+}:Al_2O_3 thin films, Opt. Lett. **33**, 608 (2008)

Xiao Z., R. Serna, C.N. Afonso: Broadband emission in Er-Tm codoped Al_2O_3 films: The role of energy transfer from Er to Tm, J. Appl. Phys. **101**, 033112 (2007)

Xu Y., M.R. Shen: Anatase TiO_2 films fabricated by pulsed laser deposition using Ti target, Appl. Phys. A **94**, 275 (2009)

Yabe T.: Simulation of laser-induced melting and evaporation dynamics by the unified solver CIP for solid, liquid and gas, in *'Mathematical modeling of weld phenomena* Vol.4', ed. by H. Cerjak (University Press, Cambridge, 1998), p. 26

Yamada A., A. Satoh, M. Konagai, K. Takahashi: Low-Temperature (600–650°C) Silicon Epitaxy by Excimer Laser-Assisted Chemical Vapor Deposition, J. Appl. Phys. **65**, 4268 (1989)

Yamaguchi A., Y. Hosokawa, G. Louit, T. Asahi, C. Shukunami, Y. Hiraki, H. Masuhara: Nanoparticle injection to single animal cells using femtosecond laser-induced impulsive force, Appl. Phys. A **93**, 39 (2008)

Yamamoto K., Y. Koga, S. Fujiwara, F. Kokai: The fraction of Sp^3 bonding in carbon thin film prepared using pulsed laser deposition, Jpn. J. Appl. Phys. **36**, L1333 (1997)

Yanik M.F., H. Cinar, H.N. Cinar, A.D. Chisholm, Y. Jin, A. Ben-Yakar: Neurosurgery: Functional regeneration after laser axotomy, Nature **432**, 822 (2004)

Yasukuni R., T. Asahi, T. Sugiyama, H. Masuhara, M. Sliwa, J. Hofkens, F.C. De Schryver, M.Van der Auweraer, A. Herrmann, K. Müllen: Fabrication of fluorescent nanoparticles of dendronized perylenediimide by laser ablation in water, Appl. Phys. A **93**, 5 (2008)

Yavas O., R. Oltra, O. Kerrec: Enhancement of pulsed laser removal of metal oxides by electrochemical control, Appl. Phys. A **63**, 321 (1996)

Ye M., C.P. Grigoropoulos: TOF and emission spectroscopy study of fs laser ablation of titanium, J. Appl. Phys. **89**, 5183 (2001)

Yoffa E.J.: Dynamics of Dense Laser-induced Plasmas, Phys. Rev. B **21**, 2415 (1980)

Yoshida A., H. Tamura, H. Takauchi, T. Imamura, S. Hasuo: Dielectric-Base Transistor using $YBa_2Cu_3O_{7-x}$/$NdGaO_3$/$SrTiO_3$ Heterostructures, J. Appl. Phys. **71**, 5284 (1992)

Yoshida S., M. Okoshi, N. Inoue: Femtosecond-pulsed laser deposition of diamond-like carbon films onto silicone rubber, J. Phys. Conf. Ser. **59**, 368 (2007)

Yoshida T., S. Takeyama, Y. Yamada, K. Mutoh: Nanometer-sized silicon crystallites prepared by excimer laser ablation in constant pressure inert gas, Appl. Phys. Lett. **68**, 1772 (1996)

Yoshitake T., T. Hara, T. Fukugawa, L. Zhu, M. Itakura, N. Kuwano, Y. Tomokiyo, K. Nagayama: Low-temperature growth of nanocrystalline diamond by reactive pulsed laser deposition under a hydrogen atmosphere, Japn. J. Appl. Phys. **43**, L240 (2004)

Yoshitake T., T. Nishiyama, T. Hara, K. Nagayama: Consideration of growth process of diamond thin films in ambient oxygen by pulsed laser ablation of graphite, Appl. Surf. Sci. **197–198**, 352 (2002)

Young E.M.: Electron-Active Silicon Oxidation, Appl. Phys. A **47**, 259 (1988)

Yu J., R. Camarero: A study of the Soret effect in laser-induced chemical vapor deposition, Appl. Phys. A **95**, 601 (2009)

Yuan C.L., P. Darmawan, Y. Setiawan, P.S. Lee: A simple approach to form Ge nanocrystals embedded in amorphous Lu_2O_3 high-k gate dielectric by pulsed laser ablation, Europhys. Lett. **74**, 177 (2006)

Zafiropulos V.: Laser ablation in cleaning of artworks, in *Laser Cleaning*, ed. by B.S. Luk'yanchuk, (World Scientific, Singapore, 2002), p. 343

Zahariev P., N. Mechkarov, G. Danev, J. Ihlemann: Excimer laser-induced microbumps on preheatd BK7-glass, Appl. Phys. A **95**, 639 (2009)

Zahner Th., R. Schreiner, R. Stierstorfer, O. Kus, S.T. Li, R. Rössler, J.D. Pedarnig, D. Bäuerle, H. Lengfellner: Off-diagonal Seebeck effect and anisotropic thermopower in $Bi_2Sr_2CaCu_2O_8$ thin films, Europhys. Lett. **40**, 673 (1997)

Zamponi F., Z. Ansari, C.v.Korff Schmising, P. Rothhardt, N. Zhavoronkov, M. Woerner, T. Elsaesser, M. Bargheer, T. Trobitzsch-Ryll, M. Haschke: Femtosecond hard X-ray plasma sources with a kilohertz repetition rate, Appl. Phys. A **96**, 51 (2009)

Zapka W., A.C. Tam, W. Ziemlich: Laser cleaning of wafer surfaces and lithography masks, Microelectronic Eng. **13**, 547 (1991)

Zeches R.J., M.D. Rossell, J.X. Zhang, A.J. Hatt, Q. He, C.H. Yang, A. Kumar, C.H. Wang, A. Melville, C. Adamo, G. Sheng, Y.H. Chu, J.F. Ihlefeld, R. Erni, C. Ederer, V. Gopalan, L.Q. Chen, D.G. Schlom, N.A. Spaldin, L.W. Martin, R. Ramesh: A strain-driven morphotropic phase boundary in $BiFeO_3$, Science **326**, 977 (2009)

Zeiger H.J., D.J. Ehrlich, J.Y. Tsao: Transport and Kinetics, in *Laser Microfabrication - Thin Film Processes and Lithography*, ed. by D.J. Ehrlich and J.Y. Tsao (Academic Press, London 1989) p. 285

Zeisel D., B. Dutoit, V. Deckert, T. Roth, R. Zenobi: Optical spectroscopy and laser desorption on a nanometer scale, Anal.Chem. **69**, 749 (1997)
Zeldovich Y.B., Yu.P. Raizer: *Physics of Shock Waves and High-temperature Hydrodynamic Phenomena*, ed. by W.D. Hayes and R.F. Probstein, 1 (Academic Press, London 1966), p. 93
Železný V., D. Chvostová, L. Pajasová, I. Vrejoiu, M. Alexe: Optical properties of epitaxial $BiFeO_3$ films, Appl. Phys. A **100**, 1217 (2010)
Zergioti I., A.W.M. de Laat, U. Guntow, F. Hutter, O. Maerten: Laser sintering of perovskite-oxide and metal coatings by the sol gel process, Appl. Phys. A **69** [Suppl.], S433 (1999)
Zergioti I., S. Mailis, N.A. Vainos, P. Papakonstantinou, C. Kalpouzos, C., C.P. Grigoropoulos, C. Fotakis: Microdeposition of metal and oxide structures using ultrashort laser pulses, Appl. Phys. A **66**, 579 (1998a)
Zergioti I., S. Mailis, N.A. Vainos, C. Fotakis, S. Chen, C.P. Grigoropoulos: Microdeposition of metals by fs excimer laser, Appl. Surf. Sci. **127–129**, 601 (1998b)
Zhakhovskii V.V., N.A. Inogamov, Y.V. Petrov, S.I. Ashitkov, K. Nishihara: Molecular dynamics simulation of fs ablation and spallation with different interatomic potentials, Appl. Surf. Sci. **255**, 9592 (2009)
Zhakhovskii V.V., N.A. Inogamov, K. Nishihara: New mechanism of the formation of the nanorelief on a surface irradiated by a fs laser pulse, JETP Lett. **87**, 423 (2008)
Zhang G.Q., T. Szörényi, D. Bäuerle: Kr^+ Laser-induced CVD of W, J. Appl. Phys. **62**, 673 (1987)
Zhang J., K. Sugioka, K. Midorikawa: Laser-induced plasma-assisted ablation of fused quartz using the fourth harmonic of a Nd^+:YAG laser, Appl. Phys. A **67**, 1 (1998a)
Zhang J., K. Sugioka, K. Midorikawa: High-speed machining of glass materials by laser-induced plasma-assisted ablation using a 532-nm laser, Appl. Phys. A **67**, 499 (1998b)
Zhang J.Y., I.W. Boyd, H. Esrom: Excimer laser-induced surface activation of alumina for electroless metal deposition, Appl. Surf. Sci. **109/110**, 253 (1997)
Zhang S.K., K. Sugioka, J. Fan, K. Toyoda, S.C. Zou: Studies on Excimer Laser Doping of GaAs Using Sulphur Adsorbate as Dopant Source, Appl. Phys. A **58**, 191 (1994)
Zhang X., S.S. Chu, J.R. Ho, C.P. Grigoropoulos: Excimer laser ablation of thin gold films on a quartz crystal microbalance at various argon background pressures, Appl. Phys. A **64**, 545 (1997)
Zhang X., J.R. Ho, C.P. Grigoropoulos: Ultra-shallow p^+-junction formation in silicon by excimer laser doping: a heat and mass transfer perspective, Int. J. Heat Mass. Trans. **39**, 3835 (1996)
Zhang X.R., X. Xu, A.M. Rubenchik: Simulation of microscale densification during femtosecond laser processing of dielectric materials, Appl. Phys. A **79**, 945 (2004)
Zhang Y.F., Y.H. Tang, N. Wang, D.P. Yu, C.S. Lee, I. Bello, S. T. Lee: Silicon nanowires prepared by laser ablation at high temperature, Appl. Phys. Lett. **72**, 1835 (1998)
Zhigilei L.V., Z. Lin, D.S. Ivanov: Atomistic modeling of short pulse laser ablation of metals: Connections between melting, spallation, and phase explosion, J. Phys. Chem. C **113**, 11892 (2009)
Zhigilei L.V.: Dynamics of the plume formation and parameters of the ejected clusters in short-pulse laser ablation, Appl. Phys. A **76**, 339 (2003)
Zhigilei L.V., E. Leveugle, B.J. Garrison, Y.G. Yingling, M.I. Zeifman: Computer simulations of laser ablation of molecular substrates, Chem. Rev. **103**, 321 (2003)
Zhigilei L.V., B.J. Garrison: Mechanisms of laser ablation from molecular dynamics simulations: dependence on the inital temperature and pulse duration, Appl. Phys. A **69** [Suppl.], S75 (1999)
Zhigilei L.V., P.B.S. Kodali, B.J. Garrison: Molecular dynamics model for laser ablation and desorption of organic solids, J. Phys. Chem. B **101**, 2028 (1997)
Zhou H., T. Rupp, F. Phillipp, G. Henn, M. Gross, A. Rühm, H. Schröder: Growth and microstructural characterizations of GaN films grown by laser induced reactive epitaxy, J. Appl. Phys. **93**, 1933 (2003)
Zhou J.-P., H. He, Y. Zhang, C. Deng, Z. Shi, C. Nan: Electric and magnetic properties of $CoFe_2O_4$/$Pb(Zr_{0.52}Ti_{0.48})O_3$ bilayer thin films prepared by pulsed-laser deposition, Appl. Phys. A **89**, 553 (2007)
Zhou Y., M.H. Hong, J.Y.H. Fuh, L. Lu, B.S. Luk'yanchuk, Z.B. Wang: Near-field enhanced femtosecond laser nano-drilling of glass substrate, J. Allo. Comp. **449**, 246 (2008)

Zijlstra E.S., J. Walkenhorst, M. E. Garcia: Anharmonic noninertial lattice dynamics during ultrafast nonthermal melting of InSb, Phys. Rev. Lett. **101**, 135701 (2008)

Ziman J.M.: *Principles of the Theory of Solids* (Cambridge University Press, London 1972)

Zimmer K., R. Böhme, D. Ruthe, T. Rudolph, B. Rauschenbach: Local growth of vertical aligned carbon nanotubes by laser-induced surface modification of coated silicon substrates, J. Phys.Conf. Ser. **59**, 318 (2007)

Zoppel S., H. Huber, G.A. Reider: Selective ablation of thin Mo and TCO films with femtosecond laser pulses for structuring thin film solar cells, Appl. Phys. A **89**, 161 (2007)

Zorba V., E. Stratakis, M. Barberoglou, E. Spanakis, P. Tzanetakis, S.H. Anastasiadis, C. Fotakis: Biomimetic artifical surfaces quantitatively reproduce the water repellency of a lotus leaf, Adv. Mater. **20**, 4049 (2008a)

Zorba V., N. Boukos, I. Zergioti, C. Fotakis: Ultraviolet femtosecond, picosecond and nanosecond laser microstructuring of silicon: structural and optical properties, Appl. Opt. **47**, 1846 (2008b)

Zorba V., P. Tzanetakis, C. Fotakis, E. Spanakis, E. Stratakis, D.G. Papazoglou, I. Zergioti: Silicon electron emitters fabricated by UV laser pulses, Appl. Phys. Lett. **88**, 081103 (2006)

Zweig A.D., T.F. Deutsch: Shock Waves Generated by Confined XeCl Excimer Laser Ablation of Polyimide, Appl. Phys. B **54**, 76 (1992)

Zweig A.D.: A Thermo-Mechanical Model for Laser Ablation, J. Appl. Phys. **70**, 1684 (1991)

Index

Note: Page numbers printed in italics refer to tables or listings of data or materials.

A
Ablation, 237, 279
  biological materials, 727
  congruent, 493
  debris, 263, 276
  fragments, 705
  incubation, 268, 733
  influence of ambient medium, 263
  liquid-phase expulsion, 196
  material damage, 251, 276, 279
  models, 242, 283
  nanosecond, 237
  organic polymers, 239, 252, 281
  particle formation, 71, 713
  photochemical, 266
  photomechanical, 273
  photophysical, 270
  photothermal, 247, 286
  pulsed-laser, 237
  rate, 238, 247, 256, 683
  resonant IR, 259
  stationary, 207, 271
  surface patterning, 237, 279
  threshold, 253, 286
  ultrashort-pulse, 279
  uniform, 495
  velocity, 205, 238
Absorption
  anomalous, 226
  cross sections, *777*
  linear, 20, 112, 133, *769*
  multilayer structures, 151, 157
  nonlinear, 14, 28, 43, 619
  plasma, 223
  waves (LSAW), 227
Acoustic monitors, 689
Activation energy, 41
Active-matrix-based displays, 540
Adhesion, 550, 607
Adsorbates, 37, 457, 463
  adsorbed-layer photolysis, 468
  BET relation, 467
  chemical (chemisorption), 458
  coverage, 466
  deposition from, 463
  doping from, 566
  influence of laser light, 462
  Langmuir equation, 463
  physical (physisorption), 458
  vibrations, 38
Alloying, 573
Amorphization, 252, 539, 541, 544, 576, 607
Analysis
  plasma/vapor plumes, 697
  processed surfaces, 694
  species, 697
  thin films, 694
Annealing, 537
Arrhenius law, 41
Artwork, 735
Avalanche ionization, 37, 302

B
Ballistic approximation, 321
Band bending, 341, 360
Band gap, 14, *769*
Beer's law, 20
Bessel function, *749*
BET equation, 467
Biological tissues, 727
Biotechnology, 729
Bistabilities, 153, 652
Blackbody radiance, 689
Bleaching, 271

Boiling temperature, *759*
Bond-breaking, 272
Bouguer–Lambert–Beer law, 20
Bubble formation, 206, 275, 719
Buffer Layers, 513
Butler–Volmer equation, 484

C
Cabrera–Mott theory, 583
Capillary waves, 623, 665
Carbonization, 259, 263, 609
Catalytic effects, 37
Cavitation, 719
Center temperature rise, 124, 127, 148
Charge transfer, 339
Chemical
  activation energy, 41
  relaxation, 18
  transformations, 544
Chemisorption, 458
Chemophoretic forces, 70
Circuit repair, 425
Cladding, 573
Clausius–Clapeyron relation, 65, 204
Cluster formation, 63, 71, 705, 713
Cold melting, 302
Colloids, 70
Columnar structures, 659, 670, 676
Confinement of excitations, 98, 279
Conical structures, 659, 670, 677
Convection
  chemical, 54
  forced, 114
  free, 114, 170
  Marangoni, 190
Coulomb explosion, 306
Coverage, 466
Crank transform, 21
Crystallization
  amorphous films, 537, 607
  explosive, 647
  fibres, 393, 578
Cutting, 231
CVD, 10, 369, 429, 446

D
Debris, 263, 278
Debye length, 585
Dember effect, 483
Dendrites, 79, 606
Deposition of microstructures
  adsorbed layers, 463
  bistabilities, 652
  direct writing, 90, 407, 617
  electrochemical, 477
  electroless, 477
  fibres, 393
  kinetics, 39, 397
  LCVD, 369
  LIFT, 528
  liquid-phase, 477
  modelling pyrolytic LCVD, 375
  morphology, 369, 395, 407
  periodic structures, 649
  photolytic (photochemical), 389
  photophysical, 422
  precursor molecules, 369
  process limitations, 392
  projection, 469
  pyrolytic (photothermal), 370
  rates, 43, 369, 393, 409, 683
  resolution, 98, 409, 470
  rods (fibres), 393
  single crystals, 395
  solid-phase, 573, 618
  spots, 370
  temperature distributions, 379, 411
  temperature measurements, 394, 689
  transport of species, 46, 399
Deposition of thin films
  adsorbed layers, 463
  cladding, 573
  electrochemical, 484
  electroless, 477
  epitaxial, 98, 505
  evaporation, 489
  heterostructures, 453, 508, 517, 521
  laser-CVD (LCVD), 429
  laser-MBE (LMBE), 471, 495
  liquid-phase, 477
  photosensitization, 28, 445
  PLD, 489
  rates, 683
Depth of focus, 92
Dermatology, 728
Design, 737
Diagnostic techniques, 681
  laser-beam profiles, 681
  processing rates, 683
  ultrafast optical, 685
Dielectric permittivity, 19
Diffusion
  electrons, 36
  equations, 46
  interstitial, 584
  length thermal, 21
  liquid-phase, 565

solid-phase, 562
surface, 458
thermal, 51
Diffusivity thermal, 19, *759*
Dimensionality of heat flow, 21
Dimensionless variables, 116
Diode lasers, 89, 196, 231, 540, *758*
Direct writing, 90
DLC, 451, 517, 543
Doping, 561
diffusion length, 563
liquid-phase, 565
local, 570
profiles, 538, 562
sheet, 565
solid-phase, 562
Drag model, 713
Drilling, 231
Droplets, 64, 291, 503, 665
Drude model, 223
Dry cleaning, 552
Dry etching
insulators, 332
metals, 327
semiconductors, 339
Dufour effect, 46
Dynamic viscosity, 191

E
Electrical
doped surfaces, 561
pn junctions, 568
sheet resistance, 567, 609, 695
Electrochemical (Nernst) potential, 481
Electrochemical plating, 484
Electromagnetic field enhancement, 37, 104
Electromotive force (EMF), 477
Electron–hole pairs, 36, 346
Embedded structures, 308, 544, 643
Energy
activation, 41
balance, 203
collisional transfer, 32
Engraving, 234
Enthalpy, 22, 41
melting, 178, 183, *775*
vaporization, 201, *775*
Epitaxial growth, 98, 505
Error function, *750*
Etching, 315, 339
atomic layers (ALE), 357
backside, 335
dark, 339
diffusive, 329
dry, 325, 339
electrochemical, 484
electroless, 362, 481
influence of crystal orientation, 348
influence of reaction chamber, 324
inorganic insulators, 332, 335
metals, 327, 335
photochemical, 343
precursor molecules, 317
rates, 316, 339, 683
resolution, 342, 364
semiconductors, 339
spontaneous, 328, 340
wet, 334, 357
EUV Lithography, 615
Evaporation, 201
Excitation
coherent, 14, 44
confinement, 98
mechanisms, 14
molecules, 25, 317, 389, 463
multiphoton, 14, 28, 43, 302
relaxation times, 15, 33
selective, 25, 32
sequential, 14, 28
surface, 14, 35
vibrational, 29, 37
Exponential integral, *750*
Extinction coefficient, 20

F
Feedback, 623, 634
Ferroelectric materials, 519
Fiber lasers, 89
Fibers
LCVD, 393
pedestal growth, 578
tensile strength, 397
Focus, 86
Fragmentation, 70
Franck–Condon principle, 26
Frank–Kamenetsky expansion, 41
Frenkel–Wilson Law, 183, 484

G
Gamma function, *751*
Gas-phase
heating, 429
nucleation, 63, 404, 713
reactions, 41, 45, 377, 408, 429, 497
recombination, 326, 437
transport, 45, 399

Gibbs free energy, 64
Glassy alloys, 576
Glazing, 541
Grashof number, 171
Gratings, 240, 359, 545
Green's function, 116

H
Hardening
  shock, 542
  transformation, 535
Heat
  flow dimensionality, 21
  transfer coefficient, 114
Heat equation, 19, 23, 111
  attenuation function, 112
  general solutions, 111
  point source, 21
  source term, 19, 112
Heaviside function, *751*
Hertz–Knudsen equation, 204
Heterogeneous reactions, 39
Heterostructures
  laser-CVD, 453
  pulsed-laser deposition, 508, 517, 521
High-temperature superconductors, 506
Hydrodynamic instabilities, 664
Hysteresis, 653

I
Implantation, 571
Infinite slabs
  interferences, 151
  temperature distributions, 147
Instabilities
  ablation, 655
  direct writing, 647
  evaporation, 655, 666
  hydrodynamic, 664
  Kelvin–Helmholtz, 192, 504, 664
  LCVD, 649
  oxidation, 646
  Rayleigh–Taylor, 192, 504, 666
  stress-related, 671
  thermochemical, 646
Interconnects, 425
Interference, 93, 151, 158, 359
Inverse Bremsstrahlung, 224
Ion implantation, 537
Ion probe measurements, 499, 688
Ionization, 222
Isotope separation, 34

J
Jacobian Theta function, *751*
Jet-Plating, 486
Junctions, 568

K
Kelvin–Helmholtz instabilities, 192, 504, 664
Kinetics
  gas–solid interfaces, 39, 397
  liquid–solid interfaces, 477
  mass transport limited, 40
Kirchhoff transform, 21, 349
Knudsen layer, 202
Kramers–Unsöld equation, 224

L
LAESI, 701
Landau–Teller relation, 34
Landau–Zener transition, 26
Langmuir equation, 463
Laplace formula, 65
Laser
  ablation, 237, 279
  absorption waves, 227
  ALE, 472
  alloying, 575
  annealing, 537
  cladding, 573
  cleaning, 549
  cutting, 231
  CVD of microstructures, 369
  CVD of thin films, 429
  drilling, 231
  enhanced plating, 480
  focused atomic deposition, 474
  implantation, 571
  induced etching, 316, 339
  induced forward transfer, 528
  induced oxidation, 581
  induced transformations, 535, 544
  induced vaporization, 201
  LIGA, 620
  machining, 231
  marking, 234, 545
  MBE, 471
  microdissection, 729
  OMBD, 473
  polishing, 542
  pulsed plasma chemistry, 590
  recrystallization, 537
  sintering, 573
  surface hardening, 535, 542

Laser beam
divergence, 86
dwell time, 4
focus length, 87
Gaussian, 85
homogenization, 681
intensity, 85
power, 85, 681
profile, 681
pulse shapes, 118, 544
Rayleigh length, 87
Lasers, 85
commercial types, 85, *757*
LCD, 540
LCVD
microstructures, 369, 393, 407
photolytic, 389
photophysical (hybrid), 422
pyrolytic, 369
thin films, 429
LIBS, 698, 737
LIF, 698
LIFT, 528
LIGA, 620
Light modulators, 93
Link cutting, 242
Liquid-phase
deposition, 477
expulsion, 196
transport, 565
Lithography, 92, 611, 615
LPPC, 590

M
MALDI, 677, 701
MAPLE, 527
Marangoni convection, 190
Marking, 234, 545
Mask repair, 425
Mass
density, *759*
spectroscopy, 699
Mass transport
gases, 399
liquids, 477
Matrix cleaning, 559
Mean free path of molecules, 174
Medical applications, 727
Melting, 177
cold, 302
depth, 178
energy balance, 180
enthalpy, 178, *775*
Frenkel–Wilson Law, 183
heterogeneous, 177, 298
homogeneous, 177, 185, 298
solidification, 183
Stefan problem, 181
surface, 184
temperature, *759*
time, 178
Microbalance, 686
Microlenses, 93, 104, 530, 616
Microscopy time resolved, 685
Microsurgery, 728
Mie theory, 105
Multilayer structures
absorptivity, 151, 157
LCVD, 453
PLD, 508, 517, 521
Multiphoton excitation, 14, 28, 43, 223, 254, 302

N
Nanoclusters, 63, 71, 705, 713
Nanocomposite materials, 522
Nanocrystalline films, 522
Nanolithography, 615
Nanopowders, 63, 70
Nanoprocessing, 90, 349
Nanotubes, 80
Nanowires, 80
Nernst potential, 481
Nitridation, 581, 591
Normalized quantities, 116
Nucleation, 63
droplets within a laser beam, 66
laser-CVD, 77
plasma plumes, 71, 705, 713
Numerical aperture, 92
Nusselt number, 172

O
Ophthalmology, 728
Optical
absorption coefficient, 20, *769*
absorption cross sections, 27, 43, *777*
absorptivity, 151
breakdown, 37, 221, 719
deflection, 684
emissivity, 689
near field, 104
penetration depth, 20, 112
reflectivity, 112, 136, 151, *769*
refractive index, 20, 156, 223

spectroscopy, 697
surface absorption, 113
transmittivity, 151
waveguides, 156, 546
Optical storage, 547
Organic materials, 239, 281, 524, 605, 727
Organic molecular-beam deposition (OMBD), 473
Ostwald ripening regime, 66
Overheating, 178, 183
Overpotential, 484
Oxidation, 581
mechanisms, 582
metals, 587
native oxide, 582
pulsed-laser plasma chemistry, 590
semiconductors, 592
spontaneous, 581
Oxide transformation, 597

P

Paintings, 736
Partial reaction orders, 41
Particulates, 501, 509, 713
Pearlite, 536
Pedestal growth, 578
Periodic structures, 623
Permittivity, 19, 151, 157, 223, 626, 634
Phase explosion, 206, 288, 300
Photochemical exchange, 608
Photochemical processes, 16
Photochemistry
alkyls, 389
carbonyls, 391
halides, 317
halogen compounds, 317
silanes, 444
Photodynamical therapy, 729
Photoeffect, 35
Photonic structures, 619
Photophysical processes, 17
Photopolymerization, 611
Photosensitization, 28, 445
Photothermal deflection, 684, 693
Physisorption, 458
Plasma
CVD, 10
formation, 221
optical properties, 223
oxidation, 581
plume, 498
plume analysis, 697, 702
plume expansion, 706
radiation, 705
waves (LSAW), 227
Plasmons, 14, 107
Plating
electrochemical, 484
electroless, 477
jet, 486
thermobattery, 481
PLD, 489
Point blast model, 710
Point source, 21
Poisson equation, 583
Polaritons, 14, 620
Polymerization, 611
Polymers
ablation, 239
PLD, 524
surface modifications, 605
Poynting vector, 19
Prandtl number, 171
Predissociation, 26
Processing
large-area, 96, 492
micro, 90
non-planar, 12, 426
optimization, 189
Projection patterning, 92
Prosthesis, 729
Pulsed-laser deposition (PLD), 489
buffer layers, 513
cross beam, 497
DLC, 517
energetic species, 500
experimental requirements, 490
film profiles, 504
heterostructures, 508, 517, 521
high-temperature superconductors, 506
insulators, 519
metals, 515
metastable compounds, 510
nanocomposites, 522
nanoparticle films, 522
organic materials, 524
particulates, 501, 509
plasma reactions, 498
semiconductors, 515
surface processes, 497
volume processes, 497
Pulsed-laser evaporation (PLE), 489
Pulsed-laser plasma chemistry (PLPC), 590
Pulse shapes, 118

Pyroelectric monitors, 689
Pyrometry, 395, 689

Q
QCM, 686
Quasi-continuum, 30

R
Radiation pressure, 217
Raman spectroscopy, 693, 697
Rapid prototyping, 575
Rapid thermal annealing (RTA), 539
Rayleigh
  criterion, 92
  length, 87
  number, 172
Rayleigh–Taylor instabilities, 192, 504, 666
Reaction
  adsorbed layers, 468
  chamber, 95, 324
  enthalpy, 22, 41
  equimolecular, 54
  heterogeneous, 39, 51
  homogeneous, 39, 59
  kinetics, 39
  order, 41
  photochemical, 17, 33, 43
  photothermal, 41
  rate, 41, 54
Recoil pressure, 216, 504
Recombination
  electron-hole pairs, 36
  species, 326, 437
Recrystallization, 537
Redox equations, 480
Reduction, 581, 598
Reflectivity, *769*
Refractive index, 20, 156, 223
Relaxation
  chemical, 18
  stresses, 671
  times, 15
Reoxidation, 581, 597
Resolution, 93
  confinement of excitations, 98
  deposition, 98, 409, 470
  etching, 342, 364
  sharpening, 135
Restoration, 735
Reststrahl oscillator, 134
Ripples, 624, 638, 676
Runaway thermal, 144

S
Saha equation, 222
Scanning knife-edge technique, 681
Scanning-probe microscopy (SXM), 94
Scribing, 234
Self-focusing, 156
Self-organization, 623
Semiconductor–liquid interfaces, 483
Shaping, 231
Sharpening, 135
Sheet resistance, 695
Shock waves, 708
Silicides, 576
Sintering, 573
Skin depth, 113
Smoluchowski equation, 54
SNOM techniques, 94, 349, 540
Solar cells, 242, 540
Solidification, 178
Soret effect, 402
Space charge layer, 340
Spallation, 288, 300
Spatial confinement, 98
Specific heat, 19, *759*
Speckles, 683
Spectroscopy
  mass, 699
  optical, 689, 697
Standard electrode potential, 481
Steam cleaning, 557
Stefan–Maxwell equations, 47
Stefan problem, 181
Step-like films, 512
Steric factor, 41
Sticking coefficient, 79, 468, 596
Stoichiometric coefficient, 41
Streak Photography, 698
Stress-related
  ablation, 273, 285
  instabilities, 671
Striations, 198
Strong explosion model, 710
Structural transformations, 535, 544
Structure formation, 623
  coherent, 623, 626
  columnar, 659, 670, 676
  degrees of freedom, 644
  direct writing, 647
  exothermal reactions, 648
  explosive crystallization, 647
  feedback, 634
  nap-type, 672
  non-coherent, 623, 626

order parameters, 625
ripples, 624, 638, 676
spatio-temporal oscillations, 644
stress related, 671
technological aspects, 676
wall-type, 672
zero isoclines, 645
Substrates
cleaning, 98
infinite slabs, 147
non-uniform, 155
pretreatment, 98
semi-infinite, 127
Superconductors, 506, 602
Superexcitation, 31
Superheating, 501, 504
Surface
cleaning, 98
deformations, 191, 298, 668, 685, 694
electric field, 340
electromagnetic waves, 626, 631
energy, 675
excitation, 35
melting, 177
polaritons, 14, 620
tension, 190
Surface modification
doping, 561
nitridation, 581, 591
oxidation, 581
polymers, 605
time resolved measurements, 685
Surgery, 728
Swelling, 607
Synthesis, 577

T
Taylor–Davies formula, 667
Teflon, 608
Temperature
boiling, *759*
jump, 114, 173
measurements, 394, 691
melting, 178, 186, *759*
Temperature distributions
ambient medium, 167, 430
analytical solutions, 116
characteristics, 123
deposits, 382, 411
infinite slabs, 147
melting, 178, 184
multilayer structures, 166
non-uniform materials, 155
parabolic approximation, 124
pulsed irradiation, 139
scanned cw laser, 137, 148
semi-infinite substrates, 127
solidification, 183, 186
thin films, 160
width, 124
TFT, 540
Thermal
activation energy, 41
conductivity, *759*
diffusion, 46
diffusivity, 19, *759*
Thermal processes, 15
Thermobattery, 481
Thermocapillary effect, 191
Thermophoretic forces, 70
Thin-film transistors (TFT), 540
Threshold fluence
ablation, 253
cleaning particulates, 550
Time of flight (TOF), 694, 700
Transformation hardening, 535
Transmission measurements, 684
Transmittivity, 151
Trimming, 242
Turbulence, 173

U
Undercooling, 178

V
Vaporization, 201
enthalpy, 201, *775*
Vapor plume, 201
Velocity
solidification, 183, 186
sound, 208
Vibrational excitation, 14, 29
Vicinal substrates, 512
Viscosity, 172, 191
Voxel, 619

W
Wagner law, 585
Waveguides, 156, 546
Welding
photochemical, 606
standard, 194
ultrashort-pulse, 196

Wet cleaning, 558
Wet etching
  backside, 335
  dielectrics, 335
  metals, 335
  semiconductors, 357
Wien approximation, 690
Wirestripping, 242

X
X-rays, 705